Proceedings of:

The Twenty-first Annual Meeting

The American Society for Precision Engineering

October 15-20, 2006
Monterey Marriott Hotel and Monterey Conference Center
Monterey, California

The American Society for Precision Engineering (ASPE) is a multidisciplinary professional and technical society concerned with research and development, design, manufacture and measurement of high accuracy components and systems. ASPE activities encompass relevant aspects of mechanical, electronic, optical and production engineering, physics, chemistry, and computer and materials science. Membership is open to anyone interested in any aspect of precision engineering.

Founded in 1986, ASPE provides a new focus for a diverse but important community. Other professional organizations have covered aspects of precision engineering, always as a sideline to their principal goals. ASPE is based on the core of generic concepts necessary to achieve precision in any application; independent of discipline, ASPE intends to be the focus for precision technology — and to represent all facets from research to application.

ASPE — The American Society for Precision Engineering
301 Glenwood Avenue, Suite 205, Raleigh, NC 27603
P.O. Box 10826, Raleigh, NC 27605
Telephone: (919) 839-8444 Fax (919) 839-8039
http://www.aspe.net

Preface

This book comprises the proceedings of the 2006 Annual Meeting. The contributions reflect the authors' opinions and are published as presented to ASPE, without change. Their inclusion in this publication does not necessarily constitute endorsement by the ASPE, or its editorial staff.

Individual readers of this book and nonprofit libraries acting for them are permitted to make fair use of the material contained in this book to be used in teaching or research; provided they copy said paper in total, as written by the author. Permission is granted to quote excerpts from the scientific or technical works in this book with proper acknowledgment of the source to include: The author's name, the book name, and the ASPE tag line. Reproduction of figures and tables is likewise permitted from the contents of this book, provided that the same acknowledgment of the same source and content is permitted.

Any other type reproduction, systematic copying or multiple reproduction of any material in this book is expressly prohibited except with the written permission of the ASPE editorial staff, addressed to the Society's headquarters.

ISBN 1-887706-41-0

2006

American Society for Precision Engineering
301 Glenwood Avenue, Suite 205
Raleigh, NC 27603

Printed in the United States of America

Welcome Note

Welcome to Monterey for the Twenty-first Annual Meeting of The American Society for Precision Engineering. The growth and success of the Society reflects the increasing importance of precision engineering in a wide variety of fields of endeavor, from manufacturing to microelectronics to basic science. The Society serves as a focus for precision engineers across all of these fields. The Annual Meeting has evolved into a premier international forum for the exchange of ideas and presentation of research results relating to precision engineering, metrology, controls, and system integration. Precision engineers and scientists from private industry, government laboratories, and universities meet to learn about the latest developments and to exchange ideas about the future directions of these technologies.

This year's meeting continues the tradition of offering two full days of tutorials presented by some of the foremost precision engineers and scientists in the world. The technical sessions and poster presentations offer the latest research results in the areas of ultraprecision machining, metrology, controls, precision grinding, micro-positioning, material processing, design, precision transducers, surface profilometry, machine tool metrology, and error compensation. The commercial exhibit will provide attendees with the opportunity to view and discuss the latest precision engineering equipment, products, and services that are commercially available.

The conference organizing committee is proud to present the program for the Twenty-first Annual Meeting of the ASPE. We welcome your participation and your feedback on how to make next year's meeting even better.

2006 Organizing & Technical Program Committee

Tony L. Schmitz, Chair
University of Florida

Vivek G. Badami, Zygo Corporation
Kenneth Blaedel, Precision Engineer
Edward D. Brehl, North Carolina State University
Keith Carlisle, Lawrence Livermore National Lab.
David A. Dornfeld, University of California at Berkeley
Thomas A. Dow, North Carolina State University
Kenneth P. Garrard, North Carolina State University
Anthony E. Gee, University College, London
David D. Gill, Sandia National Laboratories
Robin L. Hibbard, Lawrence Livermore National Lab.
Bradley H. Jared, 3M Precision Optics
Byron R. Knapp, Olympic Precision, Inc.
Don A. Lucca, Oklahoma State University
Stephen J. Ludwick, Aerotech, Inc.
Eric R. Marsh, The Pennsylvania State University
Michele H. Miller, Michigan Technological University
Richard C. Montesanti, Lawrence Livermore National Lab.
Stefan Rakuff, GE Global Research
Senajith B. Rekawa, Lawrence Berkeley National Lab.
Theodore T. Saito, Lawrence Livermore National Lab.
Richard M. Seugling, Lawrence Livermore National Lab.
Alex Sohn, North Carolina State University
Mark A. Stocker, Corning Incorporated
Pradeep K. Subrahmanyan, RAPT Industries, Inc.
E. Clayton Teague, Nat'l Nanotechnology Coordination Office
Hans-Jochen Trost, MicroFab Technologies, Inc.
R. Ryan Vallance, The George Washington University
Michael Wright, New Way Air Bearings
Allen Y. Yi, The Ohio State University

2006 Scholarship Recipient

Mr. Dariusz Golda, Massachusetts Institute of Technology
R.V. Jones Memorial Scholarship

2006 Annual Meeting
Contents

Preface . . . . . *ii*

Welcome Note . . . . . *iii*

Organizing Committee – 2006 Scholarship Recipient . . . . . *iv*

Table of Contents . . . . . *v*

Program . . . . . *vi*

Keynote Address . . . . . *vii*

Technical Exhibitors . . . . . *viii*

Sustaining Corporate Sponsors . . . . . *ix*

Corporate Sponsors . . . . . *x*

Lifetime Achievement Award *1*

Technical Paper Index *2-11*

Technical Papers *15-618*

Author Index *619-622*

Program

2006 ASPE Annual Meeting

Time	Sun., Oct. 15	Mon., Oct. 16	Tues., Oct. 17	Wed., Oct. 18	Thurs., Oct. 19	Fri., Oct. 20
8:00	Registration		Early Coffee and Registration			
9:00	Tutorials	Tutorials	Technical Session I	Technical Session III	Technical Session VI	Technical Tours
10:00			Break	Break	Break	
11:00			Technical Session II	Technical Session IV	Technical Session VII	
12:00			Lunch and Committee Meetings	Awards Lunch and Business Meeting	Lunch and Roundtable Discussions	
1:00						
2:00	Tutorials	Tutorials	Commercial Session	Poster Session	Technical Session VIII	
3:00			Break	Break		
4:00			Poster Session	Technical Session V		
5:00		Welcome Reception	Hospitality Hour	Hospitality Hour		
6:00				Open Forum		
7:00		Keynote Address	Dinner Banquet at Monterey Bay Aquarium	Open Evening		
8:00						
9:00						

☐ *Exhibit Open Hours*

Keynote Address

John (Jan) L. Hall, Ph.D.

2005 Nobel Laureate

- JILA Adjoint Fellow, University of Colorado – Boulder

- Senior Fellow Emeritus, National Institute of Standards and Technology (NIST)

Monday, October 16, 6:30 p.m.

Session Chair: Tony L. Schmitz, University of Florida

John H. Hall

John L. Hall is Senior Fellow Emeritus of the National Institute of Standards and Technology (NIST) and an Adjoint Fellow of JILA (formerly the Joint Institute for Laboratory Astrophysics), a joint institute of NIST and the University of Colorado-Boulder. Known as a preeminent laser experimentalist, Dr. Hall has contributed significantly to the development of the laser from a laboratory curiosity to one of the fundamental tools of modern science. He is known also for his training and mentoring of new generations of inspired physicists, several now being star researchers themselves.

Hall's work has concentrated on improving the precision and accuracy with which lasers can produce a specific frequency, and the stability with which they can hold that frequency. He has helped to develop a broad range of laser applications, including precision spectroscopy for physical and chemical analysis, new tests of fundamental physical "laws", measurement and redefinition of the speed of light, and other time and length metrology advances, such as the Optical Frequency Comb.

Climaxing more than 20 awards from his employer and major professional societies, Dr. Hall was awarded the 2005 Nobel Prize in Physics, sharing this honor with Theodor W. Hansch of the Max-Planck-Institute and Roy J. Glauber of Harvard University. The Nobel was awarded for their contributions to the development of laser-based precision spectroscopy, including the optical frequency comb technique. The optical frequency comb can measure the frequency of another laser with extraordinarily high precision.

The Optical Frequency Comb – a tool of many uses

The Optical Frequency Comb concept and technology was developed first as a method for optical frequency measurement, but also enables enhanced time-domain control, with broad applications in spectroscopy, metrology, and extension of nonlinear optics to the UV range and beyond. It should be a major help in frequency-based length metrology, whereby the incredible resolution is accessible ALONG WITH intrinsic resolution of the integer fringe question.

Cooperating Sponsors

Elsevier Science, Inc.

Technical Exhibitors

Accura Technics, L.L.C.

Aerotech, Inc.

ALIO Industries, Inc.

Ambios Technology, Inc.

ARC Technologies

Bal-tec

Center for Precision Metrology—
University of N.C. at Charlotte

Chardon Tool

CMPC Surface Finishes Co., Inc.

Contour Fine Tooling, Inc.

CoorsTek, Inc.

Corning Tropel Corporation

Fabreeka International, Inc.

FRT of America, LLC

Heidenhain Corporation

InsituTec, Inc.

K&Y Diamond Ltd.

Lion Precision

Machine Dynamics Research Lab. —
Penn State University

Moore Nanotechnology Systems, LLC

New Way Air Bearings, Inc.

North American EN, Inc.

Optical Perspectives Group, LLC

Philips Applied Technologies

PI (Physik Instrumente) LP

Precision Engineering Center—
N.C. State University

Precision MicroDynamics, Inc.

Precision Systems Lab.—
The George Washington University

Precitech, Inc.

Professional Instruments Company, Inc.

Queensgate Instruments, Ltd.

Renishaw, Inc.

TAC – Tour Andover Controls

The Precision Alliance

Third Wave Systems, Inc.

Commercial Session

Tuesday, October 17, 1:30 - 3:00 p.m.

Session Co-Chairs: Stephen J. Ludwick (Aerotech, Inc.)
and Byron R. Knapp (Olympic Precision, Inc.)

The Commercial Session will take place early in the week on Tuesday afternoon. This is a special session where companies and participants are free to open discussions on a less-formal basis and to promote interaction on a variety of topics. In the first part of this session, company representatives are invited to make brief presentations (five minutes) on new products associated with precision engineering. This provides participants with the opportunity to receive timely information on new technologies that have been commercialized into products and services, as well as information on advances that can be expected in the near future.

ASPE 2006 Sustaining Corporate Sponsors

3M Company
St. Paul, MN 55144
Phone: (651) 737-3790
www.mmm.com

ADCOLE Corporation
669 Forest Street
Marlborough, MA 01752
Phone: (508) 485-9100
Fax: (508) 481-6142
www.adcole.com

Aerotech, Inc.
101 Zeta Drive
Pittsburgh, PA 15238-2897
Phone: (412) 963-7470
Fax: (412) 963-7459
www.aerotech.com

Corning Tropel Corporation
60 O'Connor Road
Fairport, NY 14450
Phone: (585) 388-3500
Toll-free: (888) 4-TROPEL
www.tropel.com

Fabreeka International, Inc.
P.O. Box 210
1023 Turnpike Street
Stoughton, MA 02072
Phone: (781) 341-3655
Toll-free: (800)-322-7352
www.fabreeka.com

Lion Precision
563 Shoreview Park Road
St. Paul, MN 55126-7014
(651) 484-6544
(651) 484-6824
www.lionprecision.com

Mitutoyo America Corporation*
945 Corporate Boulevard
Aurora, IL 60504-9102
Phone: (630) 723-3619
Fax: (630) 978-6471
www.mitutoyo.com

Moore Tool Company, Inc.
800 Union Avenue
Bridgeport, CT 06607-0088
Phone: (203) 366-3224
Fax: (203) 366-5694
www.mooretool.com

New Way Precision, Inc.
4009-I Market Street
Aston, PA 19014
Phone: (610) 494-6700
Fax: (610) 494-0911
Toll-Free: (800) 394-1046
www.newwaybearings.com

Philips Applied Technologies
1140 Ringwood Court
MS16
San Jose, CA 95131-1706
Phone: (408) 991-2261
www.apptech.philips.com

Precitech, Inc.
44 Blackbrook Road
Keene, NH 03431
Tel: (603) 357-2511
Fax: (603) 358-6174
www.precitech.com

Professional Instruments Company
7800 Powell Road
Hopkins, MN 55343
Phone: (952) 933-1222
Fax: (952) 933-3315
www.airbearings.com

Queensgate Instruments, Ltd.
Woodland Road
Torquay Devon TQ2 7AY
United Kingdom
Phone: 44-1803-407710
Fax: 44-1803-4076
www.nanopositioning.com

Zygo Corporation

Zygo Corporation
Laurel Brook Road
Middlefield, CT 06455-0448
Phone: (860) 347-8506
Fax: (860) 347-8372
Toll-free: (800) ZYGO-NOW
www.zygo.com

ASPE 2006 Corporate Sponsors

Center for Precision Metrology – University of North Carolina at Charlotte
Charlotte, NC 28223-0001
Contact: Gregory W. Caskey
(704) 687-4863

Chardon Tool
Chardon, OH 44024
Contact: Michael Hunter
(440) 286-6440

Contour Fine Tooling, Inc.
Marlborough, NH 03455
Contact: Jeffrey Tomlin
(603) 876-4908

Corning Inc.
Corning, NY 14831
Contact: John Thomas
(607) 974-3842

Cranfield Precision, Div. of Landis Lund
Division of Cinetic Landis Grinding, Ltd.
Cranfield, Bedford MK43 OJR, England
Contact: Edric M. E. Brown
+44-1234-754222

euspen
Cranfield University
Bedford, MK43 OAL, United Kingdom
+44-1234-754024

Nano Corporation
Tokyo 144-0042, Japan
Contact: Akira Hayashi
+81-3-5735-6631

Reflexite Precision Technology Ctr.
200 Park Centre Drive
West Henrietta, NY 14586
Contact: Mr. Steven M. Scott
(585) 272-0290

Seagate Technology
Scotts Valley, CA 95066
Contact: Robert M. Pelstring
(831) 439-3697

Taylor Hobson, Ltd.
Leicester LE4 9JQ, UK
Contact: Daniel I. Mansfield
+44-116-2763771, Ext. 2126

Veeco Instruments, Inc.
Tucson, AZ 85706-7123
Contact: Geoffrey Anderson
(520) 741-1044

2006 ASPE Lifetime Achievement Award

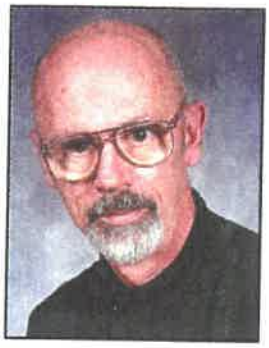

David H. Youden

David Youden was born on August 19, 1939 in Westerly, Rhode Island. He spent his early years disassembling a great many clocks and radios. He majored in electrical engineering at Worcester Polytechnic Institute from 1957 through 1959 and received a degree in mechanical engineering from Central New England College in 1967. After graduation he began work on an MBA at Clark University but the demands of a growing family ended those aspirations in 1970.

Dave's professional career began in 1959 when he accepted employment with the Heald Machine Company, a subsidiary of The Cincinnati Milling Machine Company. He started work as a draftsman, but quickly advanced to the position of R&D engineer where he worked under the tutelage of Doctor Robert Hahn, who introduced him to the study of hydrostatic bearings.

From 1969 through 1972, while working at Heald, Dave taught Instrumentation and Solid State Electronics at Quinsigamond Community College in Worcester, Massachusetts.

In 1972, during a downturn in the machine tool industry, Dave went to work for Ocean Systems, Inc. of Reston, Virginia. Ocean Systems was a start-up company in the off-shore oil industry. While there he designed and helped install large traction winches capable of one million pounds of force. These winches were used to moor tankers to buoys in the North Sea.

In 1973 the machine tool industry reclaimed Dave when he accepted employment at the Cone Blanchard Machine Company in Windsor, Vermont. Beginning as a Research Engineer, Dave advanced through a number of positions in engineering management, eventually becoming Director of Engineering. In the early '80s Dave met Frank Cooke, who described methods of using Blanchard grinders to produce spherical optics. It was at this point that Dave became a precision engineer.

When Cone Blanchard failed in 1984 Dave went to work for Don Brehm at Pnemo Precision in Keene, NH. Shortly after joining Pneumo, he met Jim Bryan and formed a lasting friendship. Between 1984 and 1994 Dave was responsible for the design of a number of notable diamond turning and flycutting machines including the ASG 2500, The Planoform 1000, and the Nanoform 600. During that period Pneumo Precision became Rank Pneumo, and then Taylor Hobson Pneumo. In 1994 Dave relocated to Raleigh, NC where he assumed the title of Director of Advanced Technology for Pneumo, and simultaneously became an Adjunct Professor in the Mechanical and Aerospace Engineering Department at NCSU.

In 1997 Dave changed jobs again, becoming an Applied Research Engineer with the Eastman Kodak Company. Continuing to operate from an office at NCSU, Dave developed a number of precision machines, including a small coordinate measuring machine that is currently at UNC Charlotte. In 2005 Dave retired from Kodak to turn his attention to more personal matters including an interest in seismology.

This respite from the commercial world did not last for long, as there was pressure on Dave to resume his career. In response, he accepted a position as Senior Engineer with Olympic Precision, Inc. of Windsor, VT. Dave, at this time, continues to design ultra-precise machine tools and metrology equipment. He also plans to pass on some of his knowledge by mentoring young engineers and teaching a series of short courses in precision engineering.

Technical and Poster Sessions Index

The technical program of the 2006 ASPE Annual Meeting contains 155 papers on precision engineering advances. Papers that lent themselves to significant verbal interaction, concise but important discoveries, or strongly visual or tactile subjects have been selected for the poster presentation. Authors will be in attendance to discuss their work on Tuesday, October 17, from 3:30 to 5:00 p.m., and again on Wednesday, October 18, from 1:30 to 3:00 p.m.

Session I
Optics & Interferometry

Tuesday, October 17, 2006, 8:30 AM - 10:00 AM

Session Chair: Senajith B. Rekawa (Lawrence Berkeley National Laboratory) and Allen Y. Yi (The Ohio State University)

1. ***Precision Interferometric Metrology (Invited Paper)** **
   Evans, C. J. (Zygo Corporation)
2. ***Phase-shifting Diffraction Interferometer for Inspecting NIF Ignition-target Shells***
   Montesanti, R. C.; Johnson, M. A.; Mapoles, E. R.; Atkinson, D. P.; Hughes, J. D.; Reynolds, J. L. (Lawrence Livermore National Laboratory) ..... page 15
3. ***A 1 m Swing-arm Profilometer for Large Telescope Mirror Elements***
   King, C. W.; Callender, M.; Efstathiou, A.; Gee, A. E. (University College, London); Walker, D. (University College, London / Zeeko Ltd.); and Lewis, A. J.; Oldfield, S.; Steel, R. (UK National Physical Laboratory) ..... page 19
4. ***Thin Film Extraction from Scanning White Light Interferometry***
   Mansfield, D. I. (Taylor Hobson, Ltd.) ..... page 23

Session II
Fabrication

Tuesday, October 17, 2006, 10:30 AM - 12:00 PM

Session Chair: Michele H. Miller (Michigan Technological University) and Bradley H. Jared (3M Precision Optics)

1. ***Reactive Atom Plasma (RAP™) Processing of Optical Surfaces***
   Subrahmanyan, P. K.; Gardopee, G.; Fiske, P. S.; Chang, A. (RAPT Industries, Inc.) ..... page 27
2. ***Two-dimensional Encoder with Picometer Resolution Using Multi-tunneling Probes Scanning Tunneling Microscope and Regular Crystalline Surface***
   Aketagawa, M.; Honda, H.; Ishige, M.; Patamaporn, C. (Nagaoka University of Technology) ..... page 31
3. ***Manufacturing the Dragonfly Eye Multi-layer, Compound Optic Array***
   Gill, D. D.; Sweatt, W. C.; Claudet, A. A.; Adams, D. P.; Vasile, M. J.; Hodges, V. C. (Sandia National Laboratories) ..... page 35
4. ***Load Force Compensation for Direct Drives in Machine Tools***
   Zirn, O.; Hoos, A. (FH Giessen-Friedberg); and Hiller, B. (Hübner AG) ..... page 39

*Abstract unavailable at press time

Session III

Thermal Considerations

Wednesday, October 18, 2006, 8:30 AM - 10:00 AM

Session Chair: Hans-Jochen Trost (MicroFab Technologies, Inc.) and Don L. Martin (Lion Precision)

1. ***In-situ Calibration of Temperature Compensation Systems Using Differential Length Measurements***
   Salsbury, J. G.; Inloes, M. (Mitutoyo America Corporation) ..... *page 43*
2. ***High-stability Temperature Control System for LISA***
   Higuchi, S.; DeBra, D. B. (Stanford University) ..... *page 47*
3. ***Sub-millidegree-stability Air Thermal Control for a Large-volume Lithography Enclosure***
   Zhao, Y.; Trumper, D. L.; Heilmann, R. K.; Schattenburg, M. L. (Massachusetts Institute of Technology) ..... *page 51*
4. ***The Design, Calibration and Use of an Ultrasonic Thickness Probe on a CMM***
   Orchard, N.; Whiteside, D. (Rolls-Royce Plc) ..... *page 55*

Session IV

Metrology I

Wednesday, October 18, 2006, 10:30 AM - 12:00 PM

Session Chair: Thomas A. Dow (North Carolina State University) and Keith Carlisle (Lawrence Livermore National Laboratory)

1. ***An Overview of the Latest Metrology Advances at NPL (Invited Paper)****
   Leach, R. (National Physical Laboratory)
2. ***Moment of Inertia Measurement Using a Five-wire Torsion Pendulum and Optical Sensing***
   Swank, A. J.; Sun, K.-X.; DeBra, D. B. (Stanford University); and Hardham, C. T. (Squid Labs, LLC) ..... *page 59*
3. ***Self-calibration for Air-bearing Rotary Encoders***
   Lu, X. (The University of British Columbia); and Trumper, D. L. (Massachusetts Institute of Technology). ..... *page 63*
4. ***Rapid High Resolution Absolute 2-D Encoding by Low Resolution Digital Imaging of a Mathematically Generated 3-tone Target***
   Chu, D. C.; Trujillo, H.; Whitney, E.; Young, J. (Agilent Technologies, Inc.) ..... *page 67*

Session V

Metrology II

Wednesday, October 18, 2006, 3:30 PM - 5:00 PM

Session Chair: Byron R. Knapp (Olympic Precision, Inc.) and Richard C. Montesanti (Lawrence Livermore National Laboratory)

1. ***Utraprecision Microscale Hole Scanning Metrology***
   Bauza, M. B.; Woody, S. C. (InsituTec, Inc.); and Smith, S. T.; Hocken, R. J. (University of North Carolina at Charlotte) ..... *page 71*
2. ***Ring Gauge for Evaluation of CMM Dynamics***
   Garrard, K. P.; Dow, T. A. (North Carolina State University); and Folkert, K. F. (Consolidated Diesel Company) ..... *page 75*
3. ***Speckle Correlation Method for 3D-deflection Measurement of the Tactile-optical Microprobe***
   Wissmann, M.; Schwenke, H. l.; Neuschaefer-Rube, U. (Physikalisch-Technische Bundesanstalt (PTB)) ..... *page 79*
4. ***Enhanced Capabilities of the NIST Fiber Probe for Micro Feature Metrology***
   Muralikrishnan, B. (University of North Carolina at Charlotte); and Stone Jr., J. A.; Stoup, J. R. (National Institute of Standards and Technology). ..... *page 83*

*Abstract unavailable at press time

Session VI

Machining

Thursday, October 19, 2006, 8:30 AM - 10:00 AM

Session Chair: Vivek G. Badami (Zygo Corporation) and Stefan Rakuff (GE Global Research)

1. ***Tunable, Ultrasonic, Vibration Assisted Diamond Turning***
   Overcash, J. L.; Cuttino, J. F. (University of North Carolina at Charlotte) . . . . . *page 87*
2. ***Modeling of Vibration in Single-point Diamond Turning***
   Sohn, A.; Lamonds, L.; Garrard, K. P. (North Carolina State University) . . . . . *page 91*
3. ***Optimizing Machining Processes for Precision: An Example Using Calculated Cutting Forces***
   Rhorer, R. L. (National Institute of Standards and Technology) . . . . . *page 95*
4. ***A Comparative Study of Part Error Contributors in High-speed Machining***
   Canning, J. S.; Zapata, R. E.; Ziegert, J. C.; Schmitz, T. L. (University of Florida) . . . . . *page 99*

Session VII

Nanotechnology

Thursday, October 19, 2006, 10:30 AM - 12:00 PM

Session Chair: Alex Sohn (North Carolina State University) and Anthony E. Gee (University College, London)

1. ***Characterization of Nano-structured Materials Using FIB and STEM Techniques (Invited Paper)****
   Jarausch, K. (Hitachi High Technologies America)
2. ***A Mechanism for Creating Variable Nanometer Gaps***
   Ma, H.; Slocum, A. H. (Massachusetts Institute of Technology) . . . . . *page 103*
3. ***Optical Near-field Directed Patterning of Submicron-sized Particles***
   Morii, H.; Ooi, T.; Tsuchiya, K.; Hamaguchi, T.; Nakao, M. (The University of Tokyo) . . . . . *page 107*
4. ***Development of a Nano-stereolithography System Using Evanescent Light for Submicron Fabrication***
   Kajihara, Y.; Takeuchi, T.; Takahashi, S.; Takamasu, K. (The University of Tokyo) . . . . . *page 111*

Session VIII

Design

Thursday, October 19, 2006, 1:30 PM - 3:00 PM

Session Chair: Pradeep K. Subrahmanyan (RAPT Industries, Inc.) and Mark A. Stocker (Corning Incorporated)

1. ***Design and Modeling of a Precision 6 DOF MEMS-based Parallel Kinematic TEM Sample Manipulator***
   Brouwer, D. M.; de Jong, B. R.; Soemers, H. M. J. R. (University of Twente) . . . . . *page 115*
2. ***Moving-magnet Planar Actuator with Integrated Active Magnetic Bearing***
   Jansen, J. W.; van Lierop, C. M. M.; Lomonova, E. A.; Vandenput, A. J. A. (Eindhoven University of Technology) . . . . . *page 119*
3. ***Design of a Robot-based Detector Manipulator for a Hard X-ray Nanoprobe Instrument System***
   Shu, D.; Maser, J.; Holt, M.; Preissner, C.; Lai, B.; Vogt, S.; Winarski, R.; Stephenson, G. B. (Argonne National Laboratory) . . . . . *page 123*
4. ***Seven-axis Tester with Servo-controlled Fly-height for Magnetic Recording Metrology***
   Crawford, T. M.; van de Veerdonk, R. J. M.; Bedillion, M. D.; Koelmans, W.; Langzettel, A. K. (Seagate Research); O'Connor, B. P.; Novotnak, R. (Aerotech, Inc.); and Lane, B. (Key Technologies, Inc.) . . . . . *page 127*

*Abstract unavailable at press time

Poster Sessions

Tuesday, October 17, 2006, 3:30 PM - 5:00 PM

Wednesday, October 18, 2006, 1:30 PM - 3:00 PM

Session Chair: Session I: David E. Brehl (North Carolina State University) and David D. Gill (Sandia National Laboratories) — Session II: Robin L. Hibbard (Lawrence Livermore National Laboratory), and Eric R. Marsh (The Pennsylvania State University)

EQUIPMENT, MACHINES & INSTRUMENTS

Analysis & Modeling

1. ***Frequency Response Prediction for Rotating Tool-holder-spindle Assemblies***
   Cheng, C.; Duncan, G. S.; Schmitz, T. L. (University of Florida) ..... *page 131*
2. ***Flexure-based Meso-level Stages Driven by Linear Piezo Motors***
   Heamawatanachai, S.; Corbin, B.; Emig, L.; Bamberg, E. (University of Utah) ..... *page 135*
3. ***A Quantitative, Constraint-based Design Method for Multi-axis Flexure Stages for Precision Positioning Equipment***
   Hopkins, J.; Culpepper, M. L. (Massachusetts Institute of Technology) ..... *page 139*
4. ***Analysis of Temperature Distribution and Optimization of the Configuration at Heating Tool in the Chip Bonding Process at Camera Module of Mobile Phone***
   Kim, I.; Kweon, S.-H.; Yang, S.-H. (Kyungpook National University) ..... *page 143*
5. ***Synthesis of the Intelligent Sensing System Using Current Signals for Manufacturing Systems***
   Kim, S.-C.; Chung, S.-C. (Hanyang University); Chung, S. (The University of Western Ontario); and Kim, K.-D. (Small Business Corporation) ..... *page 147*
6. ***Improved Analytical Chip Thickness Model***
   Kumanchik, L.; Schmitz, T. L. (University of Florida) ..... *page 151*
7. ***Dynamic Characterization of a Head Unit with a Small High Speed Spindle in Meso-scale Machine Tools***
   Lee, J.-H.; Yang, S.-H. (Kyungpook National University) ..... *page 155*
8. ***Calibration of a Parallel Manipulator with Restricted Degrees of Freedom by Means of a Redundancy Matrix***
   Meyer, P. J.; van Eijk, J. (Philips Applied Technologies) ..... *page 159*
9. ***Tool-holder Connection Modeling for Frequency Response Prediction in Milling***
   Powell, K. B.; Won, D.; Schmitz, T. L.; Duncan, G. S.; Sawyer, W. G.; Ziegert, J. C. (University of Florida) ..... *page 163*
10. ***A General Geometric Model for Determining Optimal Shapes of Planar Elastic Pivots***
    Vallance, R. R.; Haghighian, B. (The George Washington University); and Marsh, E. R. (The Pennsylvania State University) ..... *page 167*
11. ***Fractal Roundness Modeling of Experimental Profile in Turning***
    Yoon, M. C.; Chin, D. H. (Pukyong National University); and Jung, J. S. (Workers Accident Medical Corporation/Korea Orthopaedics & Rehabilitation Engineering Center) ..... *page 171*

Controls

1. ***Control of a 2 DOF Long-range and 6 DOF Short-range Stages for Nanometer Positioning***
   Buice, E. S.; Yang, H.; Smith, S. T.; Hocken, R. J. (University of North Carolina at Charlotte); Otten, D.; Trumper, D. L. (Massachusetts Institute of Technology); and Seugling, R. M. (Lawrence Livermore National Laboratory) ..... *page 175*
2. ***Active Control of Pneumatic Isolation Table by Model Following Control Using Pressure Differentiator***
   Kato, T. (Tokyo Metropolitan College of Industrial Technology); and Kawashima, K.; Kagawa, T. (Tokyo Institute of Technology) ..... *page 179*
3. ***A New Mode Switching Control for Fast Settling and High Precision Positioning***
   Kim, J.-J.; Choi, Y.-M.; Kim, K.-H.; Gweon, D.-G. (Korea Advanced Institute of Science & Technology) ..... *page 183*
4. ***Precise Position Control of a Pneumatic Servo Table System Consideration Dynamic Characteristics of Pneumatic Servo Valves***
   Miyajima, T.; Ogiso, T.; Kawashima, K.; Kagawa, T. (Tokyo Institute of Technology); and Fujita, T. (Tokyo Denki University) ..... *page 187*

5. ***Design and Control for the Pneumatic Cylinder Precision Positioning Under Vertical Loading***
Tsai, M.-H.; Cheng, C.-N.; Shih, M. C. (National Cheng Kung University) ..... *page 191*

Design & Testing

1. ***Design and Evaluation of a Prototype Instrument for Measuring Roundness Profiles of Micro Shafts***
Barraja, M.; Vallance, R. R.; Loychik, N. (The George Washington University); Marsh, E. R. (The Pennsylvania State University); and Arneson, D. A. (Professional Instruments Company, Inc.) ..... *page 195*
2. ***Microdrive and Telemetry System for Multi-Unit Extracellular Studies***
Caballero-Ruiz, A.; Ruiz-Huerta, L.; Kussul, E. (Universidad Autónoma de México); and Heredia, F. (Universidad Autónoma de Yucatán)..... *page 199*
3. ***Development of Ultra Precision Machine with High Positioning Resolution***
Fukuta, M.; Nishioka, M. (Toshiba Machine Co., Ltd.); and Suzuki, H. (Kobe University) ..... *page 203*
4. ***Development of a Hydrostatic Journal Bearing with Slit-step Compensation***
Hale, L. C. (Innovative Machine Solutions); Castro, C.; Chung, C.; Hopkins, D. J. (Lawrence Livermore National Labs.); and Donaldson, R. R. (P.E. Consultant)..... *page 207*
5. ***Development of Active Mounts for Improved Accuracy of Large Machine Tools***
Horiuchi, O.; Kato, T.; Yamaguchi, Y.; Shibata, T.; (Toyohashi University of Technology) ..... *page 211*
6. ***Development of Mechanisms and Frame Structures for a Laboratory-scale Compact Soft X-ray Microscopy***
Kang, S.-H.; Kang, D.-W.; Gweon, D.-G. (Korea Advanced Institute of Science & Technology (KAIST)); Min, J. Y. (Wonkwang University); and Yoon, K. H. (LISTEM, Co., Ltd.)..... *page 215*
7. ***Development of a Tool Alignment System in Shearing Process***
Kibe, Y.; Mitsui, K. (Keio University) ..... *page 219*
8. ***Precision Measurement of Small Diameter Hole in a Metallic Object***
Lee, K. S.; Chow, K. H.; Chan, C. K.; Chan, L. S.; Chau, W. C.; Chow, W. Y. (The Hong Kong University of Science and Technology)..... *page 223*
9. ***High Precision Modular Long Range Travel Vertical Axis***
Lotz, M.; Hackel, T.; Frank, T.; Tröbs, A.; Höhne, G.; Theska, R.; Zimmermann, K. (Technical University of Ilmenau)..... *page 227*
10. ***Development of a Design Tool Supporting Conceptual Design of Machine Tools***
Mishima, N. (Advanced Manufacturing Research Institution (AIST))..... *page 231*
11. ***Design of Air Drive Spindle***
Nakao, Y.; Mizoi, T.; Minowa, Y. (Kanagawa University) ..... *page 235*
12. ***Development of a Precision, Low-cost, Small Footprint Wire Electron Discharge Machine (WEDM)***
Orino, C.; Rakwal, D. R.; Bamberg, E. (University of Utah); and Jorgensen, J. D. (Optimation, Inc.) ..... *page 239*
13. ***Axiomatic Design Method Applied to a Parallelogram Micromachine for Low Cost Micromechanics***
Ruiz-Huerta, L.; Caballero-Ruiz, A. (Universidad Nacional Autónoma de México) ..... *page 243*

Mechatronics

1. ***Non-contact Bio Cell Manipulation by Nonlinear Micro Flow Around the Vibrated Pipette on Micro Robot***
Aoyama, H.; Chiba, N.; Fuchiwaki, O. (University of Electro-Communications); Misaki, D. (Shizuoka Institute of Science & Technology); and Usuda, T. (National Institute of Advanced Industrial Science and Technology) ..... *page 247*
2. ***New Hybrid Actuator Design with Nanometer Resolution***
Gloess, R. (Physik Instrumente (PI) GmbH & Co. KG) ..... *page 251*
3. ***Optimal Tuning of a Biaxial Servomechanism Using a Cross-coupled Controller and Disturbance Observers***
Jang, M.-S.; Kim, S.-C.; Chung, S.-C. (Hanyang University) ..... *page 255*
4. ***Fabrication of a New Position Surveying System for the Underground Pipes Using Rotary Encoders***
Hamano, T.; Kato, S. (Nippon Institute of Technology); and Ono, M. (Tokyo Metropolitan College of Technology)..... *page 259*
5. ***An In-pipe Mobile Inspection Robot Provided an Artificial Intelligence and Passable at Several T-junctions***
Kato, S.; Suzuki, T. (Nippon Institute of Technology); and Ono, M. (Tokyo Metropolitan College of Technology)..... *page 263*

6. ***Fabrication of a Snake Type In-pipe Mobile Robot Corresponding to the Different Diameters***
Ono, M.; Tanaka, M.; Ito, S.; Ikeda, S. (Tokyo Metropolitan College of Technology); and Kato, S. (Nippon Institute of Technology) . . . . page 267

7. ***Implementation of a Real-time Hysteresis Compensation for Electromagnetic Actuators***
Volkert, R.; Radler, O.; Ströhla, T. (Technical University of Ilmenau); and Zöppig, V. (STZ Mechatronik) . . . . page 271

MEMS, LIGA & Nanotechnology

1. ***Rotational Precision MEMS-based Clamping Mechanism for Stable Fixation of Elastic Mechanisms***
Brouwer, D. M.; de Jong, B. R.; de Boer, M. J.; Soemers, H. M. J. R. (University of Twente) . . . . page 275
2. ***Design of a High-speed Micro-scale Fast Scanning Stage for Two-photon Endomicroscopy***
Chen, S.-C.; Choi, H.; Kim, D.; Munro, L.; Culpepper, M. L.; So, P. (Massachusetts Institute of Technology) . . . . page 279
3. ***Formation of Micro-scale Precision Flexures Via Molding of Metallic Glass***
Chen, S.-C.; Culpepper, M. L. (Massachusetts Institute of Technology); and Bardt, J.; Ziegert, J. C. (University of Florida) . . . . page 283
4. ***Application of Input Shaping® and Hyperbit™ Control to Improve the Dynamic Performance of a Six-axis MEMS Nanopositioner***
Chen, S.-C.; Culpepper, M. L. (Massachusetts Institute of Technology); and Jordan, S. (PI (Physik Instrumente) LP) . . . . page 287
5. ***Active Mask UV Lithography System for MEMS and μ-TAS Applications***
Hayashi, T. (Osaka University); Shibata, T.; Kawashima, T. (Toyohashi University of Technology); Makino, E.; Mineta, T. (Hirosaki University); and Masuzawa, T. (Ibaraki University) . . . . page 291
6. ***Nanometer-scale Deposition of Photo-curing Resin Using a Scanning Nanopipette Probe Microscope***
Iwata, F.; Ushiro, Y.; Sasaki, A. (Shizuoka University) . . . . page 295
7. ***Recent Advances in Improving Static and Dynamic Accuracy of Nanopositioning Systems***
Jordan, S. (PI (Physik Instrumente) LP) . . . . page 297
8. ***A Novel Microfabrication Technique for Three-dimensional Metal Structures by Photocatalysis***
Okuno, M.; Takahashi, S.; Takamasu, K. (The University of Tokyo); and Aso, T. (Nomura Research Institute, Ltd.) . . . . page 301
9. ***Kinematic Assembly of Soft-polymer Biofluidic Circuits***
Trinkle, C. A.; Lee, L. P. (University of California at Berkeley); and Morgan, C. J. (University of Kentucky) . . . . page 305

Novel Systems

1. ***Design of a Miniature Dual-purpose Positioner-fixture for Six-axis Scanning and Detachable Fixturing in Nano-instrumentation***
Culpepper, M. L. ; Varadarajan, K.; (Massachusetts Institute of Technology) . . . . page 309
2. ***A Scalable Six-axis Electromagnetically-driven Nanopositioner for Nanomanufacturing***
Golda, D.; Culpepper, M. L. (Massachusetts Institute of Technology) . . . . page 313
3. ***Near-field Polarimetry Using Scanning Probe Microscope with Sub-wavelength Aperture Cantilever***
Tsuchiya, K.; Muragishi, T.; Ooi, T.; Morii, H.; Hamaguchi, T.; Nakao, M. (The University of Tokyo) . . . . page 317

METROLOGY

Analysis & Modeling

1. ***A Study of Pattern and Feature Analysis of Surface Generation in Fast Tool Servo Machining of Optical Microstructures***
Cheung, C.-F.; To, S. S.; Lee, W.-B.; Kwok, T. C.; Li, H. (The Hong Kong Polytechnic University); and Jiang, X.-Q. (University of Huddersfield) . . . . page 321
2. ***Dimensional Study of an Interference Fit Allograft***
Mauntler, N. A.; Ziegert, J. C. ; Schmitz, T. L. (University of Florida) . . . . page 325

Form & Geometry

1. ***50 m Linear Measuring Interferometer for Calibration of Surveying Tape***
Jeong, D. Y.; Suh, H. S.; Kim, J. A.; Kim, J. W.; Eom, T. B. (Korea Research Institute of Standards and Science) . . . . page 329

2 **Development and Analysis of an Optical Capability for the Measurement of Arrays**
Gill, D. D.; Claudet, A. A.; Southwell, L. M. (Sandia National Laboratories) . . . . . page 333

3. **Fast Three-dimensional Shape Measurement by Using Color-coded Illumination**
Song, C. K. (Korea Institute of Machinery and Materials); Kim, J. S. (Kafus Co., Ltd.); and Joo, B. G.; Kang, M. G. (Intekplus Co., Ltd.) . . . . . page 337

Instrumentation, Design & Testing

1. **Gravitational Reference Mass Center Determination by Velocity Modulation**
Conklin, J. W.; DeBra, D. B.; Sun, K.-X. (Stanford University) . . . . . page 341

2. **An Instrument for Nanoindentation Without Frame Stiffness Dependency**
Ellis, J. D.; Smith, S. T.; Hocken, R. J. (University of North Carolina at Charlotte) . . . . . page 345

3. **Optical Measuring Device for Radial Error of Micro-spindle Using High-speed Photo-amplifiers**
Fujimaki, K.; Mitsui, K. (Keio University) . . . . . page 349

4. **Mechanical Properties of Silicon Carbide Films Prepared by RF Magnetron Sputtering Using Targets with Different Carbon Contents**
Fujiyama, H. (Fukuoka Institute of Technology); Nakamura, M.; Sumomogi, T. (Hiroshima Kokusai Gakuin University) . . . . . page 353

5. **Nano-linear Encoder Investigation Using Dual Fiber and Grating System**
Karodkar, D. (University of North Carolina at Charlotte) . . . . . page 357

6. **Analysis and Performance of a Parallel-axis Flatness Measuring Instrument**
Marsh, E. R. (The Pennsylvania State University); and Vallance, R. R. (The George Washington University) . . . . . page 361

Machine Tool Metrology

1. **The Estimation for Errors of a Planar XY Stage from Profiles Measurement of Guide-ways**
Hwang, J.; Park, C. H. (Korea Institute of Machinery and Materials); Kim, S. W. (Korea Advanced Institute of Science and Technology (KAIST)) . . . . . page 365

2. **Development of a Trigger System to Measure Tool Position in Planetary Milling**
Kamiya, K.; Nomura, T.; Tashiro, H. (Toyama University); and Yazawa, T. (Nagasaki University) . . . . . page 369

3. **Application of 3D Optical Scanning Systems for the Measurement of Spheric and Aspheric Surfaces**
Sun, W.; McBride, J. W.; Hill, M. (University of Southampton) . . . . . page 372

Measurement Uncertainty

1. **Determination of Temperature Probability Distribution in Measurement Uncertainty**
Fang, C. Y.; Sung, C. K. (National Tsing Hua University); and Hung, C. Y.; Lui, K. W. (Center for Measurement Standards / ITRI) . . . . . page 376

2. **Cross Calibration for Primary Angle Standards by a Precision Goniometer with a Small Angle Interferometer**
Liou, H.-C.; Lin, C.-M.; Chen, C.-J.; and Chang, L.-C. (Industrial Technology Research Institute) . . . . . page 615

3. **Uncertainty Analysis for a Silicon Bulk Micromachined Dimensional Metrology Artifact**
Shilling, K. M.; Claudet, A. A.; Oliver, A. D.; Tran, H. D. (Sandia National Laboratories) . . . . . page 380

Surface & Subsurface

1. **A Serious Kinematic Coupling**
Gleason Jr., E. A. (Bal-tec) . . . . . page 384

2. **The Effect of Gaussian Filter Long Wavelength Cutoff λc in Topography Measurements and Comparisons**
Song, J. J.; Ma, L.; Vorburger, T. V. (National Institute of Standards and Technology) . . . . . page 387

3. **Study on Nano-scale Mechanical Properties of Ultra High-purity Aluminum by Nanoindentation**
Yoshida, M.; Nakamura, M.; Sumomogi, T.; Endo, T. (Hiroshima Kokusai Gakuin University) . . . . . page 391

OPTICS

Optical Fabrication

1. **Manufacturing of Glass Diffractive Optics by Use of Compression Molding Process**
Chen, Y.; Yi, A. Y. (The Ohio State University); and Klocke, F.; Pongs, G.; Demmer, A. (Fraunhofer Institute for Production Technology (IPT)) . . . . . page 395

2. ***Direct Machining of Inner Reflecting Surface for a Soft X-ray Microscope***
Chon, K. S.; Yoon, K. H. (Wonkwang University); and Namba, Y. (Chubu University) ..... *page 399*

3. ***Aspherizing the Sphere: Using Focused Ion Beam Machining to Create Aspherical Diamond Mills for Micro Optics***
Hodges, V. C; Adams, D. P.; Claudet, A. A.; Gill, D. D.; Sweatt, W.; Vasile, M. J. (Sandia National Laboratories)..... *page 403*

4. ***Manufacturing of Replicated Pt/C Multilayer Mirrors for Hard X-ray Telescopes***
Namba, Y.; Fushiki, A. (Chubu University); and Kunieda, H.; Ogasaka, Y.; Tawara, Y.; Yamashita, K. (Nagoya University) ..... *page 407*

5. ***A Magnetorheological Polishing Based Approach for Studying Magnetic/Nonmagnetic WC Hard Metals***
Shafrir, S. N.; Lambropoulos, J. C.; Jacobs, S. D. (University of Rochester) ..... *page 411*

6. ***Damage-free Processing of Silicon Carbide Optics***
Verma, Y.; Fiske, P. S.; Subrahmanyan, P. K.; Gardopee, G. (RAPT Industries, Inc.) ..... *page 415*

Optics / Interferometry

1. ***Control of Interference Fringes in a Point Diffraction Interferometer Using an Optical Saturable Absorber***
Furuhashi, H.; Uchida, Y. (Aichi Institute of Technology); Matsuda, K. (National Institute of Advanced Industrial Science and Technology); and Kono, A. (Nagoya University)..... *page 419*

2. ***Digital Periodic Error Correction: Further Testing and Results***
Schmitz, T. L.; Houck III, L. (University of Florida); and Chu, D. (Agilent Technologies, Inc.) ..... *page 423*

3. ***Phase Modulation Homodyne Interferometer with Picometer Resolution Using Tunable Laser Diode***
Ishige, M.; Matsuura, F.; Kawasugi, M.; Aketagawa, M. (Nagaoka University of Technology) ..... *page 427*

4. ***Grazing Incidence Metrology Using a Lateral Shearing Interferometer***
Kolipaka, J. P. S.; Snyder, J. J. (University of North Carolina at Charlotte); and Kuriyama, Y. (Mitutoyo Corporation) ..... *page 431*

5. ***Stitching Interferometry for Flexible Asphere Metrology***
O'Donohue, S.; Murphy, P. E.; Fleig, J.; DeVries, G. (QED Technologies) ..... *page 435*

OTHER

Precision Assembly

1. ***Assembly of Thin Gratings for Soft X-ray Telescopes***
Akilian, M.; Heilmann, R. K.; Schattenburg, M. L. (Massachusetts Institute of Technology) ..... *page 439*

2. ***Passively Aligned 100-port Micro-fluidic Connector***
Forest, C. R.; Beltran, M. J.; Hunter, I. W. (Massachusetts Institute of Technology) ..... *page 443*

3. ***Fabrication of Periodic Nano-structures Using DNA Fractions***
Hatsuzawa, T.; Yanagida, Y. (Tokyo Institute of Technology)..... *page 447*

4. ***Precision Design Verification System of Injection Molds Using Web-based 3D Viewing Technology***
Song, I.-H.; Chung, S.-C. (Hanyang University); and Chung, S. (The University of Western Ontario)..... *page 451*

5. ***An XML-based Digital Mock-up System for Heterogeneous Assembly***
Song, I.-H.; Chung, S.-C. (Hanyang University); and Kim, K.-D. (Small Business Corporation) ..... *page 455*

6. ***Design and Testing of a Tribometer for In Situ Microscopy***
Mauntler, N. A.; Dunn, A. C.; Schmitz, T. L.; Sawyer, W. G. (University of Florida) ..... *page 459*

PROCESSES

Grinding

1. ***Monitoring of Roundness-errors in Continuous Path Controlled Crankshaft Grinding Processes***
Denkena, B.; Kramer, N. J. (Hannover University) ..... *page 463*

2. ***Trueing of Micro-grinding Wheels by Diamond Tools***
Hoffmeister, H.-W.; Hlavac, M. (Technical University of Braunschweig)..... *page 467*

3. ***High Performance Grinding Wheels with Boron Doped Diamond Grits Enabling Electrical Conductivity and High Thermal Stability on Cutting Edges***
Iwai, M.; Nakagawa, K.; Uematsu, T. (Toyama Prefectural University); Sano, S. (Sodick Co., Ltd.); Tanaka, K. (Toshiba Machine Co., Ltd.); Wang, M. (OSG Co., Ltd.); and Suzuki, K. (Nippon Institute of Technology) ..... *page 471*

4. ***Study on Micro Machining of Lithium Niobate Using Single Abrasive Grinding***
Kurihara, R.; Nakamura, M.; Yoshida, M.; Sumomogi, T. (Hiroshima Kokusai Gakuin University) . . . . . *page 475*

5. ***Development of a 3-D Measuring Equipment for Surface Geometries of Grinding Wheel Surfaces***
Lee, H.-S.; Yamada, T.; Kobayashi, M. (Nihon University) . . . . . *page 479*

6. ***The Role of Crystallographic Orientation on the Forces Generated in Ultra-precision Grinding of Anisotropic Materials Such as Monocrystalline Silicon***
Marsh, E. R. (The Pennsylvania State University); and Vallance, R. R. (The George Washington University) . . . . . *page 483*

7. ***Wheel Wear During Intermittent Grinding***
Miller, M. H.; Fan, X. (Michigan Technological University) . . . . . *page 487*

8. ***Studies on Slicing Characteristics of Vibratory OD-blade Slicing***
Uneda, M.; Tsukada, H.; Ishikawa, K.; Suwabe, H. (Kanazawa Institute of Technology) . . . . . *page 491*

9. ***Study on the Contact Stiffness of Grinding Wheels Due to the Difference of Dressing Condition***
Yamada, T.; Lee, H.-S.; Morita, H. (Nihon University) . . . . . *page 495*

10. ***Development of Cross and Parallel Mode Grinding Machine for High NA Aspherical Mold and Die***
Yamamoto, Y.; Suzuki, H.; Moriwaki, T.; Okino, T.; Hijikata, Y. (Kobe University); Roblee, J. W. (Precitech, Inc.); and Miyashita, T. (Taylor Hobson Japan Ltd.) . . . . . *page 499*

11. ***Ultra-smoothness Grinding of Cemented Carbide Using Newly Developed Vertical Grinder***
Yasui, H.; Yamamoto, Y.; Miyamoto, K.; Furuya, S.; Sakamoto, R. (Kumamoto University) . . . . . *page 503*

Machining

1. ***Review of Vibration-assisted Machining Methods for Precision Fabrication***
Brehl, D. E.; Dow, T. A. (North Carolina State University) . . . . . *page 507*

2. ***Micro-structure Fabrication Using Elliptical Vibration-assisted Machining (EVAM)***
Brehl, D. E.; Dow, T. A.; Garrard, K. P.; Sohn, A. (North Carolina State University) . . . . . *page 511*

3. ***Fabrication of Micro-components Using Vibration-assisted Micro-EDM***
Endo, T.; Tsuijimoto, T.; Mitsui, K. (Keio University) . . . . . *page 515*

4. ***Polishing of Single Point Diamond Tool Based on Thermo-chemical Reaction with Copper***
Higuchi, M.; Yamaguchi, T. (Kansai University); Shimada, S. (Osaka Electro-Communication University); and Obata, K. (A.L.M.T. Corporation) . . . . . *page 519*

5. ***Tunable Holder for Boring Bars***
Houck III, L.; Schmitz, T. L. (University of Florida); and Smith, K. S. (University of North Carolina at Charlotte) . . . . . *page 523*

6. ***Development of Cutting Load Prediction System Using Monitoring Data in Micro Machining***
Ikeda, N.; Kondo, M.; Kobayashi, Y.; Shirai, K. (Nihon University) . . . . . *page 527*

7. ***Manufacturing of Micro V-groove with an Electrically Conductive Diamond Electrode in EDM***
Iwai, M.; Uematsu, T. (Toyama Prefectural University); Sano, S. (Sodick Co., Ltd.); Pan, W.; Itagaki, K.; Suzuki, K. (Nippon Institute of Technology); and Murakami, Y.; Wang, M. (OSG Co., Ltd.) . . . . . *page 531*

8. ***Condition Monitoring of Micro-drilling Processes on Glass by Using Machine Vision***
Kim, H.-H.; Kim, S.-C.; Chung, S.-C. (Hanyang University); Chung, S. (The University of Western Ontario); and Jee, W.-H. (Shinhan Diamond, Inc.) . . . . . *page 535*

9. ***Machining Parameter Selection Based on Cost-based Objective Function and Process Stability***
Kurdi, M. H.; Schmitz, T. L.; Haftka, R. T. (University of Florida) . . . . . *page 539*

10. ***Creation of V-shaped Curved Microgrooves with Two Flat-ends by Non-rotational Cutting Tools***
Moriya, T.; Ishida, T.; Teramoto, K.; Takeuchi, Y. (Osaka University) . . . . . *page 543*

11. ***Ultraprecision Turning with Binderless cBN***
Oberschmidt, D.; Uhlmann, E. (Fraunhofer Institute for Production Systems and Design Technology); and Kurz, M. (Technical University Berlin) . . . . . *page 547*

12. ***Chatter Stability Boundary Analysis Using Neural Network***
Oh, M. S.; Sim, S. B.; Yoon, M. C. (Pukyong National University); and Jung, J. S. (Workers Accident Medical Corporation/Korea Orthopaedics & Rehabilitation Engineering Center) . . . . . *page 551*

13. ***Optimizing Saw Teeth Deflection and Lumber Thickness Variation Through Precision Engineering Approach***
Okai, R. (University of Education- Winneba) . . . . . *page 555*

14. ***Characteristics of Mechanical Micromilling Using Tungsten Carbide Tools***
Ozdoganlar, B. O.; Filiz, S. (Carnegie Mellon University) . . . . . *page 559*

15. ***Effect of Low Cutting Speed on Ultra-precision Cutting of Titanium Alloy with Coated-cemented-carbide Tool***
Yasui, H.; Shinozaki, A.; Toyama, A.; Sakamoto, S.; Kajiwara, Y. (Kumamoto University) . . . . . *page 563*

Manufacturing

1. ***Self-adjustment Module for Phone Camera Lens Assembly***
Lee, C.-W.; Song, J.-Y. (Korea Institute of Machinery and Materials) . . . . . *page 567*

2. ***A Study on the Ultra Precision Progressive Die Making for Sheet Metal Forming by Computer Simulation***
Sim, S. B.; Kim, C. H.; Park, G. Y. (Pukyuong National University) . . . . . *page 571*

Non-conventional

1. ***A Single Discharge Study of Micro-EDM***
Moylan, S. P. (National Institute of Standards and Technology); and Chandrasekar, S. (Purdue University) . . . . . *page 575*

2. ***Improvement of Machining Accuracy in Wire Electrical Discharge Machine***
Sakai, Y.; Goto, A.; Nakashima, T.; Taneda, A.; Magara, T.; Hashimoto, T. (Mitsubishi Electric Corporation) . . . . . *page 579*

3. ***A Study on the Performance of Copper-graphite as Tool Material in Micromachining by Micro Electro Discharge Machining***
Sundaram, M. M.; Rajurkar, K. P. (University of Nebraska-Lincoln) . . . . . *page 583*

4. ***A New Precision Magnetic Field Assisted Finishing Process for Ferromagnetic Metallic Materials Using Plural Permanent Magnets as a Tool***
Zou, Y.; Shinmura, T. (Utsunomiya University) . . . . . *page 587*

Polishing, Lapping & ECM

1. ***Development of a Structure-controlled Fixed-abrasive Pad for Finishing of an Optical Glass***
Enomoto, T.; Fujita, T. (The University of Tokyo) and Tominaga, S.; Suzuki, M. (Roki Techno Co., Ltd.) . . . . . *page 591*

2. ***Novel CMP Technique for Copper Surface Finishing with Fullerene Nano-particle***
Tanada, H.; Miyoshi, T.; Takaya, Y.; Hayashi, T. (Osaka University); and Suzuki, K. (Nitta Haas Incorporated) . . . . . *page 595*

3. ***Studies on Oscillation Controlled Lapping Using Small Diameter Lap Tool***
Uneda, M.; Ishikawa, K.; Suwabe, H.; Tsukada, H. (Kanazawa Institute of Technology) . . . . . *page 599*

4. ***Real Time Measurement of Axial Force and Torque During Polishing***
Williams, W. B.; Mullany, B. A. (University of North Carolina at Charlotte) . . . . . *page 603*

5. ***Polisher Life in Ultra-smoothness Polishing of Magnetic Disk Substrate Using New Double Side Surface Polishing Machine***
Yasui, H.; Yamaguchi, K.; Niki, T.; Otsuka, S.; Nagata, T. (Kumamoto University) . . . . . *page 607*

Replication

1. ***Large Area Optical Devices with Glass-pressed/Metal-embedded Subwavelength Grating***
Tsuchiya, K.; Komiya, A.; Suzuki, H.; Ooi, T.; Morii, H.; Hamaguchi, T.; Nakao, M. (The University of Tokyo) . . . . . *page 611*

Technical Papers

ASPE

PHASE-SHIFTING DIFFRACTION INTERFEROMETER FOR INSPECTING NIF IGNITION-TARGET SHELLS

Richard C. Montesanti, Michael A. Johnson, Evan R. Mapoles, Dennis P. Atkinson, James D. Hughes, Jack L. Reynolds
Lawrence Livermore National Laboratory (LLNL), Livermore, CA 94550

OVERVIEW OF THE DESIGN

This paper describes the top-level design of a phase-shifting diffraction interferometer (PSDI) system for mapping the outer surface of small spherical parts (a shell), with emphasis on the PSDI head and the motion control system used to position it with respect to a shell. The method of operation of the PSDI, which consists of a laser front-end and an interferometer head, is described extensively elsewhere [1, 2, 3] and a brief description is included at the end of this paper. The interferometer head is adapted to an XYZ linear stage stack, and the shell to be measured is held by vacuum in a transfer chuck mounted to a Theta-Phi rotary stage stack (elevation-azimuth, relative to the shell). Figure 1 shows a model of this system, and Figure 2 shows a detail from that model.

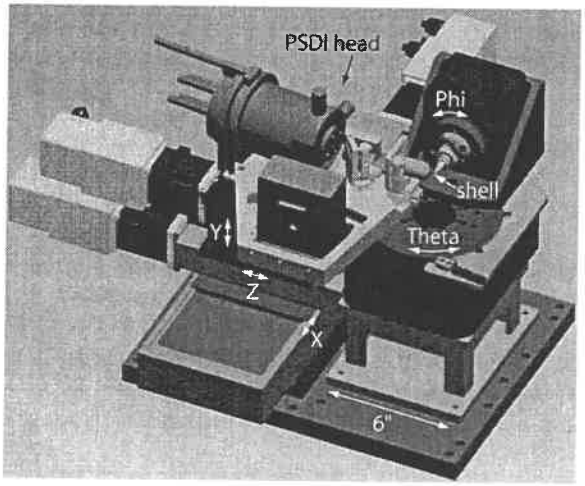

FIGURE 1. Model of the PSDI head mounted to the XYZ linear stage stack and measuring a shell held by a transfer chuck mounted to the Theta-Phi rotary stage stack.

Closed-loop computer control of the stages allows positioning the interferometer relative to the shell and then orienting the shell to measure a particular portion of its surface. The rotary stages allow mapping one half of the shell surface (hemisphere), then the shell is flipped end-for-end so that the other hemisphere can be mapped. Transfer chucks are used to mount the shell in the system, minimize handling of the fragile shells, and to facilitate flipping of a shell. The first system will be tested with a manual part loading and flipping system in September 2006, and is extendable to a future fully automated system for handling shells.

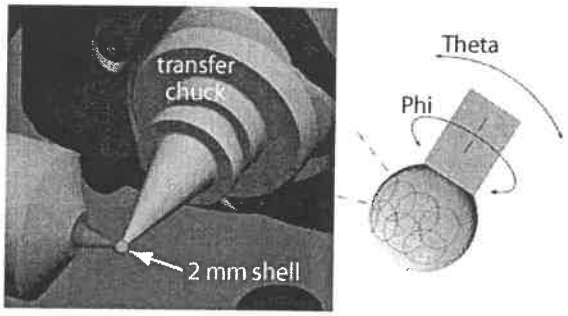

FIGURE 2. Detail of the shell, transfer chuck, and convergent rays from the PSDI head (left). Depiction of overlapping measurements on a shell surface (right).

The five motorized stages used to position the PSDI head and shell relative to each other are controlled by an Aerotech Automation 3200® machine tool controller using a LabVIEW™ user interface. The control system operates in a point-to-point position and hold mode: first positioning the PSDI head relative to the shell to acquire and center the fringe pattern, then indexing the shell after a measurement is made. The converging rays from the microscope objective in the PSDI head form a cone with a 20° included angle and its vertex at the center of the shell. Each measurement requires 3 seconds and consists of eight individual measurements averaged together. An entire hemisphere can be mapped with approximately 50 measurements, leading to 150 seconds to perform the measurements-only for a hemisphere. Additional time is needed to index the rotary stages and re-center the fringes if necessary, as well as time for data authentication and file management. Assuming that the data analysis can be performed either in parallel with the

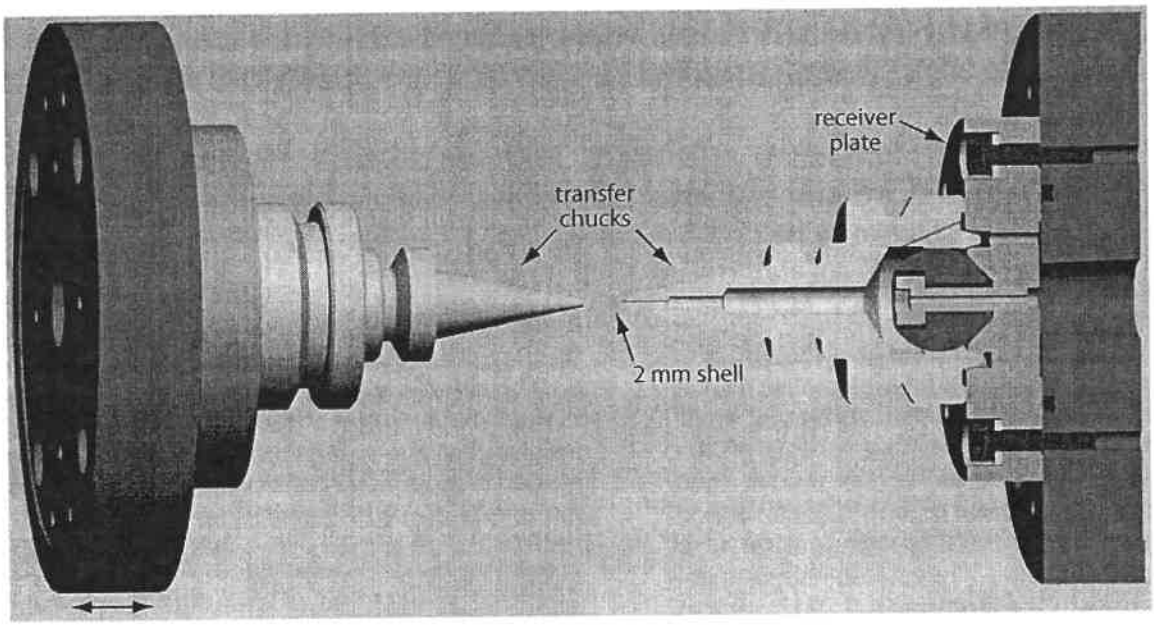

FIGURE 3. Model of two transfer chucks and their receiver plates, positioned to flip a shell. The cross-section reveals the interfaces between a chuck and receiver plate.

next measurement or off-line, a rough estimate for measuring an entire hemisphere is 7.5 minutes if each measurement, indexing and re-centering of the stages, and file management step requires 3 seconds. The five computer-controlled stages can handle that speed, but clearly the bottle neck would be manual data verification, organization, analysis, and archiving. In the near future, the user interface for the five motorized stages will communicate with an LLNL-written supervisory program that commands those stages and coordinates them with the legacy LLNL software package used to control and coordinate phase-shifting in the laser front-end and the frame grabber card for the camera. The supervisory program will also coordinate with a second legacy LLNL software package that is used to authenticate and analyze the acquired data, and will perform data organization and archiving.

Figure 3 shows a model of two transfer chucks and their respective receiver plates. A slip fit between a hardened-steel sphere and the diamond-turned bore in the transfer chuck provides the radial constraint for the chuck. The annular land on the back of the chuck mates with a diamond-turned flat surface to provide the axial and tilt constraints for the chuck and a vacuum seal. The annular protuberance at the back of the chuck is for piloting the chuck onto the receiving plate; protecting the critical diamond-turned surfaces. A source of vacuum is provided along the centerline of the receiving plate. A pressurized hood (not shown) engages the front-most groove on the transfer chuck to allow removing the chuck from its source of vacuum in the rotary stage stack and transporting it. The rear groove on the chuck accommodates a secondary, mechanical means for securing the chuck to the receiver plate, and will facilitate future automated handling of the transfer chuck. Flipping the part end for end is accomplished by positioning the receiving chuck as close as reasonably possible — using a vision system for displacement feedback — to the shell being held by the sending chuck. Vacuum is then applied to the receiving chuck and removed from the sending chuck. To first-order for a 2 mm diameter shell, a translational eccentricity between the two chucks (non-coincidence of the centerlines) causes a rotation of the shell of approximately 1 mrad for each 1 μm of eccentricity. Rotation of the shell during its flight between the chucks can add to the net rotation.

The error budget for the combined PSDI head positioning system and shell mounting system (transfer chucks) is based on a requirement that an acceptable fringe pattern is retained if the center of the shell stays within a 20 to 50 μm sphere of uncertainty relative to the PSDI head. Errors leading to the uncertainty in the knowledge of the angular orientation of each measurement site

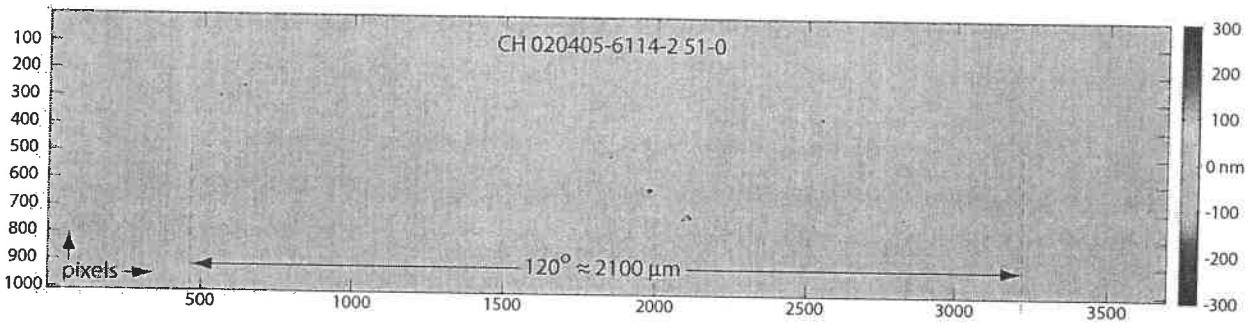

FIGURE 4. Measurement data produced by a demonstration-version of the phase-shifting diffraction interferometer. The seven overlapping measurements span one-third of the surface at the equator of this 2 mm diameter shell.

with respect to a landmark on the surface of a shell is accommodated by using observed features on the surface to stich the data together to form an accurate mosaic surface map of the shell. In this regard nature helps us, since a featureless surface is not a concern in the first place. The acceptable amount of uncertainty in knowing the angular orientation of each measurement is still being traded off against the burden on the search algorithm that stitches the measurements together, and is believed to be acceptable for the design presented.

MOTIVATION FOR DEVELOPING THIS INSTRUMENT

The application of this interferometer to the characterization of target capsules (shells) for Inertial Confinement Fusion (ICF) is due to the requirement that the surfaces of these capsules be extremely smooth and free of defects over the entire surface. Many capsules which are smooth enough on average have local defects which render them unacceptable for ICF. Figure 4 shows an example of measurement data produced by a demonstration-version of the interferometer, revealing unacceptable surface defects. Measurements such as the one shown in Figure 4 have already provided feedback needed to improve the manufacturing process for capsules. The interferometer described in this paper will provide much improved coverage much more rapidly to enable additional process improvements and will provide the throughput needed for efficient quality control of the capsules that will be used in the Ignition Campaign with the National Ignition Facility (NIF) [4]. The need for characterization over 4π steradian makes the PSDI coupled with the computer-controlled mechanical stage system described here an ideal choice for this application. An entire hemisphere of the capsule can be mapped with a lateral resolution of one micron and a height resolution of a few nanometers without handling the shell. With a single flip of the shell the entire surface is mapped. In addition, this instrument will be used to characterize inner surfaces of pieces of sacrificial shells. Furthermore, the instrument allows measurement of the radius of a shell to an accuracy governed by the mechanical stage that controls the focus direction (Z), which is within ± 2.0 μm for the unmapped system and can be improved to the sub-micron range by calibration with an artifact.

METHOD OF OPERATION OF THE INTERFEROMETER

An advantage of the optical design of this interferometer is the use of a spherical reference wavefront. The front-end of the interferometer consists of a short coherence-length laser that produces a polarized beam that is resolved into two co-linear beams having orthogonal polarizations. One of the beams passes through a delay line having a length greater than the coherence length of the laser and becomes the reference beam. The reference beam is recombined with the other (measurement) beam, and both are transmitted through a single-mode optical fiber to the back end of the fiber coupler in the interferometer head. Figure 5 shows a model of the PSDI head. Upon exiting the polished end of the fiber in the fiber coupler the beams produce a spherical wavefront that is focused onto a pinhole, which produces a more perfect spherical wavefront through diffraction. A scraping mirror sends

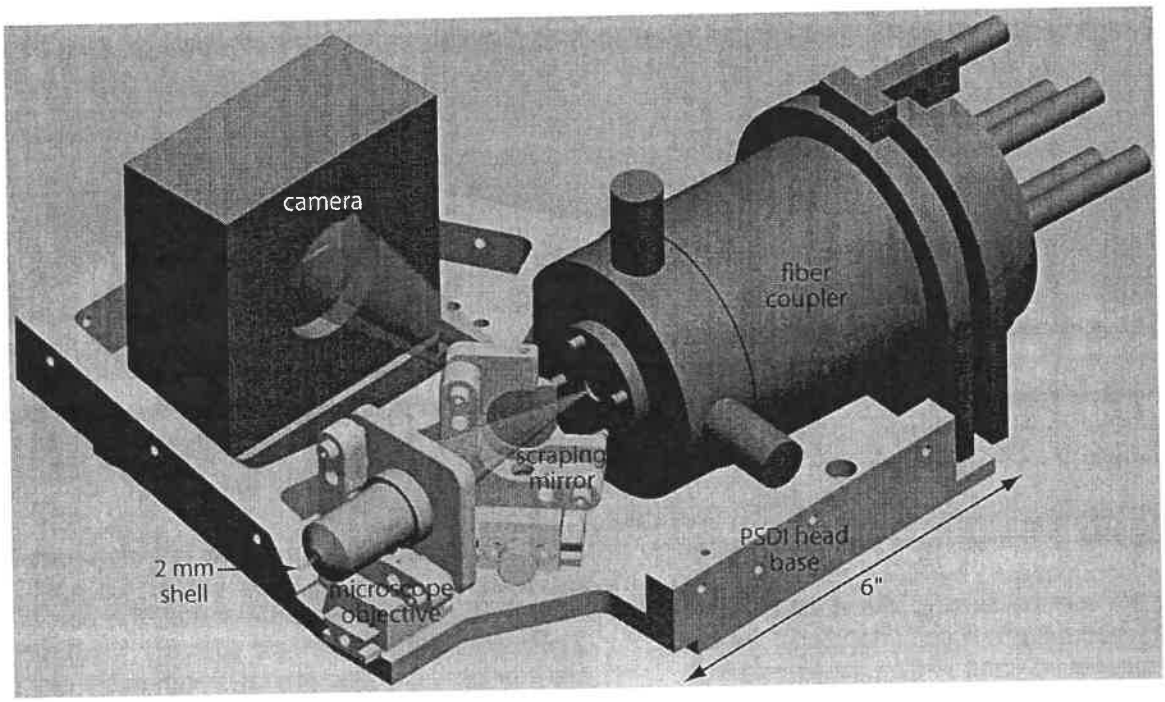

FIGURE 5. Model of the PSDI head showing its main optical components and the ray bundles emanating from the pinhole in the fiber coupler.

a portion of the combined measurement and reference wavefronts to a CCD camera, while the remainder of the combined beams are focused by a microscope objective onto the spherical surface being measured. The reflected beams from that surface are recombined with the two beams that were diverted earlier by the scraping mirror, and sent to the camera. Starting at the pinhole, the difference in optical path lengths for the two pairs of beams reaching the camera is equal to the length of the delay line in the front-end. The measurement beam from the test object and the reference beam from the scraping mirror are coherent and therefore interfere with each other. By phase shifting the reference beam relative to the measurement beam in the front-end, the amplitude and phase of the electric field at the camera can be measured. Numerical techniques are used to propagate this field to the surface of the test part to provide a measure of surface height.

ACKNOWLEDGEMENTS

In accomplishing this work, we acknowledge the helpful contributions and support of Manuel Carrillo, Marjory Jong, Stanley Edson, Steven Bretz, Steven Strodtbeck, Matthew Bono, Donald Bennett, Timm Wulff, Donald Phillion, William Behrendt, Jeffrey Atherton, and John Taylor.

This work was performed under the auspices of the U.S. Department of Energy by the University of California, Lawrence Livermore National Laboratory under Contract No. W-7405-ENG-48.

REFERENCES

[1] R. N. Smartt and W. H. Steel, *Theory and application of point-diffraction interferometers*. In Jpn. J. Appl. Phys. 14, 351-356, 1975.

[2] G. E. Sommargren and R. Hostetler, *Point diffraction interferometery at soft x-ray wavelengths*. In Soft X-Ray Projection Lithography, A. M. Hawryluk and R. H. Stulen, eds., Vol. 18 of OSA Proceedings Series Optical Society of America, Washington, D.C., 1993, p. 100.

[3] G. Sommargren, United States Patent 5,548,403, August 20, 1996.

[4] National Ignition Facility Programs. http://www.llnl.gov/nif/.

A 1 m SWING-ARM PROFILOMETER FOR LARGE TELESCOPE MIRROR ELEMENTS

Christopher W. King[1], Matthew J Callender[1], Apostolos Efstathiou[1], David D. Walker[1,3], Anthony E. Gee[1], Andrew J. Lewis[2], Simon Oldfield[2] & Robert M. Steel[2]
[1]Optical Science Laboratory, University College London, United Kingdom
[2]Engineering Measurement – Length, National Physical Laboratory
Teddington, Middlesex, United Kingdom
[3]Zeeko Ltd, 4 Vulcan Court, Coalville, Leicestershire, LE67 3FW, United Kingdom

INTRODUCTION

Advances in the requirement for large aspheric and free-form ultra-precise surfaces place difficult demands on available manufacturing techniques and the associated metrology. Modern Computer Numerical Control (CNC) polishing machines can produce surfaces to meet demanding specifications but, without complementary fast, accurate and traceable metrology, economic volume production may not be feasible for certain projects.

A major application for this metrology arises in the manufacture of Extremely Large Telescope (ELT) mirror segments which make up primary mirrors 30–100 m in diameter. One example is the Euro-50 telescope, shown in figure 1, the 50 m diameter primary mirror consisting of 618 hexagonal segments each of 2 m diameter across flats. The aspheric departures of the segments from the overall best fit sphere range from ±3 μm for segments of the inner-most ring to ±300 μm for the edge-segments. Each segment has a form tolerance of 36 nm RMS and the individual radii of curvature must conform and match to 0.5 mm. The segment manufacture will take some years and traceable metrology is required to ensure that the first segment matches the last.

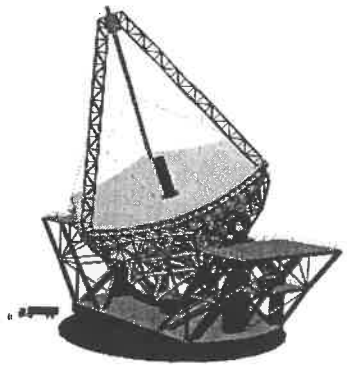

FIGURE 1. The proposed Euro-50 telescope concept: Euro-50 website www.astro.lu.se/~torben/euro50.

To address the need for high precision metrology on large optics, a tool-kit of parts is needed. As part of an on-going UK effort, a joint project between the UK National Physical Laboratory (NPL) and University College London (UCL) has developed prototype of a new design of swing arm profilometer (SAP) as shown in figure 2.

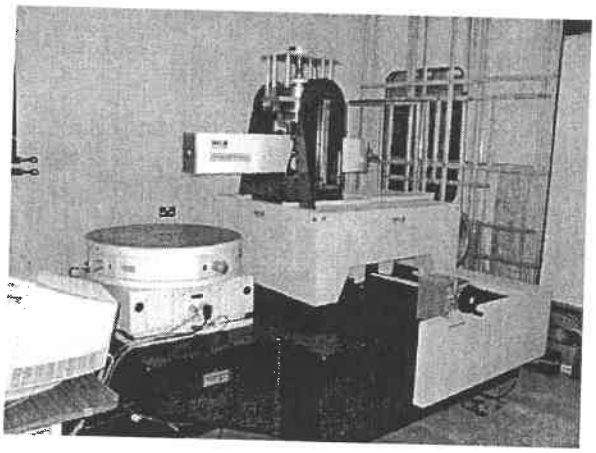

FIGURE 2. The NPL/UCL swing arm profilometer.

SWING ARM PROFILOMETRY

A swing arm profilometer [1] consists of a tilted rigid arm that rotates in space such that the end of the arm will trace out a circle.

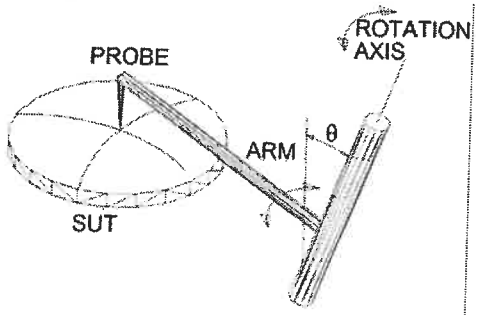

FIGURE 3. Swing-arm profilometer scheme.

When correctly aligned with the surface under test (SUT) this circle coincides with the base sphere of the SUT. A suitable probe mounted on the arm directly measures the deviation of the SUT from the best fit sphere on the path moved over the surface.

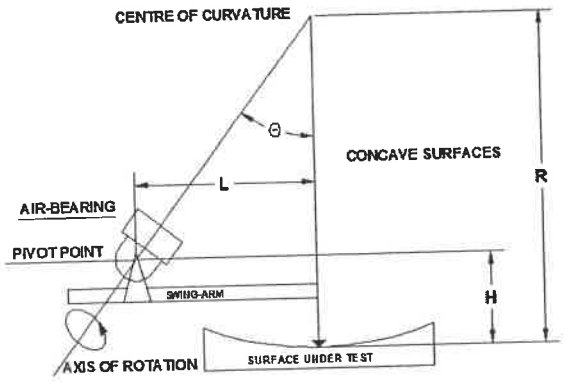

FIGURE 4. The NPL/UCL SAP geometry.

The geometry of the NPL/UCL SAP is shown in figure 4, where θ is the rotation axis tilt angle, R is the radius of curvature of the SUT, L is the length of the arm from the tilt pivot point on the rotation axis to the probe tip (the part vertex at the zero position) and H is the vertical distance between the tilt pivot point on the rotation axis and the vertex of the SUT. In our geometry the arm is held horizontally so that to align the SAP the arm rotation axis must be tilted so that:

$$\theta = \tan^{-1}\frac{L}{R-H},$$

for concave parts; for convex surfaces, the denominator on the right of the equation is equal to R+H.

As a prototype for a larger capacity instrument, the SAP has the ability to measure surfaces with diameters up to 1 m with minimum radii of curvature of 1.75 m for concave and 1.25 m for convex parts. It is aimed to achieve a form measurement accuracy of 20 nm RMS. Once complete, the prototype will be housed at the OpTIC Technium, Denbigh, North Wales, a UK national facility for the fabrication and metrology of ultra-precision surfaces.

Construction and materials

Due to the extreme performance requirements of the SAP, careful choice of components was required. The SAP support structure is built on a 2-axis translation stage from a decommissioned CMM, providing 400 mm of travel with 100 nm resolution. The SAP sits on a damped granitan base to provide stability.

The arm is a 1220 mm length of rectangular hollow section Coors-Tek alumina beam. Alumina was chosen as it has excellent stiffness and thermal properties for comparatively low density. Some key properties are given in table 1 with aluminium and steel shown for comparison.

TABLE 1. Material properties.

	Specific stiffness (GPa/gcm^{-3})	Coefficient of linear expansion ($\mu m/^{o}C$)	Density (g/cm^{-3})
Al_2O_3	95	6.1	3.9
Al	25.6	22.5	2.7
Steel	26.5	11.9	7.9

A Professional Instruments BLOCK-HEAD® 10R rotary air bearing provides arm rotation This bearing has a radial stiffness of 350 N/µm, an axial stiffness of 1750 N/µm and tilt stiffness of 11.3 Nm/µm and axial and radial run-outs better than 25 nm with working load capacities which met specifications. The bearing is equipped with a Heidenhain ERP 880 rotary encoder that gives an angular resolution of 0.36 arc sec. Drive motion is provided by a DC servo motor with a harmonic drive and is coupled to the arm and bearing via a custom-made low friction, high stiffness coupler (as off-the-shelf couplers were found to have insufficient stiffness). A precision rotary air-bearing table completes the set-up, providing an encoded rotation stage for the SUT.

At the end of the arm is an optical breadboard which allows the probe to be adjusted or completely changed as required. Instrument control and data-acquisition is performed using custom LabVIEW® software and the whole assembly is located in a temperature and humidity controlled environment.

PROBING OPTIONS

Currently any of three probes can be attached to the SAP

- Solartron LT12 linear encoder probe
- Arden Photonics AWS-50 wavefront sensor
- Fisba µ-phase interferometer

With a range of 13 mm and resolution of 12.5 nm, the Solartron LT12 can be equipped with standard metrology probe tips. It is used as a standard device for setting the SAP.

The Arden Photonics AWS-50 is a new design of wavefront curvature sensor. The key component is a specially distorted diffraction grating that provides intra- and extra-focal wave-front imaging to facilitate curvature sensing. We are currently mounting this onto the SAP for subsequent use.

The Fisba μ-phase interferometer is a compact Twyman-Green phase-stepping interferometer, fully configurable with a range of transmission spheres, phase stepping elements and reference surfaces.

While probe provides only point based measurements, the use of the optical sensors allows total surface coverage via individual sub-apertures. Software has been developed to stitch the sub-aperture images from the optical sensors to provide a complete surface map.

PROBE CALIBRATION AND RESULTS

Initial results were obtained using the Solarton LT12 which was first calibrated against a laser interferometer system. Improvements to the SAP set-up procedure and the measurement environment have allowed us to improve upon the initial measurements presented elsewhere [2].

Probe Calibration

The Solartron probe was calibrated with a NPL Jamin interferometer system and frequency stabilized He-Ne laser.

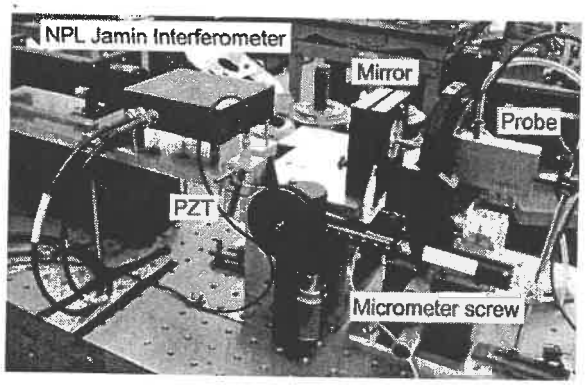

FIGURE 5. The probe calibration rig.

The calibration rig shown in figure 5 was specially configured to allow simultaneous displacement measurements both from the probe and the interferometer using a combination of a micrometer screw and PZT stack. The plot in figure 6 shows the interferometer position against the difference between the probe position and the interferometer position. The solid line represents the linear regression line and the markers represent the actual data. The linearity of the probe was calculated to be 1.4 parts per million, across the range L of the probe, using the following formula:

$$N = \frac{100 N_{RMS}}{L} \%,$$

where N_{RMS} is the standard deviation of the probe measurements from the regression line.

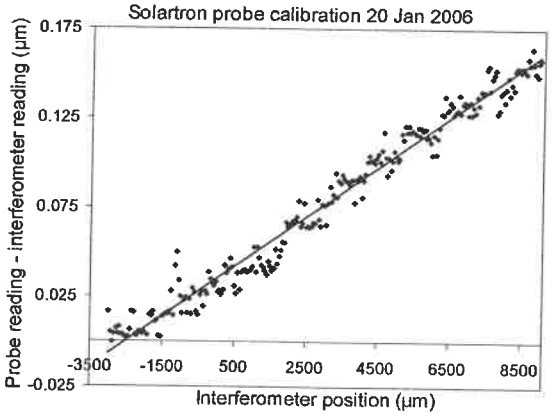

FIGURE 6. Probe calibration plot.

Results

For initial trials a 640 mm diameter *f*/9.5 concave sphere was used which has previously been verified to be spherical to λ/6 RMS at 632.8 nm (99 nm RMS form error) using a Wyko 6000 interferometer. The part has a radius of curvature of 6098 mm and is made from Pyrex glass.

After mounting and centering, the whole assembly is adjusted for tip/tilt. Measurement scans were made by swinging the arm and probe across the surface and recording data at fixed intervals. A PTFE tip was used and the arm was scanned by 20 degrees either side of the part vertex (centre).

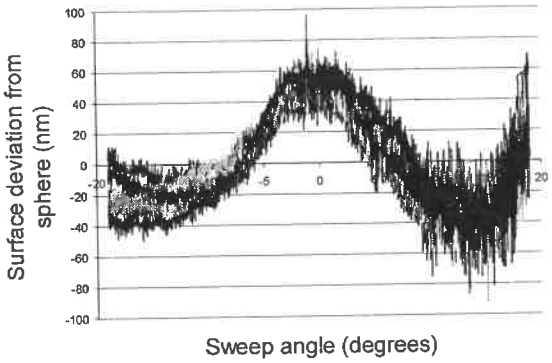

FIGURE 7. Ten repeat scans of a 640 mm diameter f/9.5 concave spherical mirror with 10 point averaging filter and tilt removed.

Figure 7 shows the results obtained from 10 scans. The data are noise-filtered using a 10 point moving average and any residual tilt has been corrected. In future a standard ISO Gaussian filter may be used to remove noise. Analysis of the data shows the repeatability of the measurement process to be better than 30 nm.

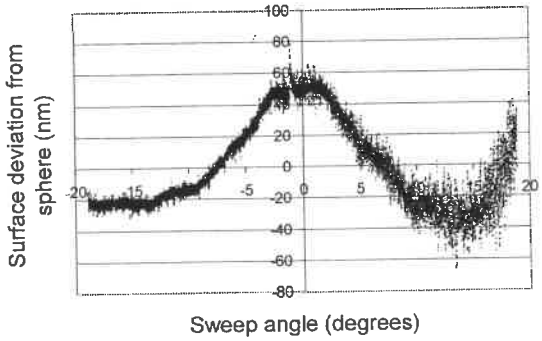

FIGURE 8. Point by point average of the 10 measurements from figure 7.

The measurement technique used is not optimal for the Solartron probe and PTFE tip used as it results in an increase in the measurement uncertainty and noise – evident to the right of figures 6 and 7. It is aimed to improve the uncertainty and noise levels by modification of the measurement technique. Further improvements to the probe mount mechanism and the use of ruby probe tips should serve to make further gains in repeatability and accuracy. Figure 8 shows the average of the 10 scans of raw data without filtering. The calculated RMS surface deviation along the scan is 28 nm, comparing favourably to a value of 40 nm obtained using the Wyko 6000 interferometer on this part of the surface.

CONCLUSION AND FURTHER WORK

The next generation of extremely large ground-based telescopes will have designs that will push to the limit our capability to manufacture large spherical and aspheric surfaces. To address this, NPL and UCL have constructed a new design of SAP that is a prototype for a larger instrument and a useful metrology tool as it currently stands.

The device can measure flats, concave and convex surfaces up to 1 m in diameter with minimum radii of curvature of 1.75 and 1.25 m respectively. We have measured surface profiles with RMS deviations of 28 nm and a repeatability of less than 30 nm.

Future work will revolve around minimizing the measurement noise and improving the mechanical probing stage. We are also in the process of attaching the Arden AWS-50 to the swing-arm using a custom 3-axis positioning stage. The interface has been designed and constructed, and we hope to report on this work in a future paper.

ACKNOWLEDGEMENTS

The NPL portion of the work on this instrument has been funded out of the UK Government's (Dept of Trade and Industry) National Measurement System Programme for Length Metrology 2002 – 2005 and the National Measurement System Programme for Engineering Measurement 2005 – 2008.

C. King is funded by a studentship from the Engineering and Physical Sciences Research Council's programme of Cooperative Awards in Science and Engineering (CASE).

M. Callender is funded by a Partice Physics and Astronomy Research Council CASE studentship.

C. King and M. Callender were also supported by the Optical Manipulation and Metrology SMART Optics Faraday project.

REFERENCES

1. Anderson, D., and Burge, J., 1995, Swing-Arm Profilometry of Aspherics, *Proc. SPIE Int. Soc. Opt. Eng.* vol 2536, pp 169—179.
2. Callender, M., Efstathiou, A., King, C., Walker, D., Gee, A., Lewis, A., Oldfield, S., and Steel, R., 2006, A Swing Arm Profilometer for Large Telescope Mirror Element Metrology, *Proc. SPIE Int. Soc. Opt. Eng.*, vol 6273, in press.

THIN FILM EXTRACTION FROM SCANNING WHITE LIGHT INTERFEROMETRY

Daniel I. Mansfield
Taylor Hobson Ltd, Leicester, United Kingdom

INTRODUCTION

Scanning white light interferometry (SWLI) is now an established technique for the measurement of surface topography. It has the capability of combining sub-nanometre interferometric resolution with a range limited only by the z-traverse, typically at least 100μm. A very useful extension to its capability is the ability to measure thin films on a local scale. For films with thicknesses in excess of ~2μm (depending on refractive index), the SWLI interaction with the film leads simply the formation of two localised fringe bunches, each corresponding to a surface interface. It is evidently relatively trivial to locate the positions of these two envelope maxima and therefore determine the film thickness, assuming the refractive index is known. For thin films (with thicknesses ~20nm to ~2μm, again depending on the index), the SWLI interaction leads to the formation of a single interference maxima. In this context, it is appropriate to describe the thin film structure in terms of optical admittances; it is this regime that is addressed through the introduction of a new function, the 'helical conjugate field' (HCF) function. This function may be considered as providing a 'signature' of the multilayer measured so that through optimization, the thin film multilayer may be determined on a local scale. Following the definition of the HCF function, examples of extracted multilayer structures are presented. This is followed by a discussion of the minimum film thickness limit of the approach.

Conventionally, thin film structures are measured using either a spectrophotometer or an ellipsometer. For large-area vacuum deposited thin films (single or multi-layer), such measurement approaches are very appropriate. In a different arena, SWLI is now an established technique for the measurement of surface topography. Typically, SWLI instruments provide a sub-micron lateral resolution (determined by the numerical aperture of the objective) and a sub-nanometre interferometric z-resolution. Within the MEMS/MOEMS industries, there is a growing requirement for the ability to measure thin film structures that only exist on a local scale. Through the development of the HCF function, the local topography capability of SWLI may be extended to include the determination of layer thicknesses and dispersive indices. An additional benefit is that, through the knowledge of the thin film structure, the phase-change on reflection (PCOR) may be compensated so that 'true' step-heights may be obtained.

Results of both single and multi-layer thin film extraction on a local scale from SWLI measurements are presented. The effectiveness of PCOR-compensation in terms of the associated step-heights at the films' boundaries is then shown.

It is useful to summarise the limits of this approach. Firstly as the thickness of a thin film decreases, the distortion of the helix reduces and so the 'signature' of the thin film structure becomes progressively featureless over the HCF bandwidth; the limit (for a thin film index ~2.2 on a BK7 substrate) is ~20nm. At the 'thick thin film' end, the single interference maximum gradually divides into two interference maxima. The multiple cavity reflections (that for thin films give rise to the standing wave electrical field pattern within the film structure) become progressively integrated out; for a single layer, the HCF function becomes progressively dominated by the sinusoidal term corresponding to the electrical fields reflected off the front and rear film surfaces. Depending on the index, this limit corresponds to a film thickness ~ 2μm.

ANALYSIS

It may be shown that through performing SWLI measurements on a thin film coated substrate (single or multi-layer) together with a 'reference' substrate, such as the glass BK7, it is possible to construct the HCF function [1]. This is defined as the product of the conjugate of the net electrical field reflectance from the 'reference' together with the thin-film/'reference' quotient of the Fourier transform positive frequency sidebands corresponding to the series of SWLI intensity values surrounding the zero path

difference

$$HCF(\nu) = \bar{r}^{*}_{sub}(\nu)\left(\frac{\Im(I_{sfilm}(\bar{z}))_{SB+}}{\Im(I_{sub}(\bar{z}))_{SB+}}\right) \quad \text{.....(1)}$$

The HCF function may therefore be determined over a range of frequencies (typically corresponding to ~480nm to ~720nm). within the two original Fourier positive sidebands. It is related to the net reflected electrical field corresponding to the thin film through :

$$\left.\begin{aligned} HCF(\nu) &= \bar{r}^{*}_{film}(\nu).e^{-i4\pi\nu\bar{\Delta}z_{HCF}} \\ \bar{r}_{film}(\nu) &= HCF^{*}(\nu).e^{-i4\pi\nu\bar{\Delta}z_{HCF}} \end{aligned}\right\} \quad \text{.....(2)}$$

The HCF function therefore has the amplitude and phase *identical* to that of the conjugate of the net reflected electrical field apart from the exponent with the linear phase term (arising from the height difference between the measured coated and 'reference' substrate). Evidently, an exponent with such a linear phase term generates a helix.

The HCF function may therefore be determined over a range of frequencies within the two original Fourier positive sidebands. If the nominal structure of the thin film (multi)layer is known, then using the angular plane-wave spectrum approach together with standard matrix-based thin film analysis [2], the net theoretical electrical field reflectance and therefore the HCF function may be evaluated over the same range of frequencies. This allows the generation of a merit function (based on the quadrature sum of the real and imaginary differences between the extracted and fitted HCF functions) so that, using optimization, the thin film structure may be determined. In this instance, the conjugate gradient approach has been used [3].

RESULTS

The bulk of the experimental work has been carried out using a CCI 6000 Ultra Low Noise instrument [4,5]. In this paper, the approach taken is to concentrate on one particular sample prior to discussing other results obtained in the same manner.

Thin film key test sample

The key sample consists of a BK7 glass substrate (25mm diameter, 5mm thick) one side of which is partially coated with a symmetrical 3-layer structure, nominally 0.5H : L : 0.5H where H and L quarter-waves respectively of TiO_2 and SiO_2 at a nominal wavelength of 0.55μm. Having the substrate partially coated is advantageous since (i) a single measurement provides both the thin film and the BK7 reference measurements and (ii) it allows for independent measurement of the thin film structure by a contact stylus. In fact half of the partially coated face was over-coated with Cr to produce a final surface in the form of a set of quadrants, (i) uncoated BK7,

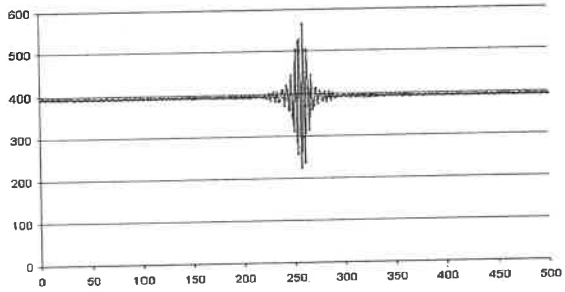

*FIGURE 1 : Interference signal corresponding to the mean of 16 locations for the triplet thin-film coating. The interference objective was a x10 Mirau (0.3NA) and the pixel-binning was 2*2. The surface area of the 16 locations was (10μm)*^{2}

(ii) triplet-thin-film coated BK7, (iii) Cr on BK7 and (iv) Cr on coated BK7. In addition to capturing the interference signals (fig. 1) for analysis, for subsequent verification purposes, the measured step-height for the 'raw' triplet edge and the Cr-coated 'correct' equivalent edge were 230nm and 189nm respectively. Additionally, a set of 5 Nanostep[5] step-height measurements gave the value 183.1± 8.8nm (2σ).

HCF extraction and fitting

Together with the equivalent SWLI measurement of the 'reference' BK7 substrate, the application of eq. (1) directly generates the HCF function corresponding to the measured triplet thin film. Given that the form of this function is that of a scaled ratio of Fourier positive-arm sidebands, there is an inevitable degradation in signal/noise as the boundaries of the two component sidebands are approached (fig. 2). Through eq. (2) and the optimization approach described, the knowledge of the nominal thin film design then enables the experimentally derived real and imaginary components of the HCF function to be matched to an equivalent synthetic pair. In this instance, the optimised parameters for the triplet and Δz_{HCF} were : 0.573H : 0.970L : 0.573H and -69.2nm where H and L are quarter-waves of

TiO_2 and SiO_2 at 550nm. The very slight departures between the extracted and fitted components of the HCF function in fig. 2 are understood to be due to using Sellmeyer representations of the component dispersive refractive indices that are not perfectly mimicking the actual values; TiO_2 in particular is known to exhibit a dispersive index that clearly is a function of the particular thin-film deposition conditions.

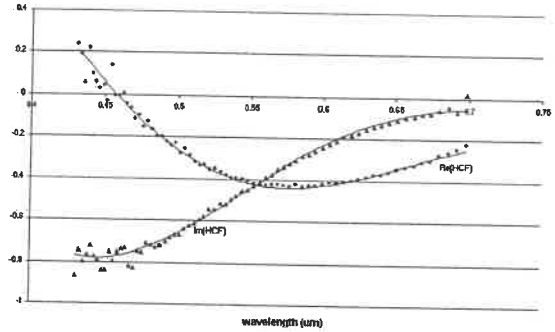

FIGURE 2 : HCF (Helical Conjugate Field) function corresponding to the triplet thin film sample. The real and imaginary components are shown. The solid lines are the corresponding real and imaginary components obtained through thin-film optimisation.

Electrical field reflectance

Having established the HCF function together with the value for Δz_{HCF}, it is then straightforward to apply eq. (2) to extract the electrical field reflectance. This is shown in fig 3.

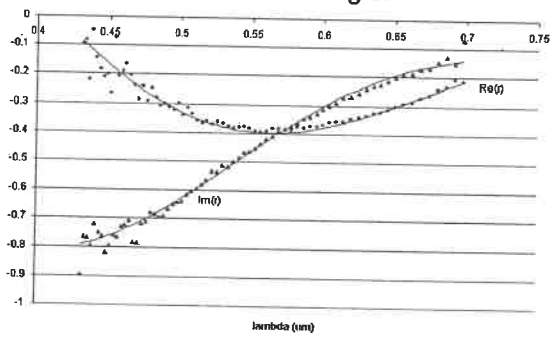

FIGURE 3 : Electrical Field reflectance for the triplet thin-film coating in terms of real and imaginary components. Also shown in solid lines are the corresponding components derived from the thin-film optimisation.

Phase-change on reflection (PCOR)

Having established the electrical field reflectance it is then trivial to re-express this in terms of PCOR. This is shown in fig. 4

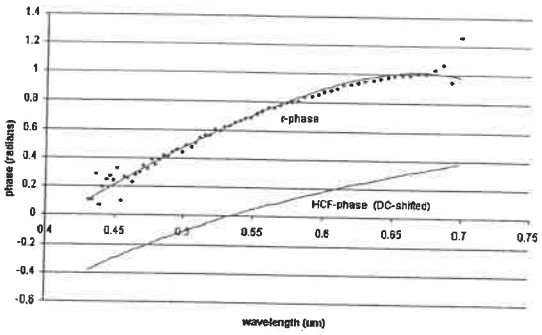

FIGURE 4 : PCOR for the triplet thin-film & (DC-shifted) HCF helical phase arising from ΔZ_{HCF}.

'Thin' thin-film measurement

The results of measuring and similarly characterising two further significantly thinner samples (A and B, respectively SiO_2 on Si and TiO_2 on BK7) are briefly presented in table 1.

	Sample A	Sample B
SWLI	3nm	82nm
PC-SWLI	35nm	79nm
Nanostep	28nm	74.9+-4.4nm
SWLI (Cr-coated)	----	75nm

Table 1 : Comparison of step-heights & film thicknesses

The corrected step-heights are clearly in broad agreement although less so than in the case of the triplet thin film. As the thin-film structure becomes progressively thinner, the phase term within the HCF function begins to be dominated by the layer dispersion and the amplitude of the HCF function becomes progressively featureless. In this regime, to maintain the level of uncertainty in the corrected step-heights, it becomes more important to characterise the dispersive index of the deposited thin film independently

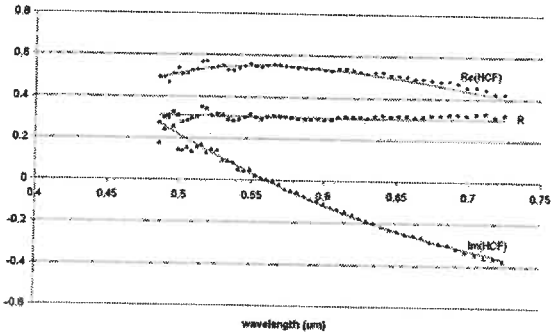

FIGURE 5 : Extracted and fitted HCF function (real and imaginary components) and spectral reflectance, $R(v)$ ($= |HCF(v)|^2$) for sample A..

Single Location Performance

The results above have all been based on HCF functions generated from sets of 16 thin-film interference signals, each corresponding to 2*2 pixel-binning. It is useful to demonstrate the extent to which the signal/noise is compromised through using the thin film interference signal corresponding to a single location. As is apparent from fig. 6, the mid-band noise does exhibit the expected 1/N behaviour whereas at the short wavelength end in particular, this is not the case. Overall, the subsequent fitted parameters for the triplet and ΔZ_{HCF} were 0.564H : 0.974L : 0.564H and -69.6nm where H and L are quarter-waves of TiO_2 and SiO_2 at 550nm. This in turn yielded a corresponding PCOR-corrected step-height of 187nm, in very close agreement with the earlier result.

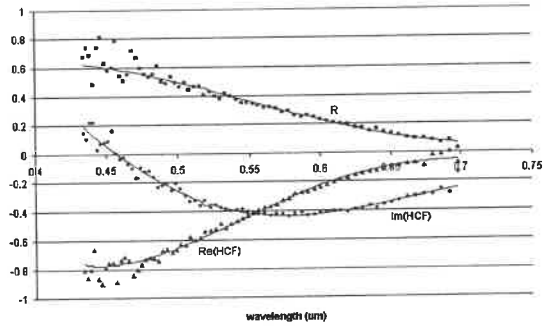

*FIGURE 6 : Extracted & fitted (solid lines) HCF functions (real & imaginary components) together with R, the reflectance corresponding to the triplet thin film sample. This data is derived from a single location interference signal set. the NA is 0.3 and the pixel-binning 2*2. The single location corresponds to an area of $(2.5\mu m)^2$.*

CONCLUSION

Scanning white light interferometry (SWLI) is now an established technique for the measurement of surface topography. It has the capability of combining sub-nanometre inter-ferometric resolution with a range limited only by the z-traverse, typically at least 100μm. Through the introduction of the helical conjugate field (HCF) function, a useful additional capability has been demonstrated; this is the ability to measure thin films on a local scale - $(2.5\mu m)^2$ has been demonstrated. In addition to single layer thin films, layer thickness extraction for a 3-layered thin film has been demonstrated. Also, the related capabilities of step-height measurement through PCOR-correction and the measurement of the spectral reflectance on the same local scale have been demonstrated. In terms of the minimum film thickness limit of the approach, it has been shown that for single layer films of less than a quarter-wave in optical thickness, the amplitude of the HCF function becomes progressively featureless while the phase becomes dominated by the material dispersion; in this context it is best to have accurate independent knowledge of such dispersion.

The author would like to thank the directors of Taylor Hobson Ltd for their support of this work.

REFERENCES

1. Mansfield, D, 2006, The Distorted Helix : Thin Film Extraction from Scanning White Light Interferometry, *Proc. of SPIE Vol.6186*
2. Macleod, F.A., 2001, *Thin-Film Optical Filters*, 3rd edition, Institute of Physics
3. Press W. *et al*, *Numerical Recipes in C - The Art of Scientific Computing*, Cambridge University Press
4. Bankhead A. *et al*, 2004, *Interferometric Surface Profiling*, GB2390676
5. Taylor Hobson Ltd, Leicester UK, 2005

REACTIVE ATOM PLASMA (RAP™) PROCESSING OF OPTICAL SURFACES

Pradeep Subrahmanyan, George Gardopee, Peter S. Fiske and Andrew Chang
RAPT Industries Inc.
Livermore, CA, USA

INTRODUCTION

Increasing demands are being made on optical surfaces, these being driven by shorter wavelengths, increased precision and the need for faster, smaller optics demanding complex aspherical surfaces to replace multiple spherical surfaces. Lately, there have been multiple innovations in final finishing (with sub-aperture, deterministic polishing steps) and metrology (stitching interferometry, computer generated holograms) of such optics. Issues such as sub-surface damage, mid-spatial frequencies, and cost and lead time of manufacturing still plague the development and deployment of precision optics.

A novel integrated manufacturing process comprising a split chemical mechanical polishing technique has been developed that addresses the issues with current modern optical manufacturing techniques.

INTEGRATED MANUFACTURING PROCESS

The conventional approach to the manufacture of precision optics relies on some form of a Chemical Mechanical Polishing (CMP) step. CMP involves pushing down mechanically on the precision surface in the presence of chemical abrasives, and invariably introduces a certain amount of damage to the surface [1]. This damage is heavily dependent on the abrasives used (mostly grit size), relative velocity between the tool and the surface, and the normal pressure applied. This damage is usually removed through a laborious process of using finer and finer grit and reduced polishing pressures over a series of iterations. Additionally, a damage mitigation step could be added to the loop and this invariably takes the form of an etching step as illustrated in *FIGURE 1*. This sequence of steps is repeated many times, until the desired precision on the surface is achieved. Surface metrology is performed in between cycles to guide the following iteration(s).

The conventional approach has been applied with great success to optics manufacturing. One of the key advances that has permitted the continued application of conventional techniques has been the advent of sub-aperture deterministic polishing techniques. However, two factors are causing the continued application of the conventional approach to break down. These are:

1. Increasingly complex geometries

   This is due to either very high aspect ratios (caused by very lightweight or thin substrates), or difficult free form geometries (caused by low f/#s in the case of aspherical optics).

2. Advent of advanced materials such as ceramics

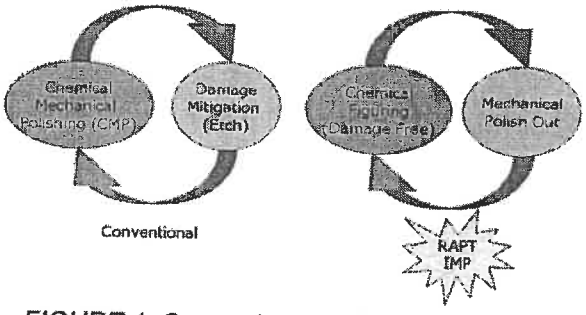

FIGURE 1. Comparison of Conventional and RAP approaches

This is because the CMP process imparts an unknown amount of stress to the surface layer. The metrology between iterations measures only the deviation from the desired geometry and there are no established techniques today to determine the state of stress/strain underneath the surface. As these substrates get thinner, this unknown surface stress causes uncontrolled deformation in the surface, either over a period of time, or worse in between and during process cycles. During subsequent cycles with finer grit and lower normal pressures, the damaged surface is removed, causing the state of stress to relax – this causes additional deformation that is uncontrolled by the process. This then leads to a very slow (undeterministic) convergence to the desired surface geometry and leads to

serious disruptions in the manufacturing process.

In this paper, we discuss a radically different approach which enables rapid, reliable, low-cost damage-free manufacturing of these precision surfaces. Our Integrated Manufacturing Process (IMP) involves serializing the chemical and mechanical steps rather than doing them in parallel as in CMP. In our process, the chemical figuring (shaping) step is responsible for imparting the desired geometry to the surface in a non-contact manner. Given the non-contact manner of the figuring step, the cycles become deterministic, as the substrate is essentially stress-free. A metrology step is used as before to determine the deviation from the desired geometry at each iteration. A mechanical buffing or polish-out step is also required as part of the cycle since the chemical etching step, by its very nature increases roughness due to selective etching at damage sites, grain boundaries, etc., which are widely prevalent on the surface being figured. The mechanical buffing step is designed to be conformal to the geometry being manufactured and uses low contact pressures to essentially provide a roughness mitigation step without altering the figure of the surface.

RAP™ Processing

Reactive Atom Plasma (RAP™) processing is a non-contact, sub-aperture, deterministic material removal technology operating at atmospheric pressure. The process involves the delivery of reactive radicals to the surface being machined. This is typically done by creating a plasma into which a reactive precursor chemical is injected and broken down into reactive radicals which are then delivered to the surface. The appropriate precursor chemistry is chosen so that the by-products of reaction with the substrate are volatile and removed in the gas phase from the substrate without redeposition or debris forming back on the surface. As a result, the surface left behind is damage and contaminant-free. One embodiment of the RAP™ technology is illustrated in *FIGURE 2*. Here, an argon plasma is created (typically by using inductively coupled RF power to excite the plasma) and a reactive precursor such as CF_4 introduced into the plasma. Other chloro or fluoro-carbons could be used just as well depending on the chemistry requirements. This gets broken down into individual carbon atoms and highly reactive fluorine radicals as illustrated in *FIGURE 2*. The stream of reactive atoms is directed onto the surface of the glass (in the example) substrate and the volatile by-products of reaction are SiF_4 and CO_2, both of which are exhausted in the gaseous form. The chemical reaction rate with the substrate is dependent on

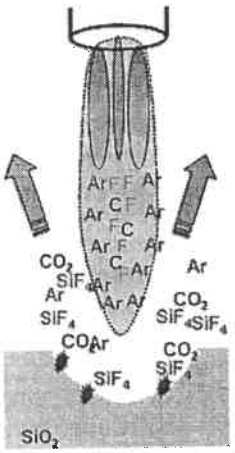

FIGURE 2. RAPT Processing

the concentration of the radicals, the chemistry of the substrate itself, and the temperature of processing. The reaction follows the Arrhenius law, and the etch rate "*Rate*" using the RAP process is given by the Arrhenius law:

$$Rate = Ae^{-E_a/RT} \qquad (1)$$

where A is a phenomenological rate constant, E_a is the activation energy, R the universal gas constant[1] and T is the absolute temperature of the reaction. It is easily seen that the etch rate varies exponentially with temperature. Practical

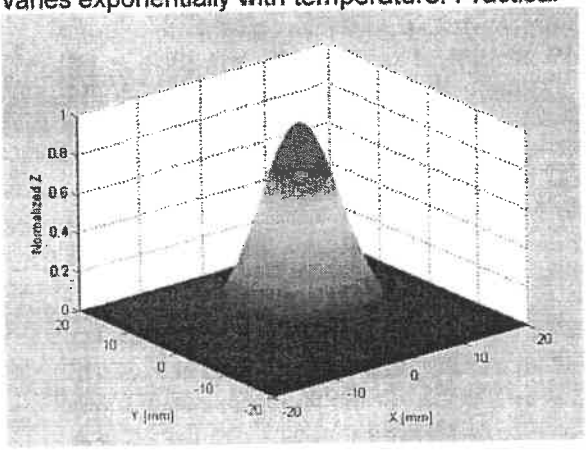

FIGURE 3. Gaussian tool footprint

issues however limit processing temperatures.

[1] R has the value of 8.314×10^{-3} kJ mol^{-1}K^{-1}

Unlike traditional sub-aperture polishing techniques which have a static footprint, the RAP™ process has a footprint that is dynamic due to the exponential temperature dependence. While this complicates the tool path algorithm, the footprint also has a smooth, symmetric Gaussian shape as illustrated in *FIGURE 3*. The Gaussian shape minimizes ringing due to high-frequency artifacts and minimizes and in certain cases eliminates mid-spatial frequency errors.

As with any other sub-aperture technique, the surface being machined is measured using metrology techniques such as interferometry or profilometry and an error map is determined by subtracting this surface map from the desired geometry. This error map is used to compute an iterative material removal map and a tool-path algorithm computes the dwell time of the plasma over the surface to be machined, by deconvolving the tool footprint from the material removal map.

Conformal Polishing

As noted before, the RAP™ process corrects the low and mid spatial frequency errors. A conformal polishing step is then used to polish out the high-frequency artifacts, without influencing the low-frequency errors

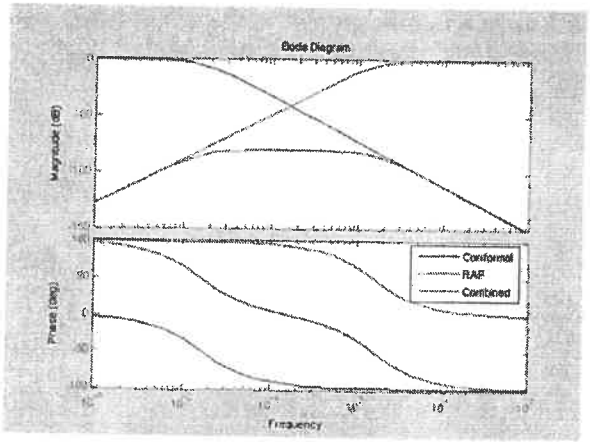

FIGURE 4. Notional frequency response of the Integrated Manufacturing Process

FIGURE 4 illustrates the RAP™ process and the conformal polishing step on a notional 1-dimensional frequency axis (chosen for ease of visualization). The RAP™ step can be modeled as a high-pass filter as discussed earlier, and the conformal polishing step is designed with the spatial frequency characteristics designed such that the combination of the two processes results in the desired attenuation of errors in the surface over the desired frequency range.

A combination of feed-forward and feedback control techniques as discussed in [2] can then be applied to ensure desired convergence. This, along with the lack of significant stress in the substrate, leads to truly deterministic and rapidly convergent manufacturing of precision optics.

RESULTS

As discussed earlier, RAP™ processing can be done with a variety of tool sizes depending on the spectral content of the error map. A range of tool sizes from 0.5mm to 50mm full-width half max have been demonstrated.

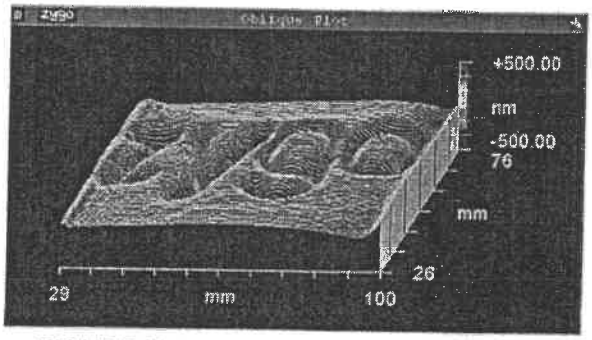

FIGURE 5. Nano-graffiti lettering. "Zygo" on fused silica

FIGURE 5 illustrates some nano-graffiti on fused silica – this is meant to demonstrate the tool-size and the control over the etching, and is not terribly useful. *FIGURE 6* illustrates a flat fused silica substrate that has a P-V error of 5 waves while *FIGURE 7* illustrates the same surface after 2 RAP™ iterations.

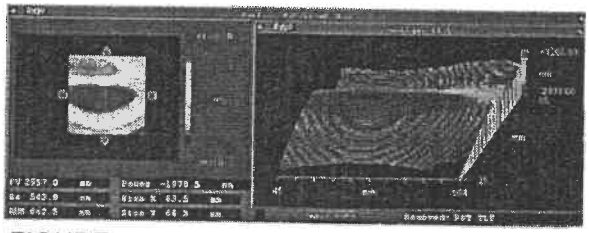

FIGURE 6. Flat surface prior to IMP (5 waves P-V)

The P-V surface error has been reduced to 1 wave P-V in less than a half hour in this example. Even more important, especially with lightweight optics is the damage removal during the figuring process itself [1].

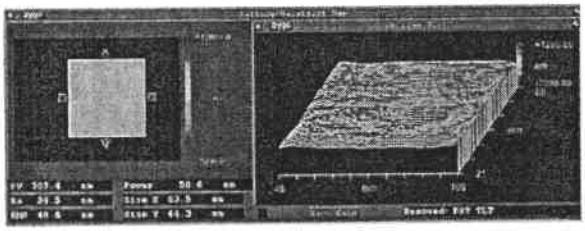

FIGURE 7. Flat surface post IMP (1 wave P-V)

The integrated manufacturing process has also been applied to the figuring of powered aspherical optics and has been shown to be a rapid cost-effective technique to fabricate damage-free precision surfaces.

CONCLUSIONS

Conventional approaches to the fabrication of high-aspect ratio precision surfaces are limited due to the damage imparted to the substrates and the resulting stress. An Integrated Manufacturing Process has been demonstrated to provide rapid and predetermined convergence to the desired shape. This IMP is being deployed to manufacture optics to about 0.25 waves P-V at which point in time, existing final finishing approaches can take over to obtain a surface with relatively little damage and with minimal mid-spatial frequency errors.

The IMP, and more specifically RAP™ process cast the manufacturing of precise optical surfaces in an entirely new light, *i.e.*, the creation of very precise surfaces with fairly imprecise tools. Given the non-contact and deterministic nature of the RAP™ process, the tool is easily implemented on a dexterous robotic manipulator. With relatively low sensitivity of the process to the height of the plasma above the surface, requirements on the impedance (stiffness) of the precision machine implementing the RAP™ process are significantly reduced. This permits the implementation of the RAP™ process on a tool with varying impedance over the workspace such as a dexterous robotic manipulator. Such a dexterous design also permits in-situ machining of pads for assembly of precision optics thus accelerating the assembly cycles and reducing the cost.

ACKNOWLEDGEMENTS

The authors are grateful to Dr. Jeffrey Carr for some of the early work on RAP. This work was supported under US. Army contracts DAAD19-03-2-0003 and W911NF-04-2-0001 and U.S. MDA contract W9113M-06-C-0067. RAP™ is a trademark of RAPT Industries, Inc.

REFERENCES

1. Verma, Y., Fiske, P.S., Subrahmanyan, P.K., and Gardopee, G., Damage-free Processing of Silicon Carbide Optics, *in Annual Proceedings of the American Society for Precision Engineering, 2006*
2. Webb, R.D., and Hardt, D.E., 1991, A Transfer function description of sheet metal forming for process control, *ASME Transactions, Journal of Engineering for Industry*, 44: 52-113.

TWO-DIMENSIONAL ENCODER WITH PICOMETER RESOLUTION USING MULTI-TUNNELING PROBES SCANNING TUNNELING MICROSCOPE AND REGULAR CRYSTALLINE SURFACE

Masato Aketagawa[1], Hiroshi HONDA[1], Masashi Ishige[1] and Chaikool Patamaporn[1]
[1]Department of Mechanical Engineering, Nagaoka University of Technology
1603-1 Kamitomioka, Nagaoka, Niigata, 940-2188 JAPAN

INTODUCTION

Nanotechnology and ultra-precision engineering have progressed very rapidly. Displacement measurements with less than sub-nanometer resolutions have become essential and critical. A scanning tunneling microscope (STM) [1] is a popular tool in surface engineering and can be used to obtain images of atoms on a crystalline surface. A graphite crystalline surface has uniform and stable 2-dimensional symmetrical periodicity, i.e. two unit lattice vectors a_1 and a_2, whose length and intersectional angle are 0.246 nm and 60° [2], respectively, over a wide mono-crystalline area of approximately 100 μm^2, when the crystal is stress-free. Therefore, the two unit lattice vectors of the graphite crystalline surface can be used, in combination with an STM, as 2-dimensional references with sub-nanometer resolution or less [3-4]. In this article, we propose a new 2-dimensional encoder using multi-tunneling-probes scanning tunneling microscope (MTP-STM) as detectors and the unit lattice vectors a_1 and a_2 on a graphite crystalline surface as references. The measurement principle, the instrumentation and the experimental results are discussed.

PRINCIPLES & INSTRUMENTATION

Three points method

Figure 1 shows an ideal atomic image of the graphite crystalline surface. In figure 1, (a_1 , a_2) and (k_1 , k_2) are the unit lattice vectors between an α sites [2] and their reciprocal vectors, respectively. The unit lattice vectors and the reciprocal vectors have the following relationship,

$$a_i \cdot k_j = \delta_{ij} \ (i, j = 1,2 : \text{Kronecker's } \delta). \quad (1)$$

In the figure 1, $k_3 = k_1 - k_2$. Topographical height $Z=Z(r)$ at an arbitrary lateral position r can be represented approximately as:

$$Z(r) = \sum_{i=1}^{3} A_i \cos(2\pi k_i \cdot r), \quad (2)$$

where A_i (i =1, 2, 3) is a contrast parameter for the atomic structure. In figure 1, we assume that three STM probes (tips) are located properly on the three points (A, B, C) which satisfy the following relationship:

$$r_A = ma_1 + na_2, \quad (3)$$

$$\left.\begin{aligned} r_B &= (m+\tfrac{1}{2})a_1 + na_2 \\ r_C &= ma_1 + (n+\tfrac{1}{2})a_2 \end{aligned}\right\}, \quad (4)$$

In the equations (3) - (4), (m, n) is a set of real numbers to show the position of the representative point A. The vector r_A also represents the relative position (displacement) vector between the multi-tips and the crystalline surface on the XY sample stage. From equations (1) - (4), we can obtain the following two relationships:

$$\left.\begin{aligned} Z(r_A) + Z(r_B) &= 2A_2 \cos 2\pi m \\ Z(r_A) + Z(r_C) &= 2A_1 \cos 2\pi m \end{aligned}\right\}. \quad (5)$$

If we locate the multi-STM tips properly on the points (A, B, C), a set of (m, n) can be determined using equation (5). This means that a 2-dimensional displacement using linear sums of the multi-tunneling-current signals of the points (A, B, C) is possible. To obtain the linear height $Z(r)$ from the tunneling currents, the use of log amplifiers for each STM tip is suggested. In the paper, the method to determine (m, n) using equation (5) is called as the three points method. The points (A, B, C) is called as the three points group.

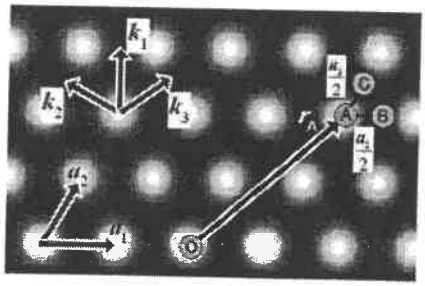

Figure 1 Ideal atomic image of a graphite crystalline surface. (a_1 , a_2) and (k_1 , k_2) are the unit lattice vectors between the α sites and their reciprocal vectors, respectively. (A, B, C) are the measurement points for the tunneling currents.

Eight points method

Figure 2 shows the locations of the multi STM tips on a double crystalline area of the graphite crystal. In the figure, the unit lattice vectors of the two crystalline areas Sα and Sβ are slightly different. However, the two crystalline areas are set on the

same XY sample stage, and the averaged planes of each crystalline area must be parallel. In figure 2, (a_1, a_2) and (a'_1, a'_2) show unit lattice vectors for the two crystalline areas, and (α, β) are intersection angles of (a_1, a'_1) to the X-axis of the sample stage. The unit lattice vectors are represented as:

$$\left.\begin{aligned} \boldsymbol{a}_1 &= d\begin{pmatrix}\cos\alpha\\ \sin\alpha\end{pmatrix},\ \boldsymbol{a}_2 = d\begin{pmatrix}\cos(\alpha+\frac{\pi}{3})\\ \sin(\alpha+\frac{\pi}{3})\end{pmatrix}\\ \boldsymbol{a}'_1 &= d\begin{pmatrix}\cos\beta\\ \sin\beta\end{pmatrix},\ \boldsymbol{a}'_2 = d\begin{pmatrix}\cos(\beta+\frac{\pi}{3})\\ \sin(\beta+\frac{\pi}{3})\end{pmatrix}\end{aligned}\right\}. \quad (6)$$

In figure 2, points A and E are representative points and vectors r_A and r_E show the position (displacement) vectors of the sample stage ($r_A = r_E$). The position vectors r_A and r_E can be written as:

$$\left.\begin{aligned} \boldsymbol{r}_A &= m_1\boldsymbol{a}_1 + n_1\boldsymbol{a}_2\\ \boldsymbol{r}_E &= m_2\boldsymbol{a}'_1 + n_2\boldsymbol{a}'_2\end{aligned}\right\}, \quad (7)$$

where (m_1, n_1) and (m_2, n_2) are sets of real numbers. From equations (6) and (7), we obtain:

$$r = r_A = r_E = \frac{\sqrt{3}}{2\sin(\beta-\alpha)}(n_1\boldsymbol{a}'_1 - n_2\boldsymbol{a}_1). \quad (8)$$

Once (n_1, n_2) can be obtained in the case β does not equal α, then the displacement vector r (= r_A = r_E) of the sample stage can be determined. In figure 2, we assume the eight STM tips are located properly at the eight points (A, B, C, D) and (E, F, G, H) satisfying equation (7) and the following conditions:

$$\left.\begin{aligned} \boldsymbol{r}_B &= (m_1+\tfrac{1}{2})\boldsymbol{a}_1 + n_1\boldsymbol{a}_2\\ \boldsymbol{r}_C &= (m_1+\tfrac{1}{2}+\tfrac{1}{8})\boldsymbol{a}_1 + (n_1-\tfrac{1}{4})\boldsymbol{a}_2\\ \boldsymbol{r}_D &= (m_1+\tfrac{1}{8})\boldsymbol{a}_1 + (n_1-\tfrac{1}{4})\boldsymbol{a}_2\\ \boldsymbol{r}_F &= (m_2+\tfrac{1}{2})\boldsymbol{a}'_1 + n_2\boldsymbol{a}'_2\\ \boldsymbol{r}_G &= (m_2+\tfrac{1}{2}+\tfrac{1}{8})\boldsymbol{a}'_1 + (n_2-\tfrac{1}{4})\boldsymbol{a}'_2\\ \boldsymbol{r}_H &= (m_2+\tfrac{1}{8})\boldsymbol{a}'_1 + (n_2-\tfrac{1}{4})\boldsymbol{a}'_2\end{aligned}\right\}. \quad (9)$$

From equations (2), (7) and (9), the following results are obtained:

$$\left.\begin{aligned} Z(\boldsymbol{r}_A) + Z(\boldsymbol{r}_B) &= 2A_2\cos 2\pi n_1\\ Z(\boldsymbol{r}_C) + Z(\boldsymbol{r}_D) &= 2A_2\sin 2\pi n_1\\ Z(\boldsymbol{r}_E) + Z(\boldsymbol{r}_F) &= 2A'_2\cos 2\pi n_2\\ Z(\boldsymbol{r}_G) + Z(\boldsymbol{r}_H) &= 2A'_2\sin 2\pi n_2\end{aligned}\right\}. \quad (10)$$

Equation (10) shows that linear sums of multi-tunneling-current signals from points (A, B, C, D) and (E, F, G, H) can be used to derive (n_1, n_2) with its fractional part, i.e., the two-displacement of the sample stage can be determined with interpolation less than the lattice spacing. In the paper, the method to determine (n_1, n_2), i.e., the displacement vector r of the sample stage, is called as the eight point method. The points (A, B, C, D) or (E, F, G, H) is also called as the four points group.

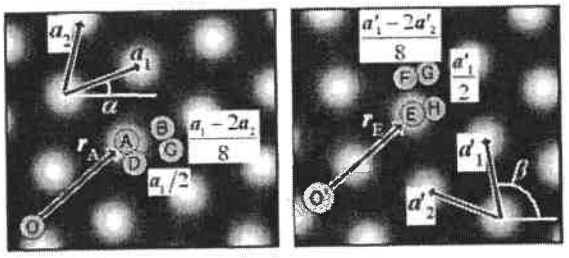

(a)Sα (b) Sβ

Figure 2 *Two ideal atomic images of the graphite crystalline surface, whose crystalline orientation in the two images are not same. (a_1, a_2) and (a'_1, a'_2) show unit lattice vectors for the two crystalline areas (a) Sα and (b) Sβ*

Semi-real time multi-probes

It is very difficult to align multi-STM tips at the proper multiple points with an accuracy of less than the lattice spacing in the three points method or the eight points method. We propose a different method to obtain multi-current-signals from multi-points using a fast lateral dither vibration applied to one STM tip. **Figure 3** shows trajectories of high-speed lateral dither vibrations applied to an STM tip for the three points group and the four points group, respectively. In figure 3 (a), to obtain tunneling currents from three points (A, B, C), a circular dither modulation is applied to an STM tip, and the data sampling interval is set to 120° in phase. In figure 3 (b), to obtain tunneling currents from the four points (A, B, C, D) or (E, F, G, H), an ellipsoidal dither modulation, whose major axis is parallel to the A-B and (E-F) line, is applied to an STM tip, and data sampling interval is set to 90° in phase.

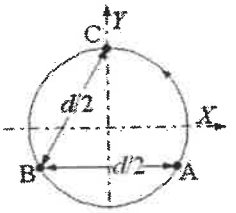

(a) Three points group

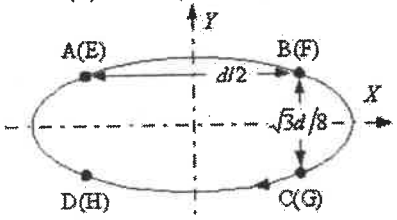

(b) Four points group

Figure 3 *Trajectories of lateral dither modulation applied to an STM tip. In the figures, the lateral axis is assumed to be the crystalline orientation.*

Instrumentation

In order to evaluate the proposed methods, a double-tunneling-probes scanning tunneling microscope (DTP-STM) was constructed, as shown in **figure 4**. The DTP-STM includes a base unit, a scanner unit, two STM heads with two STM tips, and a capacitance sensor. A tube type XY piezo-actuator is used as a sample scanner. A graphite crystal [5] is set on the sample scanner. The two STM heads are symmetrically placed with respect to the scanner. The STM heads have XYZ tube piezo-actuators as tip scanners for the Z-axis servo and high speed lateral dither modulation. Each STM head scans the three points group or the four points group using the lateral dither modulation. The capacitance sensor [6] is attached to the scanner unit to measure the displacement of the sample scanner. The measurement direction of the capacitance sensor is fixed at 45° to the X-axis of the sample scanner. Improvement of the resolution of 0.1 nm for the capacitance sensor was achieved with low pass filtering amplifier.

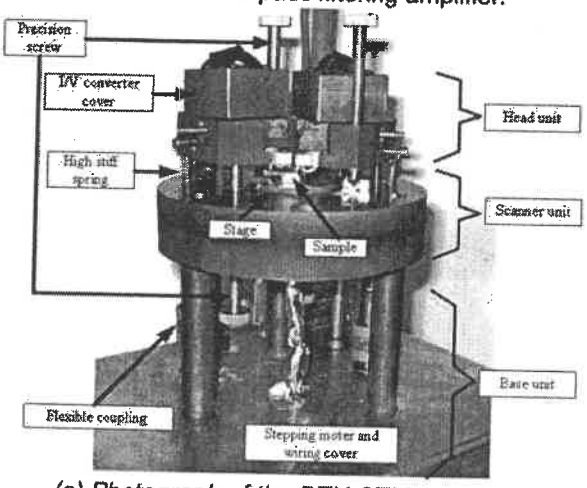

(a) Photograph of the DTU-STM

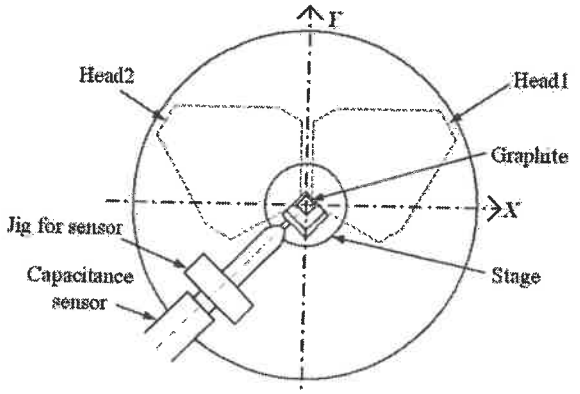

(b) Top view of a sample XY scanner unit

***Figure 4** Double-tunneling-probes scanning tunneling microscope (DTP-STM). (a) Photograph of the DTP-STM. (b) Top view of a sample XY scanner unit.*

EVALUATION EXPERIMENTS

Three points method

The three points method, wherein one STM tip is modulated with a circular dither vibration, was evaluated. The amplitude and the frequency of the dither modulation were 0.29 nm and 5.13 kHz, respectively. In the experiment, driving signals of reciprocal motion with an amplitude of approximately 40 nm and a frequency of 1.25 Hz along the 45° direction to the X-axis were applied to the scanner, and the derived displacement using the three points method was compared with the capacitance sensor. The whole measurement contains 20 reciprocal lines. **Figure 5** shows the displacement measurement comparison between the three points method and the capacitance sensor. Figure 5 (a) shows the whole displacement from the 1st to the 20th lines. Figure 5 (b) shows time variations of the difference output of the three points method and the capacitance sensor at 1st and the 20th lines after thermal drift compensation. From figure 5 (b), the time variations of the displacement at the 1st and 20th reciprocal lines coincided within a dispersion of 0.2 nm. The tip speed was around 100 nm/s.

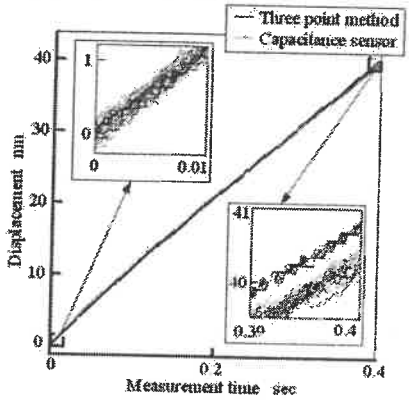

(a)

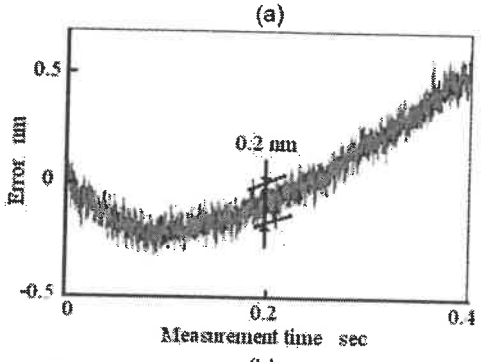

(b)

***Figure 5** Comparison of displacement measurement between the three points method and the capacitance sensor.(a) Comparison of whole displacement measurement (from 1st to 20th reciprocal lines).(b) Difference between at the 1st and 20th reciprocal lines after thermal drift compensation.*

Eight points method

The eight points method was also evaluated through comparison with the capacitance sensor. The lateral ellipsoidal dither modulations (amplitude of major and minor axes was 0.35 nm and 0.15 nm, frequency was 5.0 kHz) were applied to the two STM tips. In the experiment, driving signals of reciprocal motion with the amplitude of approximately 40 nm and frequency of 1.22 Hz along the 45° direction to the X-axis were applied to the XY scanner. The measurement result contained 20 reciprocal lines. **Figure 6** shows the displacement measurement comparison between the eight points method and the capacitance sensor. Figure 6 (a) shows the whole displacement from the 1st to the 20th lines. Figures 6 (b) shows the time variation of the difference between the output of the eight points method and the capacitance sensor at the 1st and 20th lines after thermal drift compensation. From figure 6 (b), the time variations at the 1st and 20th lines are coincident within a dispersion of 0.07 nm. Figure 6 (b) also proves that the difference between the proposed method and the capacitance sensor is approximately 0.6 nm (1.5%). The results show that the eight points method has the feasibility for 2-dimensional displacement measurement with a resolution or uncertainty on the order of 10 pm.

CONCLUSIONS

In the paper, we propose a two-dimensional (2-D) encoder with picometer resolution using the MTP-STM as detectors and the graphite crystalline lattice as a reference. We also propose a fast lateral dither vibration applied to one STM tip to obtain multi-current-signals from multi-points in semi real-time way. The proposed methods were compared with a capacitance sensor. The experimental results show that the proposed method has the capability for measuring 2-D lateral displacement with an uncertainty on the order of 10 pm with a maximum measurement speed of 100 nm/s or more.

ACKNOWLEGEMENTS

Partial finance support of the Scientific Research Fund of the Japanese Ministry of Education, Culture, Sports and Technology is gratefully acknowledged.

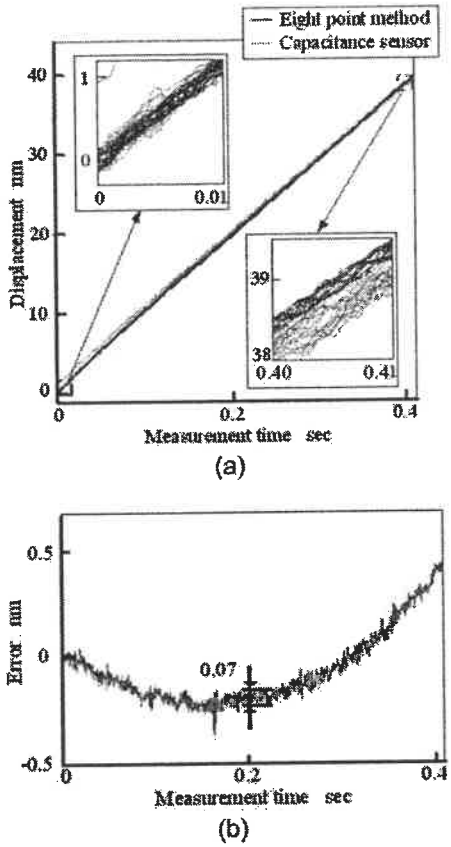

Figure 6 Comparison of displacement measurement between the eight points method and the capacitance sensor. (a) Comparison of whole displacement measurement (from 1st to 20th reciprocal lines). (b) Difference at the 1st and 20th reciprocal lines after thermal drift compensation.

REFERENCES

[1] G. Binning, H. Roher H, CH. Gerber and E. Weibel, Appl. Phys. Lett. **40** (1982), 178.

[2] S. Park, C. Quate, Appl. Phys. Lett. **48** (1986), 112.

[3] M. Aketagawa, K. Takada, K. Kobayashi et al, Meas. Sci. Technol. **9** (1998), 1076.

[4] P. Rerkkumsup, M. Aketagawa, K.Takada et al, Rev. Sci. Instrum., **75** (2004), 1061.

[5] Advanced Ceramics Corporation, ZYA-S, OH, USA.

[6] ADE corporation, Microsense, USA.

MANUFACUTURING THE DRAGONFLY EYE MULTI-LAYER, COMPOUND OPTIC ARRAY

David. D. Gill, William. C. Sweatt, Andre A. Claudet, David P. Adams, Michael J. Vasile, V. Carter Hodges
Manufacturing Science and Technology Center
Sandia National Laboratories
Albuquerque, NM, USA

INTRODUCTION

Sandia National Laboratories recently designed a novel, multi-layer, compound optic providing wide field of view in a highly compact package and based on the eye of a dragonfly. The design consists of an array of 660um diameter convex aspherical lenslets arrayed around the outer surface of a 2mm radius hemispherical shell. These lenslets are aligned with an equal number of spherical concave lenslets on the inside of the shell. The shell is positioned on a smaller hemispherical shell and the lenslet pairs are aligned with tapered conical holes that prevent crosstalk between the optical pathways. This shell is in turn positioned on the end of a spherically ground bundle of fiber optics which transmit light signals to a detector unit. The optical assembly enables an entire system for horizon to horizon (~2π steradian) viewing in a cube of less than 5mm on a side.

The manufacture of this multi-layer compound optic has presented many challenges including the creation of convex, aspherical micro optics, the alignment of the lenslets on the inside and outside of the hemispherical shell, the creation and alignment of the tapered conical holes, and assembly of the entire package. The creation of the outer hemispherical shell and its lenslets has required 5 axis motion in the diamond turning machine and the development of a means of precisely aligning the part to position the internal lenslets with respect to the external lenslets. This positioning, which would be fairly routine on a flat array, turned out to be quite challenging on the small interior of the hemispherical shell with tool clearance presenting significant challenges. A fixture was designed that leveraged the LVDT probing capabilities of the machine for alignment and part clocking. The creation of the convex, aspherical lenslets on the exterior of the shell also presented significant challenges. The challenges of creating these lenslets on the curved exterior of the shell will be described. The authors will present the challenges and the methods utilized to produce this component along with analysis of the optics produced.

THE DRAGONFLY EYE OPTIC

The dragonfly eye optic is designed as a mesoscale, multilayer optical array giving nearly a horizon to horizon (2π steradian) field of view. The optical system, shown in Figure 1, has 4 major components consisting of a 2mm radius outer hemispherical shell, a 1.4mm radius light-sizing shell, a spherically ground fiber bundle, and an imaging CCD array. This paper primarily reports on the manufacturing of prototypes of the outer shell.

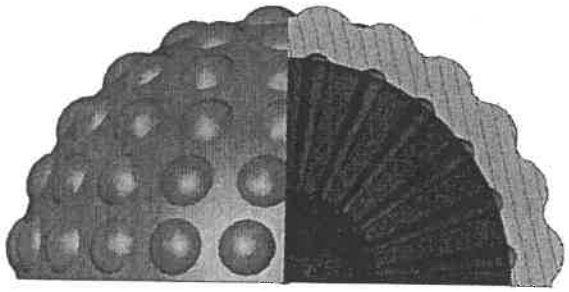

FIGURE 1. A cutaway view of the dragonfly eye optic shows the outer hemishell with convex aspherical optics and concave spherical optics, the light sizing tapered holes of the inner hemishell, and the spherically ground fiber optic bundle.

The Outer Shell

This outer shell of the assembly is a 2mm radius hemispherical shell with a wall thickness of 0.6mm. The outer surface of the shell is covered with convex aspherical lenslets spaced as closely as possible. The interior of the shell has concave spherical lenslets that are aligned with the lenslets on the exterior of the part. The exterior lenslets have a 420um radius and a 600um diameter aperture. The inner lenslets have a 780um radius and a 450um aperture. Initial prototypes have had 7 lenses around the surface of the optic.

Several means of creating the convex aspherical lenslets were considered including on center turning and diamond milling. Though on-center turning would have given the highest quality individual optics, the need to reposition the hemisphere for each new lenslet to be turned was deemed infeasible. The optics on the exterior and interior of the shell needed to be positioned within 3um radially, so the repeatability requirements for the positioning mechanism would be very difficult to achieve. It was determined that diamond milling could produce the optics with good positional repeatability and that the slight loss of clear aperture at the center of the optic would be outweighed by increased accuracy in the positioning of the optic. The concave, aspherical diamond mill used for this project is shown in Figure 2.

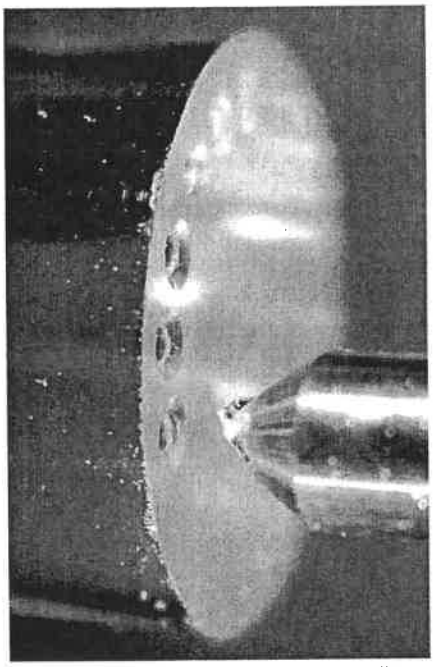

FIGURE 2. The concave aspherical diamond mill creating test lenses in acrylic.

To diamond mill the lenslets on the outer shell, a high repeatability rotary table was purchased and mounted on the Z axis of the machine such that it rotates around an axis parallel to Y and perpendicular to X and Z. The quoted positioning accuracy of the table is ±1.5 arcseconds and the repeatability is ±0.3 arcseconds. A high speed grinding spindle was mounted on top of the rotary table and aligned with the axes of the machine tool so that its axis of rotation was coaxial to the spindle axis when the rotary table was positioned at 90 degrees elevation (the pole of the hemisphere). The spindle is shown as mounted on the indexing table in Figure 3. It was now necessary to create a repeatable fixturing system to hold and position the optics and to develop a means of creating concave aspherical optics.

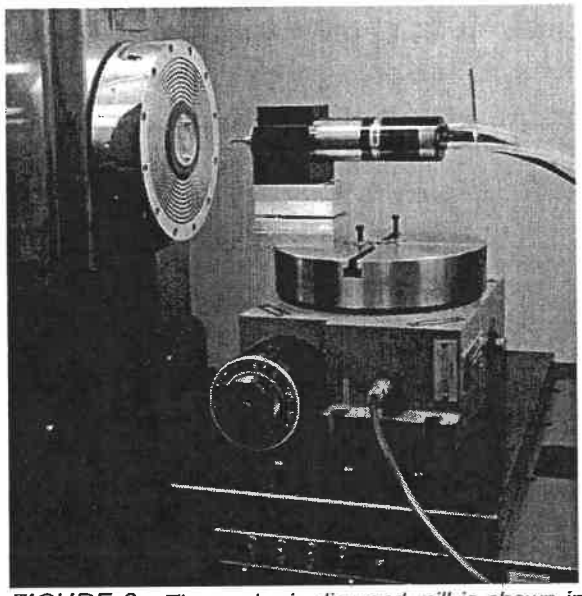

FIGURE 3. The aspheric diamond mill is shown in the collet of the high speed spindle which is mounted on a highly repeatable indexing table and positioned on the Z axis of the diamond turning machine.

Fixturing the Outer Shell

Repeatable fixturing of the optic was achieved by making the optic be part of the fixture as shown in Figure 4. A 50.4mm diameter x 2.8mm thick acrylic disk was diamond turned on both sides and on the OD such that the part could be accurately centered on the spindle vacuum chuck. The disc had two holes drilled in it approximately 180° apart. Two precision spheres (Class 5) with 0.25" diameter were glued into the holes so that the spheres protruded from the acrylic disk on both sides. A porous carbon disk was turned and faced on the machine and two concave spherical features were milled so that the precision spheres had clearance when the acrylic disk was mounted on the porous carbon on the machine spindle's vacuum chuck.

With this setup, the procedure for making dragonfly eyes required the turned acrylic disk to be mounted and centered, using an electronic indicator, on the carbon disk on the spindle of the machine. Once centered, the outer surface of the hemisphere was turned. By this method it

was centered on the acrylic disk to a within the centering resolution which is better than 100nm.

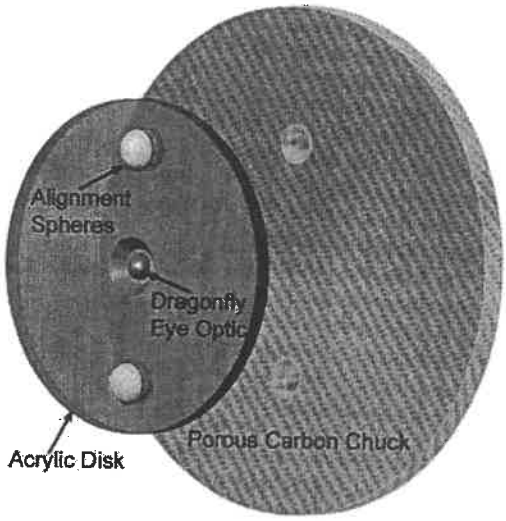

FIGURE 4. The fixturing method for manufacturing the acrylic Dragonfly Eye optic is shown in this exploded view. The acrylic disk has two precision steel spheres glued into holes approximately 180° apart. The assembly is mounted to the machine's vacuum chuck on a porous carbon disk with spherical clearance pockets for the spheres.

Next, the spindle mode was changed from free running to positioning (C-axis) mode and homed. An iterative method of aligning (clocking) the part axis to the machine's linear axes was performed. The C axis was rotated until the spheres were roughly lined up vertically and the machine's LVDT measuring system was used to traverse a horizontal trace across each sphere to find the high point of the trace as shown in Figure 5. Once the high points were located, the C-axis was rotated to move these points toward being vertical (aligned with the Y-axis of the machine). Because the distance of each sphere to the center of the part is not a precisely controlled distance, the angle of rotation cannot be accurately determined. Thus, the alignment is an iterative process repeating the tracing and rotation steps as necessary until the high points of the spheres are aligned vertically. Once aligned vertically, this angle was defined as the zero angle for the C axis.

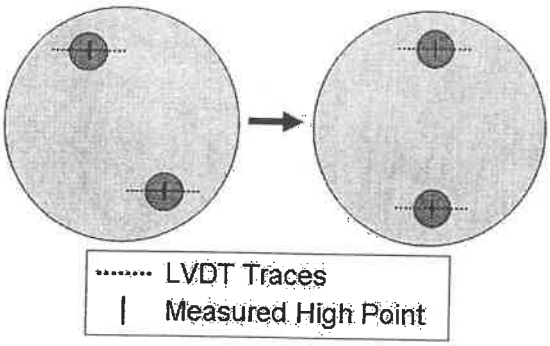

FIGURE 5. The part is aligned by horizontal traces across the two alignment spheres to find each spheres' high point. The axis is then rotated and the spheres measured again until the high points are aligned with the Y axis of the machine.

The lenslets were then machined by plunging the diamond mill into the surface of the hemisphere along the axis of the mill's rotation. The C-axis changed the machining azimuth while the indexing table changed the machining elevation. First, the pole lenslet was milled and then the rotary table was indexed, effectively changing the elevation. A lenslet was milled, the C-axis (azimuth) indexed by some amount based on the diameter of the optics and the circumference of the hemisphere at that elevation, and the next lenslet milled. This process was repeated with the C-axis making a full rotation for each rotary table setting, and the rotary table moving through approximately 45° of travel. A partial dragonfly eye prototype with a pole lenslet and a ring of 6 lenslets at 25° elevation is shown in Figure 6

Once the outer lenslets had been completed, the part was brought back to its vertical position and the part was flipped around its vertical axis. The part was recentered, the inside radius of the hemishell cut, and the part axis determined (clocked) by repeating the LVDT method. Because the part was flipped around the vertical axis, the indexing table is used at the same positions as it was for the outer diameter but it cuts on the other side of the centerline of the optic. This method leverages the inherent characteristics of an indexing table depending primarily on the excellent repeatability instead of the accuracy value which is 5 times larger.

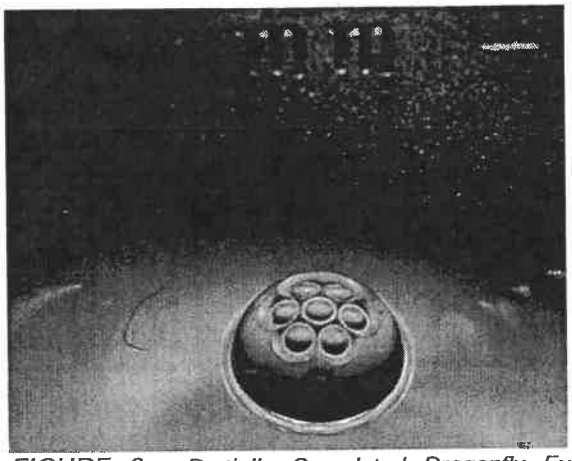

FIGURE 6. Partially Completed Dragonfly Eye Outer Shell Shows Aspherical Milled Lenslets

ERROR SOURCES AND PLANNED IMPROVEMENTS

There are several error sources identified in the production of the first dragonfly eye optics. These are being addressed to attempt to increase the accuracy of the final parts. A significant source of error is determining the location of the diamond mill in the machine. This has been done with an optical tool setter thus far and has been repeated with each increment of the indexing table because the grinding spindle is not aligned with the indexing table. In future work, the authors expect to create some angled flats which will be used to cut lenslets at each indexing of the table. The lenslets position will be used to better understand the position of the indexing table and milling tool.

There is radial rotational error in the tool that is speed dependent. Fiber optic displacement measuring probes were mounted in a custom designed fixture to measure this error at low and high speeds. The error was measured and the mill rotated in the collet until the minimum error was achieved. For this set of diamond mills, the minimum error was 8um on the radius. This error is a combination of the shaft alignment, collet errors, and spindle errors. These errors have not yet been separated to determine the major contributors.

Plunge milling the lenslets also produced some learned lessons. The first was the need to balance the radial load on the tool whenever possible. Because of the relatively large back taper on the tool, milling one optic would also mill some of the material away from above the surrounding optic locations. If an optic was milled where this loading was not symmetric around the optic to be milled, some tool deflection was experienced. This was surprising due to the relatively large diameter of the tool shank with respect to the tools. This required that the optics not be milled in order, but that every other optic be milled initially, and then the remaining optics milled. This allowed the first set of optics to be milled in virgin material and the second set of optics to have balanced interrupted cuts.

CONCLUSIONS

The manufacturing of the dragonfly eye optic has presented some significant challenges, especially in alignment of the optics. Fixtures and methods were developed to address these challenges and several lessons were learned, especially in the milling of microoptics.

ACKNOWLEDGEMENTS

Sandia is a multiprogram laboratory operated by Sandia Corporation, a Lockheed Martin Company, for the United States Department of Energy's National Nuclear Security Administration under Contract No. DE-AC04-94AL85000.

LOAD FORCE COMPENSATION FOR DIRECT DRIVES IN MACHINE TOOLS

Oliver Zirn[1], Axel Hoos[1], and Bernhard Hiller[2]
[1]Arbeitsgruppe Mechatronik, University of Applied Sciences, Giessen, Germany
[2]Hübner AG, Berlin, Germany

INTRODUCTION

The feed axis servo drive is the key component for the performance (e.g. stiffness, precision, path velocity) of a numerically controlled production machine. Replacing flexible transmission devices (e.g. ball screws, belts) by direct drives can improve the productivity. Although claimed by manufacturers of linear and torque motors, the performance of one axis test benches cannot be transferred to real multi axis machine tools.

The small masses and inertia required for linear and torque motors result in a higher disturbance sensibility of direct driven machine tools. Friction as well as gravity loads can be minimized mechanically or can be compensated in most servo controllers. Coupling forces, as discussed in the next Chapter, disturb the dynamic performance especially for high accelerations and velocities and cannot be compensated on the servo axis level.

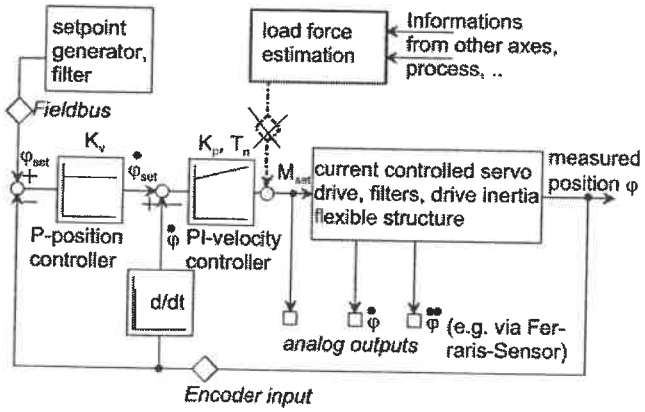

FIGURE 1. Standard machine tool control structure and interfaces.

While most robot control systems compensate the dynamic coupling forces on the numerical control level, machine tool control hardware has no such options. As shown in Figure 1 the standard machine tool control system has several analog outputs and one setpoint- and one or two encoder inputs. Closed loop force inputs are not available.

DYNAMIC COUPLING FORCES FOR DIRECT DRIVES

Figure 2 shows a typical serial machine tool manipulator with 3 direct driven degrees of freedom (DOF). The relevant system parameters are given in Table 1.

The general dynamic robot model following [2] includes centrifugal-, coriolis- and acceleration forces. For machine tools, the acceleration forces are by far the dominating coupling forces. In the example discussed here, also the excentricity of the C-axis is negligible (a=0 in figure 3). Thus the simplified dynamic model yields the coupling force F_{kX} for the X-axis and torque M_{kB} for the B-Axis:

$$F_{kX} = -(m_2 + m_3) \cdot d \cdot \cos(B) \cdot \ddot{B} \qquad (1)$$

$$M_{kB} = -(m_2 + m_3) \cdot d \cdot \cos(B) \cdot \ddot{X} \qquad (2)$$

with
- m_2 - B-axis mass (body 2 in Figure 3)
- m_3 - C-axis mass (body 3 in Figure 3)
- d - excentricity of the common gravity center

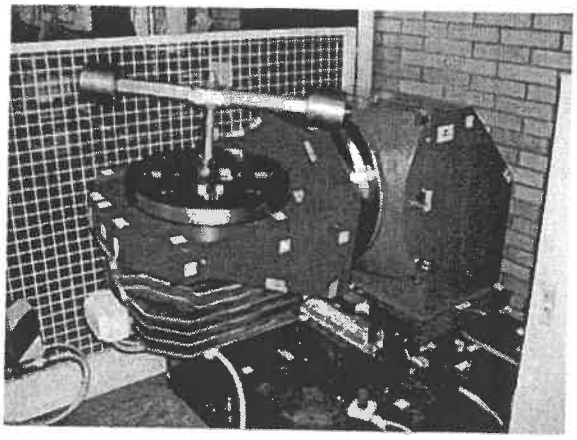

FIGURE 2. Exemplary machine tool manipulator with 3 direct driven DOF [1]

TABLE 1. Parameters for the machine tool manipulator in Figure 2

X-Axis	
Mass	$m_1 = 285$ kg
Linear Motor	Fischer Motoren GmbH
Current Converter	Simodrive 611 U
Maximum Force	$F_{Xmax} = 2500$ N
B-Axis	
Inertia	$J_2 = 13{,}7$ kgm^2
Mass	$m_2 = 285$ kg
Excentricity	d = 0,05 m
Torque Motor	Technai SA
Current Converter	Simodrive 611 U
Maximum Torque	$M_{Bmax} = 1000$ Nm
C-Axis	
Inertia	$J_3 = 1{,}3$ kgm^2
Mass	$m_3 = 138$ kg
Torque Motor	IDAM GmbH
Current Converter	Simodrive 611 U
Maximum Torque	$M_{Cmax} = 750$ Nm

The effect of the coupling forces is shown in Figure 4 for a fast 5°-positioning of the B-axis. Acceleration and braking produce heavy coupling forces for the X-axis. They lead to significant position deviations in the range of 30 µm.

The measurements in Figure 4 and Figure 5 were sampled by the current converters. The simulations in Figure 4 and Figure 5 result from a MATLAB/Simulink-model of the 3 DOF-manipulator in Figure 2 [2]. They depict the fact that the simplified dynamic model in Eqs. (1) and (2) is precise enough for the representation of the dominating coupling forces.

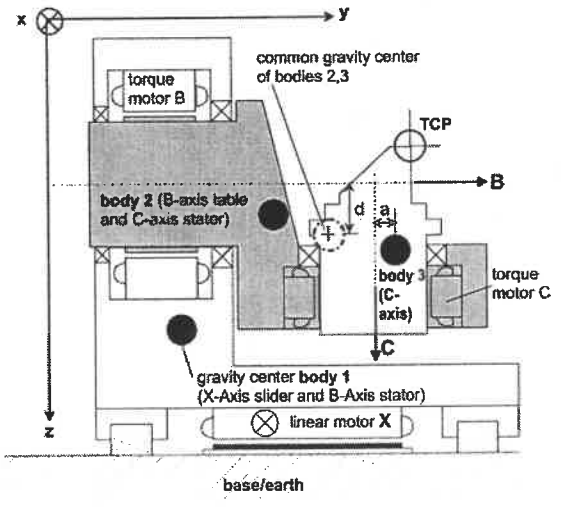

FIGURE 3. Rigid body model of the 3 DOF machine tool manipulator in Figure 2

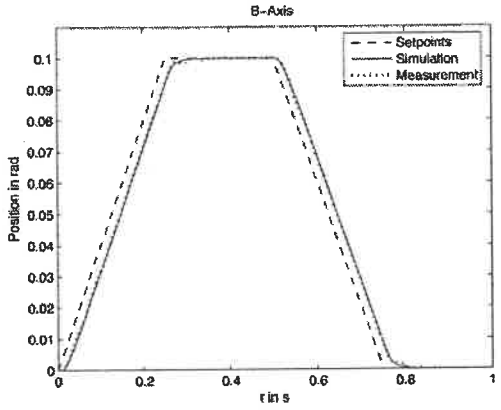

FIGURE 4. B-axis positioning trajectory.

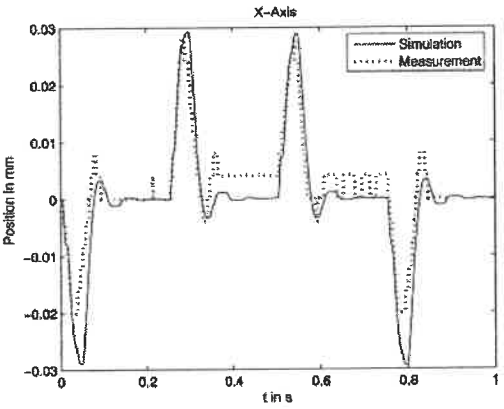

FIGURE 5. X-axis position deviation while positioning the B-axis.

As machine tool axis acceleration duration is in the range of 50..200 ms, the resulting deviation can be estimated using the static drive stiffness following [1]:

$$\Delta x \approx \frac{F_{kX}}{K_v \cdot K_p} \qquad (3)$$

with K_v - position control gain
K_p - velocity control gain

HARDWARE EXTENSION

Although standard servo controllers have no additional force input (see Figure 1), they all have two position encoder inputs for a motor encoder (velocity measurement) and a second encoder (e.g. for position measurement at the slider). Direct drives have just one encoder for position and velocity measurement. Modification of the encoder signal for the motor encoder input opens the required coupling force input for direct drives [3]. Figure 6 shows the realization of the compensation based on the universal interpolator of Hübner AG, Berlin [4]. This so

called "Blackbox" branches the measured axis position and modifies the motor position input.

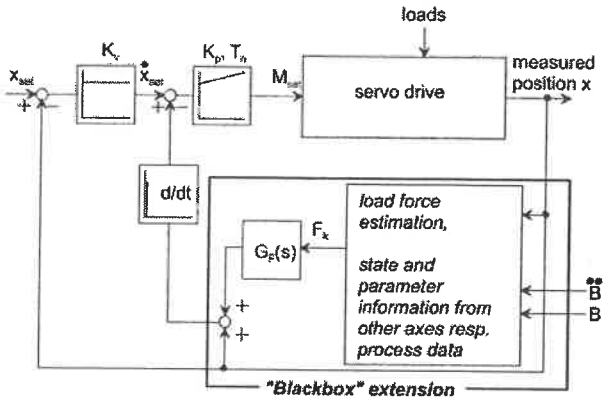

FIGURE 6. Standard machine tool control structure with a force input extension ("Blackbox")

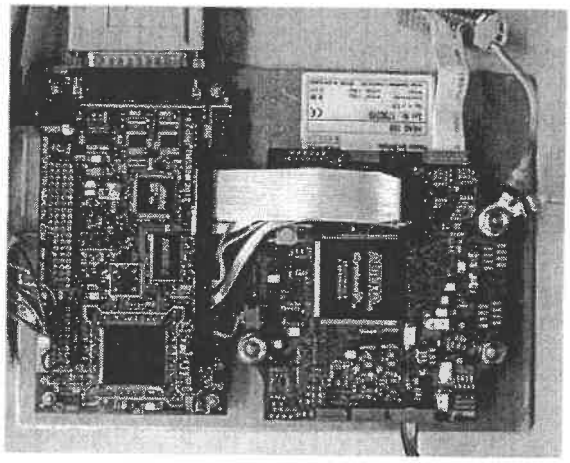

FIGURE 7. Blackbox based on the universal interpolator (courtesy Huebner AG, Berlin).

The inverse filter $G_F(s)$ compensates the motor position signal processing in the PI-velocity control loop and "mixes" the coupling force compensation to the cascade controller:

$$G_F(s) = \frac{K}{K_p \cdot (s + 1/T_n)} \qquad (4)$$

with K – compensation weighting factor (0 .. 1)

T_n – integral time constant

PRACTICAL APPLICATION

Using Eq. (1) to compensate the effect of the B-axis movement on the X-axis by considering the B-axis motor current as equivalent for the B-axis acceleration decreases the deviation significantly (see Figure 8). The complete compensation is prohibited by the delayed force generation in the current control loop as well as by friction and model uncertainities.

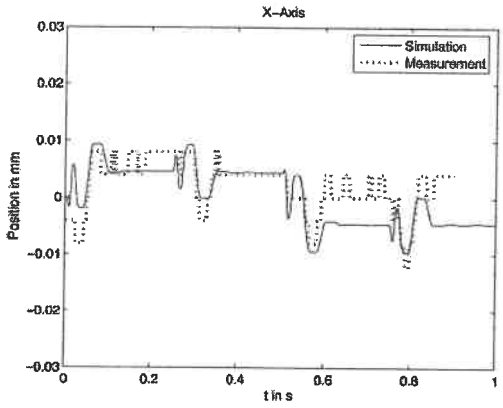

FIGURE 8. X-axis position deviation while positioning the B-axis.with load force compensation via "Blackbox"

CONCLUSIONS

This paper studied the compensation of load forces for direct drives to achieve better accuracy for machine tools and robots. A proposal for the realization on standard control hardware is worked out. The practical benefit is demonstrated by an industrial application and shows that the position resp. path deviations caused by dynamic coupling forces can be suppressed effectively.

ACKNOWLEDGEMENTS

The presented results have been worked out in the applied research project AiF-Pro-Inno KF0538601-KMH3 founded by the German Federal Ministry of Economics and Labour

REFERENCES

1. Zirn, O.; Monat, A.; Schöller, T.: Control of Direct Driven Feed Axes with Flexible Structural Components. *2005 IEEE Industry Applications Conference,* Hong Kong.
2. Zirn, O., Weikert, S.: Modellbildung und Simulation hochdynamischer Fertigungs-systeme. 367 pages, *Springer-Verlag publishing company,* Heidelberg, 2005. ISBN 3-540-25817-5

3. Zirn, O.: Herstellungsunabhängige Erweiterungsschaltung zur modellbasierten Regelung direkt angetriebener Linear- und Rundachsen. *German Patent Agency - (DPMA) Aktenzeichen DE 10 2004 027 756 A1*, February 9th, 2006.
4. Hiller, B.: Neue Entwicklungen und Anwendungen des Ferraris-Sensors. *Seminar Fortschritte in der Regelungs- und Antriebstechnik,* Universität Stuttgart, 18./19.6.2004.

IN-SITU CALIBRATION OF TEMPERATURE COMPENSATION SYSTEMS USING DIFFERENTIAL LENGTH MEASUREMENTS

James G. Salsbury[1] and Michael Inloes[2]
[1]Mitutoyo Institute of Metrology
Mitutoyo America Corporation
Aurora, IL, USA
[2]Plymouth Calibration Laboratory
Mitutoyo America Corporation
Plymouth, MI, USA

INTRODUCTION

Temperature variation can significantly impact dimensional measurements, and therefore many modern dimensional measuring instruments are equipped with built-in temperature compensation systems. These systems operate in real time during measurements and compensate for the linear thermal expansion of both the measuring instrument scales and the measured workpiece. Temperature compensation systems come standard on many instruments, such as the coordinate measuring machine (CMM).

A Mitutoyo Legex CMM was installed at Mitutoyo America's calibration lab in Plymouth, Michigan, for the purposes of doing a variety of high accuracy dimensional calibration and inspection work. One of the goals of the Legex CMM implementation was to calibrate length gages with a very low uncertainty. A large variety of length gages were considered, including step gages, length bars, linescales, ball bars, and also rings, plugs, and spheres.

Being a commercial lab, another goal of the CMM implementation was high throughput of the calibration process to reduce operational cost. The most practical solution was to use the Legex as designed, including the use of the built-in temperature compensation system. Concern existed on whether the desired uncertainty could be achieved using a standard CMM, particularly since the target uncertainty was less than the accuracy specifications of the Legex. A preliminary uncertainty budget indicated that the ability to properly measure the temperature of the length gages was critical. Since it was desired to use the temperature compensation system on the Legex, various methods were explored to calibrate and implement the system with the smallest possible uncertainty.

The final implemented solution on the Legex is a bit unique. The technique does not involve traditional thermometry methods but instead uses differential measurements of two calibrated length standards with significantly different coefficients of thermal expansion (CTE). The result is a calibration of the temperature compensation system following the same manner in which the system is actually used. The technique is straightforward to implement and has the potential to reduce dimensional measuring uncertainty associated with the combined calibration and usage of the temperature compensation system. Experimental results showed that an uncertainty of 50 mK is practical and that an uncertainty of less than 15 mK is possible. The results were verified through intercomparison of length measurements with the National Institute of Standards and Technology (NIST).

LENGTH CALIBRATION USING CMMS

CMMs have a long history of being used for the calibration of length gages. In some cases, the CMM has been equipped with an external laser interferometer [1-5]. This approach reduces the CMM to a one-dimensional measuring instrument, which would not meet the flexible needs of the Legex CMM in the Plymouth Calibration Laboratory. Another method that has been utilized involves careful error mapping and correcting the geometric errors of the CMM [6,7]; the implementation of the Legex CMM is similar to this method.

Regardless of the method utilized, the CMMs discussed in [1-7] were all located in precision temperature controlled environments. In addition, various types of temperature measurement systems were utilized to record the temperature of the measuring scale and the length gages during calibration. Understanding

the uncertainty of these systems, as implemented, is critical to understanding the overall uncertainty of the measurement process. The calibration of these temperature measuring systems can also be a challenge, for example see [6], as these systems must be calibrated on the CMM. Even with precise temperature controlled rooms and temperature measuring and compensation systems, the largest sources of uncertainty in most longer length calibrations are still related to temperature [2-6].

It is also possible to use a CMM as a mechanical comparator. Following this approach, length gages are calibrated via comparison to calibrated master gages made of similar materials. This method, which is common in applications like gage block calibration, can be very accurate but limits the range of possible measurement applications for the CMM.

LEGEX CMM IMPLEMENTATION

A Mitutoyo Legex 910 CMM was implemented in the Plymouth Calibration Laboratory of Mitutoyo America as shown in Figure 1. One of the reasons a Legex CMM was chosen is that the machine is designed to be largely insensitive to thermal variations. In particular, the measuring scales are made of CLEARCERAM-Z, which has an ultra-low CTE of 0.08×10^{-6}/K [8]. Unlike the methods presented in [1-7], which require precise measurement and correction of the machine and scale temperature, the only significant temperature related concern with the Legex is workpiece temperature measurement.

FIGURE 1. The Legex CMM (on left) in the Plymouth Calibration Laboratory of Mitutoyo America.

The Legex CMM has a built-in temperature compensation system. The workpiece sensors are thermistors encased in brass blocks, as shown in Figure 2. These two sensors are placed on workpieces during measurement and software is used to compensate for linear thermal expansion in three-dimensional space.

The Plymouth Lab was concerned with the uncertainty in the use of this temperature compensation system. Sources of uncertainty include calibration of the system, radiant influences, contact with the measured workpiece, soak-out, and self-heating. Instead of attempting to estimate these challenging sources of uncertainty, as well as implementing traditional thermometry calibration techniques on-site, such as temperature baths, the laboratory decided to calibrate the system using a novel technique of differential length measurements.

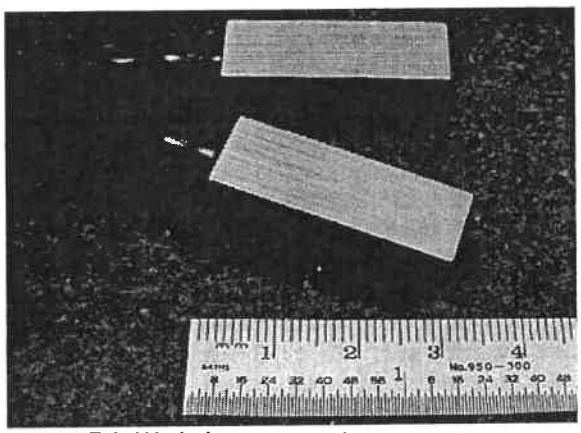

FIGURE 2. Workpiece temperature sensors.

DIFFERENTIAL LENGTH MEASUREMENTS

The workpiece temperature measurement and compensation system on the Legex CMM comes with a calibration from the CMM factory. The factory calibration is done using a temperature chamber that cycles the system over a range of temperatures to determine a calibration offset and slope. Since the Legex is used over a small temperature range, 20±0.5°C, the only significant concern is the calibration of the offset. This is done using a technique of differential length measurements. The technique requires two calibrated length gages, i.e. length standards, of nominally the same length, with different, and known, CTEs. The two length gages are then measured on the CMM using the temperature compensation system as it is normally used. The gages are placed in the same nominal location on the CMM to reduce variation from the CMM geometry. On the Legex, the two length gages are placed very near each other with two temperature sensors between them, as shown in Figure 3.

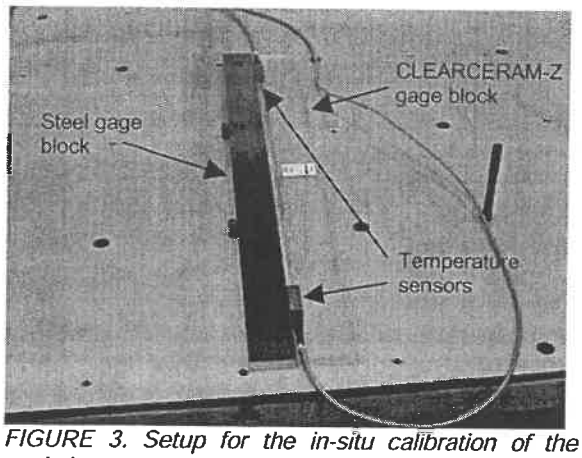

FIGURE 3. Setup for the in-situ calibration of the workpiece temperature system.

The change in length of either gage due to the influence of temperature can be expressed by:

$$\Delta L = L(T-20)\alpha \qquad (1)$$

where L is the nominal length, T is the measured temperature, and α is the CTE of the length gage. If the two gages have the same nominal length and are measured as shown in Figure 3 such that they have the same temperature, then the error in the temperature system can be determined by:

$$\Delta T = (\Delta L/L)(\alpha_2-\alpha_1)^{-1} \qquad (2)$$

This error, ΔT, can then be used to adjust the offset of the temperature measuring system. The temperature compensation system is therefore calibrated, in-situ, in the same manner in which it is used for subsequent measurements. The temperature related concerns mentioned earlier are thus reduced or eliminated. The calibration process can also be easily repeated.

The traceability of this in-situ calibration of the temperature measuring system comes completely from the calibration of the length gages. The traceability depends on the calibration of the lengths of the two gages and also the knowledge of their CTEs. No additional calibrated thermometer is required.

EXPERIMENTAL RESULTS

The temperature system on the Legex CMM in the Plymouth Lab was calibrated using the differential length measurement technique. The initial implementation utilized a steel gage block calibrated at NIST and a CLEARCERAM-Z gage block calibrated at NRC. Both gage blocks had a nominal length of 500 mm. The uncertainty of the process, as shown in Table 1, was estimated to be around 50 mK. The uncertainty of the temperature system can then be used in the estimation of the uncertainty for length measurements. For the majority of length gages, the uncertainty of the Legex CMM at the Plymouth Lab has been estimated to be a very adequate U = (0.25+0.7L/1000) micrometers (at k=2). This result is significantly influenced by the calibration of the temperature system.

TABLE 1. Uncertainty of the in-situ calibration of the temperature measurement system.

Uncertainty Source	Standard Uncertainty (nm)
Steel gage block, length calibration	82.5
Steel gage block, knowledge of the CTE (10.8×10^{-6}/K)	62.5
Low CTE gage block, length calibration	25.5
Low CTE gage block, knowledge of the CTE (0.08×10^{-6}/K)	1.0
Process reproducibility	75.0
Combined standard uncertainty = 130 nm	
Expanded uncertainty (k=2) = 260 nm	
Applying the length uncertainty to equation (2): U = 48.5 mK	

Shortly after the implementation of the in-situ temperature system calibration technique on the Legex, the Plymouth laboratory was involved with an intercomparison measurement of a step gage organized by NIST. The final results of this intercomparison were never published, but the results were made available to the participants. The timing of the intercomparison provided an opportunity to independently test the Legex and the temperature system calibration. The setup for the step gage measurements is shown in Figure 4.

The results of the intercomparison are shown in Figure 5. (While the intercomparison involved a number of labs, only the Legex deviations from the NIST results are shown.) Figure 5 shows the Legex deviations, the Legex uncertainty, and the uncertainty of the NIST calibration. The deviations, most of which are within the uncertainty from NIST, are also only about 50% or less of the estimated uncertainty of the Legex process. The most important finding, however, is that the results show no linear error, which is often indicative of temperature measurement issues. These results provide some confirmation of the Legex process and the in-situ calibration of its temperature measuring system.

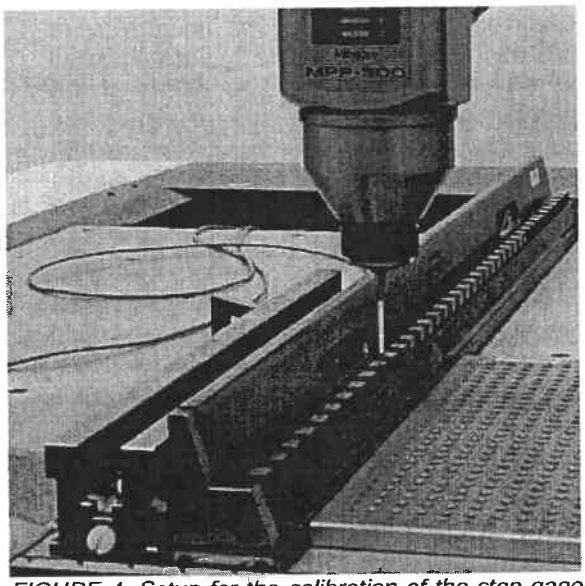

FIGURE 4. Setup for the calibration of the step gage as part of the intercomparison with NIST. The shorter Koba gage on the left is being calibrated. The Mitutoyo step gage on the right is a check standard.

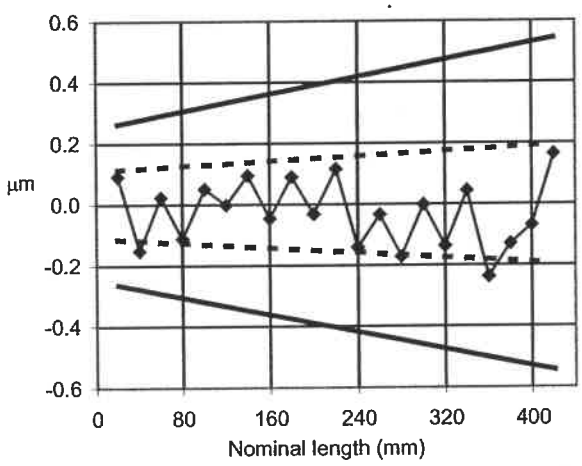

FIGURE 5. Results of the intercomparison with NIST. The solid lines are the Legex uncertainty and the dotted lines are the NIST uncertainty.

FUTURE WORK

The uncertainty analysis shown in Table 1 was based on initial work using length gages that were readily available at the time. Further research has lead to the potential uncertainty budget shown in Table 2. This is a best uncertainty based on possible improvements to the temperature calibration process. The changes include a higher accuracy calibration of the steel gage block, including the calibration of its CTE, and additional measurements to improve reproducibility. The results indicate that an uncertainty of less than 15 mK is possible.

TABLE 2. Potential uncertainty improvements.

Uncertainty Source	Standard Uncertainty (nm)
Steel gage block, length calibration	23.3
Steel gage block, knowledge of the CTE (10.8×10^{-6}/K)	6.3
Low CTE gage block, length calibration	25.5
Low CTE gage block, knowledge of the CTE (0.08×10^{-6}/K)	1.0
Process reproducibility	10.0
Combined standard uncertainty = 36.5 nm	
Expanded uncertainty (k=2) = 73 nm	
Applying the length uncertainty to equation (2): U = 13.6 mK	

SUMMARY AND CONCLUSIONS

A unique, yet straightforward, technique was presented for the in-situ calibration of built-in temperature compensation systems in the field of dimensional metrology. The technique uses differential length measurements of two length gages of significantly different CTEs. The technique avoids many thermometry calibration issues and results in the temperature system being calibrated in a manner similar to how it is used in subsequent dimensional measurements.

REFERENCES

1. Schussler, H. H., 1982, A biaxial laser interferometer for absolute calibration of bidirectional step gauges and gauge blocks, IMEKO.
2. Lingard, P. S., Purss, M. E., Sona, C. M., and Thwaite, E. G., 1991, Length-bar and step-gauge calibration using a laser measurement system with a CMM, Annals of the CIRP, 40(1):515-517.
3. Abbe, M., Starrenburg, M. P., and Sawabe, M., 1998, Results from step gauge calibration using bi-axial laser interferometer, 6th IMEKO Symposium, Vienna.
4. Osawa, S., Takatsuji, T., Noguchi, H., and Kurosawa, T., 2002, Development of a ball step-gage and an interferometric stepper used for ball-plate calibration, Precision Engineering, 26:214-221.
5. Osawa, S., Takatsuji, T., H., and Kurosawa, T., 2003, Step-gauge calibration using an interferometric CMM and the uncertainty, XVII IMEKO World Congress, Croatia.
6. Zurcher, N., 1996, Using a CMM to calibrate step gages at world class levels of uncertainty, Y/AMT-327, Oak Ridge Y-12 Plant.
7. Stoup, J. and Doiron, T., 2001, The accuracy and versatility of the NIST M48 CMM, Proceedings of SPIE, 4401:136-146.
8. Ohara Technical Data Bulletin 2001.

HIGH-STABILITY TEMPERATURE CONTROL SYSTEM FOR LISA

Sei Higuchi[1], and Daniel B. DeBra[1]
[1]Department of Aeronautics & Astronautics, Stanford University
Stanford, CA 94305, USA

INTRODUCTION

The Laser Interferometer Space Antenna (LISA) and other precision spaceflight missions require gravitational reference sensors (GRS) for drag-free control [1]. LISA uses laser metrology to measure distance between proof masses in three identical spacecrafts. The primary mission goal of LISA is detecting the gravitational waves. The total acceleration disturbance to each proof mass is required to be below $3 \times 10^{-15}\ m/s^2\sqrt{Hz}$. Optical path length variations on each optical bench must be kept below $40\ pm/\sqrt{Hz}$ over $1\ Hz$ to $0.1\ mHz$. Thermal variations due to, for example, solar irradiation, or temperature gradients across the proof mass housing are expected to be significant disturbance sources.

This article focuses on a thermal control system developed for LISA gravitational reference sensor (GRS) ground verification testing which provides thermal stability better than $1\ mK/\sqrt{Hz}$ to $f < 1\ mHz$, and which by extension is suitable for in-flight thermal control for the LISA spacecraft to compensate solar irradiation.

Stabilizing the thermal environment against low frequency disturbance is one of the most important problems for LISA performance verification. Lowering the sub-mHz thermal drift caused by diurnal variations is the main objective, with stability requirement $\delta T < 30\ \mu K/\sqrt{Hz}$ for $f > 0.01\ mHz$ measured at the sensor. Our main concern in the laboratory is the daily ambient temperature variations which causes the thermal drift of the GRS proof-mass support stage and the optical path lengths. Hence the thermal control system, which is discussed in this article, must be able to reject such thermal disturbance in the very low frequency band to realize the LISA level verification [2], [3].

In a lab environment these specifications can be met with sufficient insulation and thermal mass. For spacecraft, the very limited thermal mass calls for an active control system which can meet disturbance rejection and stbility requirements simultaneously in the presence of long time delay.

A simple proportional plus integral control law presently provide approximately $1\ mK/\sqrt{Hz}$ of thermal stability for over 80 hours. Continuing development of a model predictive feedforward algorithm will extend performance to below $1\ mK/\sqrt{Hz}$ at $f < 1\ mHz$ and lower.

EXPERIMENTAL SYSTEM

Figure 1 shows a schematic of the experimental system. The various layers of insulation correspond roughly to the layers of thermal isolation provided by the LISA spacecraft design [3], constructed from readily available lightweight materials.

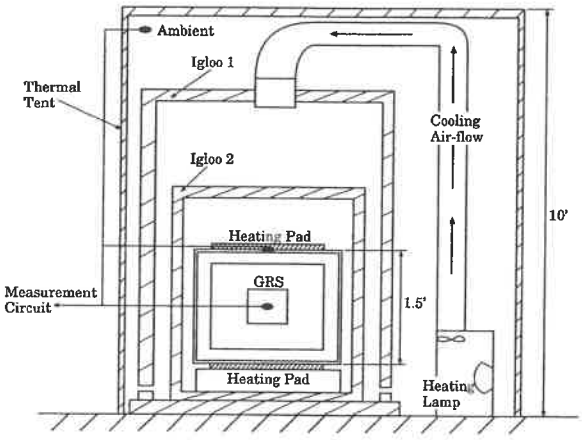

FIGURE 1. Schematic of the experimental system

The GRS sensor test-object is placed in the center of a double walled thin metal thermal enclosure, analogous to the LISA internal shield. A precision thermistor monitors the test-object with (< 100 $\mu K/\sqrt{Hz}$) noise. The enclosure is wrapped in flexible insulation, and wrapped again with copper foil. This coper foil surface corresponds roughly to the LISA Y-tube surface, and here is temperature controlled to high-precision by a heating-pad/thermocouple feedback system. Surrounding the enclosure and heater-pad apparatus is $2''$ of foil-covered polystyrene foam insulation, labeled igloo1 and igloo2, to create sealed control volumes. An improved design would use a vacuum enclosure.

The outer surface of igloo2 is maintained by a temperature regulated air-flow system which removes waste heat and provides 1st-order thermal disturbance relaxation of ambient laboratory temperature fluctuations. In this regard, the air-flow system functions to provide approximately the same level of thermal isolation, and stability as should the first layer of thermal isolation provided by the spacecraft structure. The air-flow point temperature is controlled by independent SISO controllers, which is regulated by a bang-bang control law operating a heater lamp and a mechanical relay combined with steady cold air flow from an air-chiller [4]. However, the air-flow works only as a large heat sink, simulating for space will be replaced with a cold radiator to deep space. The ambient temperature can be independently controlled using another system composed of commodity supplies (thermostats and room air-conditioners, for example). Note that our objective is not to reduce the disturbance itself, but instead to generate a compensating input so that net heat flux and thus temperature of the test object is tightly controlled.

Two heating pads, our primary actuators, are driven with an AC power source. They are installed at the top and bottom of the thermal enclosure inside igloo2. Accordingly a continuously variable computer controlled supply is the most desired equipment. However, due to the limited availability, the experiment is being conducted utilizing a 24 Vac power source, the output level of which is fixed. Therefore, the control program first computes the numerical value of the heating pad temperature (control signal) based on the desired final output and then sets as the value obtained as the reference track the reference of the control signal. Since the band width of he heating pad is significantly greater than that of the GRS, this scheme performs very well to emulate a smooth control input. Finally, the entire system is placed within a clear plastic thermal tent, primarily to cut down on air drafts.

Three temperature sensors are installed to measure the ambient temperature inside the thermal tent, the heating-pad temperatures at the copper foil outside double-walled enclosure, and the GRS test-object inside. A typical time history of the ambient and GRS test-object temperature is shown in Figure 2.

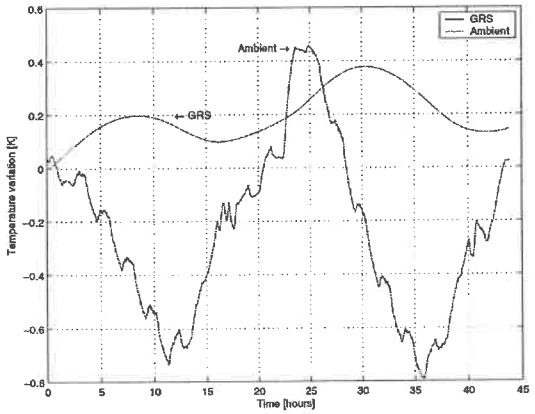

FIGURE 2. Time history of typical daily ambient temperature variation

The data was acquired without control authority and reveals significant coupling between the ambient and the GRS temperatures, which makes it difficult to reduce the fluctuations below the LISA thermal requirement [5] at least with the limited amount of thermal mass. Although the system has multiple layers of thermal insulation, the GRS test-object temperature is still varying roughly ± 0.2 K, which is obviously too large fluctuation for the LISA requirement.

In summary, the main objective of the experiment

is to develop robust control system that can suppress the ambient temperature variation as low as possible to the LISA thermal requirement level by using an active control algorithm in a limited thermal mass environment at the low frequency band, $f \sim 0.01\ mHz$. Ultimately, the control techniques being developed through experiments could be adapted to any types of systems that possess large time-delays and their dynamics are heavily dominated by them.

CONTROL SYSTEM

Figure 3 represents the control block diagram of the entire system corresponding to Figure 1.

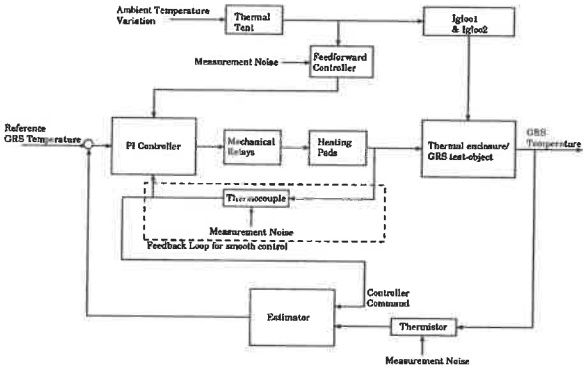

FIGURE 3. Control system block diagram

Feedback and feedforward control loops are formulated. As seen in Figure 2, the time delay between the ambient temperature and the GRS temperature is approximately 0.5 hours. Thus, by measuring the future potential disturbance that affects the GRS temperature beforehand and having the controller compute appropriate commands before the plant responds to the disturbance, the feedforward controller provides effective first-order disturbance reduction.

In addition to feedforward control, the system takes advantage of the feedback loop. In general, feedforward control performance largely depends on how accurately sensing mechanisms are able to predict the behavior of disturbance. The feedback control enhances the performance of rejecting the disturbance effects and adds robustness. The feedback loop takes a measurement at the sensor placed on the GRS. And the measured output and the control command are fed to a Smith regulator [6] [7] [8] to estimate the state so that a PI controller can compute the command signal. The parameters of the PI controller were determined from a mathematical model and numerical optimization.

The physical plant is modeled as a combination of a second-order system plus a single time-delay element. The model parameters are fitted empirically using least-square technique and MATLAB simulations. Figure 4 demonstrates dynamics of the plant in the frequency domain, which is embedded in the estimator in Figure 3.

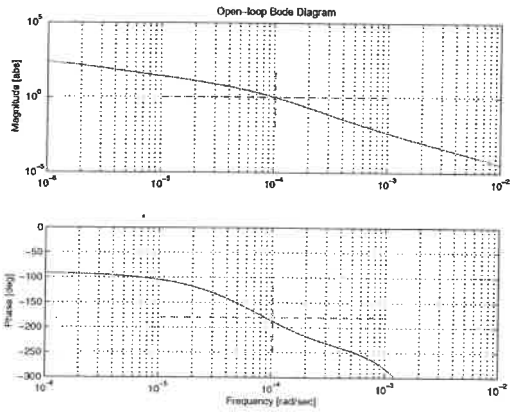

FIGURE 4. Bode plot of the plant

EXPERIMENTAL RESULTS

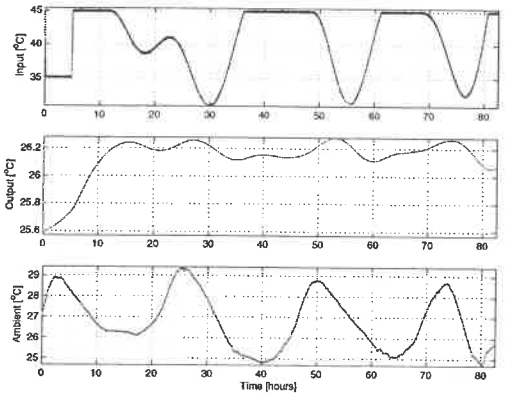

FIGURE 5. Time history of the first experiment: heating pad temperature (control effort, top), GRS temperature (output, middle), ambient temperature (disturbance, bottom)

Figure 5 demonstrates the 80-hour variation of the GRS temperature (output) together with the heating pad (input) and the ambient temperature (disturbance). The temperate is maintained approximately $\pm 20\ mK$ around $26.2\ ^oC$ over 80-hour observation. As the daily ambient temperature cycles in 24 hours, the GRS is still largely affected by such a low frequency signal ($\sim 10^{-5}\ Hz$), which is the major disturbance source.

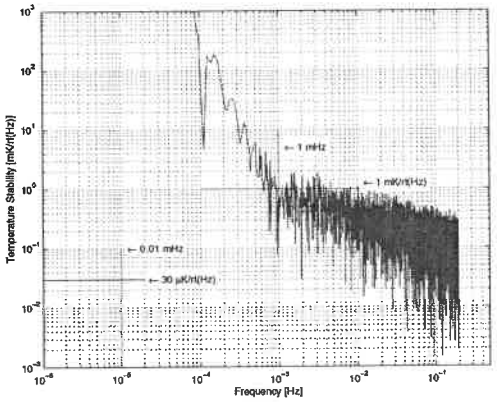

FIGURE 6. Thermal stability of the GRS test-object for 80-hour test

The mean square power spectral density of temperature variations of the GRS test-object is presented in Figure 6. The thermal stability is approximately $1\ mK/\sqrt{Hz}$ above $1\ mHz$.

CONCLUSION

The thermal experiment and corresponding results are presented. We have suppressed the ambient temperate variations by a factor of $1,000$ down to $1\ mHz$. We expect to extend the low frequency suppression to $0.01\ mHz$ and the amplitude to less than $30\ \mu K/\sqrt{Hz}$.

The LISA thermal requirement is also illustrated at the bottom left corner of the Figure 6. In order to push the spectral density curve to the region, two tasks are needed to be completed. Obviously, in order to suppress temperature variations even lower than the current level, the control algorithm has to be improved. However, the ultimate performance is limited by measurement noise from sensors. Thus, in addition to continuing development of the control system, for the better precision, less noise and more intermediate-term stability, improved measurement will be required [9] to fully satisfy the LISA thermal requirement.

REFERENCES

1. Daniel B. DeBra. Drag-free spacecraft as platforms for space missions and fundamental physics. *Classical and Quantum Gravity*, 14:1549–1555, 1997.

2. Bonny L Schumaker. Disturbance reduction requirements for LISA. *Classical and Quantum Gravity*, 20(10):S239–S253, 2003.

3. Hume Peabody and Stephen Merkowitz. Lisa thermal design. *Classical and Quantum Gravity*, 22(10):S403–S411, 2005.

4. K.M.Lawton and S.R.Patterson. A high-stability air temperature control system. *Precision Engineering*, 24(2):174–182, 2000.

5. Alberto Lobo, M. Nofrarias, and J. Sanjuan. Thermal diagnostics for ltp. *Classical and Quantum Gravity*, 22(10):S171–S176, 2005.

6. O.J.M. Smith. Closer control of loops with dead time. *Chemical Engineering Progress*, 53:217–219, 1957.

7. J.E.Normey-Rico and E.F.Camacho. Multivariable generalised predictive controller based on the smith predictor. *IEE Proc.-Control Theory Appl.*, 147(5):538–546, 2000.

8. J.J.Huang. Liquid temperatue control for precision machines. *Ph.D. Thesis, Department of Aeronautics and Astronautics, Stanford University*, 1997.

9. K. M. Lawton and S. R. Patterson. Long-term relative stability of thermistors: Part 2. *Precision Engineering*, 26(3), 2002.

SUB-MILLIDEGREE-STABILITY AIR THERMAL CONTROL FOR A LARGE-VOLUME LITHOGRAPHY ENCLOSURE

Yong Zhao[1], David L. Trumper[2], Ralf K. Heilmann[1], and Mark L. Schattenburg[1]
[1]Space Nanotechnology Laboratory, Massachusetts Institute of Technology, Cambridge, MA 02139
[2] Precision Motion Control Lab, Massachusetts Institute of Technology, Cambridge, MA 02139

INTRODUCTIONS

The thermal control of environmental enclosures is becoming increasingly critical as precision metrology, lithography and machining systems require sub-nanometer tolerances. As shown in Table 1 & 2, the thermal control of ±5 ~ 50 mK, which is typical for state-of-the-art equipment, will cause large errors on substrates. Some thermal control systems have achieved temperature stability of millidegrees or better using air-flow standard cell enclosures [1, 2] or enclosures utilizing flowing water as thermal control medium [3]. With large-volume air-flow enclosures, one-sigma air temperature stability of 2~3 mK at a single point has been demonstrated [4, 5]. In this paper we will report on how we improved the thermal control of an environmental enclosure designed for a precision lithography tool [5] to drive single-point one-sigma temperature stability down to sub-millidegree levels.

TABLE 1. Interferometer error caused by a change in the index of refraction of air inside the enclosure.

The error of temperature control	Change in the index of refraction of air	Position error for 150 mm wafers	Position error for 300 mm wafers
± 50 mK	96.80 ppb	14.5 nm	29.0 nm
± 5 mK	9.68 ppb	1. 45 nm	2.90 nm
±1 mK	1.94 ppb	0.29 nm	0.58 nm

TABLE 2. The error caused by the thermal expansion of the wafer chuck.

The error of temperature control	Coefficient of thermal expansion (Super Invar)	Position error for 150 mm wafers	Position error for 300 mm wafers
± 50 mK	0.6 ppm/K	9.0 nm	18.0 nm
± 5 mK		0. 90 nm	1.80 nm
±1 mK		0.18 nm	0.36 nm

Our environmental enclosure, whose internal dimensions are approximately 1.8-m long X 1.5-m wide X 2.1-m high, consists of two identical air handler units [5]. As shown in Fig. 1, in each unit the thermally well-controlled air flows into the chamber in the center and returns through the grills located at the top and bottom. The air returned through the top is cooled by a chiller coil and then reheated by electrical heaters to a controlled temperature. After mixing with the bottom return air, the reheated air is forced by a fan through an acoustic silencer to enter the chamber. The time for circulating the full chamber air is only 11 seconds. The thermal sensors in each unit for feedback thermal control are located in front of the central filter plane.

MEASURING THE TRANSFER FUNCTION OF THE THERMAL SYSTEM

Measuring the transfer function of a system is one of the most critical requirements to achieve the desired performance. However, sometimes it is impossible to take a direct open-loop transfer function measurement because of noise issues or field-test limitations. Alternatively, calculating the transfer function based on the closed-loop frequency response measurement is utilized. As shown in Fig. 2, with an HP 35670A Dynamic Signal Analyzer, we inject a stimulus swept sine signal (**N**) into the loop and the frequency response measurement is taken at points $\mathbf{Y_1}$ and $\mathbf{Y_2}$. The transfer function (**GTH**) of this thermal system is calculated from the measurement as below,

$$\begin{cases} |GTH| = \left|\frac{Y_2}{Y_1}\right| / |G_C| \\ \Phi(GTH) = -180^\circ + \Phi(\frac{Y_2}{Y_1}) - \Phi(G_C) \end{cases}$$

A PI compensation controller, $6(1+\frac{1}{63s})$, is utilized in the closed-loop frequency response measurement in order to make the thermal system perform around the desired temperature. Fig. 3 shows the closed-loop

frequency response measurement (Y_2/Y_1). Due to the limit in minimal frequency for the swept sine signal, we can only make the frequency response measurement down to 0.015625 Hz. However, this is low enough for us to design the controller. The calculated open-loop transfer function (**GTH**) of the thermal system is shown in Fig. 4.

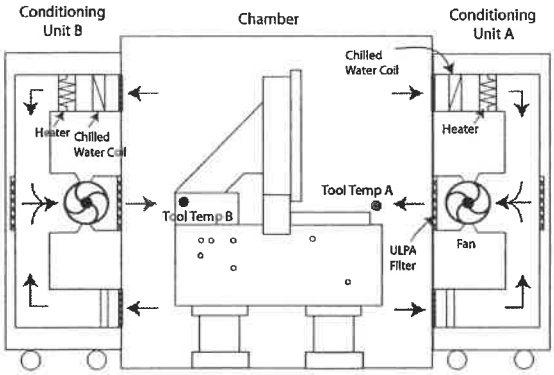

FIGURE 1. *The environmental enclosure.*

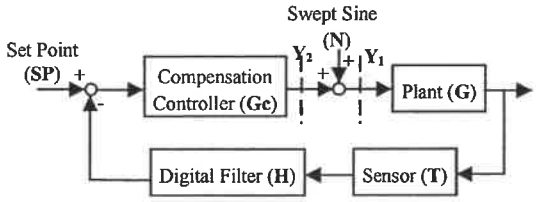

FIGURE 2. *The diagram for measuring the transfer function of the thermal system.*

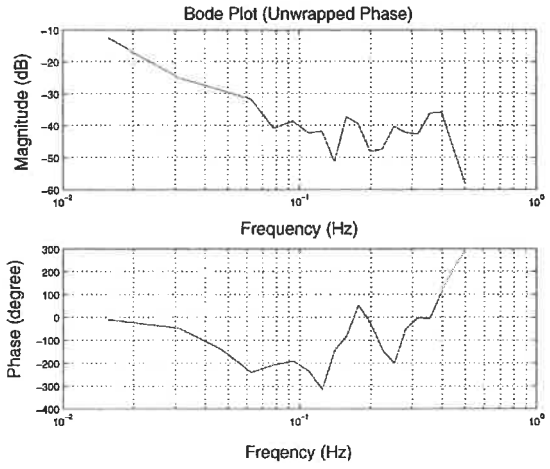

FIGURE 3. *The closed-loop frequency response measurement (Y_2/Y_1).*

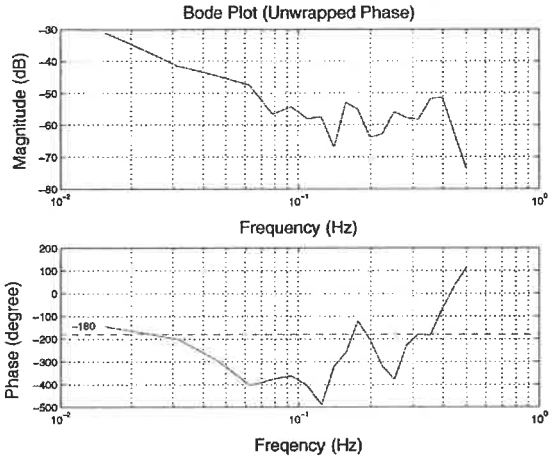

FIGURE 4. *The calculated open-loop transfer function (**GTH**) of the thermal system.*

DESIGN A CONTROLLER FOR THE THERMAL SYSTEM

Based on the transfer function of the thermal system, we design a lead compensation controller ($\frac{100s+1}{15s+1}$), which reduces the overshoot by increasing the phase margin and a faster transient response is realized by increasing the gain crossover. The bode plots of the compensated system and uncompensated system are shown in Fig. 5.

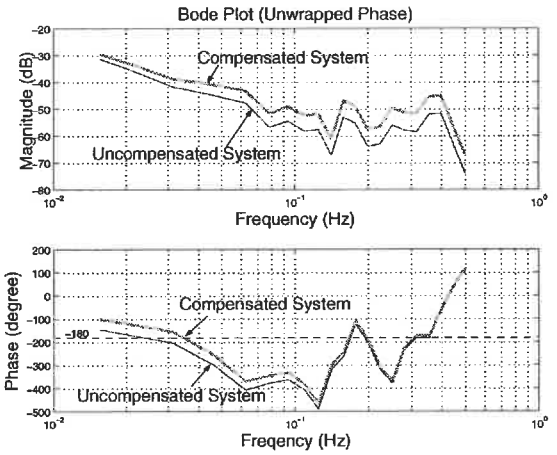

FIGURE 5. *The bode plots of the compensated system and uncompensated system.*

A PI controller $(1+\frac{1}{1000}\frac{1}{s})$ is also added into the control system in order to eliminate the steady-state error. From Fig. 6, we find the steady-state error to be around 0.2 °C with respect to the set point (20 °C) when there is no

PI controller.

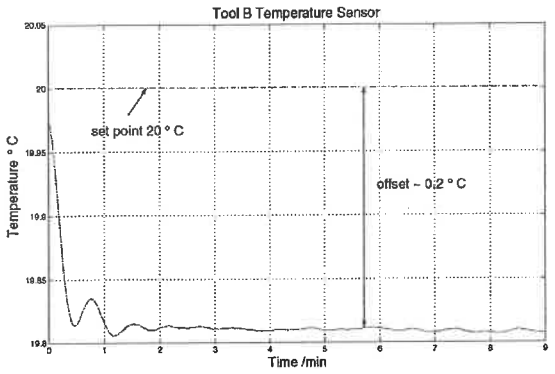

FIGURE 6. *The performance of the thermal control system when there is no PI controller.*

Figure 7 shows the diagram of our thermal control system. The controller is surrounded by a dashed line. An anti-windup block is utilized to avoid the effect of integrator windup [6]. Finally, we transformed our s-plane design to a digital implementation (z-domain).

THE PERFORMANCE OF THE THERMAL CONTROL SYSTEM AND CONCLUSIONS

With the PI-lead compensation controller, one-sigma air temperature stability of less than 1 mK at a single point over 2 hours has been achieved, which is shown in Figs. 8 (a) and (b). The temperature sensor of the thermal system measured a one-sigma stability of 0.70 mK (Fig. 8 (a)). An independent temperature sensor measured one-sigma stability of 0.50 mK (Fig. 8 (c)), perhaps due to the resolution and the response time limitations of the sensor.

In this study, a method to measure the open-loop transfer function of a thermal system has been developed. Based on the measured transfer function, a lead compensation controller together with a PI controller is designed for the thermal control of an environmental enclosure.

Sub-millidegree-stability air thermal control for a large-volume enclosure has been achieved.

REFERENCES

1. D. Sarid and D. S. Cannell, "A ±15 microdegree temperature controller", Review of Scientific Instruments, 45, 1082-1088 (1974).
2. J. Dratler, "A proportional thermostat with 10 microdegree stability", Review of Scientific Instruments, 45, 1435-1444 (1974).
3. H. Ogasawara, "Method of precision temperature control using flowing water", Review of Scientific Instruments, 57, 3048-3052 (1986).
4. K. M. Lawton and S. R. Patterson, "A high stability air temperature control system", Precision Engineering, 24, 174-182 (2000).
5. Paul T. Konkola, "Design and analysis of a scanning beam interference lithography system for patterning gratings with nanometer-level distortions", PhD dissertation, Massachusetts Institute of Technology, Department of Mechanical Engineering, June 2003.
6. Karl J. Astrom and Bjorn Wittenmark, "Computer-Controlled Systems: Theory and Design", Prentice Hall, 3rd edition (1996).

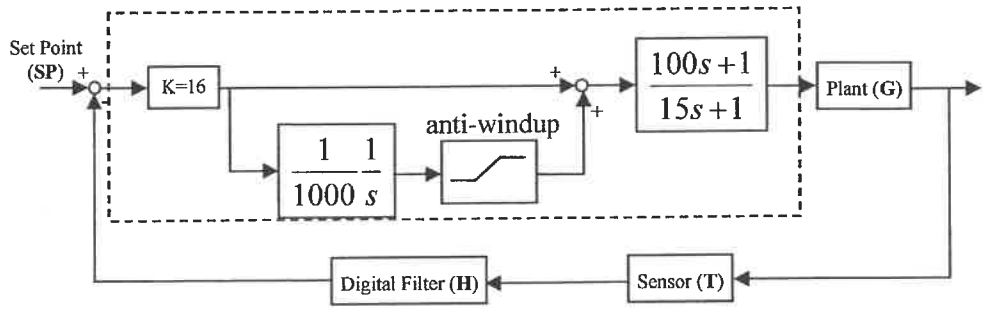

FIGURE 7. *The diagram of the thermal control system. The part inside the dashed line is the controller.*

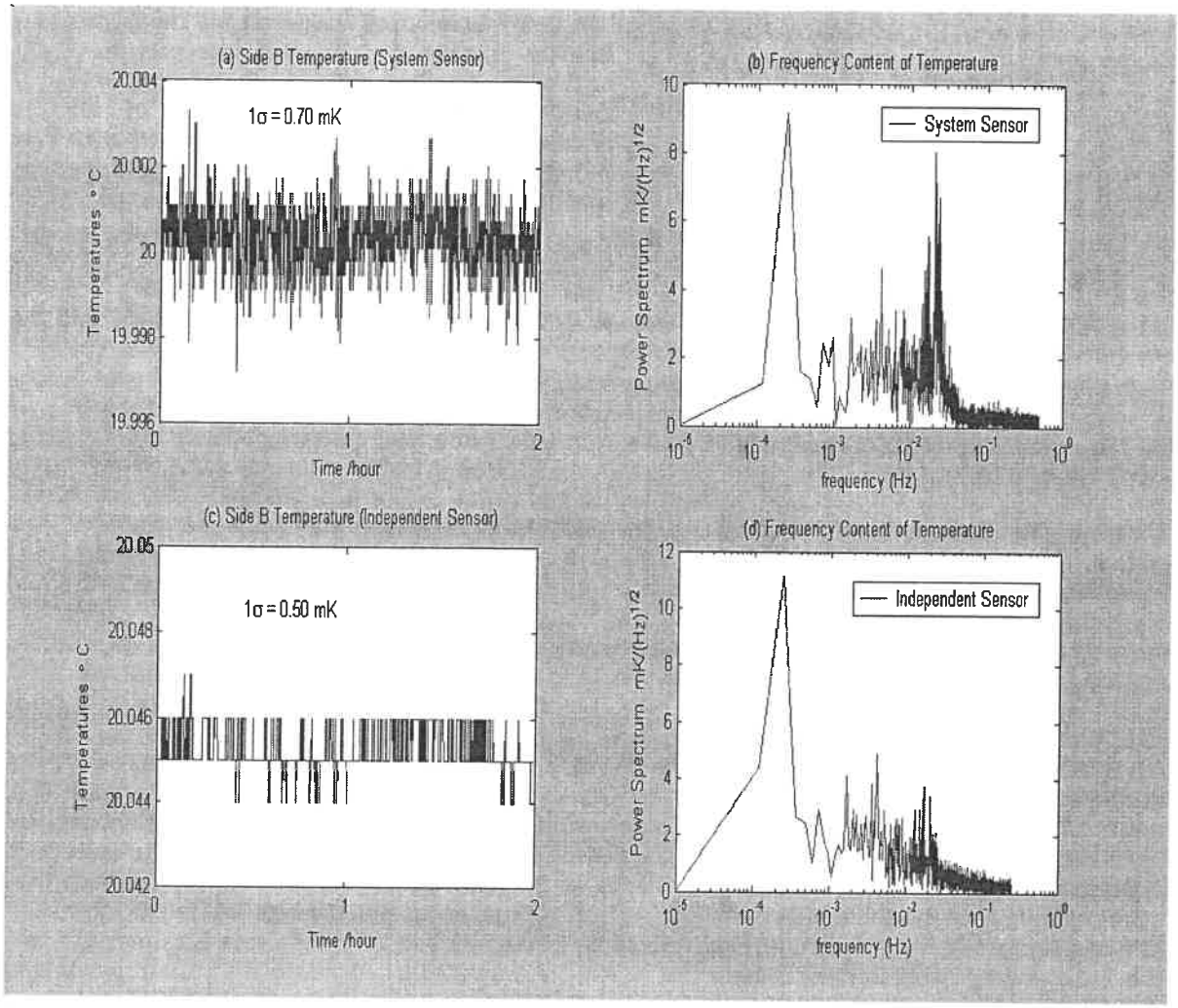

FIGURE 8. *The diagram of the thermal control system. The part inside the dashed square is the controller.*

THE DESIGN, CALIBRATION AND USE OF AN ULTRASONIC PROBE ON A CMM

Nick Orchard, Dean Whiteside
Manufacturing Technology Department
Rolls-Royce plc, Derby, UK

INTRODUCTION

Rolls-Royce has been producing wide-chord hollow fan blades for several years using the diffusion bonding and super-plastic forming process. The product of this process is the structure shown in Figure 1. This shows a typical fan blade cross-section, having a central cavity with a series of longitudinal webs that provide the required stiffness

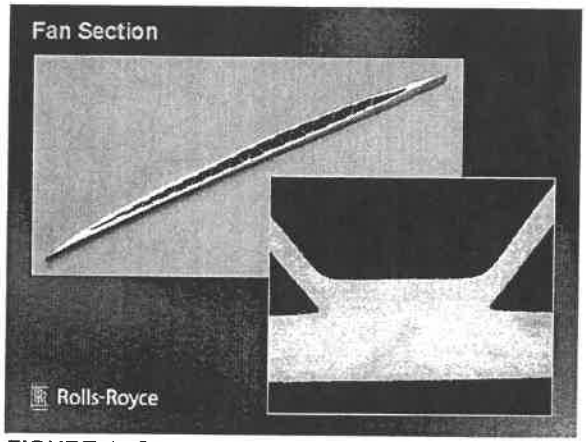

FIGURE 1. Cross-section view of a typical hollow fan blade.

After the forming process the blade is inspected to check that the wall thickness is within tolerance. This is done using an ultrasonic probe, either manually or more commonly with an automated C-Scan system. The C-Scan system has the blade fully submerged in a water bath, so that an ultrasonic probe can be rapidly traversed across the blade surface. The blade is mounted on a rotary axis so that the surface can be presented horizontally to the probe as it crosses the chord. A teach-and-learn system is used to program the 5 axis machine, but due to variations between blades the probe is held in a compliant mounting that allows about 10mm of vertical movement. While this is perfectly adequate for routine inspection, there are some times when there is a need to be able to digitise the interior surface more accurately in terms of the true position of the surface with respect to the blade datum features. The most accurate method of measuring a blade and its datum features is a CMM (co-ordinate measuring machine), but CMMs don't usually work very well under water. To solve this problem a new ultrasonic probe system has been designed that can be used automatically on a standard CMM. This paper describes how the probe has been designed to enable automatic probe changing on the Renishaw PH10 head, how the position of the probe tip is calibrated in 3D co-ordinate space, and how it is used in practice.

PROBE DESIGN REQUIREMENTS

The key design issues that had to be addressed were:

1. Light enough to be carried on a Renishaw PH10M probe head.
2. The probe transducer must be self aligning to the blade surface with 5 degrees of movement in any direction. This is to cover the limitation of the 7.5 degree index angle of the PH10, plus small variations between nominal and actual blade surface.
3. Sufficient pressure has to be applied to provide good signal coupling between the transducer and the blade surface, but the total force must not overload the PH10 or the CMM drive system.
4. Capable of being auto changed on the CMM for a conventional touch probe.
5. Hardware and software interface with the CMM so that the probe parameters can be set from CMM program control.
6. Calibration of the centre of the probe within 0.1mm in X/Y/Z axes at any PH10 position.

PROBE DESIGN

The final design of the probe is shown in Figures 2 and 3. The ultrasonic transducer has a 6mm diameter contact area. This size is a compromise between being small enough for the signal to be reasonably focussed, while being large enough to ensure that it sits flat on the surface. The transducer is held in a gimballed mount that is designed so that the axes of

rotation are as close as possible to the front face of the transducer.

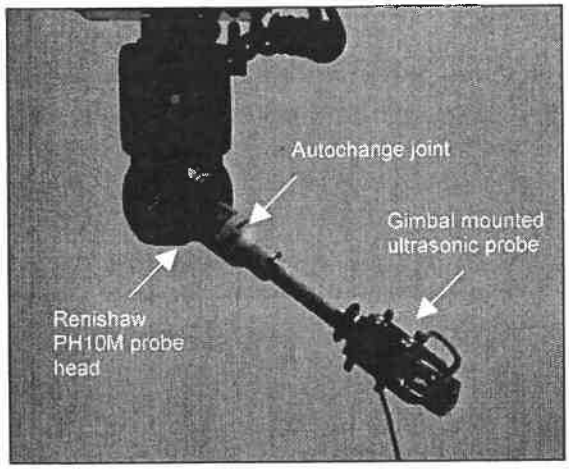

Figure 2. The ultrasonic probe system mounted on the Renishaw PH10 head.

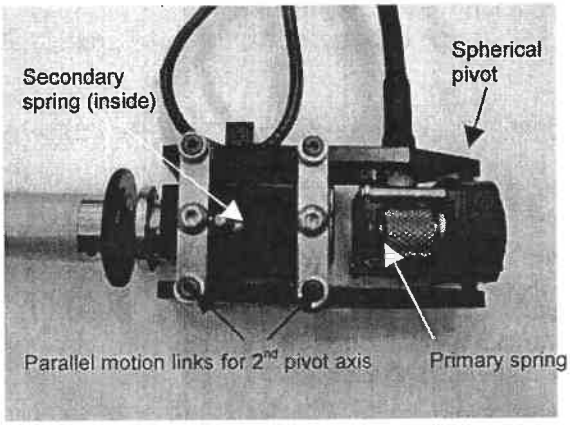

FIGURE 3. Close-up of the gimbal and spring mechanism

The transducer holder has two spherical pivots on opposite sides that locate in mating sockets in a pair of parallel motion plates. The two plates are linked so that probe can rotate about two axes without the centre of the front face moving significantly away from the probe centre line. Total movement of the head is about 10 degrees in any direction, although in practice selection of the correct PH10 angles should not require more than about 4 degrees.

Spring System

The primary spring is located behind the ultrasonic transducer. It has a spring rate that should provide adequate contact force with only 1mm of travel. The total travel is about 3mm, with the transducer itself sliding inside an outer cylinder. It is designed so that if the total travel is taken up (due to the probe being pushed too far onto the blade surface) the load will transfer to the outer cylinder, so the contact force on the transducer itself remains constant, regardless of the overall probe displacement. In other words the transducer can go below the surface of the outer cylinder. At this point the secondary spring provides further overtravel of the probe mechanism. It has a spring rate set so that the PH10 overload sensor will cut in before the end of the travel, giving it a 'soft' overload, rather than the shock overload if there was no spring present.

Auto Change Joint

Figure 2 shows how the ultrasonic probe system is mounted via a standard M8 thread to the Renishaw PAA1 Autojoint. A 50mm probe extension is used to enable the probe to fit in the Autochange rack. Although the prototype version has the transducer cable leading directly from the probe, production versions make use of the multi-wire joint and the cable runs through the CMM quill, so there is no trailing cable.

CALIBRATION

One of the main reasons for designing this system was to provide accurate data in 3D, so it is important that the true position of the ultrasonic probe can be calibrated with respect to the reference probe position. In order to do this a special artefact was designed that could be measured with both the standard touch probe and the ultrasonic probe. The artefact is shown in Figure 4.

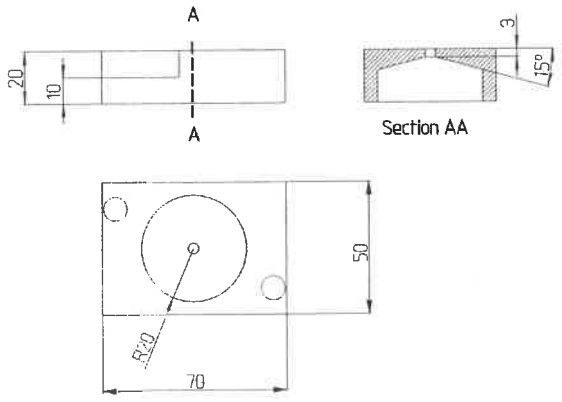

FIGURE 4. Calibration Artefact

The artefact is a rectangular block made of a similar material to the blade material (titanium alloy). The top face of the block is flat (apart from two shoulders with bolt holes to facilitate

clamping), with a small 3mm diameter hole in the centre. The underside of the block has a 20mm diameter recess that has a conical bottom, concentric with the 3mm hole. To calibrate the X/Y position of the probe, the block is first measured using the touch trigger probe. This provides the reference origin of the hole centre. The touch probe is then changed to the ultrasonic probe and a number of thickness measurements are made around the central hole, with the probe centre initially assumed to be coincident with the touch probe, see Figure 5.

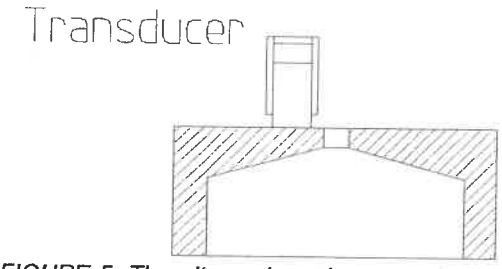

FIGURE 5. The ultrasonic probe measuring the cone thickness

The CMM software is used to convert the thickness measurements to the Z co-ordinates of a set of measurements of the cone, and then to calculate the best-fit cone to this set of points. The offset of the measured cone from the assumed origin point is the true calibrated offset of the ultrasonic probe origin. The key to the successful use of this type of artefact is to get the optimum cone angle. If the angle is too small (a flat cone) then the cone is not well constrained by the measured data, so the centre position measurement is not very repeatable. If the cone angle is too large (a steep cone) then the sound signals will be reflected away from the transducer resulting in a poor measurement signal. A cone angle of 15° has been found to give good results.

The calibration of the probe in the Z-axis is less critical than the X- and Y-axes because the need is different. In the X/Y directions it is important to know where the probe is touching the blade so that the thickness measurement can be registered in the correct position. In the Z direction the need is to make sure that the probe is in secure contact with the surface and is roughly in the middle of its range of movement. Calibration is done by driving the probe manually until it just touches the surface of the calibration block, with about 0.1mm to 0.3 mm of travel. Having previously set the Z origin to the top of the block using the touch probe, the position of the ultrasonic probe Z datum offset is given by the Z-axis reading with the opposite sign.

Transducer Response Calibration

It is important that the ultrasonic transducer response characteristic is calibrated for the specific material of the blade being measured. It is not adequate just to use a calibrated thickness sample of the nominal material because the material properties can vary from blade to blade. However, as this system has the ability to change from the touch probe to the ultrasonic probe, this can be done automatically. A thickness measurement is made using the touch probe on a suitable position on the blade, say near the edge of the aerofoil. Re-measuring the same point using the ultrasonic probe gives the true thickness calibration for that blade.

SYSTEM INTEGRATION

In order to achieve fully automatic operation, another requirement is to have the ultrasonic electronics integrated with the CMM system. The Staveley Sonic 1000PG driver/reader system is capable of remote operation via an external PC. See Figure 6. This enables various parameters, in particular the threshold levels, to be read and set from the CMM. The CMM program can make decisions about the quality of the signals that it is receiving in the course of the measurement, and make changes to try and improve it. This is important because the thickness of the blade may vary by a factor of two or more from the top to the bottom, or from the centre to the edge, and this can cause deterioration of the signal.

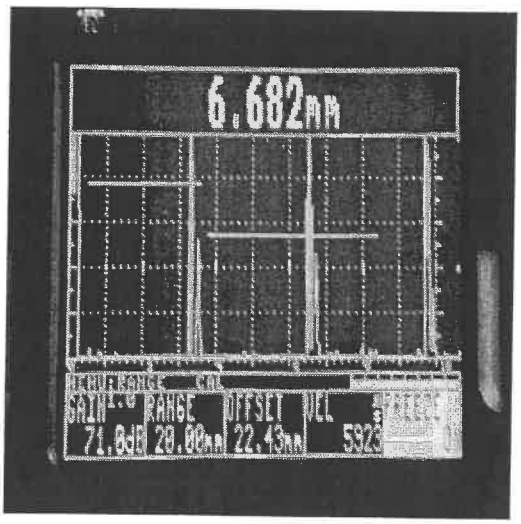

Figure 6. Staveley Sonic 1000PG system

THE PROBE IN USE

To use the probe to make true 3D measurements of the interior wall positions it is first necessary to find the actual position of the blade. A conventional touch probe is used to measure the blade datum positions, which are normally taken from either the aerofoil or the root form, and this creates the blade co-ordinate system. A contact scanning probe such as the Renishaw SP25 is then used to digitise the external blade surface at all the section heights at which internal measurements are required. This data provides the target co-ordinates and surface normals for all of the points at which ultrasonic measurements will be made. For each point the nearest PH10 head position is calculated and the ultrasonic probe is driven to a point that is nominally about 1mm below the surface of the blade. This ensures that the probe will be firmly in contact with the blade at roughly the mid-point of its travel. When the ultrasonic thickness reading has stabilised the CMM records the value. A measured point on the interior wall of the blade is then created by projecting the surface normal at the measurement position by the distance of the recorded thickness measurement.

CONCLUSIONS

We have successfully demonstrated that it is possible to calibrate a CMM-mounted ultrasonic probe in 3D, so that it can be combined with a conventional touch probe to provide accurate co-ordinate data on the inside cavity of the hollow fan blades. Patents applications have been made for several of the novel features of this technique.

ACKNOWLEDGEMENTS

The authors would like to thank the following organisations and people for their contributions to this project: Mitutoyo UK, Renishaw plc, Sperry Rail International Ltd, Corbyco (UK) Ltd, Dominic Barnard.

MOMENT OF INERTIA MEASUREMENT USING A FIVE-WIRE TORSION PENDULUM AND OPTICAL SENSING

Aaron J. Swank[1], Corwin Hardham[2], Ke-Xun Sun[1], Dan B. DeBra[1]
[1]Stanford University
Stanford, California
[2]Squid Labs
Emeryville, CA

INTRODUCTION

Typical moment of inertia measurement devices are capable of 1 part in 10^3 accuracy and current state of the art techniques are approaching capabilities of a few parts in 10^4 [1]. Introduced here is a new method for measuring the moment of inertia using a novel five-wire torsion pendulum design, which shows the prospect of improving on current state of the art.

A moment of inertia measurement apparatus typically attempts to produce a pure rotation about one degree of freedom. The measurements of rotation can have uncertainties when there are significant other degrees of freedom. Bifilar and trifilar pendulums, for example, do not constrain the swinging or lateral translation modes. The five-wire design reduces errors due to tilt and horizontal translational degrees of freedom.

The five-wire torsion pendulum is integrated with optical angular sensing using diffraction grating angular magnification. Optical sensing decouples any vertical motion from the detection sensor signal and the associated angular magnification allows for a high sensitivity measurement.

MEASUREMENT

Measurement Apparatus

When designing an apparatus to measure the moment of inertia to a high precision, care must be taken to minimize the extra degrees of freedom in the system. To improve the accuracy of a standard trifilar pendulum, the lateral pendulum modes need to be constrained. In a five-wire pendulum, two additional wires are arranged as shown in figure 1 to minimize rotations about the other two rotational axes. The

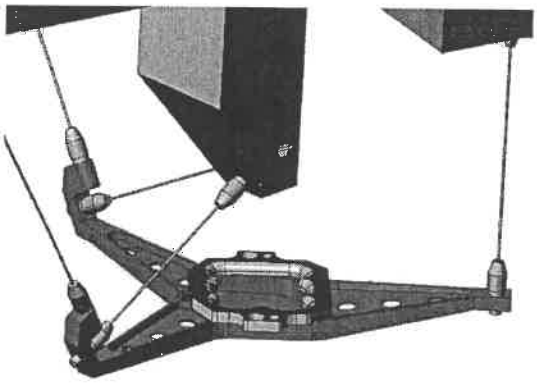

FIGURE 1. Torsion pendulum platform attach points for the five wires. A kinematic orientation fixture is in the center.

three attach points on the platform supporting the inertia to be measured are positioned equidistant from the center of rotation. At one attach point, a single vertical wire is used and the other two attach points consist of two wires. The horizontal components of the wires which are splayed out from a single attach point provide horizontal stiffness to prevent pendulum platform swinging motion. The wires are attached to the supporting frame along a line emanating from the rotation center at a point in the plane containing the mass center of the object

to be measured. The choice of the attach point locations on the supporting frame ensures a constant curvature at the platform wire mount points from each wire, which coincides with the curvature of the pendulum rotation. The constant curvature constraint is necessary to ensure proper rotation about the vertical axis.

The full moment of inertia tensor contains six independent terms. As such, a moment of inertia measurement device must be capable of determining the moment of inertia about at least six different axes of rotation. A torsion pendulum design is capable of measuring the inertia about one axis. Therefore, the apparatus requires the capability of re-orienting the measurement object to at least six independent directions. The five-wire measurement apparatus utilizes a kinematic fixture which permits changing the orientation of the object with high repeatability. A set of sleds to generate different orientations were constructed. These kinematic orientation fixtures are repeatable to $0.02°$. The fixtures are mounted to the pendulum platform using a set of v-grooves and ball bearings for a repeatable placement.

Grating Angular Sensing

The oscillatory motion of a torsion pendulum is described by the relationship between the radius of gyration R_g, or the instantaneous moment of inertia about the axis of rotation I_p, and the angular frequency ω

$$R_g^2 = \frac{I_p}{m_p} = \frac{k}{\omega^2} \qquad (1)$$

where k is the torsion coefficient or stiffness constant of the pendulum and m_p is the total mass of the pendulum. The moment of inertia for the system is therefore determined by measuring the angular frequency ω and the pendulum mass. The angular displacement of the five-wire pendulum is measured by application of a grating angular sensor [2]. A diffraction grating is attached to the pendulum platform at the center of rotation. Using a laser as a light source, the grating diffraction orders are used for angular sensing as depicted in figure 2. As the pendulum platform rotates, the

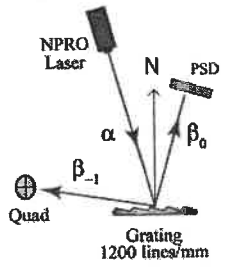

FIGURE 2. Setup of the grating angular sensor on the five-wire torsion pendulum.

diffracted beams rotate similar to a plane mirror reflection but are additionally magnified by the diffraction order angle. Any minor translational motion of the pendulum will not be magnified and vertical motion of the pendulum will not affect the diffracted beam. If the pendulum rotates (and hence the attached grating) by an angle of $\delta\alpha$, the resulting incremental rotation angle $\delta\beta_n$ of the diffracted beam for diffraction order n is given by [2]

$$\delta\beta_n = \frac{\cos(\alpha)}{\cos(\beta_n)}\delta\alpha \qquad (2)$$

where α and β_n are the angles from the grating norm for the incident beam and the diffraction angle respectively. This grating angle magnification enhances the measurement sensitivity. The grating angular sensor magnifies the angular displacement of the pendulum but does not magnify any translation.

The diffracted beams are captured by a position sensitive diode (PSD) at the 0 diffraction order and a quad photo diode at the -1 diffraction order. The diffraction order angles of $81°$ and $16.8°$ were chosen to combine the advantages of a high dynamic range sensor with high precision.

Calibration

As with any measurement device, the apparatus must first be calibrated before measurements can be made. For the five-wire torsion

FIGURE 3. Pendulum Platform. The nine large holes are used for calibration sphere placement.

pendulum, the moment of inertia for the pendulum platform must be determined. The oscillatory motion of a torsion pendulum is described by the relationship in equation 1. The unknown moment of inertia and torsion coefficient for the pendulum are determined by adding a known moment of inertia to the system. This is achieved by the addition of n calibration spheres to the platform with a known moment of inertia I_c, such that the relationship in equation 1 becomes

$$I_p + \sum_{i=1}^{n} I_{ci} = \left(m_p + \sum_{i=1}^{n} m_i \right) \frac{k}{\omega^2} \qquad (3)$$

Each calibration sphere mass m_i with radius a_i, is placed in holes at locations R_i, determined by a coordinate measuring machine. The use of fixed holes for locating the calibration spheres ensures a high repeatability for positioning and hence a consistent addition to the total system moment of inertia. Since the calibration spheres are not placed at the rotation center of the pendulum platform, the parallel axis theorem is applied and equation 3 becomes

$$I_p + \sum_{i=1}^{n} m_i R_i^2 + \tfrac{2}{5} m_i a_i = \left(m_p + \sum_{i=1}^{n} m_i \right) \frac{k}{\omega^2}$$

The calibration measurement is repeated for various combinations of calibration sphere positions. A least squares fit of the measured data is then performed to obtain the unknown parameters. During the calibration process, the same number of spheres are used to ensure a constant system mass, avoiding a change in the torsion coefficient for the system. In addition, the calibration process is performed with the orientation fixtures in place, such that the only addition to the system after calibration is the object for which the moment of inertia is to be determined.

PRELIMINARY RESULTS

The pendulum platform contains a small permanent magnet, surrounded by two wire coils, which when energized produces a magnetic field and hence a torque on the platform. By sending a pulse to the coils using a function generator, a repeatable pendulum response is generated. The time history angular position of the platform is recorded from the PSD and Quad photo diode signal. The pendulum oscillatory frequency is easily extracted by data reduction in the time domain. The response to a single disturbance to the pendulum is known to be governed by the equations for damped harmonic motion. A nonlinear curve fit is then applied to the data to experimentally determine the parameters of the pendulum response, including the natural frequency and damping coefficient. Shown in figure 4 is a representative time domain curve and fit to the data obtained during the calibration procedure with the 5° orientation fixture in place.

During the calibration process, multiple measurements of the oscillation frequency were performed for each combination of the calibration sphere positions. The individual calibration measurements indicated a repeatability on frequency determination for the time domain curve fit data to be within the standard deviation range of $\sigma = 2 \times 10^{-6}$ to 9×10^{-6} Hz for a frequency of around 2.9 Hz, depending on the particular configuration for the calibration spheres. After measuring the frequency for various combinations of calibration sphere locations, a least squares analysis was performed

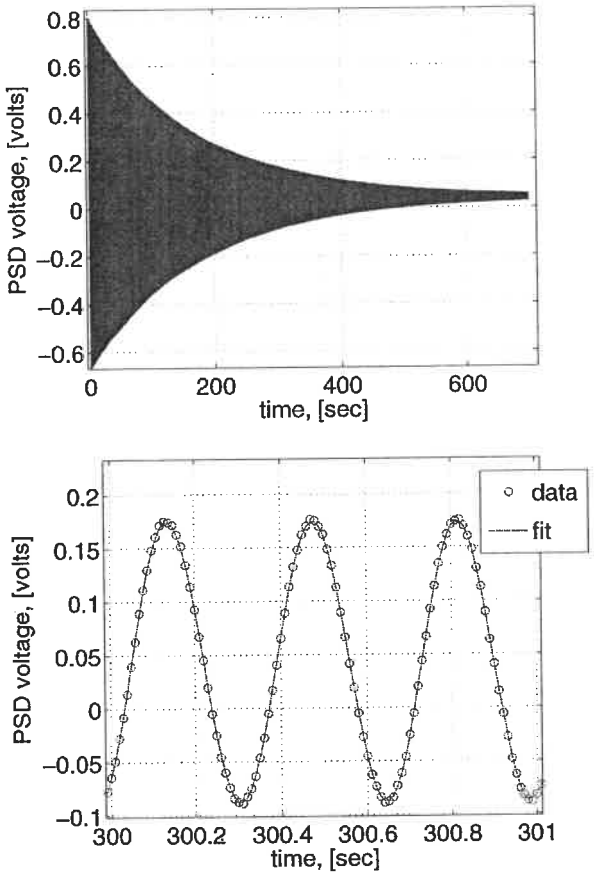

FIGURE 4. A representative segment of data for the pendulum angular position data and curve fit. The data was obtained with the 5° orientation fixture and the three calibration spheres placed in the innermost hole locations.

to determine the moment of inertia about the rotation axis for the pendulum platform with the 5° orientation fixture in place. By including different combinations of calibration measurements in the least squares analysis, a preliminary value for the pendulum platform moment of inertia with the 5° orientation fixture in place was found to be $5632\,\mathrm{g}\cdot\mathrm{cm}^2$ with a standard deviation of $\sigma = 1.0\,\mathrm{g}\cdot\mathrm{cm}^2$ resulting in a repeatable precision on the order of a few parts in 10^4.

CONCLUSIONS

The precision of the measured moment of inertia can not be more precise than the uncertainty associated with the calibration of the measurement device and the measurement of the object's mass. Currently only the calibration phase of the measurement phase has been conducted. The preliminary results indicate a repeatable precision on the order of a few parts in 10^4 for the calibration process, suggesting the measurement apparatus could be capable of near state of the art precision. The current repeatability of the frequency measurements leads us to believe that there is a possibility for improvement of the current state of the art. It should be noted that a full error analysis on the acquired data has not been completed. As such the preliminary results can only give insight into the repeatability of the measurements and not a true representation for the *accuracy* of the measurements.

ACKNOWLEDGMENTS

The authors acknowledge and thank Dr. Robert L. Byer for support and equipment. Professor Dave Beach and the precision engineering course participants Ercan Dede, Jon Glassman, Dan Kalcic, and Kristof Richmond [3] are acknowledged for apparatus construction and initial mechanical prototype design. The authors also wish to thank Graham Allen for numerous enlightening discussions.

REFERENCES

1. N. A. Lockerbie. Dynamical measurements of the gravitational quadrupole coupling to experimental test masses. *Classical and Quantum Gravity*, 18(13):2521–2531, 2001.

2. K-X. Sun, S. Buchman, and R. L. Byer. Grating angle magnification enhanced angular and integrated sensors for LISA applications. *Journal of Physics: Conference Series*, 32:167–179, 2006.

3. E. Dede, J. Glassman, C. Hardham, D. Kalcic, and K. Richmond. Inertia pendulum for the STEP project. Stanford University, ME 324 Precision Engineering Final Report, 2001.

SELF-CALIBRATION FOR AIR-BEARING ROTARY ENCODERS

Xiaodong Lu[1], and David L. Trumper[2]
[1]Dept. of Mechanical Engineering, UBC, Vancouver, BC, Canada
[2]Dept. of Mechanical Engineering, MIT, Cambridge, MA, USA

INTRODUCTION

High-accuracy rotary encoders are required for rotational axis position measurement in ultra-precision manufacturing and measurement equipments. A typical rotary encoder is made of a glass disk with a fine grating pattern and a scanning read head unit. Digital pulse trains are output from the read head to represent the disk rotary position. The angular measurement accuracy of such a rotary encoder is highly dependent on the grating pattern manufacturing error (uniformity and eccentricity of the graduation), glass disk installation on the measured rotary axis, the scanning head alignment, and signal processing circuits. All these elements unavoidably contribute to rotary encoder errors. If repeatable components of rotary encoder errors can be calibrated accurately, then they can be corrected through software mapping. Calibration of a rotary encoder needs to be conducted after the encoder is installed on the spindle end product, because this installation process may contribute to a significant amount of encoder errors. Therefore, a simple and accurate calibration method is highly desired by end users. Most existing calibration methods are based on a secondary angle sensor of higher accuracy mounted on the same rotary axis as the encoder to be calibrated. Usually that secondary angle sensor installation and setup relies on sophisticated instrument to ensure accuracy [1], and thus cannot be easily performed by end users. Self-calibration encoders have been developed to eliminate the use of a secondary angle sensor for calibration. Watanabe *et al* has demonstrated a self-calibration encoder using five identical read heads evenly distributed around a single optical disk [2]. However, that specially constructed encoder cannot calibrate error components in the 5th order spindle rotation frequencies and its harmonics. Moreover, the calibration accuracy also depends on the accuracy of these read heads installation and alignment. Most importantly, this calibration method cannot be applied to most existing encoders.

This work presents the principle, analysis, and experimental results of a novel self-calibration method for rotary encoders on air-bearing supported spindles. By recording the time of each encoder signal edge during spindle free response, calibration curve can be derived by processing the recorded data. Two distinctive features of this method are: 1) it does not need a secondary sensor as a calibration reference; 2) it can be applied to commercial rotary encoders without hardware modification. The experimental results indicate that the calibration repeatability is within 0.002 RMS grating line of the encoder.

Next, we will use our experimental setup as an example to illustrate the self-calibration method and discuss experimental results. The spindle is a Professional Instrument 4R Twin-mount motorized air-bearing spindle. Due to the lack of a high pressure air supply, the air-pressure of the spindle in the calibration process is 80 psi, instead of manufacture recommended 150 psi. A Heidenhain bearing-less optical encoder (ERO 1324-004-2500) is installed on the back of the spindle: the encoder optical disk is on the spindle rotor and the read head unit is on the spindle housing. The optical disk has 2500 grating lines.

ENCODER SIGNAL PROCESSING

As shown in Fig. 1, the encoder outputs are a pair of quadrature digital signals A/B (2500 pulse/rev) and an index signal (1 pulse/rev). Their rising/falling edges corresponds to N=10,000 spatial sampling events in each revolution to label the spindle rotary position. Essentially these sampling events are evenly spaced in spindle angle domain. The nominal spatial distance between two consecutive sampling events is Δ_0=0.25 line, where one line corresponds to 1/2500 revolution or 518.4 arc-sec. These events are numbered with reference to the rising edge of the index signal. The encoder error of the k-th sampling event is defined as

$$E(k) = \sum_{i=1}^{k} \Delta(i) - k\Delta_0 , \qquad (1)$$

where $\Delta(i)$ is the actual sampling interval between i-th and (i-1)-th event. The time span associated with $\Delta(i)$ is denoted as $T(i)$, which is captured by a circuit of 100 MHz clock. Based on this time measurement, the encoder error will be derived.

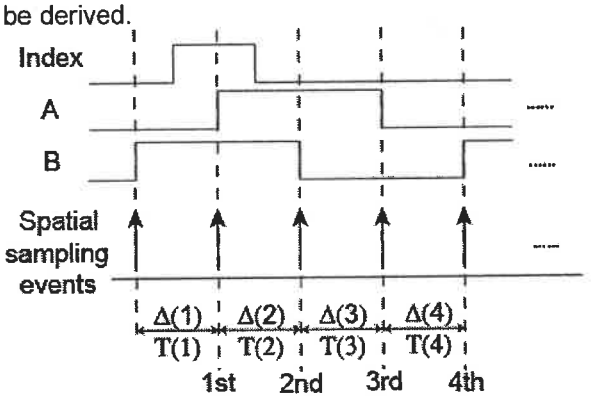

FIGURE 1. Spatial sampling events associated with encoder signals. Signal A, B, and Index are outputs from the rotary encoder. Sampling events are numbered according to the rising edge of the Index pulse.

ZERO-ORDER METHOD

The most straight-forward way to self-calibrate rotary encoder is to maintain the spindle at perfect constant speed, then the sample intervals can derived from $T(i)$ measurement as $\Delta(k)=\omega_0 T(k)$, where ω_0 is the spindle speed and can be calculated as:

$$\omega_0=\frac{\sum_{k=1}^{N}\Delta(k)}{\sum_{k=1}^{N}T(k)}=\frac{N\Delta_0}{\sum_{k=1}^{N}T(k)}. \qquad (2)$$

However, it is impractical to control the spindle speed at a constant speed accurate enough for calibration purpose, due to motor driving torque ripples and feedback sensor errors.

AIR-BEARING SPINDLE FREE RESPONSE

We propose methods to calibrate the encoder at spindle free response. The spindle is accelerated to a certain speed, and then the spindle motor is turned off, letting the spindle slows down freely. The dynamics equation of the spindle in this free response is $I\frac{d\omega}{dt}+C\frac{d\theta}{dt}=0$, where θ is the spindle angle, I is the inertia, and C is the damping constant. Equivalently in angle domain, we have:

$$\frac{d\omega}{d\theta}=-\frac{C}{I}. \qquad (3)$$

Although speed ω is not a linear function of time, it is a linear function of angle θ and thus the spindle speed at k-th sampling event $\omega(k)=\Delta(k)/T(k)$ is a linear function of sampling event index k. This is the basis of our self-calibration method. As the actual value of $\Delta(k)$ is not known yet, from time measurement $T(k)$ we can calculate apparent spindle speed $\omega_a(k)=\Delta_0/T(k)$ using the nominal value of $\Delta(k)$. This apparent speed is the combination of the spindle speed and encoder error: $\omega_a(k)=\omega(k)+(\Delta_0-\Delta(k))T(k)$. Fig. 2 shows an experimentally measured spindle apparent speed. By estimating the linear component $\omega(k)$ from measurement $\omega_a(k)$, encoder grating spacing $\Delta(k)$ can be calibrated using the first-order method derived in the next section.

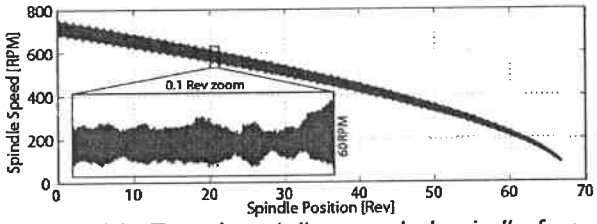

FIGURE 2. Experimentally recorded spindle free response versus spindle rotation over 65 revolutions. The insert shows the detailed apparent speed waveform within 0.1 revolution.

FIRST-ORDER SELF-CALIBRATION METHOD

Assuming the spindle damping is a constant, from Equation (3) the spindle speed can be parameterized as $\omega(k)=\omega_0+a\times k$, where ω_0 and a are unknown constants to be estimated. The spatial interval is expressed as:

$$\Delta(k)=T(k)\times(\omega_0+a\times k). \qquad (4)$$

Summing the data together over a full recorded revolution starting from the s-th sampling event, we have

$$\sum_{i=s+1}^{s+N}\Delta(i)=\sum_{i=s+1}^{s+N}T(i)\times(\omega_0+a\times i), \qquad (5)$$

where s is the starting point of the data batch over one full revolution. The left side is exactly one revolution:

$$N\times\Delta_0=\omega_0\times\sum_{i=s+1}^{s+N}T(i)+a\times\sum_{i=s+1}^{s+N}T(i)\times i. \qquad (6)$$

Combining (4) and (6), we get

$$\Delta(k)=T(k)\frac{N\times\Delta_0}{\sum_{i=s+1}^{s+N}T(i)}+a\times\left(k-\frac{\sum_{i=s+1}^{s+N}T(i)\times i}{\sum_{i=s+1}^{s+N}T(i)}\right)\times T(k)\equiv F(a,k)$$
$$k=s+1,\ \ldots\ s+N. \qquad (7)$$

However, this equation is not sufficient to estimate parameter a. Two batches of data are used as shown in Fig. 3 with starting point s_1 and $s_2 (> s_1)$, and parameter a_1 and a_2, respectively. Applying Equation (7) to both data batches, we have $2N$ equations:

$$\begin{aligned} \Delta(k) &= F_1(a_1, k), \quad k = s_1 + 1, ..., s_1 + N; \\ \Delta(k) &= F_2(a_2, k), \quad k = s_2 + 1, ..., s_2 + N \end{aligned} \tag{8}$$

Canceling out $\Delta(k)$ in Equation (8), we get

$$\begin{cases} F_1(a_1, k) = F_2(a_2, k+N), \text{for } k = s_1 + 1, ..., s_2 \\ F_1(a_1, k) = F_2(a_2, k), \text{for } k = s_2 + 1, ..., s_1 + N \end{cases} \tag{9}$$

Note, Equation (9) consists of N equations, and each of them is a linear function of two unknown parameters a_1 and a_2. Through least square fitting, we can get the best estimate of these parameters $\bar{a}_1$ and $\bar{a}_2$. Plugging $a_1 = \bar{a}_1$ back to Equation (8), we can get the calibration of sample interval $\Delta(k)$ for $k = 1, ..., N$.

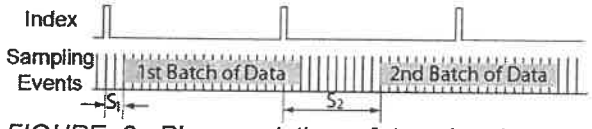

FIGURE 3. Phase relation of two batches of data for self-calibration.

EXPERIMENTAL CALIBRATION RESULTS

Applying this self-calibration algorithm to the experimental data in Fig. 2, Fig. 4 shows the calibrated grating error $\Delta(k) - \Delta_0$ at 700 RPM speed. The starting points of the two batches of data used are s_1=0 and s_2=5000, corresponding to 180 deg phase shift. Integrating this grating error according to Equation (1), the resulting encoder error is plotted in Fig. 5.

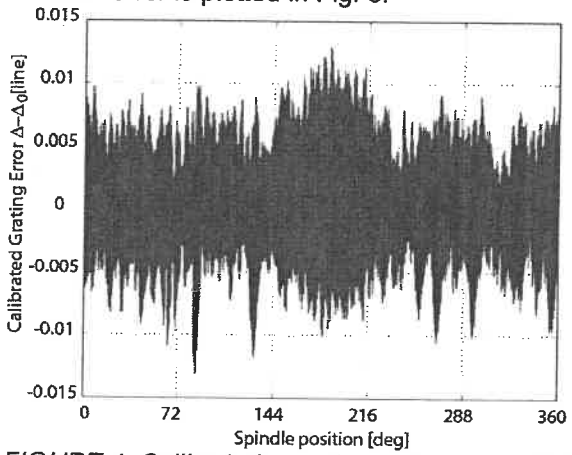

FIGURE 4. Calibrated encoder grating error. 700 rpm spindle speed, s_1=0, and s_2=5000.

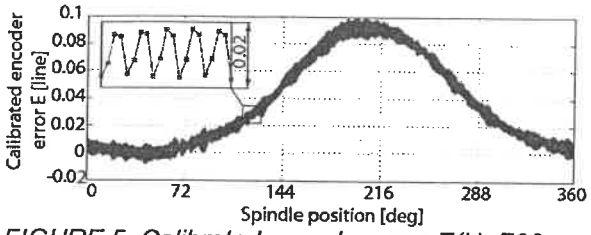

FIGURE 5. Calibrated encoder error E(k). 700 rpm spindle speed, s_1=0, and s_2=5000. The insert shows a detailed view of the encoder error.

Fig. 5 shows that this encoder has a maximum error of 0.11 grating lines. The insert indicates that significant error comes from the misalignment of two detectors for signal A and B. In spatial frequency domain, the Fourier Transform of this encoder error is shown in Fig. 6. The amplitude of the encoder error decades with the increase of spatial frequency, however, at 2500 and 5000 cycles/rev the detector misalignment error increases significantly.

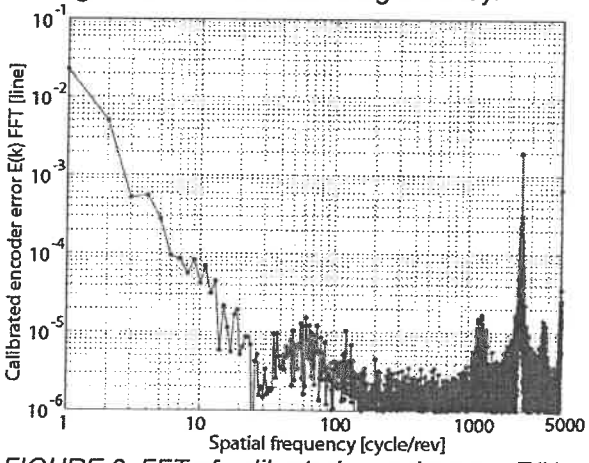

FIGURE 6. FFT of calibrated encoder error E(k). 700 rpm spindle speed, s_1=0, and s_2=5000

In order to evaluate the above calibration results, we investigated the repeatability of the calibration results at various spindle speeds and starting points of data batches.

REPEATABILITY VS DATA PHASE SHIFT

First, at 700RPM and fixing s_1=0, we applied the first-order algorithm on the same experimental data in Fig. 2 with different s_2. The calibrated encoder error map with s_2=5000 is used as a reference $E_0(k)$, and calibrated map with other s_2 is $E(k, s_2)$. The calibration repeatability $R(s_2)$ is the root mean square of the difference between two maps: $E_0(k)$ and $E(k, s_2)$

$$R(s_2)=\sqrt{\frac{\sum_{k=1}^{10000}\left(E(k,s_2)-E_0(k)\right)^2}{10000}}. \qquad (10)$$

Fig. 7 shows this repeatability as a function of the phase shifts of two data batch s_2- s_1. This result indicates that the calibration repeatability is less than 0.002 grating line for most phase shift. However, when the phase shift of two data batches is close to 0 or 10000 samples (equivalent to 0 or 360 deg of spindle rotation), the repeatability degrades significantly due to singularity of Equation (9). To ensure accurate calibration result, the phase shift of two batches should be selected between 90 and 270 deg of rotation.

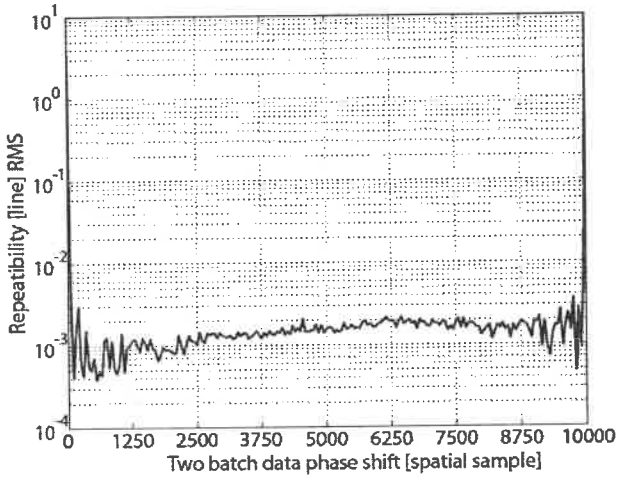

FIGURE 7. Calibration repeatability versus phase shift of two data batches. The spindle speed is 700 RPM.

REPEATABILITY VS SPINDLE SPEED

Applying the first order self-calibration algorithm to the whole data in Fig. 2 by fixing s_1=0 and s_2=5000, we investigated calibration repeatability versus spindle speed. The calibrated encoder error map at 700 RPM is used as a reference $E_0(k)$ and the calibrated map at speed n is is E(k, n). The calibration repeatability R(n) is the root mean square of the difference between two maps $E_0(k)$ and E(k, n):

$$R(n)=\sqrt{\frac{\sum_{k=1}^{10000}\left(E(k,n)-E_0(k)\right)^2}{10000}}. \qquad (11)$$

The dashed line in Fig. 8 shows this repeatability of the first-order self-calibration method as a function of the spindle speed. This result indicates the repeatability degrades as the spindle speed decrease. This is caused by the nonlinear damping of the spindle air bearing. From Fig. 2, it is obvious that the spindle damping increases as speed slows down over a large speed range. Actually, the damping of the spindle also changes even within one revolution, and thus deviates from the constant damping assumption used in first-order algorithm.

To improve the calibration repeatability, we further developed the second order algorithm, which assumes the damping coefficient to change linearly with spindle speed and thus the spindle speed can be parameterized as:

$$\omega(k)=\omega_0+a\times k+b\times k^2, \qquad (12)$$

where a and b are unknown parameters to be estimated. The mathematics of the second order self-calibration method can be derived in a similar way to the first order method. Applying second-order method to the experimental data in Fig 2, the calibration repeatability versus speed is shown by the solid line of Fig. 8. Much better than that of first-order method, the repeatability of second–order method is less than 0.002 grating line for speed range from 300 RPM to 700 RPM, Therefore, the calibration error map obtained from this speed range should be used. Once the error map is established, it can be used at any spindle speed. Through this calibration, the rotary encoder accuracy is enhanced from 0.12 lines to 0.002 lines RMS.

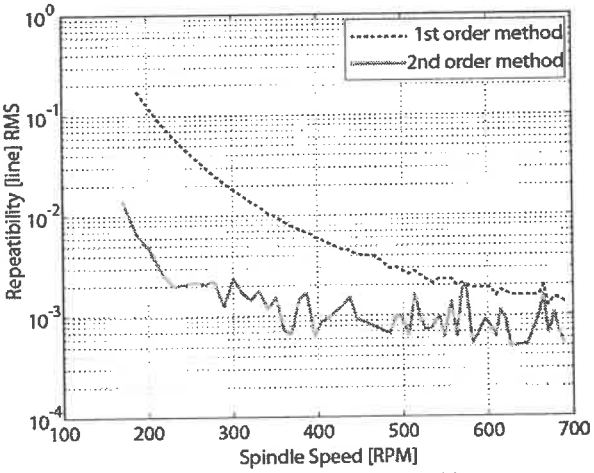

FIGURE 8. Calibration repeatability versus spindle speed. The calibration map of 700 RPM is used a reference. s_1=0, and s_2=5000.

REFERENCES

1. Satoshi Kiyono *et al*, 1997, Self-calibration of precision angle sensor and polygon mirror, Measurement, Vol 21, No 4, pp125-136.
2. Tsukasa Watanabe *et al*, 2005, Self-Calibration Rotary Encoder, 7th International Symposium on Measurement Technology and Intelligent Instruments, Journal of Physics: Conference Series 13 (2005) pp 240-245.

RAPID HIGH RESOLUTION ABSOLUTE 2-D ENCODING BY LOW RESOLUTION DIGITAL IMAGING OF A MATHEMATICALLY GENERATED 3-TONE TARGET

David C Chu, Haydee Trujillo, Evan Whitney and Jeff Young
NanoTechnology Measurement Division
Agilent Technologies, Inc.
Santa Clara, California, USA

INSTRODUCTION

A key problem in absolute 2-D encoding by imaging is to quickly and accurately identify the location of a small captured image in a large target. To 2-D correlate the image with every single subset of the target would be prohibitively cumbersome. Prior solutions include embedded codes, (pseudo-)random patterns, multi-tone pixels, and abundant pixels, [1-3]. Our system uses a deterministic target pattern consisting of white and black lines criss-crossing orthogonally over a grey background. There are only three nominal tones: white, grey, and black. (A grey region can be approximated by a checker for a 2-tone b/w target). For robustness, a 32x32 pixel subset anywhere within the target is not simply unique, but differs from any other subset with some redundancy. If he target is orthogonal and symmetric, horizontal and vertical dimensions are independently and identically decoded, with a 1-D, not 2-D, correlation-like algorithm. The target's tri-tones are represented by 1, 0, and -1. Therefore, correlation dot-product computation with such simple coefficients is realized with high-speed digital logic accumulators, without actually performing digital multiplications. Image pixel is 1:1 with sensor pixel in scale, but not necessarily in alignment. An interpolating algorithm based on statistical regression efficiently computes the optimum offsets, and provides fractional-pixel resolution of the image location in both dimensions on a "best-fit" basis.
In absolute position encoding, each frame is self-sufficient; makes no reference to any other prior frame. As a by-product, the algorithm also measures average grey-white-black intensities of the image. Imperfect target fabrication or defocusing may cause some anomaly at pixel boundaries. These systematic distortions are corrected locally after decoding.

A MATHEMATICALLY GENERATED TARGET

A small 55x55 pixel target in Figure.1 illustrates the underlying orthogonal and symmetric mathematical structure of the design. It consists of black and white lines, one pixel wide, traversing the entire target orthogonally. Periodicity is irregular, but deterministic, and symmetric about a cross-backbone labeled ccc - 3 pixels wide. The lower right shows 4 "periods" labeled 22222, 55555555, 55555555, 22222. Each period has a white-grey-black preamble followed by a number of grey pixels that is its namesake. Thus this entire target is completely defined by the short sequence 2,5,5,2. The grid

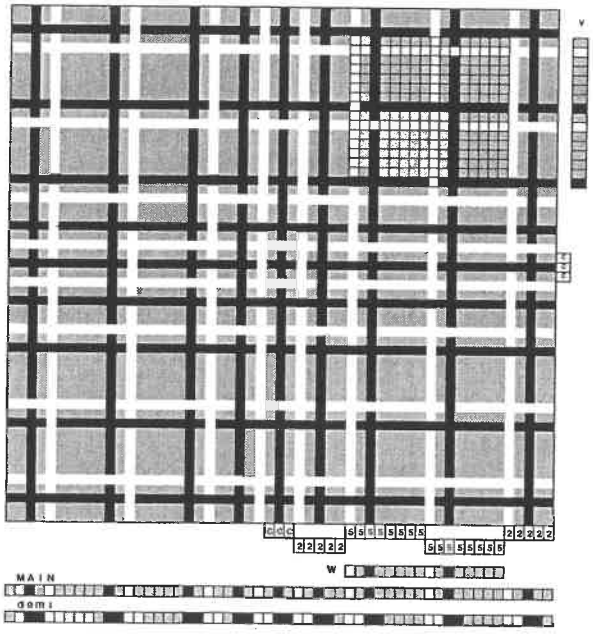

*FIGURE 1. A 55x55 pixel target consists of irregular "periods" placed symmetrically about a cross shown as ccc. Lower right shows four such periods each with a white-grey-black preamble followed by 2, 5, 5, 2 grey pixels respectively. Sequence 2-5-5-2 completely specifies the target. The grid shows a typical 16x16 pixel captured image. **V** and **W** are margin-vectors of the image. They are 1-D "correlated" against target margin-vectors **Main** and **demi** for Coarse Decoding. Identical vertical target margin- vectors are not shown.*

square shows a possible captured image. Summing rows and columns of the image pixels produces *image* margin-vectors ***V*** and ***W***. These are processed in a 1-D correlation-like operation against *target* margin-vectors ***Main*** of alphabets -1, 0, 1. For foolproof operation, they are also correlated against the *target*-margin-vector ***demi***, also with alphabets -1, 0. 1, Vector ***demi*** is the (vector-) sum of ***Main*** and its 1-right-shift neighbor. A pixel at an intersection of a black and a white line is usually assigned grey. In Figure 1, however, they are assigned black or white in a woven pattern.

Larger Target Synthesis

A 711x711 pixel target is designed with a longer sequence than 2,5,5,2. The sequence chosen is

2,5,5,2,-2, 5,4,3,2,5, 3,-4,2,4,4,
4,2,3,-5,4, -2,2,4,5,-3, 2,3,4,-5,2,
3,-3,4,3,5, 2,-4,3,4,4, -3,3,3,-5,3,
3,2,2,2,-3, 2,4,2,5,-2, 5.

Spaces are added for legibility. This sequence, ignoring for the moment the negative signs, is a sequence with four alphabets {2, 3, 4, 5} with no repeating 3-element group. It is, however, not a 4-alphabet deBruijn sequence [4] of order 3. For some larger combinations such as 5,5,4 and 5,5,5 are purposely excluded. While a sequence without the (–) signs guarantees uniqueness for any 23x23 (or larger) image, we find that worst case margin is enhanced if the black and white lines in some selected periods are reversed. These periods are indicated as (–). We are studying this phenomenon more systematically. For this design, a 32x32 image is larger than the minimum for unique decoding, and redundancy is translated into robustness. Even larger targets can be designed by increasing the alphabet size (>4) or the order (>3). Image size for larger targets, however, may also need to be larger.

DECODING ALGORITHMS

There are two parts to decoding:

1) In Coarse Decoding the image is located to between two adjacent ***Main*** vectors.
2) In Fine Decoding (Interpolation), it is further located to a much smaller pixel-fraction.

In 1), the (nonzero-mean) ***V*** and ***W*** vectors are 1-D correlated against both ***Main*** and ***demi*** target vectors in the respective dimension. These four operations are simultaneous, using identical digital logic hardware circuits. Interpolation follows 1). It is also simultaneously performed for both dimensions.

Coarse Decoding

Figure 2 shows one of four identical Coarse Decoding operations: the (nonzero-mean) ***W*** vector, generated by summing 16 columns of the captured image, is 1-D correlated against the horizontal ternary ***Main*** vector, length 55. Vectors ***M2*** and ***M1*** are the two corresponding binary vectors through this transformation:

(-1) »11; (0) » 00; (+1) » 01; (X) » 10.

The leading bit *M2* determines polarity. The trailing bit *M1* enables clocks for material summations. The sixteen elements of ***W*** occupy registers *W1-W16* as 55x2 ***M2*** and ***M1*** bits are shifted through a 2-bit wide D/FF shift-register.

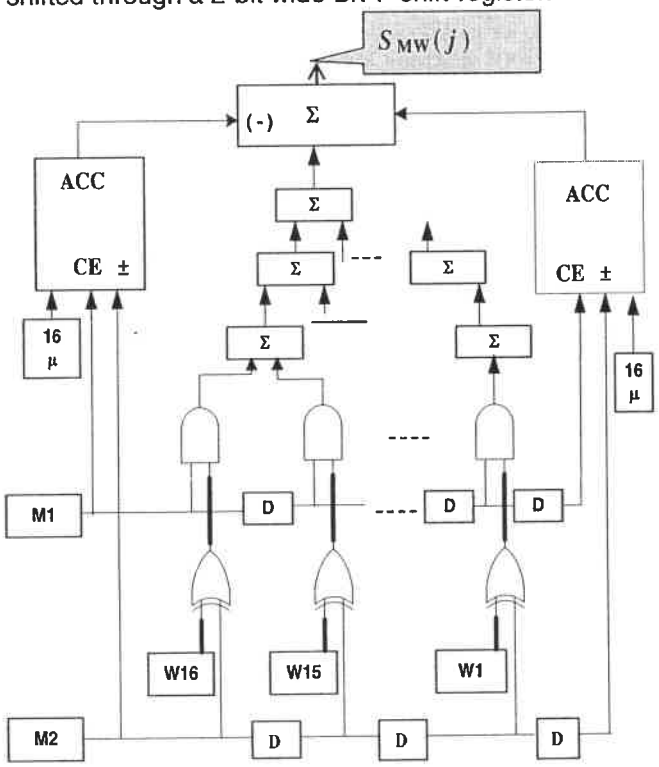

*FIGURE 2. An abbreviated schematic of hardware used in Coarse Decoding. Sixteen column sums of the captured image are housed in registers W1-W16 while the 1-D binary target representation bits **M1/M2** are shifted through. The two accumulators made meaningful processing of nonzero-mean vectors. Four such identical circuits operate in parallel. From the locations of the maximum four values provide, the coarse location of the image is determined.*

For S_{WM} to be meaningful, a term $16.\mu_W.\mu_M(j)$ must be dynamically (for each lag *j*) subtracted from the dot-product of the nonzero-mean vectors. This is the function of the two side-accumulators. Logic elements perform in 1-D the dot-product of ***W*** and ***Main*** while the latter is

shifting, culminating in a sequence S_{WM}. The constant 16μ is the sum of all image pixels/16, and is not dimension-specific. For horizontal Coarse Decoding, a maximum S_{WM} is detected at L_{WM} in ***Main***-processing; and a maximum S_{WD} at L_{WD} in **demi**-processing. It is similar to Figure 2 with **demi** binary bits **D1/D2** replacing **M1/M2**. If $S_{WD} > \sqrt{2}S_{WM}$, then the image is located between L_{WD} and $L_{WD}+1$. Otherwise it is between $L_{WM} - 0.5$ and $L_{WM} + 0.5$. Comparing the relative magnitudes of $S_{WD}(L_{WM})$ and $S_{WD}(L_{WM}-1)$ will determine whether the image is above or below L_{MW}, Vertical Coarse Decoding is identical, using vector ***V*** of row-sums. All four processes operate simultaneously.

Fine Decoding (Interpolation)

Coarse Decoding brackets the image to lie between L_M and L_M+1, (subscript *w* is dropped as both dimensions are applicable). In Fine Decoding, the best scalar partition ratio λ is estimated through statistical linear regression so vector ***W*** (or ***V***) best satisfies the relation

$$(1-\lambda)\boldsymbol{M}(L_M) + \lambda\boldsymbol{M}(L_M + 1) = \boldsymbol{W}.$$

$\boldsymbol{M}(L_M)$ is the segment of the target margin-vector at L_M and $\boldsymbol{M}(L_M+1)$ is its immediate neighbor above. Both vectors span a total of 17 elements. They bracket ***W***. To relate ***M*** to ***W*** which contains physical light intensity data, three unknowns *blk*, *gry*, and *wht* are assigned to the elements of ***M*** to replace -1, 0, 1. There are thus four unknowns and 16 equations. Linear regression produces an optimum solution for λ, the best interpolated position. For the vertical dimension, replace ***W*** by ***V***.

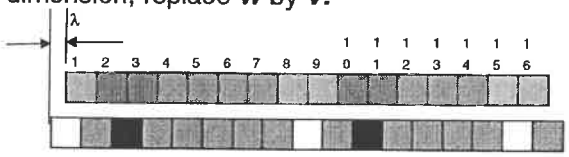

*FIGURE 3. Top bar is a visual representation of the measured **W**-vector. Due to offset λ, its 16 intensity values are linear combinations of the target margin-vector $\boldsymbol{M}(L_M)$ and its neighbor $\boldsymbol{M}(L_M+1)$, totaling 17 elements (bottom).*

The 16 equations can be partitioned into five by transition types: *g-w, w-g, g-b, b-g, g-g* For example, cell #1 is typed w-*g as it straddles a white and a grey pixel;* as do the 9th and 16th cells. Therefore one of five equations is

$$W1 + W9 + W16 = 3\cdot[(1-\lambda)\cdot wht + \lambda\cdot gry].$$

Similar logic generates the other four equations:

$$W8 + W15 = 2\cdot[(1-\lambda)\cdot gry + \lambda\cdot wht].$$
$$W3 + W11 = 2\cdot[(1-\lambda)\cdot blk + \lambda\cdot gry].$$
$$W2 + W10 = 2\cdot[(1-\lambda)\cdot gry + \lambda\cdot blk].$$
$$W4 + W5 + W6 + W7 + W12 + W13 + W14 = 7\cdot[(1-\lambda)\cdot gry + \lambda\cdot gry].$$

Digital logic hardware quickly sorts and sums them by type. Sixteen (later 32) equations are reduced to five. Solving them yields λ, as well as unknowns *blk, gry and wht.* Details are omitted.

EXPERIMENTAL SETUP

To test the encoding and decoding algorithms, a 7.11 x 7.11 mm chrome-on-glass target was made based on the 711x711 design pattern described. It is a 2-tone target with each "grey" pixel approximated by 8 black and 8 white sub-pixels arranged in a checkerboard pattern. The target is mounted on a stage with limited driven motion in one-dimension. It can be positioned manually in both dimensions spanning the entire target. On-axis illumination is provided by a 550-nm LED through a non-polarizing beam-splitter (NPBS). To minimize spherical aberration, the optical path through the NPBS is collimated. Magnification is adjusted for 1:1 between image pixel and sensor pixel, aided by an "eye-chart" pattern outside the target. Figure 4 shows the test set-up. To verify the effectiveness of the decoding algorithms, data rate is a modest 99 frames per sec with software decoding. FPGA circuitry will increase frame-rate manifold.

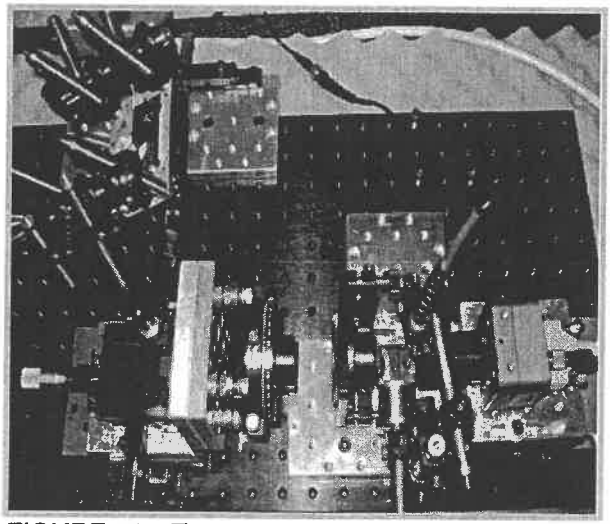

FIGURE 4. Test set-up for tracking 32x32 images captured by a digital camera (lower right) of a moving 711x711 target. The target mounted on a stage (lower left) is actuated by a mechanism (upper lerft). A LED from the top illuminates the target axially via a NPBS.

TEST RESULTS

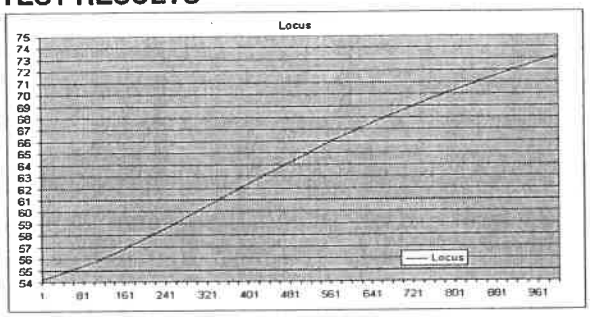

FIGURE 5. A typical test run shows the target traverses smoothly 20 pixels (0.2 mm) in 10 sec.

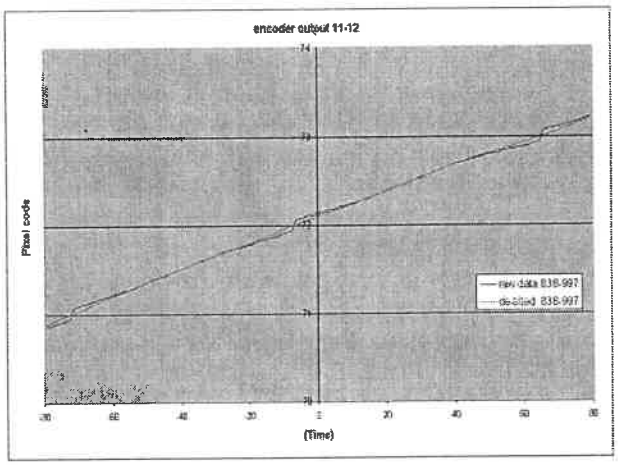

FIGURE 6. A magnified view of the data, shown with a quadratic fit, shows that the trajectory is not all that smooth. Systematic distortions are observed near pixel boundaries. This is consistent with light overfills from defocus or target-edge defect, as verified by simulation.

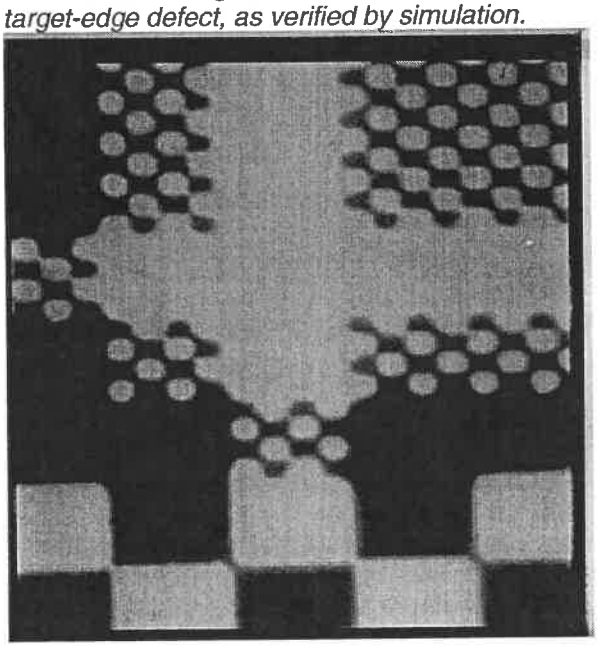

FIGURE 7. A microscopic view of the target, a 2-tone approximation to a 3-tone target (checker-board for grey), is less than ideal at pixel boundaries. The square sub-pixels are rounded, effectively making the black and white pixels larger than the grey. Pixels at the "eye-chart" (bottom) show less sign of such defects.

Subtracting off the quadratic fit magnifies further the errors shown. A global "de-curling" process effectively reduces such systematic errors.

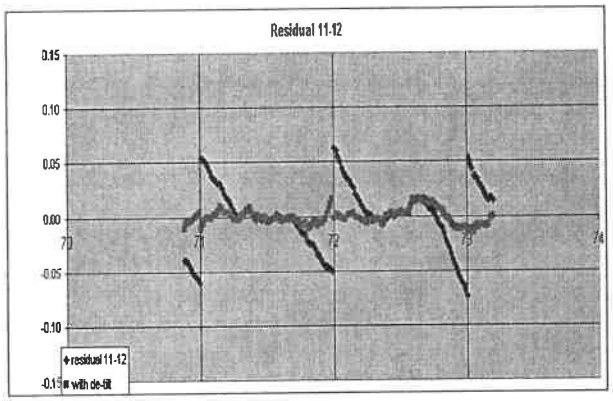

FIGURE 8. Distortion at pixel boundaries are reduced by a cubic curve compensation in the form of $C_1(\lambda-0.5)+C_3(\lambda-0.5)^3$. λ is the fractional pixel position. The same C_1 and C_3 can be used globally. The RMS error of the compensated data is 130 nm over the target, Vert: 0.5μm/div.

CONCLUSION

The feasibility and robustness of a 2-D absolute encoding/decoding architecture have been demonstrated. FPGA hardware processing will significantly reduce decoding time. A 3-tone scale, or a 2-tone approximation with reduced edge-defects, will further improve precision.

REFERENCES

1. Douglas Leviton. U.S.Patent 6,765,195 B1. Method and Apparatus for Two-dimensional Absolute Optical Encoding, 20040720.
2. B. Jones, M. Nahum. Systems and Methods for Absolute Positioning Using Repeated Quasi-random Pattern. U.S.Patent Application Pub. US 2004/218181 A1, Nov.4, 2004.
3. T. Etzion. Constructions for perfect maps and pseudo-random arrays. *IEEE Transaction on Information Theory*, 34:1308-1316, 1988.
4. N. G. de Bruijn. A combinatorial problem. *Koninklijke Nederlandse Akademie van Wetenschappen*, 49:758-764,1946.

ULTRAPRECISION MICROSCALE HOLE SCANNING METROLOGY

Marcin B. Bauza[1], Shane C. Woody[1], Stuart T. Smith[2], Robert J. Hocken[2]

[1]InsituTec Inc., 2750 East W.T. Harris Blvd, Suite 103, Charlotte, NC 28213, USA
[2]Center for Precision Metrology, UNCC ERB Bldg, 9201 University City Blvd, Charlotte, NC 28223, USA

INTRODUCTION

Measurement of high aspect ratio microscale features such as holes and channels remains a challenging metrology problem. For example, to assess a high aspect ratio small hole it is currently common to cut away a cross section and measure the features of interest using an AFM, SPM or SEM. Typically, these metrology tools may be suitable for surface finish measurement but often lack the capability for dimensional metrology measurement over these feature sizes. On the other hand, microscale probing systems currently exist which are based on the same principle of operation as systems suited for macroscale measurements. In particular, these types of probing systems often utilize a probe in the form of a shank which attaches a precision sphere on the end. As a result manufacturing complexities, the aspect ratio of these probes is small and operating frequencies are low, moreover adhesion related problems are usually difficult to overcome. During the previous annual conference, a novel probing methodology referred to as a standing wave force probe was presented and some experimental work was reported. The aim of this paper is to present measurements from this standing wave probe technique that has been integrated with a roundness measuring machine. As a result, accurate feature measurement of holes with diameters less than 100 µm are demonstrated. Moreover, the holes are scanned with thousands of data points for circular trace to correspond to information with high UPR variations.

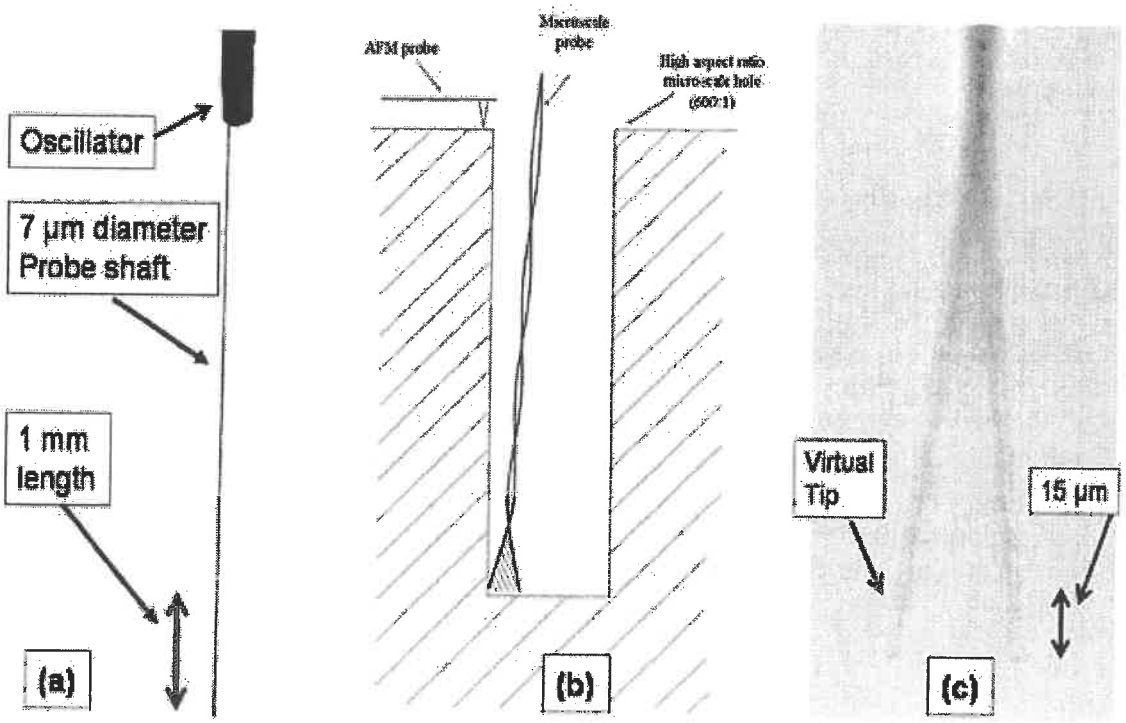

FIGURE 1. Illustrations of standing wave force probes

STANDING WAVE FORCE PROBES

The standing wave force probe uses a high aspect ratio (typically > 600:1) shaft which is mechanically bonded to an oscillator, Figure 1(a). The oscillator's resonant frequency which is currently operating at 32.76 kHz generates a forced response in the shaft, Figure 1(b). As shown, the single directional oscillation of the shank causes a point on the free end to move in a one dimensional locus. The amplitude of the oscillation located at the end of the shaft is a function of the amplitude of the signal applied to the tuning fork. Therefore, reducing or increasing the amplitude of the carrier wave to the tuning fork will result in a corresponding reduction or increase of the amplitude at the end of the fiber. Due to this characteristic behavior, this is referred to as a standing wave probe utilizing a virtual tip [1]. Moreover, as a result of the standing wave's inertia and intermittent contact, the mechanical contact interactions are not susceptible to attraction forces. A surface mount phase lock loop (PLL) circuit is employed wherein the tuning fork is locked onto a desired part of the characteristic response and the changes in frequency, phase, amplitude, or products thereof are measured. Once in contact, the PLL integrator signal changes the natural frequency to maintain a constant phase relationship. Typically, the frequency of the carrier signal is only changed by up to a few Hz during contact measurements and this is not currently monitored.

EXPERIMENTAL SETUP

A roundness gauge consisting of the standing wave microscale probes attached to scanning head in conjunction with a precision spindle was constructed and employed to perform experiments in order to investigate high aspect ratio microscale holes is shown in Figure 2. The scanning head uses constant force approach in controlling; therefore, the force probe is attached to the translator's carriage and the translator's actuator is used in closed loop control with the force gauge to maintain constant scanning forces. A displacement sensor located inside the translator monitors the displacement relative to a fixed frame [2]. This concept is the same as used in the profilometer of the previous reference except that the translator is connected, through slip rings, to a precision, custom air-free spindle that provides a rotational axis. The asynchronous radial error motion in those experiments was in a region of ±20 nm. Furthermore, the translator in the scanning head provides a single axis of motion along the radial direction of a workpiece. The roundness gauge assembly was retrofitted to Moore 1.5 measuring machine. As shown, a large scale precision spindle is retrofitted to the *Z* column and the scanning head is shown on the lower end of the spindle. The spindle houses a Heidenhain rotary encoder (ERN-120) with 16,348 TTL counts per revolution and is synchronized with the scanning head's displacement sensor. The spindle is rotated using an Aerotech frameless motor (S130-81) and linear amplifier (NL-drive). Custom slip rings are also designed and implemented to transfer electrical signals to and from the rotating scanning head.

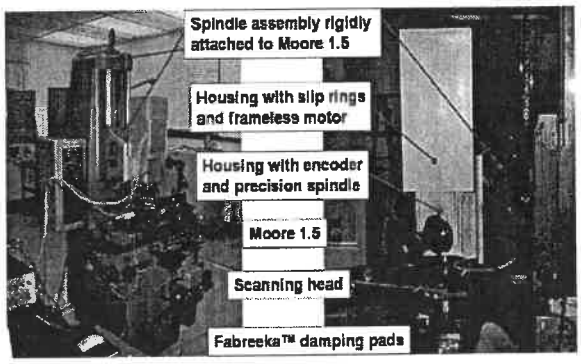
Spindle assembly rigidly attached to Moore 1.5
Housing with slip rings and frameless motor
Housing with encoder and precision spindle
Moore 1.5
Scanning head
Fabreeka™ damping pads

FIGURE 2. Experimental test stand using a Moore 1.5 and precision roundness gauge.

EXPERIMENTAL RESULTS

Form error measurements within a 128 µm hole.

As an artifact a glass ferrule made by Ozoptics Inc, Canada was chosen. The ferrule has a through hole with a diameter of 128 µm, and depth of several millimeters. In the following roundness measurement, the resulting data represents the combined radial and axial error motions that include the instrument spindle, hole's out-of-roundness, misalignments between axes of hole and spindle, electronic and mechanical system noise, and controller dynamic following errors. The glass ferrule hole was scanned at a constant applied force having a calculated value of 10-20 nN with a closed loop bandwidth of 20 Hz and approximately 14,000 data points were collected during one

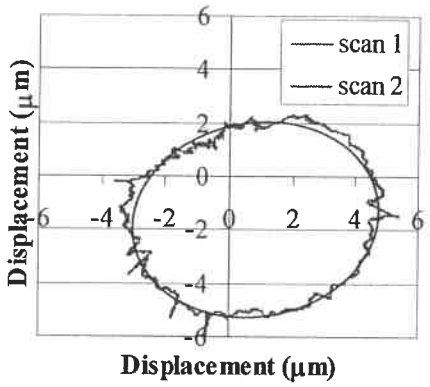

FIGURE 3. Form error measurements for the 128 µm diameter hole scanned twice.

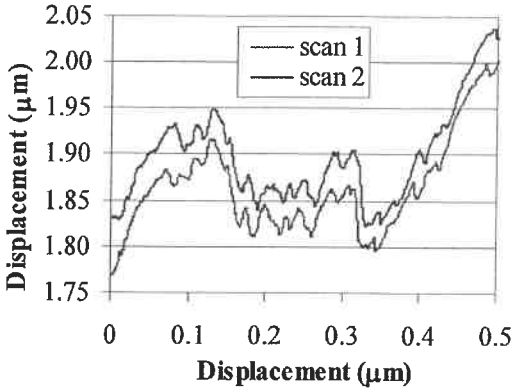

FIGURE 4. Zoom in of the scan for the 128 µm hole showing repeatability and resolution of local features.

revolution, Figure 3. The depth was set and limited to approximately 0.5 mm due to lack of automation in the setup and. alignment. Local features such as those shown in Figure 4 are highly repeatable in a range of 30 nm and the observed local misalignments are mostly related to asymmetric radial error motion of the spindle as well as possible electrical drift of the probing system. The measurement shows a 1 µm out of roundness of the measured part the dominant component of which can be observed as a 2 UPR out of roundness. Additionally, local scratches and defects are observed thereby revealing surface finish which is difficult to measure by other microscale probing systems. The repeatability of long and short wavelength features clearly demonstrates the potential of this standing wave technology. Additionally, features as high as 10-15 nm can be repeatably observed on consecutive scans. Moreover, it is possible to measure even smaller workpiece diameters; however, an automated alignment system will be necessary and is anticipated in the near future.

Touch triggering.

Touch triggering is the most commonly used method in CMM technology for both macroscale and microscale applications. Therefore, it was important to investigate the standing wave probe's ability to additionally function as a touch trigger probe. To assess this, repeatability experiments were conducted where the probe was moved towards a surface until a specified trigger voltage was reached and the corresponding reading from the displacement sensor located in the positioning mechanism was recorded. After 'contact', the probe was reversed until it was free from the surface of the specimen and the measurement then repeated, see Figure 5. As shown, 13 consecutive contacts and corresponding position at contact demonstrates a repeatability of ± 9 nm pk-pk. The time between the first and last contact measurement was approximately 6 minutes. This repeatability is expected to be a function mainly of mechanical drift of the metrology frame. The metrology loop in this experiment was grater than 2 meters. Additional uncertainties are due to electrical drift of electronics and exposed wires, and possible

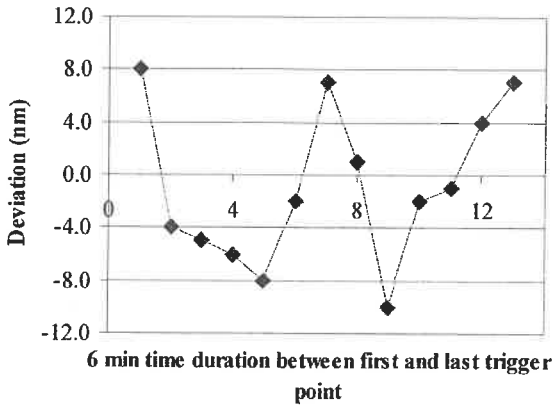

FIGURE 5. Touch trigger test as a function of the probe's sensitive oscillating axis. Note there was a 6 min. time duration between the first and last data point.

probe instability. Next steps for this research will involve designing a smaller metrology loop in the experimental setup with a significantly more compact gauge head and spindle assembly. As a result, higher repeatability is expected in future experimental results.

CONCLUSIONS

Since the space in proceedings is limited, for brevity, only two different measurements are presented. However a great number of experiments have been undertaken in an effort to establish the performance characteristics of this probe technology. Results from the tests will be presented at the conference and will include susceptibility to environmental factors (i.e. temperature and humidity), tip wear and repeatability.

ACKNOWLEDGMENTS

We would like to thank NIST for support under SBIR grants # SB134105W0840 and SB1341-06-C-0025, the Center for Precision Metrology at UNC Charlotte for supporting this project, and InsituTec Inc. for providing equipment necessary to accomplish this task.

REFERENCES

[1] Bauza M.B., Hocken R.J., Smith S.T., Woody S.C., Development of a virtual probe tip with an application to high aspect ratio microscale features. Rev. Sci. Instrum,. 76, 095112 (2005).

[2] Bauza M.B., Woody S.C., Smith S.T., Hocken R.J., Development of a Rapid Profilometer with an Application to Roundness Gauging. Precision Engineering. A05-021R (2006).

RING GAUGE FOR EVALUATION OF CMM DYNAMICS

Kenneth P. Garrard[1], Thomas A. Dow[1], and Karalyn F. Folkert[2]
[1]North Carolina State University, Raleigh, North Carolina, USA
[2]Consolidated Diesel Company, Whitakers, North Carolina, USA

BACKGROUND

An artifact has been designed and built to assess the static and dynamic performance of a Coordinate Measuring Machine (CMM). CMMs can measure a wide variety of component shapes and have accuracy and repeatability comparable with most manufacturing operations. The Y-12 National Security Complex manufactures precision parts for the government and private companies. Part acceptance is generally based on dimensional inspection and comparison with tolerance specifications. The goal of this project was to design and fabricate an artifact that can be used to expose the measurement errors in a CMM due to static (error motion of slides, control system) and dynamic sources (following error, probe dynamics). With this information, a measurement strategy for a part shape can be developed that will limit the errors to an acceptable value. If the artifact includes a broad band of excitation sources, the measurement will show how the actual gauge motion is transformed by the dynamic environment to produce a new motion with amplitude and phase errors. A ring gage was found to be the best artifact geometry for Y-12 and the addition of small sine wave features allow both static and dynamic calibration.

RING GAUGE GEOMETRY

The ring gauge has a 200 mm OD, a 150 mm ID and a thickness of 25 mm. The material was 17-4 PH stainless steel, heat treated for maximum dimensional stability and electroless nickel plated. Diamond turned flat surfaces on the top and bottom as well as circular sections on the ID and OD can be used as a standard ring gauge to measure machine geometry and the effectiveness of control systems and error correction schemes. The OD and ID have raised sections on which a sine wave features were machined to measure the dynamic response of the machine and probe.

Swept Sine Wave

The small features on the surface of the ring are designed to create a range of excitation frequencies to evaluate the response to a dynamic environment. A number of different geometries were investigated and the best candidate was a swept sine wave with constant amplitude. A swept sine wave is a sine wave with a continuously varying wavelength; that is, each point on the swept sine wave has a different wavelength. For the ring gauge, the wave begins at a long wavelength and progresses to a short wavelength in the first 90 degrees. To produce a continuous wave, the wave is "flipped" to line up with the last wave and then the wavelength increases to the starting point as it reaches 180 degrees. From 180 to 360 degrees, the wave is a mirror image of the first 180 degrees. Four quadrants of the same wavelengths allow a smaller section to be measured. Figure 1 illustrates these features.

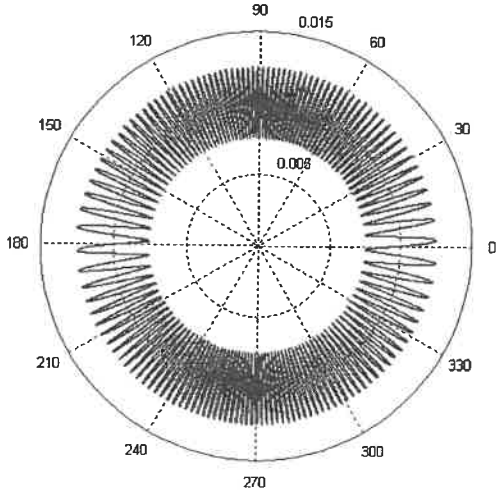

FIGURE 1. A continuous swept sine wave in polar coordinates.

The allure of the swept sine wave is that it contains a wide range of wavelengths and thus excitation frequencies. Different measurement speeds change the frequency range for the transfer function while the spatial wavelength remains the same. The linear swept sine wave from 0° to 90° is given by Equation 1 where A is amplitude, t is circumferential distance, d is the modulation parameter and f is the base wavenumber. The total number of waves over length L is $d+f$.

$$y = A \cdot \sin\left(\frac{2\pi t}{L}\left(\frac{d}{L}t + f\right)\right) \qquad (1)$$

Swept Sine Wave Excitation

The swept sine wave creates a frequency-rich environment that reveals the dynamics of the CMM, its ability to respond to small surface anomalies and the performance of the CMM as it traverses the varying wavelength features. The values of the swept sine wave were selected based on desired minimum and maximum spatial wavelength. Because the wavelengths can be considered as individual frequencies, a Fourier transform can be performed on the data set. With sampled data, the units on the frequency spectrum plot are in terms of Hertz.

However, with the generated spatial data, it is more useful to plot the results in terms of wave number[1]. The wave number is the reciprocal of the normalized spatial wavelength. Figure 2 shows the FFT of the first quadrant of the ideal wave for the ID. The magnitude is largest near the shortest wavelength at wave number 223/λ which translates to a wavelength of 0.537 µm. The phase values accumulate for half of the wavelengths and then returns to zero.

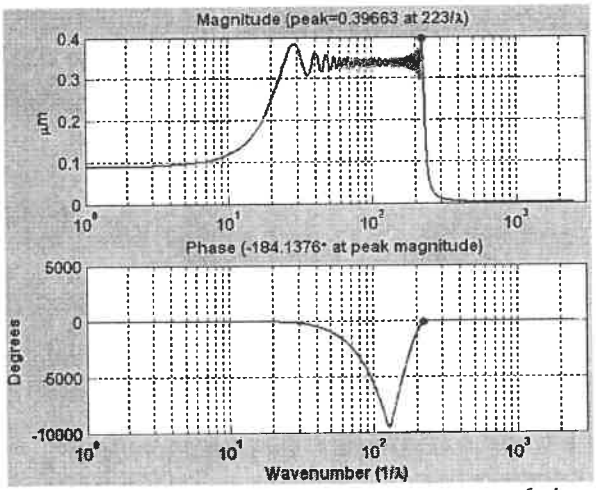

FIGURE 2. Spatial frequency spectrum of the first quadrant of the swept sine wave in Figure 1.

The FFT of the swept sine wave is more difficult to interpret than a single frequency sine wave due to the constantly varying nature of the wavelength. Rather than strictly interpreting the ideal FFT and directly comparing it to an FFT of an actual measurement, the data analysis may be simplified. A CMM has dynamic characteristics that will influence the overall measurement of the artifact and the ability of the probe to detect small perturbations changes with the radius of the probe, measurement speed, radius of the part and size of the feature. Since the swept sine wave on the surface of the ring has an 'accepted' value[2] and the CMM measurement will generate another data set, the CMM's dynamics, or transfer function, may be found by comparing these measurements using a form of deconvolution. Convolution in the time domain is the multiplication of the swept sine wave and the impulse response of the dynamic system to construct an output that shows the influence of these dynamics. Since the dynamics of the CMM are not known, the inverse of convolution, or deconvolution, is used; the CMM measurement is divided by the accepted swept sine wave. To expedite calculations, deconvolution may be executed in the frequency domain. The magnitude and phase components in the frequency domain are separated to create a Bode plot of the CMM's dynamics. Multiple measurements with different speeds can be used to create the desired frequency range of the Bode plot to determine the dynamics of the system. The transfer function of the CMM provides a significant amount of information about the machine. It specifies the natural frequency as well as the machine's performance within a frequency range. If a measurement speed is specified, the speed may be converted to frequencies present in the swept sine wave data and an appropriate CMM operating speed determined based on the transfer function and an acceptable amount of error.

ARTIFACT FABRICATION

A Fast Tool Servo (FTS) was used to machine the swept sine wave on the ring[3]. The piezoelectric stacks of the FTS are excited by the signal from a high voltage amplifier. The frequency and voltage signal affect the movement of the tool on the FTS. Feedback control from the built in cap gauge can correct for position error at low frequency. The closed loop controller uses position feedback with a proportional-integral control algorithm to correct position error. Gains are selected to shape the response of the system, to prevent overshoot

[1] The number of waves per unit distance (one quarter of the ring circumference).

[2] The actual swept sine wave may not be exactly equal to the designed shape.

[3] K. Folkert, T. Dow, K. Garrard. Metrology Artifact Design. ASPE Proceedings, 34, 462-465 (2004).

and to correct for the following error. Although the system dynamics of the FTS are improved with closed loop control, there is still significant phase error in the system at higher frequencies. Since the FTS will operate at close to 600 Hz when machining at 20 rpm, deconvolution is applied to the swept sine wave before it is input into the controller. Deconvolution uses the magnitude and phase characteristics of the FTS with the information of the desired wave output to adjust the amplitude, phase and shape of the command signal; that is, it alters the input to produce an expected output[4]. This technique greatly decreases the error to about 300 nm in the fabrication of the swept sine wave.

CONTACTING PROBE MEASUREMENTS

Determining Probe Dynamics

The dynamic transfer function of the air-bearing probe depends on the dynamics of the probe/gauge interface contact and any filtering built into the cap gauge electronics. Typical air-bearing probes capture some of the exhaust air and use it to preload the probe against the surface. This preload is a constant force independent of the deflection of the probe.

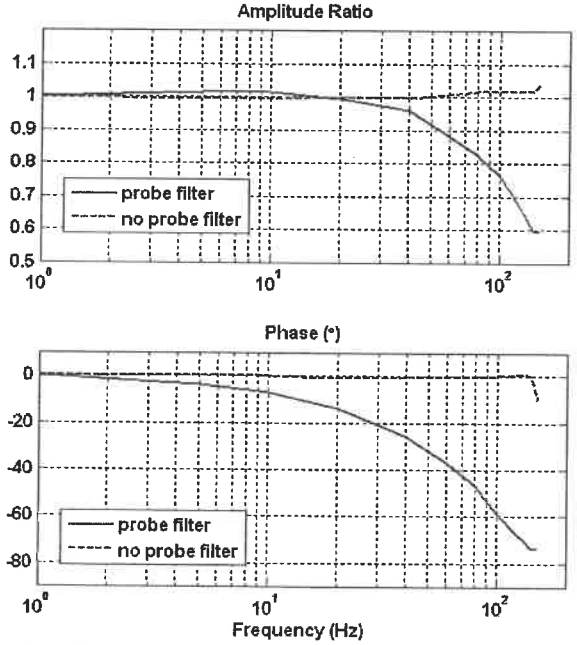

FIGURE 3. Transfer function of the air-bearing capacitance gauge with and without filtering.

When confronted with the dynamic forces from the ring gauge motion, the probe will follow the surface until the dynamic forces exceed the preload and then it will leave the surface. The initial conditions, mass and damping will determine its motion and it will bounce when it returns to the surface depending on the relative speed and interface.

Electronic filtering will change the apparent position of the probe by reducing the amplitude and introducing phase lag. An example of the probe response when excited with a sine wave motion with and without the electronic filtering is shown in Figure 3. A preload of 3.4 grams keeps the 7.4 gram mass of the probe in contact until about 150 Hz. The filtered amplitude ratio (air-bearing probe motion divided by excitation) drops as expected and is down about 3 dB (0.707) and lags the input by 64° at 113 Hz due to the filter. If the filter is removed the bandwidth is 20,000 Hz and the probe measures the motion up to the acceleration limit of 150 Hz after which it 'bounces' and contacts the surface sporadically.

The motion of the probe when it exceeds its acceleration limit will become a part of the dynamic measurement. This motion will depend on the dynamics of the probe (the friction, damping and spring constant) but not the shape of the part. A model of the motion of an air-bearing cap gauge was developed and corroborated by experimental measurements.

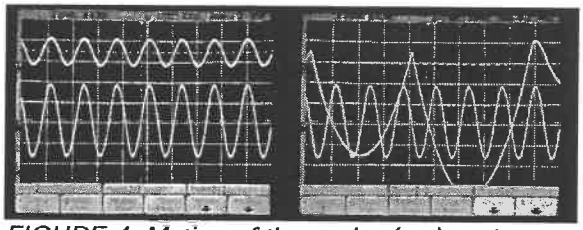

FIGURE 4. Motion of the probe (top) and gauge (bottom) in contact (left) and bouncing (right).

An example of the probe motion is shown in Figure 4 from an oscilloscope measuring probe and excitation motion at 50 Hz. The preload was reduced in the right to allow bouncing. Because of the range of the cap gauge, there is a 2.5x gain difference in the two signals. Notice that the amplitude of the probe motion grows significantly when bouncing occurs but the frequency is much lower than the excitation. The response changes depending on the gauge velocity and direction when the probe contacts it.

[4] W. Panusittikorn. Error Compensation Using Inverse Actuator Dynamics. PhD Disseration, North Carolina State University, (2004).

RING GAUGE MEASUREMENT

Measurement of the swept sine wave on the ring gauge (Figure 5) provides a rich dynamic input to assess the response of the structure, controller and probe of the CMM. The advantage of the ring gauge is that the entire CMM structural loop is included. This is also a problem because any bouncing behavior of the probe is measured.

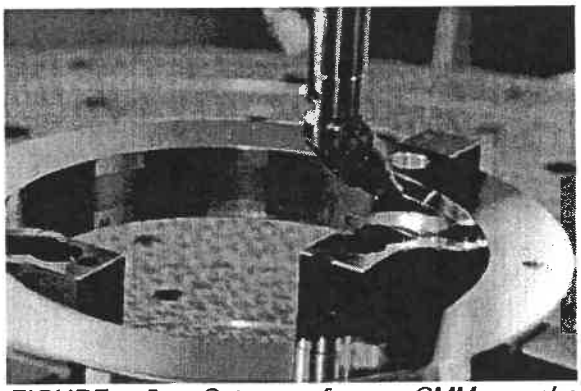

FIGURE 5. Setup of a CMM probe measurement of the swept sine waves.

As the probe moves from the low frequency region to higher frequencies, the magnitude and phase of the measured shape will be modified by the dynamics of the CMM. This change can be quantified by comparing the measured shape to the 'accepted' shape of the surface. However, the data must be modified before analysis to eliminate the non-contact regions. If the probe leaves the surface the observed system behavior will not be LTI (linear time invariant).

An algorithm has been developed to compute the CMM/probe transfer function given the gauge shape, a measurement data set and the circumferential speed of the measurement. The algorithm detects probe bounce in the measurement signal and windows the data appropriately before performing a transfer function calculation in the frequency domain.

To demonstrate the capability of this measurement technique, the air bearing probe with and without the electronic filter was used to measure the ring gauge shape. The air-bearing preload was set for contact up to about 80 Hz and a linear sine sweep was sent through a FTS to the probe. The data was collected using XPC Target and a National Instruments 6052E multifunction board at a 20 kHz sample rate. The results are shown in Figure 6 and can be compared to the probe transfer function in Figure 3. Without the filter the probe behaves as expected with unity gain and flat phase response until it loses contact. Attenuation and phase lag with the probe filter are in good agreement up to about 50 Hz.

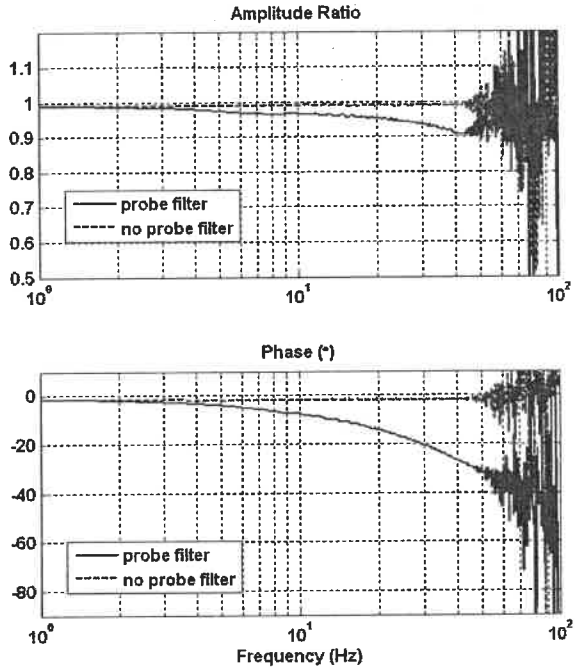

FIGURE 6. Probe transfer function derived from measurement data with and without probe filter.

CONCLUSIONS

- A ring gauge artifact with cylindrical and cylindrical with swept sine wave features has been designed and fabricated.
- Error of the ± 5 µm amplitude features is 300 nm PV and the ring is round to 120 nm PV with a surface roughness of 37 nm RMS. The swept sine wave contains spatial frequencies on the OD from 6.384 mm to 0.383 mm corresponding to 1.6 to 27 Hz at 1 rpm.
- Changing the transfer function of an air-bearing cap probe was used to demonstrate the effectiveness of the swept sine wave to measure dynamic performance.
- Algorithms were developed to extract the dynamics of the probe from the swept wave measurement. Dynamic errors change the shape and add uncertainty to the result.
- Probe dynamic response from the ring gauge measurement will allow a CMM operator to devise a measurement strategy to limit dynamic errors to a specified range.

ACKNOWLEDGEMENT

This work was supported in part by the BWXT Y-12 National Security Complex.

SPECKLE CORRELATION METHOD FOR 3D-DEFLECTION MEASUREMENT OF THE TACTILE-OPTICAL MICROPROBE

Mark Wissmann, Heinrich Schwenke, Ulrich Neuschaefer-Rube
Coordinate Metrology Department
Physikalisch-Technische Bundesanstalt (PTB)
38116 Braunschweig, Germany

INTRODUCTION

The growing number of component parts with very small functional features leads to a demand for measuring instruments that provide full 3D measurement capability for structures with dimensions clearly below 1 mm. Although there are various optical measuring techniques with resolutions in the 10 nm-range [1], tactile probing often is the preferred method for the dimensional measurement of workpieces. By tactile probing, the mechanical functional properties are measured directly and in many cases the traceability of the result is superior compared with optical measurements. Thus, over the past years an increased number of developments towards a tactile micro probe for coordinate measuring machines (CMM) have been reported [2] and some of these systems have already been successfully commercialized. Especially the tactile-optical microprobe [3, 4] has addressed a large number of applications in industry, due to its high accuracy, its very small dimensions and its robustness in daily use. At present, a major limitation of this system is the missing sensitivity in the direction of the stylus. In this paper, an novel approach to enhance the capabilities of the tactile-optical microprobe to full 3D is described. The proposed method is based on the use of a coherent light source for illuminating the fiber probe and the observation of speckle patterns generated by a target close to the probing sphere. At first, the basic principle of operation of the commercial 2D fiber probe is briefly recapitulated before the enhancement for measurements in 3D is described in detail.

THE TACTILE-OPTICAL MICROPROBE

The conventional 2D probing system

The tactile-optical microprobe combines both the advantages of tactile probing and the accurate optical measurement of the probe deflection. The setup of the microprobe system consists of a bended optical glass fiber with a small probing sphere attached to its end. The glass sphere diameter can range between 10 µm and 100 µm and the contact forces are in the order of 1 µN to 10 µN. The probing sphere is arranged in the focal plane of an imaging system and it is illuminated through the optical fiber by a LED. Thus a bright circular disk is observed when images are acquired with the integrated CCD-camera. The basic principle of the tactile-optical probe is shown in FIGURE 1.

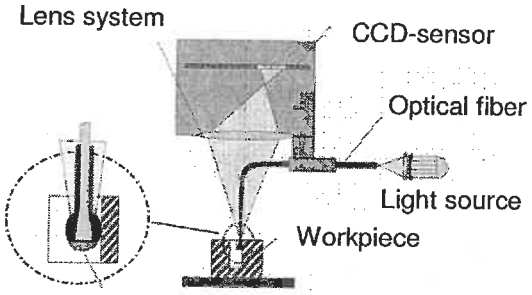

FIGURE 1.Principle of the tactile-optical probe.

Since the probing element is mounted stationary to the camera system, probe deflections caused by contacting a workpiece result in a detectable 2D-displacement of the visible probing element within the cameras view. This displacement can be measured by image processing methods and evaluated in analogy to a conventional probing system. FIGURE 2 shows acquired images of the illuminated probing element before and after contacting the inner surface of a micro bore hole which is about 200 µm in diameter.

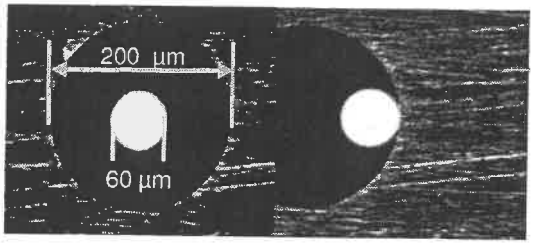

FIGURE 2. The tactile-optical 2D-microprobe before (left) and after (right) contacting the inner surface of the workpiece.

The tactile-optical probing system can deliver accuracies clearly in the sub-micron range for 2D measurements. However, the present mode of operation is quite insensitive to any out-of-plane displacements of the probing element. Thus measurements are limited to features that can be detected by 2D in-plane deflections of the microprobe in previously defined z-positions. Although this allows several adopted strategies for the 3D measurement of parts like cones and holes, measuring in full 3D is not supported yet.

Past developments to achieve 3D-sensitivity

In order to realize sensitivity in 3D, a second imaging system with a camera and an additional observable target mounted 1-2 mm above the probing sphere were used in past experiments. The second camera was arranged perpendicular to the glass fiber and recorded the out-of-plane deflection of the target when the microprobe contacted the workpiece. The deflection of the target in 3D was then obtained by combining the information extracted from both camera views. A further development has used small mirrors to fold the optical path into one integrated camera [5]. Although these approaches have proved to deliver good accuracies, the hardware has become increasingly complex. In addition, the bulky components limited the workspace and the overtravel capability of the probing system. In the following, a novel principle for the 3D detection is introduced, that combines a simple mechanical setup with a high potential to realize an accurate and robust 3D probing system for micro features.

MEASURING IN FULL 3D WITH THE SPECKLE CORRELATION METHOD

Basic principle of the speckle method

The conventional 2D tactile-optical microprobe is illuminated by a incoherent LED light source which results in a homogenous light intensity that is backscattered from the probing element. If a laser diode is used instead as a coherent light source, the observed image shows a distinctive speckle pattern that is generated by the varying length of the optical path within the multimode fiber and the probing element. The outer shape of the speckle pattern is roughly circular, the inner part of the pattern is shadowed by the optical fiber. An image of a speckle pattern is shown in FIGURE 3. Due to the stable optical path in the fiber the pattern is stationary to the probing element even when the probe is displaced in the focal plane.

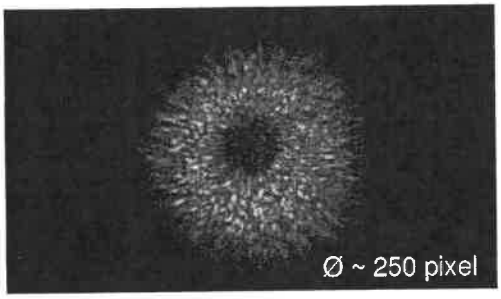

FIGURE 3. Image of typical speckle pattern.

An utilizable effect can be observed when changing the distance of the light emitting probing element to the camera: out-of-plane displacements lead to an almost radial scaling of the speckle pattern according to the numerical aperture of the imaging system. Thereby the contrast of the speckles remains almost unchanged, only the intensity changes due to the increasing distance of the light emitting sphere from the focal plane. FIGURE 4 shows a 3D visualization of a recorded image sequence while gradually changing the distance between the probing element and the camera.

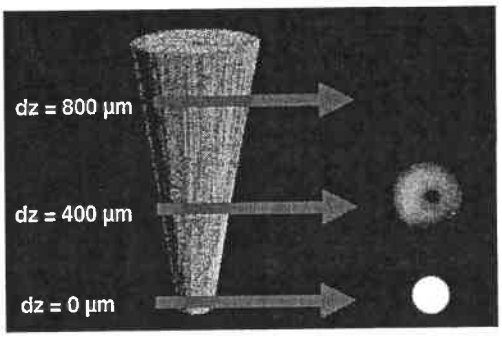

FIGURE 4. Visualization of the speckle pattern scaling effect when the light emitting sphere is defocused out of the focal plane.

As a consequence, spatial 3D information of the probing elements deflection in relation to the camera can be derived from a single speckle pattern image: x- and y- displacement by observing the shift of the whole speckle pattern, z-displacement by evaluating its shape [6]. This separable effects were the base for the developments reported in the following.

Experimental Setup

The configuration of the 3D-microprobe is based on the two-sphere probe design having a small probing sphere and an additional observation target. This design has the advantage that most of the measurements can be carried out without any negative effect caused by shadowing of the

light field during contact with the workpiece. The elastic deformation of the optical glass fiber was optimized by choosing its dimensions according to finite element simulations. In order to observe speckle pattern images with the tactile-optical microprobe, the incoherent LED was replaced by a laser diode with a wavelength of 670 nm. The light emitting target was adjusted near the focal plane of the observing imaging system. The imaging system itself consists of an objective with a 10-fold magnification and a high resolution CCD-camera. The fiber probe was arranged manually in the x-y-plane until the speckle pattern was roughly centered within the cameras view. The intensity of the laser was adjusted according to the dynamic range of the CCD-camera. The experimental setup of the 3D probe is shown in FIGURE 5.

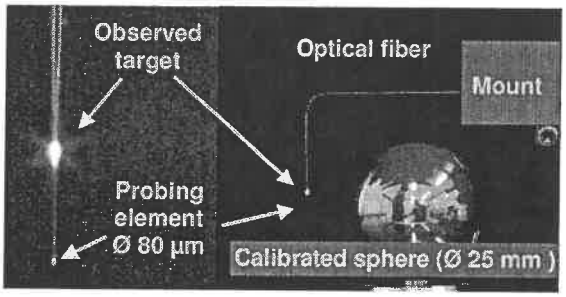

FIGURE 5. 3D-microprobe implemented in a Werth-CMM and illuminated by a laser diode.

Measurements are carried out by acquiring an image during contact of the probing sphere with the workpiece and storing the speckle image together with the current positions read out from the CMMs underlying coordinate system. The coordinates of the measured point are obtained by an algorithm as described in the following.

Image processing and evaluation software

The detection principle is based on correlation analysis of the observed speckle pattern with a set of reference images. Before the measuring, a stack of reference images with well known z-deflections is recorded (see FIGURE 4). During the measurement, the images captured by the camera are compared to this reference stack. By a correlation algorithm the maximum match within the reference stack in three degrees of freedom is evaluated: x and y in the image plane, z along the height of the reference stack. This operation can be performed with sub-pixel accuracy [7], since the speckle images are very suited to give a sharp correlation extremum (see FIGURE 6). The result of this correlation algorithm is the deflection of the target in relation to the camera. Due to the elastic deformation of the probing shaft between the target and the probing element, an additional sensitivity matrix has to be evaluated to obtain the deflection of the probing element. The coefficients of this matrix can be determined by qualification procedures comparable to the routines employed for conventional analogue probes. Based on the mechanical design of the probe the sensitivity coefficients on the main diagonal range between 0.3 to 0.7 for x and y and 1.0 for z. The 3D coordinates of the probe are finally obtained from the superposition of the probe deflection and the stored positions of the acquired speckle images within the coordinate system of the CMM. First results of the speckle correlation method are reported in the following.

EXPERIMENTAL RESULTS

Results from the correlation algorithm

The speckle correlation method performed well for test speckle images. The x-y-displacement can be obtained with sub-pixel accuracy (0.1 – 0.2 pixel) in both directions for speckle pattern images with z-distances of 0.1 µm to 1 µm. The z-position can be determined with clearly sub-micron accuracy for reference image sequences with an equidistant spacing of 0.5 µm. The correlation in x-, y- and z-directions is qualified for evaluations using parabolic best-fit functions and shows one distinctive and global extrema with low noise for appropriate speckle pairs. At present, the time to evaluate a measure point with correlation methods is about 2 minutes on our development system.

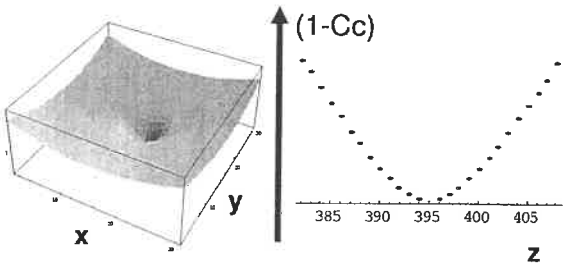

FIGURE 6. The graphical representations of the x-y-correlation (left) and the z-correlation (right) show a distinct global extremum.

Reference images and cross-sensitivities

Multiple reference image stacks were recorded to analyze the stability of the z-detection when using correlation methods. The z-deflection was stepwise incremented by 0.5 µm up to a total

z-deflection of 50 µm. The experiments showed, that z-deflections can be detected with < 0.5 µm accuracy (peak to valley) if the total z-deflection is less than 10 µm. The two mechanical cross-sensitivities dx'/dz and dy'/dz of the target and the probing element were calculated from the x-y-displacement of the whole speckle pattern as a function of the deflection in z-direction. The remaining (cross-) sensitivities were determined by in-plane deflections in both x- and y-direction, while the probing sphere was deflected in z-direction by a constant value of 20 µm to avoid slipping. The experiments showed almost linear behavior of all cross-sensitivities in x-, y- and z-direction if the absolute in-plane deflection of the probe is less than 15 µm.

Measurement of a calibrated sphere

Based on the probe test for CMMs according to ISO 10360-2 [8] the performance of the speckle correlation method was evaluated by the measurement of a calibrated sphere (Ø 25 mm) with negligible form deviations. The total number of probing points per measurement was 163 on the upper hemisphere. The measurement deviations from the best-fit sphere ranged from -1.2 µm to 1.52 µm with an average deviation < 0.4 µm. During measurement, the maximum deflection of the probe was 18 µm. This result was reproducible for four measurements carried out within a time span of 20 h. Only one single outlier was observed and its cause was identified as a blurry image. The deviations from the best-fit sphere are shown in FIGURE 7. The analysis revealed residual systematic errors which are assumed to originate from the mechanical cross-sensitivities and perhaps from form deviations of the probing sphere.

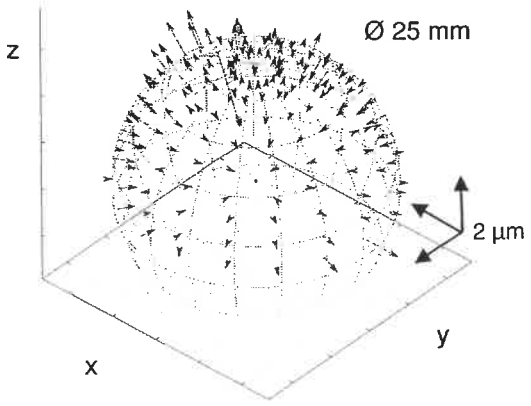

FIGURE 7. Deviation of the probing points from the best-fit sphere (163 points).

CONCLUSIONS & OUTLOOK

The experiments described here showed that the speckle correlation method can be used to enhance the capabilities of the classical tactile-optical microprobe to measure in 3D. The clearly separable sensitivity of speckle patterns for in-plane and out-of-plane deflections and the high contrast of speckles for any 3D deflection makes them well-suited for 3D measurements. After our first experiments, we believe that the proposed method has the potential to deliver sub-micron accuracy in 3D, while it preserves the benefits of a very simple and robust mechanical setup of the tactile-optical microprobe. An additional reduction of the systematic errors can be achieved by an improved method to obtain the mechanical (cross-) sensitivities. The presently long evaluation time will be strongly reduced when the correlation algorithm is optimized and implemented on appropriate hardware.

ACKNOWLEGEMENTS

This work was supported by Werth Messtechnik GmbH and Prof. Dr.-Ing. R. Tutsch from the Technical University of Braunschweig.

REFERENCES

1. Schwenke, H., Neuschaefer-Rube, U., Kunzmann, H. and Pfeifer, T., 2002, Optical Methods for Dimensional Metrology in Production Engineering, CIRP Annals, 51, 2, 2002, 685-699.
2. Weckenmann, A., Estler, T., Peggs, G. and McMurtry, D., 2004, Probing Systems in Dimensional Metrology, STC P, CIRP Annals, 51, 2, 2004, p. 657.
3. Ji, G., Schwenke, H. and Trapet, E., 1998, Opto-Tactile Sensor for Measuring Small Structures on Coordinate Measuring Machines, Proc. of the 1998 Annual Meeting of ASPE, St. Louis, USA.
4. Werth Messtechnik GmbH, Gießen, Germany, www.werthmesstechnik.de.
5. Schwenke, H., Neuschaefer-Rube, U. and Wissmann, M., 2006, Tactile Probing of Micro Features – Recent Advances in the Development of the Tactile-Optical Microprobe, Proc. of the 7th conference on Coordinate Metrology, 2006, Bielsko, Poland.
6. German Patent, DE 10 2005 021 645 A1.
7. Foroosh, H., Zerubia, J. and Berthold, M., 2002, Extension of Phase Correlation to Subpixel Registration, IEEE Transactions on Image Processing, Vol. 11, No. 3.
8. ISO 10360-2 (2001): Geometrical Product Specifications (GPS) – Acceptance and reverification tests for coordinate measuring machines (CMM) – Part 2: CMMs used for measuring size.

ENHANCED CAPABILITIES OF THE NIST FIBER PROBE FOR MICROFEATURE METROLOGY

B. Muralikrishnan[1], J. A. Stone[2], J. R. Stoup[2]
[1]Department of Mechanical Engineering & Engineering Science, University of North Carolina at Charlotte, Charlotte NC
[2]Precision Engineering Division, National Institute of Standards and Technology, Gaithersburg, MD

INTRODUCTION

In a previous publication [1] we have described a fiber probe, developed at the National Institute of Standards and Technology (NIST) that is used for coordinate metrology of microfeatures. In this paper we describe two new methods of operation of the probe. The probe, which we refer to as the NIST Fiber Probe, functions by optically imaging the fiber stem from two orthogonal directions a few millimeters away from the ball end of the fiber (see Fig. 1). Upon contacting a part, the fiber bends by a small amount; the magnitude of the deflection at the point of observation indicates the amount of over-travel of the probe. The probe is well characterized and has demonstrated performance of 70 nm (k = 2) for diameter measurements of micro holes (100 µm nominal diameter holes, 5 mm deep). This probe was essentially used as a 2D probe and also only in point-to-point measurement mode. We have since extended the capability of the probe to full 3D measurements and have also made profile measurements in point-to-point and pseudo-scanning mode. We describe these enhancements in this paper.

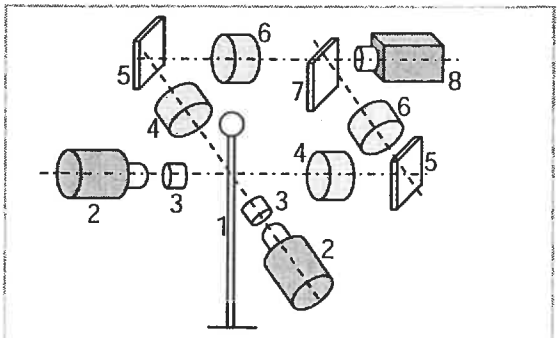

1. Fiber, 2. Source, 3. Collimating lens, 4. Objective, 5. Fold Mirror, 6. Eyepiece, 7. Thin mirror to split pixel array, 8. Camera

Figure 1: Optical setup for fiber deflection measurement

Z DIRECTION MEASUREMENT CAPABILITY - FIBER BUCKLING TECHNIQUE

In order to measure position along the *Z* direction, we exploit the fact that the fiber is slender and therefore buckles under compressive loading (see Fig. 2). We image only a 100 µm segment of the 20 mm long stem, and consequently this buckling of the fiber appears as a translation of the imaged segment along *X* and/or *Y*. This buckling behavior is experimentally determined to be repeatable (20 nm, one standard deviation) and therefore the vertical motion of the probe tip can be assessed by determining the horizontal translation of the images and using a previously determined calibration factor. We should point out that the fiber is imaged from two orthogonal axes as with the deflection method (only one axis imaging is shown in Fig. 2), and therefore the magnitude of buckling in the plane of bending can be determined.

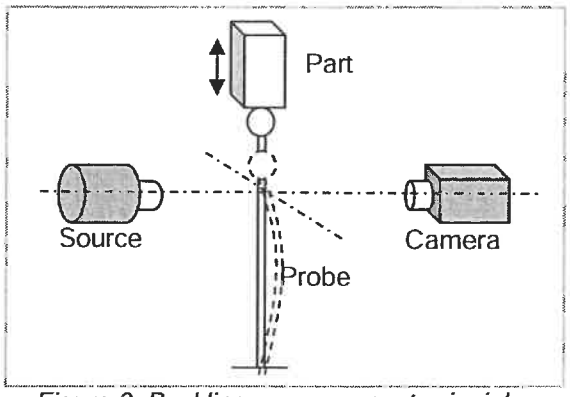

Figure 2: Buckling measurement principle

Because the fiber undergoes extremely large amounts of buckling for very small motion along *Z*, this fiber buckling technique is much more sensitive than the previously reported fiber deflection technique [1]. Fig. 3 shows a plot of the observed translation of the fiber image (in the plane of bending) as a function of motion of the tip along *Z*. From the plot, the sensitivity of the fiber buckling technique is 3 nm/pixel.

Typical sensitivity values for deflection mode measurement are approximately 300 nm/pixel. Therefore, this method yields almost 100 times improvement in sensitivity over the previous method. The measurement range is however reduced; prior knowledge of the location of the surface to within 1 μm is necessary before automatic search for surface location can be commenced.

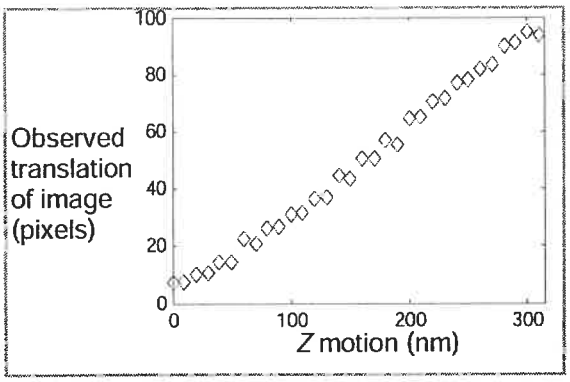

Figure 3: Plot of observed translation of image as a function of motion of tip along Z

Analysis of buckling induced deflection is reported by Stone *et al* [2]. We have measured hemispheres where the pole point was determined in buckling mode while the remaining points distributed uniformly about the hemisphere were determined in deflection mode. The overall sphericity of a ruby sphere (33 sampling points; eight sampling points per circular trace for four traces, and one pole point) was determined to be under 300 nm (one standard deviation repeatability in diameter was 30 nm), which is well within that expected for such spheres. The steepest surface normal was inclined at 22.5° with the probe axis. We are currently conducting experiments on inclined surfaces to determine if a clear transition point exists when the fiber switches from buckling to deflection mode.

PROFILING CAPABILITY – PSEUDO SCANNING BY ACOUSTICALLY EXCITING THE FIBER

Straightness profiles along the vertical direction (for surfaces whose normals are in the *XY* plane; in Fig. 4, the surface normal is along the *X* axis for the gaging surface and the measured profile is along the *Z* axis) can be obtained by simply dragging the fiber along the surface, as is done in traditional stylus profilometry. This method fails for profiles oriented horizontally (for example, a profile along the *Y* axis for the gaging surface in Fig. 4 whose surface normal is along the *X* axis) because the fiber tends to adhere to the surface and remain stuck to the previous sampling position even as the probe is commanded to move to the next position.

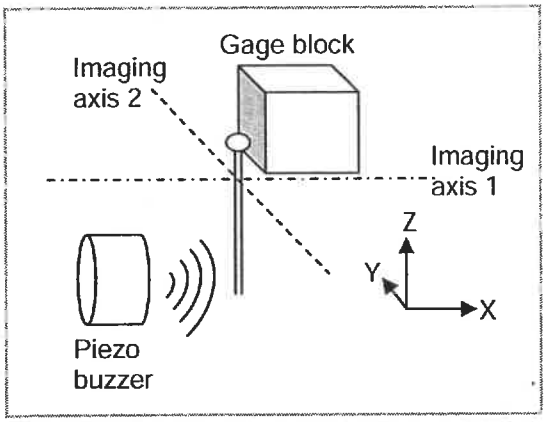

Figure 4: Fiber excited using piezo buzzer

One solution to overcome these attractive forces is to simply retract the fiber from the surface by providing a suitably large motion away from the surface and/or along *Z* before contacting the part at the next sampling location, as we typically do for circular traces inside micro-holes. This method is slow; it takes approximately 40 min to measure a typical straightness trace containing 50 sampling points. To achieve faster scanning, we excited vibrations in the fiber during the motion of the probe from one sampling point to the next to overcome the adhesive forces. To induce oscillations, we use a piezo buzzer to acoustically excite the fiber (see Fig. 4). We use this indirect method of excitation, rather than mounting the probe directly to the piezo buzzer, because it allows us to mount the fiber in a very stable V-groove assembly on a stable base. We did not achieve satisfactory stability of the fiber position when the fiber was mounted directly on the piezo.

A fiber free on one end (not contacting the test surface) and forced to vibrate in the *XZ* plane has several nodes along its length depending on the forcing frequency [3]. It is therefore possible to observe and image the fiber at one of these nodes. However, when the fiber is brought in contact with a test surface, the vibration characteristics change and a stable node is not available for imaging. Therefore, we excite the fiber only during the motion of the test surface and not during the imaging. We refer to this method as vibration assisted pseudo-scanning.

We have experimentally noticed that the fiber can stick to the surface, and will remain stuck even when the base of the probe is retracted away from the surface by as much as 400 μm. For our fiber made of glass (Young's modulus E = 80 GPa), this maximum deflection of 400 μm translates to a force at the tip of approximately 3 μN, and a stored energy of $e = \frac{1}{2}(\frac{3EI}{l^3})y^2$ [3], numerically equal to 6×10^{-10} Nm. (Here y is the deflection of the tip and l is the fiber length.) In order to break the bond via vibration, it will be necessary to provide this same force and energy, and hence it will be necessary to vibrate the probe with about 400 μm amplitude. We see experimentally that this cannot be achieved unless the driving frequency is near to a resonance frequency. Near resonance we observe extremely large amplitudes of vibration, of the order several hundred micrometers, and the fiber is able to overcome the attractive forces.

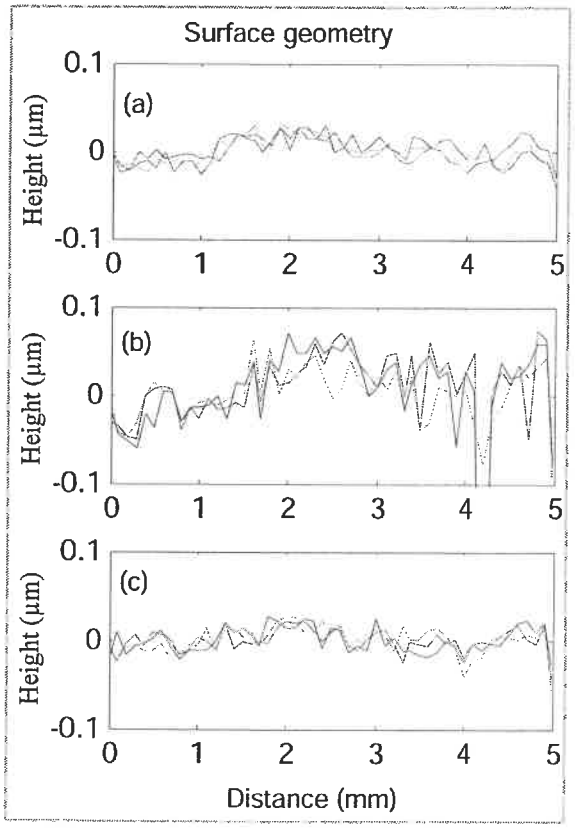

Figure 5: Surface geometry - three methods (a) point-to-point mode (bench marking technique), (b) dragging but no vibration (c) vibration assisted pseudo-scanning

Fig. 5(a) shows the actual surface geometry as detected by the active axis of the probe, in point-to-point mode (fiber retracted from surface before contacting next sampling point). Fig. 5(b) shows profiles obtained by dragging without any vibration, and Fig. 5(c) shows profiles obtained by vibration assisted pseudo-scanning. It can be seen that the data from the vibration assisted scan has a similar straightness value to that obtained with a point-to-point mode scan (≈ 75 nm), but dragging in absence of any vibration is quite noisy (≈ 200 nm after excluding large outlier).

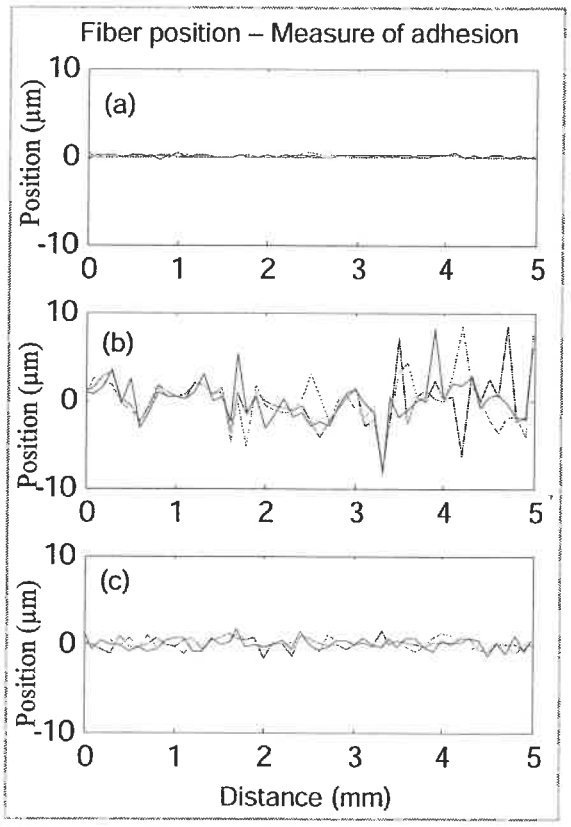

Figure 6: Fiber position for three measurement methods (a) point-to-point mode (bench marking technique), (b) dragging but no vibration (c) vibration assisted pseudo-scanning

Fig. 6 shows plots of the non-active axis (position along the surface in the direction of measurement; and therefore a measure of surface adhesion) in the three modes of measurement (point-to-point, dragging but no vibration, vibration assisted pseudo-scanning) of the fiber probe as the fiber traverses the block. In these plots, the fiber must ideally remain at a neutral position and not bend along the direction

of motion. When the probe is removed from the surface before each sampling point as in Fig. 6(a), the fiber always remains at the same unbent position. However, when dragged along the surface in absence of vibration (Fig. 6(b)), the fiber sticks to the surface and releases, resulting in significant noise. In the presence of vibration (Fig. 6(c)), the magnitude of this noise decreases considerably.

It takes only 10 min to acquire a profile (such as those in Fig. 5(c) with 50 sampling points over 5 mm length) by pseudo-scanning (a factor of 4 savings in time), and with no significant degradation in performance in comparison with our traditional fiber deflection measurement method (point-to-point measurement); therefore this technique holds considerable promise.

In its current configuration, the vibration assisted pseudo-scanning method appears to be a 1-D probing technique and is ideal for profile measurements. We have not attempted a circular scan on a CMM with this probe yet. In all our experiments, the fiber has been forced to vibrate in and out of the surface (*XZ* plane in Fig. 4). The effect of vibrating the fiber in a plane parallel to the gaging surface (*YZ* plane in Fig. 4) has not yet been investigated. We are currently exploring the possibility of adapting this probing technique in a roundness measuring machine configuration where the part is mounted on a precision spindle, to measure roundness of micro-holes.

CONCLUSIONS

We have discussed two enhancements to our fiber probing capability in this paper. First, the fiber buckling technique in combination with the fiber deflection technique allows our probe to function as a true 3D CMM probe. Second, acoustically excited vibration assisted pseudo-scanning technique allows our probe to acquire straightness profile data in any orientation (not necessarily vertical profiles). These enhancements expand our capability for micro-feature metrology

REFERENCES

1. B. Muralikrishnan, Jack Stone and John Stoup, Fiber deflection probe for small hole metrology, Precision Engineering, 30(2), 2006, 154-164
2. Jack Stone, B. Muralikrishnan and John Stoup, A fiber probe for CMM measurements of small features, Proceedings of SPIE Vol. 5879, 2005
3. Singiresu Rao, Mechanical Vibrations, Pearson Prentice Hall, 4th Edition, 2004

TUNABLE, ULTRASONIC, VIBRATION ASSISTED DIAMOND TURNING

Jerald L. Overcash, James F. Cuttino
Center for Precision Metrology
University of North Carolina at Charlotte
Charlotte, North Carolina

ABSTRACT

An ultrasonic, vibration assisted diamond turning (UVADT) device has been constructed that allows for variation of vibration frequency and vibration amplitude via a direct drive actuator [1]. This device has been used to identify the relationships between the tool vibration variables and the process parameters. Frequencies as high as forty kilohertz and amplitudes up to seven micrometers have been achieved at the tool tip during cutting. This paper discusses the tool design, the experimental results, and the model used to describe the mechanism by which vibration assisted turning reduces tool wear.

FINAL DESIGN / ACTIVE TOOLING

Prototype vibration assisted machining (VAM) devices have been described in [1] and [2]. The tool used in this work represents an integrated tool that couples the actuators directly into the tool shank, creating a UVADT device that can now be integrated with a standard tool holder mechanism on conventional precision machine tools, shown in Figure 1. The new tool also has the distinct advantage of being adaptable to conventional or hard turning operations. The tool uses multiple PZTs actuated sequentially to achieve the desired frequency.[1] Additionally, this new integrated cutting tool / actuator system is now embeddable in other systems. For example, the compact tool has been coupled with a long-range fast-tool servo (FTS). The merged technology can now realize precision free-form components produced in hard materials directly on a diamond turning machine. This technology opens a new domain of precision single point tooling, whereby, the tool becomes active during the machining process.

MODEL DEVELOPMENT

The UVADT device was used to determine that tool wear and workpiece carbon content is reduced by the VAM process. The advantage is 40% less tool wear over nearly three times the length of cut for UVADT as compared with conventional diamond turning of 12L14 steel [2]. Based upon the experimental results, a model has been developed specifically for VAM which examines the effects of dynamic heat generation from the cutting process founded on the calculated instantaneous cutting velocity. The model shows that the dynamics of the heat generation for VAM can result in a significant reduction in the average temperature during cutting. This reduction directly effects the diffusion of carbon from the diamond tool into the steel work material, subsequently reducing wear. Based on this direct link between temperature and tool wear, time dependent temperature curves have been generated.

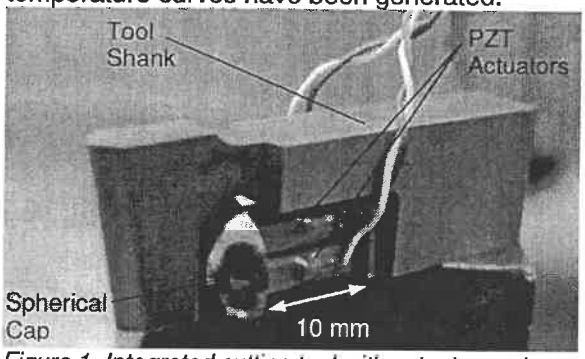

Figure 1. Integrated cutting tool with actuator system.

Tool Model

The experimentally measured tool displacement serves as the basis for the constructed model of VAM using the developed pulse activated cutting tool. The observed waveform for the cutting tool actuated at 40 kHz and 3.5 micrometers is included in Figure 2. The rise and decay times were obtained from a sample of measurements at various frequency and amplitude combinations.

Considering these effects the model approximates the tool displacement with ramp functions combined with a periodicity function. The resulting model output verifies the waveform at 40 kHz and 3.5 micrometers, shown in Figure

[1] Patent Applied for, Tunable Vibratory Actuator, serial number 10/409,746.

3. The derivatives of the displacement functions reveal the resulting periodic tool velocity. The model approximates the tool velocity as positive and constant over the extension period, negative and constant over the retraction period and zero between the pulsing intervals, as shown in Figure 4.

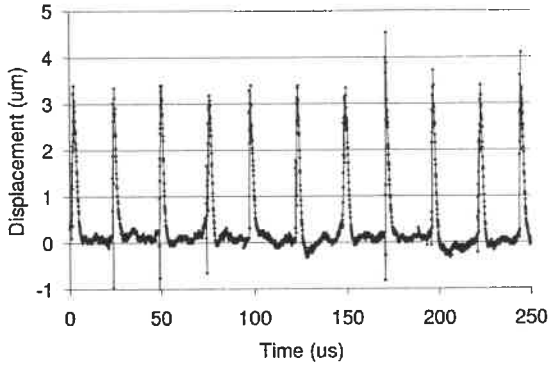

Figure 2.Measured tool displacement.

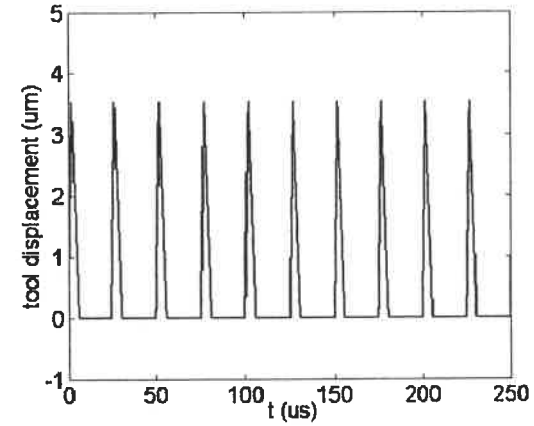

Figure 3. Model output of tool displacement.

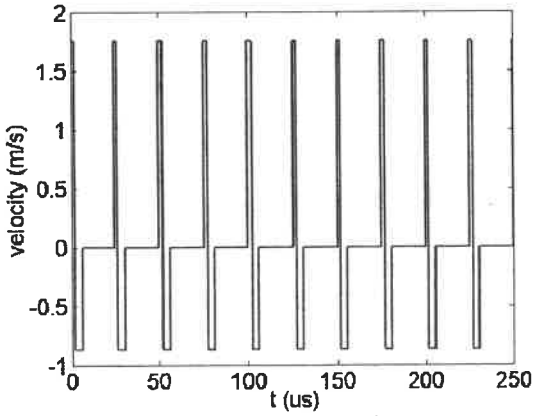

Figure 4. Model output of tool velocity.

Cutting Velocity Model

The cutting velocity for conventional turning operations is only a function of the speed of the work material approaching the cutting tool, considered to be a steady state value for constant velocity machining. The cutting velocity for vibration assisted turning has an additional term due to the tool velocity that is superimposed with the work velocity, creating a time varying cutting velocity. Therefore, the model of the tool motion was combined with the model describing the work motion to give the resulting cutting velocity, shown in Figure 5 for 40 kHz at 3.5 micrometers of tool motion and a workpiece velocity of 0.3 m/s.

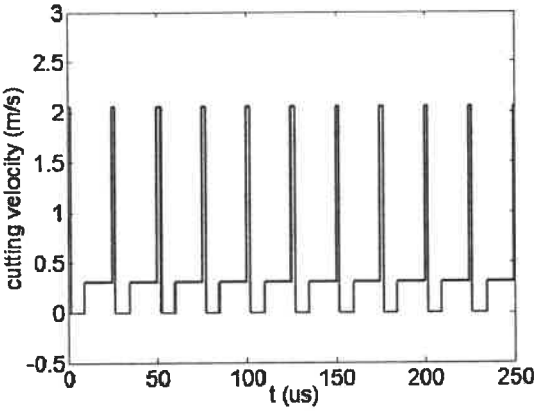

Figure 5. Model output of cutting velocity.

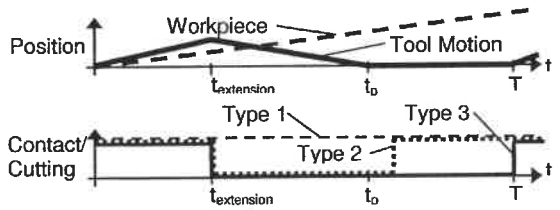

Figure 6. Displacement and contact profiles for VAM.

Through analysis of the cutting velocity, three distinct cases were identified, categorizing the pulse activated VAM process. Type 1 describes the non-separating type of vibration assisted cutting. Under these conditions, the tool remains in contact with the work surface during the entire vibration cycle due to the work velocity being greater than the tool velocity for retraction. Type 2 defines the separating type of vibration assisted cutting governed by workpiece motion where the workpiece initiates contact with the tool before the next vibration cycle is instigated. Type 3 identifies the separating type of vibration assisted cutting governed by tool motion, where, the motion of the tool dictates when cutting begins based on the ratio between tool velocity and workpiece velocity. These three categories are shown in the displacement and contact profiles as a function of time in Figure 6. As an example, Figure 5 depicts Type 2 cutting conditions.

Thermal Model

Based on the completed cutting velocity model, the cutting time is correlated to putting heat into the tool and the separation time to letting the heat be dissipated. This leads to defining the thermal time history. On this basis, a method was developed to estimate the temperature profiles for vibration assisted turning. The approach used in these simulations is adapted from interrupted metal cutting theory [3, 4]. Adapting this theory for multiple velocities is the foundation for the method developed for VAM using the pulse motion technique.

Figure 7 presents the adapted theory. At the onset of cutting, the cutting temperature increases as governed by the heating up curve at the work velocity, as shown by curve *a1*. Then, when tool motion initiates cutting, temperature is governed by the heating up curve at the tool velocity plus the work velocity, as shown be curve *a2*. Next the cutting temperature decreases as governed by the appropriate cooling down curve, as shown by curve *b*, during the separation period. After one complete cycle, the tool will usually not necessarily assume its original thermal condition, T_i; therefore, the subsequent temperature peaks will continuously increase until a limit value is reached.

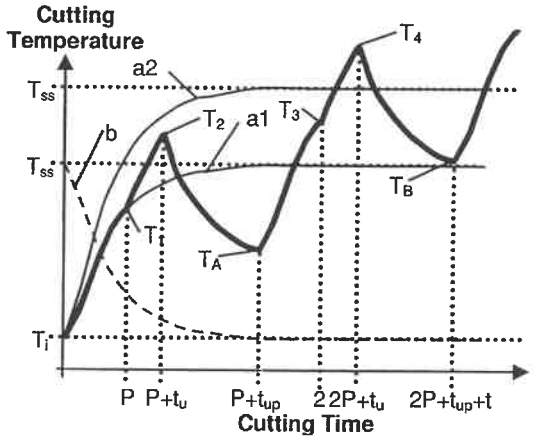

Figure 7. Model cartoon for temperatures in VAM.

Five steps were necessary to carry out the thermal model.

1. Conduct finite element modeling simulations of the cutting process under similar conditions as the experimental tests to obtain the temperature history throughout the cutting process for conventional, i.e. non-vibration assisted turning.
2. Extract the tool temperature profiles and steady state temperatures from the finite element model simulation results.
3. Adapt to vibration assisted machining by curve fitting functions to the extracted temperature data to obtain formulas that mathematically capture the profiles for the heating and cooling cycles including the thermal time constant effects.
4. Generate cutting velocity profiles founded on the combination of the work velocity with the tool displacement and tool velocity profiles.
5. Combine the curve fits of the finite element temperature data with the cutting velocity profiles to obtain estimates of the temperature profiles for vibration assisted machining.

Finite Element Results

The simulation conditions were fixed to values comparable to the experimental test conditions for conventional turning. The approach to the temperature simulation for the vibration assisted cases is to gather the temperature history for the heating and cooling cycles for conventional turning at various work velocities. Based on curve fits to the FEA data, equations were inserted into the temperature prediction program to generate the temperature histories for numerous VAM cases. The FEA simulations factor the cutting conditions into the simulations. The resulting family of curves generated by the FEA governed by constant velocity cutting adhered to the generally accepted power law function relating temperature to velocity.

Temperature Results

With the theory developed mathematically, the temperature profiles were generated based on the vibration parameters and work velocity. Numerous cases were considered such that the effects of each parameter could be realized. The temperature profiles correspond to a 20 μm depth of cut for a diamond tool in AISI 12L14 work material since the temperature equations used are based on the curve fits to the finite element model at the specified cutting conditions. The following plots demonstrate the consequence of variations in the vibration amplitude and the work velocity. Figure 8 depicts the temperature rise for a tool motion of 40 kHz at 7 micrometers and a workpiece velocity of 0.2 m/s. This demonstrates Type 3 conditions where the tool motion dictates when cutting begins and ceases. The cutting velocity is provided as a reference to show how the

temperature is reached through the process. Figure 9 shows the effect of increasing the work velocity to 0.6 m/s on the cutting temperature and the cutting velocity. Notice that the cutting state changes to Type 2 conditions and the mean cutting temperature rises approximately 15 degrees. Figure 10 demonstrates the effect of decreasing the vibration amplitude to 4 micrometers. This change reduces the separation between the tool and the work material thereby increasing the duration of the heat input and decreasing the duration of the heat dissipation, both acting to increase the cutting temperature. The result is a rise in the average temperature of approximately 7 degrees.

The results concur with experimental results that show increased tool wear as the tool motion changes from Type 3 to Type 2 to Type 1. Mapping temperature into diffusion equations resulted in trends showing this increase in tool wear; however, there were differences in the scaling between experiment and prediction.

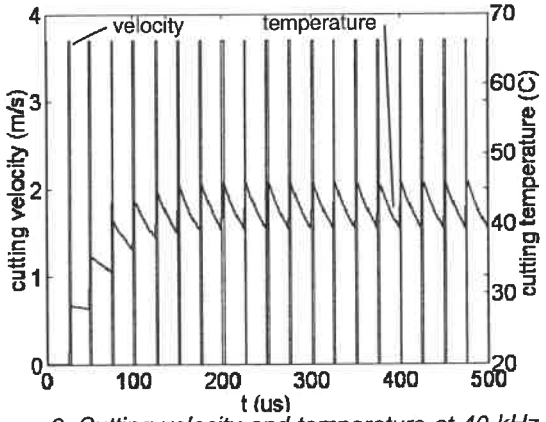

Figure 8. Cutting velocity and temperature at 40 kHz, 7 μm and 0.2 m/s

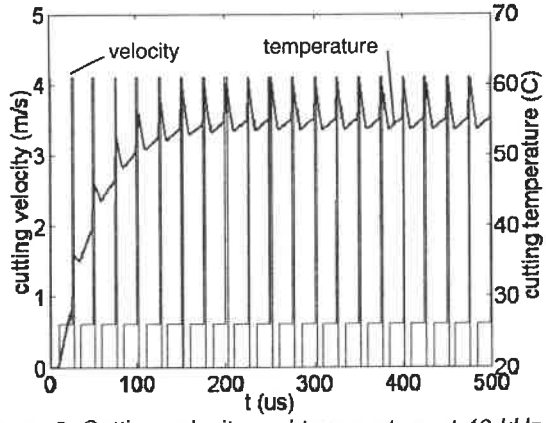

Figure 9. Cutting velocity and temperature at 40 kHz, 7 μm and 0.6 m/s

CONCLUSIONS

The simulations demonstrate that increases in the work velocity act to increase the temperature. From the same simulations, increases in the vibration amplitude and vibration frequency were found to be favorable for reducing temperature and hence diffusive wear, but must be addressed on a case by case basis for work velocity, vibration amplitude and vibration frequency for optimization.

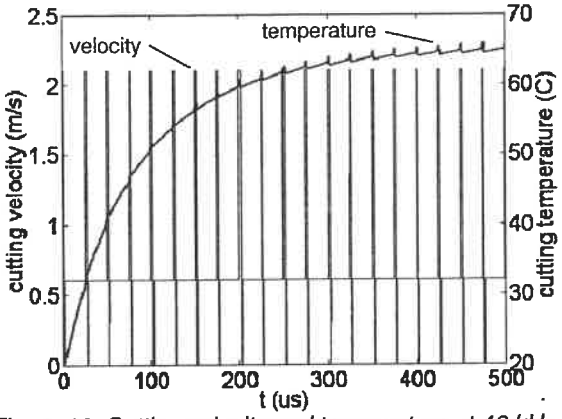

Figure 10. Cutting velocity and temperature at 40 kHz, 3 μm and 0.6 m/s

ACKNOWLEDGEMENTS

This work was supported by the industrial affiliates of the Center for Precision Metrology, a National Science Foundation Industry / University Cooperative Research Center supported under grants #EEC9811556 and #EEC0331950. Any opinions, findings, and conclusions or recommendations expressed in this material are those of the author(s) and do not necessarily reflect the views of the National Science Foundation.

REFERENCES

1. J. Overcash and J. Cuttino, "Development of a Tunable Ultrasonic Vibration-Assisted Diamond Turning Instrument", *ASPE Proceedings 2003 Annual Meeting*, 2003.
2. J. Overcash and J. Cuttino, "Tunable Ultrasonic Vibration-Assisted Diamond Turning of Steel", *ASPE Proceedings 2004 Annual Meeting*, 2004.
3. Z. Pálmai, "Cutting Temperature in Intermittent Cutting," *Int. J. Mach. Tools Manufact.*, Vol. 27, No. 2, 1987, 261-274.
4. D.A. Stephenson and A. Ali, "Tool Temperatures in Interrupted Meal Cutting," *J. of Engineering for Industry, Trans. Of ASME*, Vol. 114, May 1992, 127-136.

MODELING OF VIBRATION IN SINGLE-POINT DIAMOND TURNING

Alex Sohn, Lucas Lamonds and Ken Garrard
Precision Engineering Center
North Carolina State University
Raleigh, North Carolina, USA.

INTRODUCTION

The objective of this work is to develop a model to simulate the effects of vibration on the surface finish of single-point diamond turned parts. This model can be used to optimize cutting conditions for best surface finish and to predict geometric characteristics of the surface beyond the conventional rules of thumb. These characteristics can also have a significant impact on optical surfaces that operate in the visible range by introducing coherent scatter that produces the familiar "rainbow" appearance of diamond turned surfaces in white light.

Surface finish in single-point diamond turning is primarily influenced by four factors: Geometry, vibration, material properties, and tool edge quality. The first-order geometric model using the parabolic approximation gives the peak-to-valley roughness which is determined solely by the crossfeed (f), and the tool radius (R).

$$PV = \frac{f^2}{8R} \tag{1}$$

This approximation is often used as the sole determiner for choosing radius and feedrate even though at large radii and small feeds, the predicted finish is not achievable.

VIBRATION

Assuming suitable materials are selected and the tool edge quality is high, vibration is typically the next largest factor in determining surface finish. The origin of this vibration can be from a number of sources, although the axes of the machine or the spindle are the most likely candidates. The ASG 2500 Diamond Turning Machine at the Precision Engineering Center suffers mainly from a 65 Hz vibration of the Z-axis which has a magnitude of about 30 nm. This amplitude can vary slightly depending on spindle rpm and balance. Either of these can increase this vibration. For the purposes of the following discussions and examples, the vibration of the ASG 2500 Z-slide will be used as the source of the vibration, though the technique can be applied to any source.

The impact of vibration on a diamond-turned surface is generally to degrade the surface finish. In its simplest form, a sinusoidal vibration in the normal direction would leave an RMS surface finish of 0.707 times the amplitude of the vibration. It would seem that the surface finish could never be improved beyond this value and there would be no point in slowing the feedrate or using a larger radius tool. This assumption is, however, incorrect due to interaction between neighboring grooves at small feedrates. By modeling the surface produced by a vibrating tool, it can be shown that the surface finish is no longer limited by the vibration amplitude but can be improved by moving to finer feedrates.

THE SURFACE FINISH MODEL

A number of points along the edge of the tool are calculated for each x-position in increments of the crossfeed. The depth of cut changes around the periphery of the part with the vibration environment.

$$depth = A\sin\left(\frac{\omega x}{\Omega f}\right) \tag{2}$$

where A is the vibration amplitude, ω is the vibration frequency of the tool, x is the radial position of the tool and Ω is the vibration frequency of the spindle.

As shown in Figure 1, after multiple profiles are generated, redundant points in the overlapping regions are eliminated and only the point with the largest depth at each x-coordinate is retained. Individual cross-traces at different rotational positions of the spindle can then also be assembled into 3D profiles as shown in Figure 2.

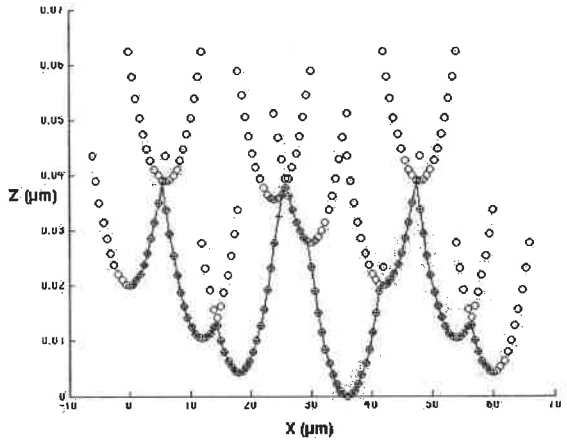

FIGURE 1. Points along multiple tool profiles, at varying depths due to vibration, produce a finished surface contour.

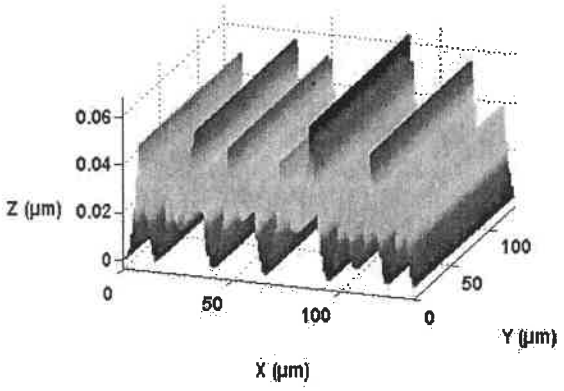

FIGURE 2. Multiple simulated surface profiles assembled into a 3-D surface.

It is at lower feedrates that the effects of tool vibration on a diamond-turned surface become interesting as illustrated in Figure 3. The illustration shows the surface left at small feedrates where the crossmarks show the tool location at each pass in the profile. A number of passes are not represented at all in the finished surface, leaving only the most extreme passes and, hence, a smoother surface than would be expected if all cuts were represented.

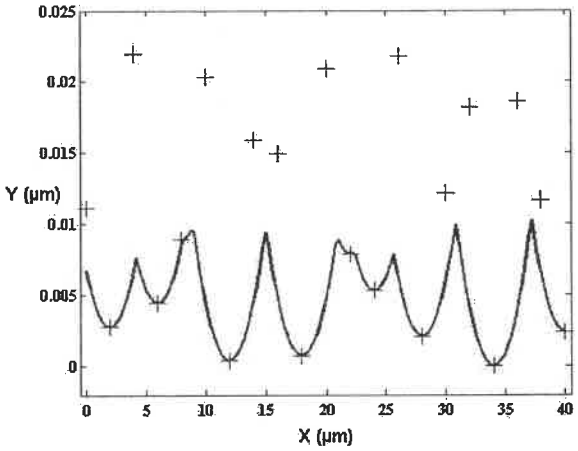

FIGURE 3. At fine feedrates, some passes of the tool (+) are not represented in the finished surface. This produces a better finish than would be expected from the RMS of the vibration alone.

EXPERIMENT

To verify the simulations, a plated copper sample was machined with the same feedrates used in the simulations. Machining experiments were performed on an ASG 2500 DTM using a 505 rpm spindle speed and a 0.5 mm radius, zero rake natural diamond tool. The laboratory temperature was controlled to 20 ±0.05°C. Petroleum oil cutting fluid (Mobilmet Omicron®) was used for lubrication and chip removal.

Eight 2 mm wide bands were machined on the 50 mm diameter sample with crossfeeds of 0.6, 0.9, 1.9, 2.7, 6.1, 8.6 and 19.1 µm/rev. The surface was ultrasonically cleaned and then measured on a Zygo NewView 5000 Scanning White-Light Interferometer (SWLI) using 50X magnification. The measurement area is 108 µm X 144 µm. Figures 4 and 5 show the typical profile measurement result. The effects of vibration on groove depth can clearly be seen in the profile at this large feedrate. The depth varies seemingly randomly as the tool traverses the part. Note a small chip is visible in the tool edge as a repeatable defect from each pass. At finer feedrates, this portion of the tool does not, however, have an effect.

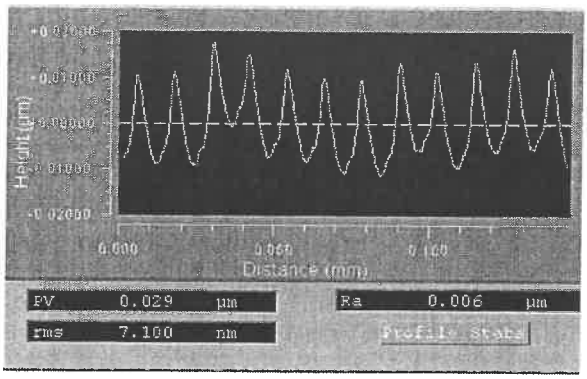

FIGURE 4. Typical surface profile measurement illustrating the depth change as a result of vibration with large feed rate of 12 µm/rev.

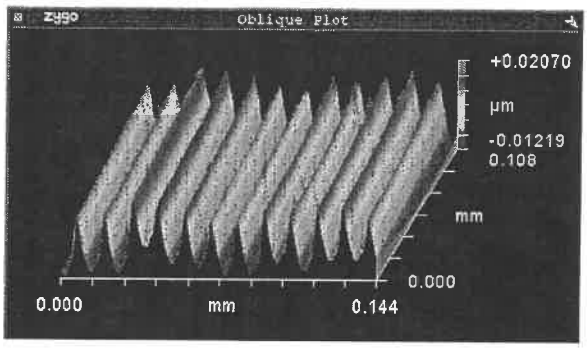

FIGURE 5. A typical measurement result in oblique plot form. This is the same machined surface shown in Figure 4.

Figure 6 shows the results for a series of simulations and cuts performed to verify the model. The plot also shows the line that represents the theoretical finish approximation for a parabolic surface.

$$RMS = \frac{f^2}{26.6R} \qquad (3)$$

Clearly, the surface finish can improve significantly beyond the RMS 7.7 nm limit of a simple sinusoidal vibration. The finish also continues to improve with finer feedrates between 2 and 5 µm, when they already deviate significantly from the theoretical approximation.

ENVIRONMENT

As the results displayed in Figure 6 show, at theoretical finishes below 2 nm RMS, the model does not predict the surface finish. At these extremely fine finishes, other factors begin to take effect such as environmental effects and material anisotropies. While the temperature in the laboratory is controlled to less than 0.1°C, even such small temperature fluctuation can have an impact. At small feedrates, the long-period fluctuations of the temperature over 1-8 min can have an impact on finish, as shown in Figure 7.

The Z-axis deadpath on the ASG 2500 interferometer was approximately 250 mm at the position where the sample was machined.

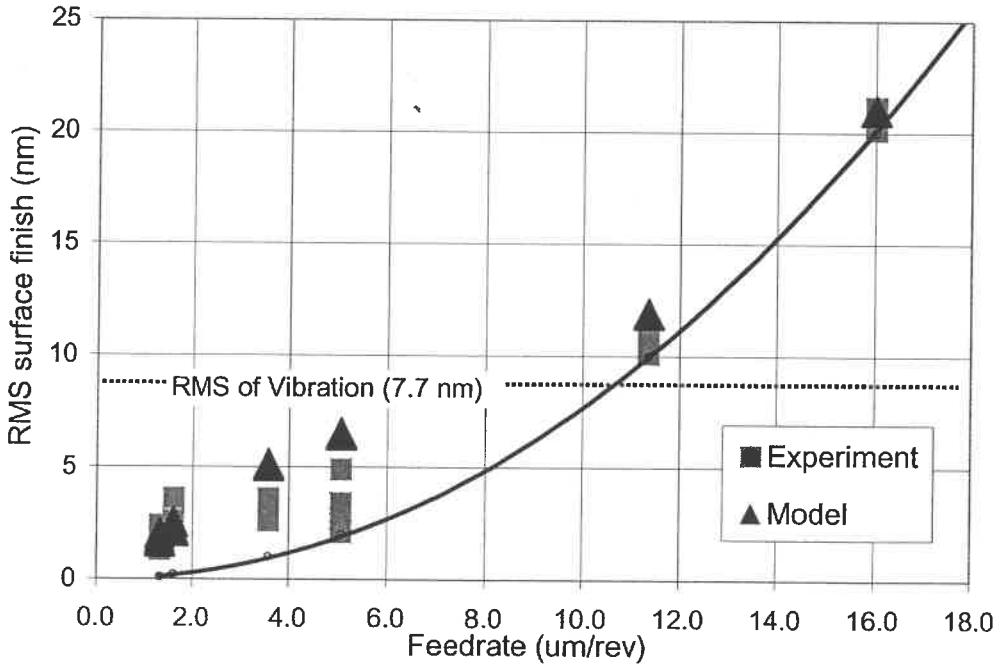

FIGURE 6. Triangles show the simulated finish with vibration and the squares show the machining results. Variation in roughness around the periphery is shown in both model and experiment.

Given a maximum temperature variation of 0.1° C, the calculated resultant deadpath error using the Edlén equation[1] is 25 nm. This limitation reflects the need to reduce deadpath, compensate for environmental fluctuations with a refractometer, operate in a vacuum, or use another means of position feedback such as a linear encoder. While linear encoders do not eliminate errors due to thermal fluctuations, expansion of the scale due to temperature changes tends to have a much longer period, so errors move into the figure error regime rather than roughness.

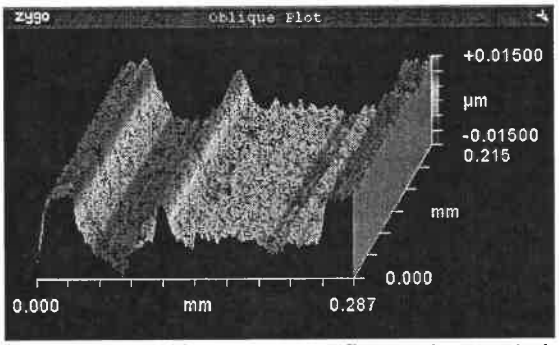

FIGURE 7. Temperature fluctuations at low feedrates can produce surface finish degradation due to deadpath error in the DTM laser interferometer.

MATERIALS

Material effects, such as inclusions or grain boundaries have a much larger impact in materials such as 6061 Aluminum[2], though apparently there are still defects even in the plated copper used as shown in Figure 8.

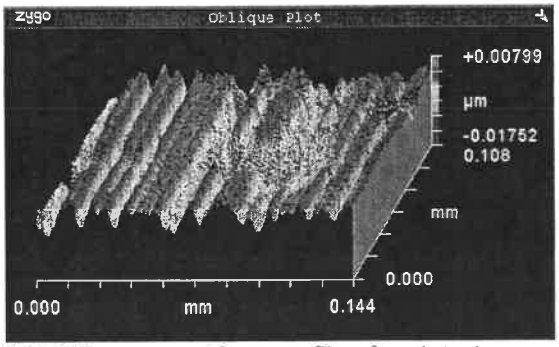

FIGURE 8. 3D surface profile of a plated copper surface machined at fine feedrates showing pits in the surface due to material defects.

The final contribution to a degraded surface finish is from errors in the control of the axes. In the case of the ASG, tests of the custom, DSP-based, controller showed tracking errors of less than 10 nm Peak-to-Valley [3]. While of some significance, the effects of this tracking error are still not as significant as those due to temperature variations and material defects.

CONCLUSION

Understanding what determines surface finish enhances the ability to improve surface finish in the most efficient manner. It also allows us to exploit all of the capabilities of a diamond turning machine to achieve the best possible finish for that machine. The conventional wisdom that there is little point in machining at lower feedrates beyond the point where the measured surface finish is worse than the theoretical finish (obtained from the parabolic approximation) simply does not hold. Ever finer feedrates continue to reduce the impact of vibration to a point where it does not impact the surface finish any more and material or environmental effects take over. In the particular case of the PEC's ASG 2500 DTM, lower feedrates than 2 µm using a 0.5 mm radius tool do not improve the surface finish. Factors other than vibration dominate below this feedrate. Until these the impact of these factors is reduced, smaller feedrates simply add time to the machining effort with little gain.

FUTURE WORK

In another application, the model can be used to perform the same analysis with the tool vibrating parallel to the surface. The advantage of this action is that the normally regularly spaced grooves formed in diamond turning that turn the surface into a diffraction grating can be randomized. This could reduce coherent scattering that produces undesirable structure in the optical output that often makes diamond-turned optics unsuitable for visible applications.

REFERENCES

[1] Alexander H. Slocum, "Precision Machine Design" 1994 John Wiley, New York.

[2] John P. Schaefer, "Progress in Precision – Single Point Diamond Turning (SPDT) of Optical Components" ASPE Proceedings 2001 Spring Topical Meeting Presentations DVD.

[3] T.A. Dow, L. Lamonds, Fabrication of Optical Surfaces and Fiducials, 2005 PEC Annual Report, pg 81.

OPTIMIZING MACHINING PROCESSES FOR PRECISION: AN EXAMPLE USING CALCULATED CUTTING FORCES

Richard L. Rhorer
Manufacturing Metrology Division
National Institute of Standards and Technology
Gaithersburg, MD, USA

INTRODUCTION

Machining process research is often directed at improving the material removal rate. However, there are some cases where the more precise one makes the component the more valuable it becomes, and so the question is: how precise can you make the part? The effect of the cutting process on the part's precision becomes the priority, not the material removal rate.

Designing a machining process for maximum precision is a motivation for cutting mechanics research. To quantify the machining process effects on the component precision, such as part deformations from cutting forces, requires understanding of the physics of the process.

Calculating cutting forces requires an adequate constitutive material model (relationship of stress-to-strain) for the work piece material. For conditions encountered in machining, this stress-strain relationship is not readily available for even common materials. A pulse-heated Kolsky bar, an experimental method being developed at the National Institute of Standards and Technology (NIST), is directed at obtaining this relationship. This same material model relating stress to strain at high temperatures is valuable when studying other high strain rate problems such as impacts and explosions.

BACKGROUND: MAXIMUM REMOVAL RATE

Optimizing a machining process for maximum material removal rate has been an ongoing research effort since the beginning of the industrial revolution. The problem can be stated in terms of an objective function describing the removal rate for a turning operation, such as:

$$Q_M = t_o \cdot w \cdot V_c \qquad (1)$$

Where Q_M is the material removal rate (mm^3/s), t_o is the uncut chip thickness, or the feed per revolution (mm), w is the chip width (mm), and V_c is the cutting velocity (mm/s). This expression describes the material removal rate for a simple turning operation, but a similar, relatively simple expression can be written for milling or grinding processes. The maximum, or optimum, removal rate is found within given boundaries, or constraints, such as power and speed limits of the machine tool. Also, there are process limits such as tool wear and the effects on part accuracy that can limit the removal rate. The optimum conditions can be found by a trial-and-error approach of calculating the removal rate for all possible parameter combinations within the constraints and looking for a maximum; however, more sophisticated mathematical methods can also be used. As part of the NIST Smart Machining Systems (SMS) Program a robust optimizer has been developed [1]. The NIST optimizer uses a linear programming approach and also handles uncertainties of each constraint and hence determines a "robust optimum."

Addressing part precision with the highest priority requires a different approach than optimizing on material removal rate. For example, increasing cutting speed increases the removal rate, but simply increasing or decreasing the cutting speed does not necessarily affect the precision of the part—additional understanding of the process is required to determine what parameters affect precision.

EXAMPLE: SHELL COMPONENT

An example component will be used to illustrate a method of studying one aspect of the precision of a machining process. The part is a cylindrical thin-walled shell. For this example, let us assume that the required material is aluminum and that the length and inside diameter of the shell are given (100 mm length and 20 mm diameter inside), but the outside diameter of the tube is not specified. The question asked is: how thin can we make the wall and still have the shell as nearly perfect as the machine is capable of making? It is an open-ended question that is frustrating for one working in a job shop

environment. However, the question is not unusual for one involved in precision engineering.

ERROR BUDGET APPROACH

An error budget is a valuable tool when answering the question: how do we improve the process of making a particular part? For example, improving the machine tool precision may not significantly improve the precision of the part if the major sources of error are from the machining process itself. We need to know the relative importance of various contributions to the overall inaccuracies of the part. An error budget is used to identify different error sources and tabulate their effect on part accuracy. We can consider the cylindricity of the outer surface of the shell due to machine tool errors and deflections due to the forces generated in cutting. The end of the tube will be larger if cutting forces are high because the tube will deflect away from the tool. There are other items like distortions due to residual stress and vibrations that would be included in a more complete analysis. As the method is carried on further, additional items can be added and compared.

The effects of relevant machine tool errors, such as the parallelism of the spindle to the axis travel and the error motions of the spindle, can be estimated for the accuracy of a particular part such as our example case. These errors might be on the order of 1 µm for a very high-precision machine tool. However, to quantify the errors due to the deflections, we need to estimate the values of cutting forces.

CALCULATING CUTTING FORCES

For well-established processes, calculating the cutting forces may not be necessary—they have either been measured or "the old-timers" know that they are not significant in making this kind of part. However, when the component is being fabricated the first time, or the material has been changed, or the question is asked "how accurate can you make this part?", calculating the cutting force is necessary. The problem is not simple and no exact mathematical expression for cutting forces is available, although good predictions can be made by several different types of models, including the finite element method (FEM). Any of the methods require knowledge of the material behavior.

For the example presented in this paper, let us consider machining the part by simple turning and further assume that the cutting geometry is close enough to the orthogonal geometry for practical purposes. Then, cutting forces can be estimated by a traditional model presented by Eugene Merchant and others in the 1940s and described in many machining textbooks, such as Kalpakjian [2]. Using this approach the cutting force can be expressed as:

$$F_C = \frac{w \cdot t_0 \cdot \tau_{flow}}{\sec(\beta - \alpha) \cdot \cos(\phi + \beta - \alpha) \sin\phi} \qquad (2)$$

Where F_C is the cutting force in the direction of the cutting speed, w is the width of the cut, t_0 is the depth of cut (or uncut chip thickness), τ_{flow} is the shear flow stress for the work piece material (assuming perfectly plastic material behavior), β is the friction angle (where the coefficient of friction, $\mu = \tan\beta$), α is the rake angle of the cutting tool, and ϕ is the shear plane angle. The thrust force, F_T, can be expressed as:

$$F_T = F_C \cdot \tan(\beta - \alpha). \qquad (3)$$

For the special case where the friction angle is equal to the rake angle, the force acting normal to the surface, the thrust force, would be zero. If we assume a coefficient of friction of 0.2, this would make the rake angle, $\alpha \approx 11°$, which is reasonable for a tool cutting aluminum. Therefore, by designing the tool with a rake angle of about 10°, the thrust force would be at least close to zero. Because of the uncertainty of the coefficient of friction, assume $F_T \approx \pm 0.1 \cdot F_C$ for our error budget estimates. The thrust force could actually be either positive or negative, making the cylindrical part either larger or smaller at the end farthest away from the holding chuck.

Determining the shear plane angle has always been a challenge, but a traditional approach finds the shear plane angle to be $\phi = 45° + \alpha - \beta$. For our special case of $\alpha = \beta$ the cutting force expression then reduces to:

$$F_C = 2 \cdot w \cdot t_0 \cdot \tau_{flow}. \qquad (4)$$

For this approach, we assume that the cutting geometry is simple and the material behavior can be expressed as a perfectly plastic response. This approach greatly simplifies the problem and makes it possible to get a reasonable value of the cutting force for given cutting conditions, assuming that we know the flow stress for the material. This can be thought of as only a starting point, and a more complete calculation could be performed using an FEM code. The FEM approach could handle more detailed geometry and would require a more complete constitutive material model.

DYNAMIC MATERIAL PROPERTIES

It would be nice if one could look up in a handbook the flow stress necessary for the expression in equation (2) above. The problem is that machining processes produce very high strains, very high strain rates, and also high temperatures with high heating rates.

A method traditionally used for obtaining dynamic material properties is the Split Hopkinson Pressure Bar, also referred to as a Kolsky Bar. This method uses two long bars with a sample of the test material sandwiched between the ends of the bars. A compression strain wave is initiated in the first bar (incident bar) which compresses the sample and causes a second wave to travel down the transmitted bar. Common variable-resistance strain-gages mounted in the center of both bars record the elastic strain waves in the bars. The strain gage signals can be used to calculate the stress-strain curve for the sample material for large plastic strains at high strain rates. The NIST Kolsky bar also has the capability to pulse heat the sample prior to the impact test and produce a stress-strain curve for the sample material at an elevated temperature. Details of the NIST Pulse Heated Kolsky bar are described by Basak [3]. An example of data obtained for an aluminum alloy is presented in Fig. 1.

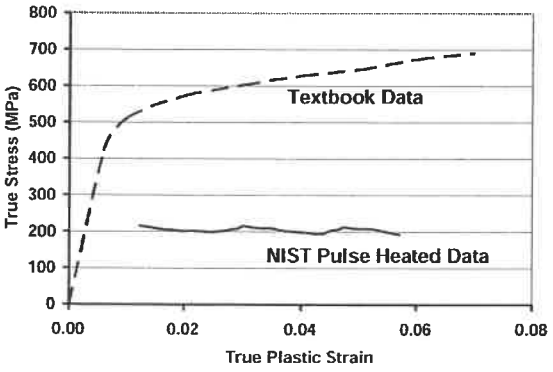

FIGURE 1. Stress-strain curve for aluminum alloy 7075-T6. Upper curve is from Meyers [4] for room temperature conditions and for strain-rates of 0.03 s^{-1} to 560 s^{-1}. The lower curve is NIST pulse heated data for a test temperature of 300°C and strain-rate of approximately 1500 s^{-1}.

EXAMPLE CALCULATION

For the example problem discussed above, the cutting forces can be estimated by assuming:
-- the width of the cut is 0.5 mm;
-- the depth of the cut (feed per revolution) is a practical minimum of about five times the edge radius (sharpness) of the tool, so we could assume a minimum of about 0.050 mm for a high speed steel tool (less for a diamond tool);
-- the tool is designed to minimize normal cutting forces, or the tool rake is about 10°;
-- the temperature in the shear zone is assumed to be elevated, in the range of 300 ° C.

Then the compression flow stress is about 200 MPa (from Fig. 1, lower curve, assuming perfectly plastic behavior), making the shear flow stress about 100 MPa (shear stress is half the normal stress assuming pure compression and using the common Mohr's circle relationship.) The cutting force is then calculated from formula (4) to be: $F_C \approx 5.0$ N. And, the thrust force would be: $F_T \approx \pm$ 0.5 N from the assumption discussed above that the thrust force would be an order of magnitude smaller than the cutting force if the tool rake angle was adjusted to minimize the thrust force.

The part will deflect away from the tool (or pulled to the tool) with the thrust force, making the part tapered. The amount of this deflection, *x*, can be estimated with a simple cantilever beam deflection equation when the thrust force is known

$$x = \frac{1}{3} \cdot \frac{F_T \cdot L^3}{E \cdot I} \qquad (5)$$

where F_T is the thrust force (≈ 0.5 N), L is the length of the part (= 100 mm), E is the modulus of elasticity (= 70 GPa). I is the area moment of inertia of the tube, $I = \frac{1}{4} \cdot \pi \cdot (R_o^4 - R_i^4)$, where R_o and R_i are the outer and inner radii of the tube cross section. To make this part with process-induced errors approximately the same as the

machine-induced errors, we should limit the deflection, x, to approximately the same as the machine tool-induced errors, or let us assume about 1 μm. We can now calculate the outer radius, R_0, for this maximum deflection using equation (5) with R_i = 10 mm. From this calculation, $R_O \approx 10.7$ mm, so the wall thickness would be about 0.7 mm.

DISCUSSION AND CONCLUSIONS

Although the calculations illustrated here are very approximate, we have provided an approach and a quantitative estimate of how thin a wall (approximately 0.7 mm) could be turned on an aluminum cylindrical tube of 100 mm length and 20 mm inside diameter. The tool has been designed to limit the effect of cutting forces on part geometry rather than to maximize the material removal rate. To further optimize the process for precision, the tool radius and feed rate will need to be adjusted to ensure the surface finish is the best obtainable for a particular machine tool.

By using a diamond tool, we could possibly decrease the depth of cut and thereby decrease the cutting and thrust forces. Therefore, an even thinner wall would appear possible with a diamond tool. However, dynamic concerns such as chatter would have to be considered when the wall thickness becomes thin.

From experience we would have to address other contributions to the error budget, such as flattening of the shell, for a complete analysis of the process for making this thin-walled part. Thermal effects causing shape and size changes in the tube must also be included in a complete error budget.

In analyzing a process to determine cutting forces as presented here, it is necessary to have a flow shear stress value for the work piece material. A more detailed process analysis, such as the use of the FEM method, can provide more exact values of cutting forces and details such as cutting temperatures. However, an even more complete material description, such as a constitutive material model based on data obtained from a series of pulse heated Kolsky bar tests, is required by the FEM method.

ACKNOWLEDGEMENTS

This work was supported through the Smart Machining Systems Program in the Manufacturing Engineering Laboratory at NIST, Dr. Alkan Donmez, Program Manager.

REFERENCES

1. Deshayes, L., Welsch, L., Vacher, A., Donmez, A., Robust Optimization for Smart Machining System: An Enabler for Agile Manufacturing, Proceedings of IMECE2005: 2005 ASME International Mechanical Engineering Congress and Exposition, Nov. 5-11, 2005, Orlando, FL.
2. Kalpakjian, S., 1991, *Manufacturing Processes for Engineering Materials, 2nd Ed.*, Addison-Wesley, Inc., Reading, MA, pp. 486-494.
3. Basak, D., Yoon, H., Rhorer, R., Burns, T., Microsecond Time-Resolved Pyro-mettry During Rapid Resistive Heating of Samples in a Kolsky Bar Apparatus, *Temperature: Its Measurement and Con-trol in Science and Industry, Vol. 7, Proceedings of the 8th Temperature Symposium*, Chicago, IL, October 2002, pp. 753-757.
4. Meyers, M., 1994, *Dynamic Behavior of Materials*, John Wiley and Sons, Inc, New York, p.300.

A COMPARATIVE STUDY OF PART ERROR CONTRIBUTORS IN HIGH-SPEED MACHINING

J. Suzanne Canning, Raul Zapata, John C. Ziegert, and Tony L. Schmitz
Department of Mechanical and Aerospace Engineering
University of Florida, Gainesville, FL, USA

INTRODUCTION

The accuracy of parts produced by machining operations has been studied extensively over the past decades. It is known that machined part accuracy has four major contributors: machine geometric errors, thermally induced errors, trajectory following errors caused by controller/structural dynamics, and errors due to the cutting forces. In computer numerical control (CNC) machining, the desired spatial trajectory of the cutting tool is ideally defined by the part program. The purpose of the part program is to place the tool tip at particular coordinates relative to the part at every instant in time, leaving behind newly created surfaces which form a workpiece of the proper dimensions. Errors in the final dimensions of the machined part are determined by the accuracy with which the commanded tool trajectory is followed, combined with any deflections of the tool, part, or machine caused by the cutting forces.

Prior research has shown that the part dimensional errors associated with the cutting force cannot be properly modeled and understood unless the vibrational dynamics of the tool-holder-spindle-machine-workpiece system are considered; and that in high-speed machining (HSM), the errors associated with cutting forces can be as large, or larger, than the errors typically associated with geometric, thermal, and controller effects for modern machine tools. Most importantly, small variations in the tool point dynamics and/or small changes in spindle speed can result in part errors which are much larger than typical tolerances. This is referred to as surface location error (SLE).

This paper reports preliminary results of a study designed to quantify the contributions of geometric, thermal, controller, and cutting force errors to the accuracy of parts produced on a modern CNC high-speed milling machine. All data reported here was collected on a Mikron UCP-600 Vario CNC 5-axis milling machine with *x*, *y*, and *z* axis travels of {600, 450, and 450} mm, respectively. The vertical Step Tec spindle accepts HSK-63A tool holders and is capable of speeds up to 20000 rpm with cutting power up to 16 kW. This machine was purchased new in 2005 and measurements undertaken soon after installation. For the purposes of this study, the machine was operated as a three-axis machine and, therefore, error motions of the B and C rotary axes are not included.

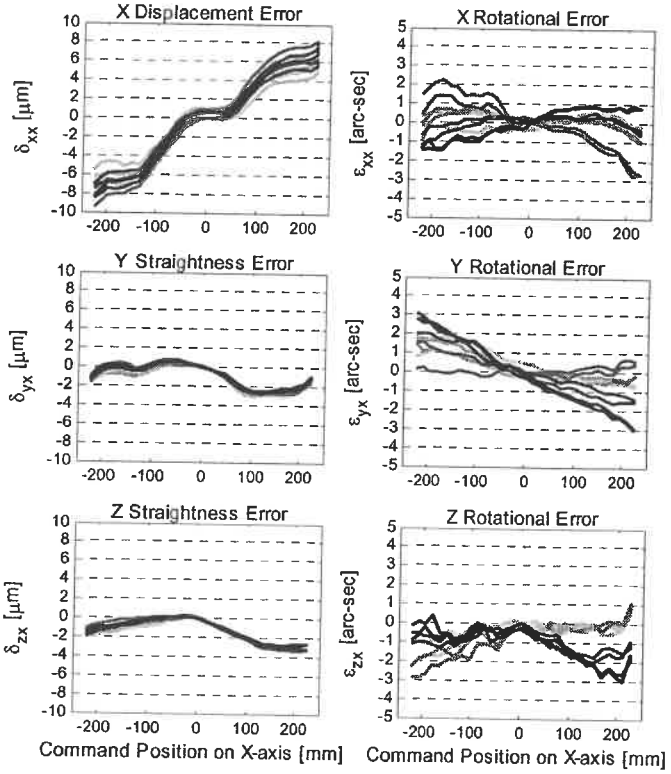

Figure 1: Error motions for the x-axis.

GEOMETRIC ERRORS

The geometric errors for the *x*, *y*, and *z* axes of the machine were measured using the Laser Ball Bar [1,2]. Six degree-of-freedom error motions (3 displacements and 3 rotations) were measured for each axis at 15 mm intervals for both the forward and reverse directions of motion. Axis orthogonality errors were also measured. All errors were measured with the machine in a cold state and were repeated five

times. Figure 1 shows measurement results for the *x*-axis. Comparable results were obtained for *y* and *z* Orthogonality errors are reported in Table 1.

Table 1: Axis orthogonality errors.

Axes	Angle (deg)	Error (arc-sec)
xy	89.99977	-0.8182
yz	89.99934	-2.3744
xz	89.99860	-5.0591

A homogeneous transformation matrix (HTM) model of the machine geometry errors was created and used to predict tool point positioning errors in a coordinate system attached to the workpiece at points along the machining tool path. An example for the *x*-axis transformation error matrices is provided in Eq. 1. The matrices for the *y*- and *z*-axes are constructed similarly. Note that orthogonality errors between the axes are included as linear terms in the appropriate straightness error functions of the axis.

$$ {}^{part}\vec{P}_{tool} = {}^{part}T_X E_X{}^X T_Y E_Y{}^Y T_Z E_Z{}^Z \vec{P}_{tool}, \text{ where} \qquad (1) $$

$$ {}^{part}T_X = \begin{bmatrix} 1 & 0 & 0 & x_{commd} \\ 0 & 1 & 0 & 0 \\ 0 & 0 & 1 & 0 \\ 0 & 0 & 0 & 1 \end{bmatrix} \quad E_X = \begin{bmatrix} 1 & \varepsilon_z(x) & -\varepsilon_y(x) & \delta_x(x) \\ -\varepsilon_z(x) & 1 & \varepsilon_x(x) & \delta_y(x) \\ \varepsilon_y(x) & -\varepsilon_x(x) & 1 & \delta_z(x) \\ 0 & 0 & 0 & 1 \end{bmatrix} $$

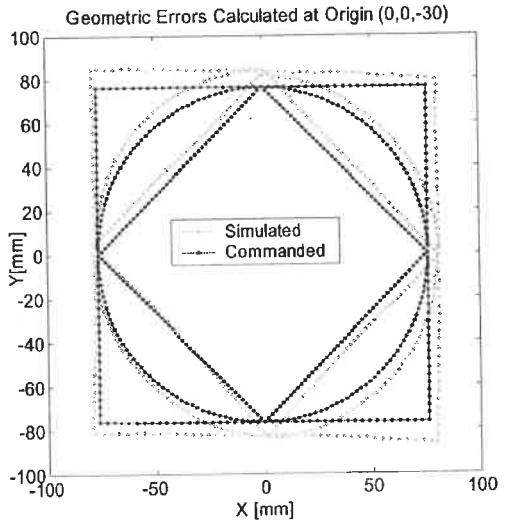

Figure 2: Part errors due to machine geometry (2000x error magnification).

The geometric errors were used in conjunction with the HTM error model to predict part errors using a Monte Carlo approach. At two to five mm increments along the part features, a value for each of the 18 machine geometric error components was selected from the distribution of the measured values at the appropriate axis location. The normal distance from the resulting tool point location to the surface of the feature being machined was then computed and saved. After a large number of iterations, statistics on the feature error at points along the surface were computed. The mean results are shown in Fig. 2 (with 2000x error magnification) for the NAS 979 test part. The points in the simulation all lie within an *xy* plane located at z = -30 mm. This is the minimum value of z for which geometric error measurements were recorded with the Laser Ball Bar.

THERMAL ERRORS

Significant heat is generated during machining, both during chip generation and from the axis and spindle motors and bearings. This heat serves to distort the machine geometry and causes errors in machined parts. Thermal errors associated with spindle thermal growth were measured using a nest of five capacitance probes reading against a cylindrical tool blank held in the rotating spindle. The capacitance probes were sampled at one minute intervals as the spindle was exercised from a cold state at speeds of 5000 rpm and 15000 rpm. Results are shown in Fig. 3.

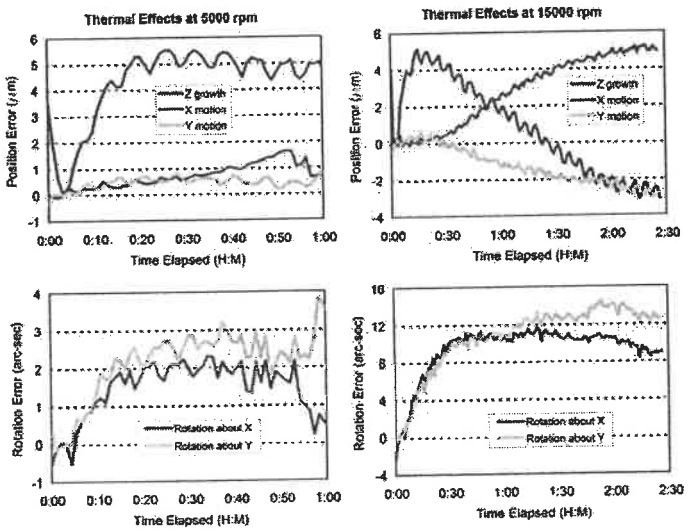

Figure 3: Spindle thermal growth errors.

CONTROLLER TRACKING ERRORS

CNC motion controllers may introduce tool path trajectory errors under high-speed motions, such as those typically encountered during HSM. These error motions were measured on the test machine using a Heidenhain grid plate encoder.

This instrument is capable of dynamic measurement of the two-dimensional trajectory of a read head held in the (non-rotating) machine spindle relative to a grid encoder plate fixed to the machine worktable. For these tests, the NAS 979 part program was modified to remove the *z*-axis motions associated with the different heights of the square, circle, and diamond features on the part. However, it is not expected that the small *z*-axis motions introduce significant geometric errors into the tool trajectory, allowing a comparison between the tool path recorded by the grid plate and the path predicted by the geometric machine model.

Figure 4 shows the tool paths measured by the grid plate at two different feed rates. A comparison between Figs. 3 and 4 shows significant similarities. Because the increase in feed rate between the two grid encoder experiments did not show significant differences, we conclude that the controller tracking errors are negligible in comparison to the geometric errors on this CNC machine.

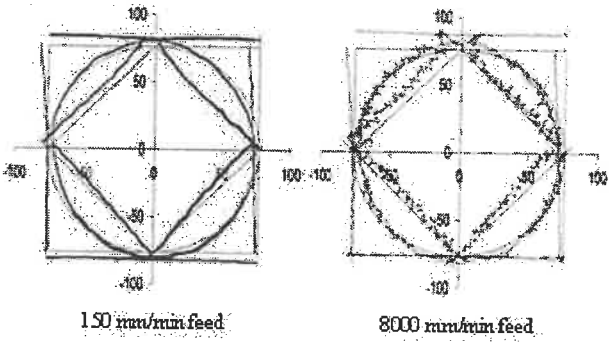

Figure 4: Grid plate measurements at two feed rates (2000x error magnification).

SURFACE LOCATION ERRORS

As noted, dynamic deflections of the cutter during stable machining can lead to significant errors in the actual location of the machined surface. Because SLE occurs due to forced vibrations, the dominant control parameter (for fixed system dynamics) is spindle speed which defines the excitation frequency (i.e., the tooth passing frequency). Previous researchers have demonstrated time-domain and semi-analytical predictions of SLE coupled with experimental comparisons [3-6]. In this study, we apply a new frequency-domain, analytical solution to SLE prediction [7]. In this approach, the tool-holder-spindle-machine dynamics as reflected at the tool point (i.e., the tool point frequency response function, or FRF) are used directly to determine the machined surface location.

To evaluate the analytical solution method, a four flute, 19.05 mm diameter carbide endmill was selected for cutting tests. It was inserted in a collet holder with an overhang length of 57 mm. The non-rotating tool point FRF (Fig. 5) was measured and cutting tests were performed to identify the force model coefficients; this data was used to make SLE predictions for a large range of spindle speeds using a 50% radial immersion (radial depth equal to tool radius).

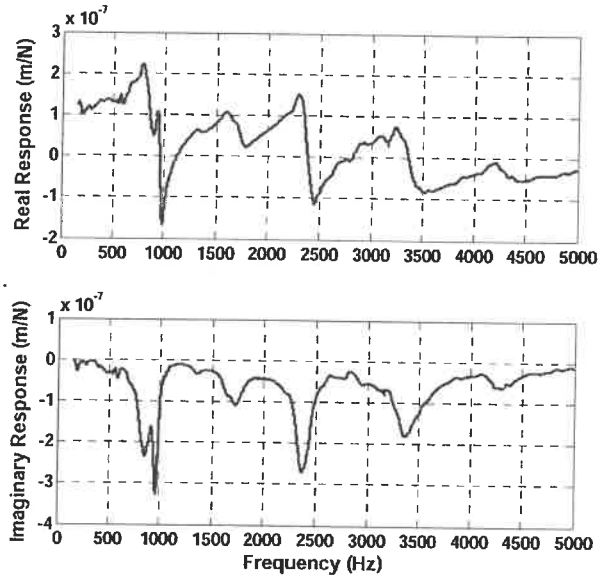

Figure 5: Tool point FRF for the 19.05 mm diameter endmill.

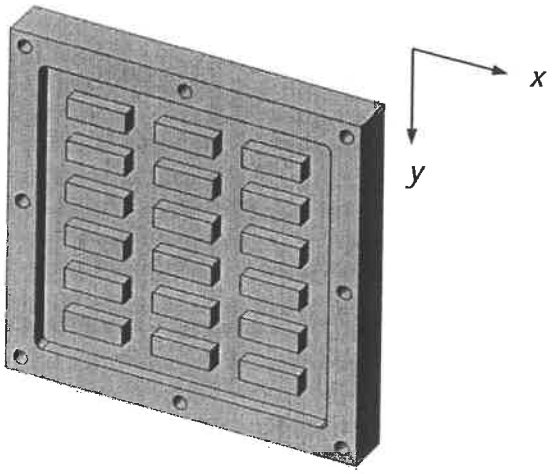

Figure 6: Diagram of the test part. Each raised boss was 50.8 mm x 17.8 mm x 12.7 mm.

The selected parameters for the cutting tests were: {7500 to 17500} rpm spindle speed range,

6 mm axial depth, 50% radial immersion, and 0.15 mm/tooth feed per tooth value. This spindle speed range was divided into 102 individual test cuts performed on 304.8 mm x 304.8 mm x 38.1 mm 6061-T6 aluminum blocks; see Fig. 6. Each block was initially machined to leave 18 evenly spaced rectangular bosses (50.8 mm long x 17.8 mm wide x 12.7 mm high) of nominally the same dimensions on each side.

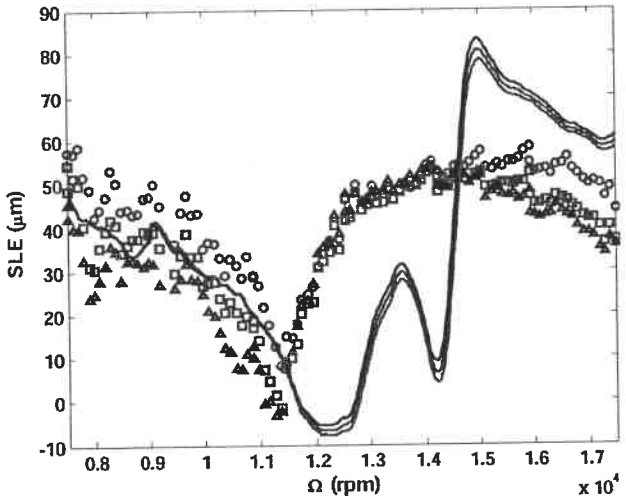

Figure 7: SLE vs. spindle speed (Ω) for experiments and prediction (lines).

These bosses were then finished machined at different spindle speeds to determine the resulting SLE. The feed direction during cutting (along the boss length, Fig. 6) was aligned with the *x*-axis of the machine to avoid any gain mismatch contouring errors. The test cuts were performed along the length of the bosses to remove roughly one-half of their width, leaving an uncut portion on the bottom as a reference. The width of the remaining top section was measured using a touch trigger probe CMM and then compared to the width of the bottom uncut portion to determine the amount of material that was removed. Surface location error was computed by comparing the amount of material removed to the commanded value. Further, measurements of the cut width were completed at three axial locations: {2 (circle), 3 (square), and 4 (triangle)} mm from the top of the boss. See Fig. 7. Reasonable agreement is observed. Discrepancies have been shown to be the result of changes in the spindle response at speed relative to the non-rotating response.

CONCLUSIONS

A comparison between the measured error sources is given in Fig. 8. For the selected tool-holder-workpiece material combination, SLE is the dominate contributor. As HSM becomes more widely accepted, it is critical that the relative contribution to part inaccuracy of all error sources, including SLE, be well understood and strategies for either avoidance or compensation be developed.

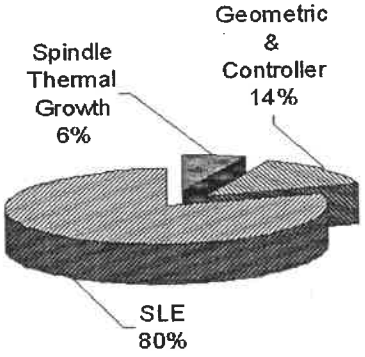

Figure 8: Relative contributions of machining error sources.

ACKNOWLEGEMENTS

This work was supported by BWXT Y-12, Oak Ridge, TN.

REFERENCES

1. Ziegert, J.C., and Mize, C.D., 1994, The Laser Ball Bar: A New Instrument for Machine Tool Metrology, *Precision Engineering: Journal of the American Society for Precision Engineering*, **16**/4: 259-267.
2. Srinivasa, N., Ziegert, J.C., and Mize, C.D., 1996, Spindle Thermal Drift Measurement Using the Laser Ball Bar, *Precision Engineering: Journal of the American Society for Precision Engineering*, **18**/2: 118-128.
3. Kline, W., DeVor, R., and Shareef, I., 1982, The Prediction of Surface Accuracy in End Milling, *Journal of Engineering for Industry*, **104**: 272-278.
4. Tlusty, J., 1985, Effect of End Milling Deflections on Accuracy, in *Handbook of High-Speed Machining Technology*, R. I. King, ed., Chapman and Hall, NY, pp. 140-153.
5. Montgomery, D. and Altintas, Y., 1991, Mechanism of Cutting Force and Surface Generation in Dynamic Milling, *Journal of Engineering for Industry*, **113**/2: 160-168.
6. Schmitz, T. and Ziegert, J., 1999, Examination of Surface Location Error Due to Phasing of Cutter Vibrations, *Precision Engineering*, **23**/1: 51-62.
7. Schmitz, T. and Mann, B., 2005, Analytical Solutions to Surface Location Error in Milling, *Proceedings of 2005 American Society of Mechanical Engineers International Design Engineering Technical Conferences and Computers and Information in Engineering Conference*, DETC2005-84805, Long Beach, CA.

A Mechanism for Creating Variable Nanometer Gaps

Hongshen Ma[1] and Alexander H. Slocum[2]
[1]Department of Electrical Engineering and Computer Science,
[2]Department of Mechanical Engineering,
Massachusetts Institute of Technology
Cambridge, MA, USA

INTRODUCTION

The creation and control of electrodes separated by a nanometer gap can provide a direct method to interface with materials and phenomenon on the size-scale of individual molecules. In particular, the study of electrokinetic properties of liquids within nanogaps may enable new measurement modalities for determining the molecular structure and composition of materials. As discussed by the theoretical work of Bazant *et al* [1] and demonstrated by the experimental work of Yi *et al* [2], the electrical impedance of fluid in nanometer channels can be dramatically different from values predicted by traditional macroscale models. When the physics of these situations are completely understood, it may be possible to apply these techniques to (1) industrial chemical processes to detect the presence of certain molecules in solution; (2) biochemical research to determine the electromechanical properties of biological molecules; and (3) molecular-electronics research to measure the electron transport properties of molecules and nanostructures. This paper reports on the development of an experimental apparatus for studying the electrokinetic properties of liquid thin films in an extremely confined state. In particular, this apparatus will act as an impedance measurement instrument where the distance between electrodes can be varied.

While a number of previous studies have demonstrated methods to create nanogap electrodes with fixed geometries using nano- and micro-fabrication technologies [3-5], few have investigated designs for a variable spacing nanogap [6]. This capability is particularly desired in electrical impedance measurements since measurement parasitics can be effectively removed by repeated measurements at different gap spacing. Furthermore, in some instances the electromechanical properties of the fluid are strongly affected by the nanoscale geometry of the gap, the electrode separation can therefore be used as a parameter to study these effects.

APPROACH

The most straightforward approach to creating electrodes separated by a variable nanometer gap is to develop a mechanism that brings together nanometer smooth, planar electrodes in a parallel manner. For example, one such mechanism, known as the Nanogate was designed as a nanoscale fluid valve [7]. As an impedance measurement cell, however, the implementation of such a design can be extremely difficult since minute non-parallelism between surfaces used to define a nanometer gap can cause the electrodes to short-circuit together, thereby altogether bypassing the fluid impedance.

The non-parallelism problem can be avoided by using spherical electrodes instead of planar electrodes. Since tangent planes through the closest points between two spheres are always parallel to each other, a small gap between two spheres approximates a small gap between two perfectly parallel planar surfaces. As long as the spheres have a smooth enough surface quality, this approximation can be improved by enlarging the diameter of the spheres. Commercially available spheres used for ball bearings and precision alignment equipment can be produced with extremely smooth surface quality. For example, a typical silicon-wafer has an RMS surface roughness of 1nm while a typical production polished tungsten carbide ball has an RMS surface roughness of 5nm. Even better surface finish can be found on balls made of specialty materials such as silicon nitride, borosilicate glass, and ruby.

A second approach to resolving the non-parallelism problem is to use the spherical electrode as a master to emboss a soft metal to create a complementary shape to the starting spherical surface. The nanogap is formed as the master sphere is pulled back precisely from its mating surface. By taking advantage of the large Hertzian stresses generated by the master sphere and choosing the proper substrate material, the deformation can be almost entirely

plastic with minimal elastic spring back. Figure 1 shows the surface profile of a tungsten carbide ball and the embossed surface in pure aluminum. The embossing process removed much of the "hills", but kept the "valleys" intact.

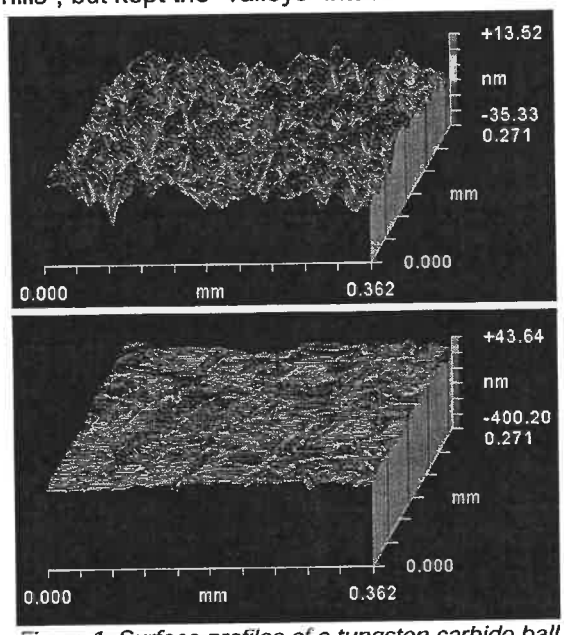

Figure 1: Surface profiles of a tungsten carbide ball (top) and the embossed pure aluminum surface (bottom). RMS roughness values are 5nm and 14nm respectively.

Both the two-spheres and the embossing approach have their advantages and drawbacks. The two-spheres approach is simple and does not require an extremely high degree of actuator reproducibility. However, a relatively larger sample volume is required because of the geometry of the impedance cell. The embossing approach requires a smaller sample volume, but is mechanically more demanding since large forces are required during the initial embossing process while the subsequent low-force return motion must follow same path precisely. The mechanism designed in this paper is amenable to both configurations. Further development work focuses on the two spheres approach, which can also be actuated using a direct piezoelectric actuator.

MECHANISM DESIGN

The mechanism described in this paper is designed to experiment with both the two-spheres and embossed configurations. The primary functional requirements of this mechanism include nanometer control of position, absolute repeatability of motion, ability to apply forces up to 2000 Newtons, and minimal noise and drift of the gap distance. A simple mechanism that fulfills such requirements is a cantilever connected by a flexural hinge.

Flexural Hinge

The chartwheel flexure, indicated as flexure 1 in Figure 2, is one type of flexural hinge with a large travel and load capacity.

The maximum stress of the chartwheel flexure can be expressed as,

$$\sigma_{max} = \frac{E\alpha t}{L},$$

where α is the deflection angle of the flexure; L is the length of both the vertical and horizontal flexure beams; t is the thickness of the flexure; and E is the elastic modulus.

Course Actuator

The position of the cantilever beam is controlled by course and fine manual adjustors. The course adjustor is a 1/4"-80 lead screw (Thorlabs: FS25AB200) that pushes near the end of the cantilever beam to achieve a 3:1 reduction at the sample position. The lead screw advances 0.3mm per revolution. Assuming 1 degree angular resolution is achievable by hand, a position resolution of 0.3um can be achieved at the electrode. Backlash in the lead screw is eliminated by an anti-backlash bushing, supplied with the lead screw. The tip of the lead screw is a ball which pushes into a carbide cup (Bird Precision: RB-25009). The radius of the carbide cup is greater than that of the ball tip in order to insure a consistent point of contact.

The effects of parasitic motion from the course actuator in both x- and y-axes are reduced by a flexible carriage as shown in Figure 2. Thin vertical flexures act like a wobble pin and allow the carriage mechanism to be flexible along the x-axis which reduces the mechanical coupling from the lead screw to the main cantilever beam. The same type of flexibility can be realized along the y-axis by thinning the flexure beams. The effect of parasitic motion along the y-axis is further reduced by flexure 2, which increases the stiffness of the main beam in that direction.

Fine Actuator

The fine actuator works in series with the course actuator by deflecting flexure 3. The fine actuator is a precision differential screw that can operate in both conventional and differential mode (Thorlabs DRV504). A piezoelectric

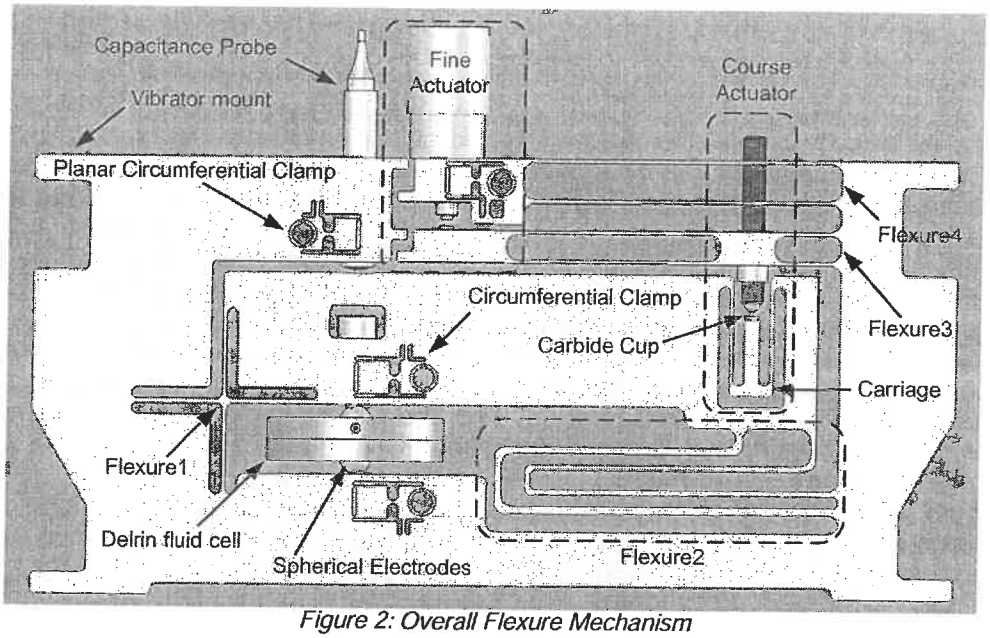

Figure 2: Overall Flexure Mechanism

actuator can also be used to achieve fine position control with no hand contact.

The fine actuator is mounted near the tip of flexure 4 and simultaneously deflects both flexures 3 and 4 to produce a large transmission ratio between the actuator to the electrode. The transmission ratio can be precisely tuned by the geometry of flexure 3 and flexure 4. The design of flexure 3 is composed of three regions: compliant double beam flexure, mount for course actuator, and stiff double-beam flexure. By adjusting the relative position of these three sections, transmission ratios from 10 to 1000 can be achieved. Flexure 4 is a compliant double beam flexure that moves in the opposite direction as the flexure 3 to provide an additional enlargement of the transmission ratio. The designed transmission ratio from the fine actuator to the electrode is 1000:1. The position of the differential screw is delineated at 1um intervals which translate to 1nm delineations through the flexural transmission.

Position Measurement

The position of the cantilever beam is measured using a Lion precision capacitive probe mounted in the flexure. The entire experimental apparatus is encased in a form box in order to minimize measurement drift caused by temperature fluctuations and air currents. Drift studies has shown measurement stability of better than 5nm per hour.

Planar Circumferential Clamp

The sample mount, both actuators, and capacitive position sensors are all cylindrical and are fixed in the flexure by flexure-based circumferential clamps as highlighted in Figure 2. The mechanism of the circumferential clamp can be separated into three parts: the clamp, the expander, and the hour glass flexure. The clamp is half a cylindrical surface which is made to press onto the desired cylinder. The expander is a 1/16" tapered pipe thread which deflects the cylindrical surface when a set screw is advanced into the hole. The hour-glass flexure provides the necessary flexibility in order to accommodate angular misalignment between the clamp and the clamped surface.

Mechanical Drift

A common problem with precision mechanisms that use leads screws in their structural loop is that residual displacement in the backlash of the screw mechanism can relax very slowly, causing a slow positional drift. One remedy for this problem is to add random mechanical energy to expediate the relaxation process. Mechanical vibration is introduced in this flexure by attaching a piezoelectric motor (Newfocus: 8302) to the flexure body. By controlling the speed of the piezoelectric motor, vibration energy can be generated at a precisely controlled frequency.

Electrode Mount

The position of each spherical electrode in the flexure is set by three smaller balls that forms a kinematic tripod mount. The three ball set is

press fitted into a 7/16" post held in the flexure by a circumferential clamp.

Fluidic Cell

The fluid cell is designed to encapsulate the sample fluid in the region between the two spherical electrodes while allowing the electrode separation to be varied. Additional functional requirements include making an electrical contact to the electrodes and minimizing dead volume.

The fluid cell is composed of two identical Delrin discs assembled together with an o-ring seal to form an enclosed chamber. The Delrin discs act as diaphragm flexures that allow the two balls to move with respect to each other. The ball electrodes are mounted at the center of each Delrin disc where a hole allows a small region of the ball to come in contact the fluid. A spherical surface with a matching diameter as the ball is machined into the Delrin disc. By applying an adhesive to this surface, a fluid seal can be produced between the ball and Delrin. Electrical contact to the electrode ball is made via a small recess in the Delrin disc where a wire can be trapped as the ball is inserted into position. Fluid connections in and out of the fluid cell are connected by 6-40 thread flangeless fittings (Upchurch: M-644-03) which adapts 1/16" tubing to the fluid cell.

EXPERIMENTAL VERIFICATION

Preliminary verification of the variable nanometer electrode gap is performed by measuring the capacitance between the electrodes in air. An exact expression for the capacitance between two spheres, C_{SS}, can be obtained from the well-known, but complex, series expression [8]:

$$C_{SS} = 2\pi\varepsilon R \sinh(\alpha)\sum_{n=1}^{+\infty} 1/\sinh(n\alpha),$$

Where $\cosh(\alpha) = 1 + d/2R$; ε is the permittivity of the intervening material; R is the radius of the sphere, and d is the separation between the two closest points on the spheres. An approximate solution was developed by Boyer *et al* [8] for the case where the spheres are very close together, *i.e.* $d/2R << 1$. The expression is then,

$$C_{SS} \approx \pi\varepsilon R\left[\ln\left(2R/d\right) + c\right],$$

where c is a constant.

The measured capacitance values obtained using the apparatus of Figure 2 are plotted in Figure 3 along with Boyer's approximate model. The value of c has been adjusted to obtain the best possible fit. Experimental values deviates slightly from the model at very small gaps and larger gaps. In very small gaps, this deviation is most likely attributed to surface roughness of the electrodes as discussed by Boyer [8]. In larger gaps, this deviation is most likely attributed higher order terms neglected by the small electrode gap approximation.

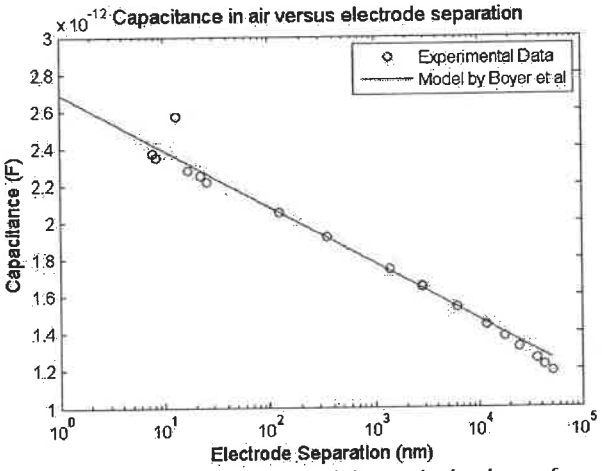

Figure 3: Experimental and theoretical values of capacitance between two spheres in air

ACKNOWLEDGEMENTS

This work has been supported by MIT's Center for Bits and Atoms under NSF Grant CCR-0122419. The authors would like to acknowledge Mark Belanger for fabrication assistance.

REFERENCES

1. Bazant, M.Z., Chu, K.T., and Bayly, B.J., *SIAM J. Appl. Math.*, 65, 5. (2005)
2. Yi, M., K. H. Jeong, and L. P. Lee, *Biosensors and Bioelectronics*, 20 (2005)
3. Oh, S., Lee, J.S., Jeong, K.H., Lee, L.P., *Proceedings of IEEE MEMS2003.* (2003)
4. Lefebvre, J., Radosavljevic, M., Johnson, A.T., *Appl. Phys. Lett.*, 76, 25. (2000)
5. Kanda, A., Wada, M., Hamamoto, Y., Ootuka, Y., *Physica E.*, 29. (2005)
6. Reed, M. A., C. Zhou, C. J. Muller, T. P. Burgin, Tour, J. M., *Science*, 278, 252. (1997)
7. White, J.R., Ma, H., Lang, J., Slocum, A.H., *Rev. Sci. Inst.*, 74, 11. (2003)
8. Boyer, L., Houze, F., Tonck, A., Loubet, J.L., Geores, J.M., *J. Phys. D – Appl. Phys.*, 27, 7. (1994)

OPTICAL NEAR-FIELD DIRECTED PATTERNING OF SUBMICRON-SIZED PARTICLES

Hiroshi Morii[1], Takeshi Ooi[1], Kensuke Tsuchiya[2], Tetuya Hamaguchi[1], and Masayuki Nakao[1]
[1] Department of Engineering Synthesis, The University of Tokyo
Bunkyo-ku, Tokyo, Japan
[2] Institute of Industrial Science, The University of Tokyo
Meguro-ku, Tokyo, Japan

INTRODUCTION

With the recent advancements in the field of fine particle engineering, it has become possible to manufacture particles of various homogeneous and composite materials in near uniform distribution sizes with diameter as small as several nanometers. Many are already widely available commercially and are considered to be directly useful as materials for bottom-up fabrication of devices such as photonic crystals, flat panel displays, and biomedical sensors. Accompanying the advancement in particle synthesis, there is an increasing interest in manipulating and ordering micron- and submicron-sized particles into patterns and structures.

The success of trapping micron-sized dielectric particles in a single beam gradient force optical trap by A. Askin *et al* has unfolded the possibility of manipulating particles using forces induced by optical fields [1]. Notably, S. Kawata *et al* have demonstrated that optical near-fields can also produce forces to move micron-sized particles [2]. Optical near-field has an advantage that it can be created on a localized area that is not exposed to the Rayleigh criterion [3]. Therefore, there are possibilities to create near-field enhanced patterns which are not subject to the diffraction limits of light. The work reported in this paper deals with manipulating and ordering submicron-sized particles dispersed in liquid using forces induced from optical near-fields. Researches involving direct manipulation of submicron-sized particles in liquid using optical near-fields have been reported by other groups; focused beam with a high numerical aperture objective lens and lithographically defined wave guides have been proposed for manipulating single or several particles [4][5]. We propose a method to order extensive particles into patterns using optical near-fields formed by multi-beam interference fringes exerted at a total internal reflection (TIR) interface. Our objective is to study the mass ordering of submicron-sized particles in a patterned optical near-field. In this paper we; 1) provide numerical estimations to derive the influence of the optical near-field pattern upon particles and 2) show experimental results of particle propulsion and ordering directed by optical near-field.

EXPERIMENTAL SETUP

The schematic of our setup is provided in Fig. 1. Samples of mono dispersed micron- and submicron-sized polystyrene particles or gold particles in water were each sealed between 100μm spaced borosilicate glass plates, and coupled to a BK7 prism using immersion oil with near matching refractive index. The glass plates were cleaned before being assembled into a target cell; they were sonicated with acetone and then with ethanol for 5 minutes respectively, dried in ambient air, and baked in an oxygen plasma oven for 10 minutes. The mono dispersed particles were sealed immediately after the cleaning of the glass plates. All experiments were done within 3 hours after the preparation of the target cell. For observations, the target cell was illuminated with incoherent white light and monitored through an objective lens. A color filter was placed after the objective lens to cut off scattering of the optical near-field by particles. Sequential images were recorded with a charged coupled device (CCD) camera. The incident angle at the glass-water TIR interface was set to an angle larger than the critical angle.

For experiments on particle propulsion, ø500nm polystyrene spheres (Polyscience Inc. Polybead® 07307) and ø250nm gold spheres (BBInternational Ltd. EM.GC250) were used. They were diluted with distilled water to 1.82×10^{9} particles/ml and 3.60×10^{8} particles/ml respectively. A linear polarized continuous wave laser with a TEM00 Gaussian beam intensity profile and wavelength of 1064nm (Coherent Inc.

Compass 1064) was converged into an elliptical spot of 100×240μm at the TIR interface of the target cell without using the beam splitters. P-polarization was used.

For experiments on particle ordering, ø1μm polystyrene spheres (Polyscience Inc. Polybead® 07310) diluted with distilled water to 2.28×10^8 particles/ml was used. A linear polarized continuous wave laser with a TEM00 Gaussian beam and wavelength of 1064nm (Keopsys Inc. KPS-BT2-SLM-YFL-1064-30-PM-COL) was split into 4 beams, converged, and merged into an elliptical spot of 50×120μm at the TIR interface of the target cell. The beams were arranged to create 5μm pitched interference fringes. S-polarization was used. The fringes were visualized, as shown in Fig. 2, by integrating sequential images of light scattered from particles without white light illumination and color filter.

NUMERICAL ESTIMATIONS

To derive the influence of the optical near-field pattern upon the particles above the TIR interface of our setup, we have performed estimations based on dipole approximation. It is known that a dielectric or metallic particle which is smaller than the wavelength of light and is located in an optical field gradient can be considered as a dipole [6][7]. If the particles are suspended in liquid, the force F induced upon a particle by the optical field is the composition of the gradient force F_{grad}, scattering force F_{scat}, and absorbance force F_{abs} given by [8],

$$\begin{aligned} F &= F_{grad} + F_{scat} + F_{abs}, \\ F_{grad} &= \tfrac{1}{2}|\alpha|\nabla\langle E^2\rangle, \\ F_{scat} &= n_m\langle S\rangle k_m^{\,4}|\alpha|^2/(6\pi c), \\ F_{abs} &= n_m\langle S\rangle k_m \,\mathrm{Im}(\alpha)/c, \end{aligned} \qquad (1)$$

where α is the polarizability of the particle, $\langle E^2\rangle$ is the time averaged electrical field strength of the optical field, n_m and k_m are the index of refraction and wave number of the surrounding medium, $\langle S\rangle$ is the time averaged Poynting vector, and c is the speed of light in vacuum. For spherical particles, polarizability α is given by [9],

$$\alpha = 3V\varepsilon_0\varepsilon_m(\varepsilon_p - \varepsilon_m)/(\varepsilon_p + 2\varepsilon_m), \qquad (2)$$

where V is the volume of the particle, ε_0, ε_p and ε_m are the dielectric constants of the

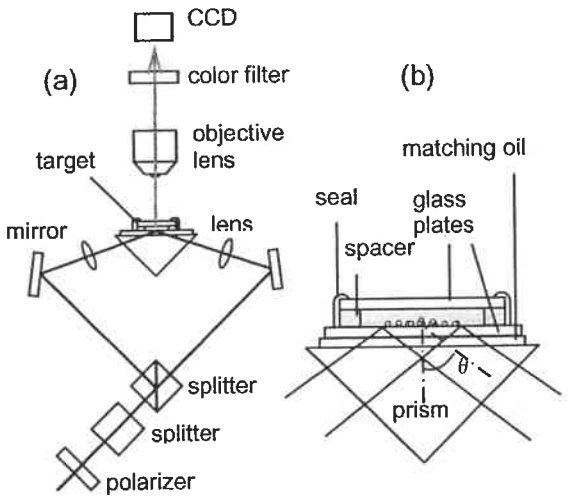

FIGURE 1: Schematic of the experimental setup; (a) overview and (b) detail of the target.

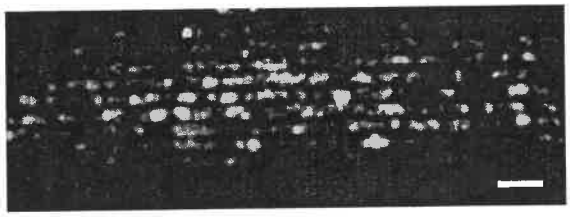

FIGURE 2: Light scattering of interference fringes by ø80nm gold particles (BBInternational Ltd. EM.GC80). A total of 100 consecutive frames were integrated at an exposure rate of 30ms/frame. Scale: 10μm.

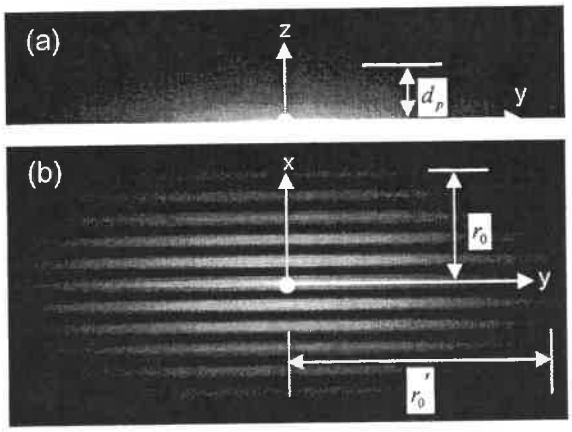

FIGURE 3: Computer simulated beam intensity profile of the near-field pattern above the TIR interface. Intensities are stronger in light colored areas.

vacuum, particle, and surrounding medium respectively. We assume a s-polarized incident light at the TIR interface and that the inclusive profile of the beam intensity of the optical near-field pattern above the TIR interface, as shown in Fig. 3, to be [10],

$$I = I_0 \exp\left\{-2\left[(x/r_0)^2 + (y/r_0')^2\right]\right\}\exp(-2z/d_p),$$
$$I_0 = I_i\, 4n_s^{\,2}\cos^2\theta/\left(n_s^{\,2} - n_m^{\,2}\right),$$
$$d_p = \lambda_0 \Big/ 2\pi\sqrt{n_s^{\,2}\sin^2\theta - n_m^{\,2}}\,, \qquad (3)$$

where r_0' and r_0 are the semi major and semi minor axis of the intensity profile at the TIR interface, d_p is the penetration depth of the near-field radiation above the TIR interface, n_s is the index of refraction of the substrate, θ is the incident angle which is larger than the critical angle, I_i is the intensity of incident light, and λ_0 is the wavelength of the incident light in vacuum. It is clear that the gradient force, scattering force, and absorption force become significantly larger as the particle approaches the vicinity of the TIR interface. The maximal gradient force $F_{grad}^{\max}$, the maximal scattering force $F_{scat}^{\max}$, and the maximal absorbance force $F_{abs}^{\max}$, at the TIR interface, are given by,

$$F_{grad}^{\max} \geq I_0|\alpha|\exp(-1/2)/(n_m\varepsilon_0 c r_0),$$
$$F_{scat}^{\max} \leq 4\pi^3 I_0 n_m^{\,5}|\alpha|^2/(\lambda^4 c),$$
$$F_{abs}^{\max} \leq 2\pi^2 I_0 n_m^{\,2}\,\mathrm{Im}(\alpha)/(\lambda c),$$
$$\lambda = \lambda_0/(n_s\sin\theta). \qquad (5)$$

For ø250nm gold particles in water; using r_0 =21.5 (μm), λ_0 =1064 (nm), ε_p =-55.5+5.62 i [11], and ε_m =1.325 [12], we find that,

$$F_{grad}^{\max} >> F_{scat}^{\max},\ F_{grad}^{\max} >> F_{abs}^{\max}. \qquad (6)$$

Because the influence of the gradient force is dominant, the force induced upon a particle can be approximated as,

$$F \cong F_{grad} = \tfrac{1}{2}|\alpha|\nabla\langle E^2\rangle. \qquad (7)$$

The potential energy U induced by the optical field is then given by,

$$U \cong \tfrac{1}{2}|\alpha|\langle E^2\rangle = I|\alpha|/(2n_m\varepsilon_0 c). \qquad (8)$$

Particles are pushed towards light intensive areas of the optical near-field pattern. To retain the particles in a pattern, the potential energy must be larger compared to thermal energy k_bT, where k_b is the Boltzmann constant and T is the absolute temperature [13]. At T =298.15 (K), θ=61°, and using incident light of 500mW, the potential energy induced by the optical field within the full width at half maximum of I follows,

$$4.1 \leq U/(k_bT) \leq 8.4. \qquad (9)$$

This indicates that the gold particles are directed onto the optical near-field pattern at the TIR interface.

EXPERIMENTAL RESULTS

Fig. 4 shows sequential images of particles propelled by optical near-field forces. The color has been converted to pseudo color so that particles show as light intensive spots. Back ground noise has been subtracted. Particles moved alongside the major axis of the elliptically illuminated spot at the TIR interface. Taking the losses of irradiance at the lenses, mirrors, and beam splitters into account, the calculated power of incident light at the TIR interface was 2.5W and 0.74W for ø500nm polystyrene spheres and ø250nm gold spheres respectively.

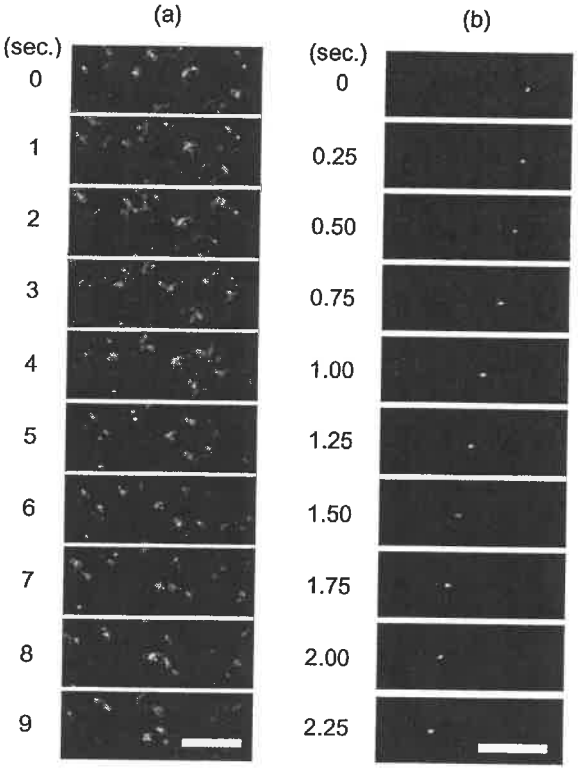

FIGURE 4: Sequential images of particles being propelled by optical near-field forces at the vicinity of the glass-water TIR interface. (a) ø500nm polystyrene spheres. (b) ø250nm gold spheres. Scales: 10μm.

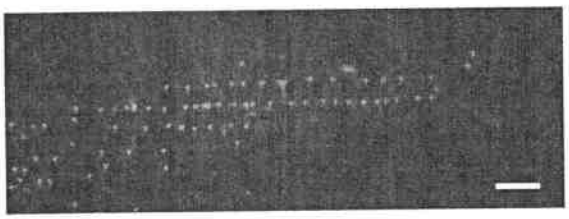

FIGURE 5: A batch of ø1μm polystyrene spheres being directed onto a 5μm pitched line and space near-field pattern. Scale: 10μm.

The speed of propulsion was 2.7μm/s and 15μm/s respectively.

Fig. 5 shows ø1μm polystyrene spheres directed onto an optical near-field pattern with 5μm pitched line and space. The calculated power of incident light at the TIR interface was 0.58W.

CONCLUSIONS

In this paper we have provided numerical estimations to derive the influence of the optical near-field pattern upon particles and have shown experimental results of particle propulsion and ordering directed by optical near-field. It has been indicated that submicron-sized gold spheres can be directed onto a pattern by optical near-fields. In addition to the propulsion of submicron-sized polystyrene or gold spheres, ordering of polystyrene spheres with size affinity to the incident light's wavelength have also been demonstrated.

REFERENCES

1. A. Ashkin, 1970, Acceleration and trapping of particles by radiation pressure, Physical Review Letters, 24 (4): pp.156-159.
2. S. Kawata and T. Sugiura, 1992, Movement of micrometer-sized particles in the evanescent field of a laser beam, Optics Letters, 17 (11): pp.772-774.
3. U. Ch. Fischer and H. P. Zingsheim, 1981, Submicroscopic pattern replication with visible light, Journal of Vacuum Science and Technology, 19 (4): pp.881-885.
4. M. Gu, J. Haumonte, Y. Micheau, J.Chon and X. Gan, 2004, Laser trapping and manipulation under focused evanescent wave illumination, Applied Physics Letters, 84 (21): pp.4236-4238.
5. L. N. Ng, B. J. Luff, M. N. Zervas and J. S. Wilkinson, 2002, Propulsion of gold nanoparticles on optical waveguides, Optics Communications, 208: pp.117-124.
6. James P. Gordon, 1973, Radiation forces and momenta in dielectric media, Physical Review A, 8 (1): pp14-21.
7. Karel Svoboda and Steven M. Block, 1994, Optical trapping of metallic Rayleigh particles, Optics Letters, 19 (13): pp.930-932.
8. Craig F. Bohreh and Donald R. Huffman, 1983, Absorption and Scattering of Light by Small Particles, A Wiley-Interscience Publication, Chap. 5.
9. J. N. Israelachvili, 1992, Intermolecular and Surface Forces 2nd Ed., Academic Press Ltd., Chap. 5: 5.7.
10. John M. Guerra, 1990, Photon tunneling microscopy, Applied Optics, 29 (26): pp.3741-3752.
11. C.L. Foiles, Editor: K.-H. Hellwege, J.L. Olsen, 1985, Landolt-Börnstein, Condensed Matter, III/15B, pp.222-235.
12. National Astronomical Observatory (Japan), 2000, Chronological Scientific Tables, Maruzen Co. Ltd., p.531.
13. A. Ashkin, J. M. Dziedzic, J. E. Bjorkholm, and Steven Chu, 1986, Observation of a single-beam gradient force optical trap for dielectric particles, Optics Letters, 11 (5): pp.288-290.

DEVELOPMENT OF A NANO-STEREOLITHOGRAPHY SYSTEM USING EVANESCENT LIGHT FOR SUBMICRON FABRICATION

Yusuke Kajihara[1], Toru Takeuchi[1], Satoru Takahashi[1], and Kiyoshi Takamasu[1]
[1]Department of Precision Engineering
The University of Tokyo
Bunkyo-ku, Tokyo, Japan

INTRODUCTION

In recent years, micro-fabrication technologies have developed dramatically and fabrication methods have become required, by which small devices on the order of micrometer can be fabricated precisely. In particular, methods of fabricating MEMS and microscopic optical devices as typified by a photonic crystal are in huge demand. Micro-stereolithography is a micro-manufacturing method that can fabricate complex 3D microstructures by curing liquid photosensitive resin in a layer-by-layer process [1]. By this method, small 3D objects with micrometer resolution can be fabricated rapidly and this method has attracted more attention.

However, conventional micro-stereolithography method has some technical issues. Since it uses propagating light as the exposure energy, surplus growth is generated, which causes a dimension error and makes it difficult to fabricate a complex structure like overhang. In addition, since the resolution of fabrication sizes is restricted by the diffraction limit, it is almost impossible to fabricate submicron structures. Various approaches have been demonstrated to resolve these issues [2][3][4][5].

In this study, we propose a novel stereolithography method that uses evanescent light instead of propagating light [6]. We consider the application of the near-field optics and use evanescent light as the exposure energy. Since the evanescent light energy does not propagate but localizes within the near-field region, surplus growth is not generated. Furthermore, the resolution is independent of the diffraction, so that it becomes possible to fabricate 3D structures with 100-nanometer scales. By this unique method, we intend to establish the nano-stereolithography that can fabricate complex 3D microstructures with a resolution of sub-micrometer.

In this paper, we develop a nano-stereolithography system that generates evanescent light and has a high-resolution imaging system. Using this developed system, we carried out fundamental experiments. The results suggest that our proposed nano-stereolithography method allows us to fabricate complex 3D structures with a resolution of sub-micrometer such as microchannels and photonic crystals.

CONCEPT OF NANO-STEREOLITHOGRAPHY USING EVANESCENT LIGHT

In this section, we describe the characteristics of evanescent light that is a key factor of our method and explain the nano-stereolithography.

Evanescent light

When light crosses materials with different refractive indices, the light beam will be partially refracted at a boundary surface, and partially reflected. Assuming that an angle of incidence is shallower than the critical angle, the light beam will stop crossing the boundary altogether and instead totally reflect back internally. Under this optical condition, nevertheless, there occurs partially localized energy at the boundary (Figure 1). The energy is evanescent light.

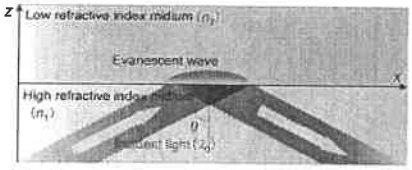

FIGURE 1: When an angle of incidence θ is shallower than the critical angle, there occurs evanescent light at the boundary.

The electric field E_2 of evanescent is expressed as follows by applying Maxwell's equations and Snell's law.

$$\mathbf{E}_2 = \mathbf{A}\exp(i\omega t)\cdot\exp(-\frac{z}{Z_{ev}})\cdot\exp(-ik_2 x\frac{n_1}{n_2}\sin\theta) \qquad (1),$$

$$(Z_{ev} = \lambda_0 / 2\pi n_2\sqrt{(n_1/n_2)^2\sin^2\theta - 1})$$

where the axis perpendicular to the boundary of Figure 1 is z, the axis equivalent to the boundary

is x, the amplitude is A, refractive indices of mediums are n_1 and n_2 ($n_1 > n_2$), the wavelength of the incident light is λ_0, the angle of incidence is θ, the angular frequency is ω, and the wavenumber in the low refractive index medium is k_2. This equation indicates that the evanescent light energy decays exponentially with distance and it is localized within the range of the wavelength.

Nano-stereolithography

Figure 2 shows a schematic diagram of the nano-stereolithography method using evanescent light. First, the incident beam at a shallower angle than the critical angle generates evanescent light at the boundary, which cures liquid photosensitive resin (Figure 2(a)). Next the cured resin adhering on the base rod is lifted and liquid resin is refilled at the boundary surface (Figure 2(b)). Then the evanescent light, which is modulated by a variable mask such as an LCD, exposes and cures a next layer (Figure 2(C)). Doing this loop repeatedly, desired object is fabricated (Figure 2(d)).

Since the evanescent light energy is localized within the range of the wavelength, the thickness of the cured resin layer is expected to be less than one micrometer. In addition, there occurs no optical transmission, which makes it possible to fabricate overhang structure. Consequently, it is expected that we can realize a flexible fabrication with a resolution of sub-micrometer.

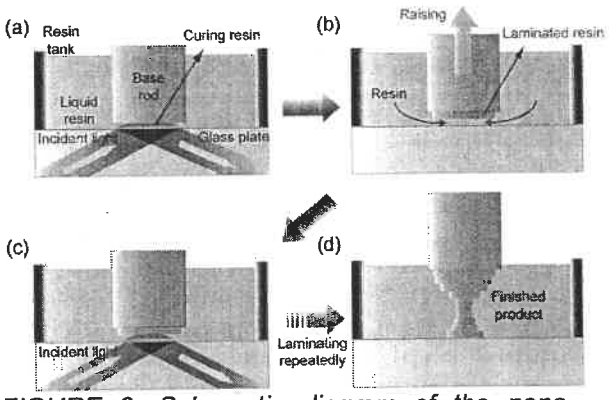

FIGURE 2: Schematic diagram of the nano-stereolithography method using evanescent light.

DEVELOPMENT OF A NANO-STEREOLITHOGRAPHY SYSTEM

Shown in Figure 3 is a developed nano-stereolithography system using evanescent light. It mainly consists of a solid state diode pumped laser providing visible output at 488nm, a high-power objective with a numerical aperture of 1.65 for forming a totally reflected beam, a resin tank located on the high-power objective, and a PZT stage, accuracy positioning of which is 1 nanometer, for lifting cured resin layers.

The light beam oscillated by the laser source propagates through a collimating lens system (Lens1 and Lens2) and is modulated by a variable mask such as an LCD or a DMD. The modulated beam is constrained to pass through

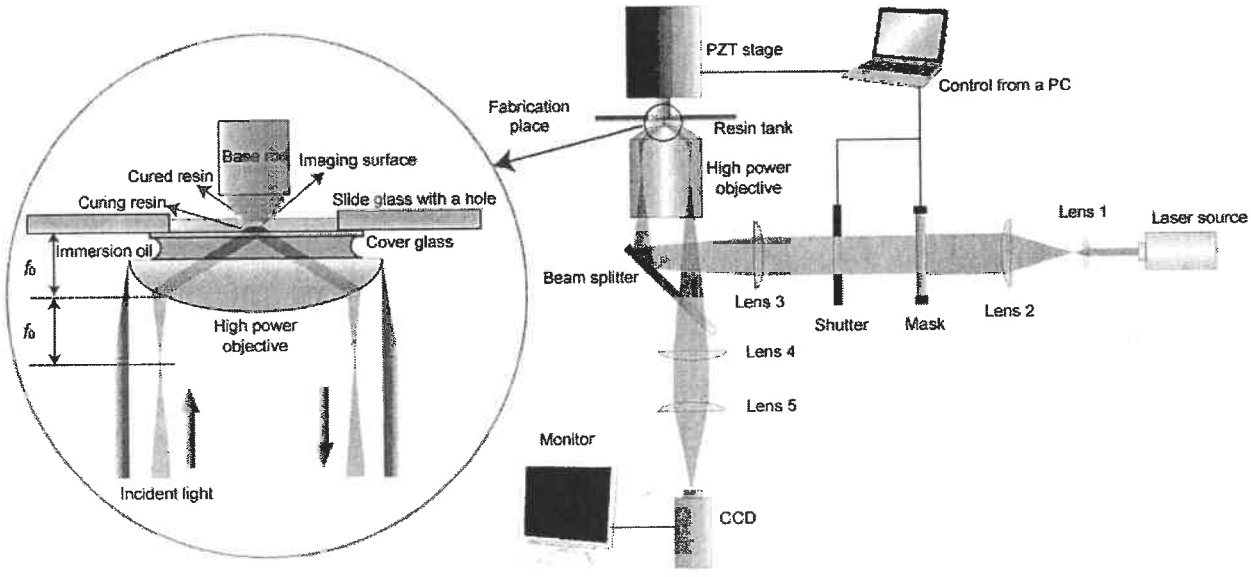

FIGURE 3: A developed nano-stereolithography system using evanescent light (Right) A modulated beam passes through the periphery of the objective's pupils and evanescent light is generated in the liquid resin. (Left) The exposure surface is equivalent of the imaging surface of the variable mask.

the periphery of the objective's pupils. It emerges from the front lens of the objective and passes into a cover glass of high refractive index through the immersion oil. Then on the top surface of the cover glass, evanescent light is generated in the liquid resin. The refractive indices of the immersion oil, the cover glass, and the photosensitive resin (KC1162, JSR corp.) are 1.78, 1.78, and 1.51 respectively. The critical angle is 57.4 degrees.

Notice that this exposure surface is equivalent of the imaging surface. The lens3 and the objective reduce the light intensity distribution 110 times from the distribution at the mask position. By installing a tube lens (Lens4 and Lens5) and a CCD, an optical microscope can be configured for infinity correction with the high power objective for evanescent generation. This microscope system allows us to directly observe a curing process of the photosensitive resin. A slide glass with a hole forms a resin tank and the PZT stage lifts the base rod during the layer-by-layer process. The mask, the PZT stage and an electronic shutter are controlled from a PC.

EXPERIMENT FOR 2D FABRICATION

In this section, we describe an experiment for 2D submicron fabrication carried out to verify the imaging system of the nano-stereolithography system.

Experimental condition

Figure 4 shows a pattern set at the mask position. With this pattern, a discoidal cured resin with a submicron groove should be fabricated by evanescent light exposure. Shown in Table 1 is the exposure condition.

TABLE 1: Exposure condition.

Angle of incidence	Exposure energy	Exposure time
65 degrees	600 mW/cm^2	4 seconds

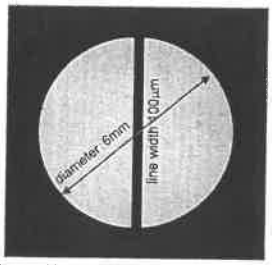

FIGURE 4: A pattern with a rectangular masking, with which a discoidal cured resin with a submicron groove should be fabricated.

Results and discussion

Exposed by the modulated evanescent light, a discoidal cured resin with a groove was fabricated. We analyzed the resin with a white light interferometer (NewView 5000, Zygo corp.) after a gold evaporation process. The result is shown in Figure 5. The thickness of the resin was about 300 nanometers, which has not been realized by the conventional method using propagating light exposure. The width of it was about 900 nanometers. This result suggests the possibility of 2D submicron fabrication and it suggests that complex shapes like a microchannel could be fabricated through the layer-by-layer process.

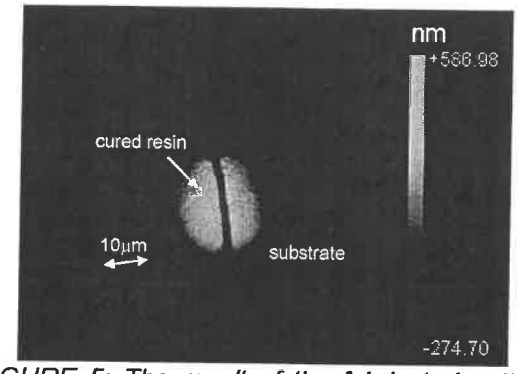

FIGURE 5: The result of the fabricated pattern analyzed by a white light interferometer, which suggests the possibility of 2D submicron fabrication.

EXPERIMENT FOR 3D FABRICATION

We describe an experiment for 3D submicron fabrication in this section. It is most important that we verify the lamination process for the layer-by-layer process of stereolithography. For the first step, we attempted to fabricate steps shown in Figure 6. The thicknesses of these steps are all about 500 nanometers.

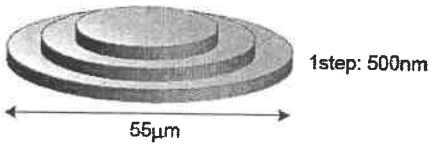

FIGURE 6: These steps are attempted to fabricate to verify the lamination process.

Experimental condition

Diameters of the mask patterns were 6mm, 4mm, and 3mm respectively, so that expected diameters of fabricated steps would be 54μm, 36μm, and 27μm respectively. The exposure condition was the same at the table 1.

Results and discussion

Figure 7 shows the fabricated steps with the developed nano-stereolithography system. The microscope image shows that the diameter of each step was approximately equal to the expected diameter. The AFM analysis shows that the thickness of each step was about 500 nanometers.

This result indicates that laminating cured resin layers of submicron thicknesses, namely nano-steps, is possible with the developed nano-stereolithography system. Applying the photofabrication of periodic submicron structures using standing evanescent light [7] to this lamination process, photonic crystals for visible range are expected to be fabricated.

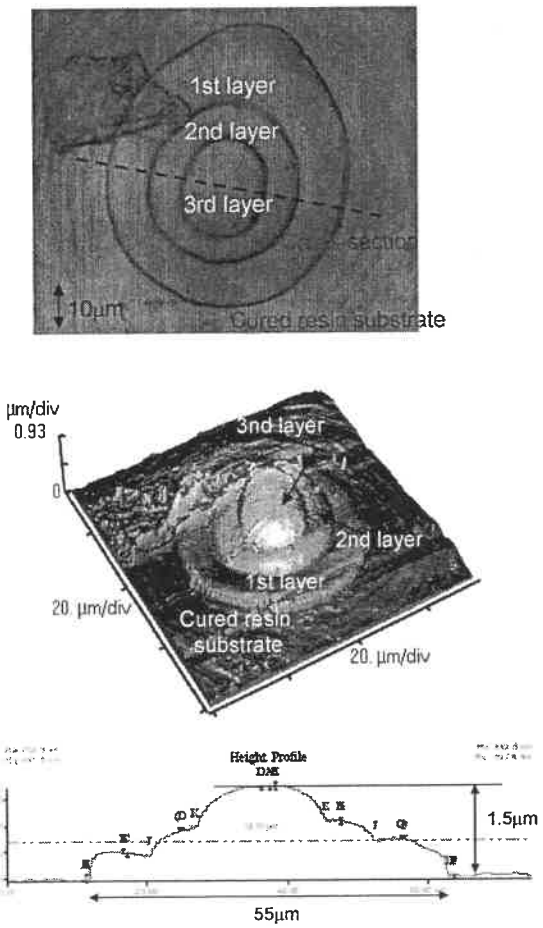

FIGURE 7: Fabricated nano-steps. (TOP) Microscope image. (Middle) AFM image. (Bottom) Cross section of the AFM.

CONCLUSION

We developed the nano-stereolithography system using evanescent light, which mainly consists of a laser at 488nm, a high-power objective with a numerical aperture of 1.65, and a PZT stage, accuracy positioning of which is 1 nanometer.

Two fundamental experiments were carried out with this system for verifying the imaging system and the lamination process. In the first experiment, a discoidal cured resin with a groove, the width of which was about 900 nanometers, was fabricated. In the second experiment, nano-steps were fabricated, the thickness of which were about 500 nanometers.

These facts suggest that complex submicron structures such as microchannels and photonic crystals could be fabricated with our proposed method.

ACKNOWLEDGEMENT

This work was partially supported by the Asahi Glass Foundation and the Research Foundation for Opto-Science and Technology. The photosensitive resin is provided by the JSR Corporation.

REFERENCES

1. Paul F. Jacobs, 1992, Rapid Prototyping & Manufacturing, *SME*.
2. T. Hayashi, T. Miyoshi, Y. Takaya and S. Takahashi, 2000, Nonlaminate Micro Stereolithography Using TFT LCD, *Proceedings of the 2nd euspen*, 1: 98-106.
3. S. Kawata, H B. Sun, T. Tanaka, and K. Takada, 2001, Finer features for functional microdevices, *Nature*, 412: 697-698.
4. S. Maruo and K. Ikuta, 2002, Submicron stereolithography for the production of freely movable mechanisms by using single-photon polymerization, *Sensors and Actuators A*, 100: 70-76.
5. Kock K. Seet, V. Mizeikis, S. Juodkazis, and H. Misawa, 2006, Three-dimensional circular spiral photonic crystal structures recorded by femtosecond pulse, *Journal of Non-Crystalline Solids*, 352: 2390-2394
6. Y. Kajihara, Y. Inazuki, S. Takahashi, and K. Takamasu, 2004, Study of Nano-Stereolithography Using Evanescent Light, *Proceedings of ASPE annual meeting*: 149-152.
7. S. Takahashi, Y. Inazuki, Y. Kajihara, and K. Takamasu, 2005, Photofabrication of periodic submicron structures using standing evanescent light for nano-stereolithography, *Proceedings of ASPE annual meeting*: 1729-1732.

DESIGN AND MODELING OF A PRECISION 6 DOF MEMS-BASED PARALLEL KINEMATIC TEM SAMPLE MANIPULATOR

Dannis M. Brouwer[1], B.R. de Jong[2], H.M.J.R. Soemers[1,3],
[1] IMPACT Institute, University of Twente, the Netherlands
[2] MESA+ research Institute, University of Twente, the Netherlands
[3] Philips Applied Technologies, Eindhoven, the Netherlands

INTRODUCTION

The relatively large dimensions of 'conventional' transmission electron microscope (TEM) sample manipulators results in typical drawbacks such as thermal drift and compromised dynamics. Especially the requested stability of 0.1 nm/min requires a new manipulator concept. Miniaturizing creates the opportunity to fix the manipulator directly to the column guiding the electron beam, isolating external thermal and vibration noise. Secondly the manipulator can be made more stable by increasing the natural frequencies, decreases the thermal drift and decreases the thermal time constant of the manipulator. Potential solutions for miniaturizing can be found in Micro Electro Mechanical Systems (MEMS). Precision manipulation in MEMS seems sparse however. In this paper a design for a 6 Degree-of-freedom (DOF) precision MEMS-based manipulator will be discussed [1]. The elastic mechanism is modeled with the specific design considerations regarding kinematic constraint design and elastic energy storage. The fabrication will not be discussed in the paper.

In general the actuators used in MEMS exhibit low work density compared to the energy storage in elastic elements. Consequently the actuators in MEMS are relatively large and the elastic elements are generally long and slender. The typical relatively large deformations of elastic hinges in MEMS result in relatively large displacements and large rigid body rotations. Geometrically non-linear elasticity theory is a necessity for accurate analysis. A software package called Spacar considers elastic elements as multi-body-like finite elements, which considerably reduces the number of elements, which makes the analysis fast and effective [2].

HEXAPOD SYSTEM DESIGN

The MEMS-based stage is designed like a parallel manipulator with elastic mechanisms. Elastic mechanisms are characterized by low hysteresis, zero backlash, no wear and high stiffness. Parallel manipulators in general have a large stiffness to mass ratio resulting in high natural frequencies and short settling times. In this case the parallel kinematics facilitates 6 actuators to be made in-plane of the wafer, using a mechanism to direct the motion out-of-plane to obtain 6 DOF (Figure 1). In this way one single technology can be used to manufacture six of the same type of electrostatic lateral comb-drive actuators as shown in Figure 2. Furthermore these can be combined with capacitive sensing by super positioning a high frequent signal on the actuation signal. The 6 comb-drives are arranged in 3 pairs, each pair controlling one of the 3 intermediate bodies in the two translational DOF of the wafer-plane. Within a pair, one comb-drive is connected to the other with a silicon leaf-spring, an intermediate body and a second leaf-spring. Three slanted leaf-springs connect the intermediate bodies to the end-effector. Because the total mechanism movement is achieved by purely elastic movements, and the mechanism is nearly exact kinematic constraint the positional repeatability will be high.

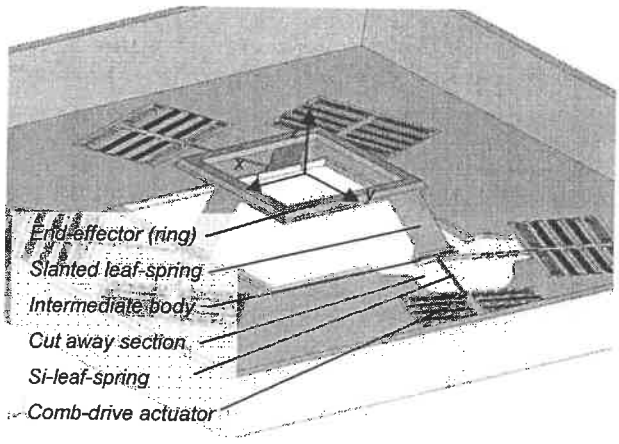

FIGURE 1: The MEMS-based hexapod design

INFLUENCE OF DRIVE STIFFNESS AND REINFORCEMENT ON LEAF-SPRING BEHAVIOR

The hexapod incorporates 6 comb-drives, each suspended by 4 folded flexures, which straight guide the actuator in actuation direction. Each folded flexure consists of 4 reinforced leaf-springs. The actuation direction of the suspension is compliant to minimize elastic energy storage. The other 5 Degrees-Of-Freedom are intended to be stiff in relation to the actuation direction. For a comb-drive a high longitudinal stiffness (Figure 2) of the leaf-springs of the folded flexures is important to minimize the possibility of side pull-in. The longitudinal stiffness however decreases with increasing deflection. Van Eijk [3] models the longitudinal stiffness of a leaf-spring while the leaf-spring is constrained at the actuated end in the actuation direction, $Cd = \infty$ in Figure 5. Legtenberg [4] leaves the translations free, $Cd = 0$. Van Eijk's model can be used for elastic guidances with a stiff drive train or a "stiff" control system at frequencies well below the control bandwidth. In MEMS however the drive train is usually in the order of the same compliance as the folded flexures, and currently, an ample control system lacks because of inadequate sensors. The longitudinal stiffness difference between the two models for relatively large deflection can be more than 2 orders of magnitude in favor of the constrained leaf-spring. The longitudinal stiffness as a function of the deflection in relation to the drive stiffness has been investigated for prismatic leaf-springs and for reinforced leaf-springs as shown in Figure 5.

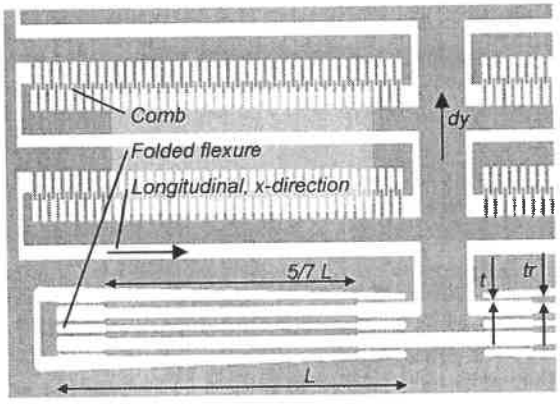

FIGURE 2. Folded flexure in a comb-drive suspension.

As folded flexures behave like individual leaf-springs, but then with half the displacement, leaf-springs are investigated. The leaf-spring dimensions (Figure 5) are taken L for length, w for width and t for thickness. A leaf-spring, prismatic or reinforced, is clamped at one end and constrained for rotation Rz at the other. An often implemented ratio of $5/7^{th}$ of the leaf-spring length is thickened. An extra one dimensional spring with spring constant Cd is attached to the free end of the leaf-spring. The displacement $dy2$ is a constrained input. The corresponding $y2$ and Cx are calculated by Spacar. Cx is related to the initial stiffness without deflection, $Cx0$.

$Cx0$ of a reinforced leaf-spring is 3.5 times larger than $Cx0$ of a prismatic leaf-spring with the reinforcement taken as a rigid body. This ratio increases during deflection in y-direction for $Cd/Cy > 100$. The reason is that by constraining the dy displacement the leaf-spring is forced in a "buckling like bending-mode" when loaded in x-direction. Reinforcement stiffens this "buckling like bending-mode" effectively, as the buckling length is shortened. Reinforcement for leaf-springs with $Cd/Cy < 100$ also increases the $Cx0$ stiffness, but the initial increase of 3.5 becomes less and reaches down to 1.9 for $Cd = 0$ at $dy/t = 30$. Loading a leaf-spring in x-direction causes the leaf-spring to deflect mainly in y-direction. The movement in x-direction is a second order effect. Therefore bending stiffness Cy dominates Cx for large y/t. The Cy stiffness of a reinforced leaf-spring is 58% larger than the Cy of a prismatic leaf-spring.

In general exact kinematic constraint design is about creating exactly those degrees-of-freedom necessary in a design by, in the case of an elastic mechanism, introducing compliance in certain directions in relation to stiffness in others. For a straight guidance for a comb-drive actuator the ratio longitudinal to actuation direction is important. Reinforced leaf-springs increase this ratio over prismatic beams at zero deflection by a factor 2.2. However this ratio decreases fast when a leaf-spring is deflected for a $Cd = 0$ situation. Also the stiffness of the reinforcement has influence on the behavior of the leaf-spring and needs a more thorough investigation. While the longitudinal stiffness is of importance for the stability of a comb-drive, the out-of-plane stiffness is important for the stiffness of the end-effector of the hexapod. The longitudinal and out-of-plane stiffness as a function of the relative deflection in relation to

the reinforcement thickness has been investigated. For the out-of-plane stiffness the length of the leaf-spring in relation to the width is important [3]. In the case of the hexapod the *L/w* ratio is 11.7.

Figure 3 shows that the longitudinal / actuation stiffness ratio gain of a reinforced leaf-spring folded flexure with respect to a prismatic leaf-spring folded flexure decreases from a factor 2.2 to a factor 1.22 at *dy/t* = 10. It must be taken into account that reinforcement given a certain leaf-spring length will need a 26% larger drive-voltage or a 58% larger comb-drive to compensate the increased actuation stiffness, if the leaf-springs can not be made thinner, as is often the case in MEMS. A comb-drive can benefit from a reinforced leaf-spring folded flexure if this leaf-spring is pre-curved and is straightened during actuation. At the point of maximum pull-in force the reinforced leaf-spring is then straight with maximum longitudinal stiffness [5].

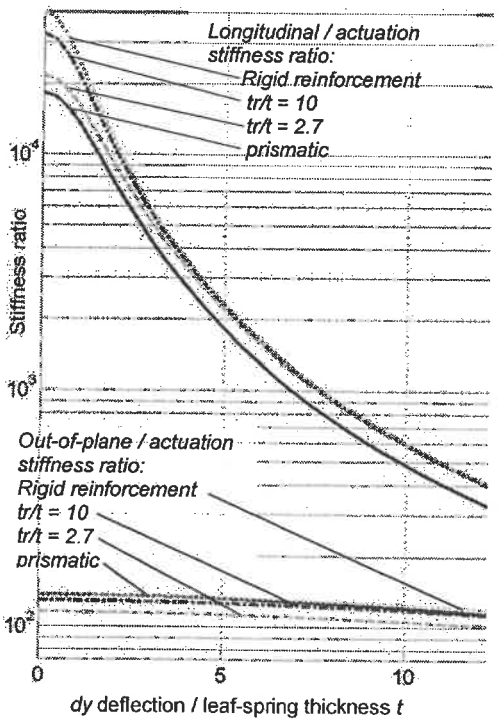

FIGURE 3. Stiffness ratios for a 4x folded flexure suspension as a function of the relative displacement. L/w = 11.7, L = 406μm, w = 35μm, t =3μm.

The out-of-plane / actuation stiffness ratio does not benefit from reinforcement at zero displacement. The bending stiffness for out-of-plane bending is increased the same amount as the bending stiffness increase in actuation direction. In fact reinforcing *tr/t* = 2.7 shows a decrease in the out-of-plane / actuation stiffness when compared to a prismatic leaf-spring. The actuation stiffness increases faster than the out-of-plane stiffness for increasing *tr*. The out-of-plane / actuation stiffness doesn't change much due to deflection, because *L/w* is relatively large [3]. A small *L/w* results in a relatively high out-of-plane bending stiffness to torsion stiffness ratio, which causes decrease of out-of-plane stiffness at deflection. *Cd* has no influence on the out-of-plane stiffness.

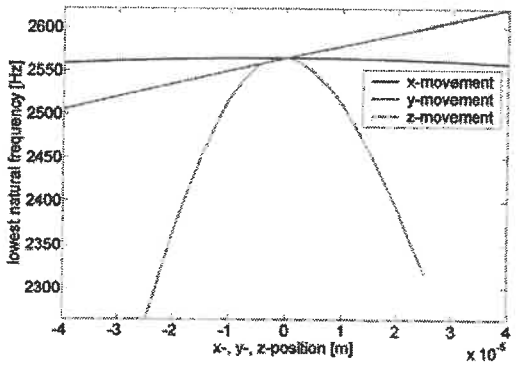

FIGURE 4. The lowest natural frequency as a function of the hexapod end-effector position in the individual x-, y- and z-direction.

THE HEXAPOD

The hexapod has been modeled by regarding the elastic energy storage in all the leaf-springs. Drive stiffness *Cd* for the six actuator suspensions is low and varies between 0.051 and 0.21. Most actuator energy is stored in the folded flexures. The lowest natural frequency in relation to a single movement in *x, y* or *z*-direction has been calculated as shown in Figure 4. The lowest natural frequency has a mode mainly in the out-of-plane direction. In the *x*- and *y*-directions the stiffness change is small compared to the stiffness change due to movement in *z*-direction. During an *x*- or *y*-displacement only the folded flexures and the silicon leaf-springs, as shown in Figure 1, are deflected. The *z*-stiffness of these flexures changes only slightly by deflection. The lowest natural frequency increases slightly when the end-effector is moved in the positive y-direction. The mass of the end-effector, which is the most important, is distributed more equal over the actuator folded flexure suspensions. The longitudinal stiffness of the slanted leaf-springs

does change significantly due to deflection when the end-effector is displaced in z-direction. Because the slanted leaf-springs are relatively thin (0.7μm) the decrease in natural frequency is relatively fast. Although an end-effector displacement of tens of micrometers shows a change in lowest natural frequency, the change in actuation force is neglectable.

CONCLUSION

The drive stiffness has great influence on the longitudinal stiffness of leaf-springs. For leaf-springs used for a relatively large drive stiffness, reinforcement is beneficial. Leaf-springs used at a relatively low drive stiffness, as is usually the case in MEMS, can also benefit from reinforcement, but only in certain cases. If the relative deflection is small there is a substantial gain in the ratio longitudinal to actuation stiffness. If the length to width ratio is small, the out-of-plane stiffness during deflection can be increased. The stiffness and so the natural frequency decrease due to deflection of elastic elements in a system can be drastic. In the proposed hexapod design the maximum lowest natural frequency shift due to a displacement of 25 μm is only 10%.

REFERENCES

1. D.M. Brouwer, et al., 2006, MEMS-based 6 DOF parallel kinematic precision micro manipulator, *Proc. of EUSPEN,* 6: 111-114.
2. Jonker, J.B. and Meijaard, J.P., 'SPACAR-computer program for dynamic analysis of flexible spatial mechanisms and manipulators', in Multi-body Systems Handbook, W.Schielen(ed.), Springer-Verlag, Berlin, 123-143.
3. J. van Eijk, 1985, On the design of plate-spring mechanisms, *Ph.D Thesis*, Delft, The Netherlands.
4. R. Legtenberg, 1996, Electrostatic actuators fabricated by surface micromachining techniques, *Ph.D thesis*, University of Twente, Enschede, The Netherlands, pp 139.
5. D.M. Brouwer, et al., 2006, Sub-nanometer stable precision MEMS clamping mechanism maintaining clamp force un-powered for TEM application, *J. of Micromech. and Microeng.* , Vol.16, No. 6: 7-12

Special acknowledgement should be given to J.B. Jonker, J. van Dijk and R.G.K.M. Aarts. They enabled the extensive calculations in Spacar.

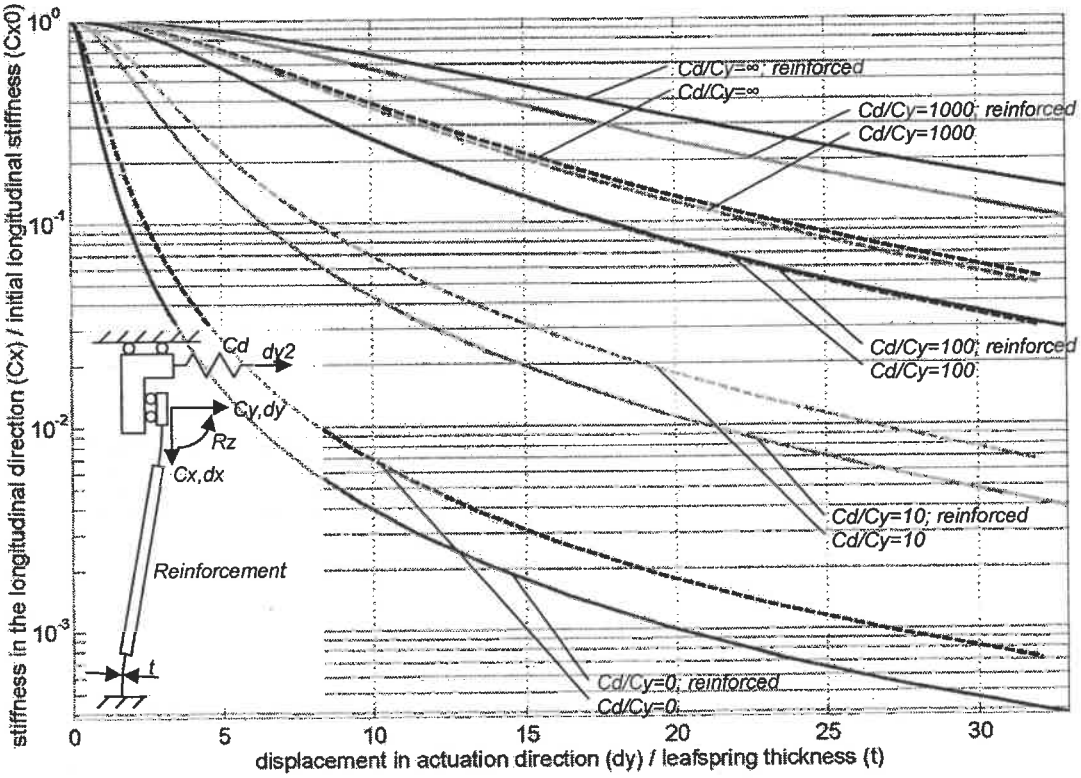

FIGURE 5. The longitudinal stiffness as a function of the deflection in relation to the drive stiffness for prismatic and for reinforced leaf-springs.

MOVING-MAGNET PLANAR ACTUATOR WITH INTEGRATED ACTIVE MAGNETIC BEARING

J.W. Jansen, C.M.M. van Lierop, E.A. Lomonova, A.J.A. Vandenput
Department of Electrical Engineering, Eindhoven University of Technology
Eindhoven, The Netherlands

INTRODUCTION

In recent years, magnetically levitated planar actuators have been developed for demanding applications such as wafer stages. Although the translator of these actuators can move over relatively large distances in the *xy*-plane only, it has to be controlled in six degrees-of-freedom (DOF) because of the active magnetic bearing. These actuators have either moving magnets and stationary coils [1] [2] or moving coils and stationary magnets [3]. The coils in the actuator are simultaneously used for the propulsion in the *xy*-plane as well as for the 4-DOF active magnetic bearing.

The advantage of a moving-magnet topology is that the coils and, therefore, the power supply and the cooling are located at the stationary part of the actuator. Consequently, no cable to the moving part is necessary. However, only the coils below the magnet array significantly contribute to the propulsion and the active magnetic bearing. For this reason, the set of active coils changes with the position of the translator in a long-stroke moving-magnet planar actuator.

Contrary to moving-coil planar actuators, symmetries in the design of a long-stroke moving-magnet actuator cannot be used to decouple the force and the torque. The strong coupling between the degrees-of-freedom combined with the need to switch between coil-sets requires new commutation techniques [4] and, therefore, new design methods.

In this paper a long-stroke moving-magnet planar actuator with integrated magnetic bearing is presented. The position dependent condition number of the commutation and decoupling matrix is used as a design criterion to predict the 6-DOF controllability of the topology.

TOPOLOGY

The topology of the planar actuator is shown in Figs. 1 and 2. The dimensions and properties are summarized in Table 1. The translator consists of a Halbach permanent-magnet array which is glued to an aluminum carrier. A Halbach permanent-magnet array is used as it increases the magnetic flux density near the coils. Although the extra permanent magnets, which are magnetized in the *x*- and *y*-directions, increase the mass of the translator, the power dissipation of the actuator is smaller compared to an actuator without these extra magnets.

The stator consists of 84 coils in a herringbone pattern. At most 24 adjacent coils are used simultaneously to control the translator in six degrees-of-freedom. All coils are connected to single-phase power amplifiers.

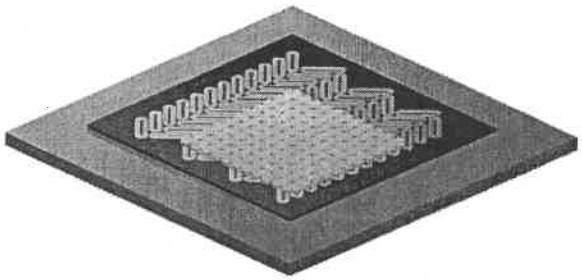

FIGURE 1. Overview of the six degree-of-freedom moving-magnet planar actuator.

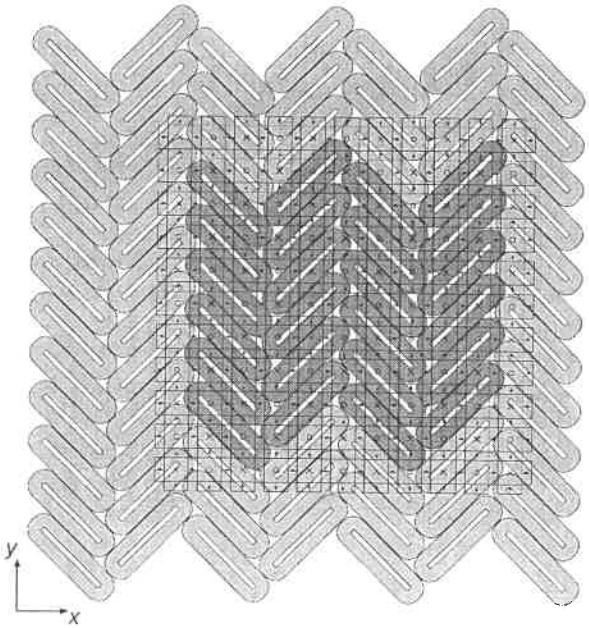

FIGURE 2. Moving-magnet planar actuator (top view).

The coils are rotated 45 degrees with respect to the magnet array. In this way, the coils can be made rectangular instead of square which will decrease the power dissipation of the actuator.

Fig. 3 shows a detail of the actuator. In the figure two groups of three coils are shown. Although the coils are individually excited by single-phase power amplifiers, the coils in each group are positioned according to a three-phase system to reduce the influence of higher harmonics of the magnetic flux density distribution of the translator on the force and the torque. Each group can produce force in two directions independent of the position of the magnet array. Both groups can produce levitation force (*z*-direction). The force produced in the *xy*-plane F_{xy} by both groups is orthogonal as indicated by the arrows in Fig. 3. Because the length l of the coils is equal to $2n\tau_n$, where n is an integer (for these coils n=2) and τ_n is the pole pitch as defined in Fig. 3, the force production in the *xy*-plane is physically decoupled [3] [5]. This reduces cross-talk between the degrees-of-freedom and, therefore, simplifies the modeling of the force and the torque in the actuator.

TABLE 1. Properties and dimensions of the actuator.

Size translator	300x300 mm
Mass translator	8 kg
Mechanical clearance (z-dir.)	1 – 2 mm
Stroke (*xy*-plane)	230x230 mm
Max speed (*xy*-plane)	1 m/s
Max acceleration (*xy*-plane)	10 m/s^2
Cooling medium	Water

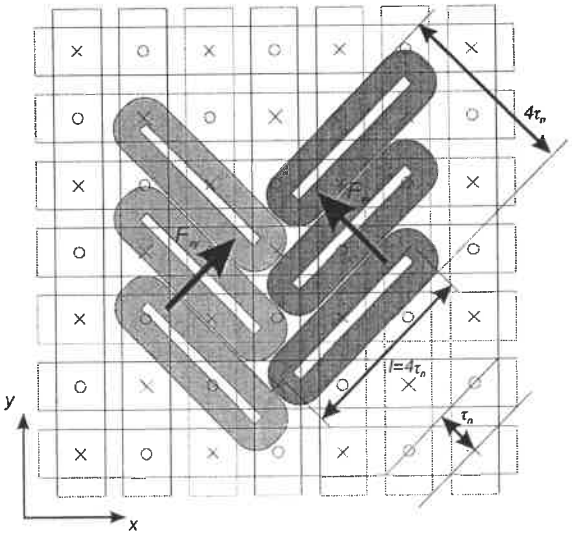

FIGURE 3. Detail of the actuator with two 3-phase coil groups.

COMMUTATION AND SWITCHING

Because the coils are responsible for both the propulsion of the magnet array and its active magnetic bearing, both the torque and the force produced by these coils should be controlled accurately. Fig. 4 shows the controller and the actuator schematically. The actuator is modeled by a position dependent non-linear mapping Γ, which maps the active currents $\vec{i}$ on the force and torque vector $\vec{w}$, and by linear time invariant (LTI) plant dynamics. In this approach rigid body dynamics are assumed.

The LTI controller calculates a force and torque set-point, the desired wrench $\vec{w}^*$, which should be converted to current set-points $\vec{i}^*$ for the active coils in the actuator. DQ0-decomposition cannot be used as a commutation algorithm as it can only decouple the force and not the torque in this actuator. Because the 6-DOF actuator is clearly over-actuated, there is a set of transformations which provide a proper linearization and decoupling of the degrees-of-freedom [4]. A solution to this problem is to minimize the ohmic losses in the coils, i.e.

$$\min_{\Gamma(\vec{p})\vec{i}^*=\vec{w}^*} \left\|\vec{i}^*\right\| = \left\|\Gamma^-(\vec{p})\vec{w}^*\right\|, \qquad (1)$$

where $\Gamma(\vec{p})$, is a matrix which contains the mapping of the current in the active coils on the force and torque exerted on the translator as a function of the position and the orientation of the translator in six degrees-of-freedom $\vec{p}$. The minimization in (1) can be solved by calculating the Moore-Penrose inverse of $\Gamma(\vec{p})$.

To decrease the computation time of the commutation algorithm, the transfer functions in $\Gamma(\vec{p})$ are analytical equations which assume an infinitely long magnet array and which can be evaluated fast [5]. Because the end-effects of the magnet array are not included in these equations, the model deviates for the coils which are near the edge of the magnet array.

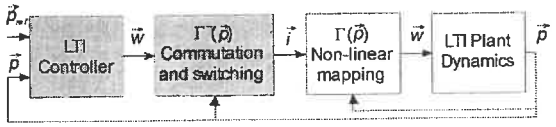

FIGURE 4. Simplified model of the actuator and controller (controller and commutation in gray), assuming ideal power amplifiers ($\vec{i} = \vec{i}^*$).

Therefore, these coils are actively switched off by smooth weighing functions $\Delta(p_x, p_y)$, which depend on the position of the translator in the *xy*-plane, p_x and p_y.

The force and torque can be decoupled again by minimizing the ohmic losses in the coils [4]:

$$\min_{\Gamma(\vec{p})\vec{i}^*=\vec{w}^*} \left\| \vec{i}^* \right\|_{\Delta^{-1}(p_x,p_y)} = \left\| \Gamma^-(\vec{p})\vec{w}^* \right\|, \qquad (2)$$

where:

$$\Gamma^-(\vec{p}) = \Delta(p_x,p_y)\Gamma^T(\vec{p})\left(\Gamma(\vec{p})\Delta(p_x,p_y)\Gamma^T(\vec{p})\right)^{-1}. \qquad (3)$$

When the translator moves in the *xy*-plane, there are 15 to 24 simultaneously active coils. In total there are 28 different sets of active coils. The weighing functions smoothly switch the coils on and off at a transition between two different sets of coils.

The effect of the weighing function is illustrated in Fig. 5. In the bottom-left figure the weighing functions do not penalize any coil and all 24 coils are active. When the translator moves in the *x*-direction, the active coils in the left column will be smoothly switched off. After they are switched off, the adjacent coils in the outer right column will be smoothly switched on (not shown). At the transition, only 18 coils are active (bottom-right figure). When the translator moves in the *y*-direction only 20 coils are active at the transition between two different sets of coils (top-left figure). In the worst case situation (top-right figure), 9 coils are penalized by the weighing function and are switched off.

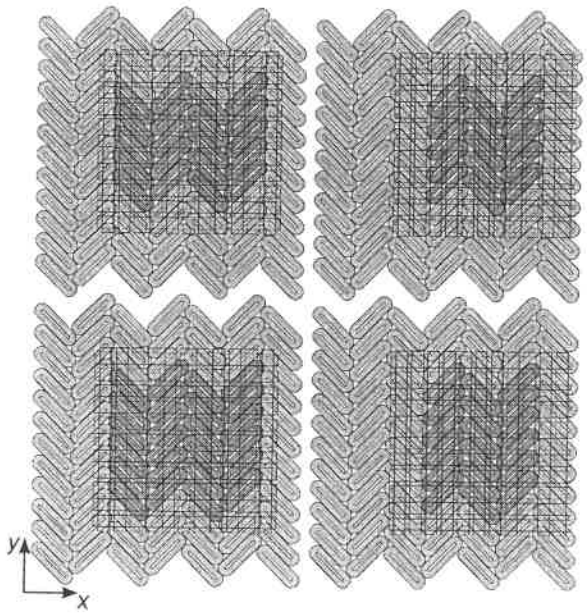

FIGURE 5. Active coils at the transitions between different sets of coils.

CONDITION NUMBER

Both the controllability and the power dissipation of a planar actuator topology are influenced by the commutation and switching algorithm. Because evaluating a large number of topologies with an accurate electromagnetic model is very time consuming, the condition number of $\Gamma^-(\vec{p})$ is calculated on a grid in the *xy*-plane to predict the controllability of a topology. If the condition number of $\Gamma^-(\vec{p})$ is sufficiently small, then all force and torque combinations can be achieved. Generally, a low condition number also results in small force and torque ripples.

Fig. 6 shows the condition number of the presented topology over a part of the stroke of the actuator. The switching between different sets of coils in the *x*-direction is most clearly visible in the condition number.

Fig. 7 shows the estimated ohmic losses for two load situations, levitation of the translator only and levitation and acceleration in the *xy*-plane of the translator. The losses are strongly influenced by the switching between the different coil sets.

Figs. 8 and 9 show the predicted open-loop force and torque ripple for the second load situation. The force and torque ripples are small and no cross-talk between the force and the torque is visible.

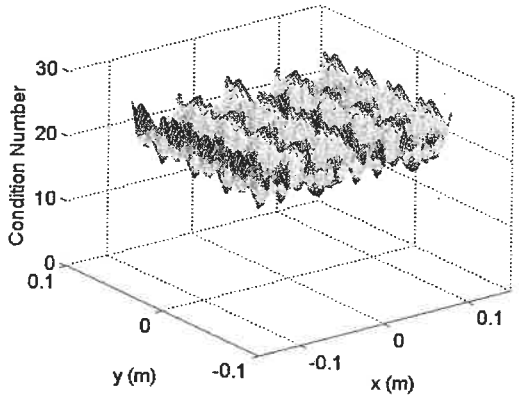

FIGURE 6. The condition number of $\Gamma^-(\vec{p})$.

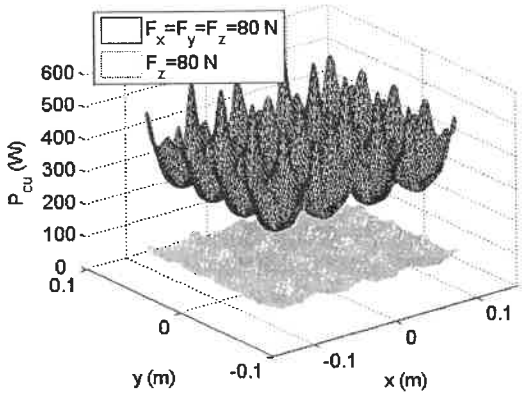

FIGURE 7. Predicted power dissipation (2 mm mechanical clearance between the stator and the translator).

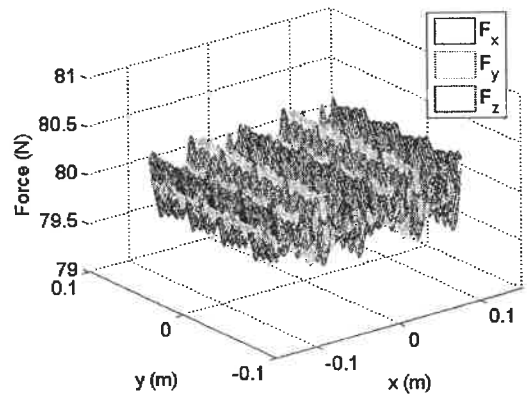

FIGURE 8. Predicted force ($F_x = F_y = F_z = 80$ N and $T_x = T_y = T_z = 0$ Nm).

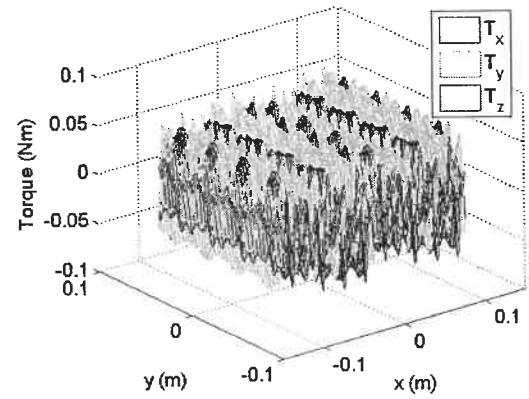

FIGURE 9. Predicted torque ($F_x = F_y = F_z = 80$ N and $T_x = T_y = T_z = 0$ Nm).

CONCLUSIONS

A moving-magnet planar actuator with integrated magnetic bearing has been presented. Simulations show that the degrees-of-freedom can be sufficiently decoupled and that the force and torque ripples are small. The switching between different sets of coils, necessary to achieve long-stroke motion, significantly influences the power dissipation.

ACKNOWLEDGEMENT

The authors would like to thank Mr. Marijn Uyt De Willigen for his assistance with the set-up. The authors would also like to thank ASML, Assembléon, Philips Applied Technologies, Prodrive, Tecnotion and Vacuumschmelze for their valuable contributions and support. This IOP-EMVT project is funded by SenterNovem. SenterNovem is an agency of the Dutch Ministry of Economical Affairs.

REFERENCES

[1] W. J. Kim, D. L. Trumper, and J. H. Lang, Modeling and vector control of a planar magnetic levitator," *IEEE Trans. Ind. Applicat.*, vol. 34, no. 6, pp. 1254–1262, Nov/Dec 1998.

[2] A. J. Hazelton, M. B. Binnard, and J. M. Gery, "Electric motors and positioning devices having moving magnet arrays and six degrees of freedom," U.S. Patent 6,208,045, 27 March 2001.

[3] J. C. Compter, "Electro-dynamic planar motor," *Precision Engineering*, vol. 28, no. 2, pp. 171–180, Apr 2004.

[4] C. M. M. van Lierop, J. W. Jansen, A. A. H. Damen, and P. P. J. van den Bosch, "Control of multi-degree-of-freedom planar actuators," *in Proc. of the 2006 IEEE International Conference on Control Applications, CCA 2006*, Munich, Germany, Oct 2006, in press.

[5] J. W. Jansen, E. A. Lomonova, A. J. A. Vandenput, and C. M. M. van Lierop, "Analytical model of a magnetically levitated linear actuator," *in Conf. Rec. 2005 Industry Applications Conference, 40th IAS Annual Meeting*, Oct 2005, pp. 2107-2113.

DESIGN OF A ROBOT-BASED DETECTOR MANIPULATOR FOR A HARD X-RAY NANOPROBE INSTRUMENT SYSTEM

D. Shu[2], J. Maser[1,3], M. Holt[3], C. Preissner[2], B. Lai[3], S. Vogt[3], R. Winarski[3], and G. B. Stephenson[1,4]

[1]Center for Nanoscale Materials
[2]APS Engineering Support Division
[3]X-ray Sciences Division
[4]Materials Sciences Division
Argonne National Laboratory
Argonne, IL 60439, U.S.A.

INSTRUCTIONS

The Advanced Photon Source (APS) at Argonne National Laboratory (ANL) is a national user facility for synchrotron radiation research. The high-brilliance x-ray beams of this third-generation synchrotron radiation source provide powerful tools for forefront basic and applied research in many fields of scientific research. A hard x-ray nanoprobe beamline is being developed at the APS. The beamline will house a hard x-ray nanoprobe instrument, one of the centerpieces of the characterization facilities of the Center for Nanoscale Materials (CNM) being constructed at ANL. The instrument will combine a scanning probe mode with a full-field transmission mode. It uses: x-ray fluorescence for trace-element mapping and spectroscopy; x-ray diffraction to obtain local structural information such as crystallographic phase and strain texture; and x-ray transmission in phase and absorption to image internal structures of complex devices [1]. The combination of diffraction, fluorescence, and phase contrast in a single tool will provide unique characterization capabilities for nanoscience.

This new probe will cover an energy range of 3-30 keV. The working distance between the nanofocusing optics and the sample will typically be in the range of 10-30 mm. With advances in the fabrication of zone-plate optics and an optimized beamline design, we expect to be able to achieve 30-nm resolution at the nanoprobe. The system is designed to accommodate x-ray optics with a resolution limit of 10 nm; therefore, it requires staging of x-ray optics and specimens with a mechanical repeatability of better than 5 nm.

This paper presents the design of three robot-based detector manipulators for microdiffraction applications with the hard x-ray nanoprobe instrument system.

TABLE 1. Design specifications for the Cartesian/articulate hybrid detector robot-arm

	Horizontal 2-D linear stages	Vertical 2-D linear robot arms
Overall Dimension (mm)	1500 (X) x 650 (Y) x 123 (Z)	604 (X) x 878 (Y) x 1217 (Z)
Normal Load Capacity (kg)	500	12
Stage type	Stepping motor with planetary gearhead	Servo motor
Encoder type	Linear encoder	Linear encoder
Travel range (mm)	1050 (X) x 200 (Y)	600 (Y) x 800 (Z)
Min. incremental motion (micron)	0.02	0.5
Unidirectional repeatability (micron)	+/- 5	+/- 10
Max. speed (mm/sec)	50	100
	Base rotary stage	**Detector bay rotary stage**
Overall Dimension (mm)	350 (X) x 336 (Y) x 118 (Z)	49 (X) x 166 (Y) x 108 (Z)
Load Capacity (kg)	360	10
Stage type	Stepping motor	Stepping motor
Travel range (degree)	90	65
Min. incremental motion (degree)	0.001	0.002
Unidirectional repeatability (degree)	+/- 0.001	+/- 0.001
Max. speed (degree/sec)	10	10

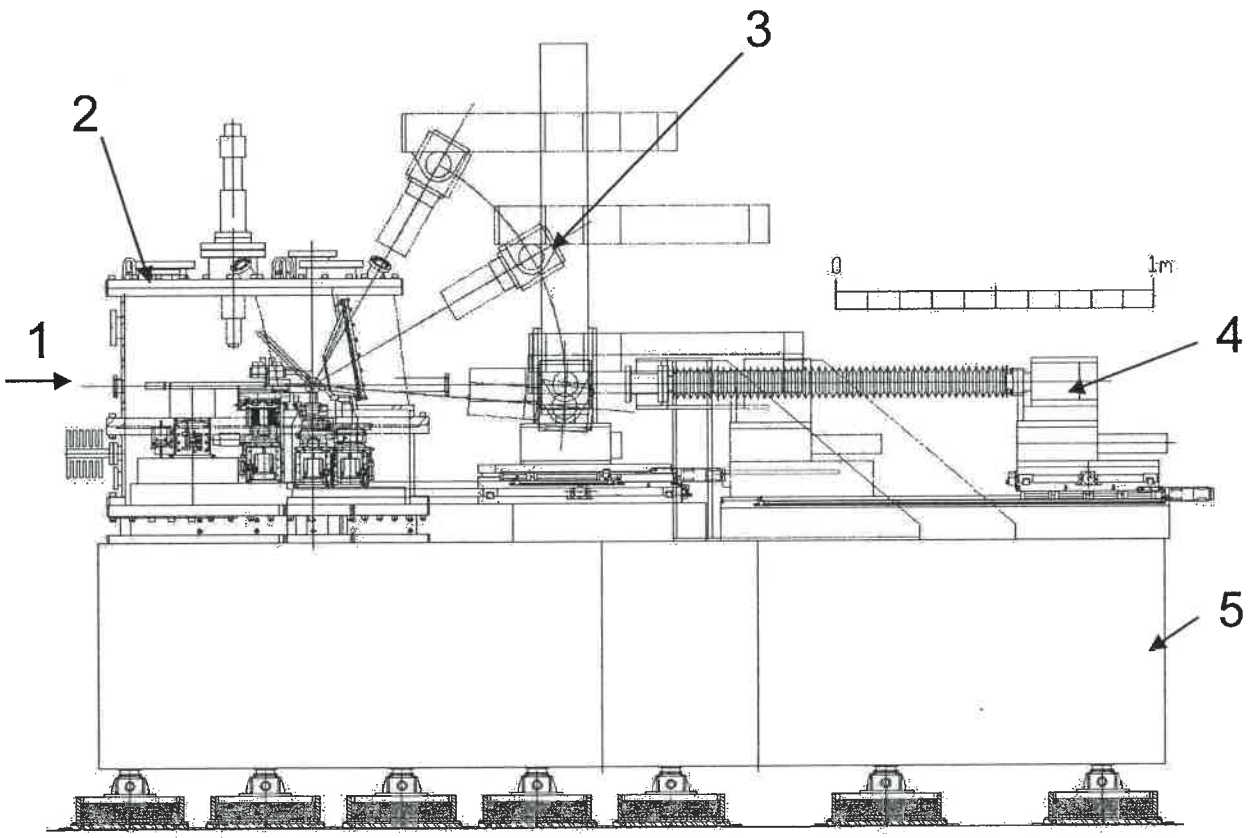

FIGURE 1. Side view of the hard x-ray nanoprobe instrument. (1) Incident x-ray beam; (2) Instrument chamber; (3) Robot-based manipulator for diffraction detector; (4) Transmission imaging detector; (5) Granite base.

GENERAL LAYOUT OF THE NANOPROBE INSTRUMENT

The nanoprobe instrument will combine a scanning probe mode with a transmission mode. The scanning probe mode will provide fluorescence spectroscopy and microdiffraction applications. The full-field transmission mode will allow 2-D imaging and tomography. Diffractive optics, such as zone plates, will be used for focusing and imaging in this instrument. High-resolution positioning and scanning is performed using the stage group for zone plate optics in a high-vacuum-compatible instrument chamber. In the same vacuum vessel, a specimen stage group is used for coarse positioning only [2].

As show in Fig. 1, the optomechanical structure for the nanoprobe presented here consists of the following major component groups: a nanoprobe instrument chamber (2), a granite base (5) to minimize the vibrations excited from the ground, a customized industrial robot-arm-based detector manipulator (3) for microdiffraction applications, and a translation stage system for the transmission imaging detector (4).

ROBOT-BASED DETECTOR MANIPULATOR FOR MICRODIFFRACTION

Limited by the geometric configuration of the nanoprobe instrument, it is not feasible to use a traditional goniometer to achieve the motions needed for a microdiffraction detector. Robot-based detector manipulators have been developed for a variety of microdiffraction detectors weighing from less than 1.5 kg up to 100 kg in three configurations. To fully support the diffraction detector when it is rotated around the specimen position, the nanoprobe instrument table has been widened significantly on the outboard side to optimize the support of the diffraction detector during rotation around the Y axis.

Detector manipulator with 12-kg load capacity

Figure 2 shows a custom-built Cartesian/articulate hybrid robot arm for detector manipulation with 12-kg load capacity and +/- 10-micron positioning repeatability. It is a combination of four linear stages and two rotary stages. A THK™ custom-built 2-D horizontal stage (2) and a Huber™ 420 single-circle goniometer (3) are mounted on a granite base (1) to perform a circular motion centered on the sample position in the horizontal plane [3,4]. A pair of IAI™ 2-D vertical Cartesian robot arms (4, 5) is mounted on the top of the Huber™ 420 goniometer to provide a circular motion centered on the sample position in a vertical plane [5]. Doubled linear robot arms are used to improve the system stiffness and repeatability. A special mechanical linkage and control scheme will be developed to ensure the synchronization between the doubled arms. The detector (7) is mounted in a U-shaped detector bay driven by a Huber™ 408 single-circle goniometer (6). Table 1 summarizes the technical specifications of the stages used in the hybrid robot-arm system.

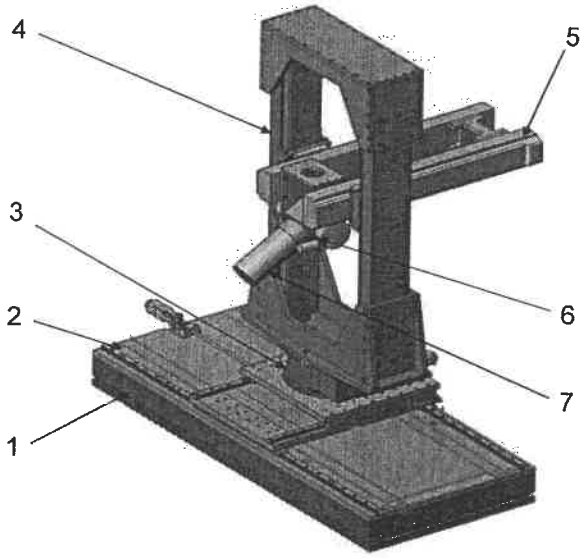

FIGURE 2. A 3-D model of the Cartesian/articulate hybrid robot-arm with 12-kg load capacity.

Detector manipulator with 1.5-kg load capacity

For detectors with a mass less than 1.5 kg, an industrial articulate robot arm could be applied to perform the circular motion in the vertical plane as shown in Fig. 3. In this configuration, a Mitsubishi™ RV-1A articulate robot arm is mounted on the top of the THK™ 2-D horizontal stage to obtain a horizontal circular motion larger than the reachable range of the RV-1A robot arm [6]. A +/- 20-micron positioning repeatability is expected for this detector manipulator system.

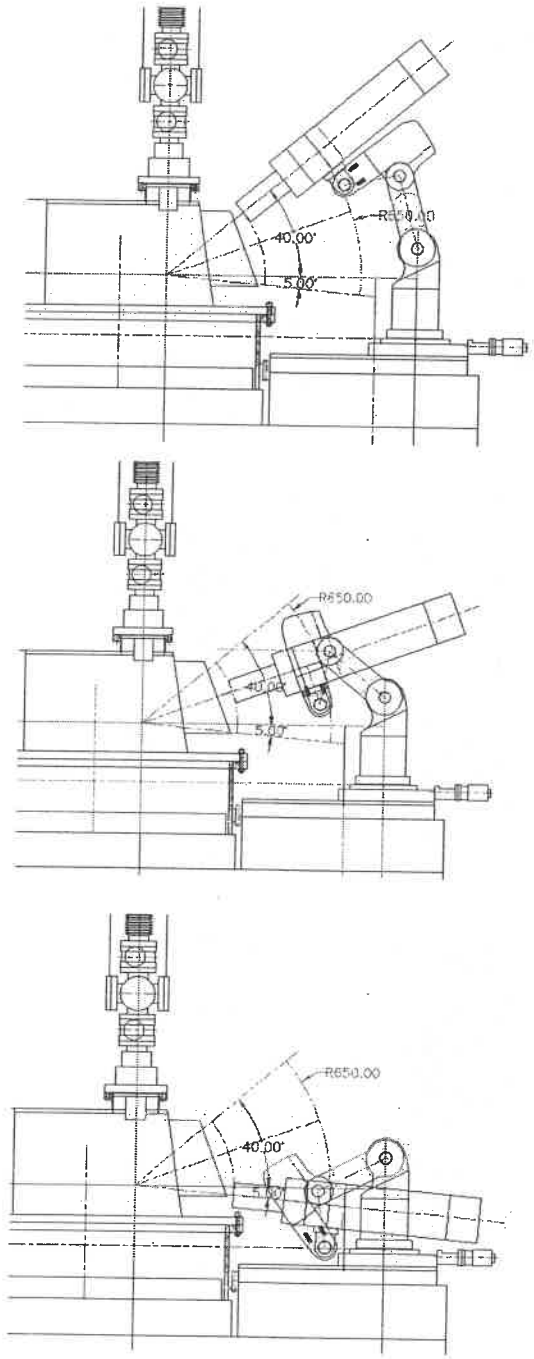

FIGURE 3. Vertical circular motion simulation with an industrial robot-arm for a 1.5-kg detector.

Detector manipulator with 100-kg load capacity

In certain microdiffraction applications, large x-ray detectors, such as the MAR™345 imaging plate or the MAR™165 CCD detector from Mar Research GmbH, will be used in the nanoprobe microdiffraction system [7]. These detectors may weigh 20 – 100 kg. Since they have large vertical acceptance, the detector manipulator only needs to provide a horizontal circular motion, as show in Fig. 4.

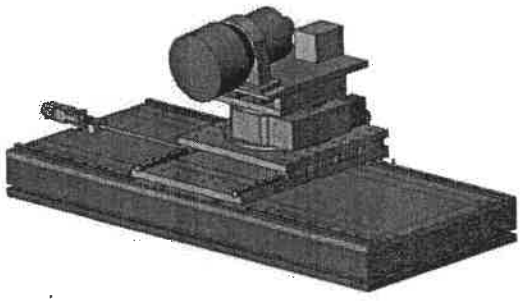

FIGURE 4. A 3-D model of the detector manipulator with 100-kg load capacity.

MASS CENTER DYNAMIC BALANCE FOR THE DETECTOR MANIPULATOR

To optimize the nanoprobe instrument positioning stability, several heavy metal balance blocks are applied on the nanoproe supporting system. They are mounted on motorized stages under the granite table. Synchronized with the detector manipulator motion, the balancing blocks keep the nanoprobe mass center position stable.

SUMMARY

This paper presents the design of a robot-based detector manipulator for microdiffraction applications with the hard x-ray nanoprobe instrument system at the APS. Applications for detectors weighing from 1.5 kg to 100 kg were discussed in three configurations.

ACKNOWLEDGMENTS

The authors would like to thank M. Muscia and A. Nyman from Argonne National Laboratory for their help in the manipulator development. This work was supported by the U.S. Department of Energy, Office of Science, Office of Basic Energy Sciences, under Contract No. W-31-109-Eng-38.

REFERENCES

1. J. Maser, G. B. Stephenson, D. Shu, B. Lai, S. Vogt, A. Khounsary, Y. Li, C. Benson, G. Schneider, SRI 2003 AIP Conf. Proc. 705, 470-473, (2004).
2. D. Shu, J. Maser, M. Holt, R. Winarski, C. Preissner, A. Smolyanitskiy, B. Lai, S. Vogt, and G. B. Stephenson, to be published in SRI 2006 Conf. Proc., AIP (2006).
3. THK Co., LTD. Catalog, Tokyo 141-8503, Japan.
4. Huber GmbH X-ray Diffraction Equipment Catalog, Rimsting, Germany.
5. IAI America, Inc. Integrated System Catalog, Torrance, CA 90501 USA.
6. Mitsubishi Electric Catalog, Tokyo 100-8310, Japan.
7. MAR USA X-ray Instruments Catalog, Evanston, IL 60201 USA.

SEVEN-AXIS TESTER WITH SERVO-CONTROLLED FLY-HEIGHT FOR MAGNETIC RECORDING METROLOGY

Thomas M. Crawford[1*], René J. M. van de Veerdonk[1], Mark. D. Bedillion[1], Wabe Koelmans[1], Anthony K. Langzettel[1], Brian P. O'Connor[2], Bob Novotnak[2], and Ben Lane[3]

[1]Seagate Research, Pittsburgh, PA

[2]Aerotech, Inc., Pittsburgh, PA

[3]Key Technologies, Inc., Baltimore, MD

(*present address – Dept. of Physics – Univ. of South Carolina, Columbia, SC)

INTRODUCTION

In magnetic data storage systems, dimensions are shrinking rapidly toward the nanoscale. Magnetic recording heads have critical feature sizes below 100 nm, while they are flown in close proximity to a fine-grained recording medium at 5-15 nm fly-heights, which are controlled in a disc drive by a hydrodynamic air-bearing on a 1×1 mm^2 slider surface. The linear density of recorded information is determined by the bit-length, which is approaching 25 nm. At these dimensions, metrology is a critical enabler for sustaining product quality and reliability. Several aspects of head performance must be quantified with precision metrology: the high-frequency performance of the write and read heads [1], the spatial extent of the magnetic field generated by the writer and the spatial field sensitivity of the read head [2-4]. None of these aspects are easily tested using conventional spin-stand recording metrology. Previous studies have shown the capability for measuring these effects at the level of individual recording heads and sliders, using scanning probe contact write/read metrology [1-4]. However, while these measurements demonstrate proof-of-principle, they are not extendable to development or production scale because of slow data gathering speeds and irreproducibility of the slider contact geometry, particularly the lack of knowledge of the head-medium or head-sensor spacing. We report here on the design and mechanical performance of a recording metrology platform with the goal of testing individual recording head sliders with a user-adjustable, servo-controlled fly height and high bandwidth electrical interconnect.

ROTARY, PITCH/ROLL, AND LINEAR STAGE ASSEMBLY

Figure 1 shows the tester. In order to deliver sufficient statistics in a minimum time, we chose to implement a rotary tester. This design uses

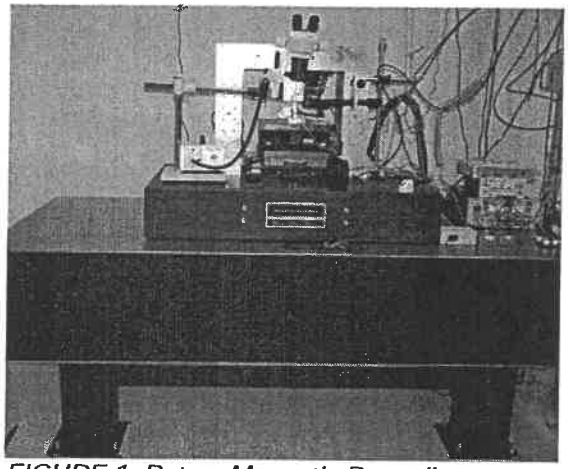

FIGURE 1. Rotary Magnetic Recording Tester

FIGURE 2. Inverted air bearing rotary stage with disc vacuum chuck

an air-bearing rotary stage which can rotate at speeds up to 400 RPM, with asynchronous error motions less than 5 nm. The rotary stage is encoded with 0.1 μRad angular resolution, enabling 2.5 nm linear resolution along the circumference at 2.54 cm radius. This stage is mounted in an inverted configuration (Figure 2), and the recording media disc is attached to the stage with vacuum. To load and unload the slider from the tester, a 4-axis positioning system is used (Figure 3 – note coordinate axes). This system includes a 300 mm linear travel air bearing stage (X-axis) with magnetic

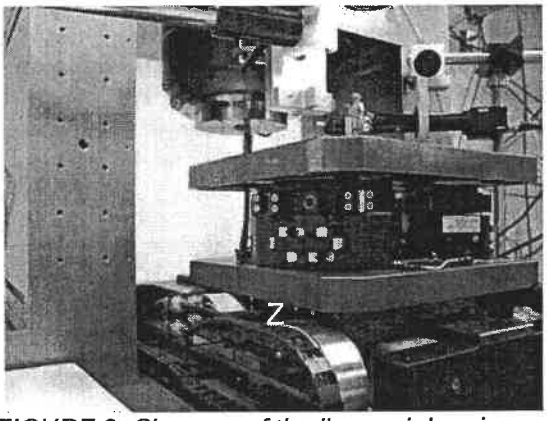

FIGURE 3. Close-up of the linear air bearing stage and one of the pitch/roll/z adjust stages

pre-load such that when the air is removed, the carrier can be locked in position. Once locked in position, the X-axis is stable to < 2 nm p-p in a 200 Hz bandwidth. To successfully perform magnetic recording, the surface of the slider must be maintained at < 5 microradian roll (about Y-axis) and 50 microradian pitch (about X-axis) with respect to the disc surface. Three wedge z-stages are mounted on the linear stage, and are arranged at 120 degree angles to provide ~ 7 milliradian angular travel with 13 nanoradian nominal angular resolution for controlling slider pitch and roll, or 1.2 mm of z-travel (z perpendicular to the disc) with 2 nm encoded resolution.

The baseplate mounted on the tip-tilt-z stage assembly has been ground and assembled parallel to the disc vacuum chuck to an angle of 5.4 μrad in the x-direction and 0.54 μrad in the y-direction (Figures 4-5). When locked in place, the stability of this baseplate relative to the disc is 1.4 nm p-p (0.23 nm rms) in a 200 Hz bandwidth (6 second capture from an optical interferometer) in the x-direction, and 3.2 nm (0.66 nm rms) in the z-direction respectively (Figure 6). For a 60 second capture, the p-p deviations are 7.1 and 8.9 nm for x and z respectively. The circular flatness of the vacuum chuck measured with respect to the system baseplate is 100 nm p-p at a 25 mm radius. With a 95 mm diameter glass disc mounted to the

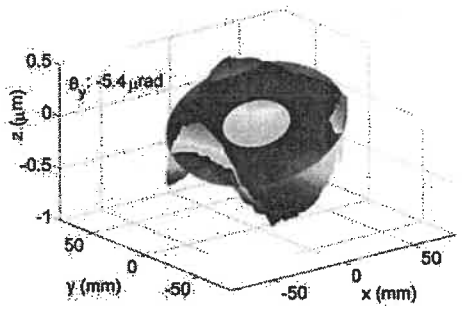

FIGURE 4. X-axis vacuum chuck parallelism relative to the tip-tilt-z platen. The angle about the y-axis is -5.4 μrad.

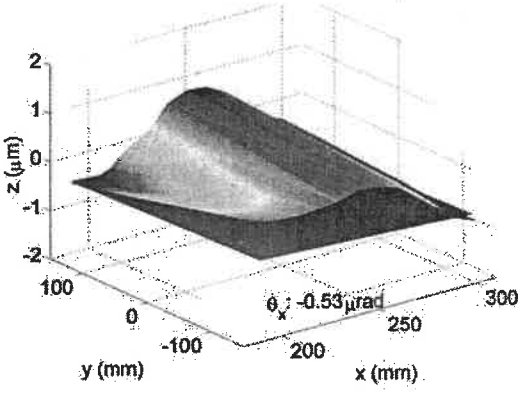

FIGURE 5. Y-axis vacuum chuck parallelism to the tip-tilt-z platen. The angle about the x-axis is -0.52 μrad.

vacuum chuck, the resulting disc circular flatness is < 800 nm p-p at a 25 mm radius, largely caused by the disc.

SLIDER MOUNTING AND PIEZO ASSEMBLY

To perform suspensionless magnetic recording at ultra-high frequencies using sliders, we require a means to hold a single slider, as well as a high-bandwidth interconnect. We also require a means to scan the slider along the radial or cross-track direction of the disc (Y-axis). Finally, the slider's distance from the disc must be controlled with nm precision. Figure 7 shows the slider clamp assembly with a 40 GHz interconnect, a 15 μm travel piezo translator, and a closed loop single-axis flexure stage (15 μm travel along the y-direction). Figure 8 displays a close-up of the slider clamp assembly

showing the clamping mechanism, the tip of an optical fiber interferometer, and a loaded slider for reference. The raised ring around the fiber tip and the pin provide reference surfaces to align the slider during loading. Finally, there is a vacuum hole directly beneath the slider, which connects to the tubing shown in the top of Figure 8, to add additional clamping force and to stabilize the slider during the loading and aligning process.

PITCH AND ROLL ADJUSTMENT

The slider roll axis is perpendicular to the linear stage. To adjust aslider roll, we employ a

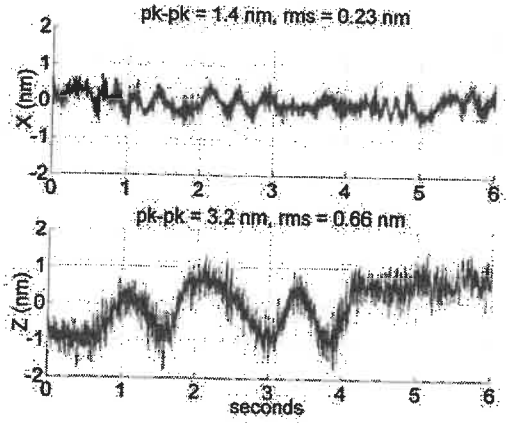

FIGURE 6. In-position stability over 6 seconds with 200 Hz bandwidth – top graph, x-axis in-position stability: p-p deviation = 1.4 nm, rms = 0.23 nm. Bottom, z-axis in-position stability: p-p = 3.2 nm, rms = 0.66 nm.

measurement station before the rotary stage, (foreground of Figure 3). This station has an optical fiber interferometer to measure the variation in slider height as the linear stage is translated. By adjusting the pitch and roll stages, a finite roll can be corrected to < 1 μrad. For a 1 mm wide slider, this angle corresponds to a height differential of 1 nm across the entire slider width. Slider pitch is controlled by scanning the z-tip-tilt stages to vary the pitch angle and measuring the change in slider-interferometer spacing. For a properly aligned interferometer with respect to the rotational axis of the pitch adjustment, a slider at zero pitch will give a symmetric response. A finite pitch angle can be introduced by offsetting this curve.

CONTROLLING SLIDER HEIGHT

The optical fiber interferometer enables us to achieve nm-scale control over the slider-to-disc separation using a digital servo control loop, which is closed around the interferometer, in order to emulate fly heights in the 5-15 nm range. The interferometer assembly modulates the gap between the fiber tip and the surface at a constant λ/2 amplitude. The interferometer signal is fed into a DSP control board, which

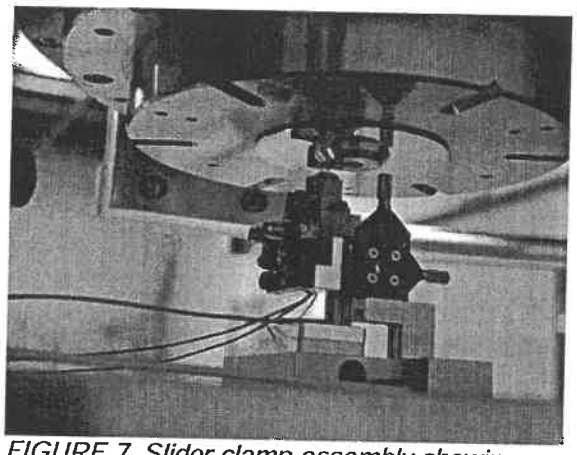

FIGURE 7. Slider clamp assembly showing 40 GHz interconnect and z-servo piezo, as mounted on the cross-track piezo stage, in proximity to the disc as mounted on the rotary stage.

performs the servo control by changing the voltage applied to the 15 μm piezo translator beneath the slider clamp assembly. Figure 9 shows the ~ 700 nm p-p circular flatness obtained when the disc is rotated and the flatness measured with the integrated optical fiber interferometer. Figure 9 shows the same signal measured with the DSP servo-control loop enabled. The maximum deviation from average over a single revolution is ~ 5 nm, and on average over a rotation, the slider is within +/- 1 nm of zero deviation. This p-p deviation of

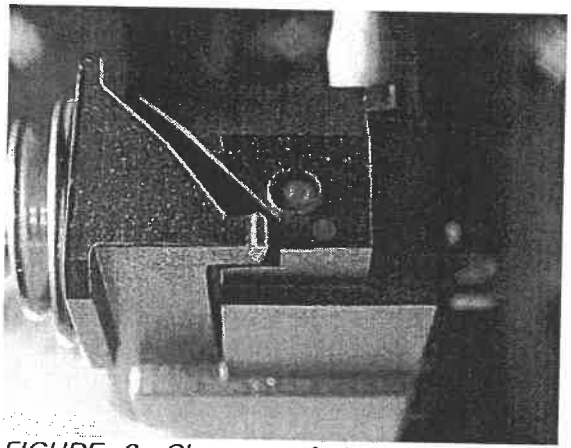

FIGURE 8. Close-up of the slider clamp showing the clamp, the slider, and the optical fiber. The slider dimensions are ~ 1x1 mm^2.

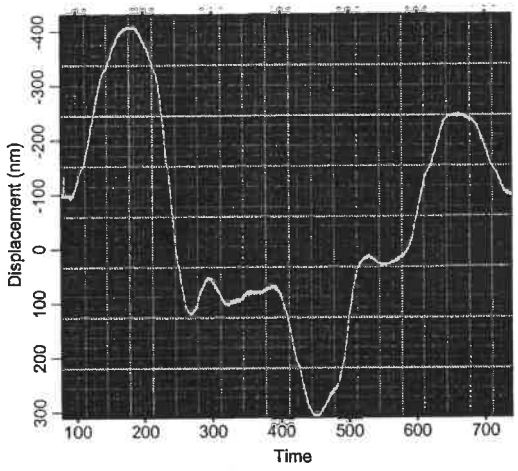

FIGURE 9. Interferometer measurement of rotating disc on vacuum chuck showing < 800 nm p-p circular flatness (rotational speed is 36 deg/sec).

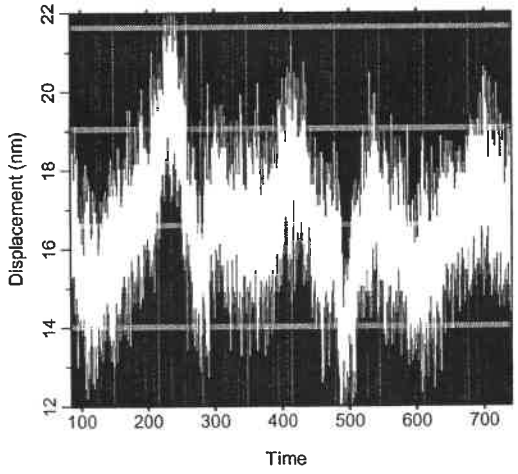

FIGURE 10. Interferometer measurement of displacement for the same disc shown in Figure 9, only with the DSP-based servo system engaged. The largest deviation from average (0-p) is ~ 5 nm, and the rms deviation is ~ 2 nm

10 nm represents a 100x reduction of the disc flatness.

CONCLUSION

A number of noise sources could potentially contribute to the observed deviation with the servo control loop enabled. For example, there is a noise peak at 1.5 kHz with higher harmonics. We suspect this noise originates in the interferometer laser or piezo power supply, as this noise was not correlated with the rotation of the disc. However, mechanical sources cannot be ruled out, such as coupling between the various z-stages, or acoustic coupling from background laboratory noise. If the data in Figure 10 is filtered at 1 kHz with a Butterworth filter, a p-p z-error signal below 1 nm can be achieved, suggesting that with additional noise reduction, for example, quieter power supplies and potential acoustic shielding, this instrument design can deliver variable fly height magnetic recording at the 5 nm level for testing and development of advanced recording components.

REFERENCES

1. R. J. M. van de Veerdonk, T. M. Crawford, S. Wang, X. W. Wu, A. K. Langzettel, A. J. Le Fèbre, S. Batra, and D. Weller, Remanent Dynamic Coercivity Measurements below 1 ns Timescales for Perpendicular and Longitudinal Recording Media – In Preparation 2006.
2. N. J. Gokemeijer, T. W. Clinton, T. M. Crawford, and M. Johnson, Recording Head Metrology at sub-100 nm Device Dimensions. J. Appl. Phys. **97**, 083912 (2005).
3. N. J. Gokemeijer, T. W. Clinton, T. M. Crawford, and M. Johnson, Direct Measurement of the Field from a Magnetic Recording Head using an InAs Hall Sensor on a Contact Write/Read Tester. J. Magn. Magn. Mat. **290-291**, 254 (2005).
4. N. J. Gokemeijer, A. K. Langzettel, and M. Covington, Write Field Measurements of a Perpendicular Head on a Soft Underlayer Film. IEEE Trans. Magn. **42**, 163 (2006).

FREQUENCY RESPONSE PREDICTION FOR ROTATING TOOL-HOLDER-SPINDLE ASSEMBLIES

Chihung Cheng, G. Scott Duncan, and Tony L. Schmitz
Department of Mechanical and Aerospace Engineering
University of Florida, Gainesville, FL, USA

INTRODUCTION

High-speed machining (HSM) is an important process for discrete part manufacturing because it can provide high material removal rates together with good surface finish and part accuracy. To realize these benefits, stability lobe diagrams, which define regions of stable cutting as a function of spindle speed and axial depth of cut, can be applied. Computation of these diagrams requires that the dynamics of the cutting system (the tool-holder-spindle-machine assembly) as reflected at the tool point be known. However, due to the diversity of available tools and holders, it is time consuming to perform impact testing, where a modal hammer is used to excite the tool point and the vibration response is measured using an appropriate transducer, on each combination.

Conventionally, the tool point FRF is measured at zero speed and is presumed to remain constant at different spindle speeds. However, researchers have reported FRF shifts at higher spindle speeds, which are typically ascribed to gyroscopic or other effects. In this paper, we present an approach for predicting rotating tool point FRFs by coupling FRFs of the spindle-machine substructure (identified using a simple geometry standard holder and inverse receptance coupling techniques [1]) to models of the tool-holder substructure. The tool-holder models are developed using Timoshenko beams including gyroscopic effects [2].

Experimental identification of the spindle-machine FRF at speed poses a number of challenges. These include runout, variations in the spindle thermal state, and noise. In this work, a time-domain technique for runout removal is presented. Tool point predictions and experimental validations are provided for a commercially-available spindle using various tool blank-holder combinations.

RUNOUT SIGNAL FILTERING

Runout of the measurement surface during rotating FRF measurements leads to unwanted content at the spindle rotation frequency. Contributors include spindle axis of rotation errors from bearing wear or misalignment, as well as the target surface itself. The runout magnitude exerts considerable influence on the FRF by producing false frequency content. Therefore, runout effects must be removed prior to converting the data to the frequency domain.

The technique implemented here is to numerically remove the runout signal by applying a time domain filter to the recorded data. A laser tachometer was used to segment the vibration signal into numerous single revolution sections. The sections prior to the hammer impact are selected to construct an average runout signal that is subtracted from the recorded data. This sequence is repeated over 50 separates files (impacts) and the results averaged to reduce the noise level. Figure 1 shows the original and filtered signals. The target was excited at t = 0.05 s.

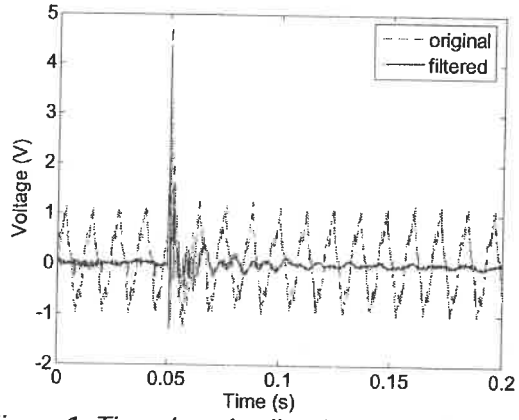

Figure 1: Time domain vibration signal filtering

SPEED-DEPENDENT FRF

Due to a number of sources (e.g., gyroscopic effects, bearings stiffness variation, mass unbalance, thermal changes, surface contact effects), the natural frequencies of the tool-holder-spindle are known to vary as a function of spindle speed. Figure 2 shows the varying FRFs at three selected spindle speeds for a 19 mm diameter, 77 mm overhang carbide tool blank

clamped in a shrink fit tool holder. To minimize thermal effects, all measurements were taken after a 40 min. stabilization period.

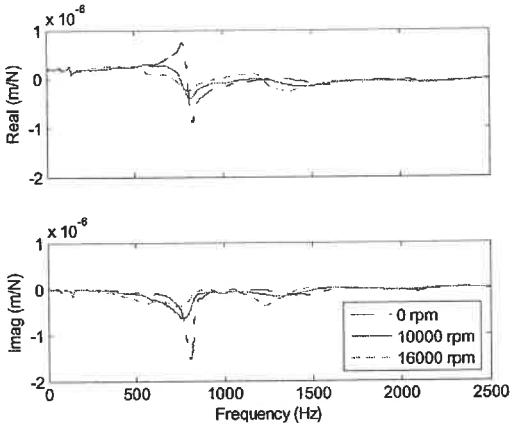

Figure 2: FRF speed dependence for a tool blank-shrink fit holder-spindle assembly.

ANALYTICAL TOOL TIP RESPONSE

In industrial applications, high-speed milling machines are typically equipped with a tool magazine that contains a number of tools-holder combinations. To reduce measurement time, it is preferred to predict the tool tip FRF rather than performing an impact test on each assembly.

Receptance Coupling Sunstructure Analysis (RCSA) was used in this study to couple spindle base receptances (identified experimentally at speed) to tool-holder models (based on Timoshenko beam theory).

A simple geometry steel "standard holder" (Figure 2, Table 1) was used to determine the spindle base receptances, R_{6a6a} . The first subscript for this 2x2 matrix indicates the sensor location while the latter indicates the hammer impact location.

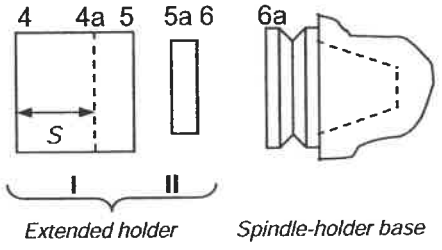

Figure 3: Standard holder geometry

Table 1: Standard holder substructure dimensions.

	OD (mm)	ID (mm)	Length (mm)
I	63.3	44.6	62.8
II	52.7	0	16.3

The notation for the structural receptances is:
R: single structure receptance matrix
RS: subassembly receptance matrix
G: full assembly receptance matrix
GS: partial assembly receptance matrix

Each receptance matrix is composed of four receptance elements H (displacement to force), L (displacement to moment), N (rotation to force), and P (rotation to moment).

The standard holder-spindle assembly displacement to force receptances are obtained by placing the sensor at coordinate 4 and the exciting the structure at the coordinates 4 (H_{44}) and 4a (H_{44a}). L_{44} is determined by first order finite difference:

$$L_{44} = \frac{H_{44} - H_{44a}}{S}, \tag{1}$$

where S is the distance between 4 and 4a (25.4 mm). By reciprocity, $L_{44} = N_{44}$. P_{44} is synthesized as:

$$P_{44} = \frac{L_{44}N_{44}}{H_{44}} = \frac{L_{44}^{\ 2}}{H_{44}}. \tag{2}$$

The standard holder-spindle assembly receptance matrix is then:

$$G_{44} = \begin{bmatrix} H_{44} & L_{44} \\ N_{44} & P_{44} \end{bmatrix}. \tag{3}$$

Given G_{44}, the spindle base receptance matrix R_{6a6a} is obtained by decoupling the extended holder:

$$R_{6a6a} = RS_{46}\left(RS_{44} - G_{44}\right)^{-1} RS_{64} - RS_{66}, \tag{4}$$

where the extended holder receptances are determined from beam models.

$$RS_{44} = R_{44} - R_{45}(R_{55} + R_{5a5a})^{-1} R_{54} \tag{5}$$

$$RS_{66} = R_{66} - R_{65a}(R_{55} + R_{5a5a})^{-1} R_{5a6} \tag{6}$$

$$RS_{46} = R_{45}(R_{55} + R_{5a5a})^{-1} R_{5a6} \quad (7)$$

$$RS_{64} = R_{65a}(R_{55} + R_{5a5a})^{-1} R_{54} \quad (8)$$

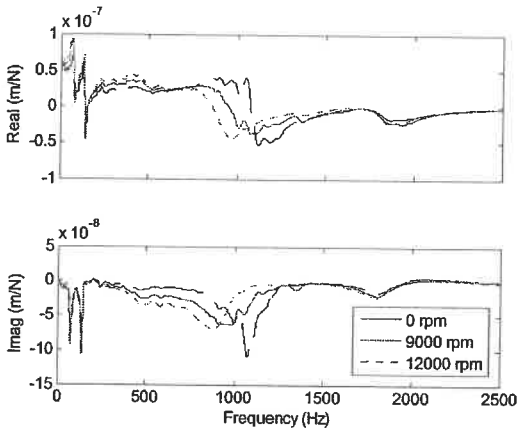

Figure 4: Standard holder H_{44} results at various spindle speeds.

Due to the speed dependence, the standard holder measurements are performed at multiple speeds within the spindle speed range of interest. See Fig. 4.

EXPERIMENTAL SETUP

Figure 5 shows the FRF measurement setup for the standard holder. Measurements were performed on a Mikron UCP 600 Vario milling machine equipped with a Step Tec 20000 rpm, 16 kW spindle. A Lion Precision C1-C capacitance probe was used to record the vibration response and a PCB 086B03 impact hammer was used to excite the system. A TTI LT-880 laser tachometer was used to record the once per revolution signal for runout filtering. A MLI MetalMax 6.0 data acquisition system was used for data collection.

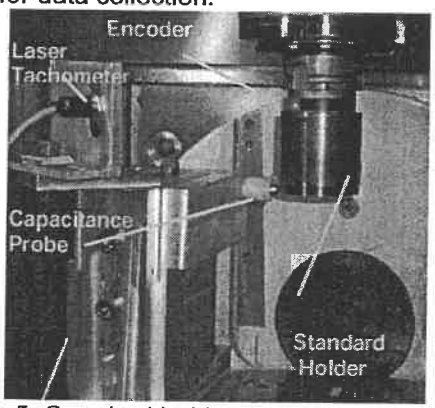

Figure 5: Standard holder rotating FRF measurement setup.

EXPERIMENTAL RESULTS

To validate the FRF predictions, experiments were conducted using a simply geometry solid holder (Figure 6 and Table 2). This holder meets the assumption of the rigidly connected beam sections.

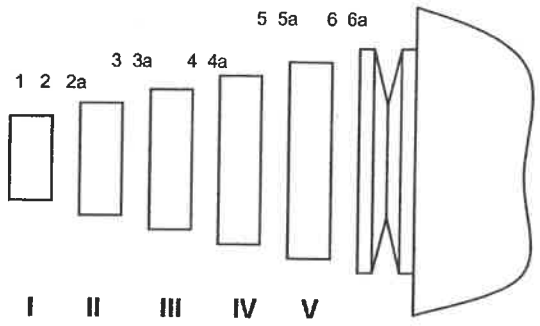

Figure 6: Solid holder geometry and coordinates.

Table 2: Solid holder substructure dimensions.

	OD (mm)	ID (mm)	Length (mm)
I	22.0	0	11.2
II	33.3	0	13.5
III	41.3	0	13.2
IV	47.4	0	11.6
V	52.6	0	13.1

Figure 7 shows a comparison between FRF measurements and predictions at {10000, 12000, and 16000) rpm for the solid holder free end. Good agreement is observed. The zero rpm measurement is also shown to identify the changes in the FRF.

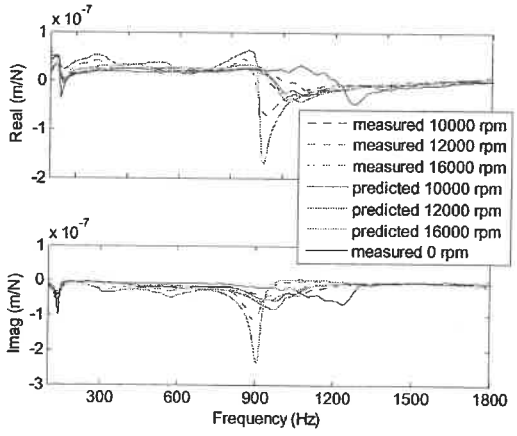

Figure 7: Solid holder FRF prediction and measurement at {10000, 12000, and 16000} rpm.

To further verify the approach, two 152.4 mm carbide tool blanks (12.7 mm and 25.4 mm diameters) were inserted in a Regofix collet holder. The overhang length was 127 mm in both cases. The dimensions of the tool-holder combinations are listed in Tables 3 and 4. The spindle speed was 10000 rpm.

Table 3: Collet holder with 12.7 mm diameter carbide blank. Here, I represents the tool overhang section and II to V represent the extended holder sections.

	OD (mm)	ID (mm)	Length(mm)
I	12.7	0	127.0
II	62.7	0	25.5
III	42.0	12.7	20.6
IV	42.0	35.1	11.5
V	42.0	0	34.0

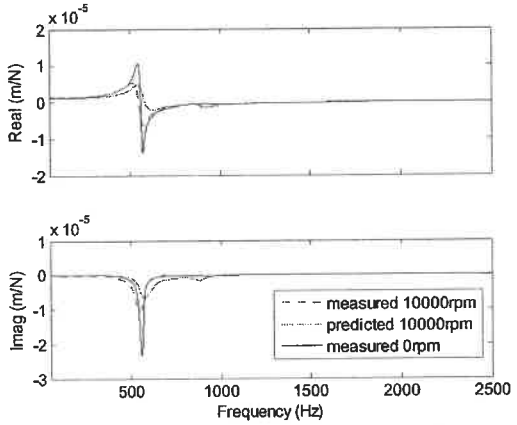

Figure 8: FRF for collet holder with 12.7 mm diameter carbide blank.

Table 4: Collet holder with 25.4 mm diameter carbide blank

	OD (mm)	ID (mm)	Length (mm)
I	25.4	0	127.0
II	62.7	0	25.5
III	42.0	25.4	20.6
IV	42.0	35.1	11.5
V	42.0	0	34.0

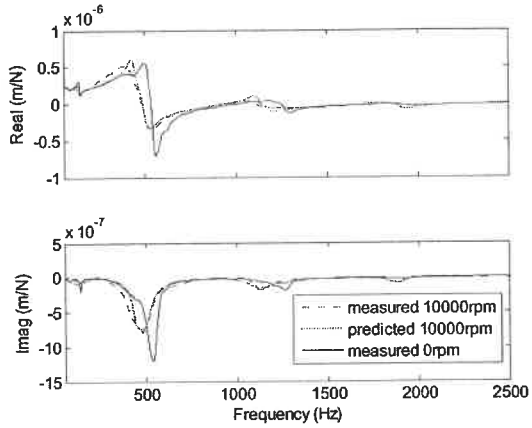

Figure 9: FRF for collet holder with 25.4 mm diameter carbide blank.

Again, the RCSA approach provides reasonable predictions. Changes in the measured and predicted rotating FRFs relative to the zero rpm measurements are observed.

CONCLUSIONS

This paper describes the application of Receptance Coupling Substructure Analysis (RCSA) to frequency response predictions for rotating tool-holder-spindle assemblies. Standard holder measurements are performed at speed to identify changes in the spindle. Then the spindle FRFs are coupled to Timoshenko beam models of the tool and holder. To improve prediction quality, it was necessary to implement time domain filtering to remove runout and averaging to reduce noise. Experimental results show good agreement with prediction and identify the variation in frequency response with spindle speed for the spindle tested here.

ACKNOWLEGEMENTS

This work was supported by the National Science Foundation (DMI-0238019) and TechSolve.

REFERENCES

1. Schmitz, T., and Duncan, G.S., 2005, Three-Component Receptance Coupling Substructure Analysis for Tool Point Dynamics Prediction, *Journal of Manufacturing Science and Engineering*, **127**/4: 781-790.
2. Nelson, H.D., 1980, A Finite Rotating Shaft Element Using Timoshenko Beam Theory, *Journal of Mechanical Design*, **102**: 793-803.

FLEXURE-BASED MESO-LEVEL STAGE DRIVEN BY LINEAR PIEZO MOTORS

Sumet Heamawatanachai, Brendan Corbin, Laura Emig, Eberhard Bamberg
Precision Design Lab, Department of Mechanical Engineering, University of Utah
Salt Lake City, UT 84112, USA

ABSTRACT

This paper presents the design and experiments of a one-axis flexural stage with a range of ±0.75 mm. The flexural stage uses a monolithic design based on flexures to eliminate stiction in combination with a piezo linear motor to avoid backlash. Closed position feedback control is achieved with a non-contact optical encoder with a resolution of 50 nanometers. The flexure element can typically be modeled as a spring element. Therefore, it ideally has a linear relation between force and deflection. But actually, the results from the experiments on this flexure stage show that it tends to have a linear relation between force and deflection at small deflections (less than 400 microns). At deflections larger than 400 microns, the relation becomes nonlinear. The experimental results on the nonlinear property of the flexure element are presented in this paper. The flexural stage is driven directly by linear piezo motors whose working principle is based on resonance of piezo-electric elements that drive the friction plate which is attached to the moving frame. The fact that the motors are based on friction has an appealing feature: When the stage reaches the target position, the motors can be turned off and hold the position by the static friction between the friction shoes and the friction plates. Hence, it can completely avoid the servo noise and also limit the heat generated from the motors. The experiments prove that this static friction is enough to hold the stage and are also provided in this paper.

INTRODUCTION

The emerging of meso-level machining creates increasing demand on developing linear stages with travels ranging from zero to a few millimeters. The short travel creates a problem for most conventional stages which tend to be based on ball screws and rolling element bearings. For short travels, the hydrodynamic lubrication layer necessary to prevent fretting of the rolling elements cannot always be formed, which can significantly reduce the life of the ball screw and bearings [1]. Flexure based stages, on the other hand, don't use rolling element bearings, thereby avoiding this issue. However, commercially available flexure stages tend to be driven by piezo-stack actuators, whose limited strain tends to limit the travel of such stages to a few hundreds of microns.

This paper presents a new type of linear stage that combines the advantages of conventional stages with those of flexure-based systems [2]. The moving part of the stage is supported by flexures and is driven directly by linear piezo motors whose working principle is based on resonance of piezo-electric elements that create very small steps on the order of nanometers at very high frequencies. This oscillation is then transferred to a friction plate, thereby generating linear motion. As such, the travel of these stages is limited by the range of the flexures but not by the motors.

As is well known, flexural bearings create extremely straight motion and if designed properly, provide tremendous stiffness in all directions except the direction of motion. They furthermore exhibit neither friction nor stiction, which is a critical feature in ultra-precision motion control where the reversal of an axis' motion typically causes a tracking error due to the change from kinetic to static friction.

The fact that the motors are based on friction has a very interesting side effect: Once the slide has reached its target position, no servo control is required to hold this position. Hence, the motors can be turned off, which not only completely avoids any kind of servo noise but also limits the amount of heat generated in the system. This, however, is only true for external forces that do not exceed the frictional force between the motor and the friction plate. There is a difficulty, though; linear piezo motors tend to exhibit a significant non-linearity in the motor velocity response versus the command voltage. The resulting dead-band where the motor creates no velocity despite a non-zero command voltage needs to be accounted for in the control system in order to minimize servo errors during a move. Also of concern is the motor mount. The

motors must be preloaded against the friction plate in order to generate a thrust force. In order to maintain preload and to account for changing distances between the motor and friction plate, a compliant mount is needed. However, to avoid backlash, the mount also needs to be very rigid.

DESIGN AND CONTROL SYSTEM

The flexural stage in Figure 1 has been designed to provide a travel of ±0.75 mm. The stage is a monolithic design where the inner frame (moving frame) is supported by four flexure beams.

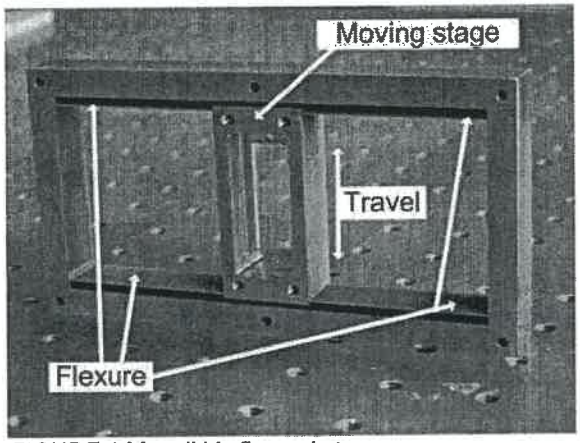

FIGURE 1.Monolithic flexural stage

The stage is driven directly by two linear piezo motors (*HR4-1-S-3*, Nanomotion Ltd) which sit on the back plate. As a result, the flexural stage provides extremely straight motion with no backlash. The friction shoes of the motors with a proper preload force push against the friction plates that are attached to the inner frame. As can be seen in Figure 2, the two HR4 motors fit inside the cavities created by the flexure beams of the moving stage and drive the moving stage from opposite sides. This requires the direction of one of the motors to be opposite from the other. Because both HR4 motors are driven by the same AB5 amplifier, a special y-connector is required where one of the motor connectors has the forward and reverse signals reversed.

The friction strips come with a sticky tape attached to the back and for typical applications, this is the recommended means of securing the strip. In this case, however, the length of the strips is rather short and the sticky tape proved to be too compliant. As a result, the moving frame drifted over time. Replacing the sticky tape with epoxy solved this issue.

The digital encoder (RGH 24, Renishaw) is fixed to the center of the back plate and read the position of the moving frame by scanning the encoder the strip that is attached to the moving frame.

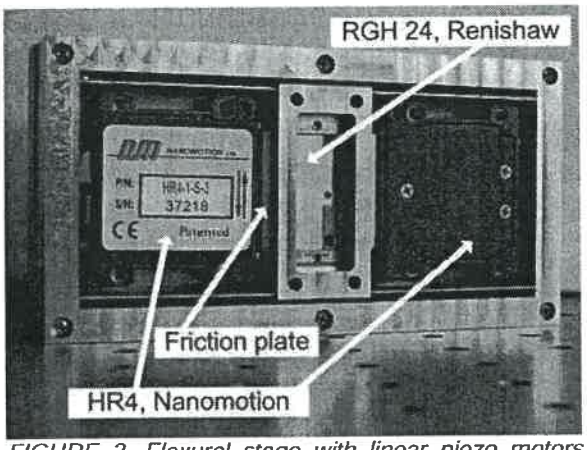

FIGURE 2. Flexural stage with linear piezo motors and non-contact digital encoder (full assembly)

The flexural stage is controlled in a closed-loop by a PID controller at a rate of 62.5 micro-seconds (*PXI-7354*, National Instruments). The position feedback from the encoder that is sent to the PID controller is a digital signal with a resolution of 50 nanometers. The motor driver (*AB5*, Nanomotion Ltd) used to drive the motors receives the command voltage from the PID controller and transforms it to a high frequency signal sent to the motors in order to create movement of the friction shoes.

EXPERIMENTS AND RESULTS

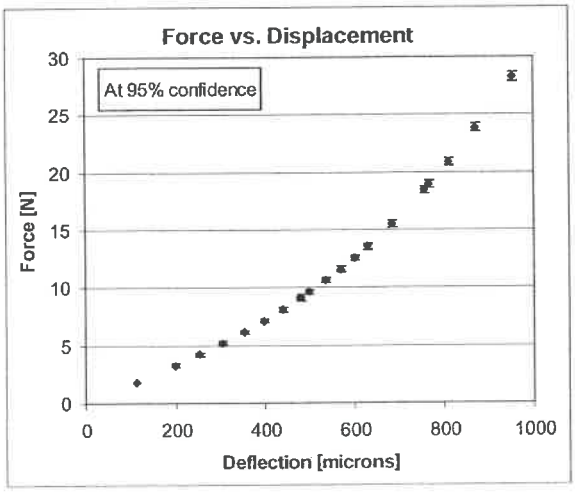

FIGURE 3. The relation of force and deflection of the flexural stage

The force vs. deflection experiment has been setup by attaching the inner frame of the flexure

stage with a set of deadweights. By increasing the weight and measuring the position from the encoder, the relation between force and deflection from the center of the flexure stage can be determined as shown in Figure 3.

From Figure 3, the results show that the flexure stage tends to have an almost linear relationship when the deflection is less than 400 microns and develops a non-linear relationship at deflections larger than 400 microns. The linear range of 400 microns is quite small when compared with the 40 mm length of the flexure beam. There are not only bending stresses applied to the beam but also an axial stress due to the symmetry constraint of this design. This axial stress limits the linearity range to less than a normal flexure system. But this design has some advantages: each flexure uses only a single beam element which reduces the chance of twisting the beams. As a result, it can hold a larger weight in the vertical direction, and it has a very compact stage size which makes it easy to manufacture. Also, the symmetry of the flexures, while limiting the axial travel, prevents any parasitic motion of the stage, thereby creating an extremely straight motion of the moving stage.

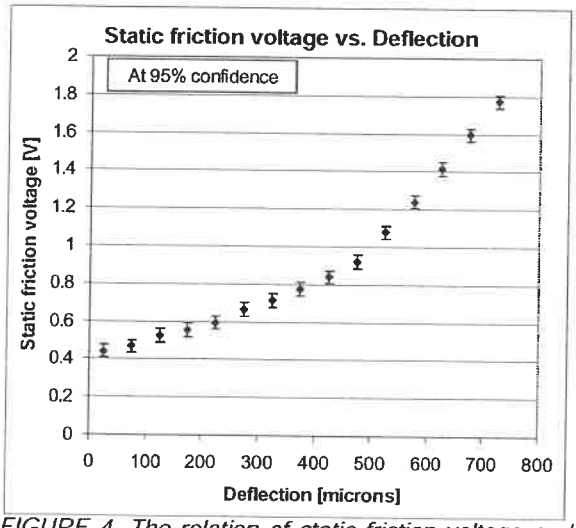

FIGURE 4. The relation of static friction voltage and deflection of the flexural stage

The static friction voltage is the minimum command voltage that is required to start the moving of the stage. This voltage offset is a result of the inherent friction in the drive system. As such, as the stage is commanded to move, the servo voltage will start at this offset rather than at zero Volts. This dramatically increases the controllability of linear piezo motors.

In the case of a flexure based system which ideally has no friction, the static friction voltage is the voltage needed to overcome the spring force of the flexure which is related with its deflection in addition to the friction of the motor. As shown in Figure 4, the static friction voltage increases linearly versus deflection for the first 400 microns from the center position. After this point of 400 microns, the relation becomes non-linear. These results agree with the results from Figure 3. In the neutral position of the stage at a deflection of 0 microns, the static friction voltage is about 0.4 V which means that the magnitude of the dead-band of these motors is 0.4 V. To improve the dynamic positioning control of the flexure stage, the static compensation voltage, which typically is a static value, may be dynamically updated according to Figure 4 to compensate for the non-linear effect.

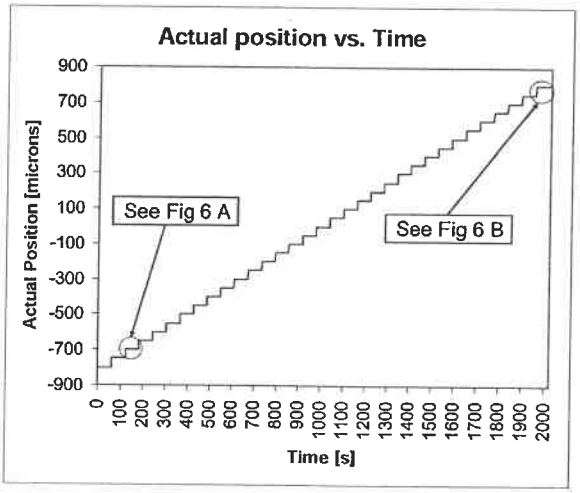

FIGURE 5. The actual position of the flexural stage vs. time (the motors are turned off at the beginning of each step and hold for 1 minute before moving to the next position)

Most servo systems, after having reached the target position, maintain this location through active servo control, meaning the drive system remains under power. As such, the system is subject to servo noise which causes small amounts of motions that induce errors.
Drive systems based on linear piezo motors can make use of the inherent friction of the drive system and allow the motors to be turned off completely once the target position has been reached. This also eliminates heat generation from the motors, thereby increasing the thermal stability of the system.
Therefore, to hold the position of the flexural stage, the static friction between the friction

shoe and friction plate is an important factor in resisting the spring force of the flexure and any applied external force as well. Figure 5 presents the results of an experiment that shows the travel of the stage over its entire range. The stage was positioned in 50 micron increments and held in place by turning off the motors at the end of each step.

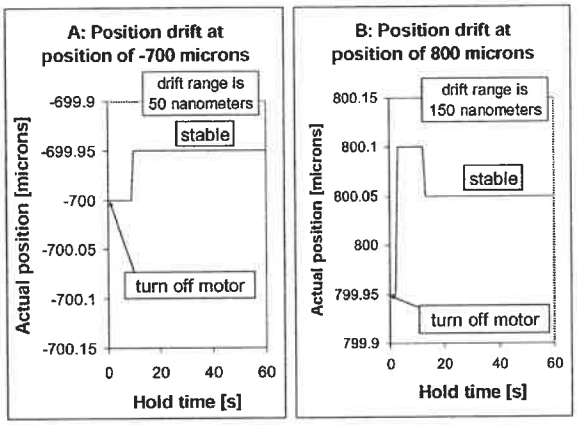

FIGURE 6. The position drift vs. time at hold position of -700 and 800 microns. The motors are turned off at the beginning of each control position and hold the position for one minute before moving to the next position.

Figure 6 shows the position of the stage as a function of time in more detail. As can be seen, the position of the stage drifts after the motors are turned off but the drift is limited to a maximum of 50 nanometers for Figure 6A and 150 nanometers for Figure 6B.

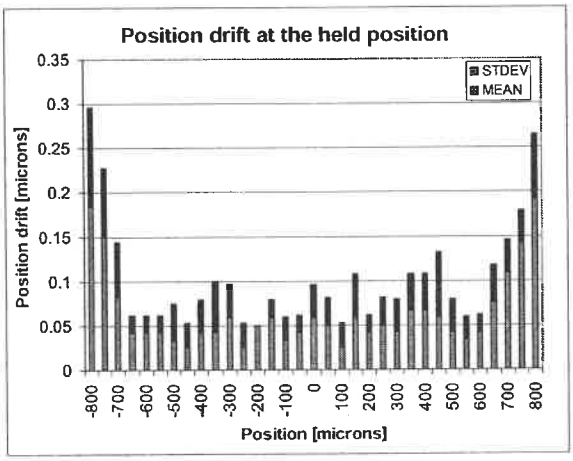

FIGURE 7. The mean and standard deviation (STDEV) of the position drift from 6 experiments (after waiting 1 minute at each brake position)

Figure 7 shows the mean values and the standard deviations from 6 experiments of the position drift after a holding time of 1 minute at each position with the motors turned off. The results show that the positions that are further away from the center tend to exhibit larger position drifts. The position drift from all experiments is less than 0.4 micron which is acceptable for most applications in meso-level machining.

CONCLUSIONS

We have shown a new type of linear stage with greatly increased travel compared to standard nanopositioning stages. The stage is a monolithic flexure-based design that in combination with two linear piezo motors exhibits no detectable backlash or error motion.

The flexure based system ideally has no friction; the major force that the motors need to overcome is the spring force from the flexure as well as any external force applied to the stage, which is predictable.

The static friction between the motor and the friction strips is sufficient to hold the stage at any position over the entire length. This allows the motors to be turned off at each position, thereby eliminating heat generation from the motors. As a result, thermal drift of the system is all but eliminated.

The quality of the mounting of the friction plates to the frame is very important. The standard sticky tape is too compliant owing to the short length of the friction strips. Replacing the tape with epoxy dramatically increases the performance of such a drive system.

FUTURE WORK

The non-linear behavior of the flexure affects the static friction voltage, which no longer is a static value but increases as the flexures are moved away from their neutral positions. For increased positioning accuracy and even better dynamic performance, a control algorithm that allows this offset voltage to be updated dynamically will be developed.

REFERENCES

[1] A.H. Slocum, "Precision Machine Design", Society of Manufacturing Engineers, 1994.

[2] E. Bamberg, S. Heamawatanachai, J.D. Jorgensen, "Flexural micro-EDM head for increased productivity of micro-holes", ASPE Proc. 2005, pp. 82-85.

A QUANTITATIVE, CONSTRAINT-BASED DESIGN METHOD FOR MULTI-AXIS FLEXURE STAGES FOR PRECISION POSITIONING EQUIPMENT

Jonathan Hopkins and Martin L. Culpepper
Department of Mechanical Engineering
Laboratory for Manufacturing and Productivity
Massachusetts Institute of Technology
Cambridge, MA 02193 USA

SYNOPSIS

In this paper we introduce a new approach to the conceptual design of flexures and compliant mechanisms that draws upon the constraint-based design (CBD) principles of complimentary patterns and principles from projective geometry. We use projective geometric primitives to create generalized sets of 3D geometries (volumes, surfaces and lines) that represent either (1) a flexure mechanism's degrees-of-freedom or (2) the possible flexure constraints that result in these degrees of freedom. These shapes are intuitive for a designer to understand and the shapes may be represented mathematically. As such, this approach provides the necessary elements for a computer (mathematics) and a designer (shapes and visualization) to cooperate during design.

The final result of the work is to provide a set of topological shapes that represent the freedoms and constraints of parallel flexure systems. These freedom and constraint topologies (FACT) provide the foundation for creating software-based design tools for precision flexures. The explanation of FACT is somewhat abstract; therefore some hardware-focused designers may find that a bit of patience is required before the utility becomes apparent to precision engineering applications. This paper ends with a section discussing the practical utility of the abstract concepts.

INTRODUCTION

The essence of constraint-based design is the process of selecting and arranging machine elements (e.g. flexures) in a geometric layout that endows a device with desired positioning and alignment performance. Constraint-based design principles are central to precision engineering as the layout of a machine's constraints set limits on a device's degrees-of-freedom, stiffness, load capacity, repeatability, stability, etc... For over 100 years [1], CBD has been practiced by using a combination of linear visualization techniques (intersection of constraint and rotation lines), practical experience and rules of thumb. These conventional techniques are easily used to create precision flexure stages wherein the motions are planar (x, y and theta-z). A great deal of CBD experience, and sometimes trial-and-error, are required to design flexures that are simultaneously capable of planar and non-planar (theta-x, theta-y and z) motions.

The subject of this paper is based upon (1) the visualization of many different types of complex 3D volumes/surface and (2) the different interactions between these shapes. The unique aspect of this method is that the shapes and their well-known equations enable designers to approach constraint-based design using (1) the conventional semi-qualitative design rules of thumb and (2) new qualitative shapes and the quantitative equations that describe them. There are over 50 shapes-equations, that represent the full range of solutions to multi-axis flexures. As such, we are unable to discuss all of them in detail herein. We choose instead to pay special attention to the case where three constraints and three degrees of freedom exist.

BACKGROUND

Degrees of freedom and constraints

A first principle of constraint-based design is that a rigid body has six degrees of freedom — three orthogonal translations and three orthogonal rotations – and any non-redundant constraint upon a body removes one degree-of-freedom. The equation that expresses this principle is:

$$R = 6 - C \qquad (1)$$

where C is the number of non-redundant constraints and R is the number of independent degrees of freedom. This is illustrated in Fig. 1.

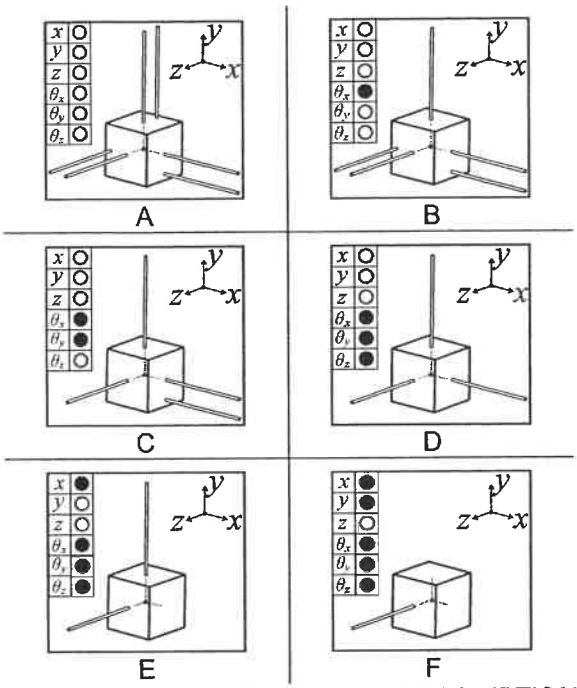

FIGURE 1. CONVENTIONAL DESCRIPTION SHOWING THE RELATIONSHIP BETWEEN CONSTRAINTS AND FREEDOMS. OPEN CIRCILES REPRESENT FREEDOMS.

It is customary in CBD to idealize flexure constraints as shown in the top of Fig. 2 [2,3]. Such constraints have zero compliance along their line of action and they have zero stiffness orthogonal to their line of action.

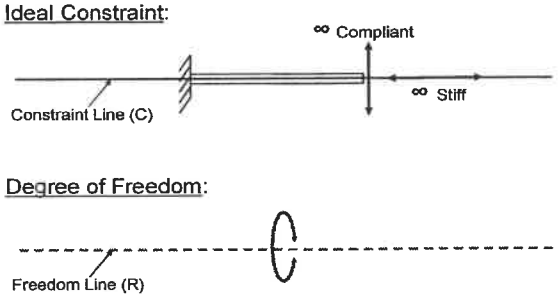

FIGURE 2. MODELING CONSTRAINTS AND FREEDOMS VIA CBD

This type of modeling approach is appropriate for finding the realistic directions of greatest compliance for a rigid stage constrained by flexible beams. Blanding observed that any stage's degrees-of-freedom could be represented by rotations about freedom lines [2]. This is shown at the bottom of Fig. 2. Blanding noted that even pure translational degrees of freedom could be modeled as a rotational freedom line that is perpendicular to the direction of translation located infinitely far away from the object translating.

The principle of complimentary patterns

Blanding's Rule of Complementary Patterns [2] defines the qualitative relationship between constraints and degrees of freedom. It states that every freedom line intersects every constraint line. Figure 3 shows an example of a block constrained by five non-redundant constraints. From Eq. 1 we would expect the block to move with only one degree-of-freedom. Blanding's Rule of Complementary Patterns finds this pure rotational freedom line to be the dotted red line. The constraints all intersect the freedom line (red dotted line). The principles of projective geometry are useful here to show that parallel lines intersect at infinity. The constraints at the bottom left therefore intersect the freedom line "at infinity". The constraints at the top and right intersect the freedom line in finite space, i.e. the top-middle-rear of the rigid block.

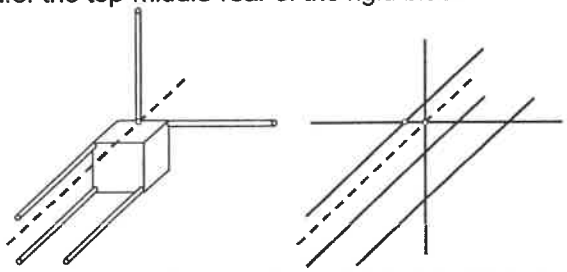

FIGURE 3. EXAMPLE OF ONE DEGREE-OF-FREEDOM FLEXURE SYSTEM

It is important to note that since the relationship between constraints and degrees of freedom is independent of the stage's shape, size, and location, the block could be removed from the picture entirely leaving only constraint lines (blue) and freedom (red) as shown in Fig. 3 to define the design problem.

THE IMPORTANCE OF DIFFERENT DESIGN CONCEPTS - FINDING ALL POSSIBLE FREEDOM AND CONSTRAINT TOPOLOGIES

The preceding principles help designers create functional designs, but they do not provide designers with a way to consider alternate concepts that possess the same functional characteristics. For instance, if one desires a flexure that has the degree-of-freedom as shown in Fig. 4, the design that is shown is necessary and sufficient – but what other designs could provide the same function? It is hard to describe the design in Fig. 4 as the best design without knowing what other designs could be used.

In many instances there are an infinite number of freedom lines that satisfy the Rule of Complementary Patterns. Consider the

example shown in Fig. 4 of a block constrained by two non-redundant constraints whose constraint lines (blue) intersect inside the block. The degree-of-freedom solutions include every freedom line (red) that intersects both constraints (blue).

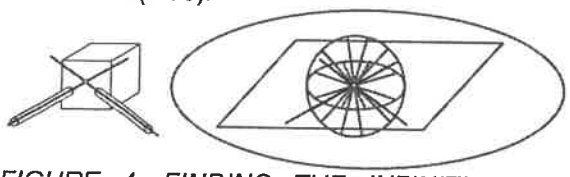

FIGURE 4. FINDING THE INFINITE PURE ROTATIONAL FREEDOM LINES (RED) FOR A BLOCK CONSTRAINED BY TWO CONSTRAINTS WHOSE CONSTRAINT LINES (BLUE) INTERSECT INSIDE THE BLOCK

It is also important to note that the constraints on the left of Fig. 4 are equivalent to any other constraints [2,3] in the plane of the first two constraints, which share the same intersection of the first two constraints. Thus a pencil can be used to represent the constraints in this design. From projective geometry, a pencil is a planar geometric shape that contains all possible coplanar lines that intersect in one point. The pencil in this case would share the intersection of the two constraints on the left of Fig. 4 and lie in the plane of the constraints shown in Fig. 4. We now have a geometric shape, which represents all arrangement of constraints that provide the same function as the design in Fig. 4.

We may do the same thing with the four degrees of freedom that must exist in this design. Considering the right side of Fig. 4 – the sphere represents an infinite number of freedom lines that satisfy this condition and intersect the constraint lines' intersection point. The plane drawn in Fig. 4 represents every freedom line that lies on the plane of the constraint lines and would therefore intersect the constraints. The hoop in Fig. 4 represents a single freedom line that is "infinitely" far from the center/intersection point within block. From projective geometry, a hoop of radius approaching infinity is equivalent to a straight line whose distance from the hoop's center is approaching infinity. A rotation about this line/hoop would yield a translation degree-of-freedom that is normal to the plane of the hoop and along the axis of symmetry of the hoop. Screw-like motions with non-zero pitch also exist as degree-of-freedom solutions for this example and could be found using screw theory. These shapes are omitted from Fig. 4 for clarity.

The preceding example shows that there is a multiplicity of freedoms that may be obtained with this design and they may be represented in general terms using the projective geometric shapes in Fig. 4. The shapes for freedoms and constraints are taken from projective geometry and equations/logical representations for them may be taken from regular geometry (e.g. equations of spheres, planes and vectors). This forms the quantitative basis for constraint-based design.

It can be shown that all flexure problems, 1 – 5 degrees of freedom, have general shapes that represent the freedoms and constraints and that these constraint and freedom shapes may be matched according to the rule of complimentary patterns. This is a powerful concept in that there are a finite number of shapes that represent all possible ways to constraint a flexure device. These shapes may then be mapped to desired motions, i.e. freedoms. As such, a designer can instantly relate desired motion, i.e. red freedom shapes, to a finite number of constraint shapes. In some instances, there are several constraint shape sets that can solve a given motion problem. In other cases, there are no solutions to a desire flexure motion problem. Either way, it is now possible for a designer to know and visualize what is possible and not possible in terms of different design concepts. The FACT shapes can be used to guide the designer in selecting the right lines from within those shapes to replace by physical flexure constraints in a real design.

Unfortunately, there are over 50 shapes and thus we are unable to discuss them all in this brief paper. Instead, we show the matches for one case, where three degrees-of-freedom are obtained with three constraints. Figure 5 shows the mapping of constraints (left) and freedoms (right). We refer to the matching sets from top to bottom as sets a – f. For instance, if the motion desired is represented by the red freedom lines in set a (the top set) – two rotations about skew lines in two different planes and a translation normal to those planes (e.g. the hoop), then these motions can be obtained by selecting three lines from the shapes on the left. The lines in these shapes are parallel within each plane and skew between each plane. If one examines these constraints and freedom topologies by overlaying them, one will find that this matching satisfies the principle of complementary patterns.

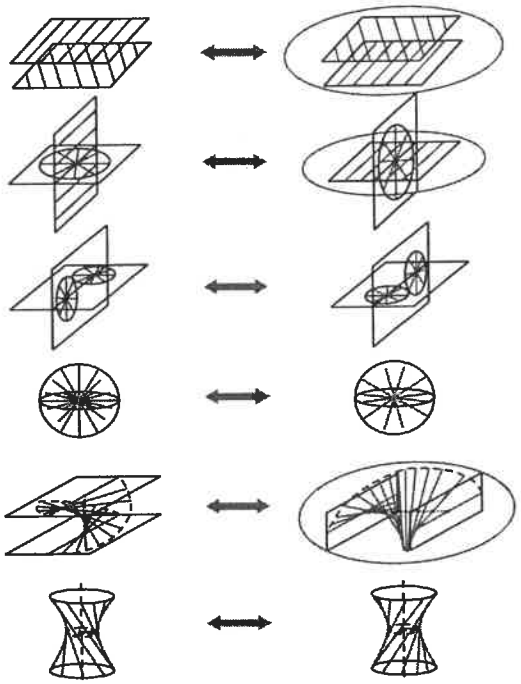

FIGURE 5. SOME EXAMPLES OF CONSTRAINT (LEFT) AND CORRESPONDING FREEDOMS (RIGHT)

Likewise set d (the spheres with radial lines) represents three rotational degrees of freedom about a central point. This function may be obtained by selecting three blue constraint lines from the left sphere. These three non-collinear constraints intersect at a common point and would therefore result in rotational degrees of freedom about the point of intersection. Again these matching satisfy the principle of complementary patterns.

THE PRACTICAL UTILITY OF THIS WORK

As noted previously, we are unable to show and fully describe all freedom and constraint topologies that are pertinent to precision flexure design. This information will come in a follow on paper. It is important however for us to describe how the full set of shapes would be useful to precision machine designers. The full set of shapes form an important design guide as they enable a designer to rapidly match a desired flexure motion performance with all possible flexure solutions. It is impractical to memorize all of the topologies and their equations and so the best way to take advantage of this knowledge is to integrate it within a software design tool that contains this information and makes it readily available to a designer in graphical and mathematic forms. We are presently working with the Virtual Reality Applications Center at Iowa State University to implement these shapes, their parametric equations and precision engineering principles to create an FEA-like design tool which uses virtual reality to display/overlap the topologies/shapes, enables a designer to select desired designs, and then performs optimization of the flexure kinematics, thermal stability and load capacity using the equations of the shapes and equations for stiffness, kinematics and thermal errors.

OTHER BENEFITS OF THE FACT METHOD

It should be noted that if one selects more than the desired number of constraints from an available constraint shape, the additional constraints do not remove additional degrees of freedom. That is, they are redundant constraints. This is an important observation as it enables flexure designers to see which constraints they may select to improve the symmetry of a flexure design (e.g. for thermal stability) or to improve the load capacity of a flexure without effecting the motions of the flexure.

ACKNOWLEDGEMENTS

This material is based upon work supported by the National Science Foundation under Grant No. DMI-0500272: Constraint-based Compliant Mechanism Design Using Virtual Reality as a Design Interface.

REFERENCES

1. Maxwell JC. General Considerations Concerning Scientific Apparatus. The Scientific Papers of James Clerk Maxwell. Dover Press. 1890;2;505–21.
2. D. L. Blanding, "Exact Constraint: Machine Design Using Kinematic Principles" (1999)
3. Hale L. Ph.D. thesis. Principles and techniques for designing precision machines. Massachusetts Institute of Technology; 1999.

ANALYSIS OF TEMPERATURE DISTRIBUTION AND OPTIMIZATION OF THE CONFIGURATION AT HEATING TOOL IN THE CHIP BONDING PROCESS AT CAMERA MODULE OF MOBILE PHONE

In Kim[1], Sung-Hwan Kweon[1], and Seung-Han Yang[1]
[1]School of Mechanical Engineering
Kyungpook National University
Daegu, 702-701, Republic of Korea

INSTRODUCTION

Recently, the demand of camera phone is remarkably increasing with the development of technology at the mobile phone market[1]. The core part of the camera phone is the camera module which consists of a Complementary Metal-Oxide Semiconductor (CMOS) chip, Adhesive conductive film (ACF) and Flexible PCB (FPCB). The camera module is manufactured in the following sequence. 1. Bonding of CMOS chip with Flexible PCB (FPCB) with ACF in between, 2. Packing and 3.Final inspection. The bonding process is carried out using flip mounting technology. The flip mounting technology is a method to attach the CMOS chip with PCB by electronic and mechanical means. The flip mounting technology varies with respect to i) the material ii) shape of bump and iii) the connecting method, Further this technology can be divided according to the connecting methods. The first method is using the soldering process, second method is

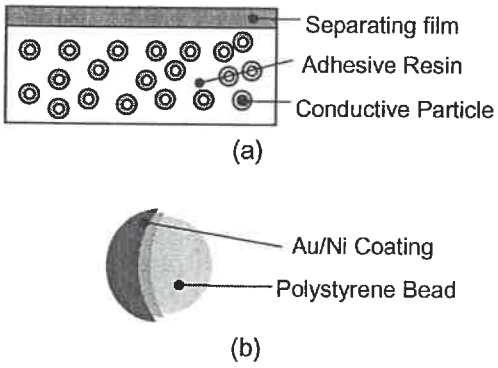

FIGURE 1. (a)Schematic Diagram of ACF (b) Conductive Particle

by employing heat-supersonic method and the third method is by using the adhesive process. This paper deals with adhesive method which is now widely used in industries.

FIGURE 1 shows the structure of ACF used in adhesive process [2-4]. The flip chip bonding process using ACF is explained as follows; The ACF consists of conductive particles and adhesive resins packed between separating films. The ACF is firmly attached with the PCB

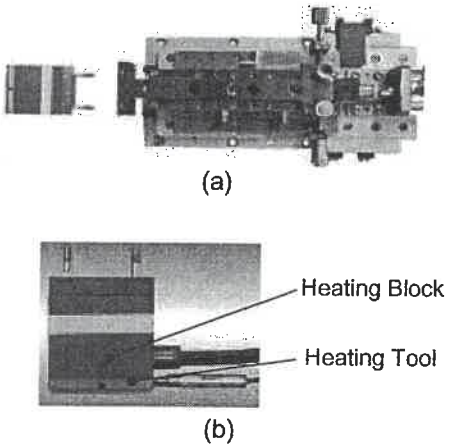

FIGURE 2. The Flip Chip Bonding Equipment (a) Whole model (b) Heating Unit

by applying a low pressure and the separating film is removed. The position of the camera module integrated chip (CMOS) is then aligned to that of the substrate. And the final bonding is accomplished by heating and pressing, as shown in FIGURE 3. At this time, the pressure is set to 2~3MPa and the temperature is set to 180~220℃, where the temperature depends on the kind of ACF used. The two opposite faces of the CMOS and the substrate with ACF now acts like an electrode. When the adhesive resin melts due to temperature and pressure, high conductivity is achieved between the faces of the electrode as the conductive particles are crashed in the small space between CMOS and PCB [5]. In the other parts except the faced electrode, high insulation is obtained. The high

adhesive strength of ACF results in firm mechanical attachment of CMOS with the PCB substrate.

In these processes, the failure of ACF attachment is considered as a serious defect. This is caused by excessive variation of temperature in the bonding surface of the flip chip bonding tool. It is observed that the temperature variation between central part and the surrounding areas of the bonding surface is high, which has resulted in poor adhesion. Therefore, minimizing temperature variation at the bonding surface is a important concern in this process.

The flip chip bonding equipment is shown in FIGURE 2. The lower part of the bonding unit is called 'Heating Unit'. The Heating unit contains of a heating block with a cylindrical cartridge type heater and a heating tool. On the upper side of the heating unit. ceramic blocks are assembled for the purpose of insulating. The heater is adjusted by a PID control. A K-type thermocouple located between the heater and the bonding surface is used as a feedback sensor.

CONFIGURATION OF THE HEATING UNIT

The purpose of this paper is to find an optimal condition to minimize the temperature variation of the bonding surface at the heating unit with a cylindrical cartridge heater as the heating source. The heating unit used in this work has several bolt holes for fixing the heater and the temperature sensor. The counter-bores also exist for assembling the heating block with the heating tool. Most of the parts have chamfer. To prevent thermal deformation the surface between the heating block and the heating tool, are made with small progressive steps.

The heat source is considered as a simple solid cylinder of radius r and length L in which energy generated as shown FIGURE 4(b). The energy generated is assumed to be constant because of PID feedback controller. It is also assumed that the temperature is not changed with respect to the time (steady-state).

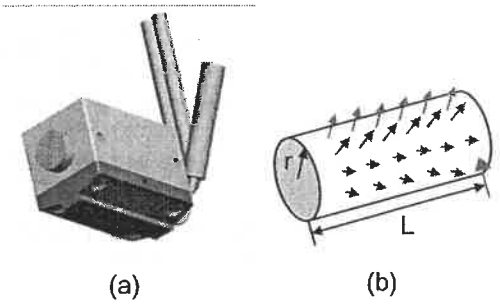

FIGURE 4. The Cylindrical cartridge heater (a) Heating Unit (b) Modeling of Heater

$$\frac{1}{r}\frac{\partial}{\partial r}(kr\frac{\partial T}{\partial r})+\frac{1}{r^2}\frac{\partial}{\partial \phi}(k\frac{\partial T}{\partial \phi})+\frac{\partial}{\partial z}(k\frac{\partial T}{\partial z})+\dot{q}=\rho c_p\frac{\partial T}{\partial t}$$

Where,

$$\rho c_p\frac{\partial T}{\partial t}=0,\quad \frac{1}{r^2}\frac{\partial}{\partial \phi}(k\frac{\partial T}{\partial \phi})=0,\quad \frac{\partial}{\partial z}(k\frac{\partial T}{\partial z})=0$$

FINITE ELEMENT ANALYSIS OF THE HEATING UNIT

Except the fixing bolt for the heater and the temperature sensor, the temperature distribution of the current model (with the bolt for only for assembly) is analyzed using a FEM software as shown in FIGURE 5(a) and 5(b). The central temperature distribution of the bonding surface

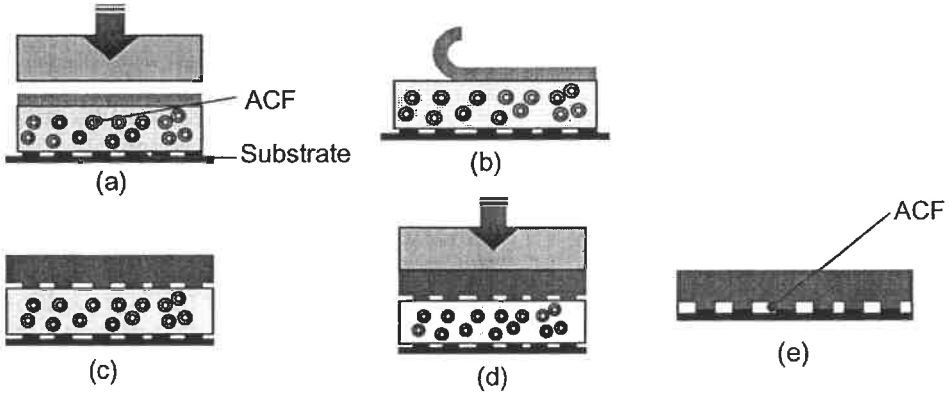

FIGURE 3. The Principle of attachment process using ACF. (a)Pre-c (b)Removing the separator film (c)Aligning the IC to the substrate (d)Final-Bonding (e)Completion

is shown in FIGURE 5(c).

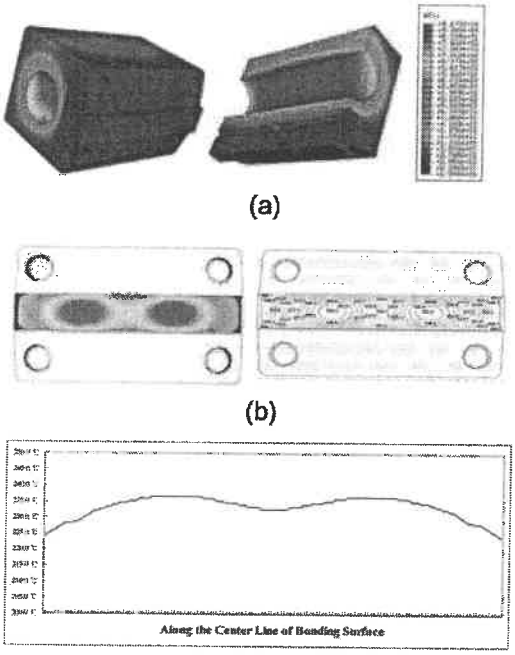

(a)

(b)

(c)

FIGURE 5. The Analyzed Result (a) The Result of whole model (b) The Result of the bonding surface (c) The temperature distribution along the center line in the bonding surface

A temperature drop at the central area in the bonding surface is noticed because the feedback sensor and fixing bolt are missing. It depends on the kind of sensor and its position. If the kind and position of sensor are known, and then the size, number and position of fixing bolt can be decided accordingly.

THE BASIC MODEL AND ANALYSIS

A basic model, which is the simplest feature without holes for assembly and progressive steps, is considered for optimization using FEM analysis and the design of experiments. From FIGURE 5, it is noted that a small bolt hole can change the temperature gradient at the bonding surface. If the fixing bolt is assembled, the temperature distribution is altered as shown in FIGURE 5. So, it is concluded that the bolt hole should not exist at the center side of the heating tool.

Suggested basic model is shown in FIGURE 6(a) and the analyzed result is shown as FIGURE 6(b) under the same conditions of FIGURE 5.

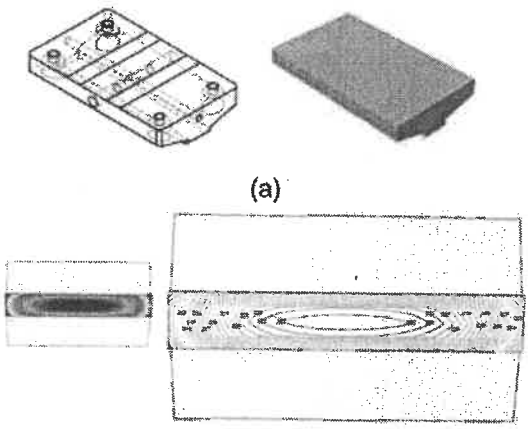

(a)

(b)

FIGURE 6. The Basic Model and the Analyzed Result (a) Current Model and Basic Model (b) The Result of the bonding surface at the Basic Model

CHANGING THE CONDITIONS

Because the fixing bolt and the chamfers are all omitted, remaining variable are the size and the position of the heater. From the heater, constant heat flux is flown out by the PID controller.

Configuration of the Heating Unit

When the size of the heater is bigger than the current model, the temperature distribution of the bonding surface is shown in FIGURE 7 under the same condition.

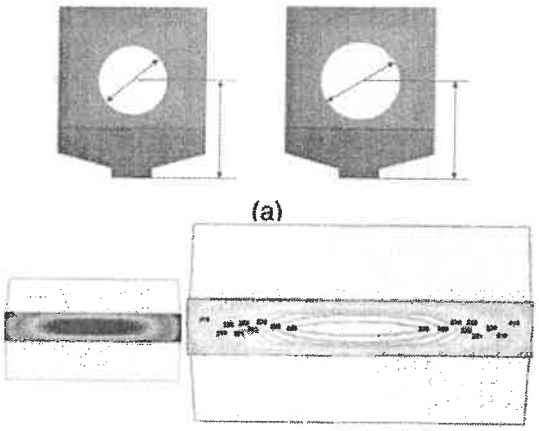

(a)

(b)

FIGURE 7. Changing size of the heater (a) Basic Model and Modified Model (b) The Result of the Modified Model

Under the same condition, the temperature distribution of the bonding surface when the

position of the heater is changed is shown in FIGURE 8.

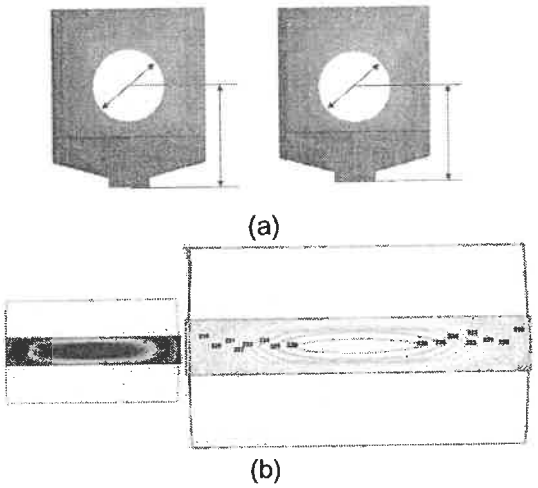

FIGURE 8. Changing position of the heater (a) Basic Model and Modified Model (b) The Result of the Modified Model

As the heater feature (cylindrical shape) approaches a flat surface similar to the bonding surface, the temperature variation along the narrow width is reduced. The result is shown in FIGURE 9

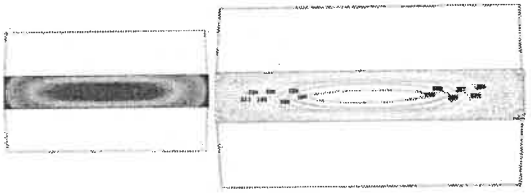

FIGURE 9. The temperature distribution of the bonding surface at changing the size and position

In the FIGURE 9, one can conclude that the temperature distribution at the bonding surface changes with the change of the size and the position of the heater and if a bigger sized cylindrical heater approximating a flat surface is used will result in reduced temperature variation.

DESIGN OF EXPERIMENTS

A design of experiment is established from the basic model with two factors.

Main factors are the position and the size of heater. The heater size and its position are limited to the cross sectional size of the heating tool unit and a constraint exists as shown in the FIGURE 10[6].

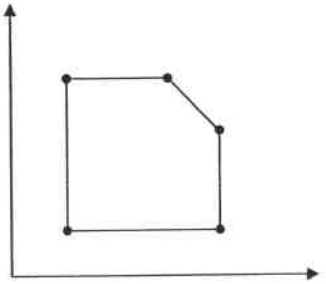

FIGURE 10. A constrained design region in two variables

CONCLUSIONS

As the heater feature approaches flat surface similar to the bonding surface, the temperature variation along the narrow width is reduced. And the temperature variation of the bonding surface is also reduced as the position of the heater is close to the bonding surface. Thus, if the cylindrical heat source of bigger size when placed closed to the bonding surface will achieve reduced temperature variation.

REFERENCES

1. D.D.Chang, J.A.Fulton, A.M.Lyons, J.R.Nis, Design considerations for the implementation of anisotropic conductive adhesive interconnection, *Proceedings of the 92nd NEPCON West Conference*, 1992
2. Y.Yamaguchi, I.Tsukagoshi, A.Nakajima, *Circuit Technol. 4, 1987.*
3. I.Tukagoshi, A.Nakajima, Y.Mikami, S.Mutoh, Z.Ikezoe, *Japan Kokai Patent(open system)*, S62-188184(1987)
4. Lindeke, R., Schoenig, Jr., F., Khan, A., and Haddad, J., 1991, Machining of a Titanium with Ultra-High Pressure Through the Insert Lubrication/Cooling, *Transactions of the North American Manufacturing Research Institution of SME*, 19: 154-161.
5. Trigger, K. and Chao, B., 1951, An Analytical Evaluation of Metal Cutting Temperatures, *ASME Transactions, Journal of Engineering for Industry*, 73: 57-68.
6. Douglas C. Montgomery, Design and Analysis of Experiments 6th, 2005, Jon Wiley and Sons, Inc.

SYNTHESIS OF THE INTELLIGENT SENSING SYSTEM USING CURRENT SIGNALS FOR MANUFACTURING SYSTEMS

Seung-Chul Kim[1], Siyon Chung[2], Kyung-Don Kim[3] and Sung-Chong Chung[1]
[1]Department of Mechanical Design and Production Engineering
Hanyang University, SungdongGu, Seoul 133-791, KOREA
[2]Faculty of Science, The University of Western Ontario, London, CANADA
[3]Small Business Corporation, Gyeonggi Regional Headquarter, Suwon, KOREA

ABSTRACT
An intelligent sensing system based on mathematical models of the servo and the cutting mechanics in end milling processes is proposed. Cutting forces in the end milling process are computed from embedded motor control signals and cutting mechanics models without additional sensors in machine tools. Using the estimated cutting forces, depth of cut (DOC) is identified during the end milling process. Performance of the devised intelligent sensing system is verified through experiments.

KEYWORDS
Control signal, Cutting mechanics, Depth of cut, End milling, Estimation, Servomechanism

INTRODUTION
In order to make unmanned manufacturing environment, intelligent manufacturing systems linked with IT technology are required. Actuators assisted with intelligent sensors are indispensable to develop intelligent machines. As the manufacturing system is actuated by motors, control signals of motors are used to develop the intelligent sensors. To improve productivity and quality in machining processes, real-time estimation and control of cutting forces are required [1,2].

In this paper, firstly, the realtime estimation of DOC in an end milling process shown in Fig. 1 is studied through kinematic modeling of cutting forces. To increase accuracy and expedite the estimation process of specific cutting forces, a two-axis circular cutting method is devised. Secondly, the cutting force estimation method through control signals of CNC machine tools is constructed from mathematical models of the spindle and feeddrive systems. Therefore, cutting torque of the spindle system, and feed and normal cutting forces are estimated accurately without additional sensors. Finally, relationships between cutting forces and DOCs in the end milling process are derived from the above two results. Using the realtime estimation results of cutting forces and DOCs, tool deflection and workpiece deflection errors, friction estimation, and condition monitoring of machine tools are available. Performance of the developed intelligent sensing system is confirmed through two-axis circular cutting experiments.

CUTTING FORCE
Force Modeling of End Milling
Cutting forces are described as functions of cutting pressure acting on an instantaneous chip load area [3-6]

$$dF_t = K_s\, dz\, h(\phi),\ dF_r = r_i\, dF_t \qquad (1)$$
$$dz = [R/\tan(\beta)]d\phi,\ h(\phi) = t_c \sin\phi$$

where dz is the thickness of the axial element of a cutting edge, $h(\phi)$ is the instantaneous chip thickness, t_c is the feed per tooth. The cutting pressure K_s is expressed as a function of the average chip thickness. In the peripheral down-milling process, instantaneous forces in the x and y directions along the chip load of a single flute are given by

$$dF_x(\phi) = -dF_t \cos\phi + dF_r \sin\phi$$
$$dF_y(\phi) = -dF_t \sin\phi + dF_r \cos\phi \qquad (2)$$

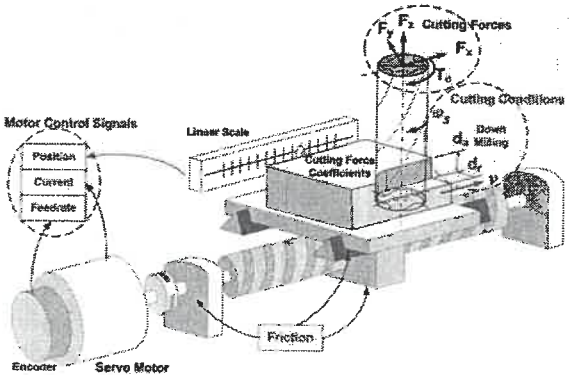

Fig. 1 Structure of the end milling process.

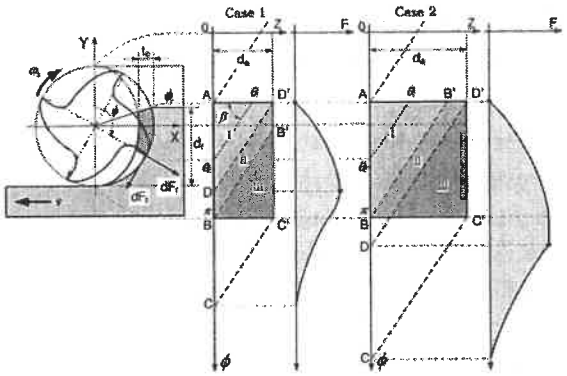

Fig. 2 Cutting mechanism of the end milling process.

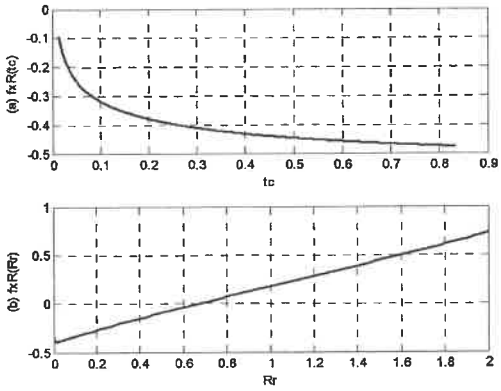

Fig. 3 f_{xR} model according to t_c and R_r

Integrating Eq. (2) within the contact range of a single tooth shown in Fig. 2 gives

$$F_{ti}(\phi) = K' \int_{\theta_1}^{\theta_2} \sin\tau d\tau \tag{3}$$

$$F_{ni}(\phi) = K' \int_{\theta_1}^{\theta_2} (\sin\tau\cos\tau + r_1 \sin^2\tau) d\tau$$

$$F_{yi}(\phi) = K' \int_{\theta_1}^{\theta_2} (-\sin^2\tau + r_1 \sin\tau\cos\tau) d\tau$$

Average forces per tooth are obtained by dividing the total cutting forces within cutting range $[\phi_A, \phi_C]$ by period of tooth $2\pi/N$. The average cutting forces for several teeth cutting are given by

$$\begin{aligned} F_{at} &= KR_a C_r \\ F_{ax} &= KR_a (A_r + r_1 B_r) \\ F_{ay} &= KR_a (-B_r + r_1 A_r) \\ F_{aR} &= \sqrt{F_{ax}^2 + F_{ay}^2} = KR_a \sqrt{1+r_1^2}\sqrt{A_r^2 + B_r^2} \end{aligned} \tag{4}$$

$$A_r = -(2R_r - R_r^2),\ C_r = 2R_r,\ K = \frac{NK_s R t_c}{2\pi}$$

$$B_r = (R_r - 1)\sqrt{2R_r - R_r^2} - \phi_r + \pi$$

In general, cutting force coefficients in Eq. (4) are functions of the average chip thickness t_a,

$$K_s = k_s t_a^{p_s},\ r_1 = k_1 t_a^{p_1} \tag{5}$$
$$t_a = t_c R_r / (\pi - \phi_r)$$

Identification of Radial Immersion Ratio

The radial immersion ratio $R_r = d_r / R$ is expressed by force ratios of the average feed force to average resultant force [5].

$$\begin{aligned} f_{xR} &= \frac{F_{ax}}{F_{aR}} = \frac{F_{ax}}{\sqrt{F_{ax}^2 + F_{ay}^2}} = \frac{A_r + r_1 B_r}{\sqrt{(1+r_1^2)(A_r^2 + B_r^2)}} \\ &= f_{xR}^{t_c}(t_c) + f_{xR}^{R_r}(R_r) + f_{xR}^{err} \\ &\approx f_{xR}^{t_c}(t_c) + f_{xR}^{R_r}(R_r) \end{aligned} \tag{6}$$

where the first term $f_{xR}^{t_c}(t_c)$ is obtained by calculating the average of f_{xR} for every t_c as shown in Fig. 3(a). The second term $f_{xR}^{R_r}(R_r)$ is obtained by calculating the average of $[f_{xR} - f_{xR}(t_c)]$ for every R_r as shown in Fig. 3(b). The error term f_{xR}^{err} and the model obtained through variable separation has the mean of 0.0032 and maximum value of 0.0215. The error term, therefore, is ignored.

FORCE ESTIMATION BY MOTOR CURRENTS

Governing equation of the servo system shown in Fig. 1 is given by

$$T_M = K_t I_M = J_e \frac{d\omega}{dt} + B_e \omega + T_f + T_d \tag{7}$$

where T_M is the motor torque, ω is the rotating speed, K_t is the torque constant, I_M is the motor current, T_d is the disturbance torque due to cutting forces, and T_f is the coulomb friction torque [2,4-6].

Using the motor currents and identification procedures of [4], the parameters of Eq. (7) are extracted from a machining center.

Spindle system

When the spindle speed is constant, the equation of motion of the spindle system is given by [2,4]

$$F_{aR} = K_{s1} I_{as} + K_{s2} \tag{8}$$

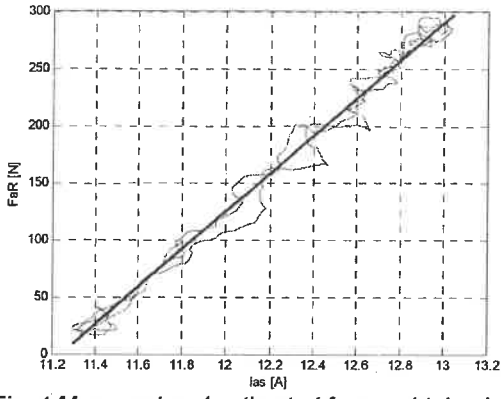

Fig. 4 Measured and estimated forces obtained from the spindle system.

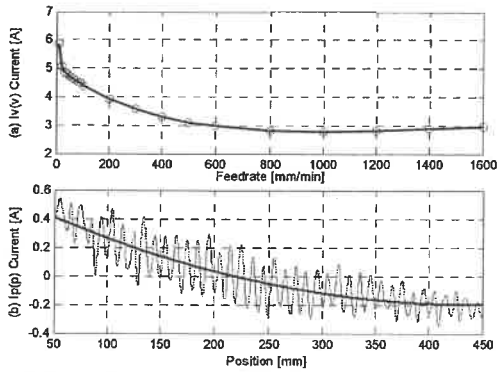

Fig. 5 Friction current models at no load case.

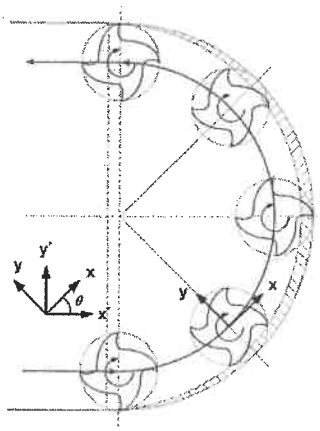

Fig. 6. Two-axis circular cutting method.

where $K_{t1}=165.2$, $K_{t2}=-1857$. Measured and estimated forces obtained from the spindle is shown in Fig. 4

Feeddrive system

Dynamics of feed drive systems are given by

$$I_c = I_M - I^n(v,p) - J\frac{dv}{dt}$$
$$F_c = K_{c1}I_c + K_{c2} \qquad (9)$$

where v is the feedrate(mm/min), p is the position of table, I_M is the measured average motor current, $I^n(v,p)$ is the motor current due to nonlinear friction torque. The cutting forces are derived from motor currents obtained by subtracting friction currents from inertia torque. The variable $I^n(v,p)$ is evaluated by measuring friction current of the feeddrive motor in no load condition. By using the results shown in Fig. 5, this variable is separated into variables of feedrate v, and table position p.

$$I^n(v,p) = I^v(v) + I^p(p) + I^{err}(p) \approx I^v(v) + I^p(p) \qquad (10)$$

where $I^v(v)$ shown in Fig. 5 (a) is the nonlinear Stribeck curve, $I^p(v)$ is shown in Fig. 5 (b). Residual current $I^{err}(p)$ is small and ignored.

EXPERIMENTS

An experimental setup is constructed for a commercial CNC machining center with a Fanuc 15MA controller. Motor control signals (positions and currents) are measured by the CNC controller. Experiments of 2-axis circular cutting are performed as shown in Fig. 6. Performances of the estimation for the cutting force and DOC are confirmed through the changes of DOC, feedrate, and feed direction in cutting.

Estimation of cutting force

Eq. (8) and (9) are used to estimate the cutting forces from the 2-axis motor control signals. The estimated cutting force $F_{x'}$ on the x'-axis is shown in Fig.7 (a), and $F_{y'}$ on the y'-axis is shown in Fig.8 (a). F_R on the spindle is shown in Fig.9 (b). Bold lines represent cutting forces measured by a dynamometer. Thin lines are estimated forces from the currents. Measured currents, positions, velocities and accelerations are shown in (b) and (c) of Figs. 8 and 9. These results are estimated relatively well except the cases of slow feedrate and/or small DOC. The reason for this is that large errors of the estimation model due to nonlinearity.

Estimation of axial immersion ratio

The resultant and feed cutting forces in Eq. (6) are required to estimate the radial immersion ratio. The feed cutting force F_x is derived from 2-axis estimated forces as

$$F_x = F_{x'}\cos\theta + F_{y'}\sin\theta \qquad (11)$$

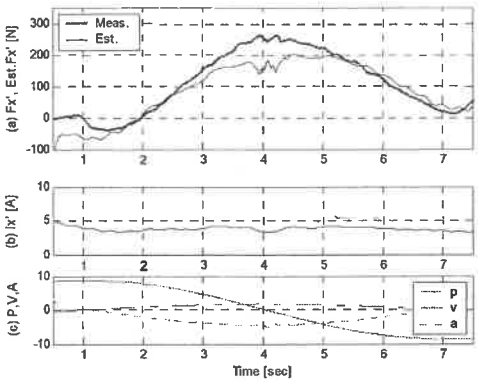

Fig. 7 Estimations of cutting force in x-axis feeddrive.

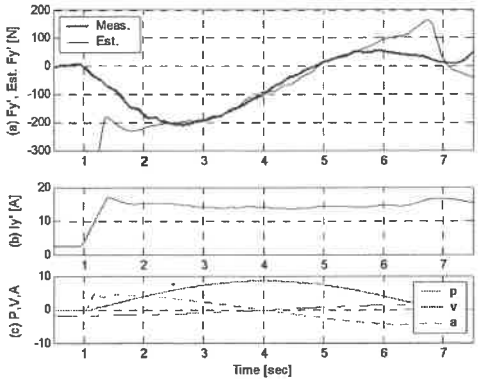

Fig. 8 Estimations of cutting forces in y-axis feeddrive.

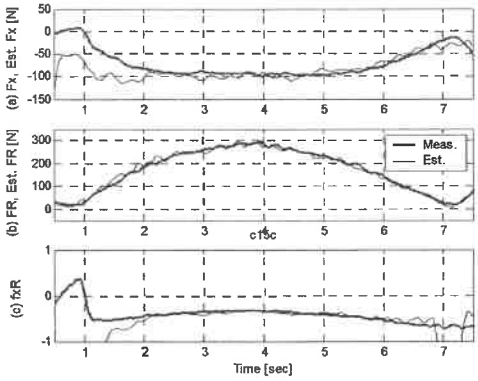

Fig. 9 Estimated cutting forces and the force ratio.

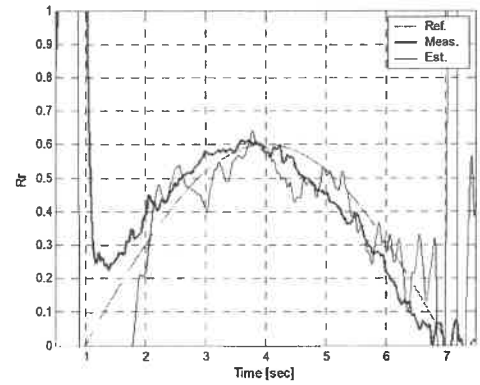

Fig. 10 Estimations of the radial immersion ratio.

The measured and estimated feed force is shown in Fig. 9(a) and Fig. 8(a), and Fig. 9(b) shows the resultant force. The force ratio that estimates DOC is shown in Fig. 9 (c). Using Eq. (6) and Fig. 9(c), the immersion ratio is estimated as shown in Fig. (10). The errors of the immersion ratio are similar to those of the estimated forces. It is confirmed that the radial immersion ratio is estimated through the motor control signal well.

CONCLUSIONS

An intelligent sensing system that estimates cutting forces and DOC through motor control signals is developed in the end milling process. Cutting force models are derived from cutter geometry and cutting mechanics. Relationships between DOC and cutting forces are also developed through the proposed force models. Cutting forces are measured indirectly through the mathematical models and observed current signals of the feeddrive and spindle servo motors. These estimated forces are applied to estimating DOC. Performance of the developed system is confirmed through the two-axis circular cutting experiments.

REFERENCES

1. Spence, A. and Altintas, Y., 1991, "CAD Assisted Adaptive Control for Milling," ASME Journal of Dynamic Systems Measurement and Control, Vol.113, pp.444-450.
2. Altintas, Y., 1992, "Prediction of Cutting Force and Tool Breakage in Milling from Feed Drive Current Measurement," ASME Journal of Engineering for Industry, Vol.114, pp.386-392.
3. Tlusty, J. and Macneil, P., 1975, "Dynamics of Cutting Forces in End Milling," Annals of the CIRP, Vol.24, pp.248-252.
4. Kim, S.C. and Chung, S.C., 1998, "Cutting Force Estimation Using Feeddrive and Spindle Motor Currents in Milling Processes", Transactions of the Korean Society of Mechanical Engineers (A), Vol.22, No.11, pp.2029-2038. (in Korean)
5. Kim, S.C. and Chung, S.C., 1999, "Robust Cutting Force Control Using Indirect Force and Disturbance Estimators in the End Milling Process", Proceedings of the ASPE,1999 Annual Meeting, pp.248-251.
6. Kim, S.C. and Chung, S.C., 2000,"Rapid Calibration of Cutting Force Control Using in the EndMilling Process", Proceedings of the ASPE, 2000 Annual Meeting, pp.276-279.

IMPROVED ANALYTICAL CHIP THICKNESS MODEL

Lee Kumanchik and Tony L. Schmitz
Department of Mechanical and Aerospace Engineering
University of Florida, Gainesville, FL, USA

INTRODUCTION

Discrete part production by macro- and micro-milling remains an important manufacturing capability. To improve process efficiency and part quality, research efforts continue with a focus on pre-process performance predictions. Important aspects of milling models include developing an accurate description of the system dynamics and cutting forces; see [1] for an overview. The cutting forces are generally taken to be a function of the time varying chip thickness. Therefore, a number of authors have studied chip thickness in milling and reported various models [2-7].

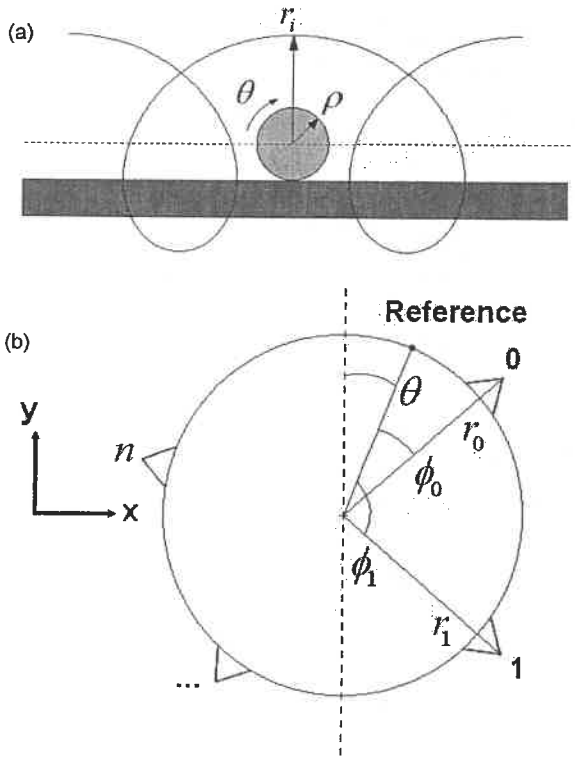

Figure 1: (a) Path for a tooth of radius r_i on circle of radius ρ. (b) Schematic of the milling tool. The reference, θ, is common for all teeth; the difference in angular position for each tooth is the angle ϕ which is measured from the reference.

In this work, we build on these previous studies to develop an analytical chip thickness model that incorporates the cycloidal trajectories of the cutter teeth and radial runout. Expressions for entry and exit angles and limiting combinations of feed rate, spindle speed, and tool radius for chip formation are also provided. It is shown that the new model is more accurate than the well-known circular tooth path approximation and the analytical model presented in [6].

NON-DIMENSIONAL TOOL PATH

The path of the ith tooth in a milling cut can be described parametrically as:

$$\begin{aligned} x_i &= \rho\theta + r_i \sin(\theta + \phi_i) \\ y_i &= r_i \cos(\theta + \phi_i) \end{aligned}, \qquad (1)$$

where $\rho = f/\omega = N_t f_t / 2\pi$ is the radius of the circle that defines the cycloidal motion of the tooth, f is the linear feed rate, ω is the spindle speed, N_t is the number of teeth, f_t is the feed per tooth, r_i is the radius of the ith tooth, θ is the instantaneous cutter angle, and ϕ_i is the angle between θ and the ith tooth. Figure 1 shows a schematic of the tool path and tool. Equation 1 can be written in non-dimensional form by dividing by the nominal tool radius, r, yielding:

$$\begin{aligned} x_i/r = X_i &= \varepsilon\theta + \alpha_i \sin(\theta + \phi_i) \\ y_i/r = Y_i &= \alpha_i \cos(\theta + \phi_i) \end{aligned} \qquad (2)$$

where $\varepsilon = \rho/r$ is the non-dimensional cutting parameter, $\alpha_i = 1 + e_i$ is the non-dimensional tool radius of the ith tooth which is nominally 1 but varies by e_i, and e_i is the runout of the ith tooth normalized with the nominal radius r. For no runout, the non-dimensional tool path of any tooth is defined solely by ε. As ε increases, the tool path becomes more elongated and the chip thickness increases. A plot of the tool path for a two tooth cutter with various ε values is provided in Fig. 2.

LIMIT OF CHIP FORMATION

The chip thickness in milling is defined as the distance between the current tooth's path and the previous tooth's path along the current tooth's edge. Figure 2c shows that, for the given

orientation, chip thickness is not defined. For the depicted orientation to be consistent with the definition for chip thickness, ε must be smaller so that the current tooth intersects the previous tooth's path as shown in Fig. 2b. The limit of chip formation is then the value $\varepsilon_{\lim}$ which allows all orientations of the current tooth in a cut to satisfy the chip thickness definition.

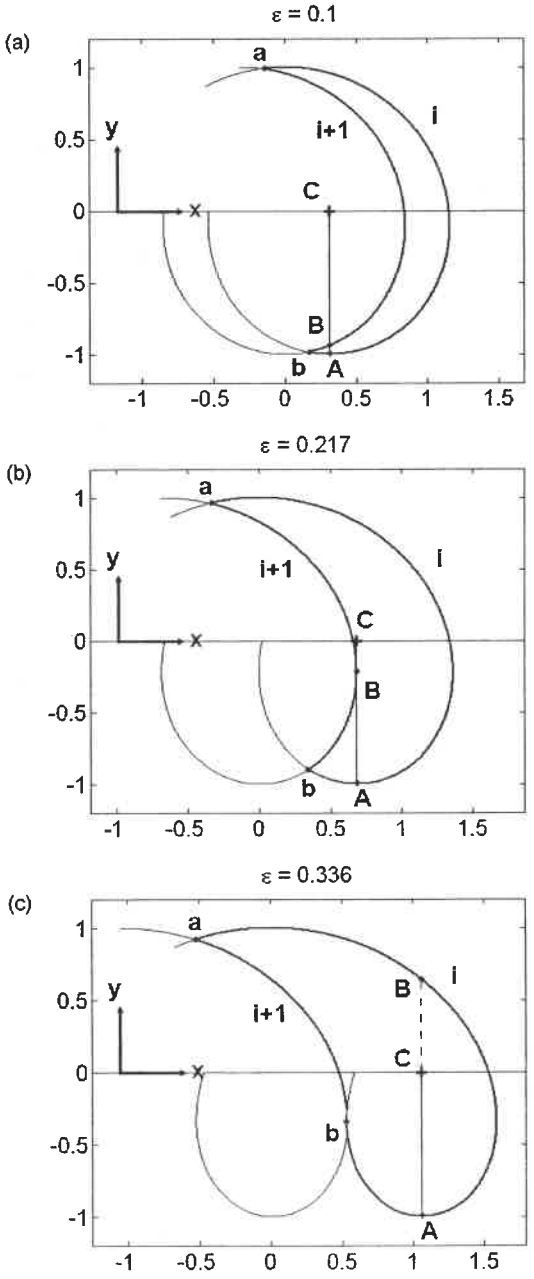

Figure 2: Non-dimensional tool path with increasing ε. Point **A** is the tooth tip, **B** is the intersection with the previous tooth's path, and **C** is the tool center. The outline of the chip being formed is identified.

As a first approximation of Fig. 2b, assume that the point of intersection, **B**, occurs on the line $Y=0$ so that at some point in time, t, the tooth, $i+1$, rotates onto the line $Y=0$ at the angle $\theta_t+\phi_{i+1}=\pi/2$. Later in time, $t+1$, the next tooth, i, rotates down to $Y=-\alpha_i$ at $\theta_{t+1}+\phi_i=\pi$. For $\varepsilon_{\lim}$ these two locations share the same x-coordinate.

$$X_i(\theta_{t+1})=X_{i+1}(\theta_t)$$
$$\Rightarrow \varepsilon\theta_{t+1}+\alpha_i\sin(\theta_{t+1}+\phi_i)=\varepsilon\theta_t+\alpha_{i+1}\sin(\theta_t+\phi_{i+1})$$
$$\Rightarrow \varepsilon(\pi-\phi_i)+\alpha_i\sin(\pi)=\varepsilon(\pi/2-\phi_{i+1})+\alpha_{i+1}\sin(\pi/2)$$
$$\Rightarrow \varepsilon_{\lim}=\alpha_{i+1}/(\pi/2+\phi_{i+1}-\phi_i) \quad (3)$$

The limiting ε is a function of the angle difference between teeth on a tool and it increases for smaller teeth spacing. Evenly spaced teeth have the same angle difference for all teeth, $\phi_{i+1}-\phi_i=2\pi/N_t$, but when considering unevenly spaced teeth the largest angle difference between any two consecutive teeth should be used. In addition, $\varepsilon_{\lim}$ is influenced by runout and so the value, α_{i+1}, of the smallest tooth should be used. In reality the point of intersection, **B**, occurs when the tooth, $i+1$, has an x-direction velocity of zero:

$$X_{i+1}{}' = \varepsilon+\alpha_{i+1}\cos(\theta_t+\phi_{i+1})=0$$
$$\Rightarrow \theta_t+\phi_{i+1}=\arccos(-\varepsilon/\alpha_{i+1})$$

The next tooth, i, still rotates to $\theta_{t+1}+\phi_i=\pi$ and the x-coordinate of these two points are coincident:

$$X_i(\theta_{t+1})=X_{i+1}(\theta_t)$$
$$\Rightarrow \varepsilon\theta_{t+1}+\alpha_i\sin(\theta_{t+1}+\phi_i)=\varepsilon\theta_t+\alpha_{i+1}\sin(\theta_t+\phi_{i+1})$$
$$\Rightarrow \varepsilon(\pi-\phi_i)+\alpha_i\sin(\pi)=\varepsilon\left[\arccos(-\varepsilon/\alpha_{i+1})-\phi_{i+1}\right]+\alpha_{i+1}\sin\left[\arccos(-\varepsilon/\alpha_{i+1})\right]$$
$$\Rightarrow \varepsilon_{\lim}=\frac{\alpha_{i+1}\sin\left[\arccos(-\varepsilon/\alpha_{i+1})\right]}{\left[\pi-\arccos(-\varepsilon/\alpha_{i+1})+\phi_{i+1}-\phi_i\right]} \quad (4)$$

Equation 4 must be solved numerically for a given angle difference. A plot of Eqs. 3 and 4 versus angle difference and the error between them is shown in Fig. 3. Most milling cuts have

values of ε that are far below the limiting value; ε_{lim} represents extremely aggressive cutting.

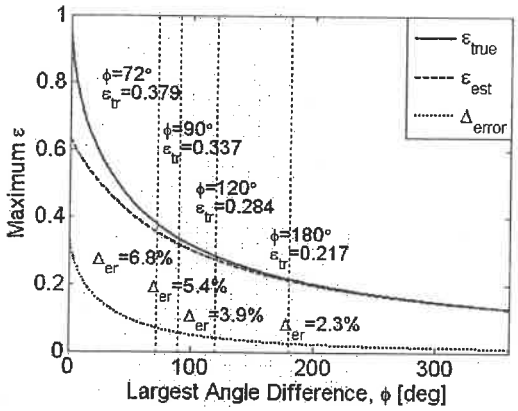

Figure 3: Maximum ε to still have normal chip formation given the angle difference between successive teeth. Smaller angle differences enable more aggressive cutting.

ANALYTICAL CHIP THICKNESS

The chip thickness in milling, h, is the distance between the current and the previous tooth paths along the current tooth's edge (Fig. 2). The non-dimensional chip thickness is then:

$$\frac{h}{r} = H = |AC| - |BC| = \alpha_i - |BC|$$

$$\Rightarrow H = \alpha_i - \sqrt{\left(X_{i+1}(\theta_t) - X_C(\theta_{t+1})\right)^2 + \left(Y_{i+1}(\theta_t) - \cancel{Y_C(\theta_{t+1})^{=0}}\right)^2}$$

$$H = \alpha_i - \sqrt{\begin{array}{l}\varepsilon^2(\theta_t - \theta_{t+1})^2 + \\ 2\varepsilon\alpha_{i+1}(\theta_t - \theta_{t+1})\sin(\theta_t + \phi_{i+1}) + \\ \alpha_{i+1}{}^2\end{array}}, \quad (5)$$

where $|AC|$ and $|BC|$ are the distance between points A and C, and B and C, respectively, in Fig. 2, and X_C and Y_C are the coordinates of the tool center ($Y_C = 0$ always). As shown in [7] but rewritten in non-dimensional form, the relationship between θ_{t+1} and θ_t is:

$$\begin{array}{l}(\theta_{t+1} - \theta_t)\varepsilon\cos(\theta_{t+1} + \phi_i) + \\ \alpha_{i+1}\sin(\theta_{t+1} + \phi_i - \theta_t - \phi_{i+1}) = 0\end{array}. \quad (6)$$

In order to make Eq. 5 a function of the current tooth's angle, θ_{t+1}, θ_t must be solved numerically from Eq. 6 [7]. However, the sinusoidal term contains the angle difference between the current and previous teeth. Depending on ε, these two angles will be nearly identical allowing the small angle approximation $\sin\theta = \theta$ to be made in Eq. 6.

$$\begin{array}{l}(\theta_{t+1} - \theta_t)\varepsilon\cos(\theta_{t+1} + \phi_i) + \\ \alpha_{i+1}(\theta_{t+1} + \phi_i - \theta_t - \phi_{i+1}) = 0\end{array}$$

$$\Rightarrow \theta_t = \theta_{t+1} - \frac{(\phi_{i+1} - \phi_i)}{\varepsilon/\alpha_{i+1}\cos(\theta_{t+1} + \phi_i) + 1} \quad (7)$$

Substituting Eq. 7 into Eq. 5 yields the non-dimensional chip thickness defined by ε and α in terms of the current cutting tooth angle, θ_{t+1}.

ENTRY AND EXIT ANGLES

The entry and exit angles for a slotting cut can be determined by setting Eq. 5 equal to zero and using the substitution $\theta_t - \theta_{t+1} = \phi_i - \phi_{i+1}$ based on the assumption that $\theta_{t+1} + \phi_i \approx \theta_t + \phi_{i+1}$,

$$H = 0$$

$$\Rightarrow \alpha_i{}^2 = \varepsilon^2(\theta_t - \theta_{t+1})^2 + 2\varepsilon\alpha_{i+1}(\theta_t - \theta_{t+1})\sin(\theta_t + \phi_{i+1}) + \alpha_{i+1}{}^2$$

$$\Rightarrow \alpha_i{}^2 = \varepsilon^2(\phi_i - \phi_{i+1})^2 + 2\varepsilon\alpha_{i+1}(\phi_i - \phi_{i+1})\sin(\theta_t + \phi_{i+1}) + \alpha_{i+1}{}^2$$

$$\Rightarrow \theta_t + \phi_{i+1} = \arcsin\left(\frac{\alpha_i{}^2 - \alpha_{i+1}{}^2 - \varepsilon^2(\phi_i - \phi_{i+1})^2}{2\varepsilon\alpha_{i+1}(\phi_i - \phi_{i+1})}\right) \quad (8)$$

The arcsine function in Eq. 8 is multivalued. To obtain the entry and exit angles that fall near $\theta_t + \phi_{i+1} = 0$ and $\theta_t + \phi_{i+1} = \pi$, Eq. 8 can be written as two equations using the principal inverse sine function.

$$\theta_t + \phi_{i+1} = \sin^{-1}\left(\frac{\alpha_i{}^2 - \alpha_{i+1}{}^2 - \varepsilon^2(\phi_i - \phi_{i+1})^2}{2\varepsilon\alpha_{i+1}(\phi_i - \phi_{i+1})}\right) \quad (9a)$$

$$\theta_t + \phi_{i+1} = \pi - \sin^{-1}\left(\frac{\alpha_i{}^2 - \alpha_{i+1}{}^2 - \varepsilon^2(\phi_i - \phi_{i+1})^2}{2\varepsilon\alpha_{i+1}(\phi_i - \phi_{i+1})}\right) \quad (9b)$$

Equations 9a and 9b define the angle of the leading tooth, $i+1$, at chip entry and exit. If used with Eq. 2, they can describe the angle of the current tooth, i, by setting the y-equations for the different teeth equal to each other and solving for $\theta_{t+1} + \phi_i$:

$$Y_i(\theta_{t+1}) = Y_{i+1}(\theta_t)$$

$$\Rightarrow \alpha_i \cos\left(\theta_{i+1}+\phi_i\right)=\alpha_{i+1}\cos\left(\theta_i+\phi_{i+1}\right)$$
$$\Rightarrow \theta_i+\phi_{i+1}= \arccos\left(\alpha_i/\alpha_{i+1}\cos\left(\theta_i+\phi_{i+1}\right)\right) \quad (10)$$

The arccosine function in Eq. 10 is multivalued. To obtain the entry and exit angles that occur near $\theta_{i+1}+\phi_i=0$ and $\theta_{i+1}+\phi_i=\pi$, Eq. (10) is split into two equations using the principal inverse cosine function in combination with Eq. 9 (Eq. 11a for entry, 11b for exit).

$$\theta_i+\phi_{i+1}= -\cos^{-1}\left(\alpha_i/\alpha_{i+1}\cos\left(\left(\theta_i+\phi_{i+1}\right)_{9a}\right)\right) \quad (11a)$$

$$\theta_i+\phi_{i+1}= 2\pi-\cos^{-1}\left(\alpha_i/\alpha_{i+1}\cos\left(\left(\theta_i+\phi_{i+1}\right)_{9b}\right)\right) \quad (11b)$$

RESULTS

In order to test the accuracy of the chip thickness equation developed here, comparison was made to other commonly used methods. The reference chip thickness was determined using the time domain simulation in [8]. The analytical methods tested were: the solution in this paper (linear), the circular tool path approximation (circular), and the solution developed in [6] (WIBT).

The first comparison was the difference in the average chip thickness over one revolution. The percent difference between each method as compared to the reference for a two tooth cutter is shown in Fig. 4a. The value ε in the plot is varied from near zero to the maximum, $\varepsilon_{\text{lim}}=0.217$. All analytical solutions lose accuracy as ε increases; however, the solution provided here is most accurate. Figure 5b shows the positive error between the time domain and analytical solutions as a function of cutter angle.

CONCLUSIONS

This paper presented an improved, non-dimensional chip thickness model that incorporates the cycloidal trajectories of the cutter teeth and radial runout.

REFERENCES

1. Smith, S., and Tlusty, J., 1991, An Overview of Modeling and Simulation of the Milling Process, *Journal of Engineering for Industry*, **113**: 169-175.
2. Tlusty, J., and MacNeil, P., 1975, Dynamics of Cutting Forces in End Milling, *Annals of the CIRP*, **24/1**: 21–25.
3. Montgomery, D. and Altintas, Y., 1991, Mechanism of Cutting Force and Surface Generation in Dynamic Milling, *Journal of Engineering for Industry*, **113**: 160-168.
4. Spiewak, S., 1994, Analytical Modeling of Cutting Point Trajectories in Milling, *Journal of Engineering for Industry*, **116**: 440-448.
5. Spiewak, S., 1995, Improved Model of the Chip Thickness in Milling, *Annals of the CIRP*, **44/1**: 39-42.
6. Bao, W.Y. and Tansel, I.N., 2000, Modeling Micro-end-milling Operations, Part I: Analytical Cutting Force Model, Part II: Tool Run-out, *International Journal of Machine Tools and Manufacture*, **40**: 2155-2173, 2175-2192.
7. H.Z. Li and X.P. Li, 2005, A Numerical Study of the Effects of Cutter Runout on Milling Process Geometry Based on True Tooth Trajectory, *International Journal of Advanced Manufacturing Technology*, **25**: 435-443.
8. Schmitz, T., Couey, J., Marsh, E., and Tummond, M., 2004, The Role of Cutter Eccentricity on Surface Finish and Milling Forces, Proceedings of American Society of Mechanical Engineers International Mechanical Engineering Congress and Exposition, IMECE2004-60232, Anaheim, CA

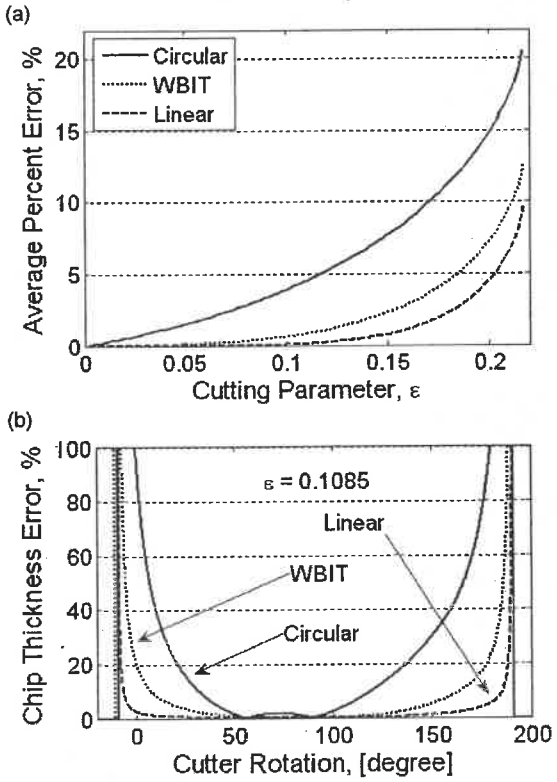

Figure 4: (a) Average error with increasing ε. (b) The positive error in chip thickness as a function of cutter angle for a two-flute cutter with $\varepsilon=0.1085$.

DYNAMIC CHARACTERIZATION OF A HEAD UNIT WITH A SMALL HIGH SPEED SPINDLE IN MESO-SCALE MACHINE TOOLS

Jae-Ha Lee[1], and Seung-Han Yang[1]
[1]School of mechanical engineering
Kyungpook National University
Daegu, S.Korea

INSTRUCTIONS

For machining process using rotation of a tool, spindle error directly affects the quality of the machined parts. Spindle error can be divided into several error components such as radial errors, axial errors, etc.[1,2] Especially, there exist two kinds of error motion in spindle error along the radial direction. Synchronous error motion due to bearing imperfection and misalignment causes out of roundness during cutting a round hole. Asynchronous error motion is related with bearing wear, improper preload and structural vibration and affects the surface finish of the machined parts. Research for identifying the radial error motion was begun long time ago. Tlusty measured spindle error motion by using non-contact capacitance sensors and an artifact such as master ball which is popularly used now.[2] This traditional measurement system assumes that there is no inaccuracy of an artifact used. For more precise measurement, the inaccuracy of the artifact such as eccentricity and roundness should be removed. Many researchers have developed various methods to eliminate the effect of the artifact.[3,4] Although the developed methods like multi-probe and multi-step method has good performance and can be used for nanometer-level measurement, some devices such as turn-table and stylus are required and it takes a lot of time to carry out measurement.[5] For measuring the error of a small spindle system in a meso-scale machine tool, a small precise artifact and an index table are needed to apply the above techniques. It is cost-effective to find an alternative way with a less precise artifact as machining system does not require tens nanometer-level precision. In this study, a method to measure radial error motion of a small spindle is proposed. It is suggested that a new and simple method to separate artifact errors from the measured data without additional devices. The spindle error can be affected by a head structure as well as a spindle itself. The dynamic characteristics of the spindle head and a spindle are the important factors to decide spindle error motion[6]. Moreover, a spindle at over tens thousands revolution per minute is needed to adapt for the required cutting speed as the small tools is used in a meso-scale system. Therefore dynamic characteristics of a head structure with a spindle become more significant in the design of the meso-scale systems. The influence of the dynamic characteristics of a spindle unit on spindle error is examined in this study.

RADIAL SPINDLE ERROR MEASUREMENT

Separation of Eccentricity

In general, the reference artifact is used to measure the spindle error. The artifact must be considered first because it has eccentricity and roundness errors. Initially, a simulation is carried out to analyze the change of measurement data based on eccentricity. Fig. 1 shows the eccentricity of the artifact which is called as master ring in this study. After selecting reference coordinate system with center of the master ring as the origin, the radius R_o is determined. The eccentricity e is expressed as the distance between the origin point of the reference coordinate system and the center of the rotating axis O. When a circle is rotating at arbitrary eccentricity e, the change in the data of circle can be evaluated.

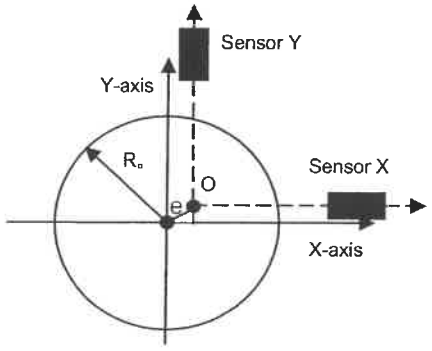

FIGURE 1. Schematic diagram of the master ring with eccentricity.

Positional information of the measured values from each sensor is taken at point O about sensor X and sensor Y as shown in Fig 1. The measured data is expressed into two circles on polar coordinate system. If axes of the sensors and axis of rotation are not coinciding, the radius of circle differ each other on the plot. Therefore, each sensor must be adjusted to get the exact data for actual measurement. Concurrently, the distance between center of the two circles and origin point of polar coordinates will coincide with eccentricity. If a different effect such as spindle error exists, the shape of ideal circle on polar coordinates can't be drawn. In this case, a best fit circle is evaluated using least square method. Hence, the eccentricity is inferred in this way.

Separation of Roundness

After removing the eccentricity of master ring, the roundness and spindle error have to be separated. It can be assumed that roundness of the artifact has a lower frequency comparing with spindle error in most operational process and its frequency has integer multiple times of spindle speed. Also, the roundness is repetitive against rotation. Therefore, the frequency characteristic of the measured data is analyzed using FFT (Fast Fourier Transform) and the cut off frequency is decided from rotation frequency of the spindle. In this experiment, five-times of rotation frequency of the spindle is selected.

EXPERIMENTS

As shown in Fig. 2, a master ring is used, instead of master ball. Non-contact capacitance sensor with 15nm resolution is constructed for measuring displacement of spindle. To measure the speed of the spindle a capacitance sensor (sensor 3) is set up at hollow part of spindle's chuck as shown in Figure 4. Bandwidth of capacitance sensor limits maximum sampling data. The larger the bandwidth is, the more sampling data is securely obtained at the large value of bandwidth. Sampling data number based on rotation velocity is calculated after selecting bandwidth of 16 kHz.

Table 1 shows the results of experiments and real error values of an artifact. Before conducting the experiments, inaccuracy of the artifact was measured to compare with the analyzed values using a CMM. The eccentricity and roundness of the artifact are 40.5 ㎛ and 1.8 ㎛, respectively. Experiments are carried out from 2,500 to 60,000 RPM. It is observed that the calculated eccentricity of the artifact increases as rotating speed is increased. As rotation speed increases, estimated eccentricity has more error. It shows that fitting error in separation of eccentricity increases as asynchronous error motion increases. In the case of roundness error, it is difficult to select the cut off frequency since the number of measured data per revolution decreases at over 20,000 PRM of spindle speed. Therefore, separation of the roundness error was done by using the analyzed roundness value at 20,000 RPM where the frequency analysis is clear. In this study a ball bearing spindle is used. As compared with fluid and air bearings spindle, ball bearing spindle displays the largest amount of asynchronous error motion.

DYNAMIC CHARACTERISTICS OF SPINDLE SYSTEM

The rotation of a spindle causes vibration of a machine tool. Structural analysis for vibration is needed to miniaturize a machine tool. Deviation of dynamic characteristics and spindle error in radial direction according to structure of spindle unit was analyzed.

Two clamping cases are selected according to headstock location as shown in Fig. 3 and a change of spindle error was analyzed in both cases during operation. To make experiments simpler, a cylinder shape artifact was used to find not quantitative result but relative difference. Therefore, measured error values include eccentricity and roundness of the artifact and chucking error. The diameter of sensors is 1.7 ㎜ and minimum target diameter is 2.3 ㎜. can be used, the diameter of the artifact is bigger than minimum target diameter.

TABLE 1. The result of experiments. (Unit: ㎛)

RPM	Eccentricity	Roundness	Spindle error	
			X-data (max, min)	Y-data (max, min)
2,430	39.80	1.94	5.59, -4.36	4.79, -4.76
4,990	39.98	1.68	4.76, -4.90	4.67, -3.98
9,380	40.15	1.92	4.05, -3.05	3.07, -2.81
14,990	40.14	1.67	3.98, -3.49	3.56, -3.39
19,990	40.55	1.62	3.66, -2.87	2.85, -2.98
25,010	41.64	-	3.82, -2.44	3.40, -2.67
28,300	42.21	-	3.31, -2.02	3.53, -2.56
40,110	44.94	-	4.28, -3.05	3.10, -3.73
60,730	49.60	-	7.90, -11.71	5.39, -6.01

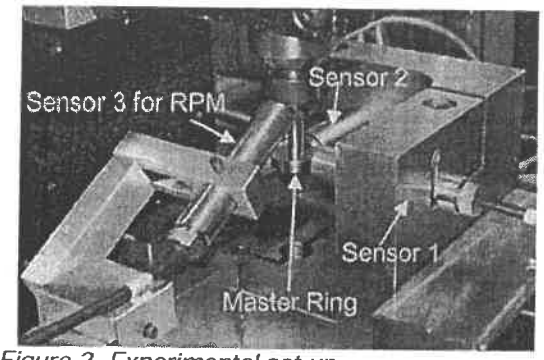

Figure 2. Experimental set-up.

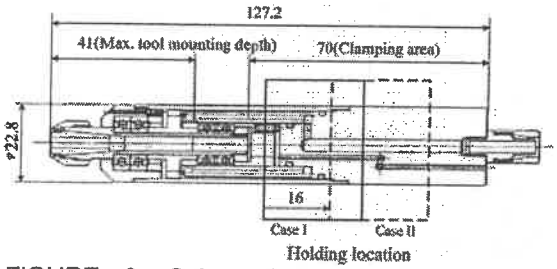

FiGURE 3. Schematic diagram of spindle (showing Case I and II).

Because the size of collet chuck is 3 ㎜ and the cylindrical shape artifact with 3 ㎜ of diameter However, target shape should be considered. Since non-contact capacitive sensors are calibrated with a flat target, measuring a target with a curved surface will cause errors. Linearity of sensing with the target was tested using a laser interferometer.

For travel range from 0 to 100 ㎛, mean value of the ratio of step displacement to a change of voltage is 22.38 [㎛/V] and standard deviation is 0.25 [㎛/V]. Because spindle error is generally within 50 ㎛ and measuring device has good linearity within 100 ㎛, measurement with the target is applicable. Table 2 shows the measured spindle error result. Both cases has similar trend that error becomes bigger as the speed increases. However, a large error occurred in case I and a small error exists in case II at 75,000 rpm. It can be assumed that this phenomenon is due to the structure of spindle unit including a headstock. Vibration test was done to verify this assumption. Through vibration test, the influence of vibration characteristic on spindle error was analyzed.

An accelerometer is attached at the end of the stator part of a spindle and impulse force is applied at near sensor position using an impact hammer.

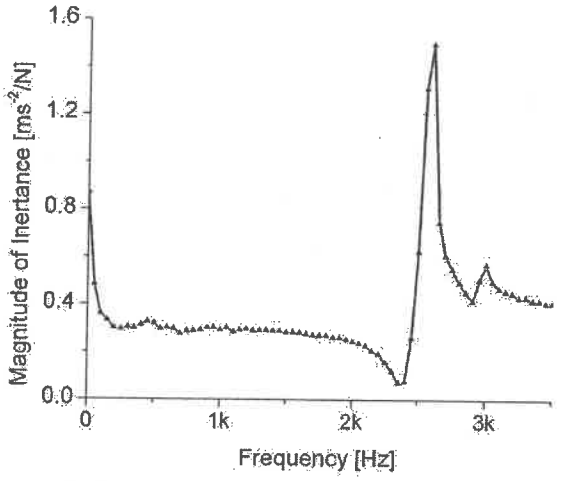

FIGURE 4. FRF plot of a spindle.

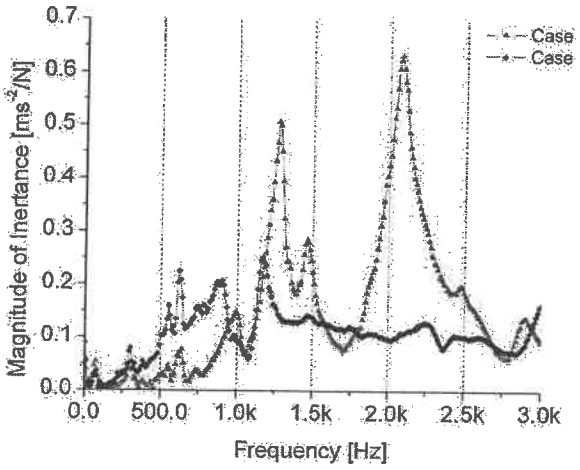

FIGURE 5. Magnitude plot of both cases.

As shown in Fig. 4, a spindle has a mass-dominant characteristic at low frequency region and its resonance frequency is 2.6 kHz. This frequency is not a matter of concern as maximum operating speed is 120,000 rpm.

There occur dominant peaks at 1258 Hz and 2060 Hz in the case I and at 610 and 1183 Hz in the case II as shown in Fig. 5 and Fig. 6. It is observed that spindle error become larger at the peak has the largest magnitude is 1258 Hz (75540 rpm, Case I) and 1183 Hz (70980 rpm, Case II). Proper spindle speed should be found according to structure to minimize the influence of vibration. Considering dynamic feature in case I, the structure is stable over 90,000 rpm. However, unbalance effect become bigger as speed increases so that spindle error becomes larger.

TABLE 2. Spindle error according to spindle speed and cases.

Spindle speed [rpm]	TIR [㎛] (Total Indicator Reading)	
	Case I	Case II
30000	10.18	12.35
45000	10.68	13.10
60000	15.60	17.03
75000	21.65	9.28
90000	13.08	16.38

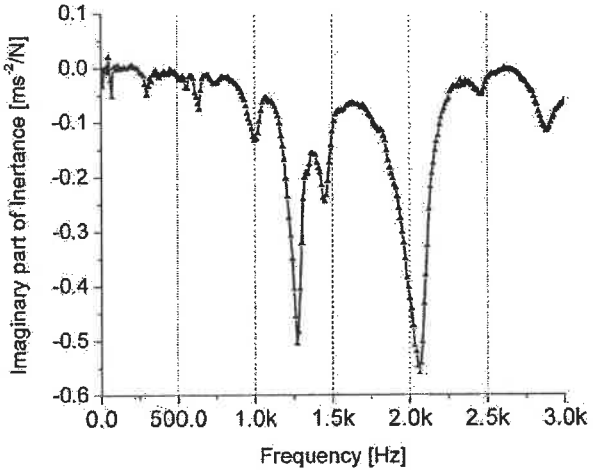

(a) Case I

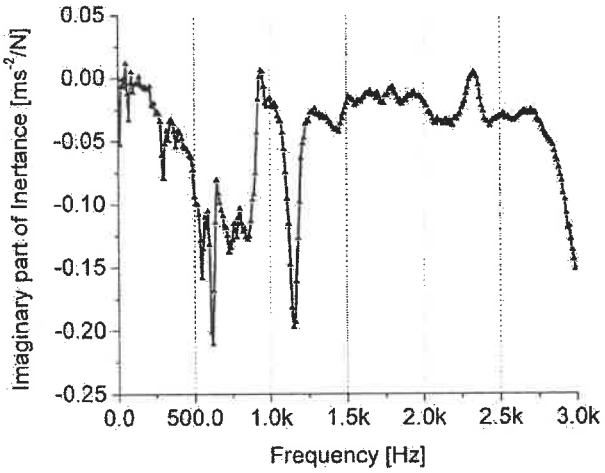

(b) case II

FIGURE 6. Imaginary part of FRF plots.

CONCLUSIONS

In this paper, radial error of a high speed meso-scale spindle is analyzed at various speeds. By using a new data analysis method, the radial error of high speed meso-scale spindle is effectively determined. The difference between calibrated real values of eccentricity and roundness error obtained using CMM and the present algorithm is less than 1 ㎛ for 2,500 to 20,000 RPM. Using the method presented in this paper for radial error analysis, it is possible to analyze the small-sized and high-speed spindle measurement data.

Though modal testing, relationship between the structure of spindle unit and spindle error were studied. Under structural limitation due to miniaturization and requirement of high speed spindle, dynamic analysis according to the structure of spindle unit is necessary to design a meso-scale machine tool.

REFERENCES

1. Martin, D.L., Tabenkin, A.N., Parsons, F.G., 1995, Precision Spindle and Bearing Error Analysis, International Journal of Machine Tools and Manufacture, 35:187-193.

2. ANSI/ASME B89.3.4M, 1992, Axes of rotation: Methods for Specifying and Testing, ASME, New York.

3. Estler, W. T., Evans, C. J., and Shao, L. Z., 1997, Uncertainty estimation for multiposition form error metrology, Precision Engineering, 21: 72-82.

4. Shoji Noguchi, Tadao Tsukada, and Atsushi Sakamoto, 1995, Evaluation method to determine radial accuracy of high-precision rotating spindle units, Precision Engineering, 17:266-273.

5. Marsh, E., Couey J., and Vallance R., 2006, Nanometer-Level Comparison of Three Spindle Error Motion Separation Techniques, ASME Journal of Manufacturing Science and Engineering, 128:180-187.

6. Liu, C.H., Jywe, W.Y., and Lee, H.W., 2004, Development of a simple test device for spindle error measurement using a position sensitive detector, Measurement Science and Technology, 15:1733–1741.

CALIBRATION OF A PARALLEL MANIPULATOR WITH RESTRICTED DEGREES OF FREEDOM BY MEANS OF A REDUNDANCY MATRIX

Piotr J. Meyer[1] and Prof. Dr. Jan van Eijk[2]
[1]Mechatronics Department
Philips Applied Technologies NA
Lynnfield, MA, U.S.A.
[2]Technology Office
Philips Applied Technologies
Eindhoven, The Netherlands

INTRODUCTION

The notions of forward and inverse coordinate transformation play an important role in the modelling and calibration of the kinematics and metrology in precision manipulators. Following an accepted convention, we shall define a Forward Transformation as a function mapping joint and/or sensor values into the spatial Degrees of Freedom (DoFs) at the manipulator's end-effector. Conversely, a function mapping the end-effector's DoFs into joint and/or sensor values shall be referred to as an Inverse Transformation. We treat both metrology and actuation aspects jointly, due to the similarity of the formalism.

One approach to dealing with machine errors in precision manipulators is to define parameters in the manipulator model, representing either deviations from the nominal layout or abstract coefficients in arbitrary expressions, such as polynomials. One can achieve this provided that the kinematics or metrology of the given manipulator can be modelled with closed-form analytical expressions. Based on the existence of such expressions in the presence of geometry parameters, manipulators can be divided into three types:

Forward Type

In this type, the forward coordinate transformation is a closed-form analytical function, while the inverse transformation is not. Examples of this type are manipulators with an open kinematic chain: certain Cartesian stages, single SCARA configurations, articulated Puma robots. Forward-type manipulators are usually applied to assembly and handling tasks, due to their relatively large workspace in comparison to size.

Inverse Type

Here, the inverse coordinate transformation is a closed-form analytical function, while the forward transformation is not. Examples of this type are parallel manipulators, i.e. ones possessing closed kinematic chains, which also allow for 6 DoF motion, such as the Stewart platform (Hexapod). Inverse-type manipulators are usually applied to precision measurement tasks, due to high motion reproducibility.

Mixed Type

In the mixed type, neither the inverse nor forward coordinate transformation can be expressed as a closed-form function, and both have to be computed with the use of numerical methods. Examples of this type are parallel manipulators, which allow for the motion of the end-effector in fewer than 6 DoFs. Some manipulators used in precision medical applications, as well as optical processing equipment are of the mixed type.

The issue of kinematics and metrology calibration for forward-type manipulators is well understood. A similar problem for the inverse type has been addressed by the Authors in [1]. In this paper, the Authors show how to adapt the formalism developed in [1] to calibrating mixed-type manipulators.

KINEMATIC AND METROLOGY MODELS

In a mixed-type manipulator, the kinematic model $\mathbf{f}_c$ consists of loop closure constraints formulated as implicit functions of the 6-DoF position $\mathbf{p}$ of the end-effector, as well as both the actuated ($\mathbf{q}_a$) and non-actuated joints ($\mathbf{q}_c$). Regarding the 6-DoF positions of all the other bodies in the manipulator, functionally and algebraically they are indistinguishable from the non-actuated joints and including them in $\mathbf{q}_c$ will

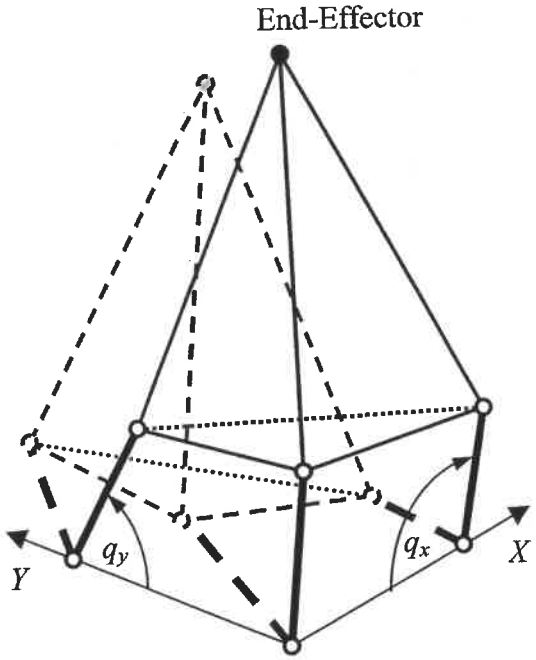

FIGURE 1. Example of a mixed-type mechanism, on which we chose to simulate our calibration method. The two actuated joints are q_x and q_y, they each have only 1 DoF, but together they fully determine the 6-DoF position of the tetrahedral end-effector. The linkage attached at the base frame origin adjusts itself in 2 DoFs as necessary. The subspace of positions reachable with the end-effector has only 2 DoFs

lead to coordinate transformations more useful in control. However, including the positions of the other bodies in $\mathbf{p}$ will also yield a correct calibration solution. The metrology model $\mathbf{f}_s$ describes the readings of some external sensors associated with the moving bodies to create redundancy beyond the limited number of DoFs in which the machine moves. In both the models, $\mathbf{g}$ is the vector of parameters representing the machine errors:

$$\begin{cases} \mathbf{f}_c(\mathbf{p},\mathbf{q}_a,\mathbf{q}_c,\mathbf{g}) = \mathbf{0} \\ \mathbf{f}_s(\mathbf{p},\mathbf{g}) = \mathbf{q}_s \end{cases} \tag{1}$$

The advantage of such a formulation is to provide for joint values as function arguments and for sensors readings as function output, which allows analytical model expressions. For the purpose of a later exposition, we shall also define the following matrices as Jacobians of the model equations:

$$\mathbf{A}_c = \frac{\partial \mathbf{f}_c}{\partial \mathbf{p}}, \quad \mathbf{B}_a = \frac{\partial \mathbf{f}_c}{\partial \mathbf{q}_a}, \quad \mathbf{B}_c = \frac{\partial \mathbf{f}_c}{\partial \mathbf{q}_c}$$
$$\mathbf{L}_c = \frac{\partial \mathbf{f}_c}{\partial \mathbf{g}}, \quad \mathbf{A}_s = \frac{\partial \mathbf{f}_s}{\partial \mathbf{p}}, \quad \mathbf{L}_s = \frac{\partial \mathbf{f}_s}{\partial \mathbf{g}} \tag{2}$$

Inverse Coordinate Transformation

Resolving the loop constraints leads to the actuated (and also non-actuated) joint values as functions of the end-effector position, hence an inverse coordinate transformation:

$$\mathbf{q}_a = \mathbf{f}_c^{-}(\mathbf{p},\mathbf{g}) \tag{3}$$

Since it is not guaranteed that the end position is reachable, we define the transformation as the minimum of a quadratic norm representing satisfaction of loop constraints ($\mathbf{M}_c$ can be used to establish a relative importance of the various DoFs):

$$E_c = \mathbf{f}_c(\mathbf{p},\mathbf{q}_a,\dot{\mathbf{q}}_c,\mathbf{g})^T \mathbf{M}_c \mathbf{f}_c(\mathbf{p},\mathbf{q}_a,\mathbf{q}_c,\mathbf{g}) \tag{4}$$

The sought minimum is attained when the gradient of criterion (4) is equal to zero (in the vicinity of the minimum, we are justified in neglecting the second term):

$$\min_{\mathbf{q}_a,\mathbf{q}_c} E_c \Rightarrow \begin{cases} \dfrac{\partial E_c}{\partial \mathbf{q}_a} = \left(\dfrac{\partial \mathbf{f}_c}{\partial \mathbf{q}_a}\right)^T \mathbf{M}_c \mathbf{f}_c(\mathbf{p},\mathbf{q}_a,\mathbf{q}_c,\mathbf{g}) = \mathbf{0} \\ \dfrac{\partial E_c}{\partial \mathbf{q}_c} = \left(\dfrac{\partial \mathbf{f}_c}{\partial \mathbf{q}_c}\right)^T \mathbf{M}_c \mathbf{f}_c(\mathbf{p},\mathbf{q}_a,\mathbf{q}_c,\mathbf{g}) = \mathbf{0} \end{cases} \tag{5}$$

In general, the model equations are non-linear; applying the Newton-Raphson method to find a zero of (5) leads to the following iterative expression for the sought joint angles:

$$\begin{pmatrix} \mathbf{q}_a \\ \mathbf{q}_c \end{pmatrix}_{i+1} = \begin{pmatrix} \mathbf{q}_a \\ \mathbf{q}_c \end{pmatrix}_i - \begin{pmatrix} \dfrac{\partial^2 E_c}{\partial \mathbf{q}_a^2} & \dfrac{\partial^2 E_c}{\partial \mathbf{q}_a \partial \mathbf{q}_c} \\ \dfrac{\partial^2 E_c}{\partial \mathbf{q}_c \partial \mathbf{q}_a} & \dfrac{\partial^2 E_c}{\partial \mathbf{q}_c^2} \end{pmatrix}_i^{-1} \begin{pmatrix} \dfrac{\partial E_c}{\partial \mathbf{q}_a} \\ \dfrac{\partial E_c}{\partial \mathbf{q}_c} \end{pmatrix}_i =$$
$$= \begin{pmatrix} \mathbf{q}_a \\ \mathbf{q}_c \end{pmatrix}_i - \begin{pmatrix} \mathbf{B}_a^T \mathbf{M}_c \mathbf{B}_a & \mathbf{B}_a^T \mathbf{M}_c \mathbf{B}_c \\ \mathbf{B}_c^T \mathbf{M}_c \mathbf{B}_a & \mathbf{B}_c^T \mathbf{M}_c \mathbf{B}_c \end{pmatrix}_i^{-1} \cdot \tag{6}$$
$$\cdot \begin{pmatrix} \mathbf{B}_a^T \mathbf{M}_c \\ \mathbf{B}_c^T \mathbf{M}_c \end{pmatrix}_i \mathbf{f}_c(\mathbf{p},\mathbf{q}_a,\mathbf{q}_c,\mathbf{g})_i$$

Based on the inverse coordinate transformation, we shall also define two auxiliary matrices which will be necessary in further exposition:

$$\mathbf{A}_c^- = \frac{\partial \mathbf{f}_c^-}{\partial \mathbf{p}}, \quad \mathbf{L}_c^- = \frac{\partial \mathbf{f}_c^-}{\partial \mathbf{g}} \tag{7}$$

To obtain those matrices, we differentiate (5) over **p**:

$$\begin{aligned} \left(\frac{\partial \mathbf{f}_c}{\partial \mathbf{q}_a}\right)^T \mathbf{M}_c \left(\frac{\partial \mathbf{f}_c}{\partial \mathbf{p}} + \frac{\partial \mathbf{f}_c}{\partial \mathbf{q}_a}\frac{\partial \mathbf{q}_a}{\partial \mathbf{p}} + \frac{\partial \mathbf{f}_c}{\partial \mathbf{q}_c}\frac{\partial \mathbf{q}_c}{\partial \mathbf{p}}\right) = \mathbf{0} \\ \left(\frac{\partial \mathbf{f}_c}{\partial \mathbf{q}_c}\right)^T \mathbf{M}_c \left(\frac{\partial \mathbf{f}_c}{\partial \mathbf{p}} + \frac{\partial \mathbf{f}_c}{\partial \mathbf{q}_a}\frac{\partial \mathbf{q}_a}{\partial \mathbf{p}} + \frac{\partial \mathbf{f}_c}{\partial \mathbf{q}_c}\frac{\partial \mathbf{q}_c}{\partial \mathbf{p}}\right) = \mathbf{0} \end{aligned} \tag{8}$$

and solve the resulting linear system for the sought matrix $\mathbf{A}_c^-$. Analogically, differentiating (5) over **g** leads to the other matrix, $\mathbf{L}_c^-$. Rewriting the results in terms of the previously defined closed-form Jacobians:

$$\begin{aligned} \begin{pmatrix} \mathbf{A}_c^- \\ \frac{\partial \mathbf{q}_c}{\partial \mathbf{p}} \end{pmatrix} &= -\begin{pmatrix} \mathbf{B}_a^T\mathbf{M}_c\mathbf{B}_a & \mathbf{B}_a^T\mathbf{M}_c\mathbf{B}_c \\ \mathbf{B}_c^T\mathbf{M}_c\mathbf{B}_a & \mathbf{B}_c^T\mathbf{M}_c\mathbf{B}_c \end{pmatrix}^{-1} \begin{pmatrix} \mathbf{B}_a^T\mathbf{M}_c\mathbf{A}_c \\ \mathbf{B}_c^T\mathbf{M}_c\mathbf{A}_c \end{pmatrix} \\ \begin{pmatrix} \mathbf{L}_c^- \\ \frac{\partial \mathbf{q}_c}{\partial \mathbf{g}} \end{pmatrix} &= -\begin{pmatrix} \mathbf{B}_a^T\mathbf{M}_c\mathbf{B}_a & \mathbf{B}_a^T\mathbf{M}_c\mathbf{B}_c \\ \mathbf{B}_c^T\mathbf{M}_c\mathbf{B}_a & \mathbf{B}_c^T\mathbf{M}_c\mathbf{B}_c \end{pmatrix}^{-1} \begin{pmatrix} \mathbf{B}_a^T\mathbf{M}_c\mathbf{L}_c \\ \mathbf{B}_c^T\mathbf{M}_c\mathbf{L}_c \end{pmatrix} \end{aligned} \tag{9}$$

We can now extend the notion of the inverse transformation and its Jacobians onto the sensor readings by appending the existing metrology model in a straightforward manner:

$$\begin{aligned} \begin{pmatrix} \mathbf{q}_a \\ \mathbf{q}_s \end{pmatrix} = \mathbf{f}_{cs}^-(\mathbf{p},\mathbf{g}) = \begin{pmatrix} \mathbf{f}_c^-(\mathbf{p},\mathbf{g}) \\ \mathbf{f}_s(\mathbf{p},\mathbf{g}) \end{pmatrix} \\ \mathbf{A}^- = \frac{\partial \mathbf{f}_{cs}^-}{\partial \mathbf{p}} = \begin{pmatrix} \mathbf{A}_c^- \\ \mathbf{A}_s \end{pmatrix}, \quad \mathbf{L}^- = \frac{\partial \mathbf{f}_{cs}^-}{\partial \mathbf{g}} = \begin{pmatrix} \mathbf{L}_c^- \\ \mathbf{L}_s \end{pmatrix} \end{aligned} \tag{10}$$

Forward Coordinate Transformation

In the presence of external sensors, the forward coordinate transformation provides the end-effector position (as well as the non-actuated joints and positions of bodies other than the end-effector) best fitting the given actuated joint and sensor values:

$$\mathbf{p} = \mathbf{f}_{cs}^+(\mathbf{q}_a, \mathbf{q}_s, \mathbf{g}) \tag{11}$$

By analogy to the inverse transformation, the best fit has to minimise a quadratic norm, which this time extends over both the loop constraints and the sensor readings:

$$\begin{aligned} E_{cs} = &\mathbf{f}_c(\mathbf{p},\mathbf{q}_a,\mathbf{q}_c,\mathbf{g})^T \mathbf{M}_c \mathbf{f}_c(\mathbf{p},\mathbf{q}_a,\mathbf{q}_c,\mathbf{g}) \\ &+\left[\mathbf{f}_s(\mathbf{p},\mathbf{g}) - \mathbf{q}_s\right]^T \mathbf{M}_s \left[\mathbf{f}_s(\mathbf{p},\mathbf{g}) - \mathbf{q}_s\right] \end{aligned} \tag{12}$$

We demand again that the gradient of criterion (12) be equal to zero. In this case, the Newton-Raphson method yields the following iterative formula:

$$\begin{aligned} \begin{pmatrix} \mathbf{p} \\ \mathbf{q}_c \end{pmatrix}_{i+1} = \begin{pmatrix} \mathbf{p} \\ \mathbf{q}_c \end{pmatrix}_i - \\ \begin{pmatrix} \mathbf{A}_c^T\mathbf{M}_c\mathbf{A}_c + \mathbf{A}_s^T\mathbf{M}_s\mathbf{A}_s & \mathbf{A}_c^T\mathbf{M}_c\mathbf{B}_c \\ \mathbf{B}_c^T\mathbf{M}_c\mathbf{A}_c & \mathbf{B}_c^T\mathbf{M}_c\mathbf{B}_c \end{pmatrix}_i^{-1} \cdot \\ \begin{pmatrix} \mathbf{A}_c^T\mathbf{M}_c & \mathbf{A}_s^T\mathbf{M}_s \\ \mathbf{B}_c^T\mathbf{M}_c & \mathbf{0} \end{pmatrix}_i \begin{pmatrix} \mathbf{f}_c(\mathbf{p},\mathbf{q}_a,\mathbf{q}_c,\mathbf{g}) \\ \mathbf{f}_s(\mathbf{p},\mathbf{g}) - \mathbf{q}_s \end{pmatrix}_i \end{aligned} \tag{13}$$

One auxiliary matrix we will need later is the Jacobian of the forward transformation over the geometry parameters. Differentiating (12) by analogy to (5) and (8), and solving the resulting linear system yields:

$$\begin{aligned} \mathbf{L}^+ = \frac{\partial \mathbf{f}_{cs}^+}{\partial \mathbf{g}}, \quad \begin{pmatrix} \mathbf{L}^+ \\ \frac{\partial \mathbf{q}_c}{\partial \mathbf{g}} \end{pmatrix} = \\ -\begin{pmatrix} \mathbf{A}_c^T\mathbf{M}_c\mathbf{A}_c + \mathbf{A}_s^T\mathbf{M}_s\mathbf{A}_s & \mathbf{A}_c^T\mathbf{M}_c\mathbf{B}_c \\ \mathbf{B}_c^T\mathbf{M}_c\mathbf{A}_c & \mathbf{B}_c^T\mathbf{M}_c\mathbf{B}_c \end{pmatrix}^{-1} \cdot \\ \begin{pmatrix} \mathbf{A}_c^T\mathbf{M}_c\mathbf{L}_c + \mathbf{A}_s^T\mathbf{M}_s\mathbf{L}_s \\ \mathbf{B}_c^T\mathbf{M}_c\mathbf{L}_c \end{pmatrix} \end{aligned} \tag{14}$$

CALIBRATION

During calibration, as the manipulator performs a sequence of movements, all the sensor readings and joint values are registered. By analogy to [1], we apply to them a composition of the forward and inverse transformations which we have defined above. This operation provides the anticipated sensor readings and joint values:

$$\mathbf{h}(\mathbf{q}_a,\mathbf{q}_s,\mathbf{g}) = \mathbf{f}_{cs}^{-}\left(\mathbf{f}_{cs}^{+}(\mathbf{q}_a,\mathbf{q}_s,\mathbf{g}),\mathbf{g}\right) \quad (15)$$

The discrepancy between the anticipated and the measured values depends on the model parameters effective in the above forward-inverse composition:

$$\Delta\mathbf{q} = \mathbf{h}(\mathbf{q}_a,\mathbf{q}_s,\mathbf{g}) - \begin{pmatrix}\mathbf{q}_a\\ \mathbf{q}_s\end{pmatrix} \quad (16)$$

The aim of calibration is to find the parameter values for which a quadratic norm of the above discrepancy (16) over all the measurement positions assumes a minimum:

$$E_{cal}(\mathbf{g}) = \sum_{k=1}^{K} \Delta\mathbf{q}_k^T \mathbf{M}_{as} \Delta\mathbf{q}_k \quad (17)$$

Matrix $\mathbf{M}_{as}$ in (17) reflects the relative accuracy of the various sensors and actuators. It can be shown that the calibration result will be optimal in the sense of Maximum Likelihood (ML) if $\mathbf{M}_{as}$ is the inverse of the sensor-actuator covariance matrix. We demand, once again, that the gradient of criterion (17) be equal to zero:

$$\min_{\mathbf{g}} E_{cal}(\mathbf{g}) \Rightarrow \frac{\partial E_{cal}}{\partial \mathbf{g}} = \sum_{k=1}^{K}\left(\frac{\partial \mathbf{h}}{\partial \mathbf{g}}\right)^T \mathbf{M}_{as}\Delta\mathbf{q} = \mathbf{0} \quad (18)$$

Applying the Newton-Raphson method to finding a zero of (18) leads to the following iterative formula:

$$\begin{aligned}\mathbf{g}_{i+1} &= \mathbf{g}_i - \left(\frac{\partial^2 E_{cal}}{\partial \mathbf{g}^2}\right)_i^{-1}\left(\frac{\partial E_{cal}}{\partial \mathbf{g}}\right)_i = \\ &= \mathbf{g}_i - \left(\sum_{k=1}^{K}\mathbf{H}^T\mathbf{M}_{as}\mathbf{H}\right)^{-1}\cdot\sum_{k=1}^{K}\mathbf{H}^T\mathbf{M}_{as}\Delta\mathbf{q}_k\end{aligned} \quad (19)$$

where the matrix **H** is a generalised version of the redundancy matrix introduced by the Authors in [1] and can be computed with the previously introduced auxiliary matrices, cf. (7), (10) and (14):

$$\mathbf{H} = \frac{\partial \mathbf{h}}{\partial \mathbf{g}} = \frac{\partial \mathbf{f}_{cs}^{-}}{\partial \mathbf{p}}\frac{\partial \mathbf{f}_{cs}^{+}}{\partial \mathbf{g}} + \frac{\partial \mathbf{f}_{cs}^{-}}{\partial \mathbf{g}} = \mathbf{A}^{-}\mathbf{L}^{+} + \mathbf{L}^{-} \quad (20)$$

SIMULATION EXAMPLE

The operation of the method has been demonstrated in a Mathematica simulation on a simple example involving a 2-DoF manipulator, whose motions in the remaining 4 DoFs are restricted by a system of mechanical linkages, and whose spatial position is measured in 3 DoFs with external displacement sensors (Figure 1).

The model involves 3 moving bodies in addition to the tetrahedral end-efector (2 actuated bodies and 1 compliant linkage), 2 actuated joints, as well as 2 non-actuated joints (at the compliant linkage). The external sensors are idealised as providing absolute distances between 3 stationary surfaces (X, Y and Z planes) in the reference frame and a point on the moving end-effector (the top vertex of the tetrahedron). The geometry parameters include the lengths of all linkages and the dimensions of the tetrahedron.

In the course of the simulation, the stage is brought to 5^2 = 25 different positions representing combinations of 5 values in each of the 2 available DoF. The simulation shows that all the geometry parameters can be calibrated from the sensor and actuator readings.

CONCLUSIONS

Our paper presents a methodology for calibrating parallel manipulators with restricted degrees of freedom. We propose a general form of an analytical kinematic model with joint values as arguments of loop closure constraints and an analytical metrology model with sensor readings as its output. We then derive iterative expressions for the inverse and forward coordinate transformations between the end-effector position and the joint and sensor values. Finally, we use the composition of both the transformations to calibrate the manipulator model by analogy to [1]. The advantage of the method is the constant, small size of the calibration matrix, irrespective of the number of measurement points.

REFERENCES

1. Meyer, P.J., van Eijk, J., 2004, In-Situ Calibration of a Redundant Measurement System for Manipulator Positioning, *Proceedings of the 2004 ASPE Topical Meeting, State College, PA, U.S.A.*

TOOL-HOLDER CONNECTION MODELING FOR FREQUENCY RESPONSE PREDICTION IN MILLING

Kevin B. Powell, Dongki Won, Tony L. Schmitz, G. Scott Duncan, W. Gregory Sawyer, John C. Ziegert
Department of Mechanical and Aerospace Engineering
University of Florida
Gainesville, FL, USA

INTRODUCTION

Discrete part production by milling is an important manufacturing capability. However, there are many potential obstacles to producing quality parts at low cost in a timely manner. One particular limitation that has received considerable attention in the literature is chatter, or unstable machining; a second is surface location error, or an error in the part dimension caused by dynamic deflections of the tool (and potentially the part/fixture) during stable cutting. In both cases, a primary factor affecting the process performance is the system frequency response function, or FRF.

The system FRF, often dominated by the flexibility of the tool-holder-spindle assembly as reflected at the tool's free end, can be obtained using impact testing, where an instrumented hammer is used to excite the tool at its free end (i.e., the tool point) and the resulting vibration is measured using an appropriate transducer. However, due to the large number of spindle, holder, and tool combinations that may be available in a particular production facility, the required testing time can be significant. Further, the measured response is often strongly dependent on the tool overhang length. Therefore, a model which is able to predict the tool point response based on minimum input data is the preferred alternative.

The purpose of this paper is to build on the previous work of Schmitz *et al.* [1-3], which describes tool point FRF, or receptance, prediction using the Receptance Coupling Substructure Analysis (RCSA) method. In these previous studies, two and three component models of the machine-spindle-holder-tool assembly were defined. In this work, we extend the three component model to include multiple connections between the tool and holder along the interference contact within the (thermal) shrink fit holder. This is shown schematically in Fig. 1, where multiple complex stiffness matrices, K_i, describe the connection parameters at each location. In this new model the fully populated K matrix is defined as shown in Eq. 1, which accounts for the displacement imposed by moment and the rotation caused by force through the non-zero off diagonal terms. Finite element models are developed to determine the position-dependent stiffness and equivalent viscous damping values for a thermal shrink fit connection between the tool and holder, which represents the preferred interface for high-speed milling applications. Using these values, the tool point FRF is predicted *a priori* and compared to measurements.

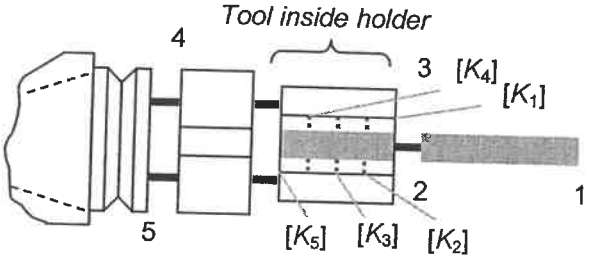

Figure 1. Three component RCSA model – the finite stiffness/damping between the tool and holder is represented by multiple K matrices determined from finite element simulation.

$$K = \begin{bmatrix} k_{yf} + i\omega \cdot c_{yf} & k_{ym} + i\omega \cdot c_{ym} \\ k_{\theta f} + i\omega \cdot c_{yf} & k_{\theta m} + i\omega \cdot c_{ym} \end{bmatrix} \quad (1)$$

RCSA MODEL

The RCSA spindle-holder-tool model is composed of three components. The spindle response is obtained by inserting a standard geometry artifact in the spindle and recording one direct and one cross FRF on the artifact. Using this data, together with a model of the artifact, the spindle receptances may be obtained by decoupling the artifact response from the spindle [3]. As shown in Fig. 1, the holder is separated into two sections: the portion with the tool inserted and the remainder of the

holder. In this work, we couple the portion of the tool inside the holder to the holder through multiple damped springs to capture the non-rigid behavior of the shrink fit connection. Finally, the portion of the tool outside the holder is rigidly coupled to the holder and spindle to predict the tool point FRF.

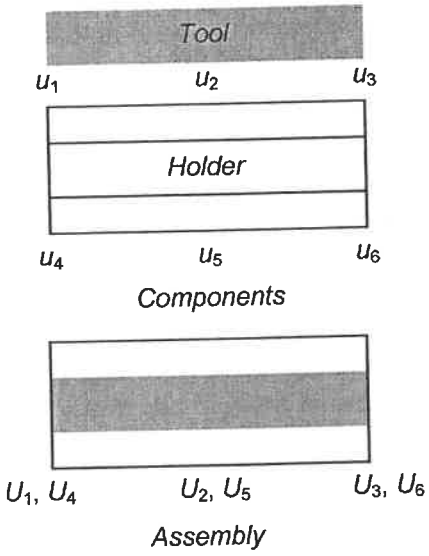

Figure 2. Tool-in-holder coordinates.

To demonstrate the coupling between the concentric inner tool and outer holder components, the case of n = 3 connection coordinates, located at the ends of the contact length and at the mid-point, is now presented. The portions of the tool and holder in shrink fit contact are treated as free-free beams. For n = 3, a total of six component coordinates is obtained – three each on the internal tool and external holder (see Fig. 2) [4]. The component displacement/rotations can be written as shown.

$$\begin{aligned} u_1 &= R_{11}q_1 + R_{12}q_2 + R_{13}q_3 \\ u_2 &= R_{21}q_1 + R_{22}q_2 + R_{23}q_3 \\ u_3 &= R_{31}q_1 + R_{32}q_2 + R_{33}q_3 \\ u_4 &= R_{44}q_4 + R_{45}q_5 + R_{46}q_6 \\ u_5 &= R_{54}q_4 + R_{55}q_5 + R_{56}q_6 \\ u_6 &= R_{64}q_4 + R_{65}q_5 + R_{66}q_6 \end{aligned} \quad (2)$$

Here, the component displacements/rotations, forces/moments, and receptances are $u_i = \{y_i \quad \theta_i\}^T$, $q_i = \{f_i \quad m_i\}^T$, and,

$$R_{ij}(\omega) = \begin{bmatrix} \frac{y_i}{f_j} & \frac{y_i}{m_j} \\ \frac{\theta_i}{f_j} & \frac{\theta_i}{m_j} \end{bmatrix} = \begin{bmatrix} h_{ij} & l_{ij} \\ n_{ij} & p_{ij} \end{bmatrix}$$

respectively. The compatibility conditions for the flexible/damped shrink fit connection are:

$$K_1(u_4 - u_1) = -q_4,\ K_2(u_5 - u_2) = -q_5, \text{ and,}$$
$$K_3(u_6 - u_3) = -q_6, \quad (3)$$

where K_i is given by Eq. 1 and the component and assembly coordinates are defined at the same spatial locations so that $u_i = U_i$, i = 1 to 6. If the assembly direct response at the left end, $G_{11}(\omega)$, is to be determined, Q_1 is applied to coordinate U_1 of the assembly (the upper case variables denote assembly coordinates, forces, and moments). The equilibrium conditions are then $q_1 + q_4 = Q_1$, $q_2 + q_5 = 0$, and $q_3 + q_6 = 0$.

G_{11} is determined in steps using the relevant equations. The first step is to insert the component displacement/rotation expressions into the compatibility conditions. The next step is to substitute $q_4 = Q_1 - q_1$, $q_5 = -q_2$, and $q_6 = -q_3$ and rearrange to obtain:

$$\begin{bmatrix} R_{11} + R_{44} + K_1^{-1} & R_{12} + R_{45} & R_{13} + R_{46} \\ R_{21} + R_{54} & R_{22} + R_{55} + K_2^{-1} & R_{23} + R_{54} \\ R_{31} + R_{64} & R_{32} + R_{65} & R_{33} + R_{66} + K_3^{-1} \end{bmatrix} \cdot$$
$$\begin{Bmatrix} q_1 \\ q_2 \\ q_3 \end{Bmatrix} = Q_1 \begin{bmatrix} R_{44} + K_1^{-1} \\ R_{54} \\ R_{64} \end{bmatrix}$$

which gives the relationship between the component forces/moments and externally applied force/moment. G_{11} can be expressed as:

$$G_{11} = \frac{U_1}{Q_1} = \frac{u_1}{Q_1} = R_{11}\frac{q_1}{Q_1} + R_{12}\frac{q_2}{Q_1} + R_{13}\frac{q_3}{Q_1}, \quad (4)$$

so the ratios $\frac{q_1}{Q_1}$, $\frac{q_2}{Q_1}$, and $\frac{q_3}{Q_1}$ are required. These can be determined from:

$$\frac{1}{Q_1}\begin{Bmatrix} q_1 \\ q_2 \\ q_3 \end{Bmatrix} =$$

$$\begin{bmatrix} R_{11}+R_{44}+K_1^{-1} & R_{12}+R_{45} & R_{13}+R_{46} \\ R_{21}+R_{54} & R_{22}+R_{55}+K_2^{-1} & R_{23}+R_{54} \\ R_{31}+R_{64} & R_{32}+R_{65} & R_{33}+R_{66}+K_3^{-1} \end{bmatrix}^{-1} \cdot \begin{bmatrix} R_{44}+K_1^{-1} \\ R_{54} \\ R_{64} \end{bmatrix} = [A]$$

where [*A*] is a 6 by 2, or 2*n* by 2, by *N* matrix (*N* is the number of points in the frequency vector, ω). The reader may note that the matrix size is 6 by 2 because R_{ij} is a 2 by 2 matrix. The matrix *A* is partitioned as follows: the first two rows of *A* give $\frac{q_1}{Q_1}$; the second two rows provide $\frac{q_2}{Q_1}$; and the final two rows give $\frac{q_3}{Q_1}$. The desired direct receptances can then be computed from Eq. 4. This 3-point coupling example can be extended to *n* coupling points by recognizing the recursive pattern in [*A*].

Once the shrink fit connection stiffness is incorporated into the tool-holder assembly as defined in the next section, the remaining components can be rigidly coupled. Assembly coordinate definitions for the overhung portion of the tool (1-2), extended holder (3-4), and spindle-holder base (5) are shown in Fig. 1. The corresponding RCSA equation for the assembly receptances at the tool point is obtained by: 1) rigidly coupling the overhung free-free tool to the free-free tool-extended holder to determine the new subassembly direct receptances at each end, GS_{11} and GS_{44}, and the cross receptances, GS_{14} and GS_{41}; and 2) using the standard holder and finite difference calculations to determine the four receptances at the free end of the standard holder, removing the portion of the standard holder beyond the flange using inverse RCSA, and defining the direct receptance at the free end of the spindle-holder subassembly, GS_{55}. See the next equation, where $H_{11}(\omega)=\frac{Y_1}{F_1}$ is the FRF generally required for milling stability and surface location error analyses. Additional details are available in references [3-4].

$$G_{11}=\begin{bmatrix} H_{11} & L_{11} \\ N_{11} & P_{11} \end{bmatrix} = GS_{11} - GS_{14}\left(GS_{44}+GS_{55}\right)^{-1} GS_{41}$$

FINITE ELEMENT MODEL

A model for a 19.1 mm diameter carbide tool blank inserted in a steel tapered shrink fit holder was developed using ANSYS. The boundary conditions were set as fixed-free and only the extended holder and tool were modeled. In this example, 6324 20-node cubic elements (SOLID184), 768 8-node contact elements (CONTA174), and 768 8-node target elements (TARGE170) were applied, where the flexible-to-flexible contact/target elements were located at the interface between the tool and holder. The coordinate directions for the model were: *x* – horizontal, *y* – vertical, *z* – along the tool axis.

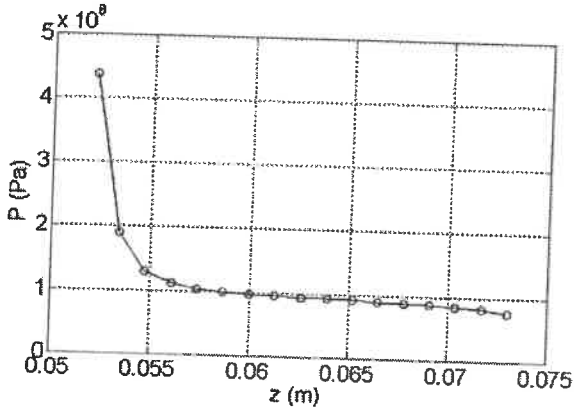

Figure 3. Simulated contact pressure profile for the shrink fit tool-holder interface (10 μm radial interference). The z axis origin was located at the fixed end of the holder.

The finite element simulations were carried out in two primary time intervals. In the first interval, the contact pressure between the tool and holder was allowed to grow due to the imposed radial interference. Figure 3 shows the simulated contact pressure, *P*, profile for the model with a 10 μm radial interference. In the second interval, the *y* direction force or couple was applied to the tool just beyond the end of contact. The forces were applied using an equivalent nodal force arrangement (to minimize localized deformation effects). For both intervals, time was divided into five equal steps.

The position-dependent stiffness values were determined using the following steps. At the end of the two time intervals, the *y* direction displacements of the tool at nodes along the tool

top centerline were recorded. The y displacements, as a function of z location, imposed by the force/couple were then computed by differencing the two results. By applying a range of forces and couples, the $k_{yf}(z)$ and $k_{ym}(z)$ stiffness values from Eq. 1 were calculated directly from the slope of the load-displacement curves for each node under consideration. For the $k_{\theta f}(z)$ and $k_{\theta m}(z)$ stiffness values, the rotation was first calculated by central finite difference from the displacement data, then the stiffness values were obtained from the load-rotation curve slope values. Example results for the $k_{yf}(z)$ values are provided in Fig. 4.

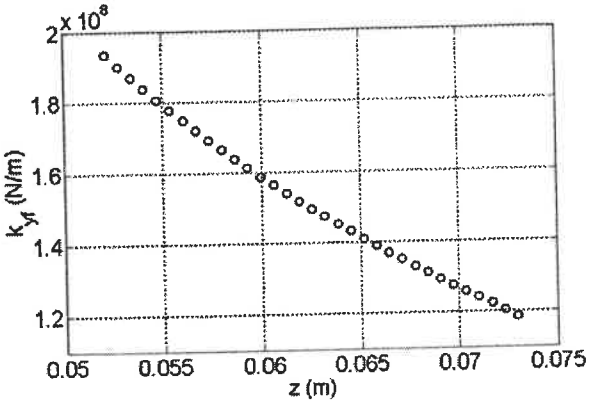

Figure 4. Stiffness values for the finite element model (10 μm radial interference).

It was assumed that energy dissipation in the shrink fit connection occurred due to relative micro-slip between the tool and holder along the tool axis during the force/couple application. This Coulomb damping was converted to position-dependent equivalent viscous damping values by: 1) computing the friction (damping) force, F_d, for each element, n; 2) calculating the viscous damping value for each element according to $c_{eq,n} = \frac{4F_{d,n}}{\pi\omega \cdot |z_n|}$ [6], where $|z_n|$ is the absolute value of the contact element displacement along the tool axis; and 3) summing the damping values for the elements located around the tool circumference for the selected z location.

RESULTS

To test the approach, thirty 19.1 mm diameter carbide tool blanks were sequentially inserted in the modeled holder and the tool point FRF was recorded. The insertion length was maintained at 22.9 mm while the overhang length varied from {66.0 to 142.2} mm. A comparison of the measurements and predictions is shown in Fig. 5. The top and middle panels show the measurements and predictions (same scale). The bottom panel shows the percent difference between the measured and predicted (dominant) natural frequencies as a function of the tool overhang length. Agreement of 2% or better is observed for all cases.

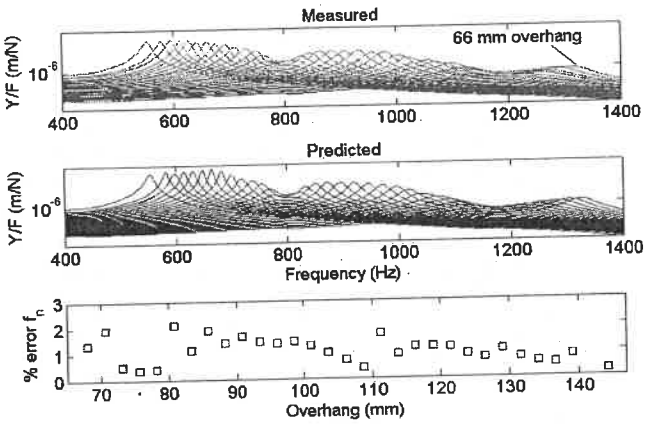

Figure 5. Top – measured FRF magnitudes; middle – predicted magnitudes; and bottom – percent difference between measured and predicted (dominant) natural frequencies, f_n.

ACKNOWLEGEMENTS

This work was supported by the National Science Foundation (DMI-0238019), the Office of Naval Research, and TechSolve. The three-component RCSA approach is patent-pending.

REFERENCES

1. Schmitz, T. and Donaldson, R., 2000, Predicting High-Speed Machining Dynamics by Substructure Analysis; *Annals of the CIRP*, 49/1: 303-308.
2. Schmitz, T., Davies, M., and Kennedy, M., 2001, Tool Point Frequency Response Prediction for High-Speed Machining by RCSA, *Journal of Manufacturing Science and Engineering*, 123: 700-707.
3. Schmitz, T. and Duncan, G.S., 2005, Three-Component Receptance Coupling Substructure Analysis for Tool Point Dynamics Prediction; *Journal of Manufacturing Science and Engineering*, 127/4: 781-790.
4. Schmitz, T., Duncan, G.S., 2006, Receptance Coupling for Dynamics Prediction of Assemblies with Coincident Neutral Axes, *Journal of Sound and Vibration*, 289/4-5: 1045-1065.
5. Thomson, W. and Dahleh, M., 1998, *Theory of Vibration with Applications*, 5th Edition, Prentice Hall, Upper Saddle River, NJ.

A GENERAL GEOMETRIC MODEL FOR DETERMINING OPTIMAL SHAPES OF PLANAR ELASTIC PIVOTS

R. Ryan Vallance[1], B. Haghighian[1], and Eric R. Marsh[2]
[1] **Precision Systems Laboratory, The George Washington University**
Washington, DC USA
[2] **Machine Dynamics Research Laboratory, The Pennsylvania State University**
University Park, PA 16802

INTRODUCTION

Elastic (flexural) pivots are commonly used in precision machines and instruments as bearings for guiding small displacements and rotations [1]. They provide accurate motion without friction and with very little hysteresis. Elastic pivots, such as those illustrated in Fig. 1, are often designed using straight beams or conic sections with circular, elliptical, parabolic, or hyperbolic shapes. Previously, each of these shapes required separate analyses using different analytical equations or finite element analysis (FEA). In this paper, we describe a general geometric model capable of representing all these shapes using two-dimensional, quadratic, rational Bézier curves. This mathematical representation of the geometry is well suited for computer aided design, analysis (either analytical or FEA), and optimization studies.

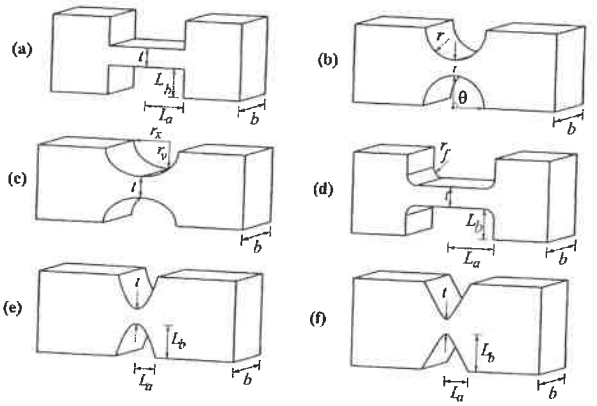

FIGURE 1. Elastic pivot shapes and their commonly used dimensions, (a) leaf spring, (b) circular, (c) elliptical, (d) corner-filleted, (e) parabolic, and (f) hyperbolic

e performance of elastic pivots depends on ee crucial aspects: compliance (or its inverse ness), accuracy of motion (e.g. rotation with- translation), and the amount of stress result- rom elastic deformation. An ideal elastic pivot would have high compliance in the intended direction of rotation and infinite stiffness in the remaining directions. Since this is not possible, designers must compromise on attributes like static stiffness, resonant frequencies, and lost motion.

Analytical estimates of compliance for several pivot shapes are available [2, 3, 4]. However, fewer analytical approaches are available for predicting the stress within the pivot, which is necessary for determining the pivots range of rotation. Therefore, it is common for designers to use analytical models to estimate compliance and then use FEA to validate the compliance, determine the stress, and determine motion range.

This design method is not ideal. Since analytical models are unique to each pivot shape, designers must consider alternate shapes independently and consecutively. Many designers therefore only consider a single shape, despite having analytical models of compliance for a variety of shapes. Those that consider alternate shapes often find that a single best choice is not obvious, especially when the designer considers several design parameters and performance factors (e.g. high resonant frequencies in multiple directions, static stiffness, manufacturing constraints, etc.). It would therefore be beneficial to have a unified geometric model applicable for most pivot shapes that is compatible with analysis techniques and optimization. This paper presents such a model, and it was recently applied and demonstrated by Haghighian [5].

QUADRATIC RATIONAL BÉZIER CURVES

Circles, ellipses, parabolas, and hyperbolas are all conic sections generated by the intersection of a plane with a cone. When these curves lie in a two-dimensional Cartesian plane, the coordinates of points along the curve satisfy an implicit equation. The explicit form of the equation gives the y-coordinate of points along the curve as a function of the independent x-coordinate. Explicit equa-

tions are typically used by others when deriving analytical estimates of compliance for elastic pivots. Alternatively, conic sections can be specified with parametric equations, such as Eq. 1 for a circle. This is more convenient for curve evaluation since the independent variable is the parametric variable $0 \leqq s \leqq 1$.

$$\begin{bmatrix} x \\ y \end{bmatrix} = \begin{bmatrix} x_o \\ y_o \end{bmatrix} + r \begin{bmatrix} cos(s\theta) \\ sin(s\theta) \end{bmatrix} \quad (1)$$

A single parametric equation can represent all of the conic sections. This is achieved with quadratic rational Bézier curves [6], which exactly represent conic sections and other shapes via the ratio of polynomial functions. The coordinates $[x, y]$ of points along a two dimensional rational Bézier curve of order n are computed with Eq. 2 in terms of the parametric variable s, the coordinates of the $n+1$ control points $\mathbf{P}_i$, and the $n+1$ scalar weights w_i that are applied to each control point. The parametric variable s varies between zero and one, and the Bernstein polynomials $B_{i,n}$, given by Eq. 3.

$$\begin{bmatrix} x \\ y \end{bmatrix} = \frac{\sum_{i=0}^{n} B_{i,n}(s)\, w_i \mathbf{P}_i}{\sum_{i=0}^{n} B_{i,n}(s)\, w_i} \quad (2)$$

$$B_{i,n}(s) = \frac{n!}{i!\,(n-i)!} s^i (1-s)^{n-i} \quad (3)$$

When the curve is quadratic (three control points and $n = 2$), Eq. 2 is expanded using Eq. 3 to obtain Eq. 4. It is sometimes convenient to divide the coefficients in the numerator by the denominator to form $n+1$ rational blending functions $R_{i,n}(s)$ since these directly blend the coordinates of the control points, as shown in Eq. 5.

$$\begin{bmatrix} x \\ y \end{bmatrix} = \frac{w_0 (1-s)^2 \mathbf{P}_0 + 2w_1 s (1-s) \mathbf{P}_1 + w_2 s^2 \mathbf{P}_2}{w_0 (1-s)^2 + 2w_1 s (1-s) + w_2 s^2} \quad (4)$$

$$\begin{bmatrix} x \\ y \end{bmatrix} = R_{0,2}(s)\, \mathbf{P}_0 + R_{1,2}(s)\, \mathbf{P}_1 + R_{2,2}(s)\, \mathbf{P}_2 \quad (5)$$

Quadratic rational Bézier curves therefore use three control points, $\mathbf{P}_i = [x_i, y_i, z_i]$ where $i = 0, 1$, or 2, to regulate their shape. The curve starts at control point $\mathbf{P}_0$ when $s = 0$, and it ends at control point $\mathbf{P}_2$ when $s = 1$. The tangency of the curve at $\mathbf{P}_0$ is parallel to $\mathbf{P}_1 - \mathbf{P}_0$, and the tangency of the curve at $\mathbf{P}_2$ is parallel to $\mathbf{P}_2 - \mathbf{P}_1$. The control polygon (triangle for second order with $n = 2$) for the curve is formed by line segments L_i that connect the control points.

Figure 2(a) shows an example that is applicable to elliptical pivots [3]. The elliptical pivot has dimensions $t = 0.002$ m, $r_x = 0.005$ m, and $r_y = 0.003$ m. It is specified with three control points $\mathbf{P}_1 = [0, t/2] = [0, 0.001]$, $\mathbf{P}_2 = [r_x, t/2] = [0.005, 0.001]$, and $\mathbf{P}_3 = [r_x, t/2 + r_y] = [0.005, 0.004]$ and three weights, where $w_0 = w_2 = 1$ and $w_1 = \sqrt{2}/2$. Figure 2(b) also shows plots of the curve's rational functions $R_{i,n}(s)$ as used in Eq. 5. The specification of one quarter of a circle is a special case of an ellipse that is obtained in a similar fashion, with the weight $w_1 = \sqrt{2}/2$.

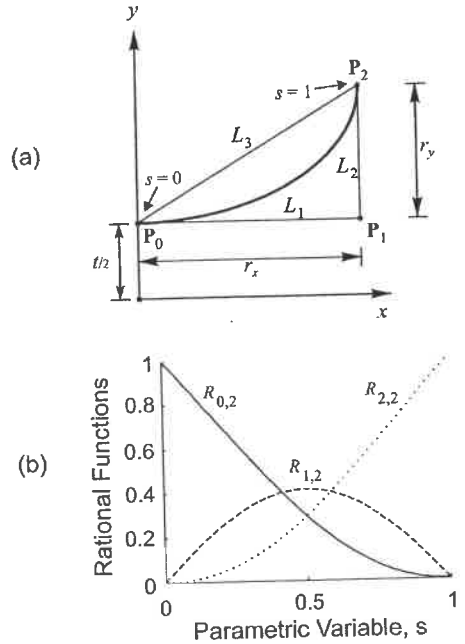

FIGURE 2. (a) Elliptical curve for elastic pivot, specified as a quadratic rational Bézier curve with three control points and its (b) rational blending functions

GENERAL MODEL

A general geometric model for half of an elastic pivot is constructed using the parametric equations for quadratic rational Bézier curves.

Figure 3 shows the model, and it consists of twelve curve segments c_i. Curve segments c_3 and c_{10} are quadratic rational Bézier curves, and all others are simple line segments with Bézier representations. The origin of a Cartesian coordinate system is located at the center of the pivot so that the two planes of symmetry coincide with the x-z and y-z planes. The shape of the pivot is governed by fifteen control points $\mathbf{P}_1$ through $\mathbf{P}_{15}$ and their corresponding weights w_1 through w_{15}. The coordinates of these control points and their weights are collected within a control points matrix cp as shown in Eq. 6.

$$cp = \begin{bmatrix} \mathbf{P}_1 & \mathbf{P}_2 & \dots & \mathbf{P}_{15} \\ w_1 & w_2 & \dots & w_{15} \end{bmatrix} \tag{6}$$

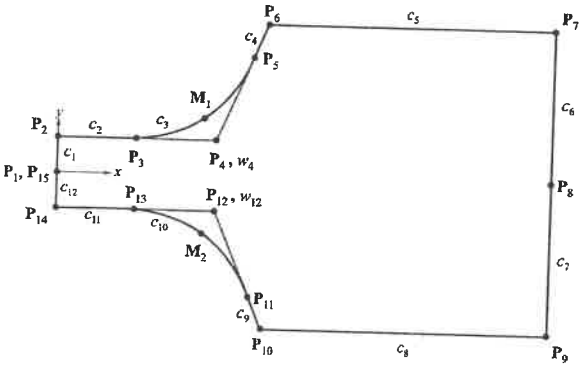

FIGURE 3. A general geometric model for the perimeter of half of an elastic pivot, based on a set of line and curve segments specified by fifteen control points and weights.

All of the pivots illustrated in Fig. 1 can be constructed using this general model, but some of these pivots do not require all of the line or curve segments. The leaf spring does not require c_3 and c_{10}, and the circular, elliptical, parabolic, and hyperbolic pivots do not require c_2, c_4, c_9 ,and c_{11}. The corner-filleted pivot requires all of the line and curve segments. Therefore, a shape vector S, given in Eq. 7, accounts for whether each curve c_i is included in the pivot's shape. An element s_i corresponds to segment c_i, and its value equals zero if the segment is not present within the shape, one if the segment is a line, and two if the segment is a quadratic rational Bézier curve. Although quadratic rational Bézier curves can represent lines, it is sometimes useful to distinguish between the two. As an example, the shape vector S for an elliptical pivot in which segments c_2, c_4, c_9, c_{11} are not present and c_3 and c_{10} are curves is given by $\mathbf{S} = [102011110201]^T$.

$$\mathbf{S} = [s_0, s_1, s_2, ..., s_{15}]^T \tag{7}$$

The coordinates of the 15 control points shown in Figure 3 and collected in cp are determined from a set of design parameters that include the following:

- t, the thickness of the pivot in the y-z plane,
- L_1, the length of line segment c_2,
- $\mathbf{T}_3 = [T_3^x, T_3^y]$, the tangency vector at control point $\mathbf{P}_3$,
- $\mathbf{M} = [M^x, M^y]$, some point along the middle of curve segment c_3,
- $\mathbf{P}_5 = [P_5^x, P_5^y]$, a position vector locating control point $\mathbf{P}_5$,
- $\mathbf{T}_5 = [T_5^x, T_5^y]$, the tangency vector at control point $\mathbf{P}_5$,
- L_2, the length of line segment c_4, and
- L_3, the length of line segment c_5.

These design parameters are collected within a design vector $\mathbf{X}$ as shown in Eq. 8, which consists of twelve scalar dimensions, coordinates, or components of the tangent vectors.

$$\mathbf{X} = [t, L_1, T_3^x, T_3^y, M^x, M^y, P_5^x, P_5^y, T_5^x, T_5^y, L_2, L_3] \tag{8}$$

The common shapes shown in Fig. 1 require that some of the design parameters be constrained to particular values. Table 1 lists the form of the shape vector S and gives equations for determining the constrained values of the design parameters for the common shapes. The tangency vector $\mathbf{T}_3$ equals $[1, 0]$ so that continuity in the first derivative is satisfied at control points $\mathbf{P}_2$ or $\mathbf{P}_3$. The components of $\mathbf{M}$, $\mathbf{P}_5$ and $\mathbf{T}_5$ are found by rearranging the implicit equations of the conic sections.

IMPLEMENTATION FOR COMPUTER AIDED DESIGN AND ANALYSIS

The geometric model was implemented by Haghighian [5] within a toolbox of scripts that run within Matlab™and enable the computer aided design, analysis, and optimization of elastic pivots. It is possible to model the shape of elastic

TABLE 1. Values of design parameters for common pivot shapes

DP	Circle	Ellipse	Corner Filleted	Parabolic
S	$[102011110201]^T$	$[102011110201]^T$	$[112111111211]^T$	$[102011110201]^T$
L_1	–	–	$L_a - r_f$	–
T_1^x	1	1	1	1
T_1^y	0	0	0	0
M^x	$r\sin\left(\frac{\theta}{2}\right)$	$r_x\cos\left(\frac{\pi}{4}\right)$	$L_1 + r_f\cos\left(\frac{\pi}{4}\right)$	$\frac{L_a}{2}$
M^y	$\frac{t}{2} + r\left(1-\cos\left(\frac{\theta}{2}\right)\right)$	$\frac{t}{2} + r_y\left(1-\sin\left(\frac{\pi}{4}\right)\right)$	$\frac{t}{2} + r_f\left(1-\sin\left(\frac{\pi}{4}\right)\right)$	$\frac{3t}{8} + \frac{L_b}{4}$
P_5^x	$r\sin(\theta)$	r_x	$L_1 + r_f$	L_a
P_5^y	$\frac{t}{2} + r\left(1-\cos(\theta)\right)$	$\frac{t}{2} + r_y$	$\frac{t}{2} + r_f$	L_b
T_5^x	$\sin\left(\frac{\pi}{2}-\theta\right)$	1	1	1
T_5^y	$\cos\left(\frac{\pi}{2}-\theta\right)$	0	0	$\frac{1}{L_a}(2L_b - t)$
L_2	–	–	$L_b - r_f$	–

pivots in four possible representations. The first representation uses the dimensions of the common pivot shapes as illustrated in Figure 1. A function named 'fptptodp' converts these dimensions into values of the design parameters using Table 1. It is then possible to convert from the design parameter representation to coordinates and weights of the control points using the 'fpdptocp' function or vice versa using 'fpcptodp'. Finally, the coordinates of points around the perimeter of the elastic pivot can be determined using the 'fpcptocoords' function.

Plane strain or plane stress FEA is automatically performed by the function 'fpfemlab2d', which builds the pivot shape within FEMLAB ™(COMSOL AB), a finite element program that operates within MATLAB. The script performs three analyses in order to determine a 2D compliance matrix C. The three analyses subject the pivot to an axial load, transverse load, and pure bending, from which the first, second, and third columns of the compliance matrix are determined, respectively. An additional function provides for superposing these results to determine stress within the pivot when simultaneously subjected to combined axial, transverse, and bending loads. Haghighian [5] validated results from our FEA method against others' analytical/fea results, and he also demonstrated the optimization of a pivot's shape using non-linear, constrained optimization techniques that employ the results of finite element analyses (e.g. compliance, deflection, and stress) within the objective function and/or constraints.

CONCLUSIONS

A general geometric model, based on Bézier curves, is described for representing the shapes of most common two-dimensional elastic pivots. The model is implemented in a set of Matlab/COMSOL scripts that permit the design and analysis of pivot shapes in an automated fashion. Although not presented in this paper, Haghighian [5] demonstrated the use of this approach in optimizing pivot shapes for particular load conditions within flexural mechanisms. This work will be presented in a future article.

REFERENCES

[1] S. T. Smith. *Flexures: Elements of Elastic Mechanisms.* CRC Press, 2000.

[2] J. M. Paros and L. Weisbord. How to design flexural hinges. *Machine Design*, pages 151–157, November 25, 1965.

[3] S. T. Smith, V. G. Badami, J. S. Dale, and Y. Xu. Elliptic flexure hinges. *Review of Scientific Instruments*, 68(3):1474–1483, March 1997.

[4] N. Lobontiu. *Compliant Mechanisms: Design of Flexure Hinges.* CRC Press, 2002.

[5] B. Haghigian. A planar model for the design, analysis, and optimization of flexural pivots. Master's thesis, The George Washington University, 2006.

[6] L. Piegl and W. Tiller. *The NURBS Book.* Springer, 1995.

FRACTAL ROUNDNESS MODELING OF EXPERIMENTAL PROFILE IN TURNING

Moon-chul Yoon[1], Jin-seok Jung[2] and Do-hun Chin[3]
[1,3]School of Mechanical Engineering Pukyong National University
San100, Yongdang-Dong, Nam-Gu, Busan, Republic of Korea
[2]Workers Accident Medical Corporation Korea Orthopedics & Rehabilitation Engineering Center
47-3 Kusan-Dong, Pupyoung-Gu, Inchon, Republic of Korea

INSTRUCTION

The characteristics of roundness can be analyzed by investigating the parameter and constant after defining the fractal roundness model. The conventional method can give the precise modeling comparatively but it cannot include the dynamic properties with less initial data in roundness modeling. In roundness presentation, it needs sometimes the dynamic properties in roundness. So, more desirable method must be used for higher dynamic properties in roundness model. For this purpose, the fractal interpolation methods with less data information were used in this study. Also, using the fractal constant in fractal interpolation the characteristic of the roundness in the workpiece is studied. Recently, many researches have been conducted using the fractal analysis. But their application is generally restricted to analyze their objects only using the parameter of fractal dimension. In this study, A fractal analysis was applied to the roundness modeling at first. And the characteristic of fractal roundness model was analyzed and its result was introduced in this study. Also, this method and parameters using fractal analysis can be applied to the several controlling and design parameters of roundness tester.

FRACTAL INTERPOLATION AND DIMENSION

In each roundness profile, the fractal dimension can be defined and calculated. Using this value, the characteristics of the roundness profile can also be defined and analyzed by comparing the values of fractal dimension among different roundness profiles. Generally speaking, it is well known that the fractal dimension in every profile data ranges from 1 to 2. The slope of the fractal geometry can be defined as fractal dimension. Also, the fractal interpolation can be represented to the following equation [1,2].

$$w_n\begin{Bmatrix} x \\ y \end{Bmatrix} = \begin{bmatrix} a_n & 0 \\ c_n & d_n \end{bmatrix}\begin{Bmatrix} x \\ y \end{Bmatrix} + \begin{Bmatrix} e_n \\ f_n \end{Bmatrix} \quad (1)$$

Where a_n, c_n, d_n, e_n and f_n are the related transformation constant in the n-th interval. And if the L is the parted distance parallel to y axis, then the following equation can be defined[1,2].

$$|d_n| = \frac{w_n(L)}{L} \quad (2)$$

Also d_n is the scaling factor having the vertical directionality and w_n is the gradient of geometry and the fractal dimension by contractive mapping can be written as follows. [1,2]

$$\sum_{n=1}^{N} |d_n|\, a_n{}^{D_F-1} = 1 \quad (3)$$

For calculating the fractal dimension in each n-th span, the parameter a_n and d_n must be defined. And after calculating the parameter a_n and d_n in all spans the fractal dimension can be calculated using eq. (3). Also another method was supposed by Strahle[3] using fixed data points. In this study, this fractal dimension is introduced for overcoming the limitation of the methods. The total roundness profile can be acquired by superposing the contractive mapping curve in each group that has two fixed data points.

If the roundness profile is observed in detail it is the combination of the flexion and extension and cause one cycle of profile. For this case the fractal dimension can be defined in another form of function. So, this fractal dimension can be defined in another equation as follows [1-5].

$$ND_F = \frac{\log(L)}{\log(d_i)} \quad (4)$$

Where, L is defined as

$$L = \sum dist\left[(x_i, y_i), (x_{i+1}, y_{i+1})\right] \quad (5)$$

Also, the notation *dist* means the distance between two consecutive points. The distance between the 1st data point and *i*-th data point can be summarized as follows.

$$d_i = \max([(x_1, y_1), (x_i, y_i)]) \quad (6)$$

MEASURED ROUNDNESS FOR FRACTAL INTERPOLATION

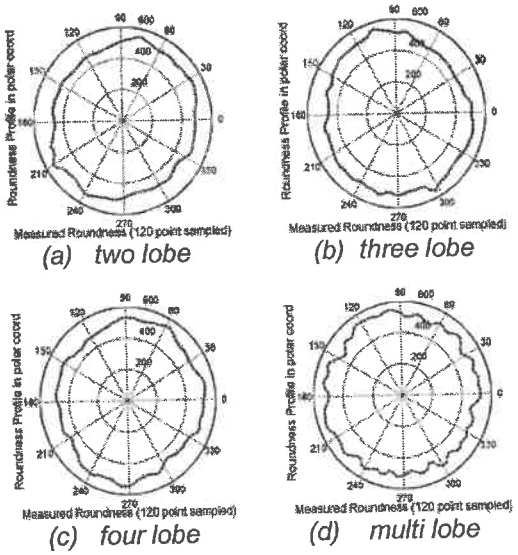

(a) two lobe (b) three lobe

(c) four lobe (d) multi lobe

FIGURE 1. Measured lobe profile of the roundness(sampled 120 points)

The verification of the experimental roundness is more realistic than theoretical one. This fractal analysis in this study uses the experimental roundness as original one and this result is more realistic than the previous work. The similar roundness was observed in the experimental results. If they were classified in the sense of lobe number, two, three and four lobe profile appear most frequently in these experiments (Fig. 1).

DISCUSSION OF FRACTAL INTERPOLATED ROUNDNESS PROFILE

The roundness profiles in Fig. 2 represent the fractal interpolated results of Fig. 1(a) that are theoretically fractal interpolated. Two-lobe profile is shown in Fig. 2(a) for scaling factor d_n of 0.1. Here, other several shapes can be generated with different scaling factor but will be discussed latter. Among nine cases of different scaling factor, the roundness has some dynamic and noise properties in the profile for a larger value of scaling factor in the lobe profile and the dynamic properties are added by fractal interpolation. Two to four-lobe roundness profiles are frequently observed in real experimental roundness, which are shown in Fig. 1. The observed results match well to fractal interpolated one and the results can be seen in Fig. 2(a)~(d) by imposing some low dynamic properties with scaling factor of 0.1 or 0.2. For fractal interpolation, the number of the fixed data points is sampled in 120 points in the profile and the total generated data points are 1440 after interpolation.

FRACTAL INTERPOLATED ROUNDNESS CONSIDERING SCALING FACTOR FOR TWO TO MULTI-LOBE

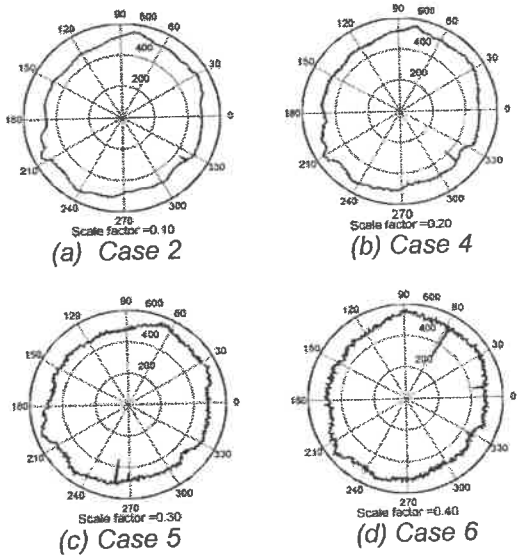

(a) Case 2 (b) Case 4

(c) Case 5 (d) Case 6

FIGURE 2. Predicted roundness model of two-lobe by fractal interpolation according to scaling factor d_n

Figs. 2(a)-(d) show the roundness profiles of two-lobe with different scaling factor ranging from 0.1 to 0.4. As the scaling factor decrease, the roundness shows some low-pass filtering properties in the roundness profile. And the dynamic noise properties in profile appear clearly by increasing the scaling factors. So the roundness profile generated by fractal

interpolation can have more diverse properties and can be generated into various profiles of different properties with the same fixed points. The fixed data point profile was shown in Fig. 1. By investigation of the results, when the original roundness is represented with small amplitude with respect to the basic datum, it is better to interpolate the roundness with small scaling factor in this study. But, if the scaling factor increases in interpolation, then the profile becomes not clear because of small amplitude between maximum and minimum radius of the roundness profile. The lobe clearness disappear by higher noise effects by fractal interpolation in this case. As a result, larger scaling factor results in higher noise and dynamic properties in roundness profile and unclear discrimination of lobe number.

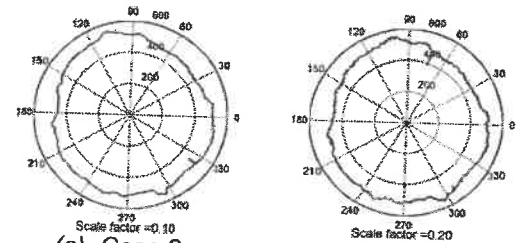

(a) Case 2 (b) Case 4

(c) Case 5 (d) Case 6

FIGURE 3. Predicted roundness model of three-lobe by fractal interpolation according to scaling factor d_n

Fig. 3(a)-(d) shows the roundness profile of three-lobe with different scaling factors. If the scaling factor decreases, then the roundness profile shows some filtering effect and also it appears the dynamic noise effect by increasing scaling factors. So the roundness profile has more diverse and different properties with same fixed points. Also, the fractal dimension was calculated in this case in Fig. 6. And it is verified that the calculated values ranges from 1.15 to 1.45 generally for the scaling factor with introduced methods. By investigating the value of fractal dimension, the results in this study show a low value of fractal dimension than the other methods. So, it is verified that the interpolation of the roundness with small scaling factor causes a small value of fractal dimension. It shows clearer roundness profile that matches to original profile but it has less dynamic properties. Also, the lobe clearness disappears with high value of scaling factor in fractal interpolation.

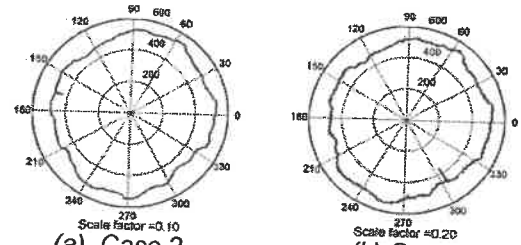

(a) Case 2 (b) Case 4

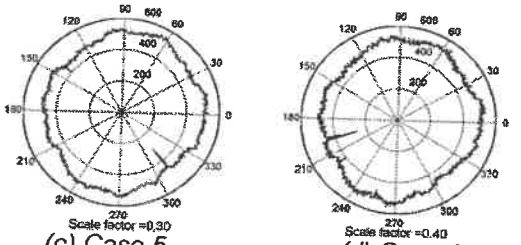

(c) Case 5 (d) Case 6

FIGURE 4. Predicted roundness model of four-lobe by fractal interpolation according to scaling factor d_n

Fig. 4(a)-(d) shows the roundness profile of four-lobe with different scaling factor ranging from 0.1 to 0.4. All phenomena are similar for the case of two and three-lobes. Also, using this fractal interpolation, the profile can be generated into various roundness of different properties with given fixed data points. Also, the fractal dimension was calculated in this case in Fig. 6. And it is verified that the fractal dimension about 1.18 to 1.4 generally low value comparing with two or three-lobe. In all cases of different lobe in Fig. 2, Fig. 3 and Fig. 4, some deviation point was detected in the interpolated profile for the case of higher value of scaling factor. It means that it has some limitations in algorithm for higher value of scaling factor in calculating the random generated parameter in fractal interpolation. But if the deviation is to be decreased, the interpolation should be performed with low scaling factor. At that case there is no large deviation in the profile and this deviation point does not show a dominant effect in roundness profile. Fig. 5(a)-(d) shows the roundness profile of multi-lobe with different scaling factor ranging from 0.1 to 0.4. The

roundness profile generated by the fractal interpolation has more diverse property and can be generated into various profiles of different properties with one fixed data point. Also, the fractal dimension was calculated in nine cases in Fig. 6, and it is verified that the calculated fractal dimension ranges from 1.16 to 1.42 generally for nine scaling factors with latter method(ND_F) using eq. (4).

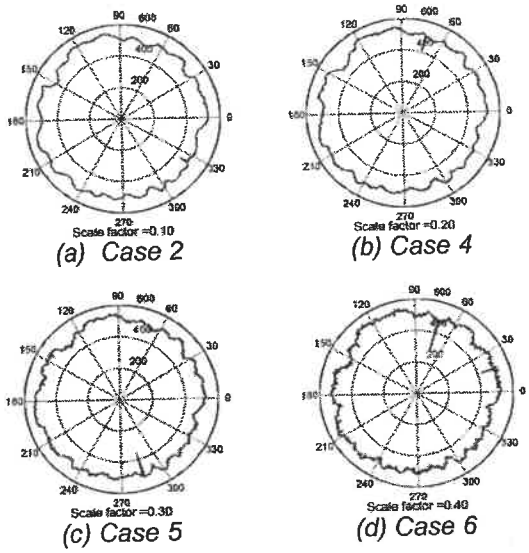

(a) Case 2 (b) Case 4

(c) Case 5 (d) Case 6

FIGURE 5. Predicted roundness model of multi-lobe by fractal interpolation according to scaling factor d_n

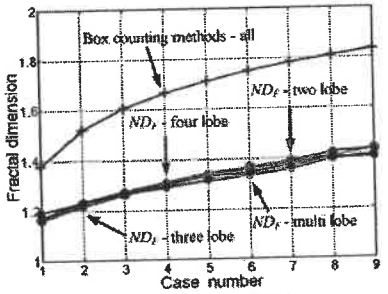

(a) fractal dimension

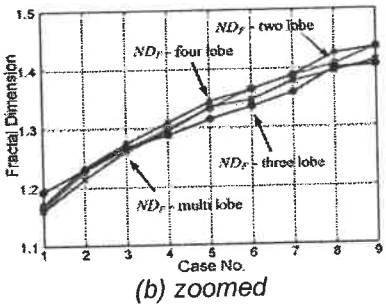

(b) zoomed

FIGURE 6. Fractal dimension of each case for all roundness

As similar as the cases of Fig. 3, Fig. 4 and Fig. 5, a larger scaling factor causes a higher noise and dynamic properties in roundness profile and unclear discrimination of lobe number. The fractal dimension depending on different scaling factors was examined. All the fractal dimensions were calculated in Fig. 6 for all lobes in this study, and it is verified that the calculated values of fractal dimension generally ranges from 1.15 to 1.45 with nine different scaling factors from 0.05 to 0.45 with an increment of 0.05. The calculated fractal dimensions ND_F using eq(4) can be seen in Fig. 6 respectively. The fractal dimensions of the profile also increase as the scale factor increases.(compare the Fig. 2, Fig. 3 and Fig. 4 with Fig.6) Considering the fractal dimension, the calculated fractal dimension ND_F generally shows lower value comparing to general fractal dimension D_F.

CONCLUSION

The original roundness profile consists comparatively well with the predicted roundness profile by fractal interpolation. This fractal interpolation can be applied in all round shape operation such as cylindrical grinding, turning, boring and drilling. Also, the fractal parameters can be used as a design and controlling parameters in roundness tester. The roundness prediction using fractal interpolation was realized with little fixed profile data. And using the fractal interpolation, the roundness involving lower or higher frequency properties in roundness profile can be generated appropriately by imposing different scaling factor in fractal interpolation.

REFERENCES

1. M.C. Yoon, B.T. Kim and D.H. Chin, 2006, Roundness modelling by fractal interpolation, *KSMTE*, 15/3: 67-72.
2. M.F. Barnsley, 1993, Fractals everywhere, *Academic Press Inc.*
3. M.A. Marvasti and W.C. Strahle, 1995, Fractal geometry analysis of turbulent data, *Signal processing*, 41: 191-201.
4. E.N. Shah, N. P. Reddy and B.M. Rothschild, 2005, Fractal analysis of acceleration signals from patients with CPPD, rheumatoid arthritis, and spondyloarthroparthy of the finger joint, *Computer methods and programs in biomedicine*, 77: 233-239.
5. M.C. Kang, J.S. Kim and K.H. Kim, 2005, Fractal dimension analysis of machined surface depending on coated tool wear, *Surface & coatin technology*, 193: 259-265.

CONTROL OF A 2 DOF LONG-RANGE AND 6 DOF SHORT-RANGE STAGES FOR NANOMETER POSITIONING

Eric S. Buice, David Otten[1], Hua Yang, Stuart T. Smith, Robert J. Hocken, David L. Trumper[1] and Richard M. Seugling[2]
Center for Precision Metrology, UNC Charlotte, Charlotte, NC 28223, USA
[1] Massachusetts Institute of Technology, Cambridge, MA 02139, USA
[2] Lawrence Livermore National Laboratory, Livermore, CA 94550, USA

OVERVIEW*

This abstract presents the work towards development of an 8 axis controller that simultaneously controls a 2 degree-of-freedom (DOF) long-range (50 mm) and a 6 DOF short range stage (4 μm, 160 μRad) [1]. The long-range stage is used for traverse in *X*- and *Y*- axis while the short-range stage corrects for any error motions generated by the long-range stage for nanometer positioning capabilities. The system can be separated into 2 controllers, long-range stage and short-range stage, cascaded together. The short-range stage operates to keep the position errors at nanometer levels with feedback from a laser interferometer (Zygo DMI 4004). The long-range stage can be controlled for position from rotary encoders while it attempts to maintain the short-range stage in its mid range.

A dSPACE real time hardware interface is used to perform all controls with a sample rate of 10 kHz while monitoring the laser interferometers, encoder and controlling in all 8 axes. Programming and system simulation is performed in Matlab™ Simulink software.

To date the short-range controller has been tested utilizing, for now, a nest of 6 capacitance gages to determine controller performance under closed loop. While actuating the z axis linearly, under closed-loop control, with a 100 nm sinusoidal amplitude a cross coupling of the X and Y axis was measured to be approximately 3 nm RMS, which is approaching the measurement resolution of this test set-up.

To further test controller strategies a single-axis system was also constructed and tested. This stage had a range of 50 mm and was also able to maintain nanometer level position errors over a 25 mm sinusoidal traverse.

Further results of controller performance and transformation matrices will be presented at the conference. Construction of the stage and integration of laser interferometer feedback is also expected to be completed. Details of construction, interfacing and performance testing will be presented. Furthermore, due to limited amount of space for this abstract the reader is encouraged to view the references for further information.

SINGLE DOF LONG-RANGE STAGE

This section provides a brief overview of an experimental program to develop and optimize control of the single axis long-range stage, see Figure 1. A more comprehensive report of this study will be prepared for publication in the near future.

To perform controller analysis a single DOF long-range stage was built utilizing ultra-high molecular weight polyethylene (UHMWPE) bearings [2] that slide against optically polished Zerodur® flats. Translations are generated with the use of an Aerotech BA10 servo amplifier and an Aerotech BMS60 brushless DC motor with an internal integral 1000 count per revolution rotary encoder with an 100 times multiplier in conjunction with an 3.1 threads per mm feedscrew and a UHMWPE nut [3]. Translations of the stage are measured with a Zygo DMI 4004 interferometer system. Located on top of the single DOF long-range stage is a single DOF piezo short-range stage with an attached planar mirror for positioning feedback. The amplifier, motor encoder, and interferometer are connected to a dSPACE 1103 PPC controller board for real time data acquisition.

Initial tests of the long-range stage were undertaken to determine the transfer functions of the stage using a simple open loop controller in conjunction with a dynamic signal analyzer for the long-range stage only.

Once the transfer function is known a closed loop controller was developed, see Figure 2.

This work was performed in part under the auspices of the U.S. Department of Energy by University of California, Lawrence Livermore National Laboratory under contract No. W-7405-Eng-48. Funding provided by NSF under grant # DMI-0210543.
UCRL-PROC-222814

The closed loop controller encompassed a backlash compensation and a variable gain to maximize performance of the long-range stage. The backlash compensation is comprised of a memory block (stores previous commanded position), sign block (determines the new direction), a gain, and a rate limiter (this is set to keep corrections within the bandwidth of the controller). The variable gain controller was advantageous since it allows the controller to be operated under different gain settings as the velocity of the stage is changed. The variable gain controller is comprised of a derivative block (this measures the speed of the stage), absolute block (abs, to assure the signal remains positive), and a saturation block (limits the gain). Lead compensation is also used to stabilize the motor drive. Figure 3 shows the closed loop response of the single DOF long-range stage under closed loop control. During short traverses (approximately 0.01 Nm torque at an input amplitude of 0.5 V is applied by the motor) the first resonant frequency occurs at approximately 150 Hz and 25 Hz for longer traverses (approximately 0.1 Nm of torque at an input amplitude of 5 V is applied by the motor). For short traverses the implied torque demand on the motor results in small rotations so that the bearings inside the motor do not rotate. Therefore, the motor during short traverses can be modeled as a stiff spring resulting in the higher resonant frequency. Figure 4 shows the single DOF long-range stage performance with the amplifier operating as a current source generating a torque at the motor of 0.1 Nm. The stage was able minimize positioning rms controller error to 0.1 μm over a traverse of 5 mm in 1000 s.

This system resulted in control of the long-range stage to within the range of the short-range mirror stage. With combined long- and short-range control it was possible to demonstrate controller errors having an rms value of 0.7 nm over a traverse of 500 μm [1]

6 DOF SHORT-RANGE STAGE

A third generation, 6 DOF, short-range stage was also tested under a simple PID closed loop controller. The short-range stage utilizes 6 single crystal PZT tubes oriented in a 2-2-2 configuration capable of traversing 4 μm and rotations of 160 μRad, for further information on the first generation see Seugling *et al.* [4]. Amplifiers from InsituTec HV150031 are used to drive the PZT's up to approximately 1000 V. The short-range stage lowest resonant frequency was determined to be approximately 210 Hz in the x-axis, while the z-axis had the highest at approximately 510 Hz. Further tests showed a cross coupling under closed loop control of the actuators to be less than 3 nm rms when the z-axis is actuated with a 100 nm sinusoidal amplitude, while monitoring the x- and y-axis, see Buice *et al.* [5] for further information.

COMPLETE CONTROLLER DESIGN

For final system implementation it is desirable to implement the above mentioned stages into one instrument giving nanometer positioning capabilities over traverses of 50 mm in 2 axis. The 6 DOF short-range stage is utilized in conjunction with the stacked long-range stage (giving 2 axis of motion) to drive the errors generated by the long-range stage into the nanometer positioning error regime. However, to further complicate the controller strategy it is desired to maintain the short-range stage in its mid traverse ranges by using the long-range stages to compensate any linear motion generated by the short-range stage in the x- and y-axis. Figure 5 shows a block diagram indicating major features of the closed loop controller that is under development. This controller includes user interface, probe (AFM, STM, *etc.*), imagining software, long- and short-range controller strategies (mentioned in previous sections), 6 DOF interferometric measurement system, and independent measurement of the short-range stage. Furthermore, the controller is a modular design to enable additional operations without requiring substantial recording of software. For instance it is desirable in the future to implement a long-range z-axis and addition of probes to allow for multiple measurements to be performed simultaneously during one operation.

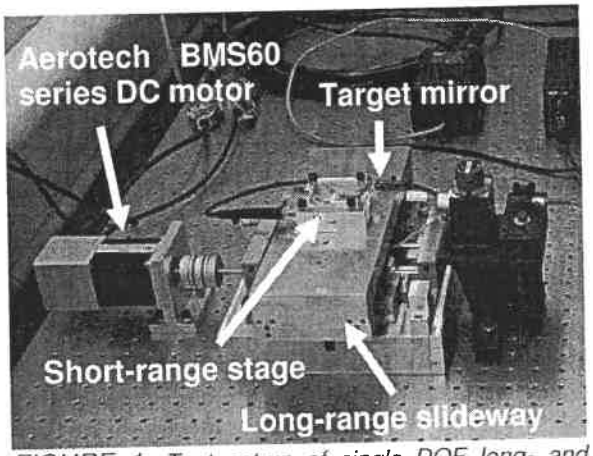

FIGURE 1. Test set-up of single DOF long- and short-range stage for controller implementation.

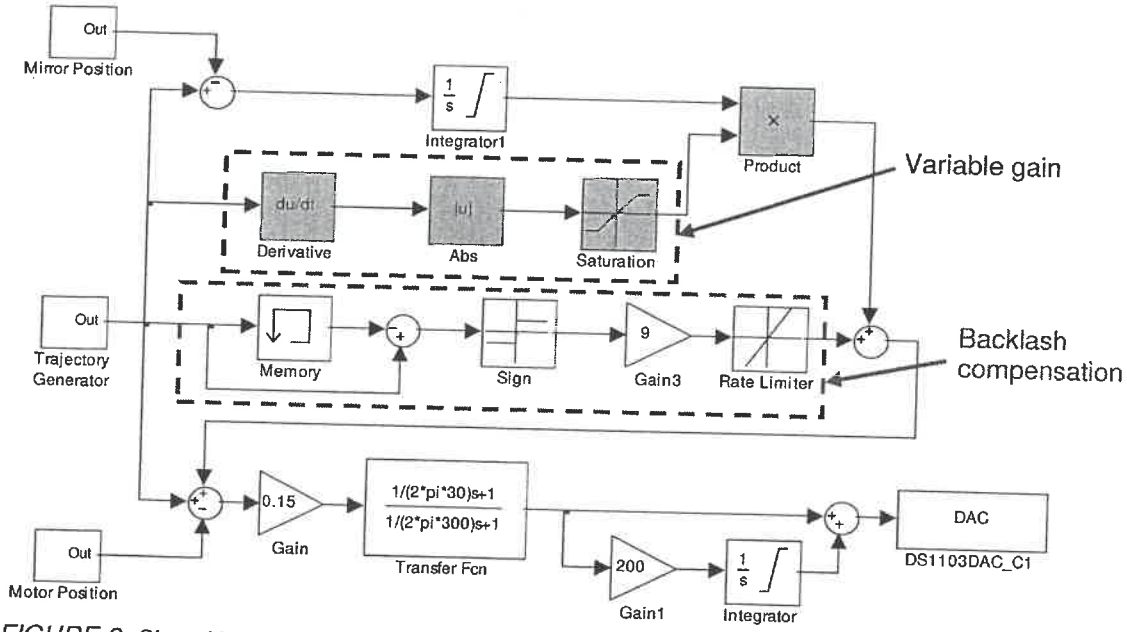

FIGURE 2. Closed loop controller for single DOF long-range stage with backlash compensation and variable gain.

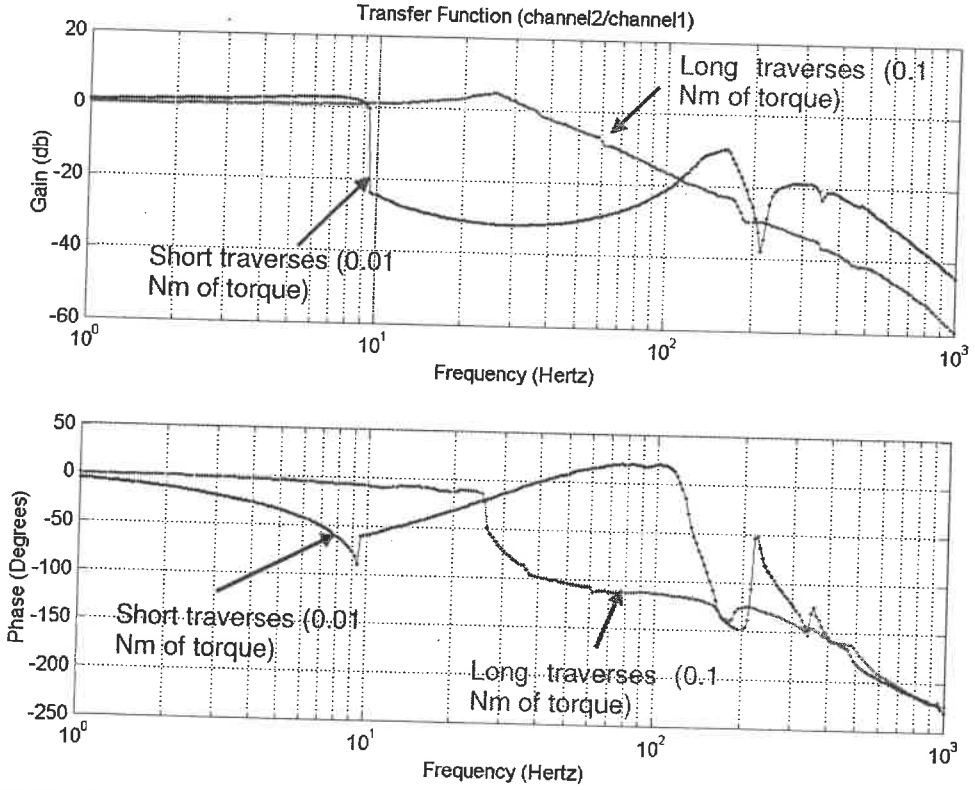

FIGURE 3. Closed loop response of motor control used in variable gain controller

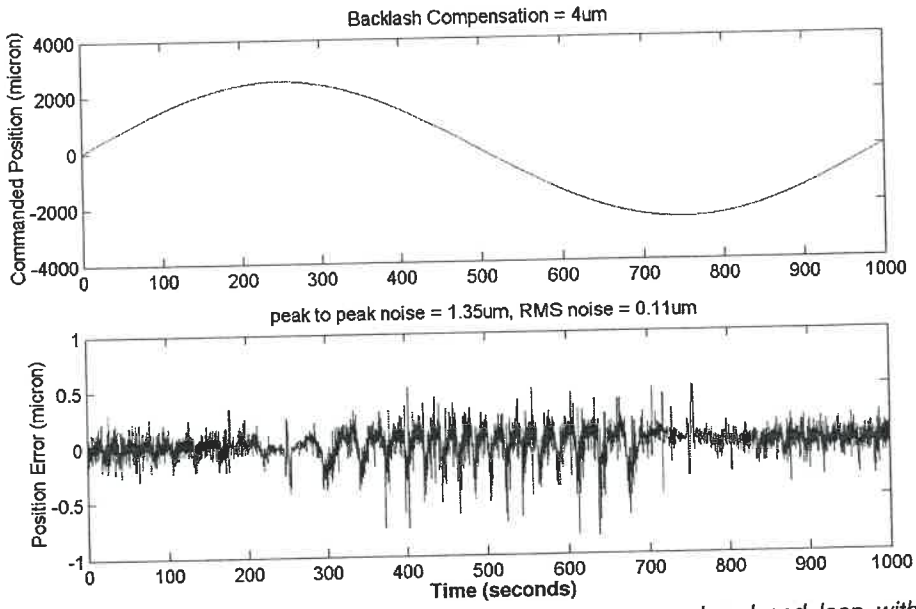

FIGURE 4. Performance of single DOF long-range stage under closed loop with backlash compensation and variable gain controller. Peak-to-peak noise is 1.35 μm with an rms noise of 0.11 μm.

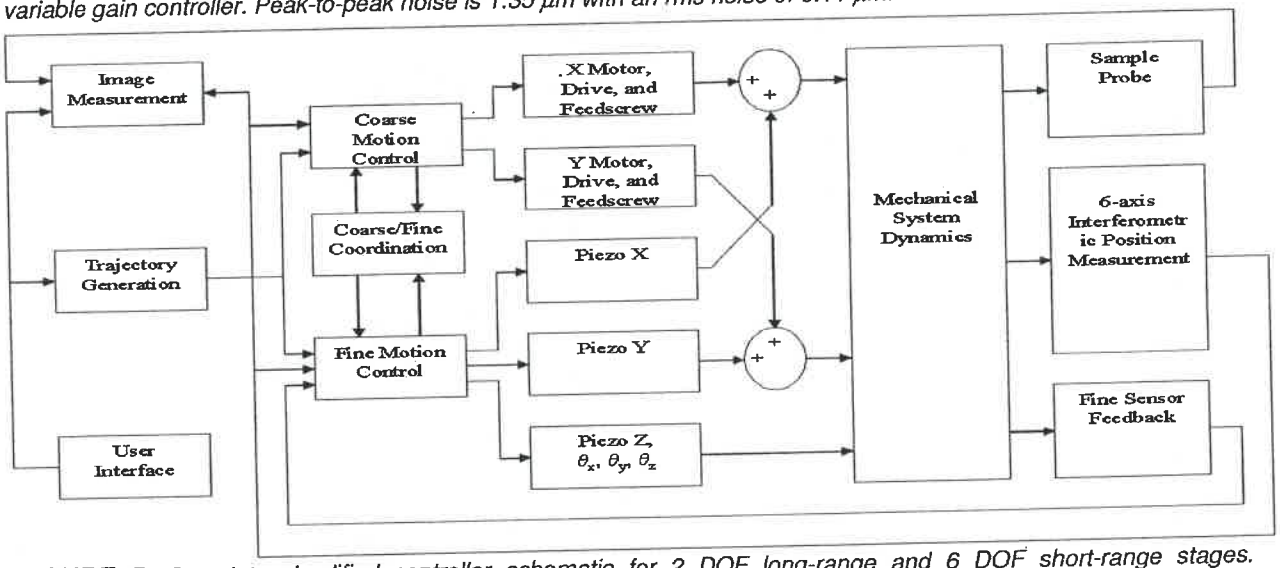

FIGURE 5. Complete simplified controller schematic for 2 DOF long-range and 6 DOF short-range stages.

1. Yang H., Buice E.S., Smith S.T., Hocken R.J., Fagan T.J., Otten D., Trumper D.L. and Seugling R.M., 2005, Design and performance evaluation of a coarse/fine precision motion control system, *Proc. EUSPEN. Annual Meeting,* Montpelier, France, 373 – 376, ISBN: 92-990035-0-5.

2. Buice E.S., Yang H., Smith S.T., Hocken R.J. and Seugling R.M., 2006, Evaluation of a novel UHMWPE bearing for applications in precision slideways, *Precision Engineering Journal*, **30** (2), 185 – 191.

3. Buice E.S., Yang H., Otten D., Smith S.T., Hocken R.J., Trumper D.L. and Seugling R.M., 2006, A comparison of drive mechanisms for precision motion controlled stages, *Proc. EUSPEN Annual Meeting*, Baden bei Wien, Austria, 321 – 324, ISBN: 0-9553082-0-8.

4. Seugling R.M., LeBrun T., Smith S.T. and Howard L.P., 2002, A six-degree-of-freedom precision motion stage, *Review of Scientific Instruments*, **73** (6), 2462 – 2468.

5. Buice E. S., Yang H., Smith S.T., Hocken R.J., Trumper D.L., Otten D. and Seugling R.M., 2006, Controller strategy for a 6 DOF piezoelectric translation stage, *Proc. EUSPEN Annual Meeting*, Baden bei Wien, Austria, 176 - 179, ISBN: 0-9553082-0-8.

ACTIVE CONTROL OF PNEUMATIC ISOLATION TABLE BY MODEL FOLLOWING CONTROL USING PRESSURE DIFFERENTIATOR

Tomonori KATO[1], Kenji Kawashima[2], and Toshiharu Kagawa[2]
[1]Tokyo Metropolitan College of Industrial Technology, 1-10-40 Higashi-oi, Shinagawa, Tokyo, Japan
[2]Tokyo Institute of Technology, 4259 Nagatsuta-cho, Midori-ku, Yokohama, Kanagawa, Japan

INTRODUCTION

Pneumatic vibration isolation systems are widely used in semiconductor manufacturing because they can support a high payload at a relatively low energy. A pneumatic isolation table is supported by several air-springs, which consist of air-filled chambers, an elastomeric diaphragm and a piston. The air-springs are often actively controlled by servo valves to attenuate the vibration transmitted from the floor and to suppress the vibration on the table. High stability and bandwidth of the isolated vibration frequency are achieved by the active control. Most of the air spring systems are controlled with nozzle flapper type pneumatic servo valves since they have both high response and high linearity.

However, such servo vales require a large amount of exhausted air flow rate in order to control pressure precisely. To decrease the exhausted air flow rate is highly required for energy saving and to cut down the running costs. In this paper, a new method is proposed to actively control an air-spring system with spool type servo valves.

A solution to decrease the exhaust flow rate is to replace the nozzle flapper type servo valve to a valve called "spool type". The spool type servo valve has much smaller amount of steady-state exhausted air flow rate and high flow rate gain. However, since it has strong non-linearity and dead-point shift in its characteristics, the valves are difficult to be used for precise pressure control like air spring systems.

In order to compensate those disadvantaged characteristics which spool type servo valves have, a model following control using the developed pressure differentiator [1] is applied. Because the pressure change in the chamber of air spring is very small, it had been difficult to obtain the differentiated value of the pressure through a discrete simultaneous differentiation of the pressure sensor signal. However, the value was successfully obtained by the developed pressure differentiator. Therefore, the model following control could be used.

In the experiment, a granite table of 1250kg is mounted on 3 air springs. Experiments are carried out on 2 control methods, conventional and the proposed control methods.

The derived results using the proposed control method are compared to those obtained by using the nozzle flapper type servo valves as a vibration isolator. In particular, the amount of steady state exhausted air flow rate, i.e., the energy loss, is measured and compared in the experiments.

A PNEUMATIC ISOLATION TABLE

Air Spring System

An actively controlled pneumatic isolation table primarily consists of a payload, air-springs, nozzle flapper type servo valves, displacement sensors, acceleration sensors and a controller. Usually, three to six air-springs are used to support the payload and isolate vertical vibration. The equation of motion of the isolation table is as follows:

$$M\ddot{x} + c(\dot{x} - \dot{x}_0) + k(x - x_0) = f_{air} \qquad (1)$$

where: M is the mass of the vibration isolated table, c is the viscous damping coefficient of the support mechanism, k is the spring constant of the support mechanism (including the air-spring), x is the displacement of vibration table, x_0 is the displacement of the floor, and f_{air} is the driving force of the air-spring.

Hereafter, x_0 is neglected in order to discuss the closed loop system of the isolated table. The following equation can be derived by differentiating the state equation of the air in the chamber:

$$P_0 \frac{dV}{dt} + V_0 \frac{dP}{dt} = GR\theta + WR\frac{d\theta}{dt} \qquad (2)$$

where: P is the pressure, V is the chamber volume, W is the mass of air, R is the gas constant, θ is the average chamber temperature, G is the mass flow rate and P_0 and V_0 represent equilibrium values.

Since the pressure changes in the camber are very small, the behavior of the air in the chamber can be

assumed to be isothermal. Thus, Eq.(2) can be written as follows:

$$P_0 A\frac{dx}{dt}+V_0\frac{dP}{dt}=GR\theta \qquad (3)$$

where: A represents the effective piston area of the air-spring.

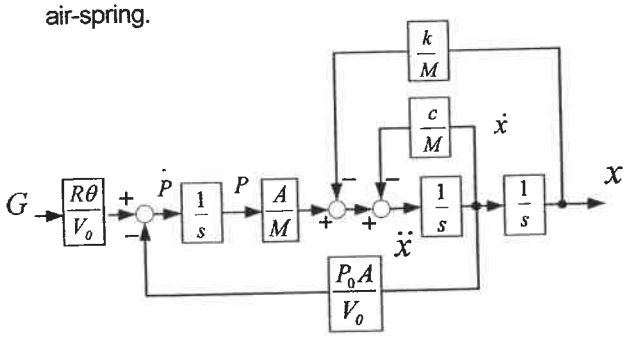

Figure 1: Block diagram of air-spring system

Nozzle-Flapper Type Servo Valve (N.F. Valve)

Nozzle-flapper type servo valves (henceforth N.F. valves) are the conventional choice for active control of air-springs. Pneumatic control systems with nozzle-flapper elements are generally approximated to first order lag systems [2]. Also, state changes of the air in the load chamber are typically assumed to be isothermal. The transfer function of these valves is given as:

$$P=\frac{K}{T_c s+1}E \qquad (4)$$

where: K is the proportional gain, T_c is the pressure time constant and E is the control signal from the controller to the valve.
The pressure time constant is given by:

$$T_c=\frac{V_0}{aR\ \theta} \qquad (5)$$

where: a is the flow rate gain.

Conventional Control Method

A block diagram of a conventional actively controlled pneumatic isolation table is shown in Fig.4. As the volume change in the chamber is very small, the term $\frac{P_0 A\,dx}{V_0\ dt}$ is neglected in this figure. From Eq. (1), the air spring can be described as a second order lag system. The input pressure to the air spring is introduced through a nozzle-flapper type servo valve. As shown in Fig.5, the desired vertical displacement of the supported payload, x_{ref}, is given as a reference input signal. A PI compensator is employed to maintain the displacement, while acceleration feedback is implemented to control the damping ratio of the isolation table.

PROPOSED PRESSURE CONTROL SYSTEM

Spool Type Servo Valve (S.P. Valve)

While the N.F. valve is categorized as a pressure control type valve, there also exists a flow rate control type servo valve called a "Spool type". The flow rate from the control port (control flow rate), Q_n, is determined by the pressure at the supply port, P_{su}, and the cross sectional area, S_e, which is adjusted by the spool displacement in the sleeve. When a controlling flow rate is not needed, the flow can be halted by the spool. Consequently, the steady state exhaust flow rate from a spool type servo valve (henceforth S.P. valve) is very small compared with that of a N.F. valve. Additionally, since it is easy to obtain large effective cross sectional area, S_e, with spool type servo valves, higher maximum control flow rates can be achieved.
However, since S.P. valves exhibit strong non-linearity and dead-point shift, they are difficult to use for applications like air spring systems which require precise pressure control.

Model Following Control

A new method to actively control an air-spring system with an S.P. valve is proposed using a previously developed pressure differentiator (henceforth P.D. sensor) [1]. Model following control is applied to compensate for the non-linearity and dead-point shift of the S.P. valve. Model following control is only possible because the P.D. sensor can accurately detect slight pressure changes. Since the pressure changes in the chamber are very small, it is difficult to obtain the differentiated pressure by simultaneous differentiation of the measured pressure using a pressure sensor. Therefore, it was measured directly with the P.D. sensor. The proposed control scheme is shown in Fig.2.

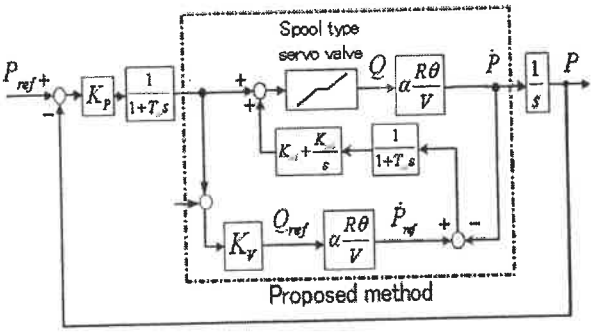

Figure 2: Proposed pressure control system

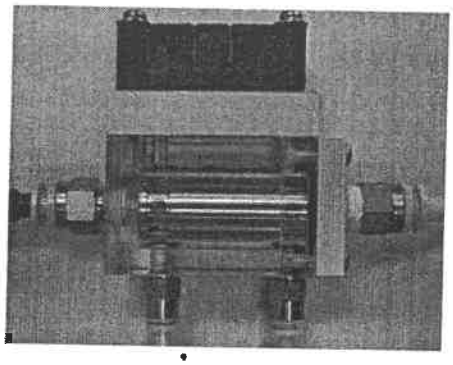

Figure 3: Pressure differentiator

It is clear from Fig.2 that the reference model of the spool type servo valve is:

$$G = K_V E' \tag{6}$$

By measuring the static characteristics of the S.P. valve, the control flow rate, Q_n, is calculated by the formulae in ISO6358. Fig.4 shows the control flow rate, Q_n, assuming a supply pressure, P_s, of 530 kPa [abs] and a control port pressure, P, of 320 kPa [abs]. Fig.4 also shows the reference flow rate obtained from Eq.(6) with K_V=10.0.

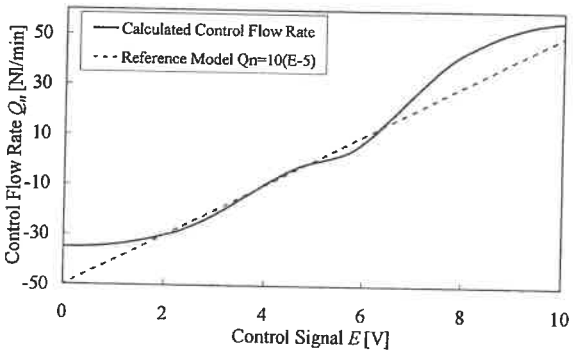

Figure 4: Characteristics of S.P. valve

The error between the reference differential pressure dP_{ref}/dt (calculated using Eq.(6)) and the actual value (measured using the pressure differentiator) is fed back to the control signal. This linearizes the characteristics of S.P. valve.

The results of the proposed pressure control method agree with both of these other results. This validates the proposed pressure control method as a lagged pressure integrator.

EXPERIMENTS ON THE AIR SPRING SYSTEM USING THE PROPOSED METOHD

Experimental Setup

To demonstrate the effectiveness of the proposed method, experiments were conducted

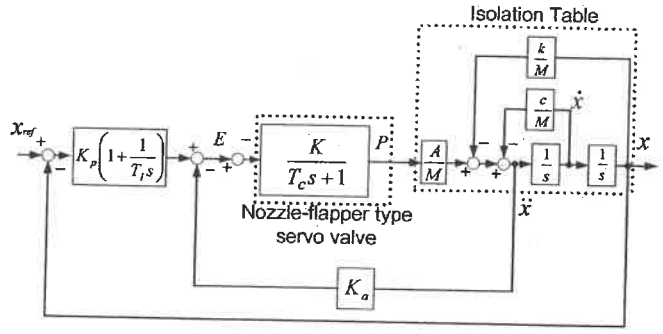

Figure 5: Block diagram of a conventional actively controlled pneumatic isolation table

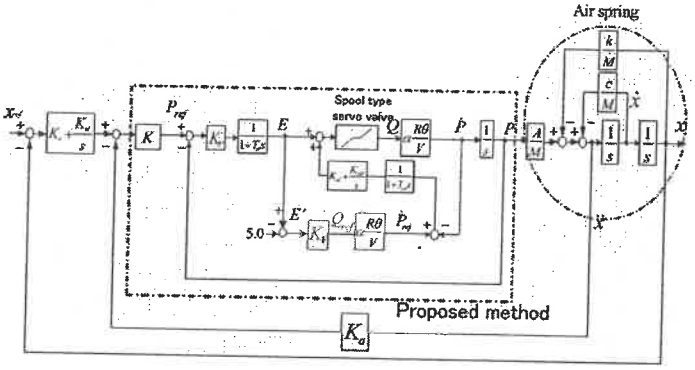

Figure 6: Block diagram of the proposed actively controlled pneumatic isolation table

using the apparatus shown in Fig.7. The payload of 1258Kg was supported by 3 air-springs in vertical direction. Accelerometers were located both on the floor and on the table to evaluate the vibration transmissibility.

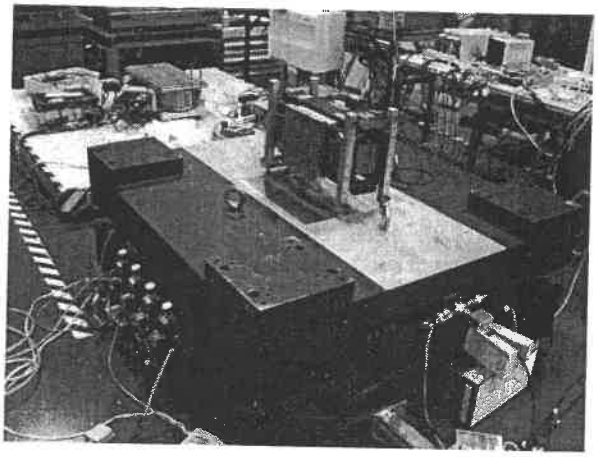

Figure 7: Actively controlled isolation Table

Measurements were fed to a PC via an A/D converter and the resulting control signal was sent from the PC to the valve via a D/A converter.

Experimental Procedure

The experiments for the conventional method were conducted using N.F. valves while those for the proposed method used S.P. valves and a P.D sensor. The two control schemes are shown in Fig.5 and Fig.6 respectively. In Fig.6, the dashed rectangular frame indicates the proposed model following controller. That part is considered to be equivalent to the N.F. valve in Fig.5. The reference displacement, x_{ref}, was set to 2 mm. PI control was conducted using displacement and acceleration feedback. The parameters for the PI controller and the acceleration feedback were selected by the passive characteristics.

The same parameters for the PI controller were used in both sets of experiments. The control parameters used in the experiments are summarized in Table 1. The isolation table was actively controlled to settle at the reference displacement. In these experiments, after the table settled at this reference value, the table displacement, table acceleration and exhaust air flow rate through each servo valve were measured.

EXPERIMENTAL RESULTS

The experimental results of vibration transmissibility, i.e. the ratio of table acceleration to ground acceleration, are presented in Fig.8.

Table 1 Parameters used in experiments

Symbol	Description	Value
K_x	Proportional gain	3.5×10^3 V/m
K_{xI}	Integral gain	2.8×10^3 V/m·s
K_a	Acceleration feedback gain	$120\,\mathrm{V\cdot s^2/m}$
K	Nozzle flapper output gain	21.0×10^4 Pa/V
K_T	Adjust gain $K_T = K$	21.0×10^4 Pa/V
K_P	Proportional gain of Pressure control	6.81×10^{-6} V/Pa
K_{ad}	Proportional gain of Model following control	2.0 V·s/Pa
K_{adI}	Integral gain of Model following control	0.5 V/Pa
T_m	Time constant of Lowpass filter	0.01s
T_{ad}	Time constant of Lowpass filter	0.01s

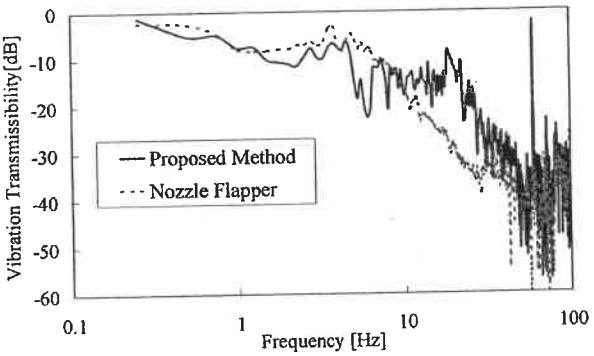

Figure 8: Experimental results of vibration transmissibility

The result obtained using the proposed control method is in no way inferior to that obtained for the standard control method using N.F. valves. The exhausted air flow rate of the N.F. valves was 9 Nl/min, while that for the proposed method (S.P. valves) was lower than 1.0 Nl/min.

CONCLUSION

In order to realize a pneumatic vibration table with lower energy consumption and higher control gain, a new pressure control method using a pressure differentiator and a spool type servo valve was proposed herein. The undesirable characteristics of spool type servo valves, i.e. non-linearity and dead point shift, were eliminated using the model following control method. This, in turn, was made possible by the use of a pressure differentiator.

The proposed pressure control system was applied to the control of a pneumatic vibration isolation table. Compared with the results for an ordinary isolation table system using nozzle flapper type servo valves, it was proven that the proposed method can greatly reduce the exhaust air flow rate of the servo valves. Additionally, this reduction was achieved without loss of vibration isolation performance.

ACKOWLEGEMENTS

This research was managed by TLO Tokyo Institute of Technology and was supported by NEDO and Tokyo Meter Co, Ltd. The authors would also like to thank Tokkyokiki Corporation for their advice and support.

REFERENCES

1. K. Kawashima, T. Kato, et. al., 2004, Development of Slit Type Pressure Differentiator using an Isothermal Chamber, Measurement Science and Technology, 16, 1150-1156.
2. K. Kagawa: Heat transfer effects on the frequency response of a pneumatic nozzle flapper, Trans. ASME Journal of Dynamic Systems, Measurement and Control, 1985, 107, 332-336.

A NEW MODE SWITCHING CONTROL FOR FAST SETTLING AND HIGH PRECISION POSITIONING

Jung-Jae Kim[1], Young-Man Choi[1], Ki-Hyun Kim[1] and Dae-Gab Gweon[1]
[1]Department of ME., Korea Advanced Institute of Science and Technology, Yusung-ku, Daejeon, South Korea

INTRODUCTION

Recently, with rapid development of digital media like semiconductor and large flat panel display, the manufacturing equipment is required to have high precision over large travel range. Moreover it should have high product throughput. To achieve high product throughput, a controller should perform fast point-to-point motion and high precision positioning after settling in spite of external disturbances or residual vibrations. A time-optimal control plays an important role in achieving high speed point-to-point motion [2]. A conventional time-optimal control algorithm like Bang-bang control has a drawback of chattering. A proximate time-optimal servomechanism (PTOS) can achieve fast settling without chattering [2]-[3]. To improve positioning accuracy after settling, robust tracking controller such as TDC, PID, H_∞, LQG, LTR and RPT should be used to increase control bandwidth and to suppress disturbances around the target position [2],[5]-[9]. A mode switching control (MSC) enables both the fast point-to-point motion and the high precision positioning. In the conventional MSC, the track seeking mode is switched to the track following mode under certain conditions. One of the design problems for MSC is the method of switching between controllers. This design problem has not yet been completely resolved, and many approaches have been tried so far [9]-[12]. Yamaguchi proposed a method called initial value compensation (IVC) to reduce the impact of the initial value during mode switching [10]-[12]. Here the initial value means the values of the states at the instance of mode switching. This method gives an additional input to a controller at the instance of mode switching. The additional input, which is an impulse response of the initial state variables of the plant at mode switching, is designed to change transfer functions from the initial variables to the controlled variables, such as position, into better ones with assigned poles [10]-[12]. The IVC algorithm, however, is highly sensitive to plant and controller model. To make smooth mode switching without transient response, we should calculate control input of tracking controller using the information of state variables such as position, velocity and control input of the point-to-point controller at the instance of mode switching. The time-delay control (TDC) algorithm uses time-delayed information (the values of the control inputs and derivatives of state variables at the previous time step) to estimate both the plant dynamics (nominal part) and the uncertainties – parameter variation, external disturbances and unknown dynamics [5]-[6]. Hence, the use of time-delayed information eliminates the need for initial value compensation during mode switching. In this paper, to improve settling and positioning performance, we propose a new MSC design, which uses PTOS for fast point-to-point motion and TDC for robust tracking.

MODE SWITCHING CONTROL ALGOTIGHM

We propose a new MSC algorithm in which the point-to-point motion is controlled by a PTOS and the tracking mode is controlled by a TDC. Each controller of these two modes can be designed independently.

A. Proximate time optimal servomechanism (PTOS)

The point-to-point motion is a time-optimal control problem. In this subsection, we recall the conventional PTOS design for VCM stage characterized by

$$\dot{x} = Ax + Bu = \begin{bmatrix} 0 & 1 \\ 0 & 0 \end{bmatrix} x + \begin{bmatrix} 0 \\ a \end{bmatrix} u, \quad x = \begin{bmatrix} y \\ v \end{bmatrix} \tag{1}$$

where x is the state vector which consists of the position y and the velocity v of the VCM stage and u is control input. Let r be the desired target position, $e=r-y$ be the position error. The PTOS control input is given by

$$u = u_{max} sat\left(\frac{k_2[f(e) - v]}{u_{max}} \right) \tag{2}$$

where the function $f(\cdot)$ is given by

$$f(e)=\begin{cases}\dfrac{k_1}{k_2}e & |e|\le y_l \\ \mathrm{sgn}(e)\left[\sqrt{2a\alpha u_{max}|e|}-\dfrac{u_{max}}{k_2}\right] & |e|>y_l\end{cases} \quad (3)$$

Here the control parameter k_2 is determined from the acceleration discount factor α *(0< α <1)*, and the closed loop poles during point-to-point motion control mode with the following continuity constraints:

$$k_2=\sqrt{\frac{2k_1}{\alpha a}} \quad \text{and} \quad y_l=\frac{u_{max}}{k_1} \quad (4)$$

where y_l is the boundary region in which the PTOS operates as a PD controller. The PTOS uses a smooth nonlinear velocity profile by introducing the acceleration discount factor α. The discounted deceleration, however, makes the rising time longer than that of the original time-optimal controller.

B. Time-delay control (TDC)

The TDC is known to be a tracking control algorithm which is robust to system uncertainties and disturbances. It uses time-delayed information to estimate both the plant dynamics and the uncertainties. The control input is given by

$$u(t)=u(t-t_s)-\bar{M}\ddot{x}(t-t_s)+\bar{M}\{\ddot{x}_d(t)+K_D\dot{e}(t)+K_Pe(t)\} \quad (5)$$

where x_d is the reference input, x is the position of the stage, t_s is sampling period, $\bar{M}$ is the estimation value of the stage mass, K_P and K_D are control parameters. Let r be the desired position, $e=r-y$ be the position error. Then, position error is decayed to zero according to error dynamics given by

$$\ddot{e}(t)+K_D\dot{e}(t)+K_Pe(t)=0 \quad (6)$$

C. Mode switching control (MSC)

Fig. 1. represents the timing diagram of the proposed MSC. During the position error is larger than switching boundary E_{SW}, the MSC operates as the PTOS to achieve fast point-to-point motion. When the position error is equal to E_{SW}, the controller mode is switched from the PTOS to the TDC. At the instance of mode switching, the TDC calculates control input using position, velocity and previous control input of the PTOS. After mode switching, the MSC operates as the TDC to achieve high precision positioning.

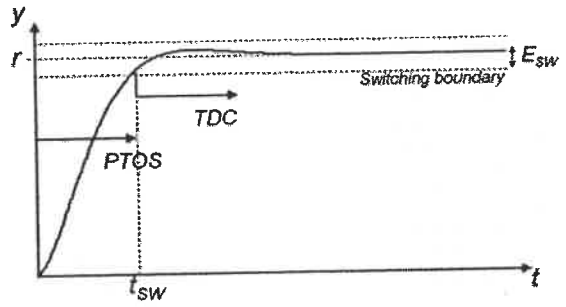

FIGURE 1. Timing diagram of the proposed MSC..

The control input of the MSC is calculated as follows

1) If $|r-y|>E_{SW}$, the MSC operates as the PTOS and control input is given by

$$u_{MSC}=u_{PTOS}=u_{max}sat\left(\frac{k_2[f(e)-v]}{u_{max}}\right) \quad (7)$$

where the function $f(\cdot)$ is given by

$$f(e)=\begin{cases}\dfrac{k_1}{k_2}e & |e|\le y_l \\ \mathrm{sgn}(e)\left[\sqrt{2a\alpha u_{max}|e|}-\dfrac{u_{max}}{k_2}\right] & |e|>y_l\end{cases} \quad (8)$$

2) If $|r-y|=E_{SW}$, the controller mode is switched from the PTOS to the TDC. At the instance of mode switching, the control input is given by

$$u_{MSC}(t_{SW})=u_{TDC}(t_{SW})=u_{TDC}(t_{SW}-t_s)-\bar{M}\ddot{x}(t_{SW}-t_s)+\bar{M}\{\ddot{x}_d(t_{SW})+K_D\dot{e}(t_{SW})+K_Pe(t_{SW})\} \quad (9)$$

where t_s means sampling period, t_{SW} is the time at which mode switches. Here, the control input of the PTOS is substituted for the previous one of the TDC as follows

$$u_{TDC}(t_{SW}-t_s)=u_{PTOS}(t_{SW}-t_s) \quad (10)$$

This guarantees smooth mode switching. Then, the control input of the MSC at the instance of mode switching is given by

$$u_{MSC}(t_{SW})=u_{TDC}(t_{SW})=u_{PTOS}(t_{SW}-t_s)-\bar{M}\ddot{x}(t_{SW}-t_s)+\bar{M}\{\ddot{x}_d(t_{SW})+K_D\dot{e}(t_{SW})+K_Pe(t_{SW})\} \quad (11)$$

3) If $|r-y|<E_{SW}$, the MSC operates as TDC and the control input is given by

$$u_{MSC}(t)=u_{TDC}(t)=u_{TDC}(t-t_s)-\bar{M}\ddot{x}(t-t_s)+\bar{M}\{\ddot{x}_d(t)+K_D\dot{e}(t)+K_Pe(t)\} \quad (12)$$

EXPERIMENTAL SETUP

To verify the effectiveness of the proposed MSC algorithm, we compared the results of applying

the MSC algorithm to the dual-stage with the corresponding results of the conventional PTOS. The implemented dual-stage is shown in Fig. 2. It consists of the coarse stage which is actuated by linear motor for large travel range and the fine stage which is actuated by voice coil motor (VCM) for high speed and high precision motion. The position of linear motor stage is measured by linear encoder and that of VCM stage is measured by laser interferometer (HP10885) with resolution of 5nm. Both stages are guided by air bearing to obtain smooth and fast motion without friction.

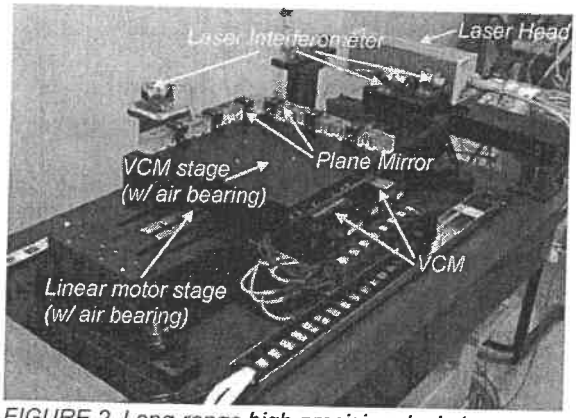

FIGURE 2. Long-range high-precision dual stage..

The performance of the dual stage is mainly determined by the fine VCM stage. It is quite conventional to approximate the dynamics of the VCM actuator by a second order model as

$$G_{VCM}(s) = \frac{X}{I}(s) = \frac{a}{s^2} \qquad (13)$$

where X is the position of the stage, I is the current input and $a=K_F/M$ is the acceleration constant, with K_F being the force constant and M being the mass of the VCM stage. The parameters of the VCM stage are shown in Table 1. The control algorithm was implemented on a dSPACE real-time DSP (ds1105) control system with sampling frequency of 10 kHz.

TABLE 1. System Parameters

Parameters	Quantity	Unit
Mass of VCM stage, M	27.4	kg
Force constant, K_F	36.2	$N \cdot A^{-1}$
Acceleration coefficient, a	1.323	$m \cdot s^{-2} \cdot A^{-1}$
Maximum current, U_{max}	4	A
Sampling period, t_s	100	μs

EXPERIMENTAL RESULTS

The proposed MSC algorithm given by (7)-(12) was implemented on the fine VCM stage. The results were compared with those of the conventional PTOS controller given by (2). The MSC and the PTOS were tuned to have the best performance. For 400 um and 10 mm step input, we adjusted the control parameters of the PTOS to $\alpha=0.9$, $k_1=10^5$ and $k_2=409$ and that of the TDC to $\bar{M}=0.75$, $K_P=10^5$ and $K_D=520$. The switching boundary E_{SW} was set to 15 um based on the simulation results. In particular, we focused on the following performance.

1) settling time at which position error becomes less than 100 nanometer to characterize the point-to-point motion (absolute error bound is important in precision measurement system)

2) standard deviation of the position error during 200 ms after settling to characterize positioning error.

Fig. 3. shows 400 um step response. As shown in Fig. 3(c) and 3(d), the MSC has faster settling performance and less positioning error. Fig. 4. shows 10 mm step response. As illustrated in Fig. 4(c) and 4(d), the MSC achieved faster settling and better positioning performance. Fig. 3(b) and 4(b) illustrate the control input of 400 um and 10 mm step response, respectively. At the instance of mode switching, the transient response in control input is negligible, which leads smooth mode switching. The experimental results with the PTOS and the MSC are compared in Table 2. As shown in Table 2, 100 nm settling time and positioning error were highly improved with the proposed MSC.

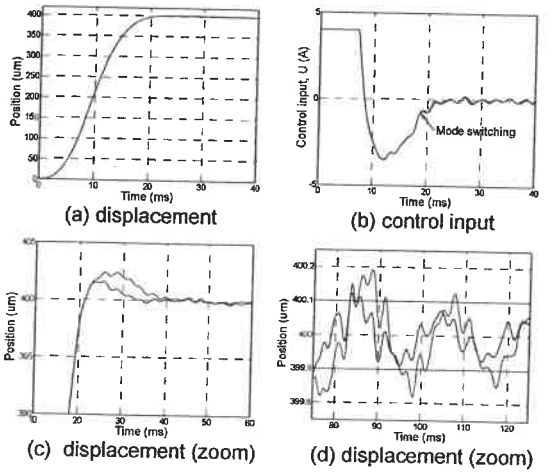

(a) displacement (b) control input

(c) displacement (zoom) (d) displacement (zoom)

FIGURE 3. 400 um step response. (dotted : PTOS, solid : MSC)

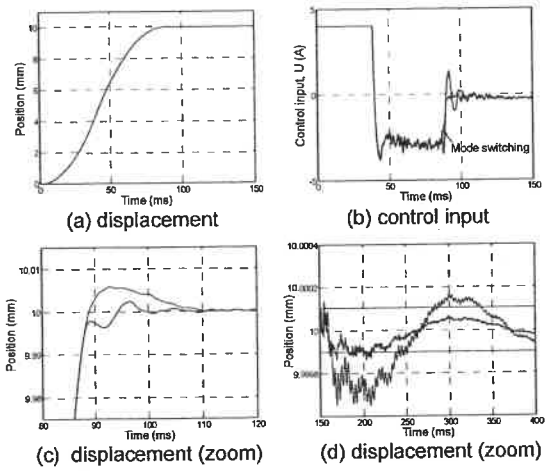

(a) displacement (b) control input

(c) displacement (zoom) (d) displacement (zoom)

FIGURE 4. 10 mm step response. (dotted : PTOS, solid : MSC)

TABLE 2. Experiment results : settling time and positioning error.

	Performance	PTOS	MSC	Improvement with the MSC
400 um	100 nm settling time	140 ms	86 ms	39 %
	Positioning error (1σ)	12 nm	6 nm	45 %
10 mm	100 nm settling time	323 ms	218 ms	33 %
	Positioning error (1σ)	22 nm	8 nm	62 %

CONCLUSION

We proposed in this paper a new MSC algorithm to achieve both the fast point-to-point motion and precise positioning after settling. Combination of the PTOS and the TDC enables smooth mode switching without any compensation of initial value. Since the TDC calculates control input using previous one of the PTOS at the instance of mode switching. The experimental results show that proposed MSC has a significant improvement in settling time and precise positioning. The proposed MSC is simple to design and can be easily applied to other servomechanism like hard disk drives that requires both the fast settling and high precision positioning.

REFERENCES

1. K. H. Kim, Y. M. Choi, D. M. Kim, B. U. Nam, D. G. Gweon, M. G. Lee and S. W. Lee, "Ultra precision dual stage system using air bearing and VCM for nanolevel scanning," *Korean Society of Precision Engineering*, vol. 22, pp. 80-86, 2005
2. G. Franklin, D. Powell and M. Workman, "Digital Control of Dynamic Systems 3rd ed.", *Addison-Wesley Press*, 1990
3. M. L. Workman, "Adaptive proximate time optimal servomechanisms," *Ph. D. Thesis, Stanford University*, 1987
4. S. Hara, T. Hara, L. Yi and M. Tomizuka, "Novel reference signal generation for two-degree-of-freedom controller for hard disk drives," *IEEE/ASME transactions on mechatronics*, vol. 5, pp. 73-78, 1998
5. K. Yucef-Toumi and I. Osamu, "A time delay control for system with unknown dynamics," *Journal of Dynamic Measurements and Control Transactions of ASME*, vol. 112, pp. 133-142, 1990
6. T. C. Hsia and L. S. Gao, "Robot manipulator control using decentralized linear time invariant time delayed joint controllers," *IEEE Proc.- Robotics and Automation*, vol. 3, pp. 2070-2075, 1990
7. S. Weerasooriya and D. T. Phan, "Discrete-Time LQG/LTR Design and Modeling of a Disk Drive Actuator Tracking Servo System," *IEEE Transactions on industrial electronics*, vol. 42, pp. 240-247, 1995
8. K. Liu, B. M. Chen and Z. Lin, "On the problem of robust and perfect tracking for linear systems with external disturbances," *International Journal of Control*, vol. 74, pp. 158-174, 2001
9. V. Venkataramanan, B. M. Chen, T. H. Lee and G. Guo, "A new approach to the design of mode switching control in hard disk drive servo systems," *Control Engineering Practice*, vol. 10, pp. 925-939, 2002
10. T. Yamaguchi, H. Numasato and H. Hirai, "A mode-switching control for motion control and its application to disk drives: Design of optimal mode switching conditions, "*IEEE/ASME Transactions on Mechatronics*, vol. 3, pp. 202-209, 1998
11. T. Yamaguchi, Y. Soyama, H. Hosokawa, K. Tsuneta and H. Hirai, "Improvement of settling response of disk drive head positioning servo using mode switching control with initial value compensation," *IEEE Transactions on Magnetics*, vol. 32, pp. 1762-1772, 1996
12. T. Yamaguchi and H. Hirai, "Control of transient response on a servo system using mode-switching control, and its application to magnetic disk drives," *Control Engineering Practice*, vol. 6, pp. 1117-1123, 1998

PRECISE POSITION CONTROL OF A PNEUMATIC SERVO TABLE SYSTEM CONSIDERATION DYNAMIC CHARACTERISTICS OF PNEUMATIC SERVO VALVES

Takashi Miyajima[1], Taro Ogiso[1], Toshinori Fujita[2], Kenji Kawashima[1], and Toshiharu Kagawa[1]
[1]Tokyo Institute of Technology, Yokohama, Kanagawa, Japan
[2]Tokyo Denki University, Chiyoda, Tokyo, Japan

INTRODUCTION

Pneumatic servo systems are used in many fields, such as pneumatic robot systems, aspherical glass molding machines, and vibration isolation systems [1]. The use of air power has a number of advantages, including compressibility, high power ratio, and low heat generation. Also air is non-magnetic and a clean energy source.

The performance of the pneumatic servo systems improved greatly as the pneumatic servo valves became commercially available in the late 1980s. At present, one of the best pneumatic servo valves has a dynamic response of 100 Hz and a spool position accuracy of 2% to the full stroke. By using these pneumatic servo valves, the precise position control by the pneumatic servo system has entered a practical stage.

There are many researches to improve the pneumatic position control system. Despite these efforts, the position controllability of the pneumatic system is inferior to the electric system. Therefore, high precise pneumatic servo positioning systems are often used electric actuators, like a piezoelectric actuator, in fine stroke [2]. However, these hybrid systems using electric actuators eliminate the advantages of pneumatic systems, which are non magnetic field generation and low heat generation.

The authors have developed a pneumatic servo table system for precise position control [3]. The system achieved position error within 0.2 μm using an air bearing to reduce friction force. We also made clear that the position controllability is dominated by the dynamic characteristic of the servo valve. Therefore, we have developed a novel pneumatic servo valve [4]. The natural frequency and the damping ratio of the servo valve could be set freely by gain tuning.

In this paper, the effect of the dynamic characteristic of the servo valve on the controllability of the pneumatic servo table system is investigated experimentally. Step response tests, frequency response tests and trajectory tracking tests of the pneumatic servo table are implemented in various natural frequencies of the servo valve.

PNEUMATIC SERVO TABLE SYSTEM

The main components of the pneumatic servo table system are a pneumatic actuator and two pneumatic servo valves. The system is shown in Fig. 1. The experimental setup including a schematic view of the pneumatic actuator is shown in Fig. 2.

Pneumatic actuator

The pneumatic actuator consists of a slider, which is 1-DOF moving part, and a fixed guide. The slider is mounted with externally pressurized air bearings. The air bearings act through holes in the surface of the guide, attaining a non-contact drive between the slider and the guide during movement. Due to the air bearing, the slider can move without stick-slip effect and can accelerate smoothly. The slider is driven by the pressure difference at both pressured chambers. The full stroke of the slider is ±70 mm. The displacement of the slider is measured by a linear transducer of resolution 0.05 μm. Values of the displacement are passed to a PC through a counter. The PC acts as a controller and sends the control signals to the servo valves.

The open loop transfer function from the control input u to the slider position x is given by Eq. (1) [3]:

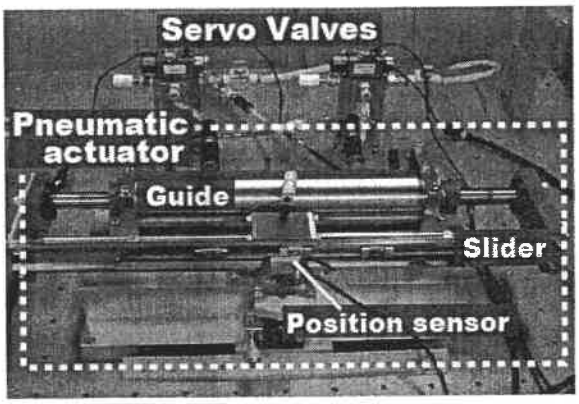

Figure 1: Pneumatic servo table system.

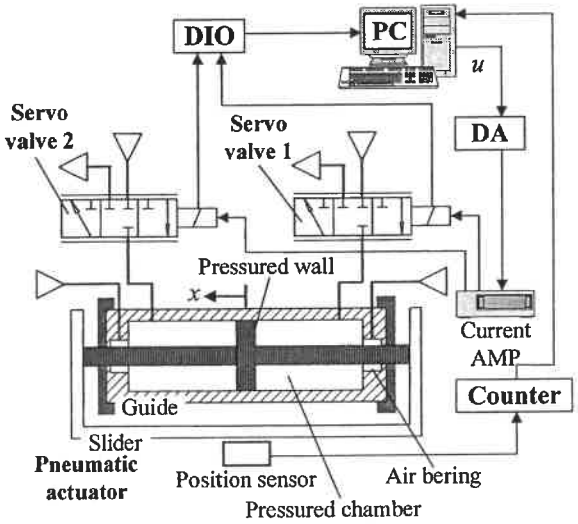

Figure 2: Experimental setup of pneumatic servo table system including a schematic view of the pneumatic actuator.

$$P_n(s) = \frac{x(s)}{u(s)} = \frac{K_n \omega_n}{s(s^2 + \omega_n{}^2)} \qquad (1)$$

Where K_n is the system gain and ω_n is the natural frequency of the actuator.

Servo valve

We have developed a High-Performance Pneumatic Servo Valve (HPPSV) [4]. The HPPSV has high dynamic characteristics and high-accuracy flow rate controllability with a digital controller. The HPPSV is a direct drive type three-port spool valve. The full stroke of the spool is ±0.9 mm. The spool position accuracy is 0.1% to the full stroke. The maximum sonic conductance is 9.0×10^{-9} m^{4}s/kg.

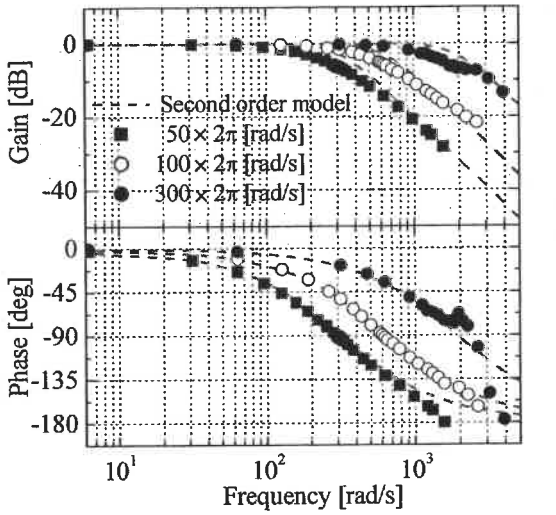

Figure 3: Frequency responses of the HPPSV.

The open loop transfer function from the control input u to the spool position x_{sp} is modeled as a second order delay system. Using the state feedback, the closed loop transfer function is as follows:

$$G_{sp} = \frac{x_{sp}(s)}{u(s)} = \frac{\omega_{sp}{}^2}{s^2 + 2\varsigma\omega_{sp}s + \omega_{sp}{}^2} \qquad (2)$$

The dynamic characteristic of the HPPSV can be determined to a desired value by setting the natural frequency ω_{sp} and the damping ratio ς. The sonic conductance C of the HPPSV is proportional to the spool position x_{sp}.

Setting several natural frequencies ω_{sp}, the dynamic characteristics of the HPPSV are changed. The damping ratio ς is fixed at 0.7. Figure 3 shows the results of the frequency response test of the HPPSV with 10% of the full-stroke. From Fig. 3, the dynamic characteristic of the HPPSV agree well with the theoretical curve at any natural frequency. Furthermore, the band width of the HPPSV is up to 300 Hz.

POSITION CONTROL

To control the pneumatic servo table system, a PDD^2 controller is used. The position, the velocity and the acceleration are used to calculate the controller input:

$$u = K_p(x - x_{ref}) - K_v\dot{x} - K_a\ddot{x} \qquad (3)$$

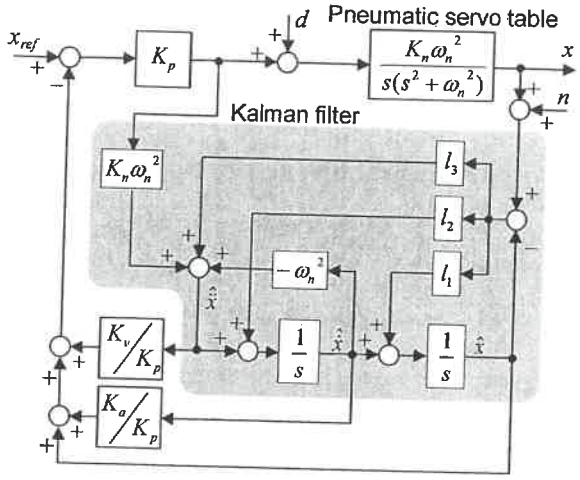

Figure 4: Block diagram of position control system with PDD² controller.

Because the velocity and the acceleration are not measurable, these values are estimated by a Kalman filter. Figure 4 shows the block diagram of the positioning system.

By using a normalized Laplace operator s_0 and dimensionless parameter α and β,

$$G_t(s) = \frac{x(s)}{x_{ref}(s)} = \frac{1}{s_0^3 + \alpha s_0^2 + \beta s_0 + 1} \quad (4)$$

The velocity gain K_v and the acceleration gain K_a can be expressed as functions of α, β and the proportional gain K_p.

EXPERIMENTAL RESULTS

Step response experiment

To improve the dynamic characteristic and the position controllability, a larger value of the proportional gain K_p is required. In the actual system, the proportional gain is limited by the nonlinearity of the system.

Table 1 shows the proportional gain of the system at the limit of stability condition with several natural frequencies of the HPPSV. The natural frequency of the HPPSV is set as 100 Hz, 200 Hz and 300 Hz. The step amplitude of the system is set as 0.1 mm and 0.5 mm. From Table 1, the proportional gain at the limit stability condition becomes larger for the higher natural frequency of the servo HPPSV, clearly.

Table 1: Comparison of stability limit proportional gain chaining valve natural frequency.

ω_{sp} [rad/s × 2π]	100	200	300
Stroke 0.1 [mm]	0.17	0.37	0.49
Stroke 0.5 [mm]	0.12	0.19	0.23

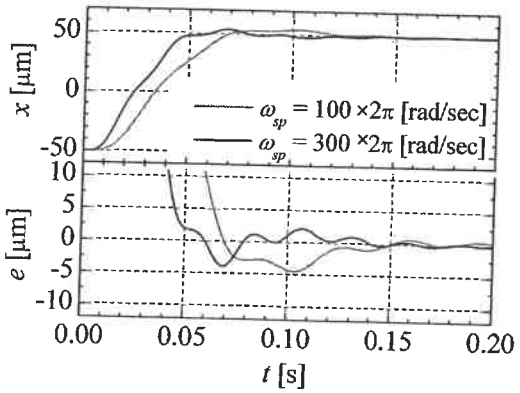

Figure 5: Experimental results of transient response.

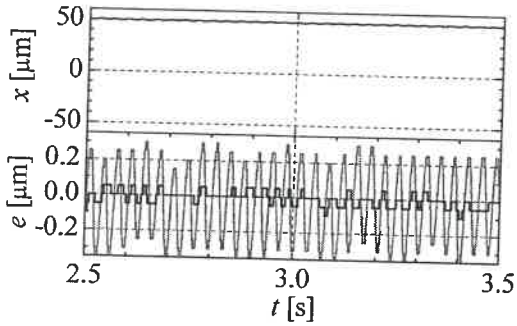

Figure 6: Experimental results of steady state error.

Step response experiments are implemented with no load at the amplitude of 0.1 mm. The proportional gain is set to the 90% of the limit of stability. Figure 5 shows the transient responses and Fig. 6 shows the steady state error. From Fig. 5, the rising time is improved by using a higher natural frequency of the HPPSV. Furthermore, it is clear from Fig. 6, that the steady state error is improved from ±0.25 μm to ±0.05 μm by changing the natural frequency of the HPPSV from 100 Hz to 300 Hz.

Frequency response experiment

Figure 6 shows the Bode diagram at the amplitude of 0.1 mm. The dashed lines in Fig. 6 show the numerical calculation results of the system based on Eq. (4). The experimental results agree well with the numerical calculation one at both gain response and phase response.

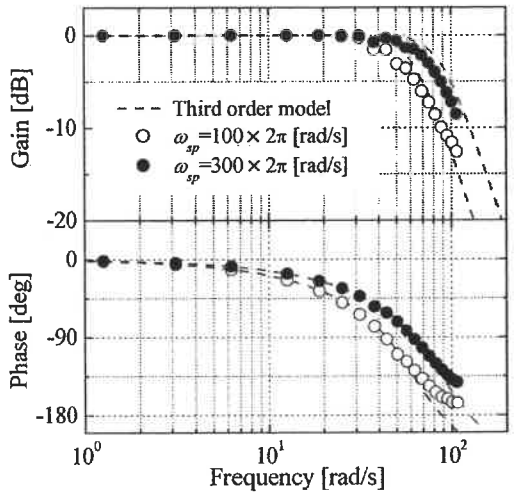

Figure 6: Frequency responses of pneumatic servo table system.

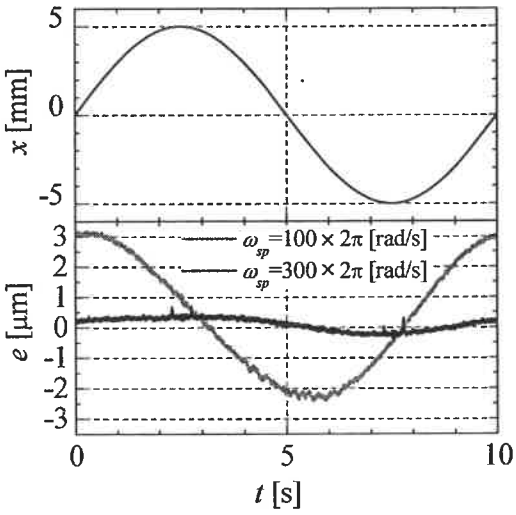

Figure 7: Experimental results of sinusoidal trajectory following test with feedforward compensator.

Using a higher natural frequency, the band width becomes wider. It means the velocity tracking ability is improved by using a higher natural frequency servo valve.

Trajectory tracking experiment

The maximum velocity of the system is restricted by the characteristic of the position encoder (300 mm/s in this system). The maximum jerk, or time variation of acceleration, of the system is restricted by the maximum sonic conductance of the HPPSV (1300 m/s^3 in this system).

From these restrictions, the selection of the reference trajectory is important to realize precise positioning. Hence, a reference trajectory of the 5.0 mm amplitude sinusoidal curve is designed with feedforward compensation. The frequency of the reference trajectory is set to 0.1 Hz. This reference trajectory is not affected by the restrictions mentioned above.

Figure 7 shows the experimental results of the tracking control test of the system. From Fig. 7, the tracking error is improved from ±3 μm to ±0.5 μm changing the natural frequency of the HPPSV from 100 Hz to 300 Hz.

CONCLUSION

Using a novel pneumatic actuator and novel pneumatic servo valves, a pneumatic precise positioning system is well constructed. The pneumatic actuator has low friction. The pneumatic servo valve has high performance. It is confirmed that the performance of the pneumatic servo system is affected by the dynamic characteristic of the servo valve.

The natural frequency of the servo valve is set three times higher than the best commercial one. We conducted several experiments and made clear that the steady state error of the system becomes lower than ±0.1 μm for step response. Moreover the tracking error of less than ±0.5 μm was realized during sinusoidal motion.

REFERENCES

1. Liu, S., Bobrow, J. E., 1988, An Analysis of a Pneumatic Servo System and Its Application to a Computer-Controlled Robot, *Transactions of the ASME Journal of Dynamic Systems, Measurement and Control*, 110: 228-235.
2. Chiang, M., Chen, C. and Tsou, T., 2005, Large stroke and high precision pneumatic-piezoelectric hybrid positioning control using adaptive discrete variable structure control, *Mechatronics*, 15: 523-545.
3. Kagawa, T. Tokashiki, L. R., Fujita, T., Sakaki, K. and Makino, F., 2000, Accurate positioning of a pneumatic servo system with air bearings, *Bath Workshop on Power Transmission and Motion Control*: 257-268.
4. Miyajima, T., Fujita, T., Sakaki, K., Kawashima, K. and Kagawa, T., Development of a Digital Control System for High-performance Pneumatic Servo Valve, *Precision Engineering* (to appear in).

DESIGN AND CONTROL FOR THE PNEUMATIC CYLINDER PRECISION POSITIONING UNDER VERTICAL LOADING

Ming-Hung Tsai, Chi-Neng Cheng, and Ming-Chang Shih
Department of Mechanical Engineering,
National Cheng Kung University
Tainan, Taiwan, R.O.C

INTRODUCTION

The pneumatic control systems have played the important roles in the industrial automation equipments owing to the following advantages - low cost, clean of the working environments, easy in power transfer, and so on. In recent years, high accuracy and high speed systems are growing up rapidly, and are important in high-tech industry. However, the precise position control of a pneumatic cylinder is very difficult due to the compressibility of air, nonlinear behavior of the air flow rate through the servo valve, the friction force between the cylinder and the piston, and the stick slip effect at the low speed of the system. The traditionally pneumatic control systems are only controlled to carry out simple on-off position and speed control by using programmable logic controller. The high precision control cannot be reached through on-off logic controller so that the modern control strategies are essential. Pandian et al [1] proposed practical design for the position and trajectory control of pneumatic actuators based on the sliding mode control approach. Shih and Ma [2] developed a control law which combines the sliding mode and modified differential PWM (M-D-PWM) control method to control the position of a pneumatic rodless cylinder. The control accuracy of the pneumatic cylinder is always under 0.1 mm. Furthermore, K.R. Pai and M.C. Shih [3] designed velocity compensator to overcome the stick-slip effect of the pneumatic table and the pneumatic table has the positioning accuracy of 20 nm. Piezoelectric actuators have been developed in recent years and already applied in pneumatic precision positioning control. Chiang et al [4] investigated pneumatic-piezoelectric hybrid positioning control system and the positioning accuracy can reach 100 nm. These papers mainly research the horizontal precision positioning control, but fewer papers study the vertical precision positioning control under loading effect. This paper is mainly to study the precision performance of positioning to the vertical pneumatic cylinder under vertical loading. In this paper, the friction force and the vertical loading have the great effect on the positioning accuracy. The hybrid fuzzy sliding mode controller with loading compensator is developed and implemented in the microcomputer to control the position of the vertical pneumatic cylinder under vertical loading in the study. Regarding the simulation of loading force, it can be accomplished by controlling the pressure of the load cylinder using pneumatic proportional valve.

LAYOUT OF THE EXPERIMENTAL DEVICES

The layout of the experimental devices for the servo pneumatic vertical position control system is shown in Fig.1. A microcomputer is applied as a controller and to get the experimental data. The displacement of the cylinder is measured by a pulse scale and the air pressure of the load cylinder is also measured and feedback to the computer. The control input signals are calculated in the microcomputer through the designed software and passed to the servo valve by the D/A capability of the data acquisition and the control card. So that the air mass flow rate can be regulated and the pressure difference of the cylinder can be built up to drive the cylinder. The simulation of loading force can be accomplished by controlling the pressure of the load cylinder using pneumatic proportional valves.

CONTROLLER DESIGN

It is difficult to obtain the accurate mathematical modal of the pneumatic system because of the strong nonlinearities, high air compressibility and significant mechanical friction. In this paper, the hybrid fuzzy sliding mode controller with loading compensator is implemented in the micro-computer to control the position of the vertical pneumatic cylinder. The fuzzy sliding mode controller is designed on the basis of human experience without accurate mathematical modal. And the stability of the fuzzy sliding mode controller can be guaranteed by using the Lyapunov approach.

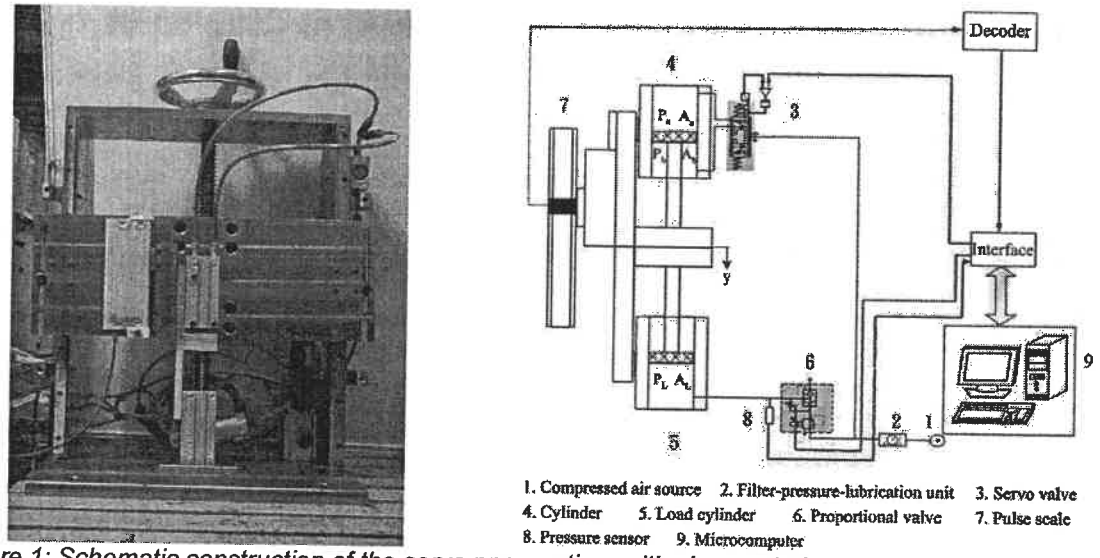
Decoder
Interface
1. Compressed air source 2. Filter-pressure-lubrication unit 3. Servo valve
4. Cylinder 5. Load cylinder 6. Proportional valve 7. Pulse scale
8. Pressure sensor 9. Microcomputer

Figure 1: Schematic construction of the servo pneumatic positioning control system.

Hybrid fuzzy sliding mode controller

The differential equation describing the piston-load dynamics is given by:

$$m\ddot{y} + b\dot{y} = (P_a A_a - P_b A_b) + mg - F_f \cdot \mathrm{sgn}(\dot{y}) - P_L A_L \quad (1)$$

where m is the piston and rod assembly mss, y is the piston position, b is viscous friction coefficient, and F_f is friction force. P_a and P_b are the absolute pressures in cylinder chambers, A_a and A_b are the piston areas. P_L is the absolute pressures in load cylinder chamber and A_L is the piston areas. The downward direction is defined as positive direction.

The actuator output force $F_{applied}$ can be controlled using servovalve and expressed as:

$$F_{applied} = P_a A_a - P_b A_b$$

The load force F_L is expressed as:

$$F_L = P_L A_L$$

The Eq. (1) can be rewritten as:

$$m\ddot{y} + b\dot{y} = F_{applied} + mg - F_f \cdot \mathrm{sgn}(\dot{y}) - F_L \quad (2)$$

The position error is

$$e = \tau - y \quad (3)$$

where τ is the command input. If the absolute position error $|e|$ is larger than the control boundary of error E_M, the control signal is set to be the maximum value ($+U_M$ or $-U_M$); if the absolute position error is smaller than the control boundary of error, the fuzzy sliding mode controller is implemented to control the position of the pneumatic cylinder. The sliding surface S is defined as:

$$S = \dot{e} + \alpha e, \ \alpha > 0 \quad (4)$$

Differentiating above equation yields:

$$\dot{S} = \ddot{e} + \alpha\dot{e} = \frac{1}{m}\left(-F_{applied} - mg + F_f \cdot \mathrm{sgn}(\dot{y}) + F_L - (m\alpha - b)\dot{y}\right) \quad (5)$$

The triangular membership functions for the input S, $\dot{S}$ and output u_f were shown in Fig. 2 and the center-of-gravity method was used for defuzzification. The fuzzy control law u_f can be determined from the rule table which was shown in Table 1.

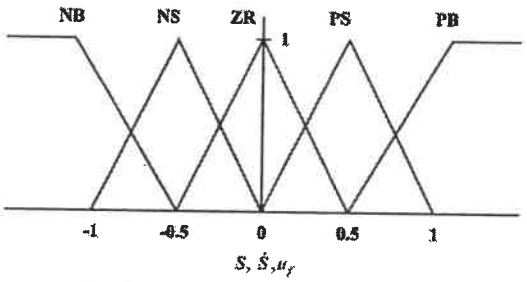

Figure 2: The triangular fuzzy membership function for the input and output signal.

Table 1: Fuzzy rule table

Ṡ \ S (u)	NB	NS	ZE	PS	PB
NB	NB	NB	NS	NS	ZE
NS	NB	NS	NS	ZE	PS
ZE	NS	NS	ZE	PS	PS
PS	NS	ZE	PS	PS	PB
PB	ZE	PS	PS	PB	PB

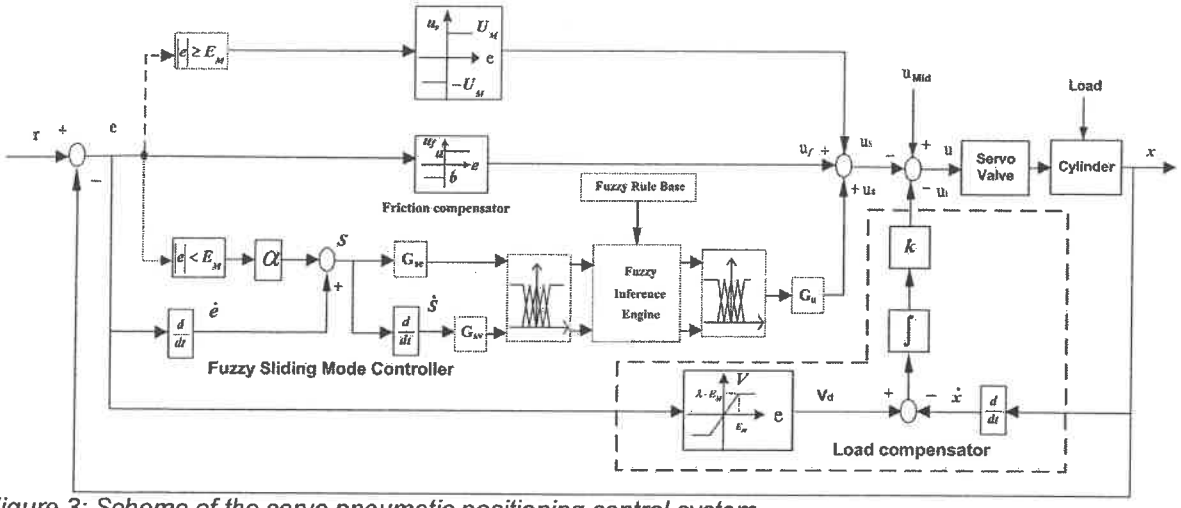

Figure 3: Scheme of the servo pneumatic positioning control system.

Loading compensator

The actuation of pneumatic cylinder is obviously influenced by the vertical loading. Moreover, the states of the position control system can not slide along the surface to track the specific time-varying state y_d and the position accuracy is decreased if the vertical loading can not be compensated well. Therefore, the loading compensator is designed to decrease the effect of the vertical loading and improve the position accuracy. The loading compensator can be written as:

$$u_L = k \cdot \int (\dot{y}_d - \dot{y}) dt \qquad (6)$$

where k is the controller gain. Because the permissible speed of the linear scale is 40 mm/s, the specific time-varying state $\dot{y}_d$ should be lower than permissible speed of the linear scale and is defined as:

$$\begin{cases} \dot{y}_d = \alpha \cdot E_M \ ; \ if \ |e| > E_M \\ \dot{y}_d = \alpha \cdot e \ \ ; \ if \ |e| \le E_M \end{cases} \qquad (7)$$

In order to get better position accuracy, the maximum value of $|\dot{y}_d|$ is set to be 20 mm/s.

Dead-zone compensator

The position accuracy is decreased owing to the dead-zone of the control system. The dead-zone of the control system is caused by the friction force and the dead-zone of the servo valve. Therefore, the compensation signal u_d is used to compensate the dead-zone of the control system.

$$u_d = \begin{cases} a \ ; \ if \ e > 0 \\ -b \ ; \ if \ e \le 0 \end{cases} \qquad (8)$$

Then combine the fuzzy sliding mode control law with compensators, the control law is redefined as:

$$u(t) = u_{mid} - u_f - u_L - u_d \qquad (9)$$

And the block diagram of the control system is shown in Fig. 3.

EXPERIMENTAL RESULTS

In this study, the sampling time is chosen to be 10 ms, the air supply pressure is set to be 5 bar. The piston diameter and the stroke of the pneumatic cylinder are 16mm and 50mm, and the load cylinder is the same size. The scaling factors of the fuzzy sliding mode controller are decided according to the experience and the reasonable mapping rage into the membership function. In order to compare the experiment results between precision positioning and precision positioning with vertical loading, the various experimental results are shown below.

Step input

For nanometer step displacements, Fig. 4 shows the time response of the multi-step positioning control. The experimental results have shown that steady state errors are within $\pm 10nm$.

Step input under constant load

Fig. 5 shows the time responses of the vertical positioning control under 4kgf upward loading force. In the experiment, the reference input is set to be 10mm and the steady state error is within $\pm 30nm$.

CONCLUSIONS

In this paper, the hybrid fuzzy sliding mode controller with loading compensator is applied to

control the vertical position of the pneumatic cylinder successfully. From the experimental results, one can make conclusions as follows:

(1) The positioning accuracy would be decreased owing to the dead-zone of the servo valve, friction force, and loading effect.

(2) From the experimental results, the vertical positioning accuracy of the pneumatic cylinder is within $\pm 30nm$, i.e. the control performance with or without loading effect is satisfactory.

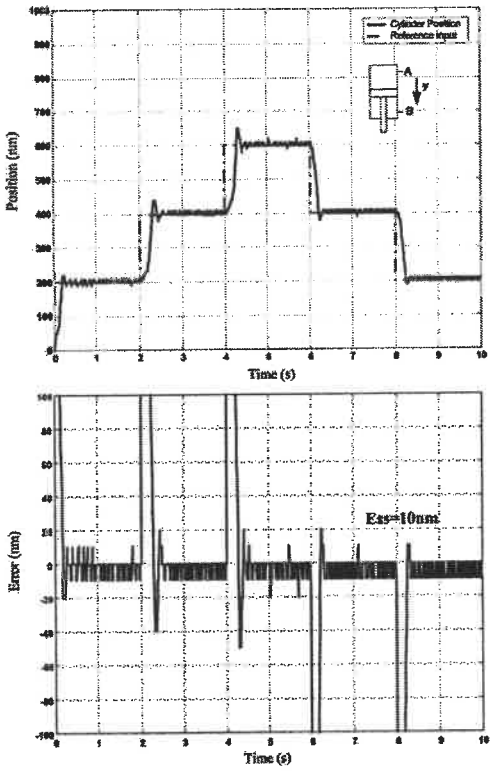

Figure 4: Time response of the multi-step positioning control.

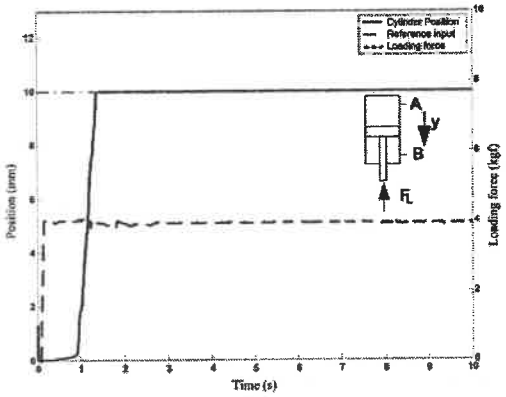

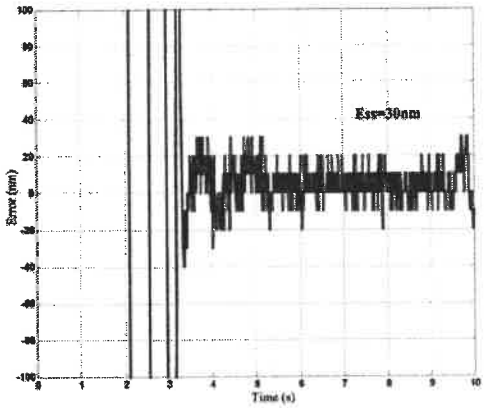

Fig. 5: Time responses of the vertical positioning control under 4kgf upward loading force.

ACKNOWLEGEMENTS

The support provided by National Science Council of Taiwan (NSC 94-2212-E-006-033) is greatly appreciated.

REFERENCES

1. S.R. Pandian, Y. Hayakawa, Y. Kanazawa, Y. Kamoyama, and S. Kawamura, 1997, Practical design of a sliding mode controller for pneumatic actuators, Transactions of the ASME, Journal of Dynamic Systems, Measurement., and Control, v119, pp. 666–674.
2. M.C. Shih and M.A. Ma, 1998, Position control of a pneumatic rodless cylinder using sliding mode M-D-PWM control the high speed solenoid valves, JSME International Journal, Series C, v 41, n 2, Jun, p 236-241.
3. K.R. Pai and M.C. Shih, 2003, Nanoaccuracy position control of a pneumatic cylinder driven table, International Journal of JSME, Series C, Vol.46, No.3, p.1062-1068.
4. M.H. Chiang, C.C. Chen and T.N. Tsou, 2005, Large stroke and high precision pneumatic-piezoelectric hybrid positioning control using adaptive discrete variable structure control, Mechatronics, v 15, n 5, June, p 523-545.

DESIGN AND EVALUATION OF A PROTOTYPE INSTRUMENT FOR MEASURING ROUNDNESS PROFILES OF MICRO SHAFTS

Mathieu Barraja[1], R. Ryan Vallance[1], Neil Loychik[1], Eric R. Marsh[2], and Dave Arneson[3]

[1] **Precision Systems Laboratory, The George Washington University**
Washington, DC USA

[2] **Machine Dynamics Research Laboratory, The Pennsylvania State University**
University Park, PA USA

[3] **Professional Instruments Company**
Hopkins, MN USA

INTRODUCTION

This paper describes the design and some initial evaluation of a prototype instrument for measuring roundness profiles of axially symmetric micro components with diameters below 500 μm. The instrument will measure form error in micro-scale cutting tools used for micro machining, small-hole metrology probes, and other high aspect ratio micro structures. The instrument will operate on the same physical principles as scanning probe microscopes, which measure surface topography using either fluctuations in tunneling of currents between probe and sample (scanning tunneling microscope or STM) or fluctuations in oscillations of a resonating cantilever beam (atomic force microscope or AFM). The instrument will measure roundness profiles using a fixed-sensitive-direction arrangement of the detector, similar to macro scale metrology instruments, as illustrated in Fig. 1. In this paper, we give an overview of the instrument and then concentrate on the design and evaluation of the instrument's axis-of-rotation.

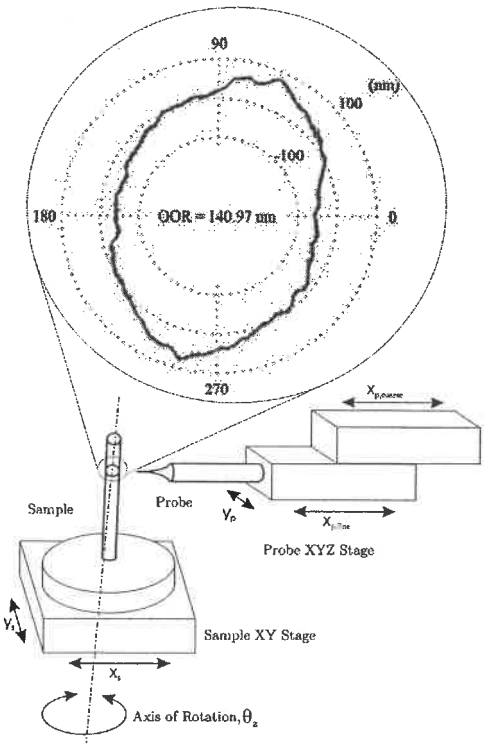

FIGURE 1. Instrument motions for fixed-sensitive direction measurement of roundness profiles on a micro shaft.

OVERVIEW OF THE INSTRUMENT

The architecture of the new instrument is illustrated in Fig. 2, and it is described in more detail by Loychik *et al.* [1]. The micro component (sample) rotates slightly more than one revolution on a spindle that is indexed with a stepper motor through a traction drive. The stepper motor and traction drive are mounted below the spindle.

As shown in Fig. 1, a nano positioning stage is attached to the top of the air bearing spindle to provide motions x_s and y_s used to center the micro component on the axis-of-rotation. The micro component is held in a collet-style holder. A support structure, symmetrically surrounding the spindle and sample, holds a second nano positioning stage that provides the probe motion in the x_p and y_p directions. A course positioning stage is being designed for the z_p direction, and it will be mounted on the probe's nanopositioning stage.

SPINDLE'S TRACTION DRIVE

The instrument requires a precise motor-driven spindle to establish an axis-of-rotation. Traditional rolling element (ball or roller) bearings are not precise enough for this application. Instead, the instrument uses an externally pressurized aerostatic spindle (Professional Instruments, Model 4R Blockhead Spindle), which exhibit radial error motions of less than 10 nm [1, 2] during coasting.

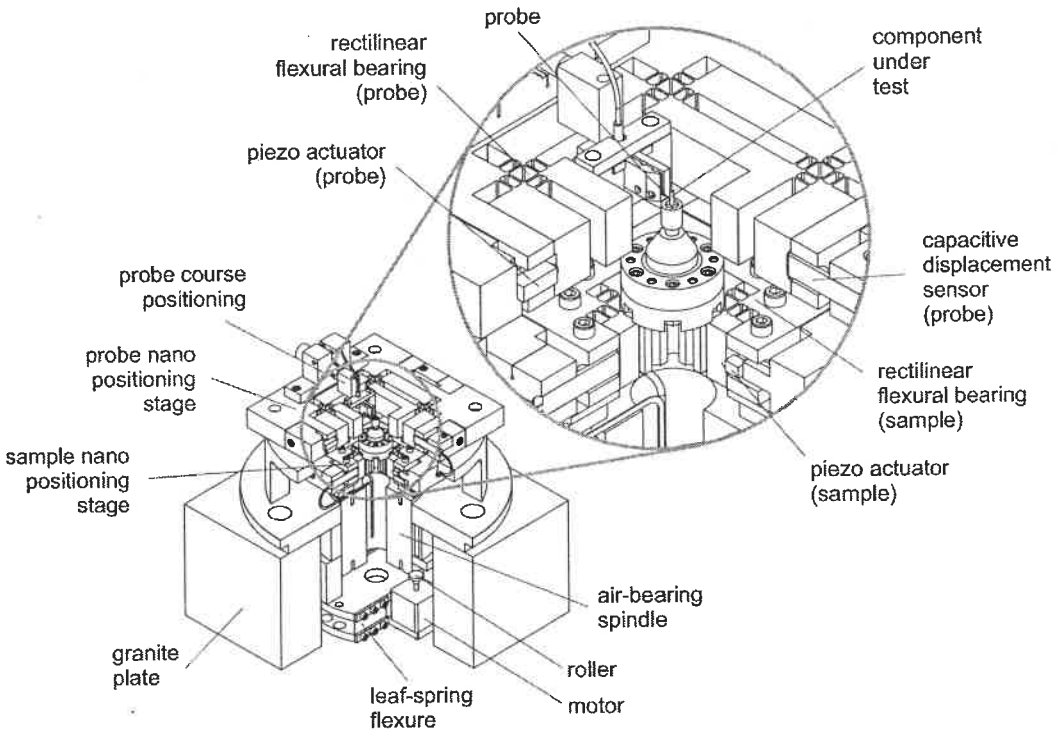

FIGURE 2. Architecture of the instrument, shown with one quarter of the solid model removed to reveal the details through to the centerline (axis-of-rotation) of the instrument.

These spindles consist of a rotor that is made of a hollow steel tube with two thrust plates and a stator that encloses the perimeter of the rotor's central tube. Pressurized air (550-1034 kPa) is supplied through the stator to a very small gap between the surfaces of the rotor and stator. Air flows out of the spindle between the annular gaps between the flange plates and stator. This produces high stiffness in the thrust, radial, and tilt directions.

The spindle is driven through a traction drive (crowned roller pressed against the perimeter of the spindle rotor) by a stepper motor (Oriental Motors, CFK544BT) mounted on a compliant flexure. The traction drive provides rolling-point contact, so a preload force is necessary to ensure that the roller remains in contact. A transmission ratio of about 7:1 is provided by the ratio of diameters for the rotor's thrust plate and the crowned roller, as illustrated in Fig. 3(a).

A compliant flexure, formed by four parallel sheet-metal springs, acts as a soft spring between the stepper motor and mechanical ground. The air gap supporting the spindle rotor is much stiffer than the compliant flexure. Therefore, radial error motion introduced from the stepper motor's shaft bearings or the roller causes the compliant flexure to move rather than the spindle's rotor, minimizing the effect on the air bearing spindle's rotor. The compliance of the flexure is adjustable using sheet metal with different width w or modulus of elasticity E, while leaving their length l and thickness t fixed. The preload force is adjusted by advancing a screw that pushes against the moving platform of the flexure. This permits adjustment of the preload force and completely disengaging the traction drive for coasting.

The angular motion of the spindle as driven by the motor is experimentally evaluated in order to determine the resolution of the traction drive and the fluctuations in steady-state position. The step-angle of the motor's controller is set to its smallest possible value, which is 2.88 millidegrees. Due to the 7:1 transmission ratio, the step size of the driven spindle is expected to be about 0.42 millidegrees. A steel lever arm is temporarily installed on the spindle. Its displacement is measured with a capacitance probe, as shown in Fig. 4. The distance between the axis of rotation of the

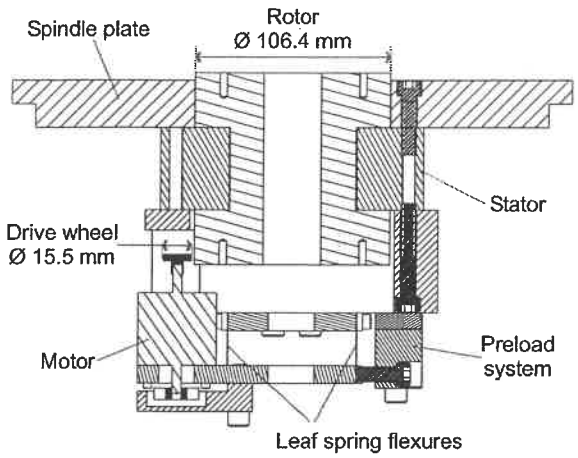

(a)

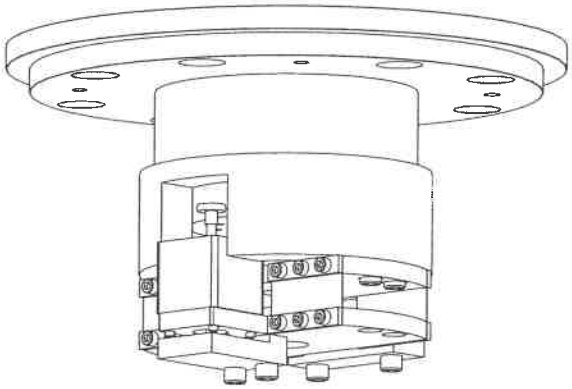

(b)

FIGURE 3. Traction drive system.

spindle and the probe has been set to 9" (228.6 mm) so that the expected range of displacement of the lever arm moved by a few steps of the motor matches the range of detection of the capacitance probe. The experiments consist of moving the motor by several steps at a frequency of 0.5 Hz, and recording the subsequent displacement of the lever arm. An anti-alias filter with a 5000 Hz cut-off frequency is used on a the analog output of the capacitance probe.

Figure 5 displays the results of these experiments run with three different enhancements to damping. The first set of experiments, shown in part (a), is conducted without any damping added to the system. As a result, the overshoot is large (78% of the step size, which leads to a damping ratio of $\zeta = 0.08$) and the settling time is relatively long (0.31 s). The gap between the thrust plate and the spindle plate is then filled with viscous

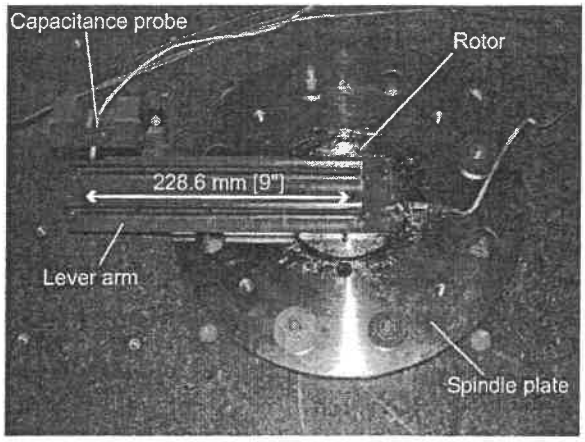

FIGURE 4. Experimental setup for measuring the spindle's step size.

grease to improve the damping and settling time, and the experiments are run again. The results illustrated in part (b) show a dramatic improvement in the damping ratio ($\zeta = 0.16$, which is double the previous value), and the settling time is reduced by more than half (0.14 s). Finally, another damping system is added to the previous one: paddles are mounted at the tip of the motor shaft, then they are plunged into a pocket filled with grease. The graph in (c) shows that the damping ratio is further improved ($\zeta = 0.23$). Throughout the experiments, a 18.3-Hz natural frequency as been constantly measured. When the rotor reaches steady-state position, it fluctuactes with a RMS value of 2.4×10^{-4} millidegrees.

It appears that these damping enhancements affected the axis-of-rotation's step size. As illustrated in Fig. 6, the average value of the spindle step size is 0.87 millidegrees, and it ranges between 0.75 and 1.05 millidegrees. With such a step-size, it would take an unreasonable 11 hours to measure a complete roundness profile, assuming that only 1 step out of 5 would be recorded and that the measured step would last 0.48 s (i.e. 4 times the settling time). Therefore, it will be necessary to increment hundreds of steps during the measurements, which will impose limits on the uncertainty in the position. A step-size of 0.87 millidegrees corresponds to a 0.15-nm step at the surface of a micro shaft with a 10 μm-radius. This suggests that the instrument resolution is smaller than the typical atomic spacing of copper or iron (0.3 to 0.4 nm, typically [3]) if the radius of the tested micro-shaft is less than 20 μm. When testing shafts with 250-μm radius, the step size would

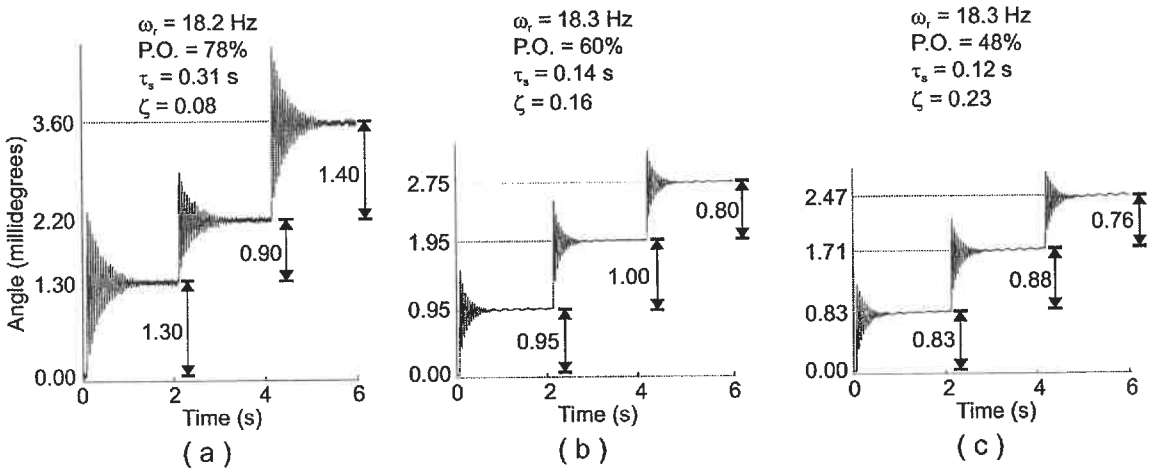

FIGURE 5. Comparison of step response with different viscous damping treatments. (a) No damping treatment. (b) Viscous grease surrounding rotor's top thrust plate. (c) Viscous grease surrounding rotor's top thrust plate and viscous paddle damper.

be about 3.8 nm.

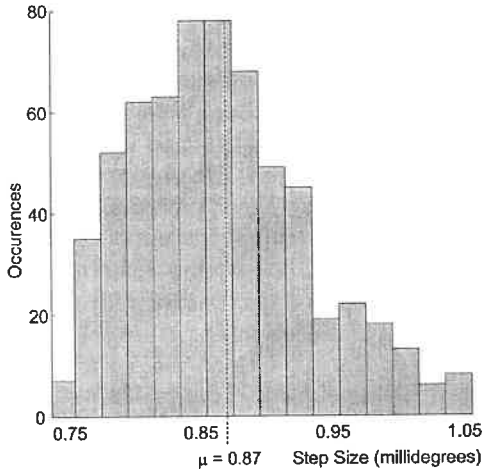

FIGURE 6. Histogram showing variation in angular step size.

CONCLUSIONS

This paper describes the design and evaluation of the axis-of-rotation for a new instrument suitable for measuring the form, waviness and roughness of axially symmetric micro components. The current non-contact metrology instruments with nanometer resolution are only suitable for flat surfaces, while this new instrument will achieve comparable measurements on axially-symmetric micro components. The first experiments performed on our prototype demonstrate that the instrument is able to span a revolved surface with a resolution ranging from 0.15 to 4 nm, depending on the diameter of the sample. The suitability of the selected traction drive system for the rotary axis of motion is confirmed. Further investigations will focus on characterizing the two nanopositioning stages that manipulate the micro component and the probe tip.

REFERENCES

[1] N. Loychik, M. Barraja, A. Khan, R. R. Vallance, E. R. Marsh, and D. A. Arneson. Mechanical design of a precision intrument for measuring the roundness profiles of micro shafts. In *Proceedings of the ASME International Conference on Manufacturing Science & Engineering (MSEC)*, October 2006.

[2] R. Grejda, E. R. Marsh, and R. R. Vallance. Techniques for calibrating spindles with nanometer error motion. *Precision Engineering*, 29(1):113–123, January 2005.

[3] Ralph W. G. Wyckoff. *Crystal Structures*, volume 1. Wiley, New York, 1963.

MICRODRIVE AND TELEMETRY SYSTEM FOR MULTI-UNIT EXTRACELLULAR STUDIES

A. Caballero-Ruiz[1], L. Ruiz-Huerta[1], E. Kussul[1], F. Heredia[2]
[1] Centro de Ciencias Aplicadas y Desarrollo Tecnológico, Universidad Nacional Autónoma de México
Mexico City, Mexico
[2] Centro de Investigación Regional "Dr. Hideyo Noguchi", Universidad Autónoma de Yucatán
Merida, Yucatan, Mexico

INTRODUCTION

In the biomedical field, the measurement of the electrical neural activity in animals enables researchers to establish valuable models of human pathologies [1] and to determine the effect of new drugs in the treatment of them [2]. In order to investigate the electrical neural activity in small animals like birds or rats by means of microelectrodes, these need to be introduced into the multiple layers of the animal's neural zone (neocortex) to register multiple neurons without disturbing its behavior [3,4].

The most common trouble being observed in this kind of measurement is the vibrations produced by the natural movement of the animal which affects the experiments. As a result of these vibrations, changes in the original position of the microelectrodes or neural damage occur and, therefore, the loss of the microelectrodes' neural signal takes place. For this reason, some researchers have proposed special systems based on devices that allow the microelectrodes to be displaced in order to record other neurons when the problem mentioned above arises.

Nowadays, manual screw-based systems are the most common mechanisms used to carry out this kind of microelectrodes displacement. However, such systems have a drawback: to rotate manually the mini lead screw that will make the microelectrodes move to a new position of study, the animal has to be immobilized (to do so, the application of anesthesia is sometimes required), which alters the results of the experiment by modifying the animal's spontaneous behavior. In the study of the neural response, it is necessary to cover some design demands to obtain reliable results, being the principal of those the study of the animal in free behavior [4-8].

In this paper, the design of an automated microdrive and a telemetry system for multi-unit extra cellular studies in rats based on a low-cost stepping micromotor is presented.

MICRODRIVES FOR EXTRACELLULAR STUDIES IN ANIMALS

Some works have reported systems for recording the electrical extracellular activity in animals using implanted microelectrodes in the animal craniums, which are placed by manual positioning devices. These works highlight the necessity of sensing some neurons simultaneously and relocating manually the microelectrodes array when the signal is lost. Nevertheless, all the information is transmitted via cables, which affect the animal's spontaneous behavior.

In this kind of studies, the process starts by setting the microelectrodes array in a fixed position into the animal's neocortex, the technique to recording the neural activity is via cables, and the positioning system is manual. Such methodologies give good results in studies in which the experimentation time is short. An experiment could go on from some minutes to some hours, but some studies require long time of experimentation to demonstrate its reliability. Therefore, in order to increase the reliability of the neural studies in animals, some research groups proposed wireless systems for recording and transmitting electrical signals, but the positioning systems are still manual [10,11]. Other authors emphasize the influence of anesthesia in the animal's neural activity [12, 13].

Another example of a system intended to increase the reliability of neural studies was presented in 2001 [14] in which a miniature

motorized microdrive was reported. In this work, an automated microdrive by means of a commercial DC micromotor was proposed. The whole system consisted of three microelectrodes moving independently. Although this system represents a good alternative to automate a microdrive, the way to record the neural activity is made by a wire system.

MICRODRIVE AND TELEMETRY SYSTEM DESIGN

Combining a wireless system for the recording of neural activity with an automated microdrive system, which is moved along the different target places of the animal's neocortex, is advantageous. In order to accomplish these tasks, the development of an automated electromechanical device (microdrive) for moving the microelectrodes and the development of a telemetry-telecommand system for recording the neural activity and for controlling the microdrive is proposed. The microdrive will be placed as implant on the rat´s head, which contains an array of four microelectrodes. The microdrive and the microelectrodes will be connected to the telemetry-telecommand system that will be placed on the rat's back. Such a telemetry-telecommand system is based on a transceiver, which will perform two tasks: one of them will be to amplify the neural signals from the array to be transmitted in a wireless way to an external PC; the other will be to receive the control signals coming from the PC to relocate the micro-electrodes when the signal is lost. Figure 1 shows the proposed system.

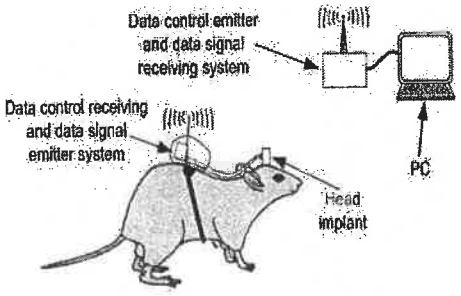
Data control emitter and data signal receiving system
Data control receiving and data signal emitter system
PC
Head implant

FIGURE 1. Automated microdrive and a telemetry system for multi-unit extra cellular studies in rats.

Automated microdrive

There are some considerations to take into account in the microdrive design: First, its maximums weight should be 25 g so that the rat can carry it on its head. Second, its size must be smaller than 15x15x15 mm, which will allow the animal to behave freely [14]. Third, the system resolution must be between 10 to 20 µm in order to allow the researcher to find new neural zones as the multiple electrodes array is relocated. Fourth, the movement range of the system must be 10 mm. Finally, the proposal has to represent a low-cost alternative.

Taking into account the experience of the researchers of the Laboratory of Micromechanics and Mechatronics in the development of micromechanical systems, and particularly in the development of micromechanical systems, as well as in the development of actuators for the automation of micromachines tools [9]; we propose an automated microdrive based on a microstepping motor, which reduces the total cost of the microdrive.

Figure 2 shows the proposed design. Basically, the microdrive is composed by a stepping micromotor (a), which is coupled to a leadscrew (b), by means of a three -gears drive (c). The leadscrew is placed between two bearings (d) A nut (g) moving along the leadscrew allows the multiple microelectrode array (i) to be displaced. The nut will be guided (h) in order to avoid free spinning. The multiple microelectrodes array is epoxy glued to the nut. The microdrive is supported by means of the principal (e) and the secondary plates (f). The microelectrodes will be guided and supported by a syringe cannula (j). The microdrive will be screwed to the rat´s head.

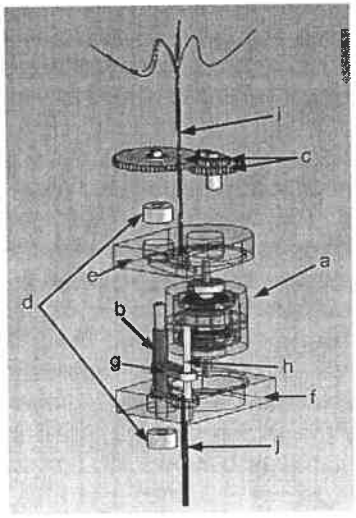

FIGURE 2. Proposed design.

Figure 3 shows how the microdrive is placed on the rat´s cranium.

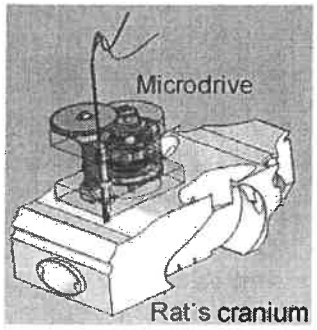

FIGURE 3. Scheme of the microdrive placed on the rat´s cranium.

Telemetry-telecommand system

This system is divided into two transceiver modules (Figure 4). One of them placed on the back rat. The second one is connected to the parallel port of a PC.

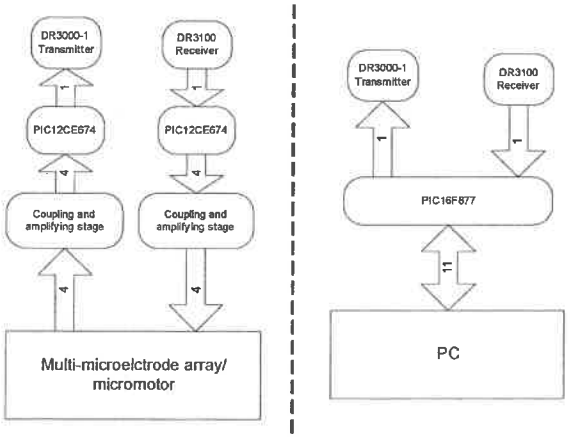

FIGURE 4. Block diagram of the rat module and the PC module.

The rat module is used to receive, via the DR3100 transceiver, the control data from the PC in order to control the microdrive. The control data is used by the PIC12CE674 microcontroller to generate the pulse sequence for controlling the position of the multiple microelectrodes array and a current amplifying stage is placed between the micromotor and the microcontroller.

In the same module, the DR3000-1 transceiver is used to transmit the neural data signals. Those signals coming from neurons are coupled by a J-FET voltage follower and amplified using a Darlington transistor. An offset voltage is added to the signals before being sent to a RISC PIC12CE674 microcontroller with 4 channels having a 8-bit A/D converter each one. Finally, the digitalized signals are sent to the DR3000-1 transceiver.

The second module employs a PIC16F877 microcontroller to receive, via the DR3000-1 transceiver, the neural data and delivers this information, via parallel port in Enhanced Parallel Port mode to a near PC. The user selects in the PC the number of steps that the motor has to execute; this information is received via the parallel port by the PIC16F877 microcontroller, which in turn transmits the data by means of its serial port to the DR3100 transceiver configured as a transmitter.

PRELIMINARY RESULTS

Figure 5 shows the first prototype of the microdrive. The employed Lorentz-Force stepping micromotor is composed by two stators to increase the torque and the rotor made by a phenolic disk which has six inserts of permanent magnet to obtain 12 steps per revolution. The current consumption of this motor is 600 mA providing a torque of about 250 µNm. This micromotor weights approximately 1 g. The micromotor is coupled to a three-gear drive with a 4.31:1 relation and a leadscrew having a pitch of 0.4 mm. The microdrive has the following characteristics:

General dimensions	13x14.5x16.6 mm
Total weight	≈5 g
Range of displacement	1.2 mm
Resolution	≈7.5 µm/step

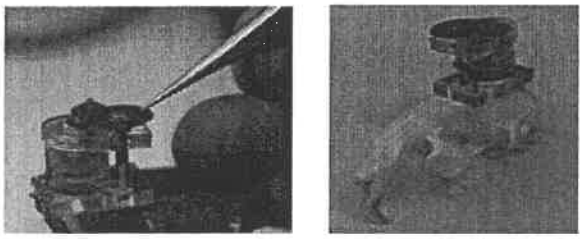

FIGURE 5. Microdrive prototype.

A prototype of an electronic circuit was developed to test the capabilities of the RF transceiver system. The system was tested using a signal generator and the results are shown in figure 6. The sample rate for this experiment was 10.5 ksamples/sec. The current

consumption of the electronic system placed on the rat´s back is approximately 30 mA.

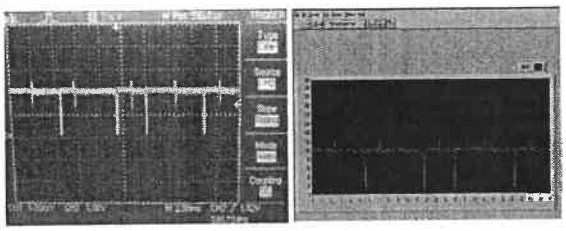

a b

FIGURE 6. A. Signal to test the telemetry data acquiring system; B. Recorded signal using the telemetry data acquiring system.

CONCLUSIONS

Automated microdrives for extracellular studies of neural response in rats represent a good application in the micromechanical field. The telemetry-telecommand system and the microdrive fulfill the requirements and will allow to develop reliable studies of neural response in animals. It is necessary to improve the micromotor design in order to decrease the current consumption. The design described in this work can include other motors in order to move each electrode independently, using a shifting system. In the near future we will present the results of the microdrive characterization.

ACKNOWLEDGMENTS

The authors want to acknowledge the enthusiastic participation of Angelica Zamora and Mario Rodriguez-Segundo in this work. This work was financially supported by grants, CONACyT 33944-U, CONACyT-NSF 39395-A, SEP/CONACyT 2003-2006 No. 2003-01-31-001-056, and DGAPA PAPIIT 112102.

REFERENCES

[1] Yannick Jeantet, YoonH. Cho, Design of a twin tetrode microdrive and head stage for hippocampal single unit recordings in behaving mice, J Neurosci Methods, 2003,129: 129-134.

[2] Heredia López Francisco J., Esquivel Loría Zoemy G, Álvarez Cervera Fernando J., Avances en el diseño y construcción de un sistema telemétrico de registro extracelular multiunitario, Congreso Nacional de Instrumentación (SOMI), México, Oct. 6-10, 2003, FHL18227.

[3] Ainsworth A, O'Keefe JA. Lightweight microdrive for the simultaneous recording of several units in the awake, freely moving rat. J Physiol (Lond) ,269(1):8P-10P, 1977.

[4] V.A. Korsunov. Miniature microdrive for extracelluar recording of neuronal activity in freely moving animals, Journal of Neuroscience Methods, 77-80, 1994.

[5] Imre Szabó, András Czurkó, Jozsef Csicsvari, Hajime Hirase, Xavier Leinekugel, Gyorgy Buzsaki. The application of printed circuit board technology for fabrication of multi-channel micro-drives. J Neurosci Methods, 2001; 105:105–110.

[6] Bilkey DK, Muir GM. A low cost, high precision subminiature microdrive for extracellular unit recording in behaving animals. J Neurosci Methods, 1999;92:87-90.

[7] A. Bragin, J. Hetke, C.L. Wilson, D.J. Anderson, J. Engel Jr, G. Buzsa´ki, Multiple site silicon-based probes for chronic recordings in freely moving rats: implantation, recordingand histological verification, J Neurosci Methods, 2000;98: 77-82

[8] J. G. Keating, G. L. Gertein, A chronic multi-electrode microdrive for small animals, J Neurosci Methods 2002;117: 201-206.

[9] Kussul E., Baidyk T., Ruiz-Huerta L., Caballero A., Velasco G., Kasatkina L., Development of Micromachine Tool Prototypes for Microfactories, Journal of Micromechanics and Microengineering, 2002; 12: 795-813.

[10] Eichenbaum H, Pettijohn D, Deluca AM, Chorover SL. Compact miniature microelectrode-telemetry system. Physiol Behav,18(6):1175-8, 1997.

[11] H. Fisher, H. Kautz, W. Kutsch. A radiotelemetric 2-channel unit for trnasmission of muscle potentials during free flight of the desert locust, Schistocerca gregaria. Journal of Neuroscience Methods, 39-45, 1995.

[12] Mark D. Kelland, Louis A. Chiodo, Arthur S. Freeman. Dissociative Anesthesia and striatal neuronal electrophysiology. Synapse , 75-78, 1991.

[13] Mark O. West. Anesthetics eliminate somatosensory-evoked discharges of neurons in the somatotopically organized sensorimotor striatum of the rat. The Journal of Neuroscience.; 9055-9068, 1998.

[14] M.S. Fee and A. Leonardo, 2001, Miniature motorized microdrive and commutator system for chronic neural recording in small animals, J Neurosci Meth, 112: 83-94.

DEVELOPMENT OF ULTRA PRECISION MACHINING WITH HIGH POSITIONING RESOLUTION

Masahiko FUKUTA[1], Masahiko NISHIOKA[1], and Hirofumi SUZUKI[2]
[1]High precision machine division
Toshiba Machine co., Ltd
2068-3, Ooka, Numazu, Shizuoka, Japan
[2]Department of Mechanical Engineering
Kobe University
1-1, Rokkodai, Nada, Kobe, Hyogo, Japan

INSTRUCTIONS

The technology for ultra-precision machining has been developed rapidly and steadily. In recent years, the demand for free form, complex and microscopic cutting has increased as a result of the need for high-value-added fabrication for items such as high NA glass lenses, micro-grooves, diffractive aspheric lenses and other optical components. The ultra-precision machine for cutting or grinding of these parts should have sufficiently high accuracy to achieve a fine surface. A highly accurate positioning system is one of the essential machine components. A good positioning system will improve the form accuracy, reduce surface roughness and increase productivity.

For several years, high-precision linear scales with 1 nm positioning have been used for ultra-precision machine. In the initial phases of such high positioning resolution, it was only possible to see the effects through the feedback signal, but not in the deviation of the actual cutting point. However, with the improvement of machining techniques and peripheral devices, it has recently become possible to see these results on the diamond-cut surfaces and even on the ground surfaces. Furthermore, there is an increasing demand for higher positioning accuracy of less than 1 nm.

Positioning accuracy of less than 1 nm has been studied and reported upon by many researchers [1]. However, most of them used the experimental table or the feedback signal to check their accuracy, i.e., they did, not measure their results at the actual cutting point. In addition, those researchers stated that a guide way using an oil static bearing was the essential factor for high accurate positioning because of the non-linearity and unexpected friction of roller bearings that can affect positioning.

In this paper, the examination of a positioning accuracy of less than 1 nm at the actual cutting point, as well as the effect of sub-nanometer positioning on the surface finish, are reported. Then, the advantages in the combination of the V-V roller bearing and linear motor are discussed based upon these results.

EXPERIMENTAL METHODS

The experiments were carried out on a four-axis numerically controlled ultra-precision machine, ULG-100D(H3) [2]. It had two air-spindles (the work spindle (C-axis) and the tool spindle), and three linear tables (X, Y and Z-axes). The X and Z-axes were mounted in a "T" configuration, and the Y-column was set vertically on the X-table. These tables were supported by V-V roller guide ways, and driven by linear motors. Figure 1 shows the photograph of the linear motor driven V-V roller guide way. Although the programming and detection resolution was 1 nm with the standard specification, the detection resolution in this study was changed to 0.1 nm in order to ascertain those effects.

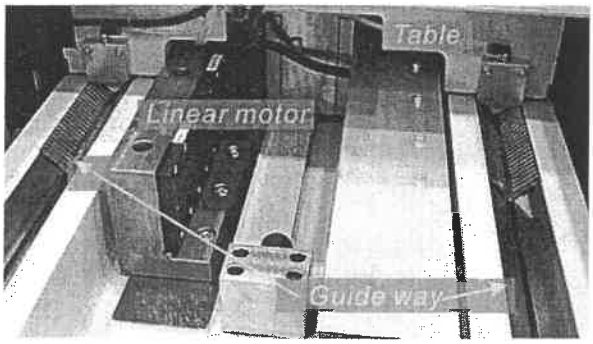

Figure 1. Linear motor driven V-V roller guide way.

The analysis of positioning accuracy in this study was carried out with three tests. The first test was the step response at less than 1 nm, which was measured at the actual cutting point with a capacitance sensor. The second test was microscopic free form cutting with a step height of a few nanometers. The third test was free form grinding, accomplished by cross-mode grinding with the air spindle tilted at 45 degrees [3].

RESULTS AND DISCUSSIONS

Step response

The step response was measured with a capacitive sensor (MICROSENSE-6810) developed for measuring sub-nanometer displacement. Therefore, the low-noise and high-stability signal at less than 1 nm could be obtained without a low-pass filter. The sensor was mounted at the side of the tool holder in the same position as the cutting location, as shown in Fig. 2, and measured the step displacement of the Z-axis. Figure 3 shows the step response for 0.5 nm, which indicates that high accuracy positioning at the actual cutting position was clearly possible. This effect is assumed to result from the reduction of the vibration from three elements: the work spindle, the drive unit, and the outer disturbance. A porous air-bearing was adopted for the work spindle, which would deliver lower air consumption and high stiffness in addition to lower vibration in the range of a few hundred Hz. The passive controlled vibration-free unit was utilized, which made it possible to decrease the outer disturbances from the floor up to a few dozen Hz. A linear motor with core was adopted as the drive unit, which was one of the most significant factors for this sub nanometer positioning. The magnet's torque ripple, which would affect the straightness of movement, could be controlled by the V-V roller guide way with a high stiffness of over 1500 N/μm horizontally and 3000 N/μm vertically. Therefore, this rigid drive unit with high torque and low current made it possible to set high position loop gain. Because a 0.1 nm step response could be detected by checking the feedback signal from the linear scale, it would become possible to measure 0.1 nm at the actual cutting position.

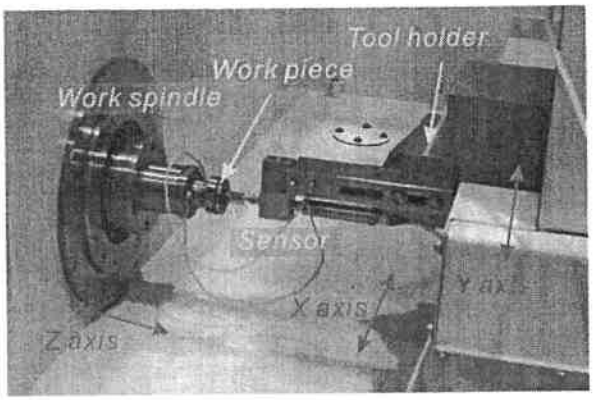

Figure 2. Setup for measuring nano-meter displacement. The capacitive sensor (MICROSENCE-6810) mounted at the side of the tool holder measured the workpiece (Electroless nickel coated harden steel) chucked on the top of the work spindle. The workpiece was cut machined with the diamond tool before measuring.

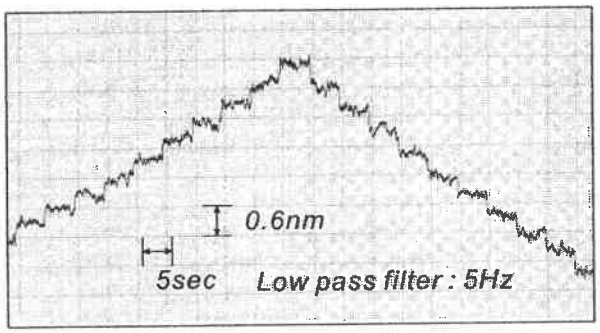

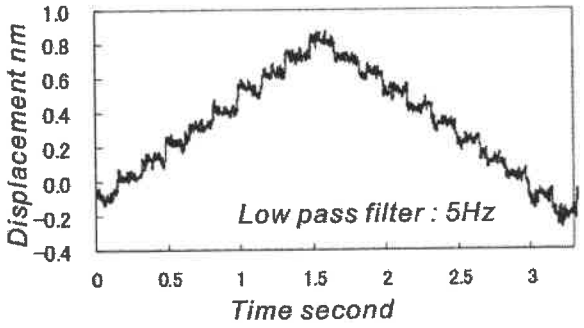

Figure 3. (Top) Step response for 0.5 nm at the actual cutting position. 5 Hz was set as a low pass filter of the analog signal recorder. (Bottom) Step response for 0.1 nm detected by checking the feedback signal form linear scale. The signal divided to 0.034 nm was sampled at 100 ms. Graph displays the result after 5 Hz low pass filtering.

Microscopic free form cutting

The second test was diamond turning of the free form using the X, Z and C-axes. The form was a designed 10 nanometer high binary pattern. In some instances of microscopic structures on an aspheric workpiece, the clear pattern and sharp edges must be formed in addition to achieving a good surface finish. Therefore, it is necessary for the Z-axis to respond quickly and steadily in sub-nanometer positioning in synchronization with the other axes. Figure 4 shows the nullified fringe pattern of the work surface and the roughness using a white-light scanning interferometer (New View 5022). The nominal height value and a uniform edge could be obtained in spite of the 10 nm step within 10 ms. Although the stick-slip caused by the guideway friction and the overshoot could not be seen, the speed of the work spindle was lower than the condition for the conventional diamond turning. It was assumed that this speed was restricted by the processing speed of the numerical controller, because the programmed pitch of the C-axis was set at 0.1 degrees in order to achieve a clear edge, which required speeds that were almost the same as the processing limit.

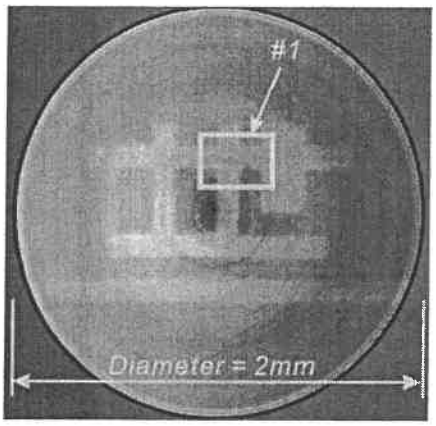

Free form grinding

The form of the third workpiece was designed based on the gray scale bitmap image. The machine tool used in this study was also adopted for making glass lens molds, which would be made from ceramic-like-materials such as cemented carbides due to their high thermal performance. Grinding with a diamond wheel would be selected for machining these difficult-to-cut materials. Although a selectable

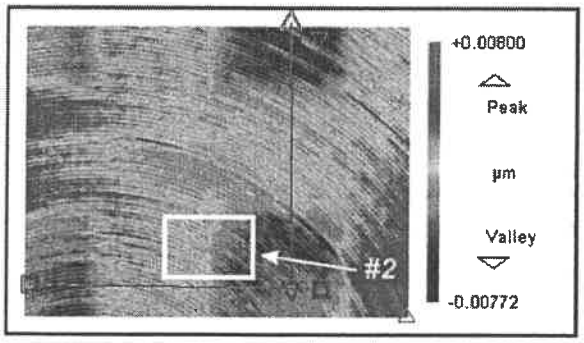

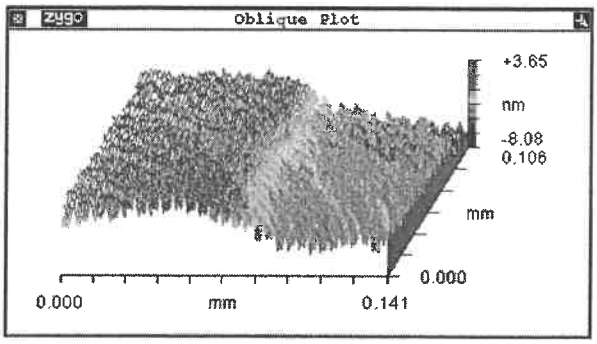

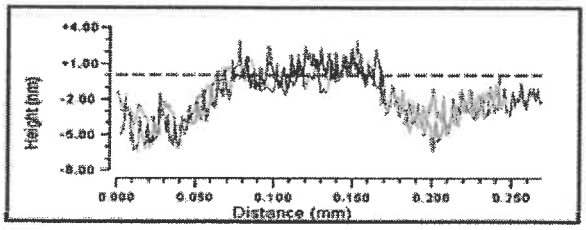

	PV nm	rms nm	Ra nm
1 T	9.245	2.268	1.988
2 S	8.375	1.715	1.433

Figure 4. (Upper left) Fringe pattern of cut machined surface. Cupper coated workpiece was cut with a diamond tool 0.5 mm in corner radius. Cutting condition were 50 min^{-1} as the work spindle speed, 0.01 mm as the feedrate and 0.005 mm as the depth of cut. (Left) Surface texture and surface profiles measured the area shown as #1 in the flinge pattern. (Right) Surface texture measured the area shown as #2 in the left figure.

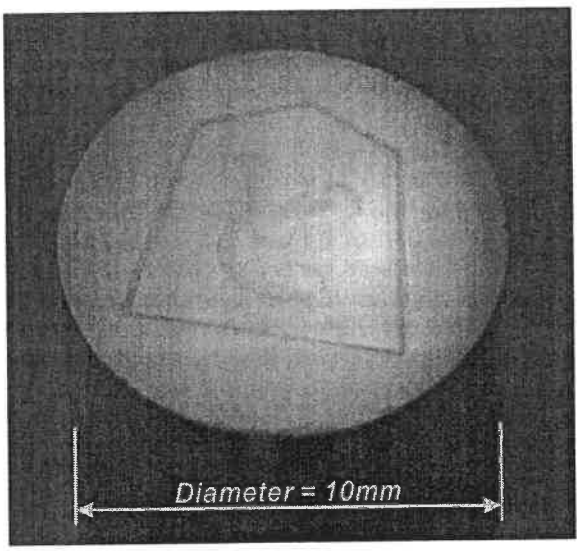

Grinding condition

Work spindle speed	*50 min^{-1}*
Tool spindle speed	*60000 min^{-1}*
Feedrate	*0.01 mm/min*
Depth of cut	*0.0005 mm*

Figure 5. Work surface ground by cross-mode grinding. (Wheel: Vetrified bonded diamond wheel, workpiece: cemented carbide)

configuration for either cutting or grinding was requested for the machine/tool, the significant change (20 kgf since the tool spindle was mounted on the Y-column) in traveling weight and the vibration caused by the imbalance in the tool spindle affected the performance of the sub-nanometer positioning. Figure 5 shows the ground surface, which indicates that a smooth surface could be obtained. However, in the detailed checking with a microscope, a little bit of chattering was detected on the flat area. In the conventional symmetric aspheric form grinding, this chatter could not be seen on the ground surface. Therefore, the chatter was caused by the low stiffness of the grinding wheel with non-continuous grinding forces. It was necessary to consider the grinding conditions because of the rapid wear on the grinding wheel in this case.

CONCLUSIONS

From the experimental results, it was clarified that the combination of the V-V roller bearing and the linear drive motor had sufficient performance to enable sub-nanometer positioning. In addition, considering the high capability of the positioning system and the wide versatility for machining methods without using any optional amplifier boards and traveling instruments, this configuration could be advantageous for flexible machine tool systems for manufacuturing free form and microscopic optical components. In the conventional precision machining of symmetric aspheric forms, a lower position loop gain made it easier to move smoothly and to achieve a good surface finish. However, the demand for more complicated and accurate machining has increased the need for a higher quality surface finish. The machine system developed in this study can meet these needs.

REFERENCES

1. Hiroshi MIZUMOTO, Makoto YABUYA, Tatuhito SHIMIZU and Yoshihiro KAMI: Comparison of positioning resolution of feed drive devices for ultra-precision machine tools, JSPE, Vol.52, No.3, 1996, pp.4582.
2. ULG/ULC series catalog 2006, Toshiba machine co.,ltd.
3. Hirofumi SUZUKI, Sunao KODERA, Shigeki MAEKAWA, Noriko MORITA, Eichi SAKURAI, Katsutoshi TANAKA, Hiroshi TAKEDA, Tsunemoto KURIYAGAWA and Katsuo SYOJI: Study on precision grinding of micro aspherical surface, JSPE, Vol.64, No.4, 1998, pp.619

DEVELOPMENT OF A HYDROSTATIC JOURNAL BEARING WITH SLIT-STEP COMPENSATION

Layton C. Hale[1], Robert R. Donaldson[2],
Carlos Castro[3], Carl A. Chung[3], David J. Hopkins[3]
[1]Innovative Machine Solutions
Dublin, CA, USA
[2]Independent Consultant
Pittsboro, NC, USA
[3]Lawrence Livermore National Laboratory
Livermore, CA, USA

INTRODUCTION

This paper describes the mathematical modeling and initial testing of an oil-hydrostatic bearing that derives compensation from both a central radial slit where fluid enters and stepped clearances near each end. Bearings using either a radial slit or stepped clearances for compensation were well studied over forty years ago by Donaldson [1]. These bearings have smooth bores uninterrupted with multiple recesses around the circumference. The present slit-step bearing achieves the best of both types with somewhat higher hydrostatic stiffness than the slit bearing and fluid shear drag lower than the step bearing. This is apparent in TABLE 1, which compares calculated values of initial (i.e., centered) hydrostatic stiffness for each type. The slit-step bearing is one of several types being studied at Lawrence Livermore National Laboratory for possible use on the Precision Optical Grinder and Lathe (POGAL).

TABLE 1. Hydrostatic stiffness (normalized to pressure, projected area and inverse clearance) for three types of compensation, all with length-to-diameter ratio ½.

Type of compensation	Clearance ratio	Hydrostatic stiffness
Radial slit	-	0.55
Stepped clearance	2	0.28
Slit plus step	3	0.73

A general understanding of the different compensation schemes may be obtained by studying FIGURES 1-3. Each one shows a cross section through the upper half of the bearing with exaggerated clearances. The pressure profile along the length of the bearing is shown at nominal clearance (solid) and either side of nominal (dashed). The supply pressure is constant and the bearing film pressure decreases to zero (atmospheric pressure) at each end. The bearing exhibits positive stiffness when the film pressure integrated over the bearing area increases as the clearance decreases.

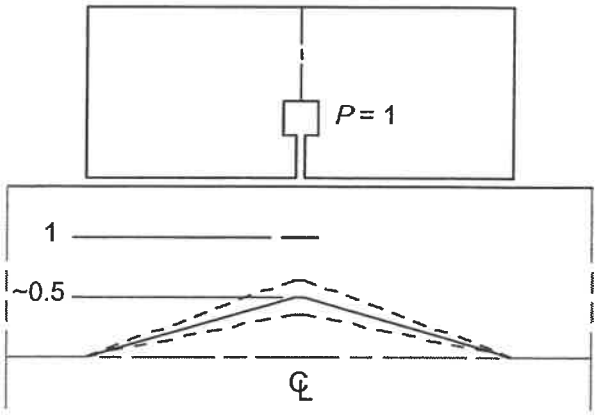

FIGURE 1. Cross section of the radial-slit bearing with the pressure profile superimposed.

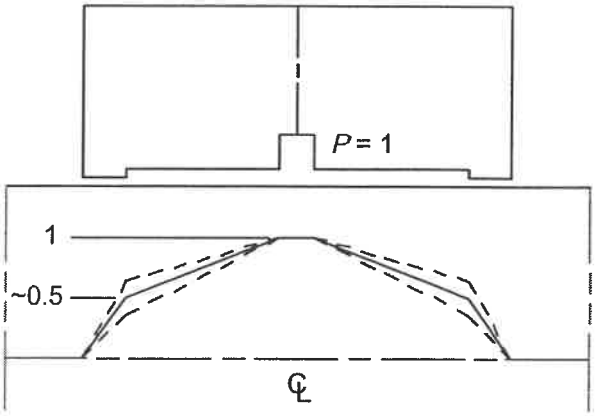

FIGURE 2. Cross section of the stepped-clearance bearing with the pressure profile superimposed.

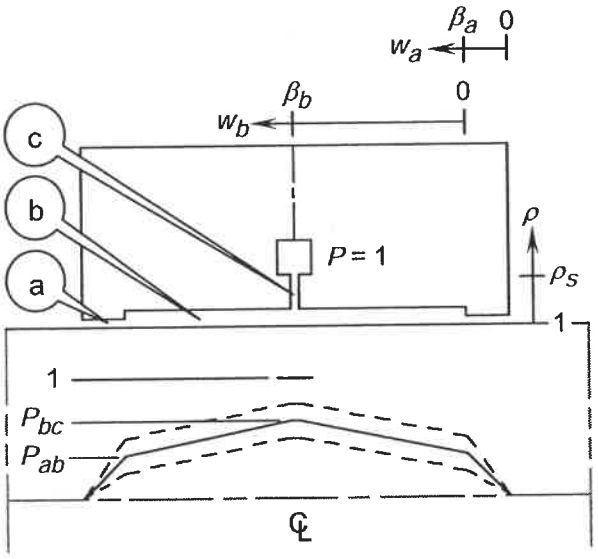

FIGURE 3. Cross section of the slit-step bearing with the pressure profile superimposed. Its has three regions: (a) land, (b) recess and (c) slit.

The stiffness advantage of the slit-step bearing results from the recess distributing the pressure response from the slit over most of the bearing length. However, the recess cannot be too deep. Fluid flows circumferentially from the higher-pressure side to the lower-pressure side more significantly for a larger recess-to-land clearance ratio and a larger length-to-diameter ratio, resulting in lower stiffness. These are important parameters when optimizing the bearing for high stiffness and low heat generation.

ANALYTICAL MODEL

The approach Donaldson used to model radial-slit and stepped-clearance bearings in [1] extends readily to the slit-step bearing of interest here. It involves piecing together solutions for partial differential equations in each region by matching flow and pressure at each junction.

The model starts with the dimensionless Reynolds equation, given in (1) for hydrostatic (HS), hydrodynamic (HD) and squeeze-film (SF) modes of operation. Being linear in pressure, the complete solution may be superimposed from separate solutions found for each mode as in (2). Our nomenclature is consistent with that in [1] except for minor changes in notation. TABLE 2 lists those variables with simple normalizations. The dimensionless parameter groups Γ and Ω appearing in (2) relate characteristic HD and SF pressures to the HS supply pressure. To further clarify, the subscripts in (2) are implied in (1) corresponding to the right-hand side, since superscripts and subscripts are needed later to identify the order and region associated with P.

$$\frac{\partial}{\partial w}\left(H^3\frac{\partial P}{\partial w}\right)+\frac{\partial}{\partial \theta}\left(H^3\frac{\partial P}{\partial \theta}\right)=\begin{cases}0 & \text{HS}\\ \dfrac{\partial H}{\partial \theta} & \text{HD}\\ \cos\theta & \text{SF}\end{cases} \qquad (1)$$

$$\frac{p}{p_s}=P_{HS}+\Gamma P_{HD}+\Omega P_{SF} \qquad (2)$$

TABLE 2. Nomenclature

Symbol	Variable	Normalized to:
P	Pressure	Supply pressure
θ	Angle (radians)	-
ρ	Radial position	Bearing radius
w	Axial position	Bearing radius
β	Bearing length	Bearing radius
H	Film thickness	Land clearance
G	Recess clearance	Land clearance
γ	Slit gap	Land clearance
ε	Eccentricity	Land clearance

Reynolds equation is accurate under the following conditions: incompressible, Newtonian fluid with constant viscosity, viscous-dominated flow, and very small clearances compared to the other length scales. In addition, the bearing surfaces are assumed to be perfectly aligned and free from deformations and form errors.

To facilitate solutions for (1), the pressure distribution is represented in (3) as a perturbation expansion in eccentricity ε. Terms up to first order are sufficient for HS and HD equations, while zero-order terms are sufficient for SF equations. This small-ε approximation will have error of order ε^2.

$$P(w,\theta)=P^{(0)}+\varepsilon\cdot P^{(1)} \qquad (3)$$

The film thickness H is constant in w for each region and has θ dependence as described in (4) for the land and recess regions, respectively.

$$\begin{aligned}H_a(\theta)&=1+\varepsilon\cdot\cos\theta\\ H_b(\theta)&=G+\varepsilon\cdot\cos\theta\end{aligned} \qquad (4)$$

Substituting (3) and (4) into (1) yields a mix of zero-, first- and higher-order terms in ε. The higher-order terms of course are discarded and like terms are collected into separate equations, (5) and (6), each of which must be satisfied. Written for the recess region, these equations also apply to the land region by setting $G = 1$.

$$\frac{\partial^2 P^{(0)}}{\partial w^2}+\frac{\partial^2 P^{(0)}}{\partial \theta^2}=G^{-3}\begin{cases}0 & \text{HS}\\ 0 & \text{HD}\\ \cos\theta & \text{SF}\end{cases} \quad (5)$$

$$\frac{\partial^2 P^{(1)}}{\partial w^2}+\frac{\partial^2 P^{(1)}}{\partial \theta^2}=G^{-3}\begin{cases}0 & \text{HS}\\ -\sin\theta & \text{HD}\end{cases} \quad (6)$$

The slit region has uniform and constant gap so the polar-coordinate form of the Laplace equation (7) holds for both zero- and first-order pressure terms.

$$\frac{\partial}{\partial \rho}\left(\rho\frac{\partial P}{\partial \rho}\right)+\frac{\partial^2 P}{\partial \theta^2}=0 \quad (7)$$

It is worth making some observations at this point to save work downstream. In the centered position ($\varepsilon = 0$), the hydrostatic pressure distribution lacks θ dependence in any of the three regions. The pressure distribution that solves the HS term in (5) is linear along the axis, as pictured in FIGURE 3. In the slit, a logarithmic pressure distribution solves (7) for the centered position.

A centered hydrodynamic bearing does not generate pressure so only the first-order HD pressure is nonzero. As noted earlier, only the zero-order SF pressure is needed for small eccentricity. Upon examining the HD term in (6) and the SF term in (5), they differ only in the forcing function on the right side, $\cos\theta$ vs. $-\sin\theta$. In both cases, the pressure distribution is generated by lateral velocity, so we should expect both solutions to be identical except for a 90° phase difference in θ. Thus only one solution need be carried further, and there is some utility in addressing the terms in (6), i.e., HS and HD.

Returning to the zero-order hydrostatic pressure, the two junction pressures along with known boundary pressures completely determine the distribution. We could choose to specify them as design parameters or calculate them from specified physical parameters. Since both slit and step bearings have only one junction, it is typical to specify the junction pressure at 0.5, the optimal value. The slit-step bearing does not have a tidy optimum so our preference is to calculate the junction pressures from physical parameters. Matching flow rates across two junctions gives two equations in (8) to solve for the two unknown junction pressures in (9).

$$\frac{1}{\beta_a}P_{ab}=\frac{G^3}{\beta_b}\left(P_{bc}-P_{ab}\right)=\frac{\gamma^3}{2\ln\rho_s}\left(1-P_{bc}\right) \quad (8)$$

$$\begin{bmatrix}P_{ab}\\ P_{bc}\end{bmatrix}=\frac{1}{\beta_a+G^{-3}\beta_b+2\gamma^{-3}\ln\rho_s}\begin{bmatrix}\beta_a\\ \beta_a+G^{-3}\beta_b\end{bmatrix} \quad (9)$$

Now the boundary conditions can be determined for the first-order pressure distributions. The three regions require a total of six equations and most are functions of θ. Two are externally imposed pressures, and the remaining four come from pressure and flow matching at the two junctions. Without further explanation, they appear in (10) through (15).

$$P_a^{(1)}(0,\theta)=0 \quad (10)$$

$$P_a^{(1)}(\beta_a,\theta)=P_b^{(1)}(0,\theta) \quad (11)$$

$$P_b^{(1)}(\beta_b,\theta)=P_c^{(1)}(1,\theta) \quad (12)$$

$$P_c^{(1)}(\rho_s,\theta)=0 \quad (13)$$

$$\left.\frac{\partial P_a^{(1)}}{\partial w_a}\right|_{\beta_a}-G^3\left.\frac{\partial P_b^{(1)}}{\partial w_b}\right|_0=-3\frac{G-1}{G}\cos\theta\begin{cases}P_{ab}\,\beta_a^{-1}\\ 0\end{cases} \quad (14)$$

$$G^3\left.\frac{\partial P_b^{(1)}}{\partial w_b}\right|_{\beta_b}-\frac{\gamma^3}{2}\left.\frac{\partial P_c^{(1)}}{\partial \rho}\right|_1=-\frac{3}{G}\cos\theta\begin{cases}P_{ab}\,\beta_a^{-1}\\ 0\end{cases} \quad (15)$$

The general solution to (6) and the applicable boundary equations is given in (16), where A_i, B_i and C_i are constants to be determined for regions (a) and (b). Likewise, the general solution to (7) for region (c) is given in (17).

$$P_i^{(1)}(w_i,\theta)=\left(A_i\sinh w_i+B_i\cosh w_i+C_i\right)\begin{cases}\cos\theta\\ -\sin\theta\end{cases} \quad (16)$$

$$P_c^{(1)}(\rho,\theta)=\left(A_c\,\rho+\frac{B_c}{\rho}\right)\begin{cases}\cos\theta\\ -\sin\theta\end{cases} \quad (17)$$

Next the solutions are substituted into the differential equations and boundary equations to determine the constants. Several constants are easily found and the remaining four are represented in a matrix equation (18) to facilitate their simultaneous solution and to easily compute the HS and HD stiffness in (19). Being nondimensional with the same normalization used in [1], it is satisfying to find numerical agreement with the two limiting cases that can be cross checked, i.e., radial-slit and stepped-clearance bearings.

$$\underbrace{\begin{bmatrix} \sinh\beta_a & 0 & -1 & 0 \\ 0 & \sinh\beta_b & \cosh\beta_b & -(\rho_s{}^2-1) \\ \cosh\beta_a & -G^3 & 0 & 0 \\ 0 & G^3\cosh\beta_b & G^3\sinh\beta_b & \frac{\gamma^3}{2}(\rho_s{}^2+1) \end{bmatrix}}_{\mathbf{M}} \cdot \begin{bmatrix} A_a \\ A_b \\ B_b \\ A_c \end{bmatrix}$$

$$= \begin{Bmatrix} \mathbf{b}_{HS} \\ \mathbf{b}_{HD} \end{Bmatrix} = \begin{Bmatrix} \dfrac{3}{\beta_a + G^{-3}\beta_b + 2\gamma^{-3}\ln\rho_s} \begin{bmatrix} 0 \\ 0 \\ 1-G^{-1} \\ G^{-1} \end{bmatrix} \\ \begin{bmatrix} 1-G^{-3}-\cosh\beta_a \\ G^{-3} \\ -\sinh\beta_a \\ 0 \end{bmatrix} \cdot \end{Bmatrix} \tag{18}$$

$$\begin{Bmatrix} K_{HS} \\ K_{HD} \end{Bmatrix} = \frac{\pi}{2(\beta_a+\beta_b)} \begin{Bmatrix} \mathbf{a}\cdot\mathbf{M}^{-1}\cdot\mathbf{b}_{HS} \\ \beta_a + G^{-3}\beta_b - \sinh\beta_a - \mathbf{a}\cdot\mathbf{M}^{-1}\cdot\mathbf{b}_{HD} \end{Bmatrix}$$

$$\mathbf{a} \equiv \begin{bmatrix} \cosh\beta_a - 1 & \cosh\beta_b - 1 & \sinh\beta_b & 0 \end{bmatrix} \tag{19}$$

Turning (19) into a dimensional form requires: the supply pressure p_s, the land clearance c_a, the bearing length L and diameter D, and the dimensionless parameter groups Γ and Ω from (2). Both Γ and Ω include the fluid viscosity μ and a characteristic velocity, which can be chosen to yield a common expression. For the HD stiffness, it is the bulk circulation frequency of the fluid at one-half the shaft speed. For the SF stiffness, it is the excitation frequency. It is convenient to express the bearing stiffness (20) as a complex number, with the real HS stiffness and the imaginary stiffness that is 90° out of phase either in space (HD) or in time (SF).

$$k(\omega) = p_s L \frac{D}{c_a} K_{HS} + (i\omega) 3\mu L \left(\frac{D}{c_a}\right)^3 K_{HD} \tag{20}$$

TEST SPINDLE

A test spindle was built with less than $500 capital investment in materials, in particular, ground-and-polished steel stock for the rotor and SAE 660 bronze bar for the journals. Other materials were found on site, and a variable-speed router motor provides an inexpensive drive solution. The authors constructed the test spindle on site. The journals and housing were turned on a Hardinge tool-room lathe and aligned concentric to one another on a Moore No. # 3 Measuring Machine.

INITIAL TEST RESULTS

The static compliance of the spindle was measured midway between the bearings by applying a force to the shaft with a force gauge and measuring the displacement of the shaft with respect to the housing using a capacitance gauge. The shear plus bending compliance of the shaft is reliably calculated to be 2.1 nm/N. Subtracting this from the total measured compliance and ignoring the compliance in the housing, the compliance for each bearing is 16 nm/N, or in terms of stiffness, 61 N/μm. The calculated stiffness using the nominal design parameters and the supply pressure of the test, 1.3 MPa, is somewhat larger at 77 N/μm. This discrepancy could result from a number of sources but we suspect larger-than-intended clearance.

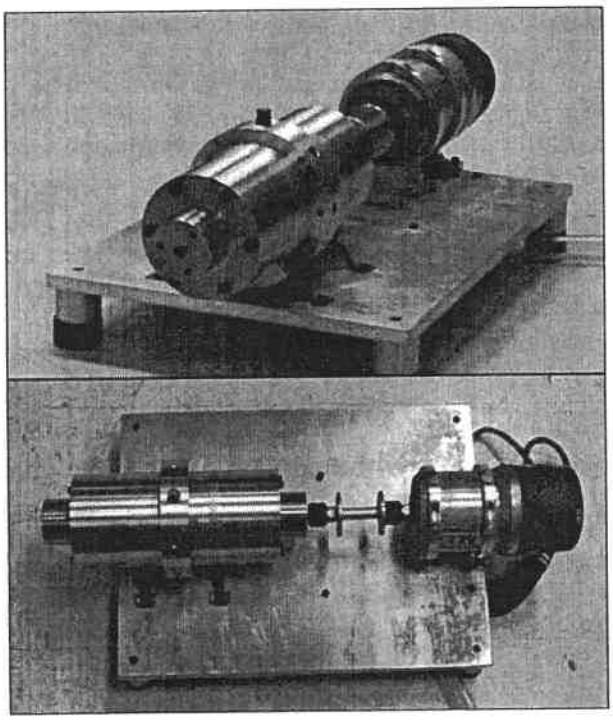

FIGURE 4. Two views of the test spindle.

ACKNOWLEGEMENTS

This work was performed under the auspices of the U.S. Department of Energy by the Lawrence Livermore National Laboratory under Contract No. W-7405-ENG-48.

REFERENCES

1. Donaldson, R.R., June 1965, *Incompressible Journal Bearings with Combined Hydrostatic-Hydrodynamic Action,* Ph.D. Thesis, Massachusetts Institute of Technology.

DEVELOPMENT OF ACTIVE MOUNTS FOR IMPROVED ACCURACY OF LARGE MACHINE TOOLS

Osamu Horiuchi, Takamichi Kato, Yoshiyuki Yamaguchi and Takayuki Shibata
Department of Production Sytems Engineering
Toyohashi University of Technology
Toyohashi, Aichi, Japan

INTRODUCTION

Generally, in manufacturing of various precision parts of an ultraprecision machine tool, accuracy of a mother machine is not enough high and a tedious correction process by scraping is indispensable. However, such a correction processing needs a lot of time and cost. Moreover, a decrease of the number of skilled technicians who can operate scraping has become a serious problem. Therefore, to remove the scraping operations, it is necessary to establish a technology for producing the machine parts only by using a mother machine. So development of an ultraprecision mother machine is demanded, which can finish up various parts of an ultra-precision machine tool.

The mother machine should be able to machine the bed, the column, the table and so on of an ultraprecision machine tool with straightness better than 0.1 μm because it guarantee the motion accuracies of the ultraprecision machine tool. The ultraprecision mother machine involved was a double column type of surface grinding machine. The most important accuracy is straightness of table motion and the error is considered mainly due to a change of vertical deformation of the bed, which is induced by moving masses, for example, the table and work. Therefore, the bed and table should have high enough stiffness in vertical direction.

In preliminary study [1][2], the influences of thickness of the bed and table on machining accuracy were investigated by FEM analysis of two-dimensional model and it was found that even a bed thicker than 3000 mm caused machining error of around 200 nm in straightness depending on the table thickness and work size.

In previous study [3], to obtain a higher accuracy independent of bed thickness or work size, active mounts have been newly proposed which can support the bed foot by pushing up forces and actively control the deformations of bed while the table traverses, as illustrated in Fig. 1. There, a hydraulic active mount developed was composed of a hydraulic cylinder and a pair of electromagnetic solenoid valves characterized by high response and small delivery. However, it had a positioning resolution of about 1 μm, which was not enough high for the ultraprecision mother machine.

In this study, to improve the positioning resolution, two different types of active mount have been newly developed and their

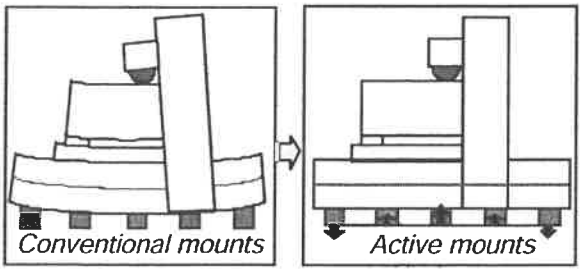

Fig. 1: Idea of active mounts

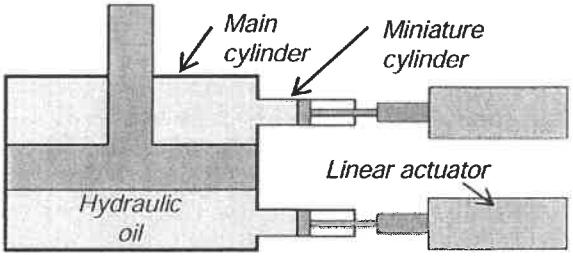

(a) Hydraulic cylinder type

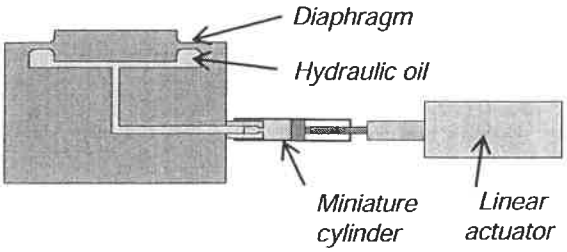

(b) Diaphragm type

Fig. 2 Two different types of active mount

Table 1: Specifications of active mounts

	Cylinder/ Diaphragm	Miniature cylinder	Ratio
Diameter mm	100	6	16.7
Cross-sectional area mm^2	7850	28	278
Maximum force N	10000	36	278
Minimum displacement μm	0.054	15	0.0036

characteristics were investigated by experiments.

ACTIVE MOUNTS

The active mount must support a heavy weight and control a fine positioning. An application of Pascal's law seemed suitable to accomplish such performance. Two different prototypes of active mount were developed. One was composed of a hydraulic cylinder and a pair of miniature cylinder driven by linear actuators, as shown in Fig. 2(a). The hydraulic cylinder was certainly driven by push and pull mode. Another type of active mount was a combination of a hydraulic diaphragm and a miniature cylinder driven by a linear actuator as shown in Fig. 2(b).

Table 1 lists the specifications of the active mounts. To obtain a high positioning resolution and a large supporting force capacity, ratio of cross-sectional area of the cylinder/diaphragm to that of the miniature cylinder was designed as large as 278. The linear actuators used for both type of active mount were driven by ball screws and stepping motors. The maximum thrust force was 100N and the minimum displacement was 15μm. Therefore the active mount had a capacity of supporting force larger than 10000N and a positioning resolution finer than 0.1μm. The active mount could elongate as far as 10μm.

EXPERIMENTAL SETUP

To investigate the characteristics of active mount, a structural model was setup assuming a part of supporting system of machine tool. The active mount was assembled at the center between a pair of steel beams which were connected by four bolts at both ends, as illustrated in Fig. 3. The upper beam and lower beam correspond to the bed of mother machine

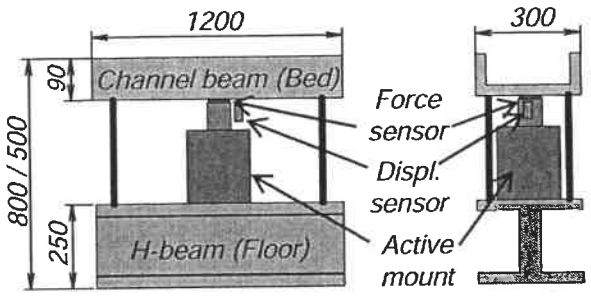

Fig. 3: Main structure of experimental apparatus

and the floor bearing the machine, respectively. The upper beam was less rigid than the lower one and pushed up by the active mount. A capacitive sensor measured the relative deflection between the beams and its output was used as feedback signal of control system. A force sensor measured the supporting load of the active mount. In the experiments, the active mount was preloaded at around 10000 N by screwing up the bolts at both ends of the steel beams.

EXPERIMENTAL RESULTS

By a series of experiments, the characteristics of the active mounts were investigated. Step response and sinusoidal response were

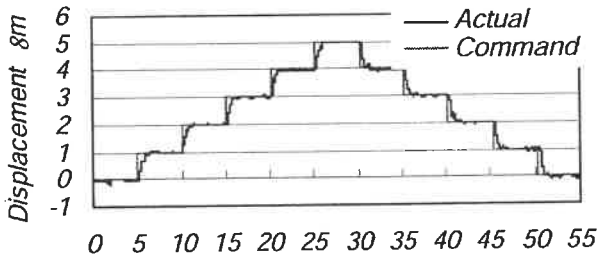

(a) Hydraulic cylinder type

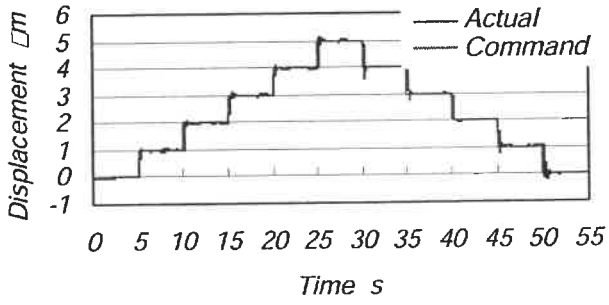

(b) Diaphragm type

Fig. 4: Step response of active mounts for 1 μm step

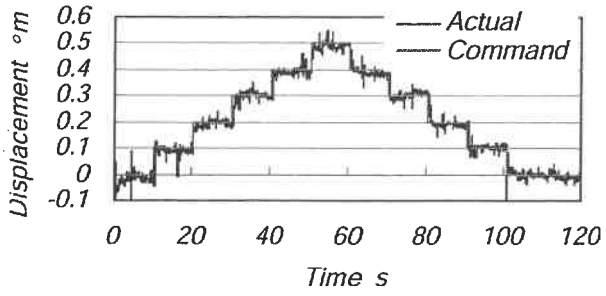

(a) Hydraulic cylinder type

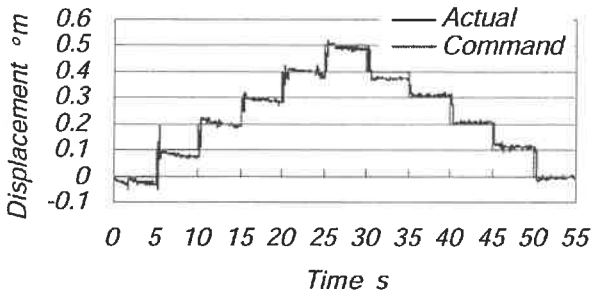

(b) Diaphragm type

Fig. 5: Step response of active mounts for 0.1 μm step

measured for different conditions.

Step response

Figure 4 shows the results of step response for 1 μm steps. Both two types of active mount could certainly make positioning with 1 μm steps. The diaphragm type of active mount showed a more rapid response and a larger overshoot than those of the hydraulic cylinder type.

Figure 5 shows the results of step response for 0.1 μm steps. Both two types of active mount seemed to have a positioning resolution of 0.1 μm. The diaphragm type could make steadier positioning than the hydraulic cylinder type.

Sinusoidal response

Figure 6 shows the results of sinusoidal response for 1 μm amplitude. Both types of active mount show a good response though a small time lag occurs between the command and the actual response. Strictly, the diaphragm type has a little bit better response than the hydraulic cylinder type.

Figure 7 shows the result of sinusoidal response for small amplitude of 0.1 μm. Both types of active mount could not response so exactly. In case of the hydraulic cylinder type, the curve of

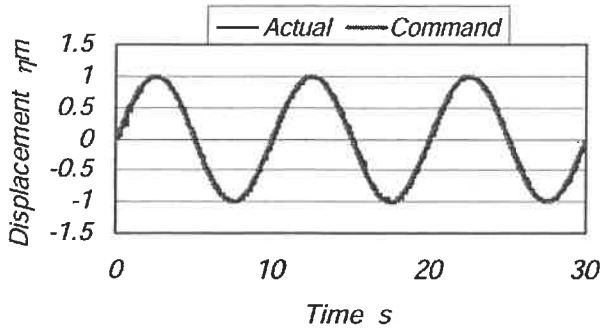

(a) Hydraulic cylinder type

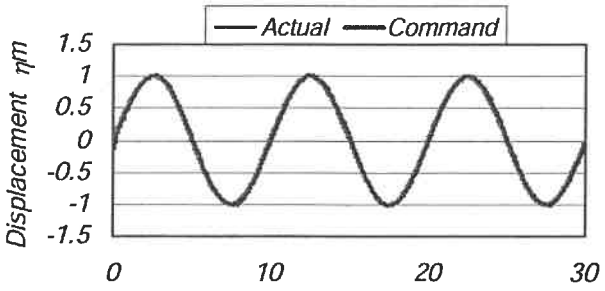

(b) Diaphragm type

Fig. 6: Sinusoidal response of active mounts for 1 μm amplitude

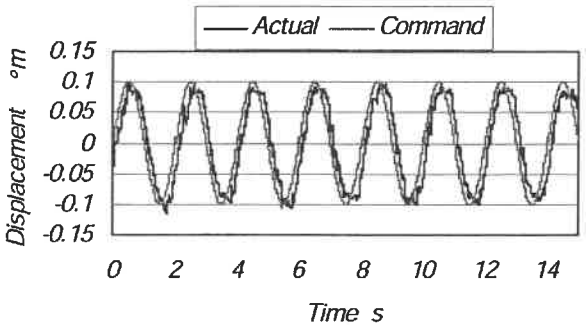

(a) Hydraulic cylinder type

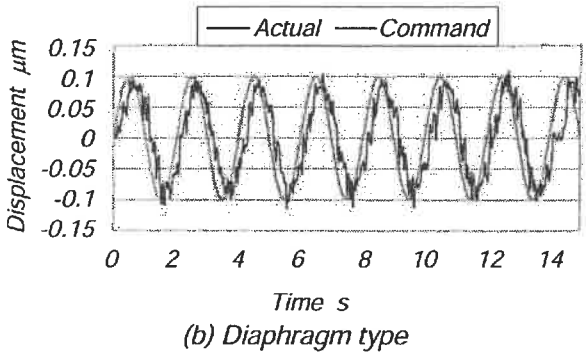

(b) Diaphragm type

Fig. 7: Sinusoidal response of active mounts for 0.1 μm amplitude

actual response looks like a trapezoidal wave. In case of the diaphragm type, however, the response curve looks like a triangular wave.

Frequency response

A series of sinusoidal response experiments was performed under various frequencies. The amplitude commanded was 1 μm. Figure 8 shows the experimental result. A frequency where the gain becomes -3 dB was 1.4 Hz for the hydraulic cylinder type and 3.3 Hz for the diaphragm type.

CONSIDERATIONS

From the experimental results described in previous section, it was found that the both types of active mount had a capability of fine positioning with a resolution better than 0.1 μm but the responses were rather low, i.e. 1.4 Hz for the hydraulic cylinder type and 3.3 Hz for the diaphragm type.

In case of the hydraulic cylinder type, the piston was driven in push and pull mode and overshoot could be suppressed if the time difference between push and pull motion was small. However a friction between the piston and cylinder might deteriorate the dynamic characteristics, for example, the trapezoidal wave caused in sinusoidal response as shown in Fig. 7(a).

In case of the diaphragm type, there was not any friction in motion of the diaphragm. Moreover the volume of concerned hydraulic oil was much smaller than that of hydraulic cylinder type. Therefore the diaphragm type is considered to be able to obtain better characteristics than the hydraulic cylinder type.

CONCLUSIONS

In order to improve the machining accuracy of large machine tools, two different prototypes of active mount were developed. One was composed of a hydraulic cylinder and a pair of miniature cylinder driven by linear actuators. Another was a combination of a hydraulic diaphram and a miniature cylinder driven by a linear actuator.

By a series of experiments, it was found that the both types of active mount had a capability of fine positioning with a resolution better than 0.1 μm but the responses were rather low, i.e. 1-3 Hz. From this result, the active mounts were considered to be effective in improving the machining accuracy if the table moved slowly such as a large surface grinder.

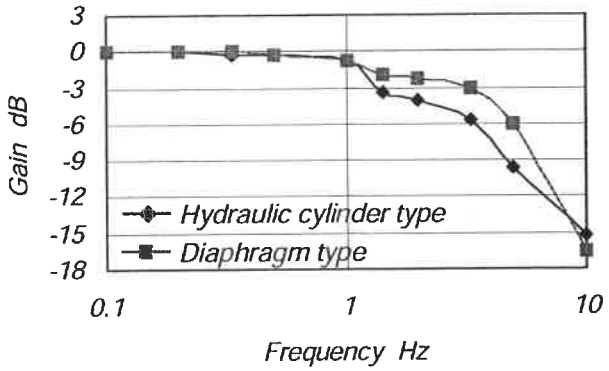

Fig. 8: Frequency response of active mounts for 1 μm amplitude

ACKNOWLEGEMENTS

This work was supported by Nagase Integrex Co.

REFERENCES

1. Suyama, A., Horiuchi, O., Shibutani, H., Suzuki, H., Yamaguchi, M., and Koizumi, K., 2002, Preliminary design of an ultraprecision grandmother machine, Proceedings of 4th International Conference on Mechanics and Materials in Design, Nagoya, Japan, 136-138.
2. Horiuchi, O., Yamaguchi, Y. and Shibutani H., 2004, Preliminary design of an ultraprecision mother machine supported by active mounts, Proceedings of 4th International Conference of euspen, Glasgow, Scotland, May-June, 404-405.
3. Yamaguchi, Y,. Kato, T., Horiuchi, O. and Shibutani, H., 2004, Hydraulic Active Mount for Improved Accuracy of a Large Machine Tool, Proceedings of 1st International Conference on Positioning Technology, Hamamatsu, Japan, June, 112-116.

DEVELOPMENT OF MECHANISMS AND FRAME STRUCTURES FOR A LABORATORY-SCALE COMPACT SOFT X-RAY MICROSCOPY

Sunghoon Kang[1], Dong Woo Kang[1], Dae Gab Gweon[1], Jin Young Min[2], and Gwon Ha Yoon[3]

[1]Department of Mechanical Engineering, KAIST, Daejeon, Korea
[2]X-ray Microscopy Research Center, Dept. of Radiology, Wonkwang University School of Medicine, Iksan, Jeonbuk, Korea
[3]LISTEM, Co., Ltd, 414-1, Chungchun-2dong, Bupyeong-gu, Incheon, Korea

INTRODUCTION

X-ray microscopy can fill the gap between optical microscopy (OM) and electron microscopy (EM). It uses the X-ray of which the wavelength lies from several nanometers to sub-nm. It makes the image resolution of X-ray microscopy much higher than OM. Recent research on micro-zoneplate for the objective of X-ray microscopy makes the X-ray image resolution even similar to that of EM[1]. X-ray microscopy can observe the samples thick up to 10um while EM can do for only 1um thick samples[2]. Especially, the interaction of soft X-ray is highly related to the atomic composition of samples therefore X-ray microscopy can be used widely from biology to industry[3].

Most of researches on X-ray microscopy used synchrotron as the X-ray source. Recently, however, rather compact X-ray sources are being used for X-ray microscopic imaging. Compact X-ray source usually has its X-ray intensity much weaker than synchrotron therefore the alignment and vibration of optical components should be one of the most important design criteria. In this paper, the mechanisms and frame structures for a laboratory-scale compact soft X-ray microscopy is presented.

CONCEPT OF A LABORATORY-SCALE COMPACT SOFT X-RAY MICROSCOPY

Soft X-ray microscope researched for this paper is full-field type and, for a laboratory-scale one, X-ray source using liquid nitrogen and high power laser is used[4]. Double-ellipsoid condenser mirror is used to illuminate the specimen and micro-zoneplate is designed to focus the specimen image on X-ray CCD. Magnification ratio is from 300 to 1000 according to the position of CCD. Total system consists of source chamber, mirror chamber and other rather small chambers. In source chamber, the components to make X-ray source as referred above, a tele-microscope to visualize the plasma and other required components is installed. Other main optical components for X-ray microscopy such as condenser mirror, specimen and Zoneplate are installed in mirror chamber.

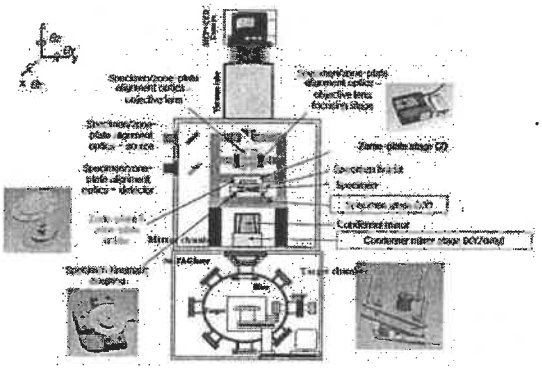

Figure 1: Conceptual design of mechanisms and frame structures of a laboratory-scale compact soft X-ray microscopy

As mentioned before, the alignment and vibration of optical components of a compact soft X-ray microscopy should be designed importantly. Due to the high magnification ratio, the misalignment of optics leads to the deterioration of X-ray image, or sometimes nothing can be detected from X-ray CCD. Vibration transmitted to optical components should blur the image therefore makes the image resolution bad.

The alignment capability of optical components is directly relate to the capability of mechanisms. Mechanisms also effect the vibration of optical components. Vibration is also influenced by the frame structure. Therefore, for the image quality of compact soft X-ray microscopy, the mechanisms for aligning optics and frame structures should be designed carefully.

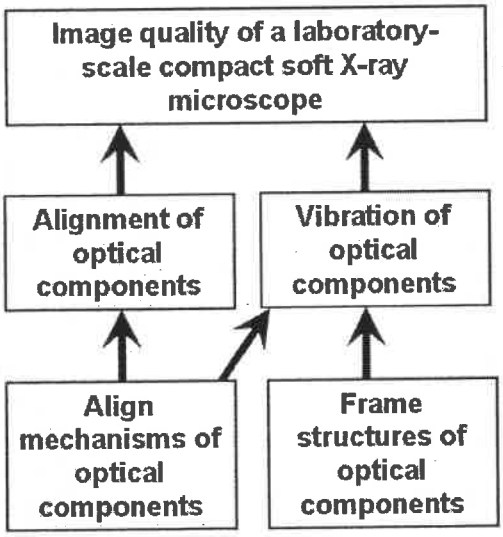
Image quality of a laboratory-scale compact soft X-ray microscope
Alignment of optical components
Vibration of optical components
Align mechanisms of optical components
Frame structures of optical components

Figure 2: Effect of mechanisms and frame structures to X-ray image quality

CONCEPTUAL DESIGN OF MECHANISMS AND FRAME STRUCTURES

In the compact soft X-ray microscope system, condenser mirror and zoneplate are most sensitive to alignment error and vibration. Because of the type of X-ray source, made by focusing the high power laser on nozzle jet of liquid nitrogen, it is desirable to correct the alignment error of condenser rather than X-ray source. Condenser mirror should have five degree of freedom from which the rotation about optic axis is excluded[4]. In addition, because the condenser mirror is 1:1 optics, Z error of condenser can be negligible to some extent. Then rest four DOF can be categorized by decenter alignment (XY) and tilt one (Θ_x Θ_y), and each can be design separately.

Another sensitive optical component is zoneplate. Z error between sample and zoneplate changes the objective distance of zoneplate, and XY error the imaging area. Due to the high magnification ratio, XY motion of zoneplate causes also the error of CCD. In addition, the alignment of zoneplate is not so easy. Therefore, in this case, specimen is aligned in XY instead of zoneplate. Objective distance still can be aligned by Z stage of zoneplate.

Frame structure can be categorized into outer frame and inner frame. Outer frame supports the total chamber body while inner frame support the components inside the chamber. Figure 3 shows the concepts of outer and inner frame structures. Outer frame consists of three hollow posts connected to the extended flange between source chamber and mirror chamber. Additional support is plate under the source chamber to lower the maximum stress and strain of flange due to system mass. This support is shaped like a cylinder for the ease of assembly.

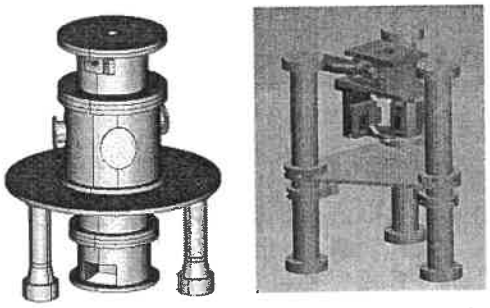

Figure 3 Concepts of outer and inner frame structures

Because of the type of X-ray source, the inner frame inside the source chamber is not easy to be installed. Therefore the inner frame in the mirror chamber only is described in this paper. As drawn in figure 3, inner frame consists of a middle plate supported by three hollow posts like outer frame. Sample is placed on the middle plate, and zoneplate and zoneplate Z stage is attached to the upper plate of mirror chamber. Specially, three posts is design to connect the lower and upper plate of mirror chamber to strengthen the stiffness of mirror chamber itself and the entire structure.

DETAIL DESIGN OF MECHANISMS

As referred before, condenser mirror stage composed of decenter stage and tilt stage. This mechanism should have high motion resolution to align the condenser finely, and have high stiffness to maintain the position of condenser after the completion of alignment. For these purposes, the condenser stage shown in figure 4 is manufactured. In XY stage, two sets of cross-roller guides are used as guide mechanisms for high stiffness, and two sets of DC linear motor with PZT tip makes the fine XY motion by dual servo control. To stiffen in motion direction, coil springs are used to provide sufficient preload. Tilt stage uses three DC linear motors to make tilt motion. At the end of each linear motor, there is a ball-shaped tip and this makes a fully kinematic contact with a v-groove. Tilt stage also is stiffened by preloading with coil springs. Same concept of XY stage of condenser stage is

applied to the specimen stage. Figure 5 shows the manufactured specimen stage.

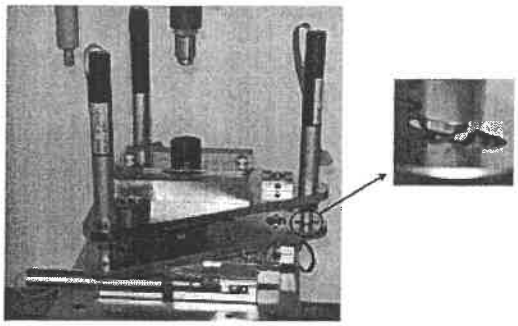

Figure 4 Manufactured condenser mirror stage

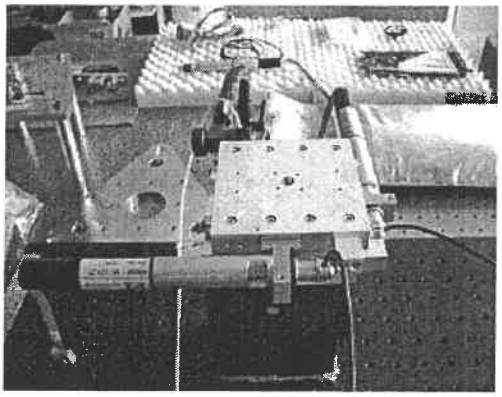

Figure 5 Manufactured specimen stage

Figure 6 and 7 shows the resolution test results of condenser and specimen stage. Condenser stage has 10nm resolution in XY, 0.08arcsec in Θ_x, and 0.04arcsec in Θ_y direction. Specimen stage has 10nm resolution in XY direction.

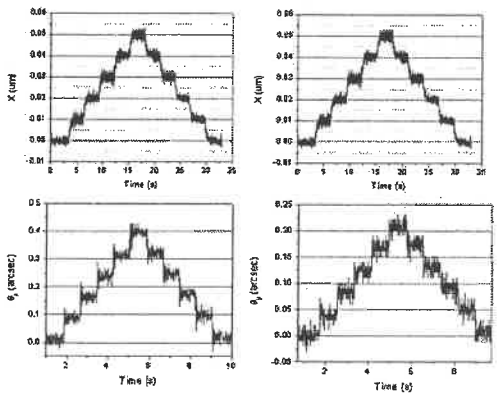

Figure 6 Resolution test result of condenser mirror stage

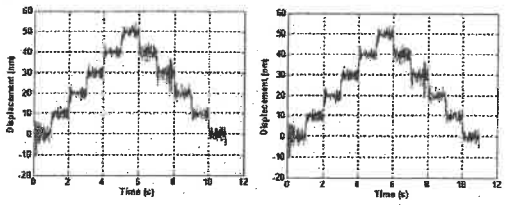

Figure 7 Resolution test result of specimen stage

DETAIL DESIGN OF FRAME STRUCTURES

The objective of outer frame is set to the 1st natural frequency above 100Hz which can ensure the stability of general structures. Natural frequencies of outer frame and total structure are calculated by FEM simulation, and feasible solution is found by changing the important dimensions of outer frame. In statics, gravity and air pressure is considered. In dynamics, some parts difficult to design in FEM is simplified using lumped masses with same mass and inertia of original parts.

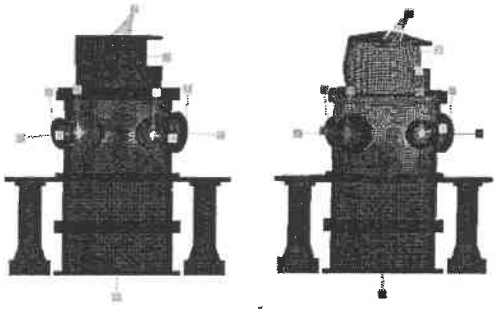

(a) *(b)*

Figure 8 FEM result of outer frame (a) statics (b) modal shape of 1st natural frequency

The design results are shown in figure 8. Statics result shows that maximum displacement does not exceed 20um and maximum stress 50MPa. Dynamics shows that the 1st natural frequency is 103Hz.

The objective of inner frame is set to be reasonable numerical values of distance change between the optical components. First, the distance change due to vibration between specimen and zoneplate should not exceed 10nm considering that the objective image resolution is 50nm. Distance changes between other optical components should be less than 1um. Inner frame is also designed using FEM simulation. Distance change between components due to vibration is obtained from FRF simulation. FRF is calculated from modal

shapes of inner frame structures, and important dimensions are modified to find the feasible solution of inner frame. Vibration sources are the turbo pump attached under the source chamber, another turbo on the side of mirror chamber, and ground vibration.

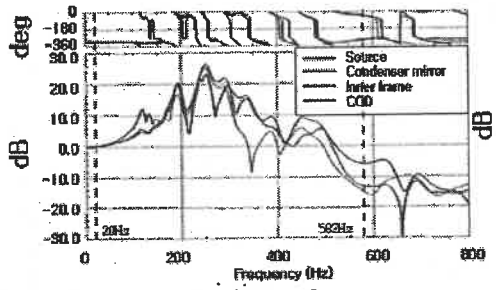

Figure 9 FRF result of inner frame

FRF graph in figure 9 is obtained in this manner, and this result shows that the objective of inner frame design is accomplished.

IMAGE ACQUISITION RESULT

Using the mechanisms and frame structures designed in this paper, a gold mesh image shows in figure 10 is acquired. The magnification ratio is set to be 325 because of the difficulty of alignment. The edge profile of the image shows the image resolution is about 120nm. This can be improved by designing the vibration of optical components more specifically.

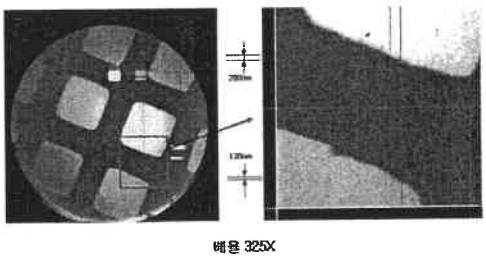

배율 325X

Figure 10 Image acquisition result of a gold mesh with 2000 pitches in 1" (X325)

REFERENCES

1. Robin Medenwaldt and Erik Uggerhoj, 1998, Description of an x-ray microscope with 30 nm resolution, *Review of Scientific Instruments*, 69: 2974-2977
2. J. Maser, A. Osanna, Y. Wang, C. Jacobsen, J. Kriz, S. Spector, B. Winn and D. Tennant, 1999, Soft X-ray microscopy with a cryo scanning transmission X-ray microscope: I. Instrumentation, imaging and spectroscopy, *Journal of Microscopy*, 197:68-79
3. Kyong Woo Kim, et al., 2006, Compact soft X-ray transmission microscopy with sub-50nm spatial resolution, *Physics in Medicine and Biology*, 51: 99-107
4. Sunghoon Kang et al., 2006, Design of a Cylindrical Flexure Jointed Stewart Platform for Aligning the Condenser in an X-ray Microscope, International Journal of Precision Engineering and Manufacturing, 7:60-65

DEVELOPMENT OF A TOOL ALIGNMENT SYSTEM IN SHEARING PROCESS

Yoshiyuki Kibe [1] and Kimiyuki Mitsui [2]
[1]Graduate School of Science and Technology
Keio University, Yokohama, Kanagawa, JAPAN
[2]Department of Mechanical Engineering
Keio University, Yokohama, Kanagawa, JAPAN

INTRODUCTION

Advances in miniaturization and weight reduction of various industrial products have demanded component parts that have both higher accuracy and quality. Small holes can be produced not only by shearing, but also with an EDM, laser, and etching. Shearing, however, is expected to be widely used because of its high productivity and machining stability.

In general, it is well recognized that the clearance most significantly influences the machining accuracy of the shearing process. However, it is quite difficult to maintain an even clearance for a same product, that is to say, to align the position of the punch and die accurately. The clearance is usually given as a value relative to the thickness of the workpiece. Therefore, when the thickness of workpiece is large, a degradation in the machining accuracy caused by tool position misalignment could be neglected. Due to the increasing demand of thin shearing products, however, it would be unwise to neglect the tool position misalignment.

For this reason, methods using static capacitance [1], wire electric discharge grinding (WEDG) [2] and image processing, which the authors helped develop [3, 4], were devised as a technique for aligning the shearing tool position accurately and maintaining an even clearance. These methods, though, correct the alignment in advance of the shearing process and cannot respond to a tool position misalignment that occurs during the shearing process. It is conceivable that a tool position could change during the shearing process because the shearing process excels at mass production.

In this research, a small punch press on a trial basis was designed to not only align the tool position in advance using image processing, but also to detect a tool position misalignment during the manufacturing process by monitoring the machining force proposed newly. Punching of circular holes was performed and the effectiveness of the system was examined.

THE SMALL PUNCH PRESS

Figure 1 shows the structure of the small punch press used in the experiments. The dimensions of the punch press are 651 mm high x 354 mm wide x 228 mm deep. A commercially available motor-driven cylinder that can apply a load up to 800 N is used as an actuator. The alignment of the shearing tool position is fine-tuned by fixing the die set on a positioning stage. The positioning stage is composed of XY and θ stages, which correspond to the alignment of various-shaped tools. The maximum shearing force of this punch press is limited to 686 N due to the maximum load of the positioning stage.

METHOD OF INITIAL ALIGNMENT

Figure 2 shows an expanded sectional view of

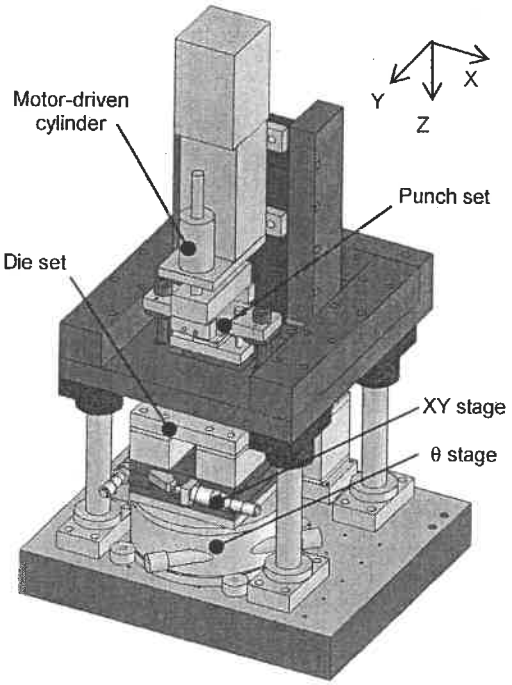

Figure 1: Small punch press on a trial basis.

the tool image acquisition system for the alignment of the shearing tool position before the shearing process. The tool images are respectively obtained in the punch side and die side, as shown in Fig. 3. The center coordinates of the tools are measured by executing an image processing technique using commercially available software. Next, the position of the die is fine-tuned using the measurement results and using the XY stage as stated above. The position of the die is determined through sequential comparison with the measurement results. It should be noted that this image acquisition and processing method can measure the center position of a circle with an accuracy of more than ± 1 μm according to previous tests.

METHOD OF MONITORING MISALIGNMENT

Lateral Force

A schematic diagram of the acting force on the tools in the initial stage of the shearing process, which is described in Maeda's paper [5], is shown in Fig. 4. Here, the acting force of the X component, that is, the lateral force F_X, is represented by

$$F_X = -F_d + \mu(P_d + H) \quad (1)$$

Consider the equilibrium of the Z component force and the moment about point P. They are obtained by

$$P_d - P_p + \mu(F_d - F_p) = 0 \quad (2)$$

$$-P_p x_p - P_d\{C(\theta) + x_d + \mu(t-s)\} + F_p y_p + F_d\{t - s + y_d - \mu C(\theta)\} - H\{x_{hd} - x_{hp} + \mu(t-2s)\} = 0 \quad (3)$$

Let $P_p = P_d = P$ and $F_p = F_d = F$, then the lateral force becomes

$$F_X = -\frac{x_{hd} - x_{hp} - \mu\{s + y_d + y_p - \mu C(\theta)\}}{t - s + y_d + y_p - \mu C(\theta)} H - \frac{(1+\mu^2)C(\theta) + x_d + x_p - \mu(y_d + y_p)}{t - s + y_d + y_p - \mu C(\theta)} P \quad (4)$$

Now, assume that a punch with external diameter D_p and a die with internal diameter D_d are used, with a gap distance ε and center angle ϕ. Then, the clearance $C(\theta)$ in angle θ is represented by

$$C(\theta) = \frac{1}{2}\{(D_d - D_p)^2 + 4\varepsilon^2 + 4(D_d - D_p)\varepsilon\cos(\theta - \phi)\}^{0.5} \quad (5)$$

Consequently, it is apparent that the summation of lateral force F_X from angle θ = 0 to 2π becomes zero at a distance of center position ε = 0. This is no different from the acting force of Y component, that is, lateral force F_Y. Therefore, it can be expected that a tool position misalignment caused during the process can be detected by monitoring the lateral force.

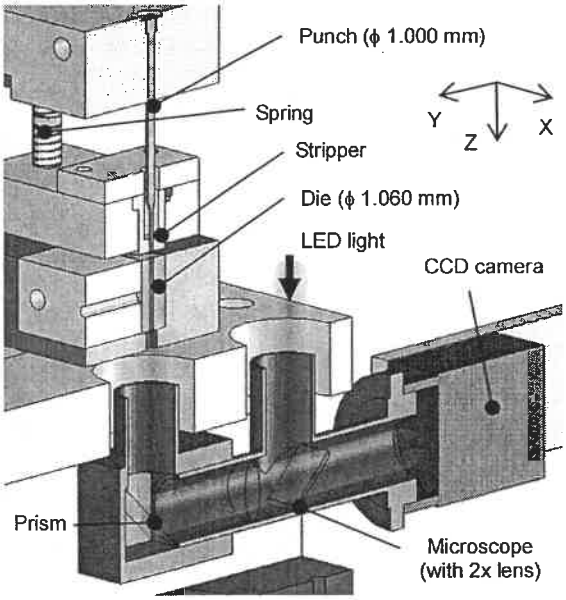

Figure 2: Expanded sectional view of tool image acquisition system

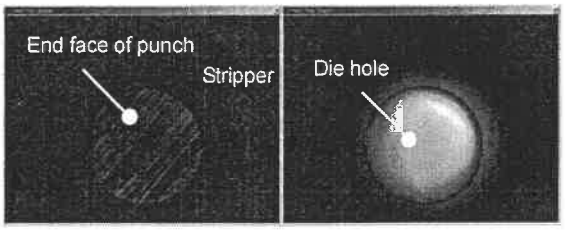

Figure 3: Obtained images: (Left) Punch side. (Right) Die side.

Machining Force Measurement Device

Figure 5 shows the device united with die set used to measure the machining force in the

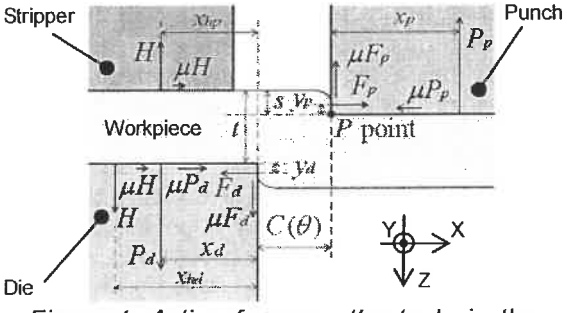

Figure 4: Acting force on the tools in the initial stage of the shearing process

shearing process. Commercially available force sensors that can measure three components (X, Y, Z) are arranged under the die and measure the shearing force and lateral force acting on the die.

In order to investigate the resolutions of this device, experiments involving applying and removing a load were repeatedly carried out for various loads and in each direction. As a result, it was confirmed that the resolutions of the X and Y directions are about 0.2 N, and the Z direction is about 0.5 N.

PUNCHING EXPERIMENT

Machining Condition

In order to confirm the effectiveness of the new method, the shearing processes were carried out under the following machining conditions.

Phosphor bronze (ISO CnSn6) with a thickness of 0.2 mm is selected as the workpiece. A commercially available punch and die made of powder high-speed steel were used as the shearing tools. The external diameter of the punch is 1.000 mm and the internal diameter of the die is 1.060 mm. The blank holding force of the stripper is set at 88 N to become about 20 % of maximum shearing force. The working speed is 1.00 mm/s, the processing temperature is RT and the feed and side bridges are secured at more than 5.0 mm so as not to have an affect on machining accuracy. Additionally, no lubrication was used in order to avoid fears that the punch could slip slightly due to the fluidity or surface tension of the lubrication.

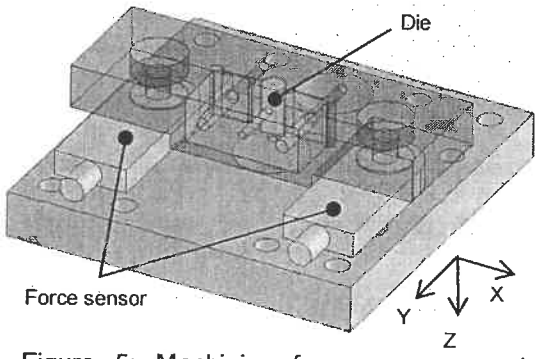

Figure 5: Machining force measurement device united with die set

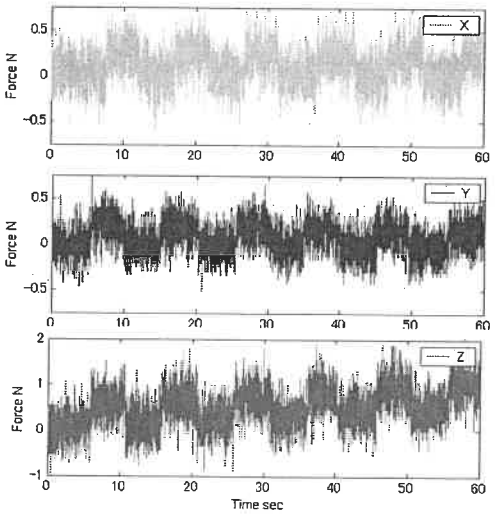

Figure 6: Resolution of each direction: (Top) X direction. (Middle) Y direction. (Bottom) Z direction.

Concerning the punch and die position alignment, the distance between the tool centers was set to be 0.4 μm in the X direction and 0.0 μm in the Y direction, using the initial alignment image processing method (Condition 1). After the several repetitions of punching in this condition, the die was moved 12.5 μm in the -X direction using the micrometer in the XY stage (Condition 2). Punching was then performed several times. Then, the die was moved another 12.5 μm in the -X direction (Condition 3), and several more punching repetitions were carried out. That is to say, expressed in clearance, the maximum clearance is 15.2 %t and the minimum one is 14.8 %t under Condition 1. In the same way, 21.05 %t is the maximum and 8.95 %t is the minimum under Condition 2, and 28.3 %t is the maximum and 2.7 %t is the minimum under Condition 3.

Experimental Results

The machining force measurement results in each direction are shown in Fig. 7. The reason the lateral force in the X and Y directions are not zero is assumed to be due to imperfect alignment, machining and assembling accuracy or elastic deformation of the small punch press.

When attention is focused on the lateral force in the X direction, it is evident that there are differences between Conditions 1 and 2 after about 0.08 seconds. Moreover, in Conditions 2 and 3, the difference becomes clear after about 0.12 seconds. On the other hand, there is almost no recognizable distinct difference in the lateral force in the Y direction and the shearing force (Z direction). Consequently, it is judged that it is possible to detect a tool position misalignment generated during the process to a satisfactory degree.

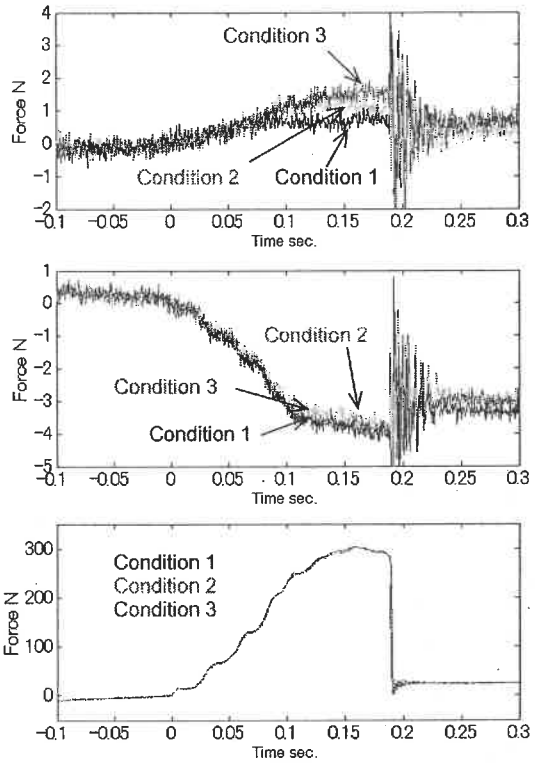

Figure 7: Machining force measurement results: (Top) Lateral force of X direction. (Middle) Lateral force of Y direction. (Bottom) Shearing force (Z direction)

SEM images of the shape of the shearing plane under Conditions 1 and 3 are shown in Fig. 8. In the top figure, it can be seen that a proportion of the shearing surface and fracture surface are distributed evenly along the outline in Condition 1. On the contrary, in the bottom figure (Condition 3), it can be seen that the proportion of the shearing surface increases from right to left and the machining accuracy isn't even in the same product.

As a whole, it can be said that monitoring the machining force is an effective method for detecting the misalignment of the tool that occurs during the process and is an important technique for maintaining machining accuracy.

CONCLUSIONS

This paper proposed a method for detecting a tool misalignment that occurs during the manufacturing process. A small punch press on a trial basis was created with two tool alignment methods, one to align the tools in advance and one to monitor the alignment in process. Actual punching of circular holes was carried under several conditions, and the effectiveness and

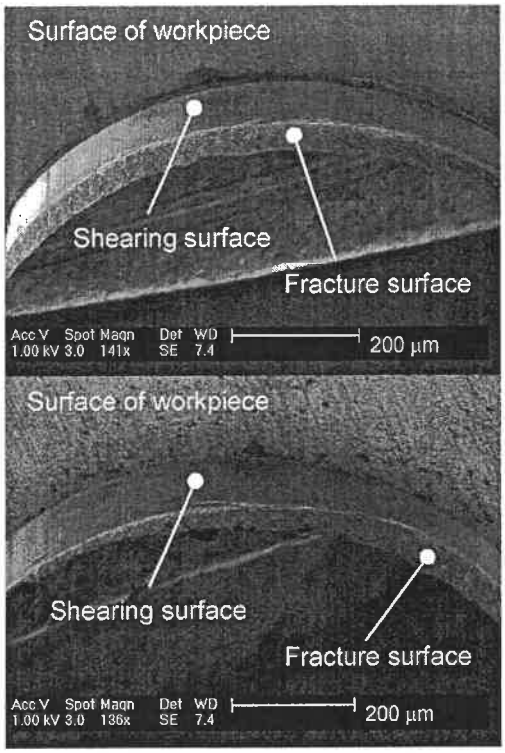

Figure 8: Shape of shearing plane: (Top) Condition 1. (Bottom) Condition 3.

importance of the proposed method were verified.

ACKNOWLEDGMENTS

This research was partially supported by the Ministry of Education, Science, Sports and Culture, Grant-in-Aid for Scientific Research (C), 17560103.

REFERENCES

1. I Aoki, 1991, Clearance setting of a blanking tool using static capacitance, *Proceedings of the Japanese Joint Conference for the Technology of Plasticity*, 42-2: 583-586. (in Japanese)
2. M Fujino, M Yamamoto and M Takahisa, 1989, Micro blanking system using wire electric discharge grinding (WEDG) method, *Symposium on Technology of Plasticity*, 122: 9-16. (in Japanese)
3. Y Okada, Y Kibe and K Mitsui, 2004, Measurement of Clearance in Micro Punch Press using Image Processing Techniques, *The 5th Manicuring & Machine Tool Conference*, 57-58. (in Japanese)
4. Y Okada, S Yoshida, K Mitsui, 2004, Optimum Clearance for Shearing Work of Sheet Metals, *Proceeding of ASPE 2004 Annual Meeting*, 418-421.
5. T Maeda and S Mekaru, 1977, Double-Side Shearing by Using Punched with High Slenderness Ratio, *Journal of JSTP*, 18-196:329-336. (in Japanese)

PRECISION MEASUREMENT OF SMALL DIAMETER HOLE IN A METALLIC OBJECT

Neville K. S. Lee, Jacky K. H. Chow, Albert C.K. Chan
Roy L.S. Chan, Angie W.C. Chau and Isabel W.Y. Chow
Industrial Engineering and Logistics Management, Hong Kong University of Science and Technology, Hong Kong

INTRODUCTION

There are a number of industrial applications such as in the aerospace and disk drive industries, which require precision measurement of small diameter holes with high aspect ratio. Some of the standard measurement systems, such as optical techniques, while capable of characterizing holes on the surface of the work piece, would face difficulties in characterizing the interior of a hole especially if the latter is a non-through hole. A novel vibroscanning method has demonstrated the possibility measurement of a 125um micro hole with level of precision better than 0.5um [1,2]. However, this technique requires a special probe, which is not widely available. Because of this, CMM using mechanical probe is still commonly used in industry. However, using CMM for small hole measurement has certain drawbacks. It is expensive, time consuming, and is a contact measuring technique. Also it is difficult to use CMM for the measurement of very small diameter holes. Therefore it is desirable to develop an alternative, more widely available cost effective precision approach.

Capacitance sensor may be a good solution as it is cost effective, widely available, and has been used for measurement of fastening holes for the aerospace industry [3]. It is the objective of this paper to refine this technique for the measurement of small diameter high aspect ratio holes. It is also the objective of this paper to see the level of precision of measurement which can be achieved using the capacitance sensor.

There is a challenging issue facing the capacitance measurement system for a small diameter hole with high aspect ratio. As the hole is small and deep, it is not practical to make the capacitance sensor much smaller than the diameter of the hole. As a result, the capacitance sensor inside the hole has the tendency to pick up signals from various regions of the hole. Therefore, an efficient way of deciphering the integrated capacitance signal for the profile of the hole is necessary. Different types of capacitance sensors have been designed, and the test results have been compared. These test results have also been compared with CMM measurement. Our preliminary result shows that the level of precision of 0.1um can be achieved by this technique. This level of resolution is more than an order of magnitude better than the small measurement technique using CMM. It is also more than an order of magnitude of improvement over the previous recorded result [3].

CAPACITIVE SENSING METHOD

In order to determine the physical geometry of a conductive work piece, the capacitance between a sensor probe and the work piece can be applied and correlated to its dimensions.. Simply speaking, for an ideal two plate capacitor, the capacitance depends on the size and shape of electrodes, distance between the two electrodes and the dielectric medium between them. If the size and shape of electrodes and the dielectric medium can be kept constant, distance variation between the probe and work piece can be interpreted.

The principle of capacitive sensing method for a small hole measurement is just applying the same concept to determine the small hole diameter from the capacitance between a cylindrical sensor probe and a small hole. In theory, the capacitance between a hole and a centering cylinder is given by

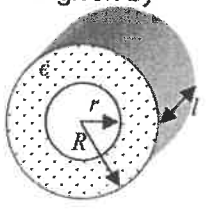

Figure 1. Coaxial cylinders.

$$C = \frac{2\pi\varepsilon l}{\ln(R/r)} \qquad (1)$$

Taking a 2.8mm hole with a 2.4mm sensor probe as an example, the capacitance versus hole sensor probe is plotted in *Figure 2*.

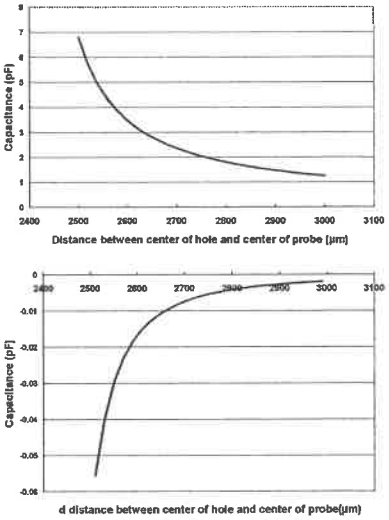
Capacitance (pF)
Distance between center of hole and center of probe (μm)
Capacitance (pF)
d distance between center of hole and center of probe(μm)

Figure 2. (Top) Capacitance signal distribution inside a hole for different hole diameters. (Bottom) Sensitivity of capacitance change with hole diameter.

Comparing the capacitance signal with the sensitivity of the capacitance change, the capacitive method in measuring hole diameter is feasible and a 6pF range with 16 bit resolution capacitance meter (less than 1fF resolution), which is common and easily found in the market (like Lion Precision and HP), can be used for this purpose. In this research, a simple, self-developed and low cost capacitance to voltage meter was used and a good performance was still achieved.

There are quite a few advantages in selecting the whole center capacitance for calculating the diameter. First, it is easy to find. Only one measuring point is needed during measurement. Fast throughput of the machine can be reached. Second, the capacitance change within the center region is quite flat (*Figure 3*). This implies that a simple alignment mechanism is good enough for the probe alignment. In a more robust case, for an eccentric cylinder configuration, the formula of capacitance can be determined as

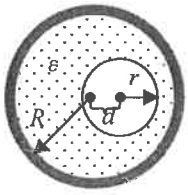

Figure 3. Eccentric cylinders of the same length l.

$$C = \frac{2\pi\varepsilon l}{Cosh^{-1}\left(\frac{R^2 + r^2 - d^2}{2Rr}\right)} \qquad (2)$$

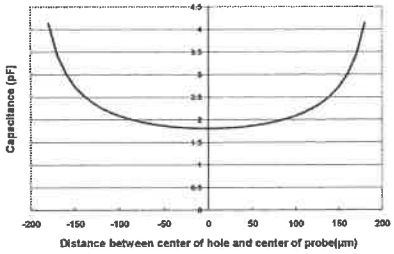

Figure 4. Capacitance signal distribution inside hole for a different probe location.

In this paper, the diameter of hole is calculated from the centered probe capacitance signal which is the minimum capacitance location between the probe and a hole. No matter how large or small the hole, there must be a minimum capacitance location. Thus, a universal reference between a hole and the probe can be found and the complexity of equipment setup can be simplified.

PROTOTYPE EQUIPMENT

To prove the practical applicability of this method, prototype equipment was built and actual measurements were carried out. The whole system architecture is as follows:

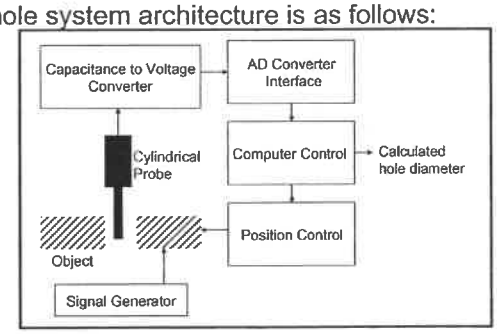

Figure 5. System Flow of the prototype equipment.

There is a basement for mounting all the equipment on it. This mounting bed is used for mounting the sample and the capacitive probe in position for the experiment. The hole sample is mounted in the X & Y direction stage which is controlled by two computer-controlled actuators for the centering of the probe. The cylindrical capacitive probe is mounted on the L stage for hole insertion. In the experiment, when the sensor probe is inserted to the hole, the computer controlled x, y stage will search the minimum capacitance position automatically. Within 10 seconds (depends on the speed of the actuator), the minimal capacitance was recorded

by the computer. Figure X shows the experimental set-up.

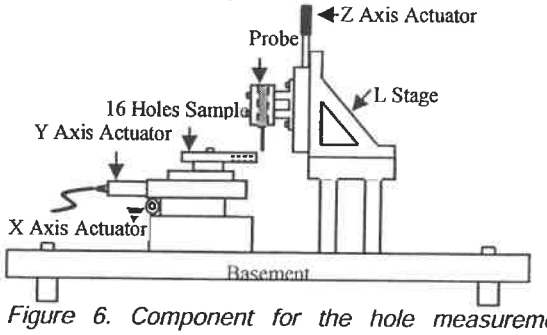

Figure 6. Component for the hole measurement systems setup.

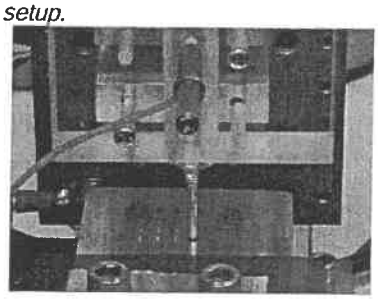

Figure 7. Sensor Probe is inserted into the hole of the sample.

EXPERIMENTAL RESULTS

In the first preliminary experiment, a 16-hole sample was used for calibration and measurement. The holes was drilled by CNC machine and the size of holes start from 2.6mm to 2.9mm with 20um difference each.

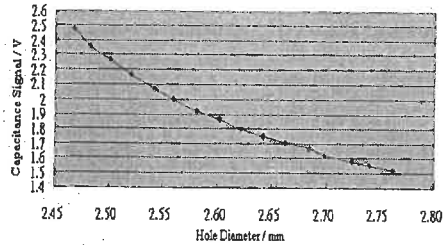

Figure 8. Experimental result for the capacitance to hole diameter.

From the experiment, a clear relation between the capacitance and hole diameter was found. From the *Figure 8*, the sensitivity of hole diameter (delta Capacitance / delta hole diameter) is equal to 0.028pF/um. With reference to our capacitance measuring equipment, less than 1fF resolution of capacitance can be detected. This implies that a less than 0.03um resolution of hole diameter can be achieved through this system configuration.

However, in practical situations, there is a difficulty to reach this high resolution for a rod sensor probe. When the probe is inserted into the hole, the capacitance is accumulated due to the increase in sensing area. The capacitance change is not as flat as the change in horizontal movement. From *Figure 9*, the capacitance between probe and hole keeps increasing when the probe is entering the hole (~1000fF/micron). As a result, if the height alignment of the sensor probe is not repeatable, there will be a large deviation of the measurement in hole diameter.

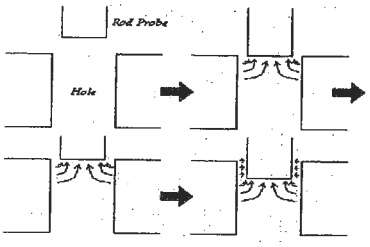

Figure 9. Rod probe is inserted into a hole.

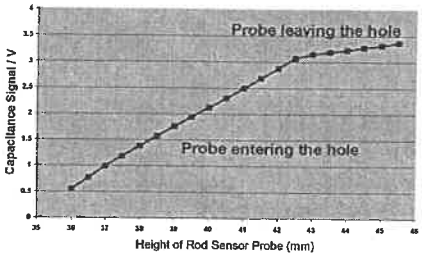

Figure 10. Rod probe signal with different height level.

On the other hand, rod probe can only be used to measure the average hole diameter of upper hole or the whole through-hole. The measurement of hole diameter at different heights level cannot be measured. Due to this reason, a disk probe (*Figure 11*) was developed for improvement.

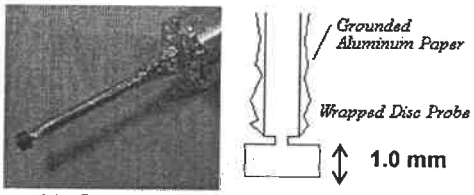

Figure 11. Design of a disk shaped ground shielded probe.

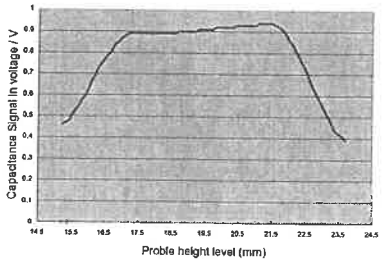

Figure 12. Effect of capacitance change for disk probe with different probe Z level.

By using the disk probe configuration, the error due to Z axis alignment is reduced by 60 times. Although the signal strength of the probe is reduced by 5 times (<0.15um resolution), the reduction in Z alignment error can compensate the loss.

TABLE 1. Effect of capacitance change for rod and disk probe with different probe Z level.

Probe	Cylindrical	Shielded Disk
Sensitivity Z level	1000 fF/um	16 fF/um
Error in diameter	0.035um/um	0.008um/um

With the help of the ground shielding disk probe, the high resolution of diameter measurement can be easily achieved by low resolution and cheap Z axis actuator. The hole diameter in different high levels can also be measured. Even for holes with 2 or more arms like *Figure 13.*

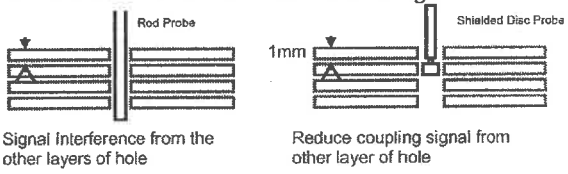
Rod Probe
1mm
Shielded Disc Probe
Signal Interference from the other layers of hole
Reduce coupling signal from other layer of hole

Figure 13. Effect of capacitance change for rod and disk probe with different probe Z level.

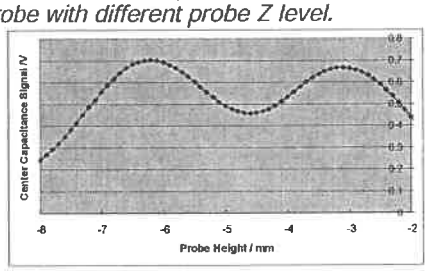

Figure 14. Effect of capacitance change for two holes in different Z level.

Within the +/- 200 um in the peak capacitance value, the slope of capacitance is limited to +/- 0.1 pF/mm (0.1fF/um). In comparing with the sensitivity of disk probe, 2fF/um, the error caused by Z level is acceptable.

CONCLUSIONS

Capacitive sensing method proved an opportunity for the industry to use low cost equipment to achieve a considerably high resolution performance. For some hole measurement applications, the circularity and the profile of a hole may not be interesting. Capacitive sensing method would be a sensible choice. In practice, cost is always in a consideration. In capacitive measuring systems, probe and circuit board are easily acquired a low prices (less than US$1,000 for a probe and circuit) by mass production.

Two types of probe are shown in this extended abstract, the rod probe and disc probe. Generally speaking, A disc probe is much better than a rod probe as the measurement results have fewer errors caused by misalignment of probe height. However, both probe designs can perform their best by being applied in different situations. Rod probe is best used to measure very small, thin through holes (low aspect ratio) with thicknesses of 1 – 2 mm. The probe can be inserted through the hole. The entire signal received by the probe comes from the thin hole. The effect of the depth of the probe position is reduced. The disk probe can be used to measure hole diameters at different height. Moreover, for a series of holes like a disk drive actuator, the disc probe performs well.

In comparing with the cycle time for measuring a hole, capacitance probe measurement measures much faster in compared with the traditional CMM probing. Using CMM requires quite a number of sample points so as to determine the average diameter of a hole. It takes at least one or a few minutes to find out the result. By using capacitance method, only the time for center searching is needed. As proved in the previous paragraph, the position of centering does not need to be accurate and line scanning would be even possible.

ACKNOWLEGEMENTS

The work described in this paper was supported by a grant from the Research Grants Council of the Hong Kong Special Administrative Region, China (Project No. HKUST6001/06E)

REFERENCES

1. Masuzawa T., Hamasaki Y and Fujino M, 1993, Vibroscanning method for nondestructive measurement of mall holes, Annals CIRP 42: 589-92.
2. Kim B., Masuzawa T., Bourouina T, 1999, The vibroscanning method for the measurement of micro-hole profiles, Meas. Sci. Technol. Vol 10: 697-705.
3. Hammond, J L, J R; Glidewell, S R, 1983, Design of algorithms to extract data from capacitance sensors to measure fastener hole profiles, IEEE Transactions on Instrumentation and Measurement (0018-9456). Vol. IM-32: 343-349.

HIGH PRECISION MODULAR LONG RANGE TRAVEL VERTICAL AXIS

Markus Lotz[1], Tobias Hackel[2], Thomas Frank[2], Anita Tröbs[3]
Günter Höhne[1], René Theska[2], Klaus Zimmermann[3]
[1]Department of Engineering Design
[2]Department of Precision Engineering
[3]Department of Engineering Mechanics
Technical University Ilmenau, Ilmenau, Germany

INTRODUCTION

High precision positioning and measuring machines have to face the demand for large moving and measuring range while realizing nanometer accuracy. Most setups of three dimensional high precision systems use fixed laser interferometers and a moving mirror stage because three dimensional applications need both horizontal and vertical motions with a high positioning resolution of the mirror which carries the object [1]. The masses of both elements have to be moved over a long travel range and hold in every position. Thus especially the objective of vertical positioning is challenging. Most state of the art high precision positioning and measuring machines have only a small vertical measuring and moving range of few millimeters or less [1, 2, 3]. But there is an increasing demand for such machines in optical industries to measure aspheric or freeform lenses and mirror shapes with a much larger moving range in vertical direction e.g. of 15 mm up to 25 mm would be appreciated [4].

This research is focused on the development of a positioning and measuring machine with a moving range of 200 x 200 x 25 mm³ [5]. Therefore a high precision vertical axis has to be designed. High precision guides and drives are needed to fulfill requirements like high resolution, high stiffness and low friction. Unfortunately drives like voice coils are not self locking. Thus they need to actively hold the masses and induce unwanted heat into the system because of power loss. Self locking spindle drives do not have the needed resolution and piezo elements have a limited moving range. Guides also have great influence to the properties of the vertical axis. Known ball guides are stiff but they are a source of stick-slip effects. Aerostatic guides are free of stick-slip but can cause vibrations and induce unwanted air flow. Flexure guides seem to be favorable but their moving range is limited. For these reasons a systematic analysis of different combinations of drives and guides is necessary. Thus the design of the vertical axis should be modular to have the opportunity to build, test and compare different setups. The aim of the research is to find an optimal overall design and combination of elements. The systematic design, virtual prototyping and realization of a modular long range travel high precision vertical axis will be presented in this paper.

DESIGN CONCEPT

The overall machine concept is a parallel kinematic design. That means the vertical axis is planar guided on a base and the horizontal axes are used only to reduce the rotational degrees of freedom (Figure 1). Design principles of short and direct force flow and symmetric design are respected. The coupling between the vertical and the horizontal axes is realized well constraint.

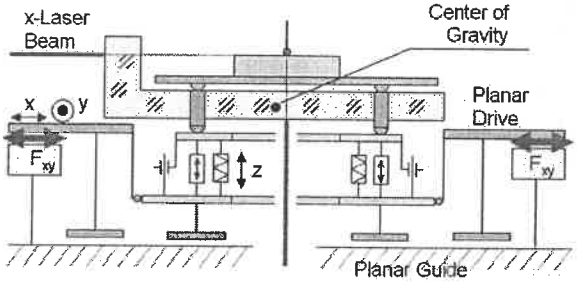

FIGURE 1: Principle design of the positioning and measuring machine.

The vertical axis itself is designed modularly. Three drives and guides are arranged symmetrically around the cumulative center of gravity. All guides stay in contact to the base through planar guides e.g. flat air bearings. The arrangement of guides and drives is serial in a short and direct force flow. Only push and pull forces arise except of lateral forces through horizontal motions.

MODULES

The vertical axis incorporates a modular design to test several different setups. This means it is

possible to apply different drives as well as different guides (Table 1).

TABLE 1: Function elements which can be combined to different setups (s – moving range, Δs – theoretical resolution).

Guide		Drive	
Ball	s > 25 mm	Spindle with Piezo	s > 25 mm Δs < 1 nm
Aerostatic	s > 25 mm	Voice Coil	s = 16 mm Δs < 1 nm
Flexure	s = 15 mm	Spindle with Voice Coil	s > 25 mm Δs < 1 nm

The used drives and guides are commercially available except of the flexure guide. For the use of voice coil actuators additional weight compensation elements are needed (not shown here). The research is focused on the development of an optimal overall design, test and comparison of different combination of elements.

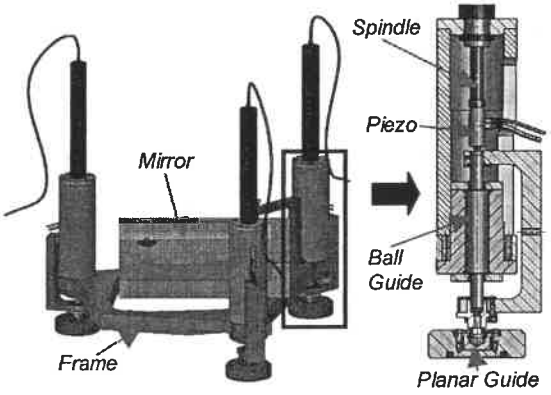

FIGURE 2: CAD model of the vertical axis with spindle and piezo drives (left) and section view of one drive unit (right).

The first combination consists of ball guides and a serial alignment of spindle and piezo drives. In Figure 2 the overall design of the vertical axis in this combination is shown. The section view shows one drive unit consisting of drive and guide. Spindle and piezo drive are collinear aligned. Through this arrangement both elements can be driven separately and work in a hybrid system. Thus a moving range of 25 mm with a theoretical positioning resolution of 1 nm can be covered. Figure 3 shows the assembled vertical axis in the described setup with a measuring mirror applied. This test device is the base for the following steps.

MODELLING AND SIMULATION

Methods of virtual prototyping are used to simulate the behavior of the vertical axis to optimize its design. The simulation of the multi-body system (MBS) is necessary to find limitations of the dynamics. Therefore an MBS of the vertical axis in its first setup was developed [6]. To get a realistic MBS the following components have to be considered and built as accurate as possible: the ball guides, the frame and the ball-V-groove coupling between mirror and frame.

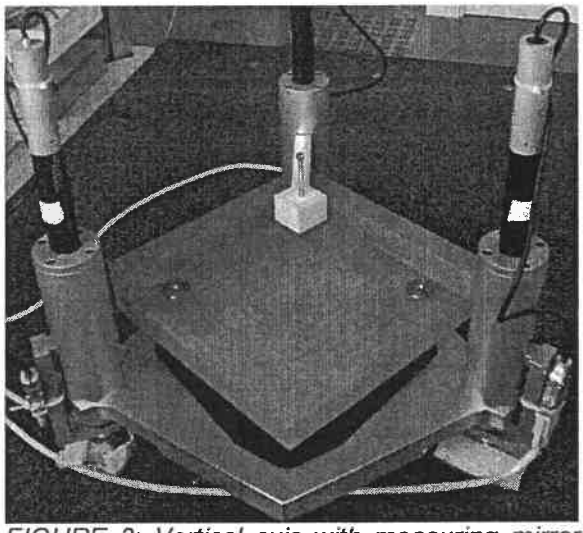

FIGURE 3: Vertical axis with measuring mirror applied.

For example the ball guides were separately modeled by two stiff bodies. These bodies are linked by elastic properties between the counter-acting cylinder / balls and between the balls / ball lining. These properties are calculated by the theory of Hertz: contact of curved areas under load. Depending from the number of balls in the guide the model is made of several radial ball bearings which are linked together. The model of one single bearing is shown in Figure 4.

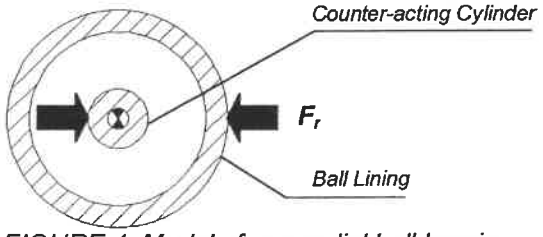

FIGURE 4: Model of one radial ball bearing.

The force F_r which acts radial is depending on the deformation between the counter-acting cylinder and the ball lining [6]. Based on this model Coulomb friction force is integrated. The normal force is calculated from the addition of the radial forces.

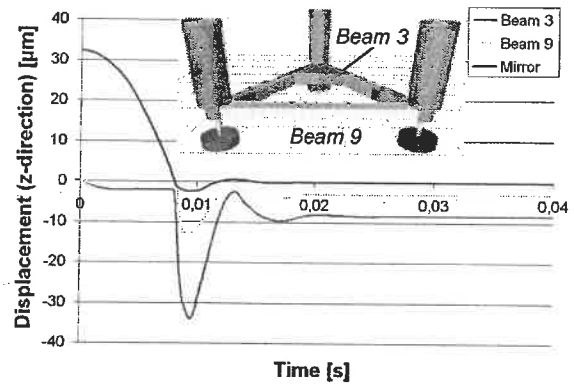

FIGURE 5: Bending of the frame vs. time in comparison to the mirror movement.

Another important element is the frame which holds the mirror. It has a bending deformation of a few µm (calculated by FEA). Thus it is modeled by a series of yield structures namely joint beams, each with five degrees of freedom. Figure 5 shows the model of the frame (top) and the simulated bending of the frame elements. In this function test of the MBS the frame is fixed and the mirror edge drops on it into the three ball-V-groove couplings (black curve). The other curves show the resulting bending of two different points on the frame. The weight of the frame itself (without the mirror) results also in a bending. When the mirror gets down to the frame a overshooting can be seen. After 20 msec the steady state is reached.

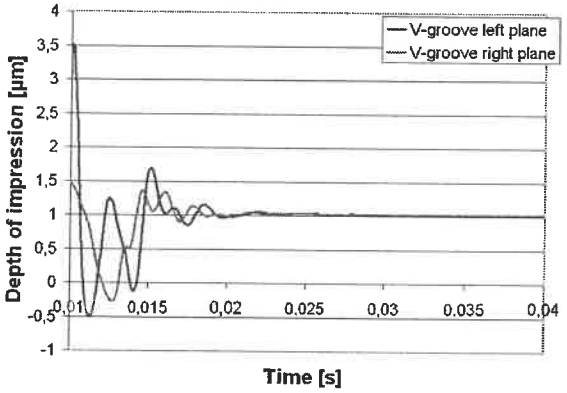

FIGURE 6: Depth of impression from the ball in the V-groove vs. time.

The couplings between mirror and frame show deformations too. Also in the second function test of the MBS the mirror drops to the frame. As a result the ball has an asymmetric position in the V-groove (Figure 6). After 20 msec (steady state) the ball enters symmetrically between the planes of the V-groove. This behavior goes back to the design especially of the orientation of the V-grooves. Through these different tests the MBS was checked and shows its function. In the next step the control will be integrated in the model to simulate the dynamic behavior. The results will be used to develop a model based control of the vertical axis.

CONTROL AND EXPERIMENTAL RESULTS

For performance testing of the axis a complete experimental setup inclusive power supply and control system was built.

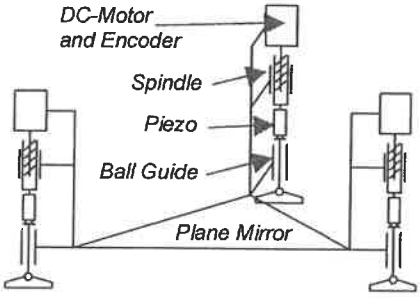

FIGURE 7: Principle design of the vertical axis.

Figure 7 shows the principle design of the vertical axis. Each drive unit consists of a coarse motion spindle drive, a fine motion piezo element and a ball guide. The three drive units move the plane mirror whose position and angle is measured by laser interferometers.

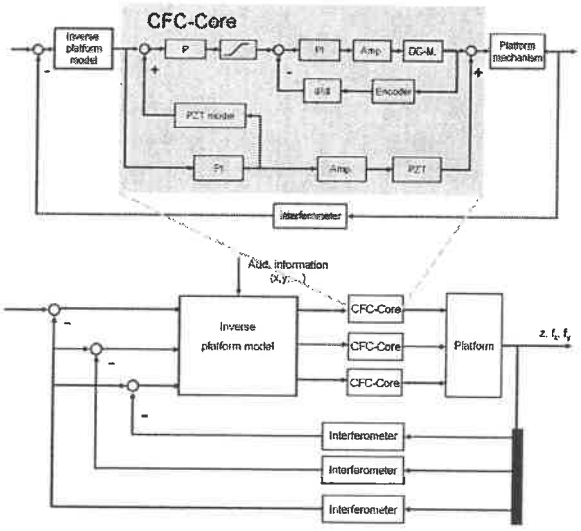

FIGURE 8: Control scheme for one drive unit and general control of vertical axis.

Figure 8 (above) shows the design of the control of one drive unit. The spindle drive is able to realize long range movements with lower dy-

namics. The piezo element realizes the short range movements below the position resolution of the spindle drive with high dynamics and accuracy. As output the sum of both movements will take effect. The positioning task is split up to the actuators by adding the piezo stroke to the control deviation of the spindle drive. The big differences in dynamics of the actuators avoid vibration. The integral element in the controller deals with non predictable stick-slip effects in the spindle drive. With the inverse platform model the position dependent difference between measuring and driving point is considered. Figure 8 (below) shows the arrangement of three drive units and three measuring tools. The idea is to reach the specified target value on this interferometer that is aligned with Abbe's point. The other measuring values are used in addition to detect and adjust the platforms angle deviation.

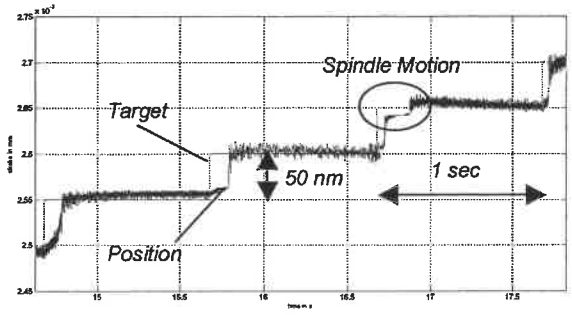

FIGURE 9: Positioning of the mirror in vertical direction in steps of 50 nm over time.

Figure 9 shows a promising plot of the device behavior following a ramp of quantized 50 nm steps each second working with a first setup of the control parameters. The white noise is around 10 nm and predominantly caused by the used measuring device (unstabilized two beam laser interferometer). The vertical axis can follow the given target position. If the moving range of the piezo drive is reached a step is performed by the spindle drive which can be seen on the diagram. Further improvement will be reached by optimizing the control parameters and using a measuring system with higher resolution. Also climate control and vibration damping of base frame will improve the behavior.

CONCLUSIONS AND FURTHER WORK

The work described here showed that the designed modular long range vertical axis can be used for high precision positioning. It also showed that a MBS-model of such device is complex but useful to examine the dynamic behavior. The measurement results of the first setup showed a good behavior of the guides as well as the drives. It was possible to reach a positioning resolution in the nanometer range with a special arrangement of different commercial components. The positioning resolution and accuracy of the test device is not limited by the mechanical components. Nevertheless there are a lot of different points which have to be solved in the future. The existing MBS-model, the control and the environmental conditions need to be further improved. After this the next steps will be the realization of other combinations (consisting of voice coils, aerostatic guides, weight compensation mechanisms and spring guides). Then the different designs can be compared to make states about the dynamic behavior and which combination is preferable.

ACKNOWLEGEMENTS

The authors would like to thank the members of the Collaborative Research Centre 622 "Nanomeasuring and Nanopositioning Machines" and the German Research Foundation (DFG) for their support.

REFERENCES

1. G. Jäger et al., 2002, Operation and Analysis of a Nanopositioning and Nanomeasuring Machine, *Proceedings of 17th ASPE Annual Meeting*
2. Ruijl, T., 2002, Ultra Precision CMM: Design, Calibration and Error Compensation, *Ponsen & Looijen, 2002*
3. Kramar, J. et al., 2005, Nanometre resolution metrology with the Molecular Measuring Machine, *Institute of Physics Publishing, Measurement Science and Technology Volume 16, Number 11, November 2005*
4. Beckstette K.-G. et al., 2006, Aspheres & Freeform Manufacturing, *Optonet Workshop 05/2006*
5. Theska, R. et al., 2004, Design Principles for Highest Precision Applications, *Proceedings of 19th ASPE Annual Meeting*
6. Gerlach, E. et al., 2004, Computergestützte Simulation der Dynamik einer Nanopositionier- und Nanomessmaschine (NPM-Maschine), *12. GMA/ITG Fachtagung. Sensoren und Messsysteme 2004, Ludwigsburg, 15.-16.3.2004, VDI-Bericht 1829*

DEVELOPMENT OF A DESIGN TOOL SUPPORTING CONCEPTUAL DESIGN OF MACHINE TOOLS

N. Mishima
Advanced Manufacturing Research Institute
National Institute of Advanced Industrial Science and Technology
Tsukuba, Ibaraki, JAPAN

INTRODUCTION

Since processes of machine tool design are rather experience basis, design procedures from conceptual design through detailed design often take long time. At the same time, the variety of target products of machine tools is growing larger and larger. Conceptual design is said to be very important to create appropriate designs and to shorten the time-to-market of products.

The series of the research [1]-[3] including this paper has been trying to develop a new design tool to support decision making at the conceptual design of machine tools. The design tool which has been proposed by the author combines the form-shaping theory [4] of and the Taguchi method [5]. It was effective in selecting generic size and structure of machine tools, or determining critical design parameters and error factors for its performance. However, since the original form-shaping theory assumes that the structural components of the machine tool are rigid, it couldn't consider deformation of the machine tool structures such as deformations caused by machine weight or thermal deformations. As the result, the values of the error factors used in the calculation were not very accurate and the accuracy of the prediction wasn't enough. This paper combines the proposed design tool with FEM analysis to determine the amount of error factors. The FEM tool is used to calculate structural deformations of machine tool structures. The proposed design tool offers a simplified method to consider not only component errors but also structural deformations, combining proposed design tool with FEM analysis. By this extension, the tool can support systematic design of machine tools.

DESIGN EVALUATION METHOD

A machine tool structure can be thought of as a chain of directly linked rigid components extending from the product through the cutting tool. An orthogonal coordinate system corresponding to each element is defined. The transformation between two local coordinate systems is represented by a coordinate transformation. Form-shaping theory represents these respective coordinate transformations by homogeneous transformation matrices (HTM) [6]. In an ordinary machine tool, HTM is represented by a parallel transition along the X, Y or Z axes or rotation around the axes. Each of these six coordinate transformations is assigned a distinguishing number, such as transformation along the X-axis being 1, and so on. By writing the HTM of ith element as A_i, vector represents the relative displacement between the product and the cutting tool, is given by equation (1). The equation is the definition of the form-shaping function that expresses the cutting motions of the machine tool. Actual machine tools have imperfect alignment, and experience thermal deformation, wear, and many other sources of error. In order to describe actual cutting motions, one must take these errors into account. Such errors can for convenience's sake be treated as errors in transformations between elements. Another homogeneous transformation matrices $A\varepsilon_i$ to generally represent transformation error between elements are defined. (Equation 2) By inserting the error component matrix $A\varepsilon_i$ between A_i and A_{i+1} in equation (1), the form-shaping function including errors, is written as equation (3). The form-shaping error function expressing the error as a quantitative deviation from the target value, is defined as the difference between the form-shaping function with and without errors, as equation (4). By analyzing the equation, it is possible to evaluate how each design parameter and error factor affects the overall performance.

$$\vec{r}_0 = A_1 A_2 \cdots A_i A_{i+1} \cdots A_n \times \vec{r}_t \tag{1}$$

$$A_{\varepsilon i} = \begin{bmatrix} 1 & -\gamma_i & \beta_i & \delta_{xi} \\ \gamma_i & 1 & -\alpha_i & \delta_{yi} \\ -\beta_i & \alpha_i & 1 & \delta_{zi} \\ 0 & 0 & 0 & 1 \end{bmatrix} \tag{2}$$

$$\vec{r}_{\varepsilon 0} = A_1 A_{\varepsilon 1} A_2 \cdots A_i A_{\varepsilon i} A_{i+1} \cdots A_n \times \vec{r}_t \quad (3)$$

$$\Delta\vec{r}_0 = \vec{r}_{\varepsilon 0} - \vec{r}_0 \quad (4)$$

$\vec{r}_0$: from-shaping function, $\vec{r}_t$: tool shape vector, $\vec{r}_{\varepsilon 0}$: form-shaping function with errors, $\Delta\vec{r}_0$: from-shaping error function

LISTING OF DESIGN OPTIONS

In creating a new design concept, there are many possible structures that have different sequences of motion axes. The issue is how to apply the proposed design evaluation method to create a design concept for a machine tool. Performances of several designs can be compared by introducing some assumptions into the Taguchi method. By assuming that every design concept has the same control factors, noise factors and their ranges of variation, the results calculated by the Taguchi method are expected to show the rank order of the designs directly. By the calculation result, a machine tool designer can determine the best design concepts for machine tools from several listed designs. It is common to represent transitional motions along the X, Y and Z axes as 1, 2 and 3, and rotational motions around the X, Y and Z axes as 4, 5 and 6. Using this convention, milling machines that have three transitional motions and one spindle rotation can be categorized into 4 major structural types. Those 4 are shown in Fig.1 (a)–(d). A significant question is which of the four commonest types has the best theoretical performance. To isolate the effect of machine tool structure, common design parameters and noise factors were defined. Tables 1 and 2 show the defined noise and control factors.

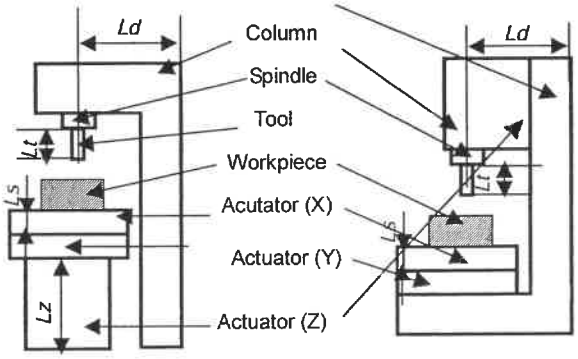

(a) Type 12306 (b) Type 12036

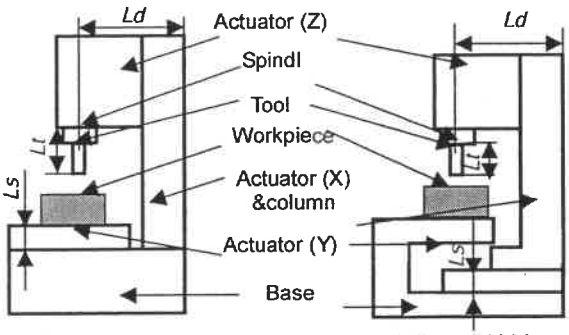

(c) Type 20136 (d) Type 01236

FIGURE 1 Design options of milling machines

TABLE 1 Control factors

Factor name	Variable
Workpiece size	*Ws*
Bearing diameter	*Db*
Rotational speed	*N*
Tool length	*Lt*
Spindle - column distance	*Ld*
Thickness of the linear actuators	*Ls*

TABLE 2 Noise factors

Name of the factor	Variable
Rotational errors of the horizontal guide ways	$\alpha_1, \beta_1, \gamma_1$
Axial error of the horizontal guide ways	δ_{z1}
Straightness error of horizontal guide ways (H)	δ_{x1}
Straightness error of horizontal guide ways (V)	δ_{y1}
Rotational errors of the vertical guide way	$\alpha_3, \beta_3, \gamma_3$
Straightness error of the vertical guide way (H)	δ_{x3}
Straightness error of the vertical guide way (V)	δ_{y3}
Axial error of the vertical guide way	δ_{z3}
Rotational errors of the spindle	α_4
Eccentricity of the spindle	δ_{x4}
Expansion of the spindle	δ_{z4}

These factors were defined in four machine tool types to clarify the effect of machine tool structure. The six control factors, *Ws, Db, N, Lt, Ld* and *Ls* from Table 1 were considered to be independent control factors. Each form-shaping error function (for the design shown in Fig.1) can be expressed using the parameters defined in Tables 1 and 2. A designer needs to compare four form-shaping error function to evaluate the performance difference of the designs with the same control and noise factors.

CONSIDERATION OF STRUCTURAL DEFORMATIONS

Although the original form-shaping theory does not handle structural deformations, those have

significant effects on machine tool performance. Therefore, most CAE tools try to calculate the deformations. However, CAE tools are not very efficient in handling component errors such as straightness errors of slides, etc. Since they based on a modeling of macroscopic shape of the machine structure, it is difficult to simulate errors caused by meso/microscopic behaviors of components, such as repetitive deviation of ball slides caused by slight differences of ball diameter, and so on. Of course it can be possible, but focusing on meso/microscopic behaviors results enormous effort in simulating overall machine structure. And it is not a practical choice in design review of machine tools in its early design stage. Because of that, the paper proposed a method to combine form-shaping theory with calculation of structural deformation based on FEM. Considered structural deformations are categorized and shown below.

(1) Deformation caused by static force.
a) Deformation caused by machine weight
b) Deformation caused by cutting force
(2) Thermal deformation.
a) Thermal deformation of a tool caused by cutting heat.
b) Thermal deformation of a spindle caused by heat generation at the motor/bearing.

Not only the above-mentioned structural deformation, but also component errors such as eccentricity of bearings or straightness errors of slides should be considered. Component errors are also important for overall machine performance. As it was mentioned, to calculate component errors would not be easy. So, the paper assumed component errors by using guaranteed value in component catalogs. Sum total of the calculated structural deformation and component errors are equivalent to the geometric errors of the machine tool element that can be written generally by equation (2) in the previous section.

COMBINING WITH FEM

To combine the proposed design evaluation method to an existing FEM based analysis, it is necessary to calculate the deformation of each structural component by FEM. Deviation between the local coordinate system assigned to one end of the component, and the one assigned to the other end, can be expressed by equation (2) in the former section. The result of the calculation by FEM expresses each element of the homogeneous transformation matrix shown in the equation. For example, expansion of the component to Z axis is equal to δz shown in the matrix, and bending around the X axis is α, as well. The next figure shows deformation of a column of a milling machine. Of course, since the purpose of the design tool is to support conceptual design of a machine tool, the detailed structures of the components have not been determined yet, in this stage. However, it is possible to roughly estimate the deformation by deciding dimensions and the material. More detailed inner structures such as ribs, wall thickness, etc. can be determined by referring examples of existing machine tool structures in the database. The result shown in Fig.2 was used to calculate the overall positioning error between the cutting tool and the workpiece, which was defined by equation (4).

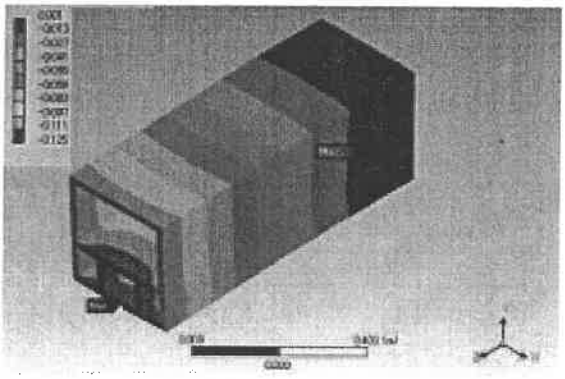

FIGURE 2 Deformation of a typical column of a milling machine

DESIGN SUGGESTIONS BASED ON THE CALCULATION RESULTS

The same ranges of noise factors and design parameters were estimated roughly, and substituted into the four form-shaping error functions of four machines shown in the previous section. Fig.3 shows comparisons of the theoretical performance. According to the figure, when the design parameters vary within some defined ranges, the lines marking the positioning error of type 12036 are always the lowest, and those of type 12306 are the highest. Among the 6 control factors defined in the Table 1, "*Ld*," which represents the spindle-column distance, is the most critical parameter affecting machine performance. The figure shows that type 12036 has better theoretical performance than types 12306 and 01236. Based on these results, type 12036 was selected as the "best" design for a milling machine from the 4 options shown in Fig.1.

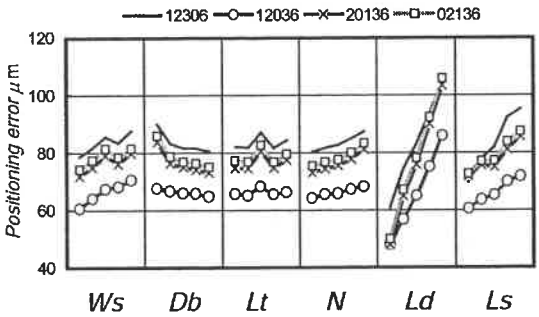

FIGURE 3 Comparison of performances

Next Fig.4 indicate influences of error factors on the overall error amount. To calculate the error contributions shown in the figure, noise factors defined in the Table 2 were changed accordingly to the assigned range of each factor. The each bar shows the difference of the overall error amount when the corresponding noise factors take the lowest and highest value.

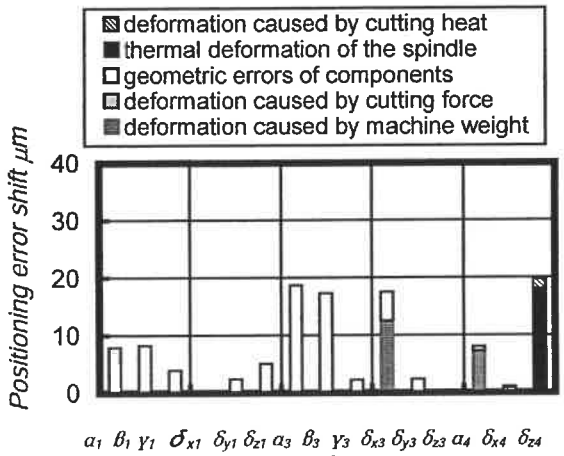
deformation caused by cutting heat
thermal deformation of the spindle
geometric errors of components
deformation caused by cutting force
deformation caused by machine weight
Positioning error shift μm
40
30
20
10
0
α1 β1 γ1 δx1 δy1 δz1 α3 β3 γ3 δx3 δy3 δz3 α4 δx4 δz4
FIGURE 4 Contributions of error sources

The information obtained by Fig.3 and 4 suggest us which design parameters should be designed carefully to obtain higher performance, and also clarify which components should have tighter tolerance to improve the machine performance. From Fig.3, following design suggestions concerning to the design parameters can be derived.

1) The most critical design parameters was the distance of the spindle from the vertical column.
2) The thickness of the slides (*Ls*) and the product size (*Ws*) had the next largest influence.
3) The diameter of the spindle (*Db*) and the rotational speed (*N*) have smaller impacts.
4) The length of the tool (*Lt*) has no evident influence on the machine performance.

From Fig.4, some design suggestions about the error factors are also possible.

1) Rotational errors of the vertical guide way (α_3, β_3, γ_3) have the largest influence on the performance of the standard machine tool.
2) Rotational errors of the horizontal guide ways (α_1, β_1, γ_1) have relatively large impacts.
3) Thermal expansion of the spindle (δ_{z4}) plays an important role. It has to be improved to obtain high accuracy.
4) Structural deformations caused by machine weight are not the primary error sources, but still have important effects.

CONCLUSIONS

The proposed design evaluation tool was effective in identifying the critical design parameters and error factors of a machine tool. By combining the tool with FEM analysis which can calculate structural deformation more precisely, it was possible to obtain guidelines for conceptual design of machine tools, without design experience and detailed calculation.
As the results of the design review, spindle-column distance had an important effect. As for error factors, geometric errors of components, especially rotational errors of vertical guides had significant influences on performances. Thermal expansion of the main spindle was also a critical error source. The results help us to determine which errors should be minimized or eliminated, in designing a precise machine tool.

REFERENCES

1. Mishima, N. and Ishii K., Robustness Evaluation of a Miniaturized Machine Tool, Proc. of ASME/DETC99, DETC/DAC-8579, Las Vegas, NV, Sept. 1999.
2. Mishima, N., Design evaluation method for miniature machine tools utilizing form-shaping theory, Proc. of ASME/DETC '02, DETC/DAC-48787, Chicago, IL, Sept. 2003.
3. Mishima, N., Derivation of design guidelines for miniature machine tools, Proc. of ASME/DETC '04, DETC/DAC-57091, Salt Lake City, UT, Sept. 2004.
4. Reshtov, D.N. and Portman, V.T., Accuracy of Machine Tools, ASME Press, New York, (1988).
5. Taguchi, G. and Konishi, S., Quality Engineering Series, ASI Press. (1994).
6. Paul, R.P., Robot Manipulators, THE MIT press, Cambridge (1981).

DESIGN OF AIR DRIVE SPINDLE

Yohichi Nakao[1], Tomohiro Mizoi[1] and Yuzo Minowa[2]
[1]Mechanical Engineering
Kanagawa University
Yokohama, Japan
[2]PENTAX Corporation, Tokyo, Japan

INTRODUCTION

A spindle of the ultra-precision machine tools, such as diamond turning/grinding machines, is an important component that determines the machining accuracy. Therefore, improvement of the spindle performance is a critical issue in designing the machine tools in order to accomplish further improvement of the machining accuracy. In addition, producing small and precise parts is another important requirement. Thus, a small spindle with improved performance is needed to meet the requirements in the precision machining.

In order to develop small in size and precise spindle, a spindle driven by water flow, named the water drive spindle, has been proposed and developed[1]-[3]. The performance of the water drive spindle has been evaluated in the theoretical and experimental studies.

The water drive spindle uses water flow for driving, supporting and cooling the spindle rotor. A small number of flow channels are specially designed inside the spindle rotor so that the water flow energy through the channels can be transformed into torque that makes the spindle rotational motion. This simple structure works as a motor, thus it is named the water drive motor. The water flow is used as the lubricant flow for the water hydrostatic bearings, as well. Water is the incompressible fluid as well as oil. In addition, the viscosity of water is smaller than that of oil, thus the water hydrostatic bearing is considered to be suitable for precision machine tools.

By the combination of the water drive motor and the water hydrostatic bearing, it is accomplish to design the small size and high performance spindle for the precision machining. In fact, the size of the water drive spindle is 22 mm in diameter and 112.5 mm in length. In addition, stiffness of the water drive spindle is 374 N/μm, as well.

The bearing stiffness and rotational accuracy are, in general, important concerns in designing the spindle for precision machine tools. In some applications, however, high speed spindle rotation becomes at the most important requirement, even bearing stiffness will degrade or the spindle size will be large. In this case, air pressure bearing is still the suitable choice for the spindle.

The present paper introduces a newly designed air drive spindle. The air drive spindle uses similar driving principle to the water drive spindle, for instance, it uses some flow channels to produce the torque to spin the rotor. However, a modification for integrating additional function to the spindle has been made so that the water/air drive spindle can rotate for both rotational directions. In the following sections, the structure and working principle of the air drive spindle are presented. A mathematical model for designing the air drive spindle is introduced, and the spindle performance is discussed through the simulation. Developed air drive spindle is evaluated through experimental studies.

AIR DRIVE SPINDLE

A basic structure of the air drive spindle is depicted in Fig. 1. The air drive spindle uses air flow for driving and supporting the spindle rotor. The spindle rotor is supported by air pressure bearings in the axial and radial directions. Since the designed air drive spindle is the prototype, the thrust air pressure bearings are located at both end surfaces of the spindle rotor for ease of the design and fabrication.

The air drive spindle is designed to be basically bilateral symmetry, except for exit channels as described later. As the water drive motor, the air drive motor is composed of a small number of flow channels inside the spindle rotor. The supplied air first enters the rotor through the channels, named the inlet channels, in the radial direction. The inlet channels are located between the outer rotor surfaces and the main channel that is formed at the center of the rotor in the

axial direction. The main channel is made so as to lead air flow to outside of the rotor through exit channels from the inlet channels. As shown in Figs. 1(b) and (c), the exit channels form bend-shaped channels. The direction of the air flow changes significantly in the exit channels. Consequently, the torque used to spin the rotor is generated by the large change in the angular momentum of the air flow.

The direction of the exit channels determines the direction of the produced torque. In order to produce torque in the opposite direction, another couple of the air drive motor structure is designed in the other side of the rotor, as shown in Fig. 1. Both air drive motor structures are the same except for the direction of the exit channels, as depicted in Figs. 1(b) and (c).

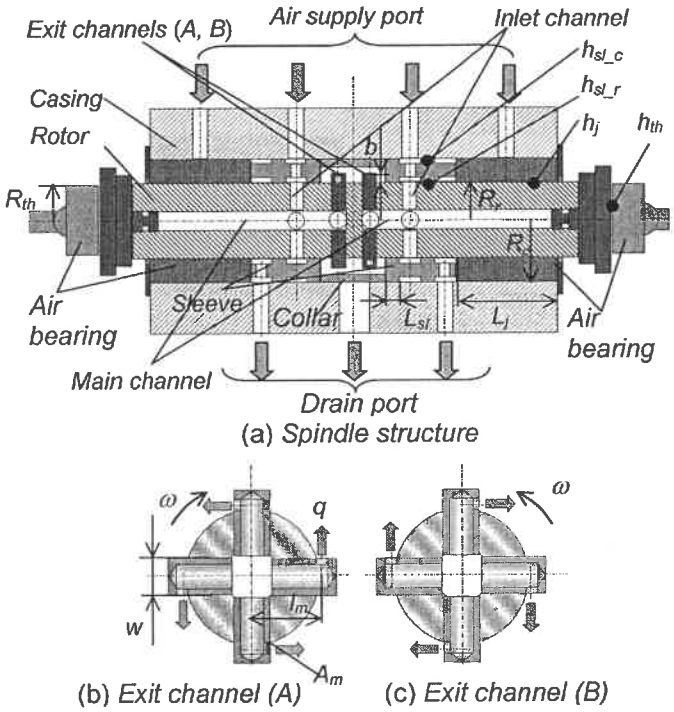

Fig. 1 Structure of air drive spindle

THEORY FOR DESIGNING AIR DRIVE SPINDLE

A mathematical model is derived for designing the air drive spindle and it uses to determine the principal spindle parameters, such as the clearance between the sleeve and rotor and the nozzle size of the exit channel. The driving torque produced by the air drive spindle can be expressed as

$$T_l = n\rho q\left(\frac{l_m}{A_m}q - R_r^2\omega\right) - \frac{4\mu\pi LR_r^3}{h_j}\omega - \frac{\mu\pi R_{th}^4}{h_{th}}\omega - 2nC_dA_{ex}\frac{\rho R_{ex}^3\omega^2}{2} \quad (1)$$

$$L = L_j + L_{sl}$$

where n is the number of the bend channels of each air drive motor, h_j and h_{th} are the clearance of journal and thrust bearings, respectively. q is the flow rate through each bend channel of the exit channels, ρ is the density of air, μ is the coefficient of the viscosity of air. C_d is the drag coefficient and A_{ex} is the projected area of the part formed on the rotor surface.

In Eq. (1), the first term represents the produced torque by the air drive motor. The second and third terms are the negative torques due to the air viscosity at the clearances between the rotor and the sleeve and journal bearing, as well as the thrust bearings. The last term represents the air resistance acting on the small parts which are placed on the rotor surface forming the exit channels, as shown in Fig. 1.

If the load acting on the spindle rotor is negligibly small, the relationship between the supplied air flow and the angular velocity of the air drive spindle can be expressed as

$$2nC_dA_{ex}\frac{\rho R_{ex}^3}{2}\omega^2 + \left[\left(n\rho q + \frac{4\mu\pi L_jR_j}{h_j}\right)R_r^2 + \frac{\mu\pi R_{th}^4}{h_{th}}\right]\omega - n\rho\frac{l_m}{A_m}q^2 = 0 \quad (2)$$

Thus, the angular velocity can be obtained by

$$\therefore \omega = \frac{-\beta + \sqrt{\beta^2 - 4\alpha\gamma}}{2\alpha} \quad (3)$$

here,

$$\alpha = 2nC_dA_{ex}\frac{\rho R_{ex}^3}{2} \quad (4)$$

$$\beta = \left(n\rho q + \frac{4\mu\pi L_jR_j}{h_j}\right)R_r^2 + \frac{\mu\pi R_{th}^4}{h_{th}} \quad (5)$$

$$\gamma = -n\rho\frac{l_m}{A_m}q^2 \quad (6)$$

If minor pressure losses can be neglected, the control pressure, p_c, is determined by the nozzle sizes of the exit channels as well as the flow rate, q, through the nozzle. Consequently, the control pressure is given by

$$p_c = \frac{\rho}{2}\left(\frac{q}{cA_m}\right)^2 \quad (7)$$

where A_m is the area of the nozzle and c is the discharge coefficient.

The clearances between the sleeve and the rotor, and between the casing and the sleeve are important parameters in controlling both leakage flow in the clearances and negative torque, due to the viscosity of the air in the clearance. The leakage flow at the clearances can be written by

$$q_{sl\_out} = \frac{\pi p_c}{4\mu L_{sl}}\left[\left(R_c + h_{sl\_c}\right)^4 - R_c^4 - \frac{\left[\left(R_c + h_{sl\_c}\right)^2 - R_c^2\right]^2}{\ln\frac{R_c + h_{sl\_c}}{R_c}}\right] \quad (8)$$

$$q_{sl\_in} = \frac{\pi p_c}{4\mu L_{sl}}\left[\left(R_r + h_{sl\_r}\right)^4 - R_r^4 - \frac{\left[\left(R_r + h_{sl\_r}\right)^2 - R_r^2\right]^2}{\ln\frac{R_r + h_{sl\_r}}{R_r}}\right] \quad (9)$$

Thus, the total flow rate is given by

$$Q_d = nq + q_{sl\_in} + q_{sl\_out} \quad (10)$$

Important spindle parameters were determined using the derived equations as shown in Table 1. Before developing the air drive spindle, performance of the designed spindle was examined through simulation. Calculated output power is given in Fig. 2. The spindle speed under no load condition is also shown in Fig. 3. Because of the air pressure limitation of the compressor for supplying air flow to the spindle, driving air pressure, p_c, is calculated. As shown in Fig. 4, it is verified that the air pressure for driving the spindle can be supplied by the commercial air compressor.

DESIGNED AIR DRIVE SPINDLE

The developed air drive spindle is shown in Fig. 5. Dimensions of the spindle rotor are 20 mm in diameter and 165 mm in length. Air pressure bearings using porous media are used in the spindle. Stiffness of the bearings at the supply pressure of 0.4 MPa are nominally 36.0 N/μm for the journal bearing and 17.7 N/μm for the thrust bearing, respectively.

Nozzle diameter of the exit channels was designed to be 1.4 mm. However, actual diameters of the eight nozzles are varied from 1.458 to 1.501 mm. Since the nozzle diameter is a principal design parameter that affects spindle performance, the exit channels are designed to be exchangeable. Thus, optimum nozzle diameter will be chosen so as to meet requirement of the spindle application. In addition, the direction of the discharge port of the exit channel can be changed, which enables all the discharge ports to set in the same direction. This setting accomplishes high speed rotation.

Table 1. Determined parameters

b	4.0 mm	w	4.0 mm
d	1.4 mm	A_{ex}	$b \cdot w$=16 mm
h_j	9.5 μm	L_j	50.5 mm
h_{sl_c}	9.5 μm	L_{sl}	1.3 mm
h_{sl_r}	11 μm	R_c	13 mm
h_{th}	5 μm	R_{ex}	R_r+b/2=12 mm
l_m	11 mm	R_r	10 mm
n	4	R_{th}	13 mm

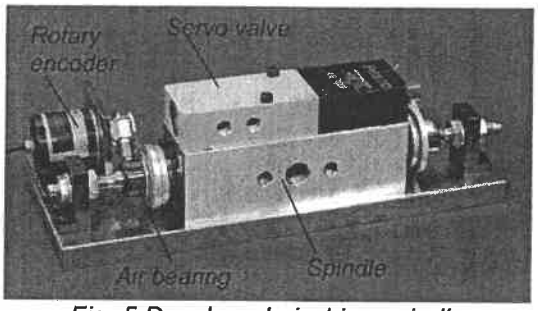

Fig. 5 Developed air drive spindle

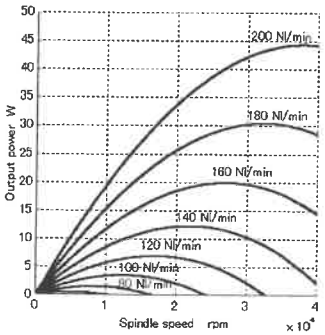

Fig. 2 Calculated output power

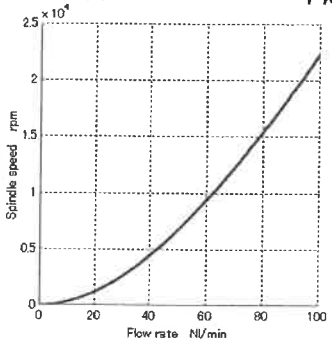

Fig. 3 Calculated spindle speed

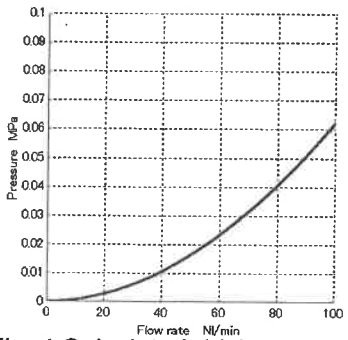

Fig. 4 Calculated driving pressure

EXPERIMENTS

The relationship between the supplied flow rate and the spindle rotation was given in Fig. 6. It is verified that bidirectional rotation was accomplished by switching the supply ports. In addition, it can be observed that the calculated spindle speed shown in Fig. 3 simulates the actual spindle speed, though it is slightly higher than the actual speed. Driving pressure, p_c, was also measured, as shown in Fig. 7. It is verified that the calculated pressure, p_c, also simulates the actual pressure.

As mentioned, the nozzle of the exit channels is a key parameter that determines the spindle speed. In addition, theoretical and experimental studies indicate that the derived mathematical model can simulate the characteristics the air drivel spindle. Thus, the influence of the nozzle diameter on the spindle speed was studied through the simulation using the derived mathematical model. In the simulation, the spindle speed, when the driving pressure reaches 0.5 MPa, was evaluated. In addition to the supply pressure limitation, maximum flow rate of the compressor, q_{max}, was considered in the calculation. The calculation result is presented in Fig. 8. From the result, it is verified that the designed nozzle diameter, d=1.4 mm, is rather large to attain high spindle speed. Since the exit channels was designed to be exchangeable, the exit channels with optimum diameter can be introduced to increase the highest spindle speed.

SUMMARY

In the present paper, an air drive spindle was proposed and mathematical model was derived for designing the air drive spindle. The air drive spindle uses the same driving mechanism with the water drive spindle that has been developed. Spindle performances were investigated through simulation studies. Then, the developed air drive spindle was tested and the result was compared to the simulation. From these investigations, it is verified that the mathematical model simulates the characteristics of the air drive spindle. Thus, optimum nozzle diameters of the exit channel were obtained for various driving conditions based on the mathematical model.

ACKNOWLEDGMENT

This research work is financially supported by the Grant-in-Aid for Scientific Research (C) of Japan Society for the Promotion of Science.

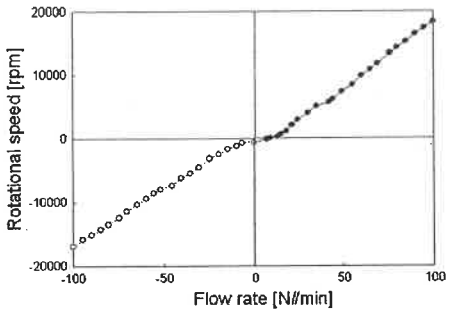

Fig. 6 Spindle speed vs. flow rate

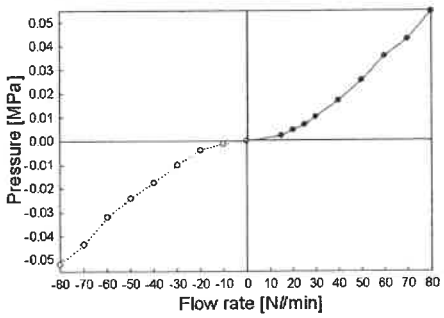

Fig. 7 Driving pressure vs. flow rate

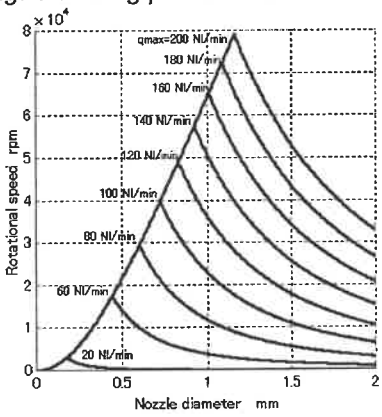

Fig. 8 Influence of nozzle diameter on spindle speed

REFERENCES

[1] Y. Nakao, M. Mimura and F. Kobayashi, Water Energy Drive Spindle Supported by Water Hydrostatic Bearing for Ultra-Precision Machine Tool, Proc. of ASPE 2003 Annual Meeting, pp. 199-202, (Portland, 2003-10).

[2] Y. Nakao, F. Kobayashi and Y. Sagesaka, Performances of Water Energy Drive Spindle Supported by Water Hydrostatic Bearing, Proc. of ASPE 2004 Annual Meeting, pp. 241-244, (Orlando, 2004-10).

[3] Y. Nakao and Y. Sagesaka, Water Drive Spindle for Diamond Turning Machine, Proc. of the third international conference on leading edge manufacturing in 21st century, pp. 449-454, (Nagoya, 2005-10).

DEVELOPMENT OF A PRECISION, LOW-COST, SMALL FOOTPRINT WIRE ELECTRON DISCHARGE MACHINE (WEDM)

Christopher Orino[1], Dinesh Rakwal[1], J. Dean Jorgensen[2], Eberhard Bamberg[1]
[1] Precision Design Lab, Department of Mechanical Engineering, University of Utah
Salt Lake City, UT 84112, USA
[2] Optimation, LLC., Midvale, UT 84047

ABSTRACT
Wire electrical discharge machining (WEDM) is a process that is highly utilized in the manufacturing industry for the cutting of material of any hardness with large aspect ratios. The most common place for its utilization is in the tool and die industry, to create molds and cutting dies very accurately with little or no polishing in the hardened heat treated state. Although it is a widely used process, a cost effective, small footprint, easy to maintain and operate machine, specified with a wide set of operating parameters has yet to be developed. With the increasing trend towards miniaturization and the development of MEMS, a need for WEDM with these characteristics is quickly coming about. This paper outlines the design and building of a prototype, innovative, cost effective, wire electric discharge machine (WEDM).

INTRODUCTION
Historically the corrosive effect of a single electrical discharge was first observed by English scientist, Joseph Priestly in 1770. It was not until 1943 when the soviet scientists B.R. and N.I. Lazarenko developed an RC circuit and control with the characteristics needed to effectively utilize electrical discharges as a material removal process [1]. Although the EDM process has been used for more than 60 years, it is currently not able to accommodate the specific needs of the development and design of micro scale systems.

The WEDM utilizes a traveling wire as the working electrode. The wire, usually 50 to 500 micrometers in diameter is stripped from a spool. It is then guided in a tensioned state between two ceramic or diamond guides, the used wire is then taken up on an additional spool. The wire is constantly moving past each of the guides. WEDM is the most versatile of the EDM processes. Intricate tapered and square geometries can be created with corner radii only slightly larger than half the wire diameter are possible. WEDM also has the capability of cutting parts with very high aspect ratios.

In discussing the prototype WEDM developed here (Figure 1); it will be broken into 3 separate systems, those being the base structure, wire tension system, and finally the power and control system. The base makes up the main structural components which include both the y- and z-axis. The wire tension system is made up of the mounting plate, cross slide, wire pull motor, and wire tension brake. The third and final system is made up of the power RC pulse generator, axis control, and control computer with its user interface.

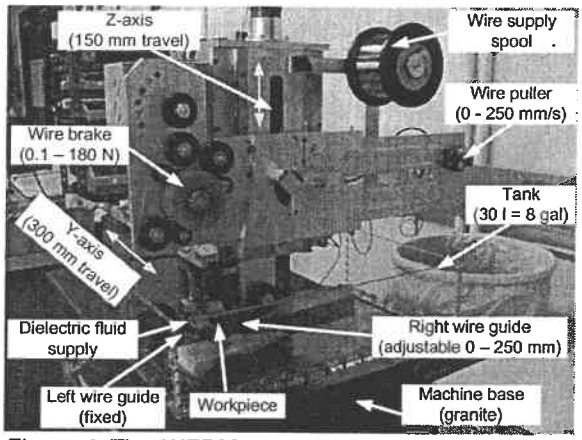

Figure 1 The WEDM prototype, pictured above, is a cost effective, small footprint (> 1 m³), easy to maintain and operate machine, specified with a wide set of operating parameters. The machine has 300 mm of travel in the Y axis, and 150 mm travel in the Z axis. The wire guides are adjustable and can be positioned from 0 mm – 250 mm.

DESIGN AND CONTROL SYSTEM

Wire Tension System
The first aspect of the design of the WEDM was to determine the basic layout and control components necessary to control both the wire traveling speed as well as the wire tension. The initial design parameter of the wire control system was the ability to tension the wire as low as 1 to 200 Newtons of force with a relative accuracy of +- 10% of the target tension. Wire tension as low as 1 Newton is required for wires

with diameters of around 20 microns. These specifications are outside of the normal range of commercially available machines, although high precision machines are now being produced that can control wires this small.
In most cases the material choice for the wire is brass. Brass is a desirable wire material because of its ability to break down from the physics of the EDM process as opposed to the work piece that is being cut. Brass also has a low ultimate tensile strength (UTS) which means that the maximum tensioning of a brass wire is relatively low.

The machine described here was designed with the ability to accommodate wire made of various materials in a range of diameters. Two additional materials that are used in WEDM machines (as in the case of the material being cut is a semiconductor) are molybdenum, and tungsten. Both of these materials have very high ultimate tensile strengths, which in turn, allow for very high tensions. The other aspect to a wide range of tensions is that as the diameter of the wire decreases, its cross sectional area decreases as an inverse square. As a result, wire with a small diameter requires dramatically reduced tension compared to the same wire with a larger diameter.

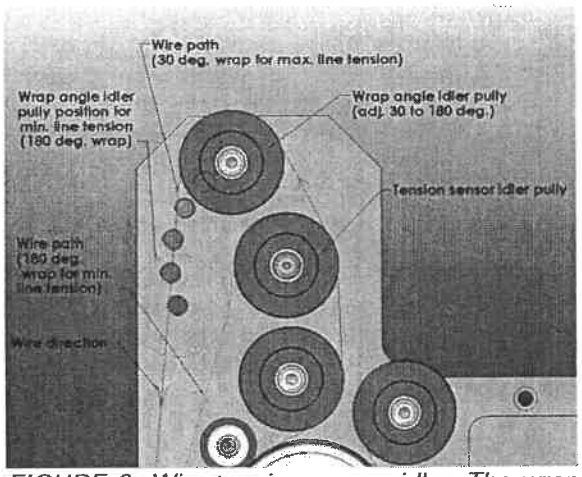
Wire path
(30 deg. wrap for max. line tension)
Wrap angle idler pully position for min. line tension (180 deg. wrap)
Wrap angle idler pully (adj. 30 to 180 deg.)
Tension sensor idler pully
Wire path (180 deg. wrap for min. line tension)
Wire direction

FIGURE 2 Wire tension sensor idler. The wrap angle idler pulley can be adjusted from 30 degrees to 180 degrees. This allows a single tension sensor to measure tension from 1 to 200 N with a +- 10% resolution. Altering the wrap angle of the wire around the tension sensor idler pulley changes the force acting on the sensor. For a 30 degree wrap angle the multiplication factor is 0.5, and for a wrap angle of 180 degrees it becomes 2.

Wire speed was also designed with both the ability to travel at a very slow speed to very high traveling speeds (0-250 mm/s). This allows a large amount of variation in control of how much of the wire is eroded away, directly affecting the maximum material removal rate as well as the quality of the surface finish.

The control of the wire tension and speed is made up of a single servo loop. This servo loop includes the wire puller motor with gearbox, line tension sensor, and a constant slip brake. The brake that was chosen was a Magtrol HB-450 hysteresis brake. The torque on the brake is continuously adjustable, resulting in a force on the wire ranging from 0 to 200 N, with unlimited slip. This fully magnetic brake was chosen over the more commonly used magnetic particle brake for its ability to remain very smooth at low rpm's. Magnetic particle brakes, on the other hand, require sufficient rotational speed, as well as heat build up in the particles, to provide smooth consistent torque.

The next component in the servo loop is a Honigmann RFS 150 tension sensor with a range from 0 to 10 N. The tension sensing is based upon readings from a strain gage mounted in the unit. To accommodate the wide range of wire tensions the machine was designed for, it is necessary to alter the wrap angle of the wire around the guide wheel that is attached directly to the sensor. Changing the wire wrap angle from 30 to 180 degrees alters the sensor reading by a factor from 0.5 to 2 times the actual line tension. For the highest tensions a wrap angle of 30 degrees is used and for the lightest tensions a wrap angle of 180 degrees is used. The wrap angle of the wire along with the amount of amplification of the signal from the sensor allows the sensor to achieve the tensions from 1 to 200 Newtons of force within the +-10% accuracy initially specified (see Figure 2).

The complete wire tension system works by first setting the wire puller motor to the desired wire traveling speed. At this point the magnetic brake is set by adjusting the current supplied to the brake which in turn tensions the wire. The wire tension sensor provides the feedback to the servo loop necessary to maintain the correct amount of tension on the wire by adjusting the current to the magnetic brake.

Having selected the necessary components for control of the wire tension system a layout of the components could be designed. One of the design goals, as stated previously, was to maintain a small foot print for the overall machine. Many options on how the wire system could be laid out were explored. Almost all commercially available machines orient the wire in the vertical direction. From that point either the position of the wire can be controlled or the position of the work piece. Both of these methods have their disadvantages. If the wire is to be positioned with respect to the work piece, the problem that arises, in the case of a vertically oriented wire, is that the tank containing the dielectric fluid be designed deep enough to completely submerge the lower wire guide along with the work piece. When designing a system with the wire oriented in such a way, the foot print of the machine, as well as the height of the machine becomes very large. If one were to move the entire tank including the work piece, the problem that arises is that the response time of the wire positioning is affected by the inertia created by moving of the dielectric fluid and work piece set up.

Considering the above arguments it was decided to orient the wire horizontally (Figure 3). By doing so, both of the issues discussed earlier could be eliminated.

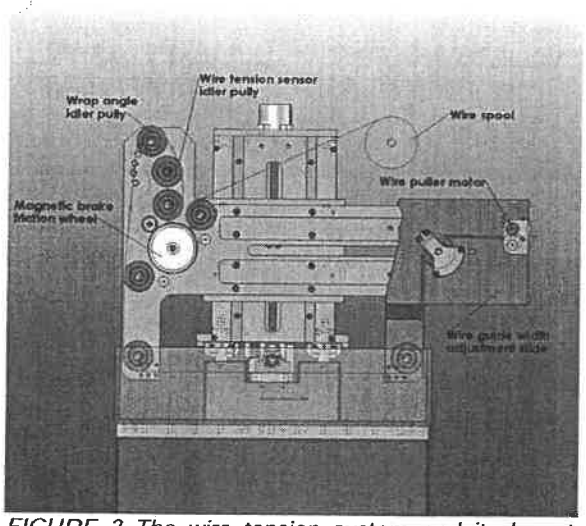

FIGURE 3 The wire tension system and its layout. The wire is first drawn off from the wire spool, directed to make almost a complete wrap around the magnetic brake friction wheel, then around the tension sensor pulley system down to the guides. The wire is pulled by the wire puller motor and exits to the right side of the machine.

The result is a simple compact wire tension system that has a constant mass, for positioning reliability, and a dielectric tank that is of minimal volume. In addition, the set up of work pieces is very simple, allowing for a wide range of set up configurations.

All of these characteristics, designed into this innovative prototype WEDM, lend themselves well to the investigation and study of parameters and techniques needed for WEDM to become an effective process for developing MEMS and miniature mechanical systems and the cutting parameters of materials used in developing these systems.

Base Structure

The base structure of the machine, which includes the two axes for positioning the wire, was designed around the decisions made for the design of the wire tension system. In order to utilize the horizontally oriented wire, it was necessary to design an axis that could be cantilevered out over the top of the dielectric tank. This made up the configuration of the Y-axis. Mounted on top of the cantilevered Y-axis is the vertical or Z-axis. Both axes are used in unison to provide the two axes that position the wire.

To begin with, the whole machine was mounted to a granite surface plate. In addition to the base being granite, a granite parallel was utilized to raise the horizontal (y-axis) above the top edge of the dielectric tank. Granite was chosen for several reasons including its stability to both tempature changes and vibration, as well as the ability to achieve a very flat surface on which the machine structure could be built.

On the granite parallel are mounted two THK roller profile rails. A plate is mounted to the two bearing rails allowing it to be positioned above the dielectric tank at any position along the tank width. The Y-axis has 300 mm of travel.

The vertical axis structure is then mounted to the horizontal axis plate. The vertical axis motion is enabled by two Schneeberger recirculating roller bearing units. These bearing units allow the wire tensioning system to be position at any depth, from slightly above to slightly below the top edge of the dielectric tank.
Finally the dielectric tank was fabricated from lexan, both for its durability, and that it is clear.

The tank was attached to a tooling plate, which had around its perimeter a tapered drain and a number of threaded holes to aid in the set up of work pieces.

Control system

The prototype WEDM is powered and controlled by a modified Optimation Profile 24 control unit that includes a 4-axis PCI motion controller from Galil, an Optimation optoisolation board that handles the IO between the WEDM, and the controller (see Figure 4).

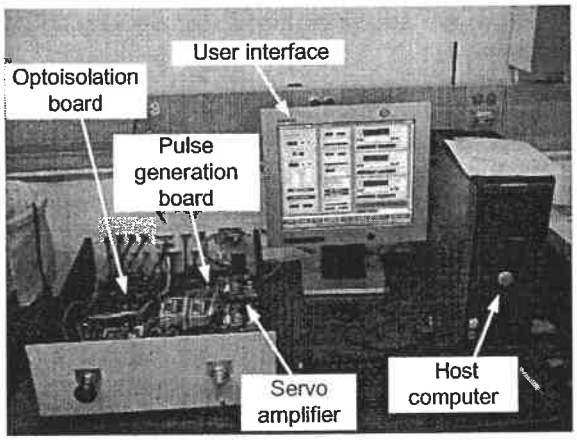

FIGURE 4 Pulse generator and control system of the WEDM prototype

Control of the system is facilitated by the use of Optimation's Opti rev 1 software and includes servo routines for the tensioning of the EDM wire as well as servo routines for the vertical and horizontal axis that adapt the feed speed to the rate at which material is being removed (Figure 5). This prevents the wire from making physical contact with the work piece and results in the fastest possible machining speed for a given set of EDM parameters.

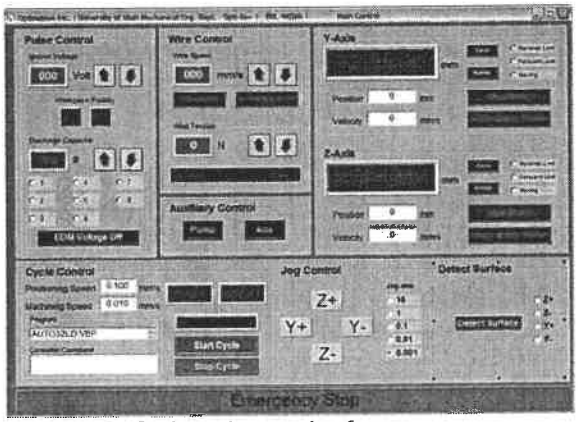

FIGURE 5 Opti rev 1 control software

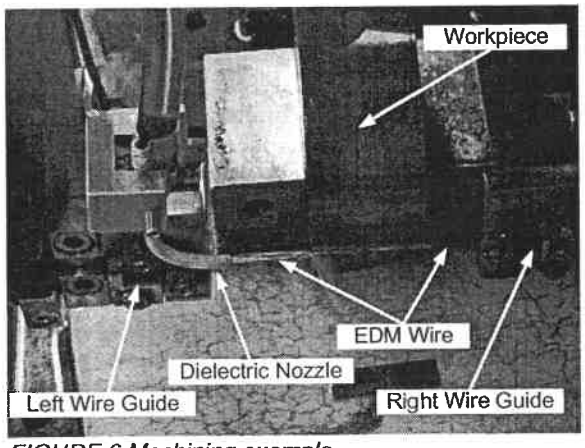

FIGURE 6 Machining example

CONCLUSIONS

In conclusion, the prototype precision WEDM that was built and tested, maintained a small foot print (> 1 m^3), is cost effective, easy to maintain and operate machine, and specified with a wide set of operating parameters. The many aspects that were considered in the development of this machine led to the successful design of a WEDM that was able to comply with the initial specifications of the development of a prototype wire EDM. The development of this prototype WEDM provides a valuable resource in the study of the WEDM processes to aid in the development of miniaturized systems such as MEMS.

The ability to have complete control over all of the major parameters involved in the WEDM process makes it possible to investigate and develop more efficient strategies in all aspects of WEDM process including, the manufacture of small parts and flexures, investigate and optimize cutting parameters of semiconductor materials, as well as more traditionally processed EDM materials.

FUTURE WORK

The dielectric flushing and filtration system will need to be improved to increase cutting efficiency, including more efficient delivery of the fluid to the wire.

REFERENCES

[1] E. Bud Guitrau, The EDM Handbook, Hanser Gardner Publications, 1997.

ACKNOWLEDGEMENTS

This material is based upon work supported by the National Science Foundation under Grant No. 0512897.

AXIOMATIC DESIGN METHOD APPLIED TO A PARALLELOGRAM MICROMACHINE FOR LOW COST MICROMECHANICS

L. Ruiz-Huerta and A. Caballero-Ruiz
Laboratorio de Micromecánica y Mecatrónica
Centro de Ciencias Aplicadas y Desarrollo Tecnológico
Universidad Nacional Autónoma de México
Circuito Exterior s/n, Ciudad Universitaria, México D.F., 04510, México

INTRODUCTION

This paper describes the experience of the Laboratory of Micromechanics and Mechatronics (LMM) at Center of Applied Sciences and Technological Development (CCADET) at National Autonomous University of Mexico (UNAM), using simple mechanisms and high level control systems to develop low cost micromechanical systems. To date, this group has developed three prototypes of micromachine tools, some models of manipulators and several versions of stepping motors for its automation. The main idea to develop low cost micromechanical systems consists of decreasing the size of the designs tested at human scale by means of generational way [1]. The first generation has overall sizes around 200mm, the second generation has overall sizes around 100mm; following this way some generations after, the n-generation could have overall sizes around some millimeters. The authors are currently working in the second generation of micromachine tools.

Using parallelograms and levers, as Richard Feynman proposed [2], the authors of this article developed a micromachine tool with resolution of 600 nm. This resolution is the same for the three translational axes and every single axis is able to move along 20 mm. Applying this low cost developed-mechanisms, the movements in each axis has a semicircular trajectory, this kind of motion requires advanced control techniques to convert it in lineal movements. Due to the goal that the authors are looking for a proper design to scale in future generations of micromachines, it is necessary to analyze and to conclude the advantages and disadvantages of the proposed design. This machine has the same setup of stepping motor, gear train, feed screw, lever, and parallelogram for every axis. The employed configuration allowed the authors to simplify the manufacture process and reduce the number of pieces required for assembly. An advantage of this design consists in the capability to place all the actuators and gear train elements far from the final motion elements, reducing the inertia problems. It is important to mention lake this mechanisms are not convenient to apply at human scale because it would result in a machine with huge components.

In order to optimize the elements associated with the motion of the micromachine, the analysis of the design by means of an axiomatic design method is presented. The results will allow the authors to improve the original version of the micromachine and to propose a better design to minimize the control requirements. The first axiom is used to know the interdependence of every function and its vulnerability in the conceptualization process, while the second axiom is used to know the operational vulnerabilities of the design. The use of the axiomatic design method results leads to some recommendations which will be considered for the design of future generations of low cost micromachine tools.

ANALYSIS

As the authors presented in [3], the lever method is a good choice to reduce problems related with backlash, but for the development of low cost micromechanics it is necessary to take care of the manufacturing process. Based on this idea, the authors analyzed two different possibilities to obtain high resolution motion while keeping the estimated low cost of around 110usd. The first alternative consists in the use of common round bars guides and carriages, figure 1. The second alternative consists in the use of the levers and parallelogram described above.

The figure 2 shows the micromachine described above, the second alternative. The points marked as B are levers, the points marked as P are parallelograms, the trajectories marked as

IM are input motion and finally the trajectories marked as OM are output motion.

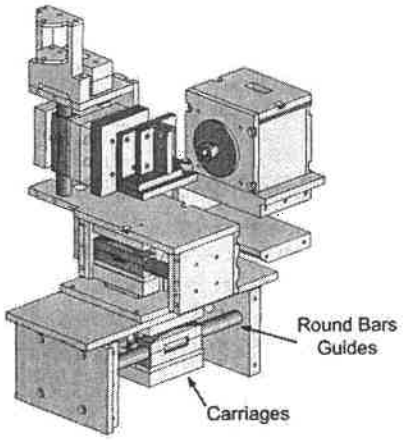

Figure 1. Micromachine based on round bars guides and carriages

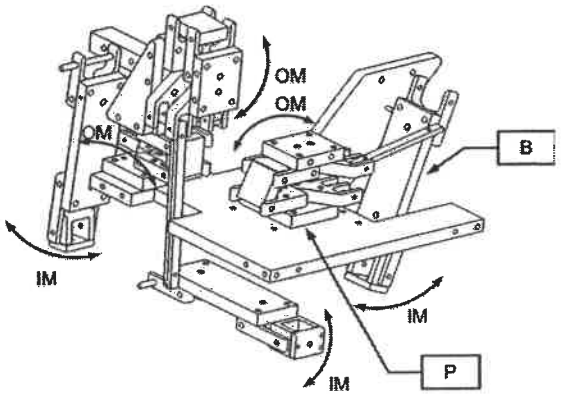

Figure 2. Micromachine based on Levers and Parallelograms.

First of all, the authors obtain and separate the main requirements to develop a micromachine tool. These requirements are:

- three dimensional motions
- independent motions
- high resolution motion and
- facility of manufacture

The independence axiom

This axiom consists in the searching process of a matrix which relates the functional FR requirements -minimum set of independent requirements that completely fulfill the design objective- to the design DP parameters -physical solutions- [4].

$$\{FR\}_{m\times 1} = [A]_{m\times p} \cdot \{DP\}_{p\times 1} \qquad (1)$$

This axiom is not fulfilled until the resultant matrix [A] is a diagonal matrix (uncoupled design) or a triangle matrix (decoupled design). These kinds of matrices allow us to keep control of the variables involved in the solution process of the design. For the case of study, which is a micro machining center, the FRs are:

$$\{FR\} = \begin{Bmatrix} FR_1 \\ FR_2 \\ FR_3 \\ FR_4 \end{Bmatrix} \qquad (2)$$

where FR_1 is the requirement of three dimensional motions, FR_2 is related to independent motions, FR_3 is related to the high resolution motion and FR_4 is the parameter which determines how easy the manufacture will be. For this last requirement we apply selection criteria on the base of the equipment installed in the LMM.

It is easy to notice that the last requirement can not be evaluated by means of the first axiom, because the independence axiom relates functional requirements to design parameters, and it is not possible to relate different values to every alternative. This could be solved by means of the second axiom, therefore:

$$\{FR\} = \begin{Bmatrix} FR_1 \\ FR_2 \\ FR_3 \end{Bmatrix} \qquad (3)$$

And the design parameters are:

$$DP = \begin{Bmatrix} DP_1 \\ DP_2 \\ DP_3 \end{Bmatrix} \qquad (4)$$

Where DP_1 is related to three axes of motion, DP_2 is related to the system of parallelograms, and DP_3 is related to the system of levers. By substituting FR and DP in equation (1) as follows

$$\begin{Bmatrix} FR_1 \\ FR_2 \\ FR_3 \end{Bmatrix} = \begin{bmatrix} 1 & 0 & 0 \\ 0 & 0 & 0 \\ 0 & 0 & 1 \end{bmatrix} \cdot \begin{Bmatrix} DP_1 \\ DP_2 \\ DP_3 \end{Bmatrix} \qquad (5)$$

It seems like the FR_2 is not related to DP_2, which results in a coupled design, and does not fulfill the independence axiom. However, the FR_2 could be fulfilled by the DP_2 when the control process is considered; which means that by using algorithms it is possible to convert complex motions (semicircular) into linear ones. Taking this into account the equation (5) is:

$$\begin{Bmatrix} FR_1 \\ FR_2 \\ FR_3 \end{Bmatrix} = \begin{bmatrix} 1 & 0 & 0 \\ 0 & 1 & 0 \\ 0 & 0 & 1 \end{bmatrix} \cdot \begin{Bmatrix} DP_1 \\ DP_2 \\ DP_3 \end{Bmatrix} \quad (6)$$

The information axiom

For this axiom the information is defined as a measure of complexity and is related to the probability of certain events occurring when information is supplied. Once different alternatives have solved the objective of a design, it is possible to apply this axiom to find the solution which best fulfill the problem [4].
The parameter information (I) is defined as:

$$I = \ln\left(\frac{SR}{CR}\right) \quad (7)$$

Where SR is the system range -the values which every alternative could take- and CR is the common range -the range which intersects the SR and the design requirement (DR)-. Based on the second axiom, it is possible to analyze the FR_2, parallelograms and the control system, as well as the FR_4, facility of manufacture (FOM).

For the FR_2 it is necessary to compare different requirements of the control system with different alternatives of mechanism. If we compare the control system of a mechanism which moves linearly with the control system of a parallelogram, we could find that they are not too different from each other, and at present, the microcontrollers have enough power of processing to complete the task promptly.

By defining as solution the capability of both, the linear motion and parallelogram system, to solve direct and inverse tasks, we could be able to execute the second axiom. Figure 3 shows a diagram of the CR, SR, and DR. Using equation 7, and defining DR as the sum of points, one per task, both systems obtain an I value equal zero.

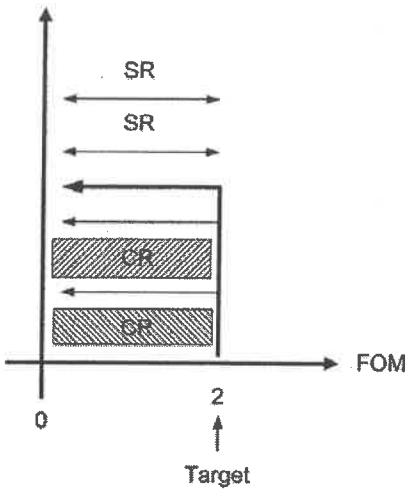

Figure 3. Graphical representation of the FR_2

$$I_{linear} = \ln\left(\frac{SR}{CR}\right) = \ln\left(\frac{2}{2}\right) = 0 \quad (8)$$

$$I_{levers} = \ln\left(\frac{SR}{CR}\right) = \ln\left(\frac{2}{2}\right) = 0 \quad (9)$$

For the FR_4, it is necessary to consider the range values which define the LOM concept. For the authors, these values are defined as the time required for fully manufacture and assembly time in units of 1 hour (TMA), the number of pieces (NP) and the number of different pieces (NDP). Every single parameter related to the FOM factor of previous designs.

$$LOM = TMA + NP + NDP \quad (10)$$

The first prototype of the micromachine tool [5] requires 20 hours for every axis, 11 pieces of which 9 are different. This results in 40 FOMs.

For the parallelograms and levers micromachine tool [6], it is possible to identify 10 hours for every single axis, 19 pieces of which 8 are different. This results in 37 FOMs.

The graphic representation of this axiom is showed in figure 4. Observe the target for the parameter FOM is located in 37 FOMs, which is the maximum time estimated to manufacture one axis.

This graph shows the values of CR and SR. Applying the equation number 7, we obtain:

$$I_{linear} = \ln\left(\frac{40}{37}\right) = 0.078 \quad (11)$$

$$I_{levers} = \ln\left(\frac{37}{37}\right) = 0 \quad (12)$$

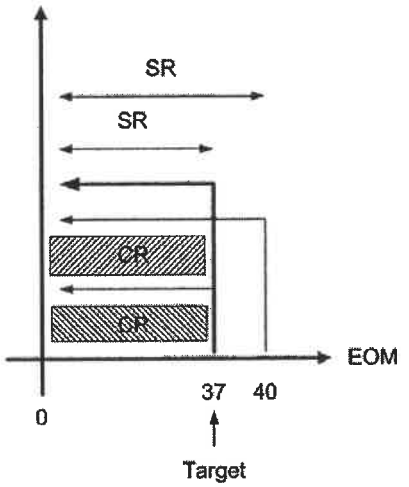

Figure 4. Graphical representation of the FR_4

By adding up of I values for linear design and for levers design, we find:

$$\sum I_{linear} = 0 + 0.078 \quad (13)$$

$$\sum I_{levers} = 0 + 0 \quad (14)$$

As showed in equations 13 and 14, the second prototype (parallelograms and levers) has a better probability of success with the proposed target. This means that the minimum information axiom is fulfilled.

RESULTS

The results presented in equations 6, 13 and 14, shown the following conclusions:

- The proposed design based on parallelograms and levers fulfills the first and the second axiom.
- The proposed design can be improved by means of the control system and the time required for manufacture.
- Using preliminary results, this micromachine tool is able to move with a resolution of 0.6μm

CONCLUSIONS

The axiomatic design method is a powerful tool in the engineering design. The advantages of using this tool lie in the minimum correction stages posterior to the conceptual design. This paper describes the application of the axiomatic design method in two different prototypes of micromachine tool developed in the laboratory of Micromechanics and Mecahtronics, CCADET, UNAM. The results confirm the viability of using parallelograms and levers as a motion mechanism to obtain a low cost and high resolution micromachine tool.

AKNOWLEDMENTS

The financial support of CONACyT, under grant CONACYT-CIAM 2002/074-3 is highly appreciated. Thanks are also addressed to Dr. Ernst Kussul for his comments.

REFERENCES

[1] E. Kussul, T. Baydyk, L. Ruiz, A. Caballero, G. Velasco, L. Kasatkina, DEVELOPMENT OF MICROMACHINE TOOL PROTOTYPE FOR MICROFACTORIES, Journal of Micromechanics and Microengineering, Vol. 12 No. 6, año 2002, pp. 795-812, UK

[2] Feynman, Richard P. THERE'S PLENTY OF ROOM AT THE BOTTOM. (California Inst of Technol, Pasadena, CA, USA) Source: *Journal of Microelectromechanical Systems*, v 1, n 1, Mar, 1992, p 60-66..

[3] Ernst Kussul, Tatiana Baidyk, Leopoldo Ruiz-Huerta, Alberto Caballero-Ruiz and Graciela Velasco, SCALING DOWN OF MICROEQUIPMENT PARAMETERS, Journal of Precision Engineering, Volume 30, Issue 2 , April 2006, Pages 211-222

[4] Basem Said El-Haik, AXIMATIC QUALITY, Wiley, 2005, USA

[5] E. Kussul, T. Baydyk, L. Ruiz, A. Caballero, G. Velasco, L.Kasatkina, DEVELOPMENT OF MICROMACHINE TOOL PROTOTYPE FOR MICROFACTORIES, Journal of Micromechanics and Microengineering, Vol. 12 No. 6, año 2002, pp. 795-812, UK.

[6] Ruiz-Huerta, L., Caballero, A., Marin, E., Velasco, G., Baydyk , T., Kussul, E., (2004), Parallelogram Micromachine For Low Cost Micromechanics. 2004 ASME International Mechanical Engineering Congress, ASME (Eds.), Anaheim, California, USA, 13/11 - 19/11, IMECE 2004-62186.

NON-CONTACT BIO CELL MANIPULATION BY NONLINEAR MICRO FLOW AROUND THE VIBRATED PIPETTE ON MICRO ROBOT

Hisayuki Aoyama[1], Naoto Chiba[1], Ohmi Fuchiwaki[1],
Daigo Misaki[2] and Takashi Usuda[3]
[1]University of Electro Communications, Tokyo, Japan
[2]Shizuoka Institute of Technology,Shizuoka, Japan
[3]National Institute of Advanced Industrial Science
and Technology,Tsukuba, Japan

INTRODUCTIONS

For these years, our group has successfully developed the precise tiny robots system for micro industrial production[1][2]. For the application toward such bio cell surgery, the cell manipulation technique is one of most important issues and there it is required to handle such the small bio cell without any damages. In this report, the unique non-contact manipulation is proposed and its basic performances are discussed with some typical experimental results.

Our small robot, which is composed of piezo elements and electromagnets, can walk with an inchworm manner to X and Y directions and rotate with the resolution of such sub micrometer in the plane under the microscope view field. The piezo driven thin glass pipette is also set on this small robot and it can be vibrated near the target bio cell which is floated in the water of schale. Then the micro non-linear flow around the vibrated pipette can be generated and the target small particle can be conveyed along the flow and rotated in the whirlpool.

We can maneuver the position of the thin glass pipette on the micro robot so that the small bio cell can move to the specified point and rotate to align the face of cell after some numerical analysis to simulate such complicated 3D flows.

In the experimental results, it is demonstrated that the egg of frog is successfully captured and conveyed to the sucking pipette. And another thin pipette can be injected to the face of egg after rotating it by the whirlpool flow.

In the conclusions, it is summarized that one of the potential benefit of the micro robot system can be assigned to such an automatic bio cell surgery with lower cost and higher reliability.

EXPERIMENTAL SETUP

In Fig.1, the overall experimental setup that is composed of the microscope, the active glass pipette, and the control electronics and PC is constructed in order to investigate the micro flow around the vibrated pipette. Here the active glass pipette as shown in Fig.2 is set under the

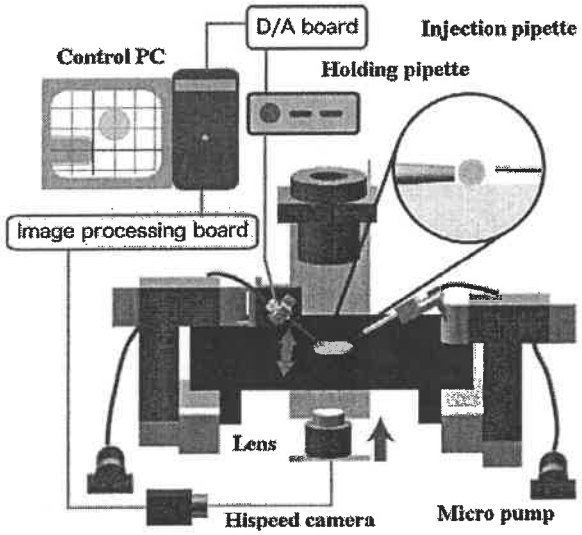

Fig.1 Experimental setup including micro microrobot with active pipette and microscope.

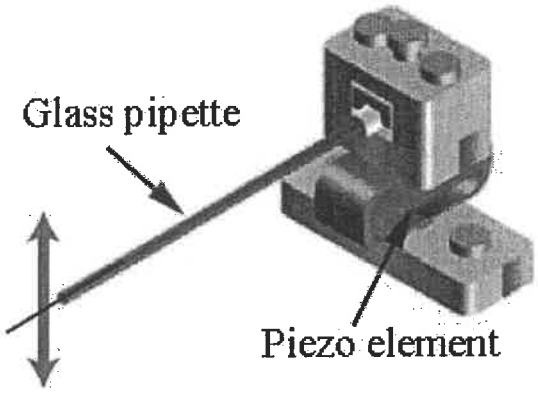

Fig.2 Piezo vibrated glass pipette for sucking and injecting bio cell.

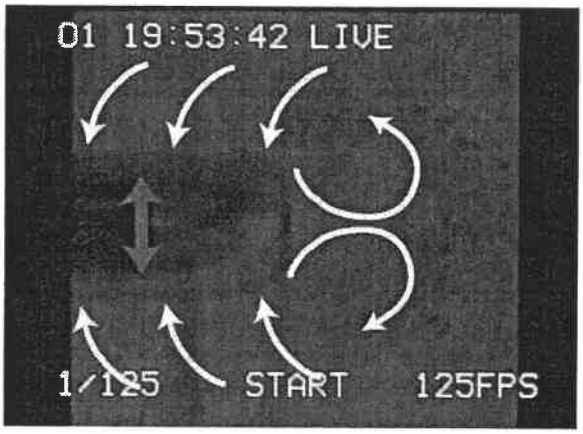

Fig.3 Top view of micro flow around the vibrated pipette.

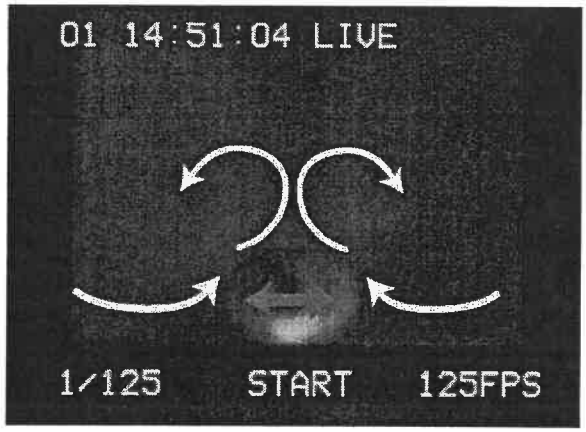

Fig.4 Side view of micro flow around the vibrated pipette.

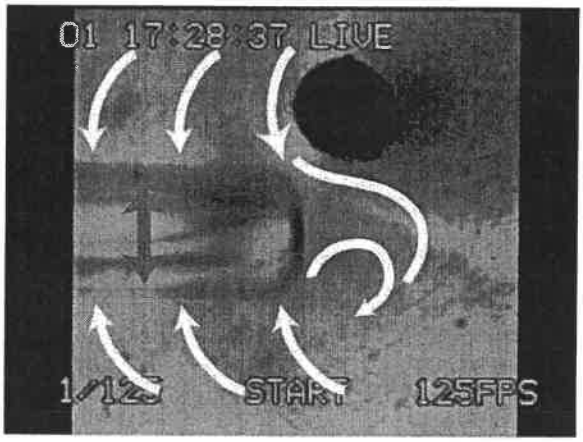

Fig.5 Top view of micro flow between the active pipette and the cylinder.

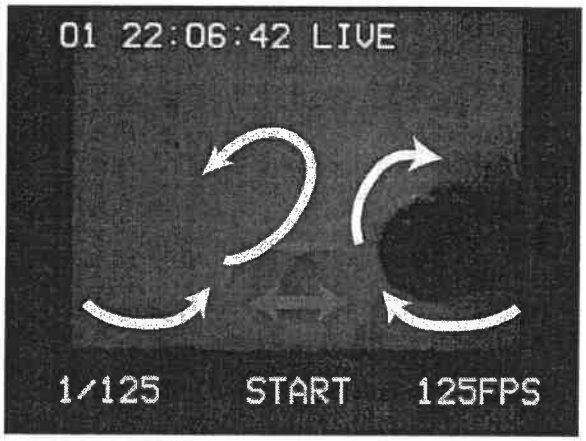

Fig.6 Side view of micro flow between the active pipette and the cylinder.

microscope. The thin glass pipette with the inner diameter of 10 micrometer is used and it can be vibrated by the piezo actuator. The optical lens and high-speed camera are set underneath the microscope and thus the image can be monitored simultaneously. This active pipette is also mounted on the XY stage and can be positioned at the specified point precisely. In order to visualize the micro flow around the vibrated pipette, the micro particle of Chinese black ink is blended into the water as a tracer. The captured image can be processed with the PC, and the position and angle of the target are presented.

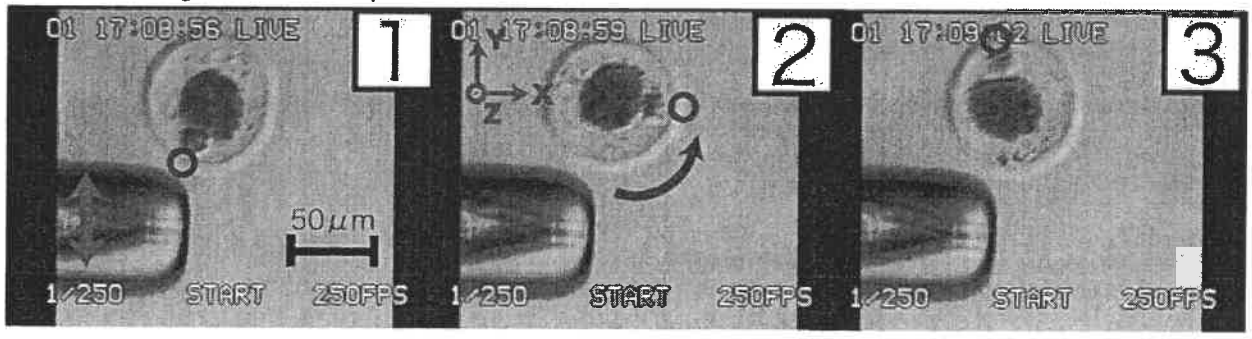

Fig.7 Bio cell can be rotated by the micro flow generated with the vibrated pipette.

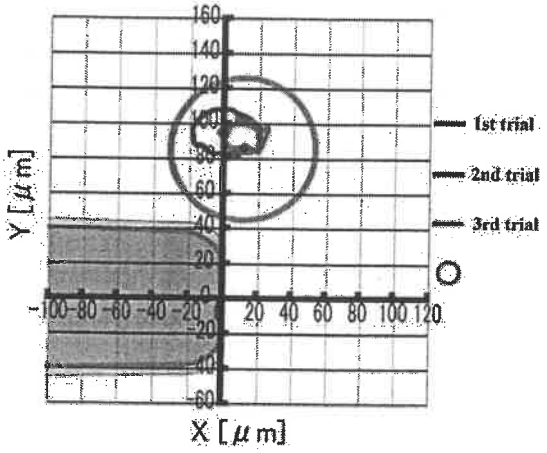

Fig.8 Measured eccentricity of the rotational motion(60Hz, 11.7 micron).

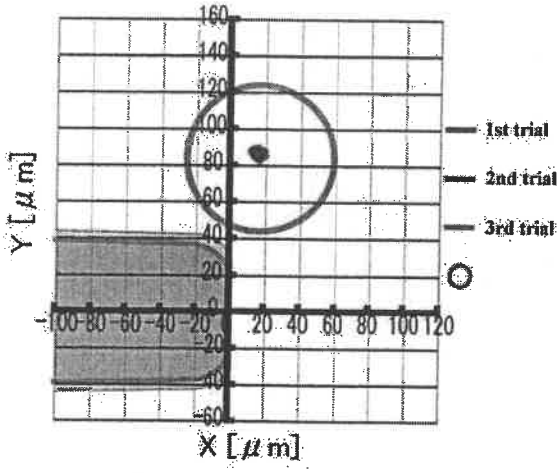

Fig.9 Measured eccentricity of the rotational motion(240Hz, 8.7 micron).

Fig.10 Rotated bio cell at the side of active pipette.

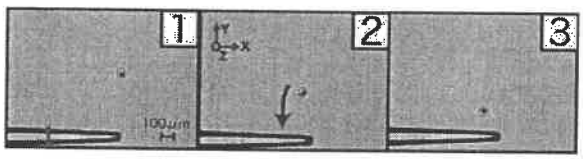

Fig.11 Bio cell conveyed by the micro flow coming from outside.

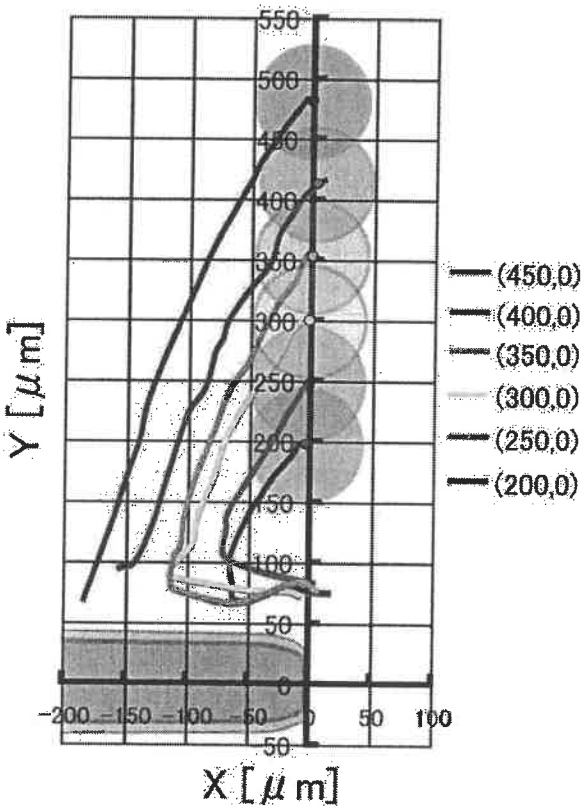

Fig.12 Measured tracks of the conveyed cell in X-Y plane from different initial positions.

EXPERIMENTAL RESULTS

In this section, we describe the basic experiments and the results. The typical micro flows around the vibrated pipette are shown in Fig.3 and Fig.4; here the top view and the side view are monitored. In the picture of the top view, it is found that the twin circle flows are generated at the end of the pipette while the other flow comes into the side of the pipette. When the frequency and the amplitude of the vibration are changed, then the flow speed can be controlled without any change of the flow pattern.

In Fig.5 and Fig.6, the micro flows are checked when the small cylinder is set near the end of the vibrated pipette. Then it is found that the flows around the cylinder of 80 micrometer in diameter are still generated and this can provide the torque force for rotation with the target located at the cylinder due to the viscous force.

In order to apply this unique manipulation to such bioengineering, we are proposing to convey and position the tiny bio cell without any mechanical contact. In Fig.7, the sequential photos are shown and it is found that the egg cell at the specified position can be rotated in either direction. This rotation is generated by the micro flow around the vibrated glass pipette. In order to check the condition that the target can be rotated, the amplitude of the vibrated pipette and the frequency are changed and the motion of the target is monitored. The target cell can not driven when the

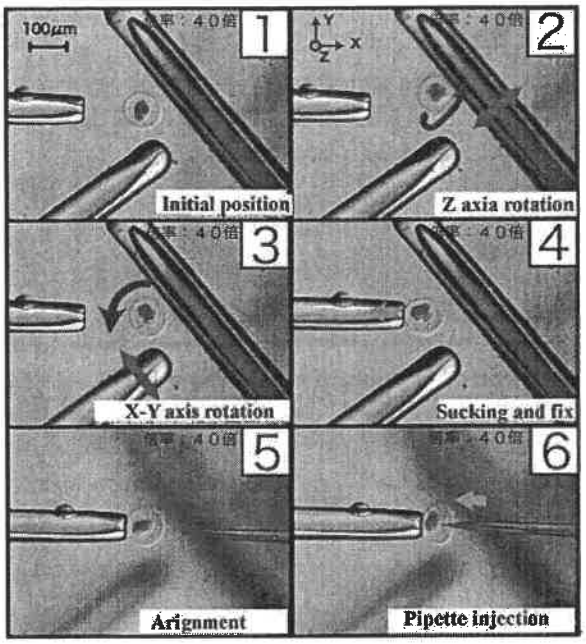

Fig.13 Three active pipettes can provide complicated manipulaion such conveying, sucking and injecting with bio cell.

amplitude of the vibration and the frequency are small while it is trembled within the higher frequency and the larger amplitude of vibration. In the appropriate condition such of 90 to 140Hz and 10 to 20 micrometer amplitude, the target can be rotated stably. This is the reason that the self-excited vibration can be given when the micro flow rate become large.

Moreover the eccentricity of the rotational motion is checked, that is shown in Fig.8 when the frequency of the vibration is 60Hz and the amplitude is 11.7 micrometer, while the frequency is 240Hz and the amplitude is 8.7micrometer in Fig.9. It is clear that the eccentricity is much better when the smaller amplitude and the higher frequency are applied to the pipette. In Fig.10, the motion of the target cell is shown when it is set in the side of the vibrated pipette. It is found that the cell can be driven to rotate with the axis parallel of the pipette. This is caused by the micro flow from the bottom to the upper around the vibrated pipette. Also unique manipulation is shown in Fig. 11, where the target small cell can be conveyed by the micro flow coming far from the pipette that is vibrated with the frequency of 160Hz and the amplitude of 48.7 micrometer.

Several tracks when the target cell is located at the different initial positions are shown in Fig.12. This results means that the micro flow around the pipette can convey the small particle such the bio cell in X-Y plane with any mechanical contact. Multiple micro robots with the active pipette can be set under the microscope and the complicated manipulation that is combined with the transnational conveying and the rotational positioning. As shown in Fig.13, the target cell is succeeded in controlled by three active pipettes and finally the bio cell can be fixed at the end of the sucking pipette and the thin pipette can be injected into the cell precisely.

CONCLUSIONS

In this paper, the unique non-contact manipulation is proposed and several experimental results showed that the micro flow around the vibrated pipette could convey and rotate the target bio cell without any physical contact. The combination of multiple active pipettes set on the micro robots demonstrated to provide the complicated manipulation for making the cell operation such as an accurate injection.

ACKNOWLEGEMENTS

A part of this project is supported by Industrial Technology Research Grant Program in 2005 from New Energy and Industrial Technology Develpment(NEDO) of Japan

REFERENCES

[1]Ohmi Fuchiwaki, Nobuyuki Tobe Hisayuki Aoyama, Daigo Misaki, Takashi Usuda,Automatic Micro-Indentation and Inspection System by Piezo Driven Micro Robot with Multiple Inner Sensors,Proc. of the IEEE International Conf on Mechatronics & Automation, pp.83 -88,NiagaraFalls,(2005)

[2]Daigo Misaki, Ohmi Fuchiwaki, Naoto Chiba, Hisayuki Aoyama, Micro •@Robotics and Its Bio-Applications,Proc. of International Confer ence on Precision Engineering and Micro/Nano Technology in Asia, pp.630-634(Shenzhen,China) (2005)

NEW HYBRID ACTUATOR DESIGN WITH NANOMETER RESOLUTION

Rainer Gloess
R&D Department, Advanced Mechatronics
Physik Instrumente (PI) GmbH & Co.KG
Karlsruhe, Germany

INTRODUCTION

Over many years the precise positioning technology was developed primarily for the semiconductor industry. This field requires mainly two-dimensional positioning with high accuracy. With the emergence of nanotechnology came the need for new types of precision positioning tools that go beyond the requirements of the conventional semiconductor sector. The functional structures of nano-devices are on the nanometer or even picometer range. Yet the dimensions of the entire devices are in most cases much larger. Thus, there are two new mechanical requirements: large travel ranges (up to one inch or more) and – at the same time – extremely accurate positioning with nanometer or sub-nanometer resolution. Furthermore, a higher number of axes is often necessary. The opto-electronic telecom market was the starting point for absolutely new technologies for many-axis alignment- often more than 12 axes. Nanotechnology requires still more resolution and accuracy. The paper describes a new design for single axis devices with extreme high resolution, high dynamics and high load capacity.

SYSTEM REQUIREMENTS

Nanotechnology envisions future positioning to occur by taking advantage of natural self-reproduction, replication, and nano-scale surface copying techniques. These exigencies can be met with a combination of various techniques: For example, motorized guided systems with incremental sensors can be used for large travel ranges.

Conventional serial positioners consist of several linear and rotary (goniometer) stages, which are mounted together in order to reach the desired number of degrees of freedom. In such a design, each single axis is simple to control, yet the overall system has some disadvantages: The system needs a lot of space, the stiffness decreases with increasing number of axes, and the dynamic behavior is axis-dependent (as the lower stages must carry the weight of the stages stacked on top). The stage cables also need to be moved, resulting in bending and friction. Most importantly, the position errors of the single stages accumulate for the overall system, resulting in large errors, often originating from rotary/tilt stage lever arms.

In high-speed nano-positioning applications, advantages of the parallel-kinematics approach over the stacked or nested serial kinematics systems is the ultra-low inertia resulting in higher resonant frequencies, faster step response, and higher scanning rates.

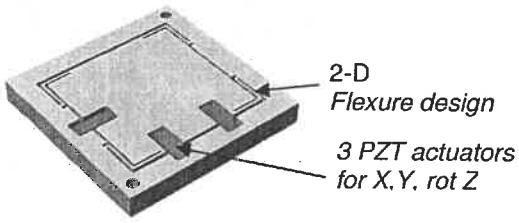

FIGURE. 1: Parallel approach in a piezo stage flexure design

Another advantage is active trajectory control on a sub-nanometer scale, which is possible when direct output metrology capacitive position sensors are integrated. Since each position sensor monitors the common platform, the smallest axis crosstalk effects are detected and can be compensated for in real time. This results in higher linearity and straighter scanning lines.

PIEZO TECHNOLOGY FOR ULTRA-HIGH PRESISION POSITIONING

One of the long-term objectives of nanotechnology – to realize von Neumann architecture for self-replicating systems – is still far from being realized on a large scale. But for studying the molecular structure of materials, accurate positioning systems down to picometer scale are necessary. Specially designed piezo

electrical positioners work on this scale. Paired with capacitive sensors, they allow for controlled sub-nm motion .

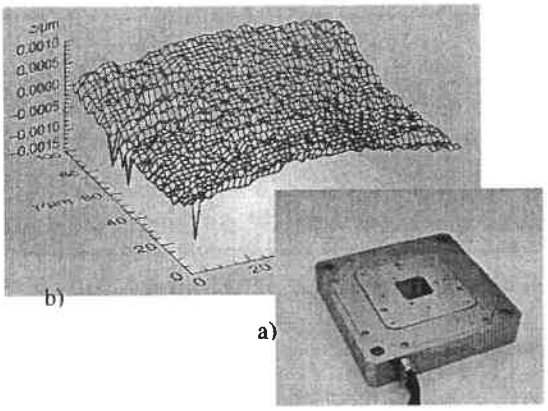

FIGURE 2 a) Reference-class piezo positioning stage with 6 degrees of freedom, made of Superinvar

FIGURE 2 b) 2D scan field with active z-error correction. Performance is better than 0.5 nm over 100x100 µm scan range.

The basic control function of piezo systems is more simple than of motorized systems, because piezo systems have a constant transfer function up to the resonance peak.
The linearized transfer function of piezo actuators can be approximated as follows:

$$T_z(p) = \frac{K_a}{1 + 2D\frac{1}{\omega_0}p + \left(\frac{p}{\omega_0}\right)^2} \qquad (1)$$

K_a Gain
D Damping coefficient
ω_0 Resonant Frequency

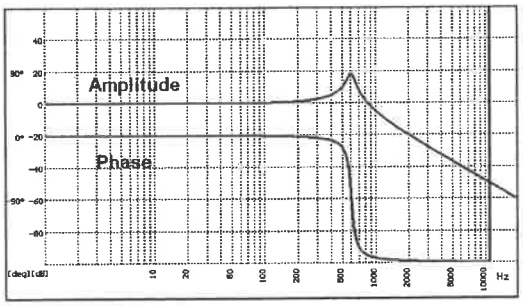

FIGURE 3: Transfer function of a piezo system $T_z(p)$

With the Nyquist criterion it can be shown that a simple PID controller function may be stable but can not offers very fast control conditions. At least a notch filter should be added into the control path, to cancel the resonant frequency peak and improve the stability. [1]

If $T_l(p)$ is the open loop transfer function defined as:

$$T_L(p) = T_C(p)*T_N(p)*T_A(p)*T_Z(p)*T_S(p) \qquad (2)$$

Where T_C is the PI-Controller transfer function, T_N is for the notch filter, T_A for the amplifier and T_S for the sensor. The Z-plane shows the real and the imaginary part over the frequency.

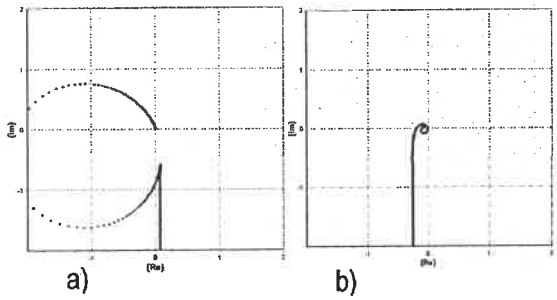

FIGURE 4: Z-plane of the Open loop transfer function a) without notch filter b) with notch filter

At PI, various methods were developed to overcome the non-linearity (hysteresis effects) as well as the creep of piezo ceramics.
The transfer function of the notch filter can be described as:

$$T_N(p) = \frac{1 + \left(\frac{p}{\omega_n}\right)^2}{1 + \frac{p}{D_n\omega_n} + \left(\frac{p}{\omega_n}\right)^2} \qquad (3)$$

D_n Damping coefficient notch filter

The Notch filter frequency is set to the system resonant frequency to avoid controller instability at this point.

$$\omega_n = \omega_o \qquad (4)$$

The transfer function of the PI (proportional/integral) term can be set to:

$$T_c(p) = \frac{K_p \cdot \left(T_i \cdot p + T_i T_g \cdot p^2\right)}{T_i p + T_i T_g \cdot p^2} \quad (5)$$

Kp	Gain
T_i	I-term time constant
T_g	Smoothing term
ω_0	Resonant Frequency

In combination with analog or digital control methods, including methods to avoid non-linearity and creep, the transfer functions of compensated piezo systems offer linear properties in the frequency domain for amplitude and phase control.

HYBRID STACKED SYSTEMS

Electromagnetic drives alone are limited in positioning accuracy due to their noise level and the stiffness relation to the guiding system. However, in combination with high-precision piezo technology, they are a very powerful tool for nano-positioning over a millimeter range. A special design principle is to combine piezo ultrasonic systems with piezo actuated stages. Piezo ultrasonic systems can reach high dynamic performance and can be controlled to very smooth motion. Additionally, if the ultrasonic system is switched off, the self-locking effect is very helpful for long-term stability and the fine adjustment with the piezo stage.

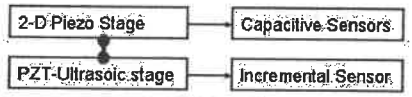

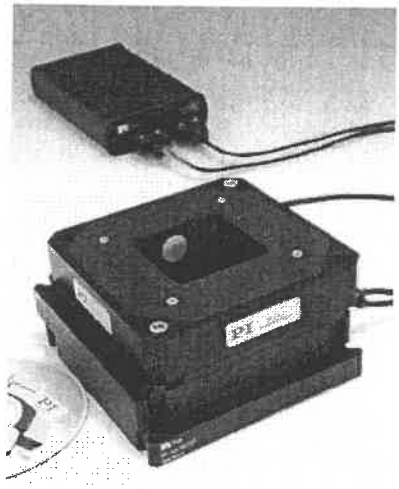

FIGURE 5: 2-dimensional piezo ultrasonic positioner combined with a 2-D Piezo stage

NEW HYBRID POSITIONING SYSTEM

The new hybrid system is the integration of one extreme high resolution incremental sensor into a stage which is driven by both - piezo and motor (or piezo-ultrasonic) actuator at the same time.

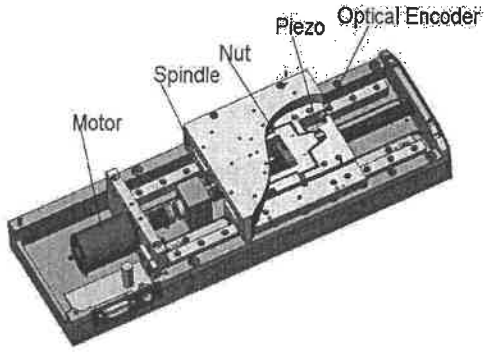

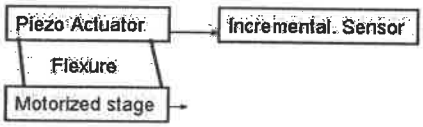

FIGURE 6: Mechatronic Hybrid system: High resolution optical incremental sensor with 2nm resolution. Motor driven stage combined with flexure guided piezo actuator for 100mm travel range.

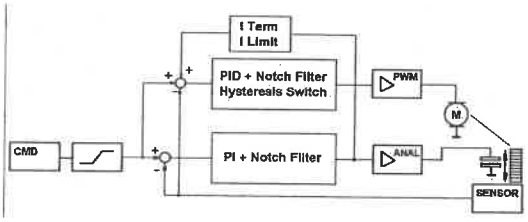

FIGURE 7: Embedded controller for hybrid system

The developed controller based on an embedded controller with hardware clock buffered sensor inputs and synchronized output buffer. The motor is driven by a PWM generated signal and the piezo amplifier is driven by a 24bit D/A converter. The sampling rate can be set between 1kHz and 200kHz, 10kHz are used for the first tests. The real time operating system "OnTime" has a very fast interrupt latency time of less than 1.5µs in worst case. Because both actuators – the piezo and the motor are working on the same stage, it is necessary to separate the control frequencies in the controller for both different drives. The piezo is used in a higher bandwidth than the motor is working. The tests show that the frequency separation should be larger than a factor of two.

The structure of the current controller has another feature: there is an integral term added between the piezo and the motor path. This term degree the piezo voltage for settling down to some volts – save for long term operation.

TEST RESULTS

A compact stage with 2µm optical scale from Heidenhain GmbH and a special 1000 time interpolation unit was designed to get a final resolution of 2nm. A super finished spindle and a small piezo with +/-2µm stroke where used. The interfacing between the stage and the controller is done by a SSI bus to get high transfer rate for the sensor data for fast motion. The small range step response is dominated by the piezo part in the system. Because of the flexure design, the stage has a very small hysteresis. Moved steps down to the resolution of the scale can be measured.

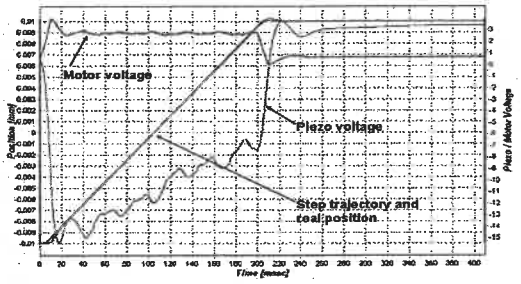

FIGURE 8: 20µm step with small overshoot to demonstrate the continuously driving mode of both actuators. The motor and the piezo are actuated at any time. The piezo voltage is controlled within a range of +/-10V for the final position (maximum +/- 36 V).

At any time both actuators – the motor and the piezo – are driven from the controller. If the piezo voltage exceed more than 10V an additional integral-term is used to drive the stage with more motor power into the position stroke of the piezo. The stage design use a piezo stroke of +/- 2µm at the moment.

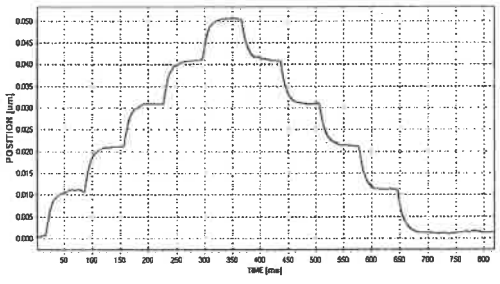

FIGURE 9: Step response of the hybrid stage for 10nm steps measured with external laser interferometer

In dynamic motion operation the piezo actuator compensates friction and roughness influence as shown in figure 10.

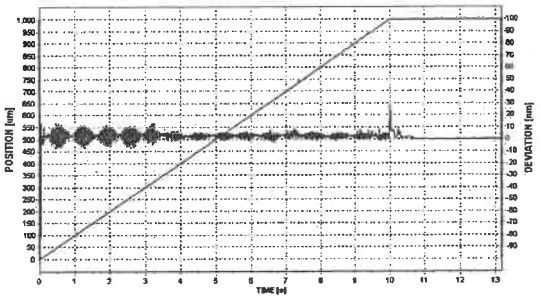

FIGURE 10: 1mm motion of the hybrid stage (velocity= 100µm/s) The deviation from the trajectory is less than 10nm. Some influence from the resonant frequency should be cancelled in future design.

5 SUMMERY

The investigation in nanotechnology requires new positioning tools with extremely high resolution combined with a large travel range. In new hybrid stage design the piezo part should be separated via flexure design and should be operate with only one incremental sensor. For high resolution hybrid systems a new type of embedded controller and a two path control algorithm shows successful results for smallest steps as for long travel range with nano/ picometer resolution.

REFERENCES

[1] R.Gloess: „Systeme zur Nanopositionierung", Teil2, F&M, Jahrg.108 (2000), Carl Hanser Verlag München, ISSN 0944-1018, 72-78

OPTIMAL TUNING OF A BIAXIAL SERVOMECHANISM USING A CROSS-COUPLED CONTROLLER AND DISTURBANCE OBSERVERS

Min-Soo Jang[1], Seung-Chul Kim[1] and Sung-Chong Chung[1]
[1]Hybrid Systems Design & Control LABoratory
Department of Mechanical Design and Production Engineering
Hanyang University, SungdongGu, Seoul 133-791, KOREA

ABSTRACT
In order to improve the contouring accuracy of a biaxial servomechanism and the robustness against disturbance, a cross-coupled controller with a disturbance observer is studied, as well as the optimal tuning based on the integrated design methodology is proposed. Strict mathematical modeling and identification process of a servomechanism are performed first. An optimal tuning problem is formulated as a nonlinear constrained optimization problem including the relevant controller parameters of a servomechanism. The objective of the optimal tuning procedure is to minimize both contour error and settling time while satisfying constraints, such as relative stability and overshoots, etc. The effectiveness of the proposed optimal tuning procedure is verified through experimental results.

KEYWORDS
Contour error, Cross-couple control, Disturbance observer, integrated design, Kharitonov's theorem, Optimal tuning, Robustness, Servomechanism

INTRODUTION
Today a high-speed and high-precision servo system is one of the most important elements in assembly, information and telecommunication, automation, and aviation industries. As time passes, more complex and precision techniques, such as several-axis control, are required. Systems ought to have high contour precision and robustness against disturbance. Ohnishi and Umeno [1] proposed a two-degree of freedom controller to improve positioning accuracy and robustness against disturbance. Koren [2] and Srinivansan [3] defined the contour errors in multi-axis systems, and proposed methods to reduce contour errors using cross-coupled controllers. However, it is very difficult to select controller parameters because the cross-coupled control system is a multivariable, nonlinear, and time-varying control system. An optimization approach to the cross-coupled control system using genetic algorithms was studied before [4], but it does not include information about its mathematical modeling and stability.

In this paper, an optimal tuning method based on mathematical models is proposed for a biaxial servomechanism. To derive the mathematical model for optimization, an integrated design methodology [5] is applied as a systematic design tool. Experiments are performed to verify the performance of the developed system.

SYSTEM IDENTIFICATION
Models of a mechanical subsystem including a velocity controller are obtained through system identification processes. In order to identify xy-table shown in Fig.1, Simulink and toolbox of MATLAB are used for the identification. As an input signal Gaussian PRBS (Pseudo Random Binary Sequence) torque command is used and the velocity signal of a motor is used as an output. The first and second order models of x and y axes obtained through the identification processes are as follows:

$$G_{mx}(s)=\frac{16442}{s^2+360.7s+46580} \qquad G_{mx}^{n}(s)=\frac{45.96}{s+111.9}$$

$$G_{my}(s)=\frac{22700}{s^2+401.9+54090} \qquad G_{my}^{n}(s)=\frac{55.52}{s+114.9}$$

CONTOUR ERROR
The objective of the cross-coupled control is to reduce contour errors, defined as the shortest distance between the desired and actual contours, by coupling two axes and controlling the relative movements, rather than to reduce position errors by controlling each axis independently. In order to implement the cross-coupled controller, it is required that contour error should be calculated correctly. In case of

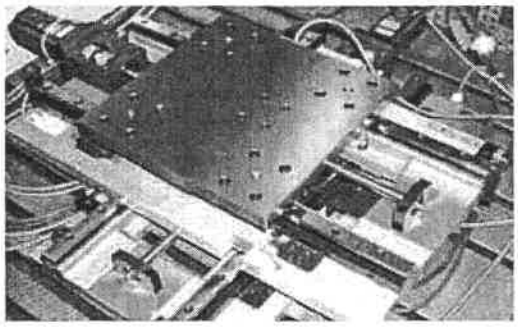

FIGURE 1. Experimental set-up (xy- table).

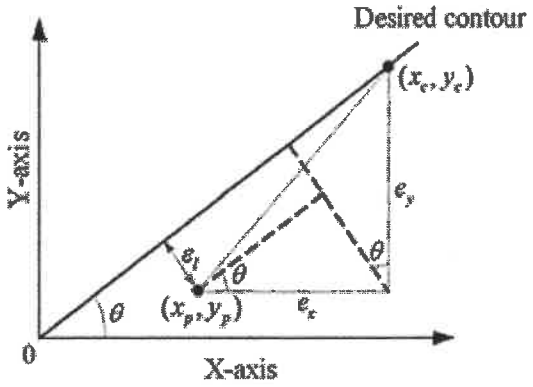

FIGURE 2. Contour error in linear motion.

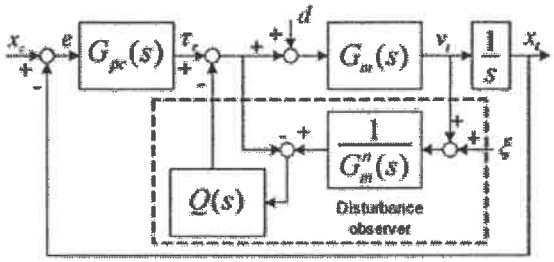

FIGURE 3. Block diagram of the disturbance observer.

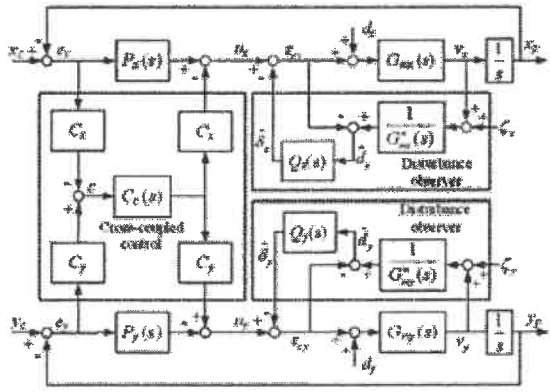

FIGURE 4. Block diagram of the overall system.

linear motion, the contour error is defined by ε_l as shown in Fig. 2. Using servo tracking errors, e_x and e_y, the contour error occurred in linear motion is given by

$$\varepsilon_l = -e_x \sin\theta + e_y \cos\theta \tag{1}$$

DISTURBANCE OBSERVER

In general, Q-filters have simple structure and good flexibility. They are appropriate to design a disturbance observer. Disturbance observer estimates disturbance using Q-filter as shown in Fig.3. Q-filters determine characteristics of disturbance observers. Disturbance elimination performance depends upon Q-filters. The velocity output v_t of the servo is represented with respect to the control input τ_r, disturbance d and measurement noise ξ as follows:

$$v_t = G_{\tau_r v_t}(s)\tau_r + G_{dv_t}(s)d + G_{\xi v_t}(s)\xi \tag{2}$$

where

$$G_{\tau_r v_t}(s) = \frac{G_m(s)G_m^n(s)}{G_m^n(s) + \{G_m(s) - G_m^n(s)\}Q(s)} \tag{3}$$

$$G_{dv_t}(s) = \frac{G_m(s)G_m^n(s)\{1 - Q(s)\}}{G_m^n(s) + \{G_m(s) - G_m^n(s)\}Q(s)} \tag{4}$$

$$G_{\xi v_t}(s) = -\frac{G_m(s)Q(s)}{G_m^n(s) + \{G_m(s) - G_m^n(s)\}Q(s)} \tag{5}$$

If $|Q(j\omega)|=1$, Eqs. (4) ~ (6) are given by

$$G_{\tau_r v_t}(s) \approx G_m^n(s) \tag{6}$$

$$G_{dv_t}(s) \approx 0 \tag{7}$$

$$G_{\xi v_t}(s) = -1 \tag{8}$$

Therefore, the real plant G_m acts like the nominal plant G_m^n and the effects of disturbance cancel each other. In this paper, the Q-filter should be selected to reduce disturbance in the low frequency region as $|Q(j\omega)|=1$, and eliminate measurement noise in the high frequency region as $|Q(j\omega)|=0$. Therefore, following type of the Q-filter is selected for the disturbance observer:

$$Q(s) = \frac{1 + \sum_{k=1}^{N-r} a_k (\tau s)^k}{1 + \sum_{k=1}^{N} a_k (\tau s)^k} \tag{9}$$

OVERALL SYSTEM

The structure of the overall system that combines the cross-coupled control system with a disturbance observer is constructed as shown in Fig. 4. In this paper, controllers, Q-filters and mechanical subsystems for the biaxial servo are defined as follows:

$$P_x(s) = K_{px} + \frac{K_{ix}}{S}\ ,\ P_y(s) = K_{py} + \frac{K_{iy}}{S}$$

$$C_c(s) = K_{pc}$$

$$Q_x = \frac{1}{\tau_x S + 1}\ ,\ Q_y = \frac{1}{\tau_y S + 1}$$

$$C_x = \sin\theta\ ,\ C_y = \cos\theta$$

OPTIMAL TUNING PROCESS

Dynamic equations of the overall system including the mechanical subsystem are represented as a state space equation. Contrary to the cross-coupled control system for linear motions, the cross-coupling gains for circular motion are nonlinear and time-varying. It is difficult to represent this type of system in a state space equation. However, all curves can be converted into a sequence of micro straight lines by an interpolator. Therefore, the cross-coupled control system for an arbitrary curve is formulated by a state-space equation based on a series of linear motion trajectories.

In this paper, the objective of optimal tuning is to improve the response and contour accuracy. Optimal tuning of the multi-objective function is performed to minimize the settling time and the contour error as [7]

$$F(\mathbf{x}) = w_1\varepsilon_l + w_2 t_s \qquad (10)$$

w_1 and w_2 are weighting factors of each objective function, ε_l is contour error, and t_s is settling time, respectively.

Modeling errors and uncertainties occur during system identification. Stability of the system has to be considered to tune the control gains. In order to secure robustness of the designed system in spite of the existence of uncertainties, relative stability criteria ought to be considered. Kharitonov theorem [6] is applied to consider the relative stability of the system which is formulated by the state-space equation. In order to secure the relative stability of the system with an uncertain parameter vector $\mathbf{q}$ in Eq. (11), following four polynomials called Kharitonov polynomials are obtained using the characteristic equation of the system.

$$\mathbf{q} = [n_{x1}\ m_{x1}\ m_{x2}\ n_{y1}\ m_{y1}\ m_{y2}]^T \qquad (11)$$

where

$$n_{i1} \in [n_{i1}^-; n_{i1}^+],\ m_{ij} \in [m_{ij}^-; m_{ij}^+],\ i = x, y,\ \ j = 1, 2$$

$$P^{++}(s,\mathbf{q}) = s^{10} + \alpha_9^+ s^9 + \alpha_8^+ s^8 + \alpha_7^- s^7 + \cdots + \alpha_1^- s + \alpha_0^-$$
$$P^{--}(s,\mathbf{q}) = s^{10} + \alpha_9^- s^9 + \alpha_8^- s^8 + \alpha_7^+ s^7 + \cdots + \alpha_1^+ s + \alpha_0^+$$
$$P^{+-}(s,\mathbf{q}) = s^{10} + \alpha_9^+ s^9 + \alpha_8^- s^8 + \alpha_7^+ s^7 + \cdots + \alpha_1^+ s + \alpha_0^-$$
$$P^{-+}(s,\mathbf{q}) = s^{10} + \alpha_9^- s^9 + \alpha_8^+ s^8 + \alpha_7^- s^7 + \cdots + \alpha_1^- s + \alpha_0^+$$

where

$$\alpha_i^+ = \max \alpha_i(\mathbf{q}),\ \alpha_i^- = \min \alpha_i(\mathbf{q}),\quad i = 1 \sim 9$$

If the roots of the Kharitonov polynomials have all negatives, the system is stable in spite of its uncertainty. If only the response of the system is considered, an excessive amount of overshoot occurs. To limit the overshoots, they should be considered as constraints. The Sequential Quadratic Programming (SQP) algorithm and optimum toolbox of MATLAB are applied to optimal tuning [7]. Plant uncertainty of ±1%, feedrate of 1*m/min* and weighting factors of $w_{1,2}$=0.5 are given for optimal tuning conditions. Table 1 shows constraints used in the optimal tuning procedure.

EXPERIMENTS

In order to verify the effectiveness of optimal tuning, experiments are performed in a precision x-y positioning system with a sampling period of 1*msec*. Instead of a circular motion 1024-polygon motion with the radius of 50*mm* is performed at the speed of 1*m/min*.

Fig. 5 shows the optimal tuning result when the xy-table is controlled only by the cross-coupled controller. Good control performance is obtained in areas where the direction of motion changes. On the other hand, the optimal tuning result obtained only through the disturbance observer shows better performance in areas where the direction of motion is constant as shown in Fig. 6. Fig. 7 shows the optimal tuning result obtained when the two controllers are combined together as shown in Fig. 4. Combining two controllers, good performance is obtained in various types of motion.

Table 1.Constarints for the optimal tuning.

Description	Equation
Relative stability	$g_1 : s_i^{++} < 0,\ s_i^{++} = \{s : P^{++}(s) = 0\},\ i = 1 \sim 10$ $g_2 : s_i^{--} < 0,\ s_i^{--} = \{s : P^{--}(s) = 0\},\ i = 1 \sim 10$ $g_3 : s_i^{+-} < 0,\ s_i^{+-} = \{s : P^{+-}(s) = 0\},\ i = 1 \sim 10$ $g_4 : s_i^{-+} < 0,\ s_i^{-+} = \{s : P^{-+}(s) = 0\},\ i = 1 \sim 10$
Maximum overshoot	$g_5 : M_x(\theta) < 5\%$ $g_6 : M_y(\theta) < 5\%$ $\quad (0^\circ \le \theta \le 90^\circ)$ $M_x = \dfrac{\max(x_p(t)) - x_{ss}}{x_{ss}} \times 100\%$ $M_y = \dfrac{\max(y_p(t)) - y_{ss}}{y_{ss}} \times 100\%$

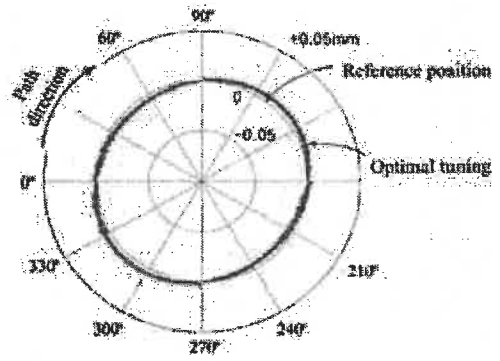

FIGURE 5. Cross-coupled control case.

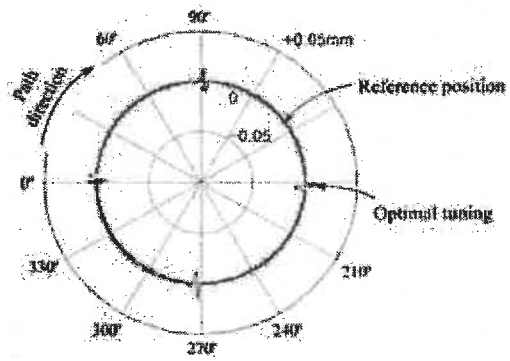

FIGURE 6. Disturbance Observer case.

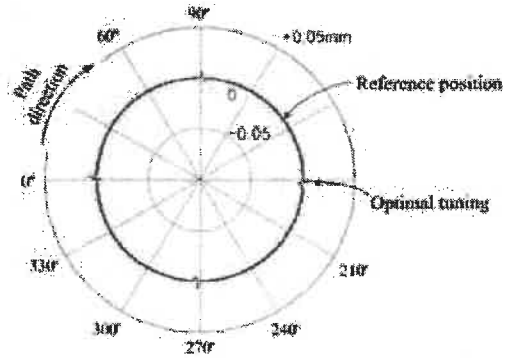

FIGURE 7. Cross-coupled control and Disturbance observer case.

CONCLUSIONS

The cross-coupled controller and disturbance observer are used to improve the response characteristics, contour accuracy and robustness against disturbance. The Optimal tuning method based on the integrated design method is proposed, and experiments are conducted on the xy-table. Experiments show that the contour error of the system with the optimal tuning results applied to it was smaller than any other systems. Combining the cross-coupled controller and the disturbance observer better performance is obtained in various types of motion.

REFERENCES

1. Umeno, T., Kaneko, T. and Hori, Y., 1993, "Robust Servosystem Design with Two Degrees of Freedom and its Application to Novel Motion Control of Robot manipulators,", *Transactions on Industrial Electronics*, Vol. 20, No.5, pp.473~485
2. Koren, Y., 1980, "Cross-Coupled Biaxial Computer Control for Manufacturing Systems," *ASME Journal of Dynamic Systems, Measurement, and Control*, Vol.102, No.4, pp.265~272.
3. Srinivasan, K. and Kulkarni, P. K., 1990, "Cross-Coupled Control of Biaxial Feed Drive Servomechanisms," *ASME Journal of Dynamic Systems, Measurement, and Control*, Vol.112, No.4, pp.225~232.
4. Tarng, Y. S., Chuang, H. Y. and Hsu, W. T., 1997, "An Optimization Approach to the Contour Error Control of CNC Machine Tools Using Genetic Algorithms," *International of Advanced Manufacturing Technology*, Vol.13, pp.359~366.
5. Kim, M. S. and Chung, S. C., 2005, "A Systematic Approach to Design High-Performance Feed Drive Systems," *International Journal of Machine Tools and Manufacture*, Vol.45, pp.1421~1435.
6. Ackermann, J., et al., 1993, *Robust Control: Systems with Uncertain Physical Parameters*, Springer-Verlag, London.
7. Bae, H, K, and Chung, S. C., 2006, "Optimal Tuning of Biaxial Servomechanisms using a Cross-Coupled Controller," *Transactions of NAMRI/SME*, Vol. 34, pp. 603~610.

FABRICATION OF A NEW POSITION SURVEYING SYSTEM FOR THE UNDERGROUND PIPES USING ROTARY ENCODERS

Toshiaki HAMANO[1], Manabu ONO[2] and Shigeo KATO[1]
[1]Nippon Institute of Technology, Saitama, Japan
[2]Tokyo Metropolitan College of Industrial Technology, Tokyo, Japan

1. INTRODUCTION

Optical fiber cable for the broad bands communication is usually covered by plastic pipe and buried under the ground. Then, we are required to grasp its real buried position before digging at the construction or the maintenance in order to prevent from the cutting of the optical fiber. However, once the optical fiber cable is buried under the ground, it is very difficult to confirm the buried position of the pipe, because the optical fiber cable and plastic cover pipe are not the metal. A former way to confirm the buried position of the optical fiber cable is the ground penetrating radar method.[1]-[3] The ground penetrating radar method is very useful for the metal. However, the optical fiber cable in plastic cover pipe is not metal.

Fortunately the cover pipe of the optical fiber cable goes through utility holes that are arranged in the hundreds meter interval. If we can insert a surveying mechanism into the cover pipe at the utility holes and detect directly the information of the buried position of the pipe by a new position surveying system that can move itself in the pipe, the problem of the former way to confirm the buried position of the optical fiber cable is solved.This research aims to identify easily the buried position of the pipe, using the information of the buried position from the pipe. We use two rotary encoders that have pulleys contacting right and left walls of the buried pipe in order to detect directly the information of the buried position of the pipe. Output of the rotary encoder contacting the wall shows the length of the wall. Average of summation of the outputs of the right and the left rotary encoder shows moving distance of a surveying mechanism of the position surveying system. The curvature of the buried pipe is obtained by difference of the outputs of the right and the left rotary encoder. The position of buried pipe is identified by the moving distance and the curvature of the pipe. It is confirmed that the new position surveying system can identify the buried position of a pipe that is 20 m long and has loose curvature in the error of 5.6 mm.

2. PRINCIPLE OF POSITION SURVEYING

Length of walls of both side of a pipe is same if the pipe is straight. If the pipe curves toward right, the length of the right wall is shorter than the length of the left wall. We measure the lengths of both side of the pipe by two rotary encoders that have pulleys. The principle of position surveying using two rotary encoders is shown in Fig. 1. Inner diameter of the pipe that has loose curvature is D. The original point is P_0 $(x_0,\ y_0)$. Present position of the surveying mechanism is P_n $(x_n,\ y_n)$. Angle between the tangential line and the x-axis is Θ. It is assumed that a difference ε is made by the both side rotary encoders when the surveying mechanism moves a small distance of s. This moved point is $P_{n+1}(x_{n+1},\ y_{n+1})$. The normal lines that cross points P_n $(x_n,\ y_n)$ and P_{n+1} $(x_{n+1},\ y_{n+1})$ make an angle θ. The radius of the curvature is assumed as R. The surveying mechanism may incline by some rolling force. The rolling angle is assumed as ϕ. Projection of the pulley is D_1 and is shown as

$$D_1 = D\cos\phi \tag{1}$$

The difference ε of the right and left rotary encoders is shown as

$$\varepsilon = \left(s+\frac{\varepsilon}{2}\right)-\left(s-\frac{\varepsilon}{2}\right)=\left(R+\frac{D_1}{2}\right)\theta-\left(R-\frac{D_1}{2}\right)\theta = D_1\theta \tag{2}$$

Then, the small angle θ is obtained as

$$\theta = \frac{\varepsilon}{D_1} \tag{3}$$

The x-coordinates and the y-coordinates of P_{n+1} are calculated from the x-coordinates and the y-coordinates of P_n as

$$x_{n+1} = x_n + s\cdot\cos(\Theta+\theta) \tag{4}$$

$$y_{n+1} = y_n + s\cdot\sin(\Theta+\theta) \tag{5}$$

The tangential angle Θ is the summation of the small angle θ and shown as

$$\Theta = \Sigma\theta \tag{6}$$

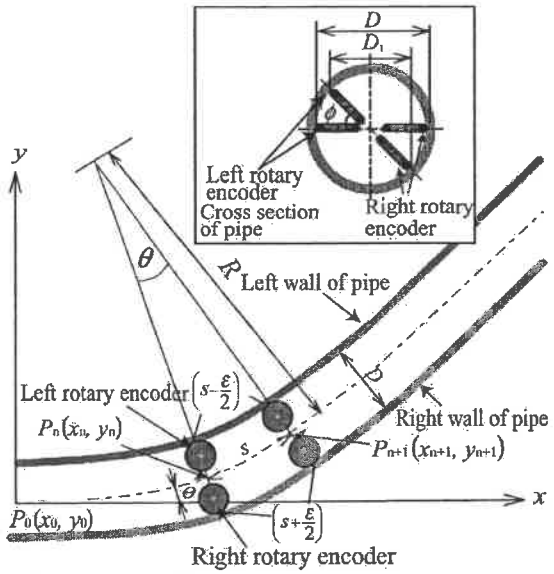

FIGURE 1. The principle of the position surveying in the underground pipe by in-pipe surveyor using rotary encoders

3. PIPE FOR SURVEYING EXPERIMENT

3.1 Coordinates of the pipe for surveying experiment

Pipe for surveying experiment is shown in Fig. 2. The pipe consists of two straight pipes and a curved pipe. The first straight pipe is 8000 mm long. The second curved pipe has a curvature radius of 36500 mm and is 4000 mm long. The third straight pipe that is attached the second pipe and is 8000 mm long. The *x*-axis of the pipe for surveying experiment is standardized by a fishing line that is 0.05 mm in diameter and is intensely tightened. Distance from the original point that is the *x*-coordinates is measured by a tape measure. The *y*-coordinates is measured by steel measure from the standard line of the fishing line. 199 *x*-coordinates are obtained, because measure is done from the original point to 19800 mm every 100 mm. The *y*-coordinates at 19800 mm of the *x*-axis is 1121 mm. The distance of 100 mm is divided into 30 in the computer, because 100 mm is coarse. Interval is 3.33 mm and number of the position coordinates is 5941. This is called as the experimental position coordinate. Errors by the division occur at the curved pipe. However, maximum of errors is less than 0.034 mm.

3.2 Small angle of the pipe for surveying experiment

Here, the ideal pipe for surveying experiment is

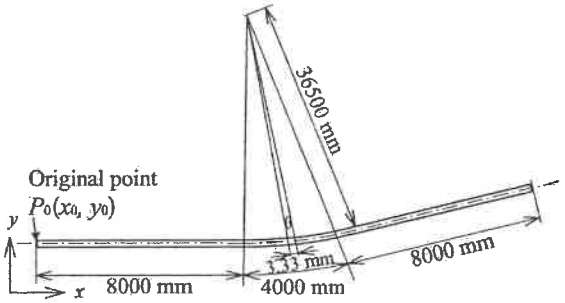

FIGURE 2. Pipe for surveying experiment

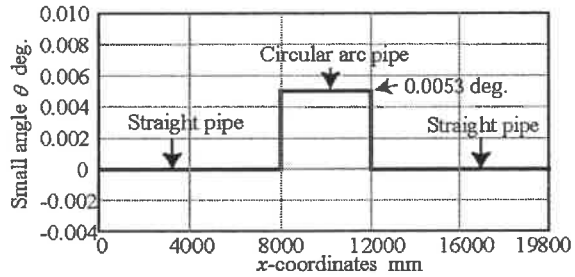

FIGURE 3. The small angle θ of the ideal pipe

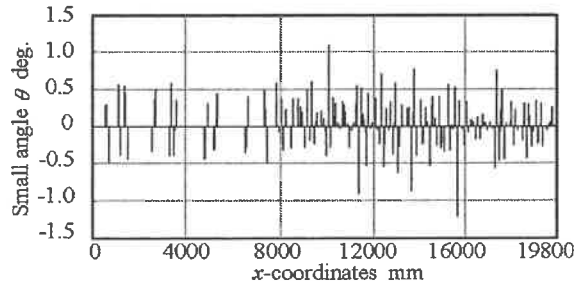

FIGURE 4. The small angle θ obtained from position coordinates of the pipe for experiment measured by the steel measure

assumed to consist from two complete straight pipes the circular arc pipe that exists between 8000 mm and 12000 mm and a complete circular arc and the small distance *s* is assumed to be 3.33 mm. Then, the small angle is 0 degree at the straight pipes and 0.0053 degrees at the circular arc pipe that exists between 8000 mm and 12000 mm of the *x*-coordinates. The small angle θ of the ideal pipe is shown in Fig. 3. Using Eqs. (4), (5) and (6), the small angle θ and the tangential angle are calculated from position coordinates of 5941 points. Relationship between the small angle θ and *x*-coordinates is shown in Fig. 4. The small angle of 0.0053 degrees that is shown in Fig. 3 is not seen in Fig. 4, because there exist errors larger than 1 degree.

3.3 Averaging process for decreasing of errors

We introduce averaging process in order to decrease large errors. Some small angle θ_n is assumed to be an average of three continuous small angles.

That is,

$$\theta_n = \frac{\theta_{n-1} + \theta_n + \theta_{n+1}}{3} \quad (7)$$

Small angles at both ends do not change. By the averaging process, all small angles except both ends are averaged and changed. The large error is changed to small error. The averaging process of 10000 times is done. The result of the averaging process is shown in Fig. 5. Errors are decreased to the order of 0.001 degrees at the straight pipe. Maximum of small angles at the curved pipe that exist between 8000 mm and 12000 mm of x-axis are 0.004 degrees or 0.007 degrees. These small angles are approximate as the small angle 0.0053 degrees of the ideal pipe. Substituting small angles shown in Fig. 5 into Eqs. (4), (5) and (6), 5941 position coordinates are obtained. These are called as calculated position coordinates. Difference between the calculated position coordinates and the measured position coordinates is shown in Fig. 6. Maximum difference is about 1.7 mm at the curved pipe. We use the calculated position coordinates as the standard position coordinates, because the error of the measured position coordinates is considered to be decreased by the averaging process of 10000 times.

4. POSITION SURVEYING SYSTEM

A new position surveying system for underground pipes is shown in Fig. 7. The system consists of a surveying mechanism that carries the right and left rotary encoders, a signal processor, an I/O interface and a computer. A weight is attached under chassis in order to prevent rolling of the surveying mechanism. However, rolling of the mechanism can not be prevented perfectly. So, rolling angle ϕ is measured by an another rotary encoder that is attached the chassis. The right and left encoders are held by arms that have pin joints and are attached the chassis of the surveying mechanis. Resolution of the rotary encoder is 44 μm. Software in the computer calculates locus of the surveying mechanism.

5. SURVEYING RESULTS BY THE POSITION SURVEYING SYSTEM

5.1 Measured small angle

We measure the position coordinates of the pipe for surveying experiment by the surveying mechanism. A sampling frequency from the rotary encoder is 20 Hz. Number of the sample is about 6800. The small distance s is about 3 mm. Obtained small angles are shown in Fig. 8. The small angle at the ideal straight must be 0 degree. However, there exist errors from 0.2 degrees to 0.4 degrees and 1 degree at 16000 mm of x-axis. The error is considered to occur at the joint bump of pipes that are 4000 mm long.

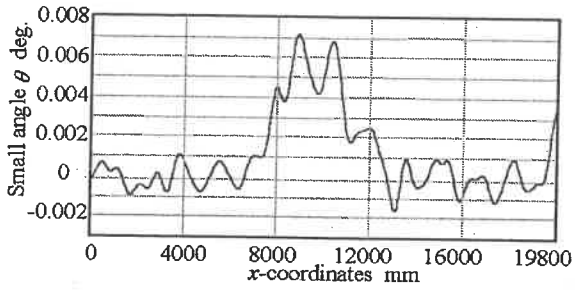

FIGURE 5. The small angle θ obtained from position coordinates of the pipe for experiment measured by the steel measure and averaged using the averaging process

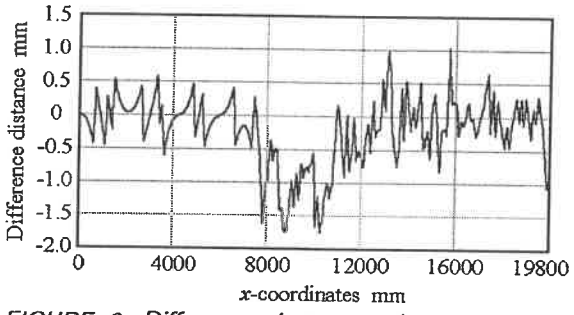

FIGURE 6. Difference between the calculated position coordinates and the measured position coordinates

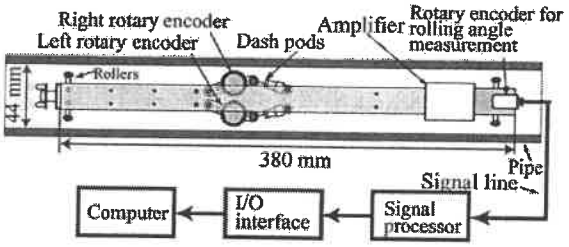

FIGURE 7. Structure of the position surveying system

5.2 Decreasing of measured error

Large error must be eliminated, because it severely affects afterwards calculation of the

position coordinates. A threshold that is a value of the large error is discussed. Optimal threshold is confirmed to be ±0.55 degrees. The difference between the position coordinate by the rotary encoder and the position coordinate by the steel measure is smallest at the optimal threshold. The small angles that are eliminated over the optimal threshold are shown in Fig. 9. The small angles that are measured by rotary encoders are averaged by using Eq. (7). Number of averaging is 10000. The averaged small angles by the rotary encoder are shown in Fig. 10 by dark line. The averaged small angles by the steel measure are also shown in Fig. 10 by gray line. They are similar.

5.3 Result of position surveying

The position coordinate by the rotary encoders and the position coordinate by the steel measure are obtained from the small angles shown in Fig. 10. Difference of both position coordinates is shown in Fig. 11. Maximum of the difference occurs at the curved pipe and is 5.6 mm. Difference of both position coordinates without the threshold processing is also shown in Fig. 11. The threshold processing is confirmed to be very effective.

6. CONCLUSIONS

1. We fabricated a position surveying system for underground pipes using two rotary encoders. Two rotary encoders measure distance of right and left walls of the pipe.
2. Some small angle is assumed to be an average of three continuous small angles. Averaging of 10000 times can decrease the measured error.
3. It was confirmed that the fabricated position surveying system can survey the position of the experimental underground pipe that consists of two 8000 mm straight pipes and 4000 mm curved pipe that has the curvature radius of 36500 mm in the error of 5.6 mm.

REFERENCES

[1] M. Sato, Subsurface Imaging by Ground Penetrating Radar, Society of The Institute of Electronice Information and Communication Engineers Trans. , Vol. J85-C No. 7 (2002), pp. 520-530.

[2] M. Tanaka, J. Takayama, S. Ohyama Imaging Process Based on Bistatic Scanning for Subsurface Radar, Trans. on Society of Instrument and Control Engineering, Vol. 39 No. 4 (2003), pp. 325-331.

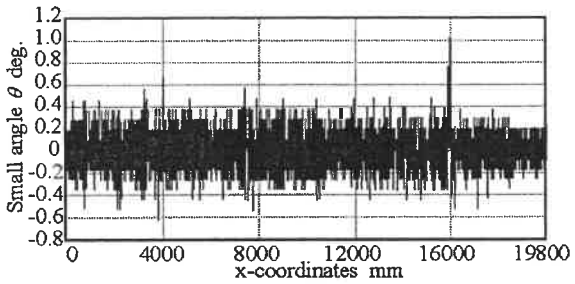

FIGURE 8. The small angle measured by rotary encoders of the position surveying system

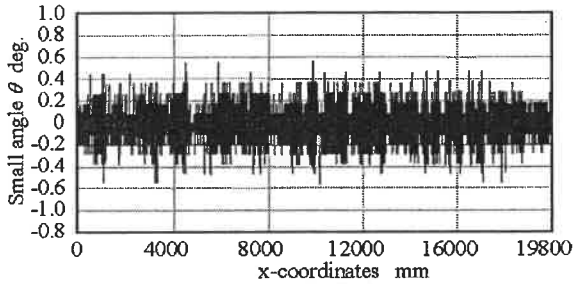

FIGURE 9. The small angle eliminated over the optimal threshold

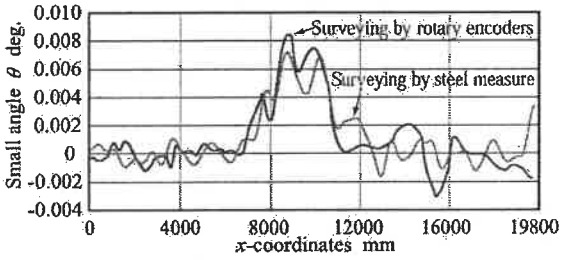

FIGURE 10. The small angle after using threshold processing and averaging processing

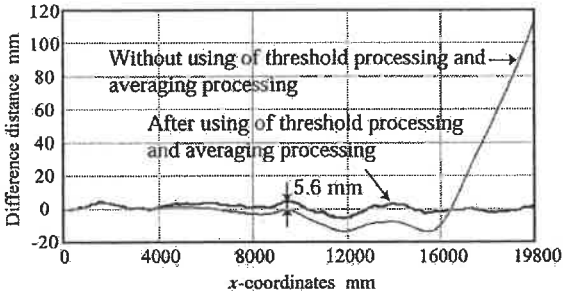

FIGURE 11. Difference between the position coordinates measured by rotary encoders and the calculated position coordinates measured by steel measure

[3] T. Miwa I. Arai, Estimaion of position of buried pipes using MUSIC algorithm with transmitting and receiving array, Technical Report of IEICE(2001), pp. 65-72

AN IN-PIPE MOBILE INSPECTION ROBOT PROVIDED AN ARTIFICIAL INTELLIGENCE AND PASSABLE AT SEVERAL T-JUNCTIONS

Shigeo KATO[1], Takachika SUZUKI[1] and Manabu ONO[2]
[1]Nippon Institute of Technology
Miyashiro, Saitama 345-8501, JAPAN
E-mail: kato@nit.ac.jp
[2]Tokyo Metropolitan College of Technology, Shinagawa
Tokyo 140-0011, JAPAN
E-mail: mana@tokyo-tmct.ac.jp

1. INTRODUCTION

Many small diameter pipes that are gas or water pipelines must be inspected in order to protect the accident previously. Since these pipes are buried in the underground or buildings, it is very difficult to inspect the pipes from the outside. Moreover, the pipes have T-junction at the point where the main pipe and the branch pipe connect. Therefore, the inspection robot must recognize the T-junction by itself and turn the T-junction of rectangular. Authors have researched in-pipe robots that are driven by air pressure and can pass Y-junction and T-junction [1], [2], [3]. However, they could not recognize the junctions by themselves, because they have no optical sensors. Now, authors fabricate a robot that has an optical sensor and artificial intelligence and can pass the T-junction by itself. The fabricated robot is confirmed to recognize the T-junction and to move to the desirable direction of the pipe.

2. STRUCTURE OF THE ROBOT SYSTEM

A structure of the fabricated robot system is shown in Fig. 1. The robot system consists of an optical sensor unit, a robot, a comparator which compares signals from the optical sensor unit and the threshold, air feeding tubes and signal line, electromagnetic valves, a computer,

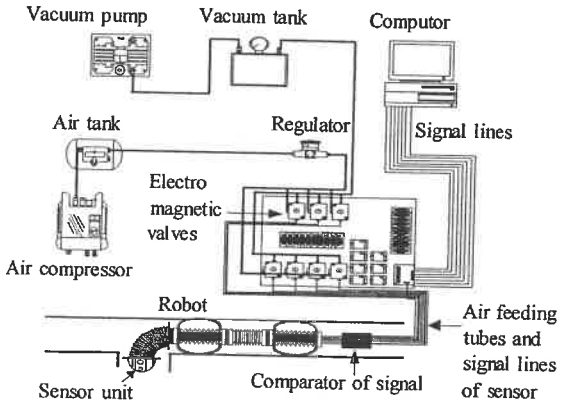

Figure 1. Structure of mobile robot system

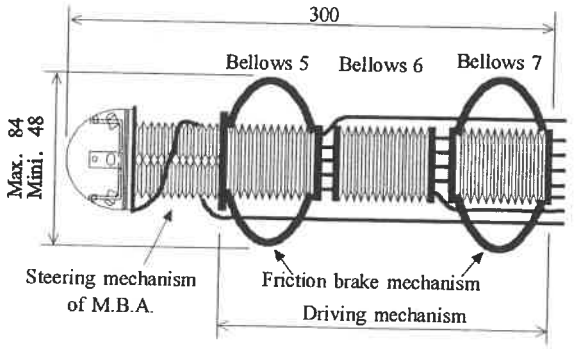

Figure 2. Structure of in-pipe robot

an electromagnetic valve controller, an air compressor which generates positive pressure and a vacuum pump which generates negative pressure.

2.1 Structure of the robot

Structure of the fabricated robot is shown in Fig. 2. The robot consists of a steering mechanism and a driving mechanism. The steering mechanism consists of a matrix bellows actuator (MBA) and is attached the front of the robot. The driving mechanism consists of three bellows that are 33 mm in outer diameter and 60 mm long. Three air-feeding tubes are independently connected to three bellows. Bulging brakes are provided to the Bellows-5 and Bellows-7. Friction brake mechanism consists of these bellows and bulging brakes. The bulging brakes are spread to radius direction and hold the pipe, when bellows of the friction brake mechanism is contracted. The bulging brakes are spread to longitudinal direction and cancel to hold the pipe, when bellows of the friction brake mechanism is stretched.

2.2 Structure of MBA and its movement

A structure of the MBA is shown in Fig. 3. The MBA consists of four bellows that are arrayed in a matrix. Each bellows is supplied positive and negative pressure independently. When the positive pressure is supplied to Bellow-2, -3, -4 and the negative pressure is supplied to Bellow-1, the head of the MBA is inclined to Bellows-1, because the bellows that is given negative pressure contracts and the bellows that is given positive pressure stretches. The MBA can steer the robot by a step of 45 degrees.

2.3 Control system of the robot

The positive pressure that is needed for stretching of the bellows is given by an air-compressor. The negative pressure that is needed for contracting of the bellows is given

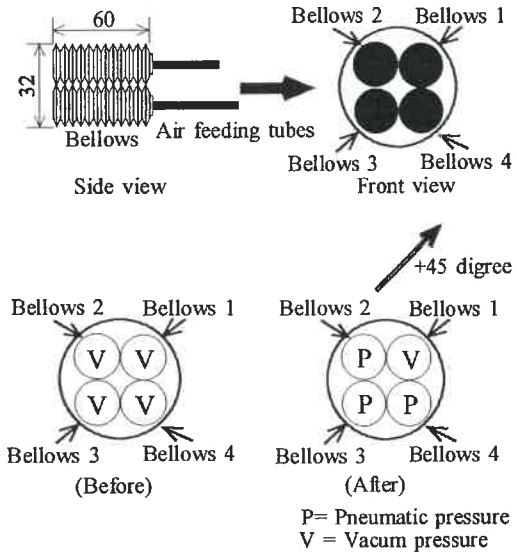

Figure 3. Structure of M.B.A.

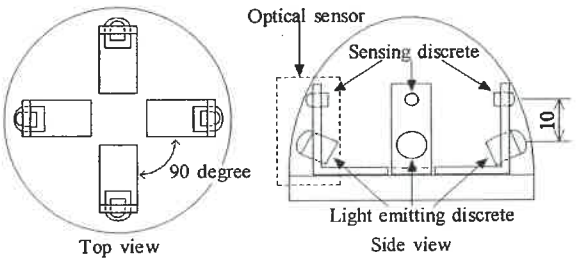

FIGURE 4. Structure of sensor unit

by a vacuum pump. The positive pressure and the negative pressure for bellows are switched by electromagnetic valves which are controlled by the computer through a valve controller. A control sequence is programmed in the computer. Since the computer can process the signal from the optical sensors, the computer can steer the robot for the direction that is desired by the operator.

2.4 Structure of the optical sensor unit

A fabricated optical sensor unit is shown in Fig. 4. The optical sensor unit consists of four optical sensors. The optical sensor consists of a light emission diode and a photo transistor.

3. MOVING PRINCIPLE

Moving principle of the robot is shown in Fig. 5. At Step-0, all of bellows are contacted by negative pressure and all of the friction brake mechanisms hold the pipe. At Step-1, the front friction brake mechanism cancels to hold the pipe. At Step-2, the front of the robot is moved to forward direction. At Step-3, the front friction brake mechanism holds the pipe and the rear friction brake mechanism cancels to hold the pipe. At Step-4, the rear end of the robot is moved to forward direction, because bellows-6 is contracted. After Step-4, the rear friction brake mechanism holds the pipe and the step returns to Step-0. During the cycle, the robot can move the displacement of the driving mechanism.

4. SENSING PRINCIPLE OF T-JUNCTION

Sensing principle of T-junction is shown in Fig. 6. The phototransistor produces analog voltage which depends on a received power of the light. At straight pipe, the phototransistor produces high voltage, because the light from the light emission diode is strongly reflected by wall of the straight pipe. At the T-junction, the phototransistor can not receive the light, because the light from the light emission diode is dissipated to the branch pipe at the T-junction and is not returned. The phototransistor produces only low voltage. Then, the T-junction is recognized by change that the phototransistor produces voltage.

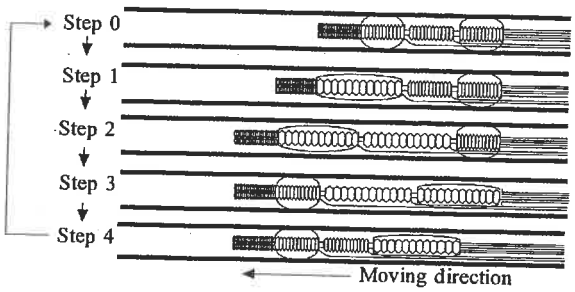

Figure 5. Moving principle of in-pipe robot

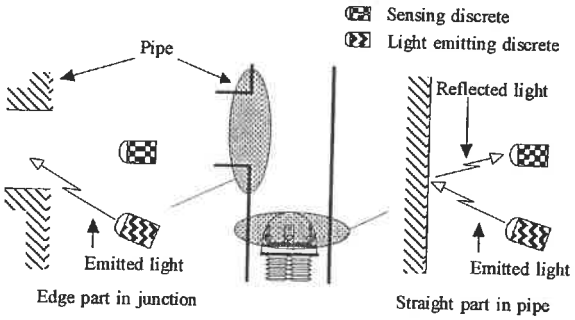

Figure 6. Sensing principle of T-junction

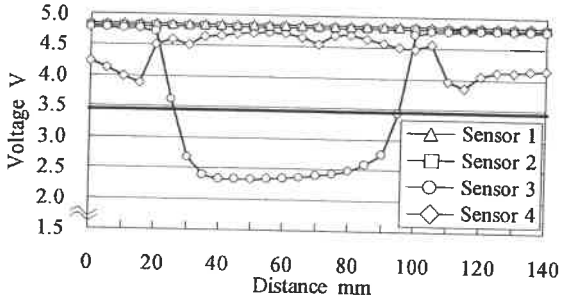

FIGURE 7. Output characteristics of sensor unit

Out put voltage of four phototransistors of the optical sensor unit is shown in Fig. 7. There are two edges of the junction at 20 mm and 100 mm of the distance. Sensor-3 is displayed to the direction of the junction. Therefore, the other sensors are displayed to the direction of the straight pipe. The output voltage which is produced by the sensor-3 is as lower as 2.5 V.

If the threshold is 3.5 V, we confirm that the junction exists to the direction where a sensor produces an output voltage more low than the threshold voltage. The output voltage produced by the phototransistor and the threshold are compared at the comparator arrayed behind the robot. The compared data are transferred to the computer. The computer confirms where the junction is.

5. MOBILE MOVING EXPERIMENT

The robot that has an optical sensor unit, a steering mechanism and an artificial intelligence is experimented to move in the pipe. (1) The robot recognizes the T-junction. (2) Then the driving mechanism stops to move. (3) The steering mechanism turns its head to the desirable direction of the pipe. (4) Then the driving mechanism restarts. The fabricated robot is confirmed to recognize several T-junctions and to move to the desirable direction of the pipe.

6. CONCLUSIONS

(1) We fabricate a robot that has an artificial intelligence and can turn the T-junction by itself. T-junction is recognized by an optical sensor unit and is passed by a steering mechanism that is made by a matrix bellows actuator (MBA).

(2) The robot is moved by a driving mechanism that consists of three bellows and bulging brakes. The robot is confirmed to have a traction force of 22 N.

(3) The fabricated robot is confirmed to recognize automatically several T-junctions and to move to the desirable direction of the pipe.

REFERENCES

[1] S. KATO, M. SHIRAKAWA, M. ONO and S. FUKUMOTO, Fabrication of In-Pipe Mobile Micromachines Driven by Pneumatic and Vacuum Pressure, Proc. of American Society for Precision Engineering 1999 Annual Meeting pp. 37-40

[2] M. ONO, S. KATO, M. SHIRAKAWA and T. HAMANO, Fabrication of an In-Pipe Mobile Microrobot with the 3D Steering Mechanism, Proc. of American Society for Precision Engineering 2000 Annual Meeting pp. 223-226

[3] S. KATO, M. KATO, S. OGAWA and M. ONO, Development of Inchworm type Mobile Robot Movable in Pipes with T-junction, Proc. of American Society for Precision Engineering 2004 Annual Meeting pp. 257-260

FABRICATION OF A SNAKE TYPE IN-PIPE MOBILE ROBOT CORRESPONDING TO THE DIFFERENT DIAMETERS

Manabu ONO [1], Miyuki TANAKA [1], Shuzo ITO [1], Shigeru IKEDA [1] and Shigeo KATO [2]

[1]Tokyo Metropolitan College of Industrial Technology
Shinagawa, Tokyo 140-0011
e-mail: mana@tokyo-tmct.ac.jp

[2]Nippon Institute of Technology
Miyashiro, Saitama, 345-8501
e-mail: kato@nit.ac.jp

1. INTRODUCTION

We have many small diameter pipes that are cooling pipes for atomic power stations, boiler pipes, and gas or water pipe lines. They must be periodically inspected in order to protect the accident previously. Diameters of these pipes are different at the place where pipes change from the main to the branch. The inspection microrobot for these pipes must move different diameter.

A step comes where the pipe changes its diameter. The in-pipe microrobot driven by wheels is very difficult to cross the step [1]. We have used cone-shape friction rings for the driving legs of the in-pipe microrobot. However, the microrobot driven by friction rings is also difficult to move in the pipe where diameter changes more than 3 mm [2].

Now, we propose a mobile microrobot that can surely move in a pipe whose diameter changes. The microrobot is constructed by the six rubber bellows as pneumatic actuator, six electromagnetic valves and six air feeding tubes. Outer diameter and natural length of the bellows are 8 mm and 53 mm, respectively. The bellows composes three somite by being arranged in two rows and three columns. The somite can make the arc like the bimetal by giving different pressure to each bellows. The arc somite can hold the pipe. The movement of the microrobot with three somite is imitating as for the accordion movement that is the movement of the snake operation.

The fabricated mobile microrobot was confirmed to move in different diameter pipes whose diameters are between 20 mm and 30 mm. Its speed was 50 mm/s.

2. STRUCTURE OF IN-PIPE MOBILE ROBOT

A structure of the fabricated microrobot is shown in Fig. 1. The microrobot is constructed by the six rubber bellows as pneumatic actuator, six electromagnetic valves and six air feeding tubes. Outer diameter and natural length of the microrobot is 15 mm and 170 mm, respectively. The bellows composes three somite by being arranged in two rows and three columns. Outer diameter and natural length of the bellows are 8 mm and 53 mm, respectively. The somite is defined forward of the microrobot as first somite, second somite and third somite. Each somite can make the arc like the bimetal by giving different pressure to each bellows. The first somite and third somite are mechanisms that hold the pipe and the second somite is mechanisms that obtain displacement.

An experimental apparatus for measuring the

characteristics of the microrobot is shown in Fig. 2. A computer controls six electromagnetic valves through a valve controller. Three air feeding tubes are connected from the electromagnetic valves to each bellows of the microrobot. An air compressor is connected to the entrance ports of the electromagnetic valves and feeds pneumatic pressure to stretch the bellows. A vacuum pump is connected to the exit ports of the electromagnetic valves and feeds vacuum pressure to shrink the bellows.

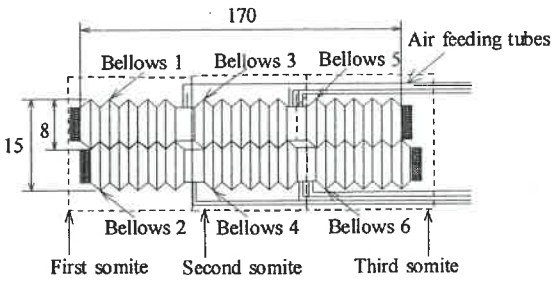

Figure 1. Structure of in-pipe mobile microrobot

3. MOVEMENT OF SNAKE IN A PIPE

We observed snake's accordion movement in pipe. Fig. 3 shows the brief movement of an snake. When the snake moves a vertical pipe,

(1) The snake bends the body like the accordion and holds the pipe by the whole body.
(2) The snake stretches oneself to the moving direction. At this time, snake's lower part of the body continues the holding of the pipe.
(3) The snake bends the upper part of the body and holds the pipe.
(4) The snake extends the lower part of the body, and releases the holding of the pipe.
(5) The snake hauled in the lower part of the body. Afterwards, the snake bends the lower part of the body and holds the pipe.

Thus, the snake can move in the vertical pipe.

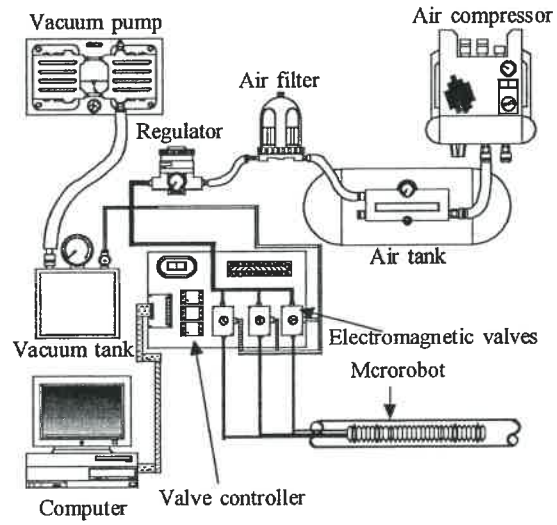

FIGURE 2. Experimental apparatus

4. Moving principle of the microrobot

The moving principle of the microrobot shown in Fig. 4. The moving principle of the microrobot referred to the accordion movement of the snake.

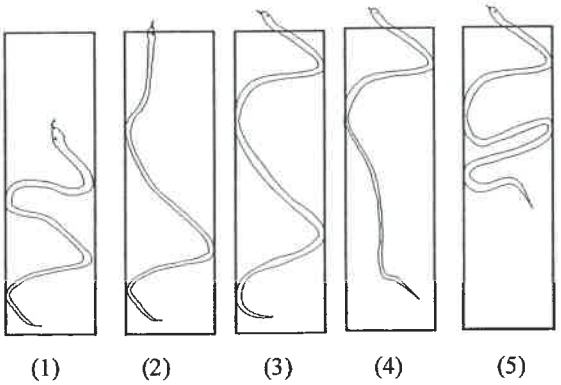

Figure 3. Accordion movement of a snake

As for step 0, negative pressure is given to all bellows.

Step 1: The third somite is bent and it holds of pipe.

Step 2: Positive pressure is given to the first

and second somite and somite are stretched.

Step 3: The first somite is bent and it holds of pipe.

Step 4: Negative pressure is given to the third somite and the holding of the pipe is released.

Step 5: Negative pressure is given to the second somite. The latter half of the robot advances in this step.

Step 6: The third somite is bent and it holds of pipe.

The microrobot can move by repeating these steps.

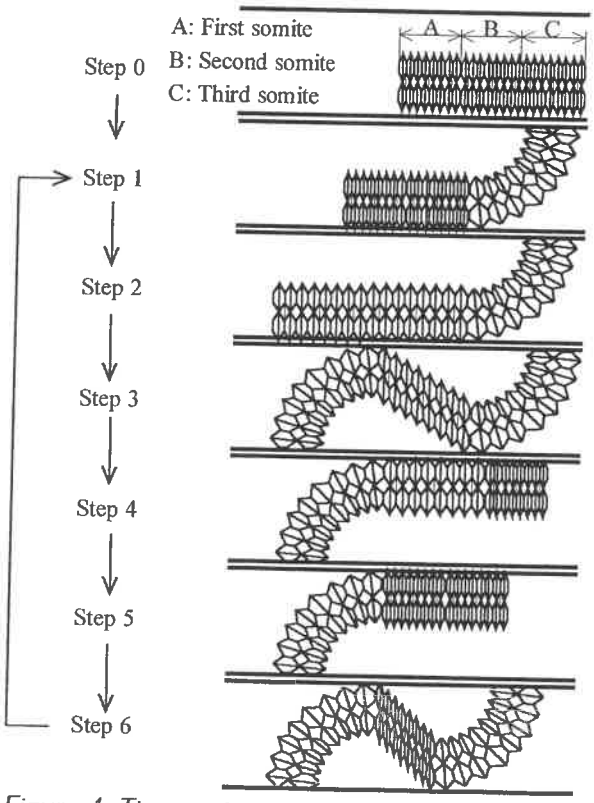

Figure 4. The moving principle of the microrobot

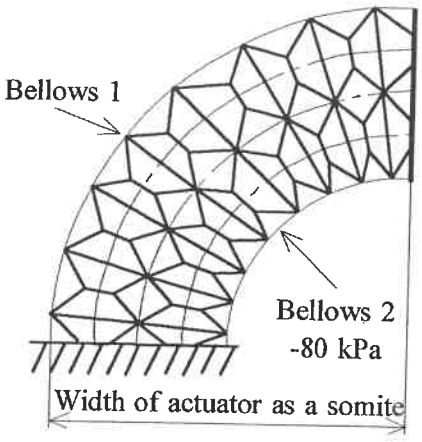

FIGURE 5. The measurement method of width of a somite

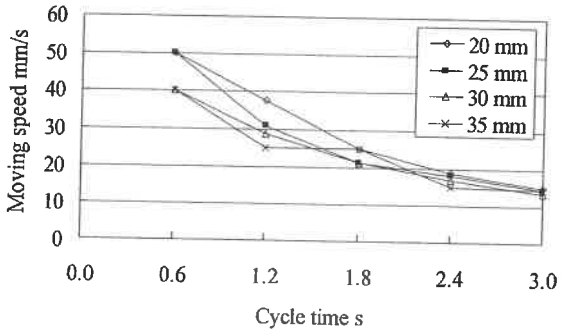

FIGURE 6. Relationship between supply pressure of bellows 1 and width of a somite

5. MOVING EXPERIMENT

5.1 Width of bending of a somite

One somite is prepared and the width of bending is measured. The measurement method is shown in Fig. 5 and the experiment result is shown in Fig. 6. The supply pressure of bellows 2 is -80 kPa and supply pressure of bellows 2 is changed from -80 kPa to +50 kPa. We confirmed to width of the somite is proportional to supply pressures and the maximum width of the somite is 37 mm at supply pressure of 30 kPa.

5.2 Moving speed of the microrobot

The moving speed of the microrobot is measured. Fig. 7 shows the experiment result.

The using pipes to experiment are 20 mm, 25 mm, 30 mm and 35 mm in the inner diameter. The microrobot is able to move in these pipes and a combined pipe of a different diameter. The air pressures used to experiment are 50 kPa and -80 kPa. We prepare five cycle times in which these air pressures were supplied. It is confirmed that the moving speed of the microrobot influenced the cycle time from Fig. 7. and maximum moving speed is 50 mm/s.

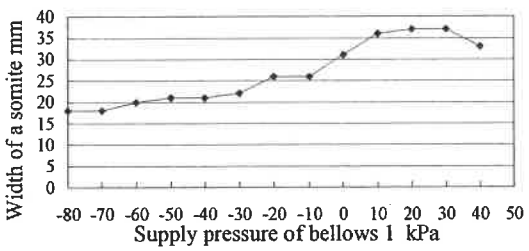

Figure 7. Relationship between moving speed and cycle time

6. CONCLUSIONS

We propose the microrobot which is imitate the snake of accordion movement. The fabricated mobile microrobot is confirmed to move in different diameter pipes whose diameters are between 20 mm and 30 mm. Its speed is 50 mm/s.

REFERENCES

[1] K. Kawaguchi, O. Yoshida, K. Iwao and T. Kikuta: Control of an In-pipe Inspection Robot for Iron Pipes, Journal of the Robotics Society of Japan, Vol 15, No. 3 (1997), 387. (in Japanese)

[2] M. ONO, T. HAMANO and S. KATO: A Basic Study of Mobile Inspection Robot Movable the Long Distance in Small Diameter Pipes, Journal of the Japan Society for Precession Engineering, Vol. 69, No. 4 (2003), 564. (in Japanese)

IMPLEMENTATION OF A REAL-TIME HYSTERESIS COMPENSATION FOR ELECTROMAGNETIC ACTUATORS

Ralf Volkert[1], Oliver Radler[1], Tom Ströhla[1], and Veit Zöppig[2]
[1]Department of Mechatronics
Technische Universität Ilmenau, Ilmenau, Germany
[2]STZ Mechatronik, Ilmenau, Germany

INTRODUCTION

By combining electrodynamic drives with planar magnetic bearings, vacuum compatible integrated multi-coordinate drives with six degrees of freedom can reliably be realized, which are required for various modern applications, e.g. for the manufacture of integrated circuits. The magnetic bearings used in these drives usually consist of several reluctance actuators. Besides the non-linearities due to magnetic saturation effects and eddy currents the control performance is influenced by the magnetic hysteresis. To attain a linear force-current relation and thus to improve the control performance compared to a simple PID controller, a more precise modelling is necessary as well as a real-time compensation of the dominating magnetic hysteresis.

There are several mathematical approaches for the accurate modelling of hysteresis effects. The hysteresis model describes, how the force F lags behind the evocative current I. This is a non-unique function $F(I)$. The implementation of the hysteresis compensation requests high CPU-intensity. It is also difficult to define the model parameters for different applications.

JILES-ATHERTON HYSTERESIS MODEL

In 1983 a method for modelling hysteresis effects was developed by D.C. Jiles and D.L. Atherton especially for electromagnetic materials [1]. It refers to the real physical processes occurring at magnetic hystereses. Due to reversible and irreversible processes resulting from the electromagnetic field strength H, the magnetization M is defined as a sum:

$$M = M_{rev} + M_{irr} . \tag{1}$$

M_{rev} represents the reversible component, M_{irr} is caused by irreversible processes. For the irreversible part applies:

$$\frac{\mathrm{d}M_{irr}}{\mathrm{d}H} = \frac{M_{an}(H_e) - M_{irr}}{k \cdot \mathrm{sgn}\left(\frac{\mathrm{d}H}{\mathrm{d}t}\right) - \bar{\alpha} \cdot (M_{an}(H_e) - M_{irr})} . \tag{2}$$

M_{an} represents the anhysteretic magnetization, H_e is the effective field strength and k and $\bar{\alpha}$ are material constants. By integration the irreversible component is calculated. According to (1) the resulting magnetization M is then:

$$M = (1-c) \cdot M_{irr} + c \cdot M_{an}(H_e) \tag{3}$$

with the reversibility coefficient c. From magnetization M and field strength H the magnetic induction B is calculated:

$$B = \mu_0 \cdot (H + M) . \tag{4}$$

In [2] a method to invert the Jiles-Atherton model is introduced, which was originally intended for FEM simulations. The magnetic induction B is stated as an independent argument. Starting from the equations

$$\frac{\mathrm{d}M_{an}}{\mathrm{d}H_e} = \frac{M_s}{a} \cdot \left(1 - \coth^2\left(\frac{H_e}{a}\right) + \left(\frac{a}{H_e}\right)^2\right) \tag{5}$$

and

$$\frac{\mathrm{d}M_{irr}}{\mathrm{d}B_e} = \frac{M_{an} - c \cdot M_{irr}}{\mu_0 \cdot k \cdot \mathrm{sgn}\left(\frac{\mathrm{d}H}{\mathrm{d}t}\right)} \tag{6}$$

with the saturation magnetization M_S, the effective induction B_e and the material parameter a, the following differential equation is derived:

$$\frac{\mathrm{d}M}{\mathrm{d}B} = \frac{1 - c \cdot \frac{\mathrm{d}M_{irr}}{\mathrm{d}B_e} + \frac{c}{\mu_0} \cdot \frac{\mathrm{d}M_{an}}{\mathrm{d}H_e}}{1 + \mu_0 \cdot (1-c) \cdot (1-\bar{\alpha}) \cdot \frac{\mathrm{d}M_{irr}}{\mathrm{d}B_e} + c \cdot (1-\bar{\alpha}) \cdot \frac{\mathrm{d}M_{an}}{\mathrm{d}H_e}} \tag{7}$$

The magnetization M is calculated by integrating (7). Together with the magnetic induction B the magnetic field strength H yields:

$$H = \frac{B}{\mu_0} - M . \tag{8}$$

Finally a coordinate transformation leads to an inverse model for the force-current hysteresis.

PARAMETER IDENTIFICATION PROCEDURE

Exemplarily the *F-I* hysteresis loops of a solenoid actuator were measured for several air gap lengths (reference points) and currents. The applicability of the Jiles-Atherton model to describe the *F-I* hysteresis had to be proven. Therefore search algorithms were used to find suitable parameter sets for the five model parameters a, M_S, $\bar{\alpha}$, k, c and the two newly introduced scaling parameters c_H and c_B, which allow an exact reproduction of the measured hysteresis loops. This task can be converted into an optimization problem with seven free parameters. To define the quality of a parameter set, the sum of deviations between calculated and measured hysteresis curve at certain measuring points is determined (9). The optimization algorithm tries to minimize this quality criterion.

$$Q_{JA} = \min\left[\sum_{j=1}^{j_{mp}} \left| F_{calc,j} - F_{meas,j} \right|\right], \qquad (9)$$

where j_{mp} denotes the number of measuring points. For higher accuracies also inner hysteresis loops are included in the parameter identification.

Optimization procedure

In [3] some optimization algorithms were investigated with regard to their applicability for this task. The possible solution space is first narrowed by the evolutionary optimization algorithm according to Schwefel in a very efficient way. Then for a more exact optimum localization the Nelder-Mead Simplex algorithm is executed starting with the parameter set found by the evolutionary search procedure. With the obtained parameter sets the measured *F-I* hysteresis can be reproduced at the reference points in a highly accurate way. Yet, a parameter interpolation for air gap lengths between the measured reference points does not lead to physically reasonable results. The hysteresis loops calculated with interpolated parameters do not run between the loops evaluated for the adjoining reference points, but rather incoherent. Further optimizations with seven free parameters showed similar results.

Reduction of the number of free parameters

For this reason the parameter optimization procedure was modified to enable a realistic reproduction of the *F-I* hysteresis for every possible air gap length at the electromagnet. Thereby it was aspired to keep constant as many parameters as possible and thus to reduce the number of free parameters necessary to calculate the hysteresis loops for different air gap lengths.

A proceeding with several optimization cycles, where the number of free parameters necessary to calculate the hysteresis loops for different air gap lengths is reduced step by step and the remaining parameters are kept constant, was successfully investigated. The best result was gained with c_H as the only free parameter. For $c_H(x)$ (dependency of c_H on the air gap length) a continuous, almost quadratic curve arises.

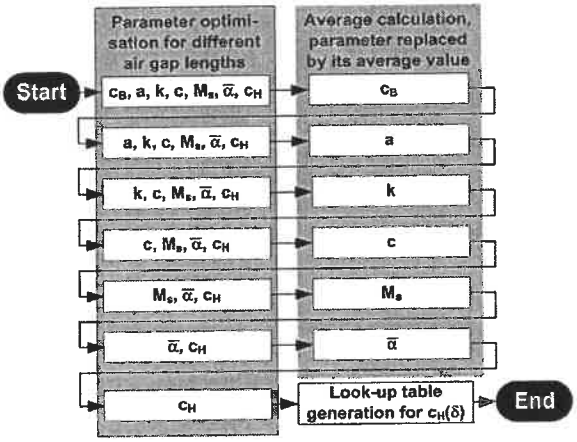

FIGURE 1. Parameter optimization procedure.

For the optimization procedure shown in Fig. 1 a MATLAB program was developed, which computes and saves the parameters needed for the hysteresis model. To verify the results, again hysteresis loops for air gaps between the reference points were calculated. Now these hysteresis loops run exactly between those for the reference points. The usage of c_H as the only free parameter implicates the advantage, that the Jiles-Atherton model can be computed with the same inner model parameters for all air gap lengths. Subsequently the result is just scaled through a multiplication by c_H.

FORCE CONTROLLER IMPLEMENTATION ON A 16-BIT DIGITAL SIGNAL PROCESSOR

The inverse Jiles-Atherton model allows a compensation of the electromagnet's force-current hysteresis. As it is based on the solution of a differential equation, it is well suited for implementation on a digital signal processor. In this case the inverse Jiles-Atherton model was programmed for a Freescale MC56F8322 DSP, which uses fixed-point arithmetic. In order to use the inverse Jiles-Atherton model for a real-time compensation, the adoption on the limitations of

the fixed-point arithmetic is crucial. The original model uses the hyperbolic cotangent (coth). This function cannot be implemented directly. This affects the calculation of the anhysteretic magnetization and the derivative with respect to the effective field strength:

$$M_{an} = M_S \cdot \left[\coth\left(\frac{H_e}{a}\right) - \frac{a}{H_e} \right], \qquad (10)$$

$$\frac{dM_{an}}{dH_e} = \frac{M_s}{a} \cdot \left(1 - \coth^2\left(\frac{H_e}{a}\right) + \left(\frac{a}{H_e}\right)^2 \right). \qquad (11)$$

It has been proven, that equation (10) can be approximated with sufficient accuracy by a linear equation. In the same way equation (11) can be approximated by a constant value:

$$M_{an} = K_2 + K_1 \cdot H_e, \qquad (12)$$

$$\frac{dM_{an}}{dH_e} = K_1. \qquad (13)$$

The inverse Jiles-Atherton model with approximation was verified by simulation. The accuracy of the compensation is not affected. Furthermore the approximation leads to a better stability and eliminates initial value problems.

Experimental results

The implemented open-loop force control, which sets force according to supplied current, shows good succession behavior both for constant and variable air gap lengths. Fig. 2 shows the hardware structure of the experimental set-up.

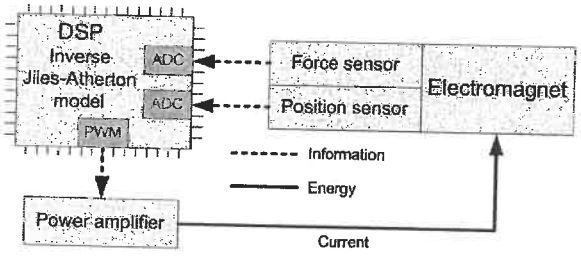

FIGURE 2. Hardware structure.

The model parameters were calculated for the stroke end position and implemented in the controller program. A serial communication is used for sending the desired force values from PC to the embedded controller. The desired force values and the measured force signals were recorded. The same desired force signal was used as input for a MATLAB simulation. In addition, the proportional solenoid was controlled without the compensation. In this case it was assumed, that the actuator has a constant current-force ratio. Fig. 3 shows the results of this experiment. The measured force signal with activated hysteresis compensation shows only small differences to the desired force curve and the simulated one.

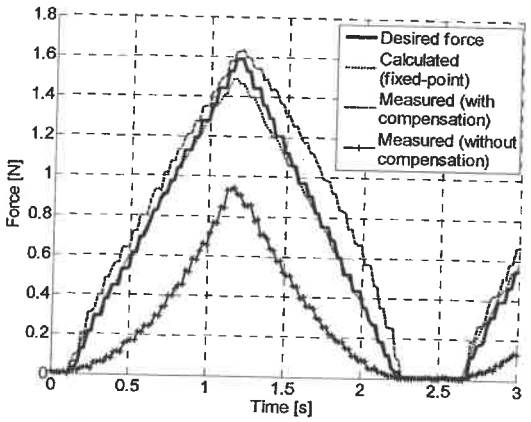

FIGURE 3. Verification of the hysteresis compensation (fixed position).

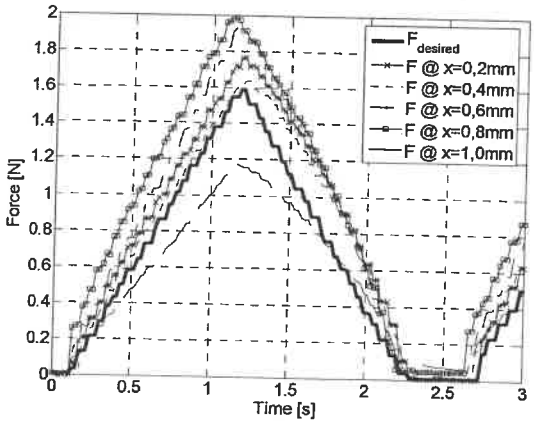

FIGURE 4. Verification of the hysteresis compensation (different positions)

In the next step the parameters of the model were adapted to the armature position. This was done in order to achieve a position-independent force control. For this purpose position-dependent look-up tables for the model constants are used. The functioning of this approach was tested by measuring the force output for a triangular desired force signal for different discrete positions. Fig. 4 shows the results of this experiment. The triangular signal shape is achieved over the whole stroke. The force is controllable with a maximum relative error of 30 %. Without compensation the signal shape differs strongly with respect to the desired triangular waveform. The accuracy of the compensation depends strongly on the quality of

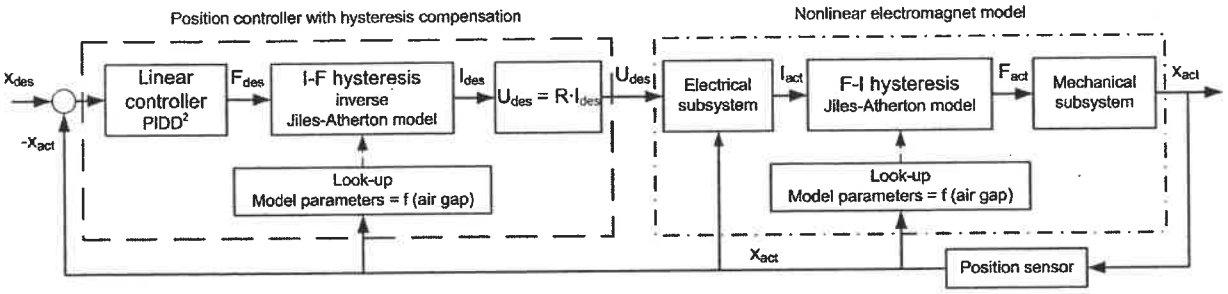

FIGURE 5. Structure of the simulation model with hysteresis compensation.

the solenoid current control. Optimizations of the current control electronics will allow a relative force error less then 10 % in the future.

POSITION CONTROLLER WITH HYSTERESIS COMPENSATION

In the next step the design of a closed-loop position controller applying linear control techniques was taken into account. By using the inverse Jiles-Atherton model as part of the controller, the electromagnet's force-current hysteresis is compensated in real-time and an almost linear actuator behavior is achieved. An electromagnet, which was originally developed as part of a magnetic bearing system, was used. At first the dynamic behavior of the position controller with hysteresis compensation was simulated in MATLAB together with an electromagnet model, which includes the dominating non-linearities. The electrical subsystem with a look-up table containing the measured relation between flux linkage and current, the force-current hysteresis described with the Jiles-Atherton model, and the mechanical subsystem were implemented. A PIDD^2 controller in combination with the inverse Jiles-Atherton model was applied. Fig. 5 shows the structure of the simulation model containing the electromagnet and the position controller with hysteresis compensation.

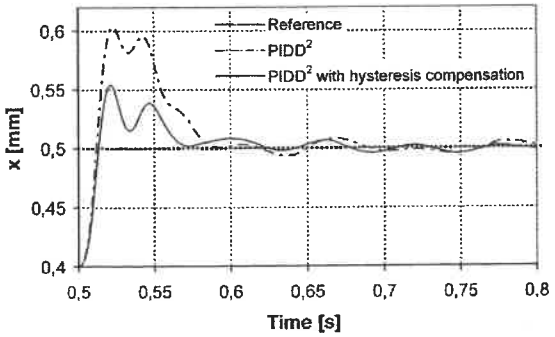

FIGURE 6. Comparison of step responses.

Based on simulation results the PIDD^2 controller parameters were manually adjusted. In a real-time hardware-in-the-loop test rig the controller was investigated. Step responses with different heights were measured. Alternatively a PIDD^2 controller without hysteresis compensation was tested. Fig. 6 shows typical results. With hysteresis compensation an overshoot reduction of about 50 % was gained. Yet settling time and steady state error remain almost constant.

CONCLUSION

By means of two different electromagnets it was exemplarily shown, that the Jiles-Atherton model, which was originally developed to describe the *B-H* hysteresis, can also be applied for the reproduction of the *F-I* hysteresis. Thus an extension of the model was performed. The model parameters can be identified in a way, that only the scaling parameter c_H depends on the air gap length. The hysteresis compensation leads to good results both for open loop force control and closed-loop position control. The applicability of the hysteresis compensation with the inverse Jiles-Atherton model has to be proven for other actuator types, like e.g. piezoelectric or magnetostrictive actuators.

ACKNOWLEGEMENTS

This work was funded by the German Research Foundation within the Collaborative Research Centre "Nanopositioning- and Nanomeasuring-Machines".

REFERENCES

1. Jiles, D.C. and Atherton, D.L., Theory of Ferromagnetic Hysteresis, *J. Magn. Magn. Mater.*, no. 61, pp. 48-60.
2. Sadowski, N., Batistela, N.J., Bastos, J.P. and Lajoie-Mazenc, M., 2002, An Inverse Jiles-Atherton Model to Take Into Account Hysteresis in Time-Stepping Finite-Element Calculations, *IEEE Trans. Magn.*, vol. 38, no. 2, pp. 797–800.
3. Ströhla, T. and Bode, S., 2004, Compensation of the Force Hysteresis of Proportional Solenoid Actuators, *Int. IEEE Conf. Mechatronics & Robotics*, Proc. vol. 2, pp. 442-445.

ROTATIONAL PRECISION MEMS-BASED CLAMPING MECHANISM FOR STABLE FIXATION OF ELASTIC MECHANISMS

Dannis M. Brouwer[1], B.R. de Jong[2], M. J. de Boer[2], H.M.J.R. Soemers[1,3],
[1] IMPACT Institute, University of Twente, the Netherlands
[2] MESA+ research Institute, University of Twente, the Netherlands
[3] Philips Applied Technologies, Eindhoven, the Netherlands

INTRODUCTION

Conventional TEM sample manipulators often lack the crucial stability of 0.1 nm/min. A MEMS manipulator attached directly to the TEM pole would greatly increase both thermal and dynamic stability. However a stable E-beam requires no interference of electric or magnetic fields. Therefore the position of the manipulator should be maintained passively. To this end a mechanical clamp is presented which clamps one of the actuators of the MEMS-based TEM sample manipulator [1]. The clamp incorporates a relatively large clamp force of 0.5 mN and is able to maintain the clamp force without external power. A theoretical basis of the clamp has been presented in previous work [2]. In this paper the design and fabrication of a second generation rotational clamp is presented. This clamp design is part of a research project for a 6 Degrees-of-Freedom MEMS TEM sample manipulator.

CLAMP DESIGN

Figure 1 shows part of the manipulator tail which has to be fixed in *y*-direction by the clamp mechanism. The clamp mechanism clamps the manipulator tail which is connected to the manipulator actuator shuttle. A transmission ratio is created to increase the clamp force and to decrease the influence of play in the rack and pin locking mechanism.

The operation of the total clamp mechanism starts by closing the parallel plate actuator. The pin moves down and the clamp shuttles are free to rotate around the pivots. The two jaws are actuated by one comb-drive collectively which results in a rotation of the jaws and shuttles around the pivots. Once a desired clamp force is established the parallel plate actuator is switched off and the pin is locked in one of the gaps of the rack. The comb-drive actuator can be switched off.

Figure 2 shows the clamp design. The jaw is suspended by leaf-springs *A* and *B*. In general, leaf-springs are very stiff in tensile direction while in bending direction they are compliant. When the two leaf-springs *A* and *B* deform together, the jaw will rotate around a virtual pivot which is the intersecting axis of leaf-springs *A* and *B*. The rotational comb operates at a larger radius than the jaw creating a force amplification. Leaf-springs *C* & *D* intersect at the same virtual pivot as leaf-springs *A* & *B*. For relatively small deflections, the rotational comb-drive will rotate around the common virtual pivot. Reinforcement *F*, is a folded leaf-spring, supporting the comb shuttle in out-of-plane direction, and leaving the other degrees of freedom compliant.

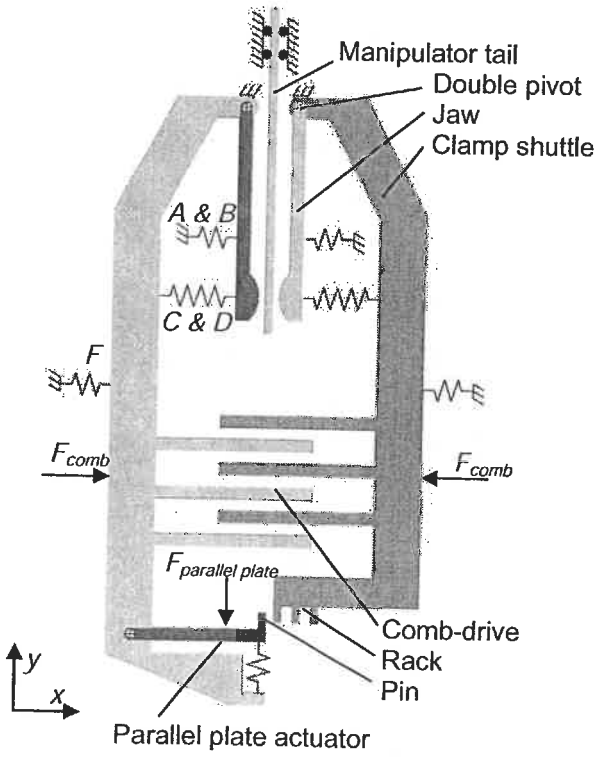

FIGURE 1. Schematic view of the clamp mechanism. The compliance of leaf-springs A, B, C, D and F are represented by 1D springs. The virtual pivots are represented by real pivots.

During the first 1.64° rotation of the jaw and 1.87° rotation of the comb-drive, the comb-drive energy is stored in leaf-springs *A*, *B*, *C*, *D* and reinforcement *F*, as the jaw does not touch the manipulator tail. After the jaw touches the manipulator tail the clamp comb-drive energy is mainly stored in leaf-springs *C*, *D* and reinforcement *F*. At the same time the clamp force starts to build up over a 0.49° clamp actuator stroke. Once a desirable clamp force is obtained, the parallel plate actuator can be gradually switched off, raising the pin in the rack. The clamp comb-drive can now be switched off. There will be some backlash due to

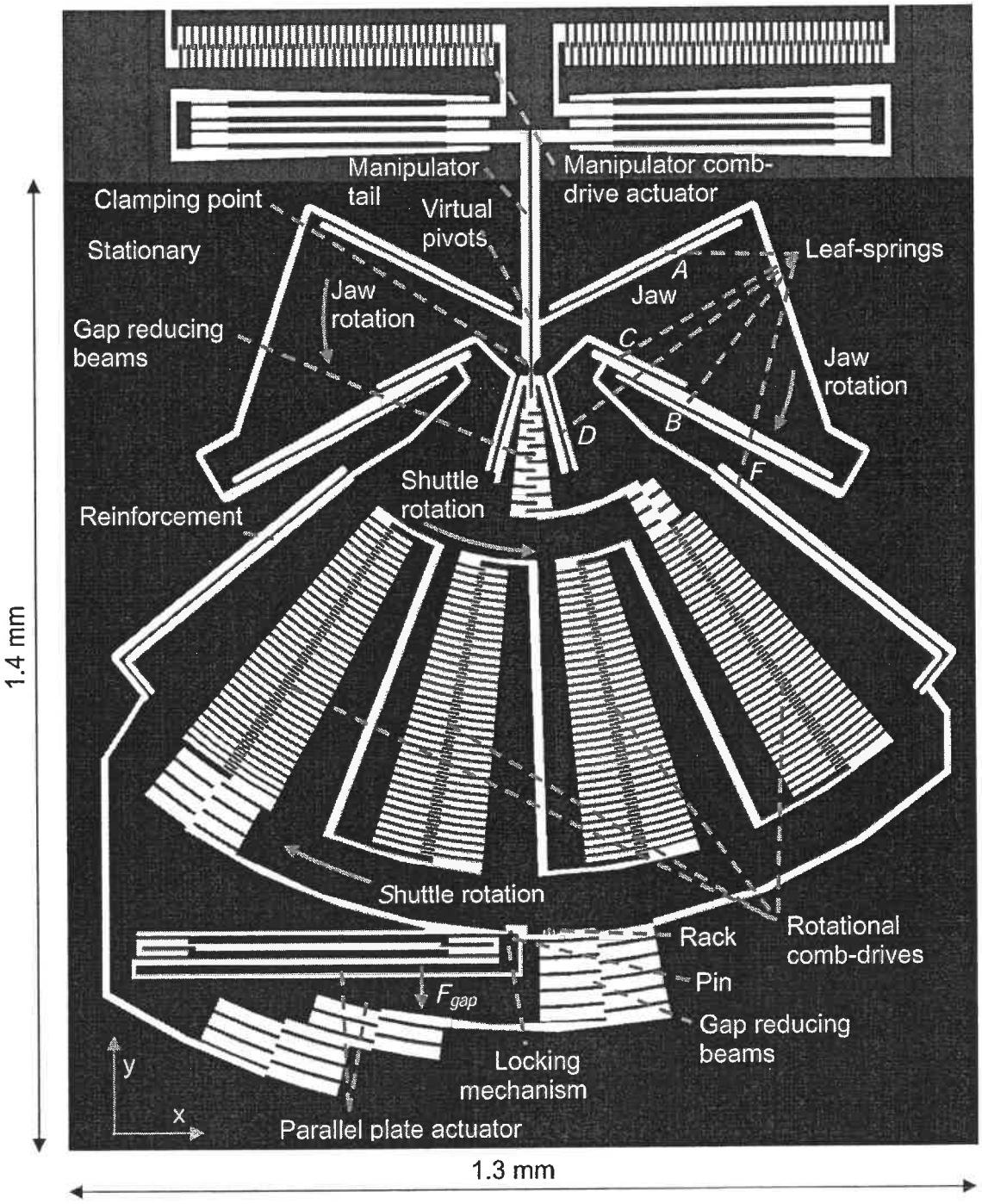

FIGURE 2. The clamp design with part of the manipulator comb-drive actuator

movement of the pin in the rack until a stop is reached. Details of first generation clamping and fixation mechanism can be found in previous work [2]. The fixation mechanism freezes the clamp force without the necessity of sustaining an electrical field. The combination of the position uncertainty due to backlash of the pin in the rack and the fabrication uncertainty should not lead to considerable clamp force loss. Therefore the bending compliance of leaf-springs *C, D* and reinforcement *F* will allow pre-tension to be built up. Making the leaf-springs too compliant will require extra stroke and actuator energy for the comb-drive. Making leaf-springs too stiff leads to unacceptable loss of clamp force when locking.

Because of large clamp forces, and therefore the risk of buckling, the relatively long and slender leaf-springs *A* & *B* are loaded with a tensile force during clamping. Leaf-springs A, B, C, & D are initially pre-curved so that at the maximum overlap of the comb-fingers, the deformation causes them to be straight. Exactly at this point the electrostatic pull-in force is greatest, and the leaf-spring's longitudinal stiffness is largest.

In order to minimize the parasitic influence of clamping on the manipulator position several measures have been taken: First, the virtual pivot is located in the middle of the manipulator-tail. Therefore nearly pure motion in *x*-direction of the jaw results, leaving the manipulator position unaffected. Second, the clamping force results in a tensile elongation of leaf-springs *A* and *B*. The leaf-spring tensile stiffnesses are tuned so the clamp force will result almost solemnly in an *x*- displacement of the jaw. The residual *y*-displacement due to the above mentioned effect is less than 1 nm. The manipulator-tail is compliant in *x*-direction to obtain an equal distribution of the clamp force in the jaws. The Hertzian contact stress due to clamping of the manipulator-tail results in an elongation of the tail of 0.19 nm in *y*-direction, which is considered to be insignificant. Consequently by clamping, the position of the manipulator will only be affected on a sub-nanometer scale.

The mechanism consists of several actuators. One actuator is used to create a controllable clamp force, the second actuator is much smaller and locks the position of the first actuator. The jaw has to build up the 0.5 mN clamp force in such a way that the manipulator position is not altered. The combination of a small locking mechanism and a larger controllable clamp actuator offers a relatively small clamping device. A comb-drive actuator is capable of realizing enough force if a transmission ratio is used. Comb-drive actuators deliver controllable force output and are relatively easy to manufacture. The applied clamp comb-drive has 144 comb-finger pairs and delivers a torque of 52nNm at 80V, which is equal to 97μN at the middle of the comb. The longest comb-fingers are 93 μm long and 3 μm wide. According to Elata [3] this geometry will not result in finger pull-in at 80V.

The symmetric design of the two combs interacting results in mostly similar geometric displacements with respect to the *y*-direction, which is beneficial for the alignment of the combs fingers.

Results obtained from modeling [2] show that 33% of the comb-drive force and 79% of the stroke is necessary for closing the 2 μm gap between the manipulator tail and the jaw. This gap is constrained by the process. The stiffness in *y*-direction of the jaw at the virtual pivot is 4.1 10^4 N/m, caused by the large tensile stiffness of leaf-springs *A* and *B*. Loading the jaw with the maximum force of the manipulator comb-drive results in 12 nm manipulator actuator movement. The highest stress occurs in leaf-spring *D*, mainly due to bending, and reaches 405 10^6 N/m^2. The calculated lowest natural frequency of the system not clamping the manipulator tail is 2.3 kHz. The associated vibration mode is a rigid body rotation of the comb-drive with jaw around the virtual pivot.

FABRICATION

The process implemented is based on the three mask process of the back side release process demonstrated by Sarajlic [4]. It offers a 35 μm thick structural layer, and a 3-20μm trench width design freedom. The fabrication is compatible with the fabrication of the parallel kinematic manipulator process.

First insulation trenches are installed in the wafer [5]. A 35 μm thick membrane is created by backside KOH etching. The mechanical structures are etched by a Bosch recipe up to 90% of the membrane depth. Etching the last 10%, the release of these suspended structures,

needs consideration. Basically there are two types of release etching: releasing by directional etching or by isotropic etching. Directional etching creates heat in the suspended devices. Although helium back-side cooling by a dummy wafer is being used, this energy has to flow through the leaf-springs, which easily break-down. In Figure 3a and 3b for example the

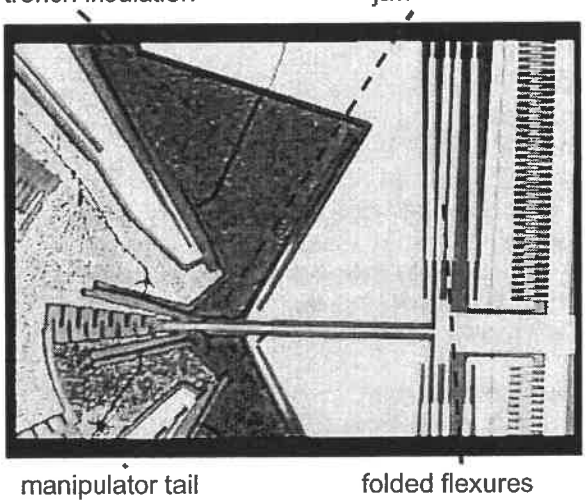

FIGURE 3a. The manipulator actuator is activated

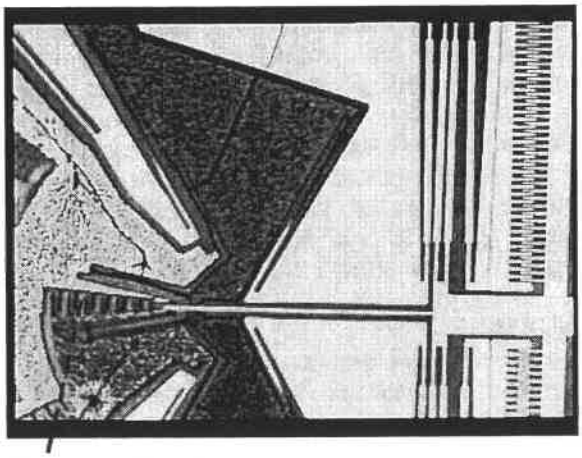

Gaps are closed

FIGURE 3b. The jaw clamps the manipulator tail.

resist has been overheated. In this case the device however is still intact. Using an isotropic release from the front or back side introduces much less heat, however it calls for the release to be confined in a short time span. The chemical etching will deteriorate the side wall passivation of devices and in the end it etches the devices themselves. In all cases the thickness of the membrane, the depth of the Bosch-like etching and the last release etching step should be uniform over the wafer area.

Figure 3a and 3b show a released clamp with test actuator. In Figure 3a the test actuator has been switched on and the folded flexures are deflected. In Figure 3b the manipulator tail has been clamped between the jaws. At present no detailed characterization has been performed.

CONCLUSION

A clamp is proposed for a micro-machined high-precision large force clamping mechanism. It includes an un-powered mechanical locking system to maintain the clamping force at 0.5 mN. Although compliant mechanism design in MEMS design requires extra attention because of the relatively large deflections, small actuations forces and relatively large actuation stiffness, the real challenge lays in designing within the limited fabrication techniques. Though still in development, the fabrication technique proposed offers 35 μm high mechanisms with a trench width bandwidth of 3-20μm. The fabrication technique is compatible with the fabrication of a 6 Degree-of-freedom manipulator.

REFERENCES

1. D.M. Brouwer, B.R. de Jong, H.M.J.R. Soemers, 2006, MEMS-based 6 Degrees-of-freedom parallel kinematic precision micro manipulator, *Proc. of EUSPEN int. conf,* 6: 111-114.
2. D.M. Brouwer, B.R. de Jong, H.M.J.R. Soemers, J. Van Dijk, 2006, Sub-nanometer stable precision MEMS clamping mechanism maintaining clamp force un-powered for TEM application, *Journal of Micromechanics and Microengineering,* Vol.16, No. 6: 7-12
3. D. Elata, V. Leus, 2005, How slender can comb-drive fingers be, *J. Micromech. Microeng.*, 15: 1055-1059.
4. E. Sarajlic, 2005, Electrostatic microactuators fabricated by vertical trench isolation, Ph.D thesis, University of Twente, Enschede, The Netherlands.
5. G Yan, Y Zhu, Z Wang, R Zhang, Z Chen, X Liu and Y. Wang, 2004, Integrated bulk-micromachined gyroscope using deep trench isolation technology, *Int. Conf. on Micro Electro Mechanical Systems MEMS*, Maastricht, The Netherlands: 605-608.

DESIGN OF A HIGH-SPEED MICRO-SCALE FAST SCANNING STAGE FOR TWO-PHOTON ENDOMICROSCOPY

Shih-Chi Chen, Heejin Choi, Daekeun Kim, Logan Munro, Martin L. Culpepper, and Peter T. So
Department of Mechanical Engineering
Massachusetts Institute of Technology
Cambridge, Massachusetts

SYNOPSIS
In this paper, we present the design, modeling, and preliminary experiments of a precision, millimeter-scale high speed 3D scanner that is to be integrated at the distal end of an endomicroscope. The scanner system consists of (1) an active Silicon optical platform which constraints, aligns, and actuates the small optics (a GRIN lens and a prism) at low speeds and (2) a high speed fiber resonator. The scanner resides within a 7mm tube and is designed to operate at 700Hz, 1 Hz, and 0.02 Hz for X, θ_X, and Z (optical) axis respectively. This will allow the focused laser to travel 100 μm for all three axes. This tight functional requirement is necessary due to the miniaturized optics and reasonable frame rate. The decoupled three axis of actuation is made possible by an optical design which incorporates a double clad photonic bandgap fiber [5].

INTRODUCTION
Presently excisional biopsy is the only way for early cancer diagnosis. This technique requires tissues to be excised, fixated, sectioned, stained and subsequently examined microscopically. The invasive nature of this process calls for the development of a supplementary non-invasive approach. Recently, a non-invasive "optical biopsy" concept has been proposed through the development of an endomicroscope containing a small scale three dimensional (3D) optical scanner embedded at the tip of a regular endoscope [1]. This endomicroscope is based on two-photon excitation [2] that enables depth discrimination and sub-micrometer resolution capabilities to perform volumetric scanning in a turbid environment. The two-photon based endomicroscope has numerous benefits over excisional biopsy. For example, (1) non-invasive optical screening may decrease the number of excision biopsies required, and (2) optical biopsy can provide more informed selection of excisional biopsy sites minimizing incorrect diagnosis due to random sampling.

The design of a two-photon imaging requires scanning of focused light to create tissue images. However, scanning technology still proves to be a bottleneck for practical endomicroscope design. Although early attempts at two-photon endoscopes have had varying success [3, 4], an integrated two-photon system with a volumetric scanning mechanism in the distal tip has yet to be developed.

SILICON OPTICAL BENCH FOR SLOW AXES IN-PLANE MOTION
The optical/scanning configuration of the endomicroscope is presented in Fig. 1, where the femto-second laser is guided to the optical platform through the resonating fiber. On the optical platform, the collimated laser first goes to the objective GRIN lens through the reflection on a millimeter scale prism. The objective GRIN lens and prism are integrated with the in-plane chevron thermomechanical actuators (TMAs) through micro-fabrication to perform scanning. The Silicon optical bench provides a micrometer level precision alignment for the small optical elements. TMAs are used in optical bench for future in vivo examination/operation due to their high force and low driving voltage nature. Although TMAs can run at high temperatures (~800^{0}K), they will introduce no harm to live tissues as long as the power is kept low (~mW).

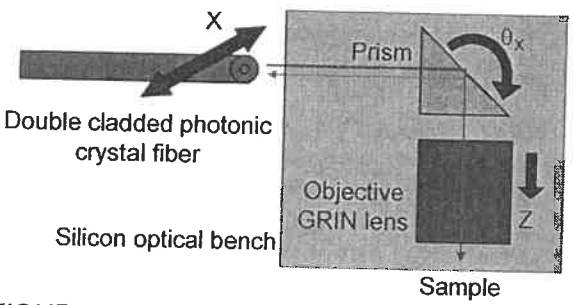

FIGURE 1: Configuration of the Endomicroscopy micro-scanner and micro-optical bench design

Figure 2 presents optimized in-plane Silicon optical bench scanning system which consists of

two sets of flexural bearings with integrated chevron TMA trains.

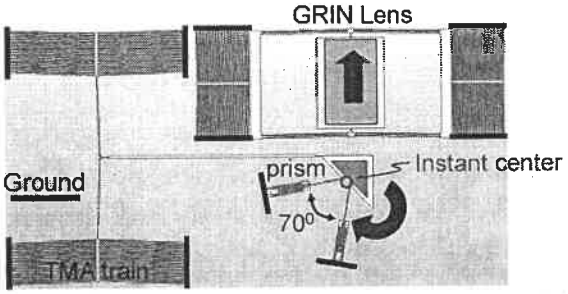

FIGURE 2: Silicon optical bench with integrated TMAs and flexural bearings that generates linear and rotary motions.

Chevron TMA train design

The chevron TMAs are optimized through the geometric contouring method [6] to provide enhanced force, displacement and reduced power consumption compared to common chevron actuators. This also allows the TMAs to be operated at lower temperature and thus makes the TMAs more suitable for precision actuation. An example of a contoured chevron TMA is presented in Fig. 3.

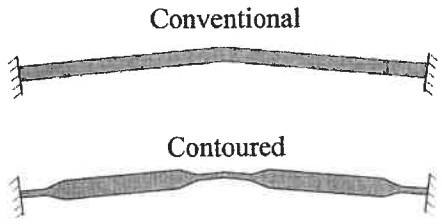

FIGURE 3: Example of a conventional and contoured chevron TMAs

Many chevron TMAs can run in parallel in order to generate larger force output without sacrificing the stroke as shown in Fig. 2. In order to model the in-plane scanning performance, a simulated experiment was conducted on the chevron TMA train using a multi-physics FEA software package (FEMLab) with temperature dependent material properties (electrical resistivity, thermal conductivity...etc). The results, shown in Fig. 4, indicate that the TMA train will reach stable scanning status within 0.2 second and is capable of scanning a 10 times faster than the required bandwidth. The smooth linear region indicated in the gray box in Fig. 4 shows promising potential for obtaining linear scan data. More characteristics of the chevron TMA train are presented in Table 1.

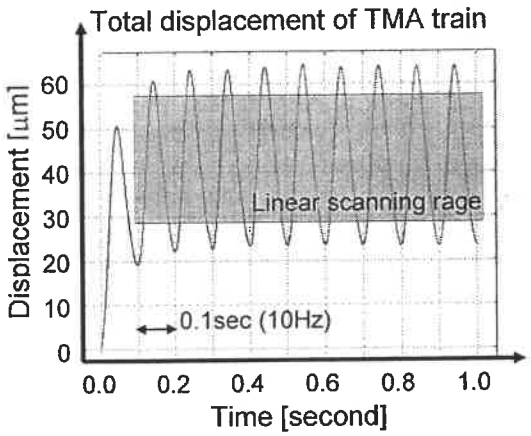

FIGURE 4: Multi-physics FEA results of sinusoidal linear displacement of the chevron TMA train.

TABLE 1. Performance table of chevron TMA train

Driving current	25mA per TMA
Operating voltage	~2.8 V
Operating temperature	580°K
TMA train bandwidth	10 Hz
Max. force output	10 mN
Number of chevron TMAs	20

Translational flexural bearing design

The flexural bearing actuated by the TMA trains provides precision guidance and reduced parasitic motion for active optical components. As shown in Fig. 2, the first flexural bearing that carries the objective GRIN lens generates linear motion and travels 100 μm. This translational flexural bearing consists of a two-stage chevron amplification mechanism and is driven by two sets of chevron TMA trains. The symmetric design prevents lateral parasitic motion. Note that only the chevron TMA train is used as an actuator, the interlinking chevron flexure is for transmitting/amplifying mechanical motion, and will remain at lower temperature.

Rotary flexural bearing design

The second flexural bearing that carries the micro-prism generates rotary motion about the instant center for 2.5°. This rotary bearing is also driven by the two-stage chevron amplification mechanism and chevron TMA train shown in Fig. 2. The shuttle that carries the prism is part of a flexural four-bar mechanism. The instant center of this four-bar mechanism is designed to be on the reflecting point of the prism's inner surface so that the parasitic translational motion can be minimized during the scanning processes. The optimization result, shown in Fig 5, suggests the two supporting flexures of the

four-bar mechanism should intersect at 70^0 which only allows 5.7nm parasitic motion at the full stroke (2.5^0) of this rotary bearing. Performances and dynamic properties of the translational and rotary bearing are presented in Table 2.

TABLE 2. Performance table of translational and rotary bearing with integrated TMA train

	Translational bearing	Rotary bearing
Range	120 μm	2.5^0
Worst gravity deflection	0.04 μm	0.3 μm
1st Resonant frequency	1346 Hz	5302 Hz
2nd Resonant frequency	8245 Hz	6105 Hz

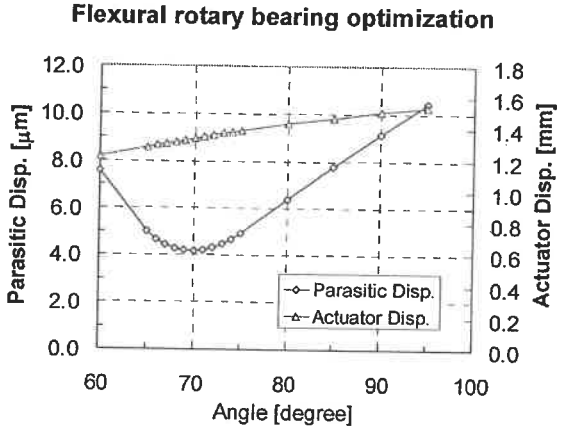

FIGURE 5: Flexural rotary bearing optimization. The results suggest at 70 the bearing will have a transmission ratio (defined as parasitic displacement over actuator displacement) equal to $2.9x10^{-3}$.

Figure 6 illustrates a proposed package for the endoscopic scanner, where the optical Silicon bench resides within a plastic housing and allows the resonating fiber to be inserted from the right side. The glass cover on top of the plastic housing protects the objective lens from direct contact with specimen tissues. Specific alignment features, such as small scale ball coupling, on the plastic housing will be developed in the near future and provides precise registration to the fiber resonator which will be discussed in the next section. The Silicon optical bench and its housing are designed to be a low cost, disposable component that will be replaced after every in vivo scan.

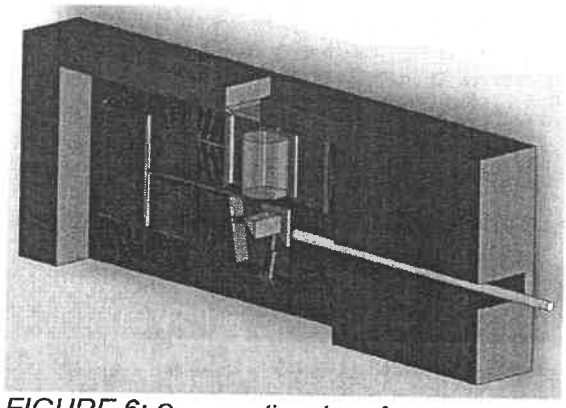

FIGURE 6: Cross-section view of a proposed package of the 3D endoscopic scanner.

FIBER RESONATOR DESIGN

A prototype fiber resonator, designed to resonate the fiber at its first mode, is constructed to characterize the mechanical and dynamic properties of the double clad photonic crystal fiber as well as to verify the single-axis displacement range, as shown in Fig. 7. The double clad fiber has a rather complex mechanical structure which consists of a Silica core with tens of hollow channels and an acrylic protection layer that introduces damping into the system [5].

The fiber resonator is actuated by PI's piezo-ceramic actuator capable of outputting a 8 mm stroke at 120V. The actuator is constrained by two metal cylinders and is preloaded by screwing down the hex bolt on the left in Fig. 7. When the fiber is constrained and actuated, a high speed camera (512x512 resolution, 15,000 fps) is used to record the motion of the resonating fiber and hence calculate the resonant frequency.

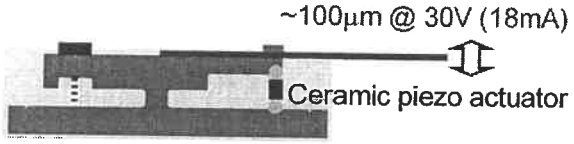

FIGURE 7: Fiber resonator design

The experimental results are presented in Fig. 8, along with the analytical theory (Equation 1), which predicts the resonant frequency accurately within 1% (~ +/- 3Hz). Equation (1) is modified from an equation for predicting the transverse resonant frequency of a prismatic cantilever beam [7]. The modified equation models the complex fiber structure as a single material (Silica) cantilever beam. The equivalent

density (d_{eq}) and radius (R_{eq}) in Equation (1) are obtained by conserving the total mass and the second moment of inertia of the double clad fiber respectively. L in Equation (1) refers the length of the fiber.

$$Frequency(Hz) = \left(\frac{R_{eq}}{2\pi}\right) \cdot \sqrt{\frac{3E_{Silica}}{d_{eq}}} \cdot (L)^{-2} \qquad (1)$$

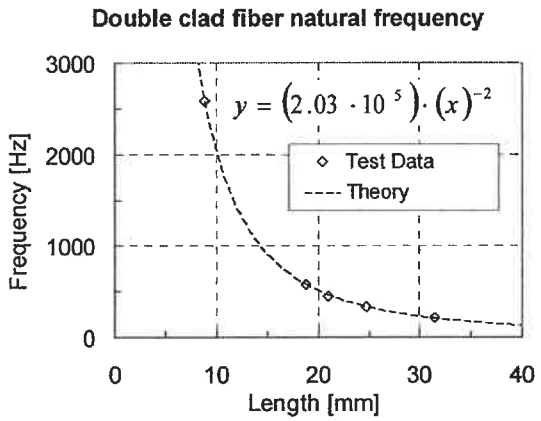

FIGURE 8. Photonic fiber resonant frequency test

The experiment showed that a 15mm long double clad fiber which resonates at 900Hz will displace ~ 100 μm at 30V which indicates that the resonant fiber should meet the functional requirement for range and speed. The experiment also shows that the fiber can achieve similar displacements at higher speed which potentially allows the endoscopic scanner to operate at a higher frame rate, for example, 10 frame/sec.

Tolerance of all parameters (such as the fiber length, the inner and outer radius of the double clad fiber...etc) have been considered. The length of the fiber protruding away from the resonator base is the most critical one of these parameters, which gives ~0.3% error in estimating resonant frequency. As a result, based on the current model, we can predict the resonant frequency within +/- 5Hz. The next generation fiber resonator will be designed to possess a device envelope less than 7mm so it can be integrated with the Silicon optical bench as shown in Fig. 6.

CONCLUSION

In this work, a high force-speed-stroke 3D endoscopic scanner for the two-photon non-invasive optical biopsy is designed, modeled and proven to be functional via a preliminary experiment.

The design and analytic modeling of an active two-axis Silicon optical bench with integrated flexural bearing and contoured chevron TMA trains are presented. The actuators on the Silicon bench are capable of generating 10mN force, and 100 μm range at 10Hz. For the fast axis, the fiber resonator is designed, tested, and characterized using a high speed camera. The parametric equation is able to predict the resonant frequency within 1%.

This two-photon endoscopic scanner can be readily modified to use other optical imaging modalities such as confocal microscopy and optical coherence tomography. Equally important, the development of high force micro-/meso-scale actuator technologies will find applications in many other unrelated areas such as telecommunications.

REFERENCES

1. Choi, H., Chen, S., Kim, D., So, P. T., and Culpepper, M. L., "Design of a Non-linear Endomicroscope Biopsy Probe," OSA Biomedical Optics Topical Meeting and Tabletop Exhibit, FL, March 19-23, 2006
2. So, P. T. C., C. Y. Dong, B. R. Masters, and K. M. Berland, "Two-photon excitation fluorescence microscopy," Annu. Rev. Biomed. Eng. 2:399–429, 2000.
3. Helmchen, et. al., "A Miniature head-mounted two-photon microscope: high-resolution brain imaging in freely moving animals." Neurotechnique, Vol. 31, 2001.
4. Jung, et. al. "Multiphoton endoscopy" Optics Letters, Vol. 28, No. 11, 2002.
5. Information about double cladding fiber is available at http://www.crystal-fibre.com/products/active.shtm.
6. S. Chen, M. L. Culpepper, "Design and Optimization of Microscale Thermomechanical Actuator Force and Stroke via Contour Shaping," to be published in the Journal of Microelectromechanical Systems., 2005.
7. Timoshenko, S., 1974, Vibration Problems in Enginerring, John Wiley & Sons, London.

FORMATION OF MICRO-SCALE PRECISION FLEXURES VIA MOLDING OF METALLIC GLASS

Shih-Chi Chen[1], Martin L. Culpepper[1], Jeffrey Bardt[2], and John Ziegert[2]
[1]Department of Mechanical Engineering
Massachusetts Institute of Technology
Cambridge, Massachusetts
[2]Department of Mechanical Engineering
University of Florida
Gainesville, Florida

INTRODUCTION

In this paper, we use experimentation and simulation to demonstrate the ability of metallic glasses to create large-displacement flexures for small-scale machines. The range of a flexure-based device scales with the product of maximum material strain and the characteristic size of the flexible elements in the device. Although small-scale flexures may be created from some moderate-strain materials, e.g. Silicon, their small size generally limits the usable range to a few micrometers. This problem is a fundamental barrier that prevents the creation of small-scale precision machines that are in immediate need.

For example, large range, small-scale flexures are presently needed to create mm-sized endomicroscopes that scan micro-optics over a volume of 200x200x200 micrometers[3]. This would enable non-invasive, in-vivo imaging that can help to detect cancer [1,2]. Other applications that could benefit include:
- Sensing structures for nanoinstrumentation
- Amplification flexures for transducers
- Multi-axis flexure-based nanopositioners
- Flexure bearings for actuators

In this paper, we focus on metallic glasses as a way to augment the range of small-scale flexures. These materials exhibit mechanical properties that enable them to achieve large elastic strains. With proper design of the flexural elements, these strains may be used to generate large, smooth and controlled precision motions. In the following, we describe the advantages of using metallic glass. This is followed by a brief description of a case study on the small-scale, flexure-based nanopositioner that is shown in Figs. 1 and 2. This device was created by micromolding its shape from the metallic glass Vitreloy ($Zr_{41.2}Ti_{13.8}Cu_{12.5}Ni_{10}Be_{22.5}$) [3].

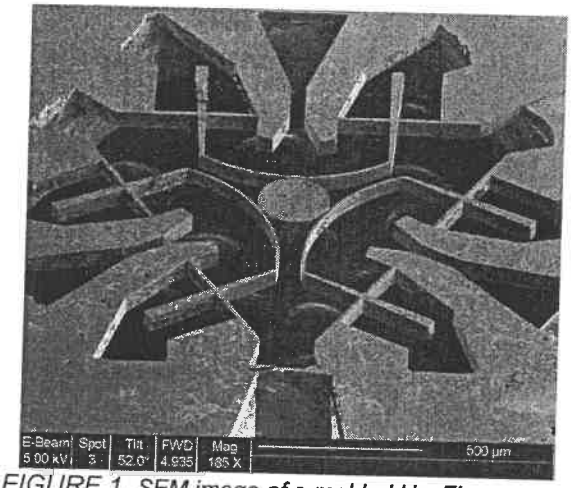

FIGURE 1. SEM image of a molded HexFlex

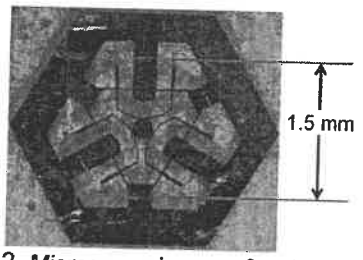

FIGURE 2. Microscope image of molded HexFlex

Brief overviews of the flexure design and fabrication process are followed by discussion of experimental results and simulation results. The results show that a micro-molded metallic glass flexure can exhibits deformation capabilities that are not normally seen in small-scale flexures.

MATERIAL PROPERTY FIGURES OF MERIT

There are two figures of merit used to compare the static and dynamic characteristics of flexure design concepts. A high ratio of yield stress to Young's Modulus (σ/E) indicates the ability to achieve higher deformations for a given flexure geometry. A high ratio of Young's Modulus to density (E/ρ) indicates a high ratio of stiffness per unit mass and so the natural frequency scales with this ratio.

Table 1 shows a comparison of these values for three common engineering materials in contrast to Vitreloy

TABLE 1. The mechanical properties of Vitreloy 1 in contrast to other common flexure materials.

	Units	Vitreloy [3].	Aluminum 6061 T6	Spring Steel	Silicon
σ_Y	MPa	1900	276	1590	120
E	GPa	96	69	210	112
σ_Y/E	---	0.020	0.004	0.008	0.001
Normalized		1.00	0.20	0.38	0.05
ρ	kg/m^3	6000	2700	7850	2330
E/ρ	m^2/s^2	$1.6x10^7$	$2.6x10^7$	$2.7x10^7$	$4.8x10^7$
Normalized		1.0	1.6	1.7	3.0

It is instructive to examine the normalized values of the ratios. The first ratios shows that for a given flexure design, Vitreloy has the capability to achieve a range that is 2.6X larger than its closest competitor (Spring steel) and 20X larger than Silicon. Unfortunately, we can expect the natural frequency to be approximately 70% lower than a device made from spring steel or 3X lower than one made from Silicon.

OVERVIEW OF FLEXURE DESIGN

A micro-scale HexFlex flexure is the subject of our experiments. The design is a derivative of a silicon-based micro-HexFlex [4]. The structure/mechanism layer is 60 μm thick and sits atop a ring-type support layer that is 250 μm thick. The mechanism layer consists of a central stage, supported by six flexural bearings with six tabs that allow external actuation as shown in Fig. 3. In-plane displacements (x, y, θz) are generated by in-plane forces applied to the tabs and out-of-plane displacements (z, θx, θy) are generated by applying out-of-plane forces to the tabs [4]. Combinations of in- and out-of-plane actuations yield six-axis displacements.

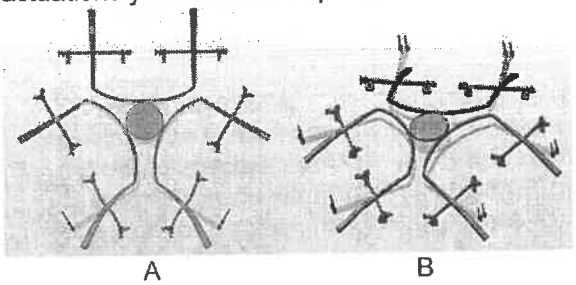

A B

FIGURE 3: Generating pure Y motion by displacing the bottom tabs in-plane (A) and generating pure Z motion by pushing all the tabs downward (B)

OVERVIEW OF FABRICATION PROCESS

The micro-molding process is conducted under a low temperature condition (400 ^{0}C) [6]. A phase change does not occur during the molding process; therefore the volume contraction during the cooling cycle of the process is less severe than one finds in conventional molding processes. This is important as many small-scale flexures depend on the bending stiffness of thin features, which in turn depend on the square or cube of the features' thickness. As such, tight dimensional control is critical to providing flexures with the desired stiffness characteristics. The bulk amorphous metal alloys tend to develop good surface finish upon vitrification, which is important because options for secondary-finishing operations are limited.

The micro-molding experimental setup uses the MTS Q-Test 5 load frame and 5000 N load cell shown in Fig 4. The individual components of the mold tooling are shown on the right of Fig. 4. The multi-step molding procedure includes (1) preload, (2) molding load, and (3) cool-down load. A master Silicon mold was patterned using DRIE. As mentioned, the molded HexFlex mechanism consists of two layers: mechanism layer and support layer. The center of the support layer is open, thus allowing the device to move. During the molding process, the metallic glass is supplied through the mechanism layer and fills the support structure until the mold is fully filled. The excess metallic glass is then removed using a fine grit abrasive process that ceases once the silicon mold can be seen. Next, the silicon mold is chemically dissolved leaving the HexFlex and support structure.

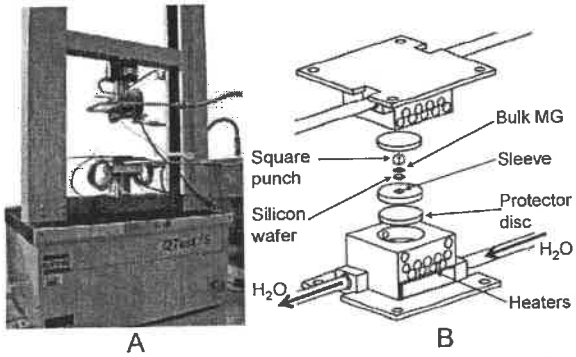

FIGURE 4. Micro-molding experimental setup: MTS Q-Test 5 load frame (A) and detail of mold tooling (B)

The micro-molding process is able to create the complex geometry with reasonable fidelity. The

nominal device thickness was desired at 60 micrometers and this has been measured to vary between 56 and 60 micrometers. The perimeters of the structural and flexural elements of the device are faithfully represented within a few microns. Inspection of Fig. 1 shows the existence of dark spots that appear to be voids or cavities in the flexural elements. These will undoubtedly affect performance, though any negative effects were not evident in our tests.

EXPERIMENTAL RESULTS

Tests were conducted on a Hysitron Nano-indenter and a Zygo profilometer in order to obtain the out-of-plane characteristics.

Hysitron Nano-indenter Test

This first test is run to ensure that the flexure of the device is as expected for the material properties and flexure geometry. This is useful to ensure that there are no cracks or other problems that would cause errors in follow on tests. Figure 5 shows the nano-indentation experimental results. The indentations were performed by pressing on the center of the stage and measuring the motion of the indenter tip as force was applied to the stage. The plot shows a bi-linear force-displacement relationship. The first, lower slope line represents a phase where the indenter is settling into the surface of the device. The early portion of the second, higher stiffness phase represents the stiffness of the stage (2700 N/m). The later half of the 2nd line reflects the effects of strain stiffening. The measured stiffness of 2700 N/m is 15% larger than the value obtained from linear FEA (2380 N/m). It is reasonable to expect this level of difference given the variability in device geometry and variability in material properties.

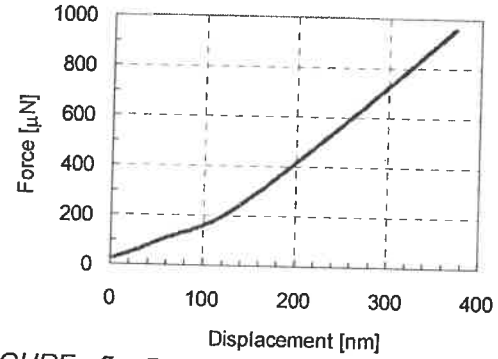

FIGURE 5: Force-displacement plot for nano-indentation on the center stage of the mechanism. The Nano-indentor is limited to exerting 1000 micro-newton force.

Zygo Profilometer Test

The second objective was to obtain the maximum elastic deformation range of the device at the (1) stage, i.e. device output and (2) tabs, i.e. device inputs. We used Cascade probes – devices with minimum step increment of 5 μm – to actuate the device.

In the first test, the probes pressed down on the center stage to see how far the stage could be displaced before failure. The displacement was measured using a white light interferometer. We were able to displace the stage in the z direction over 200 micrometers which is 3.3 times the thickness of the device. The limit of the z measuring range of the interferometer is 200 micrometers, therefore we were unable to extend the measurements beyond this. Upon unloading, the device recovered elastically, returning to its previous position.

Although we were unable to measure a failure, FEA results indicate that the stress state in the innermost, arc-shaped flexures starts to exceed the yield stress at about 200 micrometers. In contrast, a same-sized Silicon device would at best be able to displace 10 micrometers – $^1/_6$ of the device thickness – before failure.

In the second test, two probes were used to actuate the tabs at the locations shown in Fig. 6. The actuation direction was set in a direction normal to the plane of the device.

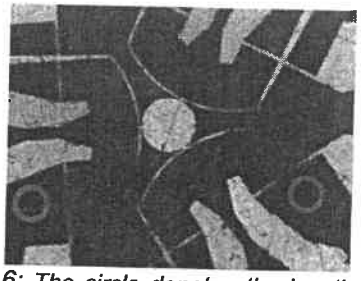

FIGURE 6: The circle denotes the location that the probe tips were pressed onto the tabs.

The probes were able to deflect the tabs by 200 micrometers – to the point where we loose the ability to measure additional deformation. The data from this test is shown in Fig. 7.

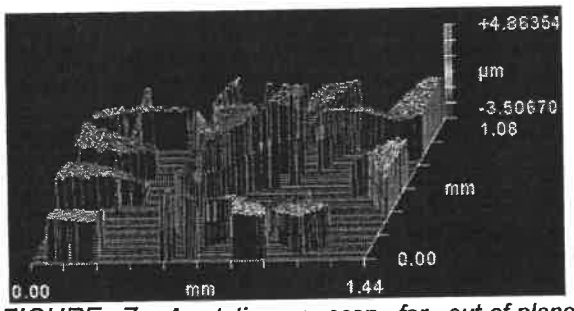

FIGURE 7: A stationary scan for out-of-plane displacement taken on a Zygo profilometer

It is difficult to visualize the degree of deformation using this data, therefore Fig. 8 is provided to augment the experimental data. Figure 8 shows a "to-scale" representation of the deformation via a side view and a 3D view of a FEA model. We note that Silicon is again only able to deform ~ $^{1}/_{20}^{th}$ the range shown in Fig. 8.

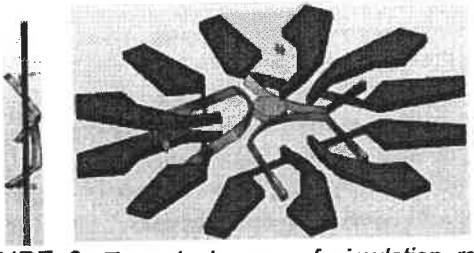

FIGURE 8: To-scale images of simulation results that show the device deflected per the actuation inputs that created Fig. 7.

Frequency Response and Mode Shapes

Figure 9 shows the results of a frequency sweep on the device. The data was obtained via a scanning Laser-Doppler Vibrometer. In the experiment, the Molded HexFlex was packaged/constrained on top of a piezo-actuated vibration stage and excited with a chirp signal. The results in Fig. 9 indicate the 1st resonance mode, at 38 kHz, is the out-of-plane motion, compared to a 40 kHz FEA prediction. Our experiment is unfortunately not equipped to extract data that would indicate the degree of damping within the material, though it is common knowledge that this effect is small in metallic glasses.

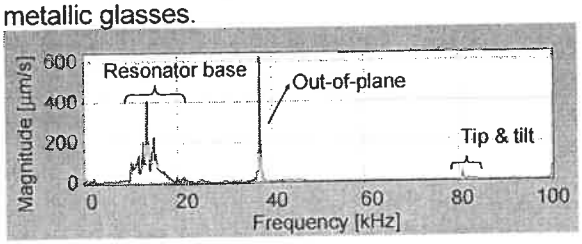

FIGURE 9: Frequency sweep, note that the resonance around 14 kHz is an artifact of the testing system. The natural frequency occurs at 38kHz.

CONCLUSION

The purpose of this paper has been to demonstrate that (1) complex, small-scale flexural machine elements can be micro-molded from metallic glasses and (2) the use of a metallic glass can endow small-scale flexures with deformation capabilities that can not be obtained by conventional engineering materials. Specifically, the advantage over Silicon shows that this material is promising for small-scale machines. The experimental results provide some confidence that a molded glass flexure may be used to solve current problems in micro-scanning stages for the biomedical imaging applications discussed in the introduction.

Future work will consist of integrating micro-actuation systems with these devices and perhaps improving the quality of the device geometry (i.e. eliminating cavities).

ACKNOWLEDGEMENTS

We would like to express our thanks to Jack Danieli of Polytec for his assistance in obtaining the dynamic response of the device.

REFERENCES

1. Choi, H., Chen, S., Kim, D., So, P. T., and Culpepper, M. L., "Design of a Non-linear Endomicroscope Biopsy Probe," OSA Biomedical Optics Topical Meeting and Tabletop Exhibit, FL, March 19-23, 2006
2. Chen, S., Choi, H., Kim, D., Culpepper, M. L., So, P. T, "Design of a High-speed, Micro-scale Fast Scanning Stage for Two-photon Endomicroscopy," submitted to the 2006 Annual Meeting of the American Society for Precision Engineering [accepted].
3. Lu, J, et al., "Deformation Behavior of the $Zr_{41.2}Ti_{13.8}Cu_{12.5}Ni_{10}Be_{22.5}$ Bulk Metallic Glass over a Wide Range of Strain Rates and Temperatures," Acta Materialia, 2003.
4. Chen, S., Culpepper, M. L., "Design of a Six-axis Micro-scale Nanopositioner—Micro-HexFlex," Journal of Precision Eng. 2006, Vol. 30, Issue 3, pp. 315-24.
5. Culpepper, M. L., Anderson, G., "Design of a Low-Cost Nanomanipulator which Utilizes a Monolithic, Spatial Compliant Mechanism", Prec Eng 2003.
6. Bardt, J., Mauntler, N., Bourne, G., Schmitz, T. L., Ziegert, J. C., Sawyer, W. G., "Metallic Glass Surface Patterning by Micro-molding". Proceedings of IMECE-2005, Nov. 5-11, Orlando, FL.

APPLICATION OF INPUT SHAPING® AND HYPERBIT™ CONTROL TO IMPROVE THE DYNAMIC PERFORMANCE OF A SIX-AXIS MEMS NANOPOSITIONER

Shih-Chi Chen[1], Martin L. Culpepper[1], Scott C. Jordan[2]
[1]Department of Mechanical Engineering
Massachusetts Institute of Technology
Cambridge, Massachusetts
[2]Department/Division
Physik Instrumente
San Jose, CA 95120

SYNOPSIS

In this paper, we demonstrate how Input Shaping® and HyperBit™ control may be used to obtain fine resolution motion and minimize vibration errors in all six axes of a six-axis, MEMS nanopositioner — microHexFlex [1]. We will first review the dynamic characteristics of the nanopositioner, including the natural frequencies and their corresponding mode shapes. We then demonstrate the effect of Input Shaping® and HyperBit™ on the nanopositioner's resolution and settling time. Using these techniques, it is possible to obtain ms settling times with sub-nanometer resolution. The practical implications of this work are that future small-scale precision devices will be able to use these techniques to provide low-cost, multi-axis positioning at high-speeds and with fine resolution.

INTRODUCTION

Six-axis nanopositioners have the ability to rectify angular misalignment and thereby correct sine/cosine errors. This capability is important to nanopositioners as angular errors may result in tens of nanometers or more position error. The ability to correct these errors enables six-axis devices to obtain levels of accuracy that are out of the reach of other types of nanopositioners. It is also important to note that six-axis positioners are capable of pivoting about an arbitrary point, i.e. a virtual pivot point, in space. This characteristic would be useful for the creation and inspection of free-form surfaces in applications, such as nano-machining, probing, scanning and manipulation.

The improved accuracy and motion capabilities are most significant if the nanopositioner moves at speeds that are required for creating or inspecting large numbers of features in a short period of time. It is therefore beneficial to possess six-axis capability in a micro-scale device that can take advantage of the beneficial scaling of natural frequency with miniaturization.

This is important for instance in high speed positioning devices for endoscopic scanners [2], integrated alignment mechanisms in micro-optic devices [3], nanoinstrumentation and positioners that are used in nano-manufacturing/data storage [4, 5]. Unfortunately, flexure-based micro-scale positioners are often made from single crystalline Silicon which has negligible damping. As a result, it is difficult to incorporate damping into these micro-/meso-scale nano-positioners. The types of dynamic problems, e.g. ringing and overshoot, which are typically addressed by damping in macro-scale machines, must therefore be addressed at the micro-scale via control techniques. In this paper, we present a study on the effect of two technologies, input shaping and Hyperbit, that can improve the dynamic performance of small-scale nanopositioners.

CASE STUDY: μ-HEXFLEX

The focus our experiments is the microHexFlex, a planar six-axis micro-scale nanomanipulator shown in Fig. 1A.

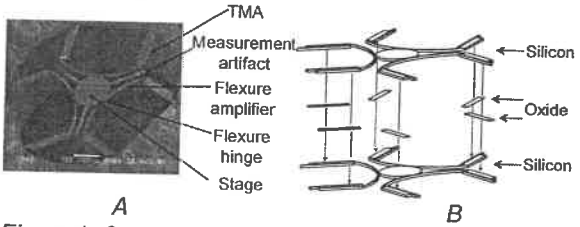

Figure 1: Overview of μ-HexFlex

The device contains teams of micro-actuators [1] that cause the stage to move in one to six axes. Motions are achieved using actuators that deform the device's compliant structure and thereby cause the stage to move in a controlled manner. Structurally, the microHexFlex consists

of two layers of single crystalline silicon with one layer of silicon dioxide that resides between them. This multi-layer architecture, shown in Fig 1B, may be used in a bi-morph mode of operation to achieve out-of-plane motions, or in a planar mode of operation to achieve in-plane motions [1]. The stage of the microHexFlex is supported by micro-scale flexures that enhance the actuation displacements from the microactuators.

The dynamic characteristics of a 2.5 mm diameter microHexFlex were obtained via a scanning Laser-Doppler Vibrometer. The first resonance mode peaks at 6.4 kHz with a mode shape that is in the z direction (out-of-the-plane in Fig. 1A). The subsequent three modes occur between 10 kHz to 13 kHz and correspond to tip and tilt mode shapes. More mode shapes, including in-plane motions and out-of-phase motions, at higher resonance frequencies were also obtained in the experiment. Given the preceding information, the modal frequencies may be selectively nullified by the Input shaping/HyperBit algorithm to generate desired motion paths.

In our tests, the thermomechanical actuators were driven via a voltage that was preconditioned using an Input shaping controller. The controller [6, 7] is an implementation of a feed-forward technique that acts to remove ringing and overshoot by modifying the input signal to the actuators to obtain the best possible performance from the positioner.

INPUT SHAPING®

An Input Shaping controller is an implementation of a deterministic and robust feed forward technique. It is designed specifically to suppress vibration excited by motion transients. The input Shaping algorithm requires only knowledge of the modal frequencies of the system, which in this case were collected experimentally. The controller is designed to reside in series between a function generator and an analog position-command input.

We prefer to observe the resultant motion of the microHexFlex driven by a 100Hz square wave that would command positive Z direction. As shown in Fig 2A, the resultant displacement of the microHexFlex without Input Shaping control exhibits a high frequency ringing effect at ~6.4 kHz. The nullification of this resonant behavior can be observed after the resonance characteristics (frequency ~6400 Hz, damping ζ ~ 0.005) are provided to the Input Shaping controller, as shown in Fig 2B. Note that the drift/slope in Fig 2 is attributable to an integration constant that is obtained when the data (velocity) is integrated to obtain position.

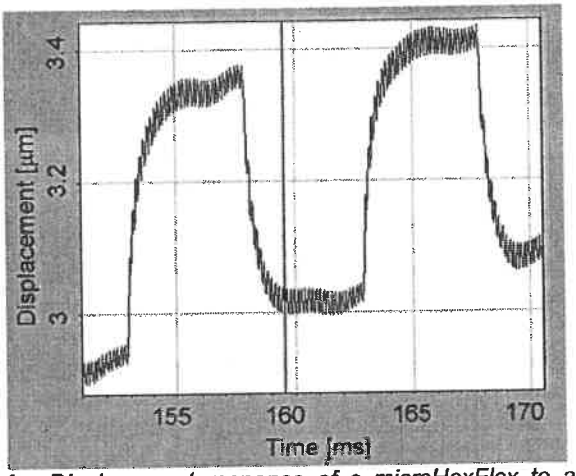

A: Displacement response of a microHexFlex to a 100-Hz square-wave without Input Shaping

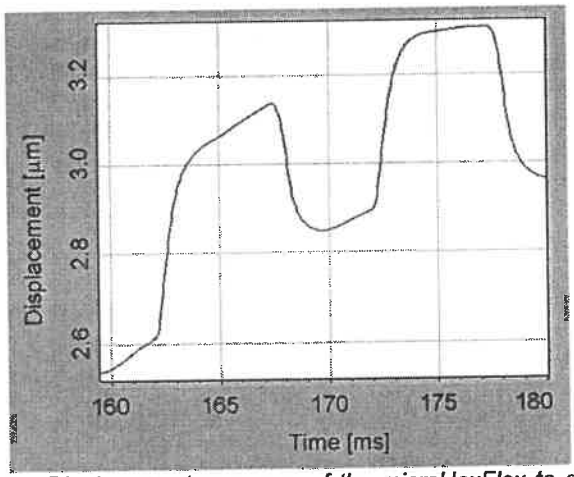

B: Displacement response of the microHexFlex to a 100-Hz square-wave with Input Shaping

FIGURE 2. Performance enhancement after applying Input shaping control.

HYPERBIT™ CONTROL

HyperBit™ is a recently-developed technique [8, 9, 10] for extending the resolution of digital-to-analog converters (DACs), which is otherwise fixed by the number of addressable bits in a DAC's command input. In its simplest implementation, the technique involves pulse-width modulation (PWM) of the least-significant bits (LSBs) of the DAC. As DAC update rate capabilities are generally significantly faster than the bandwidths of the devices being driven, this

technique allows the idle time-domain capacity of the DAC to be converted into resolution, as shown in Equation (1).

$$res_{bits} \rightarrow res_{DAC} + \log_2\left(\frac{DAC\ Rate}{PWM\ Frequency}\right) \quad (1)$$

HyperBit is of particular interest to MEMS developers as less silicon real-estate or off-die circuitry is required to achieve a target resolution, enabling a cascade of fabrication cost savings and density improvements. As the microHexFlex is a flexure-based device where friction is negligible, its resolution is typically limited by its drive electronics' DAC granularity. A to 3H shows laser Vibrometer results demonstrating resolution enhancement of microHexFlex under waveform actuation using "bitness-limited" DACs.

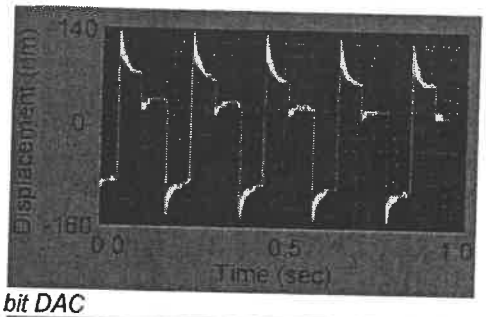

A: 3 bit DAC

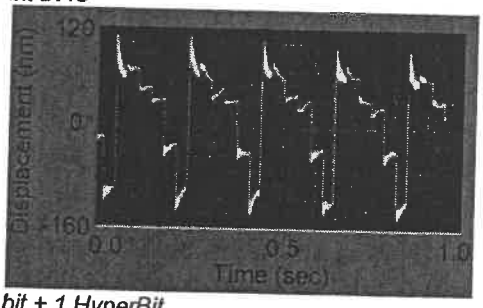

B: 3 bit + 1 HyperBit

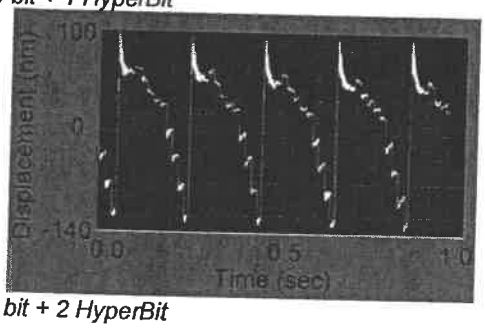

C: 3 bit + 2 HyperBit

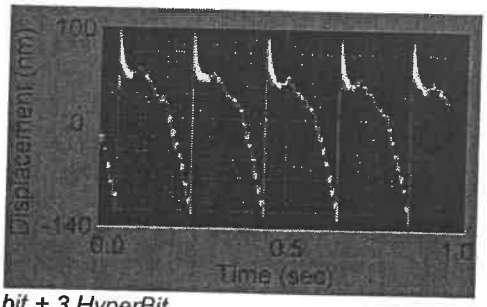

D: 3 bit + 3 HyperBit

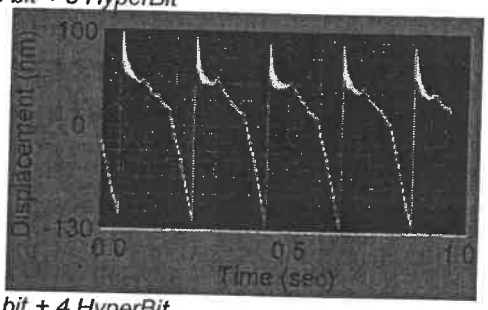

E: 3 bit + 4 HyperBit

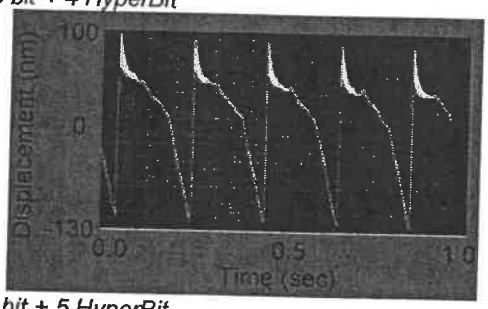

F: 3 bit + 5 HyperBit

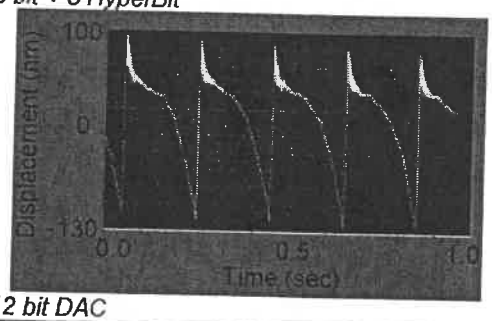

G: 12 bit DAC

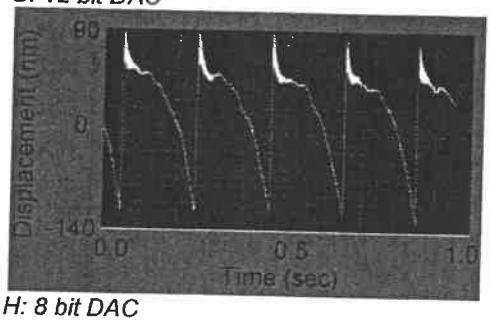

H: 8 bit DAC

FIGURE 3. MicroHexFlex actuation vs. HyperBit configuration. Amplitude chosen for 3 bit transitions of 3-bit DAC. No Input Shaping® is seen in these

examples therefore some ringing can be seen after vertical edge of sawtooth.

CONCLUSION:

We have provided an experimental demonstration of the utility of combining a micro-scale six-axis nanopositioner with Input Shaping and HyperBit Control. The end result of this combination is to show that even though small-scale nanopositioners may have high natural frequencies, this characteristic will not be enough to enable nanometer resolution positioning at high speeds. Damping is difficult to add to micro-scale systems and therefore additional technology is required to realize high-speed nanopositioning via micro-scale devices.

Input Shaping has been shown to have a significant effect via our experimental investigation. The software-based HyperBit technology has also demonstrated the ability to enable low-bit DACs emulate high-bit DACs. The implications of the high-bit DAC emulation are the simplification and further miniaturization of future electronic circuits for on-chip nanopositioners. With the combined technologies, we can now achieve ~5nm resolution at 100 Hz.

We envision that in the near future Input Shaping and Hyperbit control technology will be extensively used in micro-scale positioning systems in various fields. microHexFlex with Input Shaping control, for example, can be used in manufacturing processes that require moving/aligning parts with nanometer resolution, as is the case with many fiber optics components. MicroHexFlex can also be embedded directly into a silicon optical bench, containing numerous smaller devices that need to be kept in alignment over the life of the component.

REFERENCES

1. Chen, S., Culpepper, M. L., "Design of a Six-axis Micro-scale Nanopositioner — MicroHexFlex," Journal of Precision Eng. 2006, Vol. 30, Issue 3, pp. 315-24.
2. Choi, H., Chen, S., Kim, D., So, P. T., and Culpepper, M. L., "Design of a Non-linear Endomicroscope Biopsy Probe," OSA Biomedical Optics Topical Meeting and Tabletop Exhibit, FL, March 19-23, 2006
3. Haake J. M, Beranek M., "Integrated Microelectromechanical Alignment and Method for Fiber Optic Module Manufacturing," US Patent No.: 6164837.
4. Eleftheriou, E., et al., Millipede - a MEMS-based scanning-probe data-storage system. IEEE Transactions on Magnetics, 2003. 39(2): p. 938-45.
5. Mita, M., et al., Bulk micromachined tunneling tips integrated with positioning actuators. J. of Microelectromechanical Systems, 2005. 14(1): p. 23-28.
6. Singer, N. C., Seering, W. P., "Design and Comparison of Command Shaping Methods for Controlling Residual Vibration," in Proc. IEEE Conf. Robotics Automat., 1989, pp.888-893.
7. Singer, N. C., "Residual Vibration Reduction in Computer Controlled Machines," Ph. D. dissertation, AI-TR 1030, Artificial Intell. Lab., MIT, Cambridge, MA, Jan. 1989.
8. Jordan, S. C., "Method and Apparatus for Increasing Effective Resolution of Analog Output of Digital-to-analog Converter (DAC) Having Predetermined Digital Word Size, where DVC Drives Plant" U.S. Patent 6950050,2005
9. Jordan, S. C. and Lawrence, E., "Vibration Nullification of MEMS Devices using Input Shaping", SPIE Smart Structures 2003, http://www.polytecpi.com/ftp/MachTools/SS03.PDF
10. Jordan, S. C., "Eliminating Vibration in the Nano World", Photonics Spectra, July 2002, http://www.physikinstrumente.de/pdf/extra/NanoVibrationControl.pdf

ACTIVE MASK UV LITHOGRAPHY SYSTEM FOR MEMS AND μTAS APPLICATIONS

Terutake Hayashi[1], Takayuki Shibata[2], Takahiro Kawashima[3],
Eiji Makino[4],Takashi Mineta[4], Toru Masuzawa[5]
[1]Department of Mechanical Engineering, Osaka University, Suita, Osaka, Japan
[2] Department of Production Systems Engineering,
Toyohashi University of Technology, Toyohashi, Japan
[3]Department of Electrical and Electronic Engineering,
Toyohashi University of Toyohashi, Japan
[4]Department of Intelligent Machines and System Engineering,
Hirosaki University, Hirosaki, Japan
[5]Department of Mechanical Engineering, Ibaraki University, Hitachi, Ibaraki, Japan

INTRODUCTION

Rapid and accurate fabrication of 3D microstructures is very important for developing devices that are used in microelectromechanical systems (MEMS) and micro total analysis systems (μTAS). Manufacturing such miniaturized 3D devices is typically accomplished by complex processes with multiple etching and deposition steps. Since the method requires a repetitive exposure procedure, the preparation of the multiple photomasks and the repetitive exposure procedure prevents the rapid fabrication of 3D microstructures[1,2].

In order to simplify the fabrication process, an active mask fabrication technique for the small-lot production of 3D microstructures is proposed; it is a photolithographic technique that utilizes a liquid crystal device (LCD) as an electrically controllable photomask. The advantages of this system are as follows: The computer-generated photomask serves as an active photomask in the LCD lithography system. The positions of photomasks can be precisely controlled by a unit of the LCD pixel without any mask alignment procedure. This allows the rapid fabrication of microstructures as well.

It is expected that this system will rapidly and precisely fabricate complicated 3D structure such as a μTAS chip and MEMS devices in small-lot production. The production time and cost of microdevices can be improved significantly using this system.

This paper describes the following: 1) development of the LCD mask exposure system with UV light source, 2) experimental confirmation of high resolution such as 11 μm in the case of exposure using grid patterns.

DESIGN OF LCD LITHOGRAPHY SYSTEM

A photolithography system with an LCD as an active mask developed here used a conventional high-pressure mercury lamp as an ultraviolet (UV) light source in order to fabricate microstructures by using commercially available photoresists. The optical configuration of the LCD lithography system was determined from the following experiments. First, the contrast of the LCD mask to the UV light was evaluated as a function of irradiated light intensity. Next, an appropriate incident angle of the UV light for the LCD mask was investigated in order to obtain the highest contrast in the system. We also examined optical aberrations on the image plane of the system with the LCD mask in order to improve the pattern exposure resolution.

Contrast of LCD mask against UV light of 365nm

In the LCD, polysilicon thin-film transistors (TFTs) are used as switching elements for pixels. Therefore, in order to prevent damage to the LCD that must decrease the contrast of the LCD during UV exposure, the UV light irradiation on the TFT substrate part should be reduced[3,4]. In this experiment, we selected the LCD integrated with microlens array, resulting in a high numerical aperture (NA) of more than 54%, which is greater than that of a conventional LCD. This type LCD has an advantage; the microlens decreases the UV light irradiation on the TFT substrate part that will reduce the above problems to a minimum. In addition, the loss of UV light through the LCD mask effectively decreases.

The contrast of the LCD mask against UV light centred at 365 nm selected from a high-

pressure mercury lamp (Ushio Inc., SX-UI 500HQ) through an optical filter was investigated under varying irradiation conditions with the basic configuration of an experimental optical setup shown in Fig. 1. Two important factors—light intensity and incident angle—were considered since they would affect the LCD mask contrast. We calculated the LCD mask contrast by using two parameters — I_{255} and I_0; they denote the transmitted light intensity when LCD mask grey levels are of 255 (Open) and 0 (Close), respectively. The contrast was defined as I_{255}/I_0. As shown in Fig. 1, a polarizer changes the polarization of incident light from the mercury lamp into a linearly polarized light. The polarized light is then focused by a lens with a variable aperture and passed through the LCD mask. A pair of polarizers is placed in the orthogonal polarization direction at the front and back of the LCD mask.

Fig. 2 shows the influence of light intensity on LCD mask contrast as a function of F-number. The F-number (F = f/D) is defined as the ratio of aperture diameter (D) to the effective focal length of a lens (f). It expresses the divergence angle of focused light rays, that is, an increase in the F-number will decrease the divergence angle. An F-number of 5.7 gives approximately 5° divergence angle with respect to an optical axis, which is a maximum value in this experiment. The data (denoted by a △ symbol) were taken by changing the optical density of a neutral density (ND) filter at the same aperture diameter in order to change the light intensity only. The mask contrast slightly increased with an decrease in the light intensity less than 150 mW/cm^2.

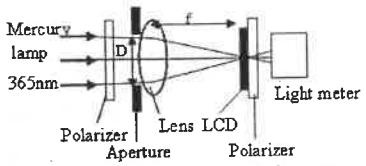

Fig. 1 Experimental setup for characterization of LCD mask contrast.

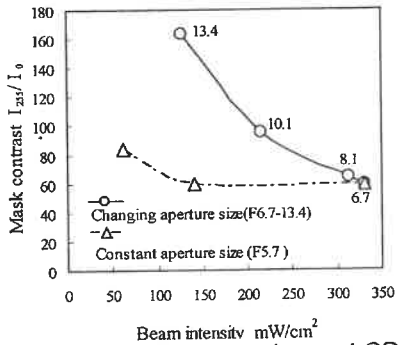

Fig. 2 Influence of light intensity on LCD mask contrast as a function of F-number.

On the other hand, the LCD mask contrast (denoted by a ○ symbol) were measured at varying F-numbers with changing the aperture diameter. The mask contrast increased markedly with an decrease in the light intensity, where the F-number increased simultaneously. At a light intensity of 150 mW/cm^2, the mask contrast at F = 13.4 was approximately three times larger than that at F = 5.7. These results suggest that the effect of the divergence angle corresponding to the F-number on the improvement in the mask contrast was greater than that of the light intensity. Therefore, the perpendicular incident direction to the LCD mask with a well-collimated incident light is required to achieve high LCD mask contrast.

OPTICAL DESIGN OF UV LITHOGRAPHY SYSTEM WITH LCD ACTIVE MASK

As mentioned above, a pattern projection system with high LCD mask contrast could be achieved by using collimated UV light that perpendicularly illuminated the LCD mask as well as low light intensity. Based on this concept, we designed the optical configuration of an UV lithography system with an LCD active mask as shown in Fig. 3. By applying a reduction optical system, the LCD mask can be placed just behind the mercury lamp, and consequently, it will be illuminated by well-collimated light with relatively low intensity. The energy density of the light passed through the LCD mask can be intensified on an exposure plane by the reduction optics. This will allow patterning conventional UV-sensitive photoresists. Moreover, the pattern exposure resolution can be improved because the reduction image of the mask pattern displayed on the LCD is projected on the exposure plane.

The optical system was composed of three parts, namely, a uniform irradiation optical system that generates collimated light with a low

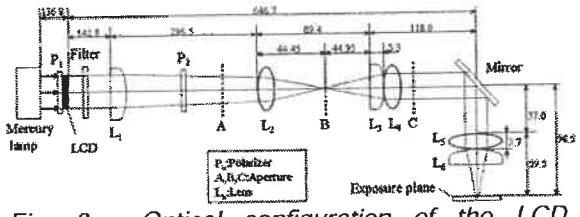

Fig. 3. Optical configuration of the LCD lithography experimental system.

energy density, reduction optical system that reduces the LCD mask pattern at 15%, and relay lens optical system that transfers the LCD mask image to an exposure plane. A wavelength of 365 nm was selected from the mercury lamp using an optical filter with a transmittance of 82.7% before illuminating the LCD mask. The lens arrangement and specifications were determined by considering the balance of optical aberrations based on ray-tracing simulation results. In order to reduce the light absorbance to a minimum, we used anti-reflection coated lenses with a transmittance of 99.0% and a mirror with a reflectance of 99.0 % at 365 nm. In this system, the LCD mask, consisting of a pair of polarizers and the LCD itself, showed very low transparency at 365 nm, resulting in a transmittance of only 1.1%. As a result, the overall transmittance of the optical system (from the mercury lamp to the exposure plane) was estimated to be as low as 0.8%.

However, as the LCD lithography system designed here is a projection system with a 6.5:1 reduction, the UV light intensity on the exposure plane can be maintained to be approximately 35% of that of the mercury lamp.

EVALUATION OF PATTERN RESOLUTION ON LCD LITHOGRAPHY SYSTEM

Fundamental experiments were conducted by using a binary mask image displayed on the LCD in order to achieve high resolution on the LCD lithography system. In this chapter, we discuss the effect of apertures on pattern exposure resolution. Three apertures A, B and C were set as shown in Fig. 3. They will strongly depend on optical aberrations on an exposure plane.

Effect of apertures on pattern exposure resolution

A computer generated mask image on the LCD composed of four square patterns with a size of 19×19 pixels (342×342 μm^2). The squares are located diagonally with a gradually increasing interval. This mask image is reduced by 15%, and consequently, the size of each square pattern will be of 52.3×52.3 μm^2 on the exposure plane. Fig. 4(a) shows a typical photoresist pattern formed by using the LCD mask image without any aperture on the LCD lithography system. A positive photoresist (Tokyo Ohka Kogyo Co. Ltd., OFPR-800) layer with a thickness of about 1.4 μm was spin-coated onto a silicon substrate, and then exposed by 365 nm UV light. The resulting square-shaped photoresist patterns (in width Wa) were equivalent to the transparent image area of the LCD mask. However, in the neighbourhood of each square pattern, interference fringes were observed. Since the interference fringes are originated in the change in photoresist thickness, this region (in width Wb) can be also considered as a light irradiated area, but the photoresist was still remained in a development process probably due to underexposure. Such geometric error is mainly caused by optical aberrations on the exposure plane. Therefore, the pattern resolution must improve as the width W_b of the exposed area approaches the width W_a of the patterned area by adjusting the position and diameter of the apertures.

The exposed area did not change despite the addition of aperture A. It did not change even when the aperture diameter of B was decreased. However, the exposure area decreased with the aperture diameter of C.

Exposure results obtained without the aperture C has an interference fringe The resolution is considered to improve as the area of Wb approaches that of Wa. The resolution of pattern exposure is optimum when the aperture C with a diameter of 8 mm is used; in this case the exposure area is the minimum.

From the above result, it was confirmed that the exposure area could be optimized by adjusting the aperture diameter of C. Therefore, the aperture diameter of C was the dominant parameter for achieving the appropriate irradiation conditions.

The aperture A was considered to control the light amount and remove the high order diffracted light. The aperture B was

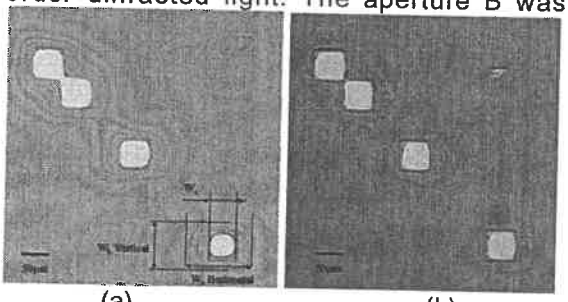

(a) (b)

Fig. 4. Typical positive photoresist patterns formed by using LCD mask with LCD lithography system: (a) Exposed at exposure energy of 66 mJ/cm² (0.168 mW/cm² × 390 s) without any aperture; (b) exposed at exposure energy of 15 mJ/cm² (0.025mW/cm² × 600 s) with 8mm-diameter aperture C.

considered to remove the stray light. The aperture C was considered to decide the resolution of reduction optical system. However the reduction optical system had long optical path from lens L1 to L3, the frame of lens worked as well as the aperture A and B. On the contrary the aperture C could control the angle of the field on relay lens imaging system, that is composed from lens L3 to L6, at the behind of lens L4. The resolution thus depended on the size of the aperture C.

Evaluation of resolution using line and check patterns with different aperture sizes of A, B and C

Line pattern were produced in order to investigate the resolution by using the reduction optical system. The line pattern with a 10 μm gap could be fabricated when the aperture C was set to a diameter of 8 mm. The pattern resolution corresponded to the contrast of light intensity between the exposed area and its surrounding area. The resolution decreased significantly with an increase in the exposure line width because of overexposure.

Fig. 5 shows the fabrication result of the line pattern with a width of 10.8 μm. The diameter of C was 8 mm. The resolution did not improve with any change at B. The highest mask contrast was obtained by adjusting C of 8 mm in the designed optical system.

It was confirmed that the line pattern with a line width of 10.8 μm could be precisely fabricated using OFPR-800. It was confirmed that our designed optical system, which uses UV light as a light source, was useful for 2D device fabrication.

CONCLUSION

In this study, we designed the LCD mask exposure system for applying the LCD as a UV photomask. The patterning resolution of the LCD mask was evaluated. It was experimentally confirmed that the line pattern of 10 μm in width could be fabricated by using the developed system.

The experimental results are summarized as follows.

(1) The mask contrast lowered with an increase in the angle of light emitted in the LCD. In particular, the contrast decreased rapidly when the range of the incident light angle was greater than 5°.

(2) The patterning resolution of the reduction optical system without any aperture was 48.6 μm (18 pixels). The finest pattern could be fabricated by installing the aperture C of 8 mm. The resolution was 10.8 μm (4 pixels) in the line width and 5.4 μm (2 pixels) in the line space.

It was expected that this technique could be applied to the fabrication of μTAS chips such as the flow channel with tapered shape. 3D MEMS devices could also be fabricated without the multistep procedure. In addition, this technique could be applied widely for controlling the lighting area and light intensity distribution in order to control various photochemical reactions. This technique is expected to be applied for the synthesis technology of DNA chip production.

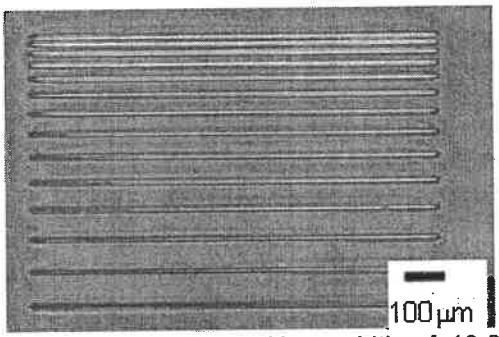

Fig. 5 Line pattern with a width of 10.8 μm width at 12.9 mJ/cm2

REFERENCES

1. Maboudian, R,1998, Surface processes in MEMS technology, Surface Science Reports 30 (6), 207-269
2. Bustjllo, J.M., Howe, R.T., Muller, R.S. 1998 Surface micromachining for microelectromechanical systems, Proceedings of the IEEE 86 (8), 1552-1573
3. Yong-Hyuk LEE, Se-Jin KYUNG, Jong-Hyuk LIM and Geun-Young YEOM, 2005, A Study of Electrical Damage to a-Si:H Thin Film Transistor during Plasma Ashingby a Pin-to-Plate Type Atmospheric Pressure Plasma, Japanese Journal of Applied Physics, Vol. 44, No. 48, L 1456–L 1459
4. Gosain, Dharam Pal, Westwater, Jonathan, Usui, Setsuo, 1995 High performance bottom gate TFTs by excimer laser crystallization and post hydrogenation Japanese Journal of Applied Physics, Part 1: 34 (2 B), pp. 937-941

NANOMETER-SCALE DEPOSITION OF PHOTO-CURING RESIN USING A SCANNING NANOPIPETTE PROBE MICROSCOPE

Futoshi IWATA, Yuhki Ushiro, and Akira SASAKI
Department of Mechanical Engineering,
Faculty of Engineering, Shizuoka University
Johoku, Hamamatsu, 432-8561, Japan

INTRODUCTION

Scanning Probe Microscopes (SPMs) are well known as surface imaging techniques at nanometer scale resolution. SPM can be used not only for surface observation but also for local surface fabrication. The typical fabrication technique using SPM is directly scratching on surfaces with the probe. However in this case, high loading force must be applied between the probe and the surface, which induces some undesirable problems such as cutting particles and probe edge wearing. Therefore, other fabrication techniques are required.

Recently, we have developed novel nanometer-scale fabrication using a scanning shear-force microscope with a nanopipette probe. The nanopipette probe was used for delivering materials to any points on the substrate surface [1]. Furthermore, local metal plating was also achieved using the nanopipette probe filled with metal ionic electrolytes [2].

In this paper, we describe nanometer scale fabrication method of photo curing resin using near field optical illumination. Dot array and line pattern were sequentially fabricated on the glass substrates.

EXPERIMENTAL METHOD

Figure 1 shows a schematic diagram of a scanning shear-force microscope using a nanopipette probe for local surface fabrication. This scanning probe microscope system was constructed by us. A capillary glass tube, having 1.0 and 0.6 mm outer and inner diameters, respectively, was thermally pulled using a filament-type nanopipette puller (Narishige, PD-5). The diameter of the probe aperture was approximately 200 nm as shown in Fig. 2. The nanopipette probes could be filled with any kind of liquids for delivery and fabrication. In regard to the topographical observation of the surface, the shear-force control technique was employed. The pipette probe was fixed on a dither PZT and oscillated laterally at its resonant frequency of approximately 20 kHz with the amplitude of 1 nm. As the probe is approached to the surface, the amplitude is damped. Thus the distance between probe and surface could be controlled.

As for the photo curing resin, liquid state photo curing resin was filled into the nanopipette probe. After deposition of the liquid state resin, the resin was cured by irradiation of light. The peak of the absorption spectrum of the photo curing resin is about 500 nm. Thus Ar^+ laser was employed due to almost same wavelength of 488 nm. In order to avoid undesired cure of the liquid state resin inside the pipette, evanescent wave was employed on the triangle prism in total internal reflection.

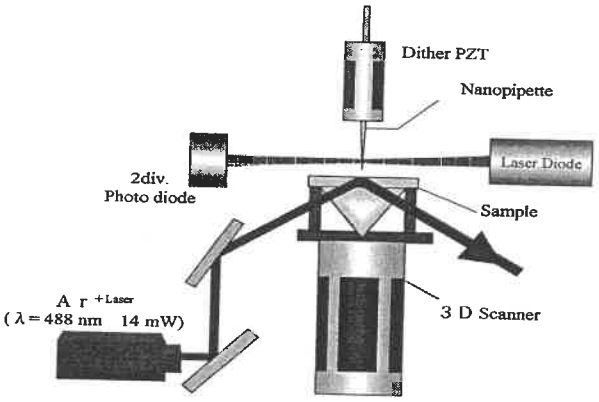

Figure 1: Experimental setup of the nanopipette probe microscope. Glass substrate is put on the triangle prism fixed on the PZT tube scanner. Ar^+ laser (wavelength of 488 nm) is employed to cure the photo curing resin.

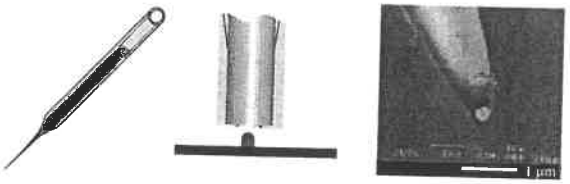

Figure 2: Nanopipette probe. The nanopipette probe was prepared by thermally pulling from the capillary glass tube.

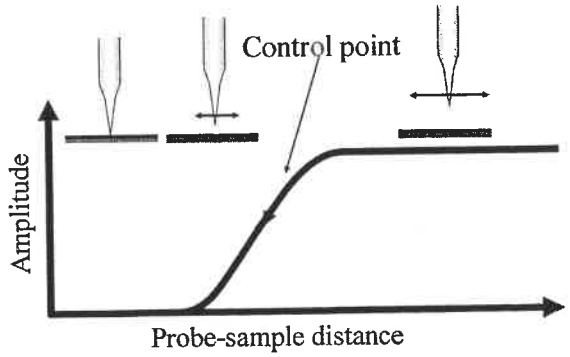

Figure 3: Shear force distance control Nanopipette probe was oscillated laterally at its resonance frequency with amplitude of 1 nm.

EXPERIMENTAL RESULTS

Figure 3 show the dot deposited by this method. Figure 3(a) shows the dot before laser illumination. Liquid state dot could not be observed due to dragging by the probe during scanning. On the other hand, Figure 3(b) shows dot structure after laser illumination. As shown in this figure, clear dot structure could be observed. Thus, the dot structure was cured by photochemical reaction. In general, intensity of such evanescent illumination is not strong. However, in our experiment, with respect to the incident beam of 14 mW power, the exposure time about 1 sec was enough to cure it.

The amount of deposition can be controlled by changing deposition time. Figure 4(a) shows the smallest dot in our experiment. Figure 4(b) shows the cross-sectional profile. The height and width of the dot are 10 nm and 180 nm, respectively. Figure 4 (c) shows the dot array of the photo curing resin deposition. The dot array was sequentially fabricated during surface scanning by varying the probe-surface distance under shear-force control. Figure 4(b) shows cross-sectional profile. High reproducibility can be confirmed.

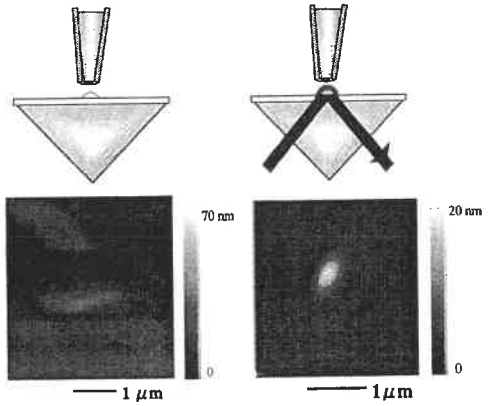

Figure 3: Dot structures before curing and after curing. (a)Dot without laser illumination. (b) Dot structure with laser illumination.

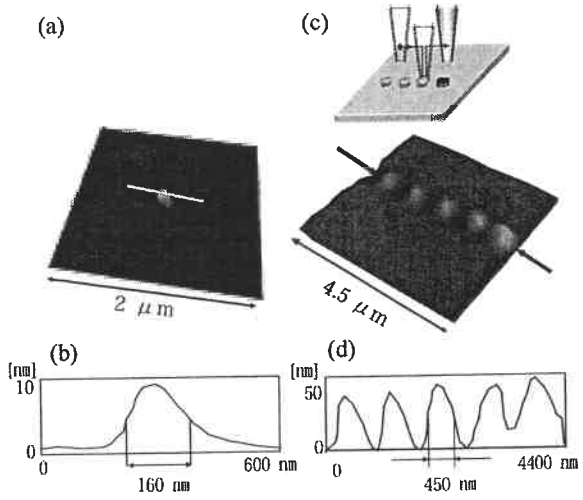

Figure 4: (a) Smallest dot deposited by this method. (b) Cross-sectional profile of the dots structure. (c) Dot array (d) Cross-sectional profile of the line patterns.

CONCLUSION

Novel fabrication techniques of local surfaces were performed using a scanning probe microscope with various liquids filled nanopipette probes. Liquid state photo curing resin was successfully deposited on the substrate, then, the liquid resin could be cured with evanescent wave light generated by total internal reflection configuration in triangle prism attached under sample holder. Dot array structures could be realized. These fabrication techniques might be conceivable for many fields such as precision engineering and biological manipulations.

REFERENCES

1. F Iwata, Y Sumiya, S Nagami and A Sasaki "Submicrometer-scale fabrication of polycarbonate surface using a scanning micropipette probe microscope", *Nanotechnology* 15 (2004) 422.

2. F Iwata, Y Sumiya, S Nagami and A Sasaki "Nanometer-scale metal plating using a scanning shear-force microscope with an electrolyte-filled micropipette probe", *Jpn. J. Appl. Phys* 43 (2004) 4482.

RECENT ADVANCES IN IMPROVING STATIC AND DYNAMIC ACCURACY OF NANOPOSITIONING SYSTEMS

Scott C. Jordan
PI (Physik Instrumente) L.P.
San Jose, California USA

BACKGROUND

Not long ago, nanopositioning was a laboratory curiosity. Today it is a vital industrial commodity, fundamental to industries as diverse as semiconductors, data storage, biotech and defense, and an entire new field of nanomanufacturing promises fresh challenges of immense economic importance. Fortunately the field of nanopositioning enjoys rapid innovation which addresses emerging issues. Drawing from contributions from developers around the globe, we review recently-introduced technologies with particular impact on improving accuracies in high-throughput processes.

PROBLEM STATEMENT

A characteristic of virtually all current and emerging industrial applications of nanopositioning is a focus on throughput [1]. "Time is money," so a prerogative has been to provide not just better nanometers but faster nanometers. Unfortunately, higher resolution needs are physically at cross-purpose to higher-throughput needs. In this way, industry's need-for-speed coupled with unrelenting pressure for ever-finer resolution capabilities have exposed fundamental limitations of traditional nanopositioning technologies, especially for controls [2]:

- Electronic bandwidths, limited by amplifier, sensor and servo-processing capabilities, cause phase-lags, nonlinearities, and "rounding of corners" in waveform motions.
- Mechanical stiffness, characterized by the resonant frequency (F_{res}), limits the controllability in high-dynamic applications, necessitating time-consuming settling intervals. Classical mechanics demonstrates that the time to settle a damped mechanism exponentiates as the settling criterion tightens, which of course relates to the scale of the structures being processed.
- Economic prerogatives which prioritize throughput often dictate larger-area processing as well. Long-travel nanopositioners can be resolution-limited by DAC granularity since a fixed number of bits is spread over a larger area; higher-bitness DACs can pose drawbacks in stability, speed, etc.
- Throughput considerations can necessitate processes be performed without pause, throwing an additional spotlight on positioning and communications bandwidth, synchronization capabilities, and dynamic accuracy.
- Constrained or coordinated motions across multiple degrees-of-freedom pose additional challenges for real-time control, metrology, kinematics and dynamic compensation of parasitic errors.

Previous approaches to improving matters include using higher-power amplifiers, faster servo update-rates, stiffer materials, and similarly obvious nostrums. However, these merely push the margins of system performance back slightly, and often with a poor cost/benefit ratio. Meeting the needs of current and emerging industrial applications demand fundamentally new advancements.

Origins of Piezo Inaccuracy

If piezoelectric actuation resulted in a perfectly proportional relationship between instantaneous voltage and position, the story would end here. But even statically (FIGURE 1), the proportionality is not linear, and hysteretic effects are seen.

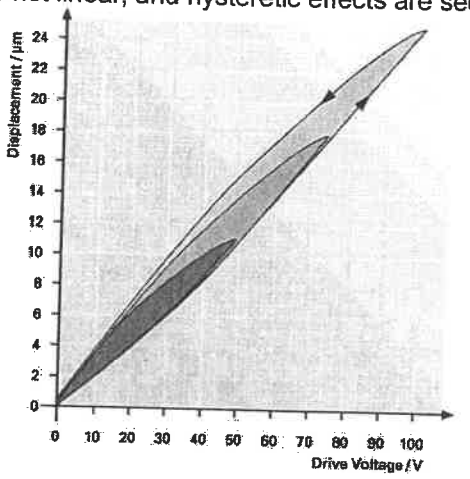

FIGURE 1. Piezo hysteresis, nonlinearity and creep necessitate closed-loop actuation in most applications.

From a dynamical standpoint, piezoelectric actuators are electrical capacitors, so there is a non-zero time required to inject charge into the material. Improving the current capabilities (power) of the amplifier helps, but relaxation phenomena in piezo materials will persist, leading to an asymptotic approach to target position unless servo-controlled in closed-loop using position feedback, for example by a capacitive position sensor or strain gauge. This in turn introduces sensor and servo bandwidths and latencies. These new errors tend to be frequency dependent, so they vary by motion profile and application and cannot be calibrated-out as static nonlinearities can be.

THE SOLUTIONS MATRIX

Optimization of the Mechanics

The stiffer the mechanics, the crisper the responsiveness to motion commands: F_{res} rises, and rolloff is pushed to the right in the system's Bodé plot, reducing dynamic inaccuracy. Mechanical stiffness must be optimized in the positioner design process, for example by selecting thicker-cross-section piezo stacks and taking into account a host of other design considerations which can impact stiffness. In particular, travel and form factor requirements may necessitate lever amplification. Lever amplifiers profoundly influence the stiffness in the motion direction of a nanopositioner; the stiffness coefficient diminishes with the square of the lever amplification ratio (EQUATION 1).

$$C_n = \frac{C_{Piezo}}{r^2} \quad \text{r : lever amplification ratio}$$

EQUATION 1. Lever amplification for longer travels impacts mechanical stiffness.

For the load, the moment arm of the center-of-mass with respect to the symmetry axis of the motion device's platform should be kept as short as possible. In rapid actuation, center-of-inertia offsets above or to the side of the symmetry axis can excite pitch and yaw moments, respectively; dynamic accuracy can sometimes actually be improved by counterbalancing in these situations, even if this means adding mass. And certainly the mounting hardware should be as rigid as possible; stiffnesses combine as a sum of quotients as in EQUATION 2:

$$\frac{1}{C_{effectire}} = \frac{1}{C_{PiezoSystem}} + \frac{1}{C_{fixture}}$$

EQUATION 2. The effective stiffness of a mechanism and its fixturing

After a motion impulse, the amplitude of the resonant ringing of each element in a structure scales as $e^{-t/\tau}$ where τ is the time constant for each element's resonant characteristics (EQUATION 3):

$$\tau \approx \left(\omega_n \zeta^{-1}\right)$$

EQUATION 3. Time constant for decay of resonant vibration of precision structures.

...where ω_n is the resonant angular frequency and ζ is the ratio of the damping for the resonance versus critical damping. For the rigid materials used in precision positioners, $\zeta \rightarrow 0$ [3]. Together with EQUATION 2 it is clear that settling times worsen (exponentiate) as settling tolerances tighten due to Moore's Law and similar market and application dynamics.

Optimization of the Controls

Downloadable Servo Parameters

Digital controllers allow instant download of servo parameters for different loads, rather than forcing the user to deploy a lowest-common-denominator parameter set for safe operation with all anticipated loads and operation modalities.

Notch Filters

Desensitization of the servo to F_{res} can be addressed via notch filters in the controller. Amazingly, not all piezo controllers have notch filters, necessitating softer servo settings to eliminate the risk of oscillation and runaway. Softer settings mean poorer dynamic accuracy.

Simple Feedforward

This technique, popular with motor controllers, involves injecting a portion of the command signal directly to the amplifier, bypassing the servo. This tends to be a "tweaky" technique; but throughput benefits can be substantial, particularly in the case of external servos, as in the emerging generation of track-following spinstands for testing disk-drive heads. PI offers a patent-pending "fast/precise" digital interface which facilitates such applications.

Eliminating motion-driven vibrations

Recoil-driven oscillations of load and adjacent componentry follow EQUATION 3 but may not be observable by the motion feedback sensor, so finessing servo settings is of limited utility in

addressing them. A patented feedforward technology tradenamed Input Shaping® was developed based on research at the Massachusetts Institute of Technology and commercialized by Convolve, Inc., (Armonk, NY). This time-domain technique nullifies any motion-driven resonances. The systems integrator first quantifies the frequency of the vibrations (which often falls out of the system's work product, e.g., FIGURE 2); the controller is then informed of these. Thereafter, no commanded motion will excite the resonances. The technique accommodates any number of resonances, non-orthogonal resonances, any motion profile, and any degree of

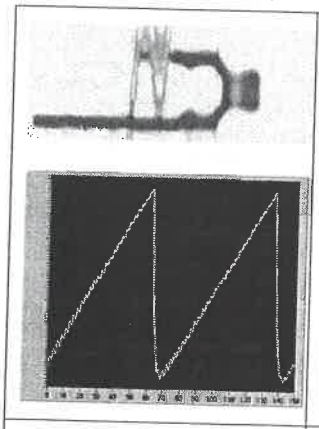

FIGURE 2. Scanned laser confocal microscopy image. Note periodic anomalies. Laser vibrometry of the scanning optic reveals motion-driven ringing somewhere in structure (bottom).

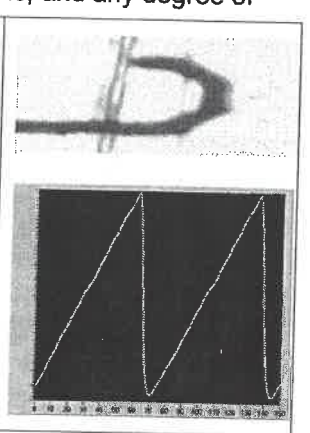

FIGURE 3. Same as FIGURE 2, with resonances nullified by Input Shaping®. Smears formerly seen in image are revealed to be a streak of contaminant; the phantom blob to the right of the original image is eliminated.

damping. It is an integrated option for PI's top-end digital piezo controllers and also available as an add-on module for existing open- and closed-loop controls. It is similarly available as a firmware option for a variety of popular motor controllers, and it is effective in MEMS [4], [5].

Eliminating following errors

Digital Dynamic Linearization™, a new technique, virtually eliminates following errors in repetitive motion patterns and scanning. The controller integrates an internal algorithm into the metrology and servo logic; this optimizes the internal command generated for a repetitive waveform according to the error signal detected with the internal sensor. A brief (typically <1 second) auto-optimization is commanded by the user (or a reload of previously-saved optimizations) when changes in motion parameters, desired waveform or loading occur. After this, following errors are reduced to approximately the noise level of the system [5], [6], [7].

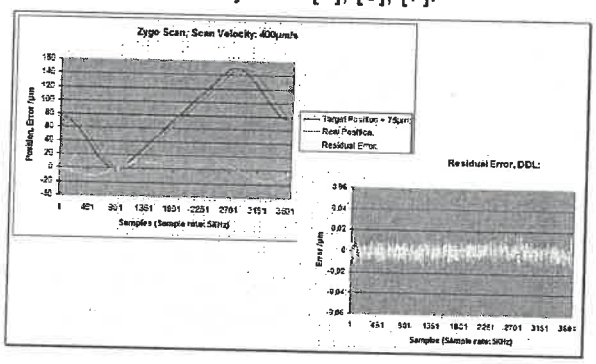

FIGURE 4. Test with a PI P-721K099 nanopositioner with and without DDL, as visualized with a Zygo ZMI-2000 laser interferometer. In this fast-waveform test, the following error is reduced from up to 10µm to 15nm or less—an improvement of three orders of magnitude.

This capability is integrated into the latest generation of PI digital controllers and is supported by internal waveform generators and extensive software drivers including COM objects, DLLs and LabVIEW libraries.

Eliminating the Travel/ Resolution Trade-Off

Recall FIGURE 1 shows how piezo actuation is roughly proportional to applied voltage, which is typically generated by a digital-to-analog converter (DAC) driving an amplifier. Hence the number of addressable positions for a piezo mechanism is 2^{bits} –reflecting the bit-width of the DAC's digital input. The resolution of the nanopositioner can be no better than its travel divided by this number. Process economics have driven the development of longer- and longer-travel nanopositioners; thus, achieving tight resolution goals requires higher and higher DAC bitness.

Until now, a DAC's limitations were permanent characteristics of the specific chip chosen by the designer. A PC user usually chooses between 12- and 16-bit cards for their PC to drive their piezo controller, for example-- higher-resolution cards are uncommon, and most users prefer to stick with popular and well-supported National Instruments I/O cards, which generally top out at 16 bits. Deployed (for example) with PI's P-628.1 PIHera® stages, with 950µm travel, 16 bits ≈ 15nm resolution, and many applications re-

quire better resolution than that. OEM engineers designing their own controls might choose a 20- or 24-bit DAC for their custom circuit design, but care must be taken, as such DACs can present drift issues, poor step response or other drawbacks. And sometimes a new design is not economically practical, yet end-user demands for higher and higher resolution persist. (Digital controllers do typically integrate high-bitness DACs, but inside the servo loop where the stage's metrology allows drift compensation.)

The missing element in the discussion above is time. DACs are typically very fast compared to motion devices, even one as responsive as a piezo-driven mechanism. This is what allows DACs to generate smooth arbitrary waveforms. It also means there is unused analog-output bandwidth in a typical nanopositioning setup. The recently-patented HyperBit™ technology[1] leverages this under-utilized time-domain capability, converting it into many additional bits of physical positioning resolution (FIGURE 5) [8].

HyperBit™ employs modulation of the least-significant bit(s) of a DAC to accomplish this. For example, the LSB can be dithered using pulse-width modulation at a rate higher than the positioning system's bandwidth. The positioner acts like a flywheel to provide smooth, stable motion with much higher resolution than the DAC's native resolution can provide, with no tradeoffs.

$$Bits(effective) \rightarrow Bits(DAC) + \log_2\left(\frac{DAC\_rate}{PWM\_freq}\right)$$

EQUATION 4. Rule of thumb for resolution enhancement

HyperBit can be implemented in software or hardware. It is available for license by OEM users and is a cost-effective software option for users of NI analog I/O hardware. Example implementations and options include HyperBit-enabled LabVIEW subVIs, a Windows DLL for programmers using C or other popular languages, and HDL for designers using FPGAs, as well as hardware and embedded approaches. Point-to-point and waveform actuation are supported. Since the time-domain capability of the DAC would otherwise be unused, there is no impact on system bandwidth, responsiveness or speed.

[1] US Pat. #6,950,050, foreign Patents pending.

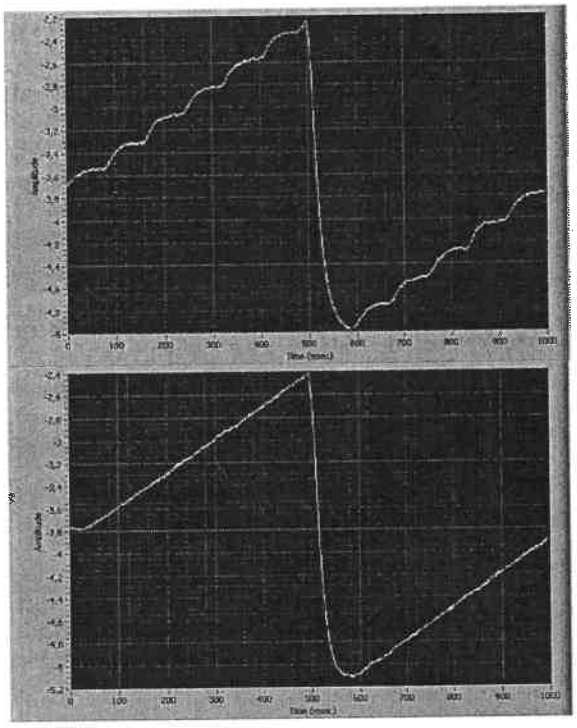

FIGURE 5. Fine nanoactuation, per laser vibrometer, showing DAC granularity (top) vs. superior resolution (bottom) with HyperBit™.

REFERENCES

[1] Jordan, S. (interview), 2003, Stage Technology Confronts New Demands, *Semiconductor International*, July

[2] Jordan, S., 2005, Piezo Scanning Technologies at *Scanning*

[3] Ogata, K., 1970, *Modern Control Engineering*, Prentice-Hall, ref. Pp271-272

[4] Jordan, S, Lawrence, E., 2003, Vibration Nullification of MEMS Devices using Input Shaping, proceedings of *SPIE Smart Structures*

[5] Chen, S.-C., Culpepper, M., Jordan, S., 2006, Application of Input Shaping and HyperBit Control to Improve the Dynamic Performance of a Six-axis MEMS Nanopositioner, at *ASPE 2006*

[6] Jordan, S., 2003, Novel approaches to maximizing micromachining throughput by minimizing positioner inertia, servo following errors, and unobservable resonant responses, *SPIE Conference on Micro-machining Technology for Microoptics and Nanooptics*

[7] Jordan, S., 2003, Technologies Address the Resolution/Speed Tradeoff & Approaches for Minimizing Tracking and Vibratory Errors In High-Bandwidth Beam Steering, *MEDSCI*

[8] Jordan, S., 2006, Optical Traps Enter New Era of Nanomanipulation, *Biophotonics International*, February

A NOVEL MICROFABRICATION TECHNIQUE FOR THREE-DIMENSIONAL METAL STRUCTURES BY PHOTOCATALYSIS

Masaki Okuno[1], Tasuku Aso[2], Satoru Takahashi[1], and Kiyoshi Takamasu[1]
[1]Department of Precision Engineering
Graduate School of Engineering, The University of Tokyo
Hongo, Bunkyo-ku, Tokyo, Japan
[2]Nomura Research Institute, Ltd.
Marunouchi, Chiyoda-ku, Tokyo, Japan

SUMMARY

Though there are a variety of microfabrication techniques, one that can fabricate three-dimensional metal structure by simple procedure is rarely seen. Given this fact, we suggest a new method for three-dimensional microfabrication that is characterized by photocatalytic deposition. The setup for this method consists of a wavelength 405nm laser diode, a numerical aperture 0.9 objective lens, and a motorized linear stage. With this setup, it was observed that a converging near-ultraviolet laser beam caused deposition of Ag at the beam waist in $AgNO_3$ solution including TiO_2 nanoparticles. Furthermore, we succeeded in fabricating a microbox and a microcoil by sweeping the beam waist in the solution.

INTRODUCTION

Microfabrication is one of the most important technologies in the manufacturing industry. Large Scale Integrated (LSI), Micro Electro Mechanical System (MEMS) or other electronic devices depend on it. On top of that, in biochemical fields, this technology is needed to manufacture cutting-edge devices such as Micro Total Analysis System (μ-TAS) and DNA Microarrays.

Therefore a lot of microfabrication techniques are under study, but one that can fabricate three-dimensional metal structure by simple procedure is rarely seen. Beyond that, apparatuses used for microfabrication tend to be expensive. For example, lithography requires complicated processes and the Focused Ion Beam (FIB) method is too expensive for mass-production.

Now we propose a new microfabrication technique that uses photocatalysis. In $AgNO_3$ solution including TiO_2 nanoparticles, it was observed that a converging laser caused photocatalytic reduction and Ag was deposited at its beam waist. Furthermore, we succeeded in fabricating a microbox and a microcoil by sweeping the beam waist in the solution.

PHOTOCATALYTIC OXIDATION-REDUCTION REACTION OF TiO_2

Our microfabrication technique is based on the theory of photocatalytic oxidation-reduction (redox) reaction. When a photocatalyst absorbs light energy that is greater than its bandgap energy, electrons in the valance band transfer to the conduction band [1]. In this study, we selected a TiO_2 photocatalyst because it is very active and stable throughout the redox reaction. TiO_2 absorbs light with wavelength that is shorter than about 400nm, and then it generates pairs of holes and electrons. The holes are so oxidative that they can break apart the water molecules to form hydrogen gas and hydroxyl radicals. And the electrons can reduce oxygen molecules to form super oxide anions (*Fig. 1*).

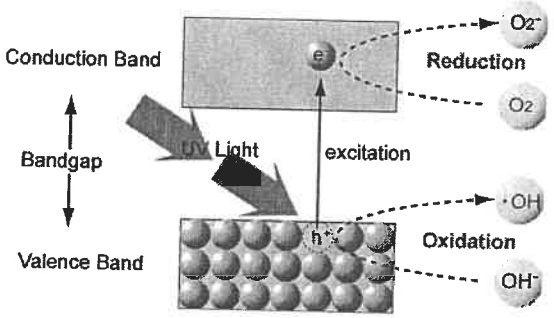

Fig. 1 Redox reaction of excited TiO_2. Electrons in the valance band are elevated to the conduction band by UV-light energy that is greater than bandgap energy.

If excitation of TiO_2 occurs in ionic solution of noble metal whose ionicity is lower than H^+, reduction of the metal ions is possible. Actually, it was reported that when TiO_2 was illuminated with UV-light, it caused deposition of metal, such as Ag [2] and Pt [3].

CONCEPT OF MICROFABRICATION WITH PHOTOCATALYSIS

We thought that photocatalytic deposition of metal could be applied to three-dimensional microfabrication. The key point of our idea is to use a metal ion solution in which TiO_2 nanoparticles are dispersed. If a converging laser beam illuminates the TiO_2 nanoparticles in the solution, a cluster of metal will appear at the beam waist by the photocatalytic redox reaction. Therefore, by sweeping the beam waist, a three-dimensional structure would be formed along the path of the beam waist (*Fig. 2*).

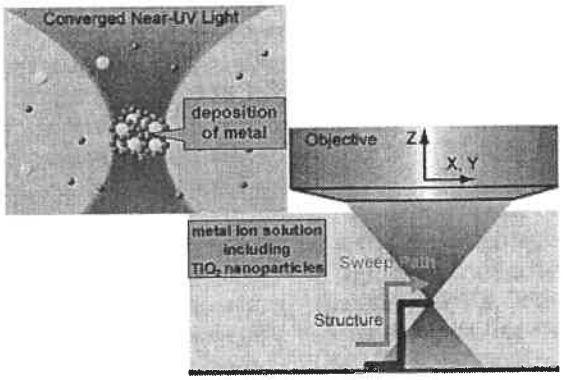

Fig. 2 A metal structure formed by beam waist sweep. In metal ion solution, excited TiO_2 nanoparticles deposits the metal at the beam waist of a converging laser beam. Therefore, by sweeping the beam waist within the solution, any shapes of three-dimensional structures will be fabricated.

EXPERIMENTAL SETUP

To realize our conception, we set up a fabrication system, which is illustrated by *Fig. 3*. The light source of the system is a wavelength 405nm laser diode whose maximum output is 55 mW / cm^2 (LDM Series Blue, Omicron Laserage). Its exit aperture is connected with a single-mode optical fiber with a 3.3μm diameter (LDM-405 FAS, Omicron). The end point of the fiber can be positioned by a motorized linear stage under computer control (LINEAR-BALL GUIDE, SURUGA SEIKI ltd.). With this stage, it is possible to position the fiber end by 2 μm.

After going through the fiber, the light is gathered together to a parallel beam by a collimating lens with a focal length 48 mm, and a 8 mm effective diameter (06GLC205, MELLES GRIOT). Via a beam splitter, the laser beam enters a 40x objective with a 0.9 numerical aperture (CFI S Fluor 40x, NIKON). By the objective, the laser beam is converged at a point on the sample stage.

And a CCD camera enables observation of the fabrication process in real time. To avoid CCD saturation, a dichroic mirror is inserted in front of the CCD imaging lens.

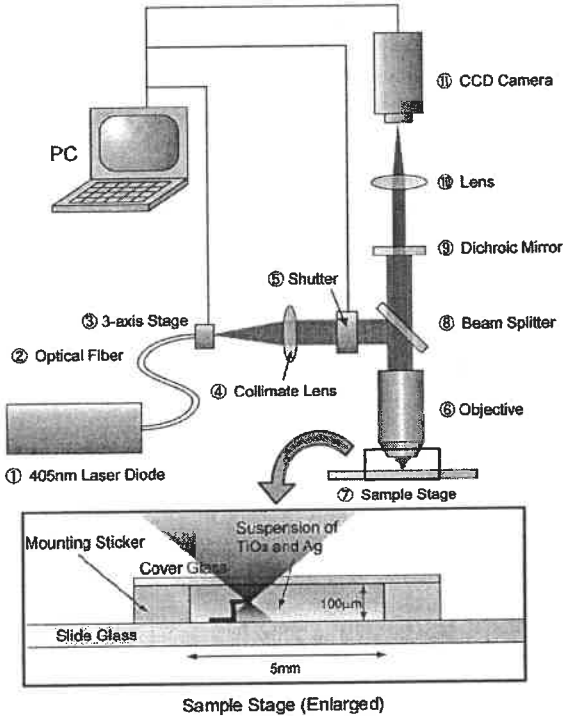

Fig. 3 Diagram of our experimental setup. The laser diode on the left side of the diagram provides a wavelength 405nm laser beam. Via an optical fiber, a collimating lens, a beam splitter and an objective, the laser is converged at a point on the sample stage on the right side of the diagram. The fiber end can be positioned by a computer-control stage, so that it is possible to manipulate the beam waist with the computer.

FEASIBILITY OF PROPOSED METHOD

With the setup mentioned in previous section, we tested the feasibility of the proposed microfabrication method. In this report, we used $AgNO_3$ solution as a metal ion solution. This was because Ag has the lowest electric resistivity among all metals so that microstructure of Ag should be worthy for electric usage. On top of that, Ag microstructure may be applied to optical devices because Ag nanoparticles show unique optical properties such as photochromism that is based on surface plasmon resonance [4].

The first step was preparation of a sample, $AgNO_3$ solution in which TiO_2 nanoparticles

were dispersed. We used suspension of brookite TiO_2 nanoparticles with a 10 nm diameter on the average (NTB-1, Showa Denko K.K), and 0.1 mol / l $AgNO_3$ solution. They were mixed at the same rate. Then a drop of the mixture was clipped between a slide glass and a cover glass.

When the sample was illuminated at 7mW / cm^2 with our setup, a dark spot with a 10 μm diameter appeared in the sample solution (*Fig. 4 (a)*). And we swept the beam waist at 2μm / sec during illumination, a line was formed along the sweep path of the beam waist (*Fig. 4 (b)*).

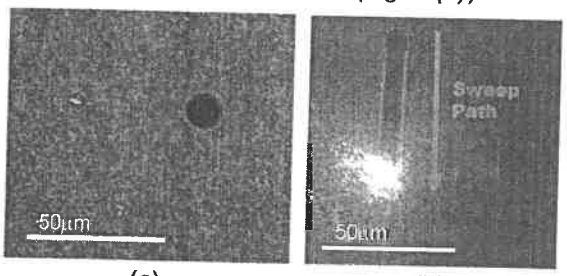

(a) (b)

Fig. 4 (a) A photograph of a dark spot that appeared after near-UV laser illumination with our setup. The diameter was about 10μm. (b) A line that was formed along the sweep path of the beam waist.

To investigate composition of the deposited substance, we analyzed it with an X-Ray Diffraction (XRD) Spectroscopy apparatus. *Fig. 5* shows the analysis result. The diffraction angles at which the spectrum peaks appear match those of Ag and TiO_2. This means that the deposited substance was composed of Ag and TiO_2, therefore the proposed microfabrication method turned out to be feasible.

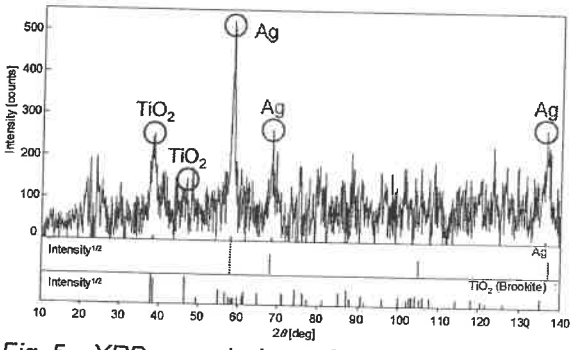

Fig. 5 XRD analysis of the deposited substance that was obtained with our setup. X-ray diffraction patterns of Ag and TiO_2 are attached at the foot of the obtained pattern. The diffraction angle 2θ at which a spectrum peak appears matches that of Ag and TiO_2.

RELATIONSHIP BETWEEN LINE WIDTH AND SWEEPING VELOCITY

It is important to figure out the characteristics of the proposed microfabrication, so we examined how sweeping velocity v would influence the line width of deposited Ag w at a certain light intensity. As a result, it was observed that w monotonously decreased with increasing v. *Fig. 6* shows variations in w versus v at 7mW / cm^2. Then it turned out that w was approximately proportional to $v^{-1/2}$. This can be explained with the hypothesis that deposited metal grows with geometric similarity, and its amount is linear with exposure. If deposited Ag grows similarly, cross section area of the line S is proportional to $w^{1/2}$. And if amount of deposited Ag has linearity with exposure, S is proportional to v^{-1} because the time period in which a certain cross section can receive exposure energy is proportional to v^{-1}. Therefore w is proportional to $v^{-1/2}$, so that it is possible to control line width by sweeping velocity.

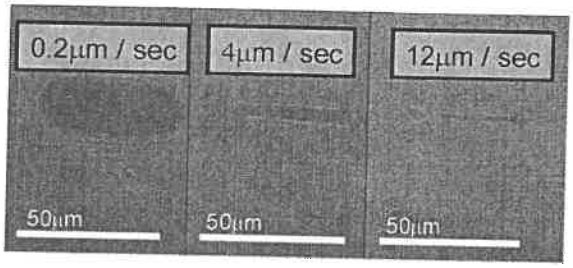

(a)

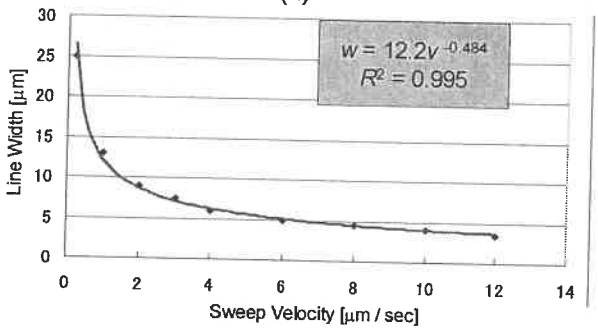

(b)

Fig. 6 (a) Three photographs of line-shaped deposited Ag. They were deposited at 7mw / cm^2. Line width w decreases as sweeping velocity v gets faster. (b) Plot of w versus v. Under the condition of fixed light intensity, w was approximately proportional to $v^{-1/2}$.

DEMONSTRATIONAL FABRICATION OF THREE-DIMENSIONAL MICROSTRUCTURE

Here we tried to fabricate two different types of structures as a demonstration. One structure

was a microbox shown in *Fig. 7 (a)*. It is a cuboid with sides of 60μm, 60μm, 30μm, and two decoration circles suspended in the squares. The other was a microcoil with a 60μm diameter and a 12μm pitch, which is shown in *Fig. 7 (b)*.

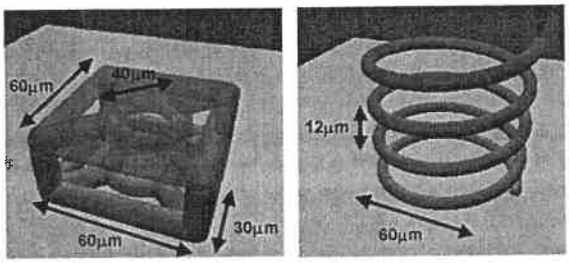

(a) (b)

Fig. 7 Design of three-dimensional structures for demonstrational fabrication. (a) A microbox with sides of 60μm, 60μm, 30μm, and two decoration circles suspended in the squares. (b) A microcoil structure with a 60μm diameter and a 12μm pitch.

We prepared the sample in the same way as the previous sections. The two structures were fabricated on a slide glass. In this experiment, the laser output was 7mW / cm^2, and the sweeping velocity was 2μm / sec.

The microbox was shown in *Fig. 8 (a)*. The frame of the microbox structure was fabricated completely along the sweep path. The microbox wasn't too weak to collapse immediately. It was seen that when the microbox came off the slide glass, it turned over in the solution with its shape kept. Thus parts of the microbox were combined with some strength.

The microcoil was fabricated by sweeping the beam waist in a spiral (*Fig. 8 (b)*). Presently, the maximum number of pitches is just two, so we'll try to fabricate longer coil in the further study.

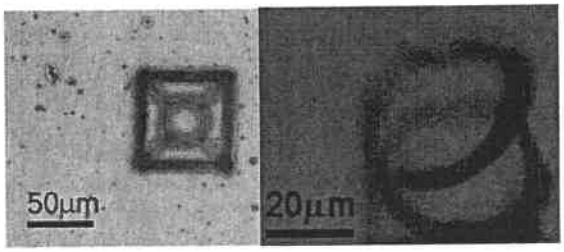

(a) (b)

Fig. 8 (a) A microbox with 60μm x 60μm bottom and top, and four 30μm columns. Sweep path of the beam waist completely matches the frame of the microbox. (b) A microcoil with a 60μm diameter and a 12μm pitch.

CONCLUSION

In conclusion, we have shown the feasibility of the new microfabrication technique based on photocatalytic deposition Ag. First, we actually set up a microfabrication system with a wavelength 405nm laser diode and a 0.9 numerical aperture objective.

Then, with our setup it was possible to cause deposition of Ag at the beam waist. If the beam waist was swept in the sample solution, deposited Ag formed a structure along the sweep path of the beam waist.

And inspection of the relationship between line width w and sweep velocity v made it appear that w was proportional to $v^{-1/2}$. Therefore the line width was controllable by the adjustment of the sweep velocity.

Finally, we succeeded in fabricating two types of three-dimensional structures, a microbox and a microcoil. In particular, the microbox was strong enough to rotate in the solution without being broken. From now on, we'll search for how to fabricate smaller, stronger and more complicated structures.

REFERENCES

1. Fujishima, A., Honda, K., 1972, Electrochemical photolysis of water at a semiconductor electrode, *Nature*, 238: 37.
2. Herrmann, J., Disdier, J., Pichat, P., 1988, Photocatalytic Deposition of Silver on Powder Titania: Consequences for the Recovery of Silver, *Journal of Catalysis*, 113: 72-81.
3. Ishii, H., Juodkazis, S., Matsuo, S., Misawa, H., 1998, Photoelectrochemical Fabrication of Submicrometer Platinum Pattern on Titanium Dioxide Single Crystal Surface, *Chemistry Letters*, 7: 655-656.
4. Ohko, Y., Tatsuma, T., Fujii, T., Naoi, K., Niwa, C., Kubota, Y., Fujishima, A., 2003, Multicolour photochromism of TiO2 films loaded with silver nanoparticles, *Nature Materials*, 2: 29–31.

KINEMATIC ASSEMBLY OF SOFT-POLYMER BIOFLUIDIC CIRCUITS

Christine A. Trinkle[1], Christopher J. Morgan[2], and Luke P. Lee[3]

[1]Department of Mechanical Engineering
[3]Department of Bioengineering
University of California, Berkeley
Berkeley, CA 94720

[2]Univeristy of Mechanical Engineering
University of Kentucky
Lexington, KY 40506

INTRODUCTION

Micro-scale biofluidic networks are providing researchers with a powerful new tool to perform useful biological assays. These Biofluidic Application Specific Integrated Circuits (BioASICs) can be designed for medical diagnostics, high throughput drug discovery, cell culturing, proteomics, functional genomics, protein crystallization, or any number of other important quantitative biology and medical applications [1-3]. Performing these tests using microfluidic technology not only makes them more portable when compared to their traditional counterparts, but also decreases testing time and cost.

One widely used method of creating BioASICs uses a soft polymer (Poly-dimethylsiloxane, PDMS) to replicate a silicon master mold in a technique known as soft lithography. This method can be used to create polymer microchannels rapidly and inexpensively, but complete assembly of these BioASICs requires precision alignment and bonding of the PDMS to a glass substrate that has proteins or metal electrodes patterned on the surface. PDMS' low modulus of elasticity makes it difficult to achieve this alignment by mechanical means, so the assembly must be performed manually under an optical microscope, leading to alignment errors that may be over an order of magnitude larger than feature dimensions in the BioASICs.

The paper presents a process that enables multiplexed assembly of PDMS/glass BioASICs with better than 5 μm precision, as compared to 20-40 μm error generated using current technology. By employing kinematic constraint and an integrated flexural bearing, the assembly device (shown in Figure 1) allows passive mechanical alignment and assembly of the microfluidic components. This decreases

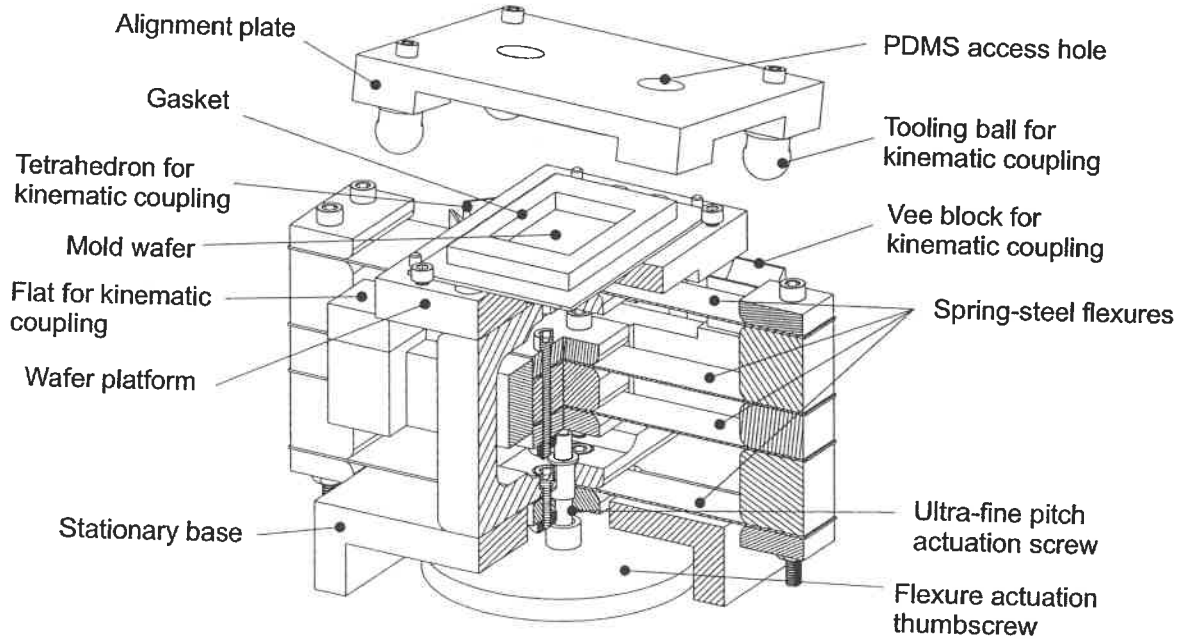

Figure 1. Sectioned diagram of kinematic soft-polymer alignment device.

fabrication time, increases alignment accuracy and eliminates the need for complicated optical alignment equipment. The necessary hardware for this system can be manufactured at a cost more than an order of magnitude smaller than comparable devices and it is possible to extend this technique to high-throughput automated assembly and use with other polymer materials.

PRIOR WORK

The first microfluidic and biofluidic devices were created in silicon and glass using semiconductor processing technology [4, 5]. This requires access to expensive etching machinery, and so was soon replaced in many labs by soft lithography [6]. This process requires a master mold created through the process shown in Figure 2, steps 1-4. A photosensitive polymer, such as SU-8 photoresist, is spin-coated onto a silicon wafer and then exposed to UV light through a patterned mask. The polymer which has not been exposed is subsequently removed during a developing step, leaving behind a positive relief mold.

Negative replicas of the mold are made by the process shown in Figure 2, steps 5-8; first, uncured PDMS prepolymer is poured over the entire mold. A single mold will generally contain multiple copies of the same pattern, thus the PDMS microfluidic networks for multiple BioASICs can be cast simultaneously. The PDMS is heat cured, removed from the mold and manually cut into individual components. Each PDMS microfluidic component undergoes optical alignment and bonding to a second substrate, forming closed channels. Patterned features—such as proteins or metal electrodes—on this second substrate make proper alignment between the components critical.

The current standard for BioASIC assembly involves using tweezers to manually suspend the PDMS microfluidic component over the glass substrate while they are aligned visually using a microscope. The PDMS is then released, bringing the two substrates into contact. The precision attained using this technique depends heavily on the user; even the most experienced technicians produce tens of microns of error during assembly.

Some researchers have attempted to improve assembly by replacing the hand-held tweezers with precision translation stages. This has

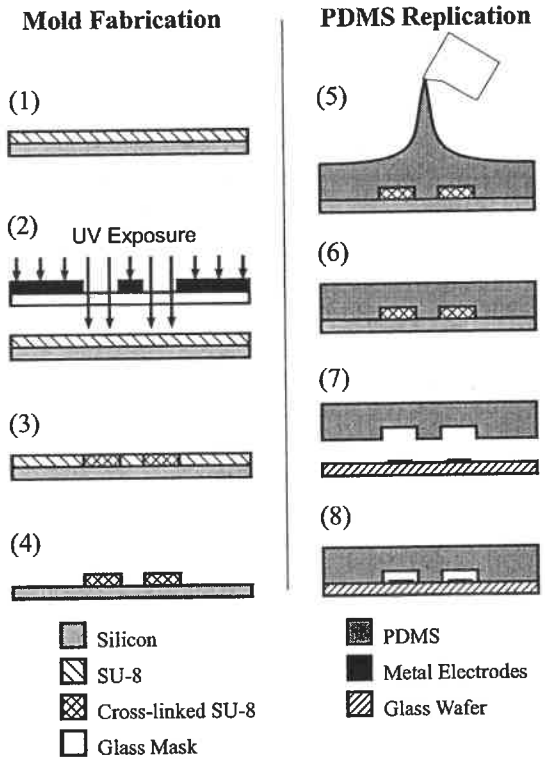

FIGURE 2. Traditional soft lithography: mold fabrication (a) begins by spin coating a silicon wafer with SU8 photoresist (1), then exposing it to UV through a patterned mask (2), causing exposed areas to crosslink (3). A chemical developer removes areas which have not crosslinked to leave a positive-relief mold (4). Mold replication is performed by pouring PDMS prepolymer over the mold (5) and curing until the material is rigid (6). The PDMS can then be removed from the mold (7) and aligned and bonded to a glass substrate (8).

increased the accuracy of optical alignment, but even with a very thoroughly designed multiple-stage setup it is difficult to attain less than 10 µm error [7]. Other drawbacks of this approach include high cost of the alignment machine and inability to process multiple BioASICs simultaneously.

Jo, *et al.* [8] reported 15 µm accuracy in aligning thin PDMS films by biasing them against a reference edge and using surface tension forces provided by a methanol surfactant. This approach removes the need for optical alignment, but the resulting error is larger than desired, and the approach is limited to use with components whose mass is small enough to be shifted via surface tension forces.

KINEMATIC ALIGNMENT DEVICE

The kinematic alignment device shown in Figure 1 removes the need for optical alignment, increases alignment accuracy, and is scalable to assemble multiple BioASICs simultaneously. The new technique, shown schematically in Figure 3, uses the same molds as traditional lithography. However, the difference lies in using a kinematic coupling to provide accurate placement in the horizontal plane and a flexural bearing to produce precise, repeatable motion in the vertical direction.

The novel soft lithography process starts by placing the mold onto the stationary base and assembling the gasket and alignment plate (steps 1-2). The PDMS prepolymer is poured into the mold cavity through an access hole in the alignment plate (step 3). The entire assembly is heated in an oven to cure the PDMS (step 4). After curing, the alignment plate is removed, retaining contact with the cured PDMS part (step 5). Then the mold is removed from the stationary base and replaced with a patterned glass substrate. The alignment plate/PDMS assembly is then mated with the base; the kinematic coupling provides passive alignment in the x-y plane. A flexural bearing in the base allows careful control of the gap between the two components, allowing them to be brought into precise contact (step 6). The assembled BioASIC can then be removed from the alignment mechanism.

The kinematic coupling is a deterministic mounting system that employs a set of three tooling steel balls and six contact points to exactly constrain the alignment plate in all six degrees of freedom. Thus, alignment between the two main components of the system is achieved with repeatability in the sub-micron range. [9] The optics-free nature of the system provides the opportunity to scale this technique to perform wafer-level assembly of BioASICs. Removal of optical alignment also means that the technique can be used with any number of polymers, even those that are not optically transparent.

Initial testing of the kinematic coupling placement accuracy was performed using Lion Precision C1 capacitive sensors. The data from n=10 trials has a range of just under 1 μm in each direction, with standard deviation of 0.33 and 0.34 μm in the x- and y-directions, respectively.

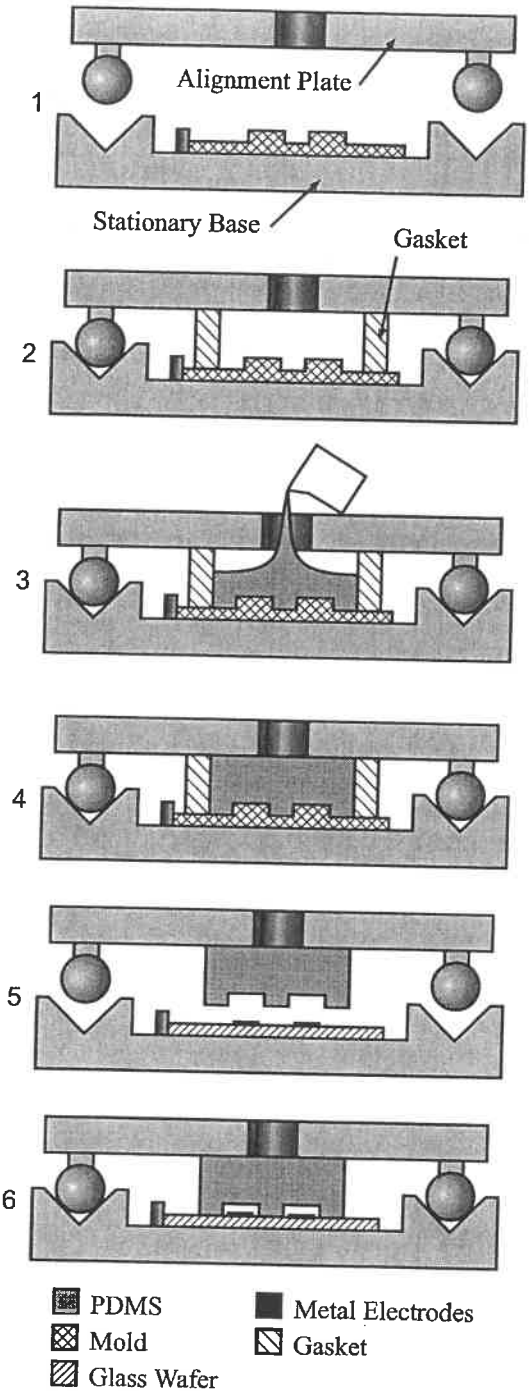

FIGURE 3. Soft lithography with kinematic alignment. A mold is aligned to the stationary base (1); a gasket and the alignment plate form a closed cavity (2). PDMS prepolymer is added via an access hole in the alignment plate (3), and PDMS is heat cured (4). The PDMS is removed from the mold and gasket, but retained with the alignment plate; the mold is replaced with a glass substrate (5). The alignment plate is reseated, bringing the PDMS and glass substrate into contact (6).

A double-compound flexural bearing is integrated into the stationary base of the alignment device. The bearing is actuated using an ultra-fine pitch screw (100 tpi, from ThorLabs) connected to a thumbwheel, which are both also integrated into the stationary base. By actuating this system, one can manually control the spacing between the alignment plate and the mold or glass substrate. This provides accurate control over PDMS thickness during the casting process and contact pressure during alignment and bonding steps. The system has a travel range of over 1 mm and was chosen because its geometric symmetry minimizes error due to long time scale thermal fluctuations.

Use of the alignment plate as a backbone during the PDMS curing and assembly process also allows better control over thermal expansion of PDMS. The large coefficient of thermal expansion (310 μm/m/K) of this material makes it very sensitive to ambient temperature fluctuations: change of a single degree Kelvin leads to an expansion of 3 μm over a standard 1 cm x 1 cm die size. Constraining the PDMS to the alignment plate forces the PDMS to conform to the thermal deformation of the stiffer (and less thermally expansive) backing material [10], thus increasing its dimensional stability with respect to temperature fluctuations by at least an order of magnitude. Careful matching of material CTE and thermal centroid location in future generations of this device should reduce thermally induced error even further.

CONCLUSIONS AND FUTURE WORK

A novel kinematic system for PDMS-based microfluidic casting and alignment has been developed for creation of biofluidic integrated circuits. Precision machine design techniques such as kinematic constraint can be used to provide low-cost passive alignment device capable of better than 5 μm precision. Initial testing of the kinematic coupling alignment has shown submicron placement repeatability. The elimination of optical alignment and ability to simultaneously assemble multiple BioASICs provides a significant improvement in efficiency and opens the door to automated and wafer-level assembly. This technique could easily be extended to other uses PDMS devices, such as microcontact printing; it could also be adapted for use with any number of other soft polymers.

ACKNOWLEDGEMENTS

The authors would like to thank the Intel Corporation for their financial support of this project. This material is based upon work supported under a National Science Foundation Graduate Research Fellowship.

REFERENCES

1. Auroux, P.A., Iossifidis, D., Reyes, D.R., and Manz, A., 2002, Micro Total Analysis Systems. 2. Analytical Standard Operations and Applications, *Analytical Chemistry*, 74: 2637-2652.
2. Breslauer, D.N., Lee, P.J., and Lee, L.P., 2006, Microfluidics-Based Systems Biology, *Molecular Biosystems*, 2: 97-112.
3. Tudos, A.J., Besselink, G.A.J., and Schasfoort, R.B.M., 2001, Trends in Miniaturized Total Analysis Systems for Point-of-Care Testing in Clinical Chemistry, *Lab on a Chip*, 1: 83-95.
4. Harrison, D.J., Fluri, K., Chiem, N., Tang, T., and Fan, Z.H., 1996, Micromachining Chemical and Biochemical Analysis and Reaction Systems on Glass Substrates, *Sensors and Actuators B-Chemical*, 33: 105-109.
5. Wilding, P., Pfahler, J., Bau, H.H., Zemel, J.N., and Kricka, L.J., 1994, Manipulation and Flow of Biological-Fluids in Straight Channels Micromachined in Silicon, *Clinical Chemistry*, 40: 43-47.
6. Duffy, D.C., McDonald, J.C., Schueller, O.J.A., and Whitesides, G.M., 1998, Rapid Prototyping of Microfluidic Systems in Poly(Dimethylsiloxane), *Analytical Chemistry*, 70: 4974-4984.
7. Kim, J.Y., Baek, J.Y., Lee, K.A., and Lee, S.H., 2005, Automatic Aligning and Bonding System of Pdms Layer for the Fabrication of 3d Microfluidic Channels, *Sensors and Actuators a-Physical*, 119: 593-598.
8. Jo, B.H., Van Lerberghe, L.M., Motsegood, K.M., and Beebe, D.J., 2000, Three-Dimensional Micro-Channel Fabrication in Polydimethylsiloxane (Pdms) Elastomer, *Journal of Microelectromechanical Systems*, 9: 76-81.
9. Slocum, A.H., 1992, *Precision Machine Design*: Prentice Hall, Englewood Cliffs, N.J.
10. Kunnavakkam, M.V., Houlihan, F.M., Schlax, M., Liddle, J.A., Kolodner, P., Nalamasu, O., and Rogers, J.A., 2003, Low-Cost, Low-Loss Microlens Arrays Fabricated by Soft-Lithography Replication Process, *Applied Physics Letters*, 82: 1152-1154.

DESIGN OF A MINIATURE DUAL-PURPOSE POSITIONER-FIXTURE FOR SIX-AXIS SCANNING AND DETACHABLE FIXTURING IN NANO-INSTRUMENTATION

Martin L. Culpepper and Kartik M. Varadarajan
Department of Mechanical Engineering
Laboratory for Manufacturing and Productivity
Massachusetts Institute of Technology
Cambridge, MA 02193 USA

SYNOPSIS

The purpose of this paper is to demonstrate a detachable fixture system that can provide, (1) positioning with sub-micron repeatability and accuracy and (2) rapid (100 Hz) scanning. Such systems may be used in nano-instrumentation (e.g. SEM, STM, AFM) and nanomanufacturing equipment to repeatably fixture, accurately position in a quasi-static mode, and/or execute fast scanning motions. This device is called a dual-purpose fixture-positioner (DPF) due to its ability to perform as a fixture and positioner.

INTRODUCTION

Exact constraint fixtures, such as the kinematic coupling shown in Fig. 1A, are capable of sub-micrometer repeatability. The accuracy of such a device depends on the geometric quality of their components and the accuracy of their assembly [1]. Their accuracy is typically limited to 10 micrometers [2].

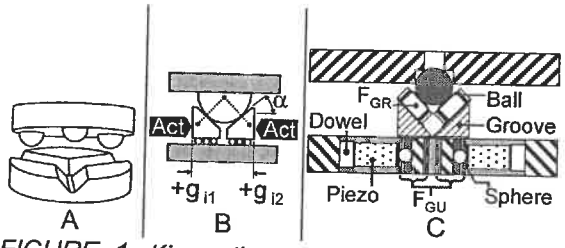

FIGURE 1. Kinematic couple (A), schematic of a moving groove DPF ball-groove joint (B) and cross section of miniDPF ball-groove joint (C)

However, one may actively adjust an exact constraint fixture's geometry so as to modify the relative location of the fixtured components, thereby improving fixturing accuracy. Achieving this can be done for instance by repositioning the balls or grooves via external actuation.

This has been demonstrated by creating kinematic couplings, a type of exact constraint fixture, wherein two [3] and three [4] axis corrective motions may be achieved. For ultra-precision applications it is important to be able to have accurate alignment in all six axes. This makes it possible to (1) achieve any combination of position-orientation and (2) to correct parasitic alignment errors. Recently, several devices have been created for this purpose – a manually adjustable coupling based upon adjustable links [5], a DPF that uses an eccentric ball-shaft to adjust position [2] and a DPF wherein motion was generated via a moving groove design [6,7].

In this paper, we investigate the performance of a miniaturized moving groove DPF. Whereas preceding DPFs were designed for static operation, the scaling down to the present miniaturized design (lower mass to stiffness ratio) enables fast motions.

CONEPT AND DESIGN DETAILS

A cross-section of a ball-groove joint from a moving groove DPF is shown in Fig. 1B. The grooves are attached to a guiding bearing and actuated along the horizontal by actuators (Act). In the miniDPF design, the grooves sit atop a guiding flexure (F_{GU}) as shown in the miniDPF-specific ball-grove joint of Fig. 1C. As each of the j grooves (j = 6) may be actuated an amount, g_{ij}, it is possible to achieve displacements in all six degrees-of-freedom. The components of the miniDPF are shown in Fig. 2A. The dimensions of the prototype are roughly 5 x 5 x 5 cm.

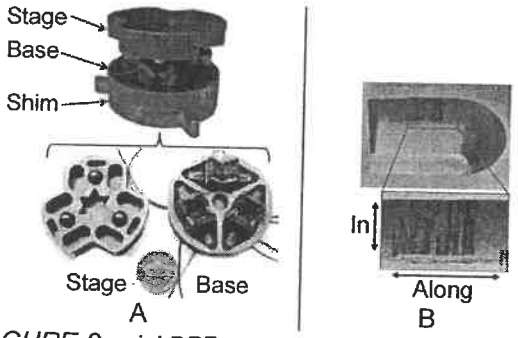

FIGURE 2. mini DPF assembly and components (A) and damage on groove surface due to sliding (B)

The miniDPF consists of a top component (stage) to which the balls are rigidly attached and a bottom component that contains flexures and piezo actuators (piezos) that work together to cause changes in the fixtured position/orientation. Figure 1C and 2A show how the flexures and actuators are integrated within the DPF.

Within this design there are:

(a) Six guide flexures – The guide flexures guide the motions of the groove flexures as shown in Fig. 1B and 1C. The groove flexures are part of the monolithic base as shown in Fig. 3A.

(b) Six piezo actuators – The actuators are assembled into the monolithic base by preloading within their respective guide flexures. The piezos interface with the guide flexures via a dowel pin on one end and a sphere on the other end. The guide flexures are sized so that the series of sphere-piezo-dowel pin is slightly oversized with respect to the fit with the guide flexures. During assembly, the guide flexure therefore deforms when the sphere, piezo and dowel are set into place. This provides a preload that is necessary to extract the best stiffness-range combination from the piezos. The dowel pin and sphere are used to avoid over constraining the piezo.

(c) Six groove flexures – A pair of groove flexures form each contacting groove surface of the device. A detail of a groove flexure is shown in Fig. 3B. The groove flexures are stiff in the direction normal to the ball-groove contact and compliant in directions perpendicular to the normal contact. This layout of stiffness and compliance maintains a stiff coupling while permitting flexing for adjustment of position and orientation. A more detailed justification for the groove flexures follows.

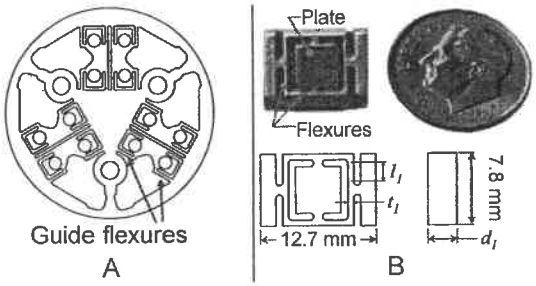

FIGURE 3. Illustration of guide flexure (A) and groove flexure (B)

When the grooves are actuated, the balls must slide along the grooves in order to maintain geometric compatibility between the ball and groove patterns [2]. Figure 2B shows the wear marks that result from a ball sliding along a groove when groove flexures are not used. The groove flexure are important as they prevent relative sliding between the balls and grooves. That is, if there is an impetus for the balls to move parallel to the groove surface, it is the groove flexure deformation that allows this motion rather than an undesired, relative sliding between the balls and grooves.

Kinematic couplings have been made by replacing the ball-groove contacts with air bearings [8], but here we have chosen flexure bearings as they are vacuum compatible and require no supporting electronics or fluid systems. They have also demonstrated utility in other fixture applications, for instance to minimize friction hysteresis effects [9], to prevent over constraint [10, 11] and to enable sealed contact [12]. Figure 4 shows top and bottom views of the miniDPF base with all flexures and actuators assembled.

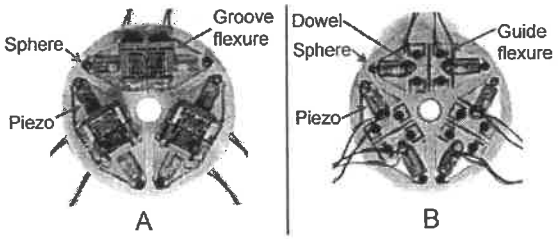

FIGURE 4. Detailed top (A) and bottom (B) views of DPF base

EXPERIMENTAL RESULTS

The HPF was designed according to the physical principles and models used to design a large-scale, moving groove DPF [6,7]. The miniDPF is shown encapsulated within a cap probe-based metrology system in Fig. 5A. Six probes take displacement readings on the positions corresponding to the numbered locations in Fig. 5B. The measurements were taken while a magnet preload was applied between the top and bottom components.

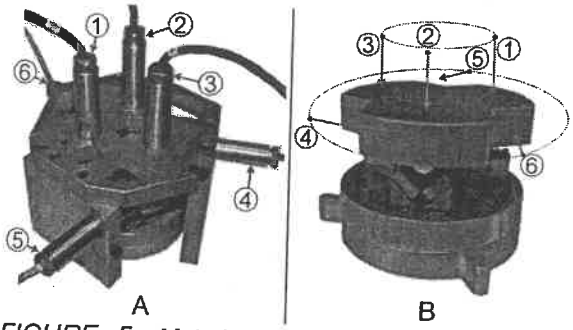

FIGURE 5. Metrology system (A) and diagram showing location where probes 1 - 6 measure off of miniDPF stage.

In our first experiment, we conducted repeatability tests on the device in fixture mode. In this mode, the actuators are energized to a constant state. They are not actively adjusted in order to improve the accuracy or repeatability of the fixturing operation between cycles. This enables us to test the repeatability of the exact constraint interface. Figure 6 and Table 1 show the results of the repeatability test.

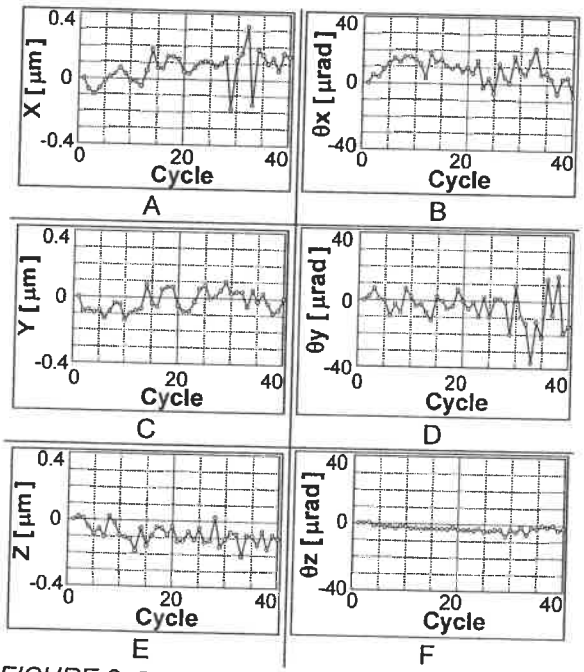

FIGURE 6. Static repeatability test results

In previous tests on DPFs, we used an automated test rig to collect data over hundreds of mate-unmate cycles. Due to the small size of the miniDPF, we are unable to use this automated system and therefore it was only practical to conduct the tests by hand over 40 cycles. This prevented us from obtaining the worn-in repeatability, the best repeatability of a kinematic coupling that most often occurs after several hundred cycles. The tests show that the miniDPF is capable of approximately one quarter micrometer and tens of µradians before wear-in has occurred. This is comparable to the performance of conventional kinematic couplings [13]. More tests are to be run in order to determine if the repeatability approaches the 50nm repeatability of prior DPFs [7].

TABLE 1. Static repeatability test results. Values given in standard deviation, σ, and half, ½ R, of the range of measurements, i.e. ½ (max–min).

	X nm	Y nm	Z nm	θx µrad	θy µrad	θz µrad
3σ	290	192	167	21	30	4
½ R	250	120	120	15	26	4

Our next test was run to determine the potential for high-speed scanning with the DPF. The miniDPF has a natural frequency over 1 kHz. In our test, we commanded the six actuators to act in concert so as to move the stage in an x-y raster scan pattern. This scan was completed at less than 10% of the natural frequency, 100 Hz, over one third of the devices range of 3x3x3 micrometers[3]. The results are shown in Fig. 7.

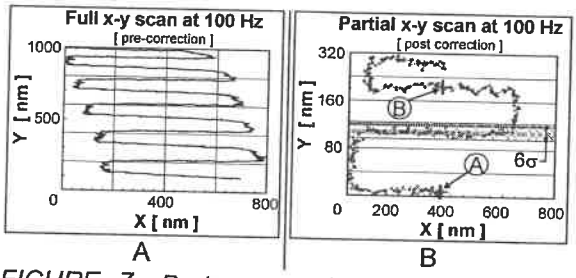

FIGURE 7. Raster scan data in raw (A) and corrected form (B)

The miniature piezo actuators used in the device are not equipped with sensors that allow us to perform closed loop control. We are therefore only able to run the piezos in open loop and measure the resultant motions via the metrology system. This means that there is to be a certain degree of hysteresis and creep expected in the piezo actuators that will be reflected in the device behavior. This is indeed seen via the raw experimental data shown in Fig. 7A. When this data is corrected to remove the piezo creep and hysteresis effects, the motion better-resembles the commanded x-y raster scan profile. A section of the corrected scan data is shown

enlarged in Fig. 7B. The variation from linear is within the 6σ capability of the sensing system. This range is denoted by the shaded region in Fig. 7B.

SUMMARY

To date, this work has shown the capability of a DPF to serve as a high-speed, sub-micron precision dual-purpose fixture-positioner. We have obtained a few hundred nanometer repeatability and tens of microradian repeatability. We have demonstrated that the device has the potential to scan at 100 Hz with accuracy on the order of tens of nanometers. Achieving this in a practical way will require the addition of closed-loop control. Current efforts are focused upon fulfilling this goal. Additional tests are under way to ascertain the worn-in repeatability of this device. Past work has shown that the incorporation of groove flexures into kinematic couplings can improve their repeatability to better than 100 nm, possibly improving this to tens of nm. Continued work seeks to determine if the worn-in repeatability of the miniDPF will approach these results.

REFERENCES

1. Barraja, M., and Vallance, R. Tolerancing Kinematic Couplings, Prec Eng 2005;29;101-12.
2. Culpepper, M. L., M. K. Varadajan and M. Dibiaso, "Design of integrated eccentric mechanisms and exact constraint fixtures for micron-level repeatability and accuracy," Precision Engineering, 29 (1), 65 – 80, January 2005.
3. Taylor JB, Tu JF. Precision X-Y microstage with maneuverable kinematic coupling mechanism. Precision Eng 1996;18(2):85–94.
4. Chui, MA, Roadmap of mechanical systems design for the semiconductor automatic test equipment industry, MIT Ph.D. thesis, 1998.
5. Hale, L. Adjustable link for kinematic mounting systems. United States Patent 5,642,956, July 1997.
6. Varadarajan, MK. Culpepper, ML. A Dual-purpose Positioner-Fixture for Six-axis Nanopositioning and Precision Fixturing – Part I: Modeling and Design. Submitted to Precision Engineering.
7. Varadarajan, MK. Culpepper, ML. A Dual-purpose Positioner-Fixture for Six-axis Nanopositioning and Precision Fixturing – Part II: Experiment and Calibration. Submitted to Precision Engineering.
8. Tymianski V. and Ziegert J., Air Bearing Kinematic Couplings. In: Proceedings of the 2005 ASPE Annual Meeting; Norfolk, VA; 2005.
9. Schouten CH, Rosielle PCJN, Schellekens PHJ. Design of a kinematic coupling for precision applications. Prec Eng;20;46-52.
10. Hale, LC., Principles and techniques for designing precision machines, MIT Ph.D. Thesis, 1999, Cambridge, Ma.
11. Culpepper, M. L., "Design of Quasi-Kinematic Couplings," Precision Engineering, 28 (3), 338 – 357, July 2004.
12. Culpepper, M. L., A.H. Slocum and F. Z. Shaikh, "Compliant Kinematic Couplings for Use in Manufacturing and Assembly," Proceedings of the 1998 International Mechanical Engineering Congress and Exposition, Anaheim, CA, November 1998, pp 611 – 8.
13. Slocum AH. Donmez A. Kinematic couplings for precision fixturing- Part 2: Experimental determination of repeatability and stiffness. Prec Eng 1988;10;115-22.

A SCALABLE SIX-AXIS ELECTROMAGNETICALLY-DRIVEN NANOPOSITIONER FOR NANOMANUFACTURING

Dariusz Golda[1], and Martin L. Culpepper[1]
[1]Department of Mechanical Engineering
Massachusetts Institute of Technology
Cambridge, MA, USA

ABSTRACT
This paper presents the design and demonstrated performance of a low-cost, centimeter-scale, six-axis nanopositioner driven by electromagnetic actuators with applications in nanomanufacturing and scanning-probe microscopy. The planar device can operate linearly with a range-of-motion of nearly 8 micrometers in the x-, y- and z- directions with a first resonance of 120 Hz. Sensor-limited repeatability of better than 20nm has been demonstrated, while the minimum measured step size is 10nm. The system is a first step toward the design of a high-speed meso-scale six-axis device. As such, it can be scaled down to several millimeters in size, enabling high-speed and precise positioning of small samples such as probe tips and thin-film materials.

INTRODUCTION
Multi-axis meso-scale nanopositioners can enable high-speed and precise positioning and measurement in the biological sciences, data storage, probing equipment for nano-scale measurements, and more recently, nanomanufacturing processes [1-5]. Emerging applications in these fields would benefit from portable, multi-axis, nanometer-level positioning over tens-of-microns at speeds of hundreds to thousands of Hertz. Several design challenges must be overcome in order to achieve high-speed multi-axis sample positioning using a meso-scale device: 1) multi-axis actuator and bearing design and integration; 2) position sensing for feedback control; 3) power dissipation; 4) sample integration. We have designed, constructed, and tested a low-cost, centimeter-scale 6-axis nanopositioner of planar geometry as a potential solution to the first design challenge. The system is a first step towards the design goal of a meso-scale system.

DESIGN OF THE PROTOTYPE SYSTEM
The nanopositioner is shown in Fig. 1a), while cross section A-A depicting the actuator layers is shown in Fig. 1b).

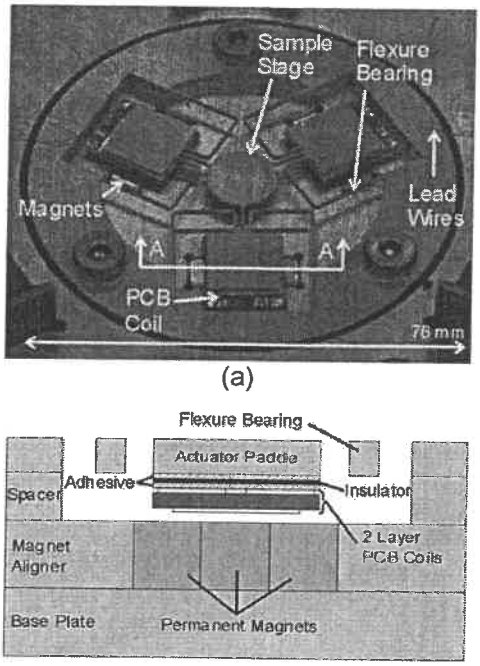

FIGURE 1. a) Bench-level prototype nanopositioner. b) Cross-section A-A of the nanopositioner showing actuator components.

The device operates in open-loop, and is comprised of a planar, spatially compliant 6061 aluminum flexure bearing [6], and three sets of two-axes moving-coil actuators. The system has six total actuator inputs, and six possible position outputs. The aluminum flexure arms are approximately 0.82mm thick and 0.64mm wide. The actuators consist of planar-coils fabricated on a printed circuit board (PCB) suspended above a set of three alternating-pole permanent magnets. An aluminum spacer is used to achieve the correct gap between the PCB coils and the permanent magnet structure. The PCB coils are bonded to the underside of the flexure bearing actuator paddles, and protected from shorting to the aluminum via plastic insulator layer. Thin 36-gauge insulated lead wires are used to supply the moving coils with current while adding negligible stiffness to the structure. The three-way symmetric design

[6] and relatively small out-of-plane profile mitigate thermal errors in the stage position.

When powered, the actuators apply forces to deflect the flexure bearing. Electromagnetic simulations have been used to predict the force output of the actuators as a function of current. Assuming linearity, the set of input currents required to achieve some static output state **x** is related through:

$$\mathbf{i} = (TK_a)^{-1} K\mathbf{x} \qquad (1)$$

The actuator matrix K_a is derived from the electromagnetic analysis, and relates the command currents to actuator forces. This is multiplied by the kinematic transformation matrix T that maps forces at the actuator location to the structure. The structural stiffness matrix K is then multiplied to map the applied force on the structure to the output displacement. In practice, this input-output mapping is measured and results in a linear calibration matrix.

The flexure dimensions were designed such that the force-limited system has a range of motion of roughly 10 μm when the actuator coils are powered with the maximum sustainable current of 500mA. The resulting first mechanical natural frequency of the system is roughly 125 Hz, as computed using finite element analysis (FEA). Figure 2 shows the first mode of the system, which is tilting out-of-the-plane.

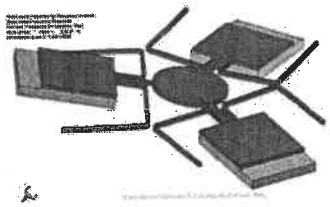

FIGURE 2. First mode of the nanopositioner at 125Hz as computed using FEA.

The planar geometry of the flexure bearing and coil actuators enable scaling of the system via lithographic microfabrication. Miniaturization to the meso-scale would result in improved performance through: a) reduced thermal error; b) increased natural frequency; c) more efficient coil actuators.

EXPERIMENTAL RESULTS

The prototype centimeter-scale nanopositioner has been calibrated and tested using a set of six capacitance probes and target fixture. Data was collected with a DSpace 16 bit real-time data acquisition system operating at 1000Hz. Lion Precision capacitance probes were used to obtain position measurement from the multi-axis probe target. A custom-built 6-channel voltage-current amplifier was used to power the coils. Figure 3 shows the nanopositioner with capacitance probe target mounted to the sample stage, and the six-probe fixture. In practical applications a smaller target/metrology system would be used. The relatively large size of the target used in our experiment is as small as permitted by our current sensing/data acquisition system.

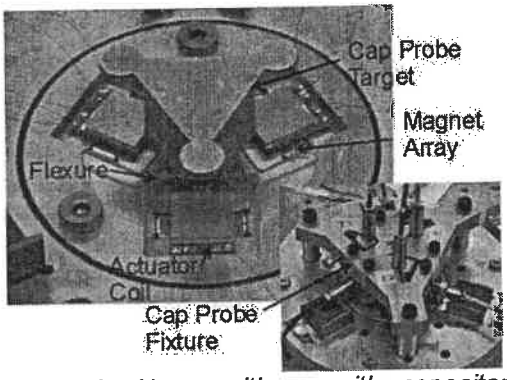

FIGURE 3. Nanopositioner with capacitance probes and measurement target.

The range-of-motion of the positioner is measured to be close to ±4 microns in each of the X-, Y-, and Z-directions. Figures 4 and 5 show the input-output relationship of the system in the x- and z- direction, which is limited by the current-carrying capability of the PCB coils.

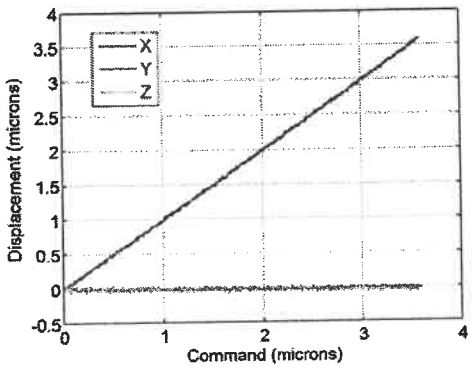

Figure 4. Measured vs. commanded displacement in the x-direction.

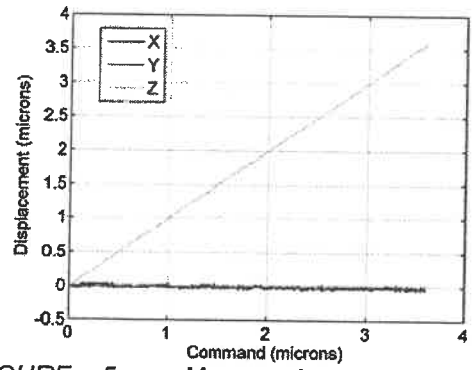

FIGURE 5. Measured vs. commanded displacement in the z-direction

The dynamics response of the system has been measured by referencing one capacitance probe off the sample stage without using the probe target which adds considerable mass to the system. Figure 6 shows the frequency response of the system in the out-of-plane direction (z-direction). The predicted out-of-plane first natural frequency of 125 Hz closely matches the first measured peak at 120 Hz.

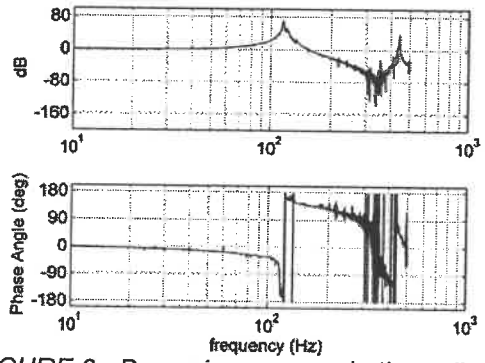

FIGURE 6. Dynamic response in the z-direction without probe target.

The in-plane repeatability and step response was measured with the capacitance probe target and 6-probe setup. The system was commanded to step in the x-direction by 600nm and return. The measured x-, y-, and z- motions are shown in Fig. 7. The under-damped system tends to ring for a few seconds in response to the step input in all three axes as a result of the tilting mode harmonics. The figure indicates that although the system rings, the repeatability is on the order of the measurement noise, which in this case is roughly 20nm.

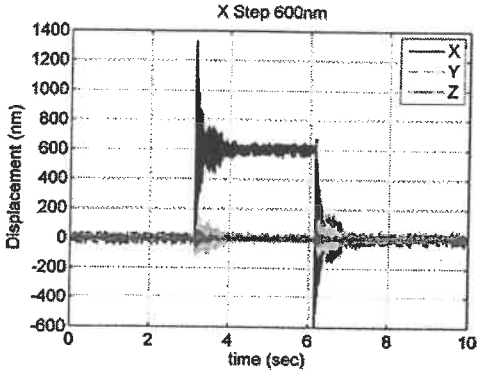

FIGURE 7. Nanopositioner response to a 600nm step input in the X-direction with 6-axis capacitance probe target.

Out-of-plane repeatability and step response was also measured, but without the capacitance probe target. In this case, a single probe referenced directly to the sample stage surface. Figures 8-10 show the results of commanded 10nm, 100nm, and 1000nm steps. Again, the under-damped system overshoots the target step height, but the oscillations damp out in less than 0.5 seconds. The oscillations could be damped in open-loop using techniques such as input pre-filtering, or by adding visco-elastic elements. The data indicates that the repeatability of the system is approximately that of the noise floor of 20nm in all three cases.

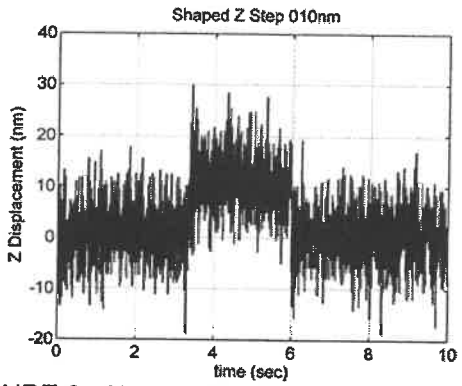

FIGURE 8. Nanopositioner response to a 10nm step in the z-direction without the capacitance probe target.

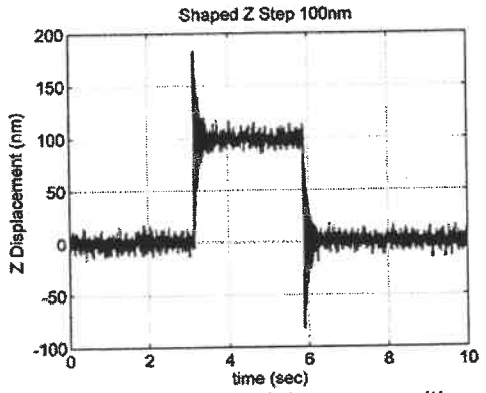

FIGURE 9. Response of the nanopositioner to a 100nm step in the z-direction, without the capacitance probe target.

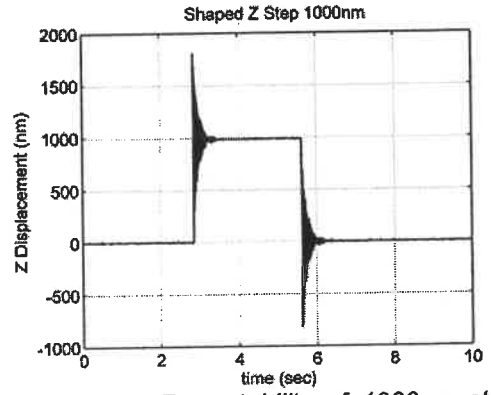

FIGURE 10. Repeatability of 1000nm step in the z-direction without 6-axis probe target.

In order to demonstrate the full three-dimensional capabilities of the nanopositioner, the system was commanded to traverse a 1 μm spiral trajectory in open-loop. The six-probe fixture and probe target were used to record position. The commanded and measured data is plotted in Fig. 11.

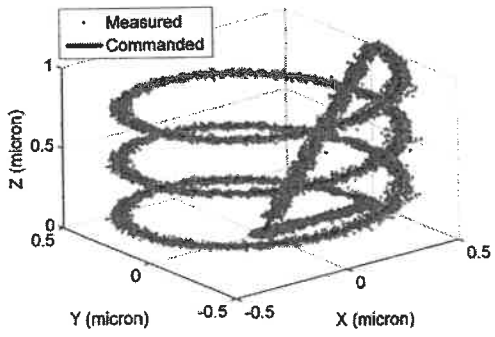

FIGURE 11. Measured trajectory of the nanopositioner when commanded to follow a 3-loop spiral trajectory with diameter and total traversed height of 1000nm.

The data indicates that the positioner follows the desired trajectory to within the noise of the measurement system.

CONCLUSION

A centimeter-scale, electromagnetically-driven nanopositioner has been designed and tested to have 8 microns range-of-motion and repeatability of better than 20nm. The low-cost prototype nanopositioner design is scalable down to the millimeter size through microfabrication. Miniaturization would lead to several performance benefits including increased bandwidth, increased coil current density, and favorable thermal performance. Target applications for the meso-scale system include high-throughput nanomanufacturing and scanning probe microscopy. The prototype is currently being integrated into a bench-top electric-pen lithography system for demonstration of low-cost nanomanufacturing.

REFERENCES

1. Lutwyche, M., et al., "Planar Micromagnetic X/Y/Z Scanner with Five Degrees of Freedom," presented at Proceedings of the 194th Meeting of the Electrochemical Society, Boston, 1998.
2. Rothuizen, H., et al., "Compact Copper/Epoxy-Based Electromagnetic Scanner for Scanning Probe Applications," presented at 15th IEEE International Conference on Micro Electro Mechanical Systems MEMS 2002, Jan 20-24 2002, Las Vegas, NV, 2002.
3. Rothuizen, H., et al., "Fabrication of a Micromachined Magnetic X/Y/Z Scanner for Parallel Scanning Probe Applications," *Microelectronic Engineering*, vol. 53, pp. 509-512, 2000.
4. Pantazi, A., et al., "A Servomechanism for a Micro-Electromechanical-System-Based Scanning-Probe Data Storage Device," *Nanotechnology*, vol. 15, pp. 612-621, 2004.
5. Malshe, A. P., et al., "Investigation of Nanoscale Electro Machining (Nano-Em) in Dielectric Oil," presented at 55th CIRP General Assembly, Antalya, Turkey, 2005.
6. Culpepper, M. L. and Anderson, G., "Design of a Low-Cost Nano-Manipulator Which Utilizes a Monolithic, Spatial Compliant Mechanism," *Precision Engineering*, vol. 28, pp. 469-482, 2004.

NEAR-FIELD POLARIMETRY USING SCANNING PROBE MICROSCOPE WITH SUB-WAVELENGTH APERTURE CANTILEVER

Kensuke Tsuchiya[1], Takayuki Muragishi[2], Takeshi Ooi[2], Hiroshi Morii[2], Tetsuya Hamaguchi[2], and Masayuki Nakao[2]
[1]Institute of Industrial Science, The University of Tokyo, Meguro-ku, Tokyo, JAPAN
[2]Department of Engineering Synthesis, The University of Tokyo, Bunkyo-ku, Tokyo, JAPAN

INTRODUCTION

Optical devices with micro-features of sizes close to light beam wavelengths have recently been gathering much attention [1]. Advancements in micro-fabrication and form transfer have realized development of optical devices with a variety of functionalities. Nevertheless, fabrications of such devices are always accompanied with form errors and thus the performances of the optical devices are also affected. Measuring the far-field electromagnetic fields and comparing the measurements with computational estimates can quantify the effects of such errors. Direct measurement of the near-field electromagnetic intensities and the direction of polarization would, however, give better understanding of the phenomena and would eventually cut down the time and cost of developing optical devices.

Instrumentation for measuring the electromagnetic field near devices mostly use optical fiber probes [2-6]. A typical instrument has an optical fiber installed as the probe of the atomic force microscope (AFM) and measures, at the detector in the back, the light that enters the probe from the tip. This method has the advantage of small noise interference because optical fibers provide connection from the tip to the detector. On the other hand, however, the configuration of the tip is difficult to control and measuring polarized light is difficult. Our studies solved this problem by fabricating a micro-aperture on the AFM cantilever, and we propose a new system for measuring the optical device surface configuration, its near-field electromagnetic field and polarized lights.

INSTRUMENTATION WITH A MICRO-APERTURE CANTILEVER

Figure 1 shows the concept of the system we proposed in our study. The primary components of this system include a cantilever with a micro-aperture, an AFM that drives it, a lens and aperture, and a photomultiplier tube. A Focused Ion Beam (FIB) cuts the micro-aperture at the tip of the cantilever to an arbitrary shape.

An AFM generally scans optical device surfaces with the cantilever to measure the surface shape configuration. The system of our study injects a beam to the optical device, and the cantilever with a micro-aperture measures the surface configuration. The beam emission from the optical device surface that passes the micro-aperture reaches the PMT detector. This method allows measuring the electromagnetic field intensity at the position together with the shape configuration. Also, scanning the space directly above the optical device measures the 3D spatial electromagnetic field distribution there. Unlike measuring with an optical fiber probe, however, the cantilever sensing allows light to reach the PMT through paths other than through the micro-apertures; such light beams are noise for our measurement. To reduce such noise, the cantilever itself and the aperture in front of the PMT shut out beams from paths other than the micro-apertures.

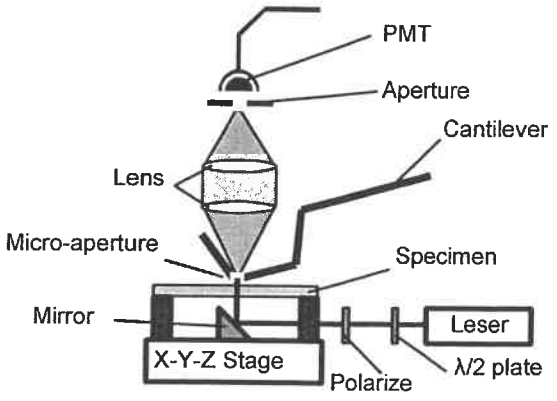

Figure 1: Configuration of the proposed system including a cantilever with a micro-aperture, an AFM, a lens and aperture, and a photomultiplier tube.

For measuring polarized light, we can cut slit-shaped micro-apertures with width equal to or less than the half-wavelength of the light, because a slit with a width of half-wavelength or less only passes a polarized light component with its electrical field vibration oriented perpendicular to the slit. If we change the direction of detection and measure the polarized light components in two directions, we can determine the direction of polarization at the point. With these principles we measured the optical device surface shape, and the electromagnetic field intensity and polarization in the near-field.

We constructed our system with a cantilever, (OMCL-HA100-WS, Olympus Corporation), an AFM (SPI3800N/SPA400, Seiko Instruments Inc.), a lens (M Plan Apo SL 20, Mitutoyo Corporation), an aperture (IRIS DIAPHRAGM MOUNT 03623-H, Edmund Optics Inc.), and PMT (R1463, Hamamatsu Photonics K.K.).

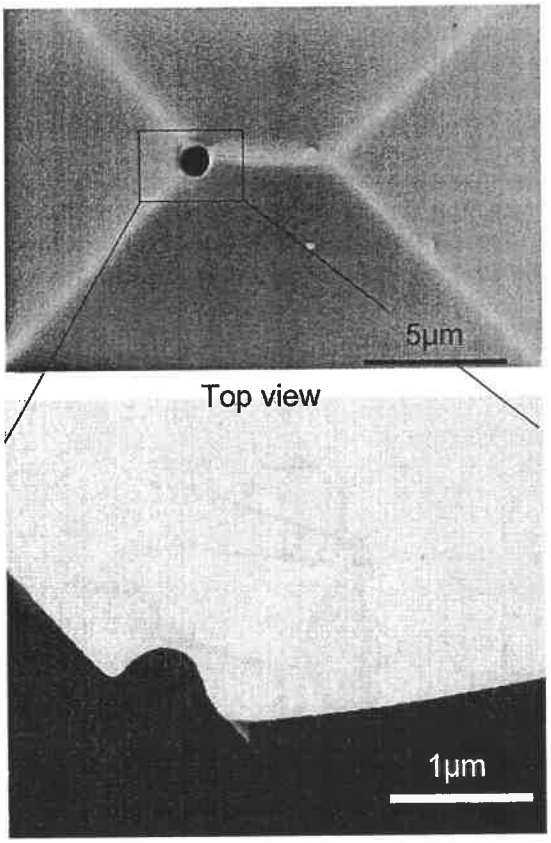

Figure 2: SEM images of the cantilever with a circular micro-aperture fabricated by FIB.

ELECTROMAGNETIC FIELD INTENSITY MEASUREMENT TEST

We first tested the measuring of the electromagnetic field intensity in the near-field of an optical device.

Similarly to an optical-fiber probe micro-aperture, we made a circular micro-aperture on the cantilever. The test took several measurements by varying the distance between the aperture and the device surface. The circular aperture on the cantilever had a diameter of 1.1μm. Opening this hole removed the bulge at the tip of the cantilever for shape measuring and we made an approximately 300nm bulge near the micro-aperture with Electron Beam Deposition (EBD). Figure 2 shows the SEM image of the cantilever with a micro-aperture.

We prepared specimen with four 0.5μm x 5μm slits arranged in a 1.5μm pitch. The slits were prepared by sputtering an approximately 200nm thick Au film on a glass substrate and then removing the Au over the slits with FIB. Our input beam was He-Ne laser (wavelength: 632.8nm) and PMT measured the electromagnetic field intensity distribution above a 10μm x 10μm area by increasing the distance between the cantilever and specimen from the approached state (where the specimen and micro-aperture were about 100nm apart for measuring the surface configuration) to a distance of about 9μm.

Figure 3 shows the measurement results and Figure 4, the simulation results with similar conditions except with 3 slits. The measurement in the approached state produced PMT output results (optical image) with slits similar to the ones observed with shape measurement results (shape image). The 500nm or so offset of the optical image to the shape image was due to the approximately 500nm distance between the bulge of the cantilever tip and the center of the micro-aperture.

The results from continually changing the distance between the specimen and the micro aperture from 1 to 10μm shows the optical interference pattern. These results matched the simulation well. Our results demonstrated that a cantilever with a micro-aperture can measure the electromagnetic field spatial intensity distribution in the field near optical devices.

POLARIZED LIGHT MEASUREMENT TEST

The previous section showed the results from a cantilever with a 1.1mm diameter circular aperture. As explained in Section 2, we needed to fabricate slit apertures with widths of half

wavelength of the beam or less for polarized light measurement. We thus, applied FIB to open three 1.5μm x 0.2μm slits apart by a pitch of 0.4μm on the cantilever tip. Figure 5 shows the SEM photograph. The slit lengths were set so the open area approximately equals that of the circular aperture.

We used the above cantilever to verify that it could measure specific polarized lights when differently polarized lights coexisted. The specimens were made similarly to the previous section by sputtering metal on glass and removing part of the metal. The input beam was a laser from underneath. Figure 6-(1) shows the specimen with five 0.22μm x 2.5μm slits apart by a pitch of 0.53μm. We prepared 4 sets of such slit arrangement that were rotated by 90 degrees. Each slit on the specimen passes the input beam component with its direction of electrical field vibration perpendicular to the slit. Injecting a beam with its direction of electrical field vibration at a 45 degree angle with the slits would produce an outgoing beam with an electromagnetic field with polarized lights that are 90 degrees apart.

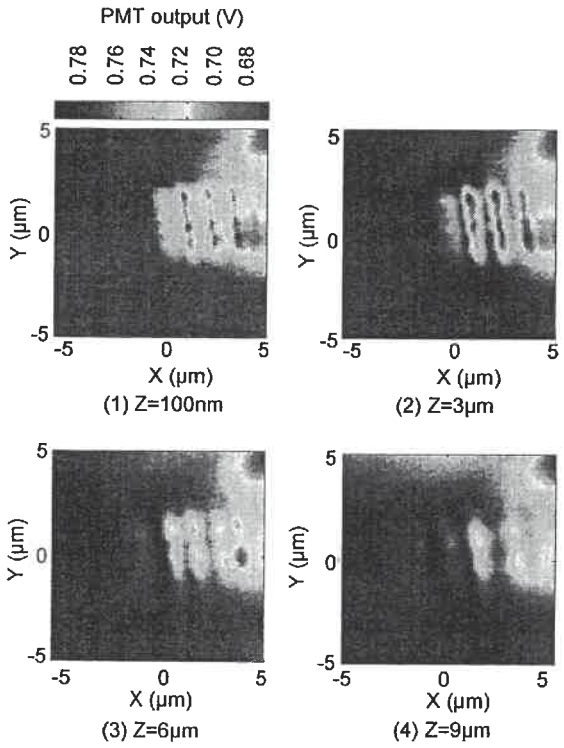

Figure 3: Measurement results of the electromagnetic field intensity distribution above a specimen.

We measured a 10μm x 10μm area above the specimen that covered the specimen slit area by reciprocate scanning of 100 lines at a speed of 1μm/sec. Using cantilevers with a circular aperture and slit apertures, we measured, with the method described in Section 2, the specimen surface configuration and the distribution of the electromagnetic field intensity in the area above the specimen.

Figure 6-(2)(3)(4) show the results. The cantilever with a circular aperture detected the beam output from all the slits. The cantilever with slit apertures, on the other hand, detected beam output only when the slits of the cantilever and those of the specimen were parallel. These results demonstrate that the cantilever with slit micro-apertures can measure the electromagnetic field intensities for specific

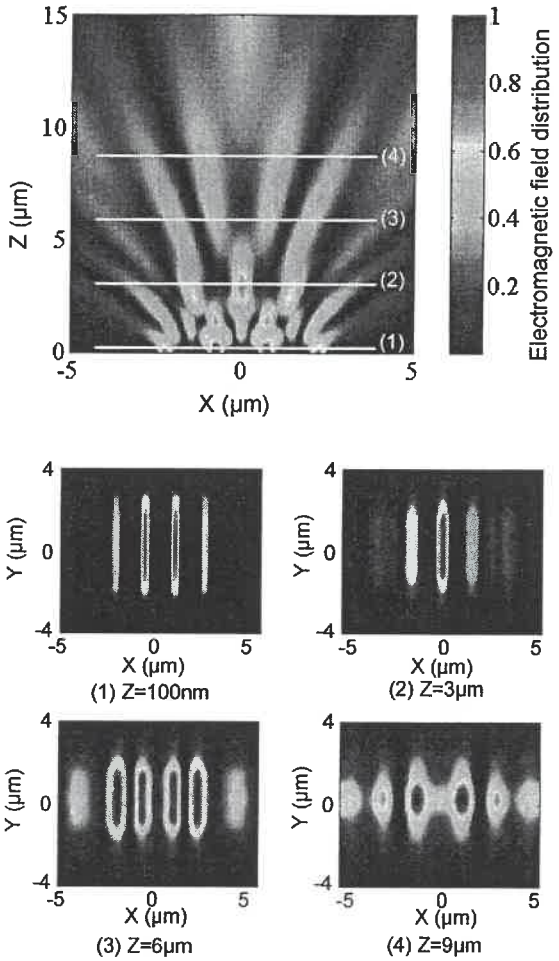

Figure 4: Simulation results of the electromagnetic field intensity distribution above a specimen with the similar conditions except with 3 slits.

polarized components. The slit apertures, however, failed to identify the optical interference like in the results of the previous section. This was due to the large apertures with sizes 1 to 2μm that caused lack of resolution.
To enhance the resolution, we need to reduce the aperture size, however, when they are made smaller than the beam wavelengths, the beams that pass the aperture turn into near-field beams and cannot reach the PMT. We need to develop mechanisms to convert a near-field beam into a diffusion beam by placing scatterer material like silver or carbon inside the apertures. The efficiency of conversion into a diffusion beam partially depends on the aperture shape. Since FIB allows freely aperture arbitrary shapes for the apertures, we can minimize the decay of light by sizing and forming adequate apertures depending on the wavelengths of the beams to detect.

CONCLUSIONS

This study developed a system to measure the surface configuration of optical devices and spatially measure the electromagnetic field intensity and polarized light in the near field. Micro-apertures at the tip of the cantilever beam on AFM allowed simultaneously measuring the device shape configuration and the electromagnetic field intensity. We also showed that slit shaped micro-apertures can measure the electromagnetic field intensity for specific polarized light components.

REFERENCES

1. M. L. M. Balistreri, J. P. Korterik, L. Kuipers, N. F. van Hulst, 2000, Photon scanning tunneling optical microscopy with a three-dimensional multiheight imaging mode, *Appl. Phys. Lett.*, 77(25): 4092-4094.
2. C. Peeters, E. Fluck, A. M. Otter, M. L. M. Balistreri, J. P. Korterik, L. Kuipers, 2000, Photon scanning tunneling microscopy of tailor-made photonic structures, *Appl. Phys. Lett.*, 77: 142-144.
3. E. Fluck, N. F. van Hulst, W. L. Vos, L.Kuipers, 2003, Near-field optical investigation of three-dimensional photonic crystals, *Physical Review E*, 68: 015601.
4. A. Nesci, R. Dandliker, M. Salt, H. P. Herzig, 2002, Measuring amplitude and phase distribution of fields generated by gratings with sub-wavelength resolution, *Optics Comunication*, 205: 229-238.
5. Th. Dziomba, Th. Sulzbach, O. Ohlsson, Cj. Lehrer, L.Frey, H. U. Danzebrink, 1999, Ion beam-treated silicon probes operated in transmission and cross-polarized reflection mode near-ingrated scanning near-field optical microscopy, *Surface And Interface Analysis*, 27: 486-490.
6. Quidant, J.-C. Weeber, A. Dereux, G. Leveque, J. Weiner, C. Girard, 2004, Addressing and imaging microring resonators with optical evanescent light, *Physical Review B*, 69: 081402.

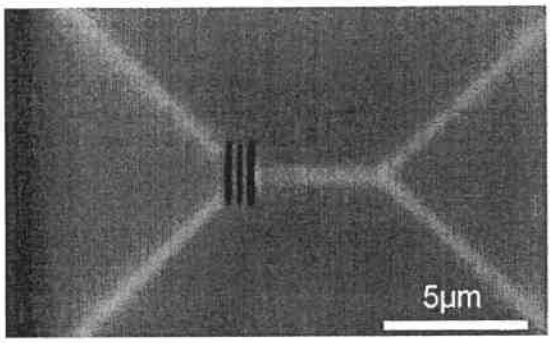

Figure 5: SEM images of the cantilever with slit shaped micro-apertures, which allows measuring the electromagnetic field intensity for specific polarized light components.

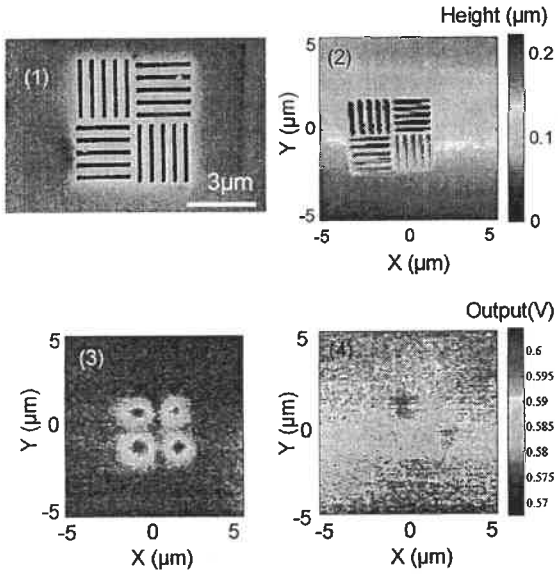

Figure 6: (1) SEM images of the specimen with five 0.22μm x 2.5μm slits apart by a pitch of 0.53μm, and measurement (2) AFM image, (3) optical image measured using cantilevers with a circular aperture, (4) optical image measured using cantilevers with slit apertures.

A STUDY OF PATTERN AND FEATURE ANALYSIS OF SURFACE GENERATION IN FAST TOOL SERVO MACHINING OF OPTICAL MICROSTRUCTURES

C.F. Cheung[1], X.Q. Jiang[2], S. To[1], W.B. Lee[1], T.C. Kwok[1] and H.F. Li[1]

1. Advanced Optics Manufacturing Centre, Department of Industrial and Systems Engineering, The Hong Kong Polytechnic University, Hung Hom, Kowloon, Hong Kong.
2. Centre for Precision Technologies, University of Huddersfield, UK.

ABSTRACT

Nowadays, there are lack of definitive international standards, surface parameters and techniques for the characterisation of the surface generation of optical microstructures with the articulation to their quality specifications in practical applications. This paper presents a study of factors affecting the surface generation in FTS machining of optical microstructures. The surface quality and defects of the machined surfaces are examined by a non-contact interferometric surface profiler. Surface features and patterns are analysed based on power spectrum analysis and are correlated with the surface quality of the optical microstructures. The results form the basis for the development of the pattern and feature analysis algorithms for the characterisation of surface generation in FTS machining of optical microstructures.

Keywords: Fast Tool Servo Machining, Optical Microstructures, Pattern and Feature Analysis, Surface Generation, Surface Characterization.

1. INTRODUCTION

Nowadays, the role of optical microstructures such as micro-lens arrays is becoming increasingly important as the need for the parallelism and density grows for display, communication, and storage applications. This trend toward highly parallel compact optical systems leads to a growing need for high performance optical microstructures such as micro-lens arrays [1]. Optical microstructures are small scale topologies generally classified as grooves, pyramids, microlens arrays, lenticulations and echells. Applications of optical microstructures can be found in the flat panel displays used in hand held devices such as mobile phones, personal data assistants (PDA) and broad band optical fibre connectors.

Although ultra-precision machining based on fast tool servo (FTS) machining provides a solution for machining optical microstructures with sub-micrometer form accuracy and nanometric surface finish without the need for any subsequent post processing, the methodologies for the characterisation of surface generation have received relatively little attention. Optical microstructures are usually characterized by their surface quality such as surface roughness and their optical properties. Most previous research work on micro-optics testing is based on interferometric methods [2-4] and wavefront measurement such as Mach-Zehnder interferometer (MZI) [2]. Some research work has been found in the application of (2D) discrete Fourier transform (DFT) of the interference microscope image to evaluate the fabricated grid surface [5]. However, the interferometric testing of micro-optics incurs certain difficulties due to their small dimension such as Fresnel diffraction artefacts, coherent noise and distributing interferences, etc [6]. On the other hands, they fail to articulate the surface quality of the optical microstructures to the functional specifications of the micro-optics systems.

The surface quality of a FTS machined optical microstructures depends largely on the selection of cutting conditions and of the tool path. Nowadays, the achievement of functional specifications of the optical microstructures still depends largely on the experience of the optics designer through an expensive trial-and-error approach when new optics design is used. As the optimal optics design for ensuring good quality depends largely on the functional specifications, machine tolerance and measurement errors. There is a need for a characterisation system and standardized tools which can characterize the effect of different factors on surface quality and hence the functional specifications of the optical microstructures. As a result, this paper presents a preliminary study of characterization of surface

generation of optical microstructures using pattern and feature analysis.

2. PATTERN AND FEATURE ANALYSIS

In the present study, the factors affecting the surface generation in FTS machining optical microstructures were identified and analyzed through a series of cutting tests conducted on the Nanoform 200 ultra-precision machine incorporated with a FTS system located in the Ultra-precision Machining Centre of The Hong Kong Polytechnic University. The surface quality and defects of the machined surfaces were examined by a non-contact interferometric surface profiler (Wyko NT8000). Power spectrum analysis is used to extract the patterns and features from the measured surfaces. The power spectrum analysis is done by Vision software. The features are correlated with the quality specifications of the optical microstructures. This forms the basis for the development of the pattern analysis algorithms for the characterisation system.

The characterisation system is composed of three major components which are the data acquisition module, the pattern analysis module and the characterisation module, respectively. The data acquisition module is used to acquire surface data from measurement instruments based on a stitching algorithm. Hence, the measurement data are analyzed by pattern analysis algorithm built based on power spectrum analysis. In the characterisation module, the spectrum features are correlated to different types of defects and errors artifacts of optical microstructures.

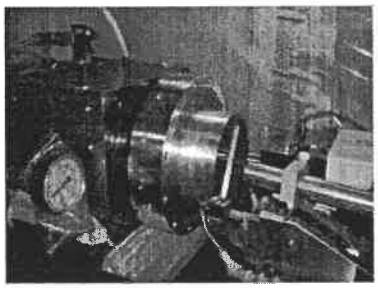

Figure 1 Configuration of the experimental setup

3. EXPERIMENTAL

A series of cutting experiments were conducted on FTS of microlens array under various surface speeds and feed rate conditions. The experiments are basically divided into two groups i.e. Group A and Group B. Group A consists of cutting tests conducted under different surface speed while Group B consists those conducted under different feed rates.

The configuration of the machine setup is shown in Figure 1 while the geometrical patterns and specifications of microlens array are shown in Figure 2 and Table 1, respectively. Tables 2 and 3 summarize the cutting conditions in the present study. To determine the variation of surface quality of the microlens array with respect to the distance from the centre of the workpiece, the form error and surface roughness of the microlenses were measured at location L4.

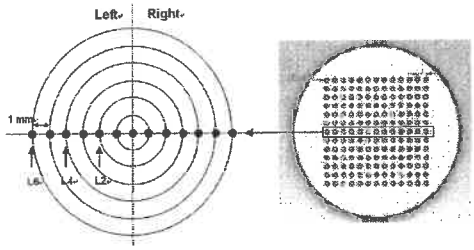

Figure 2 Geometrical pattern of microlens array

Table 1 Design specifications of microlens array

Dot Spacing	1 x 1 mm2
Radius of curvature of the microlens	1.1705 mm
Angle of curvature of the micolens	13°
Depth of the microlens	0.03 mm
Number of the microlens	13 x 13
Diameter of the lens	0.5266mm

Table 2 Cutting conditions for Group A

Cutting Conditions	A1	A2	A3
Surface speed, V_s (m/s)	1.25	2.50	8.00
Feed rate, f (mm/min)	1.00	1.00	1.00
Depth of cut, d_c (μm)	5	5	5

Table 3 Cutting conditions for Group B

Cutting Conditions	B1	B2	B3
Surface speed, V_s (m/s)	1.25	1.25	1.25
Feed rate, f (mm/min)	0.50	1.00	5.00
Depth of cut, d_c (μm)	5	5	5

4. RESULTS AND DISCUSSION

4.1 Effect of surface speed

Figure 3 shows the results of the effect of surface speed on the surface generation in FTS of microlens array. The surface measurement was done at location L4. It is interesting to note that the geometry of the lens change with increasing surface speed. As surface speed decreases, better surface quality can be achieved.

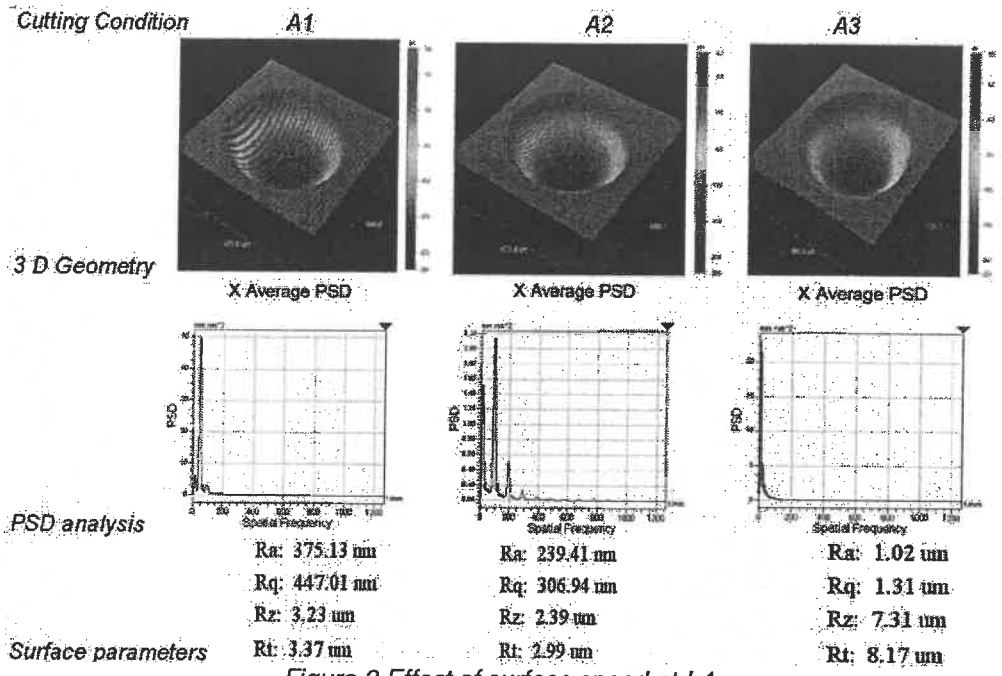

Figure 3 Effect of surface speed at L4

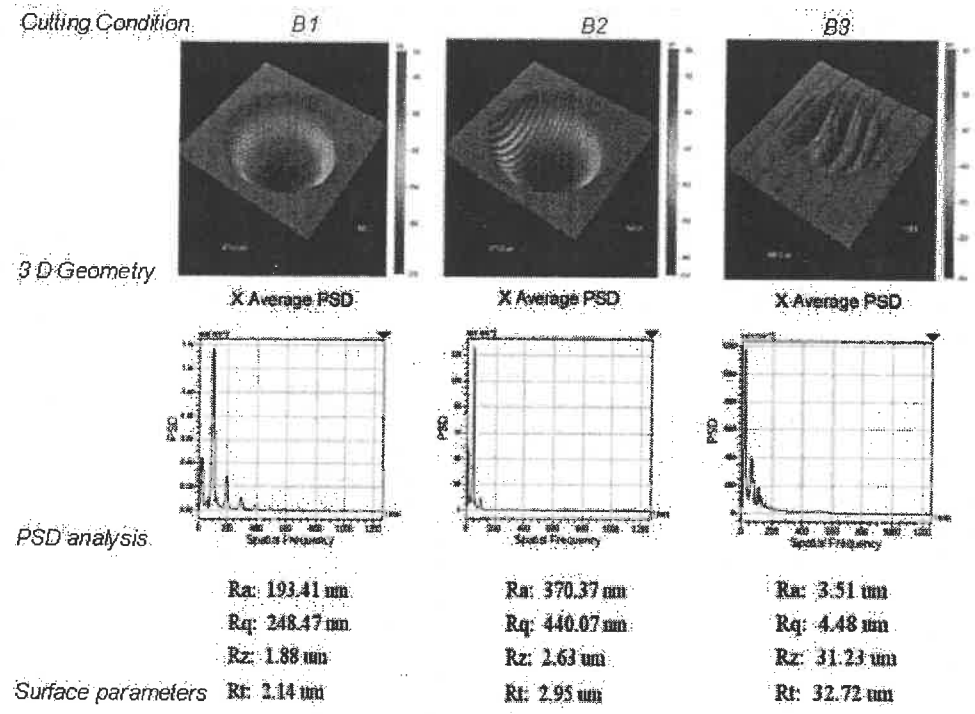

Figure 4 Effect of feed rate at L4

The distortion is not desired for practical applications and can be described as the failure of cutting path positioning. The diffraction efficiency and thus the optical performance are severely degraded. It may be due to insufficient time for FTS to stack back the diamond tool between two successive cuttings. Therefore, the diamond tool cannot perform accurately during the cutting process.

In the PSD plot, it appears that the patterns of the power spectrum change with increasing surface speed. The spark peaks shift to a lower

frequency as surface speed increases. This provides an important means for correlating the features of the power spectrum with surface quality of the microlens array.

4.2 Effect of feed rate

Figure 4 shows the effect of feed rate on surface generation in FTS machining of mirolens array. Different feed rates were used while the other cutting conditions were kept constant. It is interesting to note that deeper and wider tool marks were formed on the microlens with a higher feed rate. In other words, the surface roughness of the microlens increases as feed rate increases and imperfect surface profile of the micro lens is found as feed rate is high.

This may be due to the tool feed rate which is defined as the ratio of the feed rate and the spindle rotational speed. As tool feed rate increases, the width and the depth of the tool marks formed on the surface increase. An increase in feed rate together with decreasing spindle rotational speed results in an increase in tool feed rate and hence the formation of imperfect surface profile in the microlens array. It is found that the power spectra of the surface profiles change with the variation of feed rate. This infers that the power spectrum of the surface profile is possible to be used to characterize the surface generation under different feed rates.

5. CONCLUSION

Although ultra-precision machining based on fast tool servo (FTS) machining provides a solution for machining optical microstructures with sub-micrometer form accuracy and nanometric surface finish without the need for any subsequent post processing, the methodologies for the characterisation of surface generation have received relatively little attention.

In this paper, the factors affecting the surface generation in FTS machining optical microstructures are identified and analyzed through a series of cutting tests. The surface quality and defects of the machined surfaces are examined. Patterns and features are extracted by power spectrum analysis based on the experimental findings and they are correlated with surface qualify of the optical microstructures.

The preliminary results indicate that the form accuracy and surface roughness of the microlens array are significantly affected by the surface speed and feed rate, respectively. Better form accuracy can be achieved with a lower surface speed while the surface profile of the microlens distorts significantly as the surface speed increases. Such a distortion reduces the diffraction efficiency and thus the optical performance. It is also found that the surface roughness of microlens array increases with increasing feed rate. Moreover, it is interesting to note that the patterns and features of the power spectrum of the machined surface can be correlated to the form and surface roughness of the optical microstructures. This not only provides an important means for the surface characterisation but also forms the basis for the development of the pattern analysis algorithms for the surface characterisation system for optical microstructures.

ACKNOWLEDGEMENTS

The authors would like to express their sincere thanks to the Research Committee of The Hong Kong Polytechnic University for their financial support for the project (Project Code: YE95). Many thanks are also due to Precitech Inc. for the support of the research work.

REFERENCES

[1] Quan, C. et al., 2003, Integrated optical inspection on surface geometry and refractive index distribution of a microlens array, *Optics Communications*, 225:223–231.

[2] Sickinger, H., Schwider, J. and Manzke, B., 1999, Fiber based Mach-Zehnder Interferometer for Measuring Wave Aberrations of Microlenses, *Optik*, 110 (5):239-243 (1999).

[3] Schwider, J. and Sickinger, 1997, Arraytest for Microlenses, *Optik*, 107:26-34.

[4] Moench, W. and Zappe, H., 2004, Fabrication and Testing of Micro-lens Arrays by All-liquid Techniques, *Journal of Optics A: Pure and Applied Optics*, 6:330-337.

[5] Gao, W., Araki, T., Kiyono, S., Okazaki, Y. and Yamanaka, M., 2003, Precision Nano-fabrication and Evaluation of a Large Area Sinusoidal Grid Surface for a Surface Encoder, *Precision Engineering*, 27:289-298.

[6] Reichelt, S., Bieber, A., Aatz, B. and Zappe, H., 2005, Micro-optics Metrology Using Advanced Interferometry, *Proceedings of SPIE*, 5856:437-446.

DIMENSIONAL STUDY OF AN INTERFERENCE FIT ALLOGRAFT

Nathan A. Mauntler, John C. Ziegert, Tony L. Schmitz
Department of Mechanical and Aerospace Engineering
University of Florida, Gainesville, FL, USA

INTRODUCTION

The University of Florida and Regeneration Technologies, Inc. (RTI) are currently participating in a research collaboration to extend their understanding of the interference fit pin connections that join the multiple cortical/cancellous bone layers in allograft assemblies used in spinal fusion surgeries. As production rates for the allograft assembly increase, the scrap costs associated with failed interference fit become increasingly significant. The focus of the work is determining dimensional variations of the hole and pin diameters during the various stages of the manufacturing process, including machining operations and subsequent post-machining/assembly procedures. These include the proprietary BioCleanse™ sterilization process and lyophilization (i.e., freeze drying). These dimensional variations not only provide RTI with information about their process capabilities, but are also incorporated into mechanical models of the interference fit.

DIMENSIONAL MEASUREMENTS

The systematic measurement of the interference fit components is central to the analysis. For each of ten donors, the components for six assemblies were measured. Each assembly consists of a cancellous block and two cortical bone plates held together by two cortical interference pins (see Fig. 1). Prior to pin insertion, the pin and hole diameters were measured on a three-axis coordinate measuring machine (CMM) using a touch trigger probe. Pins were measured while clamped in a manual collet holder. Cortical plates were measured in the RTI fixture in which they were machined. Half of the cortical/cancellous stack-ups were then removed from the machining fixture and the cortical plate holes were measured again. The three stack-ups per donor which remained in the machining fixture were then returned to RTI for the final assembly/machining steps. Measurements of the pin and hole diameters were repeated after BioCleanse™, lyophilization, and a recommended thirty-second hydration.

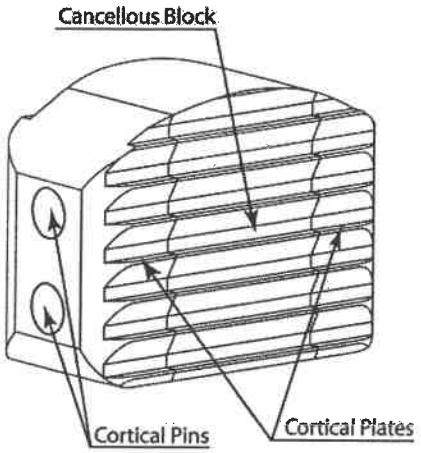

Figure 1: The Cornerstone™ ASR cortical-cancellous allograft produced by RTI.

Figure 2 shows the average diametric interference predicted from measurements of the loose pin and plate hole diameters following each of the manufacturing processes. The shaded region represents the nominal diametric interference specified by RTI for the as-machined allografts. The data indicates a 21 μm average drop in the predicted diametric interference and an increase in interference variability following lyophilization. A thirty second hydration of the parts resulted in an average recovery of 9 μm of interference.

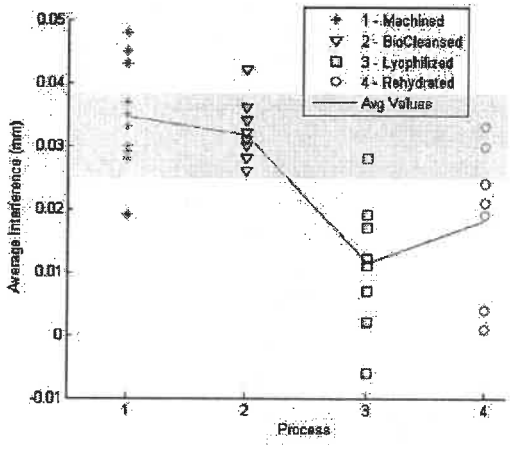

Figure 2: Average predicted diametric interference following each manufacturing process.

FINITE ELEMENT ANALYSIS

The data collected from the dimensional measurements was incorporated into a finite element model of the interference fit (Fig. 3, ANSYS 10, ANSYS, Inc, Canonsburg, PA). To simplify the model, the 11 mm radius on the top of the graft was neglected and a symmetry boundary condition was applied across the plane through the pin centers. The pin diameter was set equal to the average of all pin diameters from the dimensional study. The diameter of the holes was set equal to the pin diameter minus the average predicted interference value from the dimensional study. Twenty-node brick elements were used to mesh the pin and the plate. To simulate the interference fit, contact and target elements were created at the pin-plate interfaces.

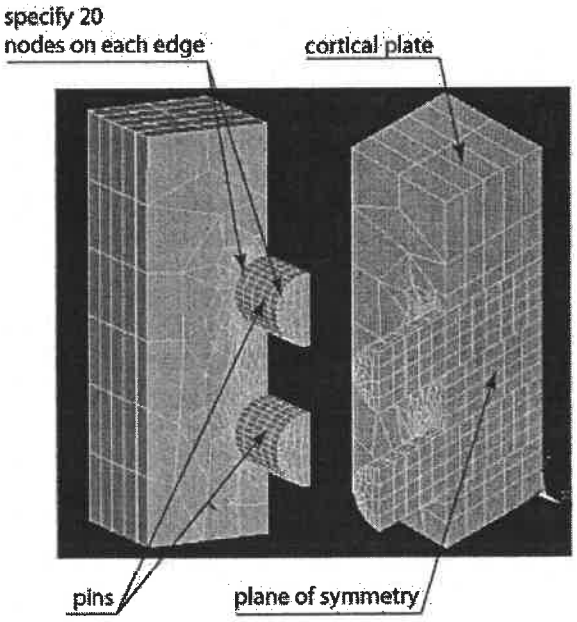

Figure 3: The solid model and mesh used in the finite element analyses.

Three trials of the finite element model were completed using three different sets of geometric and material property inputs (Table 1). In the first trial, the average pin diameter and the diametric interference values obtained after thirty seconds of hydration were used. For the second and third trials, the model geometries were created using the average pin diameter and diametric interference values measured after lyophilization.

Table 1: Geometry and material property values used in the finite element analyses.

Trial	1	2	3
E_r (GPa)	12.0	12.0	9.0
E_c (GPa)	12.0	12.0	9.0
E_l (GPa)	18.0	18.0	14.0
G_{rc} (GPa)	3.3	3.3	2.9
G_{rl} (GPa)	3.3	3.3	2.9
G_{cl} (GPa)	3.3	3.3	2.9
$\nu_{\square\square}$	0.50	0.50	0.5
$\nu_{\square\square}$	0.40	0.40	0.4
$\nu_{\square\square}$	0.25	0.25	0.25
□	0.29	0.29	0.29
□□□□□□□ □□□□□□	1.948	1.936	1.936
□□□□□□□□□□□ □□□	18	11	11

In all trials, transversely isotropic material symmetry was assumed. The first and second trials used material properties obtained by Reilly and Burstein in 1975 [1]. In the third trial, the elastic and shear modulus values are reduced by one standard deviation from the mean value.

The finite element model used two load steps. First, a static analysis was used to predict the von Mises and contact pressure distributions in the allograft. In the second step, a 100 μm relative motion between the pins and the plate was commanded. The sum of the axial direction forces on the contact elements during the second load step was used to estimate the pull-apart force.

Results from the finite element analyses are shown in Table 2. The three trials predict maximum von Mises stress values in the cortical plates between 35 MPa and 81 MPa. Comparing these values to a tensile failure stress on the order of 53 MPa [1] suggests that material failure is likely at higher interference values. Additionally, the finite element model predicts that the force required to separate the interference fit is between 95 N and 216 N.

Table 2: Von Mises stress and pull-apart force predicted by the finite element analyses.

□□□□	$\sigma_{\square\square}$ □□□□ □□□□	□ □□□
1	81	216
2	45	120
3	35	94

Figure 4 shows the contact pressure stress distribution along the two pins. It should be

noted that no stress concentration is predicted at the boundary of the contact.

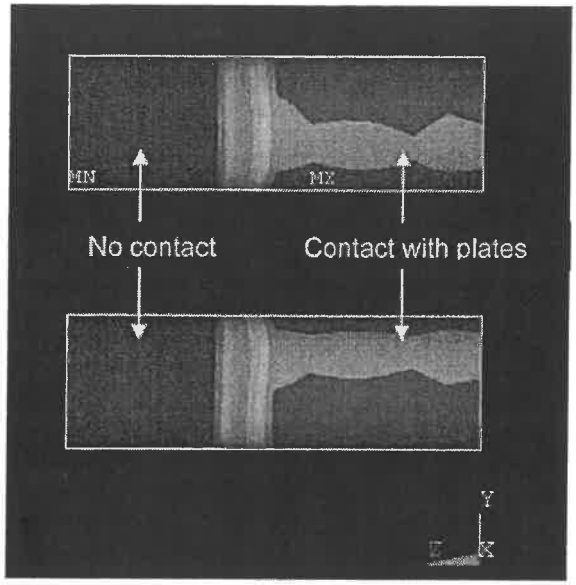

Figure 4: Contact pressure distribution on the cortical pins.

MONTE CARLO SIMULATION

An analytical interference fit model formed the basis for a Monte Carlo simulation used to predict the rate of pull-apart and material failure for the assembled grafts.

Analytical Shrink Fit Model

The analytical shrink fit model applied in this simulation is shown in Fig. 5. This model assumes isotropic material properties and a cylindrical geometry of both pin and plate.

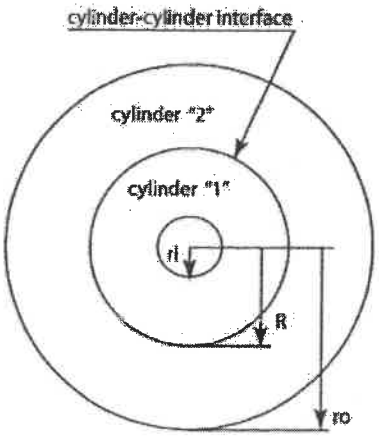

Figure 5: Geometry of the analytical shrink fit model.

The analytical model uses thick-walled cylinder stress-strain theory to predict the contact pressure at the pin-plate interface and the maximum von Mises stress in the cortical plate (Eqs. 1 and 2) [2]. The force required to remove one interference pin can be calculated as the integral of the differential product of the local stress concentration factor, the contact pressure, the area in contact, and the coefficient of friction (Eq. 3). Variable definitions are provided in Table 3. The stress concentration factor Kt is applied to account for finite or unequal lengths of the pin and plate.

$$p = \frac{\delta}{\frac{R}{E1}\cdot(1-\nu 1) + \frac{R}{E2}\cdot\left(\frac{ro^2+R^2}{ro^2-R^2}+\nu 2\right)} \quad (1)$$

$$\sigma v2 = p\cdot\sqrt{Kt^2 + Kt\cdot\left(\frac{ro^2+R^2}{ro^2-R^2}\right) + \left(\frac{ro^2+R^2}{ro^2-R^2}\right)^2} \quad (2)$$

$$F = \int Kt(x)\cdot p\cdot(Ac)\cdot\mu\, dx = \int Kt(x)\cdot p\cdot(2\cdot\pi\cdot R\cdot Lc)\cdot\mu\, dx \quad (3)$$

Table 3: Analytical shrink fit model variables.

Parameter	Symbol
Radial Interference	δ
Young's Modulus (Pin)	E1
Young's Modulus (Plate)	E2
Poisson's Ratio (Pin)	v1
Poisson's Ratio (Plate)	v2
Stress Concentration	Kt
Friction Coefficient	μ
Length of contact	Lc

This analytical model has several limitations. First, it cannot account for the combined stresses of two interference pins in close proximity. Also, the model cannot incorporate material anisotropy. Finally, the model cannot accommodate non-cylindrical plate geometry. To deal with this final issue, the outer cylinder radius, ro, was treated as a fitting factor to match analytical to finite element results.

Monte Carlo Simulation

The Monte Carlo simulation was carried out by calculating the von Mises stress in the plate and the pull-apart force over 250,000 iterations. In each iteration, the model input parameters were selected randomly within one standard deviation of the mean value. The material properties and geometric values used in the simulation were the same as those used in the third finite

element trial (Table 4). Standard deviations were drawn from the literature [1] and the statistical distribution of the measured geometric values.

Table 4: Monte Carlo input parameters

Parameter	Mean Value	Standard Deviation
Diametric interference (μm)	11	9
Pin Young's modulus (GPa)	9	1
Plate Young's modulus (GPa)	9	1
Pin Poisson's ratio	0.41	0.15
Plate Poisson's ratio	0.41	0.15
Pin diameter (mm)	1.937	0.021
Plate outer radius (mm)	1.2	0
Stress concentration factor	1	0
Contact length (mm)	7.0	0.3
Coefficient of friction	0.3	0.15

The Monte Carlo simulation predicts the average plate will be subjected to a mean von Mises stress of 65 MPa with a standard deviation of 39 MPa. If the failure stress of the bone material is assumed to be 53 MPa, the simulation predicts a material failure rate of 57%. Furthermore, the simulation predicts that an average of 133 N (standard deviation 141 N) is required to pull an allograft apart. The model predicts a pull-apart failure rate of 13%.

MECHANICAL TESTING

Thirty assembled allografts were tested for pull-apart failure on a mechanical load frame in order to verify the finite element model and Monte Carlo simulation. The graft cortical plates were epoxied to grooved aluminum blocks (Fig. 6) held in the load frame grips so that the interference fit would not be compromised by clamping forces nor reinforced with epoxy.

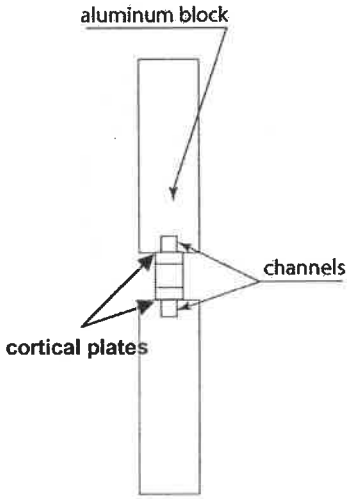

Figure 6: Allografts were attached by epoxy to grooved aluminum blocks for mechanical testing.

Prior to mechanical testing, the lyophilized grafts were tested manually for interference failure and visually inspected for cracks according to RTI quality assurance procedures. Of the 30 allografts considered, 4 (13%) were manually pulled apart without appreciable force. Cracks were observed in one or both of the cortical plates of 17 of the allografts (57%). The frequencies of these failures closely agree with the frequencies predicted by the Monte Carlo simulation.

Following manual inspection, the grafts were attached to the aluminum blocks, hydrated for 30 seconds, and pulled apart. The epoxy bond failed prior to the interference fit for 10 of the allografts tested. Of the remaining 20 tests, the average force required to separate the interference fit was found to be 83.4 N with a standard deviation of 25.9 N. For the seven grafts that were pulled apart and showed no signs of cracking, the average pull apart force was found to be 100.6 N with a standard deviation of 28.5 N. The average pull-apart forces were comparable to the 94 N value predicted by the finite element model (trial 3).

CONCLUSIONS

The components of thirty interference fit allografts were measured at various points in the manufacturing process. Lyophilization was found to have the largest effect on feature size and variability. Data collected from the dimensional measurements was then used to create a finite element model and a Monte Carlo simulation of the allograft. The 94 N pull-apart force predicted by the finite element analysis based on reduced modulus values and lyophilized pin and plate diameters was comparable to the average values measured in mechanical testing. The predicted frequencies of pull-apart failure (13%) and material failure (57%) agreed with those observed in the assembled allografts.

ACKNOWLEDGEMENTS

This was supported by a grant from RTI.

REFERENCES

1. Reilly, D. and Burstein, A., 1975, The Elastic Modulus and Ultimate Properties of Compact Bone Tissue, *Journal of Biomechanics*, 8: 393.
2. Shigley, J. and Mischke, C., 2001, *Mechanical Engineering Design*, McGraw-Hill, New York, NY.

50 m LINEAR MEASURING INTERFEROMETER FOR CALIBRATION OF SURVEY TAPE

Don Young Jeong, Ho Suhng Suh, Jong Ahn Kim, Jae Wan Kim and Tae Bong Eom
Korea Research Institute of Standards and Science
Yousong, Daejeon, 305-340, S. Korea

INTRODUCTION

Line standards such as survey tape and rigid rule still form important roles in the traceablility chain for dimensional measurement. Their calibration is usually performed by a comparison method. The reference and measurement tapes are stretched side by side and the length difference of two graduations is measured. This comparison method requires a reference tape, which is traceable to length unit. Therefore the absolute measurement of the reference tape is required. Most of national metrology laboratories (NMLs) designed and constructed their own instruments.[1,2] Korea Research Institute of Standards and Science(KRISS) had designed and constructed a 50 m tape measuring system 20 years ago. Recently we modified it for automatic measurement. The image of the graduation of the tape is captured by the CCD camera of optical microscope and wireless-transferred to the computer. The computer determines the center of the graduation. And it also controls the stage position up to 50 m by wireless communication. In our system, the calibration of the tape is carried out by a comparison measurement as well as an absolute measurement traceable to SI unit of length and the long distance measuring instruments such as ultrasonic distance meter or lased distance meter can be directly calibrated by laser interferometer.

SYSTEM DESCRIPTION

A 50 m linear measuring interferometer for the calibration of survey consists of a precision laser interferometer, a guide rail, a moving carriage, and optical microscope with CCD camera and an image processor. The entire instrument is housed in a 56 m tunnel where temperature is controlled. General view of the system is shown in Fig. 1.

Rail system

The base of the system is a reinforced concrete pier, 51 m long, cast in 33 segments on the concrete floor. 32 steel plates, which cemented on the concrete pier, support the steel profile of length 51 m which consists of rigidly bolted steel channel boxes, 3 m long, 0.1 m high and 0.35 m wide. The profile is constrained laterally but is free to move axially to accommodate the thermal expansion difference between concrete and steel. The track, on which the carriage moves and the surveying tape seats, consists of two rails which are made up of 42 ground rods of diameter 60 mm and length 3 m. 80 sleepers are rigidly fixed on steel profile at 0.65 m intervals. The sleepers support the rods and provide the lateral and vertical adjustments of rods for straight motion of the carriage.

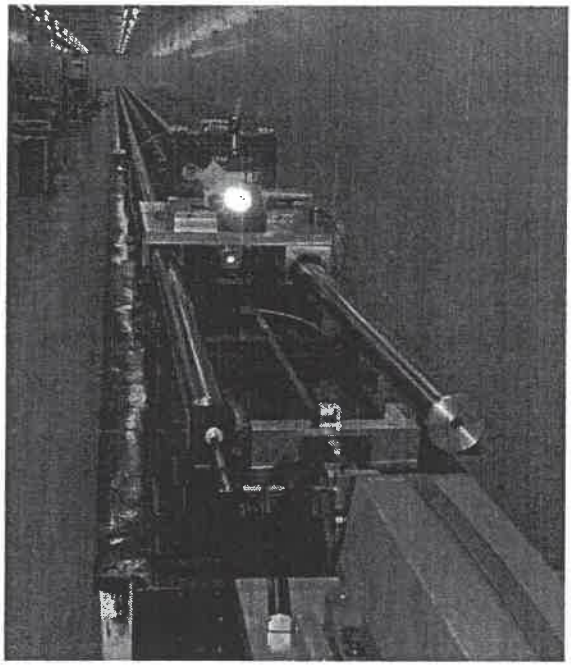

Figure 1: Overview of the 50 m tape measuring system.

The straight motion of the carriage is very important. To obtain the good straight motion, two rails, which consist of ground rods, should be accurately aligned. First, using water level, the heights of both ends of the rails are adjusted to be same height. Using the laser beam and the position sensitive photodiode (PSD) fixed on the

carriage, the vertical and horizontal positions of the rails adjusted. Finally the electronic level is used to adjust tilting angle of the rails, which is related to the pitch and the rolling motion of the carriage.

Carriage

The carriage, supported by 3 ball bushing bearings, is driven by a DC geared motor along the guide rail with rack gear. It is moved along the rail. On this carriage, a small translator with short moving range is fixed to provide a fine motion by micrometer. It also carries a corner cube of the laser interferometer and an optical microscope. The DC geared motor of the carriage is wireless-controlled by the computer. It has to be noted that the carriage can be manually driven by hand

Tape support and tape tensioning system

In our system, the tape calibration is carried out by the comparison method or direct method by laser interferometer. In comparison method the reference and test tapes are stretched out side by side and the length of the test tape is determined in terms of the reference tape. This comparison method requires the reference tape traceable to meter. In order to reduce the friction between tape and tape supporting system, 80 round supporters are sat on the sleepers at 0.65 m intervals. The supporters are Teflon-coated to reduce friction and their height variations are less than 0.05 mm. Both ends of the tape are connected to hanging weights by wires.

Detection of the graduation

At the absolute measurement by laser interferometer, the center of the line can be automatically determined. The line image of tape is captured by the CCD camera of the optical microscope and wireless-transferred to the frame grabber of the computer to calculate the deviation between the center of the line and the center of the field of view of the CCD camera. This deviation is used as error signal to control the motor. This signal is also wireless-transferred to control unit to serve the carriage until it reaches nearly zero. The distance between lines is calculated by the displacement of the carriage measured by laser interferometer and the deviation of the line center from the center of CDD. The rechargeable batteries at carriage supply the electric power for motor, CCD camera and lamp of microscope. This feature doesn't need the ducting for electrical control signal and leads to a simple driving mechanism.

Measurement of environment parameters

The temperature of tape is measured by 6 thermister probes. For calculating the refractive index of air, air pressure, humidity and air temperatures at 3 different positions were measured. The sensors are calibrated at laboratories of KRISS.

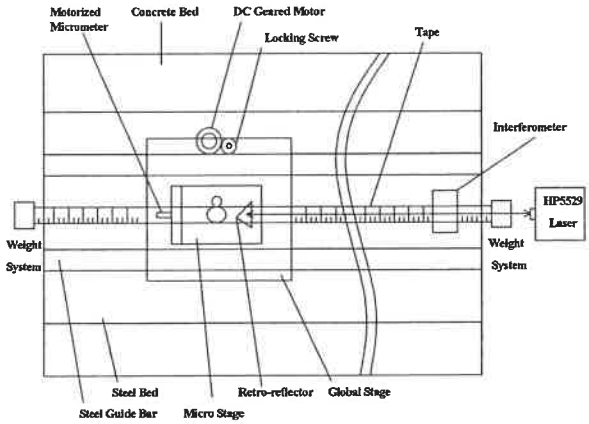

Figure 2: Schematic diagram of the tape calibration system.

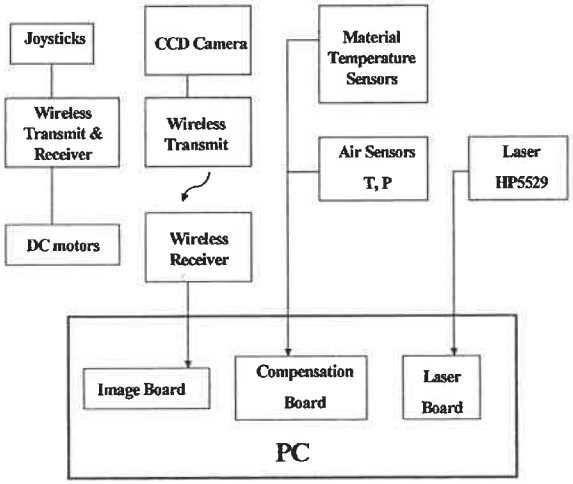

Figure 3: Electronic control of the tape calibration system.

MEASUREMENT SOFTWARE AND SYSTEM PERFORMANCE

The software to control the system and determine the center of the graduation is written in LABVIEW. The software controls the DC motor to drive carriage, and it reads the data from laser interferometer and environmental

parameters such as air temperature, pressure and humidity. The displacement of the carriage is determined. The image of the graduation is captured by CCD camera and transferred to a frame grabber of the computer. The computer calculates the image profile and determines the center of the graduation. Finally the distance between the measuring graduation and the reference graduation is determined. In order to determine the center of the graduation, we use three different algorithms. First, the image profile over specified threshold level is fitted in even order 6th polynomial and the axis of the polynomial is used as the center of the line. Second, the left side and right side areas at the center of the image profile are calculated so that two areas are same. Third, the left and right edges of the image profile are determined at every intensity level of the image and the center of the graduation is calculated as an average of the centers of the left and right edges at all intensity levels. The difference between distances determined by three center detection algorithms depends on image quality and is usually less than 10 μm.

Sources of uncertainty	Standard Uncertainty
Determination of center of graduation	11.6 μm
Abbe error	
(Pitch)	2.6 μm
(Yaw)	0.8 μm
Dead path error	0.2 μm
Laser frequency	0.6×10^{-8}
Refractive index of air	8.0×10^{-7}
Cosine error	2.0×10^{-8}
Temperature measurement	3.1×10^{-6}
Friction force	1.0×10^{-6}
Drift	2.0 μm
Combined standard uncertainty	$(12.2 + 3.3 \times 10^{-6}$ L) μm , L: m
Expanded uncertainty (k = 2)	$(24.4 + 6.6 \times 10^{-6}$ L) μm , L: m

Table 1: Uncertainty evaluation in measurement of tape.

The Abbe offset in vertical direction can not evitable in our system, so it is required to reduce the pitch error motion. In our system, the Abbe offset in vertical direction and horizontal direction are less than 25 mm and 4 mm respectively. Pitch and yaw error along movement range of 50 m were determined using automatic autocollimator. Roll error was also measured by electronic level. Fig. 5 illustrates the angular error motions of the carriage during travel of 50 m in 1 m intervals.

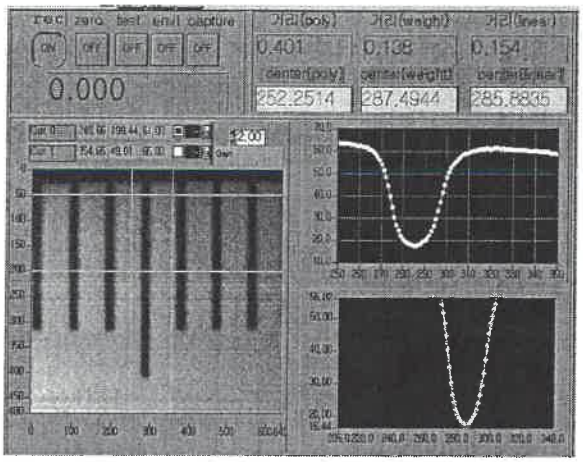

Figure 4: Output window of the software.

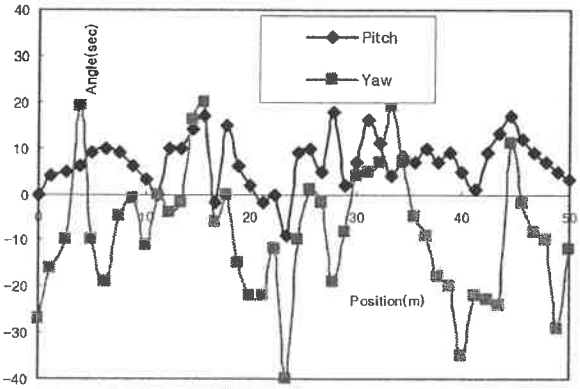

Figure 5: Angular error motion of the carriage over travel of 50 m.

The measurement uncertainty of the system was estimated according to the ISO guide for the expression of uncertainty in measurement. Details in uncertainty contributions are outlined at Table 1. As shown at table, main contributions are from determination of center of graduation, temperature measurement and friction force.

OTHER TASKS : TESTING EDMs

The system can be adapted to several other tasks. For example, ultrasonic distance meter and laser interferometer can be calibrated in this system. And also the short-range performance

of electronic distance meter (EDM) is tested in the tape measurement system.

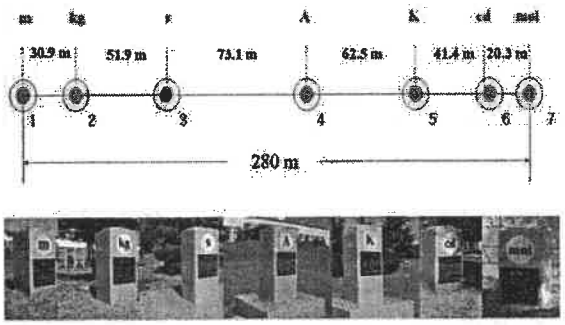

Figure 6: KRISS 280 m baseline for calibrating the electronic distance meter.

The EDMs are normally used for measuring large engineering structures such as ships, dams and tunnels and still have a key role for establishing the position in surveying. The EDMs can generally measure the distance up to a few km with resolution better than 0.1 mm. Usually we calibrate its scale factor and cyclic error.[3] In KRISS the scale factor of EDM is calibrated using 280 m baseline. (see Fig. 6) To calibrate the cyclic error of the EDM, we use the tape calibration system. The calibration is straightforward. The EDM is set on other side of the tape bench and a corner cube for EDM is fixed at opposite side of a corner cube for laser interferometer. And the reading of the EDM is compared with the reading of the laser interferometer. Fig. 7 is the calibration result of an EDM. The figure shows the cyclic error with period of 3 m.

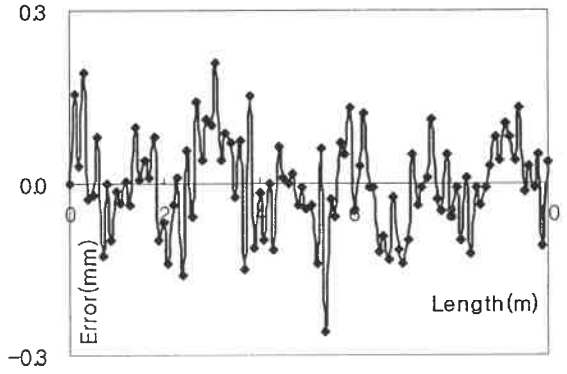

Figure 7: Cyclic error of an EDM.

CONCLUSION

Laser interferometric measurement system for calibration of tape up to 50 m had been constructed and was recently modified for automatic measurement. It consists of a precision laser interferometer, a guide rail, a moving carriage, and optical microscope with CCD camera and an image processor. The calibration of the tape is generally carried out by a comparison measurement as well as an absolute measurement traceable to SI unit of length. The system can be adapted to several other tasks. For example, ultrasonic distance meter and electronic distance can be calibrated in this system.

REFERENCES

1.P. E. Ciddor, K.H. Edensor, K.J. Loughry and H.M.P. Stock, 1987, A 70 metre Laser Interferometer for the Calibration of Survey and Mapping, *The Australian Surveyor*, 33: 493.

2.Rosenberg C.B., Munteanu C.S., and Ferguson R.A., 1997, Calibration of the Flexible Tapes to ppm Accuracy Level, *OIML Bulletin*, 38: 25-29.

3.R.A. Veugen, 2002, Cause of Cyclic Error at the Calibration of EDM Devices with a Laser Interferometer, Report number PE 2002-083 Eindhoven.

DEVELOPMENT AND ANALYSIS OF AN OPTICAL CAPABILITY FOR THE MEASUREMENT OF ARRAYS

David D. Gill, Andre A. Claudet, and Larinn M. Southwell
Manufacturing Science and Technology Center
Sandia National Laboratories
Albuquerque, NM

INTRODUCTION

The Mesoscale Manufacturing and Systems Development Department at Sandia National Laboratories has developed the capability to measure optical arrays in response to customers' needs. It has been a specific need to measure an array of miniature spherical optics where the optical surface was only a very small spherical surface patch. Previous attempts to use a coordinate measuring machine proved to have too much uncertainty due to the very small portion of the spherical surface available for measurement. In response, a small form-measuring interferometer was mounted in a 4-axis diamond turning machine. This combination allowed the high accuracy positioning of the diamond turning machine to be utilized with the capabilities of the interferometer, which has proven to be a very versatile tool. In addition to the measurement of optical arrays, the system allows rapid measurement of diamond turned surfaces for tool centering, tool radius error compensation, feature positioning, and part radius of curvature measurements.

This paper includes a description of the system, the results of an uncertainty analysis, and applications for which this system is proving most useful.

SYSTEM DESCRIPTION

The multi-axis interferometer system utilizes a Zygo PTI 250P form measuring interferometer, a Moore Nanotechnology Systems 350FG 4-axis diamond turning machine, and a kinematic mount for repeatable positioning on the Z axis of the machine tool. The first iteration of utilizing the interferometer in the diamond turning machine is shown in Figure 1. The interferometer is mounted in the machine and then adjusted in pitch and yaw such that it is aligned with a surface, such as the vacuum chuck, which has been diamond turned in the machine and is thus assured of being aligned to the axes of the machine. In this machine, the interferometer is on the Z axis while the part to be measured is on the spindle C axis which is mounted in the Y axis and stacked on the X axis. This setup allows the interferometer to move in only one axis while the part moves in three axes. This is helpful, especially with cable management from the interferometer. The interferometer is attached to a kinematic mount because it is often necessary to remove the interferometer from the machine. When this occurs, the kinematic mount is covered to preserve cleanliness.

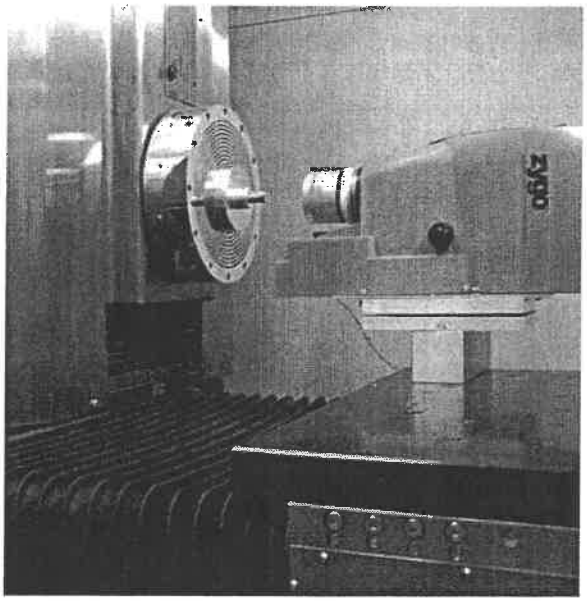

FIGURE 1. The interferometer (right) is shown mounted in the diamond turning machine on the Z axis. The spindle axis, holding the workpiece to be measured, is mounted in the Y axis which is stacked on the X axis of the machine tool.

The interferometer matches this application well due to its small size and low weight making it easy to install in the machine over and around other turning tools and equipment. The maximum aperture of the interferometer is 25mm which is sufficient for many of the surfaces created by the authors. The PTI 250P utilizes a temperature stabilized solid state laser

which keeps the power consumption and subsequent heat generation to a minimum within the machine environment. The turning machine shell was modified to have a through hole allowing for cables to enter the machine. The power and communication cables extend from the interferometer to the computer and its image capture board which is kept outside the machine. The interferometer has bayonet mount transmission spheres and flats, giving easy and repeatable optics interchangeability.

The Nanotechnology Systems 350FG is a 4-axis precision machining center with X,Y,Z motion and a positionable spindle (C axis). The machine has demonstrated form accuracy better than 100nm over a 75mm spherical test part for the linear axes and has a stated accuracy of ±2 arcsec for the spindle C axis.

The initial iteration of testing, shown in Figure 1, utilized available tooling blocks which required that pitch and yaw adjustment of the interferometer be achieved by manually "tapping in" the mount and by shimming the mounting plate. The tooling block was not well suited for this task due to the large cantilevered portions of the interferometer. To address these concerns, a new mount has been designed that gives the user micrometer adjustments of pitch and yaw while giving the interferometer better support over its entire base. The improved mount was not completed in time for this submission but will be discussed at the poster presentation.

UNCERTAINTY ANALYSIS

In order to utilize the system for customer needs, an uncertainty analysis was performed for the whole system. Because of the information available at the time, the uncertainty analysis has the flavor of an error budget. The analysis included error contributions from temperature effects, the kinematic mount, the interferometer laser, and the machine axes. In addition, it was determined that the most conservative method for the analysis would be to include a Repeatability and Reproducibility (R&R) study of the whole system including operator variability.

Repeatability and Reproducibility Procedure

The R&R utilized 3 operators taking measurements of a diamond turned concave spherical surface over the course of 3 weeks. The test surface has an aperture of 0.5 inches and was measured with an f/1.5 transmission sphere. The interferometer and kinematic mount were positioned in the machine using a transmission flat and the diamond turned face of the machine's vacuum chuck was used to align the interferometer to the machine axes. After this initial alignment, the pitch and yaw axes of the kinematic mount base, and thus of the interferometer, were not adjusted for the duration of the 3 week test. However, each operator lifted and replaced the interferometer on the kinematic mount before that day's measurement. The operator then moved the axes to locate the reference surface with the interferometer, and took measurements of the part. Within a set of measurements (for all 3 operators on a single day), the measured surface stayed fixed to the vacuum chuck, but between days it was necessary to remove the part due to other machine usage. The interferometer was removed from the machine each day after data collection, but remained powered on for the duration of the 3 week testing.

The measurement procedure required that the operator find the catseye position for rough positioning and then move to the confocal position. The operator took multiple measurements of the surface and moved the machine along the Z (optical) axis until the measured power was minimized. At this point, the axis location, optical power, form PV, form RMS, and the 10^{th} order Zernike polynomial terms were noted and the machine was moved in X, Y, and Z before beginning the next operator's measurements. The results of the R&R study are shown in TABLE 1. The table presents results for machine position (position of the confocal point representing the center of the measured sphere) and for the PV and RMS form errors measured by the interferometer at the confocal position.

TABLE 1. Standard deviation determined from the R&R study for machine position of the confocal (sphere center) location in X, Y, and Z, and PV and RMS form errors measured at the confocal point. The part position was different each day so measurements within a day were compared and the resulting deviations averaged.

σx (mm)	σy (mm)	σz (mm)	σPV (nm)	σrms (nm)
0.00507	0.00207	0.00141	2.847	0.591

Error Budget Results

The thermal, interferometer, axes, and kinematic mount error contributors were assumed to have rectangular distributions while the R&R results were assumed to follow a normal distribution. For each contributor, the variance was determined and totaled for all error sources. The total system standard deviation was determined from the variance and a factor of 2 standard deviations is reported as the expanded uncertainty for the system giving a 95% confidence interval. The results of the uncertainty analysis are given in TABLE 2.

TABLE 2. Results of the expanded uncertainty analysis. See Discussion section for explanation of error sources.

	X	Y	Z
Expanded Uncerainty	10.35um	4.69um	3.30um

R&R Discussion

As is common in this type of analysis, the results of the R&R study overwhelmed the other error contributors. There are several proposed causes of the poor performance of the system in the R&R study. The initial implementation of the system utilized already existing tooling blocks which were not well suited for the application. The interferometer was cantilevered a long distance over the tooling block leading to a possible lack of repeatability in positioning the system. A second issue was poor cable management. Because the interferometer had to be placed in the machine and removed after every test, the cables were not permanently affixed to the axis to give uniform cable strain. This strain primarily causes a yawing of the interferometer on the mount and is expected to be the source of the large X uncertainty. In future testing, the cable will be fitted with a cable tie to attach to a bolt on the Z axis so that the cable strain will be more uniform in testing. A third source of error is the utilization of inexperienced students for the testing. This was determined to be the most conservative method of testing. The operators were all students who had no prior diamond turning or interferometric metrology experience. A set of work instructions was created for the students to follow, and they followed it carefully. Where an experienced operator might have a bit better perspective on the measurement and how to achieve the most accurate measurement, the students primarily followed the work instructions and any deficiency in the instructions was directly transferred to the results. A fourth source of error was improper maintenance of the kinematic mount. The mount was new and was not properly lubricated. The newness and the lack of lubrication may have had a small contribution to the error by changing the interferometer's position over time. And finally, a source of concern for the mathematics of the R&R was the necessity to remove the measured artifact from the machine every day. The removal of the artifact meant that the X, Y, and Z positions could only be compared within a day's testing (3 operators taking 1 measurement each). Having only 3 measurements for the day makes the day's standard deviation a bit questionable. This was a tradeoff between doing all of the measurements back to back or doing all of the measurements across a span of 3 weeks to include environmental fluctuations in the study. The authors have designed a new mount for the interferometer and plan to try the R&R study again with the operator testing being done consecutively allowing the artifact to remain in the machine. Additionally, the mentioned cable holder will be utilized as will updated work instructions.

APPLICATIONS

The interferometer/diamond turning machine combination has proven useful for many applications. The most basic of these is for tool centering. Typical tool centering for a research machine (i.e., one that is using a variety of tool geometries, setups, cutting planes, etc.) requires that the rough position of the tool is found using an optical tool setter or by eye. The height of the tool is then fine tuned by cutting a spherical surface and measuring the diameter and shape of a center residual feature. And, finally, the feed axis (X) position is fine tuned by cutting the spherical surface and measuring the form. In addition, tool radius errors can be determined if there is a means of measuring the radius of the surface. When using this methodology, it is usually necessary to take the part out of the machine after each cut of the spherical surface. In many instances, this will require that the part be removed from the machine many times. Each time, the part must be centered again when it is put back on the spindle. However, the introduction of the interferometer in the machine tool allows the tool to be centered without the part having to leave the machine. This results in a great time savings.

Another example part is the metrology target shown in Figure 2. Several of these parts were

diamond turned on Sandia's 350FG. Two of the optics were mounted in an assembly and the customer needed to know the position and radius of each of the 10 optics in the assembly. The spherical optics contain only a small surface patch of the sphere, so CMM measurements were not felt to be of sufficiently low uncertainty. Instead, the assembly was placed in the diamond turning machine and the interferometer was used to measure position and radius for each of the 10 optics in reference to an origin also measured on the part. This system provided valuable information in a short timeframe for this customer.

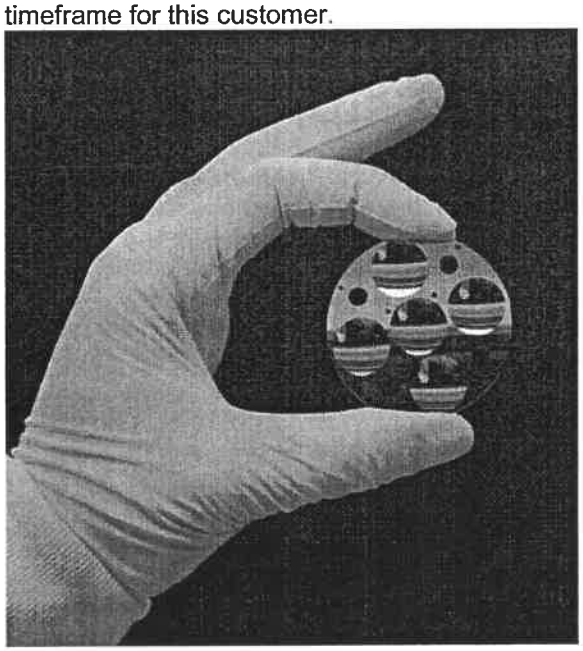

FIGURE 2. An example application for the reported measuring capability was this metrology target for which the customer needed to know optical radius and position for the 5 optics with respect to each other and 5 other optics in and assembly.

ACKNOWLEDGEMENTS

Sandia is a multiprogram laboratory operated by Sandia Corporation, a Lockheed Martin Company, for the United States Department of Energy's National Nuclear Security Administration under Contract No. DE-AC04-94AL85000.

FAST THREE-DIMENSIONAL SHAPE MEASUREMENT BY COLOR-CODED ILLUMINATION

Chang Kyu Song[1], Jeong Sik Kim[2], Byeong Gwon Joo[3] and Min Gu Kang[3]
[1]Intelligent Machine Systems Center
Korea Institute of Machinery and Materials, Daejeon, Korea
[2]Kafus Co., Ltd., Chungnam, Korea
[3]Intekplus Co., Ltd., Daejeon, Korea

INTRODUCTION

Three-dimensional (3-D) shape measurement plays an important role in information technology(IT) industries such as semiconductor industry and TFT-LCD industry. Some examples are BGA coplanarity measurement of semiconductor chip and spacer height measurement for TFT-LCD. One feature of these measurements is on-line inspection, so measurement time must be very fast. Light interference methods have been used for measuring 3-D surface profile. The white light scanning interferometry (WSI) is typical method. These interference methods are not suitable for on-line inspection because they need phase-shifting process. The color-coded illumination method does not need phase-shifting process so it is suitable for on-line measurement of semiconductor and TFT-LCD applications [1-6].

In this study, a color-coded illumination method for 3-D surface profile measurement is suggested and it is verified that this method is available for on-line measurement because it is simple and fast. The principle of the method is that color beam of rainbow pattern is projected onto the object and the reflected light beam goes to color line CCD camera in which the color has analyzed to Red-Green-Blue intensities. Then inherent characteristic of the color, hue, is calculated from RGB intensities and the height of the object coincident pixel of the camera is calculated from hue also. RGB intensities have phase difference of 90 degrees respectively so phase-shifting process does not need.

Experimental setup has been built and some experiments have been done. A prism and cylindrical lenses are used to make color beam and the beam size is 500 micrometers. It is showed that the beam size is related to measurement resolution and the thinner beam size leads to the better resolution, so how to make an optical system for thin beam size is mentioned. As a light source, both a halogen lamp of 150W and a metal halide lamp of 250W have been used and the comparison has carried out in respect of measurement result. Some software algorithm has also been coded such that hue and height are calculated from captured RGB intensities.

PRINCPLE OF MEASUREMENT

In this study, color's proper characteristic, hue, is used. Light is projected onto the measuring object and the reflected light is acquired by CCD camera. The hue value is calculated by using CCD pixel intensity.

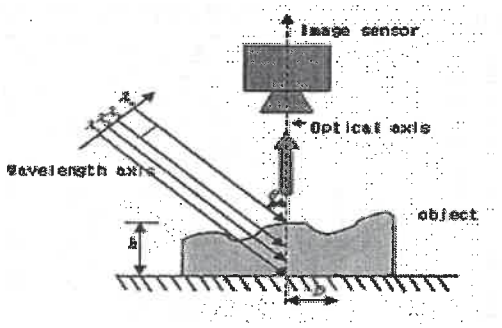

FIGURE 1. Optical geometry of the measuring system

Optical geometry of the measuring system is provided in Fig. 1. As the figure shows, there is measuring object which has shape's height variation in level of decades or hundreds micrometers. Multiple wavelength light is projected onto the measuring object tilting angle θ with respect to optical axis and the reflected light is grabbed by image sensor. If the bandwidth of multiple wavelength is same as that of visible light, input light will show rainbow pattern. The image sensor is a sort of color CCD so outputs of image sensor are red(R), green(G), blue(B) intensities. Hue is calculated by using these RGB intensities.

In Fig. 1, if the multiple wavelength illumination light is projected on a point P then color distribution of P is represented as follows;

$$p = \begin{pmatrix} R \\ G \\ B \end{pmatrix} \quad (1)$$

Where R, G, B in equation (1) are red, green, blue intensities, respectively. There is achromatic point A which has equal color intensities with point P and represented as follows;

$$A = \begin{pmatrix} i \\ i \\ i \end{pmatrix} \quad i = (R + G + B)/3 \quad (2)$$

The representation of the red color is in Eq. (3).

$$R = \begin{pmatrix} 1 \\ 0 \\ 0 \end{pmatrix} \quad (3)$$

The hue value H at the point P can calculate by using the equation (1)~(3).

$$H = \cos^{-1}\left[\frac{\langle P - A, R - A\rangle}{(|P - A|)(|R - A|)}\right] \quad (4)$$

Where the symbol <> means scalar product.
The height H of the P point can be represented by the function of hue value H.

$$Z = f(H) \quad (5)$$

It should be pointed out that the height H is determined by only H and does not relate with θ. As the illumination light composed several coherent light or white light are generally used. White light from tungsten halogen lamp is separated by prism.

EXPERIMENTAL SETUP

In this study, an optical system with prism is manufactured. Fig. 2 shows that prism transform the white light to rainbow pattern. After passing through the prism white light can be reformed rainbow pattern and a three-color line CCD camera is useful to capture the RGB intensities of the line of rainbow pattern.

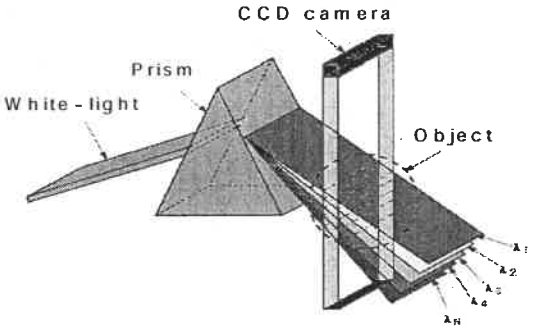

FIGURE 2. The optical system with prism.

The conceptual diagram for optical system is showed in Fig. 3 and photography of optical system is showed in Fig. 4. A halogen lamp of 150W and a metal halide lamp of 250W are used as optical source and a prism located in front of an illumination lens. Role of the illumination lens is to maintain focal distance and magnification of the light. After passing through the prism light source is separated to rainbow pattern and pass a cylindrical lens. The cylindrical lens makes beam size thin.

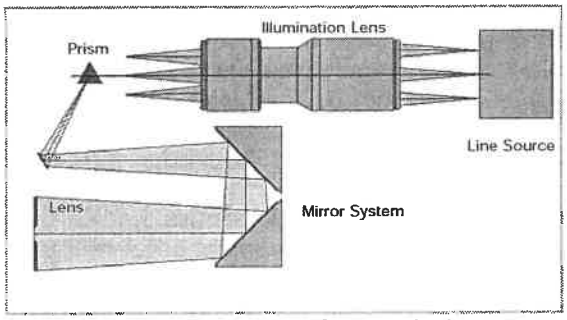

FIGURE 3. Configuration of the optical system

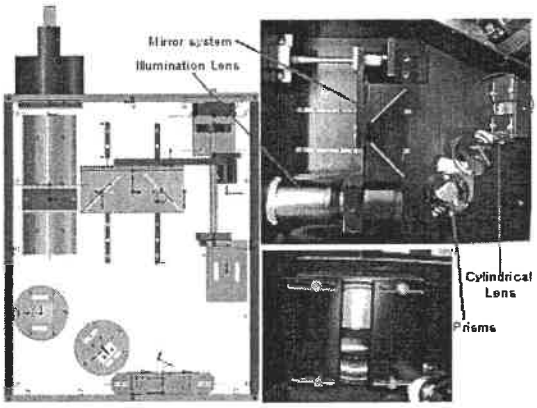

FIGURE 4. Photography of the optical system

The whole measurement system is composed of optical system, moving stage, three-color line

CCD camera and PC as provided in Fig. 5. Color beam from optical system is linearly projected on surface of the object and when the stage is moved color beam is scanned the whole surface area. Used frame grabber is Metro II of Matrox and line CCD is HVSOLO of Hanvision. The moving stage is constituted of ballscrew and LM guide and controlled by PC-based motion control board (MEI).

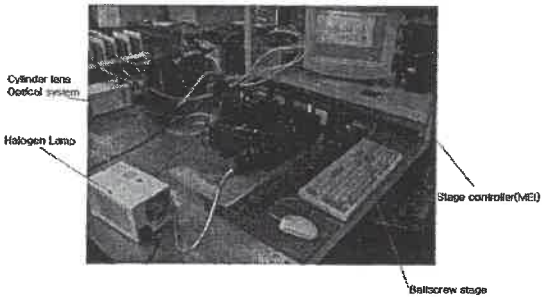

FIGURE 5. Photography of the measurement system

This color-coded illumination method has an advantage for in-line measurement. Since phase of R, G, B has been shifted previously so the moving stage is not necessary to stop for phase shifting but to scan at uniform speed. This uniform scan capability is the key for in-line measurement.

In this system, phase difference of R, G, B should be 90 degrees in each other. But Initial phase difference of RGB is not equal 90 degrees. The three-color line CCD camera has a function to change the color space as provided in Fig. 6. So equally-phase-shift RGB can be acquired by adjust camera's transformation matrix. Fig. 7 showed that initially white light(Left) is captured by CCD camera(Center) and is transformed phase shift image(Right).

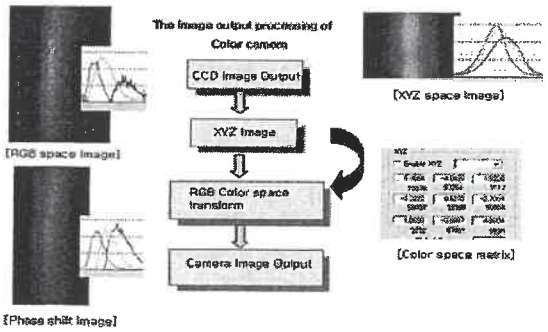

FIGURE 6. Color space transformation process of the color line CCD camera.

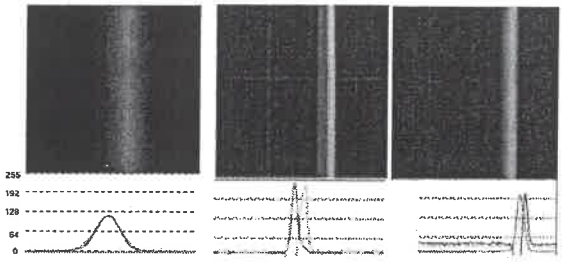

FIGURE 7. R,G,B phase shift processing.

EXPERIMENTAL RESULTS

A measurement result for height standard (195μm) by the color-coded illumination method is provided in Fig. 8. In this experiment the halogen lamp of 150W is used as light source and stage scanning speed is 30mm/sec. Used beam size is 500 μm. If thinner beam size is used, system resolution will be better but phase difference between RGB is not uniform so accuracy of the measurement result gets worse. In Fig. 9 RGB phase distribution of the 300 μm, 500 μm, 700 μm beam size is showed. The phase distribution of 300 μm beam size is composed so this beam size is not suitable for color-coded mesurement.

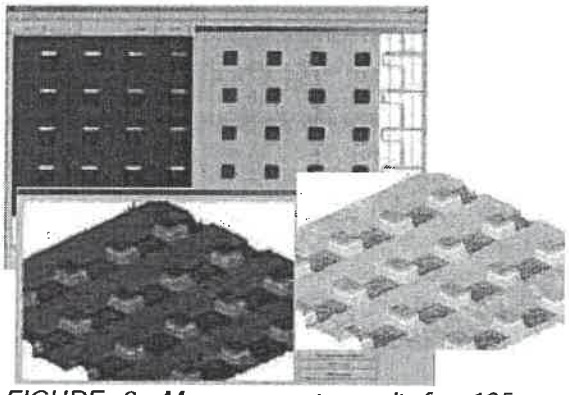

FIGURE 8. Measurement result for 195 μm height standard with halogen Lamp of 150W.

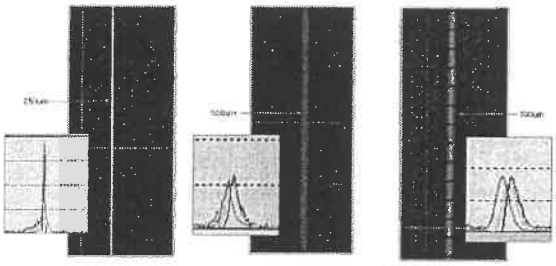

FIGURE 9. Phase of R,G,B with respect to beam size.

The surface roughness of the measured surface in Fig. 8 is very rough. This reason is that the

light after passing the optical system has small power so it is necessary to raise the camera gain to 6X but this gain setting leads to noisy result. Solution of this problem is power up of light source.

The measurement result for same standard with metal halide lamp of 250W is provided in Fig. 10. Surface roughness is better than that of halogen lamp.

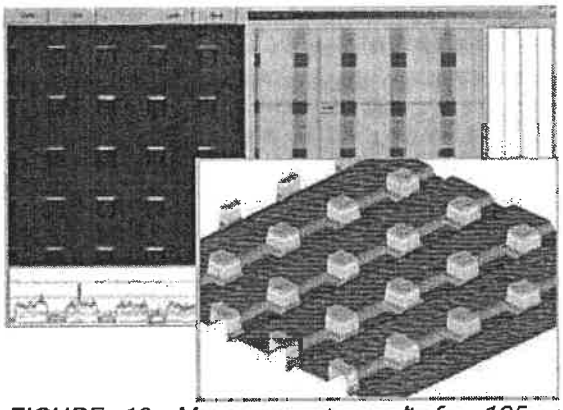

FIGURE 10. Measurement result for 195um height standard with metal halide Lamp of 250W.

CONCLUSIONS

In this study a color-coded illumination method for measuring micro features is suggested. This method is used previously phase shifted color so very suitable for in-line measurement which needs fast measurement. It is possible to scan the measuring object because the color-coded illumination method does not need phase-shifting process. An optical system composed of prism and some lenses is manufactured and computer program code is implemented. To prove usefulness of this method experiments has been done. The measurement results of halogen lamp and metal halide lamp are compared and these experiment results showed that the color-code illumination method is useful for measurement of hundreds of micrometers features.

REFERENCES

1. Weiyi Liu, Zhaoqi Wang, Guoguang Mu and Zhiliang Fang, 2000, Color-coded projection grating method for shape measurement with a single exposure, *Applied Optics*, 39: 3504-3508.
2. E. Hasman, V. Kleiner, 2001, Color-coded optical profilometry with $>10^6$ resolved depth steps, *Applied Optics*, 40: 1609-1616.
3. Gerd Hausler and Dieter Ritter, 1993, Parallel three-dimensional sensing by color-coded triangulation, *Applied Optics*, 32: 7164-7169.
4. H. Fan, H. Zhao, and Y. Tan, 1997, Automated three-dimensional surface profilometry using dual-frequency optic fiber phase shifting method, *Opt. Eng.*, 36: 3167-3171.
5. S. Tang and Y. Hung, 1990, Fast profilometer for the automatic measurement of 3-D object shapes, *Applied Optics*, 29: 3012-3018.
6. Liu, W.-y., Yu, D.-y and Hou, Q.-h., 2002, 3-D Dynamic Object Shape Measurement by Using Color-coded Method, *Optoelectronics Laser*, 13: 169-172.

GRAVITATIONAL REFERENCE MASS CENTER DETERMINATION BY VELOCITY MODULATION

John W. Conklin[1], Ke-Xun Sun[2], and Dan B. DeBra[1]
[1]Department of Aeronautics & Astronautics, Stanford University
Stanford, CA, U.S.A.
[2]Edward L. Ginzton Laboratory, Stanford University
Stanford, CA, U.S.A.

INTRODUCTION

Future space-borne gravitational experiments such as the Laser Interferometer Space Antenna (LISA) and the Space Test of the Equivalence Principle (STEP) require test masses whose mass center (MC) location must be known with unprecedented accuracy. Motion of the MC is the primary science signal in these experiments, because it is the MC of a drag-free test mass that follows a perfect geodesic.

The STEP differential accelerometer will use two concentric belted cylinders to measure the equivalence principle to a part in 10^{18}. LISA will detect gravitational waves by measuring distance variations between test masses housed in three drag-free spacecraft separated by 5 Gm with an accuracy of 10 pm/$\sqrt{\text{Hz}}$. LISA may use two cubic test masses or possibly a single spinning spherical test mass per spacecraft. For the cubic LISA test masses, the mass center should be as close as possible to the geometric center (GC) to reduce cross coupling between the rotational and translational degrees of freedom. For a spinning spherical test mass, geometric irregularities are averaged out, but the MC offset from the GC must be less than 0.1 μm to reduce the dynamic range of the optical sensor.

The current state of the art method for determining the MC location of a sphere involves pendulous techniques which are typically limited to MC offsets > 1 μm due to the increase in low frequency instrumentation noise ($1/f$ noise) as the MC and GC come closer together and the pendulous frequency approaches zero.

A new technique potentially capable of determining the MC offset of a sphere to 0.1 μm or better has been developed. The new method avoids the $1/f$ noise boundary by rolling the sphere down a set of parallel rails, thus spectrally shifting the MC offset information to the rolling rate frequency. The sphere's trajectory is measured optically by recording the times that the sphere crosses a series of optical gates. A Monte Carlo parameter search is used to recover the magnitude and phase of the sphere's MC offset. The rolling ball technique was first attempted by Hahn and DeBra in 1985 [1].

Numerical simulations accounting for expected experimental error, including an overall timing accuracy of 100 ns, show that the velocity modulation method is capable of determining the MC location of a sphere to at least 0.1 μm. Initial validation of the method using a 2 inch (50.8 mm) diameter sphere with a known MC offset of $\sim$ 44 μm achieved a measurement error of σ = 1.5 μm.

Later, the apparatus may be modified to accommodate cylindrical or faceted test masses like those used for the STEP and LISA missions.

MECHANICS

The velocity modulation technique for MC determination shifts the frequency at which the measurement is made to the rolling rate frequency of the sphere. The sphere is rolled down two parallel rails which restricts the motion to rolling about a single axis. The only forces acting on the sphere are gravity and the forces at the contact points with the two rails. Any irregularities in either the sphere or the rails affect the forces acting on the sphere. The velocity modulation caused by the mass center offset acts at the rolling rate frequency and can therefore be extracted from other irregularities. The uncertainty in the optical gate locations and the geometric effects of the rails, which are a combination of the inclination and the ran-

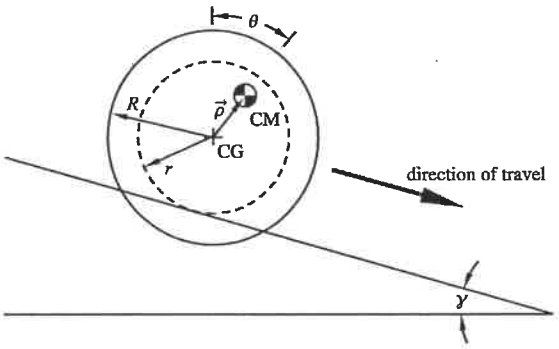

FIGURE 1. Simplified model of the rolling sphere

domly distributed surface irregularities, are fixed in the laboratory, while the geometric effects of the sphere (including MC offset) depend on the initial orientation of the sphere. Therefore, to separate these effects, the needed information is obtained by systematically changing the initial phase of the sphere by known quantities.

Sphere shape irregularities can be a smaller order of magnitude than the mass center offset for which only low order harmonics are significant. Therefore, shape irregularities are spectrally separable from the MC offset. The resulting measurement of the sphere MC location is currently limited by the level of sphericity, which can be less than 10^{-6} for 25 to 100 mm diameter spheres.

The simplified geometry of the sphere and rails is provided in Figure 1. The radius of the sphere is R and the instantaneous radius of rotation is r. The rails are assumed to be perfectly straight without any irregularities and inclined at an angle γ. The projection of the vector from the GC to the MC into the plane perpendicular to the axis of rotation has magnitude ρ and phase θ relative to the vertical. With these assumptions and geometry, the governing equation of motion obtained using D'Alembert's method to sum torques on the sphere is as follows.

$$I\ddot{\theta} + mr\ddot{\theta}[r + \rho\cos(\theta - \gamma)] - m\rho\dot{\theta}^2 r\sin(\theta - \gamma) + m\rho\ddot{\theta}[\rho + r\cos(\theta - \gamma)] = mg(r\sin\gamma + \rho\sin\theta) \quad (1)$$

Since the asphericity and material inhomogeneity can be at least as small as the MC offset, it is a good approximation to take the moment of inertia to be that of a perfectly uniform sphere $I = \frac{2}{5}mR^2$, so that the mass of the sphere m fall out of (1).

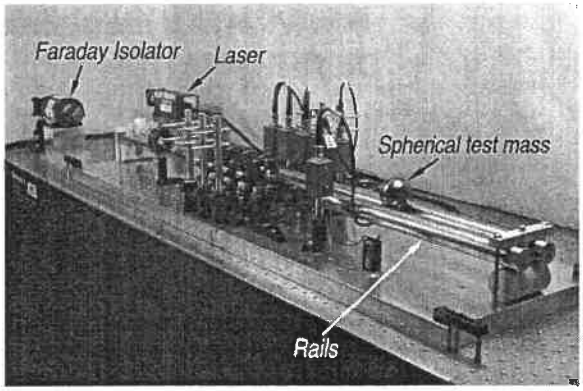

FIGURE 2. Experimental apparatus general layout

EXPERIMENTAL APPARATUS

Mechanical Equipment

The experimental setup is shown in Figure 2. The apparatus consists of a 1.25 inch (32 mm) thick aluminum base plate mounted on an optical bench with two 1.25 (31.8 mm) diameter steel rails supported above the base plate by aluminum cylinders laying on their side. The axes of the two $\sim$ 1 m long rails are separated by 1.95 inches (49.5 mm). There are five optical gates spaced 2 inches (50.8 mm) apart so that sensing of the sphere's trajectory only occurs over an 8 inch (203 mm) section of the rails. This allows space to roll the sphere by hand on one side of the optical gates and to catch the sphere on the other.

Since the sphere is nearly uniform, a mark must be placed on its surface to set the sphere's initial phase relative to the location of the optical gates. A pair of orthogonal great circles are drawn on the spherical test mass [2] and a coordinate system is defined relative to the great circles. The location of the mass center relative to the geometric center is then determined in this coordinate system.

Before each roll of the sphere, one of the great circles is aligned by eye with one of three pairs of wires mounted perpendicular and above the two rails. These phase alignment wires can be seen in Figures 2 and 3. The three pairs of wires are mounted such that they cross the rails exactly between two optical gates. This allows one to set the initial phase of the sphere by aligning one of the great circles vertically with the phase alignment wires while using the optical sensing system to set the position of the sphere on the rails.

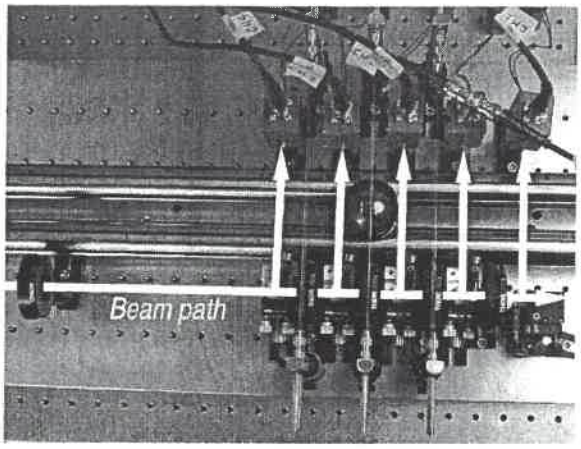

FIGURE 3. Optical sensing system.

Optical Sensing System

Modulation of the sphere's velocity is measured optically by recording the precise times that the sphere crosses the optical gates. Infrared laser light (λ = 1064 nm) is emitted by a 30 mW NPRO laser. The light is aligned parallel to the rails at the exact height of the sphere's geometric center. The beam then passes through a Faraday Isolator before entering the bank of five optical gates. Each gate consists of a $\lambda/2$ wave plate and a polarizing beam splitter (PBS). Each PBS is mounted on an adjustable stand that allows the reflected light to cross the trajectory of the sphere's GC perpendicular to the rail axes. The reflected light is collected by reverse-biased photo-diodes mounted on the other side of the rails. The layout of the optical sensing system and beam path are shown in Figure 3. The beam enters the figure from the left. The $\lambda/2$ wave plates and PBSs can be seen at the bottom of Figure 2 and the photo-detectors at the top. A 2 inch spherical test mass is also shown between two reflected beams.

Measurement of the sphere's location is made by a *pair* of adjacent photo-detectors. The reflected laser beams and photo-detectors are aligned so that exactly half of the incident light is occulted when the sphere is precisely between two detectors as is shown in Figure 3. The voltage produced by the pair of photo-detectors is differenced so that when the voltage difference is zero, the sphere is exactly between the two optical gates. Fluctuations in laser intensity are consequently eliminated in the differential signal because laser intensity variations are common to all detectors.

With five optical gates spaced exactly one diameter of the sphere apart, four differential signals are produced so that each time the sphere is rolled, four time/position measurements are made. If the first measurement is thought of as a reference measurement, then a total of three measurements are made relative to the reference. Three measurements is the minimum number needed to observe the modulation of the sphere's velocity.

Before a measurement can be made, the voltages produced by each photo-detector must be balanced so that equal quantities are subtracted to produce the differential signal. The five $\lambda/2$ wave plates are used to adjust amount of light illuminating each detector. This allows the detector voltages to be balanced without using electronic amplifiers that may add noise to the system. With the laser light fully illuminating all five photo-diodes, the five $\lambda/2$ wave plates are adjusted until all detector voltages are equal.

MEASUREMENT TECHNIQUE

To collect the data necessary to determine the MC location, the sphere is rolled three times, each time setting the initial phase with a different pair alignment wires. Each roll, three time/position measurements are taken, so a total of nine time/position measurements are made in the laboratory. In order to recover the MC location, the measured times are compared with times computed by numerically integrating (1).

First the experiment is performed measuring the MC location in a plane defined by one of the great circles. To determine the MC location in three dimensions, the experiment is performed again measuring the projection of the MC offset onto the plane defined by the orthogonal great circle.

DATA REDUCTION

The nine times measured in the laboratory are compared with times computed by numerically integrating (1). A Monte Carlo parameter search is used to fit the MC location as well as other parameters in (1) that can not be measured to the required level of accuracy.

Parameters g, R and r are well known or measurable quantities. The goal is to determine $\vec{\rho}$, but in order to do so, the inclination of the rails, the location of each optical gate, and the initial velocity of the sphere must also be fit to the data.

If a cost function J is defined as the RMS difference between the measured and computed times, then J provides an estimate of the measurement error since there is nearly a one-to-one relation between timing error and position error for a sphere rolling at $\sim$ 1 m/sec. A nonlinear optimization problem suitable for a Monte Carlo parameter search has now been defined: Find the set of parameters in (1) that globally minimizes J.

PRELIMINARY RESULTS

Initial validation of this method was performed using a 2 inch (50.8 mm) diameter BeCu sphere with two holes forming a "V" to generate a MC offset of $\sim$ 44 μm [3]. A Cartesian coordinate system aligned with the two great circles was drawn on the sphere to define measurement planes. Five independent measurements were made in the $z-x$ plane of the sphere and three in the $x-y$ plane.

Figure 4 shows the results of the five measurements made in the $z-x$ plane. The geometric center is shown on the right side of the figure at coordinates (z, x) = (0, 0) μm. The expected MC location is also shown at coordinates (z, x) = (-38, 0) μm, which is the projection of the 44 μm total MC offset onto the $z-x$ plane. The estimated error for each measurement is also depicted as error circles surrounding each measured MC location. The radii of the error circles are the minimum J achieved for each data set.

All five measurements are self consistent, *i.e.* all measurement error circles overlap, and all five measurements are consistent with the expected MC location. The mean magnitude of the MC offset using all eight measurements is 41.2 μm, with a standard deviation of 1.5 μm.

FUTURE WORK

Several sources of measurement error in the current apparatus are known and work continues toward achieving a measurement accuracy $<$ 0.1 μm. Ultimately, the accuracy will be limited by the sphericity of the test mass. However, the mechanics model can be improved to include the effects of second order and higher harmonics of the sphere's shape. With these improvements, the measurement accuracy would then be limited by the level of knowledge of the sphere's shape.

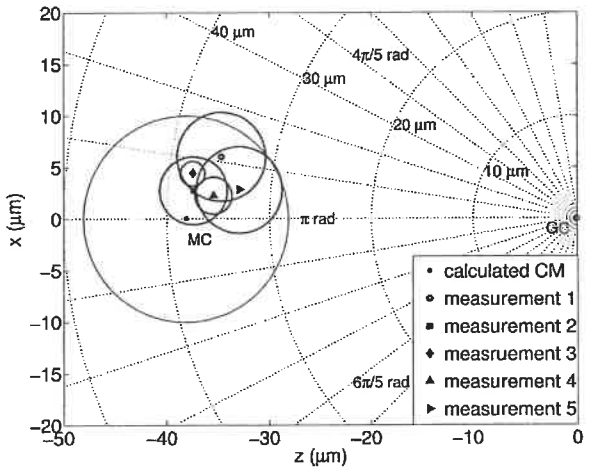

FIGURE 4. Preliminary experimental results

ACKNOWLEDGEMENTS

The authors would like to thank Professor Robert L. Byer of Stanford University for equipment and support, the Stanford Product Realization Lab staff, especially Will Beecher and Craig Milroy, for assisting in the fabrication of mechanical components, Aaron Swank for help assembling the data acquisition system, Jennifer Bower, Eric Nelson and Mike Thielvoldt for producing the calibration spheres, Peter Frykman and Rachanna Vang for developing the great circle marking device, and Aurora M. Aguero for photography.

REFERENCES

1. Hahn, Nam-Hee, December 1985, Rolling Ball Technique, *Stanford University Department of Aeronautics & Astronautics, Engineer Thesis.*

2. Frykman, P., and Vang, R., June 2006, Drawing Great Circles on a Spherical Test Mass, *Stanford University, ME 324 Precision Engineering Final Report.*

3. Bower, J., Nelson, E., and Thielvoldt, M., June 2005, Sphere with Adjustable Mass Center for the LISA Project, *Stanford University, ME 324 Precision Engineering Final Report.*

AN INSTRUMENT FOR NANOINDENTATION WITHOUT FRAME STIFFNESS DEPENDECY

Jonathan D. Ellis, Stuart T. Smith, and Robert J. Hocken
Center for Precision Metrology
University of North Carolina at Charlotte
Charlotte, NC, USA

INTRODUCTION

Hardness is typically measured by indenting a specimen and then correlating the applied force to the projected area, surface area or depth of the indent. Because the hardness measurement requires force, displacement and sometimes geometric measurements, there are still many areas of discrepancy such as instrument frame deflection compensation, quantifiable units, traceable uncertainty, and geometrical errors in the indenter stylus. The purpose of this research is to establish a unique methodology for measuring hardness, nanohardness in particular, and address the aforementioned issues.

The measurement of nanohardness is of increasing value for several fields including thin-films for tool coatings and adhesives, micro-electrical mechanical systems (MEMS), and semiconductor process characterization. The goal of nanohardness measurements is to quantify material properties at the nanoscale. Some of the current techniques for calibrating nanohardness instruments require using material properties that are "known" on the macroscale. This is ambiguous because the material properties differ as the size-scale varies [1]. Additionally, the compliance variations within the instrument may vary considerably with scale and contribute to the uncertainty of the measurement.

A considerable contribution to the uncertainty of nanohardness measurement is the correlation between the indenter geometry and the depth of indent [2] and the characterization of the frame stiffness under loading. An alternative instrument design that reduces the dependency on frame stiffness will reduce the uncertainties in the force and depth measurements. In a typical instrument, the metrology loop and the force loop are largely coincident, Fig. 1. This coincidence is the source of the uncertainty associated with frame stiffness and thus, force and depth uncertainties. When the size of the indent is small, the stiffness of the indent may be the same order of the magnitude as the stiffness of the frame and stage. In general, the deflections in the sample, frame, and stage behave similar to three springs in series, all nominally the same value because the stiffness of each element is comparable. By reducing the size of the metrology loop and removing a majority of the coincidence with the force loop, uncertainties can be estimated more accurately and at a lower magnitude.

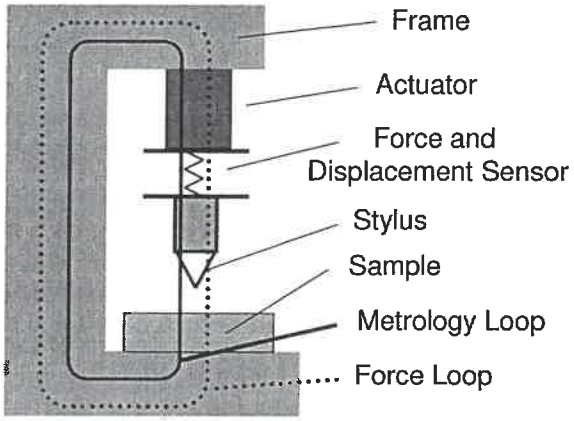

FIGURE 1: Coincident metrology and force loops within a C-Frame hardness measuring instrument.

Figure 2 depicts a new hardness instrument which significantly reduces the dependency on the frame stiffness. Because the area of the indent is difficult to measure directly at nanometer scales, as with other commercially available instruments, this instrument also measures the depth of indent as a function of applied force. Force is measured using a conventional load cell based on the displacement of a linear flexure of known stiffness. Measurement of the indenter penetration into the surface is obtained from a surface probe that is maintained at constant force. This force is maintained using a piezoelectric actuator (2^{nd} actuator in Figure 2) as a load is applied to the indenter through the load cell. The depth of penetration is obtained from a displacement sensor that measures the translation of the second actuator. In this design,

deflections in the frame and stage are compensated and thus, a large contributor to uncertainty is significantly reduced.

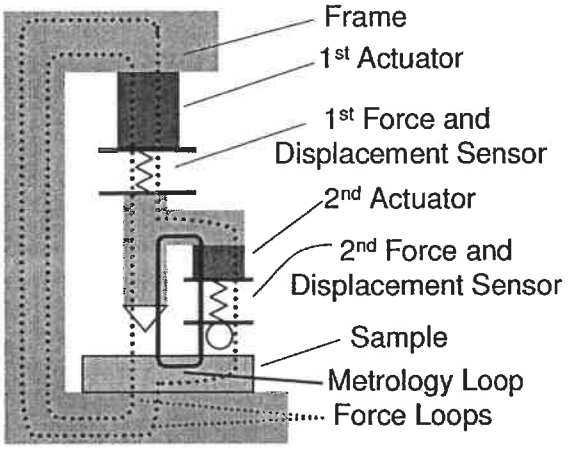

FIGURE 2: Hardness instrument compensating for frame and stage deflections where the metrology loop is much smaller than the force loops.

INSTRUMENT DESIGN

To measure nanohardness, this instrument requires a constant force feedback loop. This feedback is accomplished through an atomic force microscope (AFM) probe, shown as the second force and displacement sensor in Figure 2. The desired force level (pre-determined) is held constant using a piezoelectric transducer (PZT). Because the AFM probe does not deflect during an indent, calibration, although desired, is not necessary. The reference force mechanism is connected directly to the body of the indenter, shown in Fig. 3, and the load cell, F_{LC}, measures the total force from the indent, F_I, and the reference force, F_R.

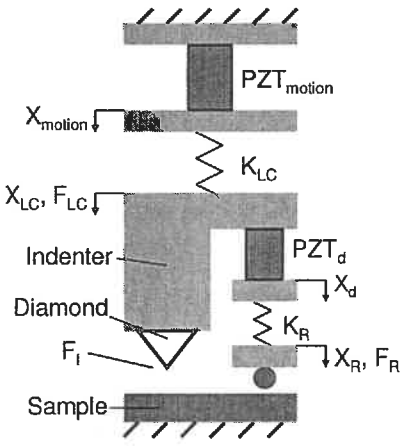

FIGURE 3: Theoretical model of an indentation instrument with a constant reference force mechanism to compensate for deflections in the instrument frame.

The force due to indentation is measured as the change in force and therefore does not include the reference force. Figure 4(a) illustrates the operation of the indenter during a simple indent showing the typical signal from the load cell during an indent cycle. The dashed line is the force due to the reference force, F_R, and the solid line is the force of the indent, F_I, and is used for determining the characteristics of the indent and subsequently the material properties.

When the indent occurs, the indenter stylus penetrates the surface of the sample and causes components in the force loop to deflect. Components in the metrology loop that coincide with the force loop deflect, causing errors in determining the displacement due to penetration versus displacement due to deflections. The displacement X_d is the total depth of indent plus the deflections of metrology loop. Because of the relatively high stiffness of the indenter body, deflections within the metrology loop are estimated to be insignificant compared with the depth of indent. Based on the idealized model of Fig. 3, the total depth of indent, X_h, is defined as

$$X_h = X_d - X_{met} \tag{1}$$

where X_d is the measured displacement of the servo (2nd actuator) and X_{met} is the deflection of metrology loop. The deflection of the metrology loop may be determined experimentally or estimated using analytic models but is considered insignificant in this case. The total depth of indent plus all deflections in the instrument, X_D, is

$$X_D = X_{motion} - X_{LC} \tag{2}$$

where X_{LC} is the deflection of the load cell and X_{motion} is the translation of the indenter and instrument frame. These measurements include an arbitrary vertical offset such that the measurement is zero when the indent begins, as noted in Fig. 4(b). By measuring these two signals simultaneously, as shown in Fig. 4(b), their difference shows the deflections in the frame and stage.

Once the depth and force of the indent is determined, the hardness is

$$H = \frac{F_I}{A(X_d)} = \frac{F_I}{aX_d^2} \tag{3}$$

where F_I is the force on the indent from Fig. 4(a), A is the area of indent, X_d is the depth of the indent extrapolated from Fig. 4(b), and a is a

correlation constant that depends on the indent stylus geometry and depth. Additional properties of the material can be found from the force-displacement curve, as shown in Fig. 5. From this curve, characteristics such as modulus [3], yield strength, and other mechanical properties can be determined [4]. This enables other phenomenon to be studied, such as adhesion across boundaries [5], phase transformations in silicon [6], or soft tissue samples [7].

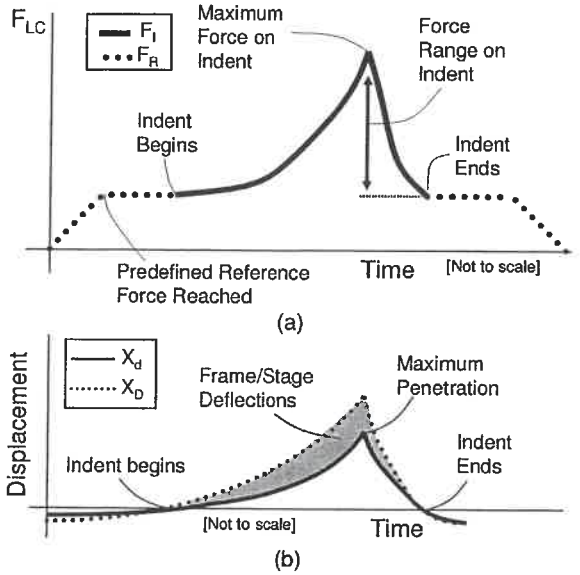

FIGURE 4: (a) Schematic of the force signal from the load cell during an indent sequence. The dashed line represents the force contributed by the reference sensor and the solid line is the force due to the indent. (b) Schematic of the measured depth of indent and the frame and stage deflections during indentation.

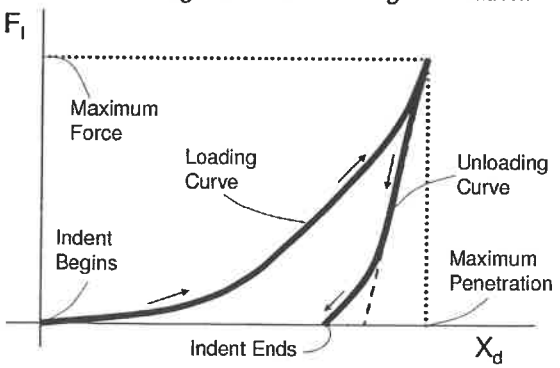

FIGURE 5: Loading and unloading curve compiled from the force extrapolated from Fig. 4(a) and from displacement (depth) from Fig. 4(b).

DESIGN SPECIFICATIONS

The purpose of this instrument is to have an accurate, traceable means of measuring hardness for nanometer scale indents. To achieve this, it is necessary to develop a comprehensive estimate of combined uncertainty for any given measurement. In addition, a high natural frequency is desired to reduce susceptibility to vibration. A higher natural frequency also makes it possible to operate the instrument faster and with greater control. In this design, the natural frequency of the mass on the load cell spring, K_{LC}, is predicted to be greater than 85 Hz. Also, the load cell (a capacitance sensor) adds considerable damping with a predicted damping ratio of 0.35.

The three capacitance sensors (measuring X_{motion}, X_{LC}, and X_d) will be calibrated using a traceable Helium-Neon laser source which has an uncertainty of less than 1 part in 10^7. To reduce errors in this calibration, the output of the capacitance sensor is fit to a polynomial therefore removing any periodic errors due to heterodyne beam mixing. Once the load cell sensor is calibrated, traceable weights will be used to determine its stiffness. Theoretically, the 0.07 nm (6σ) noise floor of the load cell combined with the stiffness of the load cell should result in a minimum force resolution of near 500 nN. The theoretical noise floor from X_d (depth of indent) is approximately 0.37 nm. Both of these displacement sensors will be bandwidth limited at 1000 Hz.

The reference force sensor is an AFM probe and the force and displacement values are not required, only that the values can be held at a constant value. Therefore, calibration of the ARM probe is not necessary. Given the resolution of the data acquisition system and a natural frequency approaching 2900 Hz for the PZT setup, a closed loop control on the position of the AFM should be able to compensate for less than nanometer deflections in the frame and stage at 500 Hz. A typical AFM probe has a stiffness less than 200 N m^{-1} and displacement resolutions better than 1 nm. Consequently, it is expected that the force can be held constant with deviations of less than 0.5 μN.

Although nanohardness is intended for indents of less than 200 nm [8], the maximum depth of indent with this instrument will be approximately 7 μm and a maximum force of 50 mN.

While other instruments may state to resolve smaller displacement and force increments, the purpose of this instrument is to provide nanoscale hardness measurements with traceable uncertainties.

SIMPLIFIED UNCERTAINTY

Because the dependence on the frame and stage stiffness has been significantly reduced the uncertainty budget is simplified. The simplified expanded uncertainty in hardness, Equation (3), is

$$U_H^2 = \left(\frac{\partial H}{\partial F_i}\right)^2 \sigma_{F_i}^2 + \left(\frac{\partial H}{\partial X_d}\right)^2 \sigma_{X_d}^2 \quad (4)$$

The load cell and displacement sensor measurements are independent and therefore coupling terms are removed. The force and indent area coupled term can be found from finite element modeling. For materials of significantly lower modulus and hardness than diamond, this would typically be significantly less than the other uncertainty contributors and can therefore be considered zero.

The area function $A(X_d)$ is typically determined by using the geometry of an ideal Berkovich probe. In practice, there is no ideal probe due to manufacturing errors as well as an additional uncertainty contribution from the tip radii. Notwithstanding the problem of AFM tip deconvolution, it is possible that the indent area can be measured using a calibrated AFM [9]. Once the area is determined, effects of indenter orientation with respect to the central axis of the indenter can be evaluated mathematically. For an ideal Berkovich diamond a misalignment of 0.5 degrees, the change in area is 0.0022%. This increases nonlinearly with respect to the tip and tilt angles. For extreme misalignments of 5.0 degrees, the change in area only increases to 0.25%. These uncertainties will be measured and quantified prior to testing. However, determination of uncertainties in the correlation constants between depth and area represent a substantially unexplored challenge and require further research if these are to be verified in practice.

The uncertainties in the depth measurement include electrical noise in measuring X_d, thermal effects, Abbe offset between the indenter and the reference AFM, distortions of the components sharing the force and metrology loops (indenter body and indenter), and controller errors on the position of the AFM.

The majority of the uncertainty of the force measurement is from electrical noise in measuring X_{LC}, calibration of stiffness K_{LC}, thermal effects, and errors in the vibration isolation. Although the theoretical force resolution is 500 nN, the smallest reliable, traceable force measurement is only approximately 5 μN [10], which represents the current limit for all instruments.

The detailed error budget has not been completed yet. Some of the uncertainties must await the construction and characterization of the instrument, which will be completed by the end of this year.

ROUND ROBIN TESTING

The instrument described here will be used for measurements at UNC Charlotte for the CIRP International Comparison of Nanoindentation. It consists of the measurement of three samples, single crystal aluminum, fused silica, and rolled tungsten, to determine the realization of the ISO Standards 14577-1, 2, 3.

REFERENCES

1. Pethica, J., Hutchings, R., and Oliver, W., 1983, Hardness measurements at penetration depths as small as 20 nm. *Philosophical Magazine*, 48: 593-606
2. Herrmann, K., Jennett, N., Wegener, W., Meneve, J., Hasche, K., and Seeman, R., 2000, Progress in determination of the area function of indenters used for nanoindentation, *Thin Solid Films*, 377-378: 394-400.
3. Doerner, M. and Nix, W., 1986, Interpreting data from depth sensing indentation instruments. *J. Mater. Res.*, 1: 601-609.
4. Bowden, F. and Tabor D., 1964, *The Friction and Lubrication of Solids: Part II.* Oxford University Press.
5. Daniels A,, Smith S., and Lewis M., 1994, A scanning electron microscope based hardness indentation tester, *Rev. Sci. Instrum.*, 65: 632-638.
6. Kailer, A., Gogotsi, Y., and Nickel, K., 1996, Phase transformations of silicon caused by contact loading, *J. Appl. Phys.*, 81: 3057-3063.
7. Lim, C., Zhou, E., and Quek, S., 2006, Mechanical models for living cells – a review, *J. of Biomechanics*, 39: 195-216.
8. International Standard 14577-1, 2002
9. Herrmann, K., Jennett, N., Wegener, W., Meneve, J., Hasche, K., and Seeman, R., 2000, Progress in determination of the area function of indenters used for nanoindentation, *Thin Solid Films*, 377-378: 394-400.
10. Pratt, J., Kramar, J., Newell, D., and Smith, D., 2005, *Meas. Sci. Technol.*, 16:2129-2137.

OPTICAL MEASURING DEVICE FOR RADIAL ERROR OF MICRO-SPINDLE USING HIGH-SPEED PHOTO-AMPLIFIERS

Kengo Fujimaki[1] and Kimiyuki Mitsui[2]
[1]School of Integrated Design Engineering
Keio University, Yokohama, Kanagawa, Japan
[2]Department of Mechanical Engineering
Keio University, Yokohama, Kanagawa, Japan

INTRODUCTION

In recent years, micro machine tools have been studied and developed for space, energy and resource savings. A micro-spindle, which is a miniaturized spindle, is one of the main components of miniaturized machine tools. It is comparatively easy for a micro-spindle to run at high speed because the rotor of the micro-spindle is thin and lightweight. Therefore, a micro-spindle system with a maximum rotation speed of 300 krpm has already been demonstrated [1].

The measurement of the spindle rotation accuracy, which is the width of the run-out, is very important to verify the machining accuracy. A conventional measurement method uses capacitive displacement sensors and a reference object such as a high-precision ball or cylinder. However, the target attached to a micro-spindle must be small and light to avoid an imbalance of the spindle axis. In addition, capacitive displacement sensors have limitations in the applicable radius of the target and are not suitable for measuring the displacement of a small target at ultra-high speed. Therefore, a conventional measuring method cannot precisely measure the rotation accuracy of the micro-spindle.

The authors have proposed an optical measuring method for the rotation accuracy of micro-spindles [2] after researching an optical method using a concave mirror [3], which is based on Holster's method [4]. In this method, the rotation accuracy is evaluated according to the movement of the reflected light from the target sphere attached to the spindle end, and a small target sphere can be targeted because the light beam is condensed by the objective lens. In addition, this method has advantages such as a non-contact, long working distance and little susceptibility to electric noises. Moreover, the authors have succeeded in relaxing the effect of the surface of the target sphere for measurement accuracy by applying the algorithm of the three-point method [5].

In this study, we tried to improve the response speed and the noise characteristics after reconsidering the sensor board of the measuring device. This paper first describes the basic principle of the optical measuring method and then shows the improved measuring device and some of the measurement data for the rotation accuracy of a micro-spindle. Finally, the results are summarized.

MICRO-SPINDLE SYSTEM

The micro-spindle system used in this research is shown in Figure 1. The rotational axis is supported by ball bearings, and the maximum rotational speed is 200 krpm. The collet chuck on the end can hold an object of 1-mm diameter. A steel ball of grade 16 is attached to the collet chuck in the measurement.

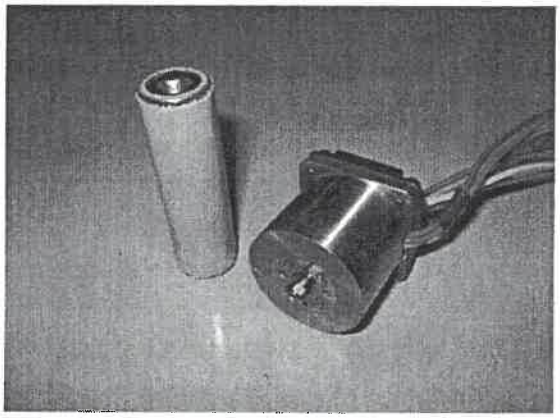

Figure 1. Micro-spindle for a miniaturized machine tool. (This trial spindle was produced in cooperation with NSK Ltd.)

MEASURING DEVICE

Figure 2 shows the principle of the optical measurement method, which is based on a laser collimator. The optical spot on a QPD (Quadrant Photo Diode) moves according to the

displacement of the steel ball attached to the spindle axis. The QPD is composed of four photo cells (photo diodes), and the outputs V_x and V_y of the QPD in the X and Y directions are calculated for the differences between the outputs of the four photo cells as the following expressions.

$$V_x = (S_1 - S_2 - S_3 + S_4)/(S_1 + S_2 + S_3 + S_4) \quad (1)$$

$$V_y = (S_1 + S_2 - S_3 - S_4)/(S_1 + S_2 + S_3 + S_4) \quad (2)$$

The displacements of the spindle axis in the X and Y directions are the values V_x and V_y divided by the sensitivity, which is estimated by the calibration.

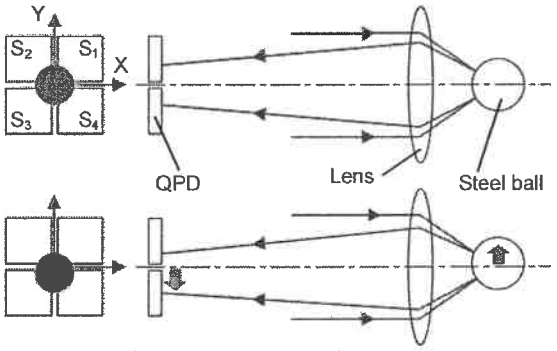

Figure 2. Measurement principle

The configuration of the optical measuring device is shown in Figure 3. Because the outputs of the photo cells on a QPD are faint current signals, the outputs are converted into voltage signals on a circuit board to void electric noises.

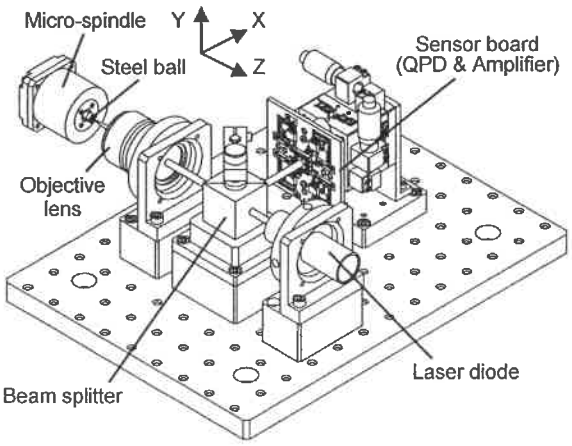

Figure 3. Configuration of the optical measuring device.

RESPONSE TEST

Figures 4 and 5 show the response of the sensor (the QPD and the amplifier) to light modulation by rectangular signals of 1 kHz. The response was sampled at 40 MHz. From this result, it is found that the response frequency of the sensor is about 1 MHz, which is equal to the specification value of the integrated circuit of the amplifier. Because there is a need for a response frequency of at least 167 kHz in order to measure the frequency components to 50 upr (undulations per revolution) at the rotational speed of 200 krpm, this sensor meets the response requirement for measuring the run-out of the micro-spindle. In addition, the overshoots shown in Figure 4 are probably due to the characteristics of the A/D converter without analog low-pass filters.

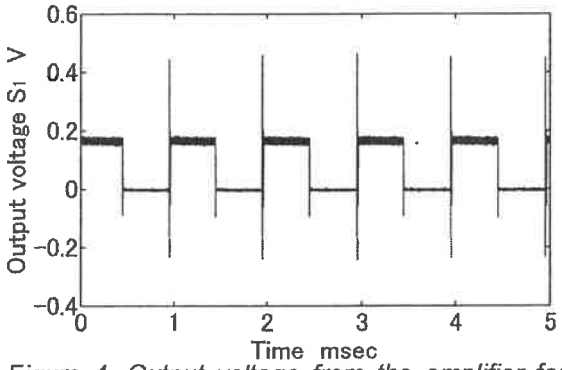

Figure 4. Output voltage from the amplifier for light modulation by rectangular signals.

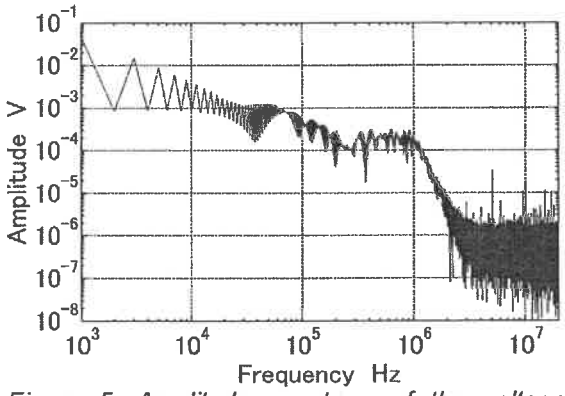

Figure 5. Amplitude spectrum of the voltage output from the amplifier for light modulation by rectangular signals.

NOISE TEST

Figures 6 and 7 show the noise signals in the same condition as the measurement of the micro-spindle but without the rotation of the spindle axis. These data were sampled at 20

MHz and were calculated using Equations (1) and (2), assuming that the sensitivity is -0.1 μm^{-1}. Then, it is found that the standard deviation of the noise level is about 9.5 nm and the power spectrum of the noises mainly exists in the frequency band of 1 MHz.

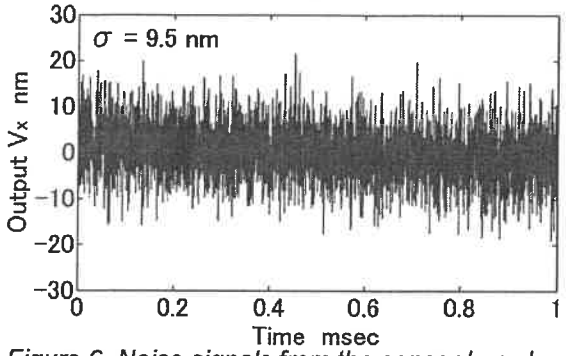

Figure 6. Noise signals from the sensor board.

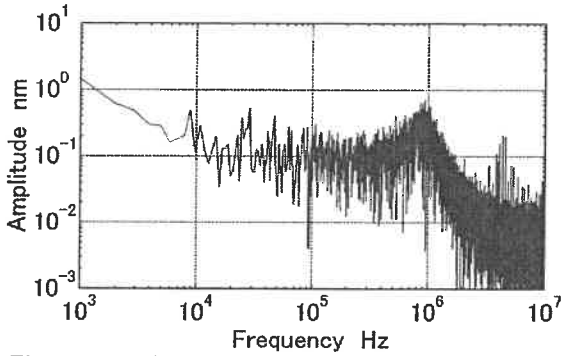

Figure 7. Amplitude spectrum of the noise signals.

MEASUREMENT OF THE MICRO-SPINDLE

Figures 8-10 show the measurement results of radial error motions of the micro-spindle by the optical measuring device. The scale factor of the figure at 200 krpm is twice that of the others. These data were recorded by the A/D converter through analog low-pass filters of 500 kHz in cut-off frequency, and afterward they were not filtered by the digital processing. Because these data were sampled at 5 MHz and the Nyquist frequency is 2.5 MHz, it is enough to record the analog signals. The data length is about 16 revolutions. Then, the sensitivities in the X and Y directions were -0.0545 μm^{-1} and -0.0707 μm^{-1}, respectively; the difference between these is due to the light intensity distribution of the output beam from the laser diode. Therefore, the resolutions in the X and Y directions are estimated at 3.1 nm and 2.4 nm based on the bit number and the measurement range of the A/D converter. Moreover, the standard deviations of

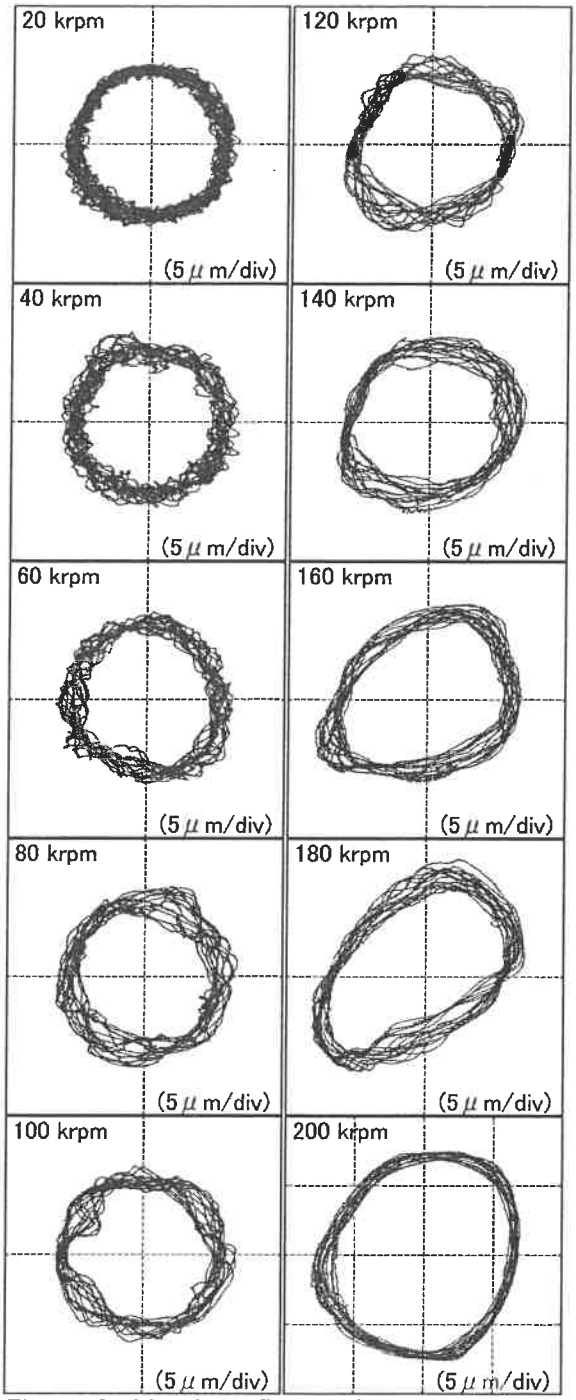

Figure 8. Lissajous figure of the radial error motions of the micro-spindle. (The vertical and horizontal directions show X and Y.)

the noise levels in the X and Y directions are estimated at 17.4 nm and 13.4 nm, respectively. From these results, it is found that the radial error motion becomes smoother with increasing spindle speed. The reason is probably the

spindle axis cannot mechanically respond to the ultra-high-speed vibration sources such as the radial error motions of the built-in bearings. In addition, the increase of TIR (Total Indicated Reading), which is the circumscribed circle diameter of the Lissajous figure with speed-up, is due to the centrifugal force. This trend is roughly in agreement with the results of the very simple measurement in Ref. [6], which introduced a micro-spindle similar to the one used in this paper.

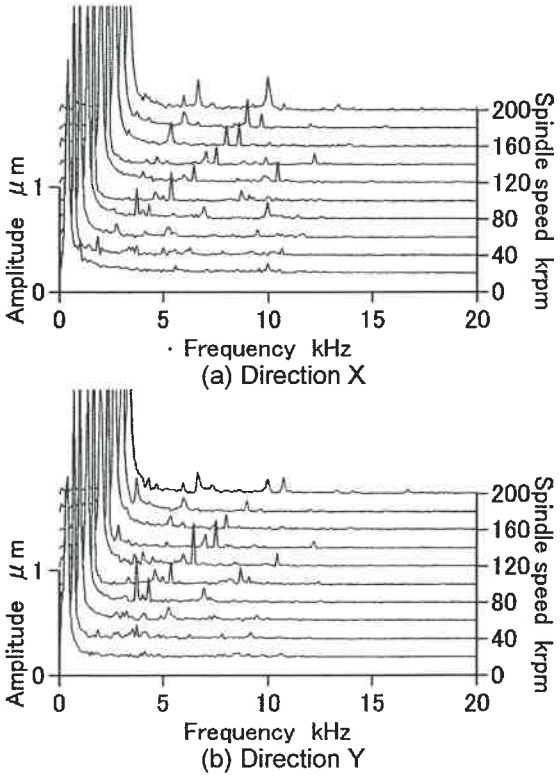

Figure 9. Frequency analysis of the radial error motion.

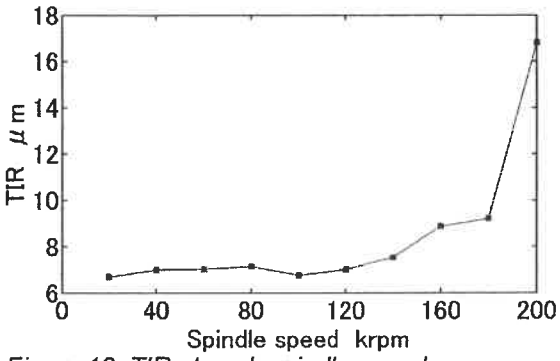

Figure 10. TIR at each spindle speed.

CONCLUSIONS

The results obtained in this paper are summarized as follows.

- It became clear that the radial error motions of a micro-spindle running at the maximum rotational speed of 200 krpm can be measured by the optical measurement method using a small steel ball, which is based on a laser collimator.
- The radial error motion of the micro-spindle running at ultra-high speed tends to become smoother with the increase in rotational speed.
- The TIR of the micro-spindle drastically increases as spindle speed increases.
- There is a need to verify the validity of the measurement results in future work.

ACKNOWLEDGEMENT

The authors would like to acknowledge NSK Ltd. for the cooperation with the trial spindle system.

REFERENCES

1. Okazaki Y. Desk-top ultra-high-speed milling machine with 300krpm spindle and linear motor stages. Proc ASPE 2004 Annual Meeting. 2004. p. 277-80.
2. Fujimaki K, Mitsui K. Development of an optical measuring device for rotation accuracy of micro-spindle. Proc ASPE 2005 Annual Meeting. 2005. p. 287-90.
3. Mitsui K, Ling Ji, Hashimoto Y, Nunome K, Hibi K. Development of an optical measuring method for radial spindle error. Proc 7th Int Precision Engineering Seminar. 1993. p. 506-17.
4. Holster PL, Jacobs JAHM, Sastra B. Measuring the radial error of precision air bearings. Philips Tech Rev. 1983/1984;41 (11/12):334-7.
5. Mitsui K. Development of a new measuring method for spindle rotation accuracy by three points method. Proc 23rd Int MTDR Conf. 1982. p. 115-21.
6. Okazaki Y, Mori T. Development of a desktop milling machine equipped with an ultra-high speed spindle (6th report). Proc JSPE spring meeting 2004. 2004. p. 327-8. (in Japanese)

MECHANICAL PROPERTIES OF SILICON CARBIDE FILMS PREPARED BY RF MAGNETRON SPUTTERING USING TARGETS WITH DIFFERENT CARBON CONTENTS

Hirokazu Fujiyama[1], Masayoshi Nakamura[2] , and Tsunetaka Sumomogi[2]
[1] Department of Intelligent Mechanical Engineering, Fukuoka Institute of Technology, Fukuoka, JAPAN
[2] Department of Mechanical Engineering, Hiroshima Kokusai Gakuin University, Hiroshima, JAPAN

INTRODUCTION

Silicon carbide is an attractive thermally and chemically stable material. Its mechanical properties, such as low friction coefficient and high hardness, make it promising for use as a wear resistance coating for different types of steel. Among the many methods of growing silicon carbide films on steel substrates, radio-frequency (rf) magnetron sputtering, which permits low-temperature film deposition, is most effective because high-temperature film deposition causes damage to the substrate. However, there is very little information on silicon carbide films deposited by rf magnetron sputtering [1]. We do not know of any studies in which the hardness, internal stress, friction coefficient, and other mechanical characteristics of silicon carbide films, all of which are important factors when such films are used for surface protection, were examined. If a target containing a volatile element, that is, carbon, oxygen or nitrogen, is used for sputtering, a film without this volatile component is generally produced. Therefore, in sputtering with a compound target containing a volatile element, volatile component gases contained in the target are often added to the gas for reactive sputtering [2-5]. The silicon carbide film composition improved when acetylene or methane was added to argon gas. However, it is difficult to determine the optimum partial pressure of such a gas mixture for obtaining films with excellent mechanical properties. Four silicon carbide mixture targets (mixture targets) with carbon contents of 50 mol%, 55 mol%, 60 mol% and 67 mol% were used to evaluate the characteristics of sputtered silicon carbide films as functions of the carbon content of the target. Furthermore, the stoichiometric SiC target (compound target) was also used to enable comparison with the characteristics of films sputtered with mixture targets.

EXPERIMENT

Sputter deposition

Figure 1 shows a schematic view of the rf magnetron sputtering apparatus used in this work. Four mixture targets with carbon contents of 50 mol%, 55 mol%, 60 mol% and 67 mol% and the compound target, with diameters of 50 mm and thicknesses of 5 mm were used. Three types of substrate were used: borosilicate glass plates of 26×36 mm^2 and 1.2 mm thickness for monitoring film thickness; stainless-steel plates (SUS304) of 10×26 mm^2 and 70 μm thickness for internal stress measurements; and SUS304 of 26×36 mm^2 and 1.4 mm thickness for all other measurements. The substrate was cleaned in a supersonic bath of acetone for 15 min and then

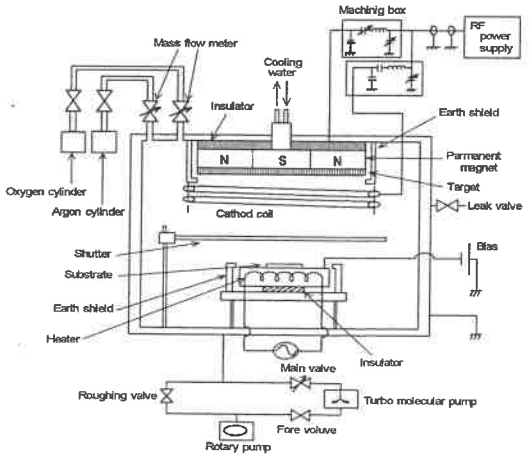

Figure 1: Schematic view of RF magnetron spattering apparatus.

TABLE 1. Sputtering and sputter etching conditions.

	rf power (W)	rf power density (W/cm^2)	Working pressure (Pa)	Argon gas flow rate (sccm)	dc bias (kV)
Sputtering	150	7.7	8×10^{-2}	10	0
Sputter etching	30	1.54	1×10^{-1}	30	1

TABLE 2. Hardness and chemical composition (mol. %) of pin (SUJ2) and substrate (SUS304)

	Fe	C	Cr	Ni	Mn	Si	DH (GPa)
SUS304	72.92	0.08	18.0	8.2	0.8	—	3.7
SUJ2	97.25	0.95	1.6	—	—	0.20	5.5

placed on a substrate holder. The sputtering apparatus was first evacuated to 5×10^{-4} Pa with a turbomolecular pump to reduce the influence of residual gases, and then the working gas (99.99% pure argon) was introduced into the chamber through an electrically controlled mass flow controller. After the pressure was stabilized at 4×10^{-1} Pa, the substrate and target were cleaned by sputter etching for 10 min. The film deposition was carried out under the conditions shown in Table 1. In all cases, the pressure of the gas during film deposition was 8×10^{-2} Pa.

Hardness test

Film hardness was measured with a nanoindentation tester (Shimadzu, DUH-201) using a Berkovich indenter at room temperature. A load of 30 mN was employed with a dwell time of 15 s. To obtain reasonably good accuracy, ten impressions were made on each specimen and their values were averaged.

X-ray diffraction test

The crystallographic structure of the films was examined by X-ray diffraction (XRD) analysis using a Shimadzu XRD-7000 goniometer with a constant incidence angle of 1° using Cu$K\alpha$ radiation. The excitation voltage and current were 40 kV and 30 mA, respectively.

Electron probe microanalysis

An electron probe microanalyzer (EPMA) was used to analyze the composition ratio of Si and C, the Ar content in the films and the composition in the wear region. The measurements were performed under the following conditions: an accelerating voltage of 10 kV, a sample current of 100 nA and a beam diameter of 1 μm.

Atomic force microscopy

Atomic force microscopy (AFM) was also performed to observe the surface topography of the films prepared. The tip used in the AFM was a rectangular microcantilever, with a radius of 20 μm, made of Si_3N_4. The images were obtained in the constant-force mode at a tip load of 40-50 nN.

Friction and wear test

The friction and wear test apparatus is of the pin-on-disk type, as shown in Fig. 2. The pin (SUJ2, diameter=2 mm) was pressed onto the rotating table at a normal load. A new pin was used for each test and it was cleaned in a supersonic bath of acetone for 15 min before each run. Friction force was measured by strain gauges located on both sides of the plate spring. Sliding velocity was maintained constant by adjusting the rotation speed of the pulse motor and the radius of the wear track. Experimental

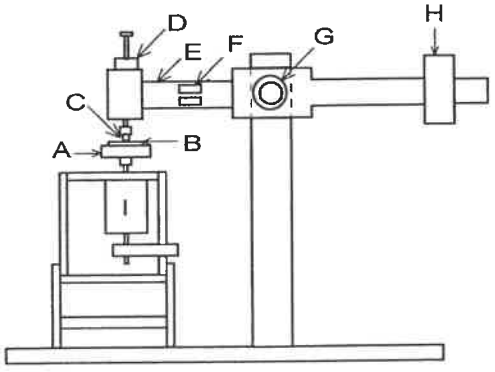

A: Rotation table B: Sample C: Pin D: Normal load
E: Plate spling F: Strain gauge G: Bearing H: Weight balance
I: Pulse motor

Figure 2: Schematic view of pin-on-disk wear apparatus.

conditions throughout the test were a load of 0.4 N, a sliding velocity of 4 mm/s, and dry friction in open air. The hardnesses and chemical compositions of the pin and the substrate (SUS) are shown in Table 2.

EXPERIMENTAL RESULTS AND DISCUSSION

Film hardness

Hardness is one of the importance factors governing wear resistance, as reported by Rabinowicz et al. [6], who showed that the inverse of abrasive wear resistance is proportional to hardness. A hardness test, therefore, was carried out to evaluate the hardness of SiC films sputtered using mixture targets and the compound target. Figure 3 shows the results. The hardness of films sputtered with the mixture targets increases with increasing carbon content of the target. On the other hand, the hardness of film sputtered with the compound target was comparable to that of the film sputtered using the target with a carbon content of 60 mol%.

The most influential factors affecting film hardness are the crystal structure,[7] composition,[8-9] and particle size.[10] Therefore, these factors were measured in this study by XRD analysis, AFM and EPMA. First, XRD was used to determine whether the film was crystalline or amorphous. It was found that the crystal structure of the sputter-deposited films was amorphous with all targets investigated. This suggests that the crystal structure does not affect film hardness in this study. The film composition was further examined by EPMA. The silicon and carbon contents in sputter-deposited SiC films using the mixture target and the compound target are shown in Fig. 4. The carbon content in the film increases with increasing carbon content of the target, whereas the silicon content in the film decreases. These EPMA results indicate that a film sputtered using a mixture target with a carbon content of 60 mol% has the optimum stoichiometry. On the other hand, the film hardness increases to a maximum value at the carbon content of 67 mol%; this indicates a good correlation with the carbon content in the films. Therefore, the film composition might be one of the factors affecting film hardness. To verify the influence of particle size, the surface shape of the films was observed by AFM. Figure 5 shows

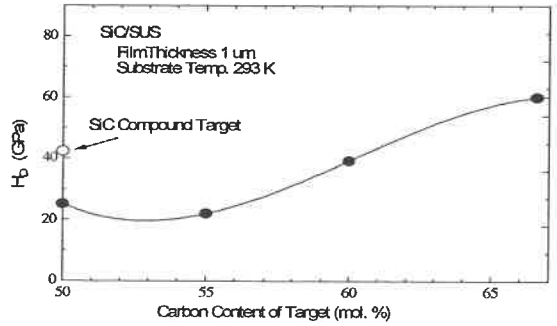

Figure 3: Film hardness with a load of 30mN as a function of carbon content of mixture target (•) and SiC compound target (○).

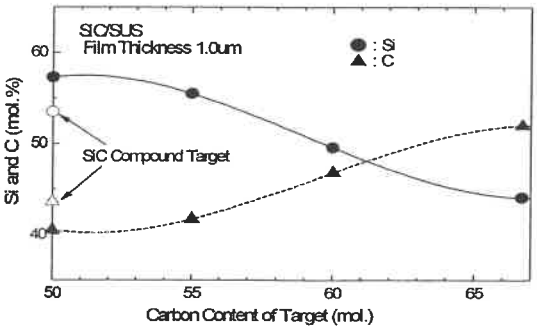

Figure 4: Silicon and carbon contents in sputter-deposited SiC films as a function of carbon content of mixture target (•: Si ▲: C) and compound SiC compound target (○: Si △: C) .

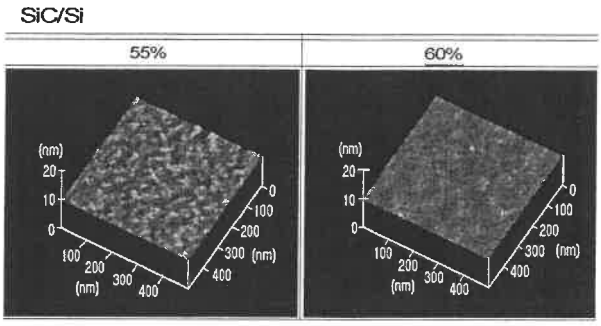

Figure 5: Atomic force microscopy image of SiC films sputter-deposited using targets with carbon contents of 55 mol% and 60 mol%.

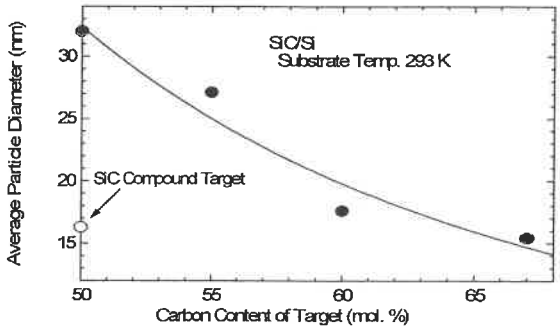

Figure 6: Number of particles per unit area in atomic force microscopy image as a function of carbon content of mixture target (•) and SiC compound target (○).

the AFM images of SiC films sputtered using the mixture targets with carbon contents of 55 mol% and 60 mol%. As can be seen, the surface of the former tends to have a more acicular structure and that of the latter has structures that are more spherical in shape. Figure 6 shows the relationship between the carbon content of the mixture target and the diameter of the surface structures obtained from AFM images. It was found that the average particle diameter decreases with increasing carbon content of the mixture target. This correlates well with the film hardness. On the basis of these results, the film composition and particle size might be the factors affecting the film hardness.

It is thought that the film sputtered by adjusting composition ratio of a mixture target offers stoichiometoric compound and desired properties to compound target and indicates the possibility of great development industrially.

Friction coefficient and wear resistance

Figure 7 shows the friction and wear test results for the SUS304 substrate and SiC films sputter-deposited using the mixture targets and the compound target. It can be seen that the friction coefficients of the SiC films sputter-deposited using the mixture targets with carbon contents of 60 mol% and 67 mol% and using the compound target are small after 3000 or more wear test cycles. In particular, the films sputter-deposited using the mixture target with a carbon content of 67 mol% shows a steady low friction coefficient of 0.2 after 10000 wear test cycles. According to these results, the carbon content of the target might be expected to affect mechanical properties such as the hardness, the friction coefficient and the wear resistance of the film.

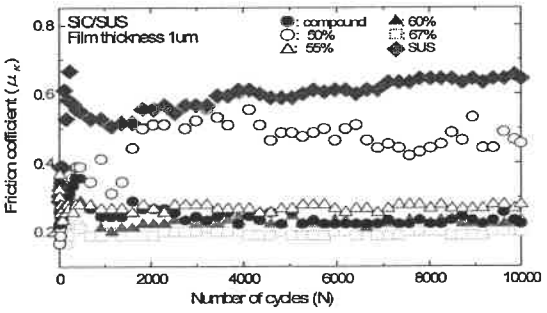

Figure 7: Change in friction coefficient with number of cycles for SUS substrate and SiC films sputtered using mixture targets with different carbon contents and using compound target

CONCLUSION

The mechanical properties of SiC films deposited by rf magnetron sputtering using mixture targets with different carbon contents and using the compound target were studied. The following results were obtained.

1. Film hardness increases with increasing carbon content of the mixture target.
2. The crystal structure of the films is amorphous at all the carbon contents investigated.
3. The carbon content increases with increasing carbon content of the mixture target, whereas the silicon content of the films decreases.
4. The average particle diameter of the film decreases with increasing carbon content of the mixture target.
5. The friction coefficient of the films decreases from 0.5 in the case of using a mixture target with a carbon content of 50 mol% to 0.2 in the case of using a mixture target with a carbon content of 67 mol%.

REFERENCE

1. A. Sathyamoorthy and W. Weisweiler, 1982, Studies of the Sputter Deposition of Carbon, Silicon and SiC Films, Thin Solid Films, **87**: 33-42.
2. M. K. Olsson, K. Macák and W. Graf, 1999, Reactive D. C. Magnetron Sputter Deposited Al_2O_3 films: large-area coatings for industrial applications, Surface and Coating Technol., **122**: 202-207.
3. P. J. Kelly, O. A. Abu-Zeid, R. D. Arnell and J/ Tong, 1996, The Deposition of Aluminum Oxide Coatings by Reactive Unbalunced Magnetron Sputtering, Surface and Coating Technol., **86/87**: 28-32.
4. K.Mumtaz, J. Echigota, H. Enoki and Y. Shindo, 1996, RF MagnetronSputted Aluminum Oxide Coatings on Iridium, J. Mater. Sci., **31**: 5247-5256.
5. T. Semba, H. Fujiyama and H. Satoh, 1998, Development of Resin-Bonded Diamond Wheels with Improver Wear Resistance Using Surface Modified Fine Grains Treated by Radio-Frequency Magnetron Sputtering, Annals of the CIRP, **47/1**: 271-274.
6. Rabinowicz E., L. A. Dunn, and P. G. Russell, 1961, A study of Abrasive Wear under three-Body Conditions, Wear, **4**: 345-355.
7. I. Manika, and J. Maniks. 1992, Characteristics of deformation localization and limits to the microhardness testing of amorphous and polycrystalline coatings, Thin Solid Films, **208**: 223-227.
8. J.-E. Sundgren, 1985, Structure and properties of TiN coatings, Thin Solid Films **128**: 21-44.
9. J.-E. Sundgren, B.-O. Johansson, S.-E. Karlsson, and H. T. G. Hentzell, 1983, Mechanisms of reactive sputtering of titanium nitride and titanium carbide II: Morphology and structure, Thin Solid Films **105**: 367-384.
10. W. Hoffmeister and M. Zuegel,1968, Thin Solid Films **3**:35-40.

NANO-LINEAR ENCODER INVESTIGATION USING DUAL FIBER AND GRATING SYSTEM

Devendra D. Karodkar[1]
Department of Mechanical Engineering
University of North Carolina at Charlotte, Charlotte, USA

ABSTRACT

Measurement of linear displacement to nanometer levels represents a relative broad industry need within the variety of assemblies currently under development as part of the nanotechnology. In the area of manufacturing, some notable examples that require nanometer level measurement include miniature machine tools, microlithography position stages, dip-pen and imprint lithography stages, and scanned probe microscopes to name but a few.

In present encoder technology linear encoders comprise a wavelength dependent dual grating system, with an illumination source, beam splitter and a detector. This paper presents an investigation to eliminate the optics and use dual fiber (illumination) system, one grating and a detector. Two optical fibers are separated by a distance $\lambda/4$ or $(2m-1)\ \lambda/4$, each optical fiber will produce a sine wave and, because they are separated by $\lambda/4$ (a spatial phase shift of 90^0), will produce an A/B output. Detail mathematical study on dual fiber and grating interaction is being undertaken. A mathematical model and is presented. From this model using Matlab diffraction was observed with separation distance between grating and fiber as 5 mm. Along with theoretical developments an experimental program is in progress. The experimental apparatus consist of a grating attached to a computer controlled PZT driven platform and the stationary dual fiber system running over the grating. Constant separation distance between the grating and the fiber maintained using flexure based support and a skid mount. Dual fibers run over the grating relatively with collection of the intensity variation data from a photo diode (FDS 100) located below the grating. Data acquisition was accomplished using LabView program. Near filed approach using dual fiber- grating system is considered as future steps of the investigation.

INTRODUCTION

Length measurements in the nanometer-scale regime are accomplished by a number of methodologies, including, capacitance, inductance, tunneling, atomic-force, electron, and visible and ultraviolet light optical interactions (usually interference). Computer modeling and standards development are also integral parts of the measurement process. Optical Encoders with gratings divided into micro-meter pitch are widely used on machines and metrology systems. Renishaw, SONY and Heidenhain manufacture encoders with resolution to a few nanometer levels or below. Principally these encoders measure displacement by monitoring the phase change of a laser beam as it passes through, or reflects from, a grating. These include either two grating system or single grating double pass system. Figure-1 below shows the typical operation principal of the SONY laser scale.

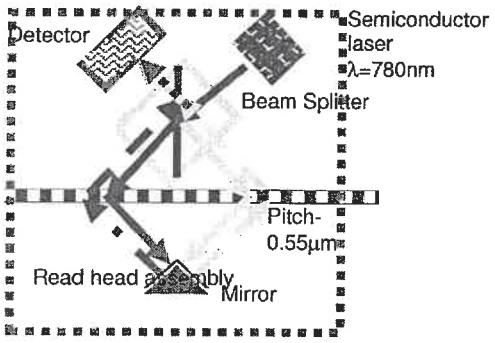

FIGURE-1 OPERATIONAL PRINCIPAL OF SONY LASER SCALE

The beams are collected at the detector where the detector system converts the interfering beams into electrical signals. Most optical encoder systems are arranged to produce A/B quadrature, when the scale moves, phase of the two signals changing in proportion to the direction and amount of travel. The encoder resolution is limited by several factors such as the grating pitch (that is, in turn, limited by the wavelength of the illuminating beam), light collected back at the detector, the phase shift added by the return path light with incident light. It has been found that the installation of detector and the grating scale assembly requires

considerable skill when work volumes are highly compact using present encoders.

Accuracy and resolution of an encoder can directly be enhanced by reducing the pitch of the encoder gratings. When using diffractive based sensing methods, reduction of pitch leads to a higher reflected beam angle, so partial reflected light will be collected at the detector. This will increase the size of the detector as well as creating an ambiguity in phase discrimination thereby imposing a limitation with current designs. The goal of this project is to investigate the possibility of using dual fiber probes as phase producing elements along with a high pitch grating, to measure displacement.

THEORY

To understand the theory of dual fiber and grating interaction a mathematical model is defined as shown in the Figure-2 below.

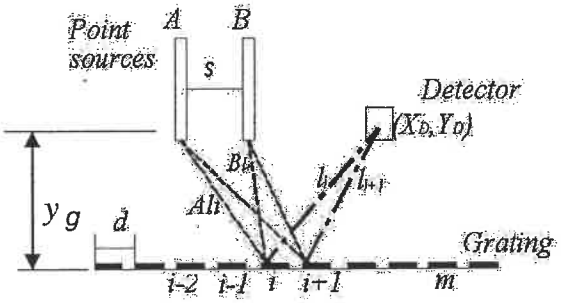

FIGURE-2 MATHEMATICAL MODEL FOR GRATING AND DUAL FIBER

Let *d* is the spacing between the grating lines, s is the separation distance between dual fibers (A & B), x_0 is the distance from a reference to first fiber, let yg is the constant separation distance between fibers and the grating and the wavelength of light is 633 nm. The amplitude of the illumination at each point on the diffraction grating in a 2-D model can be obtained from the vector sum of the (assumed) coherent illuminations of amplitude A_0 from the two point sources. To determine this, it is necessary to know the path length between each source (*A* and *B*) and the I^{th} point on the grating. And that can be given by

$$
\begin{aligned}
{}^{A}l_i &= \left((id - x_o)^2 + y_g^2\right)^{1/2} \\
{}^{B}l_i &= \left((id - x_o - s)^2 + y_g^2\right)^{1/2}
\end{aligned}
\qquad (1)
$$

The phase of the incident illumination from each source is proportional to path length and given respectively by the equations

$$
\begin{aligned}
\phi_{Ai} &= \frac{2\pi}{\lambda}\left((id - x_o)^2 + y_g^2\right)^{1/2} \\
\phi_{Bi} &= \frac{2\pi}{\lambda}\left((id - x_o - s)^2 + y_g^2\right)^{1/2}
\end{aligned}
\qquad (2)
$$

Consequently, these two illuminations will combine vectorilly to produce a new source at the point *i* on the grating of magnitude

$$
A_{0i}^{'} = A_0\left[\frac{1}{{}^{A}l_i^2} + \frac{1}{{}^{B}l_i^2} + \frac{2}{{}^{A}l_i\,{}^{B}l_i}\cos(\phi_{Ai} + \phi_{Bi})\right] \qquad (3)
$$

Substituting (1) and (2) into (3) gives

$$
A_{0i}^{'} = A_0\left[\frac{1}{(id - x_o)^2 + y_g^2} + \frac{1}{(id - x_o - s)^2 + y_g^2} + \frac{2\cos\left(\frac{2\pi}{\lambda}\left[\left((id - x_o)^2 + y_g^2\right)^{1/2} + \left((id - x_o - s)^2 + y_g^2\right)^{1/2}\right]\right)}{\left((id - x_o)^2 + y_g^2\right)^{1/2}\left((id - x_o - s)^2 + y_g^2\right)^{1/2}}\right]
$$

Additionally, it is necessary to know the phase of the source at each I^{th} point on the grating.

$$
\begin{aligned}
\phi_{oi}^{'} &= \tan^{-1}\left(\frac{\left[\frac{1}{{}^{A}l_i}\sin\phi_{Ai} + \frac{1}{{}^{B}l_i}\sin\phi_{Ai}\right]}{\left[\frac{1}{{}^{A}l_i}\cos\phi_{Ai} + \frac{1}{{}^{B}l_i}\cos\phi_{Ai}\right]}\right) \\
&= \tan^{-1}\left(\frac{\left[{}^{B}l_i\sin\phi_{Ai} + {}^{A}l_i\sin\phi_{Ai}\right]}{\left[{}^{B}l_i\cos\phi_{Ai} + {}^{A}l_i\cos\phi_{Ai}\right]}\right)
\end{aligned}
$$

Having an expression that transforms from the fiber sources to the amplitudes and phases at each I^{th} scattering point on the grating, it is possible to express the amplitude of the reflected illumination at a detector location (x_D, y_D). For an infinite grating, this is simply the sum of all illuminations arriving at the detector from each point on the grating given by

$$
\sum_{i=-\infty}^{\infty}\frac{A_{0i}^{'}}{l_{Di}^{'}}\cos\left(\phi_{oi}^{'} + \frac{2\pi}{\lambda}l_{Di}^{'}\right) = \sum_{i=-\infty}^{\infty}A_{Di}\cos(\varepsilon_i)
$$

Where l'_{Di} is the distance from the i^{th} scattering point on the diffraction grating to the detector. The above can be reduced to a simple amplitude A and phase θ of the form

$$A_D = R\cos(\theta)$$

Where

$$R = \left[\sum_{i=-\infty}^{\infty} (A_{Di}\cos(\varepsilon_i))^2 + \sum_{i=-\infty}^{\infty} (A_{Di}\sin(\varepsilon_i))^2 \right]^{1/2}$$

$$\theta = \tan^{-1}\left(\frac{\sum_{i=-\infty}^{\infty} (A_{Di}\sin(\varepsilon_i))}{\sum_{i=-\infty}^{\infty} (A_{Di}\cos(\varepsilon_i))} \right)$$

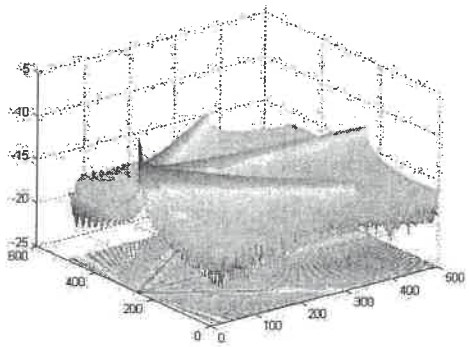

FIGURE-3 DIFFRACTION ORDERS FOR 1 μm GRATING SPACING AND DUAL FIBER GRATING SEPARATION OF 5 mm

The 3D plot of the intensity computed from this analysis is as shown in the Figure-3 for a separation distance of 5 mm which is a typical example of fraunhaufer diffraction. Various parameters such as grating spacing, separation distance between grating and fibers, fiber separation distance were analyzed. Intensity plots variations were observed with change in especially grating spacing and grating separation distance.

Based on the theoretical analysis in Matlab the dual fiber and grating interaction in far field yields a diffraction solution

Experimental Setup

Figure-4 below shows the schematic representation of PZT driven and flexure based computer controlled displacement measurement platform setup used for experimentation.

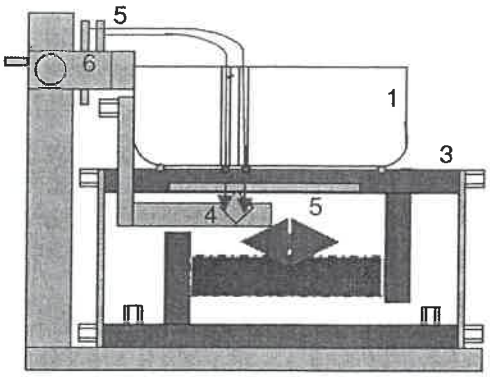

FIGURE-4 SCHEMATIC REPRESENTATION OF DISPALCEMENT MEASUREMENT SETUP
1. SKID-MOUNT, 2.PZT, 3.FLEXURE-STRUCTURE, 4.PHOTO-DIODE, 5.GRATING, 6.DUAL FIBER

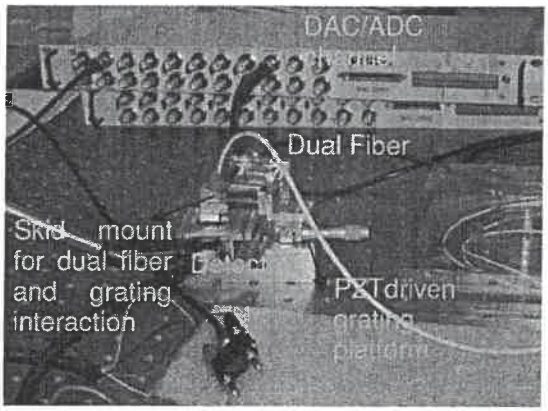

FIGURE-5 EXPERIMENTAL SETUP FOR DISPALCEMENT MEASUREMENT USING DUAL FIBER ANG GRATING

The skid mount and the flexure support makes the fibers run over the grating with constant separation distance. For course motion of the skid mount in the initial adjustments with detector position linear stage is used (Newport-M-SDS25). The laser source used is 633 nm wavelength pigtailed lasers (FDRV0635-005SFO) from Bluesky research co. This laser is operated on 5 V DC source with output power of 5mW, using a fiber coupler and a standard FC connector output from the laser is distributed among two fibers. Two bare fibers were coupled with the coupler fibers using fusion splice technique. Shielding provided on the bare fibers and the ends of the bare fibers were held together by bonding them into a ferrule. Photo diode used in the data collection is FDS 100 from Thorlabs. This photodiode was characterized for the noise, and sensitivity before the experimentation. Based on the characterization results the sensitivity of the diode is 95% and the noise power spectral

density when observed on the spectrum analyzer (SRS 780) is $1mV^2/Hz$ for 120 Hz bandwidth. Using an adjustable dial indicator stand the photodiode is positioned below the grating. The photodiode is operated with 15V reverse bias operation. Using electronic circuits for noise and amplitude detector performance was improved. The flexure based platform on which the grating is mounted is calibrated for the 17 micrometer of displacement using a capacitance gauge (Lion Precision™). Voltage is applied to the PZT using LabView program, through a DAC channel, and single channel piezo driver (MDT691 Thorlabs). The output signal from detector was recorded using an ADC. Low pass filter was used in the output signal from detector to eliminate aliasing effect.

RESULTS

Currently the experimental apparatus is being developed to measure the displacement and address issues like repeatability of data. An investigation in near field sensing is also ongoing.

CONCLUSION

The theoretical study has been initiated to identify the diffraction for far field situation. This study also helps understand the details of mathematical modeling of grating and dual source interaction.

Near field approach is considered as next steps of investigation. The future steps are to redesign the platform for grating mounting such that feedback system can be incorporated for near filed experimentation. Also design of holding ferrule for dual fiber at some constant separation distance is important. Detector positioning design is critical for collecting signal from the near filed interaction.

ACKNOWLEGEMENTS

This work is supported by SINAM UCLA and Charlotte Research Institute Charlotte NC. Special thanks to Dr Robert Hocken and Dr. Stuart Smith for their support through out the work.

REFERENCES

1. Eugene Hecht, OPTICS (4^{TH} Edition), Addison Wesley 2001
2. Yves Jourlin, Oliver Parriaux, Alexander V. Tischenko, Phase relationship in two beam grating combiner, Optical Engineering 40(8) 1464-1470 2001
3. Chich Kung Lee, Chyan-Chyi WU, Shih-Jui Chen, Liang Bin Yu, Design and Construction of Linear Laser Encoders that possess high tolerance of mechanical run out
4. David S. Nyce, Linear Position Sensors, Theory and Application, John Wiley & Sons INC, 2004

ANALYSIS AND PERFORMANCE OF A PARALLEL-AXIS FLATNESS MEASURING INSTRUMENT

Eric R. Marsh[1], R. Ryan Vallance[2]
[1]Mechanical Engineering
Penn State University
University Park, PA, USA
[2]Mechanical Engineering
George Washington University
Washington, DC, USA

ABSTRACT

This paper describes the design, analysis and performance of a flatness inspection instrument to measure workpieces with up to one millimeter departure from flatness. The instrument uses two air bearing spindles arranged with parallel axes to simultaneously rotate a workpiece and slowly pass a capacitance probe over the spinning surface. Capacitance probes offer user-selectable sensitivity to provide multiple combinations of measurement range and resolution. In tests with a high sensitivity probe, the instrument demonstrated measurement repeatability of 25 nanometers on a Ø75 mm workpiece. This paper presents a complete homogeneous transformation matrix analysis of the propagation of errors into the measurement as well as sample measurements on diamond-turned workpieces.

INTRODUCTION

In this work we introduce an instrument for measuring flatness that bridges the performance gap between the CMM and interferometry in range, resolution, and surface finish requirement. This instrument, shown in Figure 1, uses two air bearing spindles in place of the linear bearings found in CMMs. Falter and Dow used this same rotary bearing configuration, with the addition of a piezoelectric actuator, for diamond turning nominally flat workpieces [2]. Rotational bearings offer more accurate motion than linear ways at the expense of flexibility in the allowable workpiece topology; in practice the rotary bearing configuration is suitable for plano (flat) and/or axisymmetric parts. The accuracy of a spindle-type instrument is high and the rotational error motions can be quite small (less than 25 nanometers) compared to other contributors to measurement uncertainty such as thermal growth and machine geometry. Furthermore, the scanning speed of a spindle-type instrument can be somewhat higher than a CMM while maintaining this high level of accuracy.

This paper describes the parallel axis flatness measuring instrument, the propagation of its geometrical and spindle errors into the measurement as predicted by homogeneous transformation matrix (HTM) models, and its performance on diamond-turned workpieces. As will be shown, the HTM model analysis leads to a self-checking procedure that reduces the residual measurement error to the order of 50 nm. Furthermore, sample measurements show 25 nm repeatability for workpieces with sub-micron flatness.

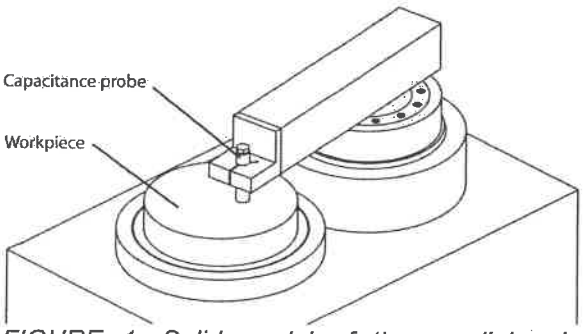

FIGURE 1. Solid model of the parallel axis flatness instrument.

The flatness measurement is carried out by scanning the part with a non-contact displacement sensor such as a capacitance probe. A workpiece is placed on an air bearing spindle and rotated at a few hundred revolutions per minute while a second spindle swings the displacement indicator over the part in the same way as the read head passes over the spinning disk in computer hard drives. The measurement data provide a scan of the workpiece that may be gathered as either a continuous spiral or discrete rings. The largest friction source in an

air bearing spindle occurs as a result of shearing the thin film (a few micrometers) of externally-pressurized air and is so small that the workpiece spindle can be unmotorized to eliminate the influence of motor pole cogging on the flatness measurement, which can be 10 to 100 nanometers in amplitude, even with high quality frameless, brushless motors [3]. In the prototype instrument introduced in this work, the probe arm sweeps the part in discrete steps across the rotating workpiece surface. The concentric rings of data are digitized and subsequently post-processed in software with synchronization provided by rotary encoders on each air bearing spindle.

The workpiece and probe arm spindles exhibit error motion typically between 5 and 25 nanometers in instrument-grade air bearing spindles [3]. Any axial and face spindle error motion will erroneously appear in the measurement as form error of the part being measured, as shown in Figure 3. Furthermore, the contribution of each spindle's face error motion is a function of the radial location of the displacement sensor. For the workpiece spindle the radius gets smaller as the probe approaches the axis of rotation while for the probe spindle, the radius is fixed.

The non-parallelism of the two spindles' axes of rotation leads to additional inaccuracies in the flatness measurement results. If the spindles are not perfectly aligned, the error manifests itself in different ways depending on the direction of the tilt. Care must be taken to properly account for the Abbé errors based on the alignment of the axes of rotation for the two spindles.

The effects of spindle error motions and the alignment/geometrical errors may be explored quantitatively using homogenous transformation matrix models of the instrument [2]. The HTM method allows the systematic modeling of various error sources in an instrument including spindle error motion and geometry errors (e.g., squareness, parallelism). The HTM method is well documented in the literature; Slocum [2] provides additional insight for the specific application of precision machine design and spindle analysis. The method tracks the geometric location of coordinate frames during the simulated motion of a machine using matrix-based calculations. The transformations between coordinate frames are mathematically represented by 4×4 translation and rotation matrices in Denavit-Hartenberg notation. This approach is readily adapted to predict how the flatness instrument's errors affect the measurement.

It is possible to evaluate the instrument accuracy at a single measurement point using a complete (i.e., nonlinear) analysis or by first linearizing the terms in Equation 3 by assuming small angles and ignoring higher order terms. Since both approaches only evaluate the error at a single point, neither calculation can predict the shape of the error surface without further analysis, but either approach allows for the estimation of the relative importance of the various contributors. This accuracy estimate is a function of the nominal instrument geometry, the alignment and spindle errors, and the angular position of the two spindles.

In practice, we are interested in measuring the flatness of an entire surface. Therefore, a complete investigation of the machine performance requires repeated evaluation of the HTM model, post processing to remove piston and tilt (using a least-squares fit plane) from the resulting surface, and examination and interpretation of the remaining errors as computed by exercising the HTM model. Piston is an arbitrary displacement along the axis of rotation and tilt (or wedge) is the inclination of the workpiece surface to the axis of rotation. Either error could be caused by a piece of debris under the workpiece and neither is relevant for a flatness measurement; both errors must be properly removed in software by least-squares removal of a plane from the data set.

The error values used in the simulation are based on careful measurements on prototype hardware. The values for geometry errors (parallelism, etc) were obtained from measurements taken on a prototype flatness instrument using a Moore measuring machine. The spindle error motion values are based on previous measurements published by Grejda and others [1]. These representative values are used to quantify the contribution of individual error components, but would not be sufficiently accurate or stable for nanometer-level correction of the measurement results.

Figure 2 shows typical results from the HTM model simulation with the ten contributing errors. The illustrations are individually scaled so that the character of each component is plainly

visible. The numerical values show that the largest contributor to measurement error is the alignment between the two spindles and the wedge (out-of-parallelism between the two sides) of the workpiece. In general, the contribution of the spindle errors is small compared to the geometrical alignment errors. However, as will be seen in the next section, the largest geometrical errors can be removed by an error separation procedure that was developed in the course of this research and verified using the HTM model. Wedge is removed by the least-squares fit plane.

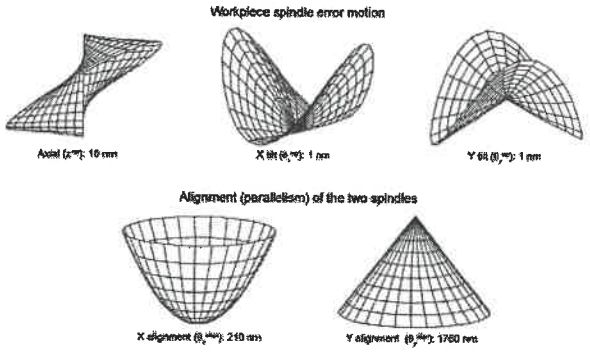

FIGURE 2. Schematic of the effects of the ten geometry errors on the flatness measurement.

EXPERIMENTAL SETUP

A prototype instrument demonstrates the utility of the parallel-spindle arrangement to flatness measurements. The prototype instrument was designed to measure conventionally-turned, diamond-turned, milled, ground, or lapped parts up to 150 mm in diameter and 70 mm thickness. The spindle layout of the instrument is small yet scalable to measure larger workpieces given air bearing spindles of sufficient capacity. There are a variety of issues to be considered in the instrument design that are summarized here.

The two instrument-grade spindles (Professional Instruments 4R) used in the flatness instrument exhibit synchronous axial error motions of less than five nanometers [1,3]. The additional contribution of tilt error motion leads to synchronous face error motions of less than 10 nanometers at a radius of 200 mm, as shown in Figure 3. Both spindles have 4096-count per revolution rotary encoders for angular position feedback. The probe arm spindle is motorized via a stepper motor drive with a friction (capstan) drive on the underside of the spindle. A friction drive was chosen for its relatively small influence on the spindle. Importantly, the stepper drive is not enabled or moved during the measurement so that the scans are made on discrete radial bands of constant radius.

All displacement measurements were made using a capacitance probe (Lion Precision C1-C with DMT 12 driver). These non-contact sensors were calibrated with a sensitivity of 2.5 nm/mV and a resolution of two nanometers at 20 kHz bandwidth. For non-conductive workpieces, the same sensor may be used in conjunction with a diamond stylus on a frictionless, air bearing movement (Lion Precision Contact Adaptor Probe). When low-pass filtered to a cutoff frequency suitable for this application (200 Hz), the electrical noise floor of the capacitance probe is 1 nm peak-to-valley (over 30 seconds) and 0.2 nm RMS including both the sensor system and the data acquisition system.

The data are sampled at intervals triggered by the rotary encoders (approximately 14 kHz) on the prototype instrument. Analog anti-aliasing filtering is handled using a 4-pole low-pass Butterworth filter with a 200 Hz cutoff frequency. At a workpiece speed of 200 RPM, this allows the first 60 undulations per revolution of workpiece features to pass through unattenuated. Additional digital filtering is applied in post-processing to provide a sharp cutoff of content beyond 50 undulations per workpiece revolution.

The mechanical dynamics of the structure were verified using modal analysis. The first mode of vibration is characterized by the probe arm bending in the sensitive (measurement) direction at 665 Hz. Therefore, the critical dynamics of the test structure are automatically removed from the measurement signal by the anti-alias and digital filters. The modal analysis shows that the mechanical response of the system is linear to within 5% in the 200 Hz measurement bandwidth.

The static stiffness of the workpiece-to-sensor metrology loop is 2 N/micrometer. For this geometry, the theoretical static stiffness of the air bearing spindles is over 20 N/micrometer at a radius of 150 mm. Most of the compliance is in the probe arm, which is deliberately lightweight to achieve a high natural frequency to improve instrument linearity within the desired bandwidth.

The flatness measurement is made with multiple rings of data at each discrete location of the

probe arm spindle. Any measurement averaged over multiple revolutions has a calculable average (synchronous) component and a remainder (asynchronous) component. The workpiece is inherently stable, so the asynchronous component is removed with the benefit of reducing the uncertainty of the measurement. To obtain the highest possible accuracy, it is still important to always work to reduce the asynchronous component, which will include contributions from electrical noise, data acquisition issues, air bearing spindle air pressure fluctuations, and thermal effects. In a properly conducted measurement, the asynchronous component will be small. The prototype parallel axis flatness measuring instrument typically had a maximum asynchronous component less than 12 nm peak-to-valley. Measurements that exceed this value may be discarded and retaken.

The repeatability of the instrument was assessed experimentally by checking the circular flatness of a diamond turned artifact. The standard deviation of these ten individual circular flatness tests is 1.1 nm. The peak-to-valley range of the flatness results is 3.4 nm.

EXPERIMENTAL RESULTS

The prototype instrument was used to measure the flatness of a Ø75 mm diamond turned 6061 aluminum workpiece. The lathe used to turn the measured surface has an air bearing spindle with a high-torque brushless, frameless motor. This arrangement is known to cause imprinting of the lathe spindle imperfections into the surface of cut workpieces. A 1.5 mm radius, single point monocrystalline diamond tool was used in the machining.

Figure 3 shows a representative flatness measurement to demonstrate the repeatability. The average measured flatness over ten such measurements is 123 nm with a standard deviation of 7.4 nm and a peak-to-valley difference of 30 nm. A number of interesting features show up clearly in the flatness results, including the expected print-through of the diamond turning lathe used to cut the part. The straightness of the lathe's linear motion also appears as imperfections in the radial direction of the surface. These results demonstrate the ability of the parallel axis flatness instrument to resolve small amplitude features on the measured workpiece surface. The results also show the excellent repeatability of results obtained on this instrument. The measurement has accuracy on the order of 50 nm, it is highly repeatable and stable to a bandwidth of 50 undulations per revolution of the workpiece.

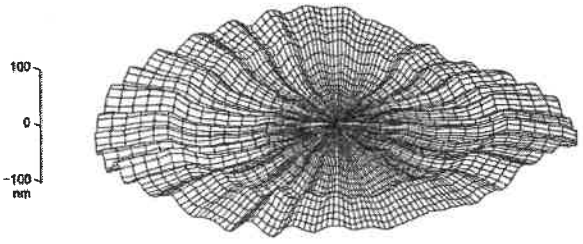

FIGURE 3. Flatness results from a typical measurement revealing motor pole cogging and machine straightness error in the diamond turned part.

CONCLUSION

The prototype instrument was then used to measure the flatness of a Ø75 mm diamond turned 6061 aluminum workpiece. The lathe used to turn the measured surface has an air bearing spindle with a high-torque brushless, frameless motor. This arrangement is known to cause imprinting of the lathe spindle imperfections into the surface of cut workpieces. A 1.5 mm radius, single point monocrystalline diamond tool was used in the machining.

REFERENCES

1. Grejda R. D., E. R. Marsh, and R. R. Vallance, *Precision Engineering* 29, 111-123 (2005).
2. Slocum A. H., Precision machine design (Prentice Hall, Englewood Cliffs, NJ, 1992).
3. Evans C. J., R. J. Hocken, and W. T. Estler, *Annals of the CIRP* 45, 617-634 (1996).
4. Bruning J. H., D. R. Herriott, J. E. Gallagher, D. P. Rosenfeld, A. D. White, and D. J. Brangaccio, *Applied Optics* 13, 2693-2703 (1974).
5. Falter P. J. and T.A. Dow, *Precision Engineering* 9, 185-190 (1987).
6. Grejda R. D., Use and calibration of ultraprecision axes of rotation with nanometer level metrology (Ph.D. Thesis, The Pennsylvania State University, 2002).
7. Abbé E., *Journal for Instrumental Information* 10, 446-448 (1890).

THE ESTIMATION FOR ERRORS OF A PLANAR XY STAGE FROM PROFILES MEASUREMENT OF GUIDE-WAYS

Jooho Hwang[1], Chun-Hong Park[1], and Seung-Woo Kim[2]
[1]Intelligent Machine Research Center, Korea Institute of Machinery and Materials, Daejeon, Korea
[2]Department of Mechanical Engineering, Korea Advanced Institute of Science and Technology, Daejeon, Korea

INTRODUCTION

A planar XY stage is frequently used as a precision positioning system for equipment producing semiconductors or flat panel display. Therefore, higher velocities and better accuracies are required to reach higher productivity and performance measures. A planar XY stage, for which an H-shaped frame is usually used as a base stage, is driven by two actuators, such as linear motors, with two position feedback sensors, such as linear scales or interferometers on the scanning motion axis. The stage is frequently used as main frame of the equipment. Therefore the machining and assembly process of rail and bed of the stage is one of first process during the equipment is built. The 2D position error, motion error and flatness of the stage can be measured when the real test is performed. If the errors of stage didn't meet the requirement of it's specification, the stage must be corrected for machining and assembly process again. It is difficult and time consuming work, if assemble and disassemble process is repeated for such a big stage.

In this paper, the estimation method for errors of a planar XY stage is suggested, which is applied during the rails and bed of stage is evaluated. To estimate the errors of a planar XY stage, profiles measurement, estimation of motion error and 2D position estimation model is used.

CONFIGURATION OF PLANAR XY STAGE

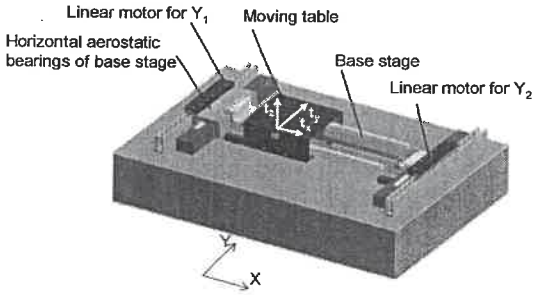

Figure 1: Schematic diagram of a planar XY stage

As shown in Figure 1, the moving table of a planar XY stage is translated along the X-axis on the base stage, which has an H-type structure and is driven by two simultaneously controlled linear motors (LM310-4, Trilogy) along the Y-axis. The stroke of each axis is 300 mm, which can be measured using a precise optical linear scale (LIP481, HeidenHain). A PC-based motion control board with a PID filter(PMAC2, Delta Tau) is used to control the position of the stage. The X and Y axes move on a granite bed, which is used as a vertical guide of vacuum preloaded aerostatic bearings for two stages to avoid deflection of the table and base stage and to reduce the moment force in high acceleration motions. A double pad aerostatic bearing is used to constrain horizontal motion. As shown in Fig. 1, the base stage is constrained against horizontal motion only at the aerostatic bearing on the Y_1-axis.

PROFILE MEASUREMENT OF GUIDE-WAYS

The profile of guide way is measured by three-probe system, that can be used to measure the parallelism and straightness of a pair of rails simultaneously [1]. The parallelism is measured using a modified reversal method, while the straightness is measured using a sequential two-point method as shown in Figure 1. The profile can be expressed as

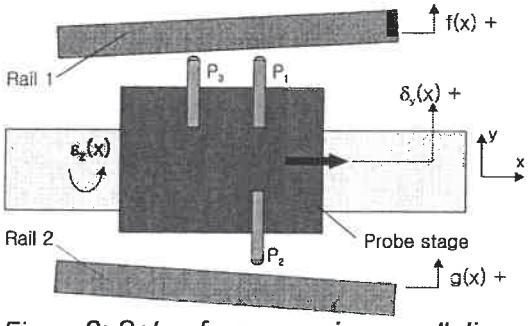

Figure 2: Setup for measuring parallelism and straightness

$$f(x_i) \approx f_d(x_i) = f_d(x_{i-1}) + m_1(x_i) - m_3(x_i) + l\varepsilon_z(x_i)$$
$$g_d(x_i) \approx f_d(x_i) - (m_1(x_i) + m_2(x_i)) \quad (1)$$

Where, $m_1(x)$, $m_2(x)$ and $m_3(x)$ are measured data of corresponding probes. The measured profiles of each guide-ways are shown in Figure 1~3.

ESTIMATION OF THE MOTION ERROR

Static equilibrium model of stage

The static equilibrium modeling, which is considered by change of reaction force and displacement for single porous pad of aerostatic stage, is shown in Fig. 6. Where, W is external load of table including weight; m is number of the pad in table; X_{ci} is distance from center of table to center of pads; L is length of rails; $F_i(x)$ and $Z_i(x)$ are i^{th} reaction force and corresponding displacement of center of pads, while position of center of table is x; $\theta(x)$ is slope of the table.

If the relationship between the profile of rails and each pads of table is considered, the pad of table is moved to new equilibrium state owing to changed aerostatic reaction force($f_{ei}(x)$) and new displacement of stage ($z_i(x)$), while the reaction force is $F_i(x)$.

Assuming the stiffness of aerostatic pads are constant within the small displacement of stage, the relation ship between the $f_{ei}(x)$and $z_i(x)$ is explained as

$$f_i(x) = f_{ei}(x) - K_0 z_i(x) \quad (2)$$

Considering the Eq. (2), moment equilibrium from reaction force of pads is explained as Eqs. (3) and (4).

$$\sum_{i=1}^{m} \{ f_{ei}(x) - K_0 z_i(x) \} = 0 \quad (3)$$

$$\sum_{i=1}^{m} f_{ei}(x) \left(X_{ci} - R_i(x) + \frac{ml}{2} \right) = \sum_{i=1}^{m} K_0 z_i(x) \left(X_{ci} + \frac{ml}{2} \right) \quad (4)$$
$$x = \frac{ml}{2}, \cdots, L - \frac{ml}{2}$$

The Fourier transformed profiles of rails ($e(x)$) is explained as

$$e(x) = a_0 + \sum_{k=1}^{n} \left(a_k \cos \frac{2k\pi}{L} x + b_k \sin \frac{2k\pi}{L} x \right) \quad (5)$$

Computation of motion error

The aerostatic bearing pads of the stage are same shape and multi supported configuration in same plane, as shown in Figure 6. Therefore, the error motion of the moving table of the stage can be calculated, from geometric relationship of each pads and calculated characteristic of one pad. It has advantage of fast calculation time during assembly process of the stage.

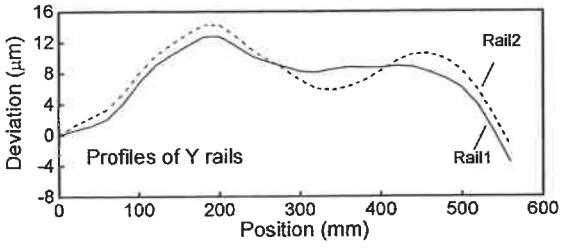

Figure 3: The profiles of Y axis rails

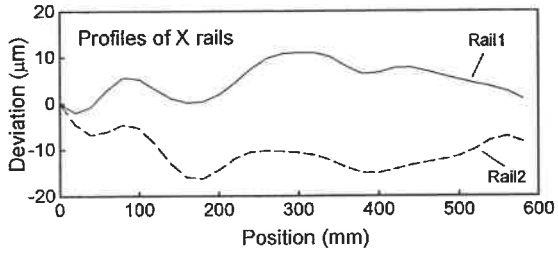

Figure 4: The profiles of X axis rails

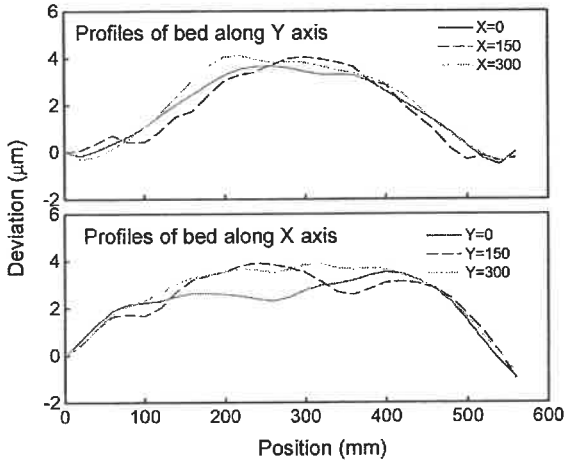

Figure 5: The measured profile of bed along X and Y axis

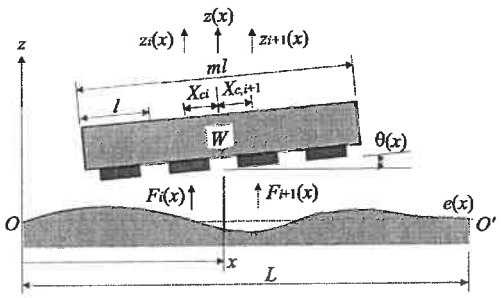

Figure 6: Equilibrium state of a porous aerostatic stage

When a porous pad is moving along the rails and the center of pad has same coordination with rails, the profiles of rails in Eq.(5) and change of reaction force of a porous pad($f_e(x)$) can be explained as spatial frequency(ω). The spatial frequency is defined as $\omega=2\pi/\lambda$, where, the wavelength for one of the sinusoidal profiles of rails id defined as λ. And, in the case of wave length is as same as length of pad (l), the spatial frequency is defined as $\omega_1 = 2\pi / l$. The change of reaction force($f_e(x)$) has same spatial frequency with rails, if the profile of rail, which has profile $e(x)$ with only single spatial frequency ω. From this relationships, the motion transfer function will be defined as

$$K(\omega)=\frac{f_e(\omega)}{e(\omega)} \qquad (6)$$

linear motion error and angular motion error may be represented by

$$z(x)=\frac{1}{K_0 m}\sum_{i=1}^{m} f_e(x+X_{ci})$$
$$\theta(x)=\frac{12}{K_0 m(m^2-1)l^2}\sum_{i=1}^{m}\left\{f_e(x+X_{ci})\left(X_{ci}-R_i(x+X_{ci})\right)\right\} \qquad (7)$$

Where, the $f_e(x)$ and $R(x)$ can be represented by Eq.(8) and Eq.(9)[2].

$$f_e(x)=\sum_{k=1}^{n} K\left(\frac{2k\pi}{L}\right)\left(a_k\cos\frac{2k\pi}{L}x+b_k\sin\frac{2k\pi}{L}x\right) \qquad (8)$$

$$R(x)=l\sum_{k=1}^{n} G\left(\frac{2k\pi}{L}\right)\left(a_k\cos\frac{2k\pi}{L}x+b_k\sin\frac{2k\pi}{L}x\right) \qquad (9)$$

The motion errors of stage can be acquired by sequential repetition calculation along moving directions.

THE ESTIMATION OF 2D POSITION AND FLATNESS ERRORS FROM THE MOTION ERRORS

The 2D position errors estimation model of planar XY stage was introduced about same stage, it is represented by Eq. (10)[3].

$$\begin{bmatrix}\delta P_x(i,j)\\ \delta P_y(i,j)\end{bmatrix}=\begin{bmatrix}-t_y\left(\varepsilon_{z1}(j)+\varepsilon_{z2}(i)\right)+t_z\varepsilon_{y2}(i,j)+\delta x_1(j)+\delta x_2(i)\\ t_x\left(\varepsilon_{z1}(j)+\varepsilon_{z2}(i)\right)-t_z\varepsilon_{x2}(i,j)+a_2(i)\varepsilon_{z1}(j)+a_2(i)\theta_{12}+\delta y_1(j)+\delta y_2(i)\end{bmatrix} \qquad (10)$$

In Eq. (13), each error motion contains an i or j index, or both. These are intermittent steps of the estimation and measurement process of the 2D error in the X and Y directions, respectively. The motion errors of the stage were compared in Figure 7, between measured by inter-

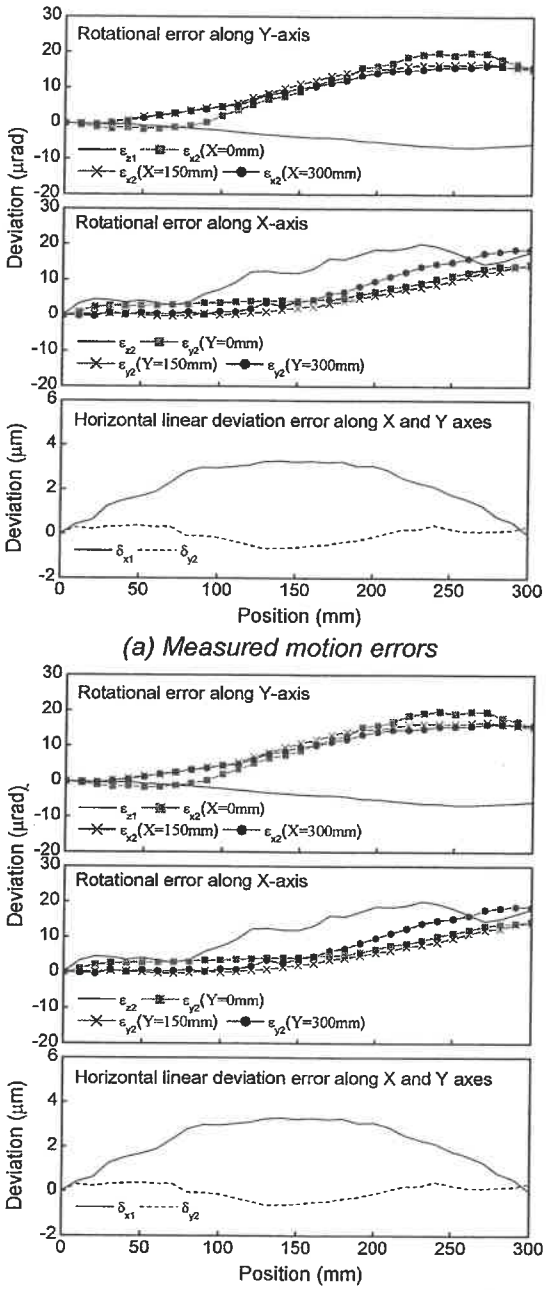

(a) Measured motion errors

(b) Estimated motion errors

Figure 7: Comparison between measured and estimated motion errors of the planar XY stage

ferometer and estimated motion error using Eq. (7) and the results of Fig. 3~5. The yaw motion of base stage (ε_{z1}) is affected by controlled position of each of y1 and y2 axis. Therefore, measured data of ε_{z1} was used in estimation of 2D position both of the cases. As shown in Fig. 7, the most of motion errors are similar, but yaw motion of moving table along X axis was shown in little bit different shape.

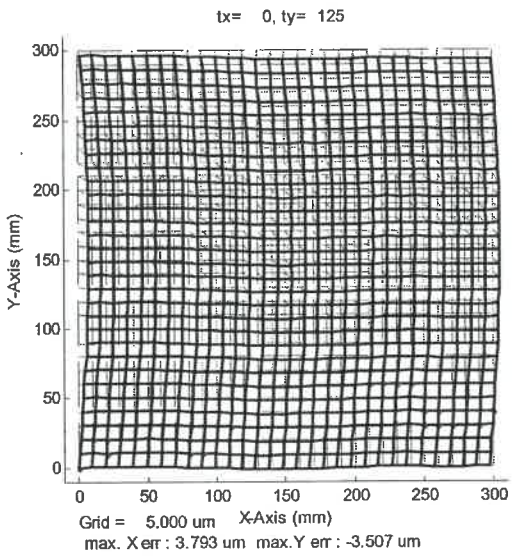

(a) From measured motion errors

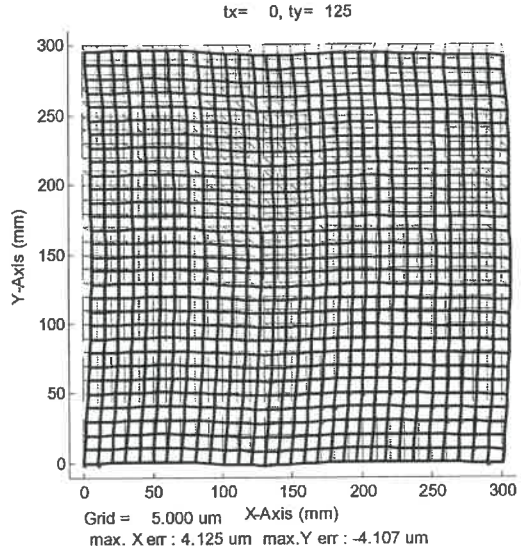

(b) From estimated motion errors

Figure 8: Comparison of 2D position errors of the planar XY stage at the center

The 2D position error of the stage was estimated from the sum of the motion errors every 10 mm over the 300 × 300-mm translational area. The 2D position errors were compared in Figure 8 for t_x = 0 mm, t_y = 125 mm, t_z = 60 mm, and θ_{12} = 0. Interpolation was used to estimate the pitch errors $\varepsilon_{x2}(i,j)$ and $\varepsilon_{y2}(i,j)$, which had similar shapes at the three different measured positions because the position difference of 150 mm was less than the span of the aerostatic bearings of the moving table (270 mm).

The straightness of flatness can be simply calculated from summation of each interpolated

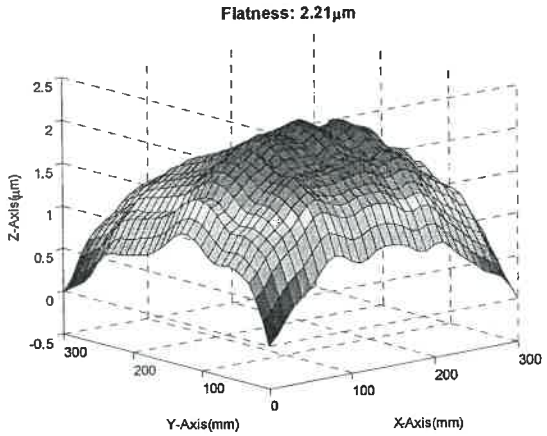

(a) From measured straightness

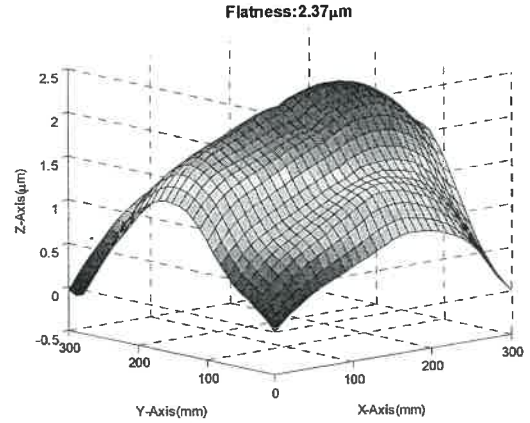

(b) From estimated straightness

Figure 9: The comparison between measured and estimated flatness

straightness data which can be measured directly or estimated from measured profile data. The comparison of flatness data were shown in Fig. 9. As shown in Fig. 9, the flatness also can be estimated from measured profile of surface of granite bed.

REFERENCES

1. J. Hwang, C.-H Park, W. Gao, S.-W. Kim, A three-probe method for measuring parallelism and straightness of a pair of rails for ultra precision machine tools, Proceedings of ASPE 2005 Annual meeting, pp.315-18, 2005
2. C.H. Park and H. Lee, Motion Error Analysis of the Porous Air Bearing Stage Using the Transfer Function, J. of KSPE Vol. 21, No. 7, pp. 185-194, 2004,
3. J. Hwang, C.-H. Park, C.-H. Lee, S.-W. Kim, Estimation and correction method for the two-dimensional position errors of a planar XY stage based on motion error measurements, I. J. of Machine Tools & Manufacture, Vol. 46, pp. 801 - 810, 2006.

DEVELOPMENT OF A TRIGGER SYSTEM TO MEASURE TOOL POSITION IN PLANETARY MILLING

Kazuhide Kamiya[1], Takashi Nomura[1], Hatsuzo Tashiro[2], and Takanori Yazawa[3]
[1]Department of Intelligent Sytems Design Engineering
Toyama Prefectural University,
Kurokawa, Imizu, Japan
[2]Department of Mechanical and Intellectual Systems Engineering
Toyama University,
Gofuku, Toyama, Japan
[3]Department of Mechanical System Engineering
Nagasaki University,
Bunkyocho, Nagasaki, Japan

INTRODUCTION

In a normal ball end milling, the relative velocity between tool and material becomes zero at the rotation axis of the tool. The relative velocity is necessary to machine materials suitably. A planetary milling method[1)] is proposed to generate relative velocity at the rotation axis of the tool, so that a high quality dimple texture can be manufactured to append surface technologies to the materials.[2)]

In the planetary milling method, the dimple shape is distorted. The ball center of the tool is not set to the intersection point of the rotation axis and the revolution axis of the tool. Therefore an optical edge detection method and an image processing technique is proposed to adjust the position of the tool for the dimple. [3,4)] The tool position should be adjusted dynamically, because the tool turns at more than 40,000 revolutions per minute. And it is necessary that the image acquisition synchronize with the revolution of the tool, because the position analysis needs images observed from the same angle. However, as a rotary encoder is not installed in the tool spindle of a general milling machine, a trigger system is needed to synchronize acquisition with the revolution.

In this paper, a simple trigger system is proposed for position measurement in planetary milling working tools. In the proposed method, marking, add-on devices etc. are unnecessary because the proposed method uses light reflected at the tool. Experimental results shows that, trigger signals obtained by the proposed method are better than the one by using marker on the tool. In the image acquisition, there were no errors with the proposed trigger system.

PLANETARY MILLING

The principle of planetary milling is shown in Fig. 1. The planetary milling method is proposed to manufacture a high quality dimple. In the planetary milling, the ball end mill turns around the rotation axis and the revolution axis. The rotation axis and the revolution axis cross each other on the center of the curvature of the cutting edge in the ball end mill. In the proposed method, the dimple shape becomes distorted if the center of the curvature of the cutting edge of the ball end mill is not set to the intersection point of the rotation axis and the revolution axis of the ball end mill. As the ball end mill turns at more than 40,000 revolutions per minute, the position of the ball end mill should be adjusted dynamically.

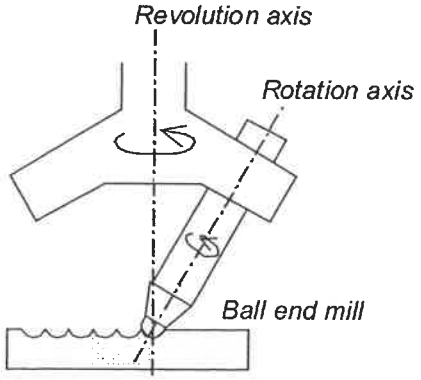

Figure 1: Principle of planetary milling

PRINCIPLE OF TOOL EDGE MEASUREMENT SYSTEM

An optical edge detection method and an image processing technique is proposed to adjust the position of the tool for machining the dimple texture. Figure 2 shows a schematic drawing of tool edge measurement system. The lens 1 and the lens 2 are Fourier transform lens and Inverse Fourier transform lens respectively.[5] The anti pinhole is put on the Fourier plane at the lens 2 for the high pass filter to generate an edge image of the tool. The lens 3 and the lens 4 magnifies the image of the tool. An edge image of the tool is captured by the CCD during spindle turning. The edge image is analyzed and the tool position is calculated by a computer.

TRIGGER SYSTEM

As rotary encoders are not installed in the spindle of the planetary milling machine, a trigger system is needed to synchronize acquisition with the revolution. Figure 3 shows a trigger system that uses the intensity of a reflecting light from a mark on the tool. It was not suitable because the signal changes depending on the size of mark and the revolution speed of the tool. A relationship between the rotary position and the signal obtained by conventional type trigger system is shown Fig. 4. The trigger signal in the old system is not responsive.

Therefore a method is proposed that uses light reflected at the tool edge. Figure 5 shows the shape of the tool edge. In this paper, the light reflected at the colored area in the flank face is used for the trigger signal. Figure 6 shows a proposed trigger system. Figure 7 shows a photograph of experimental setup. Figure 8 shows a trigger signal obtained by the proposed method. The trigger signal obtained by the proposed method is more responsive than the trigger signal obtained by the conventional system. Sensitivity has increased by seven times.

To evaluate the performance of the proposed trigger signal, tool images were captured. Figure 9 shows an edge image. As the result, there is no wrong image in 300 images captured by the proposed trigger signal.

CONCLUSIONS

In this paper, a simple trigger system is proposed for the position measurement in planetary milling while a tool is turning. As the results of experiments, the trigger signals by the proposed method are better than one using a marker on the tool. Sensitivity of the trigger signal has increased by seven times. In the image acquisition, there were no errors with the proposed trigger system.

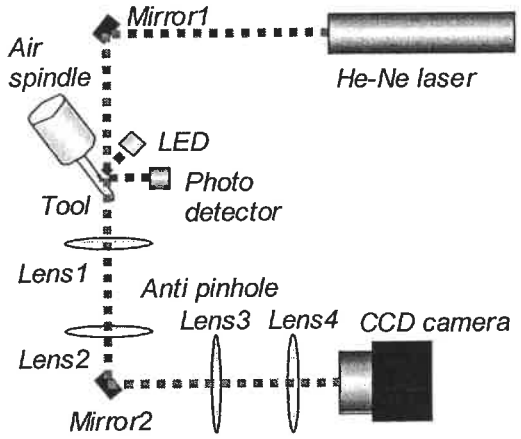

Figure 2: schematic drawing of experimental setup

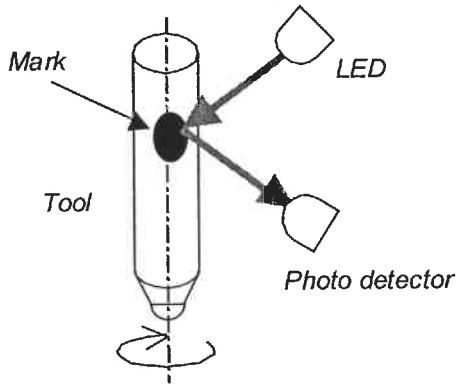

Figure 3: Conventional trigger system

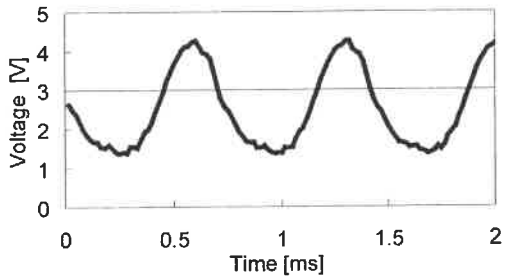

Figure 4: Trigger signal obtained by old type trigger system

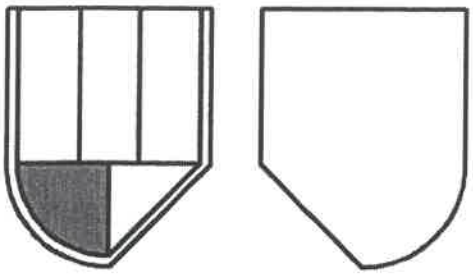

(a) Flank face (b) Rake face

Figure 5: Diamond ball end mill

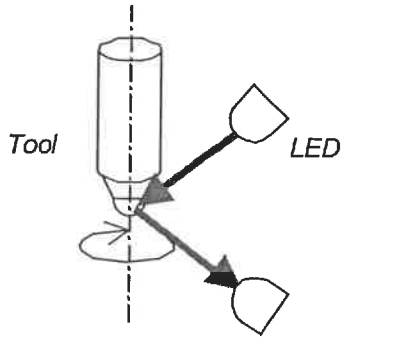

Figure 6: Proposed trigger system

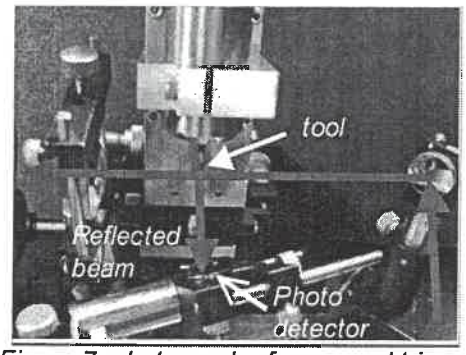

Figure 7: photograph of proposed trigger system

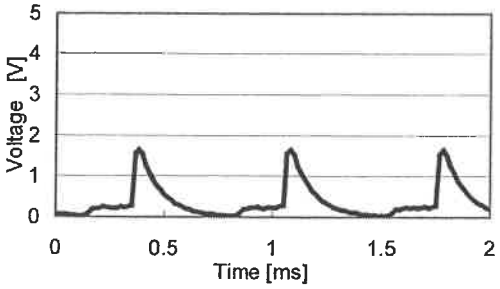

Figure 8: Trigger signal obtained by proposed trigger system

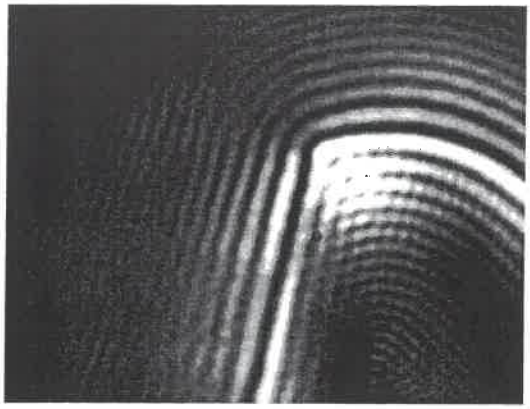

Figure 9: An edge image

ACKNOWLEGEMENTS

This work was financially supported in part by a special grant in aid from Toyama Prefectural University.

REFERENCES

1. T. Yamai, T. Yazawa and M. Masuda , Precision planetary milling for R0.1 dimple texture, Proceedings of Semestrial Conference of Japan Society of Precision Engineering, Vol.2003A , (2003), pp.428-428.
2. M. Masuda, Overview of Micro Machining Processes for Functional Surfaces, Journal of the Japan Society of Precision Engineering, Vol.68, No.2, (2002), pp.161-166.
3. K. Kamiya, T. Nomura, Y. Miyamoto, H. Tashiro and T. Yazawa, Position measurement of planetary milling working tool (2nd report), Proceedings of Semestrial Conference of Japan Society of Precision Engineering, Vol.2005S, (2005), pp.225-225.
4. K. Kamiya, T. Nomura, Y. Miyamoto, H. Tashiro, T. Yazawa, Development of position measurement system of planetary milling working tool, Journal of the Japan Society of Advanced Production Technology, Vol.24, No.1, 2006, pp.44-50.
5. W. Lauterborn, T. Kurz, M. Wiesenfeldt, Coherent Optics : Fundamentals and Applications, Springer Verlag, 1995, pp.149-180.

THE APPLICATION OF 3D OPTICAL SCANNING SYSTEMS FOR THE MEASURMENT OF SPHERICAL AND ASPHERIC SURFACES.

Wenjuan Sun, John W. McBride and Martyn Hill
School of Engineering Sciences
University of Southampton, Southampton, United Kingdom

INTRODUCTION

Optical scanning systems are widely used for precision surface measurements because they offer increased scanning speeds over stylus systems and are also non-contact measurements. The 3D optical scanning system is one type of optical scanning machine, which combines three-axis control with an optical displacement sensor in the Z axis. This type of system is widely used in precision surface measurements, and shows the potential for the 3D measurement of both spherical and aspheric surfaces.

In this paper, the systematic errors of a confocal the white light (WL) measurement system are studied, with a view to improve the performance for the measurement of spherical and aspheric surfaces. The dominant systematic errors include, positioning error, table flatness and sensor error related to surface slope. Three stages of experiments are presented identify these systematic errors. They are single line scans, optical flat measurements and calibration ball measurements. At the end of the paper, the complex circumstance, where more than one systematic error overlapped each other has been discussed. Computer simulation process also has been used to assist the identification of the systematic errors, and these are applied to the measurement of a spherical reference surface.

SYSTEM INTRODUCTION

The system used in the study uses a raster scan of the surface, with precision ball-screw motion stages in all axes. The system specification outline is given in Table 1. The motion path of the XY coordinate system is designed to scan the X axis with an increment in the Y axis. The optical sensor detects the height of the surface during the motion of XY coordinate system. The system is able to allow for data stitching in the Z axis but this is not used in this study.

White Light Sensor Head

The optical setup of the WL system is based on the chromatic depth scan principle [1] with an extended Z axis field. The system configuration is shown in Fig.1. A white-light source is used for illumination. The light focuses on various heights along the Z axis through an objective lens with longitudinal chromatic aberration. The Z position of the measured point is obtained by spectral coding of the Z axis; therefore the sensor is able to determine the Z value within a range of the chromatic aberration. The specification for the sensor used is given in Table 1.

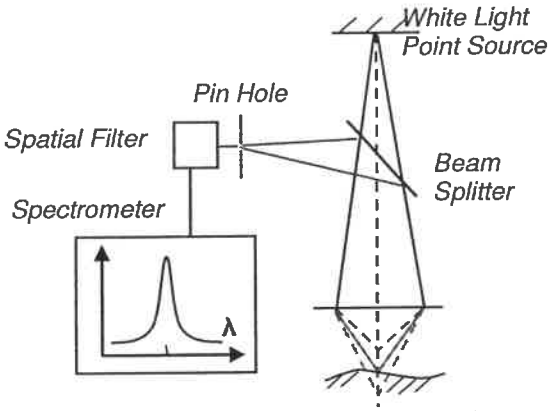

FIGURE 1. Configuration of sensor head

TABLE 1.System specification

Table Resolution	100nm
Table On Axis Accuracy	1μm
Table Range	25mm
Sensor Resolution	10nm
Sensor Gauge Range	350μm
Sensor Spot Size	7μm
Sensor Angular Tolerance	30°
Sensor Axial Accuracy	60nm

System Limitations

It can be seen from Fig. 1 that without mechanical motion of the sensor head, the maximum vertical measurable range is determined by the range of dispersed white light covered. This limitation along the optical axis is defined as gauge range, which is one of the sensor limitations. In addition the measurement is also limited by the angle of the measured

surface. Only part of the light can be reflected back to the pin hole if the surface is tilted and the surface can not be measured if the surface angle reaches certain limit. This limit is defined as angular tolerance. With these two limitations, to measure a 22mm calibration ball, the maximum measurable length of square sampling area is 5.5mm, which is approximately 14.36 degree of segment angle. The maximum scan length along the crown is 7.77mm.

SYSTEMATIC ERRORS

There are a number of potential systematic errors with the scanning system. However, only a few are dominant which can be identified in measurements. They are positioning error, table flatness and sensor error. It is assumed here that all axes are pre-aligned.

Positioning Error

The positioning error of the tables can cover a wide range of issues. The system used provides position feedback for the table, reducing back-lash and hysteresis. The dominant table error is therefore associated with the synchronisation of the sensor data acquisition with the position of the table during dynamic motion of the X axis.

There are three speed options designed for the scanning system. They are low speed (LS), medium speed (MS) and high speed (HS) modes. The differences between these modes are the scanning speed and the number of sensor readings averaged for each sampling point (refer to Table 2).

TABLE 2. Specification of different speed mode ('N' stands for the number of sensor readings averaged for each sampling point, 'SS' stands for the state of the stage (XY coordinate system)

Speed Mode	N	SS
LS	128	Stationary
MS	16	In motion
HS	2	In motion

A single line experiment was designed to test the differences between these 3 speed modes in the measurement of a 22mm radius calibration ball. The differences between different speed modes in both the scans along the X axis and Y axis are displayed in Fig. 3. The measurements covered a 7.1mm scanning length by using 143 data points.

With feed-back from the table position, the Low Speed (LS) mode where the table is stationary during sensor sampling should be the best option for measurement with low uncertainty. However a measurement using a large number of data points will take considerably more time than the dynamic measurement modes. This can lead to additional environmental influences. Therefore, it is only advisable to use this mode when the number of required sampling points is low (depending on whether the system is installed in a well conditioned environment). In the X axis the comparison shows that the MS mode produces a better result over the LS mode, which suggests that the MS mode reduces the synchronisation errors.

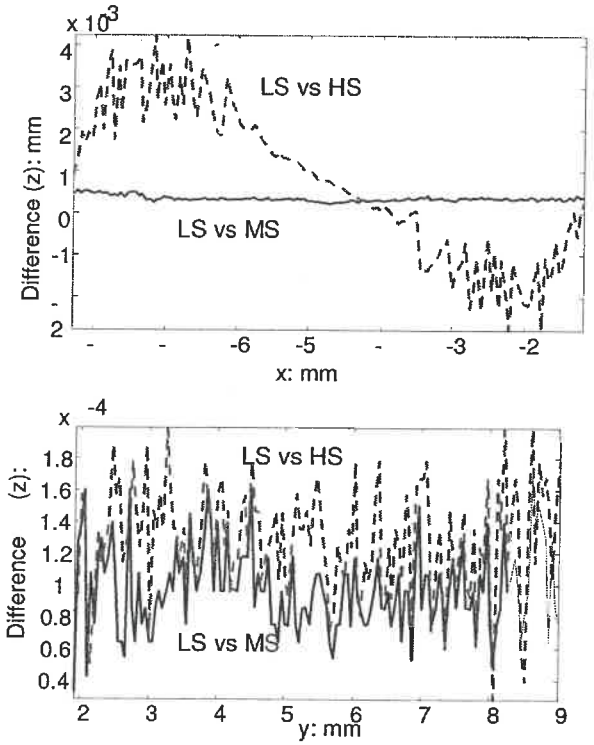

FIGURE 2. Comparisons of measurement results between different scanning modes. (Top)Along X axis (Bottom) Along Y axis Blue solid curves and red dotted curves indicate the difference between LS and MS, LS and HS modes respectively.

Table Flatness

Table flatness is defined as the maximal vertical deviation of the slide motion within a stroke length for the stage or table. It is the vertical displacement of the coordinate system. This error is significant in the measurement of flat surfaces and near plane surfaces, and can have

a fundamental influence on the sphere fitting methods used for spherical surfaces.

An optical flat (OF) surface was utilised to investigate this error. In the experiments, the OF was fixed on the stage. Therefore, any slight displacement of the stage in vertical direction will be reflected in the measurements of the OF and superimposed on the surface form. Fig. 3 shows the residuals of the OF measurement with the best-fit plane removed. The measurement is over 24mm x 24mm area by using 481 x 481 data points, which covers more than 92% of the maximum measurable area of the stage. It has been noticed that this measurement result and the residual pattern are repeatable. Although the measurement took around 26 minutes to be finished, the environmental effects, such as thermal drift do not show a significant effect in the repeat measurement, as evident from the repeated patterns on both contours, see Fig.3. The repeatable map allows for table flatness compensation.

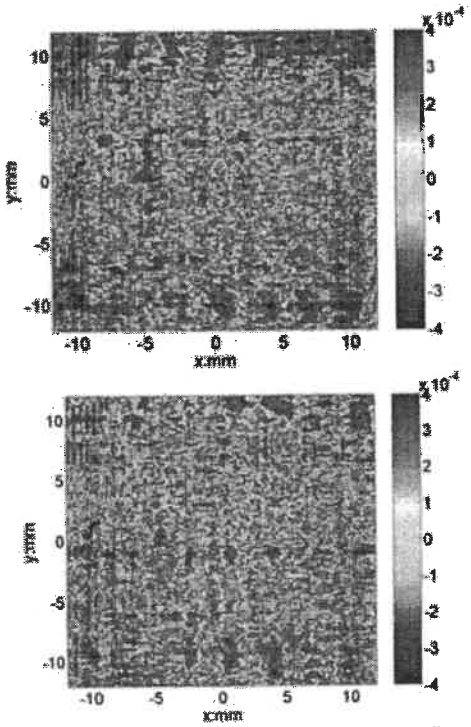

FIGURE 3. Residuals with the best-fit plane removed (the scanning result of an optical flat surface and its repeat scanning result).

Sensor Errors

In the measurement of the 22mm calibration ball, with the best-fit sphere removed, the residuals shows a centro-symmetric pattern as shown in Fig. 4, where the scan covers a 5.5mm x 5.5mm area by using 79 x 79 data points. The error is related to the optical performance of the sensor. To eliminate the error source, the calibration ball surface also has been verified by a 2D measurement system (Talysurf), which ensures the error is not due to the deformation of the CB surface. In Fig. 1, the white light sensor is limited by the gauge range and the angular tolerance. The optical setup determines the error may be related to the surface angle and the surface height, or both of them, where the residual patterns are symmetric with respect to the crown of the sphere in all of the situations.

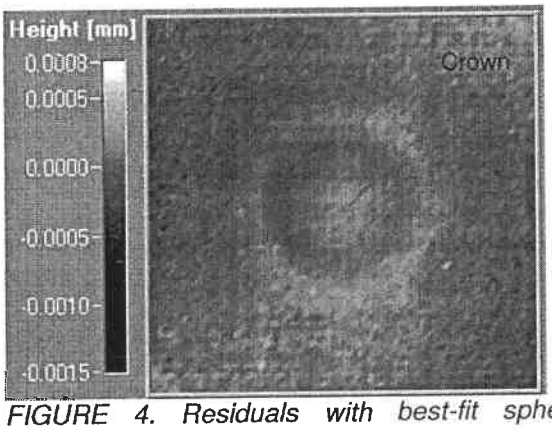

FIGURE 4. Residuals with best-fit sphere removed.

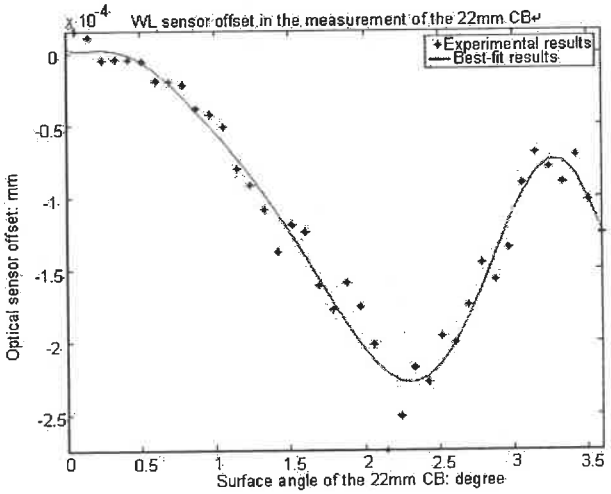
x10^-4
WL sensor offset in the measurement of the 22mm CB
Experimental results
Best-fit results
Optical sensor offset: mm
Surface angle of the 22mm CB: degree

FIGURE 5. Sensor error in the measurement of the 22mm CB.

The error relative to the crown of the surface has been further investigated, referring to the area within the dotted circle in Fig. 4. The modelling of the sensor error allows for a compensation of the data on the spherical reference surface as shown in Fig. 5 with respect to surface angle.

However, the experimental result is not sufficient to confirm the relationship between the sensor error and the surface angle as well as the surface height. Thus the results can not be generally used in the sensor error analysis. More information is required to account for the error.

Computer Simulation of Combined Systematic Errors

In the experiments, it is common to have more than one systematic error dominant in the measurement. For example, Fig. 6 shows the residual pattern with best-fit sphere removed from the 22mm CB measurements. In addition to the sensor error this is a misalignment error shown in the diagonal of the residual pattern. Empirically, it has been shown that this can be caused by the orthogonal error of the axes [2].

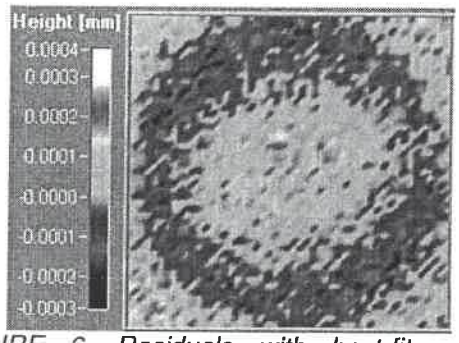

FIGURE 6. Residuals with best-fit sphere removed from the 22mm calibration ball measurements.

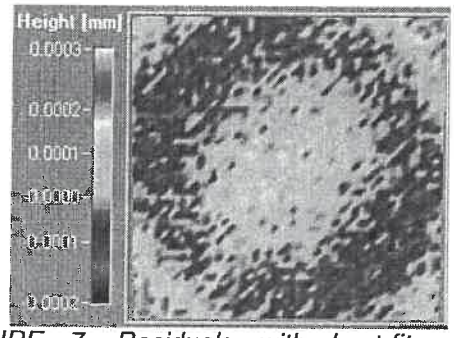

FIGURE 7. Residuals with best-fit sphere removed from the computer simulated surfaces.

A computer simulation process has been used to reproduce the combined systematic errors. A 22mm calibration spherical surface within 2.0mm x 2.0mm by using 51 x 51 data points (the same as experimental data set) was simulated. The ideal surface was then superimposed with sensor error as discussed in previous section as well as orthogonal error. A random error also has been considered [3] and added to the simulated surface. The residual pattern of the simulated surface is shown in Fig. 7. Further comparison between the measured surface and computer simulated surface is shown in Table 3, which confirms the similarity between the experimental result and the simulation result.

TABLE 3. Comparison between the experimental result and the simulation result. 'Exp' stands for experiment. 'Sim' stands for simulation.

Type	Radius: mm	Std of Residuals
Exp data	21.95304	0.088 μm
Sim data	21.94981	0.088 μm

CONCLUSIONS

In this paper, systematic errors of a WL scanning system have been briefly discussed. These errors are caused by the imperfection of different system components, where the common dominant systematic errors are the positioning error, table flatness and sensor error. A combined model for more than one systematic error has been discussed. The systematic errors discussed are unique for individual system. The character of the systematic errors may changes due to any change of the circumstance. However, the methods to study systematic errors discussed in the paper generally can be applied to the system within the same category.

This study shows how error compensation can be used in 3D scanning system to allow precision scanning of spherical surfaces. This can also be extended to spherical studies on aspheric surfaces.

REFERENCES

1. Molesini, G., et al., 1984, Focus-wavelength Encoded Optical Profilometer. *Optics Communications*, 49(4): 229-233.
2. Zhang, D., 2003, The *Assessment and Application of Form Evaluation Algorithms in Coordinate Metrology*, University of Southampton (UK), Ph.D. Thesis, 176.
3. Sun, W., McBride, J.W. and Hill, M., 2005, A Comparison between the Errors in Simulated and Experimental Data in Non-contact Surface Measurement Systems, *Proceeding of 5th EUSPEN Conference*, Montpellier, France, 37-40.

DETERMINATION OF TEMPERATURE PROBABILITY DISTRIBUTION IN MEASUREMENT UNCERTAINTY

C. Y. Fang[1], C. K. Sung[1], C. Y. Hung[2], and K. W. Lui[2]
[1]Department of Power Mechanical Engineering, National Tsing Hua University
Hsinchu, Taiwan 300, R.O.C.
[2]Center for Measurement Standards/ITRI, Hsinchu, Taiwan 300, R.O.C.

ABSTRACT
Temperature is one of the uncertainty sources in precision dimensional measurement. It is better to be evaluated by a Type B evaluation instead of a Type A evaluation, since the latter takes times and costs. A probability density function of temperature change is derived by mathematical model. Simulated data and statistical graphic analysis are used to verify the temperature probability distribution by goodness-fitting test. Results show that it has high confidence in the evaluation of the temperature uncertainty to be represented by a U-shaped distribution.

INTRODUCTION
Precision dimensional measurement is highly sensitive to the environmental temperature. A temperature of 20 °C is recommended to be the standard temperature in order to obtain the best measurement results [1], but temperature control has its limitations. The grade E of class AA laboratory proposed by JIMS 5 is delimited at ±0.5 °C [2]. Thus, measurement uncertainty due to temperature should be estimated. According to ISO GUM [3], the temperature uncertainty is usually estimated by Type B evaluation, but not by Type A evaluation due to cost consideration.

One of the main procedures for Type B evaluation is to hypothesize the probability distribution expressed by temperature effects and then deduce the Type B uncertainty from this probability distribution. If the hypothesis of the probability distribution is not appropriate, this will cause inappropriate uncertainty estimation. Tarapčík made an attempt at finding a probability distribution [4] by numerical simulation, which is mostly applied in normal and rectangular distributions, but there is no further description on the probability distribution of temperature changes. For the measurement uncertainty evaluation, the commonly used probability distributions are normal distribution, U-shaped distribution, rectangular distribution, and triangular distribution. In this paper, the probability density function of laboratory environmental temperature changes is derived from mathematical model. Simulated data and statistical analysis are used to test and verify its probability distribution by goodness of fit test. Proof of the probability distribution generated by temperature changes can be provided for users having high confidence data on Type B uncertainty evaluation and boost the quality of uncertainty evaluation. The size of laboratory and air conditioning performance may be also the influential factors to the uncertainty evaluation, but these factors will not be discussed in this paper.

PROBABILITY DENSITY FUNCTION OF THE TEMPERATURE DISTRIBUTION
The environmental temperature of a dimensional measurement laboratory is recommended to keep at (20 ± A) °C. For temperature correction in precision measurements, it is usually to observe the temperature at a specific time period ($0 \le t \le b$) which is a rectangular distributions. The room temperature variation of a temperature-stabilized laboratory against time will perform as a sine function. The temperature at time t can be represented as $Y(t)=A\sin\omega t$, where A is the half bound of the temperature variation range and ω is the sampling rate ($\omega=2\pi/b$). $Y(t)$ can be rewritten to give the equation of t, which is then used to derive the probability density function (pdf). We get $t=\frac{\sin^{-1}\left(Y/A\right)}{\omega}$ and $\frac{dt}{dY}=\frac{1}{\omega\sqrt{A^2-Y^2}}$. After a variable transform, we obtain the probability density function, $f_Y(y)$, as follow.

$$f_Y(y)=\frac{1}{\pi}\cdot\frac{1}{\sqrt{A^2-Y^2}} \quad (1)$$

Equation (1) performs a U-shaped distribution as shown in Fig. 1 and it is subjected to mathematical integration to obtain the probability sum, which is $\int f_Y(y)dy=\int\frac{1}{\pi\sqrt{A^2-Y^2}}dy=1$.

It meets the basic assumption of probability

density functions. Therefore, it is known that its probability density function is expressed in a U-shaped distribution when the laboratory temperature is in a sine distribution.

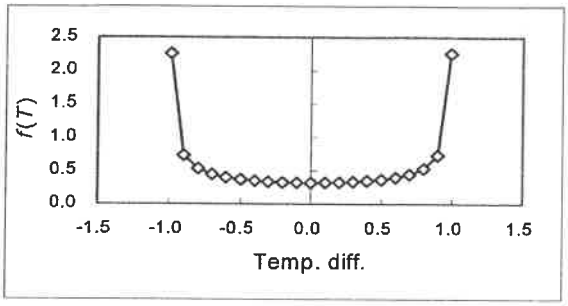

FIGURE 1. U-shaped probability density function.

VISUAL OBSERVATION OF TEMPERATURE PROBABILITY DISTRIBUTION

The environmental temperature of a dimensional laboratory is usually controlled at (20 ± 1) °C. The laboratory temperature changes in a sine function with time can be expressed as $T(t)=20\pm\sin\omega t$. We collect one measured temperature data every minute for 8 hours, which is the usual business hour for most laboratories. We can use statistical charts to help observing the distribution of the collected data. We calculate the frequency of data points by EXCEL Pivot Table Reports and then draw a bar chart as shown in Fig. 3 by using statistical table tools. Figure 3 shows data tending to be U-shaped, which meets the derived results in last section.

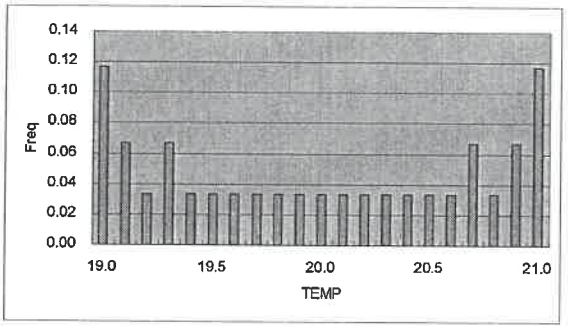

FIGURE 2. Bar chart of temperature probability distribution.

However, the charts can only facilitate the determination of data distribution patterns since the probability distribution in Fig. 2 may also tends to be a rectangular distribution. Therefore, statistical methods should be used to confirm its probability distribution, so as to minimize the probability misestimate and increase the reliability of uncertainty estimation.

STATISTICAL TESTING OF TEMPERATURE PROBABILITY DISTRIBUTION

The most common and powerful statistical methods for goodness of data fitting are Chi-square test, Kolmogorov-Smirnov test (K-S test), and A-D test. The K-S test is the most typical method among these three statistical testing models. As our collected temperature data are continuous, probability histograms are used to determine the probability distribution. Prior to draw a chart, it is necessary to determine the number of groups and its range. We can group the collected data into k groups by Stauge grouping formula, $k=1+3.32\cdot\log N$, where N is number of collected data. Since there are 480 sets of collected data, a group number (k) of 10 is obtained. The range (R) of the entire group of data is 2.0 °C. We get R/k to be 0.2 °C.

Prior to the test, we assume that the data values may appear as Beta, normal or rectangular probability distribution. We substitute the collected data into the software for testing. Table 1 summarized the results obtained from these three statistical tests at a statistical significance level of 5 %. We can firstly determine the data probability distribution by observing the mean, variance, the skewness and kurtosis of the probability distribution. Table 1 shows that the data values are close to Beta distribution.

According to Table 1, the three distributions tested by chi-square test are all rejected. This implies that the testing results of the three above-mentioned distributions are not retained. However, according to the results of K-S test and the A-D test, there is no sufficient evidence to reject the temperature data not to be expressed in a Beta distribution, i.e. U-shaped distribution. Such findings conform the previous hypothesis of this study. This means that its probability density function appear to be a Beta distribution when laboratory's temperature changes in a sine function with time. Figures 3 to 5 are comparisons of data histogram with their probability density function. The histograms in the charts are the distribution of collected data, whereas the curves show the probability density function fitted by the distributions. Figure 3 fits the above-mentioned hypotheses the best among these charts, whereas the probability density functions of Fig. 4 and Fig. 5 clearly do not meet these data histograms. Therefore, it can be assured that this data histogram is expressed in a Beta distribution

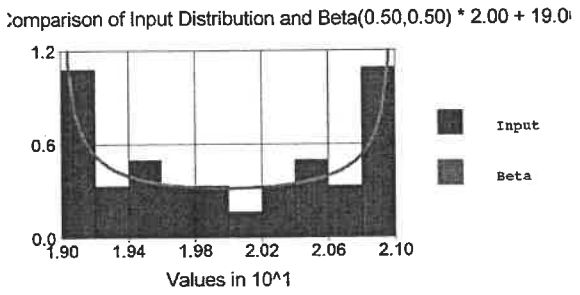

FIGURE 3. Beta distribution test.

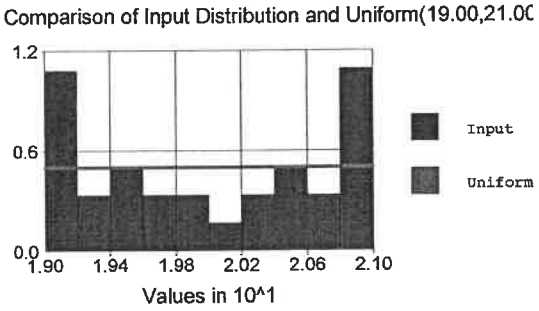

FIGURE 4. Uniform distribution test.

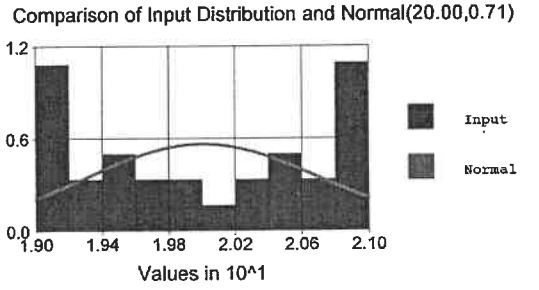

FIGURE 5. Normal distribution test.

GROUP DATA DIFFERENCES

Probability distribution of data is not determined only based on charts, but also the objective data and scientific methods. Otherwise, it may cause misestimate. If data are equally grouped into 50 sets by one's intuition instead of statistical grouping methods, the histograms of Beta distribution test and Uniform distribution test will be respectively drawn as shown in Figures 6 and 7. Data values should be expressed in a U-shaped distribution according to the original hypothesis, but they tend to a rectangular distribution in Fig. 7. If users are not observant enough, they will misuse the Type B uncertainty estimation for probability distribution and thereby underestimate the uncertainty. Although the Type B uncertainty estimation is obtained by non-statistical methods, it is practically better to use statistical methods so as to avoid underestimation or misestimate.

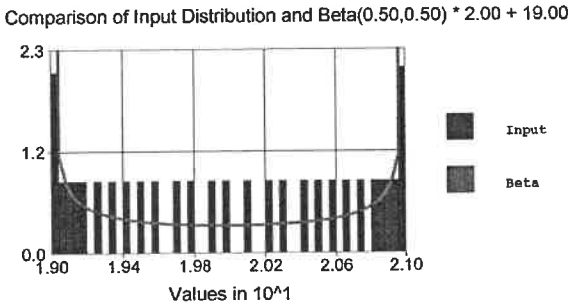

FIGURE 6. Beta distribution test (k = 50).

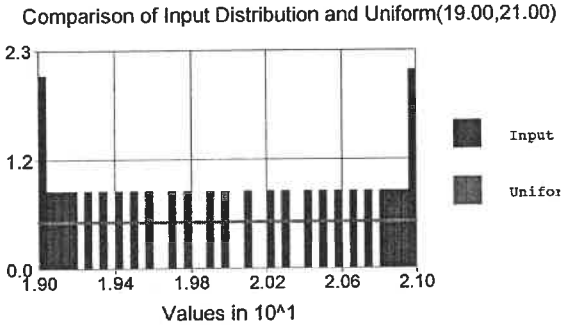

FIGURE 7. Uniform distribution test (k = 50).

TIME INTERVAL OF DATA COLLECTION

If the data acquisition interval is now 0.5 minute, 960 sets of data will be collected. The histogram and the probability density function are shown as in Fig. 8. It is found that Fig. 8 and Fig. 3 are not exactly the same, but both give a U-shaped distribution curve. Data can also be drawn in P-P chart as shown in Figure 9. In Fig. 9, the horizontal axis is the probabilities calculated from the collected data and the vertical axis is the probability values of the Beta probability distribution. When the curve closes to diagonal, the original hypothesis (i.e. is the data values approach to a Beta probability distribution) becomes more accurate. This implies that the collected data really tend to a Beta distribution (or a U-shaped distribution).

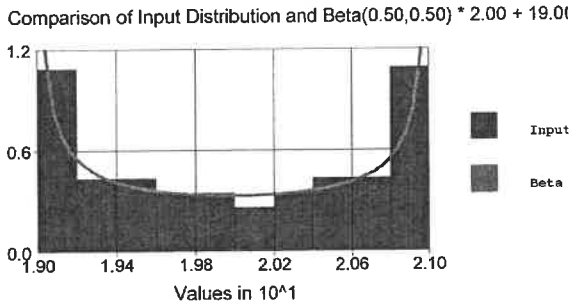

FIGURE 8. Beta distribution test (N = 960).

When the temperature probability distribution is tested by histograms, the test results appear to be unrelated to the data-sampling interval. In other words, it is not necessary to make too much consideration on the sampling interval. However, if Fig. 8 is compared with Fig. 3, Fig. 3 appears to be smoother and easily visually observed to be a Beta distribution (U-shaped distribution). Thus, The more the data sampling, the easier is the visual observation of data.

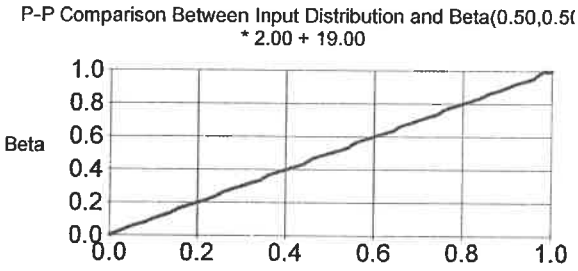

FIGURE 9. P-P chart of Beta distribution (N = 960).

CONCLUSIONS

This paper first proves that temperature stably changes in a sine function with time through the derivation of mathematical formulae, and its probability density function is a U-shaped distribution. Then, we use numerical simulation with actual data, histograms, and statistical tests to test and verify that the probability density function to be truly a U-shaped distribution. While actually executing environmental monitoring, another factor affecting the test results is the sampling size. This study shows that sampling size does not make a great impact on the results of probability distribution derivative. Therefore, too much consideration in sampling size is not necessary. However, when more data are collected, it is easier to determine its probability distribution and even visual observation can achieve the determination of probability distribution. While evaluating the uncertainty for precision dimensional measurements, Type B evaluation is usually used for temperature, but its probability distribution can only be used as a hypothesis. After applying distribution tests and verification, it is relieved to estimate the temperature effects to be an U-shaped distribution in the future. Moreover, if environmental monitoring can be computerized, the environmental temperature and relative humidity information of the laboratory can be easily accessed online in a real-time basis. By the high efficient and speedy computer computation capability, instantaneous temperature probability distribution can be immediately computed to provide the users with more convenient and accurate data to boost measurement quality.

REFERENCES

1. ISA RP52.1, Recommended Environments for Standards Laboratories, 1975.
2. 標準室のガイドライン，JIMS 5，財団法人日本産業技術振興協会，1978。
3. Guide to the expression of uncertainty in measurement, Reprinted ed., ISO, 1995.
4. P. Tarapčík, et al. "Measurement uncertainty distributions and uncertainty propagation by the simulation approach", Accreditation and Quality Assurance, Vol. 6, pp.352-359, 2001.

TABLE 1. Statistical test of Beta, normal, and uniform distributions

#Classes : 10	Interval Width : 0.2	Sample : 480		
Statistics/Distribution	*Source*	Beta	Normal	Uniform
Formula		Beta(0.50,0.50) * 2.00 + 19.00	Normal(20.00,0.71)	Uniform(19.00,21.00)
Minimum	19	18.999949		18.999949
Maximum	21	21.000051		21.000051
Mean	20.002079	20.002079	20.002079	20
Standard Deviation	0.708434	0.708434	0.708434	0.577379
Variance	0.501879	0.501879	0.501879	0.333367
Skewness	-4.16E-03	-3.92E-03	0	0
Kurtosis	1.490279	1.489988	3	1.8
Test		Beta	Normal	Uniform
Chi-Square		55.026011	583.08534	180.651536
Confidence		Rejected	Rejected	Rejected
Kolmogorov-Smirnov		0.02894	0.114786	0.123275
Confidence		>0.15 *	Rejected	Rejected *
Anderson-Darling		0.635193	15.04502	33.235429
Confidence		>0.15 *	Rejected	Rejected *

UNCERTAINTY ANALYSIS FOR A SILICON BULK MICROMACHINED DIMENSIONAL METROLOGY ARTIFACT

Meghan Shilling, Andre A. Claudet, Andrew D. Oliver, Hy D. Tran
Sandia National Laboratories
Albuquerque, New Mexico

ABSTRACT

A mesoscale dimensional artifact based on silicon bulk micromachining fabrication has been developed with the intention of evaluating the artifact both on a high precision Coordinate Measuring Machine (CMM), and on a video-probe based measuring system. A high accuracy touch-probe based CMM can achieve accuracies that are as good as the 2-D repeatability of video-probe systems. While video-probe based systems are commonly used to inspect mesoscale mechanical components, a video-probe system's certified accuracy is generally much worse than its repeatability. By using a hybrid artifact where the same features can be extracted by both a touch-probe and a video-probe, the accuracy of video-probe systems can be improved.

In order to use the micromachined device as a calibration artifact, it is important to understand the uncertainty present in the touch-probe measurements. An uncertainty analysis is presented to show the potential accuracy of the measurement of these artifacts on a high precision CMM.

ARTIFACT DESIGN

The design for the micromachined calibration device takes inspiration from the macroscale, where the step bar is an accepted calibration artifact. Step bars contain measurement planes at well-defined intervals, and are used to determine scale errors along an axis. In order to create an artifact with a measurable step interval on the mesoscale level, bulk silicon etching is used.

Anisotropic bulk micromachining creates structures with crystallographic angles which are based on fundamental physical phenomena, and thus have intrinsic angle accuracy. The edges created between etch planes are sharp to the nanometer level. The micromachined artifact is made of bulk <100> silicon anisotropically etched in a KOH solution, which creates side walls at an angle of 54.74 degrees to the near-vertical <100> plane.

For the mesoscale calibration artifact, 1.5 mm thick, 100 mm diameter silicon is used. Various sizes of trenches, which simulate a step bar, and pitches are designed to have different aspect ratios including some where the etch pits are terminated by the <111> etch planes instead of having a flat bottom. Additional shapes are created on the artifact to serve as tools for the exploration of additional calibration structures. The manufactured calibration artifact is shown in FIGURE 1 [1].

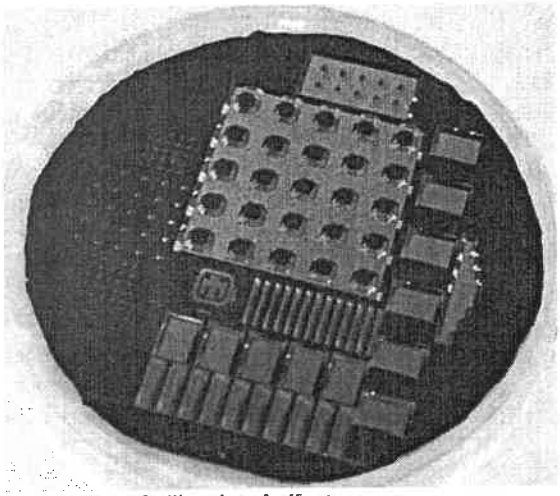

FIGURE 1: Calibration Artifact

The geometric features of the calibration artifact have are sharp edges, which can be determined via an optical probing system or reconstructed by measuring points with a CMM. The sharp edges that exist between the top and etch planes can be seen in FIGURE 2, a close-up view of a mesa structure.

A Moore M48 CMM will be used to probe both the etched planes and the horizontal planes. The computed intersection of the planes is a line segment, which can be imaged with a vision-based inspection system using coaxial lighting.

The spacing between the edges is analogous to the spacing between planes in a step bar.

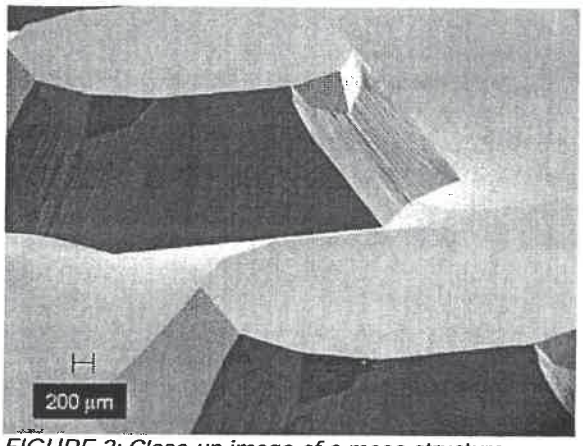

FIGURE 2: Close-up image of a mesa structure.

UNCERTAINTY ANALYSIS METHODOLOGY

In order to use the micromachined device as a calibration artifact, it is important to understand the uncertainty present in the touch-probe measurements. One of the most critical features is the line created by the intersection of the etch plane and the top plane. The touch-probe does not measure this line directly, but instead calculates it based on the intersection between two best-fit planes. It is necessary to understand the uncertainty in the calculated line because the position of the intersection line calculated from data collected on the CMM will be compared to the line directly measured by the video-probe system.

The standard method for uncertainty evaluation is described in the U.S. Guide to the Expression of Uncertainty in Measurement (GUM) [2]. Unfortunately, due to the complexity of the intersection line calculation, using the GUM methodology to determine the associated uncertainty is exceedingly complicated because sensitivity coefficients can not be derived analytically [3].

An alternative to this calculation is to use a Monte Carlo simulation to estimate the uncertainty. Monte Carlo simulations estimate the uncertainty in a measurement by assessing the uncertainty present in a large number of trials whose input conditions are varied according to the expected magnitude and distribution of uncertainty sources.

Monte Carlo simulation has been used by Schwenke et al. [3], Cox et al. [4], Trapet et al. [5], Balsamo et al. [6] and others to assess measurement uncertainty. Future revisions of GUM will include supplemental guides that deal with the use of Monte Carlo simulation as a tool for evaluation measurement uncertainty through the propagation of distributions [4].

In order to determine the uncertainty using a Monte Carlo simulation, it is necessary to first understand the individual sources of uncertainty which contribute to the overall uncertainty of the measurement, and their respective probability distribution functions (PDF).

Once these sources are identified, a model is built to mimic the process which calculates the quantity of interest. In this case the model is dictated by the methods used to calculate each of the best-fit planes and the line formed by their intersection.

Sources of Uncertainty

For this work, the uncertainty lies in the measurement points. Measurement point uncertainty comes from two sources – the touch-probe and the imperfect surface of the part.

Touch-probe uncertainties used for this investigation are modeled based on the repeatability values for each axis of the CMM over a span of time. Based on repeatability tests, the one-sigma repeatability values for the Moore M48 were found to be 15 nm for the two horizontal axes, and 25 nm for the vertical axis. A Gaussian distribution is used to model these uncertainties.

Uncertainty due to surface imperfections is a result of the combination of surface roughness and surface planarity. These numbers are taken from previous experimental work and wafer manufacturer specification, respectively. Surface roughness is 50 nm peak-to-valley. Surface planarity is stated as 1 µin over 1 in, which translates to 25 nm over 25 mm. The uncertainty values due to surface imperfections are modeled as uniform distributions.

Mathematical Model

Given data points lying on two distinct planes, the goal is to calculate the intersection line of the two best-fit planes. To do this, a plane is first fit to each of the sets of data points. Shakarji [7] specified a highly accurate least-squares reference algorithm that is commonly used to fit

CMM data to a plane. The algorithm uses Lagrange multipliers on a constrained minimization problem. Resulting from this algorithm is a point that lies on the plane and a normal vector for each of the fit planes. The line of intersection is then calculated directly from these quantities using widely available analytic equations.

Monte Carlo Simulation

With an understanding of magnitude and sources of point uncertainty and a mathematical model, a Monte Carlo simulation can be run. An example of the data from a single test case is given in FIGURE 3. Each test case starts with the intended measurement points and adds a randomized variation based to the point uncertainty model to create simulated measured data points. The simulated data points are evaluated to determine an intersection line using the algorithm described above. A large number of test cases are run and the set of all intersection lines from the test cases is evaluated to estimate the uncertainty of the intersection line under the given conditions.

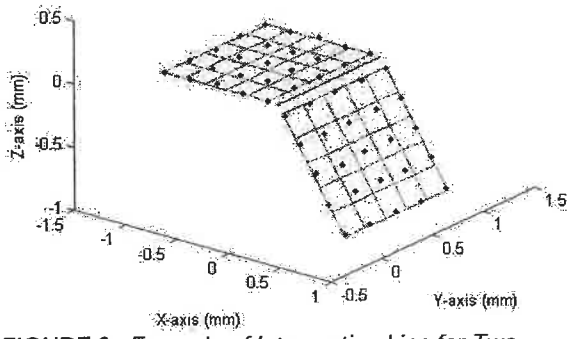

FIGURE 3. Example of Intersection Line for Two Planes

RESULTS

The results presented in FIGURE 4 are from a Monte Carlo trial based on the expected touch-probe measurement locations and associated point uncertainties. In the case of FIGURE 4, a total of 1000 data sets were generated with an intersection line calculated for each trial. FIGURE 4 shows X-Z cross sections of the set of lines at the ends and center of the measurement area. The uncertainty region appears elliptical and varies in size by position along the intersection, with the smallest variation in the center of the measurement area.

In order to quantify the uncertainty, the standard deviations (σ) along the major and minor axes of the elliptical region are calculated. An improved algorithm is used to determine the major axis, as standard routines assume no uncertainty in the abscissa.

The 2σ values at different points along the fit line for a Monte Carlo simulation with 25,000 data sets are given in FIGURE 4. As expected based on the pattern seen FIGURE 5, the deviations are higher at the ends of the line than in the middle. The k=2 uncertainty (95% confidence, or 2σ value assuming Gaussian distributions), along the major axis is approximately 40 nm at the ends, and 32 nm in the center of the measurement area. The uncertainty along the minor axis is approximately 20 nm at the ends, and 16 nm in the center.

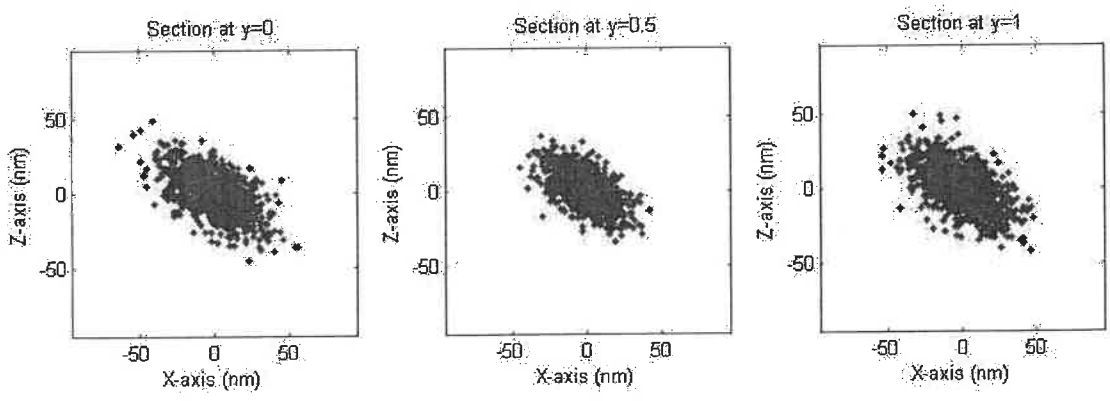

FIGURE 4: Sections at Ends and Center of Intersection Line.

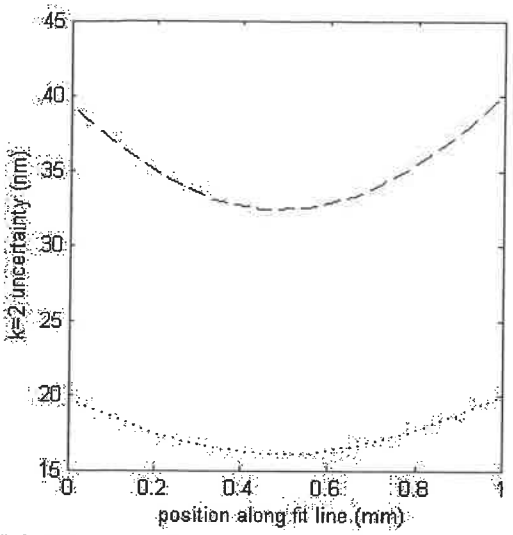

FIGURE 5: 2σ Uncertainty along Intersection Line Based on 25,000 Test Runs

Additional tests were run that varied the number of trials. A variation of a few nm was found in repeated tests with 25,000 trials. This number decreased to less than 1 nm with 250,000 trials. In addition to the number of trials, several other quantities were investigated. It was found that the number of collected data points varies quadratically with measurement uncertainty. To reduce the uncertainty by a factor of two, approximately four times the number of points is required.

Additionally, it was found that, although the area over which the points are collected does not have an effect on uncertainty, the uncertainty varies linearly with the offset of the closest measurement points from the edge. Smaller offsets produce smaller uncertainties.

SUMMARY

The goal of this project is to increase the accuracy of an optical measurement system by increasing the accuracy of the calibration artifact. Current optical calibration artifacts have uncertainty levels around 1 μm. The hope to create an artifact that can be measured with a CMM that has uncertainty levels at 1/10 of the current value, or approximately 100 nm. The numbers calculated by simulation, > 50 nm, are more than 20 times better than the accuracy of current calibration artifacts.

The uncertainty values used in these simulations were taken from literature and from previous experimental work on other artifacts. It is necessary to check the numbers, both for the artifact uncertainty and the CMM uncertainty, to make sure that they agree with the fabricated artifact under current measurement conditions. Even with slight changes in the expected uncertainty values, the overall (k=2) uncertainty of the line fit should remain below 100 nm.

ACKNOWLEDGEMENTS

This work is a product of the Laboratory Directed Research and Development program at Sandia National Laboratories. Sandia is a multiprogram laboratory operated by Sandia Corporation, a Lockheed Martin Company, for the United States Department of Energy's National Nuclear Security Administration under contract DE-AC04-94AL85000.

REFERENCES

1. Oliver, A. D., Tran, H. D., Claudet, A. A., 2006, Design of a Silicon Micromachined Artifact for Hybrid Dimensional Measurement, *Proc. of ASME Int'l Conf. on Mfg Sci. Eng. (MSEC).*
2. ANSI, 1997, American National Standard for Calibration – U.S. Guide to the Expression Of Uncertainty in Measurement, ANSI/NCSL Z540-2-1997.
3. Schewenke, H., Siebert, B. R. L., Wäldele, F., Kunzmann, H., 2000, Assessment of Uncertainties in Dimensional Metrology by Monte Carlo Simulation: Proposal of a Modular and Visual Software, *Annals of the CIRP*, 49:395-398.
4. Cox, M., Harris, P., Siebert, B. R.-L., 2003, evaluation of Measurement Uncertainty Based on the Propagation of Distributions Using Monte Carlo Simulation, *Measurement Techniques*, 46(9):824-833.
5. Trapet, E., Savio, E., De Chiffre, L, 2004, New advances in the traceability of CMMs for almost the entire range of industrial dimensional metrology needs, *Annals of the CIRP*, 53:433-438.
6. Balsamo, A., Di Ciommo, M., Mungo, R., Rebaglia, B. I., Ricci, E., Grella, R., 1999, Evaluation of CMM Uncertainty Through Monte Carlo Simulations, *Annals of the CIRP*, 48:425-428.
7. Shakarji, C. M., 1998, Least-Squares Fitting Algorithms of the NIST Algorithm Testing System, *Journal of Research of NIST*, 103(6):633-64

A SERIOUS KINEMATIC COUPLING

Eugene A. Gleason, Jr.
Bal-tec, Los Angeles, California, USA

What are the design parameters for a kinematic coupling that must repeat to a few microradians and have an unheard of minimum life of 20,000 insertions and extractions? Actually 120,000 cycles were achieved, at which point testing was stopped.

When the level of repeatability required of a kinematic coupling is in the realm of nanometers and microradians, instead of micrometers and microinches, serious attention must be paid to every detail.

At the first physical contact between the component parts, of the two platforms, of kinematic system, elastic compliance sets in. The deterministic limits, of the repeatability, of the system, begin to manifest themselves, right here.

Rather than dwelling on the inherent weaknesses we will concentrate on those positive factors that we can control to maximize function. The sum total of all the features of a serious kinematic system is that it must provide a "slippery slope" between the elements.

Slipping fosters continuous motion, of the removable platform, as contrasted with a premature sticking or stopping. The slippery part of this axiom can be enhanced by using the stiffest material possible. Stiffness here is simply the highest Young's modulus and the lowest Poisson's ratio possible. Imagine the asperities on the surfaces coming into contact, between two very stiff and then two very compliant materials. The enhanced propagation of continued movement between very stiff surfaces will be apparent.

The practical choices of ideal materials for these high-end devices are greatly simplified by the limited availability and extreme price sensitivity of most of the candidates. In addition friability is a very undesirable quality for kinematic systems, but it is very characteristic of many of the apparent candidates. Good examples of friable materials are sapphire and silicon carbide.

Cermets such as tungsten and titanium carbides, where the particles of ceramic are cemented together with a binder metal, are much tougher than true ceramics where only partial fusion of the particles occurs. Cemented carbides have the additional advantage, in that they are electrically conductive, so that they can be inexpensively machined using the EDM (electrical discharge machining) process. An additional advantage for the cemented carbides is that they are available in micro-grain (sub-micrometer particle size) material that is hot iso-static pressed (HIPED) for near 100% density.

The material chosen for this specific project was a 94 percent tungsten carbide 6 percent cobalt, micro grained, hot iso-static pressed material. This material has a Young's modulus of elasticity that exceeds 100,000,000 psi (in compression) and a hardness of 91 HRA.

The second element in the slippery part of the axiom is the surface texture. Here we are emphasizing total surface texture over simple micro finish, because the waviness element of surface texture literally provides teeth in the surfaces that can lock together and impede the slippage of the system to true mechanical equilibrium. Conventional ground surfaces have tiny undulations that aren't really slippery. Just try sliding the ends of your finger nails over a ground surface. Even the finest ground surfaces, will feel "chalky".

A really slippery surface has the grain structure of the material truncated off to a single plateau.

A good gage block has a surface texture of about one microinch (0.025 micrometer) Ra. In contrast, the surface quality of really high quality kinematic components is between 0.1 to 0.2 microinches (0.003 micrometers), (2.5 to 3 nm) Ra.

The slope part of the equation starts with the contact angle between the component parts of the system. Although a 45 degree angle is commonly used in conventional components, the very best slope for repeatability is 60

degrees. Tests have been conducted that showed repeatability of plus or minus one nanometer at this angle. Although this quite steep slope gives the best location, it dramatically reduces the load carrying capacity of the system.

Immediately, after coming into contact, with each other, the components of the two platforms slide, in at least two directions. As they move together, they rotate, and slide as they find mechanical equilibrium. To minimize stiction between the elements, the overall two-axis slope can be increased by using a sphere against two cylinders, instead of a sphere against flat prismatic surfaces. Unfortunately this increased slope is achieved with a considerable sacrifice in load carrying capacity. The total load (platform and payload) on this project was six pounds.

When the surfaces of the component parts come into physical contact, they are placed under high Hertzian elastic stress. The slipping between the two contacting surfaces, as they move to achieve mechanical equilibrium, can be a serious source of wear.

It is imperative that we understand the mechanism of this tendency for wear, if we are to minimize or eliminate it. This initial wear mechanism is similar to fretting in many ways but we prefer to use more accurate description of short stroke wear, to separate it from the true, in place fretting that can occur when the two kinematic platforms are fully engaged.

When the two component parts of the kinematic system come into physical contact, the molecular interfaces actually adhere to each other. This adhesion can be so strong that it approaches or even equals the shear strength of the materials involved. As the two surfaces, which are under high Hertzian stress, slide over each other, the molecules in the surface layers become confused. They lose their identities, and easily separate from their native materials. Under the high stresses involved at these sliding interfaces, the surface temperatures at the molecular level can be raised to a reaction level and chemical by products result. The amount of these compounds generated is minute for each insertion or extraction, but they are steadily fused by the pressure and temperature into sizable platelets. Compressive stresses exude this material from the interfaces as a thin plate. This thin sheet of chemical compound is usually an oxide of the base material, and it is very brittle. The compressive stresses that exude this material out of the intersection between the kinematic elements results in tensile stresses within the thin brittle plate that causes it to break up into small thin bricks. The thickness of these bricks, in the system under study, appears to be on the order of one micrometer, as estimated from the SEM. photomicrographs.

This relatively thin turbidity causes a significant decrease in the repeatability of the kinematic coupling. The almost certain cause of this dilemma is that these brick-lets lodge under the sphere as it approaches mechanical equilibrium. These brick-lets act as chocks that stop the sliding motion of the platform far short of its proper end position.

As is often the case in kinematic coupling systems, the allowable freeboard on this system was very limited. A six-pound load may not seem like much, but as the ball size is driven down by the constraints of the allowable free board and is exacerbated by the steep sixty-degree contact angle and the need to use cylinders instead of prismatic surfaces, the requirement for a large support radius for the cylinders becomes imperative. The ball diameter was limited to one half inch (12.7 mm), which required a three quarter inch (19.05 mm) diameter cylinder, to give an adequate safe load factor. The freeboard constraints wouldn't allow these large diameter cylinders, to be used, so the quarter round concept was employed. In this scheme the cylinders are split up into four individual components. This dramatically reduces both the height and the width of the structure.

The very rigid system employed for mounting the half-inch diameter ball consisted of burying one half of the ball in a spherical pocket and holding it in place with an M4X0.7 cap screw from behind. This configuration is a good example of the need for electrical conductivity, so that the threaded hole could be machined in the incredibly hard tungsten carbide ball, by EDM.

The three quarter inch (19.05 mm) diameter quarter rounds were housed in three sets of precision-machined trenches and were held in place by M4X0.7 cap screws.

The layout of the kinematic system was a nice symmetrical Maxwell setup, with the three vees laid out in an equilateral 120 degree pattern. The platforms were both simple aluminum plates, without any whistles or bells.

One of the factors that have not been discussed is the basic, coefficient of friction, between the materials rubbing against each other. We haven't found a lot of published data on either the breakout or running friction of the otherwise desirable materials, but we have been privy to limited information from tests performed by the materials manufacturer that indicate good to excellent performance.

After 7500 insertions and extractions were made some sporadic disparities in location began to appear. A slight modification of the coupling that connected the robotic arm to the upper platform was made. This modification changed the angle of attack very slightly. This slight change altered the path of the upper platform minutely and restored the original accuracy that repeated thru 12,000 cycles.

I believe that there is considerable significance to this ploy. By systematically altering the attack angle between the platforms, a significant improvement in the accurate life of kinematic systems could be assured.

This kinematic system was designed to ultimately be used in a moderate vacuum. After achieving excellent repeatability, but less than desired longevity, a vacuum compatible lubricant was applied to the elements of the kinematic system. Extensive testing under ambient conditions showed good results, so the system was placed in vacuum and the test was resumed. At 120,000 cycles the repeatability was still within specification and the test was concluded.

In seeking even further improvements in the performance of this really "serious kinematic coupling" testing of titanium carbide cylinders against tungsten carbide balls and against silicon nitride ceramic balls is being pursued.

THE EFFECT OF GAUSSIAN FILTER LONG WAVELENGTH CUTOFF λc IN TOPOGRAPHY MEASUREMENTS AND COMPARISONS

John Song, Li Ma* and Theodore V. Vorburger
National Institute of Standards and Technology (NIST), Gaithersburg, MD 20899
*** Guest Researcher, Kent State University, Kent, OH 44242**

1. QUANTIFYING SURFACE TOPOGRAPHY DIFFERENCES USING CCF_{max} AND D_s

Topography measurements play an important role in surface and nano-metrology, production quality control, tribology, bio-technology and forensic science [1]. Dozens of surface parameters are specified in national and international standards [2, 3]. Although none of these are designed for topography comparisons, statistical methods of auto- and cross-correlation function (ACF and CCF) may be adapted to this purpose. At the National Institute of Standards and Technology (NIST), we use the CCF maximum (CCF_{max}) and a new parameter we call the profile (or topography) difference, D_s, to quantify differences between 2D profiles or between 3D topographies [4, 5]. The CCF_{max} is the value of the cross-correlation function when the two correlated 2D profiles or 3D topographies, A and B, are located in their maximum correlation position (or "zero-shift" position) after registration. At this position, profile (or topography) difference, B – A, is calculated. The parameter of the profile (or topography) difference, D_s, is defined as [4, 5]:

$$D_s = Rq^2 (B - A) / Rq^2 (A), \quad (1)$$

where Rq^2(B - A) and Rq^2(A) represent the mean square roughness for the topography difference (B – A) and the reference topography A. Rq^2(A) is used here as a normalization factor. From Eq. 1, it can be seen that when two compared topographies are exactly the same, B = A, then Rq^2 (B – A) = 0, and D_s = 0. That means when D_s = 0, the two compared 2D profiles or 3D topographies must be exactly the same (point by point).

A 2D and 3D topography measurement and comparison system was established at NIST [6]. This system includes data acquisition stations using a stylus instrument and a confocal microscope, and a program to calculate the correlation parameters D_s and CCF_{max}, and the surface parameters root-mean-square (r-m-s) roughness Rq (or Sq for 3D) and r-m-s waviness Wq [2, 3]. Detailed information can be found in Ref. 6.

2. EXTRACTING SURFACE ROUGHNESS FROM WAVINESS AND FORM IN TOPOGRAPHY COMPARISONS

Surface topography includes a wide range of surface wavelengths, from the form in the extreme long wavelength domain, through surface waviness to surface roughness in the extreme short wavelength domain [2, 3]. However, many topography measurements are interesting only in a limited wavelength range, for example, surface roughness. An unambiguous extraction of roughness components from waviness and form plays a key role in topography measurements. A high-pass Gaussian filter, characterized by the long wavelength cutoff λc, can be used for this purpose [2, 3].

The optimum selection of λc for the extraction of roughness from waviness and form has a particular importance in ballistics identification. When bullets and casings are fired or ejected from guns, both the macro- and micro-features on the gun parts are picked up by the bullets and casings, thus creating characteristic topographies on the surfaces. For bullets, the macro-features include the number, shape, direction and angle of the twists of the gun barrel; and the geometrical size, curvature, form and waviness of the barrel surface contacting the bullets during the firing process. For casings, the macro-features include the form and waviness of the firing pin, breech face and ejector which contact the casings during firing. The macro-features represent the common characteristics of a group of guns manufactured from the same design, manufacturer and tooling process. When the macro topography feature is striated or impressed on the surface of the bullets or casings, the common characteristics form the "Class Characteristics" (as they are called in forensic science) [7] on the surface of the bullets or casings. The "Class Characteristics" are basically the similar markings for all bullets or casings fired from guns manufactured from the same production line. In forensic science, "Class Characteristics" are used for the identification of the type and the manufacturer of a weapon [7].

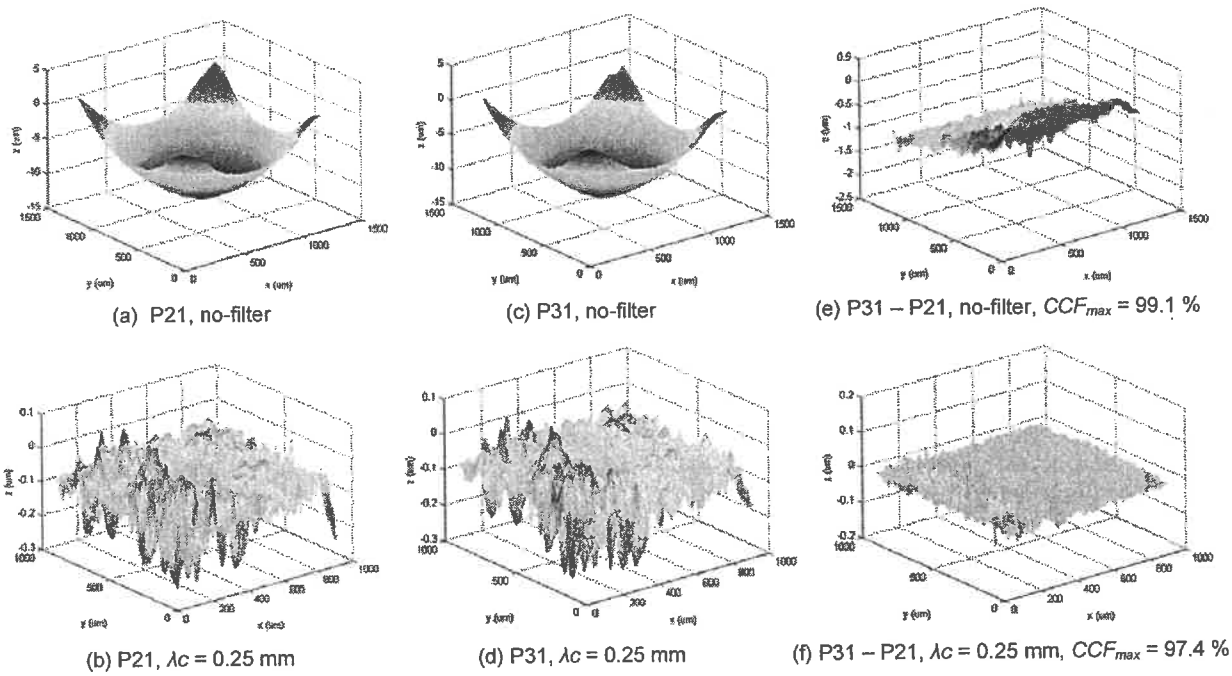

(a) P21, no-filter (c) P31, no-filter (e) P31 – P21, no-filter, CCF_{max} = 99.1 %

(b) P21, λc = 0.25 mm (d) P31, λc = 0.25 mm (f) P31 – P21, λc = 0.25 mm, CCF_{max} = 97.4 %

FIGURE 1. Topographies of the firing pin impression of P21 (a and b) and P31 (c and d) prototype standard casings are compared with no-filter (a and c) and with a Gaussian filter having λc = 0.25 mm (b and d); (e) and (f) show the corresponding topography difference, P31 – P21. The slope in (e) indicates slight differences in the calculation of the least squares mean planes between (a) and (c).

On the other hand, the micro topography or surface roughness on the gun parts represents, in addition to stochastic differences, the unique characteristics of the gun. These are different for different guns even those manufactured from the same manufacturing line one after another. When the micro topography of the gun parts is striated or impressed on the surface of the bullets or casings, those unique characteristics comprise the "Individual Characteristics" [7], or ballistics signatures. In forensic science, "Individual Characteristics" are used for the identification of an individual firearm, and for connecting the fired bullet or casing to a firearm and criminal act [7].

Figure 1 shows a 3D topography comparison between the firing pin impressions of two NIST prototype standard casings [8] P21 (Fig. 1a and 1b) and P31 (Fig. 1c and 1d). These surfaces were measured by a stylus instrument. Their 3D topographies were compared using both no-filter mode (Fig. 1a and 1c) and a Gaussian filter with long wavelength cutoff λc = 0.25 mm (Fig. 1b and 1d). The standard casings were manufactured by an electro-forming technique [9] from the same master casing, and show nearly identical surface topographies [8]. However, small differences can be detected from the topography differences, B - A, as shown in Fig. 1e and 1f.

When no-filter mode is used, the two casing topographies (see Fig. 1a and 1c) are mainly compared for their form and waviness. The topography difference D_s (see Fig. 1e), as calculated by Eq. 1, is equal to 1.8 % at the location of the cross-correlation function maximum CCF_{max} calculated to be 99.1 %. Both the high CCF_{max} and the low D_s values mainly indicate the high similarity of the waviness and form. Those could be considered "Class Characteristics" of the two standard casings. When a Gaussian filter with a long wavelength cutoff λc = 0.25 mm is used for the extraction of the roughness topography from the waviness and form, only the roughness topography is compared, as shown in Fig. 1b and Fig. 1d. The topography difference D_s (see Fig. 1f) calculated from Eq. 1 is equal to 4.2 %; the CCF_{max} is 97.4 %. Both parameters indicate the high similarity of the roughness topographies, or the "Individual Characteristics".

3. FUNCTIONAL RELATIONSHIP BETWEEN CORRELATION PARAMETERS D_S AND CCF_{max} AND SURFACE PARAMETERS *Rq* (OR *Sq*), *Wq* AND λ_C

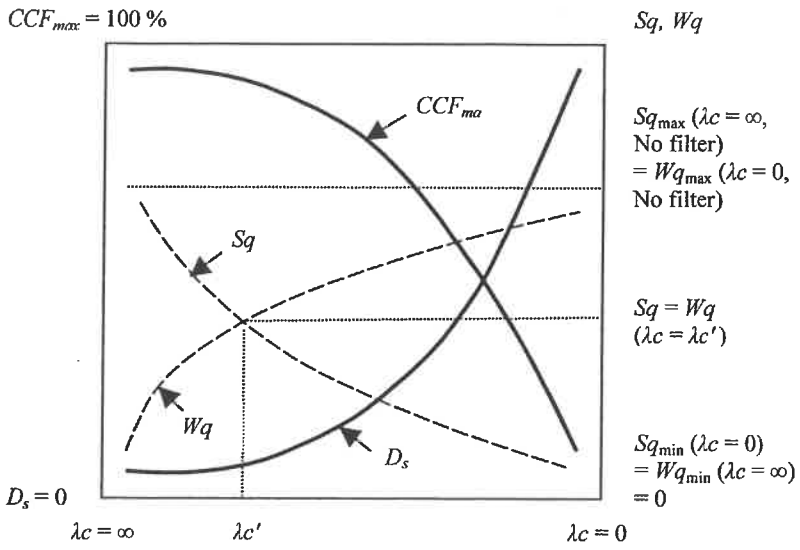
CCF_{max} = 100 %
Sq, Wq
CCF_{ma}
Sq_{max} ($\lambda c = \infty$, No filter) = Wq_{max} ($\lambda c = 0$, No filter)
Sq
$Sq = Wq$ ($\lambda c = \lambda c'$)
Wq
D_s
Sq_{min} ($\lambda c = 0$) = Wq_{min} ($\lambda c = \infty$) = 0
$D_s = 0$
$\lambda c = \infty$
$\lambda c'$
$\lambda c = 0$

FIGURE 2. Theoretical relationship between the Gaussian filter long wavelength cutoff λc, and the correlation parameters D_s, CCF_{max}, and the surface parameters Sq, Wq, assuming the topography comparisons were conducted between two 3D topographies with the same form and waviness and different but correlated roughness.

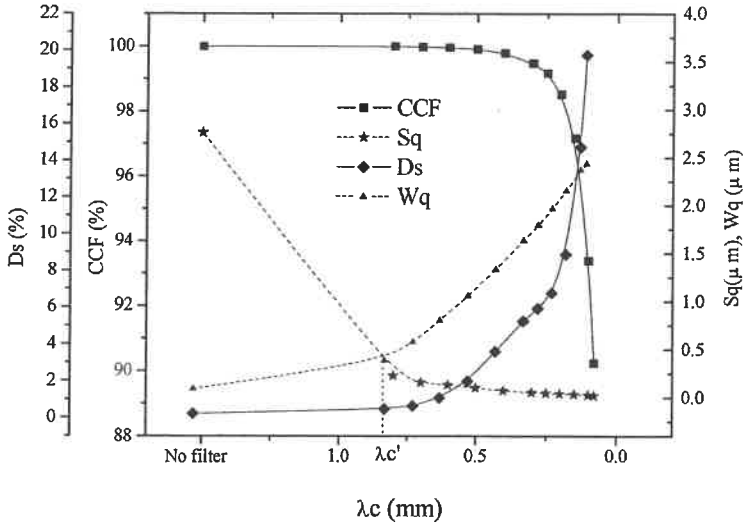

FIGURE 3. Experimental results between the Gaussian filter long wavelength cutoff λc, and the correlation parameters D_s, CCF_{max}, and the surface parameters Sq, Wq. Topography comparisons are performed on NIST prototype standard casings P21 and P31 as shown in Fig. 1. The Sq and Wq values are measured on P21 standard casing. Standard uncertainties (k = 1) are approximately 2 % of full scale for D_s, Sq and Wq and approximately 1 % for CCF_{max}.

Figure 2 shows a theoretical analysis of the functional relationship between λc and D_s, CCF_{max}, Rq and Wq [1], assuming that the topography comparisons are conducted between two 3D topographies having essentially the same form and waviness and having different but correlated roughness, such as those of the NIST prototype standard casings shown in Fig. 1. With the decrease of the long wavelength cutoff λc for roughness measurement, which also represents the short wavelength cutoff for waviness measurement [2, 3], the roughness, Sq, decreases and the waviness, Wq, increases (see Fig. 2). Meanwhile, the CCF_{max} for the roughness correlation decreases and the roughness topography difference D_s increases, because successively fewer waviness and form components are compared; and the two topographies are compared more via their roughness components, which are correlated but have small differences in the fine details. With the increase of long wavelength cutoff λc, the roughness Sq increases because more waviness and form components are included as roughness topography. That results in a large CCF_{max} and small D_s, because the similar waviness and form components dominate the comparison.

Figure 3 shows experimental results supporting the theoretical relationship shown in Fig. 2. In Fig. 3, topography comparisons are performed between two 3D topographies of NIST prototype

standard casings P21 and P31 (as shown in Fig. 1) using different λc ranging from 0.08 mm to 0.8 mm, and a no-filter mode. The experimental results in Fig 3 support the theoretical analyses shown in Fig 2. From Fig. 2 and 3, it can be seen that at the cutoff of $\lambda c = \lambda c'$, the roughness and waviness have equal value for Sq and Wq. That suggests an approach for the optimum selection for the Gaussian filter long wavelength cutoff, $\lambda c'$, by which the roughness topography is extracted from the waviness and form at the level where $Sq = c \times Wq$ $(c < 1)$, and c is a constant to be experimentally determined, which produces an optimum correlation for ballistics signatures from the same gun.

4. OPTIMIZING THE GAUSSIAN FILTER LONG WAVELENGTH CUTOFF λc IN FORENSIC BALLISTICS IDENTIFICATION

In ballistics identifications, poorly selected λc might result in the "Class Characteristics" being inappropriately included in the "Individual Characteristics", resulting in a sub-optimum correlation. Furthermore, a fired bullet may be deformed or even broken when striking hard objects, and fired casings may show different deformations due to the change of firing conditions. As a result, the "Class Characteristics", or the size, form and waviness on the fired bullets and casings, might be completely changed. However, the micro roughness topography, or the "Individual Characteristics", can still exist on the surface of the fired bullets and casings, and can be used as evidence for ballistics identification. In that case, by using a Gaussian filter with a correctly selected long wavelength cutoff λc, the "Individual Characteristics" (surface roughness) can be unambiguously extracted from the "Class Characteristics" (waviness and form) for ballistics identification.

The NIST 2D bullet signature measurement system [6] has been enhanced for 3D casing signature correlations. A standardized Gaussian filter cutoff λc = 0.25 mm is currently used for the correlations of 3D casing signatures [10]. However, we have found that when the form of the two compared casings shows large differences, the cutoff of 0.25 mm might be only suitable for one casing but not for the other. As a result, after the Gaussian filter using λc = 0.25 mm, some waviness and form components may still remain in the roughness topography for correlation, which yields a sub-optimum correlation.

We are therefore planning to optimize the choice of long wavelength cut off to improve casing signature correlations. It is possible that the information content in this process will be optimized by maintaining a fixed ratio between roughness and waviness i.e. $Sq = c \times Wq$.

REFERENCES

1. Song, J. and Vorburger, T., "Topography Measurements and Applications," 2006 International Symposium on Precision Mechanical Measurements (ISPMM), Urumqi, China, August 2006.
2. ASME B46-2002, *Surface Texture (Surface Roughness, Waviness and Lay)*, ASME, 2002.
3. ISO/WD 4287-1997, *Geometrical Product Specification (GPS) – Surface Texture: Profile Method – Terms, definitions and parameters of surface texture*, ISO, 1997.
4. Song, J. and Vorburger, T., "Proposed Bullet Signature Comparisons Using Autocorrelation Functions," *Proc. 2000 NCSL*, July 2000, Toronto.
5. Song, J., Vorburger, T., Ma, L., Libert, J. and Ballou, S., "A Metric for the Comparison of Surface Topographies of Standard Reference Material (SRM) Bullets and Casings," *Proc. of 2005 ASPE*, October 2005, VA.
6. Ma, L., Song, J., Whitenton, E., Zheng, A., Vorburger, T. and Zhou, J., "NIST Bullet Signature Measurement System for RM (Reference Material) 8240 Standard Bullets," *J. Forensic Sci.*, **49**, (4), July 2004, pp. 649-659.
7. Moenssens, A. et al., *Scientific Evidence in Civil and Criminal Cases*, 4th ed., Foundation Press, NY, 1995.
8. Song, J., Whitenton, E., Kelley, D., Clary, R., Ma, L and Ballou, S., "SRM 2460/2461 Standard Bullets and Casings Project", *J. Res. Natl. Inst. Stand. Technol.* **109,** (2004), pp. 533-542.
9. Song, J., Vorburger, T. and Rubert, P., "Comparison Between Precision Roughness Master Specimens and Their Electroformed Replicas," *Precision Engineering* **14** (2) 1992, pp. 84-90.
10. Vorburger, T., Yen, J., Bachrach, B., Renegar, T., Filliben, J., Ma, L., Rhee, H., Zheng, A., Song, J., Riley, M., Foreman, C. and Ballou, S., "Surface Topography Analysis for a Feasibility Assessment of a National Ballistics Imaging Database," to be submitted to the *J. Forensic Sci.*

STUDY ON NANO-SCALE MECHANICAL PROPERTIES OF ULTRAHIGH-PURITY ALUMINUM BY NANOINDENTATION

M. Yoshida[1], M. Nakamura[2], T. Sumomogi[2] and T. Endo[2]
[1]Graduate School of Engineering, Hiroshima Kokusai Gakuin University
6-20-1 Nakano, Aki-ku, Hiroshima 739-0321 JAPAN
[2]Faculty of Engineering, Hiroshima Kokusai Gakuin University
6-20-1 Nakano, Aki-ku, Hiroshima 739-0321 JAPAN

1. INTRODUCTION

By advance of an ultraprecision machining, it has been becoming important to grasp the mechanical properties on microscopic scale. The depth of cut at the machining is several tens nanometers ~ several micrometers, and the grain size of work piece is larger than the deformation volume at the cutting. It is thought that the impurities, initial dislocations, oxide layers and surface asperities and so on, are influenced considerably with decreasing of the depth of cut. Although the machining process has been thought as cutting behavior on microscopic scale, the little effort has been placed on the strength and the deformation properties of metallic single crystals in microscopic scale [1].

In order to understand the mechanical properties on microscopic scale, the nanoindentation of metallic single crystals, such as Au, Ag and Al, has recently been the focus of intense research [1-5]. The results of the numerous nanoindentation studies have revealed that the elastic and the plastic property, the theoretical share strength and the hardness of materials, changes at small indentation depth. This behavior has been considered as the atomic-level processes that contribute to the initial nucleation, motion and multiplication of dislocation, but the mechanism is unresolved[6]. Therefore, it has been necessary for us to obtain a detailed understanding of the behaviors on microscopic scale.

In this study, the nanoindentation system that is able to obtain indentation load vs. penetration depth curves is employed. The experiments are performed on (111), (110) and (100) surface of single crystal aluminum 99.9999%. Moreover, the purity dependence of mechanical properties is investigated using aluminums with purity levels: 99.9999%, 99.99% and 99%.

2. EXPERIMENTAL PROCEDURES

The materials used in this study are 99.9999% (6N) ultrahigh-purity aluminum of (111), (110) and (100) surface. In order to clear the purity dependence of the mechanical properties, commercial purity aluminums 99% (2N), high purity aluminum 99.99% (4N) are used in addition to ultrahigh-purity aluminum. The sample size is 10mm×10mm×1mm. All samples are electoropolished, and are annealed between at 500℃ for 5 hours in a vacuum of 2×10^{-5}Pa. Furthermore, 6N and 4N samples are cyclically annealed between 90℃ and 300℃ 8 times in a vacuum of 2×10^{-5}Pa.

The average space between dislocations is about 300μm in the 6N and about 30μm in the 4N. The average space between dislocations in the 2N becomes unclear, but it is considered to be several micro meters. From the results, the test region under nanoindentation in the 6N is considered to be a nearly perfect crystal [1].

The nanoindentation experiment is performed using a Hysitron TriboScope which is an indentation attachment to a scanning force microscope (SPM). A cube corner tip with an apex angle of 90 degrees is used. The tip radius in nanoindentation system is 40nm, 75nm and 100nm, respectively. The Indentation loading rate is $4\mu N\cdot s^{-1}$, and the dwell time at the selected maximum load is 0 second for each indentation. The sample is indented at least seven~ten times.

3. RESULTS AND DISCUSSIONS

3.1 ONSET OF PLASTIC DEFORMATION

Figure 1 shows an example of the indentation load vs. penetration depth curve for 6N, in which the indentation load is 50μN and 19μN (the inset of Fig. 1). In the curve of the maximum load 50μN, the penetration depth suddenly increases to 30nm at 20μN. Several researchers have reported that the initial penetration depth burst corresponds to the initiation of plastic deformation, namely, the yield point [3-9]. In the case of the maximum load 19μN (the inset of Fig. 1), both of loading curve and unloading curve nearly consist. Furthermore, the indentation mark is not observed after the indentation. From

the results, the indentation behavior before the indentation burst at 20μN is considered to be elastic deformation and the following process is considered to be plastic deformation.

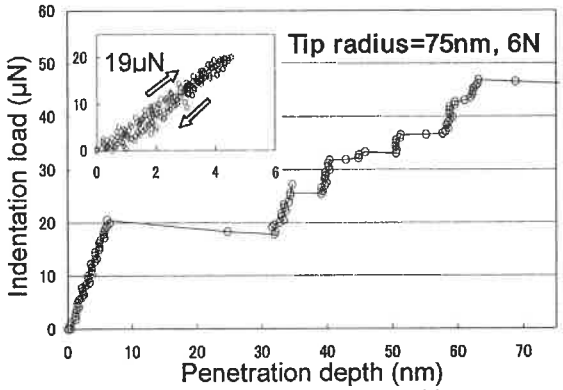

Fig. 1 Deformation behavior induced by nanoindentation on the 6N sample.

Figure 2 shows relationship between the yield load and the loading rate for various purity aluminums. Each plot is the average of more than five measurements. The yield load of 4N and 6N shows higher value than that of 2N.

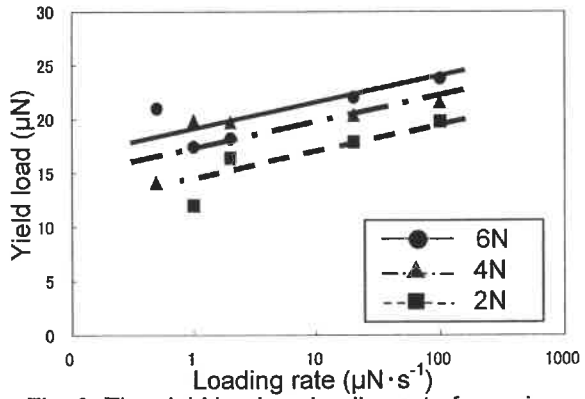

Fig. 2 The yield load vs. loading rate for various purity aluminums.

Using these yield loads, let us calculate the maximum shear stress of aluminum samples. Indenter contacts with the sample elastically under the load lower than yield load, so the maximum pressure P_m under an indentation can be given by [10],

$$P_m = \left(\frac{6 P_Y E^{*2}}{\pi^3 R^2} \right)^{1/3} \quad (1)$$

where, P_Y is the yield load, and R is the tip radius. The reduced modulus E^* combines the modulus of the indenter and the specimen [10], and R=75nm and E^*=71GPa are used. The maximum shear stress τ_{max} is given by [10],

$$\tau_{max} = 0.31 P_m \quad (2)$$

The estimated maximum shear stress is in the range 4.4 ~ 4.8GPa. This maximum shear stress on microscopic scale has higher value than that, $2 \times 10^{-3} \sim 2 \times 10^{-2}$GPa [11], obtained from the tensile test on macroscopic scale. The maximum shear stress τ_{max} calculated from shear modulus μ is 4.2GPa, using $\mu/2\pi$. This value is the same order with that calculated from yield load P_Y. The calculated maximum shear stress increases with increasing of the purity. It is assumed that the properties on microscopic scale differ remarkably from that on the macroscopic scale.

In 6N sample, the no initial dislocations and no impurities exist in the region subjected to nanoindentation. Therefore, it is considered that the ideal strength is obtained in the nanoindentation for 6N aluminum. Moreover, the crystal becomes a more perfect state as the purity increases, so the maximum shear stress increases with increasing of the purity. The present yielding behavior occurs when the maximum shear stress approaches the ideal strength.

3.2 MECHANICALLY CUTTING SURFACE

The 2N aluminum sample is face-turned with a single crystal diamond tool. The machining condition is cutting speed 447m·min^{-1}, feed rate 0.05mm·rev^{-1} and depth of cut 4μm.

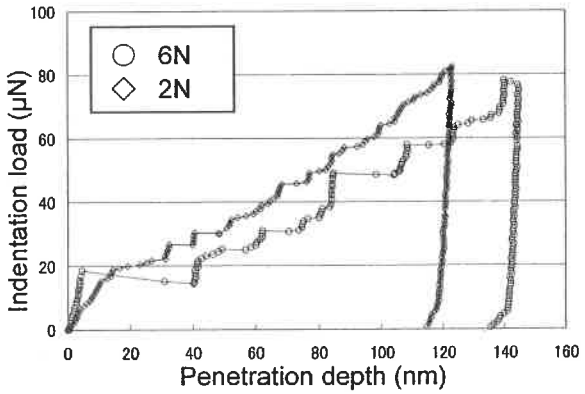

Fig. 3 Indentation load vs. penetration depth curves for 6N and machined 2N aluminum.

Figure 3 shows Indentation load vs. penetration depth curves for cyclic annealed 6N sample and the machined 2N sample. In the 2N sample

machined by cutting, penetration depth burst decreases, and nearly continuous deformation is observed. The penetration depth burst exhibits a dependence on purity level and dislocation density.

The impurities in sample resist the movement of the dislocation, so the movable distance becomes shorter, and the penetration depth burst decreases. Furthermore, for machined 2N sample, the yield load of 6μN is obtained. The yield load of 19μN for 6N shows higher value than that for machined 2N sample. In the ideally perfect crystal, the high stress is necessary to create a dislocation. The penetration depth burst occurs when the resolved shear stress becomes closer to the ideal strength. It is suggested that the defect free region has high resistance to dislocation nucleation.

3.3 EFFECT OF SURFACE ORIENTATION

Figure 4 shows the yield load vs. the distance of initial penetration depth burst for (111), (110) and (100) surfaces. The distance of initial penetration depth burst increases with increasing of the yield load. It is considered that the total elastic energy stored in the sample during the initial elastic deformation induced by nanoindentation is exhausted by nucleation and emission of dislocations. The remarkable difference in the yield load exists between the (100) surface and the (111) and (110) surfaces. The yield load of (100) is the highest of all, and the yield load of (111) is slightly less than that of (110).

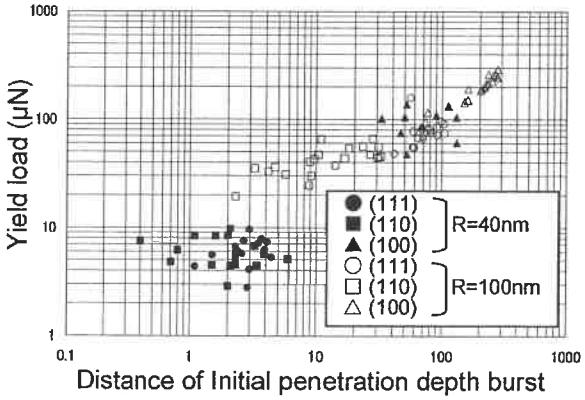

Fig. 4 The yield load vs. distance of initial penetration depth burst for surfaces (111), (110) and (100).

The differences of the yielding behavior are considered as the number of {111} planes that intersect the indented surface shown in Fig. 5. The two, three and four {111} planes intersect the (110), (111) and (100) surfaces, respectively. It is assumed that the total elastic energy stored in the sample changes with the number of {111} planes that intersect the indented surface, but to understand how slip plane affects indentation, a model based on a critical shear stress for slip must be developed in the future.

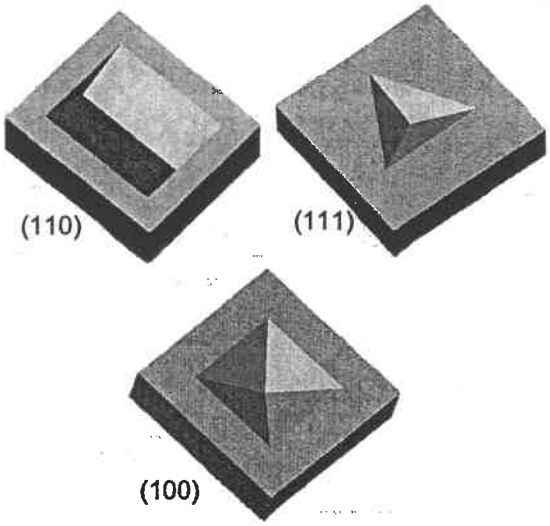

Fig. 5 Schematic illustration of the {111} planes.

Figure 6 shows Hardness vs. indentation load for surface planes (111), (110) and (100). There is no remarkable in the hardness between (111) and (110), and the values for the hardness obtained by nanoindentation are 1 ~ 3GPa. However, the hardness of (100) surface of 15~ 70μN is much higher value than that of (111) and (110) surface.

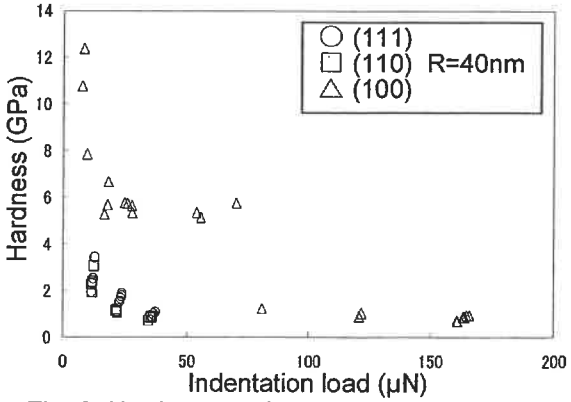

Fig. 6 Hardness vs. Indentation load for surface orientation (111), (110) and (100).

Figure 7 shows scanning probe microscope images of the (100) surface after the indentation at indentation load 90μN. Although the

indentation load is just prior to the initial penetration depth burst, the indent mark is made on the (100) surface. The similar result has been reported on Au by J. D. Kiely et. al [12]. It is considered that the yielding behavior has two types, which are the minor penetration depth burst and major penetration depth burst. Therefore, the hardness of (100) surface in the range of 15μN～70μN is much higher than those of (111) and (110), as shown in Fig. 6, because major penetration depth burst does not occur.

Fig. 7 Scanning probe microscope images of the (100) surface after the indentation at indentation load 90μN

4. CONCLUSION

In order to investigate mechanical properties of metals in microscopic scale, nanoindentation test was performed on aluminum samples with the various purities: 99.9999% (6N), 99.99% (4N) and 99% (2N), and with surface (111), (110) and (100). The following results are obtained.

1) The initial penetration depth burst is the initiation of plastic deformation, namely, a yielding behavior. The maximum shear stress estimated from the yield load is closer to an ideal strength of aluminum. Moreover, the estimated maximum shear stress increases with increasing of the purity. The results indicate that a perfect crystal is harder than an imperfect crystal.
2) Deformation behavior on microscopic scale shows discontinuous deformation. In the 2N sample machined by cutting, penetration depth burst decreases, and nearly continuous deformations are shown. Deformation behavior on microscopic scale exhibits a dependence on purity level and dislocation density.
3) The distance of initial penetration depth burst increases with increasing the yield load. It is considered that the total elastic energy stored in the sample during the initial elastic deformation induced by nanoindentation is exhausted by nucleation and emission of dislocations.
4) The remarkable difference in the yield load exists between the (100) surface and the (111) and (110) surfaces. The yield load of (100) is the highest of all, and the yield load of (111) is slightly less than that of (110).
5) It is suggested that the yielding behavior has two types, which are the minor penetration depth burst and major penetration depth burst.

ACKNOWLEDGEMNTS

The authors wish to thank to Professor H. Maeta, Hiroshima Kokusai Gakuin University and Mr. Fujii, the technical staff of the Research Institute of Advanced Technology of Hiroshima Kokusai Gakuin University for fabricating all the samples used in the present study.

REFERENCES

[1] M. Yoshida, T. Sumomogi, H. Maeta and T. Kino: The 3rd International Conference on Leading Edge Manufacturing in 21st Century, Nagoya. Japan. October 19-22 (2005) 375-380.
[2] T. Sumomogi, M. Yoshida, M. Nakamura, H. Osono and T. Kino: Mater. Trans. JIM. 46 (2005) 1996-2002.
[3] A. M. Minor, J. W. Morris, Jr. and E. A. Stach: Appl. Phys. Lett. 79 (2001) 1625-1627.
[4] S. G. Corcoran, R. J. Colton, E. T. Lilleodden and W. W. Gerberich: Phys. Rev. 55 (1997) 57-60.
[5] A. Gouldstone, H. J. Koh, K. Y. Zeng, A. E. Giannakopoulos and S. Suresh: Acta. Mater. 48 (2000) 2277-2295.
[6] K. J. V. Vliet, J. Li, T. Zhu, S. Yip and S. Suresh: Phys. Rev. B. 67 (2003) 104105. 1-15.
[7] T. Ohmura, K. Tsuzaki and F. Yin: Mater. Trans. 46 (2005) 2026-2029.
[8] M. Yoshida, T. Sumomogi, T. Endo, H. Maeta and T. Kino: Mater. Trans. JIM. 70 (2006) in press.
[9] J. D. Kiely and J. E. Houston: Phys. Rev. B. 57 (1998) 12588-12594.
[10] K. L. Johnson, Contact Mechanics (Cambridge University Press, Cambridge, 1996).
[11] D. A. Didenko and V. V. Pustovalov: J. Low. Temp. Phys. 11 (1973) 65-76.
[12] J. D. Kiely, K. F. Jarausch, J. E. Houston, P. E. Houston and P. E. Russell: J. Mater. Res. 14 (1999) 2219-2227.

MANUFACTURING OF GLASS DIFFRACTIVE OPTICS BY USE OF MOLDING PROCESS

Yang Chen[1], Allen Y. Yi[1], Fritz Klocke[2], Guido Pongs[2], and Axel Demmer[2]
[1]Department of Industrial, Welding and System Engineering
The Ohio State University, Columbus, OH, USA
[2]Fraunhofer Institute for Production (IPT), Aachen, Germany

INSTRUCTIONS

Growing demands on high-speed data, voice and video signals transmissions depend on low cost and reliable optical components to convert optical signals to electrical signals or vice versa. Microlenses, diffractive optical elements (DOE) and micromirrors are increasingly playing an important role in these applications [1-2]. The basic concept of a DOE relies on constructive and destructive interference of spherical sources to produce the desired illumination geometry. For example, in the simplest design, two parallel slits illuminated by a collimated beam (planar wave front) such as a laser. As the light propagates from the slits, both slits act as independent light sources and the light from each propagates in a spherical shape, see figure 1. At some distance, the two spherical waves

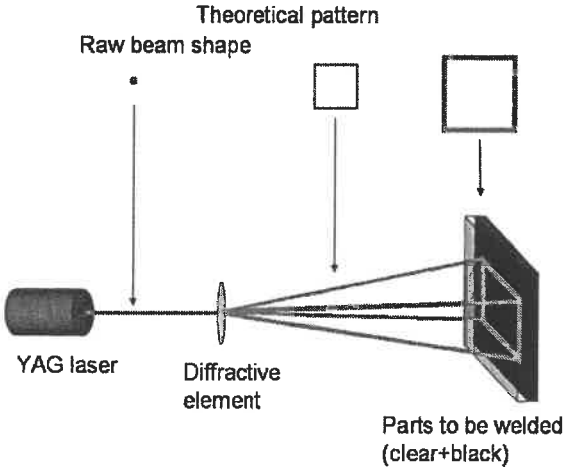

Figure 1: Schematic of a DOE design

interact with each other. In order to produce 2-dimensional patterns, such as the square depicted in figure 1. In this setup the line pattern is replaced by a 2-dimensional pattern, which appears to be very complicated. In order to design this pattern, an Inverse Fast Fourier Transforms (iFFT) of complex arrays is used. More specifically, in order to design a mask to produce a square, the image is constructed as a bitmap graphics based on the intensity mapping of the image. The image is then inverted from the center to the corners, and an inverse (iFFT) is performed on the inverted image based on equation 1 [3].

$$F(f_x, f_y) = \int_{-\infty}^{\infty}\int_{-\infty}^{\infty} f(x,y)e^{-j2\pi(f_x x + f_y y)}dxdy \qquad (1)$$

where $f(x,y)$ is a function that includes the complex values of the original bitmap image (inverted) at the index locations x and y, and $F(f_x,f_y)$ is the phase domain of the image (complex amplitudes) of the bitmap at index locations x and y. f_x, and f_y are the spatial frequencies. The details of the DOE design can be found in reference [4].

EXPERIMENTS

Glassy Carbon Mold Preparation

Glassy carbon wafer was selected for its excellent chemical stability at high temperature and its optical polishability. Compared with other traditional mold materials such as fused silica or tungsten carbide, operating temperature of glassy carbon can reach up to 2000°C. In addition, no special coating was needed on the glass carbon wafer surface because there are very low sticking between glassy carbon and glass workpiece, these ideal material properties are essential for an economical mold making process. These properties also make glassy carbon mold more suitable for fabricating diffractive optical elements (DOEs) or microlens array where thin film protection coating layer can be difficult to apply.

The glassy carbon wafer was fabricated using micromachining process and followed up with plasma dry etching as seen in figure 2. The photoresist was Shipley S1813 and it was deposited with a thickness of 1.4 _m in order to assure that the photoresist withstand the etching procedure. The wafer with photoresist was

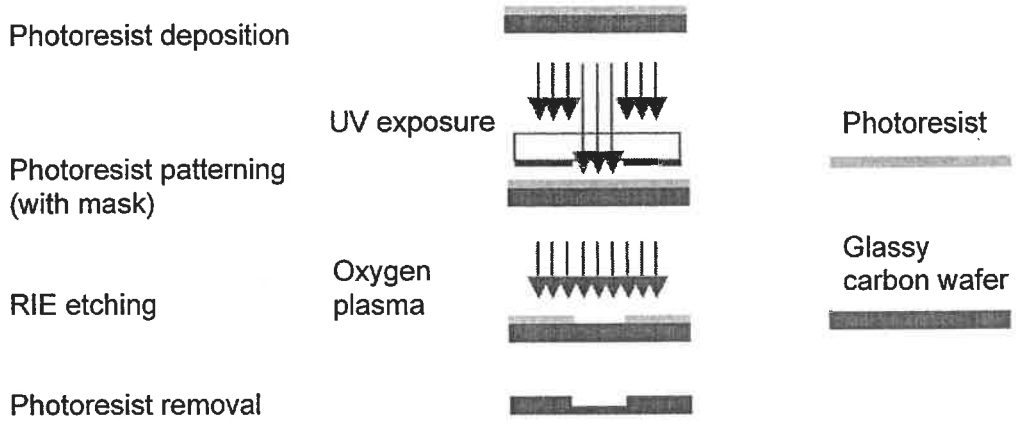

Figure 2: Micromachining process for glassy carbon wafer

exposed to UV radiation (MJB-3 365 nm) for 5 second at a density of 11 mW/cm2. The wafer was then developed for 1.5 minutes using MF 319 developer and water rinsed followed by a spin dry. A bench top RIE (Reactive Ion Etching by Technics Micro-RIE Series 800II) unit was used for reactive ion etching of the wafer. The pressure during etching was 150 mTorr with an RF power of 200W. The oxygen flow rate during etching was 20 cm^3/minute and total etching time was 10 minutes. After etching, the remaining photoresist was removed by Acetone.

Molding Process

The DOE molding experiments discussed in this paper were performed on a Toshiba GMP 211V machine at the Fraunhofer Institute for Production Technology (IPT). The glassy carbon wafers used in this research were manufactured by Tokai Carbon Co. Ltd., Tokyo, Japan). The glassy carbon wafers were optically polished before the diffractive pattern was fabricated in the cleanroom. The shaded component in the figure is the optical glass workpiece. The glass workpiece used in this experiment was also optically polished on both sides and placed manually on the lower mold. During each experiment, vacuum was applied at the beginning to ensure that no air remained in the gap between the mold and DOE. This was immediately followed by nitrogen purge to further remove oxygen residual. Figure 3 shows schematically the molding process using glassy carbon wafer mold and the optical glass materials. Figure 4a and 4b are the process conditions used for B270 glass. These conditions were found to be effective but they are not necessarily the optimal conditions [5].

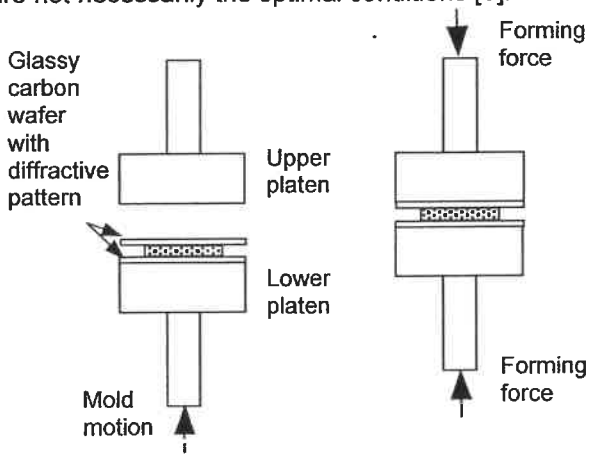

Figure 3: Illustration of a DOE molding process

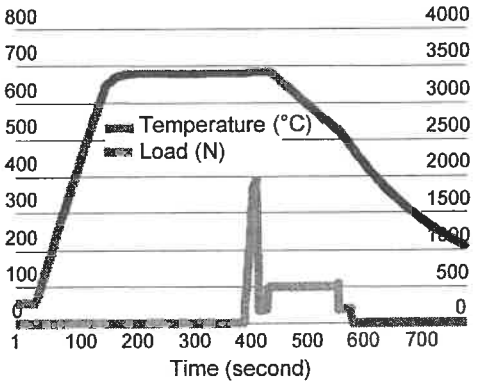

(a)

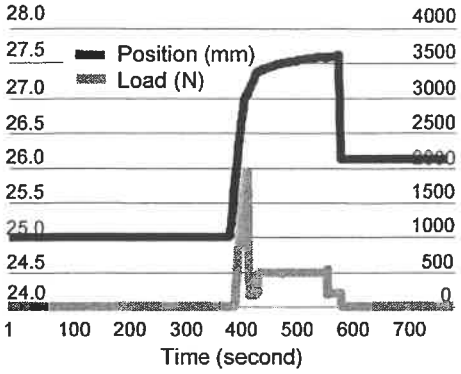

(b)

Figure 4: Molding conditions for B270 DOE molding process

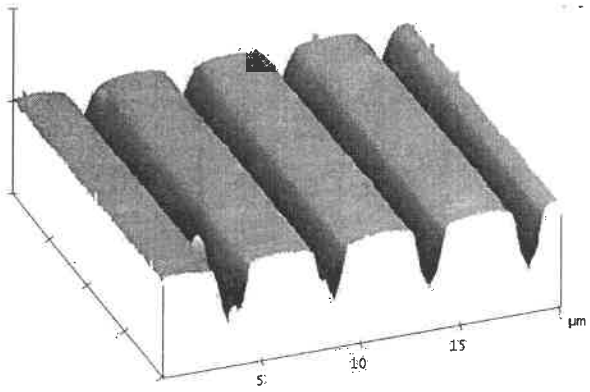

(a)

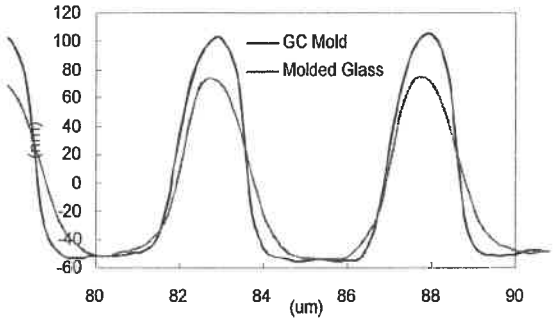

(b)

Figure 5: Molded B270 glass DOE

RESULTS AND DISCUSSION

Replication Accuracy

The molded DOEs were measured for geometric accuracy and surface finish. Figure 5a shows the molded DOE measured on a Digital Instrument's AFM (Veeco NanoMan Dimension 3100 with NanoScope IV SPM Control Station, lateral scale is 5 μm/div and vertical scale is 300 nm/div). To ensure a valid comparison, Wyko (Veeco NT3300 optical profiler) scans were performed on the same area on the glassy carbon mold and the molded B270 glass DOE. Figure 5b shows the comparison between the glassy carbon mold and the molded B270 DOE. Using the AFM scans again, the surface roughness (R_a) of the molded DOE was measured to be 35 nm versus 40 nm for glassy carbon mold.

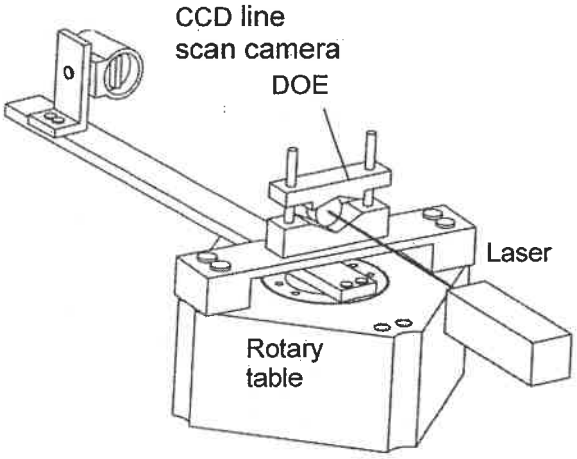

Figure 6: Optical performance test setup

Optical Performance

To analysis the optical performance of the molded glass, an experimental setup was assembled as shown in figure 6. The molded glass was placed about 350mm away from the laser source (HP-5517B). The diffractive pattern was measured by a Charge Coupled Device (CCD) line scan camera that was set 350 mm away from molded glass DOE (Model 1000 line scan camera Entwicklungsb_ro, Reinholdstra_e, 5D –12051Berlin, Germany). The 1000 model is equipped with a Sony line scan CCD sensor ILX553 that has 5150 pixels, and each pixel has a 7x7_m^2-sensing area. To measure the diffractive peak of different order at different position, a rotary table (Soloist single-axis rotary stage by Aerotech, Inc., Pittsburgh, PA) was operated through a computer to move at a fixed speed to control the line scan camera to scan the entire diffractive area. The diffractive pattern of the molded glass after filtering out the zero

order light was then plotted in figure 7. For more details of the optical setup, readers can go to reference [5-6]. The result shows that the molded glass DOE can work as predicted for beam-shaping with a high signal noise ratio.

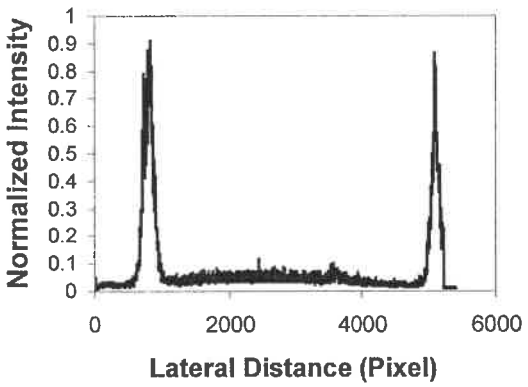

Figure 7: Optical performance test result

CONCLUSION

Through design, fabrication and measurement of compression molded low T_g glass DOE as well as measuring the optical performances of the molded glass DOEs, we have demonstrated that compression molding can be a promising process for high volume production of precision DOEs with micro and nano scale features. Geometrical characterizations of the molded DOEs were demonstrated using different optical metrology techniques.

The proposed strategy for DOE fabrication has several inherited advantages over existing technologies. First, it is flexible in that there are several hundred optical glasses available versus only a few optical plastics. Second the molded DOEs can preserve the optical quality of the mold surfaces, therefore, no post molding processes are needed, i.e., it is a net shape manufacturing process. Third, this method can be applied to fabricating many different optical components thus making it a very powerful tool to mass produce various optical elements at low cost which opens the door for enhanced and more affordable optical systems. Finally, the compression molding process can be used to fabricate other components with micro and nanoscale features at an affordable cost, for example, microfluidic devices for biomedical applications.

ACKNOWLEGEMENTS

This work was supported in part by the German Research Foundation (DFG) within the SFB/TR4 "Process Chains for the Replication of Complex Optical Elements." The authors also would like to thank MicroMD at the Ohio State University for assistance in providing Micromachining Facility (www.micromd.org). The research was also supported by the National Science Foundation (USA) under Grant No. 0547311. Any opinions, findings, and conclusions or recommendations expressed in this material are those of the authors and do not necessarily reflect the views of the National Science Foundation.

REFERENCES

[1] M. R. Wang, H. Su, "Laser Direct-Write Gray-Level Mask and One-Step Etching for Diffractive Microlens Fabrication," *Applied Optics*, 37 (32), 7568-76 (1998).

[2] H. Chase, M. A. Handschy, M. J. O'Callaghan, F. W. Supon, "Improvement of spatial light modulator optical input/output performance using microlens arrays," *Optics Letters*, 20 (12), 1444-6 (1995).

[3] L. Li, A. Y. Yi, C. N. Huang, David Grewell, Avraham Benatar, Y. Chen, Fabrication of Diffractive Optics by Use of Slow Tool Servo Diamond Turning Process, in press, *Opt. Eng.*, March (2006).

[4] D. Grewell. *Modeling of Molecular Healing for Micro-Laser Welding of Plastics with Diffractive Optical Elements as Spatial Modulators*. The Ohio State University, Columbus, OH, Ph.D. (2005).

[5] F. Klocke, A. Y. Yi, T. Bergs, A. Demmer, G. Pongs, "Compression Molding of Precision Micro and Diffractive Glass Optical Components," European Society for Precision Engineering (Euspen) Annual Meeting, Baden, Austria, May (2006).

[6] A. Y. Yi *, Y. Chen, G. Pongs, F. Klocke, D. Grewell , A. Benatar, "An innovative precision compression molding process of glass diffractive optics by use of fused silica wafer mold and low Tg optical glass," in press, Journal of Micromechanics and Microengineering, July (2006).

DIRECT MACHINING OF INNER REFLECTING SURFACE FOR A SOFT X-RAY MICROSCOPE

Kwon Su Chon[1], Yoshiharu Namba[2], and Kwon-Ha Yoon[1]
[1]Institute for Radiological Imaging Science
Wonkwang University
Iksan, Jeonbuk, Korea
[2]Department or Mechanical Engineering
Chubu University
Kasugai, Aichi, Japan

INTRODUCTION

A soft X-ray microscope can be used to investigate hydrated specimens, particularly living cells, with a high resolution about several times better than that of a visible light microscope. It can also extend to material science, plasma fusion research, magnetic research, environment science, and so on. The reflecting optics used in a soft X-ray microscope requires supersmooth surface and highly accurate figure.

Single-point diamond turning (SPDT) is a very useful optical fabrication method in manufacturing aspheric optics particularly. This method can overcome disadvantages of conventional optical fabrication methods of grinding and polishing. However, substrates used in SPDT are limited as non-ferrous material and plastics [1].

An aspheric X-ray mirror, Wolter type I mirror, with axial symmetric inner reflecting surface is manufactured by an epoxy replication method [2]. This fabrication method has several advantages compared to the direct machining of inner reflecting surfaces. However, in a practical application of the mirror, i.e., in a soft X-ray microscope, one critical problem is found. The soft X-ray can be generated from carbon solid target focused Nd:YAG laser [3]. The generated plasma also brings out carbon debris which covers the reflecting gold surface. The reflectivity of soft X-rays continuously decreases by the debris. Because the gold surface of the epoxy replicated mirror is very weak, cleaning of the surface is almost impossible. Therefore, the life time of the replicated mirror is limited. To overcome this critical problem under the laser-produce plasma source, the reflecting surface needs to hard enough to remove debris and to refresh the mirror used in the soft X-ray microscope. In this paper, we consider a Wolter type I mirror as a condenser optic. We will examine the fabrication possibility of the mirror with axial symmetric inner reflecting surface by SPDT.

OPTICAL DESIGN

A Wolter type I mirror, condenser optic, for an X-ray microscope is composed of two coaxial, confocal ellipsoidal and hyperboloidal surfaces of revolution as shown in Fig 1.

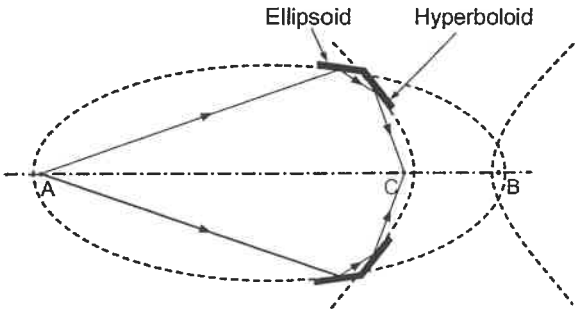

FIGURE 1. A Wolter type I focusing mirror used in a soft X-ray microscope based on a laser-produced X-ray source.

The shape and size of a Wolter type I mirror can be determined by four independent parameters [4]. We considered a Wolter type I mirror for focusing soft X-rays with a magnification of 1/4 X, a central grazing incidence of 2 degrees, an object-to-image distance of 437 mm, and a length of ellipsoid of 26 mm. The working distance of the mirror was approximately 64.5 mm, and the distance between a source and the front of the mirror was 323.6 mm.

To reduce effectively carbon debris on the mirror surface, the source-to-mirror distance should be over 200 mm. Even if the distance was large enough, the debris was gradually deposited on

the reflecting surface of the mirror. The debris decreased the optical performance, reflectivity, of the mirror because it increased surface roughness of the mirror. Figure 2 shows the reflectivity of the surface of electroless nickel for single reflection as a function the surface roughness. Because soft X-rays were reflected twice on the Wolter type I mirror, the reflectivity of the mirror decreased more rapidly than that shown in Fig. 2.

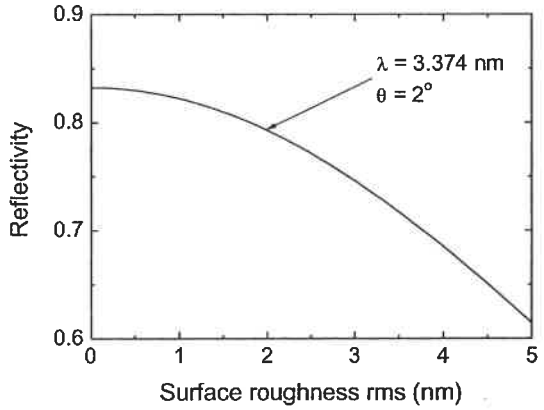

FIGURE 2. Calculated reflectivity for a reflecting surface of electroless nickel as a function of surface roughness. X-ray wavelength and grazing incidence angle are fixed as 3.374 nm and 2 degrees, respectively.

The dimension of the mirror to be fabricated by SPDT is shown in Fig.3. The mirror considered here had approximately 19 mm in diameter. In order to obtain a reflectivity of over 50 % which was the goal in this study, the surface roughness of the mirror had to be less than 4 nm rms (root-mean-square).

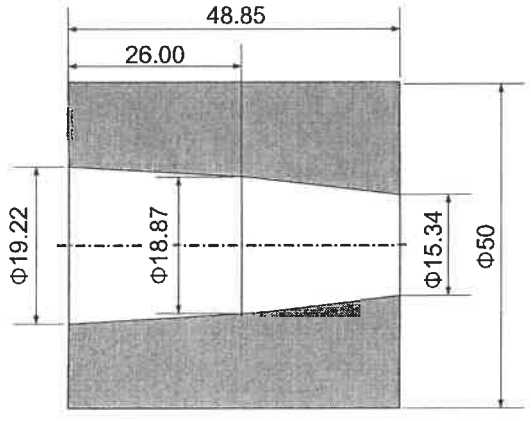

FIGURE 3. Dimensions of a Wolter type I focusing mirror.

EXPERIMENTAL SETUP

Generally, electroless nickel which was alloy of nickel and phosphorous was plated on aluminum alloys or steel. We prepared electroless nickel plated on the aluminum alloy A7075 substrate. A conventional numerical control lathe was used for machining base mirror substrates. Using an ultra-precision machine tool, the base mirror substrate was machined to a thickness of below 75 μm from the ideal contour of the designed Wolter type I mirror. The thickness of electroless nickel was 110 μm. The plated electroless nickel showed amorphous structure [5]. In machining point of view, this structural state was useful to obtain smooth surface by SPDT because of no grain boundary and anisotropy [6]. Electroless nickel also had an advantage in the optical performance, i.e., reflectivity. The reflectivity of electroless nickel was much higher than that of high Z-materials, for example, gold.

The diamond turning machine tool used in this experiment had two perpendicular slide tables (Z and X axes), an air bearing spindle on the Z-slide table, and a rotary table (B-axis) with a tool post. A laser interferometer system used to determine accurately positions. X and Z-tables could be controlled within 1 nm positional step. The B-table could be rotated with an angular step of 0.0001 degree. However, in this experiment the B-table was fixed. The machine tool was set up within a vibration isolator and supported by air mounts to prevent external vibrations. The environment was maintained by a clean room of the class 100 and controlled within temperature of 0.1 K. A sample substrate was attached on the special jig which was fixed on the main spindle. The jig had four holes to extract cutting chips.

Figure 4 shows the experimental setup for fabricating a Wolter type I focusing mirror with the inner reflecting surface using SPDT. The kerosene mist with air pressure of 0.2 MPa sprayed on the cutting face, which also helped to remove chips during machining. The mist was supplied through a small hole in the shank of the tool because uniform mist supplement was not easy from the outside directly.

Figure 5 presents a single-crystal diamond tool used in this experiment. The single-crystal diamond tool of which the crystallographic plane (110) was the rake face were used; the rake and clearance angles were 0 and 5°, respectively,

and the window angle was 55°. The shank of the diamond tool was made of tungsten carbide to prevent bending during machining because the arm of the shank was very long, and nose radius of the diamond tool was 1 mm. The diameter of left edge of the shank was approximately 14 mm which was very close to the smallest ideal diameter of the mirror, 15.34 mm. The arm of the diamond tool except for fixing part to tool holder on tool post of the diamond turning machine tool was 55 mm. Cutting edge of the diamond could be new by rotating the tip which was fixed by a screw on the shank when the cutting edge was worn. Thus, the life time of the tool could be extended more.

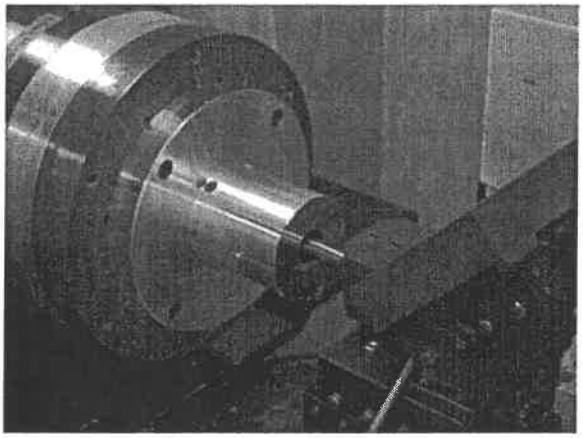

FIGURE 4. Experimental setup for fabricating a Wolter type I focusing mirror with inner reflecting surface by single-point diamond turning.

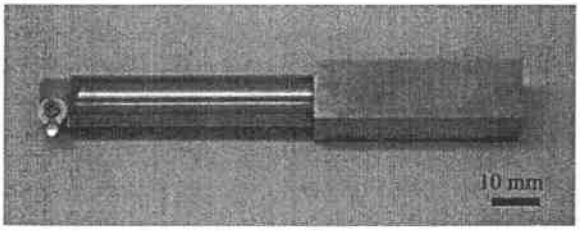

FIGURE 5. Single-crystal diamond tool with tungsten carbide shank. The shank has a small fiber of 1 mm diameter to supply cutting oil during machining.

DIRECT MACHINING OF INNER REFLECTING MIRROR

The mirror had an aspect ratio of approximately 3.2, which was defined as the ratio of the length to the diameter. From a geometrical point of view, the machining of the mirror had large space to meet machining vibration during cutting the inner reflecting surface of electroless nickel. The machining vibration was generated generally by the resonance of the machine tool vibration [7]. In order to avoid the machining vibration, the choice of machining conditions was very important. Main sources of the machining vibration were the rotation of main spindle and feed rate.

To achieve a smooth surface, a rapid rotation of main spindle and a low feed rate was required. In addition, the machining vibration should be also considered in machining the mirror. Approximately 1 μm/rev in feed rate was almost lower limit, and 600 rpm (rotation per minute) in spindle rotation was the upper limit. Depth of cut was not crucial factor in generating the machining vibration. In our experience, the depth of cut of from 1 to 3 μm was no difference in surface roughness with respect to the fixed cutting conditions of the spindle rotation and the feed rate. Under a slow feed rate of 1 μm/rev in a depth of cut of 1 μm, the spindle rotation was limited as 250 rpm. In this case, the machining time was approximately 195 minutes. A long machining time could have possibility to degrade surface roughness and figure accuracy of the mirror. As final cutting of the mirror substrate, a feed rate of 3 μm/rev, a spindle rotation of 450 rpm, and a depth of cut of 1 μm were chosen, and the machining took approximately 36 minutes. The diameter of the mirror was control within ± 1 μm.

Figure 6 (a) and (b) shows surface roughness and figure error of the machined mirror, respectively. These were obtained with a contact mode surface profiler. Because the machined mirror was not carried out post polishing, the curve of figure error was not smooth. The left and the right from zero in Fig 6 (a) mean the ellipsoidal and the hyperboloidal parts of the mirror, respectively. The figure error of the machined mirror was 277 nm PV (peak-to-vallley), and the surface roughness was 2.8 nm Ra and 18.5 nm Ry. The surface profile shown in Fig 6 (b) almost was closed to an average surface roughness of the mirror (3.5 nm rms). The ellipsoidal part of the mirror showed relatively rougher than hyperboloidal part. Figure 7 shows the machined mirror by SPDT.

CONCLUSIONS

We examined the fabrication possibility of a Wolter type I mirror, which would be used for a condenser optic in a soft X-ray microscope, with inner reflecting surface of electroless nickel by

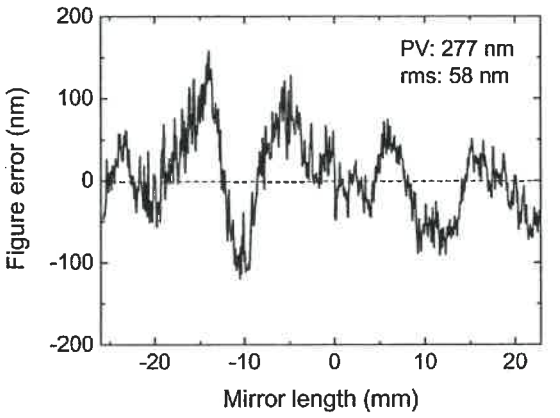

(a) Figure error

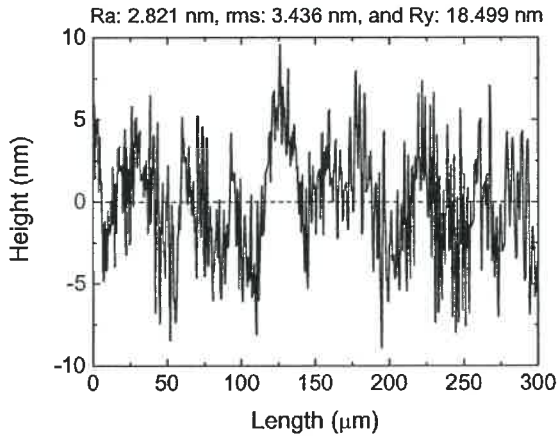

(b) Surface roughness

FIGURE 6. Measured figure error (a) and surface roughness (b) of the mirror machined by SPDT.

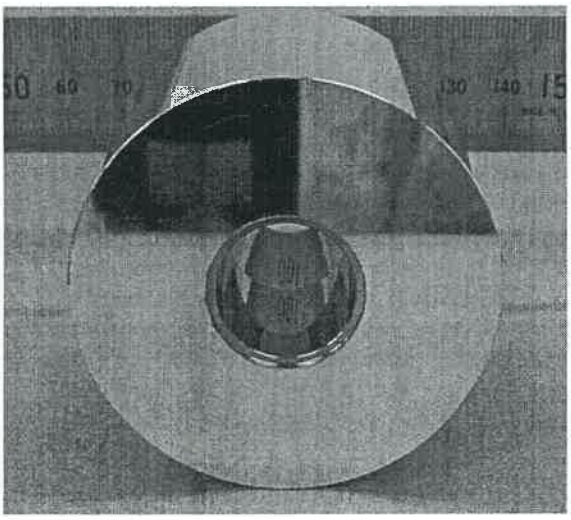

FIGURE 7.Machined Wolter type I mirror by SPDT.

direct machining, i.e., SPDT only. Because of long arm of the single-crystal diamond tool, machining vibration was happened frequently. Possible machining conditions were restricted because of avoiding the machining vibration. Spindle rotation and feed rate were crucial factors causing the machining vibration. The machined Wolter type I mirror showed 277 nm PV in figure error and 2.8 nm Ra in surface roughness. The Wolter type I mirror fabricated by SPDT can be used for a condenser optic only (not imaging optics) in a soft X-ray microscope.

ACKNOWLEDGEMENTS

Part of this work was supported by the Grant KOSSF F01-2006-000-10092-0 and the Grant ITEP No. 10006942 of Korea Ministry of Commerce, Industry and Energy. And also part of this work was supported by the Grants-in-Aid for Scientific Research (B) Nos. 15360075 and 18360073 from the JSPS, and also the Grants-in-Aid for Scientific Research on Specially Promoted Research No. 15001002 from the Ministry of Education, Culture, Sports, Science and Technology, Japan.

REFERENCES

1. Rhorer R. and Evans C., 1995, *Fabrication of optics by diamond turning*, OSA Handbook of Optics 2nd Ed. Vol 1, McGraw-Hill, Washington DC.
2. Chon K.S., Namba Y., and Yoon K.H., 2006, Precision machining of electroless nickel mandrel and fabrication of replicated mirrors for a soft x-ray microscope, *JSME International Journal Series C*, 49: 56-62.
3. Kühne M. and Thornagel R., 1990, Soft x-ray emission from a laser-produced carbon plasma, Ed. Michette A.G., Morrison G.R., and Buckley C.J., in *X-ray microscopy III,* Springer-Verlag, Berlin.
4. Chon K.S., Namba Y., and Yoon K.H., 2006, Optimization of a Wolter type I mirror for a soft x-ray microscope, *Precision Engineering*, 30: 223-230.
5. Hibbard D. L., 1997, Electroless nickel for optical applications, *Proceeding of SPIE*, CR67: 179-205.
6. Yean Z., Lee W., Yao Y., and Zhou M., 1994, Effect of crystallographic orientations on cutting force and surface quality in diamond cutting of single crystal, *Annals of the CIRP*, 43, 39-42.
7. Myler, J.K., Parker, R.A. and Harrison, A.B., High Quality Diamond Turning, Proc. SPIE, Vol. 1333 (1990), p.58-79.

ASPHERIZING THE SPHERE: USING FOCUSED ION BEAM MACHINING TO CREATE ASPHERICAL DIAMOND MILLS FOR MICRO OPTICS

V. Carter Hodges[1], David P. Adams[1], Andre A. Claudet[1], David D. Gill[1], William C. Sweatt[1], Michael J. Vasile[1]
[1]Sandia National Laboratories
Albuquerque, New Mexico, USA

INTRODUCTION

Sandia National Laboratories has developed a method for using diamond mills to fabricate arrays of convex aspherical micro-optics. The optics are on the surface of a 2 mm radius hemisphere and have a 420 μm radius and a 660 μm diameter aperture. Conventional diamond tool production methods can create mills with spherical concave cutting edges (actually cylindrical when considering the clearance angle). However, when a design requires an asphere, there are not many options. Focused Ion Beam (FIB) shaping in combination with ultraprecision machining has been demonstrated to produce micro-scale components in a variety of materials [1-3]. We procured concave, spherical diamond mills and utilized focused ion beam shaping to modify the tool geometry into an aspherical mill.

In fabricating the asphere on the diamond mill, there are many steps of the process from design to final part. The most significant include optical design of the aspheres, selection of a best fit radius, spherical tool manufacturing, optical redesign to utilize the actual tool radius, FIB process planning, FIB shaping, and ultraprecision machining of the desired optics using the new tool. In this report we describe each of these steps. As expected, we found that the accuracy of the final optics was dependent on the errors within each of the fabrication steps.

OPTICAL DESIGN AND THE BEST FIT RADIUS

The optical design was done using the ZEMAX [4] commercial ray tracing software. The design is for the visible spectrum using acrylic lens material. The software also provides the ability to determine the material that must be removed in rough grinding of the optic. This feature was used to determine the maximum inscribed sphere (i.e., the best fit sphere that leaves material to be removed during the focused ion beam shaping of the spherical tool, similar to a most material condition.) The ray trace for the optical design and the corresponding inscribed best fit sphere are shown in FIGURE 1.

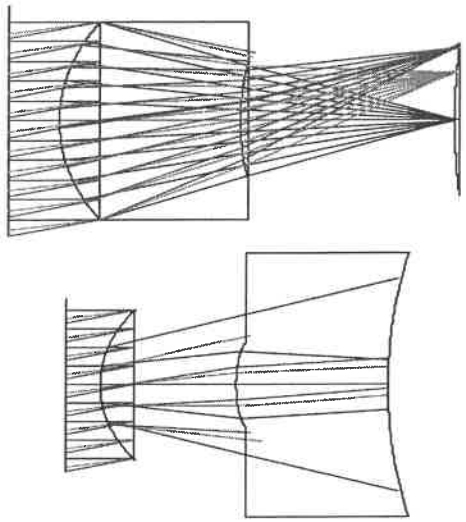

FIGURE 1. The optical design (top) and the corresponding inscribed best fit spheres (bottom) shown as the material to be removed.

SPHERICAL TOOL MANUFACTURING

Diamond concave cutting edge tools were procured from Chardon Tool [5] at a specified radius of 420 μm. The quoted accuracy for the specified radius was ±10 μm due to the difficulty of lapping the concave tool. The tools are single crystal synthetic diamond brazed onto the tip of a 3.175 mm diameter steel shank. The concave edge is created with ~6 μm of arc past the center of the tool to assure full cutting even if there is some radial error in the tool motion. The tool has a 0° rake angle and a cylindrical clearance angle which varied from 6 to 10° across the face of the tool. To maintain a constant clearance angle, the tool would have required a conical clearance angle which was deemed to be unnecessary for the application.

OPTICAL REDESIGN

Once the tool was delivered, the optical design was performed again to match the actual radius of the supplied tool. This included changing the mean radius of the aspheric lens and then recalculating the inscribed best fit sphere. Once the optical design was complete, the tool was ready for aspherizing process planning and modification.

FIB PROCESS PLANNING

The FIB system is equipped with a secondary electron imaging capability so that the beam can be controlled in the image coordinate system. With this flexibility in mind, an image of the as-fixtured tool was captured (FIGURE 2) and processed externally. To maintain precise image alignment, the tool was not moved in the time between when the image was captured and the shaping was performed. Additionally, none of the beam parameters, e.g., energy, current, lens voltage, were changed.

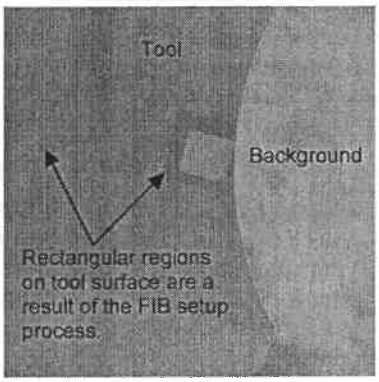

FIGURE 2. As fixtured diamond tool.

The edge of the tool is detected using image processing algorithms and a least squares best fit radius is determined in image coordinates. The tool radius is known from inspection at the tool manufacturer and yields a pixel to length factor. The pole is determined to be the point tangent to the concave cutting edge on a line that is parallel to the tool flat (FIGURE 3).

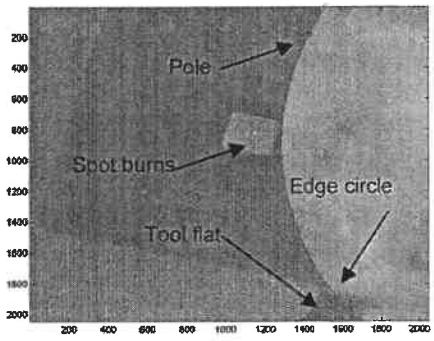

FIGURE 3. Tool edge and pole determination.

The optical design input to the process is an analytic definition of the aspherical tool profile of the form

$$f_a(x) := \frac{C \cdot x^2}{1 \cdot mm + \sqrt{1 \cdot mm^2 - (1+k) \cdot C^2 \cdot x^2}} + A_1 \cdot x + A_2 \cdot x^2 + A_3 \cdot x^3 + A_4 \cdot x^4 \ldots + A_5 \cdot x^5 + A_6 \cdot x^6 + A_7 \cdot x^7 + A_8 \cdot x^8$$

where C, k, and A_i are asphere parameters. A best fit circle is determined for the asphere equation and the residual deviation plot gives an idea of the amount of FIB modification required (FIGURE 4).

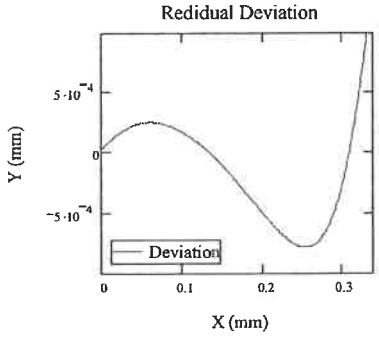

FIGURE 4. Asphere residual deviation.

With the circular edge and pole location known, the aspherical curve is overlaid on the tool and a bitmap pattern determined. The pattern in FIGURE 5 is white where material is to be removed.

FIGURE 5. Bitmap pattern.

The positional relationship between the binary pattern image and the original captured image is known and allows the pattern to be imported into the FIB user interface software.

FIB SHAPING

We chose to orient the tool with the cutting face closest to the ion source. Throughout the FIB shaping process, careful consideration was given so as to maintain the sharpness of the cutting edge. The ion beam intensity has a Gaussian distribution. Parts of the beam are known to reach outside of user-defined patterns and cause rounding of edges. To protect the cutting edge from rounding effects of the ion beam, an adhesion layer of chromium was deposited directly onto the tool face followed by a protective layer of molybdenum.

The tool was loaded into a coupler that would allow it to be fixtured on a rotation stage within the vacuum chamber to which the FIB column is mounted. For this procedure, a tip/tilt stage and white light interferometer were utilized to ensure that the tool was leveled in X and Y axes to within one tenth of one degree with respect to the tool coupler.

The coupler and tool were then positioned to the desired beam orientation within the vacuum chamber using a rotational stage. As shown in Figure 3, the ion beam was focused and stigmated through a series of iterative test spots on the face of the tool for the purpose of optimizing the beam profile. As described earlier, an image of the tool was captured and processed externally to generate the bitmap pattern. The bitmap pattern was imported and aligned using parameters defined by the FIB user interface software.

The FIB has an energy of 30 keV and a current of 7nA was chosen from the variable aperture strip of the FIB system. For FIB sputtering, the yield of diamond is ~0.09 $\mu m^3/nC$ when the beam angle of incidence is normal [6] and the volume of diamond to be removed was estimated using a CAD drawing. The FIB user interface software calculates an ion dose based on these parameters. The area of the bitmap pattern combines with the above mentioned parameters to determine the total time required to deliver the full ion dose.

Once the FIB shaping was completed, the cutting edge of the tool was imaged with scanning electron microscopy (FIGURE 6). Analysis of the image indicates that the edge was successfully milled into an aspherical pattern. The modified end relief varies in length as would be expected when some areas of the pattern overlap the edge more than other areas. An even stronger indication is that the longer areas of relief coincide with the areas of larger overlap in the pattern.

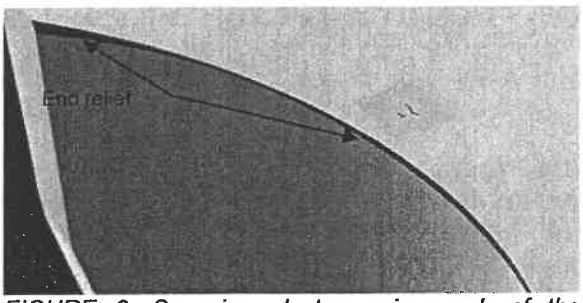

FIGURE 6. Scanning electron micrograph of the cutting edge.

ULTRAPRECISION MACHINING

The completed tool was used to mill optics on the exterior of the outer hemisphere of the dragonfly eye optic. The tool was put into the collet of a high speed spindle mounted on a rotary table positioned on the Z axis of the machine. The acrylic workpiece was mounted on the C-axis (positionable spindle) of the diamond turning machine. The FIB modified tool was then plunged into the surface of the polymer to create convex aspheric lenses. These lenses are undergoing metrology to determine the actual shape produced.

CONCLUSIONS AND FUTURE WORK

In conclusion, we have demonstrated a method for using FIB shaping to modify a diamond tool so that it has an aspherical cutting edge. An optical design was generated for use with conventional diamond tool production methods. A commercially available tool was procured according to that design. The as-received tool geometry was characterized and the optical design was adjusted accordingly. An aspherical bitmap pattern was generated and successfully transferred to the cutting edge. The tool was used to machine optics, which are currently being evaluated. Now that this capability is proven, future tool modifications will use precision fixturing techniques to customize the tool geometry, i.e., optimal rake and relief angles can be included in the tool design. In addition, the optical properties of the machined lenses will be characterized as this will be the most critical data for evaluating the success of this technique.

ACKNOWLEDGEMENTS

The authors would like to thank Armando Fresquez for physical vapor deposition and Bonnie McKenzie for scanning electron microscopy. Sandia is a multiprogram laboratory operated by Sandia Corporation, a Lockheed Martin Company, for the United States Department of Energy's National Nuclear Security Administration under Contract No. DE-AC04-94AL85000.

REFERENCES

1. Adams, D.P., Vasile, M.J., Krishnan, A.S.M., 2000, Microgrooving and microthreading tools for fabricating curvilinear features, *Precision Engineering*, 24: 347-356.
2. Adams, D.P., Vasile, M.J., Benavides, G., Campbell, A.N., 2001, Micromilling of metal alloys with focused ion beam-fabricated tools, *Precision Engineering*, 25: 107-113
3. Picard, Y.N., Adams, D.P., Vasile, M.J., Ritchey, M.B., 2003, Focused ion beam-shaped microtools for ultra-precision machining of cylindrical components, *Precision Engineering*, 27: 59-69
4. ZEMAX® Zemax Development Corp. Bellingham, WA 98004-8017 www.zemax.com
5. Chardon Tool Chardon, OH 44024 www.chardontool.com
6. Russell, P.E., Stark, T.J., Griffis, D.P., Phillips, J.R., Jarausch, K.F., 1998, Chemically and geometrically enhanced focused ion beam micromachining, *Journal of Vacuum Science & Technology B,* 16: 2494-2498

MANUFACTURING OF REPLICATED Pt/C MULTILAYER MIRRORS FOR HARD X-RAY TELESCOPES

Yoshiharu Namba[1], Atsuya Fushiki[1], Hideyo Kunieda[2], Yasushi Ogasaka[2], Yuzuru Tawara[2] and Koujun Yamashita[2]
[1]Department of Mechanical Engineering
Chubu University
Kasugai, Aichi 487-8501, Japan
[2]Department of Physics
Nagoya University
Nagoya, Aichi 464-8602, Japan

INTRODUCTION

Recent soft X-ray telescope satellites such as Chandra [1], XMM-Newton [2] and Suzaku [3] had launched in July, 2000, December, 2000 and July, 2005, respectively. All three telescopes are now working in order to observe new phenomena in the space. Figure 1 shows the structure of such X-ray telescope which is constructed by nested multiple reflecting mirrors. The grazing incidence reflecting mirrors need light weight and higher shape accuracy with very smooth surfaces. The telescope used a Wolter type I mirror which was consisted by a paraboloid and hyperboloid of revolution.

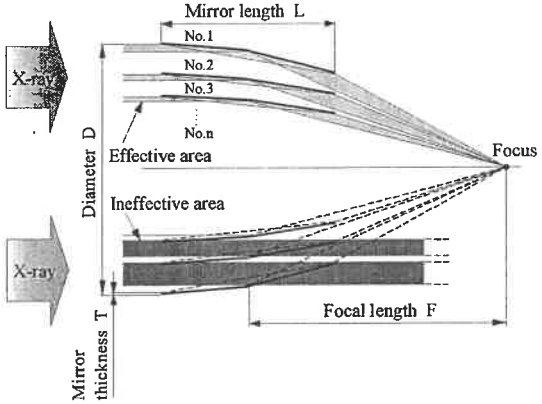

FIGURE 1. Structure of a grazing incidence X-ray telescope.

Chandra's aspheric X-ray mirrors were made of zero thermal expansion glass-ceramics, called ZERODUR and well polished and coated iridium inside mirror surfaces. The maximum diameter of the telescope is 1,200 mm and they have 4 aspheric mirrors as the first and second reflection, respectively. Chandra has the highest imaging resolution among three satellites, needed the longest manufacturing time and was the most expensive one. XMM-Newton was made by replication processes, that is, polishing aspherical electroless Ni mandrels, coating gold on the mandrels, electro-forming nickel of 1mm thickness on the mandrels, and separating the electro-formed nickel shell with gold film from the mandrel. Suzaku was made by different replication processes, that are, coating gold on glass tubes in the market, attaching an aluminum foil on gold-coated glass tube by a resin adhesive, curing them in the vacuum, and peeling off the foil with gold film from the glass tube. Each gold-coated foil mirror was a quarter arc of a circular cone and four mirrors were assembled in a circle.

Focusing optics in hard X-ray region above 10 keV will open a new window of the universe, where extremely hot astrophysical phenomena or non-thermal high energy phenomena like jet occur in unknown way [4]. This paper deals with a novel manufacturing process of replicated Pt/C multilayer mirrors which will be used for the next-generation hard X-ray telescope after 2012. The specifications of such mirrors are as follows; shape accuracy of aspherical mirrors is less than 100 nm and surface roughness is also less than 0.3 nm rms. The mirror tolerance is tighter than soft X-ray telescope, because of shorter wavelength application.

MANUFACTURING PROCESS

In the case of a grazing incidence hard X-ray telescope, more than hundred of Pt/C multilayer mirrors of aspherical shape in high precision are needed for collecting X-ray from the galaxy. The weight of the telescope has to be light due to the space application, and the mirror surface area has to be larger for collecting power, so that the next-generation X-ray telescope consists of nested mirrors having Pt/C multilayer. For

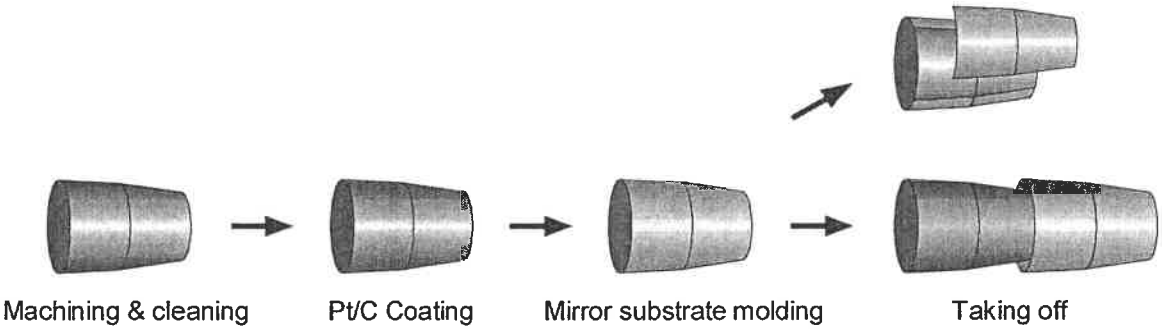

FIGURE 2. Manufacturing process of replicated mirrors for hard X-ray telescopes.

obtaining light-weight mirrors, replication technology is essential.

Figure 2 shows a manufacturing process of replicated Pt/C multilayer mirrors. The only material which can be ultra-smoothly polished is an amorphous material such as glass and electroless nickel. In this paper we used the latter one as molding die or mandrel material, because it is easy to be diamond-turned into aspherical shapes. Diamond turned aluminum mandrels are covered with electroless nickel plating and diamond turned again, then polished in to smooth surfaces less than 0.3 nm rms. After that, the polished surface has to be cleaned up. Pt/C multilayers are deposited on the electroless nickel mandrel after the deposition of a thin film for separation and glued a metal shell over the mandrel. All parts are put into a vacuum chamber for curing and then put into cold water in order to separate the Pt/C multilayer mirror from the mandrel.

The Upgraded hard x-ray telescope with Pt/C multilayer supermirrors for the InFOCμS balloon experiments were performed [4-6] by our group, in this case cylindrical glass tubes were used as the mandrel material like the Suzaku's mirrors. It is easy to separate the Pt/C multilayer from the glass mandrel by a quarter arc of an aluminum foil. However, no one has succeeded in separate the Pt/C multilayer from electroless nickel mandrels, though machining of electroless nickel is much easier than that of glass.

EXPERIMENTAL PROCEDURE

Electroless nickel deposited aluminum samples were turned in to plane, conical or aspherical shapes by a single-point diamond turning machine as shown in Fig. 3. The machine was installed on a vibration proof foundation in a temperature controlled clean room.

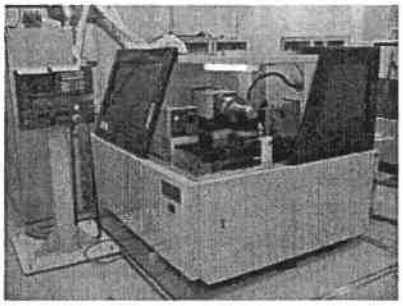

FIGURE 3. Single-point diamond turning machine in a temperature controlled clean room.

The diamond-turned samples were optically polished or float polished or hand-polished.

The Pt/C multilayer was deposited on polished plane dies, conical and aspherical mandrels by DC magnetron sputtering. The number of layer pair was 30 and the periodic distance was 4 nm. Various materials were used as an intermediate layer between the electroless nickel and platinum for separation.

Substrates for mirrors were separately prepared by inner-turning of steel. In the case of plane mirrors, we used thick glass plates as a substrate. The Pt/C coated mandrel and substrate were fixed with epoxy resin, and cured in a vacuum camber, then dipped in cold water for separation.

EXPERIMENTAL RESULTS

There are so many problems for establish the manufacturing process of replicated Pt/C multilayer mirrors for hard X-ray telescope. In this paper we will explain some of the experimental results.

Polishing of plane electroless mandrel

Electroless nickel samples of 30 mm in diameter and 10mm in thickness were diamond turned and optically polished as well as float polished. Figure 4 shows the surface roughness of machined plane samples, measured with a scanning probe microscope (SPM). Diamond turned and float-polished samples show the surface roughness of 0.90 nm rms and 0.11 nm rms, respectively. The latter surface satisfies the specification for hard X-ray telescope mirrors. The smoothest diamond-turned surface of 0.344 nm rms was obtained on an electroless nickel plane surface at the cutting conditions of 1 μm depth of cut, 0.5 μm/rev feed rate, 15m/s cutting speed with a sharp single point diamond tool having 10 mm nose radius. This number does not satisfy the specification of hard X-ray telescopes even on a plane surface, so the ultra-precision polishing is essential after the diamond turning.

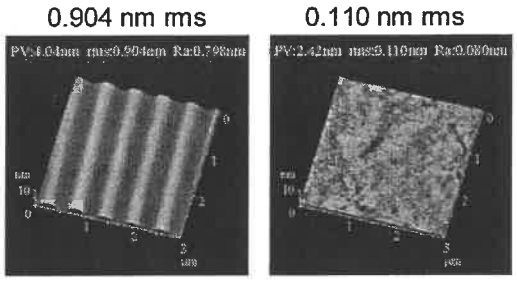

(a) Diamond turned (b) Float polished

FIGURE 4. Surface roughness of machined electroless nickel sample, measured with an SPM.

Replication of plane mirrors

In the case of separation of the Pt/C multilayer from the glass mandrel, the intermediate layer is not necessary [6]. However, we need the intermediate layer between an electroless nickel mandrel and Pt/C multilayer for separation.

Various materials were tested as an intermediate layer such as carbon, titanium, gallium, gold, vapor of silicon oil as well as Langmuir-Blodgett film. The coated intermediate layer has to be smooth on the surface less than 0.3 nm rms and very thin. Separation and transference of the die surface were good in the case of using carbon, titanium and Langmuir-Blodgett film as an intermediate layer. The gold is the perfect separation material, however the coated gold film is not smooth enough for this purpose.

Figure 5 shows the surface roughness of the float-polished electroless nickel plane die and the replicated Pt/C multilayer plane mirror after separation, measured with ZYGO NEWVIEW 200. The surface roughness are 0.136 nm rms and 0.155 nm rms on the electroless nickel plane die and replicated Pt/C multilayer mirror, respectively. In this case, we used the carbon intermediate layer.

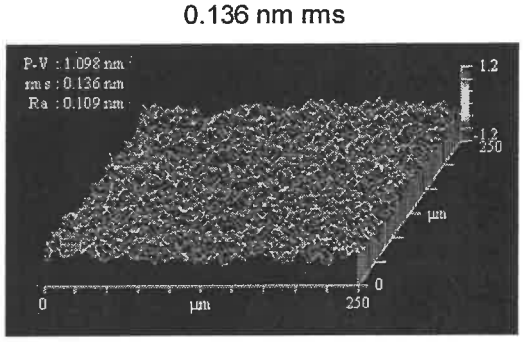

(a) Float-polished electroless nickel plane die

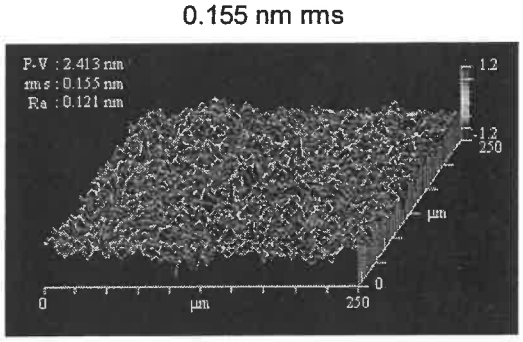

(b) Replicated Pt/C multilayer plane mirror

FIGURE 5. Surface roughness of electroless nickel plane die and replicated Pt/C multilayer plane mirror after separation.

The shape accuracy is also important in the replication process as well as the surface roughness. The flatness of replicated Pt/C multilayer on a glass plate of 8 mm thick was about the same flatness on the electroless nickel die plate.

Replication of conical mirrors

Figure 6 shows a conical mandrel made of aluminum alloy coated with electroless nickel on

the left, and a replicated Pt/C multilayer inner mirror on the right. The maximum diameter and mirror length were 38 mm and 35 mm, respectively on the mandrel, and the vertical angle of the cone was 20 degrees. This angle is much steeper compared with the hard X-ray telescope mirrors of less than 0.3 degrees. The thickness of carbon steel substrate was 5 mm. We could separate the Pt/C multilayer from the electroless nickel mandrel only when we used titanium as an intermediate layer. The picture shows the status of mandrel and replicated mirror just after the separation in cold water.

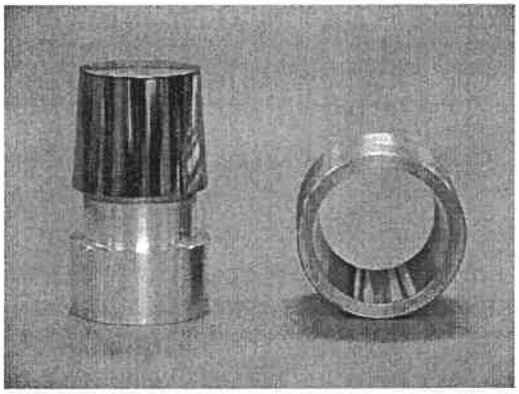

FIGURE 6. Diamond turned and polished conical electroless nickel mandrel (left) and replicated Pt/C multilayer conical mirror (Right).

Replication of aspherical mirrors

Electroless nickel mandrels of 102 mm maximum diameter and 75 mm in mirror length were machined for making a Wolter type I mirror of 8 m in focal length. The outer shape of mandrel was composed by a paraboloid and hyperboloid of revolution. The mandrel was coated by titanium in 10 nm thickness and deposited with Pt/C multilayers.

Carbon steel mirror substrates of 5 mm thick were mounted on the Pt/C multilayer coated mandrel with epoxy resin. However, Pt/C multilayer mirrors were not separated from the mandrel by the above-mentioned way up to now.

A glass fiber cloth was dipped in epoxy resin and a Pt/C multilayer-coated mandrel was partially covered with the fiber cloth. After curing, we can peel off the Pt/C multilayer-coated cloth of 0.5 mm thick from the mandrel. Titanium was used as an intermediate layer of 10 nm thick. This is another way of making replicated Pt/C multilayer mirrors.

The manufacturing method of whole circumference of replicated Pt/C mirrors will be still remained as the next step research.

SUMMARY

In order to obtain replicated Pt/C multilayer mirrors for a next-generation hard X-ray telescope, some basic experimental works have been done using electroless nickel mandrels which were single-point diamond turned and polished.

The surface roughness less than 0.2 nm rms was obtained on electroless nickel plane dies by the float polishing, and also we could get Pt/C multilayer plane mirrors less than 0.2 nm rms in surface roughness by replication technology using an intermediate layer. We succeeded in the separation of Pt/C multilayer from a cone mandrel. Titanium is one candidate as an intermediate layer between an electroless nickel mandrel and Pt/C multilayer from the view point of separation and transferability. The perfect replicated Pt/C mirrors for next-generation hard X-ray telescopes could not obtained yet.

ACKNOWLEDGEMENTS

This study was supported in part by the Grants-in-Aid for Scientific Research (B) Nos. 15360075 and 18360073 from the Japan Society for the Promotion of Science, and also the Grants-in-Aid for Scientific Research on Specially Promoted Research No. 15001002 from the Ministry of Education, Culture, Sports, Science and Technology, Japan.

REFERENCES

1. http://chandra.harvard.edu/
2. http://xmm.vilspa.esa.es/
3. http://www.astro.isas.ac.jp/suzaku/index.html.en
4. Tawara, Y., Yamashita, K., Ogasaka, Y., Tamura, K., Haga, K., Okajima, T., Ichimura, et. al., 2002, InFOCμS balloon-borne hard x-ray experiment with multilayer supermirror x-ray telescope, *Proc. SPIE*, 4496: 109-114.
5. Ogasaka, Y., Tamura, K., Okajima, T., Tawara, Y., Yamashita, K., Furuzawa, A., Haga, K. et. al., 2003, Supermirror hard x-ray telescope and the results of first observation flight of InFOCμS, *Proc. SPIE*, 4851: 619-630.
6. Okajima, T., Tamura, K., Ogasaka, Y., Haga, K., Takahashi, S., Ichimaru, S., Kito, H. et. al., 2002, Characterization of the supermirror hard X-ray telescope for the InFOCμS balloon experiment, *Appl. Opt.*, 41: 5417-5426.

A MAGNETORHEOLOGICAL POLISHINING BASED APPROACH FOR STUDYING MAGNETIC/NONMAGNETIC WC HARD METALS

Shai N. Shafrir[1, 2], John C. Lambropoulos[1, 2], and Stephen D. Jacobs[2]
[1]Mechanical Engineering, Materials Science Program, University of Rochester
Rochester, NY, USA
[b]Laboratory for Laser Energetics, University of Rochester
Rochester, NY, USA

1.0 INTRODUCTION

Magnetorheological finishing (MRF) is a commercial polishing process for the manufacturing of precision optics [1, 2]. MRF is a subaperture polishing technique that uses magnetic particles and a nonmagnetic polishing agent (abrasive particles) in either an aqueous or nonaqueous carrier fluid. The viscosity of the fluid is changed significantly in the presence of a magnetic field. This has traditionally limited the process to only nonmagnetic glasses, metals, crystals, and polycrystalline materials. In recent work [3] it was demonstrated that MRF can also be used to determine subsurface damage depth for optical crystals and glasses.

The purpose of this study is to expand this technique to tungsten carbides (WC) hard metals with significant microstructure. This is the first study where MRF is demonstrated to apply to a large variety of both magnetic and nonmagnetic tungsten carbide (WC) hard metals, Co-based and Ni-based, respectively.

Our goal is to have a better understanding of the correlation between WC response to microgrinding and nanopolishing with the resulting surface microroughness. In this study, we demonstrate that MRF spots can be placed on ground WC and that the spots can be used to evaluate the depth of the damaged layer. We focus on commercially available WC, with different microstructures and mechanical properties.

2.0 EXPERIMENT PROCEDURES

2.1. Tungsten carbide

Two different groups of commercial WC were used for this study. The first group of materials included five nonmagnetic WC samples (i.e., nickel (Ni) based binder), including one binderless material, whereas the second group included six magnetic WC samples (i.e., cobalt (Co) based binder). All the materials tested were selected on the basis of their binder content and grain size as well as their mechanical properties. Relevant microstructural, mechanical, and physical properties are listed in Table 1, ranked according to increasing value of the Vickers hardness.

2.2. Grinding experiments

The grinding experiments were performed on the OptiPro SX50 platform [4], a deterministic computer numerical control (CNC) ultraprecision grinding machine. For all our grinding experiments, a contour-tool grinding configuration for flat surfaces was used with three different diamond tools, rough, medium, and fine (40-, 10- to 20-, 2- to 4-μm grit size, respectively). Table 2 lists the grinding conditions used.

2.3. MRF spotting of ground surfaces

MRF was used in our experiment to measure the depth of the deformed layer from grinding and the quality of the subsurface subsequently exposed. Two sets of experiments were performed on different MRF CNC platforms for the nonmagnetic and magnetic materials, respectively, as follows:

1. Spot taking machine (STM) with an experimental nanodiamond [5] MRF fluid for Ni-based materials [6].
2. QED Q22-Y with a commercial MRF fluid designated as D10 for Co-based materials [7, 8].

Using these platforms we were able to polish spots onto the surface of a nonrotating part by lowering the part surface into contact with a rotating magnetic fluid ribbon under CNC control. The material removal rate is determined from the amount of material removed, i.e., ratio of spot volume, to spotting time. Machine parameters such as the magnetic field strength (~2–3 kG), wheel speed (250 rpm), pump speed

(125 rpm), ribbon height (1.6-mm), and depth of the part penetrating into the ribbon (0.3-mm) were kept constant and the spotting time was varied. Spotting was done on unetched regions of rough-ground, medium-ground, and fine-ground surfaces of each material.

2.4 Microscopy of processed surfaces

Surfaces were studied using a white-light interferometer [9], scanning electron microscope (SEM) [10], contact profilometer [11], and atomic force microscope (AFM) [12]. Before analyzing the surfaces, the samples were ultrasonically cleaned in acetone and then rinsed with alcohol; surfaces were dried using a nitrogen gun after ultrasonication and after rinsing.

3. EXPERIMENTAL RESULTS

Surface roughness data after each grinding stage were taken using the white light interferometer. For the first set of materials (nonmagnetic), the p–v surface-roughness varied from ~3.3 μm (BC12N) to ~5.8 μm (M10) with the coarse tool, from ~0.6 μm (K801) to ~3.9 μm (M10) with the medium tool, and from ~0.05 μm (M45) to ~0.09 μm (BC12N) with the fine tool. The smoothest surface after fine grinding was ~7 nm rms (M45), see Shafrir et al [6].

TABLE 1. Materials microstructural and mechanical properties [a]

Matl. ID	Dim. (mm) / # of samples	Density ρ, (g/cm^3)	Grain size, μm	Binder wt%	Hardness Rockwell A	Young's Modulus E, (GPa) [b]	Vickers Hardness H_v, (GPa) [c]	Fracture Toughness K_c, (MPa m$^{1/2}$)	Ductility Index DI, $(K_c/H_v)^2$ (μm)
Non magnetic materials (Ni based)									
BC12N	30 x 26 / 2	14.35	1.0	12	87.5-89.0	(614) [d]	12.01±0.13	12.98 [e]	1.17
K801	40 Φ / 3	14.85	7	6.3	90.7	618	13.71±0.17	10.15 [e]	0.55
M45	30.01 Φ / 3	14.40	0.6-1.3	12.5 [f]	89.5	500	14.78±0.17	8.06 [e]	0.30
M10	30.01 Φ / 3	14.25	0.2-0.6	9.5 [f]	92.5	510	18.54±0.2	6.35±0.1 [c, g]	0.12
Cerbide	56 x 32 / 2	>15.45	0.4	none	95.5	620	24.72±0.61	5.75±0.04 [c, g]	0.05
Magnetic materials (Co based)									
K3520	40 Φ / 3	13.28	10	20	84.2	485	9.3	16.9	3.3
K3833	40 Φ / 3	14.39	6	11	89.4	561	13.5	10.0 [e]	0.6
K94	40 Φ / 3	14.12	6	11.5	89.8	549	13.6	12.7	0.9
BC14S	40 Φ / 3	14.12	0.8	14	89.0-90.5	483	13.7 [d]	9.2 [e]	0.5
K714	40 Φ / 3	13.29	5	6.9 [h]	92.8	555	18.6	6.7 [c, g]	0.1
JO5	40 Φ / 3	14.6-14.7	??	2-3 [f, i]	92.5-94.0	570	19.5	5.5 [c, g]	0.08

[a] Catalog values, unless specified otherwise. [b] Converted from PSI. [c] Using a Tukon micro-indenter equipped with a Vickers diamond indenter and a microscope (50× objective), averaging the diagonals of five random indents on the surface with a load of 1-kg and duration of 15 s. [d] Estimated value. [e] Calculated values by using Laugier's correlation [13-15], $K_c = 2.15x10^6 (E/H_v)^{0.6} (1+0.012\ E/H_v)^{0.6} H_v^{-1.5}$, for WC-Co composites containing a ductile (i.e., binder) phase, where E is the Young's modulus, in units of MPa, and H_v is the Vickers hardness, in units of MPa, for $H_v \geq 10{,}000$ MPa. [f] Approximate values from EDS measurements. [g] Fracture-toughness values were calculated from the observed cracks using the Evans correlation [16]. [h] Cr-Co. [i] Ti.

TABLE 2. Contour grinding conditions used on the OptiPro SX50, in a single pass [a]

Tool grit size (μm)	Depth of cut (μm)	In-feed (Z-axis) mm/min)	Duration of single pass (sec)	Cross-feed (X-axis) (mm/min)	Duration of single pass (min)
40 [b]	100	0.5	12	1.0	30-40
10-20 [b]	20	0.5	2.4	1.0	30-40
2-4 [c]	5	0.5	0.6	5.0	6-8

[a] The following parameters remained constant: Wheel speed, Ω_t = 6800 rpm, Work spindle speed, Ω_w = 100 rpm. [b] Bronze bonded, 75 diamond concentration. [c] Resin bonded, 75 diamond concentration.

MRF spots of various durations were taken on all ground surfaces. After the location of the spot deepest point of penetration (ddp) was identified, using the contact profilometer, surface-roughness measurements at five random locations within the ddp region were taken with the white-light interferometer. Figure 1 shows the evolution of surface roughness with the maximum amount of material removed by MRF. The initial ground surface roughness is reduced for BC12N, K801, M45 and Cerbide when the MRF penetrates past 2.1-2.6 μm of the deformed surface layer thickness. However, surface roughness eventually increases with increasing MRF material removal. For M10, surface roughness decreased monotonically with increasing material removal. SEM images taken within the ddp region of the optimal spot (i.e., least roughness) confirmed that the deformed layer induced by grinding is completely removed by the MRF process [6].

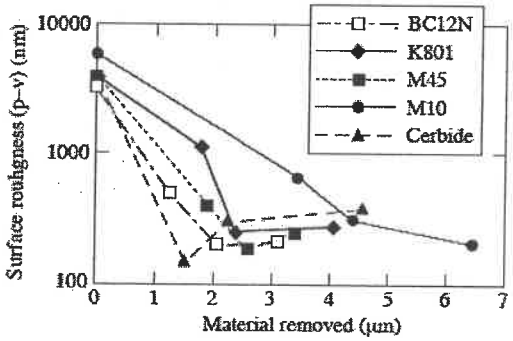

FIGURE 1. Evaluation of surface roughness, p-v (nm) semilog, vs. MRF spot material removed (μm). The starting condition is the rough ground surface (p-v roughness in the range of 3.3-5.8 μm). After removing 2-3 μm of material from the surface, the p-v roughness decreases to 180-310 nm.

A further investigation on K801 shows that the deformed layer induced by grinding (see Fig. 2(a)) is not completely removed after 1.8 μm of material is removed by the MRF spot (see Fig. 2(b)). However, when a total of 2.4 μm is removed (see Fig. 2(c)) the undisturbed subsurface is exposed. AFM scans confirmed that additional material removal slightly increased the surface roughness due to preferential polishing of the nickel binder (for a more detail discussion, see Ref. [6]).

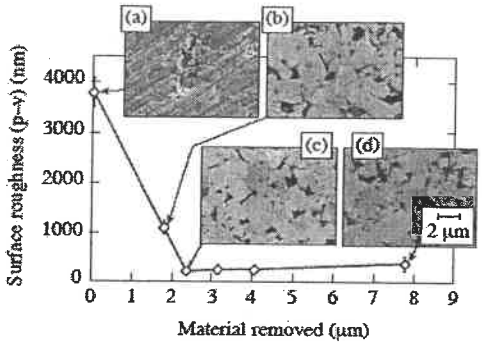

FIGURE 2. Surface roughness in the MRF spots, p-v (nm), vs. amount of material removal in microns for rough ground K801. Each data point represents a spot time of (as rough ground), 3, 6, 12, 18, and 40 min. SEM images correspond to the: (a) initial rough ground surface and (b) 1.8 μm, (c) 2.4 μm, and (d) 8 μm material removed (within the spot ddp region). The error bars represents the standard deviation of five areal measurements.

This technique was also tested for the second set of materials, i.e., magnetic WC. We found that an MRF spot can be placed on previously ground/lapped magnetic WC materials, which may be used to evaluate the depth of SSD, for more details see Shafrir et al. [8]

4.0 CONCLUSIONS

We have demonstrated that a MRF spot can be place on ground surfaces of tungsten carbides and that the spot can be used to evaluate the depth of the surface deformed layer, also known as SSD. We found that for the rough and medium tools, SSD depth is in the range 1.5-2.7 μm. The surface roughness of the MRF spot at the deepest point of penetration (ddp) can be used as a guide for establishing the optimal amount of material to be removed by subsequent grinding or polishing steps. By utilizing both surface-roughness measurements and SEM imaging at the spot ddp, we were able to estimate the depth of the deformed layer. Thus, we showed that the depth of the deformed layer can be estimated in two ways. An optical profilometer-based measurement of the p–v surface microroughness of the ground surface provides an upper bound to the deformed layer thickness. This is a desirable estimate given the noncontact nature of this metrology technique. On the other hand, the MRF spot can also be used to reveal the true depth of the deformed layer while reducing the surface-roughness.

5.0 ACKNOWLEDGMETS

The authors acknowledge the Laboratory for Laser Energetics at the University of Rochester for its continuing support. One of the authors (S. Shafrir) is a LLE Horton Fellow. This work was supported by the U.S. Department of Energy Office Confinement Fusion under Cooperative Agreement No. DE-FC52-92SF19460, the University of Rochester, and the New York State Energy Research and Development Authority. The support of DOE does not constitute an endorsement by DOE of the views expressed here.

6.0 REFERENCES

1. Jacobs SD, Pollicove HM, Kordonski WI, Golini D. Magnetorheological finishing (MRF) in deterministic optics manufacturing. International Conference on Precision Engineering (ICPE). Taipei, Taiwan, 1997. p.685.
2. Shorey AB, Jacobs SD, Kordonski WE, Gans RF. Experiments and observations regarding the mechanisms of glass removal in magnetorheological finishing. Applied Optics 2001;40.
3. Randi JA, Lambropoulos JC, Jacobs SD. Subsurface damage in some single crystalline optical materials. Applied optics 2005;44:2241.
4. OptiPro Systems, Inc., Ontario, NY.
5. Jacobs SD. Nanodiamonds Enhance Removal in Magnetorheological Finishing. Finer Points 1995;7:47.
6. Shafrir SN, Lambropoulos JC, Jacobs SD. A magnetorheological polishing-based approach for studying precision microground surfaces of tungsten carbides. Precision Engineering 2006;Article in press.
7. QED Technologies, Rochester, NY.
8. Shafrir SN, Lambropoulos JC, Jacobs SD. Technical note: A magnetorheological polishing-based approach for studying magnetic WC-Co hard metals. Precision Engineering 2006; Submitted for publication.
9. Zygo NewView 5000 white light interferometer, Zygo Corp., Middlefield, CT. Average microroughness data (peak-to-valley, p-v, and root-mean-square, rms) were obtained with a Zygo NewView 5000 non-contacting white light interferometer over five 350 μm by 250 μm areas, randomly distributed across ground and un-etched areas. This instrument has a lateral resolution of ~1 μm and a vertical resolution of ~0.3 nm.
10. LEO 982 FE SEM equipped with a secondary electron detector, a backscatter detector, and also an energy dispersive x-ray spectroscopy detector (EDS). The preferred imaging configuration was a mix signal of the in-lens and in-chamber secondary electron detectors.
11. Taylor Hobson TalySurf 2 PGI profilometer, Taylor Hobson Inc., Rolling Meadows, IL. 120 mm traverse unit, 10 mm gauge range, 12 nm vertical resolution, and 0.1 μm accuracy. Stylus specifications: 60° tip angle and 2 μm tip radius.
12. Digital Instruments/Veeco Metrology Dimension 3000 Atomic Force Microscope system, Veeco Instruments Inc., Woodbury NY. Surface scans for selected spots were taken over three 10- x 10-μm^2 areas randomly distributed across areas in spots where the deepest point of fluid penetration (ddp) occurred. This instrument has a vertical noise resolution of less than 0.5-Å.
13. Laugier MT. Palmqvist toughness in WC-Co composites viewed as a ductile/brittle transition. Journal of Materials Science Letters 1987;6:768.
14. Laugier MT. Comparison of toughness in WC-Co determined by a compact tensile technique with model predictions. Journal of Materials Science Letters 1987;6:779.
15. Laugier MT. Palmqvist indentation crack analyses for toughness determination in WC-Co composites. Key Engineering Materials 1989;32:77.
16. Evans AG. Fracture Toughness: The role of Indentation Techniques. In: Fierman SW, editor. Fracture Mechanics Applied to Brittle Materials, vol. 678. Philadelphia: American Society for Testing and Materials, 1979. p.112

DAMAGE-FREE PROCESSING OF SILICON CARBIDE OPTICS

Yogesh Verma, Peter S. Fiske, Pradeep K. Subrahmanyan, George J. Gardopee

RAPT Industries, Inc., 6252 Preston Ave., Livermore, CA 94551

ABSTRACT

Mechanical grinding and shaping of optical materials imparts damage that manifests itself as defects and cracks that can propagate well below the surface of the optic. Mitigation of damage is necessary to preserve the integrity of the optic and to relieve residual stress that can be detrimental to its performance. This damage can also cause instability in optical performance with changes in the ambient conditions. In certain high laser fluence applications or under transient stresses, it can also lead to catastrophic failure. This residual stress is usually relieved by grinding with progressively smaller grit sizes but often times this process will still leave behind a small amount of stress from the final polishing step.

Reactive Atom Plasma (RAP), a novel non-contact, atmospheric pressure plasma-based process, has been shown to reveal and mitigate sub-surface damage in optical materials. Twyman stress tests on thin glass and Silicon Carbide (SiC) substrates demonstrate RAP's ability to relieve this stress. We will show how RAP processing can enhance and accelerate fabrication of precision SiC optics.

INTRODUCTION

Optics fabrication relies on various machining, grinding and polishing steps that remove material through either brittle or ductile mode shearing [1]. This not only leaves behind a fractured surface but most of those fracture points have cracks that extend well below the surface. This is usually referred to as sub-surface damage (SSD). The presence and amount of SSD influences the amount of time required to polish the optic to final specification not only because SSD can create surface defects but also because of the high state of stresses in the damaged zone. SSD can also be a limiting factor in the ultimate tensile strength of brittle materials by providing nucleation sites for catastrophic failure [2].

Sub-surface damage is typically reduced through a series of grinding steps using successively finer grit sizes that remove the damage from prior grinding step but leave behind a thinner damage zone which has to be removed in subsequent grinding steps. Opticians often use rules of thumb such as removing 3x the depth of material corresponding to the previous grit size used. However, depending on the process parameters, there is damage that is lurking deeper than this. Final polishing with sub-micron abrasive particles is thought to prevent the introduction of new damage but will leave behind a surface that has substantial residual stresses from plastic deformation [3, 4].

Sub-surface damage can be detected and qualitatively assessed using a variety of techniques including ball-dimple tests, optical and acoustical microscopy and a variety of other non-destructive tests. The stress associated with SSD can be quantitatively determined by measuring the change in shape of thin disks before and after a grind step. This type of analysis is referred to as Twyman analysis and was first observed by an Englishman by the same name in the early 20th century [5].

SiC and SSD

SiC is a material finding increased adoption in the optical community due to a number of reasons. It has excellent thermal and mechanical properties with a specific stiffness of >120 N-m/KG (second only to Beryllium and without the accompanying toxicity issues). Its thermal stability is better than Zerodur in environments where there is rapid and large fluctuation in temperatures. However, its widespread adoption has been limited by manufacturability issues. SiC's hardness is such that the only known

technique to mechanically polish the surface is to use diamond based abrasives and employ high contact forces. This process ends up putting a significant amount of sub-surface damage into the substrate and, in the case of lightweight optics, the high contact force causes print-through. In the case of high-performance glass optics, a wet acid-etch step is sometimes inserted between hard machining steps in order to arrest further propagation of sub-surface damage. In the case of SiC, the only known (hazardous and slow) chemistry for an etching step is using molten potassium hydroxide at an elevated temperature.

Rapid damage removal using Reactive Atom Plasma (RAP™) processing

Reactive Atom Plasma processing is a novel manufacturing technology with the potential to significantly reduce the time and cost of manufacturing optics [6]. The process uses an atmospheric pressure inductively coupled Ar plasma to breakdown CF_4 gas into carbon and fluorine atoms and is discussed in detail in a companion paper [10].

EXPERIMENTAL PROCEDURE

For these tests thin disks (75mm diameter by 2mm nominal thickness) of fused silica (Corning 7980) and sintered SiC (CoorsTek SC30) were used. Both sides of each disk were ground on a 3 micron fixed abrasive lap to remove about 250 microns of material so that any damage from prior process steps is removed The glass disks were then acid etched in a buffered HF solution to remove 50-60 microns of stock from both sides. In the case of SiC, the RAP process was used to strip off about 20 microns of material on both sides. At this point the disks had no sub-surface damage and no residual stress.

The front side of each disk (designated S1) was measured for shape either on a phase shifting interferometer (in case of fused silica) or an optical profiler microscope (in case of SiC). Samples were then ground on the back side (designated S2) using down pressures of 0.6 to 2.6 psi on fixed abrasive laps with either 9 micron or 3 micron grit. A total of 25 microns was removed in this grinding step. The grinding step produced a uniform compressive stress in S2 which caused it to bend in a convex shape, resulting in a concave shape change on S1.

The shape change on S1 was measured. This change in shape is radially symmetric and is commonly referred to as sag. Opticians refer to it as power change. Subsequently a RAP removal was performed on the back side to remove a small amount of damage layer. This caused a slight stress relaxation and a resultant change in sag. This change in sag of S1 was again measured. This procedure was repeated until further RAP removals didn't change the shape any further. The cumulative amount of RAP removals (based on weight loss measurements) gives the depth of SSD.

The Stoney equation can be used to correlate the change in sag of a disk to a change in the state of surface stress [6] where:

$$\sigma = \frac{4\delta E d^2}{3(1-\upsilon)t_{ssd}D^2}$$

σ = Twyman stress (MPa)
ν = Poisson's ratio
E = Young's Modulus (MPa)
t_{ssd} = Damage layer thickness (nm)
δ = Circular plate deflection (nm)
d = Substrate thickness (mm)
D = Substrate diameter (mm)

This is the biaxial form of the equation and is valid for aspect ratios greater than 1:50 between depth of SSD and thickness of the substrate. The equation above further approximates the radius of curvature and is valid for small plate deflection. t_{ssd} is determined by the depth of removal required to restore the disk to its original pre-ground shape.

RESULTS

Using the Stoney equation and plugging in the total depth of SSD (t_{SSD}) the stress change after each RAP hit was determined based on the amount of sag change. The following results are shown as plots of change in stress as a function of RAP assisted material removal.

Results on glass

Figure 2 shows the decrease in stress as a function of RAP removal in glass disks subjected to grinding at 0.6, 1.3 and 2.6 psi

on a 9 micron fixed abrasive lap. The resulting roughness after lapping on the 9 micron lap was 140-150 nm Ra and did not vary with downward pressure. The surface stress from grinding with the 9 micron lap ranges from 25-30 MPa for all samples: no variation in initial stress is observed as a function of grinding pressure. The depth of SSD is around 10 microns in the surfaces ground at 0.6 and 1.3 psi but the surface ground under 2.6 psi of pressure shows stress and damage extending at least 16 microns into the material. In general, the relaxation of stress is not linear – the initial few RAP removals remove more stress than later RAP steps.

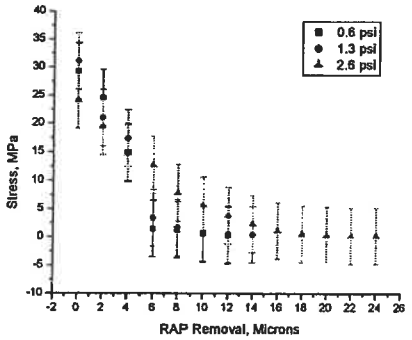

Figure 2. Residual stress in fused silica glass ground on 9 μm fixed abrasive lap under various pressures as a function of material removed by RAP processing.

Results on SiC

Figure 3 shows the decrease in stress as a function of RAP removal in a SiC disk ground under 1.3 psi using a 9 micron fixed diamond abrasive lap.

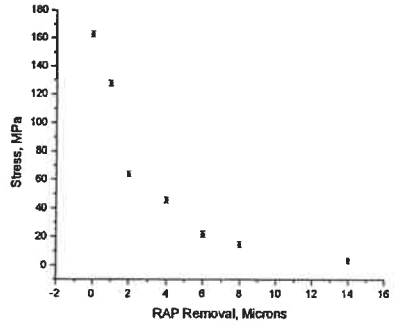

Figure 3. Residual stress in Coorstek SC30 SiC ground on 9 μm fixed abrasive lap under various pressures as a function of material removed by RAP processing.

Our results on glass are in accordance with a number of prior observations and measurements of damage in brittle materials [4]. The depth of SSD (and associated stress) correlates with the pressure during lapping.

DISCUSSION

The roughness produced by this lapping step was 170-200 nm Ra. The post-grinding state of stress is 160 MPa and falls off with depth in a relationship similar to that observed in the glass disks. The depth of SSD is roughly 14 microns.

Like previous studies, our results on both glass and SiC suggest that stress is not uniformly distributed within the damage zone but rather is concentrated at the surface and falls off with depth in a rough power law relationship. Similar behavior is observed in the distribution of micro-cracks in Corning 7980 fused silica ground under a variety of conditions [9].

Since the RAP process is chemical in nature it works by attacking the most (chemically) active sites first, so rather than remove a specific depth of material it would remove the most damaged and stressed material first. This makes it difficult to derive an exact relationship between stress and depth of SSD from our data.

We observe that under comparable lapping conditions SiC exhibits about 5.5x the stress associated with SSD compared to glass. As shown in earlier studies the magnitude of stress is dependent on physical material properties of the substrate and SiC has a modulus of elasticity that is about 5.5x higher than glass (410 GPa vs. 72.1 GPa).

Despite the differences in physical properties between glass and SiC, the thickness of the damage layer in this variety of SiC appears to be comparable to that in glass lapped under similar conditions. This suggests that using an all conventional process, opticians will have to remove at least as much material in SiC as in glass to achieve a surface with low damage. Using higher downward force during grinding may increase the material removal rate but it will also increase the depth of damage and necessitate larger volumes of stock removal

during subsequent process steps. Thus, higher pressure grinding may not reduce overall manufacturing cycle times for SiC optics at all but will increase the risk of catastrophic failure of the optical substrate during optical fabrication.

CONCLUSIONS

Residual stress in ground surfaces of SiC are roughly a factor of 5 times higher than those measured in glass ground under identical conditions. The depth of sub-surface damage in ground SiC can extend at least as deep as that observed in ground glass. Manufacturing precision, low-damage SiC optics using purely conventional processes will thus require extremely long cycle times.

Irrespective of the magnitude or origin of the stresses observed in these materials, we have demonstrated that RAP can be used to quickly and deterministically mitigate the stress by removing the damage that causes it. In the case of glass, RAP provides an alternative to buffered etching – with the added advantage of allowing for localized removal in areas of concentrated damage as well as shape control and figure improvement.

In the case of SiC, RAP is the only method we are aware of that can rapidly and cost-effectively remove the damage caused by abrasive grinding while simultaneously improving the shape of the optical surface, thus greatly reducing the time required to finish high-performance SiC optics

ACKNOWLEDGEMENTS

The authors are grateful to Mr. Francois Piche and Mr. Jeffrey Maloney (L-3 Brashear) for providing the glass disks for this study and to Dr. Jeffrey Carr for inspiring this work. This work was supported under US. Army contracts DAAD19-03-2-0003 and W911NF-04-2-0001 and U.S. MDA contract W9113M-06-C-0067. RAP is a trademark of RAPT Industries, Inc.

REFERENCES

1.Preston, F. W., 1921, The structure of abraded glass surfaces, *Trans. Opt. Soc. v. 23*, 141-164.

2.Li, K., and Liao, T. W., 1996, Surface/subsurface damage and fracture strength of ground ceramics, *J. Mat. Proc. Tech. v. 57*, 207-220.

3.Golini, D., and Jacobs, S. D., 1991, Physics of loose abrasive microgrinding, *Appl. Optics v. 30*, 2761-2777.

4.Lambropoulos, J. C., Xu, S., Fang, T., and Golini, D., 1996, Twyman effect mechanics in grinding and microgrinding, *Appl. Optics v. 35*, pp 5704-5713.

5.Dalladay, A. J., 1922, Some measurement of the stress produced at the surfaces of glass by grinding with loose abrasives, *Trans. Opt. Soc. London* v. *23*, 170-173.

6.Yogesh V., Peter S. F., Andrew K. C., John W. B., Kenneth F., George J. G., Jude K., Thomas K., Jeonghwa L., Nick L., David P., Phillip R. S. and Pradeep S., 2006, *Proceedings of SPIE, Astronomical Telescopes and Instrumentation, 2006.*

7.Randi, J. A., Lambropolous, J. C., and Jacobs, S. D., 2005, Subsurface damage in some single crystalline optical materials, *Appl. Optics v. 44*, 2241-2249

8.Johnson, J. S., Grobsky, K., and Bray, D. J., 2002, Rapid fabrication of lightweight silicon carbide mirrors, *in Optomechanical Design and Engineering 2002 (A. E. Hathaway, ed.), Proceedings of SPIE v. 4771*, p. 243-253.

9.Miller, P. E., Suratwala, T. I., Wong, L. L., Feit, M. D., Menapace, J. A., Davis, P. J., and Steele, R. A., 2005, The distribution of subsurface damage in fused silica, *in Boulder Damage Symposium 2005.*

10.Subrahmanyan, P.K., Gardopee, G., Fiske, P.S., and Chang, A., Reactive Atom Plasma (RAP) Processing of Optical Surfaces *in Annual Proceedings of the American Society for Precision Engineering, 2006*

CONTROL OF THE INTERFERENCE FRINGES IN A POINT DIFFRACTION INTERFEROMETER USING AN OPTICAL SATURABLE ABSORBER

Hideo Furuhashi[1], Yoshiyuki Uchida[1], Kiyofumi Matsuda[2] and Akihiro Kono[3]
[1]Department of Electrical and Electronics Engineering
Aichi Institute of Technology
1247, Yachigusa, Yakusa-cho, Toyota, 470-0392 Japan
[2]Graduate School for the Creation of New Photonics Industries, Japan
[3]Graduate School of Engineering, Nagoya University, Japan

INTRODUCTION

A point diffraction interferometer (PDI) is a common-path interferometer that can be used to easily measure either the variation in the phase across a wavefront or the change in the refractive index of a transparent phase object [1-4]. Point-diffraction interferometers have a simple construction and are inherently stable. Thus they are useful for testing and evaluating optical elements, and analyzing phase objects, fluid flow diagnostics, for example. However, the filter in a PDI has an extremely small dot, and it is difficult to focus the wavefront on such a small dot. Therefore, we have proposed a PDI that employs an optical saturable absorber. In this system, the small dot is generated automatically on the film and the focal point is self-aligned. One disadvantage of this system, however, is that the fringe contrast decreases over a long period of time. We have demonstrated that this problem can be overcome by stabilizing the fringe pattern by applying blue light [5].

It is difficult to vary the transparency of the film in a conventional PDI, making it impossible to control or optimize the fringe contrast, since the contrast depends on the light intensity passing through the PDI dot. However, the technique using blue light has the advantage that the characteristics of the filter (the transparency and the size of the dot) can be adjusted, so that the maximum contrast can be obtained.

In this paper, the control of the fringe pattern contrast in a PDI using an optical saturable absorber and blue light is discussed in detail.

THEORY

Figure 1 shows a schematic diagram of a conventional PDI system. A transparent dot filter is employed in a conventional PDI system. A wavefront in the object plane is focused on the filter using a Fourier-transform lens. The interference image is observed in the image plane. The optical image intensity is given by [5]

$$I = A^2\left\{\alpha^2 + \gamma^2\cdot\left(\alpha_{foc}-\alpha\right)^2 + 2\cdot\alpha\cdot\gamma\left(\alpha_{foc}-\alpha\right)\cdot\cos\left[i\phi(x,y)\right]\right\} \quad (1)$$

Here, A and $i\phi(x,y)$ are the absolute amplitude and phase of the wavefront in the object plane respectively, x and y are orthogonal coordinates, α and α_{foc} are the amplitude transmittances of the filter outside and inside the dot respectively, and γ is the ratio of the light passing through the PDI dot.

The fringe contrast is defined as

$$V = \left|\frac{2\cdot\alpha\cdot\gamma\cdot\left(\alpha_{foc}-\alpha\right)}{\alpha^2+\gamma^2\cdot\left(\alpha_{foc}-\alpha\right)^2}\right|. \quad (2)$$

Therefore, the contrast changes with γ. It has a maximum value of 1 when

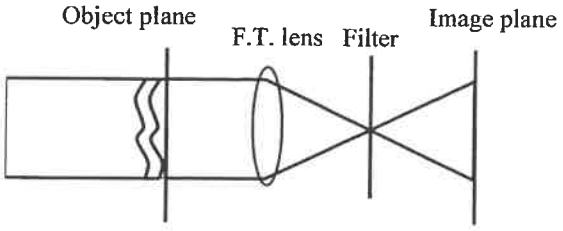

FIGURE 1. Schematic diagram of a PDI system. F.T. lens: (Fourier transform lens)

$$\gamma = \left| \frac{\alpha}{\alpha_{foc} - \alpha} \right|. \qquad (3)$$

It is difficult to vary the transparency of the film in a conventional PDI.

Figure 2 shows the experimental set-up of a PDI that employs a saturable absorber. A saturable absorber, photochromic bacteriorhodopsin (BR) film, is used as the filter. Figure 3 shows a schematic diagram of a simplified photocycle of a BR film. BR568 is the ground state, while M412 is the excited state. The film absorbs light having wavelengths between 500 and 700 nm by the excitation of molecules in the ground state to the excited state. It has a very high resolution of over 5000 lines/mm and a low saturation energy. It has a relaxation time, (defined as the time taken for 63% (1/e) of all excited state molecules to return to the ground state) of 40-80 s at a temperature of 22°C.

If a wavefront from a collimated laser, which has an output wavelength in the range 500-700 nm, passes through a transparent phase object and is focused on the film, the point becomes transparent. Thus, the BR-film acts as a PDI filter. The film has a maximum absorption at 568 nm, therefore He-Ne lasers having output wavelengths of 633 nm and 543.5 nm were used in this experiment. We then applied blue light from a xenon lamp, which de-excites the M412 state to the BR568 ground state. The film absorbs light with a wavelength below 500 nm by de-excitation.

The absorption rate of the film is given by [5]

$$\beta_{abs} = k_{12} \cdot \frac{N_0}{I' \cdot k_{12} + I'' \cdot k_{21}} \left[I'' \cdot k_{21} + I' \cdot k_{12} \cdot \exp\left\{ -\left(I' \cdot k_{12} + I'' \cdot k_{21} \right) t \right\} \right] + \beta_0 \qquad (4)$$

Here, k_{12} and k_{21} are the absorption coefficients for the excitation light in the ground state and for the de-excitation light in the excited state respectively, N_0 is the molecular surface density, β_0 is the background absorption rate of the film, and I' and I'' are the optical intensities of the excitation light and the de-excitation light at the film, respectively. After a long time, it becomes

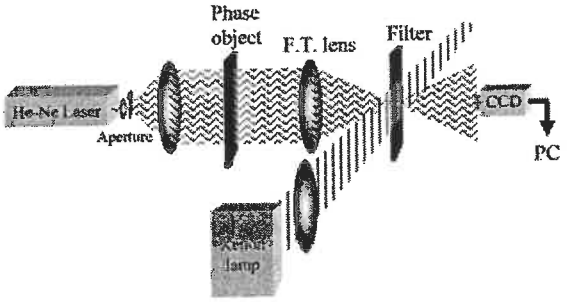

FIGURE 2. Experimental set-up of a point diffraction interferometer using a saturable absorber, He-Ne laser and blue light.

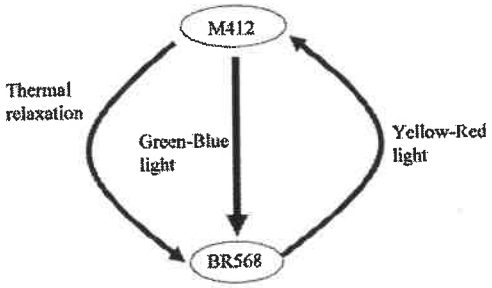

FIGURE 3. Schematic diagram for a simplified photocycle of the BR film.

$$\beta_{abs} = N_0 \cdot k_{12} \frac{1}{1 + \frac{I'}{I''} \cdot \frac{k_{12}}{k_{21}}} + \beta_0 . \qquad (5)$$

If the excitation light intensity I' is very high, the absorption becomes small.

The absorbencies for the ground-state film and excited-state film used in this experiment are 2 and 0.7 for the 633-nm-wavelength radiation of the He-Ne laser, respectively. Those for 543.5 nm are 6 and 0.9, respectively. Therefore, $N_0 \cdot k_{12} = 1.3$ and $\beta_0 = 0.7$ for the 633-nm-wavelength He-Ne laser. $N_0 \cdot k_{12} = 5.1$ and $\beta_0 = 0.9$ for the 543.5-nm-wavelength He-Ne laser.

The amplitude transmittances α of the filter outside the focal point are 0.37 and 0.05 for wavelengths of 633 nm and 534.5 nm, respectively. The saturated amplitude transmittances are 0.7 and 0.64 for the

wavelengths of 633 nm and 534.5 nm, respectively. Figure 4 shows the fringe contrast calculated using equation (2). Figure 4(a) is for the 633-nm laser while Fig. 4(b) is for the 534.5-nm laser.

Since the amplitude transmittance inside the focal point is larger than that outside the focal point, maximum contrast is obtained when $\alpha_{foc} = \left(1+\frac{1}{\gamma}\right)\alpha$. However, the maximum amplitude transmittances α_{foc} of the filter inside the focal point are 0.7 and 0.64 for 633 nm and 534.5 nm, respectively. Therefore, maximum contrast is obtained at the maximum α_{foc} of 0.7 for the 633-nm-wavelength laser having a wavelength of 633 nm. It is smaller than 1. On the other hand, a maximum contrast of 1 is obtained by controlling the transmittance α_{foc} between 0.05 to 0.64 for the 534.5-nm-wavelength laser.

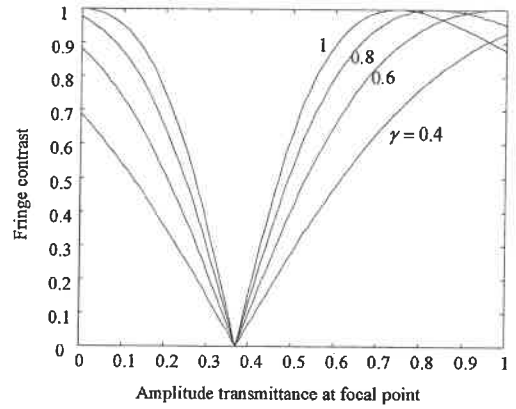

(a)

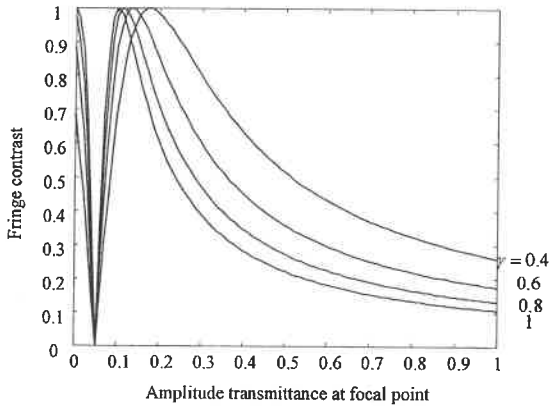

(b)

FIGURE 4. Relationships between fringe contrast and amplitude transmittance at the focal point for the (a) 633-nm-wavelength and (b) 534.5-nm-wavelength He-Ne laser.

In general, the necessary condition for obtaining a fringe contrast of 1 is

$$\frac{\alpha|_{\max}}{\alpha} > 1+\frac{1}{\gamma}. \qquad (6)$$

Here, $\alpha|_{\max}$ is the saturated amplitude transmittance of the film. This condition can be written as follows in terms of the absorbance of ground state b_{BR} and that of the excited state b_M for the exciting light.

$$\exp\left(\frac{b_{BR}-b_M}{2}\right) > 1+\frac{1}{\gamma} \qquad (7)$$

Therefore, the 534.5-nm-wavelength laser gives good contrast. However, the large absorption of BR state at this wavelength results in a low intensity of the fringe. Therefore, if $\gamma \approx 1$, the 633-nm-wavelength He-Ne laser is the most suitable for measuring the fringes for the BR film used in this experiment. Better fringe contrast is obtained by using a thinner film for the 534.5-nm-wavelength laser.

Next we consider the focused plane wave which has an optical intensity profile on the focal point given by

$$I'_{plane} = I_p \left\{ \frac{2J_1\left(\frac{a}{\lambda \cdot f} r\right)}{\frac{a}{\lambda \cdot f} r} \right\}^2 . \qquad (8)$$

Here, I_p is the peak intensity at the focal point, f and a are the focal length and radius of the Fourier-transform lens, respectively. The

amplitude transmittance profile is given as follows.

$$\alpha_{foc}(r) = \exp\left(-\frac{N_0 \cdot k_{12}}{2} \frac{1}{1 + \frac{I'_{plane}}{I''} \cdot \frac{k_{12}}{k_{21}}} - \frac{\beta_0}{2} \right) \quad (9)$$

Figure 5 shows the amplitude transmittance of plane wave calculated by using equations (8) and (9). The transmittance can be changed by changing the intensity of the de-excitation light. The PDI dot size can be also changed. Therefore, the contrast can be controlled by varying the intensity of the de-excitation light.

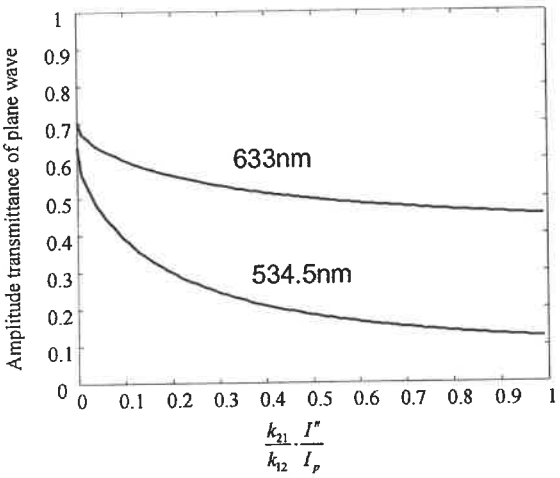

FIGURE 5. Calculated amplitude transmittance profile applied He-Ne laser. (a) 633 nm, (b) 543.5 nm

CONCLUSIONS

In conclusion, control of the contrast of the fringe pattern in a PDI using an optical saturable absorber and blue light has been discussed in detail. The contrast can be varied by the adjusting the intensity of the blue light. Therefore, it is possible to obtain good contrast for a wide variety of wavefronts by using this method.

REFERENCES

1. R. N. Smart, Jpn. 1975, Theory and application of point-diffraction interferometers, J. Appl. Phys. Suppl. 14: 351-356.
2. C. P. Grover, 1975, Random partial diffuser as beam splitter in a new, common path interferometer, Opt. Commun, 13: 335-337.
3. R. N. Smart, 1979, Special applications of the point diffraction interferometer, Proc. SPIE, 192: 35-40.
4. Hideo Furuhashi, Atsushi Shibata, Yoshiyuki Uchida, Kiyofumi Matsuda and Chander P. Grover, 2004, A Point diffraction interferometer with random-dot filter, Opt. Commun. 237, 17-24.
5. Hideo Furuhashi, Atsushi Shibata, Yoshiyuki Uchida, Kiyofumi Matsuda and Chander P. Grover, 2004, Point diffraction interferometer using an optical saturable absorber, Proc. 9th Annual ASPE Meeting.

DIGITAL PERIODIC ERROR CORRECTION: FURTHER TESTING AND RESULTS

Tony L. Schmitz[1], Lonnie Houck III[1], and David Chu[2]
[1]Department of Mechanical and Aerospace Engineering
University of Florida, Gainesville, FL, USA
[2]Agilent Technologies, Inc., Santa Clara, CA, USA

INTRODUCTION

Differential-path interferometry is often applied in situations requiring accurate displacement measurement, such as lithographic stages for semiconductor fabrication, transducer calibration, and axis position feedback for precision cutting and measuring machines. In many instances, a two frequency (or heterodyne) Michelson-type interferometer with single, double, or multiple passes of the optical paths is selected. These systems infer changes in displacement of a selected optical path by monitoring the optically-induced variation in a photodetector current. The phase measuring electronics convert this photodetector current to displacement by digitizing the phase progression of the photodetector signal. Due to non-ideal performance, mixing between the two heterodyne frequencies may occur, which results in periodic errors superimposed on the desired displacement data. First or second order periodic errors, with amplitudes that vary cyclically with the target position, are commonly observed. First order periodic error, which appears as single sideband modulation on the data at a spatial frequency of one cycle per displacement fringe, often dominates. However, second order periodic error, with a spatial frequency of two cycles per displacement fringe, is also often present.

Although modifications to traditional optical setups may be implemented to reduce periodic error, a digital correction scheme offers the advantage that no changes to the existing optical configuration are required. This paper describes experiments used to evaluate the real time, first order periodic error reduction scheme developed by Chu and Ray [1] for a variety of conditions. The results described here were obtained using a single pass, heterodyne Michelson-type interferometer that enabled: 1) isolation of periodic error as the primary uncertainty source in displacement measuring interferometry; and 2) variation of the frequency mixing that leads to periodic error so that the error amplitude could be changed. During target motion (achieved using an air bearing stage) at various velocities, the real time first order error correction was digitally applied in hardware and both the uncorrected and corrected measurement signals were recorded. Various frequency mixing levels were realized by adjustment of the setup optics. Additionally, data was collected during non-constant velocity motion and the time-dependent uncorrected and corrected results are provided.

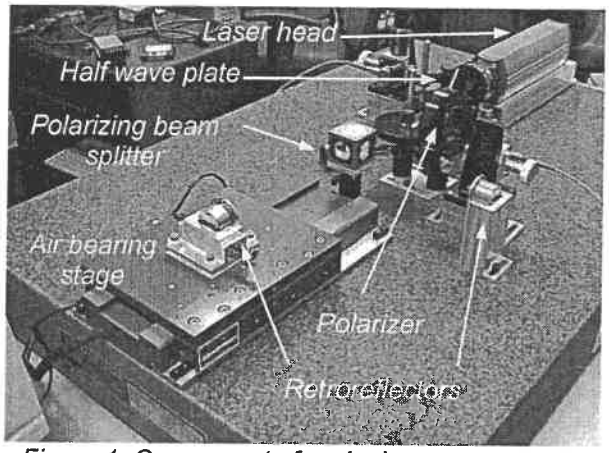

Figure 1: Components for single pass, heterodyne interferometer experimental setup.

EXPERIMENTAL SETUP

A photograph of the setup is provided in Fig. 1. The orthogonal, linearly polarized beams with a split frequency of approximately 3.65 MHz (Helium-Neon laser source) first pass through a half wave plate. Rotation of the half wave plate enables variation in the apparent angular alignment (about the beam axis) between the polarization axes and polarizing beam splitter; deviations in this alignment lead to frequency mixing in the interferometer. The light is then incident on a non-polarizing beam splitter (80% transmission) that directs a portion of the beam to a fiber optic pickup after passing through a fixed angle sheet polarizer (oriented at 45 deg to the nominal laser orthogonal polarizations). The pickup is mounted on a two rotational degree-of-

freedom flexure which enables efficient coupling of the light into the multi-mode fiber optic. This signal is used as the phase reference in the measurement electronics.

The remainder of the light continues to the polarizing beam splitter where it is (ideally) separated into its two frequency components that travel separately to the moving and fixed retroreflectors. In this design, motion of the moving retroreflector is achieved using an air bearing stage. After the beams are recombined in the polarizing beam splitter, they are directed by a 90 deg prism through a polarizer with a variable rotation angle. Finally, the light is launched into a fiber optic pickup. This serves as the measurement signal in the measurement electronics (0.3 nm resolution for single pass configuration).

The intent of the setup design was to minimize other well-known error contributors and enable variation in the periodic error nature, first or second order, and amplitude. To isolate periodic error, the setup was designed with zero Abbe offset (i.e., the measurement axis was collinear with the motion axis) and zero dead path difference (i.e., the distance between the polarization beam splitter and the moving retroreflector was equal to the distance between the polarization beam splitter and the fixed retroreflector at initialization). The measurement time (~100 ms) and motion amplitude were kept small to minimize the contribution of air refractive index variations due to the environmental changes. Additionally, careful alignment of the air bearing stage axis with the optical axis resulted in small beam shear.

EXPERIMENTAL RESULTS

In this section, we describe the analysis procedures and provide experimental results for two primary scenarios: 1) constant velocity tests with variable half wave plate and polarizer orientations; and 2) non-constant velocity tests with fixed polarizer and half wave plate angles.

Variable polarizer angle

In these tests the half wave plate angle was held fixed at its nominal orientation and the polarizer angle was systematically varied over a wide range. The velocity for the air bearing stage (and moving retroreflector) was 540 mm/min. The measurement and reference signal data from the interferometer were sampled at 312.5 kHz by the phase measuring hardware during constant velocity conditions; displacement was then determined from these signals. Output files included the uncorrected position data and the corrected data with the first order periodic error removed using the algorithm described in reference [1].

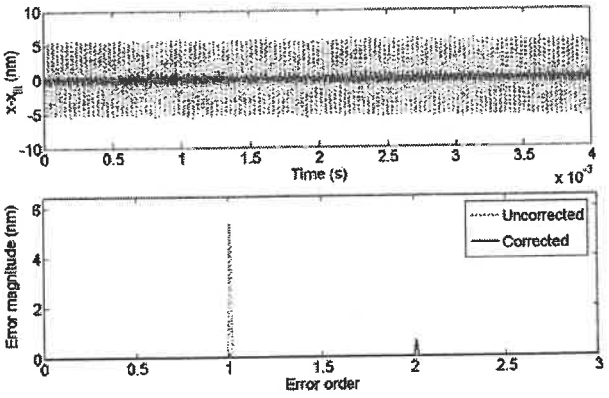

Figure 2: (Top) Time domain uncorrected (dashed) and corrected (solid) displacement signals after removing best fit line. (Bottom) Frequency domain representation of error normalized to error order. A first order error reduction from 5.4 nm to 0.1 nm is observed.

To isolate the periodic error content for these constant velocity tests, a least squares linear regression was performed and the best fit line, x_{fit}, subtracted from both the uncorrected and corrected signals. For the single pass Helium-Neon interferometer setup used here, first order error repeats every 633/2 = 316.5 nm, while second order completes a full cycle in 633/4 = 158.3 nm. To identify the first and second order error amplitudes, the discrete Fourier transform of the error (vs. nominal displacement) was computed and the spatial frequency axis normalized to periodic error order. Typical results are shown in Fig. 2 where the first and the second order error amplitudes are 5.4 nm and 0.4 nm, respectively, for the uncorrected signal. The corrected signal amplitudes are 0.1 nm and 0.7 nm, respectively.

The first and second order periodic error variation with polarizer angle is displayed in Fig. 3. The top panel shows successful attenuation of the first order error to sub-nm levels; the bottom panel shows that the algorithm does not affect the second order error. The percent reduction in first order error is provided in Fig. 4. Reductions of 90% or better are seen in all instances that the uncorrected first order error was 2 nm or greater. Slightly lower percentages are observed for small uncorrected error levels.

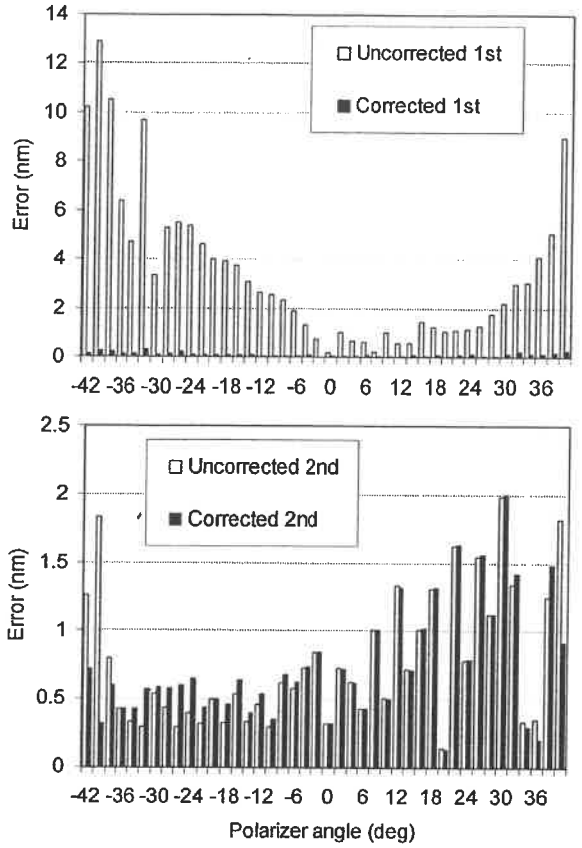

Figure 3: (Top) First order periodic error variation with polarizer angle. (Bottom) Second order variation. The 0 deg angle corresponds to the nominal 45 deg polarizer orientation.

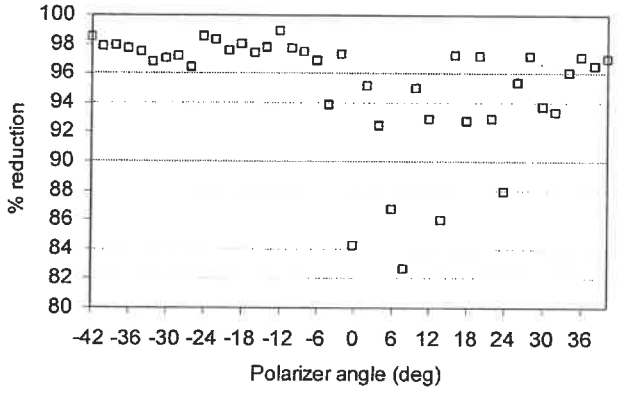

Figure 4: Percent error reduction in first order periodic error with variable polarizer angle.

Variable half wave plate angle

In this case the half wave plate angle was varied while the polarizer angle was held fixed at its nominal orientation. The stage velocity was 560 mm/min. The first and second order periodic error variations with half wave plate angle are displayed in Fig. 5. Large second order amplitudes are observed in the bottom panel for the extreme half wave plate angles. Under these conditions, the first order error in the corrected signal increases somewhat; percent reduction values of less than 90% are seen for deviations greater than 12 deg from the nominal in Fig. 6.

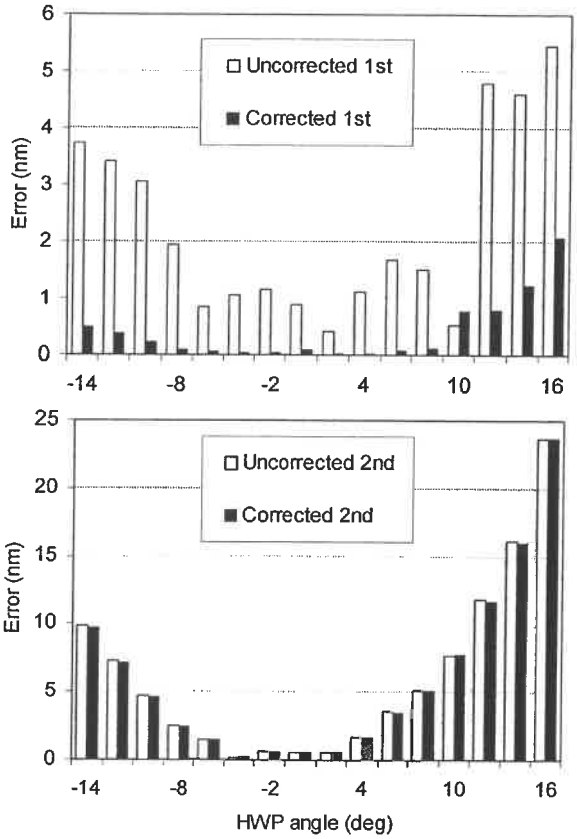

Figure 5: (Top) First order periodic error variation with half wave plate (HWP) angle. (Bottom) Second order variation. The 0 deg angle corresponds to nominal alignment between the HWP fast axis and laser head vertical polarization.

Additional constant velocity tests

To demonstrate the insensitivity of the digital correction algorithm to the commanded velocity, tests were also completed using fixed optical setups with data collected at a discrete number of constant velocities. Figure 7 shows first order error levels (uncorrected and corrected) for velocities between 650 mm/min and 3000 mm/min using two polarizer orientations (case I – 35 deg polarizer misalignment, case II – 15 deg polarizer misalignment; the nominal half wave plate angle was selected in both instances). In all tests, the percent error reduction is greater than 95%.

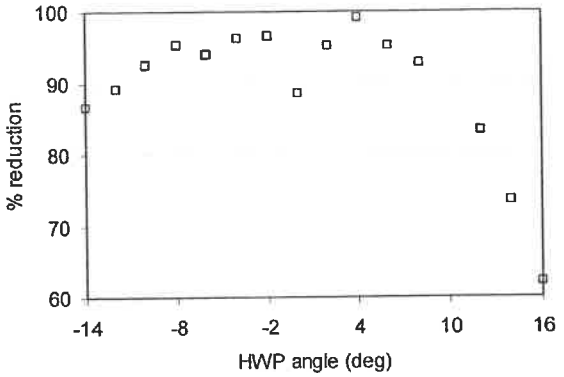

Figure 6: Percent error reduction in first order error with variable half wave plate angle. No data point is shown at 10 deg because the error level increased slightly (sub-nm level).

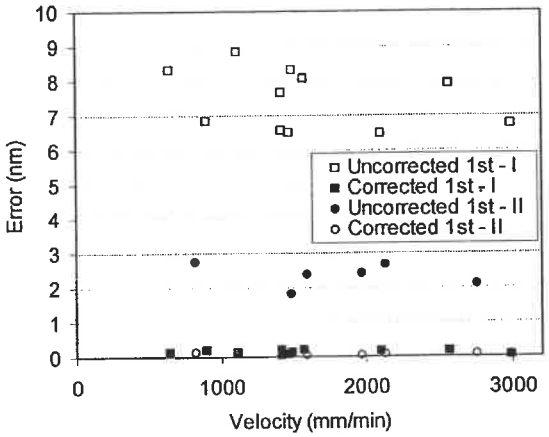

Figure 7: First order error reduction for two optical setups (cases I and II) as a function of commanded velocity.

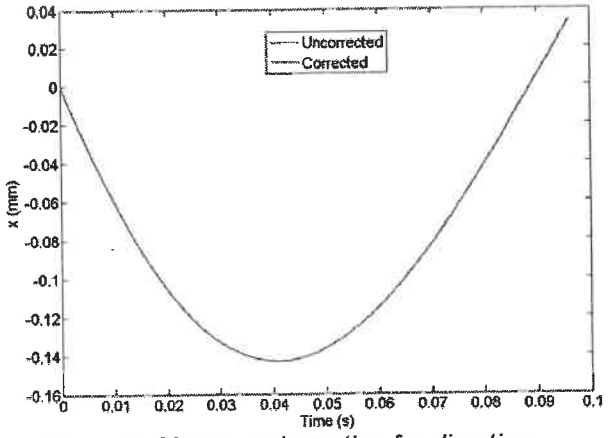

Figure 8: Macro-scale motion for direction reversal and velocity sign change.

Non-constant velocity

Here, data was collected during non-constant velocity profiles. Example data for a change in motion direction is provided. Figure 8 shows the macro-scale motion. Figure 9 (top) displays the uncorrected and corrected periodic error signals (after removing a least squares polynomial fit) for the time interval that contains the direction reversal; the middle panel shows the first order error amplitudes identified by the Chu and Ray method pre- and post-correction[1]; and the bottom panel shows the correction applied by the digital algorithm. Successful reduction of first order error under non-constant velocity conditions is observed.

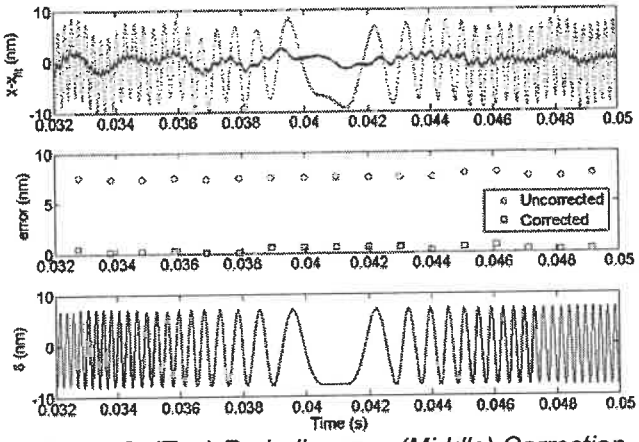

Figure 9: (Top) Periodic error. (Middle) Correction amplitudes. (Bottom) Digital correction signal.

CONCLUSIONS

The tests described here showed that the Chu and Ray digital correction algorithm [1] is able to successfully identify and reduce the first order periodic error level to sub-nm levels in nearly all constant velocity cases. In addition to the strong performance under constant velocity conditions, first order error reduction for non-constant velocities was also demonstrated.

ACKNOWLEGEMENTS

This work was supported by Agilent Technologies, Inc., the National Science Foundation (DMI- 0555645), and Aerotech, Inc.

REFERENCES

1. Chu D. and Ray, A., 2004, Nonlinearity Measurement and Correction of Metrology Data from an Interferometer System, Proceedings of 4th **euspen** International Conference, Glasgow, Scotland (UK), May-June, 300-301.

[1] Note that the Fourier technique cannot be applied to non-constant velocity motions.

PHASE MODULATION HOMODYNE INTERFEROMETER WITH PICOMETER RESOLUTION USING TUNABLE LASER DIODE

Masashi ISHIGE[1], Fumio MATSUURA[1], Masaaki KAWASUGI[1] and Masato AKETAGAWA[1]
[1]Nagaoka University of Technology
1603-1 Kamitomioka, Nagaoka Niigata 940-2188 Japan

INTRODUCTION

Since nanotechnology has progressed rapidly, a measuring method for length or displacement with resolution of picometer must be required in the near future[1)]. Nowadays, the laser interferometry is of the industrial standard. A lot of commercial interferometers are widely used in industries. However, it is very difficult to determine an arbitrary length or displacement with an accuracy of nanometer using the commercial interferometer, because it suffers from the nonlinearity problem of fringe interpolation[2)].

A phase modulation homodyne interferometer (PMHI) is proposed by Basile et al. in 1991[3)]. In the PMHI, a phase of an incident light is modulated with an Electro-optic modulator (EOM) and the output signal of a photodiode at the end of interferometer is demodulated with the modulation signal using a lock-in amplifier. (LIA) From this configuration, it is possible to determine an optical path difference L of wavelength λ × integer N (= mode number) with an accuracy of 10 pm or less using the null-method, because the lock-in demodulation can transfer a dark fringe (in the case, $L = \lambda \times N$) into a null-cross-point of the lock-in output signal. However, it is impossible to determine an arbitrary length or displacement using this method.

We propose a new displacement measurement method using the PMHI and a tunable laser diode (TLD) as a light source, to determine an arbitrary length with resolution of picometer. In the proposed instrument, a displacement of movable mirror in the interferometer can be converted to a frequency shift of the TLD. The features of proposed system are shown below.

(1) Displacement of the target can be measured by an optical frequency change of the TLD.
(2) There should be no periodic errors caused from phase interpolation.
(3) The principle of the system ensures the traceability of the meter.

In this paper, we discuss the principle of the proposed method, the instrumentation and the experimental results. In the experiments, we compare the proposed method with the commercial heterodyne interferometer[4)].

PRINCIPLE

Since interference signals of the Michelson interferometer have always offset part, it is difficult to determine a bright (or dark) fringe accurately in the signals. However, an application of the EOM and the lock-in detection to the homodyne interferometer allows to determine optical path difference L of wavelength λ × integer N with picometer resolution using null method[3)].

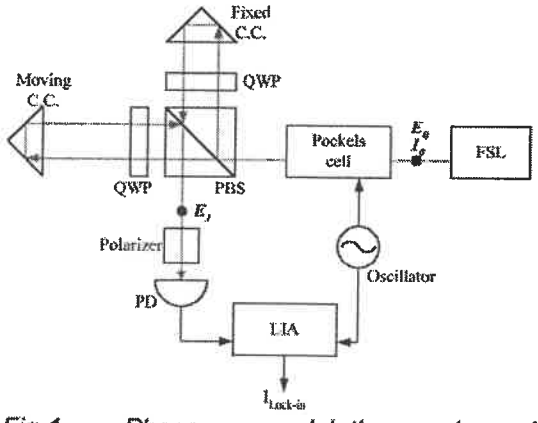

Fig.1 Phase modulation homodyne interferometer

Fig. 1 shows a system of the phase modulation homodyne interferometer. The system includes a frequency stabilized laser (FSL), a Pockels cell, a polarized beam splitter (PBS), quarter wave plates (QWPs), corner cube prisms (CCs), a photodetector (PD), a lock-in amplifier (LIA), a oscillator, and a polarizer. The light beam from FSL passing through the Pockels cell is divided into the reference and the measurement arms, respectively, by the PBS. And, the light beams reflected from the fixed and the moving CCs are mixed by the PBS. The mixed beam passing through an analyzer enters to the PD. The light from the FSL is linearly polarized and its angle is

45°from vertical. Its Jones vector can be written as,

$$\vec{E}_0 = \begin{pmatrix} E_x \\ E_y \end{pmatrix}. \quad (1)$$

The light passed through the Pockels cell and the interferometer is written as

$$\vec{E}_1 = \begin{pmatrix} 1 & 0 \\ 0 & e^{i(\delta + a\cos(\omega t))} \end{pmatrix} \begin{pmatrix} E_x \\ E_y \end{pmatrix}, \quad (2)$$
$$= \begin{pmatrix} E_x \\ E_y e^{i(\delta + a\cos(\omega t))} \end{pmatrix}$$

where δ, a and ω are a phase difference of optical path difference of interferometer, a modulation depth of Pockels cell and a modulation frequency, respectively. An intensity of the light detected in the PD is written as

$$I_1 = |E_1|^2$$
$$= \frac{1}{2}\left\{E_x^2 + E_y^2 + 2E_x E_y \cos(\delta + a\cos(\omega t))\right\}$$
$$= \frac{1}{2}\left\{1 + \Gamma\cos(\delta + a\cos(\omega t))\right\}, \quad (3)$$

where,

$$I_0 = E_x^2 + E_y^2, \quad (4)$$

$$\Gamma = \frac{2E_x E_y}{E_x^2 + E_y^2}. \quad (5)$$

And the output of the interferometer shown in (3) is synchronously detected by the LIA. Then the output of the LIA is written as

$$I_{lock-in} = \frac{1}{2\pi}\int\left[\frac{1}{2}I_0\left\{1 + \Gamma\cos(\delta + \cos(\omega t))\right\}\right]\cos(\omega t)\cdot dt(\omega t)$$
$$= \frac{1}{2}I_0\Gamma\sin(\delta)\times J_1(a), \quad (6)$$

where $J_1(a)$ is a first order of the Bessel function. The newly proposed system is shown in Fig.2. The system includes the PMHI, the TLD as a light source of the PMHI, the FSL for getting a beat signal between the TLD, and a servo unit for adjusting a frequency of the TLD.

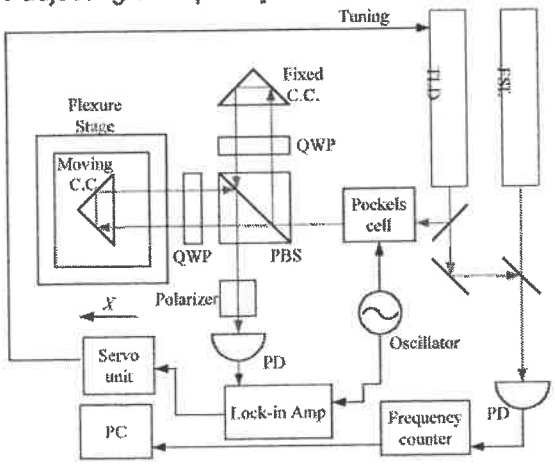

Fig.2 Constraction of proposed system

At a null-cross-point of the PMHI, we obtain next equation

$$L = \frac{c}{2fn}N, \quad (7)$$

where c, n and N are the speed of the light, a refractive index and a mode number, respectively. When moving CC is displaced, an optical frequency of the TLD is controlled to maintain the null-cross-point, then we obtain,

$$\frac{\Delta L}{L} = -\frac{\Delta f}{f} + \frac{\Delta N}{N}, \quad (8)$$

where ΔL, Δf and ΔN are changes of the optical path, the frequency and mode number, respectively. In the case, we assume $\Delta n = 0$. In the system, since one of the null-cross-points must be kept by adjusting a frequency of the TLD, the change of the mode number (= ΔN) must be null. Therefore, ΔL can be determine from Δf, which can be derived from the beat signal between the TLD and the FSL

EXPERIMENTAL RESULT

In the system, in order to determine ΔL, L must be known before the experiment. L can be derived from the free-spectral-range (FSR) which equals the frequency difference between neighboring modes. The FSR is written as

$$FSR = \frac{c}{2nL}. \quad (9)$$

The FSR can be measured in the LIA signal by scanning the frequency of the TLD. Fig.3 shows the measurement result of the FSR. In the figure, a frequency shift between neighboring null-cross-points is regarded as the FSR.

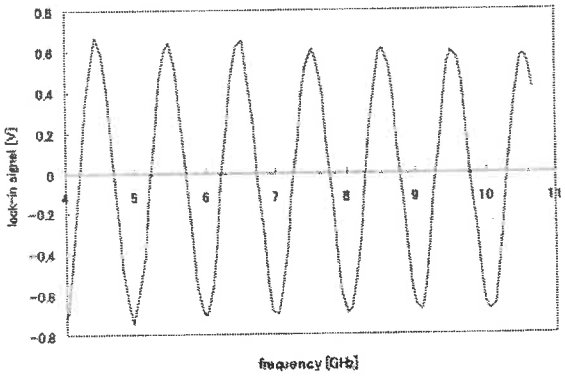

Fig.3 Measurement of the Free Spectral Range

From the Fig.3, the FSR equals to 1.01528GHz and L can be determine as,

$$L = \frac{2.9979\times10^8}{2\times1.00027\times1.01528\times10^9} = 147.60 \ [mm], \quad (10)$$

where refractive index of air is compensated with Cidder's equation[5]. The proposed system

was compared with commercial heterodyne interferometer. Experimental configuration is shown in Fig.4. In the configuration the moving CCs of the PMHI and the heterodyne interferometer are set on the same X-axis stage. When the X-axis stage is scanned, the both interferometer can synchronously measure the displacement of the stage. In the comparison measurement, a scanning frequency and a range for the X-axis stage are 0.05 Hz and 800 nm respectively. Fig.5 shows time variations for the heterodyne interferometer and the frequency change of the proposed system. Fig.6 shows the relationship between the displacements from the hetrodyne interferometer and the frequency change of the TLD. By using (8)～(10), the periodic error (= an output of the heterodyne interferometer - the output of the proposed method) was obtained. The result is shown in Fig.7. In Fig.7, half wavelength periodicity is clearly recognized.

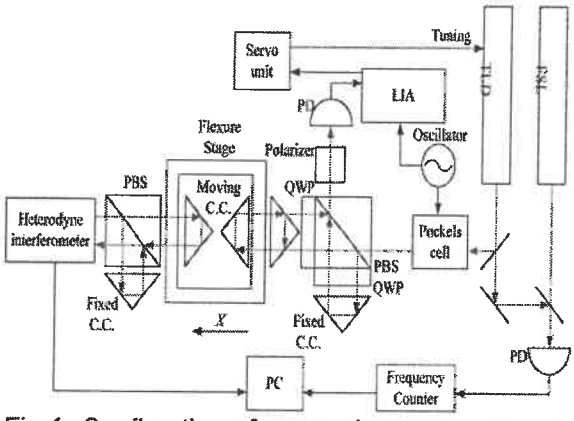

Fig.4 Configration of comparison measurement between proposed system and commercial heterodyne interferometer

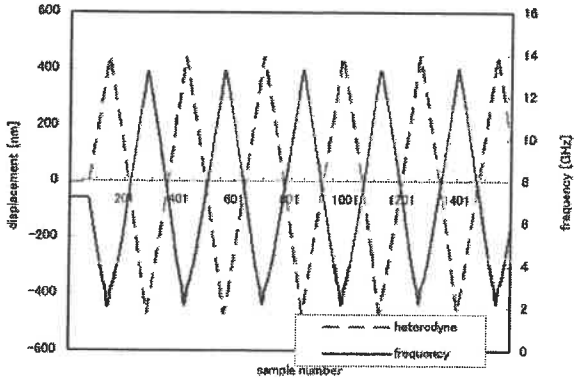

Fig.5 Relationship between signal of commercial heterodyne interferometer and signal of proposed system

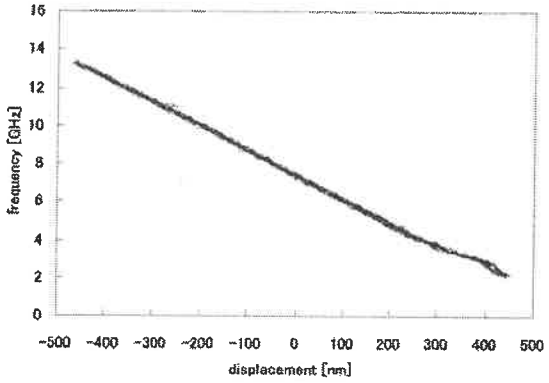

Fig.6 Relationship between signal of commercial heterodyne interferometer and signal of proposed system

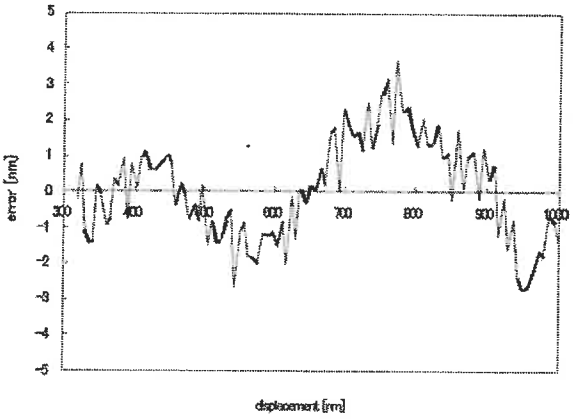

Fig.7 Periodic error of commercial interferometer

CONCLUSION

The method for measuring the displacement with high resolution by adjusting the optical frequency of the TLD is proposed. Its system is constructed by combining with the PMHI, the TLD and frequency tuning electronics. For measuring displacement optical path difference is determined by averaging FSR which is measured by observing the lock-in output when optical frequency scanned. Comparison measurement between proposed system and commercial heterodyne interferometer has carried out to evaluate performance of proposed system. From the experimental results, periodic error of commercial interferometer is detected. Its amplitude is less than 3nm and its period is about 310nm.

ACKNOWLEGEMENTS

Partial finance supports of the Scientific Research Fund of the Japanese Ministry of Education, Culture, Sports and Technology is

gratefully acknowledged. The Mitsutoyo Association for Science and Technology (MAST) and the Research Foundation for Opto-Science and Technology (RFOST) are also gratefully acknowledged.

REFERENCE

1. International Technology Roadmap for Semiconductor: http://public.itrs.net/
2. Norman Bobroff; Measuremnet Science and Technology. 4 (1993) 907
3. G.. Basile, A. Bergamin, G. Cavagnero and G. Mana; 28 (1991) 455.
4. Agilent technologies Laser positioning system : http://laser.taiyo.co.jp/gijyutsu/img/optic_component_220806.pdf
5. Philip E.Cidder; Applied Optics, 35,9(1996)1566

GRAZING INCIDENCE METROLOGY USING A LATERAL SHEARING INTERFEROMETER

Janaki P. Kolipaka[1], Yutaka Kuriyama[2], and James J. Snyder[1]
[1] Center for Precision Metrology, Department of Mechanical Engineering, University of North Carolina at Charlotte, Charlotte, NC, USA
[2] Guest Researcher (Mitutoyo Corporation), Department of Mechanical Engineering, University of North Carolina at Charlotte, Charlotte, NC, USA

INTRODUCTION

A novel approach to measure the straightness error of machined surfaces with the help of non contact optical techniques is described in this report. This approach combines the concepts of grazing angle of incidence and phase shifted lateral shearing interferometry to perform the measurement. Measurement of such surfaces is generally hampered by the non specular characteristic of its surface. To increase the specular reflection from the surface, the test beam is incident at grazing angle of incidence. The use of a lateral shearing interferometer physically separates the test object from the interferometer, thereby reducing the components required for the experimental setup.

EXPERIMENTAL SETUP

The experimental procedure involves the use of a collimated He-Ne laser beam that is incident onto the test object. The reflected beam is distorted and it contains information about the straightness of the test surface. The distortion is in the form of curvature of the beam and the analysis of this beam and the calculation of the curvature is carried out as a part of the experiment. The beam is incident onto the test object at grazing angle. The reflected beam then hits the shearing interferometer and is then captured by the CCD camera.

Collimation of the laser beam is an important aspect for the measurement. For this purpose a collimating lens of focal length 150mm is used and a collimated beam having a diameter of about 5mm is achieved. Beam from the laser emitter first passes through a microscope objective and then through the collimating lens. A folding mirror is used to direct the beam onto the test object. The angle of incidence is controlled by the angle of the folding mirror with respect to the beam from the collimating lens and also with respect to the target object. The angle of incidence can be varied by varying the position of the folding mirror, thus changing the angle of rotation of the mirror and in turn the angle of incidence. Schematic representation of the experimental setup is as shown in Figure 1.

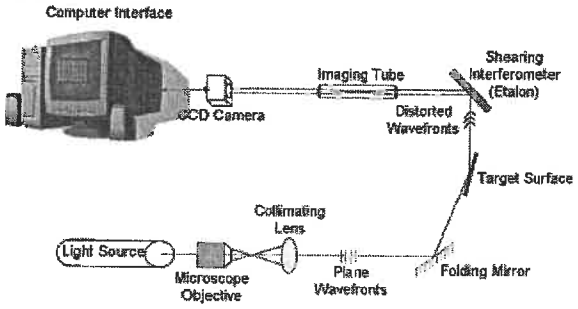

Figure1. Schematic of experimental setup.

The distorted beam reflecting from the test surface carries the information about the surface. This beam undergoes shearing at the shearing interferometer and the sheared interferograms are captured by the CCD camera and analyzed. We follow a 4-step phase shift technique to calculate the phase of the interferograms and then to reconstruct the profile of the target surface based on the analysis done using this technique. The interferograms are formed by the interference of the two sheared beams coming as an output from the shearing interferometer.

A program processed in LABVIEW operates the working of the CCD camera and the shearing interferometer. In our setup phase shift is achieved by rotating the shearing interferometer at particular angles. This rotation is also controlled by the program. The program gives signals in terms of voltage to the galvonometer that rotates the shearing interferometer. Detailed explanations regarding the various concepts utilized in the setup have been provided in this report. Some of the results obtained during the process of measurement have also been discussed. Figure 2 shows a photograph of the experimental setup with the target placed in

position for measurement.

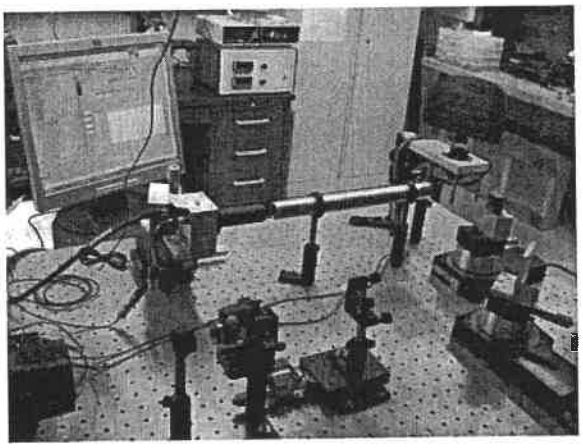

Figure 2. Photo of the experimental setup for testing the straightness error of a die (also seen in the picture). The output of the measurement is displayed on the monitor.

The above figure gives a picture of the actual setup to perform the measurement task. In this picture we are measuring a die for its straightness. The angle of incidence as already mentioned is decided by the position of the folding mirror.

GRAZING ANGLE OF INCIDENCE

Objects produced by machining processes often possess non specular surface. Such surfaces do not generally support their measurement using optical techniques for straightness error since reflection from specular surfaces is meager compared to normal surfaces. To enhance the specular reflection of such surfaces the test beam is incident at a very shallow angle known as the grazing angle.

Considering the normal roughness height of the test surface to be 'h', when a beam is incident at an angle of '_' onto the surface, the effective roughness height becomes '*hcos_*'.

SHEARING INTERFEROMETER

A solid etalon made of fused silica and consisting of two reflecting surfaces is used as a shearing interferometer. The incident beam is reflected twice, initially at the front surface and then at the back surface and the two beams are sheared. This phenomenon can be seen in the figure 3.

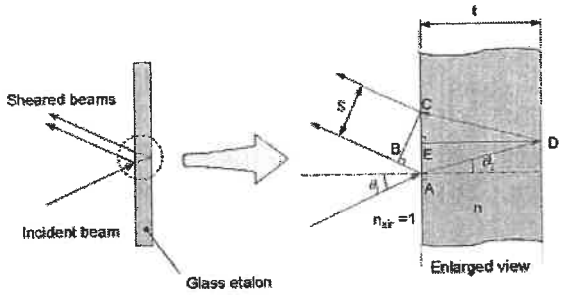

Figure 3. The introduction of shear to the incident beams by the shearing interferometer

In this figure we can see a beam is incident at an angle _ onto the shearing interferometer of refractive index '*n*' and thickness '*t*' and is reflected both from the front and the back surfaces. The reflected beams are sheared by a distance '*S*'. The relationship between angle of incidence to both amount of shear and the optical path difference (OPD) of the reflected beams is as given below;

$$S = \frac{t \sin 2\theta}{\sqrt{n^2 - \sin^2 \theta}}$$

$$OPD = 2t\sqrt{n^2 - \sin^2 \theta}$$

The OPD and the shear are dependent on the angle of incidence. The change in OPD for a given change in the angle of incidence is

$$\frac{\partial OPD}{\partial \theta} = -S$$

The angle at which the incident beam hits the shearing interferometer is also to be checked. In our setup the incident beam is directed onto the shearing interferometer at an angle of 45°. Since the amount of shear introduced depends on the angle of incidence and also based on the formula mentioned above the angle of incidence at which we obtain the maximum amount of shear has been found to be about 45°. The measured amount of shear for an incidence angle of 45° has been found to 0.837mm.

The fringes formed by the shearing interferometer are of constant slope along the direction of shear unlike many other interferometers. Also the fringes generated are of order (N-1), considering the shape of the surface to be of order 'N'. A flat wavefront

generates a solid fringe (constant phase) independent of wavefront tilt and a spherical wavefront produces fringes that are straight and parallel.

Typical interferograms obtained in the course of measurement of a 20m radius of curvature concave mirror that was tested on a preliminary note are as shown in figure 4. These interferograms are obtained by the overlapping of the actual beam and the sheared beam coming out of the shearing interferometer. This interference phenomenon is the key aspect of the shearing interferometers.

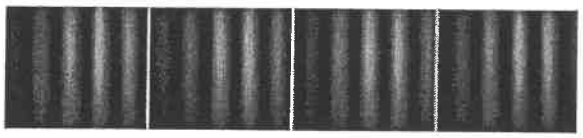

Figure 4. Sheared interferograms with a _ wave phase shift obtained when a 20m radius of curvature concave mirror was used as the test object.

The shearing interferometer is a self referencing common path interferometer, making it insensitive to environmental disturbances such as vibrations. This feature of the setup enables it to be used in industrial environments where vibrations are the major cause of measurement errors.

EXPERIMENTAL PROCEDURE

A 633nm wavelength He-Ne laser is collimated using an achromatic lens and is directed onto the test object at a grazing angle of incidence. The reflected beam from the target surface then hits the shearing interferometer at 45° incidence angle. The sheared beams then pass through the imaging optics and are captured by the CCD camera.

The CCD camera has a resolution of 640 X 480 pixels with the pixels at 7.4μm square. The phase values of the four interferograms captured by the CCD are calculated and a phase map based on these values is generated by the LABVIEW program. The program then does the unwrapping of the phase. The unwrapped phase is then fit to a 3rd order polynomial according to [1] and the coefficients related to the wavefront are obtained. These coefficients are then used to form the profile of the surface under test.
At normal incidence the measurement area observed by the CCD with its effective resolution of 637 X 477 pixels is 4.7 X 3.5mm. The width of the same is elongated when viewed at oblique angles and varies by a factor of 1/cos_, where _ is the angle of incidence. For example, measurement area for an 82° grazing angle of incidence is 33.9 X 3.6mm.

PRELIMINARY RESULTS

To evaluate the performance of the interferometer and also to test the accuracy of the measurement done by the instrument, we have measured the radius of curvature of a mirror of specified radius 2000±6mm. The measured radius at an incident angle of 69.7° was 2002.7±0.7mm which as well under the specified tolerances. The measured sag in the mirror was 11.522±.004μm for an effective measurement area of 13.6 X 3.5 mm.

We have also measured the straightness error of a 30mm long ceramic gage block of nominal thickness 1.5mm to be about 132±4nm over a measurement area of 13.6 X 3.5 mm. The 13.6mm measurement length on the gage block was spread centrally at an incidence angle of 69.7°.

Flatness of the same gage block was measured by a Fizeau interferometer to be around 90nm in the central 13.6mm region. The reason for this discrepancy in the measured value is still to be found, mainly attributed to the variation in the method of mounting of the test specimen. A photograph of the gage block being measured is shown in the figure 5.

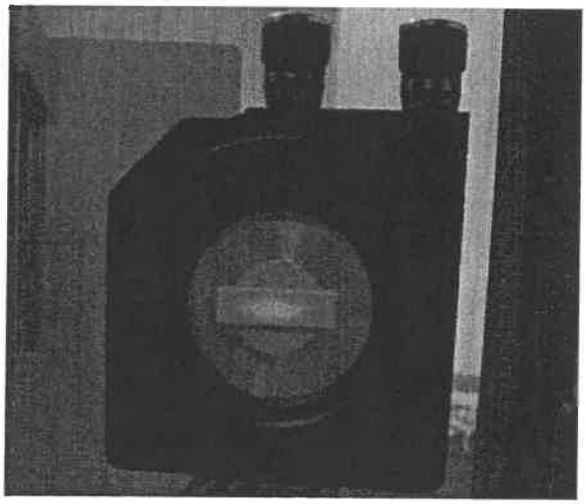

Figure 5. Illuminated gage block being measured at 70° incidence angle

We are currently measuring for the radius of curvature and sag of a die. The photograph of the same is shown in figure 6.

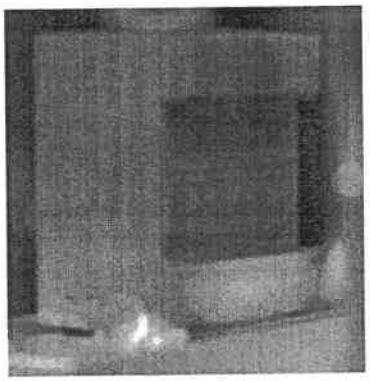

Figure 6. Illumination on the die at an incident angle of 70°

FUTURE WORK

Our future tasks would involve the measurement of artifacts with known values of radius of curvature and straightness errors in order to facilitate the comparison of the obtained results and accordingly vary the interferometer constraints.

REFERENCES

1. D. Malacara, Optical Shop Testing-2nd edition
2. Peter de Groot, Diffractive Grazing-Incidence Interferometer

STITCHING INTERFEROMETRY FOR FLEXIBLE ASPHERE METROLOGY

S. O'Donohue, P. Murphy, J. Fleig, and G. Devries
QED Technologies
Rochester NY, U.S.A.

ABSTRACT
Manufacturing precision aspheric surfaces is often limited by the availability of surface metrology. Interferometric tests of aspheres have traditionally needed dedicated null lenses, which require significant time and expense to design and fabricate. The costs of null lenses are recurrent because each is specific to one particular asphere prescription. Although sub-wavelength uncertainty is attainable, the accuracy of null tests is often limited by alignment errors and inadequate calibration techniques. Aspheric surfaces can also be tested with scanning instruments and profilometers. These devices are more flexible than null lenses because they are compatible with a variety of geometries and prescriptions. Accuracy, however, is typically limited by errors in the machine axes, and the time required for a full aperture map can be problematic for a manufacturing environment.

In 2004, QED Technologies introduced the Subaperture Stitching Interferometer (SSI®) to automatically stitch large diameter and high numerical aperture spherical surfaces (including hemispheres). This system also boosts accuracy with in-line calibration of systematic errors such as reference wave and imaging distortion. More recently, the system's aspheric testing capability has been developed, which effectively extends the longitudinal dynamic range of a standard interferometer by an order of magnitude or more.

We present the SSI_A™: a flexible and robust method of stitching non-null aspheric phase measurements. Through the use of novel compensation schemes and in-line system error calibration, our subaperture stitching system can provide high accuracy interferometric measurements of surfaces with tens of microns of departure from the best-fit sphere. This is done *without* the use of dedicated null lenses, and can be applied to a wide variety of mild aspheric surfaces. The system reports a full-aperture map, which can then be used in conjunction with a deterministic finishing process. An example stitched asphere measurement is shown along with null test data for comparison.

1. PRINCIPLES OF NON-NULL STITCHING

In practice, Fizeau interferometers are typically used in a "null" configuration. This occurs when the test and reference wavefronts closely match each other. One example of a non-null test is measuring a rotationally symmetric aspheric surface against a spherical reference wave. Although a non-null test is simple in principle, it does present some difficult challenges. The most significant constraint is the resolution of the interferometer itself. A non-null aspheric test is effectively limited to only a few microns of aspheric departure, due to the fringe density and resolution of the detector. Other challenges include non-common path effects, and an increased susceptibility to scaling, alignment, and imaging errors. These types of errors can cause inaccurate removal of the aspheric shape, which directly degrades the measurement accuracy.

Subaperture stitching can alleviate many of these issues. One of its biggest advantages is achieved by dividing a wavefront that, measured all at once, is beyond the interferometer's capability into smaller sections that are measurable individually. This characteristic effectively increases the longitudinal dynamic range of a Fizeau interferometer by an order of magnitude or more. It also significantly improves the lateral resolution of the instrument. By measuring a small section of the surface with the same interferometer and camera that is used for full aperture measurements, the lateral resolution can be improved by 3x or more. These are examples of how the *acquisition* process associated with stitching can be advantageous for aspheric surfaces. Once the data is collected, however, it must then be properly reconstructed to provide an accurate map of the surface form error.

2. MEASUREMENT DESIGN

The first responsibility of the user is to properly input the prescription of the aspheric surface to be tested. Figure 1 shows two plots calculated based on the prescription of an aspheric surface that was tested on the SSI_A; on top is a plot of the departure from best fit sphere, and the graph on the bottom shows the two principle curvatures of the surface (radial and tangential). Both graphs are plotted as a function of the distance from the center of the surface. Once the aspheric surface to be tested is defined, the location of each subaperture must be determined. The optimal measurement design, termed the *"lattice"*, is automatically computed for each asphere. An example asphere lattice can be seen in Figure 2. It uses a number of parameters to perform this calculation including, but not limited to; local curvatures, interferometer resolution, magnification available from each transmission sphere, as well as other guidelines that make the stitching process more robust. After the user selects their preferred option, a lattice is automatically calculated. The software has parameters that allow adjustment of the overlap to accommodate varying requirements for relative speed and accuracy.

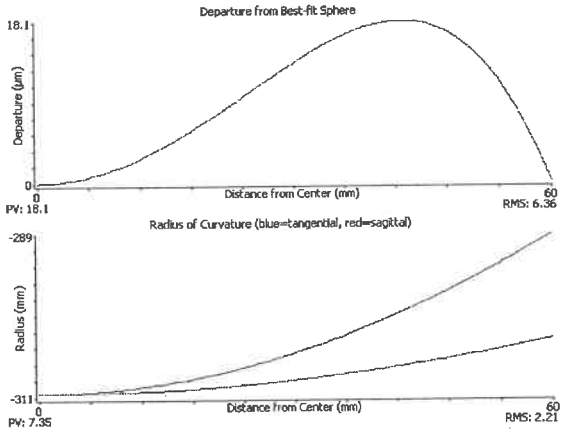

Figure 1. Departure and curvature plots of an aspheric mirror measured with the SSI_A.

Previous work in aspheric stitching utilized a method known as "zonal" or "ring null" stitching[4,5]. Zonal stitching involves acquiring nearly nulled measurements in ring-shaped subapertures (the annular "zones"). A different measurement zone is achieved by adjusting the distance of the aspheric test part from the interferometer (by moving through the optical axis). The size of measurable data from each ring null is relatively small compared to the area of the detector. One of the SSI_A workstation's capabilities rests in its freedom to move the surface off-axis with respect to the interferometer. This allows the system to acquire subapertures that utilize far more pixels on the detector. Figure 3(a) shows a simulated ring null fringe map, where (b) is an off-axis measurement nulled to a local best fit sphere.

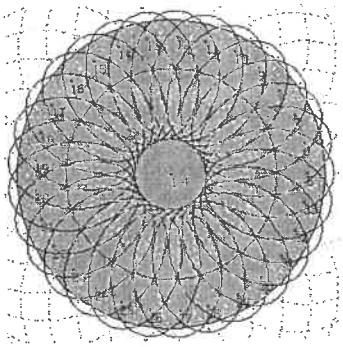

Figure 2. SSI_A lattice design for measuring a concave asphere with ~18 microns of departure. The measruement consists of 33 subapertures.

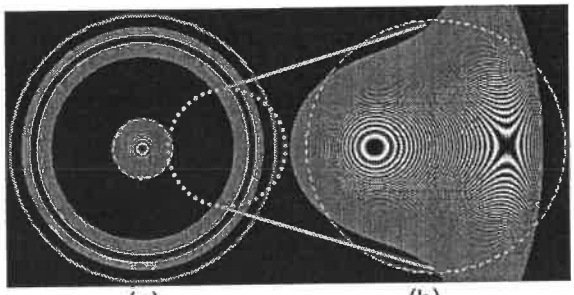

Figure 3. Simulated fringe patterns for a mild asphere: (a) A ring null subaperture measurement provides a limited area of data. (b) Choosing an off-axis region using a local best-fit sphere dramatically increases the resolvable region.

3. HIGH ACCURACY RESULTS

Adequately sampling the non-null fringes is simply the first step in accurately reconstructing aspheric figure. The common-path property of Fizeau interferometry strictly only applies to null fringe fields; accuracy can degrade rapidly when measuring non-null wavefronts. The SSI_A can estimate and correct for a significant fraction of systematic error present in non-null measurements. This compensation is automatically performed inline with the stitching process, therefore it is a "real-time" calibration.

A mild aspheric mirror with ~ 18 microns of departure from best-fit sphere was measured

with the SSI_A system. The departure and curvature plots for this surface can be seen in Figure 1. Figure 4(a) displays the full aperture stitched map computed by the SSI_A software with the nominal aspheric shape removed. Figure 4(b) and (c) are example interferograms from the central and outer zones, respectively.

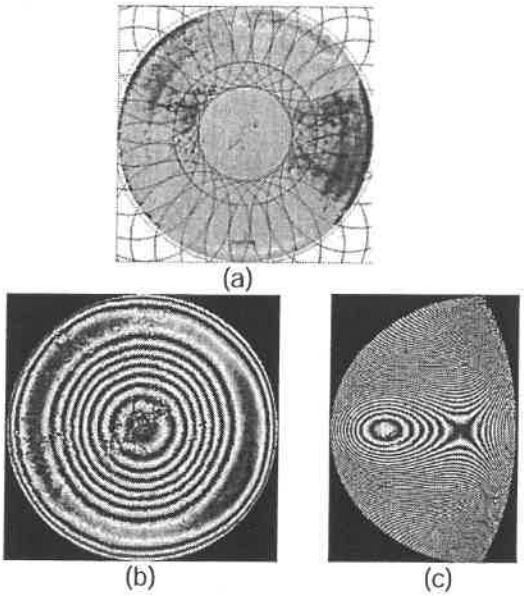

Figure 4. (a) Full aperture stitched map of an asphere reported by the SSI_A software. (b) central subaperture and (c) subaperture from the outer zone.

The same surface was also measured with a null test that required a computer-generated hologram. The results of both measurements are shown in Figure 5, where very good low order agreement can be seen (oblique plots are used to make form comparison possible). Smaller features and surface defects, however, are more evident in the stitched measurement. This difference can be attributed to stitching's inherent increase in resolution over a full aperture measurement[6].

4. IMPROVING LEAD TIME

In a manufacturing environment, total lead time is an increasingly important metric. When producing precision aspheres, lead time is often driven by the time required to produce a custom null lens as well as the individual manufacturing steps. Null lenses can take anywhere from weeks to months to produce, and they are specific to one aspheric prescription only.

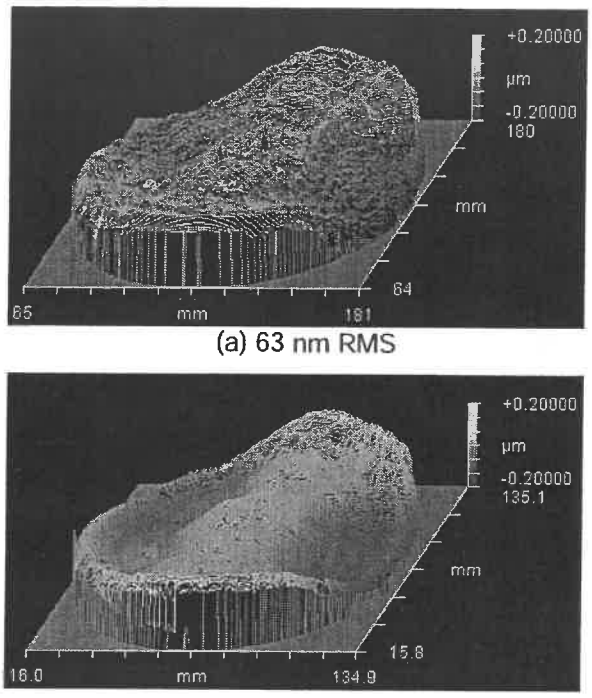

Figure 5. The full aperture stitched map is shown in (a), and the CGH null test measurement can be seen in (b). Both maps are on the same lateral (120 mm) and vertical scales (+/- 0.2 microns).

If the surface prescription changes even slightly, a new null lens must be designed and manufactured. The SSI_A utilizes a Fizeau interferometer and standard transmission spheres, therefore it has the flexibility to measure a wide variety of surfaces without making modifications to existing or purchasing new hardware. Contact profilometers are also flexible and have a large dynamic range, however they typically only provide a two dimensional trace with relatively low lateral resolution. Furthermore, identifying any asymmetric errors, such as astigmatism, requires multiple scans which can be labor intensive.

Another example aspheric surface, this time with ~50 microns of departure, was measured with the SSI_A. The surface required 35 subapertures in order to provide a high resolution, full aperture map. Under normal conditions, each subaperture takes 20-30 seconds to acquire, therefore this particular measurement was completed in ~15 minutes. A different lattice (measurement design) was then generated with

only 12 subapertures. This measurement was designed to significantly decrease the cycle time by measuring merely a "slice" across the diameter of the surface. Figure 6 shows both the full aperture and faster measurement designs.

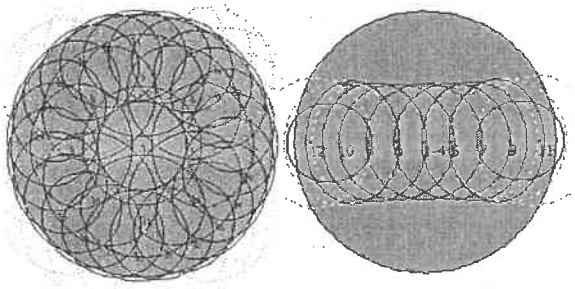

(a) (b)

Figure 6. (a) is the standard lattice design for providing a full aperture map and consists of 35 subapertures. (b) decreases the measurement time by a factor of 2 by only acquiring data across a slice of the surface.

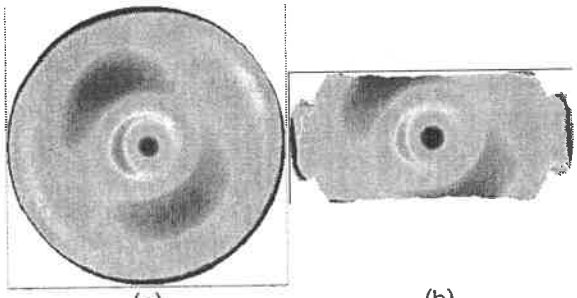

(a) (b)

Figure 7. (a) full aperture stitched map and (b) stitched result from the faster "slice" measurement. Both vertical scales are +/- 0.5 microns.

Figure 7 shows the stitched maps from the full aperture and faster "slice" acquisitions in (a) and (b), respectively. Both maps have the same lateral resolution and nearly identical low order form. Measurement (b) still provides precise data regarding radial (symmetric) errors. The same center feature and astigmatic form can also be identified seen in both maps, however the (b) measurement only required ~7 minutes to complete. The combination of speed and accuracy makes this type of measurement ideal for in-process metrology after, for example, a polishing process that removes the grinding and subsurface damage. The full aperture stitched measurement can then be used for deterministic finishing and final quality testing.

5. CONCLUSION

Subaperture stitching has been able to enhance lateral range and resolution of an interferometer for some time. With QED's introduction of the SSI, this capability became commercially available for spherical surfaces, with improved accuracy over a conventional test (due to its inline calibration capability). Now with the SSI_A software, the system can stitch mild aspheres quickly, automatically and accurately *without any dedicated null optics.*

QED has demonstrated that the SSI_A process is capable of obtaining nanometer-level quality measurements on mild aspheres. Most recently, this instrument successfully measured more aggressive aspheric surfaces with ~ 70 microns of departure. These capabilities are a breakthrough improvement to an interferometer's lateral and longitudinal dynamic range capability.

REFERENCES

1. J. Thunen and O. Kwon, "Full aperture testing with subaperture test optics," *Wavefront sensing; Proceedings of the Conference, San Diego, CA, August 1982,* N. Bareket, and C.L. Koliopoulos, Eds., **351**, 19-27, SPIE - The International Society for Optical Engineering, Bellingham, WA, 1983.
2. W. Chow and G. Lawrence, "Method for subaperture testing interferogram reduction", Optics Letters, **8**, 468-470, 1983.
3. P. E. Murphy, *et al.*, "Stitching interferometry: A flexible solution for surface metrology," *Optics and Photonics News*, **14**, 38-43 (2003).
4. Y-M. Liu, G. Lawrence and C. Koliopoulos, "Subaperture testing of aspheres with annular zones," Applied Optics, 27, 4504-4513, 1988.
5. Tronolone, *et al.*, "Method of testing aspherical optical surfaces with an interferometer," US Patent #5,416,586; Tropel Corporation.
6. S. O'Donohue, G. DeVries, P. Murphy, G. Forbes, and P. Dumas, "New methods for calibrating systematic errors in interferometric measurements," *Optical Manufacturing and Testing VI,* H. Philip Stahl, Ed., Proc. SPIE **5869**, SPIE, Bellingham, WA, 2003.

ASSEMBLY OF THIN GRATINGS FOR SOFT X-RAY TELESCOPES

Mireille Akilian*, Ralf K. Heilmann and Mark L. Schattenburg
MIT Kavli Institute for Astrophysics and Space Research
Massachusetts Institute of Technology
Cambridge, MA 02139

INTRODUCTION

Optics used as mirrors and gratings in space telescopes must withstand launch forces, vibrations and harsh environment conditions. High resolution and efficiency are required for the imaging and spectroscopy of light from stellar objects. For the soft x-ray band, large areas of substrates used for both reflective optics and reflection gratings must be shaped to a tight tolerance, requiring the substrates to be extremely flat. This is achieved by either using thick substrates that are polished using standard processes, or by stacking thousands of relatively thin, smaller-area substrates. In both cases, the overall mass of the substrates must be kept at a minimum to meet cost limitations. Once the substrates are worked to their final shape, they have to be aligned and assembled into ready-to-fly modules with high accuracy and precision to avoid optic surface degradation during assembly.

This article discusses a new method of assembling numerous thin substrates using precision spacers. The substrates used are 140 mm x 100 mm x 0.4 mm in dimension. In their flat configuration, the assembled substrates can be used as gratings. Imaging mirrors require introducing a curvature onto the assembled substrates for focusing x-rays using the Wolter I or the Kirkpatrick-Baez configuration [1].

The substrates are connected to one another using three precision spacers epoxied on each individual substrate, as shown in Figure 1. Identical spacers are used to attach all the substrates to a rigid starting block, which is to be mounted on the telescope structure. This scheme allows for a rigid assembly with a high natural frequency, yet the additional mass due to the small cross-section spacers is maintained low.

* Email makilian@mit.edu
URL: snl.mit.edu

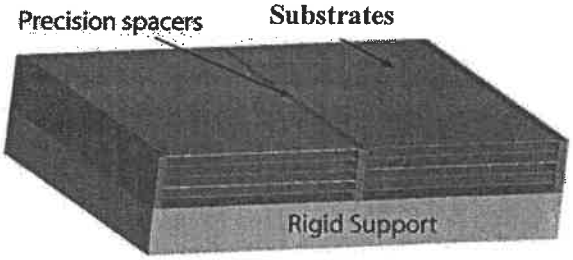

Figure 1. Assembled substrates epoxied to one another and to a rigid support using precision spacers

ASSEMBLY TOOLS AND PARTS

Shack-Hartmann Metrology Tool

Metrology plays a critical role in assembly, since it provides feedback throughout the process. The Shack-Hartmann metrology system is used to obtain surface maps of flat substrates with a repeatability of 0.4 arcsec [2].

Thin Optic Metrology Truss

Measuring the surface of the unconstrained substrate is crucial for generating a reference map. After the optic or grating is assembled, its surface is measured and compared to the unconstrained reference surface to evaluate any deformations introduced during the assembly process. During metrology, the pre-assembled substrate has to be constrained such that the effects of forces such as gravity, friction and thermal stresses are minimized. This is done by using the *thin optic metrology truss* shown in Figure 2, which was developed at the *Space Nanotechnology Laboratory* at MIT. This tool uses sets of monolithic flexures to constrain 100 mm diameter circular or 140 mm x 100 mm rectangular optics having a nominal thickness of 0.4 mm with a repeatability of 1 arcsec [3].

Rigid Support and Precision Spacers

The starting block in the assembly process is the rigid support, which is comprised of a plate, optically polished to a flatness of 50 nm. Three precision spacers with a cross-section of 2 x 2 mm^2 and a length of 100 mm, the length of the substrates, are stacked on the rigid support. Since the area on the substrate making contact

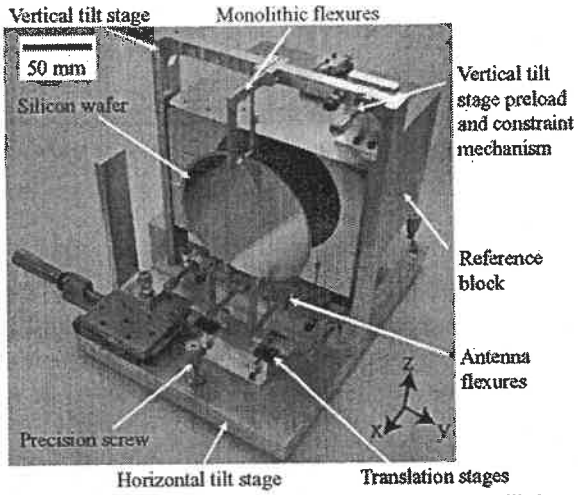

Figure 2. The thin optic metrology truss utilizing monolithic flexures to constrain circular and rectangular optics with minimal distortion

with the spacers can no longer reflect the incoming x-rays, the width of the spacers is made as narrow as possible without compromising their bending stiffness. For the dimensions chosen for these spacers, the area on the substrate that does not see the x-rays is less than 5% of the overall surface area. The height of the spacers, which provides the gap through which x-rays can pass and hit the surfaces of the substrates, is chosen to be equal to the width to avoid any orientational placement errors during assembly.

Vacuum Chuck

The key component in this scheme is the vacuum chuck, a plate that has been machined to be left with four windows and three ribs, as shown in Figure 3. The ribs have the same width as the spacers. Three holes are drilled starting from one edge of the plate through the three ribs, which themselves have grooves machined on their surfaces. By connecting the grooves to the holes, a vacuum channel is formed on each rib. The part is optically polished to 50 nm flatness such that the ribs with the vacuum channels are flat. The vacuum chuck is what transports the substrate from the thin optic metrology truss, where its free surface was measured, to the rigid support. This is done by placing the grating or mirror surface of interest, i.e. the x-ray reflecting surface, against the flat ribs and turning the vacuum on, as shown in Figure 4. Because the ribs are flat, the overall flatness of the thin substrates is improved once they are rigidly constrained by the vacuum chuck. It should be noted that as the thickness of the substrates increases, their compliance

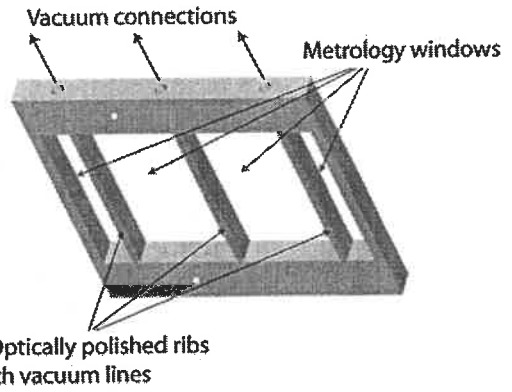

Figure 3. Optically polished vacuum chuck showing the three flat ribs with vacuum lines and the metrology windows

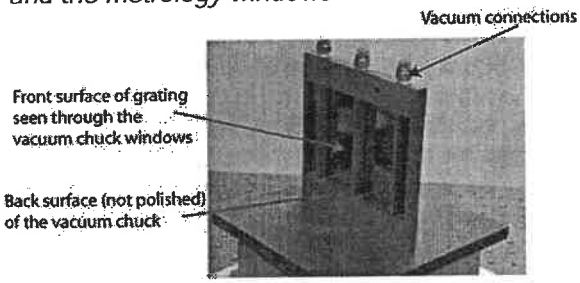
Vacuum connections
Front surface of grating seen through the vacuum chuck windows
Back surface (not polished) of the vacuum chuck

Figure 4. A silicon substrate constrained by the vacuum chuck. The x-ray reflecting surface of the substrate is seen through the windows in the vacuum chuck. This surface is placed against the optically polished surface of the vacuum chuck, which is facing away from the camera.

decreases, and this method eventually reaches its limits. The windows between the ribs allow for metrology of the x-ray reflecting surface while the substrate is rigidly constrained and maneuvered in space until it is in the right position to be assembled onto the spacers on the rigid support.

ASSEMBLY STEPS

Once the free substrate surface is measured using the Shack-Hartmann and the metrology truss, it is ready to be assembled onto the rigid support. Three precision spacers are placed on the three ribs of the vacuum chuck. When the vacuum is turned on, the spacers are fully constrained by the vacuum chuck. At this point, a thin layer of epoxy is applied on the exposed surface of the spacers, as shown in Figure 5(*a*). The vacuum chuck with the spacers is placed against the rigid support and held at that position with the vacuum on until the epoxy fully cures. The vacuum is then turned off, and the vacuum chuck is removed leaving the precision spacers epoxied on the rigid support. The thin substrate

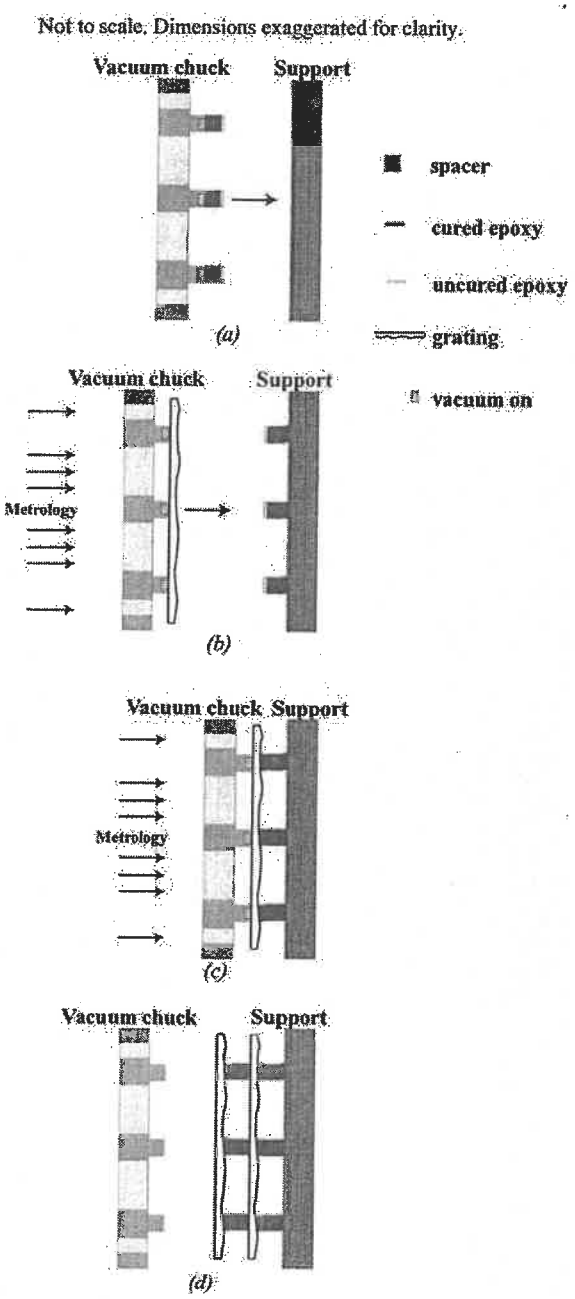

Figure 5. Assembly steps. (a) Spacers constrained by vacuum chuck, and a thin layer of epoxy applied on one face. (b) Spacers mounted on rigid support with a fresh layer of epoxy on their exposed face while substrate constrained by vacuum chuck. (c) Substrate assembled on spacers and vacuum chuck retracted after curing of epoxy. (d) Second substrate assembled following previous steps.

can now be placed on the vacuum chuck, as shown in Figure 5*(b)*. The compliance of the thin substrates allows for them to conform to the shape of the rigid, optically polished ribs of the

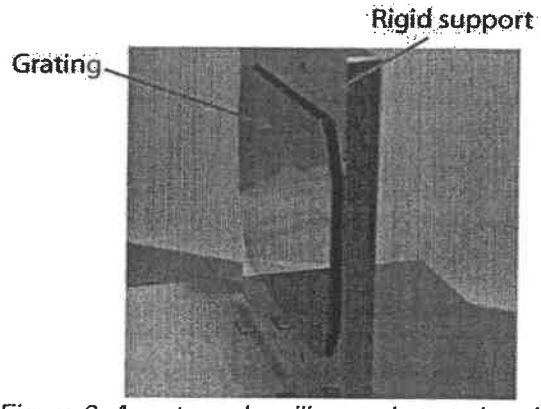

Figure 6. A rectangular silicon substrate bonded to spacers on the rigid support. Spacers (not seen) are between the grating and the support.

vacuum chuck once the vacuum is turned on. This in turn improves the overall flatness of the substrates, particularly at the areas of contact with the ribs.

Metrology on the front surface of the now constrained substrate can still be performed through the windows in the vacuum chuck, which is maneuvered in space until the substrate is at its final position with respect to the rigid support and the precision spacers. At this point, the vacuum chuck is moved slightly closer to the spacers so the substrate makes contact with the epoxy on the spacers, as shown in Figure 5*(c)*. The vacuum is left on until the epoxy fully cures to counteract shrinkage forces associated with the epoxy curing process. When the epoxy is fully cured, the vacuum is turned off and the vacuum chuck is removed from the system. The x-ray reflecting surface of the now assembled substrate is ready to be measured to evaluate the process, as shown in Figure 6.

More substrates can be stacked on top of the first one by repeating the same steps, as shown in Figure 5*(d)*.

RESULTS AND DISCUSSION

The role of the vacuum chuck is not only to improve the overall flatness of the substrates, but also to transfer the substrates onto the precision spacers without compromising this flatness. Figure 7*(a)* shows the surface map of a silicon substrate to have a distortion of 9.4 μm peak-to-valley (p-v) and 1.7 μm rms with an angular distortion of 52 arcsec rms. Figure 7*(b)* shows the same substrate after it has been constrained by the vacuum chuck to have a

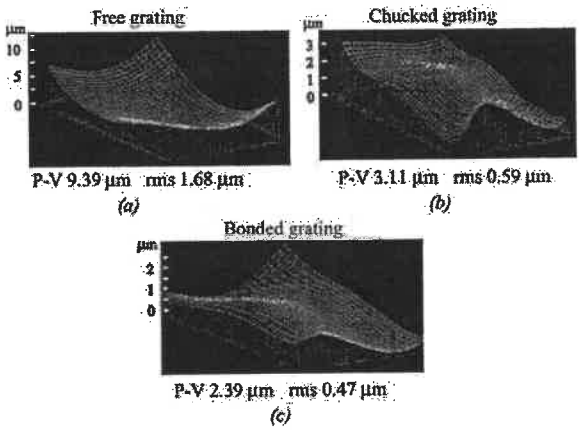

Figure 7. Surface topography of a substrate before and after assembly. This is the area of the substrate surface seen through one of the windows of the vacuum chuck. (a) Free substrate when constrained by the thin optic metrology truss. (b) Substrate constrained by the vacuum chuck leads to a significant improvement in surface overall flatness. (c) Assembled substrate bonded to precision spacers.

distortion of 3.1 μm p-v and 0.6 μm rms with an angular distortion of 30 arcsec rms. A significant improvement in the overall flatness is observed as a result of the substrate compliance to the flatness of the ribs on the vacuum chuck. Figure 7*(c)* shows the substrate once it has been epoxied on the precision spacers. A slight improvement is observed in the surface flatness, which is measured to be 2.4 μm p-v and 0.5 μm rms with an angular distortion of 27 arcsec rms.

The effect of epoxy creep with time for different types of epoxy is to be studied to eliminate any variations in the substrate's surface maps with time. The substrate chosen for this experiment was randomly picked from commercially available 6" diameter silicon wafers. It has been die-sawed to its final rectangular dimensions. No shaping processes were conducted on this substrate before it was assembled, and that explains the large initial non-flatness. Commercially available 6" diameter silicon wafers that are ~0.4 mm thick have a typical surface topography ranging between 10 μm and 30 μm p-v, whereas glass substrates with the same dimensions have a surface topography that can reach to up to 0.6 mm p-v. As a result, silicon has been chosen for this experiment. Working with better substrates that have a smaller initial surface warp can provide better results. A surface shaping process is needed. Silicon wafers are usually double-side polished after they are sawed, but that only improves the overall thickness uniformity of the wafer and not its flatness, since once the wafer is removed from the tool, it springs back to its original shape. Magnetorheological finishing is one method that can be used to improve the overall flatness of the wafer surface, but the process is time consuming and expensive for wafers with an initial surface warp exceeding 3 μm p-v [4]. The advantage of following this assembly scheme is that the tolerances on the shaping processes can be loosened; the free substrate does not have to be extremely flat, since the assembly step will improve the overall flatness of the individual substrates.

REFERENCES

1. Eberhard Spiller. Soft X-Ray Optics. SPIE Optical Engineering Press, 1994.
2. Craig R. Forest et al. Metrology of thin transparent optics using Shack-Hartmann wavefront sensing. Optical Engineering, 43:742-753, 2003.
3. Mireille Akilian et al. Thin optic constraint. Journal of Precision Engineering, accepted for publication Apr. 2006.
4. Ralf K. Heilmann et al. Shaping of thin grazing-incidence reflection grating substrates via magnetorheological finishing. Proc. of SPIE, 5900:73-80, 2005.

PASSIVELY ALIGNED 100-PORT MICRO-FLUIDIC CONNECTOR

Craig R. Forest, Michael J. Beltran, and Ian W. Hunter
BioInstrumentation Laboratory, Department of Mechanical Engineering
Massachusetts Institute of Technology
Cambridge, MA, USA

ABSTRACT

Widespread application of micro-fluidic systems has been hindered by the challenge of repeatable, accurate interfacing between integrated channels or wells and external loading, detecting, or stimulating devices. We are developing a repeatable, accurate, 100-port micro-fluidic connector to interface to a 100 capillary array. The capillaries are passively aligned for connection with a combination of precision guide pins and conical tapered holes, and sealed with a PDMS layer after insertion. Using the connector device, an array of 100 loosely-assembled capillaries with 1 mm spacing can be aligned to 20 μm radial accuracy and high repeatability, with only 5% failure after 10,000 insertions. We have confirmed electrical and fluidic connectivity as well. This device can be simply manufactured and adapted for numerous micro-fluidic interface applications.

INTRODUCTION

During the past decade, micro-fluidics has become increasingly important in biological, chemical, and engineering fields due to the increased need for manipulation of small quantities of materials. Advantages can include lower costs due to less waste or fewer starting templates, higher surface area to volume ratio, and rapid, portable analysis. Devices capable of these small scale manipulations accomplish a variety of tasks such as chemical synthesis, DNA amplification reactions, and DNA sequencing.

Despite these compelling advantages, there are numerous complications for micro-fluidic device design and manufacturing. A key challenge is fluidic connectivity, which is often required to deliver or withdraw nanoliter-scale volumes from the device [1,2]. These fluidic connections are often an essential link between an integrated channel or well and external loading, detecting, or stimulating devices. Previous work has been limited to only a few micro-fluidic ports [3,4], whereas hundreds or thousands of ports can be required in applications which fully exploit the potential of miniaturization.

We are developing a 100-port micro-fluidic connector as a proof-of-concept for an effort to build a 10,000 capillary mutational spectrometer instrument capable of sorting through the requisite 10^{12} gene fragments to discover statistically significant correlations between mutation and disease [5]. The discovery of the genetic causes for common diseases could lead to simple genetic tests for risk and to targeted preventative or therapeutic strategies [6]. The mutational spectrometer instrument, shown in Fig. 1, enables parallel loading, electrophoretic separation, detection, and collection of DNA mutations from pools of 100 persons per channel for 10,000 parallel capillary channels simultaneously and continuously. We have created this micro-fluidic connector to service either end of the capillary array.

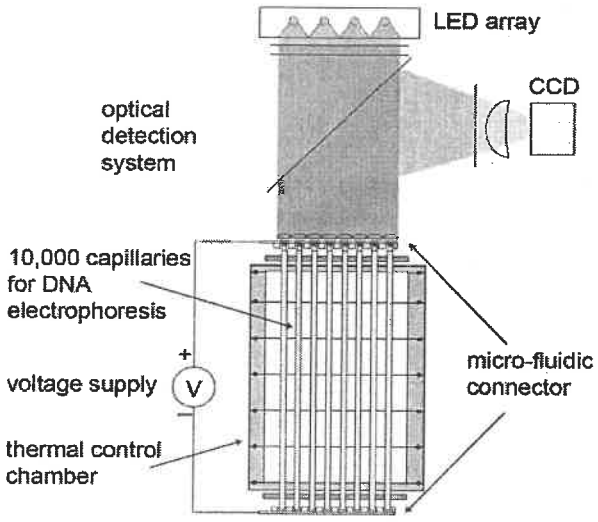

FIGURE 1. Schematic of the ultra-high-throughput mutational spectrometer for scanning 10,000 samples of DNA for mutations simultaneously. Ten-thousand capillaries, 300 mm long, are arranged in a 3-D array with 1 mm spacing. Micro-fluidic connectors at either end of the capillary array enable DNA loading, separation, detection, and collection.

Scanning gene fragments in this instrument requires repeated interfacing to the ends of the 10,000 capillary array reliably, repeatably, and accurately. In quick succession, these capillaries must be sanitized, injected with a viscous polymer matrix, loaded with DNA, and immersed in a buffer solution. Rapid connection (<10 s) with inherent sealing mitigates evaporation and prevents contamination. We desire to have the individual capillaries simultaneously and passively aligned to less than 50 μm radially to facilitate mechanical access and optical detection. Furthermore, the micro-fluidic connector must tolerate a high-voltage (10 kV), chemically-active environment.

In this paper we will present the theoretical and physical design, manufacturing approach, and experimental results for the 100 port micro-fluid connector. Repeatability, alignment accuracy, and voltage performance of the device with the prototype 100 capillary array will be described.

THEORY

In order to predict repeatability and accuracy of insertion for the capillaries into a connection interface, we created a system error budget [7]. With the capillary tip as the "tool," and the fluid connection port as the "workpiece," we proceeded to trace random errors through the structural loop to predict the maximum mechanical alignment error. Random errors were tallied from the capillary tip to a guide pin interface to conical entry ports through eight coordinate systems. These errors were dominated by machining tolerances and capillary radial misalignment. Random error results are displayed in Tab. 1; systematic errors were negligible, as were axial (z) errors.

TABLE 1. Error budget for capillary alignment structural loop.

	Random errors (mm)	Root-Sum-Squared random errors (RSS) (mm)	Average of random & RSS (mm)
Δx, Δy	0.38	0.21	0.30

Thus the predicted maximum alignment error between the capillary tips and the conical fluidic ports is 0.30 mm. We therefore designed the entry port for each capillary to have a radius large enough to tolerate this misalignment; 0.5 mm radius entry ports can tolerate a misalignment of 0.32 mm.

MATERIALS AND METHODS

The main challenge in mechanical design of the fluid connector is to permit the maximum predicted error while enabling reliable, repeatable, and accurate interfacing. This is initially accomplished with the use of two 6 mm steel guide pins to align the device prior to capillary insertion, as shown in Fig. 2. The connector is then translated along the guide pins, causing each capillary tip to be directed by a pair of conical tapers (primary and secondary) into a 400 μm hole. These conical ports independently and passively bend the capillaries into an aligned grid with 20 μm radial accuracy, spaced 1 mm apart. The aligned capillary array within the connector is shown below in Fig. 3.

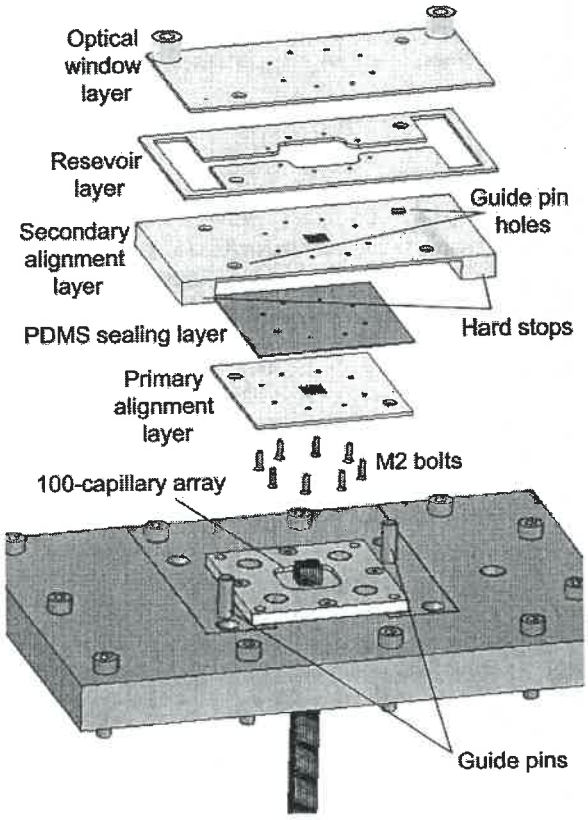

FIGURE 2. Exploded model of the 140 mm x 70 mm micro-fluidic connector above capillary array and guide pins. Entry ports on the primary alignment layer are registered to those on the secondary alignment layer. This secondary alignment layer has reamed guide pin holes which are machined in the same setup as the conical ports for accurate registration. After the guide pins provide coarse capillary alignment, the primary and secondary alignment layers engage the capillaries.

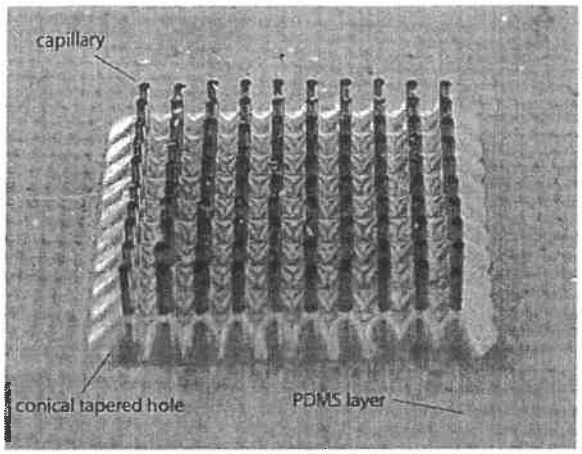

FIGURE 3. Photograph of 100 capillaries (diameter 360 μm) inserted and sealed into the micro-fluidic connector. The conical ports, spaced 1 mm apart, align the capillaries accurately to 20 μm radially. The PDMS layer seals and inhibits evaporation. Insertion of the 100 ports requires approximately five seconds by hand.

The entire device (see Fig. 2), is constructed using four separate layers of 1.5 mm thick polymethyl methacrylate (PMMA), fluidically sealed with a layer of poly-(dimethyl siloxane) (PDMS) and bonded with PMMA solvent methylene dichloride. Each PMMA layer is laser cut (Trotec Speedy 100) and selectively milled.

As the capillaries are inserted into the device, they pass through the PDMS layer, which and seals around their perimeters. When the capillaries are removed, the silicone reseals, preventing escape of fluid from the reservoir.

Translation along the guide pins is limited by hard stops on the secondary alignment layer, preventing capillary damage. During electrophoretic separation of DNA within the capillaries, a 5 mL buffer solution in the reservoir layer permits application of high voltage (up to 10 kV tested) to the capillaries via a platinum wire electrode, as well as collection of the eluted DNA. Detection of DNA is permitted by a PMMA optical window layer. (Fig. 3 photograph taken through this window.)

EXPERIMENTAL RESULTS

Capillary radial alignment accuracy

For each of the capillaries shown in Fig. 3, we measured the capillary tip alignment before and after insertion into the 100 port connector. For the 100 capillaries tips protruding 8 mm from an elastomer constraint device [8], the 3σ radial deviation from a regular grid with 1 mm pitch is 187±7 μm. Since the holes in the fluidic ports are only 400 μm in diameter, the 360 μm diameter capillaries must be aligned to, at worst, 20 μm radially after insertion.

Repeatability

The repeatability of insertion was measured by a 100 trial experiment. The micro-fluidic connector was inserted to the 100 capillary array 100 times, resulting in a total of 10,000 individual capillary insertions. During the course of these trials, 6 capillaries were rendered unusable. In total, 9517 out of 10,000 capillaries were successfully inserted, 95.2%.

Electrical and fluidic connectivity

A test to verify electrical and fluidic connectivity was conducted. During electrophoretic operation, the capillaries, filled with a polymer matrix, are inserted into micro-fluidic connectors at either end. In this experiment, we inserted the ends of a single, gel-filled capillary into two connectors containing buffer solution. Platinum electrodes were used to apply a 4 kV potential difference between the ends. A current of 8 μA was measured indicating electrical and fluidic connectivity.

CONCLUSIONS

This proof-of-concept describes the design of a 100 port micro-fluidic connection for application to high throughput capillary electrophoresis instrumentation. We have completed devices for both ends of the capillary array. This interface technique allows for a repeatable, accurate method of introducing a fluid reservoir, electrical connectivity, and 20 μm radial alignment to 100 capillaries, and potentially more, by hand.

This interface is a low cost, easily constructed method of alignment for multiple ports, which in future work will be scaled up to a 10,000 port assembly for the final version of an ultra-high throughput mutational spectrometer. Applications to other micro-fluidic fields, such as cell manipulations and DNA applications, as well as microchip interfacing and chemical mixing are simple, require only minor modifications to the device for chemical compatibility and fluid requirements.

Future progress in DNA detection using this device at the ends of a 100 capillary array will be reported at the ASPE annual meeting.

ACKNOWLEGEMENTS

We gratefully acknowledge the generous support of the National Science Foundation, Sandia National Laboratories, and the MIT BioInstrumentation Laboratory.

REFERENCES

1. Gray, B.L., Collins, S.D., Smith, R.L., 2001, *Proceedings of the Micro Total Analysis Systems* 2001, Kluwer Academic Publishers, Dordrecht, The Netherlands 2001, pp. 153–154.
2. Gartner, C., Becker, H., Anton, B., O'Neill, A., Rotting, O., 2003, Polymer based microfluidic devices - examples for fluidic interfaces and standardization concepts. *Proceedings of the SPIE*, 4982: 99-104.
3. Nittis, V., Fortt, R., Legge, C.H., Mello, A.J., 2001, A high-pressure interconnect for chemical microsystem applications, *Lab on a Chip*, 1: 148–152.
4. Yang, Z., Maeda, R., 2002, A world-to-chip socket for microfluidic prototype development, Electrophoresis, 23: 3474-3478.
5. Forest, C.R., Ball, N.B., So, P., Thilly, W.G., Hunter, I.W., 2006, Two-dimensional capillary array electrophoresis end-column fluorescence detection, Electrophoresis, (under revision).
6. Morgenthaler, S., Thilly, W.G., 2005, Summed multi-allelic risk: logical and a statistical models for discover of carrier genes in human populations, Mutation Research, (submitted).
7. Slocum, A.H. 1992, *Precision Machine Design*, Prentice Hall, Inc.
8. Forest, C. R., Woodruff, B., Hunter, I. W., 2006, Accurate, repeatable, and replaceable constraint of capillary arrays using a micro-fabricated device, Proceedings of the *20th International Symposium on MicroScale Bioseparations* (MSB), Amsterdam, Netherlands, January 22-26.

FABRICATION OF PERIODIC NANO-STRUCTURE USING DNA FRACTIONS

Takeshi Hatsuzawa and Yasuko Yanagida

Precision and Intelligence Laboratory,

Tokyo Institute of Technology

4259-R2-6, Nagatsuta-cho, Yokohama, 226-8503, JAPAN

INTRODUCTION

Molecular self-assembling is one of the important technical fields for the fabrication of nano-mechanisms by the bottom-up technique. Among many kinds of biopolymer, DNA has advantages such as creativity of arbitrary base sequence using DNA synthesizer, sub-nm self-positioning resolution in hybridization, and well- developed cut-and-paste techniques for the double helix structure, which is very attractive for nano-mechanism fabrication. So far, pre-hybridized DNA blocks - DNA tiles in rectangle or triangle shape have been developed to form 2D structures by designed base sequences and ligation[1]. Also, labeling technique to the DNA enables nano-particle positioning by the base pitch of 0.33nm, which cannot be obtained by the mechanical method. By using the positioning ability, periodic gold nano-particle arrays with 2D pitch of tens of nm has been developed by Zhang et.al.[2]. Also by using a long single strand DNA and "staple" DNA's, the "DNA origami" to form 2D structures has been developed by Rothemund[3].

In this report, a linear nano-structure with periodically positioned metal nano-beads is developed using ligation of short DNA double strands for a nano scale application. Also, two applications of DNA strands combined with biotic protein rather than metal particles are proposed. First, a DNA folding process with IHF2 protein is shown for sensor and actuator use. And then, branches at a designated position on the DNA strand is proposed by using RecA protein for complicated structures.

1D PERIODIC STRUCTURE

CONSTRUCTION PRINCIPLE

Figure 1 illustrates construction principle of the 1D periodic structure by DNA fraction. Two single strand DNA's with a length of *L* mer are chemically synthesized, and one of the DNA has a chemical coupler – biotin for the particle

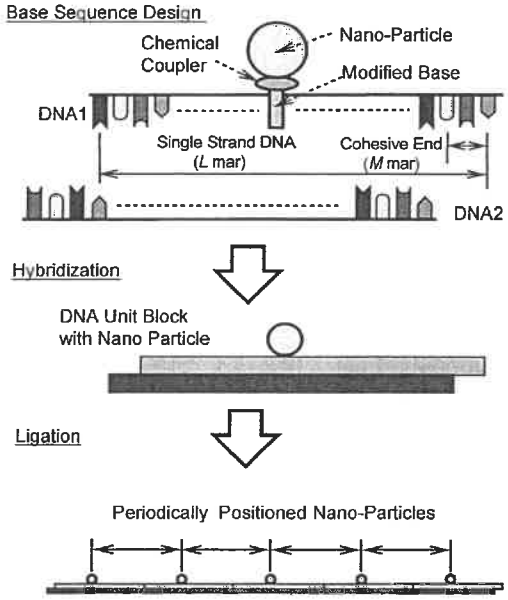

FIGURE1. Construction principle of the periodic nanostructure by DNA.

labeling. They are hybridized to form the unit block with a cohesive offset of *M* mer. And then, the unit blocks are serially connected each other by using a ligase, which firmly connects the phosphodiester bond at the both side of DNA. Finally, nano-particles are positioned by the chemical coupler, typically avidin-biotin coupling, and the periodic nano-structure can be obtained.

DESIGN OF BASE SEQUENCE

Base sequence has been optimized by a computer simulation so that two DNA's are hybridized only in one way. According to an earlier study[4], requirements for the base sequence are

1) no 6 mar or longer subsequence is existed in the single strand,
2) 5 mar subsequence is rare in the sequence.

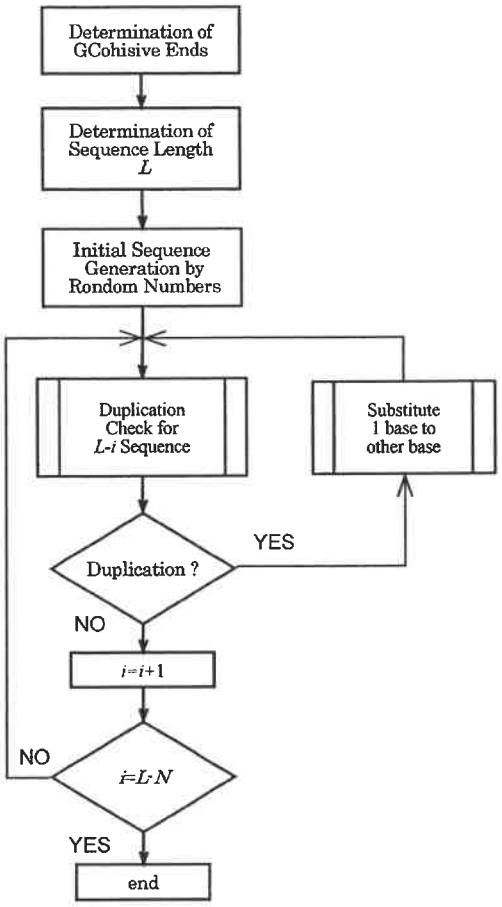

FIGURE2. Flow chart for optimization of base sequence.

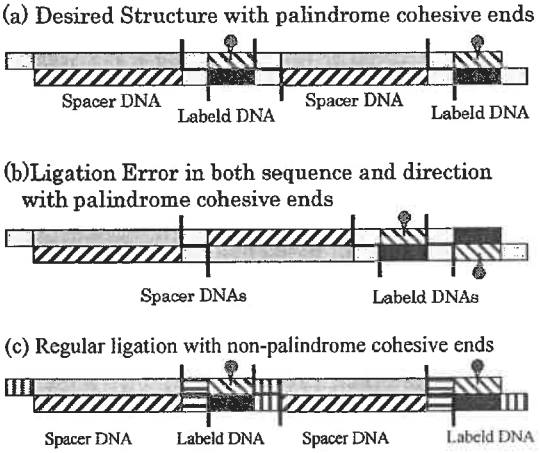

FIGURE3. Connection variation in the multi-block configuration.

Figure 2 shows the flow chart to find the base sequence, in which an initial base sequence is generated randomly. When the doubled sequence is found, it is replaced by other base sequence, and this process is performed until the obtained sequence meets the requirements. Direction of the DNA blocks. Usually, each design of cohesive ends are another importance, since it controls the connecting cohesive end has a palindrome base sequence, which is recognized by restriction enzyme, however, it may cause direction and sequence error for multi block configuration shown in figure 3. To realize single formation, non-palindrome cohesive ends are adopted.

Table 1. Example of the optimized base sequence.

DNA1a 30mer (Labeled)	5'-GTATGGTTCATCC[b]GCCGGCAAGACTTACG-3'
DNA1b 30mer (Labeled)	5'-CTCTACGTAAGTCTTGCCGGCAGGATGAAC-3'
DNA 2a 50mer (Spacer)	5'-TAGAGGTAACCTATTTCCGGAGAAT-GACTGCTCGCGTTGGCCATCACAAG-3'
DNA 2b 50mer (Spacer)	5'-CATACCTTGTGATGGCCAACGCGA-GCAGTCATTCTCCGGAAATAGGTTAC-3'

Table 1 is an example for the multi-block DNA serial nano-structure for "Labeled" (with coupler) and "Spacer" (no label) DNA's. In this case, unit block length of 80bp(base pair) is obtained, corresponding to 26.4nm.

EXPERIMENTS

In the hybridization, two types of the unit DNA – Labeled and spacer are hybridized separately in a plastic test tube. The density and volume of the DNA is adjusted so that the number of DNA is almost the same. After 5 min incubation at 90℃, it is cooled down to room temperature for 18hours. And then, the labeled and spacer unit is hybridized at cohesive ends at a low temperature of 50 ℃ to avoid dissociation of unit DNA's. Next, a ligase (Takara Ligation Kit Ver.1) is introduced for 30min at a temperature of 16 ℃ to make phosphodiester bond at the both side of DNA. Finally, avidin coated gold nano-particle with a diameter of 5nm(BB international) is positioned

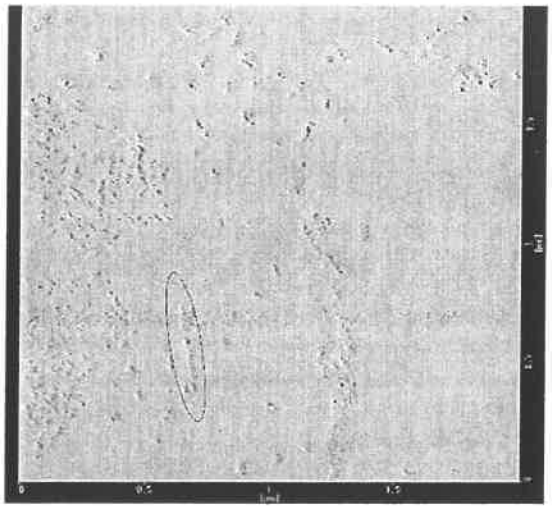

FIGURE 7. An AFM micrograph for the DNA labeled gold chain (Scanned within 2 x 2(m)

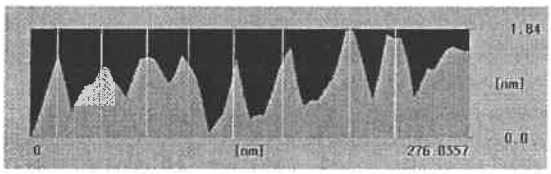

FIGURE 8. Cross sectional measurement on the DNA labeled gold chain

on the designated position of the DNA chain. For this purpose, TE buffer dissolved DNA with a volume of 10μg/ml is mixed with the gold colloid of 3.4 μg/ml, incubating for 1hour at a temperature of 25℃.

Figure 4 is an AFM (SII, SP400) micrograph of the periodic DNA nano- structure observed on a mica substrate at a tapping mode frequency of 120Hz. DNA is static- electrically fixed on the mica by Mg+ ion, which is obtained by the pre-treatment of the substrate by the $MgCl_2$ solution.

A long DNA chain is observed in the right part of the micrograph, though, it does not seem to be continuous because of the labeling error or crack in the fixation process. In the elliptical part of the micrograph, a cross sectional analysis is performed, which is shown in figure 8. Average pitch measured from fig.8 is 27nm ± 4.7nm, which is almost identical to theoretical pitch of 26.7nm(80bp).

According to the electrophoresis of the DNA , more than 90 unit of the labeled and spacer DNA repetition is confirmed, and thus, periodic 1D nano-structure can be fabricated, and can be applied for nano-scale[5].

ZIGZAG CONFIGURATION WITH IHF

A biotic protein IHF(Integration host factor) recognize special base sequence on the DNA and selectively self-hold to the place, which is called IHF box. It usually have a base sequence **atcaaxxxxtt**, where **x** is an arbitrary nucleic acid of DNA. When IHF hold to DNA, it bend the double strand like a hairpin. By using this characteristics, a zigzag configuration can be formed, which is shown in fig.9. First, a DNA block with the IHF box sequence is synthesized chemically, and

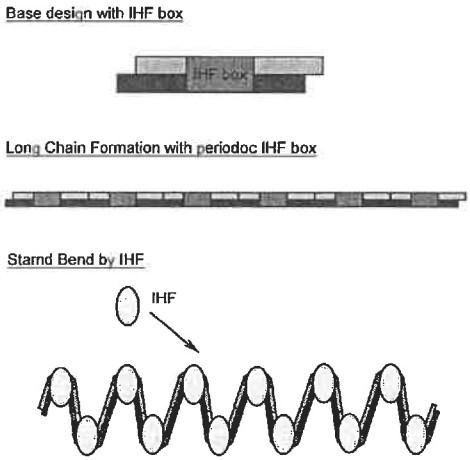

FIGURE9. Principle of the DNA zigzag configuration with IHF protein.

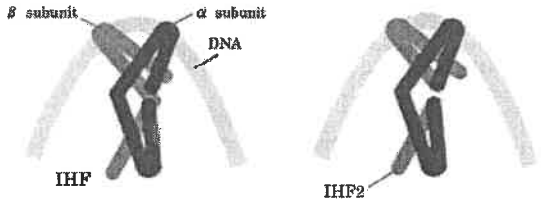

FIGURE10. 3D structure of IHF (dimmer) and IHF2 (monomer).

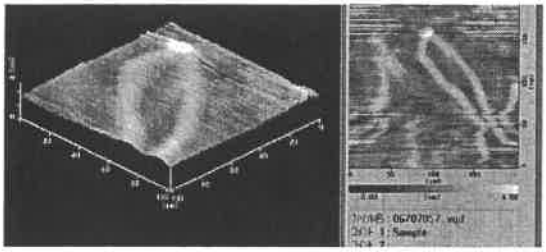

FIGURE11. An AFM micrograph at the bending corner of the zigzag configuration.

ligated to form a long DNA strand. Secondly, IHF protein is added to the DNA and it automatically positioned to the IHF box and bend the strand, resulting in a zigzag formation.

IHF consists of a dimmer with α and β subunit protein shown in fig.10, which makes extraction process difficult. An alternative monomer IHF2 has been is proposed[6] and can be made by *E.coli* culture with recombinant DNA. Fig.11 is an example of AFM micrograph at a corner of the zigzag configuration, which was obtained by the IHF2 and a DNA double strand with 8 IHF boxes. The corner is bent by the IHF2, and looks slightly thick because of the IHF2 adhesion, which demonstrates the usefulness of this method.

COUPLER ARRANGEMENT BY RecA

In the pervious methods, the coupler should be designated beforehand by placing biotin or IHF box in the DNA strand. By using RecA protein, it is possible to put the coupler at arbitrary position of the DNA strand, provided that the base sequence at the place is known. RecA protein works as a recombination mechanism to make DNA triple strand partially, where the base sequence of the single strand can be hybridized to one of the double strand sequence. It clips the single strand to the double strand just like in fig.12. When the single strand DNA has an excess base sequence, which cannot be hybridized to the double strand, branch from the DNA can be constructed. Also, with a chemical modification at the end of the single strand DNA, nano-coupler can be placed at the designated places.

To confirm this arrangement, a long DNA double strand with a length of 1600bp, which consists of 8 unit blocks(200bp), is produced by recombinant cloning of *E.coli*. A 90mer single strand DNA with the hybridization length of 80mer and a biotin coupler at the non-hybridization end is mixed with the long DNA and RecA(Bio Labs). After 3-hour incubation of the DNA in a test tube, a long DNA with periodic branches are formed. Figure 13 is an AFM micrograph for the nano-structure. DNA's with periodical thick parts are observed form the micrograph, which demonstrates the branch construction by the proposed method.

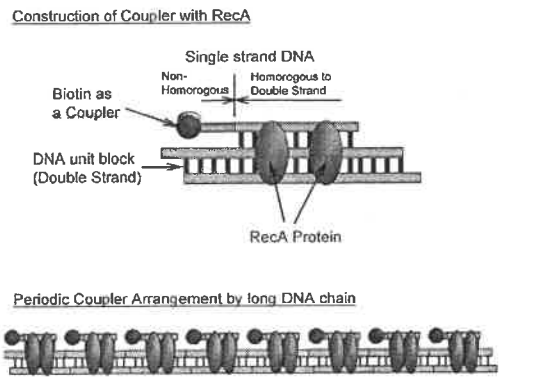

FIGURE12. Principle periodic coupler arrangement by RecA protein and Single strand DNA.

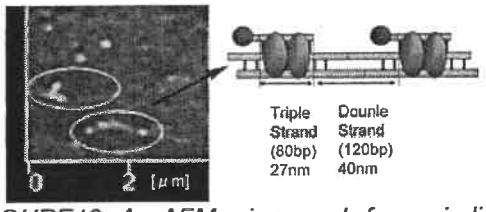

FIGURE13. An AFM micrograph for periodical branch by RecA.

CONCLUSION

Periodic nano-structure by DNA are proposed as follows.

1)DNA with gold labeling,
2)DNA with IHF box and IHF2 protein,
3)DNA and single strand DNA with RecA protein.

ACKNOWLEGEMENTS

This work is partially supported by Grants-in-Aid of Scientific Research, JSPS (B-17360112).

REFERENCES

1. C.Mao,et.al., 1999, A Nanomechanical Device Based on the B-Z Trasition, Nature, 397,144-146
2. J.Zhang, et.al., 2006, Periodic Square-Like Gold Nanoparticle Arrays Templated by Self-Assembled 2D DNA Nanogrids on a Surface, Nano Lett. 6(2), 248-251
3. P.W. K. Rothemund, 2006, Folding DNA to create nanoscale shapes and patterns, Nature, 440, 291-302
4. E.Winfree, et.al., 1998, Design and self-assembly of two-dimensional DNA crystals, Nature 394(6), 539-544
5. T.Hatsuzawa, 2004, Nanoscale Artifact by DNA Strand and Gold Labeling, First Int'l Symposium on Standard Material and Metlorogy for Nenotechnology, 201- 204
6. T.Corona et.al., 2003, Activation of site- specific DNA integration in human cells by a single chain integration host factor, Nucleic Acid Research, 31, 5150-5148

PRECISION DESIGN VERIFICATION SYSTEM OF INJECTION MOLDS USING WEB-BASED 3D VIEWING TECHNOLOGY

In-Ho Song[1], Siyon Chung[2] and Sung-Chong Chung[1]
[1]Hybrid Systems Design & Control LABoratory
Department of Mechanical Design and Production Engineering
Hanyang University, SungdongGu, Seoul 133-791, KOREA
[2]Faculty of Science
The University of Western Ontario, London, Ontario, CANADA

ABSTRACT
An efficient and precision hybrid interference verification algorithm for the web-based interference verification system is studied for injection mold design processes. In order to design a collaborative system over the distributed environment, the proposed system uses lightweight CAD files produced from the optimally transformed CAD data through ACIS kernel and InterOp. This proposed system allows collaborative developers to verify interferences among parts over the Internet without any commercial CAD systems. The system gives benefits to collaborators by reducing production cost, errors and lead-time to the market. Validity of the developed system is confirmed through case studies.

KEYWORDS
Collaboration, Injection mold, Interference verification, Internet, Lightweight CAD file.

INTRODUTION
Injection-mold industry is important for the human life. Demands for shorter design and manufacturing lead-time, good dimensional accuracy and quality, and rapid design changes have become significant issues in the injection mold design and manufacturing industries. In order to reduce lead-time in the production process of accurate molds, most companies use 3D CAD systems and attempt to apply design collaboration tools to the design process of molds. Communication difficulty between collaboration divisions or companies, loss of accurate inspection tools to verify designed molds, the file conversion difficulties among several CAD systems, etc. have increased the lead-time and decreased the production efficiency [1]. To overcome these problems, commercial web-based viewing tools, such as Spinfire of Actify Corporation and AutoView of Cimmetry system have been used. However, the commercial viewing tools have only simple measurement functions and do not have accurate interference verification functions applicable to injection mold design processes [2]. In addition, as they are general viewers, it is difficult to apply the viewers to the design process of injection molds.

In this paper, to design a precise viewer with accurate measurement functions, a web-based design verification system is studied through ActiveX control. To apply this system to the interference verification process of injection molds, a draft verification module [2] according to the parting surface is incorporated into the web-based precise measurement system. An optimized lightweight CAD file [3], produced from a commercial CAD file, is applied to overcome communication difficulties. In addition, assembly verification of injection molds is developed through the axis aligned bounding box tree [4] and the data structure of the lightweight CAD file [2].

Performance of the developed system is verified through various case studies over the Internet. Using the developed web-based 3D viewer, it is possible to reduce lead-time and manufacturing cost.

CLASSIFICATION OF INTERFERFERENCE PARTS IN INJECTION MOLDS
Interferences of injection molds primarily occur by slide cores, angle pins, ejector pins, bolts, etc. Interference of a slide core occurs at the curved surface between the slide and the lock. In this case, the slide core is not assembled well due to the interference. Fig. 1(a) shows an example of the interference between the slide and the lock. An angle pin is a locking unit that fixes a slide core to prevent interference between the product and the injection mold. Interference changes the length and the inclination angle of the angle pin

according to working distance of the slide core. Interference between the angle pin and the angle pin evasion hole occurs according to length and inclination angle of the angle pin. The interference damages slide cores. Fig. 1(b) shows interference between the angle pin and the angle pin evasion hole. Interferences of ejector pins or bolts mainly occur owing to not only the position errors between the ejector pin and the ejector pin hole, but also the long length of the ejector pin. Bolt interference occurs when the bolt is longer than the depth of a hole. Fig. 2(a) shows an example of interference between the ejector pin and the bolt.

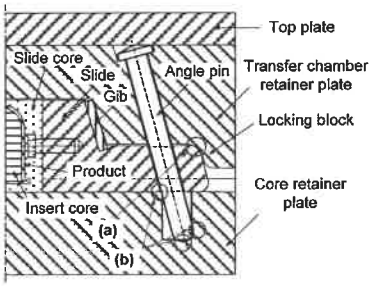

FIGURE 1. Interference between: (a) slide and lock, (b) angle pin and angle pin hole.

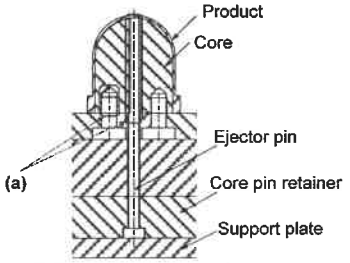

FIGURE 2. Interference between the ejector pin and the core.

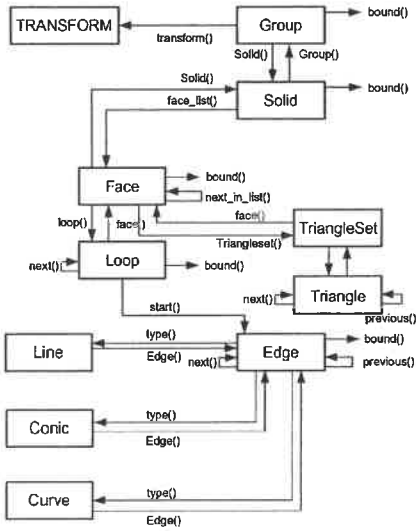

FIGURE 3. Structure of the lightweight CAD file.

HYBRID INTERFERENCE VERIFICATION

Data Structure

An efficient interference verification algorithm is accomplished by using the hierarchical data structure of the previously developed lightweight CAD file [3]. The data structure shown in Fig. 3 is used to propose a hybrid algorithm which uses the AABBtree [4] and the structure of the lightweight CAD file [2] to verify interferences effectively. The name 'Solid' means a solid entity of a CAD file. The 'Face' includes surface information of a solid. Face is composed of triangular meshes and edges. The triangular meshes are applied for the visualization of CAD files. Using this data structure, the solids, faces and triangular meshes are able to be successively searched for interference verification. To reduce the interference inspection time between solids and faces, the AABBtree is applied to exclude non-selecting entities during the inspection process.

Interference Verification Algorithm

Fig. 4 shows the hybrid interference verification process using the lightweight CAD file. Following 5 steps are used for the interference verification:

(1) First step is the computation of a BV of a face. Maximum and minimum values of vertexes included in faces are extracted from the vertex information. In Fig. 5, BV is computed by the maximum and minimum values ($FV_{i,j}$) that is stored at the class of face ($F_{i,j}$). The BV of solid (SV_i) is computed by the BV values of the generated face in the class.

(2) Second step is the computation of a BV of a solid. Comparing maximum/minimum values of $FV_{i,j}$ included in S_i, SV_i is obtained. In Fig. 5, BV of the j th face ($F_{i,j}$) in the i th solid (S_i) is given by SV_i.

(3) Third step is the interference verification of solids. The interference verification of SV_i, BV of the ith solid, and BV of other solids is performed repeatedly. If no interference is found, interference verification of SV_{i+1}, BV of the next solid, and BV of the rest of the solids is executed. These processes are iterated to complete the interference verification of BV of all solids. A more detailed method of interference verification of BV of solids is suggested in [3].

(4) Fourth step is the interference verification of faces. $F_{i,j}$ is one of the faces included in the solid of S_i. If interference is detected in BVs of two solids, interference verification of BV of $F_{i,j}$ and BV of faces of S_{i+1}, which has already been interference verified, is performed. This process is repeated to execute interference verification of BV of all faces contained in the two solids.

(5) Fifth step is the interference verification of triangular meshes. If interference between two faces occurs, the first triangular mesh $T_{i,j,k}$ of $F_{i,j}$ is selected and interference verified with triangular meshes of $F_{i,j+1}$. If no interference is found, $F_{i,j}$'s next triangular mesh $T_{i,j,k+1}$ and triangular meshes of $F_{i,j+1}$ undergo interference verification. In this case, k is the order of triangular meshes. The process is iterated to perform interference verification of all triangular meshes. The color of meshes with interference changes to show results of the interference verification. Using this procedure, it is possible to find the interference spot of an injection mold in the injection mold design process.

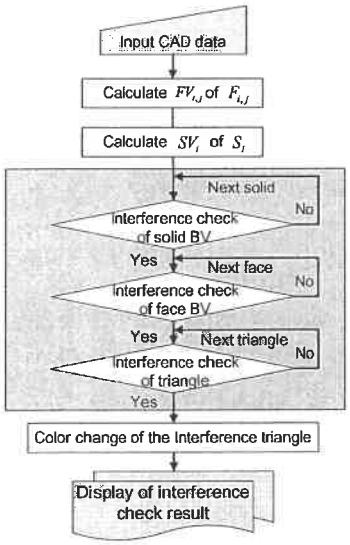

FIGURE 4. Hybrid interference verification algorithm.

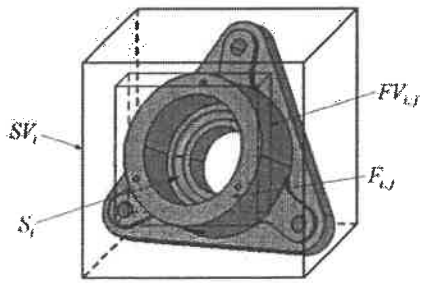

FIGURE 5. BVs of a solid and faces.

SYSTEM PERFORMANCE

In order to verify the efficiency of the proposed algorithm, the total number of calculation to check interference of two solids is compared. The two solids include faces, and the numbers of the faces of the two solids are denoted by f_l and f_m, respectively. The number of pairs of faces with interference is f_n. The numbers of triangular meshes included in each of the faces are t_l and t_m, respectively.

In an extreme case, where interference inspection of two solids does not have a hierarchical structure like VRML, the total number of calculation to inspect interference is calculated according to the whole search method [5,6] of triangular meshes as given by Eq. (1). However, the proposed number of calculation of the interference inspection is calculated according to Eq. (2). As Eq. (1) includes a lot of multiplication and Eq. (2) is expressed in smaller amount of multiplication and addition, the proposed method, Eq. (2), is faster and more efficient. In addition, if two solids interfere at only one pair of faces, when f_n is 1, $N_{proposed}$ decreases dramatically.

$$N_{worst} = f_l f_m t_l t_m = 10 \times 10 \times 100 \times 100 = 1{,}000{,}000 \quad (1)$$

$$N_{proposed} = f_l f_m + f_n t_l t_m = 10 \times 10 + 1 \times 100 \times 100 = 10{,}100 \quad (2)$$

For example, each of two solids A and B consists of 10 faces, and each face is made of 100 triangular meshes. It is assumed that there is only one face interfering each other. Then, the fourth and fifth columns of Tab. 1 show the number of calculations required to inspect the interference between the two solids composed of triangular meshes. Using the proposed method, even with about 2% of calculation, exact interference locations are able to be extracted. It is effectively applicable to the injection mold design process with small size of interference.

TABLE 1. Calculation numbers to inspect interference between the worst and proposed cases.

	A	B	Worst-	Proposed
Solid	1	1	-	1
Face	10(f_l)	10(f_m)	-	100
Triangle	100(t_l)	100(t_m)	1000000	10000

CASE STUDY

Efficiency of the proposed interference verification system is verified through actual

CAD files for the injection mold process. The injection mold is designed on commercial CAD systems, and the CAD data are registered through the web page of the developed system. The registered CAD files are converted into lightweight CAD files trough the translation server. When an injection mold CAD data is searched on the web and is requested to be verified, the viewer is automatically plug-in on the user's web-browser, and the searched lightweight CAD file is downloaded and visualized.

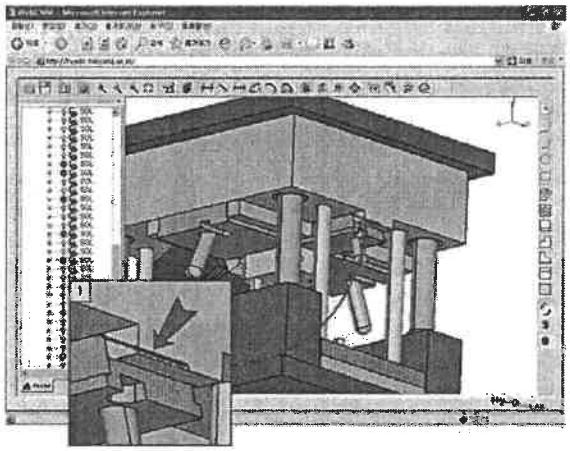

FIGURE 6. Interference verification between angle pin and hall.

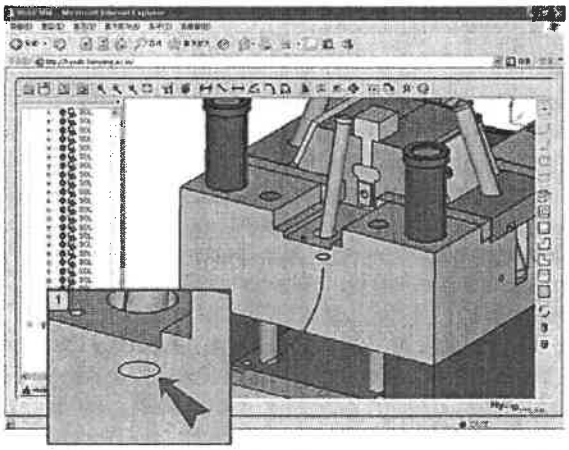

FIGURE 7. Interference verification between slide and lock.

Fig. 6 shows the result of interference verification of the angle pin and the evasion hole. Interference comes from contact between the angle pin and the evasion hole due to the longer length of the pin. Result of interference verification is displayed on the screen in black as shown in ① of Fig. 6. Based on the result, designers are able to modify the length of the angle pin or size of the evasion hole, and apply the changes to the design of the injection mold. Fig. 7 shows the interference between the slide and the locking block. In this case, interference occurs at the corner where the slide and the locking block contact together. The reason is that the radius of curvature of the slide is smaller than that of the locking block. The interference region is made distinguishable through color change and is shown in ① of Fig. 7.

CONCLUSIONS

Following conclusions have been obtained:

(1) Major interference cases of injection molds have been classified and a hybrid interference verification algorithm has been proposed.

(2) As the developed interference verification algorithm is incorporated into the previously developed web-based collaborative viewing system, commercial CAD systems are not required for assembly verification.

(3) Using the developed interference verification system, collaborators are able to verify design results and dimensions without using expensive commercial CAD/CAM system.

(4) The effectiveness of the proposed system is verified through the case study.

REFERENCES

1. Ye, X. G., Fuh, J. Y. H. and Lee, K. S., 2000, "Automated Assembly Modeling for Plastic Injection Molds," *Internal Journal of Advanced Manufacturing Technology*, Vol. 16, No. 10, pp. 739~747.

2. Chung, S. C., Yeon, K. H. and Song, I. H., 2005, "Web-based Draft Verification System for Injection Mold Design," *Transactions of the KSME*, A, Vol. 29, No. 10, pp. 1353~1360.

3. Chung, S. C. and Song, I. H, 2006, Design of Lightweight CAD Files with Dimensional Verification Capability for Web-based Collaboration, *Transactions of the KSME(A)*, 30: 488-495.

4. Bergen, G., 1997, "Efficient Collision Detection of Complex Deformable Models Using AABB Trees," *Journal of Graphics Tools*, Vol. 2, No. 4, pp. 1~13.

5. Gottschalk, S., Lin. M. C. and Manocha, D., 1996, OBBTree: A Hierarchical Structure for Rapid Interference Detection, *Computer Graphics Proceeding (SIGGRAPH)*, 30: 171-180.

6. Ar, S., Chazelle, B. and Tal, A., 2000, Self-customized BSP Trees for Collison Detection, *Computational Geometry: Theory and Applications*, 15: 91-102.

AN XML-BASED DIGITAL MOCK-UP SYSTEM FOR HETEROGENEOUS ASSEMBLY

In-Ho Song[1], Kyung-Don Kim[2] and Sung-Chong Chung[1]
[1]Hybrid Systems Design & Control LABoratory
Department of Mechanical Design and Production Engineering
Hanyang University, SungdongGu, Seoul 133-791, KOREA
[2]Small Business Corporation,
Gyeonggi Regional Headquarter, Suwon 443-766, KOREA

ABSTRACT
Digital Mock-Up(DMU) system, a tool to build a virtual mock-up in the design stage, has been used to prevent interferences and mismatches during precision design processes. Using the virtual assembly tool, engineers are able to design precision and interference free parts without making physical mock-ups. Instead of a single CAD source, several CAD systems are used to design a complex product in the distributed design environment. In this paper, a heterogeneous multi-CAD assembly method is proposed through an XML and the lightweight CAD file. XML data contains hierarchy of the heterogeneous multi-CAD assembly. The lightweight CAD file produced from various CAD files through ACIS kernel and InterOp includes not only mesh and B-Rep data, but also topological data. It is used to visualize CAD data and to verify dimensions. The developed system is executed on desktop computers. It does not require commercial CAD systems to visualize 3D assembly data. Assembly of heterogeneous models is conducted to verify the effectiveness of the developed DMU system on the Internet.

KEYWORDS
Assembly, Digital Mockup, Heterogeneous CAD, lightweight CAD file, XML

INTRODUTION
Design of cars and aircrafts requires a lot of engineering collaborators. Most of design modifications, related to manufacturability and assembility, are required due to mismatches and interferences between neighboring parts. To reduce such mismatches and interferences, a real mock-up has been used. CAD systems are applied to verify and check the assembly process. DMU systems have been used to prevent the interferences and miss matches during precision design processes. Using DMU systems, designers are able to design precision and interference free parts without making physical mock-ups.

Rezayat[1] has applied XML to exchange CAD information. In order to exchange CAD data, Rezayat translated topological CAD information into XML data by using KBPD(Knowledge-Based Product Development). In addition, he proposed a DTD type schema called CADML(CAD Markup Language). Chen et al.[2] studied a real-time web-based collaborative design for assembly, which is called e-Assembly. By using ACIS kernel and the model of CAR (collaborative assembly representation), they devised a real-time collaborative tool applicable to verifying assemblies. Jezernik and Hren[3] developed a low cost VR(virtual reality) system by using XML and VRML. JT of UGS[4] and HSF of HOOPS[5] visualize assembled parts composed of heterogeneous CAD data. However, they do not generate visual data efficiently in various PDM systems because they are not interfaced with XML or STEP/PDM schema.

In this paper, visualization of an XML based DMU system for assembled parts composed of heterogeneous Multi-CAD data is proposed through the visualization of the lightweight CAD file [6]. The developed system does not require expensive commercial CAD systems. Cost of ownership is cheaper than other systems. In addition, the system has a function of real-time interference check, dimensional check, and design verification of heterogeneous multi-CAD assembled parts on the Internet environment. Lightweight CAD data [6] are used for sharing model information. XML is used for displaying and interfacing BOM (bill of material) of assembled parts. By designing a schema based on an international standard of ISO/STEP PDM,

the developed system are able to interface with most commercial PDM systems. In order to interface with other systems, modified positional information generated in the assembly process is stored as an XML format and is registered in the PDM system database.

VISUALIZATION OF ASSEMBLY

In this paper, visualization of assembly is designed by PDM schema of STEP standard. Fig. 1 shows an XML schema structure of the assembly and parts. In Fig. 1, the XML schema structure consists of subordinate assembly, sub-assembly, and its part, component. The sub-assembly is able to adopt another assembly or parts.

The parts and assemblies have matrix data to represent position information. The matrix data containing position information are formed with transformation matrix (V1~V9) and position vector (T1~T3) of parts or sub-assemblies at 'Position'. 'Name' on Fig. 1 means a name of the part or sub-assembly on BOM. 'Id' is a number to distinguish assemblies or parts. 'Type' means a kind of the link data. According to the 'Type', users select appropriate translator for visualization. 'Version' describes the version of drawings. 'Higher_info' is an entity representing higher level information, and it supports a searching function of a hierarchy in the multi-level assembly. 'Link' in a assembly supports the connection between sub-assemblies or parts. 'Link' in a part links physical visualization data. In this paper, XML schema expresses up to N level assemblies and accesses CAD BOM. As the XML data is designed according to DMU of the multi-level assembly, higher and/or lower stage searches are conducted conveniently. Therefore, various CAD data registered in various PDM systems are easily interfaced to the developed XML schema.

SYSTEM ARCHITECTURE

Fig. 2 shows overall structure of the proposed system. The system consists of following modules: CAD API (application programming interface), PDM server and data base, Web server and servlet engine for web interface, data translator for visualization, and PDM-viewer client.
Operating procedure of the system is conducted as follows: Various CAD data are registered in PDM by selecting the 'Check in' menu of the

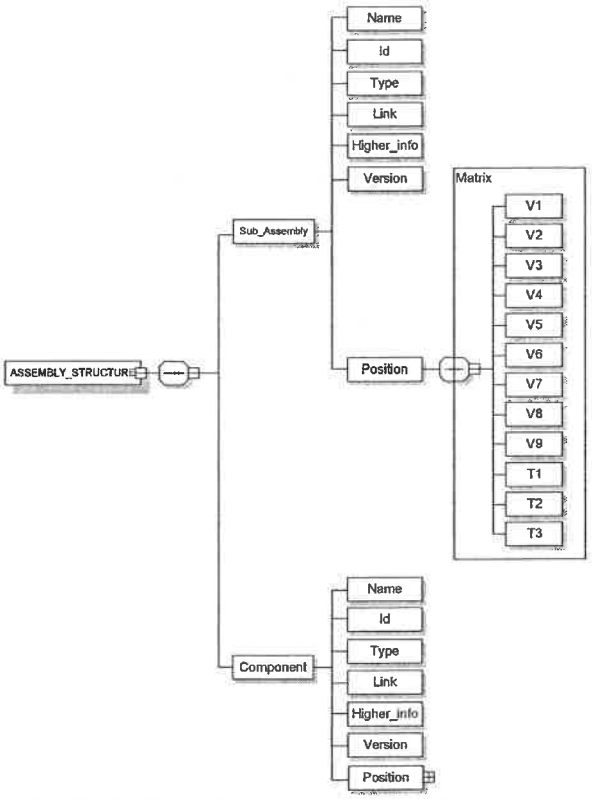

FIGURE 1. XML schema structure for assembly.

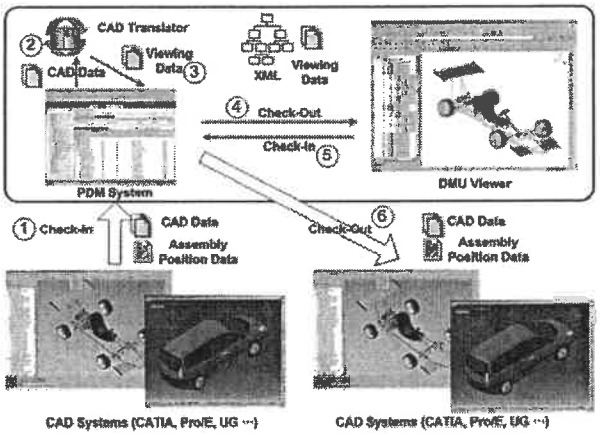

FIGURE 2. Overall framework of the DMU system.

PDM system. The PDM menus are constructed by CAD API. When the CAD data are registered into the PDM, the system extracts position and assembly information of the CAD data by using the CAD API as shown in Fig. 2 ①, and register them to the PDM data base.

The CAD data, registered in the PDM system, are translated to visual data by the CAD Translator as shown in Fig. 2 ②, and managed

by the PDM system as shown in Fig. 2 ③. When users check out an assembly needed to be verified, then the DMU web viewer is plugging into the web browser. The assembly XML and the lightweight CAD file as visual data of components are visualized on the web viewer as shown in Fig. 2 ④. After verification by the assembly DMU, the system checks in the assembly on the viewer, and then delivers the changed assembly position by XML and shows it. The verified file, checked by DMU web viewer, is able to be verified again on CAD systems. To be verified on the CAD system, the file should be searched through the PDM system, and then 'Check-out' to the CAD system. According to these procedures, users are able to check whether the CAD data have interferences. If there are interferences, clients are able to modify those interferences, and register modified data through check-in procedure of the PDM system.

GENERATION OF VISUAL DATA

Most PDM systems convert CAD data to visual data for efficiency and security. In this paper, visual data are generated separately as the component file and the assembly information. CAD data corresponding to parts generate visual data after conversion, but the other CAD data corresponding to assembly store both connecting and position information as matrices including visual data. These assembly data corresponding to sub-parts of the PDM system data is obtained without conversion. Using the information, clients are able to search the data on the PDM. An XML-writer generates an XML files to be used for visualization. The XML-writer was developed by using Xerces XML Parser.

In general, the generation process of visual data converts all CAD data of an assembly at once in the translation server. To do like this, a high performance translation server is required. However, using the proposed method of this paper, only the conversion of parts of the visual data is required. Minimum requirement of the translation server is limited to the size of the maximum part. If an assembly is composed of duplicated parts, the visual data might be reduced remarkably. If there is frequent design modification, the translation server should have big capacity for data storage. However, as only the visual data of the modified parts are required in this paper, clients save memories and reduce the server size.

CASE STUDY

Application of the XML schema

To implement the developed assembly verification system using XML, previously developed lightweight CAD translator [6] and the XML file composer developed in this paper are used. Oracle is used as a database of the PDM system. Fig. 3 shows an example of an XML file and the lightweight CAD data generated when the visualization data is required at the PDM system. Ⓐ of Fig. 3 saves relative position data of each part to 'Position'. Ⓑ of Fig. 3 saves link information of the real visualization data to 'FilePath'. The visualization data link of Ⓑ is connected to ⓒ of Fig. 3 to visualize data. When these parts are connected to the CAD system, they are replaced with CAD data. Eventually, it allows the DMU verification is conducted on the CAD system.

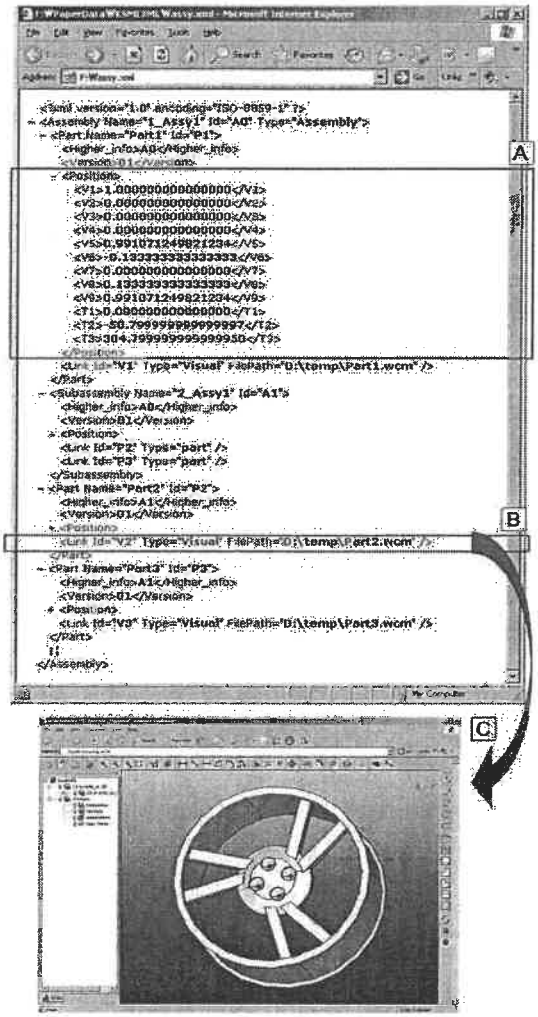

FIGURE 3. CAD assembly using an XML file.

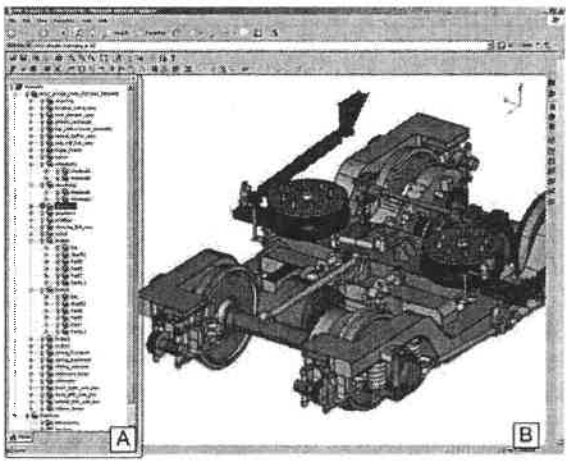

FIGURE 4. Bogie assembly for multi-level DMU.

Application of Multi-level Assembly

A bogie assembly shown in Fig. 4 [B] is used as a case study. It is a 3-level assembly. CAD data designed by a CAD system are registered in the PDM system through the 'Check in' function. Using this function, all part files and conversion matrices at each level of the assembly are registered on the PDM system at once. The registered assembly file is verified step by step through the various searching functions of the PDM system. The assembly at each level is able to be visualized and DMUed by the viewer developed in this paper. In addition, this system represents BOM structure of an assembly as shown in Fig. 4 [A]. It confirms the case study is a 3-level assembly as shown in Fig. 4 [A]. It is concluded that the developed system are able to be applicable to visualization and DMU of any levels of assembly.

CONCLUSIONS

By designing an XML based Digital Mock-up system for heterogeneous multi-CAD assembly, following conclusions are obtained:

(1) Using XML technique, the data structure of the heterogeneous multi-CAD assembly is constructed. The XML-based DMU system has been devised and verified.

(2) As the XML-based assembly system is designed according to the international standard, STEP PDM schema, the developed system is interfaced with various PDM systems.

(3) As the feature information is constructed through the lightweight CAD data and the assembly data are designed by XML, multi-level assembly and visualization of the feature data are performed efficiently.

(4) Visualization data of an assembly are divided into parts and sub-assemblies. As the parts include feature data and the sub-assemblies include only the position data of each part, all visualization data are generated and managed very efficiently.

(5) As the system is applicable to visualization of the assembly data through the generation of modification of parts, advantage of the developed system is maximized when it is used to design an assembly requiring frequent design modification.

(6) Effectiveness of the multi-level assembly of heterogeneous CAD files linked with the PDM and DMU viewer systems is confirmed through the case study.

REFERENCES

1. Rezayat, M., 2002, Knowledge-based Product Development Using XML and KCs, *Computer Aided Design*, 32: 299-309.
2. Chen, L. Song, Z. and Feng, L., 2004, Internet-enabled real-time collaborative assembly modeling via an e-Assembly system : status and promise, *Computer-Aided Design*, 36: 835-847.
3. Jezernik, A. and Hren, G., 2003, A Solution to Integrate Computer-Aided Design (CAD) and Virtual Reality (VR) Databases in Design and Manufacturing Processes, *Int. J. Adv. Manuf. Technol.*, 22: 768-774.
4. UGS-PLM, http://www.ugs.com.
5. HOOPS corporation, http://www.hoops3d.com.
6. Chung, S. C. and Song, I. H, 2006, Design of Lightweight CAD Files with Dimensional Verification Capability for Web-based Collaboration, *Transactions of the KSME(A)*, 30: 488-495.

DESIGN AND TESTING OF A TRIBOMETER FOR IN SITU MICROSCOPY

Nathan A. Mauntler, Alison C. Dunn, Tony L. Schmitz, and W. Gregory Sawyer
Department of Mechanical and Aerospace Engineering
University of Florida, Gainesville, FL, USA

INTRODUCTION

Surface contacts represent a severe environment for even the most robust materials. High localized pressures and temperatures at asperity peaks can lead to a wide variety of wear regimes and chemical events that ultimately lead to the failure of a bearing surface.

Wear rates of sliding surfaces can be measured in a variety of ways. Mass measurements can be taken before and after tests to provide an average wear rate, provided that the materials of interest do not uptake or outgas mass in the test environment. A wide range of commercially available profilometers, interferometers, and optical/electron microscopes can be used to geometrically characterize material loss once a test is complete.

It is often desirable to perform real-time wear measurements and observe initial run-in (or transient) periods, sudden material failures, and other wear events. One approach is to monitor the relative normal displacement between two surfaces, then calculate a wear rate from knowledge of the contact geometry. This can be troublesome if both components of the contact are simultaneously wearing. Chemical events can also be monitored in real time through the use of in-situ spectroscopy [1].

In order to realize *in situ* surface analysis, we have developed a reciprocating tribometer that is easily adapted for use under multiple microscopes and analytical instruments. If wear evolution is a concern, a scanning white light interferometer (SWLI) can be used to monitor the wear of specific regions after each pass rather than at the end of the test. Optical microscopy can be applied to visually inspect the counterface for wear or wear debris during testing. Additional components will be developed in the future to make the design compatible with a Raman/Fourier Transform Infrared (FTIR) spectroscopy unit in order to observe chemical bond changes during tribological tests.

TRIBOMETER DESIGN

A schematic of the tribometer configured for use under a scanning white-light interferometer is shown in Fig. 1. The tribometer operates by reciprocating a flat plate under a normally-loaded hemispherical pin. Relative motion between the pin and counterface is provided by a servo-controlled lead screw stage. The normal force between the pin and the counterface is adjusted by raising or lowering a manual micrometer stage. Normal and friction forces are measured by a six channel load cell. When adjusting the normal load with the micrometer stage, the load cell is kept in alignment with the sliding surface by a leaf spring parallelogram-type flexure (Fig. 2). Additionally, poly-etheretherketone (PEEK) insulators make electrical contact resistance testing possible.

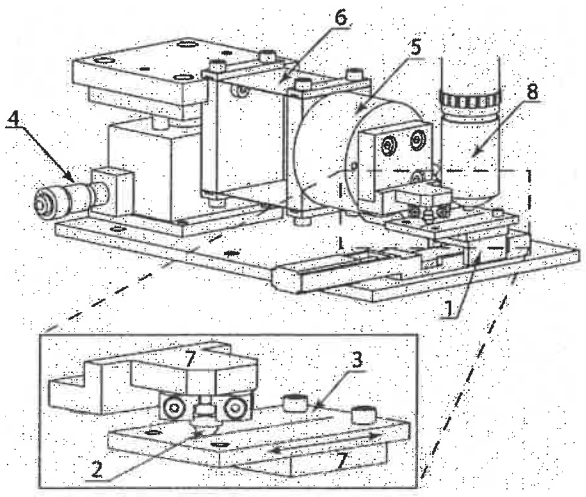

Figure 1: Linear reciprocating tribometer design. (1) Reciprocating stage (2) Pin (3) Counterface (4) Normal load micrometer stage (5) Load cell (6) Leaf spring flexure (7) PEEK insulators (8) Microscope objective for wear observation (9) V-block pin holder

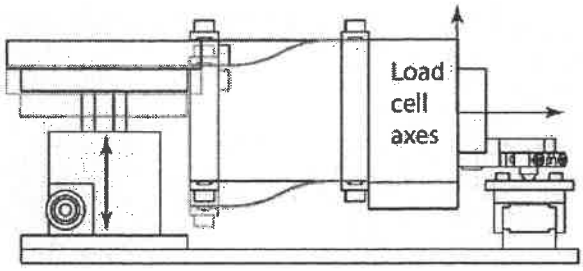

Figure 2: The leaf spring parallelogram-type flexures keeps the load cell axes aligned.

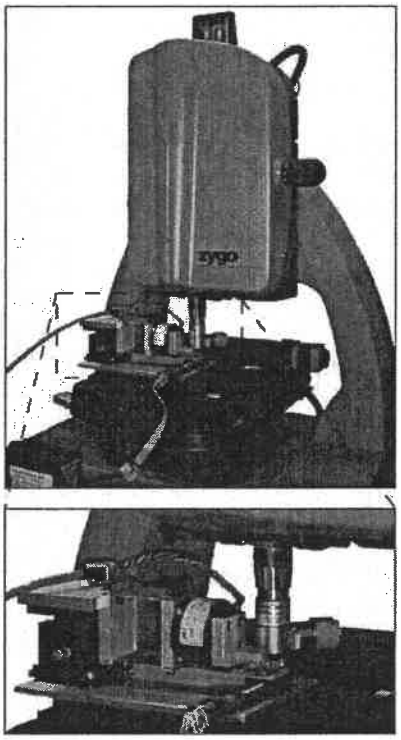

Figure 3: In situ tribometer mounted on SWLI stage.

TESTING UNDER A SCANNING WHITE LIGHT INTERFEROMETER

As previously discussed, the reciprocating tribometer can be configured to complete friction tests under a scanning white light interferometer in order to monitor wear development as a test progresses (Fig. 3). Such testing is accomplished by executing single or multiple reciprocations of the stage while monitoring normal and friction forces. After a given number of cycles (one or more), the wear track area of interest is moved under the interferometer objective in order to perform surface measurements. In this way, average friction coefficient data and surface metrology data can be compared on a cycle-by-cycle basis. In one such test, a polished stainless steel counterface was reciprocated under a stainless steel sphere.

Test Conditions

The stainless steel pin used in this test was mounted with epoxy to a piece of steel tubing which was, in turn, clamped in the V-block holder (Fig. 1). After mounting the pin and counterface on the tribometer, the micrometer stage was lowered until a normal force of 3.5 N was achieved. With the assumption that the counterface could be modeled as an elastic half-space, the initial Hertzian contact pressure between the 3.2 mm diameter sphere and counterface was calculated to be 1.2 GPa. The stage was reciprocated over a 30 mm track length at a commanded sliding speed of 3 mm/s.

Test Results

The test continued for 120 cycles until the epoxy bonding the pin to the steel tubing failed. The average friction coefficient data and a three-dimensional surface map of a portion of the wear track were recorded after each cycle. The test results at several cycles are shown in Fig. 4. Surface height data has been magnified by a factor of 10.

Figures 4a and 4b show the evolution of the wear track as new scratches form and grow on the counterface surface. The combined friction and wear data allow the development of these scratches to be linked with increases in the friction coefficient as seen between cycles 1 and 7. Additionally, the SWLI surface data can be used to calculate surface roughness evolution and monitor the accumulation of wear debris (cycles 7-120).

FUTURE WORK

Currently, a chamber is being constructed to enable operation of the tribometer in a variety of gas environments. Additionally, future tests will include passing current through the pin and into the counterface to study contact resistance evolution. Finally, the tribometer will be modified to operate under a Raman/FTIR apparatus to monitor chemical changes under the contact.

REFERENCES

1. Wahl, K., Dunn, D., and Singer, I., 1999, Wear Behavior of Pb–Mo–S Solid Lubricating Coatings, *Wear*, 230: 175-183.

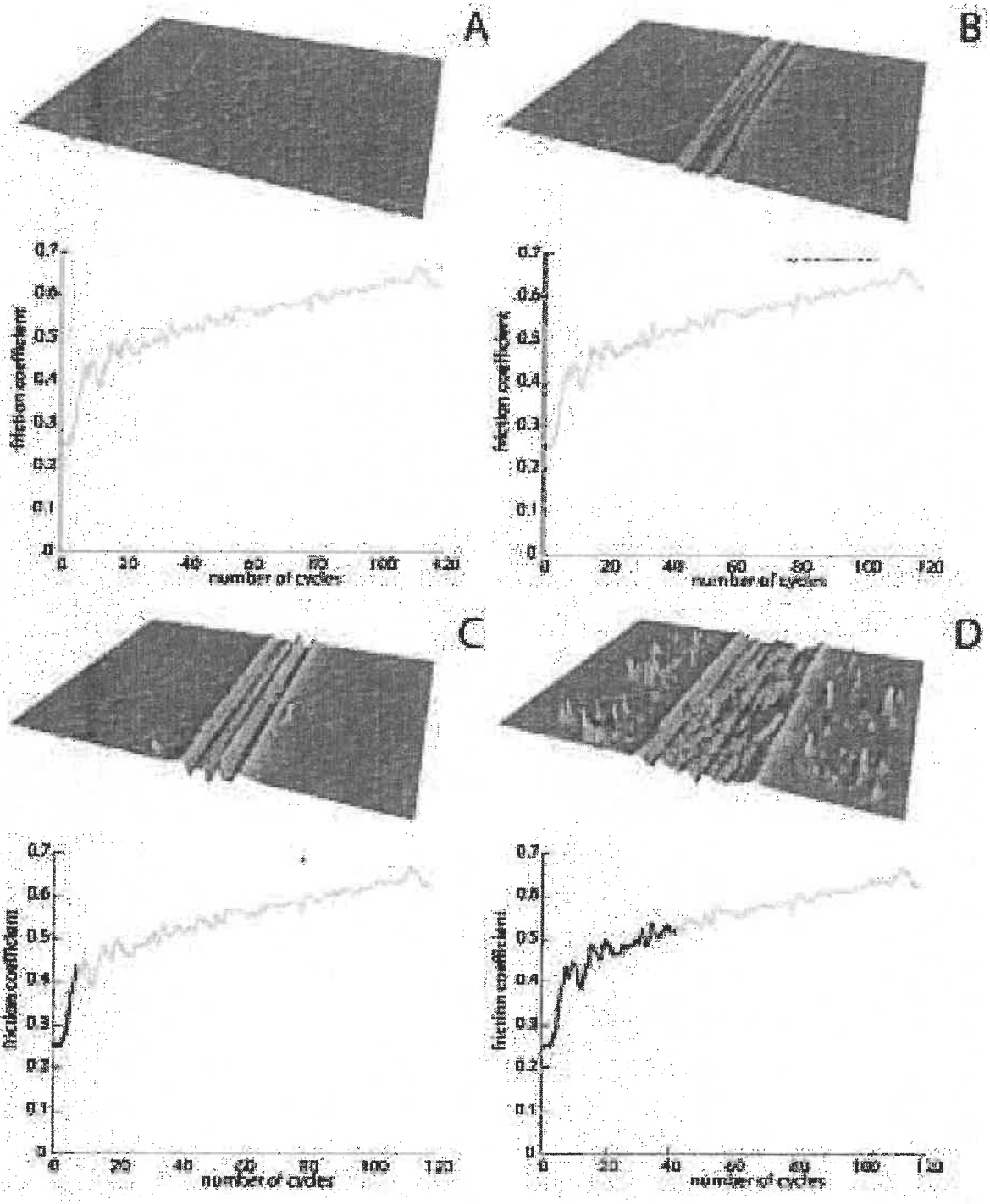

Figure 4a: Friction and wear results for a steel pin on a steel plate under a 3.5 N normal load. (A) Cycle 0, the nascent surface. (B) Cycle 1. (C) Cycle 7. (D) Cycle 40, debris is seen outside the wear track.

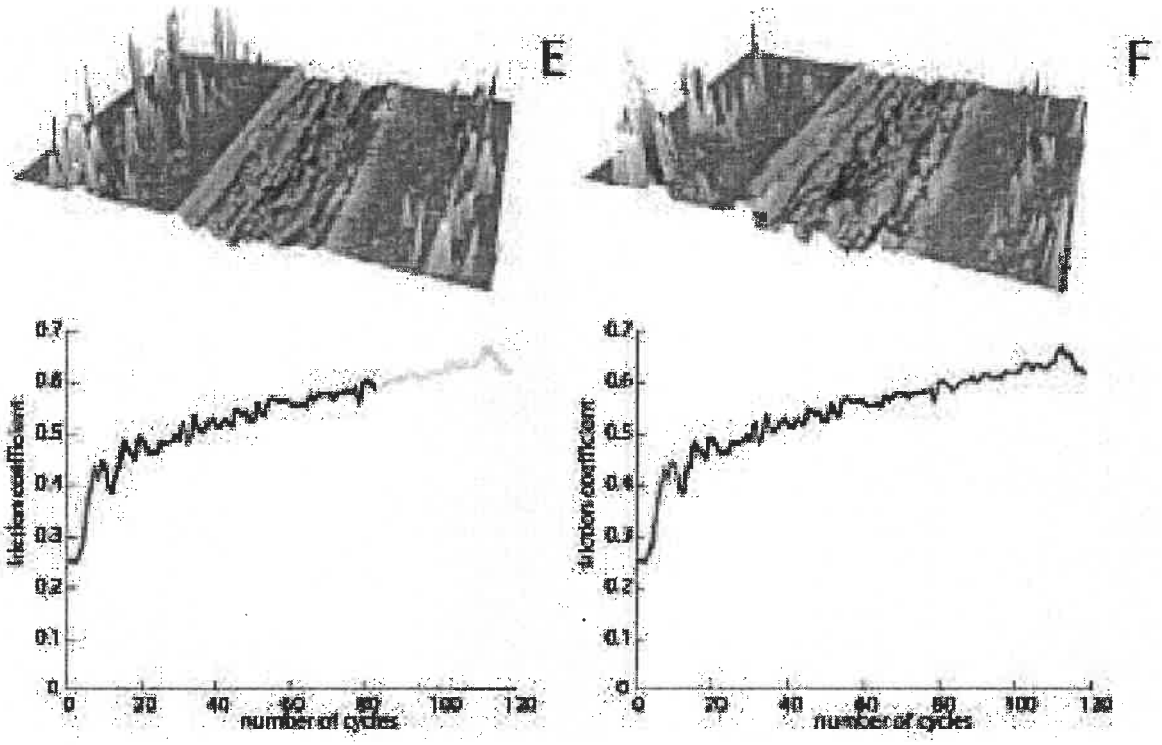

Figure 4b: Friction and wear results for a steel pin on a steel plate under a 3.5 N normal load. (E) Cycle 80, additional debris is observed. (F) Cycle 120.

MONITORING OF ROUNDNESS-ERRORS IN CONTINUOUS PATH CONTROLLED CRANKSHAFT GRINDING PROCESSES

Berend Denkena[1], Niklas Kramer[1]
[1]Institute of Production Engineering and Machine Tools
Hannover University, Hannover, Germany

INTRODUCTION

Crankshafts are typical parts for nowadays grinding operations. A very productive manufacturing process is supposed to machine hardened materials in order to create a long lasting, high performance part of superior quality. Since the beginning of this millennium, worldwide more than 55 million cars are produced every year. This emphasizes the importance of an economic production process providing stable quality and short machining times.

Due to the increasing performance of combustion engines and the ever-rising quality demands of the customers, the geometrical tolerances of the crankshaft are continuously narrowing (FIGURE 1). At the same time, ecological aspects and climbing oil prices call for light-weight and small parts while the load is increasing.

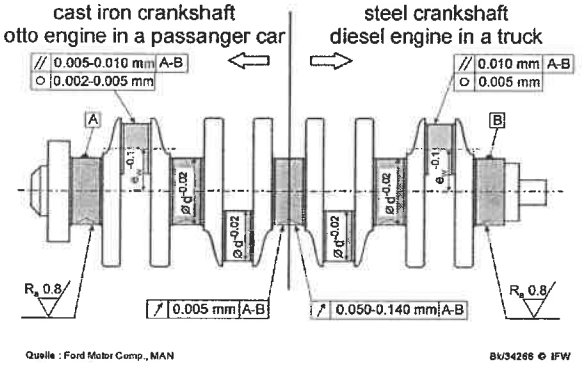

FIGURE 1. Geometrical requirements for crankshafts.

Continuous path controlled grinding of crankshafts is believed to be the most productive and – regarding quality - superior process for hard-fine machining of crankshafts. Nevertheless, the specific geometry of a crankshaft is still a challenge for grinding processes because of its angle depending stiffness. Hence the geometrical precision can only be achieved economically by an extensive knowledge and understanding of the process.

CONTINUOUS PATH CONTROLLED GRINDING OF CRANKSHAFTS

Kinematics and Forces

The specific geometry of crankshafts features more than one rotational axis. In order to grind the bearings, specially designed chucks and tailstocks are used. These clamping devices allow the positioning of each rotational axis of the crankshaft congruent to the machine axis. This involves additional set-up time and the risk of positioning errors.

Modern machines are capable of grinding all the bearings in one set-up. This is done by a sinusoidal movement of the feed axis which allows the grinding wheel to follow the eccentric rotational movement of the crankpin. As a result no more re-clamping is necessary and set-up times are significantly reduced.

The moving speed and the needed acceleration of the radial feed axis are directly depending on the eccentricity and diameter of the crankpin as well as of the rotational speed. In order to maintain the positioning accuracy the traveling speed of the wheel-head is limited and therefore small rotational speeds apply. Generally, in crankpin grinding similar material removal rates are used as in normal plunge grinding operations. Nevertheless, the small rotational speed causes a significantly higher feed per rotation. Therefore specific normal forces are approximately twice as high as in outer plunge grinding processes [1, 2, 3, 4].

Deflection of the Crankpin during Grinding

In shaft grinding, the limited stiffness of the part causes a permanent diameter error, which is varying with the part's length and provoked by the deflection due to the grinding forces. This error can easily be corrected by adapting the radial position of the grinding tool according to the deflection line. As Fujiwara et al. [2] showed, the stiffness of a crankshaft is depending on the rotational angle. Additionally, each bearing features a different stiffness depending on the axial position within the shaft (FIGURE 2).

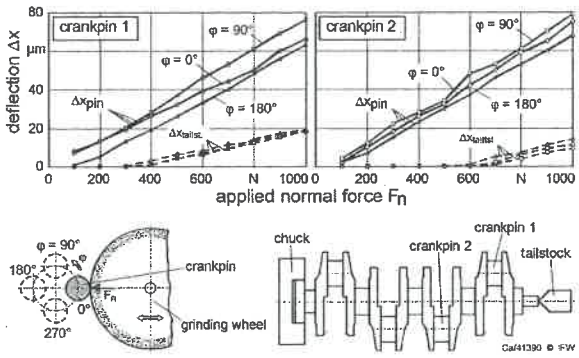

FIGURE 2. Deflection of a force loaded crankshaft during grinding.

This causes a roundness error, which cannot be eliminated by a constant re-positioning of the tool (TABLE 1). The roundness error will be persistent, as long as significant grinding forces are applied, even when the chip thickness is held constant by keeping a constant contact point speed, as Becker and Fujiwara suggested [1, 2].

TABLE 1. Roundness and diameter errors due to grinding forces (assumption: $Q'_w = 16$ mm³/mms; $F_n = 600$ N).

crankpin		angle φ				error	
		0°	90°	180°	270°	diameter	roundness
1	stiffness c [N/μm]	19.3	15.0	23.0	15.0	83 μm	13 μm
	deflection Δx [μm]	39	46	33	46		
2	stiffness c [N/μm]	14.3	12.5	16.7	12.5	87.5 μm	11 μm
	deflection Δx [μm]	42	48	37	48		

Analytical Model of Roundness Generation Mechanism

A process model based on this knowledge implies that there is a persistent roundness error as long as any radial feed or normal grinding force is applied to the crankpin grinding process, whereas an ideal round part is only generated if no force and no feed is present. Therefore the roundness of a part is mainly generated during the spark-out time. The roundness error existing just before the spark-out process is system innate and can be observed even when a perfectly round part was given into the grinding process. Therefore a multi-stage process is necessary, to economically grind crankshafts with a satisfactory geometrical accuracy. In such a process high material removal rates imply higher forces and thus higher roundness errors, which will elongate the necessary spark-out time. In order to minimize the total grinding time, information on the roundness error, its generation and removal behavior have to be known throughout the process. Hence only an in-process measurement system is capable of gaining the needed data to implement an optimized multi-stage process and an adapted spark-out time, depending on part, grinding wheel, cutting parameters and the individual stock allowances and roundness errors.

EXPERIMENTAL EVALUATION

In an experimental approach, a plunge grinding operation was used to simulate crankpin grinding. The goal was to confirm the analytical model and to identify major influences on the roundness generation process in order to develop a monitoring strategy.

Experimental Setup

To simulate and record grinding conditions like in a crankpin grinding process, a steel ring was clamped in a pneumatic chuck of limited stiffness. The used rings feature a radial bore, which causes a changing contact area and simulates the angle depending stiffness of the crankpin. To provoke the needed roundness error of the pre-ground parts metal sheets of different thickness were put into the chuck. The effects of stock allowance and grinding wheel sharpness were investigated by using two allowances and different grinding wheels.

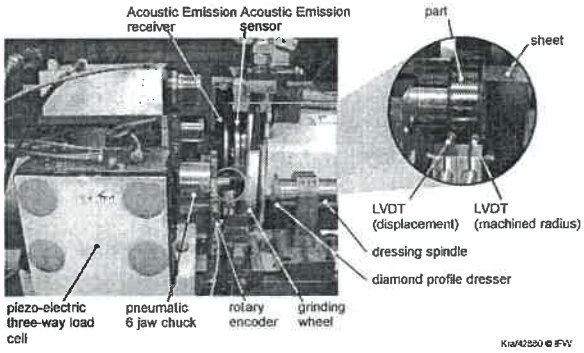

FIGURE 3. Experimental set-up.

Two tactile displacement measurement devices (LVDT: Linear Variable Displacement Transducer) were installed in such a way to detect the current radius of the ground surface as well as the displacement of the part in the unmachined surface. Additionally, the grinding forces were recorded by a three-way piezo-electric load cell. Also RMS Acoustic Emission (AE) signals were recorded by means of a rotating, wireless transmitting sensor placed on the body of the grinding wheel (FIGURE 3). All the data was measured continuously by a single high speed A/D card, so all signals were analyzed using the same time base.

Observations

The data gained in the experiments approves the analytical model. Although the sharpness of the used wheel has a major influence on the generation of round parts, the actual roundness error is not minimized during the feed movement. The in-process measurements reveal that the fluctuations of the forces are constant during the infeed motion. The part diameter itself is lessened during the infeed process, but the roundness error is persistent and only reduced during the spark-out time. This is due to the weak clamping resembling a part of low stiffness. The generation of roundness errors by the grinding process itself was also observed. Varying contact areas cause deviating radii in the area of the bore. This confirms the above described model, which predicts that no round parts can be ground as long as grinding forces are present and a part with an angle-depending stiffness is ground.

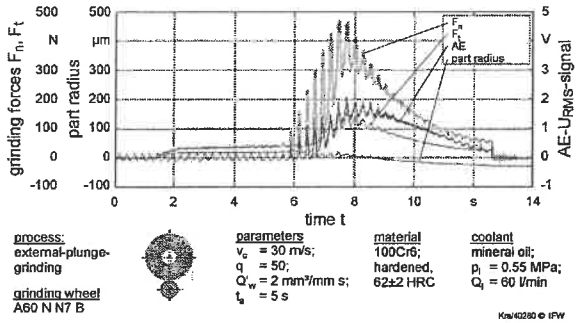

FIGURE 4. Monitoring of roundness generation in grinding by AE, forces and LVDT.

The recorded RMS AE signals correlate to the process. The general amplitude follows the force signal and is therefore corresponding to the current material removal rate [5]. Hence the AE signal is modulated by the roundness error. Thus the AE signal will show such fluctuations as long as a non-round part is identified by the LVDT sensor (FIGURE 4).

Signal Correlation

In order to see whether the AE signal is capable of distinguishing between round and non-round parts, the AE and the LVDT signals were correlated (FIGURE 5). If both signals are processed by a band pass filter and the pass frequencies are chosen alike the rotational frequency of the part, only the signals from the roundness error remain while the influence of the material removal rate in the multi-stage process is eliminated.

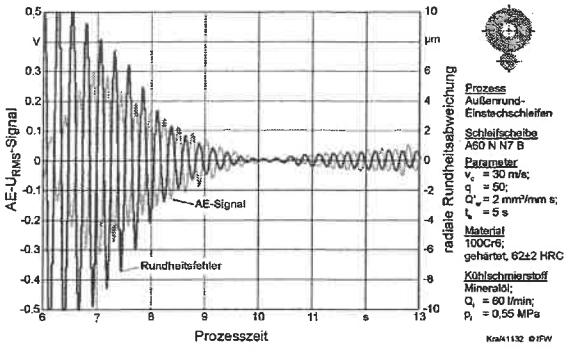

FIGURE 5. Identification of roundness errors in-process by AE RMS signals.

A statistical approach was chosen to identify the main effects on the LVDT and AE roundness signals. The modulation of the envelope curve covering the amplitudes of the two signals during the spark-out time was extracted from the measurements. This data was used to perform an analysis of variance and the main effects were plotted (FIGURE 6).

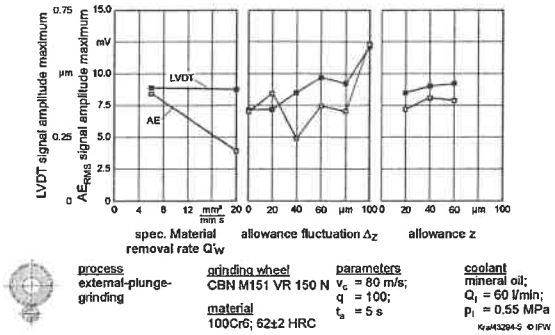

FIGURE 6. Main effects on the in-process measured roundness signals.

The collected data shows that the grinding wheel stiffness and its cutting ability are of great influence regarding the removal behavior of the roundness error. In order to identify the effect of the parameters which can be changed in a multi-stage process design, only all variations within one tested grinding wheel test were chosen as predictors. It can be observed that the stock allowance is of low influence, as the analytical model predicted. The initially provoked roundness error created by the metal sheet inside the chuck is of effect to the persistent roundness error and shows a strong influence for both in-process recorded signals, the LVDT and the AE. Nevertheless, the effect of the specific material removal rate on the two measuring methods is of great difference. While

the LVDT signal is not influenced by the material removal rate, the AE signal is strongly depending on it.

To evaluate if the AE signal can be used to quantify the exact dimension of the roundness error, the maxima of the LVDT and AE signal at the end of spark-out time were correlated within one set of trials, thus eliminating the influence of grinding wheel, allowance and material removal rate (FIGURE 7). The comparison of the quantified modulation of the signals due to the geometrical error of the part reveals that a describing envelope of the signal amplitudes would be of different order. While the tactile geometry information must be in linear correlation with the roundness error, the AE signal is very sensitive even if only small geometrical deviations occur. Nevertheless, this sensitivity decreases and any further increase of the roundness error will only marginally increase the AE signal level (comp. FIGURE 5).

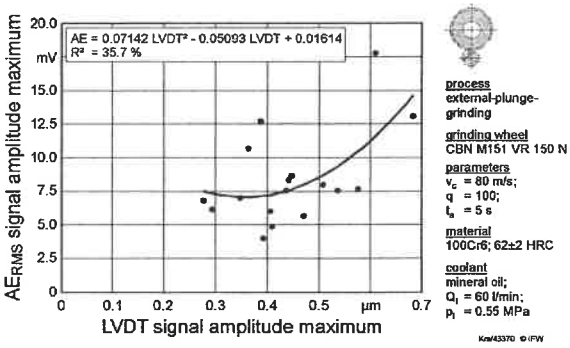

FIGURE 7. Correlation of AE signal with the roundness error dimension.

CONCLUSION

In crankshaft grinding, roundness, especially of the crankpins, is a critical quality parameter. Due to the specific movement of the wheel-head in continuous path controlled grinding processes and the limited, angle-depending stiffness of the crankshaft, the part's roundness can only be created during spark-out time. This behavior was described in an analytical model and proven experimentally.

Detection of non-round parts

The accomplished research proves that in-process measured AE signals are able to distinguish between round and non-round parts. During the spark-out time, the current roundness error of the part shows a huge influence on the AE RMS signal amplitude modulation. As FIGURE 5 shows, the signal is especially sensitive for small errors. Therefore, an adaptive control of the spark-out time by the AE readings is possible.

Determination of the roundness error

In order to implement an adaptive controlled feed motion, which would efficiently generate round parts during a very small number of spark-out revolutions; it is necessary to quantify the roundness error. The statistical evaluation of the main effects and the correlation of the LVDT and AE signals reveals that the AE RMS signal is not proportional to the roundness error (FIGURE 6 and FIGURE 7). Also, the AE signal's magnitude is depending on additional effects, such as the material removal rate or the type of grinding wheel. Therefore, AE signals cannot be used to quantify the actual roundness error, unless the process parameters remain unchanged and the transfer function is determined.

ACKNOWLEDGMENTS

The authors of this work wish to acknowledge the financial support of the German Research Association (DFG) within the project TFB 49 "Qualitymonitoring and –control in grinding of non-round and eccentric parts".

REFERENCES

1. Becker, J.C., 2004, Bahngesteuertes Schleifen von Kurbelwellen (Path-Controlled Grinding of Crankshafts), *Dr.-Ing. Dissertation, Hannover University.*
2. Fujiwara, T.; Tsukamoto, S.; Miyagawa, M., 2005, Analysis of the Grinding Mechanism with Wheel Head Oscillating Type CNC Crankshaft Pin Grinder. *Key Engineering Materials Vols. 291-292 "Advances in Abrasive Technology VIII":* 163-168
3. Czenkusch, C., 1999, Technologische Untersuchungen und Prozessmodelle zum Rundschleifen (Technological Investigations and Process Modells for OD-Grinding), *Dr.-Ing. Dissertation, Hannover University.*
4. Brinksmeier, E., 1991, Prozess- und Werkstückqualität in der Feinbearbeitung (Process- and Partquality in Precision Manufacturing), *Professional Dissertation, Hannover University.*
5. Meyen, H.P., 1991, Acoustic Emission (AE) – Mikroseismik im Schleifprozess (AE in Grinding Processes), *Dr.-Ing. Dissertation, RWTH Aachen.*

TRUEING OF MICRO-GRINDING WHEELS BY DIAMOND TOOLS

Hans-Werner Hoffmeister[1], Marcus Hlavac[1]
[1] **Institute of Machine Tools and Production Technology, Technical University Braunschweig, Germany**

INTRODUCTION

The micro-grinding process with diamond micro-grinding wheels and abrasive pencils enables a fast and high-quality fabrication of microstructures in various hard and brittle materials [1, 2, 3]. When using cubic boron nitride (CBN) as abrasive, even hardened steels can be machined by micro-grinding [1, 4, 5, 6]. Micro-grinding wheels are very suitable for the machining of straight and open structures, but usually they can only fabricate structures with rectangular geometries because of their restriction of profile. The usage of micro-grinding wheels with a special profile, as for example a V-profile, is uncommon. This is due to the fact that micro-grinding wheels with a special profile are difficult to manufacture. Furthermore, the renewing process after the profile has worn is difficult to accomplish. A new approach is the trueing of CBN micro-grinding wheels by diamond tools.

APPROACH

The technology of trueing grinding wheels by rotating diamond tools is highly favoured and well-established in macroscopic grinding technology. Trueing by rotating diamond tools is a reproduced process. The profile of the diamond trueing tools is the negative geometry of the desired grinding wheel profile. By moving the rotating grinding wheel against the also rotating trueing tool, the profile is machined into the peripheral surface of the grinding wheel, because the diamonds of the trueing tool are much harder than the CBN grains and the bonding of the grinding wheel. An easy kinematic, high quality and short processing times make this technology very efficient. Furthermore, this technology allows a periodical renewing of the profile inside the grinding machine. The approach to develop micro-diamond tools in order to realize a trueing pro-cess for CBN micro-grinding wheels is just a consequence of the named technological advantages.

EXPERIMENTAL AND ANALYSIS

Generally, the miniaturizing of approved macroscopic production technologies is not a simple step. The process parameters and the process conditions often have to be optimized according to the requirements of micro dimensions. The aim of this study was to determine all influences on the trueing process and the trueing result. Besides the process parameters, the influence of the specification of the CBN micro-grinding wheels was one of the focuses in this study. CBN micro-grinding wheels are available with different bonding materials. These bonding materials, synthetic resin, bronze and nickel, are characterized by their different mechanical properties. In conventional grinding technology, grinding wheels with metallic bonds are very difficult to true by a mechanical process. In micro-grinding technology especially wheels with metallic bonds are favourable for many applications. So the focus of the endeavours was to develop a technology to true those micro-grinding wheels with metallic bonds.

Another question which had to be answered was how strong the influence of the specification of the chosen micro-diamond tool on the trueing process and the trueing result is. In this study three diamond trueing tools with different specification were tested (figure 1). Two of those tools were miniaturized wheels made of steel with a V-groove of an angle of 90 degrees. Both tools are covered with a single layer of electro-plated diamonds (46 micron and 15 micron). The SEM pictures of the trueing tool with the diamond grains of 46 micron in diameter showed a closed surface. The projection of the diamond grains was large and inhomogeneous as well as the chip space. Compared to this tool the surface of the trueing tool with the diamond grains of 15 micron in diameter seemed to be quite smooth. The projection of the diamond grains was small and also inhomogeneous.
A complete different type of tool were specially developed CVD-diamond trueing tools. The technology of CVD-diamond coats enables to be free in the design of tools and the thin coat covers very precisely the form of the tool body. Furthermore, the rough surface structure of this special diamond coat enables the machining of hard materials. In contrast to electro-plated diamond tools this synthetic diamond coat is characterised by a high homogeneous crystal structure and grain projection [7].

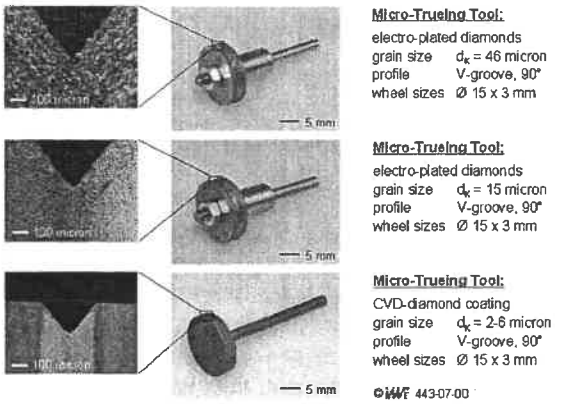

FIGURE 1: Micro-diamond tools for trueing CBN micro-grinding wheels.

For the experiments, a second spindle system for the trueing tools was integrated into the micro-grinding machine (figure 2). This spindle has a maximum rotation of 160,000 min^{-1}. Such high rotations were required because of the small diameter of the trueing tools (about 15 mm) and the high rim speed of the trueing tools which varied between 12 m/s and 72 m/s during the experiments. By this set-up, trueing and grinding experiments could be realized with high accuracy because no tool change was necessary.

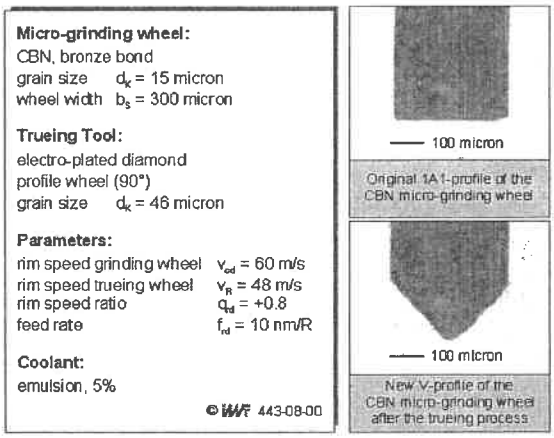
Micro-grinding wheel:
CBN, bronze bond
grain size d_k = 15 micron
wheel width b_s = 300 micron
Trueing Tool:
electro-plated diamond
profile wheel (90°)
grain size d_k = 46 micron
Parameters:
rim speed grinding wheel v_{cd} = 60 m/s
rim speed trueing wheel v_R = 48 m/s
rim speed ratio q_d = +0.8
feed rate f_{rd} = 10 nm/R
Coolant:
emulsion, 5%
©IWF 443-08-00
100 micron
Original 1A1-profile of the CBN micro-grinding wheel
100 micron
New V-profile of the CBN micro-grinding wheel after the trueing process

FIGURE 2: Experimental set-up for trueing CBN micro-grinding wheels with diamond tools inside the precision tool machine.

After each trueing process the machining result was controlled by grinding a groove into a small steel sheet with a thickness of just 40 micron with the trued CBN micro-grinding wheel. The geometry of this groove was analysed by optical measurement. The quality of the trueing result was characterised by the accuracy of the profile angle, the accuracy of the profile geometry and the radius of the micro-grinding wheel tip.

EXPERIMENTAL RESULTS

The first experiments were done with the CVD-diamond trueing tool. When using this trueing tool, all kind of CBN micro-grinding wheels could be trued. The quality of the created profile flanks was sufficient, and so was the performance of this tool. In contrast to the electro-plated trueing tools made of tool steel, the body of the CVD-diamond tool made of sintered carbide is very heavy. High rotation speeds (about more than 30,000 min^{-1}) could not be realized because of increasing dynamic forces and the incresing danger of a tool break. Another disadvantage is the difficult fabrication of the bodies for this kind of trueing tools because of the low machining ability of sintered carbide. During the fabrication of these tool bodies, the used grinding tools were affected by strong wear, so the realized profile of the trueing tool was not sufficient. This fact could be seen when using this CVD-diamond tool. The tip radius was about r_s = 115 micron.

In order to obtain an optimized trueing tool, the CVD-diamond tools were further developed. Instead of heavy sintered carbide, light silicon was chosen for the fabrication of the tool body. With a newly designed prototype of a CVD-diamond trueing tool very high rotation speeds could be realized. Also the quality of the profile geometry could be increased and the tip radius was reduced down to 40 micron. With this new prototype tool, the experiments were continued and the trueing possibilities of all three kinds of micro-grinding wheel bonding material were tested. The grain size of the used micro-grinding wheels was about 15 micron and the width of the grinding wheels was 100 micron. In the experiments the rim speed of the micro-grinding wheels was v_{sd} = 60 m/s and the rim speed of the diamond trueing tool was v_{rd} = 48 m/s, so the rim speed ratio was q_{rd} = +0.8. As coolant an emulsion of 5% was used. In order to obtain the machining efficiency of the CVD-diamond trueing tools and the trueing process, the feed rate was increased stepwise beginning from 1 nm per revolution.
The highest material removal rates were determined when trueing the micro-grinding wheel with the resin bond. The soft bonding material enabled feed rates up to f_{rd} = 0.1 micron per revolution. At a feed rate of f_{rd} = 0.2 micron per revolution the filigree micro-grinding wheel was damaged. Disruptions on the micro-grinding wheel were determined which point to high process forces and a too aggressive cutting process. Consequently, when trueing this kind of

CBN micro-grinding wheels the feed rate should be smaller than 0.1 micron per revolution. However, when grinding a control groove into the thin steel sheet no distinctive profile could be identified. After the trueing process a machined profile could be seen under microscope, but this profile of the 100 micron thick resin bonded micro-grinding wheel was very unstable, so that the newly created profile wears even under the low forces of the control grinding operation. Consequently, small CBN micro-grinding wheels made of a resin bond seemed not to be suitable for trueing and structuring. In contrast to this, micro-grinding wheels with metallic bonds seemed to be very expedient. When trueing these tools the quality of the profile was high, but the hardness of these bondings allowed only a slow trueing process with feed rates of just a few nanometers per revolution. Increasing the feed rate up to 10 nanometers per revolution or more, the thin micro-grinding wheels or the CVD-diamond trueing tool was damaged.

When using the electro-plated trueing tool with the large diamond grain size of 46 micron, micro-grinding wheels with a resin and a bronze bonding as well as a wheel width of 300 micron down to 100 micron could be trued well. The rough surface topography of this diamond trueing tool showed an efficient machining performance. High material removal rates and feed rates up to 0.1 micron per revolution could be realized. But the large diamond grains and the inhomogeneous grain projection created profile flanks with a low quality (figure 3). Furthermore, the possible minimal tip radius was also limited to r_s = 35 micron because of the surface structure of this trueing tool. CBN micro-grinding wheels with a nickel bond could not be machined well with this diamond tool. Damages, as cracks and disruptions of material, could be noticed when machining this kind of micro-grinding wheels. The cutting process of this trueing tool with its large diamonds was too aggressive and inhomogeneous for this very hard metallic bonding material.

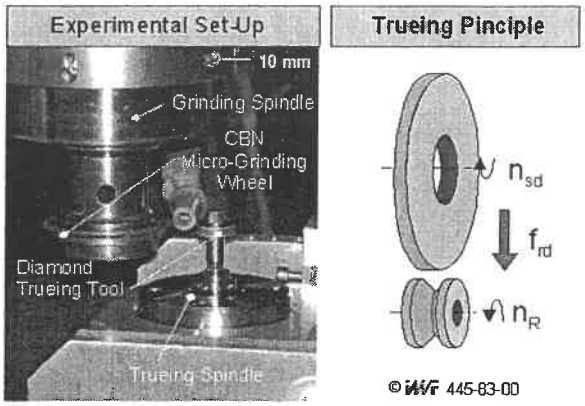

FIGURE 3: Trueing of a CBN micro-grinding wheel by an electro-plated diamond trueing tool with grain size of 46 micron

When using the electro-plated trueing tool with the smaller diamond grain size of only 15 micron CBN micro-grinding wheels with a resin bonding could be trued well. In contrast to that, the bronze bonding caused a closing of the small chip removal space. Furthermore, the inhomogeneous cutting process, because of the also inhomogeneous surface topography of this trueing tool, was again not suitable for the machining of CBN micro-grinding wheels with a hard nickel bond. Consequently, the application of this trueing tool specification was quite limited.

Generally, analysing the CBN micro-grinding wheels by SEM-pictures after all trueing processes, a quite smooth surface topography could be seen. As a consequence of that, the projection of the abrasive grains was extremly small, because the CBN grains were also cut as the soft bond material. This means that after the trueing process the CBN micro-grinding wheels are not really ready for an efficient machining process. Especially for those micro-grinding wheels with a metallic bonding a following sharpening process will be neccessary.

SUMMARY AND OUTLOOK

Micro-grinding with CBN tools is a very favourable method for microstructuring of hardened steels. Micro-grinding wheels with different profiles increase the structuring possibilities. Trueing of grinding wheels with rotating diamond tools is well known in conventional grinding technology. By the approach to miniaturize this special trueing technology, the fabrication of new profile geometries on CBN micro-grinding wheels as well as the renewing of those profiles could also be achieved now. The identified advantages of this new micro-technology are the

easy and precise trueing process, which smoothly produces a symmetric profile on the filigree CBN micro-grinding wheels with a minimum width of just 100 micron. Furthermore, this technology is characterized by high precision and high efficiency because the micro-trueing device is directly integrated into the micro-grinding machine. That means that no accuracy failures occur because of a tool change of the micro-grinding wheel between grinding and trueing operation. As a consequence of that the run of the micro-grinding wheels is extremely good.

Different specifications for diamond trueing tools were tested in this study. The best results could be obtained when machining with a CVD-diamond trueing tool because of its homogeneous surface topography. Electro-plated diamond trueing tools sometimes enabled a fast trueing process, but the inhomogeneous projection of the diamond grains caused a lower machining quality. The used micro-grinding wheels with three different bonding materials could be machined with quite different effects. Best machinability was determined for resin bonded micro-grinding wheels, but this kind of tools were also subject to a strong wear, so that the application of these trued micro-grinding wheels was not very favourable. In contrast to that, metallic bonded micro-grinding wheels were difficult to machine. A bronze bond often caused a close of the chip space of the fine-grained diamond trueing tools. Nickel bonded micro-grinding wheels had to be trued very slowly because the hard material of these tools reacted quite brittle when machining too strong. However, these hard micro-grinding wheels showed the best trueing results and performance. Generally, all CBN micro-grinding wheels had an insufficient projection of the abrasive grains after the trueing process. Consequently, a sharpening operation will be neccessary after trueing these grinding tools.

Within further studies optimized CVD-diamond trueing tools made of silicon bodies will be tested. These tools are characterized by profiles with a very small radius and different angles. Furthermore, the fabrication of complex profiles onto the CBN micro-grinding wheels as well as the performance of trued CBN micro-grinding wheels will be the focus of further studies.

ACKNOWLEDGEMENT

- This work is sponsored by the Deutsche Forschungsgemeinschaft DFG ("German Research Foundation").

REFERENCES

1. Weck, M. (ed.): *Mikromechanische Produktionstechnik.* Abschlusskolloquium DFG Schwerpunktprogramm 1012, Aachen, 21. Mai 2003, Shaker Verlag, Aachen.
2. Hesselbach, J. (ed.): *mikroPRO – Untersuchung zum internationalen Stand der Mikro-produktionstechnik.* Vulkan Verlag, Essen, 2002.
3. Wenda, A.: *Schleifen von Mikrostrukturen in sprödharten Werkstoffen.* Dissertation Technische Universität Braunschweig, Vulkan Verlag, Essen, 2002.
4. Hoffmeister, H.-W.; Hlavac, M.: *Grinding of Microstructures in Hardened Steel with CBN Tools.* Proceedings of the **euspen** International Topical Conference, Aachen, Germany, May 19th/20th 2003, pp. 337-340.
5. Hoffmeister, H.-W.; Hlavac, M.: *Dressing of Micro-Grinding Wheels.* Proceedings of the **euspen** International Conference, Glasgow, Scottland, May 31st-June 2nd 2004, pp. 135-136.
6. Hesselbach, J.; Hoffmeister, H.-W.; Hlavac, M.: *Micro-Grinding – Efficient Technique for Micro-Structuring Hardened Steels.* WGP - Production Engineering, Vol. XII/1, 2005, pp. 1-4.
7. Gäbler, J.; Schäfer, L.; Hoffmeister, H.-W.; Wenda, A.: *Development and application of CVD Diamond Micro Tools for Milling and Grinding.* Proceedings of the 1st **euspen** International Conference, Bremen, Germany, May 31st–June 4th 1999, pp. 434-437.

HIGH PERFORMANCE GRINDING WHEELS WITH BORON DOPED DIAMOND GRITS ENABLING ELECTRICAL CONDUCTIVITY AND HIGH THERMAL STABILITY ON CUTTING EDGES

Manabu Iwai[1], Kiyotaka Nakagawa[1], Sadao Sano[2], Katsutoshi Tanaka[3], Tetsutaro Uematsu[1], Wang Mei[4], and Kiyoshi Suzuki[5]

[1]Toyama Prefectural University, Imizu, Toyama, Japan
[2]Sodick Co. Ltd., Yokohama, Kanagawa, Japan
[3]Toshiba Machine Co., Ltd., Numazu, Shizuoka, Japan
[4]OSG Co., Ltd., Toyokawa, Aichi, Japan
[5]Nippon Institute of Technology, Miyashiro, Saitama, Japan

INTRODUCTION

The authors have proposed the development of an "electrically conductive (EC) cutting edge diamond wheel" utilizing the electrically conductive CVD diamond thick film or electrically conductive diamond grits as shown in Fig.1 [1~3]. In the case of diamond grinding wheels utilizing conventional diamond grits, it is impossible to shape the tip of the diamond grits. However, in the case of the electrically conductive diamond grits wheel, it was shown that the tip of the diamond grits can be shaped by using electrical discharge machining (EDM), and therefore, it is possible to perform grinding using these shaped diamond grits. Furthermore, as the boron doped diamond grits possess higher oxidation temperature, this is thought to be advantageous with respect to removal machining. From the results of experiment conducted on grinding of optical glass, it is found that in the case of the boron doped diamond grits wheel there is a large reduction in the wear of the grinding wheel compared to a conventional grinding wheel [4,5].

In this research work, metal and resin bonded diamond wheels, containing boron doped electrically conductive diamond grits are trial manufactured. The electrodischarge truing (ED truing) performance along with the grinding performance of these diamond wheels on difficult-to-grind materials are investigated and compared with the conventional diamond grits wheel.

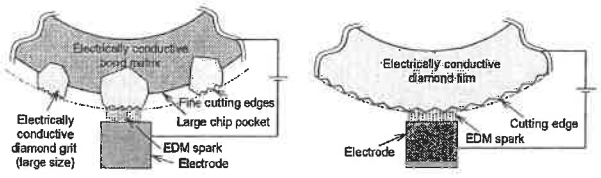

(a) Electrically conductive diamond grits wheel *(b) Electrically conductive diamond layer wheel*

FIGURE 1. Formation of cutting edges on electrically conductive diamond wheels by ED trueing/dressing.

BORON DOPED DIAMOND GRITS WHEEL

Boron doped electrically conductive diamond grits (BDD-S, grain size: 120/140 US mesh) were trial manufactured by a special technique. Although the boron doped diamond grits are not particularly good in crystal morphology, they are approximately equivalent to the conventional diamond grits in terms of impact strength. Moreover, the oxidation resistance of the boron doped diamond grit is superior to that of the conventional diamond grits by about 200K. A higher oxidation temperature means that the diamond cutting edge can resist the temperature rise occurring during grinding operation. Due to this, it is expected that the boron doped diamond grits will show an excellent grinding performance in the grinding of difficult-to-grind materials and even ferrous materials in the case of which the rise in the temperature induces wheel wear. Although the specific resistance of these trial manufactured diamond grits has not been measured, the diamond grits are expected to possess a value of specific resistance of the order of $0.4\sim1\times10^{-3}\Omega\cdot m$ similar to the commercially available electrically conductive CVD diamond thick film (CVDITE-CDE), which is sufficient for successfully forming the diamond grits by ED truing.

In this research work, metal bonded and resin bonded diamond grinding wheels ($\phi100\times t5mm$) utilizing boron-doped diamond grits were manufactured for grinding test. For comparison a conventional diamond-grinding wheel having similar friability was used. The condition of the wheel surfaces is shown in Fig.2, and the experimental conditions are shown in Table 1.

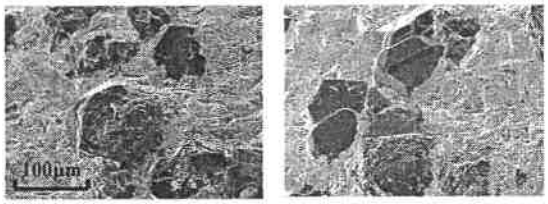

(a) Normal diamond grits wheel (b) Boron doped diamond grits wheel

FIGURE 2. Comparison of metal bonded wheel surfaces with different diamond grits after truing using a vertical type truer with conventional GC wheel.

ED TRUING PERFORMANCES OF BORON DOPED DIAMOND GRITS WHEEL

ED Truing Performances

As shown in Fig.3(a), ED truing of the bottom surface of the boron doped diamond wheel was performed using a copper block of 5mm in thickness, and the removal efficiency (removal rate) was investigated. The EDM area used was 25mm^2. The EDM conditions used were, electrode [+], no load voltage u_i=60V, pulse t_e/t_o=50/50μs and set peak current i_P=3~15A. Oil was used as the dielectric and the EDM time was set to 10min. The experimental result along with a comparison with the non conductive normal diamond grits wheel is shown in Fig.3(b). The removal efficiency of the boron doped diamond grits wheel is 3~4 times higher than the normal diamond grits wheel. This is thought to be because of the fact that, in the case of the boron doped diamond grits wheel, the EDM of both the diamond grits as well as the bond material takes place.

ED Truing of Abrasive Tip and its Grinding Properties

The ED truing of the tip of boron doped diamond grits was carried out on a surface grinder using water soluble grinding fluid as the medium. The grinding properties of the grinding wheel with the abrasive tip flattened by the on-machine ED truing were investigated.

ED truing of the abrasive tip

As shown in Fig.4, a rotating copper disc electrode (ϕ55×*t*1mm) was set perpendicular to the grinding wheel and truing was performed by traversing the copper disc electrode in a direction parallel to the rotation axis of the grinding wheel. Truing was performed for 30 minutes using the discharge conditions of u_i=90V, i_P=3A, t_e/t_o=8/10μs. The effect of the

TABLE 1. Experimental devices and conditions.

Machine	· Die sinking EDM machine (AQ35R, Sodick) · NC surface grinder (NSP-50, Nachi) + EDM power source (SUE-87, Sodick)
Grinding wheel	Straight type wheel, ϕ30×t3, ϕ100×t5mm · Boron doped electrically conductive diamond grits wheel: SDE120Q80M · Normal diamond grits wheel: SD120Q80M
Working fluid	Oil (Vitol 2, Sodick) Grinding fluid (Synthetic, Syntilo GX, 2%, BP)
Truing / dressing	· Mechanical truing: Vertical type truer (GC) · Electrodischarge (ED) truing: Copper electrode (Block, Disc (ϕ55×t1mm)) u_i=60, 90V, i_e=3~15A, t_e/t_o=8/10, 50/50μs
Work piece	Cemented carbide (WC, HV1350) Die steel (SKD11$_{JIS}$, HRC63) Optical glass (BK7), *l*=100mm
Grinding condition	V_S=26m/s, V_W=5m/min, *a*=2~40μm, *b*=3mm Surface plunge grinding, Coolant flow rate: 6 L/min

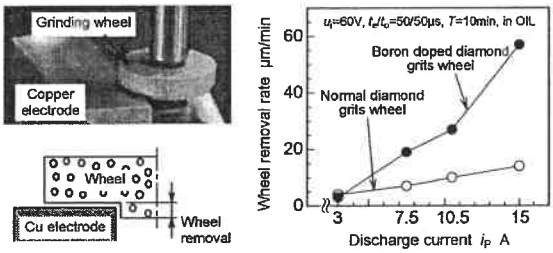

(a) Experimental setup of ED truing (b) Wheel removal rate by ED truing

FIGURE 3. Comparison of wheel removal rate by ED truing between normal diamond grits wheel and boron doped diamond grits wheel (in oil).

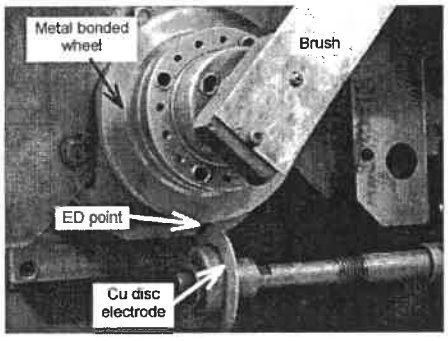

FIGURE 4. Setup of on-machine ED truing.

wheel polarity was initially investigated. As shown in Fig.5(a) and (b), in the case of the grinding wheel [+], EDM marks are not observed on the bond surface, but the EDM appears to have taken place on all the abrasive tips. On the other hand, in the case of the grinding wheel [-], no change in the abrasive tip due to EDM is

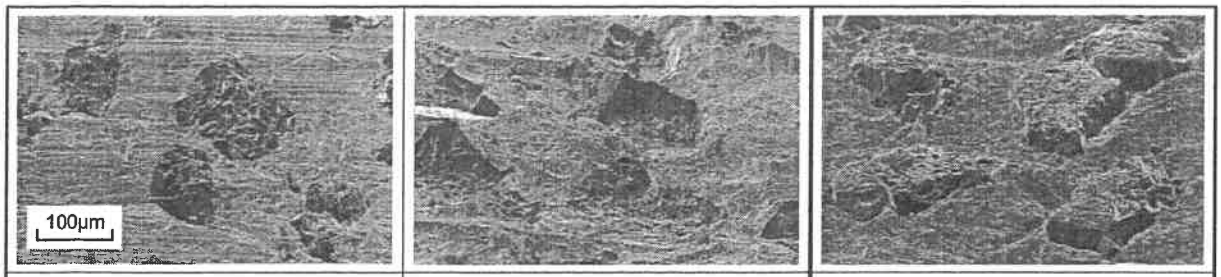

(a) Polarity: Wheel [+] (t_e/t_o=8/10μs, 30mins)	(b) Polarity: Wheel [-] (t_e/t_o=8/10μs, 30mins)	(c) Polarity: Wheel [+] (t_e/t_o=4/10μs, 3hrs)

FIGURE 5. Change of the tip of boron doped diamond abrasive by ED truing
(Metal bonded boron doped diamond grits wheel, ED conditions: u_i=90V, i_p=3A)

observed. Moreover, at the short pulse condition (t_e=4μs), though the efficiency of EDM of the abrasive is low, flattening of the abrasive tips can be achieved after performing EDM for 3 hours as shown in Fig.5(c).

The effect of the flattened abrasives on grinding ability

Using the flattened abrasive tips shown in Fig.5(a), the grinding ability of the grinding wheel was investigated. Grinding of 50 passes on optical glass and cemented carbide (l=20mm) were performed under the conditions of V_S=26m/min, V_W=5m/min, a=2μm, b=3mm.
Grinding was also performed using a grinding wheel trued using a vertical type rotary truer with a GC wheel and a comparison of the results is shown in Fig.6. The grinding resistance in the case of the grinding wheel with the flattened abrasive tips was 3 times higher for any of the work materials, but the workpiece surface roughness improved by 70%.

GRINDING PROPERTIES FOR VARIOUS WORK MATERIALS

The grinding ability of the boron doped diamond abrasive wheel was investigated by grinding cemented carbide, die steel and optical glass (l=100mm) for a long time. The truing and dressing of the grinding wheel was performed using a vertical type rotary truer with a GC wheel. Grinding conditions used were V_S=26m/s, V_W=5m/min, a=2~40μm and b=3mm. For the various work materials, normal grinding force at the end of grinding, grinding ratio except for the initial grinding period, and the workpiece surface roughness are shown in Figs.7~9.

(1) Cemented carbide (Fig.7): For the resin bonded as well as the metal bonded boron doped diamond grits wheels the grinding ratio is

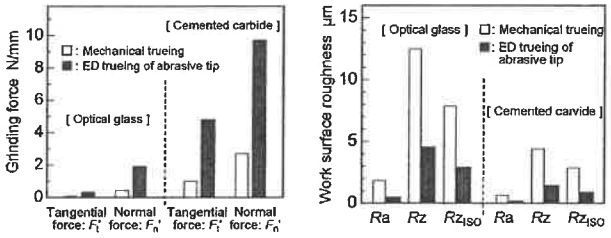

(a) Grinding force *(b) Work surface roughness*

FIGURE 6. Grinding performances of boron doped diamond grits wheel with abrasive tips flattened using ED truing (V_S=26m/s, V_W=5m/min, a=2μm, b=3mm, 50pass)

20~30% higher compared to the normal diamond grits wheel. Although no difference in the grinding resistance is observed, the surface roughness for the grinding depth a=2μm improved by 30%.

(2) Die steel (Fig.8): In the case of the resin bonded grinding wheel, experiments were performed for varying the grinding depth. Although no change in the grinding ratio or grinding resistance is observed, for the grinding depth a=2μm and 10μm, the workpiece surface roughness using the boron doped diamond grits wheel showed a slight (5% and 15%) improvement.

(3) Optical glass (Fig.9): The results using a resin bonded wheel at a grinding depth of a=40μm is shown. The grinding ratio increases by about 70% and the grinding resistance is reduced by 30%. A 20% improvement in the workpiece surface roughness can be observed.

CONCLUSION

The ED truing properties of the boron doped electrically conductive diamond grits wheel as

well as its grinding properties were investigated. The results can be concluded as below.

1. Due to the ability of EDM removal on the boron doped diamond grits in oil, the ED truing efficiency of the boron doped diamond grits wheel is 3~4 times higher than the normal diamond grits wheel.
2. The flattening of the tip of the diamond grits could be achieved on a surface grinder using a water-soluble grinding fluid by keeping the polarity of the grinding wheel [+]. Although the grinding resistance using this grinding wheel was higher compared to a grinding wheel trued using a mechanical truing method, the workpiece surface roughness was 70% better.
3. From the results of the grinding test for a long period of time, with respect to the cemented carbide and optical glass workpieces there was a marked improvement in the grinding ratio in the case of the boron doped diamond grits wheel.

ACKNOWLEDGMENTS

The authors would like to express their cordial gratitude to Element Six Ltd. for their kind cooperation in this research.

REFERENCES

1. Suzuki K., Iwai M., Uematsu T. et al., 2003, Application of electrically conductive diamond to removing processing (3rd report), *Proc. of JSAT conf., ABTEC2003*, 171. (in Japanese).
2. Suzuki K., Iwai M., Uematsu T. et al., 2003, Development of a Grinding Wheel with Electrically Conductive Diamond Cutting Edges, *Advances in Abrasive Technology VI, Key Engineering Materials (Trans Tech Publications)*, 257-258: 239.
3. Suzuki K., Iwai M., Uematsu T. et al., 2005, Development of diamond grinding wheel having electrically conductive diamond cutting edges (1st report), *Journal of JSAT*, 49-6: 347. (in Japanese)
4. Suzuki K., Iwai M., Uematsu T. et al., 2004, Development of an electrically conductive diamond grits wheel, *Proc. of JSAT conf., ABTEC2004*, 487. (in Japanese)
5. Suzuki K., Iwai M., Uematsu T. et al., 2005, A new diamond wheel containing boron doped diamond abrasives enabling electrically conductive cutting edge and high thermal stability, Advances in Abrasive Technology VIII, Key Engineering Materials (Trans Tech Publications), 291-292: 57.

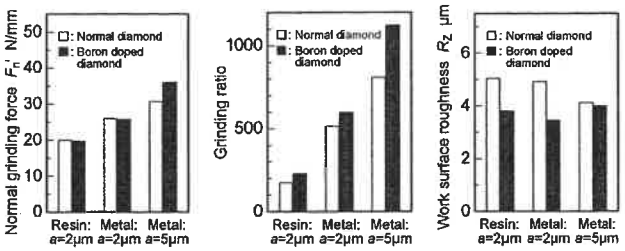

(a) Normal grinding force *(b) Grinding ratio* *(b) Work surface roughness*

FIGURE 7. Grinding properties for cemented carbide using various diamond wheels
(V_S=26m/s, V_W=5m/min, b=3mm, a=2,5μm, Q'=2800,3000mm^3/mm)

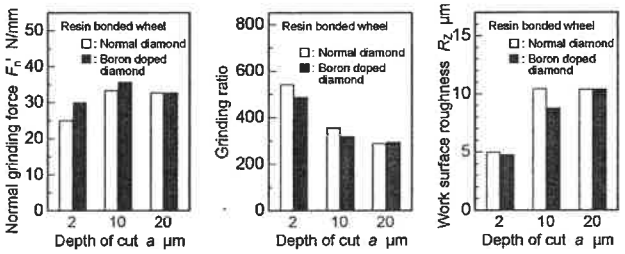

(a) Normal grinding force *(b) Grinding ratio* *(b) Work surface roughness*

FIGURE 8. Grinding properties for die steel ($SKD11_{JIS}$) using various resin bonded diamond wheels
(V_S=26m/s, V_W=5m/min, b=3mm, a=2,10,20μm: Q'=1800,5000, 4600mm^3/mm)

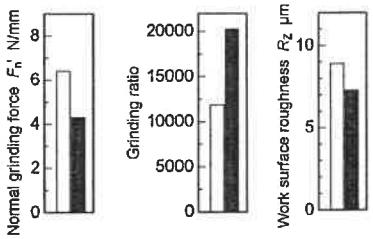

(a) Grinding force *(b) Grinding ratio* *(c) Surface roughness*

FIGURE 9. Grinding properties for optical glass (BK7) using various resin bonded wheels
(V_S=26m/s, V_W=5m/min, b=3mm, a=40μm: Q'=28000mm^3/mm)

STUDY ON MICRO MACHINING OF LITHIUM NIOBATE USING SINGLE ABRASIVE GRINDING

R. Kurihara[1], M. Nakamura[2], M. Yoshida[1], and T. Sumomogi[2]
[1]Graduate School of Engineering Hiroshima Kokusai Gakuin University,
Nakano 6-20-1, Aki-ku, Hiroshima, Japan
[2]Faculty of Engineering, Hiroshima Kokusai Gakuin University,
Nakano 6-20-1, Aki-ku, Hiroshima, Japan

1. INTRODUCTION

With improvements in many precise instruments, the necessity of high quality surfaces for optical devices or memory devices has been of major concern nowadays. Examples of materials that have been adopted for such optical devices or memory devices are KDP, glass, and silicon. Of these, silicon has been widely applied to the field and studied for finish machining for many years [1]. Llithium niobate ($LiNbO_3$) has been used with excellent optical and electrical characteristics in a wide range of the optical fields in recent years. In addition, lithium niobate has been studied as the material for holographic data storage (HDS) [2].

In order to obtain those high quality surfaces, new methods for finish machining of brittle materials, the nano-scale machining by ultra precision grinding and cutting, known as ductile mode machining, need to be considered. The machining of silicon and glass, using single abrasive grinding, has been studied by T. Sumomogi and M. Nakamura [3, 4], and obtained no cracks surfaces by a very small depth of cut. Furthermore, it has been discovered that subsurface cracks occur before surface cracks are observed. In this study, lithium niobate with (0001) plane was focused on the propagation of surface cracks with some experimental conditions.

2. EXPERIMENTAL DETAILS

2.1 Lithium niobate

The workpiece material employed in the present experiment is single-crystal lithium niobate with (0001) plane. Table 1 shows the properties of lithium niobate [5].

Table 1 Properties of Lithium Niobate [5].

Lattice parameters (Å)	Melting point (℃)	Density (g/mm^3)	Thermal conductivity (W/mK)
a= 5.15 c=13.86	1250	4.655	4.2

Concerning the crystal orientation of lithium niobate, it is reported that the material has a trigonal structure, which is sectioned by 120° with the cleavage plane $\{10\bar{1}2\}$. Figure 1(a) and (b) show the crystal orientation of lithium naiobate used as one of the experimental conditions.

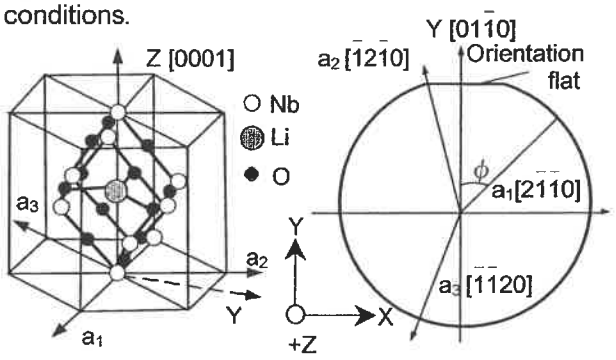

(a) Crystal structure of lithium niobate (b) Crystal orientation of lithium niobate

Fig. 1 The crystal structure and orientation of lithium niobate.

2.2 Hardness test

A microhardness tester is used for hardness measurements and observing the propagation of cracks occurred. The tip adopted for the indentation is a Vickers diamond indenter with an apex angle of 136 degrees. The indentation loads are used in the range, 0.25N and 0.5N, and the indentation speed is 30 μ m/s. The indentation is performed from 5 to 7 times for each load, and observed by a scanning laser microscope (SLM).

2.3 Nanoindentation test

In order to investigate the crack behaviors and also mechanical properties of lithium niobate in detail, the nano-scale test is executed. The instrument is Hysitron Triboscope system attached to a scanning probe microscope (SPM). The triangular pyramid with an apex angle of 90 degrees has tip radius of 40nm. Figure 2 shows

the indentation load-penetration depth curves for indentation, and Young's modulus and hardness can be obtained from this curve [6].

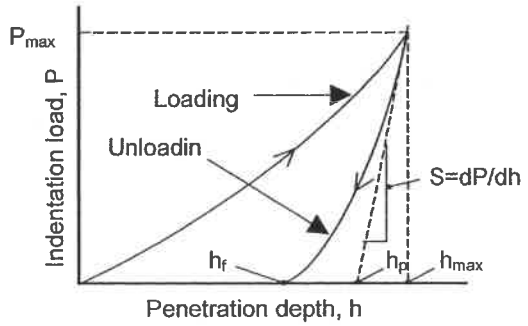

Fig. 2 Indentation load vs. penetration depth curve for nanoindentation.

2.4 Grinding test

A Vickers diamond pyramid indenter with an apex angle of 136 degrees is used as the grinding tool. The ultra precision turning machine consists of an aerostatic bearing spindle for workpiece revolution and a roller bearing slide for tool feed. Face-turning of the workpiece is carried out from the center to the outside with the fixed feed rate of 30 μ m/rev. Grinding speed, relative speed of the tool and the workpiece, is from 17 to 1700m/min. The workpiece is mounted on a vacuum chuck. A partial inclination is given to the mounted workpiece by a partly inserted spacer between the workpiece and the vacuum chuck surface. Machining the inclined workpiece generates various depths of grooves, as shown in Fig. 3. Table 2 shows the experimental conditions. The angle ϕ is determined clockwisely from the orientation flat to the machined position, as shown in Fig. 1(b).

SPM is used to measure the depth of grooves and the surface crack ratio of each groove. This is the ratio of the total length of surface cracks generated along a groove to the length of the groove in the observation area on the scanning force microscope, as shown in Fig. 4.

Table 2 The experimental conditions for the grinding test in lithium niobate.

Workpiece	Lithium niobate with z-axis (0001) surface 76-mm (3 in.) wafer
Tool	Vickers diamond indenter
Grinding speed	17 to 1700 m/min
Feed rate	30 μ m/rev
Grinding direction	ϕ =0° , 30° , 60° <01$\bar{1}$0> and <$\bar{1}$2$\bar{1}$0>

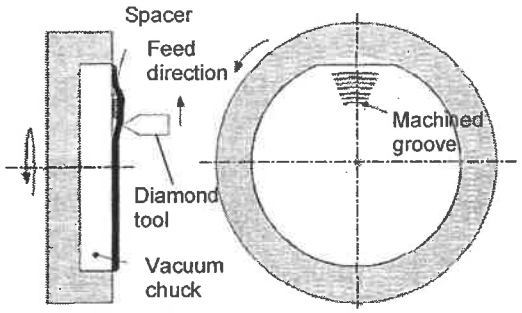

Fig. 3 Schematic of the machining of the main part.

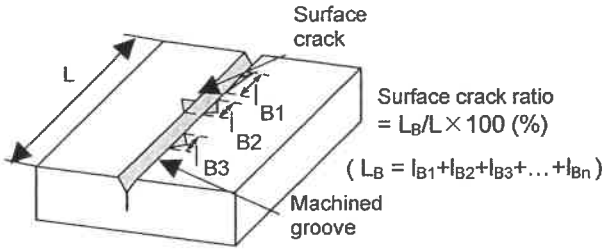

Fig. 4 Observations of the surface cracks.

3. RESULTS AND DISCUSSION

3.1 Hardness test

The characteristics of the fracture depended on the crystallographic directions are studied by the hardness test with a load of 0.5N. The results show that a large number of cracks occur to the cleavage direction <$\bar{1}$2$\bar{1}$0>, as shown in Fig. 5(a). Figure 6 shows the number of cracks generated in each crystal orientation, <$\bar{1}$2$\bar{1}$0> and <01$\bar{1}$0> with a load of 0.5N. It is showed that the cleavage directions <$\bar{1}$2$\bar{1}$0> have the large number of cracks estimated from the apexes of indented mark where the maximum stresses are generated, as shown in Fig. 6.

Compared to the surface of single-crystal silicon tested by the hardness test, it can be seen that lithium niobate seems to be more fragile material than silicon due to many chipping occurred under the same conditions, as shown in Fig. 5.

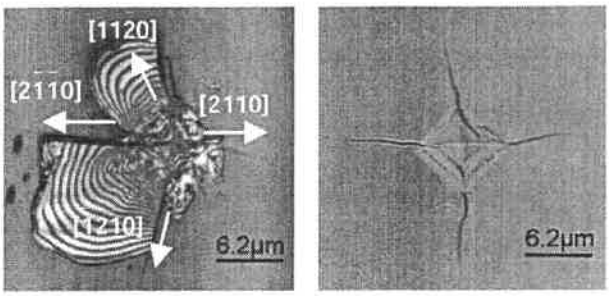

(a) Lithium niobate (b) Silicon

Fig. 5 Indented surfaces with a load of 0.5N.

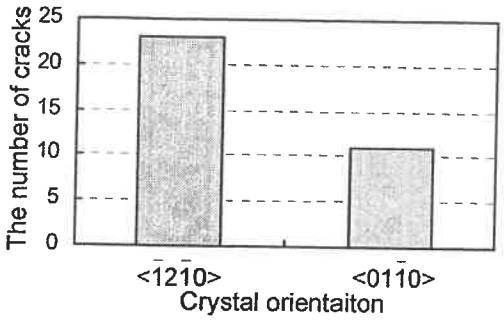

Fig. 6 The number of cracks generated in each crystal orientation, <01$\bar{1}$0> and <$\bar{1}\bar{2}$10>, with a load of 0.5N.

3.2 Nanoindentation test

Figure 7 reveals the difference between the indentation load-penetration depth curves for indentation by Triboscope, in which the indentation load is 500 μ N. Generally speaking, Knoop hardness (kg/mm^2) is 610 for BK7, 1150 for silicon [7], and 570 for lithium niobate [8], respectively. Results of nanoindentation, however, showed the different results. Lithium niobate is the hardest material in the three under the nanoindentation test. The reason is being considered that the hardness test is indented in micro-meter scale although the nanoindentation test is indented in nano-meter scale.

Figure 8 shows the results of the test for the crystallographic dependence. As mentioned above, the hardness test has shown that lithium niobate and silicon produce their crystallographic dependence. However, the results as presented in Fig. 8 show similar curves, which means that the crystallographic dependence is not observed.

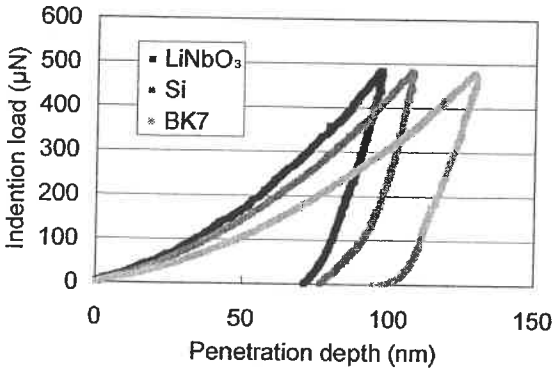

Fig. 7 The indentation load-penetration depth curves for indentation in each material.

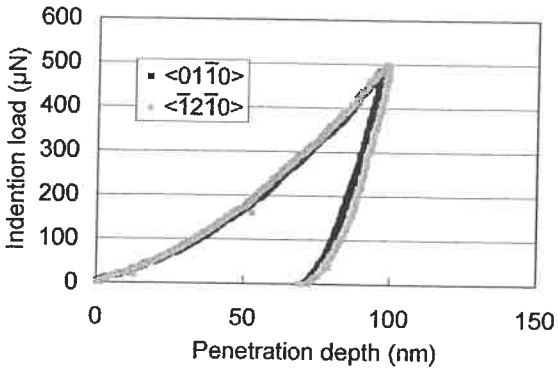

Fig. 8 The crystallographic dependence by the nanoindentation test in lithium niobate with a load of 500 μ N.

3.3 Grinding test

Figure 9 shows an image of the surface of lithium niobate by an optical microscope and SPM. It is discovered that the surface cracks in a grove of depth 27.3nm are not observed, which suggests the surface remains crack-free during machining. Figure 10 shows the crystallographic dependence of surface crack ratio as a function of groove depth for grooves machined at a grinding speed of 80m/min. Bellow depth of approximately 40nm, crack-free machining seems to be accomplished in both directions. When the depth of the grooves becomes deeper, the surface crack ratio increases gradually. Arrows in the figure show the points at which the surface crack ratio reaches 100%.

Compared to the crystallographic directions, <01$\bar{1}$0> and <$\bar{1}\bar{2}$10>, the depth of the grooves in <$\bar{1}\bar{2}$10> direction reached large-scale fractures, approximately 160nm, is shallower than that of <01$\bar{1}$0>, approximately 260nm. It is expected that the reason is crystallographic dependence as mentioned above. However, at a grinding speed of 1700m/min shown in Fig. 11, a difference is not so obtained.

Figure 12 shows that the effect of tool geometry, ridge line direction and face direction, to the surface crack ratio at a grinding speed of 80m/min. Because of the difference of its tool geometry, a case of face direction reached surface crack ratio of 100% at a shallower depth than that of ridge line direction.

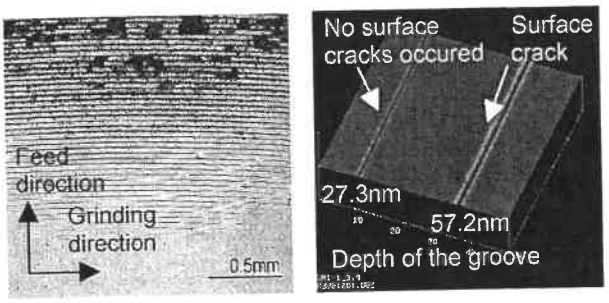

(a) The image of surface of lithium niobate by the optical microscope

(b) The image of surface of lithium niobate by SPM

Fig. 9 Images of lithium niobate surface with crystallographic direction <01$\bar{1}$0> machined at a grinding speed of 80m/min.

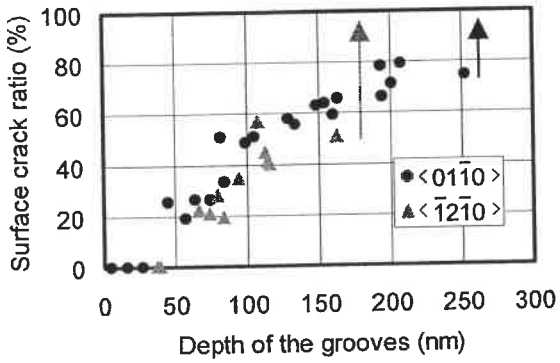

Fig. 10 The crystallographic dependence of surface crack ratio as a function of groove depth for grooves machined at a grinding speed of 80m/min.

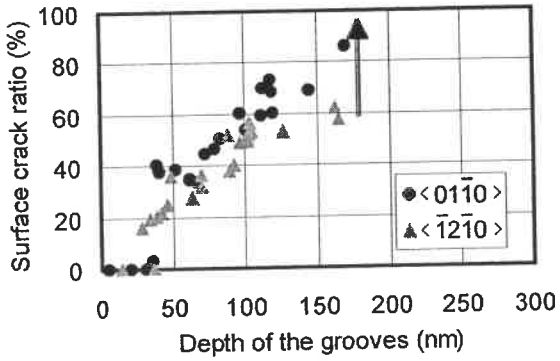

Fig. 11 The crystallographic dependence of surface crack ratio as a function of groove depth for grooves machined at a grinding speed of 1700m/min.

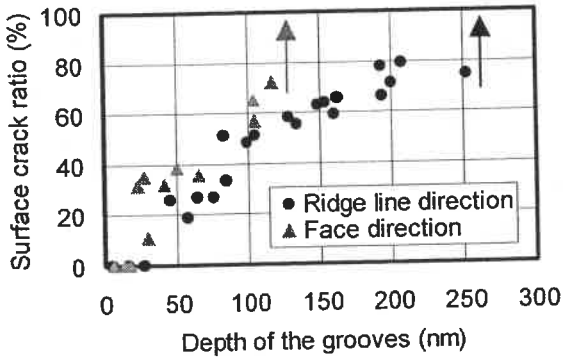

Fig. 12 The effect of tool geometry, ridge line direction and face direction, to the surface crack ratio at a grinding speed of 80m/min.

4. CONCLUSIONS

The following results are obtained.

1) In the microhardness test, compared to silicon, lithium niobate is much more fragile under the same conditions. Moreover, the crystallographic dependence is obtained that the direction <$\bar{1}$2$\bar{1}$0> had the large number of surface cracks.
2) In the nanoindentation test, the properties of lithium niobate are discovered. It shows the different hardness charactristcs of lithium niobate, silicon, and glass from the hardness that has been previously known.
3) In the grinding test, crack-free surfaces are obtained. Crystallographic dependence in lithium niobate is observed.

REFERENCES

1. P. N. Blake: J. Am. Ceram. Soc., **73** (1990) 949-957.
2. L. Hesselink, S. S. Orlov, A. Liu, A. Akella, D. Lande, and R. R. Neurgaonkar: Science., **282** (1998) 1089-1094.
3. M. Nakamura, T. Sumomogi, and T. Endo: Surface & Coatings Technology., **169-170** (2003) 743-747.
4. T. Sumomogi, M. Nakamura, T. Endo, T. Goto, and S. Kaji: Materials Characterization., **48** (2002) 141-145.
5. K. K. Wong and B. L. Weiss: EMIS datareviews Series., **28** (2002) 8.
6. W. C. Oliver and G. M. Pharr: J. Mater. Res., **7** (1992) 1564-1583.
7. Yunn-Shiuan Liao and Ying-Tung Chen: J. Micromech. Microeng., **15** (2005) 2433-2440.
8. K. G. Subhadra, K. Kishan Rao, and D. B. Sirdeshmukh: Bull. Mater. Sci., **23** (2000) 147-150.

DEVELOPMENT OF A 3-D MEASURING EQUIPMENT FOR SURFACE GEOMETRIES OF GRINDING WHEEL SURFACES

Hwa-Soo LEE, Takazo YAMADA and Masaaki KOBAYASHI
Department of Mechanical Engineering, College of Science and Technology, Nihon University, Tokyo, JAPAN

ABSTRACT

A principle of non-contact measuring method with a laser displacement sensor for the distributions of three basic elements of grinding wheels has been proposed. In this method, scanning a surface of grinding wheel, 3-D geometries of grinding wheel surface are displayed by using a computer graphic software. Applying this method, geometric shapes of abrasive grains can be measured and evaluated quantitatively. Consequently, the distributions of abrasive grains and their wear behaviors can be displayed and evaluated.

In the present study, based on the proposed principle, a 3-D measuring equipment for actual grinding wheels is developed. This equipment consists of main spindle for loading measured grinding wheel, two laser sensors, linear feeding axes and a laser sensor for measuring the rotating phase of grinding wheel spindle. All of these elements are controlled by a personal computer. Furthermore, measured data are transported to the same personal computer and 3-D geometric data are displayed by means of a computer graphics software. These data can be used to evaluate the distributions of abrasive grains and cutting edges. Additionally, applying these geometric data, surface geometries of ground workpiece surfaces may be also estimated.

INTRODUCTION

In grinding operations, workpiece surfaces are generated based on the copy principle. Therefore, in order to obtain accurate workpiece surfaces, surface geometric shapes of grinding wheels have to be controlled appropriately. From such a viewpoint, a new measuring method for 3-D geometrical shapes of grinding wheel surfaces is developed [1]. In this method, scanning the surface of measured grinding wheel by a laser displacement sensor, 3-D geometric shapes are obtained and evaluated by means of a computer graphics software. Applying this proposed method, it has been confirmed that the distributions of abrasive grains can be measured three-dimensionally.

This study aims to develop an equipment to measure the actual grinding wheel based on the proposed measuring principle. In this paper, a developed measuring equipment is introduced and an example of evaluations of the abrasive grains wears by means of the developed equipment is discussed.

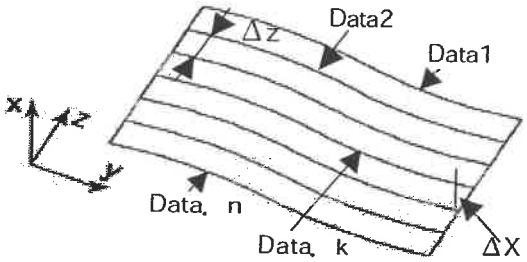

Figure 1: Principle of surface measurement for grinding wheels

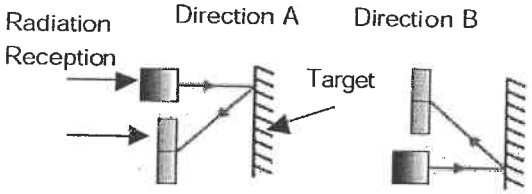

Figure 2: Measuring directions

PRINCIPLE OF A 3-D MEASURING METHOD

Newly developed measuring equipment is depending on a measuring principle previously proposed [1]. An outline of the proposed measuring principle is as follows.

Rotating the measured grinding wheel around the spindle axis Z, distance ΔX in X axis are measured by a laser displacement sensor. Fig.1 shows a 3-D displaying method of measured data. That is, displacement data showing

geometrical shape in a certain periphery ΔX is measured and this data is named as data 1. And feeding the monitoring position to ΔZ in Z axis, data 2 is monitored as same as data 1. Repeating this procedure in n times, geometrical shapes surrounding grinding wheel periphery, (Ym, Zn), can be displayed.

The laser displacement sensor utilized in this measurement uses diffused reflections for measuring displacement. Therefore, in case of that measured targets have some large steps in its surfaces, accurate measurement cannot be carried out and measuring errors take place. In order to avoid such errors, a new measuring method is proposed. Namely, grinding wheel surfaces are measured in two opposite directions A and B as shown in Fig.2, and these two data ΔX are compared. In case of that these data are not same amount, larger data, which means no error takes place, is identified as a data at this point. In such a identification, measuring errors due to some large steps in measured surfaces can be avoided.

MEASURED EXAMPLE BASED ON THE 3-D METHOD

A surface geometry of CBN grinding wheel with #120 is measured. Comparing the measured surface geometry with a microscopic photo, it is confirmed that the 3D geometries of abrasive grains can be monitored accurately. Based on this confirmation, a perspective view of grinding wheel surface is shown in Fig.3. In this figure, the geometries in the surface layer where the depth is less than 120 micron from the most external peak are shown. From this figure, the distribution of the abrasive grains in external layer can be observed.

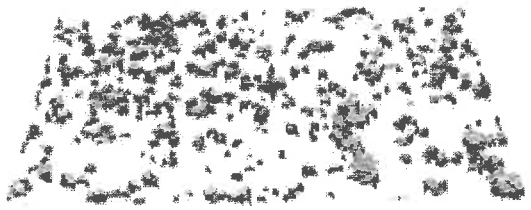

Figure 3: Perspective view of a CBN wheel (#120)

From the measured example shown in Fig.3, it is confirmed that surface geometries of grinding wheels can be measured by the proposed method.

3-D MEASURING EQUIPMENT

Developed 3-D measuring equipment is shown in Fig.4. A measured grinding wheel is located on the main spindle as same as ordinary grinding machines. The main spindle is rotated around Z axis by a stepping motor. Since this rotation is synchronized with the laser sensor, sampling is carried out. While, this main spindle is fed and positioned in Z axis by another motor, and 3-D geometries of grinding wheel surface are sampled. These sampled numerical data are accumulated in a personal computer. The resolutions of the developed equipment are shown in table 1.

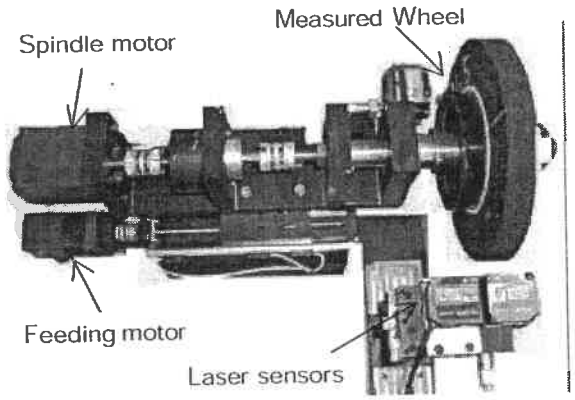

Figure 4: Developed measuring equipment

Table 1: Resolutions of feed system

	Resolutions
Wheel rotation	4×10^{-4} (deg / pulse)
Z axes	2.0 (Micron / pulse)

MEASURED EXAPMLES BY DEVELOPED EQUIPMENT

A plunge grinding is carried out under the condition shown in table 2 by means of a cylindrical grinding machine. Measured examples of grinding wheel surface before and

after grinding are shown in Fig.5(a) and (b). Where, volume of ground workpiece is 1100mm^3/mm. In these figures, the region where left hand side from 3mm in horizontal axis are used in grinding operations, and right hand side region are not used. In these figures, only the data less than 200micron depth from the external peak point of grinding wheel are shown, and then the data deeper than 200micron are not displayed. Being focusing only the external layer as shown in these figures, the layers concerning grinding operations can be and evaluated easily.

Table 2: Machining condition

Grinding	Grinding wheel	WA60J7V
	Workpiece	S50C Hardened
	Wheel speed	1900 m/min
	Work speed	18 m/min
	Depth of cut	10 micron
	Width of cut	5 mm
	Coolant	Soluble type
Dressing	Depth of cut	30 micron
	Lead	0.4 mm

Fig.5(a) shows the geometric shape, and the distributions of abrasive grains and cutting edges can be monitored. Fig.5(b) shows the geometry in the same position after grinding, and it can be known that, in the left hand side region from 3mm in horizontal axis, the distribution of abrasive grains is coarser than the same region shown in Fig.5(a). It means that the number of abrasive grains in this region decreases in the grinding operation. Fig.6 shows a result of substitution of Fig.5(b) from Fig.5(a). This figure shows the worn surface of grinding wheel in the grinding operation while the ground volume of workpiece is 1100mm^3/mm. It is known that no wheel wear takes place in the right hand side region, while a lot of wear takes place in the left hand side region. Based on these data, the worn areas in each depth from the external peak are shown in Fig.7. It can be known from Fig.7 that 100% of abrasive grains are worn where the depth is less that 50micron, and in the deeper layer the worn ratios gradually decrease and 30% of abrasive grains are worn at depth is 200micron.

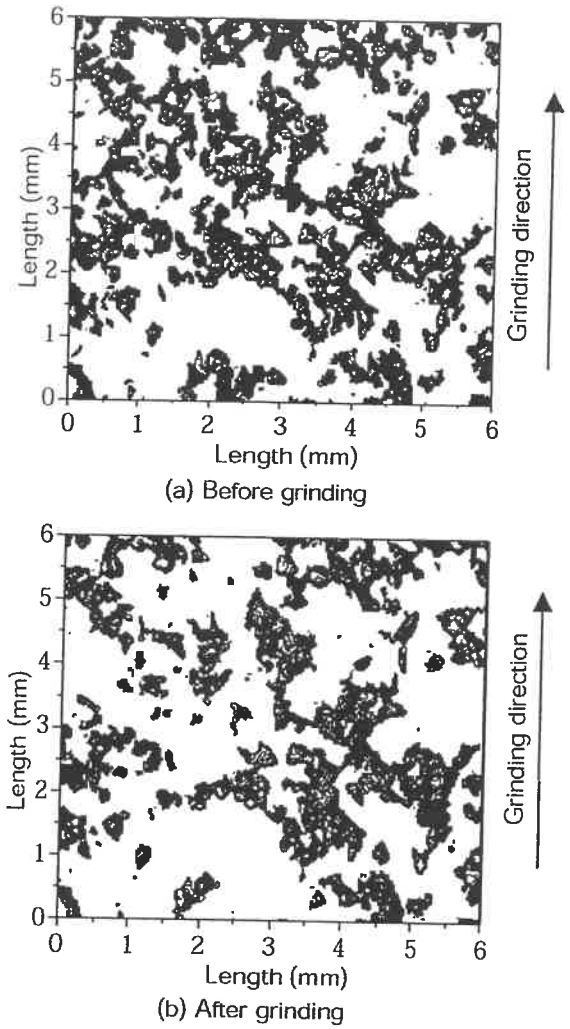

Figure 5: Measured examples

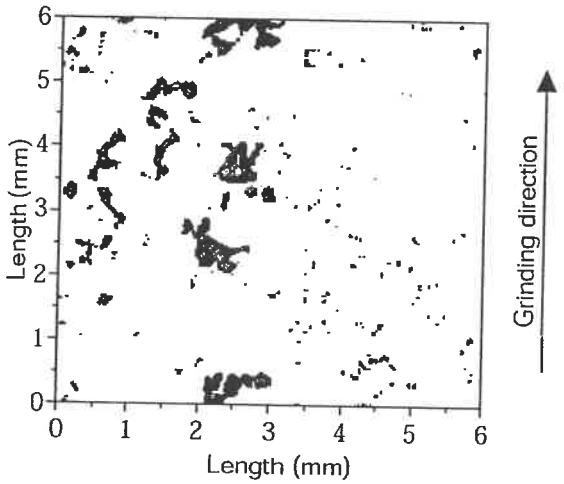

Figure 6: Worn surface in grinding operation

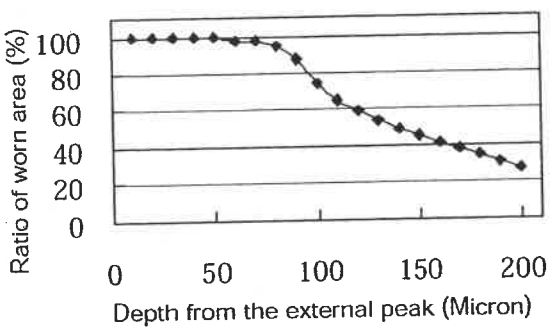

Figure 7: Ratio of worn area in external layer

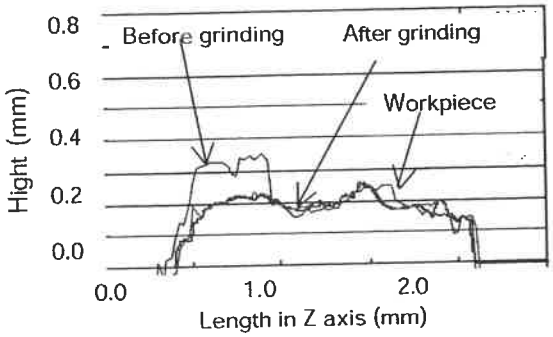

Figure 8: Surface profiles before and after grinding

As shown above, it is confirmed that utilizing the developed 3-D measuring equipment, the grinding wheel wear can be can be evaluated quantitatively.

Fig.8 shows grinding wheel profiles of before and after grinding operation in a certain section in spindle axis Z. In this figure, a profile in the same part of a ground workpiece is also shown. According to this figure, the grinding wheel profiles after grinding coincides with the profile of ground workpiece. Therefore, It can be understood that workpiece geometries are generated based on the copy principle. In Fig.8, the profiles of before and after grinding are different each other where Z=5-10, and their difference is about 300 micron. Taking into account the average size of abrasive grain of the wheel with #60 is 240 micron, it can be estimated that one or two abrasive grains in this part have released from the wheel surface. As shown in this example, using developed 3-D measuring equipment, it can be said that the sort of grinding wheel wear can be identified clearly.

CONCLUSIONS

A 3-D equipment to measure the geometrical shapes of grinding wheel surfaces is developed. Using this equipment, the worn abrasive grains in grinding operation can be measured and evaluated quantitatively. Although any results are not shown in this paper, the worn volume of grinding wheel can be also evaluated. Furthermore, using this equipment, the sort of grinding wear can be identified and then estimation of the grinding wheel wear may be carried out.

REFERENCES

1. Hwa-Soo LEE, Kazuki KAWAGUCHI and Takazo YAMADA, Three-dimensional measurement of the surface geometries of grinding wheel by using a laser displacement sensor, Proceedings of the ASPE 2004 Annual Meeting, (2005.10), CD/ROM.

THE ROLE OF CRYSTALLOGRAPHIC ORIENTATION ON THE FORCES GENERATED IN ULTRA-PRECISION GRINDING OF ANISOTROPIC MATERIALS SUCH AS MONOCRYSTALLINE SILICON

Eric R. Marsh[1], R. Ryan Vallance[2]
[1]Mechanical Engineering
Penn State University
University Park, PA, USA
[2]Mechanical Engineering
George Washington University
Washington, DC, USA

ABSTRACT
This work presents a system of measuring grinding forces in precision applications. Several experiments demonstrate the performance in monitoring diamond wheel dressing, detecting workpiece contact, and process monitoring. The system appears promising for monitoring precision wafer grinding since this approach provides excellent sensitivity, high signal resolution, and good bandwidth.

INTRODUCTION
Ultra-precision grinding is a subset of precision machining where sub-micrometer geometric form errors and nanometer-level surface finishes are obtained using fixed abrasives and machine tools with high static and dynamic stiffness, high-resolution controls, and environmental isolation systems. For example, manufacturers of silicon wafers and precision optics often require tenth-wave form error and nanometer surface finish.

The literature documents a comprehensive exploration of the properties and behavior of silicon and crystallographically similar diamond. Both materials show directionally-dependent behavior including preferred orientations for best results with various material removal processes [1,2,3]. For example, Wilks and Wilks showed that diamond polishing rates vary when working the crystal in different directions [4]. Furthermore, silicon turned with single point tools shows radial spokes of damage in the directions predicted to be the most difficult by Wilks and Wilks. Blackley et al. explained the orientation dependent machining damage in silicon by examining the variation in resolved tensile stress on the {111} slip planes [5].

The anisotropy of monocrystalline silicon causes machining properties like the critical chip thickness, or the ductile-to-brittle-cutting transition depth, to vary with the crystal orientation. Furthermore, the orientation of the crystal lattice during grinding plays a very significant role in the wafer form and surface quality. Recent wafer processing research focused on the roles of each of these components to analytically predict wafer shape and quality. For example, Pei et al. has done extensive research in understanding the geometrical parameters of the workpiece chuck shape, the wafer shape and the process parameters (work speed, wheel speed, feed rate, abrasive grit size, coolant geometry) for fine grinding [6].

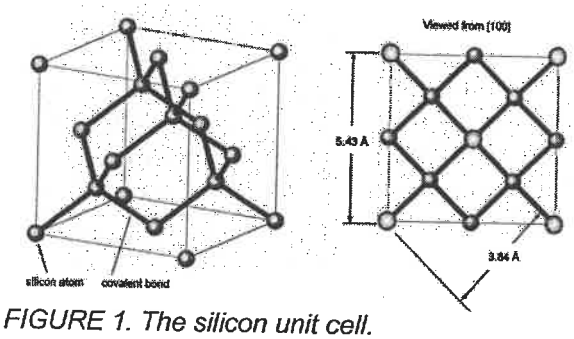

FIGURE 1. The silicon unit cell.

The crystal structure of silicon (diamond cubic at room temperature) is shown in Figure 1. The structure of the crystal lattice and atomic arrangement are extremely important in understanding the anisotropy of silicon because it affects its mechanical, electrical, chemical and optical properties. The mechanical anisotropy is especially influential on the orientation-dependent results obtained when machining silicon and other crystalline materials.

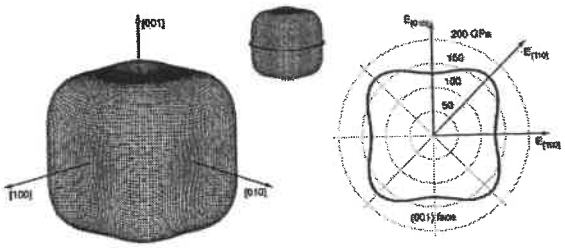

FIGURE 2. Modulus variation as a function of crystal orientation.

One example of the anisotropy in the mechanical properties of silicon is found in the elastic modulus variation. The variation of the elastic modulus on individual crystal planes is found by taking slices of the three-dimensional surface through the origin of the crystal axes. Figure 2 also shows the elastic modulus variation on the cubic face of monocrystalline silicon. On the cubic crystal plane (001 plane), a 4-lobed pattern emerges in the elastic modulus variation. This variation mirrors the atomic structure on the (001) crystal face shown in Figure 1, and a pattern repeating every 90° is evident. As expected, the direction with the highest atomic density yields the highest elastic modulus.

EXPERIMENTAL SETUP

Figure 3 shows the hardware designed specifically for measuring forces in the normal and tangential directions during cylindrical grinding. The design features an aerostatic spindle (Professional Instruments 4R Twin-Mount) with a frameless, brushless, DC motor (MCS) and a 1024 count rotary encoder (Heidenhain) for synchronized data acquisition. Four high-resolution capacitive displacement sensors (1 mV/nm, Lion Precision C1-C) are used to measure the relative motion between the spindle rotor and stator. This arrangement allows the calculation of both radial and axial loads without compromising the structural loop stiffness of the machine tool.

All experiments were carried out on a two-axis grinding machine (Moore CNC 450) with a programmable resolution of 0.1 micrometers. During experiments, an oil-based coolant is applied as a mist using pressurized air. The sensing area of the capacitance probes is kept clean and dry by the positive air pressure flowing through the air bearing spindle.

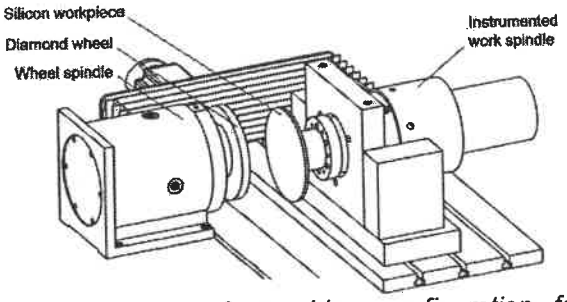

FIGURE 3. CNC machine configuration for silicon grinding experiments.

The spindle instrumentation measures the relative motion between the work spindle stator and rotor. The axial, radial, and tilt stiffnesses are known for the spindle, so the force calibration values can be computed directly by real-time analysis software. An additional consideration is that the capacitance sensors target a rotating steel surface with 100 nm form error. The software removes this form error automatically using the rotary encoder for synchronization. Data acquisition and analysis is carried out by custom LabWindows/CVI software with nearly real-time force feedback and a usable bandwidth of 150 Hz.

The grinding experiments described below are on the outer diameter of cylindrical (100) silicon workpieces Ø150 mm by 10 mm thick. The results and approach are also applicable to face and contour grinding. The work spindle rotates at 500 RPM and the abrasive wheel spins at 3600 RPM. The diamond wheel is a Ø200 mm, 220 grit synthetic diamond wheel (Coors Ceramic SD 220). During the diamond wheel dressing experiments, the diamond wheel rotates at a much slower 400 RPM and a silicon carbide dressing wheel that is mounted in place of the workpiece rotates at 3000 RPM. During dressing and grinding the axial feed rate is 150 mm/min while the radial infeed varies and is reported individually for each experiment.

EXPERIMENTAL RESULTS

The first experiment demonstrates the importance and capability of real-time instrumentation in ultra-precision silicon wafer grinding. Because the typical material removal rates of a brittle material such as silicon are so low, the amount of energy generated in grinding is small and difficult to accurately detect. The same situation applies to diamond wheel dressing, which is notoriously time consuming because of the inherent strength of diamond

wheels. While it is important that the grinding wheel be properly trued for use in precision grinding, the condition of the diamond wheel can be difficult to quantify. For example, a newly installed diamond grinding wheel will have a certain amount of eccentricity and out-of-roundness when mounted on the grinding spindle. It is difficult to quantify the wheel runout because of its rough surface. Diamond wheels are trued and dressed by a variety of methods depending on the particular application. In some situations, if the diamond wheel runout is large, it can take hundreds of passes of the dressing wheel to properly true the diamond wheel. Without adequate feedback, it is easy to stop the dressing operation to early and leave the diamond wheel out-of-true or to waste time dressing an already round wheel.

The second experiment compares grinding forces under different wheel conditions, i.e., a dull wheel and freshly re-conditioned wheel while grinding a silicon sample. The upper time trace of Figure 4 shows the fluctuation in force that occurs as a worn and untrued wheel is used to grind the outer diameter of a silicon workpiece. The lower trace shows data taken with a properly trued wheel. Because the diamond wheel is now geometrically round and dressed so that the many abrasive grits are in a similar condition, the grinding force is more uniform and the once-per-revolution of the grinding wheel force is no longer seen in the inset.

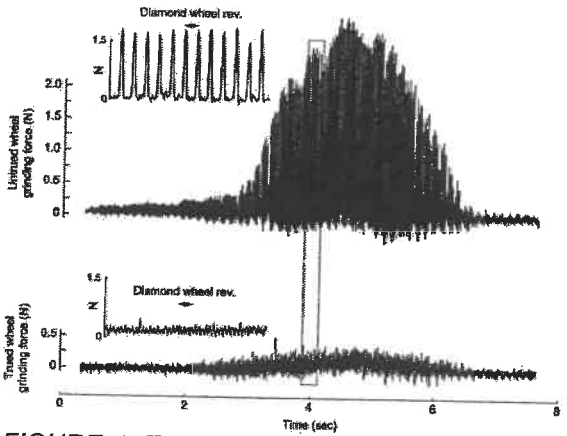

FIGURE 4. Time traces of grinding force with a untrued (upper) and trued (lower) wheel. Without the benefit of the force feedback it would be difficult or impossible to detect the higher force fluctuation of the untrued (worn) wheel.

In the third experiment, we establish the correlation between the measured grinding forces and workpiece crystal orientation. In this experiment, a cylindrical (100) silicon workpiece was ground with a partially worn diamond wheel on the outer diameter. Figure 5 shows how the force data can be visualized over the geometry of the cylindrical workpiece. Although the figure has the familiar appearance of a form error measurement, these data show the fluctuation in grinding force obtained while grinding the outer diameter of the silicon. The forces have been essentially plotted over the cylindrical geometry and then unwrapped and also stretched as shown to make the figure.

The left-hand surface shows the raw grinding force after low-pass filtering the measurement data with a cut-off frequency dictated by the instrument dynamics (150 Hz). This plot shows two interesting phenomena. The first is the regular, but asynchronous, lobing associated with the rotating grinding wheel that occurs approximately nine times per revolution. By counting in the workpiece diameter direction, the force fluctuates approximately nine times per revolution of the workpiece, which corresponds to the ratio of the grinding wheel speed to the workpiece speed. These lobes occurring at approximately nine times per workpiece revolution do not fall in neat lines along the length of the workpiece because the grinding wheel spindle does not rotate at a precise integer multiple of the workpiece spindle speed.

The right-hand surface plot shows the same data, but with additional filtering to a low-pass frequency cutoff below the grinding wheel speed. Readily apparent is the characteristic four lobe pattern that occurs due to the anisotropy of the silicon crystal when machined on the outer diameter of the (100) face. Note that the four-lobe characteristic can be seen in the left-hand surface but it is partially concealed by the higher frequency grinding wheel force fluctuations.

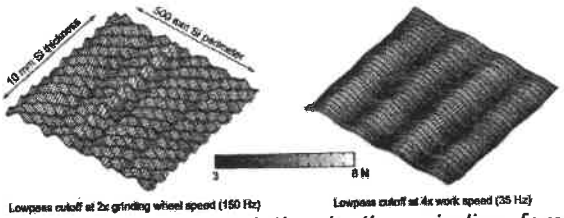

FIGURE 5. The variation in the grinding force measured on a particular pass of the rotating diamond wheel over the rotating silicon workpiece.

The final experiment reveals the crystal anisotropy with a waterfall plot of the grinding force spectra made from a single pass of the diamond grinding wheel over the rotating silicon workpiece. The workpiece spindle speed is 500 RPM (8.3 Hz) and appears, along with many harmonics, in Figure 6 through the contact of the silicon workpiece with the wheel. The fourth harmonic is particularly strong because of the crystal lattice structure (33.3 Hz). Also seen is the significant fluctuation in the grinding force at the frequency of the grinding wheel speed (3600 RPM or 60 Hz). As additional parts are ground with this wheel, the 60 Hz wheel speed component will continue to grow as the wheel wears and breaks down. Eventually the wheel will have to be retrued at which point the 60 Hz component will again be small compared to the work rotation and its harmonics.

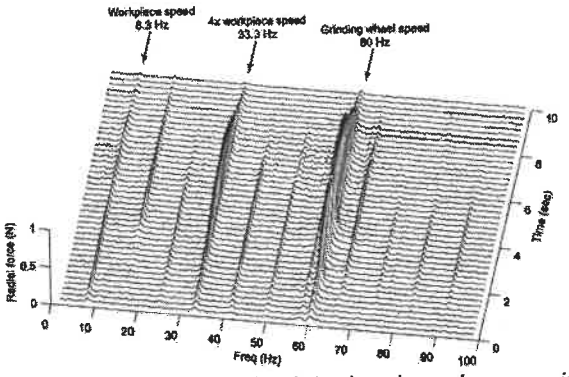

FIGURE 6. Waterfall plot showing changes in grinding force spectra as the grinding wheel makes one pass over the silicon workpiece.

CONCLUSION

Monitoring process variables such as force in ultra-precision grinding of anisotropic crystalline materials is advantageous in optimizing material removal rates, improving process control, and producing high quality parts. However, this is challenging in several applications where aerostatic spindles and small (micro or even submicron level) depths of cut and use of coolants are common. This paper demonstrates an approach to provide force feedback with a resolution on the order of 25 mN and capable of quantitatively resolving the variation in grinding force that accompanies the cyclic change in crystal orientation as an anisotropic workpiece is ground.

Experiments demonstrate the capability of the force-sensing approach in ultra-precision grinding of silicon wafers. The selected experiments show that diamond wheel dressing, wheel condition monitoring, and workpiece crystal lobing are all adequately resolved with sufficient bandwidth to assist in process optimization.

REFERENCES

1. Syn C, Taylor J, Donaldson R, Shimada S. Ductile-brittle Transition of Cutting Behavior in Diamond Turning of Single Crystal Silicon. LLNL UCRL-98100, 1988.
2. Bifano T, Dow T, Scattergood R. Ductile-regime grinding of brittle materials: experimental results and development of a model. *Proceedings of the SPIE: Advances in Fabrication and Metrology for Optics and Large Optics*. 1988;966;108-115.
3. Blake P, Scattergood R. Ductile-regime machining of germanium and silicon. *Journal of American Ceramic Society* 1990;73(4);949-957.
4. Wilks J, Wilks E. Properties and Applications of Diamond. Oxford: Butterworth-Heinemann Ltd., 1991.
5. Blackley W, Scattergood R. Crystal Orientation Dependence of Machining Damage – A Stress Model. *Journal of American Ceramic Society* 1990; 73(10); 3113-3115.
6. Pei ZJ and Strasbaugh A. (2001) Fine grinding of silicon wafers, *International Journal of Machine Tools & Manufacture*, Vol. 41, pp. 659-672.

WHEEL WEAR DURING INTERMITTENT GRINDING

Michele H. Miller[1] and Xiaorui Fan[2]
[1]Department of Mechanical Engineering-Engineering Mechanics
Michigan Technological University
Houghton, MI
[2] American Showa, Inc.
Sunbury, OH

INTRODUCTION

Grinding is widely used for manufacturing components with fine tolerances and smooth surface finish. Compared to other machining processes, grinding requires large energy per unit volume of material removed, which in turn leads to high forces and heat generation. Intermittent grinding, which may be realized with segmental wheels or vibration assistance, offers a way to reduce average force and temperature [1-5]. Although the average material removal rate is the same as in conventional grinding, the distribution of the instantaneous material removal rate is different for intermittent grinding. Because specific energy decreases with MRR (due to the "size effect"), the average segmental wheel grinding force is less than in regular grinding. Other benefits of segmental grinding, such as improved surface finish [4,6] and reduced wheel wear [7] have also been reported. The effect of intermittent grinding on wheel wear is not straightforward. On the one hand, lower temperatures would slow wheel wear. On the other hand, the high peak forces inherent to intermittent grinding would accelerate wheel wear. The purpose of this paper is to take a closer look at this issue.

PREDICTIONS OF AVERAGE AND PEAK FORCES

We developed a model based on empirical specific energy data that can predict forces in surface grinding with segmental wheels [5]. Figure 1 illustrates the surface grinding setup and describes the wheel and workpiece for which the force model was calibrated and validated. For the wheel-work combination described in Figure 1, the force model is:

$$F_z = 5.35(MRR)^{0.74} + 0.74$$
$$F_x = 3.25(MRR)^{0.76} + 0.43 \qquad (1)$$

where F_z and F_x are the thrust and tangential forces, respectively, in Newtons, and *MRR* is the material removal rate in mm^3/s.

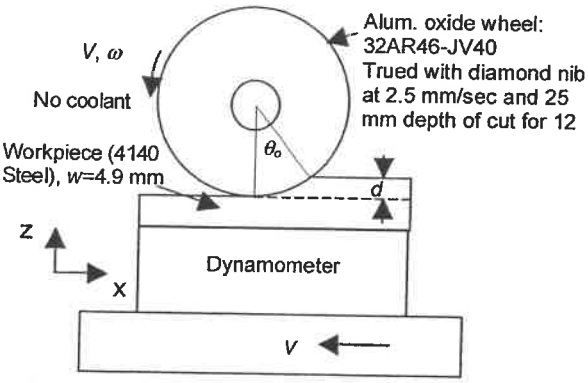

FIGURE 1. Experimental setup for surface grinding force measurements.

The material removal rate, *MRR*, for surface grinding is:

$$MRR = Awdv \qquad (2)$$

where v = table speed, d = depth of cut, and w = width of cut. For a perfectly true wheel grinding a flat surface, the material removal rate is constant and the coefficient A equals 1. With segmental wheels, the material removal rate cycles between a maximum and minimum value as each segment passes; the coefficient A may range from 0 to 1. The chip formation geometry for a square segment wheel, such as shown in Figure 2, was analyzed to determine the A values. The segmental wheel is characterized by the following quantities:

Wheel radius, r
Number of segments, n
Intermittency ratio, $\eta = \dfrac{\text{segment length}}{\text{space length}}$
Wheel engagement angle, $\theta_0 = \text{acos}\left(\dfrac{r-d}{r}\right)$

Space (or notch) angle, $\theta_n = \frac{2\pi}{n}(1-\eta)$

Segment angle, $\theta_s = \frac{2\pi}{n}\eta$

Wheel rotational frequency, ω

Feed per segment, $f = \frac{2\pi v}{n\omega}$

Table 1 summarizes the *A* coefficients for the grinding cycle of one segment. The information in Table 1, in combination with Equations (1) and (2) can be used to calculate the forces in segmental wheel grinding.

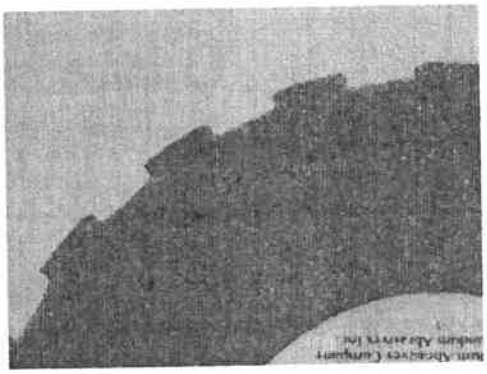

FIGURE 2. Photograph of segmental wheel with intermittency ratio η of 0.5.

Table 1. Multiplier of wdv for calculating instantaneous MRR.

Start time	End time	A
0	$\frac{\theta_o}{\omega}$	$2\left(\frac{\theta_n}{\theta_o}-1\right)\frac{\omega t}{\theta_o}+3\left(\frac{\omega t}{\theta_o}\right)^2$
$\frac{\theta_o}{\omega}$	$\frac{\theta_s}{\omega}$	1
$\frac{\theta_s}{\omega}$	$\frac{\theta_s+\theta_o}{\omega}$	$1-\left(\frac{\omega t-\theta_s}{\theta_o}\right)^2$
$\frac{\theta_s+\theta_o}{\omega}$	$\frac{\theta_s+\theta_n}{\omega}$	0

The force model was used to investigate how number of segments and intermittency ratio influence the normal and tangential grinding forces (both average and peak). Figure 3 shows that average forces increase with number of segments while peak forces decrease. Figure 4 shows that average forces increase with intermittency ratio while peak forces decrease. These effects reflect the fact that larger spaces between segments lead to higher peak forces and lower average forces. (Note that an intermittency ratio of 1 corresponds to a continuous conventional wheel.)

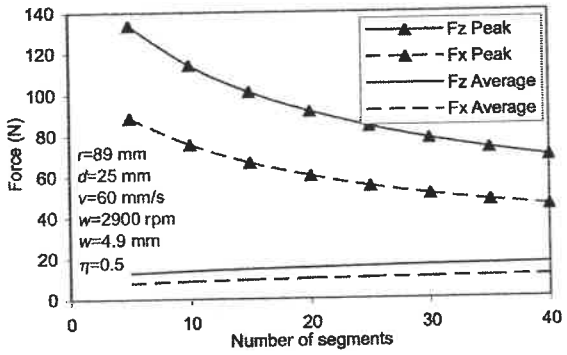

FIGURE 3. Predicted effect of number of segments on average and peak forces.

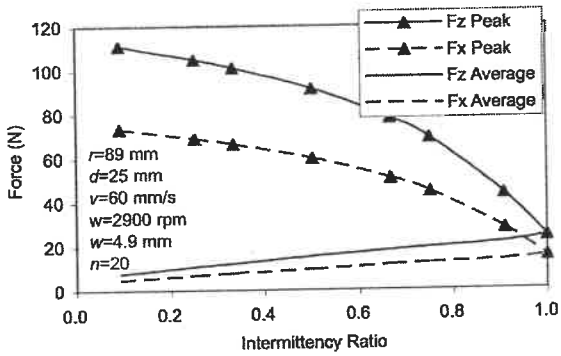

FIGURE 4. Predicted effect of intermittency ratio on average and peak forces.

The model was validated for a several different segmental wheels. The model does a good job predicting average force but tends to underpredict peak force. We believe that non-trueness of the wheel is the reason that the recorded peak force tends to be higher than predicted.

MEASUREMENTS OF WHEEL WEAR

To investigate the effect of segmentation on wheel wear, tests were conducted under the conditions shown in Table 2.

A conventional wheel was compared to several segmental wheel geometries. In each case, a 12.7 mm wide wheel ground a 6.35 mm wide steel workpiece. An imprint of the wheel profile was made by periodically grinding a softer steel material (Rockwell B72). After determining the volume of wheel wear from the wheel profile imprint, a G Ratio (volume of work material removed divided by

volume of wheel material removed) was calculated. After truing, each wheel removed a total of 1966 mm^3 of tool steel. Imprints were made at 492, 983, 1474 and 1966 mm^3 of removal. Then the wheel was retrued, and the wear test repeated. The wheel volume loss for the two trials was averaged before calculating the G Ratio for each wheel.

Table 2. Grinding conditions for wheel wear tests.

Grinding wheel	Aluminum oxide, 32A46-IVBE, 178 mm dia., 12.7 mm wide Trued with diamond nib at 5 mm/sec and 25 μm depth of cut for 12 passes
Work material	Tool steel, Rockwell B83, 152 mm long by 6.35 mm wide
Table speed	180 mm/sec
Wheel speed	27.0 m/sec
Coolant	Castrol Clearedge 6519, 5% concentration 3 liters/min
Depth of cut, per pass	10 μm, up grinding

Figure 5 compares the G ratios for the 5 wheels. For all of the wheels, wear was rapid initially (low G Ratio) and then slowed for a period of time (higher G Ratio) before increasing again. Figure 6 presents the test data in a different way. The G Ratio is calculated based on the cumulative volume removed since the beginning of the test (rather than the volume lost since the last measurement was made). This figure shows the G Ratio for the 2 tests and for the average of the 2 tests. Note that the data appears less noisy when presented in this way.

The same reduction in diameter for a conventional and segmental wheel corresponds to different amounts of actual wheel volume loss. The "absolute" G Ratio is based on the actual wheel material volume lost. The "apparent" G Ratio is based on the envelope of wheel material lost. Table 3 compares the "absolute" and "apparent" G Ratios for the 5 wheels based on a work volume of 1966 mm^3. Figures 5 and 6 show apparent values; the data in the "apparent" column correspond to the average data points at 1966 mm^3 from Figure 6.

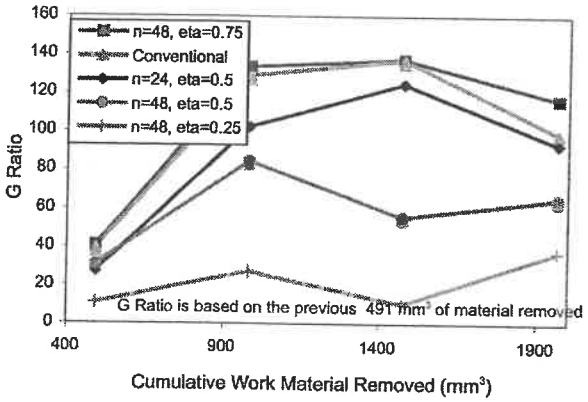

FIGURE 5. G Ratio comparison based on wear measurements made at 4 times after truing.

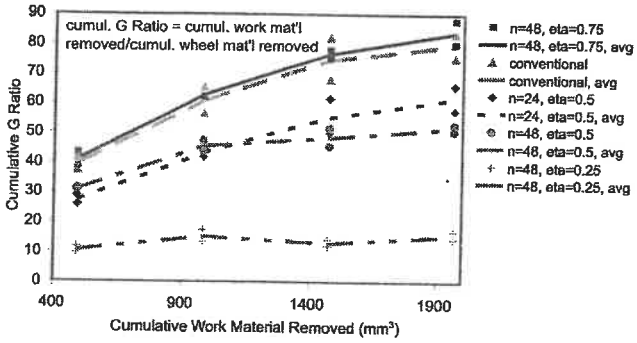

Figure 6. Cumulative G Ratio comparison showing 2 tests at each condition and the average of the 2 tests.

Table 3. G Ratio comparison for 1966 mm^3 of work removed.

Wheel	G Ratio (apparent)	G Ratio (absolute)
Conventional	79	79
n=48, η=0.75	84	112
n=48, η =0.5	52	103
n=48, η =0.25	16	62
n=24, η =0.5	62	123

The Table shows that the 48-segment wheel with small spaces (η=0.75) has a slightly higher G Ratio than the conventional wheel. The wheels with η=0.5 have slightly lower G Ratios than the conventional wheel. Finally, the wheel with η=0.25 has a significantly lower G Ratio. The absolute G Ratios for the segmental wheels (except for the η=0.25 wheel) are higher than the conventional wheel. This is probably due to the reduced average force (and temperature) of grinding

with segmental wheels. The lower absolute G Ratio for the η=0.25 wheel suggests that high peak force is causing rapid wear.

REFERENCES

1. Shaw, M. C., 1971, Wheels for higher-speed grinding. *Mechanical Engineering* 93(8): 19-23.
2. Nakayama, K., Takagi, J., Abe, T., 1977, Grinding Wheel with Helical Grooves—An Attempt to Improve the Grinding Performance. *Annals of the CIRP* 25(1): 133-138.
3. Degtyarenko, S. M., 1989, Contact area between the component and the intermittent working surface of the grinding wheel. *Soviet Engineering Research* 9(11): 54-59.
4. Kim, J. D., Kang, Y. H., Jin, D. X., Lee, Y. S., 1997, Development of discontinuous grinding wheel with multiporous grooves. *Int. J. Mach. Tools Manufact.* 37(11): 1611-1624.
5. Fan, X., Miller, M. H., 2004, Force Analysis for Segmental Grinding. *Proc. of the ASPE Annual Meeting*: 84-87.
6. Brecker, J. N., Shaw, M. C., 1975, Segmental Cup Grinding Wheel. *Avtomaticheskaya Svarka*: 441-452.
7. Gordeev, A. V., 1997, Wear Resistance of Segmental Diamond Wheels. *Machines & Tooling (English translation of Stanki i Instrument)* 48(2): 21-22.

STUDIES ON SLICING CHARACTERISTICS OF VIBRATORY OD-BLADE SLICING

Michio UNEDA[1], Hiromasa TSUKADA[2],
Ken-ich ISHIKAWA[1], and Hitoshi SUWABE[1]
[1]Kanazawa Institute of Technology
7-1 Ohgigaoka, Nonoichi, Ishikawa, 921-8501 Japan
[2]Graduate School of Kanazawa Institute of Technology
7-1 Ohgigaoka, Nonoichi, Ishikawa, 921-8501 Japan

INTRODUCTIONS

With recently increase of quantities of use of hard and brittle materials such as ceramics, the improvement of the high precision slicing/cutting techniques has been demanded. In the slicing techniques for these materials, establishment of improvable technique which ensures high efficiency and accuracy is especially imperative. Moreover, it is required to reduce waste of materials such as kerf-loss caused by slicing because those materials are extremely expensive. With these backgrounds, OD-blade slicing is widely used to slice hard and brittle materials, and then, it tends thinner blades to be used. However, the use of the thinner blade gives rise to the deterioration of slicing accuracy caused by blade elastic deformation during conventional slicing. Therefore, the several studies about the OD-blade slicing have been performed to establish above demand, and then the low frequency vibration slicing technique has been studied as one effective method by research group of us. Figure 1 shows the schematic drawing of our vibration slicing technique. We already reported the slicing characteristics by theoretical and experimental considerations that the vibration slicing method can decrease the slicing force. This paper describes the results of the slicing accuracy characteristics examined in detail.

EXPERIMENTAL METHOD

The vibratory OD-blade slicing apparatus was produced to test the slicing characteristics. This apparatus has mechanical vibration spindle which can apply the circular vibration at the amplitude of 100μm and at the frequency of 5 to 20Hz to the blade. Moreover, this apparatus installs the piezoelectric vibration exciter to apply the perpendicular vibration at the amplitude of 0 to 30μm to the workpiece. Table 1 shows the experimental conditions. To evaluate the slicing accuracy, waviness and roughness of sliced surface were measured a tracer surface roughness tester. Figure 2 shows the illustration of the measurement lines of the waviness. The waviness was measured at "Upper" and "Bottom" lines, and both surfaces

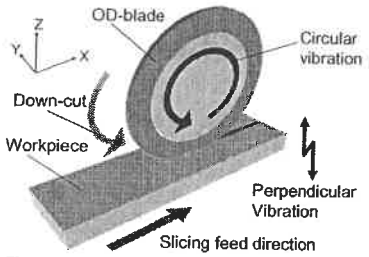

FIGURE1: Schematic drawing of our vibration slicing technique

TABLE1: Experimental conditions

OD-blade	φ125×1mm^t
Slicing depth	11mm
Frequency	20Hz
Workpiece	Soda glass, Slicing length 150mm
Slicing feed velocity	42,102mm/min
Amplitude: Perpendicular	15,25μm
Amplitude: Circular	100μm
Speed of rotation	5000rpm
Slicing method	Down-cut

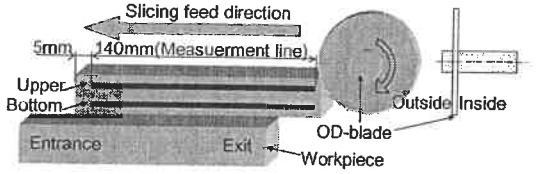

FIGURE2: Illustration of measurement lines of waviness

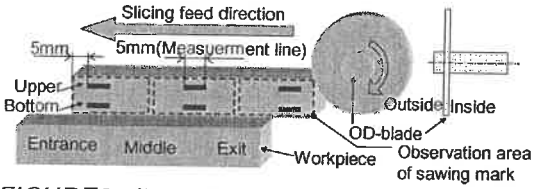

FIGURE3: Illustration of measurement lines of roughness and the observation areas of sawing mark

for a total of four lines. In these measurement lines, the side where the blade comes in contact with the workpiece was defined as "Entrance", the side where the blade separates from the workpiece was defined as "Exit". On the other hand, Figure 3 shows the illustration of the measurement lines of the roughness. The roughness was evaluated as an arithmetical mean deviation of the assessed profile: Ra. The roughness was measured at "Upper" and "Bottom" parts, "Entrance", "Middle" and "Exit" parts, and both surfaces for a total of 12 parts. Furthermore, sawing mark was observed to evaluate the slicing accuracy, too. The area surrounded with the dotted lines in Fig.3 means the observation areas of sawing mark, hence, the sawing mark was observed at as same as the roughness measurement for a total of six areas. The sawing mark was also observed through an optical microscope.

SLICING ACCURACY

Waviness

Figure 4 shows the example profiles of waviness examined both the non-vibration slicing and the vibration slicing. This figure indicates that the waviness profile by the vibration slicing resembles one by the non-vibration slicing well, and then, each profile draws a large curve in the vicinity of the exit. The reason for the deterioration of waviness is thought to be dependent upon elastic deformation of the blade during slicing as shown in Fig.5. First, the slicing force acts in the blade when the blade comes in contact with the workpiece as shown in Fig.5-(a), and then the elastic deformation of the blade occurs. Next, the blade with the elastic deformation continues slicing the workpiece as shown in Fig.5-(b), and then the sliced groove inclines in the feed direction. Finally, in the exit as the vicinity of the slicing where the blade separates from the workpiece, the elastic deformation reduced due to decrease of slicing force. Therefore we conclude that the sliced profiles draw curve.

On the other hand, Fig.6 shows the maximum waviness and its distribution. The maximum waviness was defined as the maximum of four lines data obtained by one pass slicing, and each plotted value is the average of those maximum data. From this figure, the averaged value in the vibration slicing is approximately as same as the non-vibration slicing, however, the distribution of waviness in the vibration slicing decreases compared with the non-vibration slicing. This reason is considered as repeating

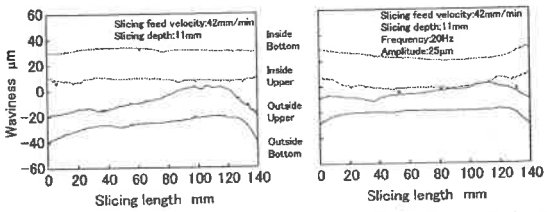

(a) Non-vibration slicing (b) Vibration slicing

FIGURE4: Example profiles of waviness

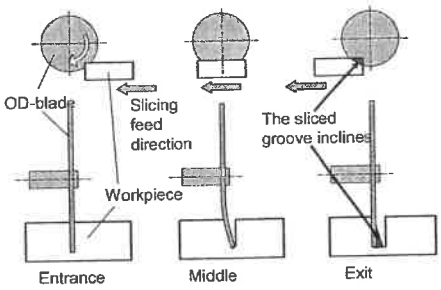

FIGURE5: Illustration of blade elastic deformation during slicing

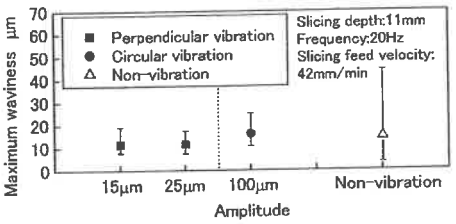

FIGURE6: Maximum waviness and its distribution

phenomena with contact and separation between the blade and the workpiece. Hence, the blade elastic deformation returns to the neutral position during separation per once each cycle. This prevents the blade from deflecting as it does in the non-vibration slicing. Consequently, this phenomenon is called as OD-blade self corrective effect. Therefore, we conclude that the vibration slicing can obtain stable waviness compared with the non-vibration slicing.

Roughness

Figure 7-(a) shows the distribution of roughness Ra of both the non-vibration slicing and the vibration slicing. The numerical value in figures is an averaged value of Ra. From these figures, the averaged value of Ra of the vibration slicing is slightly larger than of the non-vibration slicing. The reason for slight deterioration of roughness in the vibration slicing is thought to be higher actual feed velocity of the OD-blade during slicing. However, the distribution width of Ra in

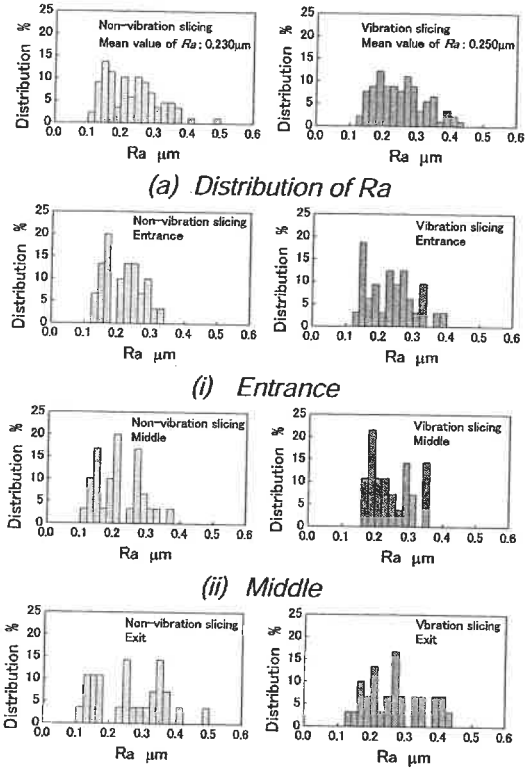

(b) Distribution of Ra at the each parts

FIGURE7: Distribution of roughness Ra at parts of "Entrance", "Middle", and "Exit" to evaluate relationship blade elastic deformation and Ra in detail
(Slicing feed velocity:42mm/min, Slicing depth: 11mm, Amplitude:25μm, Freqency:20Hz)

the vibration slicing decreases compared with the non-vibration slicing. Therefore, in the case of waviness equally, we consider that the vibration slicing can obtain stable roughness compared with the non-vibration slicing.

Here, Figure 7-(b) shows the distribution of Ra at the parts of "Entrance", "Middle", and "Exit" to evaluate relationship between the blade elastic deformation and Ra in detail. From these figures in the non-vibration slicing, the distribution width of Ra increases as the workpiece sliced with the order of "Entrance", "Middle", and "Exit". We consider that the reason for this result that the blade with the elastic deformation continues slicing the workpiece as shown in Fig.5. On the other hand, in the vibration slicing, the distribution width of Ra at the "Middle" shows the most narrow. Therefore, we conclude that the vibration slicing can decrease the blade elastic deformation due to the blade self-corrective effect, and then the vibration slicing can also

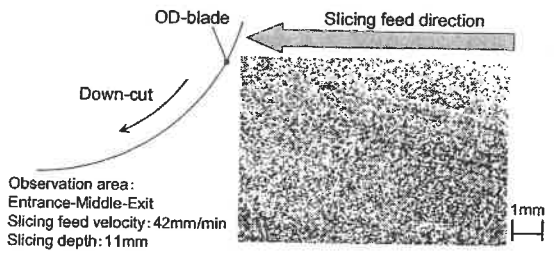

FIGURE8: One example result of opposite sawing mark

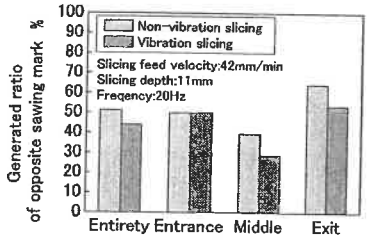

FIGURE9: Generated ratio of opposite sawing mark

decrease the distribution width of Ra. Moreover, from Fig.7-(b) again in the non-vibration slicing and the vibration slicing, distribution width of Ra at the Exit part increases compared with the Entrance and the Middle parts. This phenomenon has high correlation in waviness profiles; hence, this is caused by the deterioration of waviness at the Exit parts.

Sawing mark

The sawing mark occurs in the blade sliced surface as the grinding trace, and then, this paragraph examines the relation between the sawing mark and the roughness. From the pre-observation results, this paragraph evaluates an "opposite sawing mark" which means the sawing mark opposite of the slicing feed direction. Figure 8 shows one example result of the opposite sawing mark. This evaluation method is appropriate because the opposite sawing mark is generated by the blade back side surface which does not participate directly in slicing the workpiece. Figure 9 shows the generated ratio of the opposite sawing mark. From this figure, first, the vibration slicing decreased the generate ratio compared with the non-vibration slicing. Next, to evaluate the ratio with a change of the observation parts, the generated ratio at the Exit and the Entrance parts is higher than the Middle part in both non-vibration slicing and the vibration slicing. Therefore, we conclude that the sawing mark became the deterioration factor of the roughness, and then the vibration slicing can

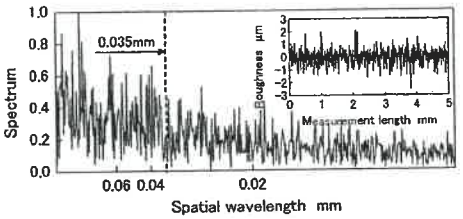

(a) Non-vibration slicing

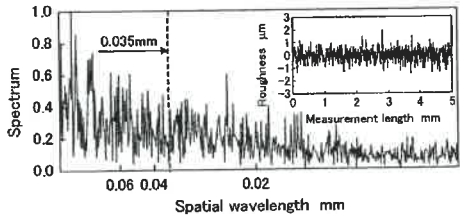

(b) Vibration slicing

(i) Slicing feed velocity is 42mm/min

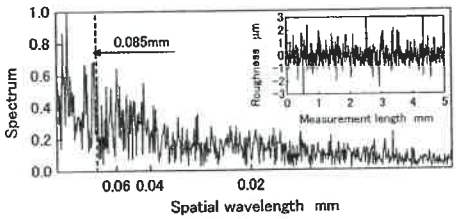

(a) Non-vibration slicing

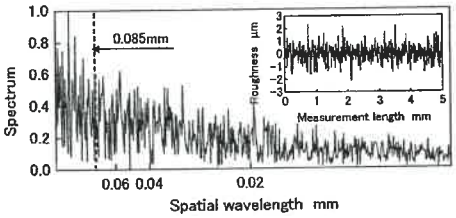

(b) Vibration slicing

(ii) Slicing feed velocity is 102mm/min

FIGURE10: Analyzed results of spatial wavelength spectrum (Slicing depth:11mm, Amplitude:25μm, Freqency:20Hz)

decrease the distribution width of waviness, roughness, and the generated ratio of sawing mark.

Spectral analysis on roughness

In the above discussions, waviness, roughness and sawing mark have been evaluated. Here, the vibration slicing has the separation and contact phenomenon between the blade and the workpiece. Therefore, this paragraph discusses the effect that this phenomenon gives the roughness profile; hence, the spatial frequency/wavelength spectrum of the roughness profile is evaluated. Figure 10 shows the analyzed results of spatial wavelength spectrum at the feed velocity of 42mm/min and 102mm/min, at the frequency of 20Hz. On the other hand, the slicing feed amount Δ in one vibration period can be expressed as follows;

$$\Delta = \frac{f}{\dot{X}/60} \quad (1)$$

where, f is frequency and $\dot{X}$ is slicing feed velocity. Therefore, Δ is 0.035mm in Fig.10-(i), and Δ is 0.085mm in Fig.10-(ii); hence, these lengths correspond to the spatial wavelength of spectrum. In other words, if the spectrum peak is not generated in this wavelength, it means that the separation and contact phenomenon in the vibration slicing does not give the roughness profile deterioration effect. From these figures, the spectrum peaks are not generated in each wavelength. Therefore, we conclude that the vibration slicing does not have the deterioration effect for the roughness profile.

CONCLUSIONS

As the evaluation results of the vibration slicing, the following points have been noted.

(1) The waviness profile tends to draw a large curve in the vicinity of the exit.
(2) The distribution widths of waviness and roughness in the vibration slicing decrease compared with the non-vibration slicing.
(3) The vibration slicing can reduce the generation of opposite sawing mark.
(4) The vibration slicing does not have the deterioration effect for the roughness profile.

ACKNOWLEDGEMENT

The authors gratefully acknowledge a research grand from The Osawa Scientific Studies Grants Foundation for this work.

REFERENCES

1. Michio UNEDA, Hiromasa TSUKADA, Ken-ich ISHIKAWA and Hitoshi SUWABE, 2006, Studies on Vibratory OD-Blade Slicing Characteristics using Mechanical Circular Vibration Spindle, *J. Jpn. Soc. Abrasive Tech.*, 50, 4: 206.
2. Michio UNEDA, Ken-ich ISHIKAWA and Hitoshi SUWABE, 2000, Experimental Study of OD-Blade Self Corrective Effect by Vibration Slicing, *J. Jpn. Soc. Precision Eng.*, 66, 7: 1115.
3. Masahiro MIZUNO and Toshirou IYAMA, 2002, Simulation of sawing processing with OD-Blade, *J. Jpn. Soc. Abrasive Tech.*, 46, 11: 56.

STUDY ON THE CONTACT STIFFNESS OF GRINDING WHEELS DUE TO THE DIFFERENCE OF DRESSING CONDITION

Takazo YAMADA , Hwa-Soo LEE and Hironori MORITA
Department of Mechanical Engineering, College of Science and Technology,
Nihon University, Tokyo, JAPAN

INTRODUCTION

As shown in figure 1, stiffness of grinding system consists of static stiffness of grinding wheel system, of workpiece system and contact stiffness between grinding wheel and workpiece. By clarifying the amounts of these stiffness, it can be expected to control the elastic deformation between grinding wheel and workpiece in grinding operations deeply affecting on the spark-out time and on the occurrence of chatter vibrations.

In order to make clear the relationship between the stiffness of grinding operation system and these phenomena, discussions have been carried out so far, and the effects of these static stiffness on dynamic phenomena are made clear[1]. However, since static stiffness of grinding wheels has wide dispersion depending on the construction and/or their manufacturing process. On the other hand, dressing condition may also affects on the stiffness as shown figure 1, and then, it is called to be difficult to identify the amount of static stiffness actually.

From such a viewpoint, a mathematical model of grinding wheels as shown in figure 2 was proposed in the previous study, in this model grinding wheel consists of rigid body as abrasive grain and spring element as bond[2][3]. Applying this mathematical model to FEM analysis, contact stiffness between grinding wheel and workpiece, and elastic deformations of grinding wheel due to centrifugal forces can be estimated quantitatively.

In this paper, in order to make clear the contact stiffness of grinding wheels due to the difference of dressing condition, analysis depending on the proposed mathematical model of grinding wheel and experiments used actual grinding wheel for any dressing condition are carried out.

MEASUREMENT OF NUMBER OF ABRASIVE GRAINS IN GRINDING WHEELS SURFACES

Number of abrasive grains in grinding wheel surface varies depending on the dressing

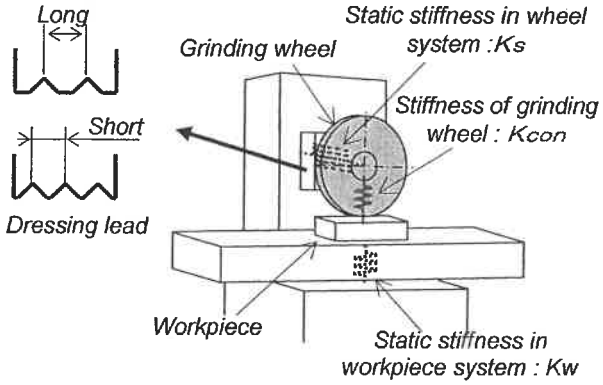

Figure 1: Schematic model of grinding system and dressing lead

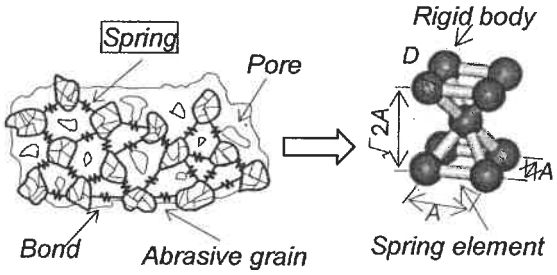

Figure 2: Proposed mathematical model of grinding wheels

condition. It is considered that contact stiffness between grinding wheel and workpiece varies depending on the difference of number of abrasive grains, too. In the first steep of this study, number of abrasive grains in the grinding wheels surfaces under different dressing condition is evaluated. In this experiment, a resinoid wheel WA60J6B, which external diameter is 150mm and width is 10mm, is used. After carrying out the dressing under the condition that depth of cut is 50μm and dressing leads are 0mm/rev. , 0.5mm/rev. and 1.0mm/rev., the distributions of surface abrasive grains are measured by copying the surface geometries to carbon papers.

Since it is estimated that the copied number of abrasive grains depends on the contact load of grinding wheel to carbon paper, the numbers of abrasive grains are measured under some different contact load. The measured numbers of abrasive grains per unit area corresponding to the copy load are shown in figure 3. From this figure, it is known that the numbers of copied abrasive grains increase with the increase of the contact loads. According to this result, when analyzing the contact deformations using the grinding wheel model, it is needed to set the number of abrasive grains appropriately for each contact load.

Figure 4 shows the relationship between dressing lead and the number of abrasive grains of grinding wheel surfaces. The number of abrasive grains, in case of dressing lead 0mm/rev. is the most numerous, and number of abrasive grains decrease with the increase of dressing lead, and increase from a certain dressing lead. This minimum number of abrasive grains may be affected on the contact width between dresser and grinding wheel. From figure 4, it is known that the minimum number of abrasive grains coincides with the contact width due to the amount of dresser's wear. As the results of these experimental results, it is known that number of abrasive grains of grinding wheel surface depends on dressing lead and amount of dresser's wear. Consequently, taking into account these relationship, grinding wheel have to be model.

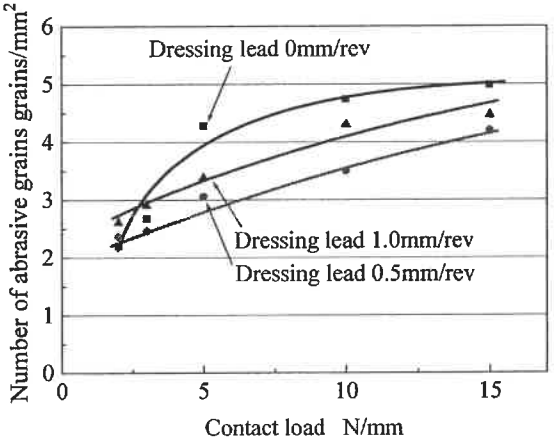

Figure 3: Relation between contact load and amount of abrasive grain

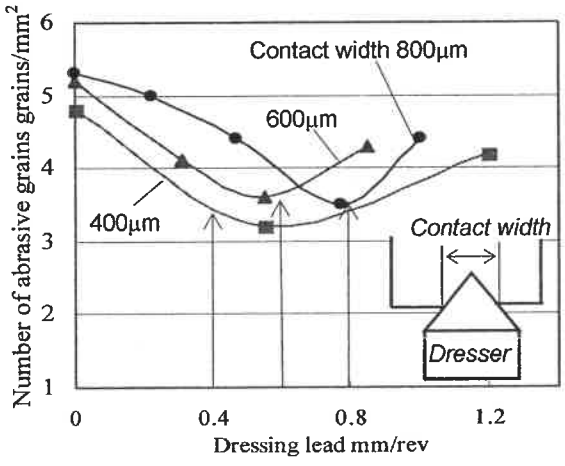

Figure 4: Relation between dressing lead and contact width of dresser

EXPERIMENT OF CONTACT STIFFNESS WITH ACTUAL GRINDING WHEEL

Using actual grinding wheel, contact stiffness between grinding wheel and workpiece are measured. Figure 5 shows schematic diagram of contact tester [3]. In this tester, a grinding wheel is fixed to a shaft, the load is acted to the surface of grinding wheel through a ceramic plate and acting load is measured by a force sensor. Deformations of the loaded grinding wheels are measured as follows. Deformations are measured at a ceramic plate, at an internal part of wheel and at the bottom point of wheel by electric micrometers respectively. Substituting the deformations at internal part and at the bottom of wheel from the amount at ceramic part, the deformation of grinding wheel can be obtained. In this measurement, the same grinding wheel with previously written is used. And dressing leads are 0, 0.5 and 1.0mm/rev, and the depth of dressing is 50μm.

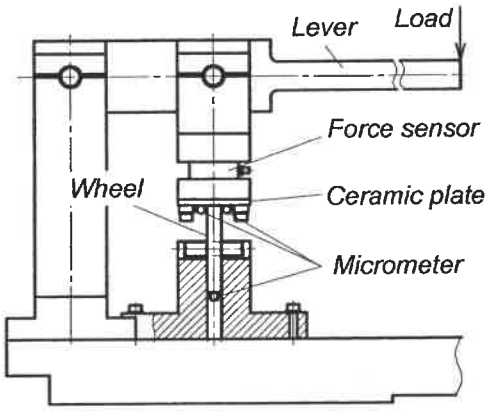

Figure 5: Schematic diagram of contact tester

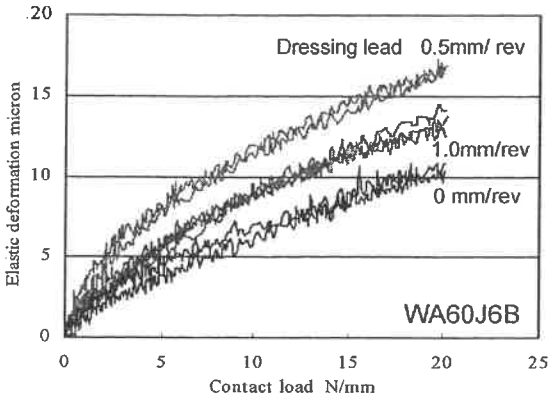

Figure 6: Relation between contact load and elastic deformation

Figure 6 shows the relationships between the contact loads and elastic deformations of grinding wheels for different dressing condition. Experiments are carried out three times for each dressing lead. Comparing elastic deformations for each dressing leads, deformation for dressing lead 0.5mm/rev. is the largest amount, and deformation for 0mm/rev. is the smallest. It is known that contact stiffness varies depending on the difference of dressing condition. As shown in figure 4, number of abrasive grains of surface for 0.5mm/rev. is the smallest amount, on the other hand, one for 0mm/rev. is the largest. According to the results shown above, it is considered that contact stiffness of grinding wheels are reflected the difference of number of abrasive grains.

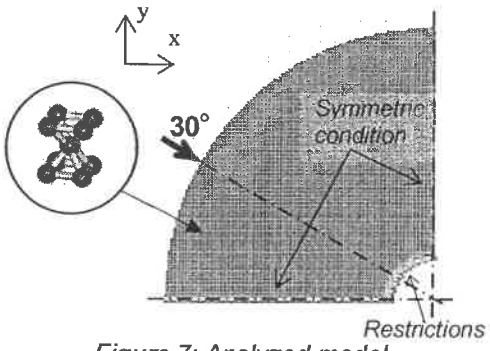

Figure 7: Analyzed model

ANALYSIS OF CONTACT STIFFNESS WITH PROPOSED GRINDING WHEELS MODEL

In previous studies, the mathematical model of grinding wheel consisting of rigid body as abrasive grain and spring element as bond was proposed so far[2][3]. Appling this proposed model to FEM analysis, contact elastic deformation between grinding wheel and workpiece can be calculated quantitatively. So, using proposed model, elastic deformations between grinding wheels and workpiece due to the difference of dressing lead can be analyzed.

In this analysis, a quarter model is used and contact direction is 30° as shown in figure 7. Certain deformations are given to each rigid body, and resistance forces are treated as

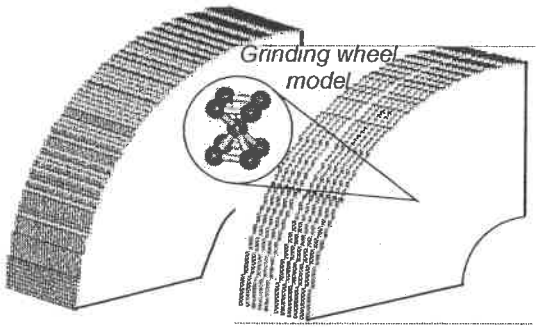

(a) Initial model *(b) Dressed model*

Figure 8: Grinding wheel model

contact loads between wheels and workpiece. In this model, the number of abrasive grains is set depending on the dressing condition. Figure 8 (a) shows initial model, and (b) shows a dressed model taking into account the dressing lead. In these models, the numbers of abrasive grains are 2.2, 3.2, 4.5 and 5.2grains/mm^2 from the results shown in figure 3 and 4. Figure 9 shows analyzed results. From this figure, it is known that elastic deformations of contact area decrease with the increase of number of abrasive grains of wheel surfaces. As shown in figure 3, the number of abrasive grains varies with the contact load between grinding wheel and workpiece. From above, relation between contact load and deformation is calculated as follow. At first, elastic deformations corresponding to contact load with each dressing lead are calculated. And next, connecting the results of each elastic deformation, final analyzed result of each dressing lead are obtained.

Figure 10 shows analyzed results of relationship between contact load and elastic deformation. From this figure, it is confirmed that the elastic

deformation when the minimum number of grains under dressing lead is 0.5mm/rev. is maximum. On the other hand, it is also confirmed that the deformation for maximum number of grains, that is, lead is 0mm/rev. is minimum. These analyzed results coincide with the experimental results. Consequently, it is shown that actual elastic deformations can be obtained from proposed model considered dressing condition.

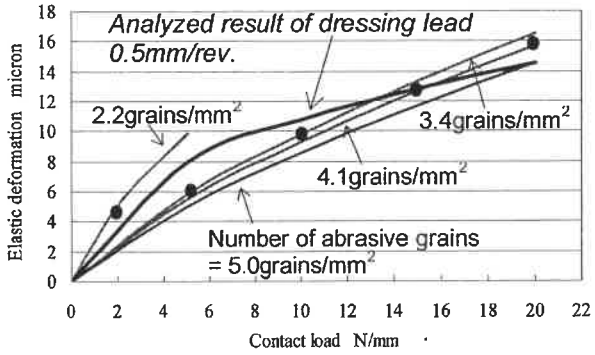

Figure 9: Analytical method of relation between contact load and deformation

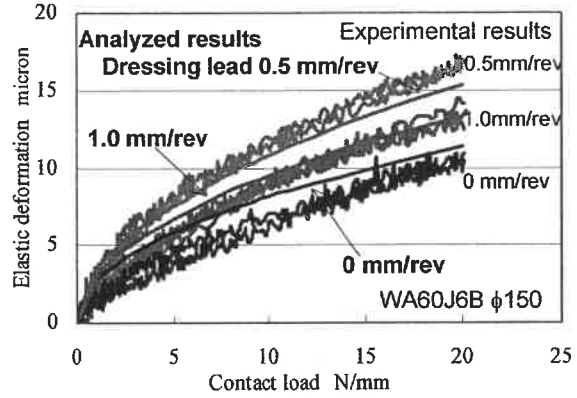

Figure 10: Comparison between experimental results and analyzed results

Based on the results shown above, the effect of the contact stiffness on the elastic deformations occurring in grinding operations will be discussed. In this case, the condition is that the depth of cut is 15 μm, normal grinding force is 70N and the dressing leads are 0 and

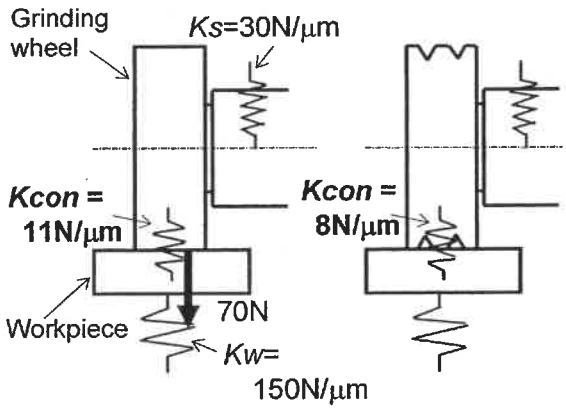

Deformation = 9μm **Deformation = 11μm**

(a) 0mm/rev. *(b) 0.5mm/rev.*

Figure 11: Elastic deformation taking into account grinding machine

0.5mm/rev. The contact stiffness corresponding to the dressing leads 0 and 0.5mm/re. can be obtained as 11 and 8N/mm from figure 10. Assuming that the static stiffness of grinding wheel system and of workpiece supporting system are 30 and 150N/μm, the amounts of elastic deformations in grinding operations can be estimated as 9 and 11μm for dressing lead are 0 and 0.5mm/rev. respectively.

As shown above, contact stiffness between grinding wheel and workpiece can be calculated from the dressing leads, and the elastic deformations under grinding operations can be estimated quantitatively.

CONCLUSIONS

Since the numbers of abrasive grains in contact area depend on the dressing lead, it is clarified that the contact stiffness between grinding wheel and workpiece can be estimated quantitatively by means of the proposed mathematical model of grinding wheel.

REFERENCES

1. H.S.LEE and Y. FURUKAWA: Journal of the Japan Society for Precision Engineering, 48(1982), 106.
2. T. YAMADA et al: Identification of the Static Stiffness of Grinding Wheels with Resin Bond, Proceedings from ASPE2002 Annual Meeting, ASPE(2002-10), 521.
3. T. YAMADA et al: A Study on the Contact Stiffness of Grinding Wheels, Advances in Abrasive Technology VI, ISSAT(2003), 263.

DEVELOPMENT OF CROSS AND PARALLEL MODE GRINDING MACHINE FOR HIGH NA ASPHERICAL MOLD AND DIE

Yuji Yamamoto[1], Hirofumi Suzuki[1], Toshimichi MORIWAKI[1], Tadashi OKINO[1], Yoshio HIJIKATA[1], Jeffrey ROBLEE[2] and Tsutomu MIYASHITA[3]

[1] Department of Mechanical Engineering, Kobe University, Kobe, Hyogo, JAPAN
[2] Precitech Inc., Keene, NH, USA
[3] Taylor Hobson Ltd., Shinagawa, Tokyo, JAPAN

1. INTRODUCTION

Needs of the digital camera and the mobile phone with camera increase, and the necessity of a micro and high NA aspheric glass lens has been increased in recent years. Such micro aspheric glass lenses of high NA must be molded with ceramic dies and molds made of tungsten carbide, and that are ultra-precision ground with aspherical grinding machine with micro diamond wheel. Moreover blue lasers have been increasingly used to make wavelengths short and the maximum tangent angle of the aspheric shape has increased. Therefore ultra-precision grinding technology of ceramic dies became to be a core technology. There are the cross-grinding method and the parallel-grinding method in the micro aspherical grinding. In the cross-grinding, where the wheel rotational direction is cross to the workpiece rotational direction, form accuracy and surface roughness are usually fine compared with the parallel-grinding. In the recent digital cameras or mobile phone with lenses many aspherical lenses have to be install. In some aspherical shape, parallel-mode grinding is superior in precision grinding. Because in that case the grinding wheel with large diameter and small tip radius can be used, the wheel wear can be reduced and workpiece form deviation can be increased. Then grinding machine with the cross mode and parallel mode grinding has been required.

2. MICRO ASPHERICAL GRINDING

2.1 Problem of the cross grinding

Most of the aspherical grinding, the cross-grinding is usually used because of its superior ground surface. But in some aspherical shape such as high NA lens, small radius r_t of the wheel must be used to contact to the minimum local workpiece curvature in case of the cross grinding as shown in Fig.1 (a).

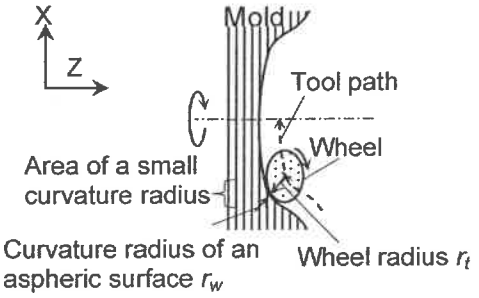

(a)Cross grinding

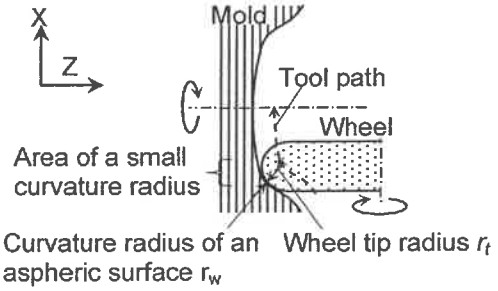

(b) Parallel grinding

Figure 1: Grinding of an aspherical surface

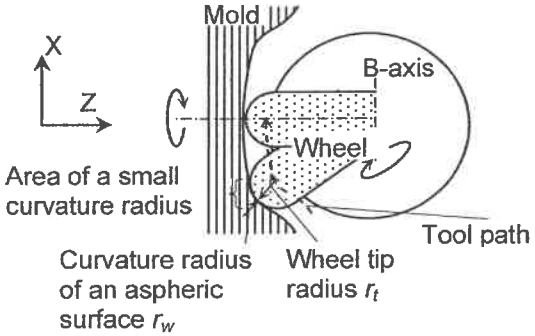

Figure 2: The illustration of the simultaneous 3 axis (X, Z, B) controlled parallel grinding method

In this case, the grinding area on the workpiece A_w becomes much larger than that on the wheel

A_t (Wheel diameter $\times \pi \times$ contact width), then the wheel wear will be large and it will be difficult to obtain a fine form accuracy.

2.2 Parallel-grinding

Then in this case, the parallel-grinding must be applied to use large diameter of the wheel. The wheel tip radius r_t must be smaller than the minimum local workpiece curvature, however a large radius wheel can be used as shown in Fig.1 (b). Then the wheel wear can be decreased.

However, the waviness and surface roughness of the wheel surface are completely transferred to the workpiece surface, and then it is necessary to true or form the wheel surface smoothly with so much truing process in order to obtain the superior wheel surface. Furthermore, the workpiece form accuracy will become large because of the unequal distribution of wheel wear. In order to improve these problems, a rotary B axis has to be added to the grinding machine and grinding point on the wheel surface will be fixed as shown in Fig.2.

In this study, the ultra-precision grinding machine of simultaneous 3-axes (X, Z, B) control was developed. Moreover, although the conventional rotational axis had insufficient positioning accuracy, the rotational axis of new oil hydrostatic pressure slide was developed to be used as a B axis.

3. GRINDING MACHINE/SYSTEM

A view of the grinding machine is shown in Fig. 3. The specifications of the machine are shown in Table 1. The grinding wheel was actuated with X, Z linear motor driven tables of 8.4 nm (X, Z) in positioning resolution. B axis rotary table is the oil hydrostatic rotary table with high stiffness and high resolution in the wedge. In the grinding experiments, the aspherical workpiece was vacuum chucked with the jig onto the workpiece air spindle. The grinding wheel was installed to 45 degrees tilted and high-speed spindle with collet chuck and the grinding spindle was set on the B-axis rotary table. Each axis was controlled with PC based NC system. The cross-grinding mode or parallel grinding modes can be selected by exchanging a jig.

4. GRINDING EXPERIMENTS

4.1 Cross-grinding

Figure 4 shows an illustration of the 45 degrees tilted grinding method. As a grinding spindle, the high speed air spindle was installed, and is driven by simultaneous 2 axis (X,Z). A micro cylindrical type of resinoid bonded diamond wheel was chucked into the grinding spindle with a cullet chuck.

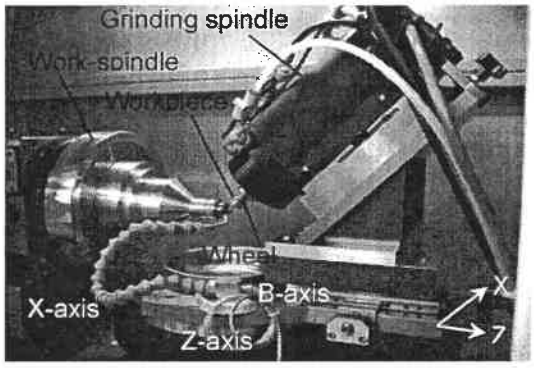

(a)Cross grinding

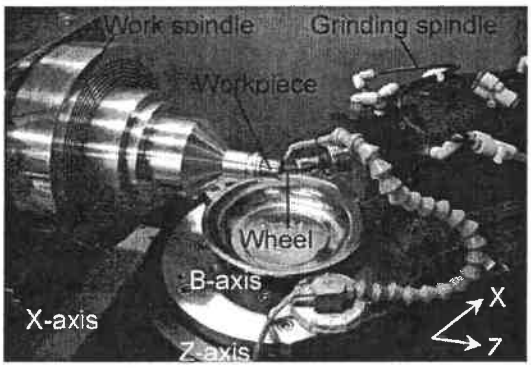

(b) Parallel grinding

Figure 3: Appearance of the developed grinding

Table 1 Specifications of grinding machine

Axes	Travel (mm)	Resolution
X	190	1.4 nm
Z	190	1.4 nm
B	Endless	1/10000 degree

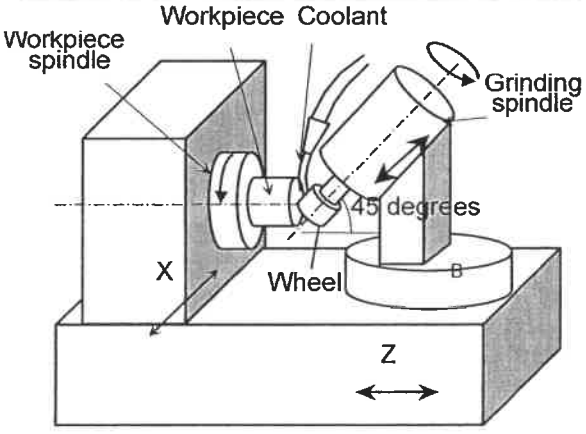

Figure 4: Cross-grinding mode of simultaneous 2 axes (X, Z) controls

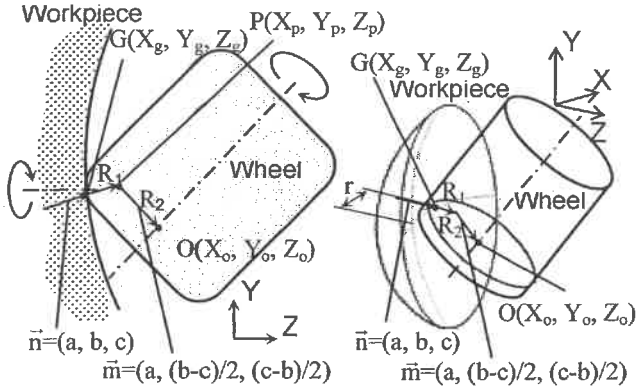

Figure 5: Tool path in cross-grinding of simultaneous 2 axis (X, Z) control

Table 2 Grinding conditions (Cross grinding)

Grinding wheel	Resinoid bonded diamond wheel
Grain size	# 1200
Diameter	2 mm
Rotational rate	40,000 min^{-1}
Workpiece	Tungsten carbide
Rotational rate	200 min^{-1}
Depth of cut	2 μm/path
Feed rate	0.1 mm/min
Coolant	Oil mist

(a) Wheel path

The wheel center point O (X_o, Y_o, Z_o) can be obtained from the coordinate of grinding point G (X_g, Y_g, Z_g) and the normal vector $\vec{n}$ (a, b, c) at the grinding point as shown in Fig. 5 by the following formulae.

$$\left.\begin{aligned} X_o &= X_g + \frac{a}{l}\cdot R_1 + \frac{a}{L}R_2 \\ Y_o &= Y_g + \frac{b}{l}\cdot R_1 + \frac{b-c}{2\cdot L}R_2 \\ Z_o &= Z_g + \frac{c}{l}\cdot R_1 + \frac{c-b}{2\cdot L}R_2 \end{aligned}\right\} \quad (1)$$

Where, $|\overrightarrow{GP}| = R_1$, $|\overrightarrow{PO}| = R_2$, $l = \sqrt{a^2+b^2+c^2}$ and $L = \sqrt{a^2+0.5\cdot(b-c)^2}$. Moreover, this system is actuated by 2-axes (X, Z) drives, the wheel center point (X_o, Z_o) that realize $Y_o = -R/2^{0.5}$ is calculated numerically by using Newton-Raphson method.

(b) Grinding conditions

Table 2 shows the grinding conditions. As a wheel, a resinoid bonded diamond wheel of # 1200 was used and diameter was about ϕ 2 mm.

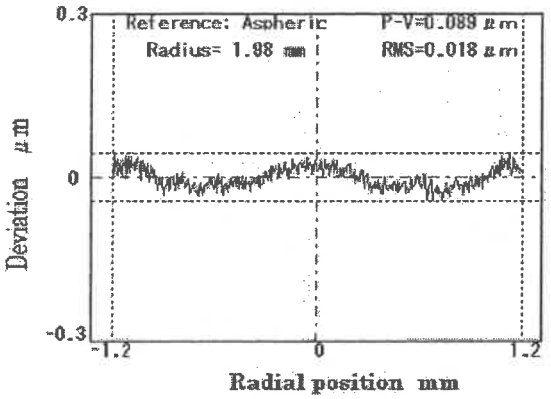

(a) Form deviation (0.09 μmP-V)

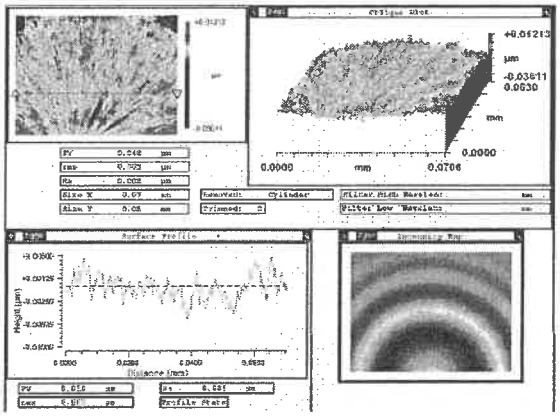

(b) Surface roughness (10nmRy, 1nmRa)

Figure 6: Grinding results (Cross grinding)

The wheel shape was cylindrical shape and the wheel edge was trued to 0.8mm in the radius curvature. As a workpiece, molding die of 2 mm in radius curvature was tested and the material was tungsten carbide.

(c) Grinding results

Figure 6 shows a deviation profile and surface roughness profile after final grinding. The form accuracy of 0.09 μmP-V and mirror surface were obtained.

4.2 Parallel-grinding

Figure 7 shows an illustration of the parallel-grinding, which actuated by simultaneous 3-axes control X, Z, and B. Grinding spindle was set on the B axis rotary table and grinding point on the wheel was controlled to be fixed.

(a) Wheel path

The wheel center point O (X_o, Z_o, B_o) can be obtained from the coordinate of grinding point G (X_g, Z_g, B_g), distance from wheel tip to B axis rotation center R_{tB} and the tangential angle θ of

the grinding point, as shown in Fig. 6 and by the following formulae.

$$\left.\begin{aligned} X_o &= X_g + R_{tB} \cdot \sin\theta \\ Z_o &= Z_g + R_{tB} \cdot (1-\cos\theta) \\ B_o &= \theta \end{aligned}\right\} \quad (2)$$

(b) Grinding conditions

Table 3 shows the grinding conditions. As a wheel, a resinoid bonded diamond wheel of # 1200 was used and diameter was about ϕ 5 mm.

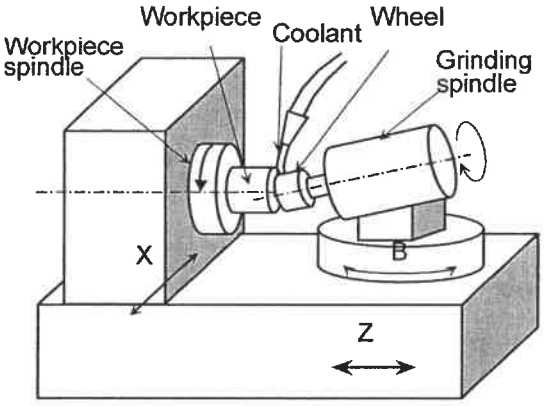

Figure 7: Tool path in parallel-grinding of simultaneous 3-axes (X, Z, B) control

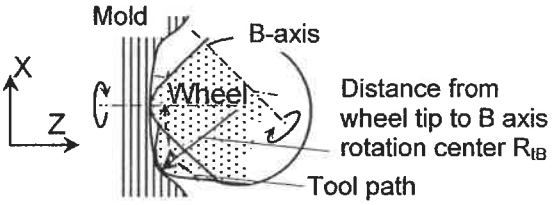

Figure 8: Parallel-grinding of simultaneous 3-axes (X, Z, B) control

Table 3 Grinding conditions (Parallel grinding)

Grinding wheel	Resinoid bonded diamond wheel
Grain size	# 1200
Diameter	5 mm
Rotational rate	40,000 min^{-1}
Workpiece	Tungsten carbide
Rotational rate	200 min^{-1}
Depth of cut	2 μm/path
Feed rate	0.2 mm/min
Coolant	Oil mist

(c) Grinding results

Figure 9 shows a deviation profile and surface roughness profile after final grinding. The form accuracy of 0.13 μmP-V and mirror surface were obtained.

CONCLUSIONS

The grinding machine with crossing mode and the parallel mode was developed. As a result, the good result was obtained in the two modes.

REFERENCES

(1) Yuji Yamamoto, Hirofumi Suzuki, et al., Ultra Precision Grinding of Micro Aspheracal Surface, Proceedings of 2004 ASPE Annual Meeting, FL (USA), Oct, 558-561.

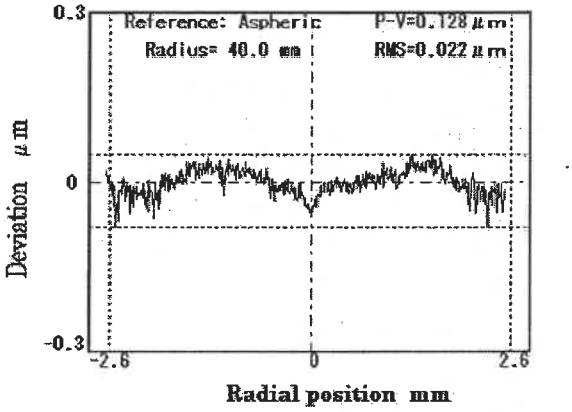

(a) Form deviation (0.13 μmP-V)

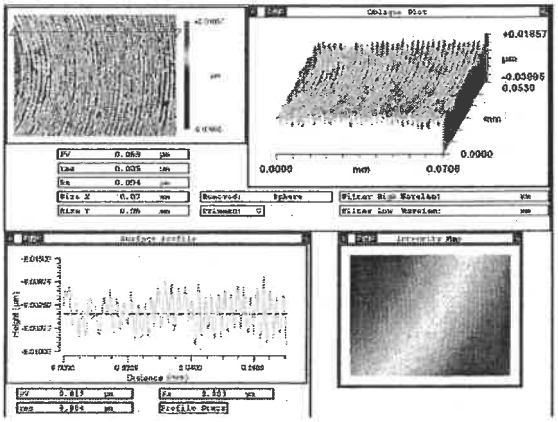

(b) Surface roghness (19nmRy, 3nmRa)

Figure 9: Grinding results (Parallel grinding)

ULTRA-SMOOTHNESS GRINDING OF CEMENTED CARBIDE USING NEWLY DEVELOPED VERTICAL GRINDER

Heiji YASUI[1], Yuki YAMAMOTO[2], Kensuke MIYAMOTO[2], Shogo FURUYA[2], and Ryushiro SAKAMOTO[2]
[1]Department of Mechanical System Engineering, Kumamoto University Kumamoto city, JAPAN
[2]Graduate School of Science and Technology, Kumamoto University Kumamoto city, JAPAN

INSTRUCTION

Difficult-to-cut cemented carbide is one of the most important materials. With the increase of demand of high quality of tool, components and so on, high efficient ultra-smoothness grinding method for cemented carbide has recently been required strongly. In the previous research, the ultra-smoothness grinding method is developed and applied to horizontal surface grinder. From the result, the ground surface roughness of cemented carbide attains below 50 nm (R_z)[1)].

However, the removal rate is small thought it is larger than polishing. To resolve this problem, In the research, vertical ultra-smoothness grinding method is developed. Furthermore, using newly developed vertical ultra-smoothness grinder, the grinding characteristics of cemented carbide is examined.

ULTRA-SMOOTHNESS GRINDING METHOD

The schematic diagram of ultra smoothness grinding method is shown in FIGURE 1. First of all, in the new method, the contact width of workpiece-wheel is ground by feeding the workpiece toward the direction normal to grinding direction. The normal feed per a wheel revolution, f_{Gn}, must be smaller than the wear width of cutting edge normal to grinding direction.

Secondly the workpiece is slightly step-fed a small length, f_p, toward the direction parallel to grinding direction.
The parallel step-feed, f_p, however, is determined so that the geometrical surface roughness, H_p, which is formed by overlapping the cross-section of two wheel circles before and after step-feeding becomes smoother than the required surface roughness. After the parallel step-feed, thirdly the workpiece-wheel contact width is ground again by feeding reversely the workpiece toward the direction normal to grinding direction. The whole surface of workpiece is finished by repeating such grinding procedure.

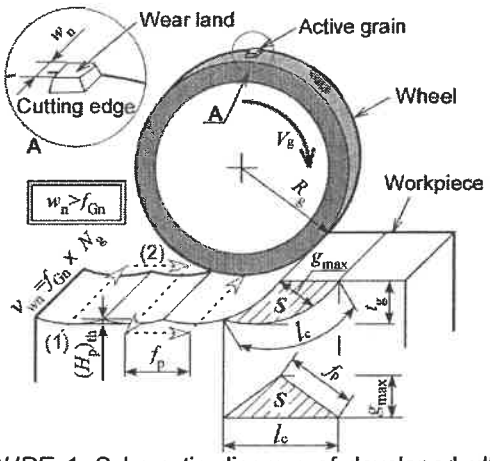

FIGURE 1. Schematic diagram of developed ultra-smoothness grinding method

INCREASING METHOD OF REMOVAL RATE

As considered from FIGURE 1, the removal rate M in the ultra-smoothness grinding method is approximated as follows;

$$M = t_g \times f_p \times f_{Gn} \times N_g \qquad (1)$$

where t_g and N_g are depth of cut and wheel revolution number. From the equation (1), there are four elements related to the removal rate.

Depth of cut, t_g, of the first element can not increase selfishly because it is limited below the allowance removal depth. Concerning parallel step-feed f_p of the second element, the surface roughness $(H_p)_{th}$ formed geometrically due to f_p must be smaller than the required surface roughness. The $(H_p)_{th}$ is expressed as follows;

$$H_p \fallingdotseq f_p^2/(4 \times D_g) \qquad (2)$$

where D_g is wheel diameter. Accordingly the increase of f_p must be below a given value decided by the equation (2). From the equation (2), the f_p can be increased by making the wheel diameter larger under the same geometrical

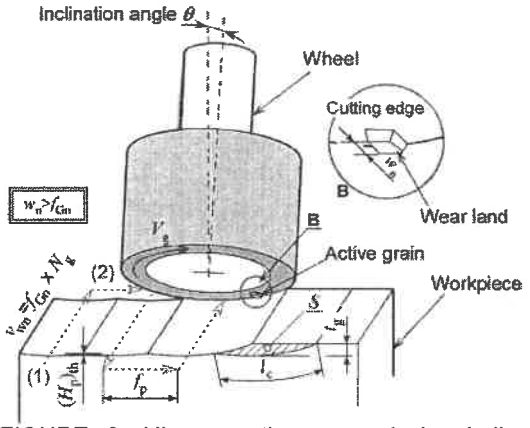

FIGURE 2. Ultra-smoothness vertical grinding method

surface roughness. Thirdly the normal feed per a wheel revolution, f_{Gn}, as mentioned above, needs smaller than the wear width of active grains normal to grinding direction. Therefore, the maximum normal feed per a wheel revolution value, $(f_{Gn})_{max}$, in the range below which the ultra-smoothness grinding is possible depends on the wear width of active grains. According to the separate experiments in the horizontal grinding method[3], the $(f_{Gn})_{max}$ is remarkably small value below 50 micro-meters. In the present state, the increase of the $(f_{Gn})_{max}$ can not be expected for increasing the removal rate.

Finally the maximum wheel revolution number, $(N_g)_{max}$, is related to the allowance wheel speed $(V_g)_{cr}$ or the maximum value, $(D \cdot N)_{max}$, obtained from the product of wheel spindle diameter, D, and spindle revolution number, N which equals to wheel revolution number, N_g. Namely the $(N_g)_{max}$ is calculated by C_g/D_g or C/D where C_g or C is $(V_g)_{cr}/\pi$ or $(D \cdot N)_{max}$., respectively.

From the consideration mentioned above, two methods are thought for making suitably the removal rate larger. Those are to increase the f_p. and N_g. Both methods are related to the wheel diameter. The increase of f_p under the same surface roughness must be accompanied with raising the wheel diameter to the 2nd power. Therefore the wheel diameter must be increased steeply as the f_p becomes large. The wheel diameter, however, is limited on manufacturing of wheel, grinder size and so on.

On the other hand, the increase of $(N_g)_{max}$ under the same limitation needs to decrease proportionally the wheel diameter. The high speed spindle in which the spindle revolution number is over twenty times more than ordinal

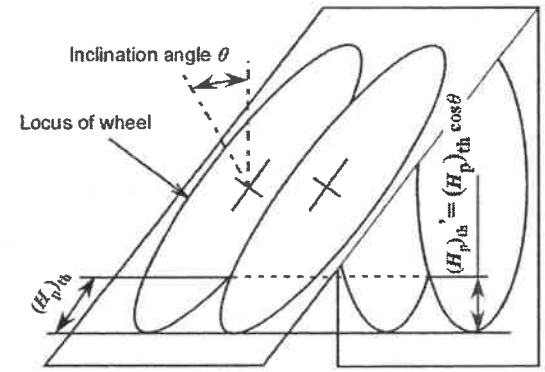

$(H_p)_{th}$:Geometrical surface roughness using **horizontal grinder**
$(H_p)_{th}'$:Geometcila surface roughness using **vertical grinder**

FIGURE 3. Effect of axis inclination on surface roughness

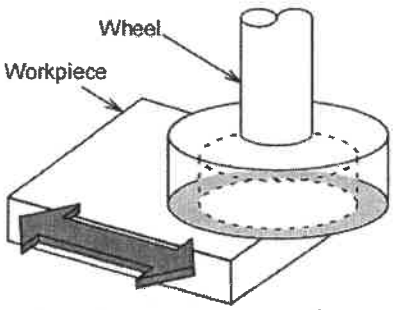

FIGURE 4. Schematic diagram of conventional vertical grinding method

spindle can increase relatively easy the $(N_g)_{max}$ though the wheel diameter is small.

From the point of view, the ultra-smoothness vertical grinding method shown in FIGURE 2 is devised. There are two reasons for the decision to the vertical grinding method. One is that the high speed spindle of small diameter is difficult to apply to the horizontal grinding method. Another is that in the vertical grinding method, the f_p can be made larger than the horizontal grinding method because the geometrical surface roughness in the vertical grinding method becomes so smaller than the horizontal grinding method.

FIGURE 3 shows the effect of the inclination of wheel axis on the surface roughness. In the vertical grinding method, the geometrical surface roughness of parallel direction $(H_p)_{th}'$ is expressed for the $(H_p)_{th}$ in the horizontal grinding method as follows;

$$(H_p)_{th}' = (H_p)_{th} \times \cos\theta \qquad (3)$$

where θ is inclination angle. From the equation (3), the smaller the θ becomes, the smaller the $(H_p)_{th}'$ becomes. To execute grinding at the $\theta=0$ as shown in FIGURE 4, however, is considered

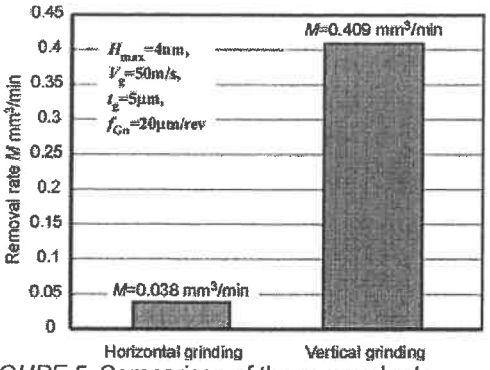

FIGURE 5. Comparison of the removal rate obtained using horizontal surface grinder with using vertical surface grinder in the same geometrical surface roughness
[Horizontal grinding: D_g=100mm, N_g=159rps, f_p=40 micro-meters]
[Vertical grinding: θ=3° , D_g=14mm, N_g=1137rps, f_p=60 micro-meters]

difficult from the point of the effect of grinding fluid supply and the occurrence of loading.
FIGURE 5 shows the comparison of removal rate obtained using horizontal grinding method with vertical grinding method in the same geometrical surface roughness. In the calculation, the setting geometrical surface roughness, H_{max}, is 4nm. The wheel speed is the same of V_g=50 m/s. The wheel diameters used are D_g=100 mm in the horizontal grinding method and D_g=14 mm in the vertical grinding method, respectively. The inclination angle of wheel in the vertical grinding method is 3 degrees. From the figure, the removal rate in the vertical grinding method is found over 10 times larger than the horizontal grinding method.

EXPERIMENTS

FIGURE 6 shows the vertical grinder manufactured newly on trial. The main specifications of the grinder are listed in TABLE 1. The grinder is constructed with the mechanism of 4 axes. The grinder equips with the air spindle and X-Y table holding the workpiece whose movement accuracies are 62 nm. Wheel spindle is possible to be inclined with small angle from vertical direction. The vertical movement accuracy is 62nm.

The experiments are done with the new vertical grinder. The experimental conditions are listed in TABLE 2. The grain size and concentration of wheel used is #140 and 50, respectively. The workpiece and grinding fluid used are cemented carbide and soluble type. Normal feed per a wheel revolution ranges from 10 micro-

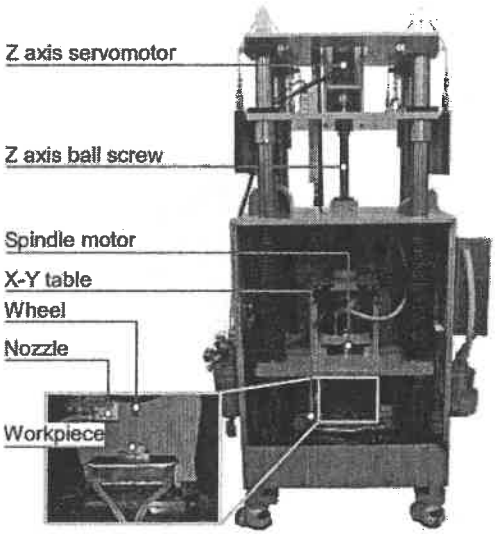

FIGURE 6. Appearance of vertical grinder manufactured on trial

TABLE 1. Specifications of vertical grinder

Maximum feed length	X,Y:200 mm Z:180 mm
Feed accuracy	X,Y,Z:62 nm
Table working area	170 x 170 mm
Wheel revolution	12,000 - 150,000 rpm
Wheel inclination angle	0 - 6.5 degree
Size	730 x 555 x 1920 mm
Weight	900 kg

TABLE 2. Experimental conditions

Workpiece		Cemented Carbide (P20)
Wheel		SD140Q100M
Wheel revolution	:N_g	30,000 rpm
Wheel speed	:V_g	15 m/s
Depth of cut	:t_g	5 micro-meters
Normal feed	:f_{Gn}	5 - 100 micro-meters / rev
Table speed	:v_{wn}	2.5 - 50 mm/s
Parallel feed	:f_p	10 micro-meters
Grinding fluid	Type	Soluble type
	Dilution	1 / 100

meters/rev to 100 micro-meters/rev. The workpiece surface and its surface roughness are observed with Nomarski microscope and SEM, and measured with a surface interferometer (WYKO:TOPO-3D).

RESULTS AND DISCUSSIONS

FIGURE 7 shows the cemented carbide surfaces ground at f_{Gn}=10 micro-meters/rev and f_{Gn}=100 micro-meters/rev using the new grinder. At the f_{Gn}=10 micro-meters/rev, there are no cracks and grinding grooves on the surface. At the f_{Gn}=100 micro-meters/rev, on the other hand, lots of cracks and grinding grooves are observed. The reason is considered why the f_{Gn} exceeds the wear width of active grain. It is clear from the result that in the vertical grinding method as well

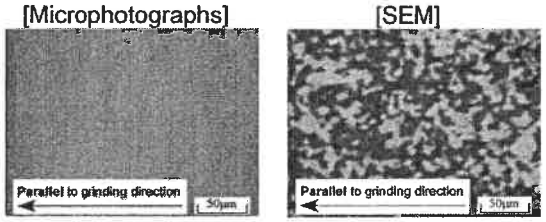

(a) f_{Gn}= 10 micro-meters/rev

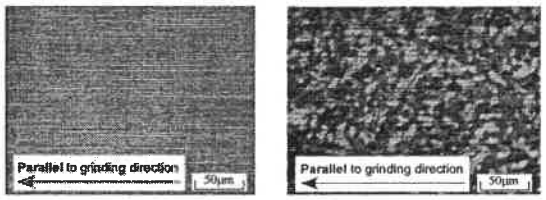

(b) f_{Gn}= 100 micro-meters/rev

FIGURE 7. Cemented carbide surfaces ground by ultra-smoothness vertical grinding method [Cemented carbide, SD140Q100M, V_g = 15 m/s, t_g = 5 micro-meters, f_p = 10 micro-meters]

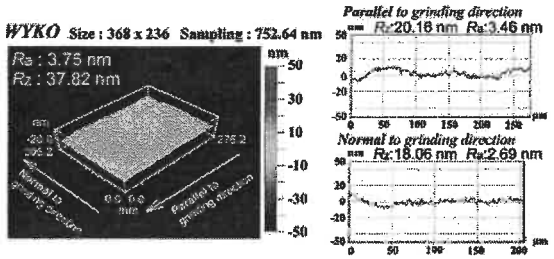
WYKO Size : 368 x 236 Sampling : 752.64 nm
Ra : 3.75 nm
Rz : 37.82 nm
Parallel to grinding direction
Rz:20.16 nm Ra:3.46 nm
Normal to grinding direction
Rz:18.06 nm Ra:2.69 nm

(a) Vertical grinding

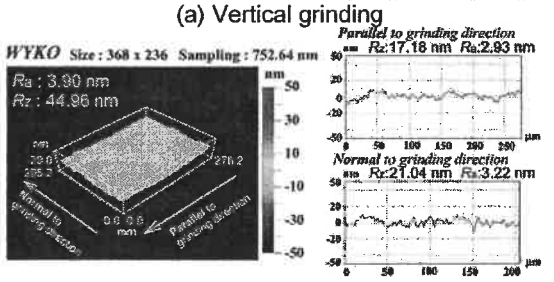
WYKO Size : 368 x 236 Sampling : 752.64 nm
Ra : 3.90 nm
Rz : 44.96 nm
Parallel to grinding direction
Rz:17.18 nm Ra:2.93 nm
Normal to grinding direction
Rz:21.04 nm Ra:3.22 nm

(b) Horizontal grinding

FIGURE 8. Surface roughness of cemented carbide formed by using ultra-smoothness vertical grinding method and horizontal grinding method [Cemented carbide, SD140Q100M, V_g = 15 m/s, t_g = 5 micro-meters, f_p = 10 micro-meters, f_{Gn}= 10 micro-meters/rev]

as the horizontal grinding method, the f_{Gn} can be increased in the range of only small value.

FIGURE 8 shows the comparison of the surface roughness formed by the vertical grinding method with the horizontal grinding method. The grinding conditions in horizontal grinding method is the same as that used in the vertical grinding method shown in Fig.7 except the D_g=100 mm. In both methods, the 3D surface roughness is about 40 nm (R_z) or 4 nm (R_a). It is referred that the surface smoothness in the ultra-smoothness

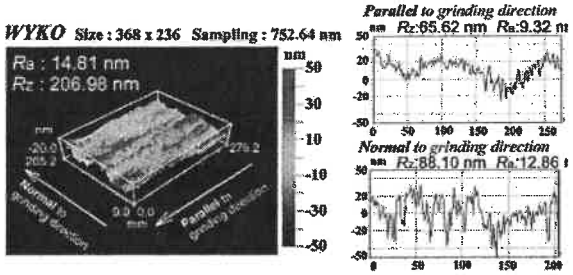
WYKO Size : 368 x 236 Sampling : 752.64 nm
Ra : 14.81 nm
Rz : 206.98 nm
Parallel to grinding direction
Rz:65.62 nm Ra:9.32 nm
Normal to grinding direction
Rz:88.10 nm Ra:12.86 nm

FIGURE 9. Cemented carbide surface roughness formed by ultra-smoothness vertical grinding method [Cemented carbide, SD140Q50M, V_g = 15 m/s, t_g = 5 micro-meters, f_p = 10 micro-meters, f_{Gn} = 100micro-meters / rev]

vertical grinding method can be formed to almost the same as the level in the horizontal grinding method.

FIGURE 9 shows the surface roughness of the cemented carbide as shown in FIGURE 7(b). The 3D surface roughness is about 207 nm (R_z), or 15 nm (R_a). Compared with the surface roughness in FIGURE 8(a), Its roughness is found so large.

SUMMARY

The main conclusions obtained are as follows:

1. The ultra-smoothness vertical grinder which is ground, in the design, with ten times higher removal rate than horizontal grinder is manufactured successfully on trial.
2. The vertical grinder equips with high revolution spindle. For ultra-smoothness grinding, the small diameter wheel is used under high revolution.
3. Cemented carbide surface ground at f_{Gn} = 10 micro-meters/rev using vertical grinder attains about 32 nm (R_z), 5 nm (R_a).
4. The critical normal feed per a wheel revolution $(f_{Gn})_{cr}$ exists for obtaining ultra-smoothness surface.

ACKNOWLEDGEMENT

The authors would like to thank Noritake Super Abrasive Industries Co. Ltd. and Yushiro Chemical Industry Co. Ltd. for providing grinding wheels, grinding fluid. A part of the research is supported by GRNT-IN-AID for Scientific Research (2004) [Project No. 15360072], in Japan

REFERENCES

1.Heiji YASUI: Development of Polishingless Ultra-Smoothness Grinding Method (1st Report), J. Japan Society for Precision Eng., Vol.69, N0.12, (2003)pp.1713-1717

REVIEW OF VIBRATION-ASSISTED MACHINING METHODS FOR PRECISION FABRICATION[1]

D. E. Brehl, T. A. Dow
Precision Engineering Center
North Carolina State University
Raleigh, North Carolina, USA

INTRODUCTION

In "vibration-assisted machining" (VAM) a cutting tool moves at high frequency in a small-amplitude (10's of μm) path. This motion can be linear ("1-D VAM") or elliptical ("2-D VAM"). The oscillating tool motion is superimposed on the main upfeed motion of the workpiece. When the vibration parameters are properly selected relative to the upfeed motion, the tool will separate from the uncut work material for a portion of each cycle. Several notable benefits result from this interrupted cutting characteristic. Tool forces (thrust and cutting forces) are smaller than in conventional cutting. Tool life is extended--most dramatically when VAM is used with diamond tools on ferrous metals, which generally cannot be precision-machined by conventional means. Surface finish and form accuracy are improved.

VAM MOTION

In 1-D vibration-assisted machining the tool is driven harmonically in a linear path parallel to the workpiece upfeed motion. For VAM frequency f, vibration amplitude A, and upfeed velocity V, the position $X(t)$ and velocity $X'(t)$ of the tool relative to the workpiece are

$$X(t) = A * \cos(2\pi ft) + V * t \qquad (1)$$
$$X'(t) = -2\pi f * A * \sin(2\pi ft) + V \qquad (2)$$

From Eq. (2), when $2\pi fA < V$ the tool will separate from the uncut work material for a portion of each cycle. This is depicted in Figure 1. At $t=0$ the tool initially contacts the workpiece. At $t=t_1$ it has finished cutting and is about to move backwards relative to the work. Between t_1 and t_2 the tool is separated from the work and not cutting. At $t=t_2$ the tool is again in contact with the uncut work material and is about to cut. Figure 2 shows 2-D vibration-assisted machining. The tool moves at frequency f in an ellipse with horizontal amplitude A and vertical

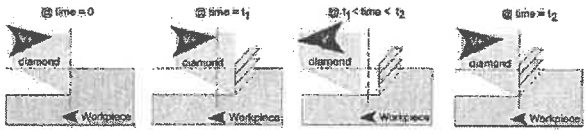

FIGURE 1. 1-D vibration-assisted machining

amplitude B. The horizontal position and velocity relative to the work are again given by Eq. (1) and Eq. (2). The vertical position $Z(t)$ and vertical velocity $Z'(t)$ are

$$Z(t) = B * \sin(2\pi ft) \qquad (3)$$
$$Z'(t) = 2\pi f * B * \cos(2\pi ft) \qquad (4)$$

Again, when $2\pi f*A < V$ the tool will separate from the uncut work material for a portion of each cycle.

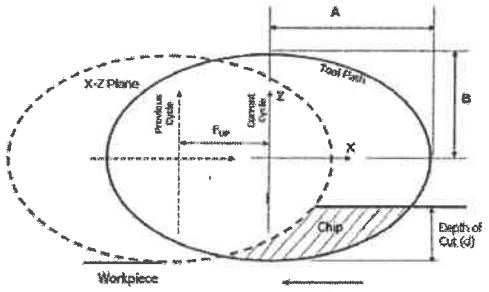

FIGURE 2. 2-D vibration-assisted machining

The operating point of a VAM system can be characterized by three terms. The "upfeed index" F_{UP} (Eq. 5) is the distance traveled by the tool relative to the work in one cycle. The "horizontal speed ratio" HSR (Eq. 6) relates the peak cutting speed of the tool to the upfeed velocity.

$$F_{UP} = \frac{V}{f} \qquad (5) \qquad HSR = \frac{V}{2\pi f * A} \qquad (6)$$

Small values of F_{UP} and HSR lead to low theoretical surface roughness. The third

[1] Work sponsored by NSF grant DMI-423315, monitored by G. Hazelrigg

characterizing term, "duty cycle", is the proportion of each cycle the tool is cutting.

VAM SYSTEMS

A typical 1-D VAM system uses a piezoelectric or magnetorestrictive actuator to create a reciprocating harmonic motion at ultrasonic frequency but small amplitude. This motion is amplified by a shaped-acoustical waveguide booster and horn. A cutting tool is attached to the end of the horn, aligned so that the rake face is normal to the direction of vibration. 1-D VAM systems operate at discrete frequencies of 20-40 kHz, achievable by commercial ultrasonic generators. Amplitude is typically 10 to 25 μm.

"Resonant" 2-D VAM systems create elliptical tool motion by causing the tool support structure to vibrate at its resonant frequency in two directions. Figure 3 is a resonant 2-D VAM system developed by Moriwaki and Shamato [1]. Piezoelectric actuators are attached to the side faces of the beam structure, and are activated in opposed pairs to induce bending in two directions at right angles to one another. The beam is supported at its nodal points. Bending vibration of the beam ends at the 3rd resonant frequency amplifies the motion induced by the piezo strips. The diamond tool is mounted on the end of the beam. The combination of the two bending vibrations makes the tool move in an elliptical path. This system operates at discrete frequencies above 20 kHz.

"Non-resonant" 2-D VAM systems use a mechanical linkage to convert the expansion and contraction of piezoelectric actuators into an elliptical tool path. Figure 4 shows a system developed at North Carolina State University [2]. Sinusoidal voltages, with a phase difference between them, are supplied to the two parallel actuators. The toolholder acts as the linkage. This system operates at up to 4 kHz with ellipse dimensions as large as 36 μm x 6 μm. The ellipse size, aspect ratio and orientation can be varied by changing the phase shift between the stacks and/or the voltage signal amplitude. The frequency can also be varied. This design requires a cooling system because of large actuation and hysteresis history.

VAM BENEFITS

Cutting Dynamics and Reduced Tool Forces

VAM's interrupted cutting results in a small chip being formed during each machining cycle, at lower tool force. The high vibration frequency means that many cycles take place in a specified time interval. Therefore in VAM many small chips are made, instead of a large continuous chip as in conventional cutting. Also, the tool moves with lower average force for a much larger cumulative distance in repetitive passes, compared to conventional machining in the same amount of time. For the same volumetric material removal, the work performed by VAM is therefore consistent with that of conventional machining.

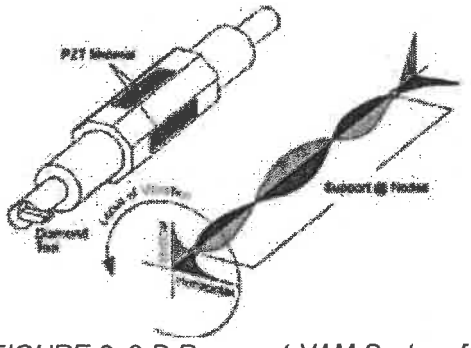

FIGURE 3. 2-D Resonant VAM System [1]

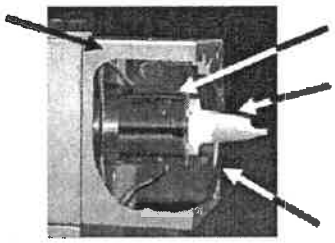

FIGURE 4. 2-D Non-resonant VAM system

1-D and 2-D VAM have different cutting dynamics. Figure 5 compares instantaneous 1-D VAM thrust and cutting forces to those of conventional machining. These results are from an experimental system operating at up to 6 Hz [3] (instantaneous force measurements are difficult to obtain at ultrasonic frequencies because of the high sampling rate required).[2] The peak VAM forces are the same as the steady-state forces. Interrupted cutting is the cause of smaller average forces seen in 1-D VAM. A rough estimate of the average force can be found by multiplying the steady state

[2] Another concern for ultrasonic VAM systems: when the operating frequency is much larger than the measurement system's natural frequency forces transmitted to the sensor are highly attenuated. Unless corrections are made based on the vibration response of the specific measurement setup, the force measurements will be inaccurate.

force by the duty cycle. The shape of the instantaneous 1-D VAM profiles reflects material loading transitions from elastic to plastic regimes, and changing strain rates.

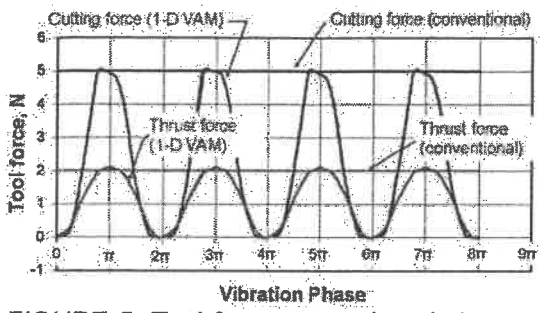

FIGURE 5. Tool force comparison between 1-D VAM and conventional cutting. Steel tool, copper work. f=6 Hz Redrawn from [3].

Figure 6 shows instantaneous thrust and cutting force measurements for 2-D VAM at 1 kHz [2]. Only the portion of the overall cycle when the tool is cutting in the material is shown. Thrust and cutting forces are seen to be always smaller than the forces for conventional machining. The peak VAM thrust force is 38% of the conventional thrust force and the peak VAM cutting force is 54% of the conventional cutting force. Integrating the instantaneous forces over one cycle gives an average VAM cutting force 8%, and an average VAM thrust force 5%, of the respective values for conventional machining. In 2-D VAM, the tool force reduction is due to making chips that are thinner than the overall depth of cut in conventional cutting. These thin chips occur because of the consecutive overlapping elliptical tool paths. See Figure 2.

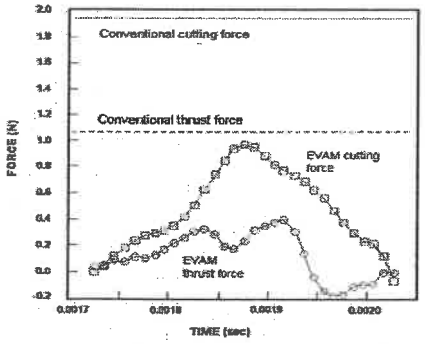

FIGURE 6. Tool force comparison between 2-D VAM and conventional machining. Diamond tool, copper work. f = 1000 Hz [2].

Limited published work exists on quantitative prediction of VAM tool forces. Babitsky [4] and various collaborators carried out theoretical, finite element, and experimental studies of 1-D VAM. They modeled individual tool/work contact cycles as viscoelastic interactions. Cerniway [5] developed a tool force model that evaluated the varying chip thickness due to the consecutive overlapping elliptical tool paths, as well as variation in tool contact area and rake angle resulting from the 2-D motion through the work. Model predictions agreed well with experimental results at frequencies up to 4 kHz.

Extended Tool Life

Increase in surface roughness with cumulative machining distance can be used as an indication of tool wear. Figure 7 shows surface roughness vs. cutting distance for a diamond tool machining hardened steel, for 1-D and 2-D VAM. 2-D VAM is seen to extend tool life in steel to almost 2000 m cutting distance (compared to < 100 m for conventional diamond-machining). Thermochemical mechanisms are mainly responsible for diamond tool wear in ferrous metals. VAM's interrupted cutting extends tool life by reducing the duration of tool-work contact, limiting the time for these mechanisms to operate. VAM may also reduce tool temperature, limiting the driving potential for the relevant reactions. Tool life in ferrous metals for 2-D VAM is superior because in 1-D VAM the tool cutting edge can chip from accidental contact with the workpiece during the non-cutting portion of the machining cycle.

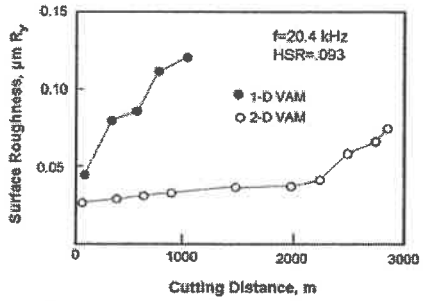

FIGURE 7. Tool wear (indicated by surface roughness) as a function of cutting distance for 1-D and 2-D VAM. Diamond tool, hardened steel work. Redrawn from [1].

VAM extends tool life for other combinations of tool and work materials. 1-D VAM improved the life of carbide tools by a factor of 20, when machining glass ceramics [6]. Another experiment used 1-D VAM and carbide tools to machine stainless steel. After 500 m, conventional machining caused a 350 μm wear land in the tool, compared to 100 μm for VAM

[7]. In these examples abrasive-mechanical wear mechanisms dominate. VAM appears to reduce wear because smaller instantaneous and average tool forces lead to reduced local stress in vulnerable parts of the tool.

Surface Finish and Form Error

Surface finish in VAM is frequently superior to conventional machining for the same combination of tool and workpiece materials. The cyclic nature of VAM allows the tool to traverse the cut area from the preceding cycle and remove material peaks left over from the last pass. Small F_{UP} and *HSR* give low theoretical surface roughness by maximizing the overlap between successive cycles. The smaller forces in 2-D VAM, and the smaller average forces in 1-D VAM, lead to improved form accuracy and surface finish by decreasing relative vibration between tool and work. The reduced tool forces also inhibit chatter.

APPLICATIONS

2-D VAM appears to be well-suited to traditional precision machining applications, where a feature must be made to precise form and nanometer-scale surface roughness. Figure 8 shows microstructures machined in hard plated copper by the non-resonant 2-D VAM system of Figure 5 using diamond tools. The Angstrom symbol is 200 µm x 200 µm overall with the smallest feature (vertical bar of the topknot symbol) only 15 µm wide. Surface roughness is ~20 nm RMS. The trihedron array has structures 80 µm tall on a 112 µm pitch, and also includes interstitial trihedrons 10 µm tall. These parts show burr-free edges in an SEM at 2000x magnification. Figure 9 shows micromolds in hardened die steel made using the resonant 2-D VAM system in Figure 3. This system has also machined steel optical parts including flat mirrors up to 91 mm x 121 mm.

1-D VAM systems have been used in applications requiring significant material removal (e.g. depths of cut .01 to 1 mm). Here the objective often is to achieve a desired finish in hard-to-work materials with economical tool life. Babitsky *et al* [9] aimed to machine Inconel and titanium while extending carbide tool life with 1-D VAM As another example, thin aluminum camera drawtubes (0.8 to 1.2 mm wall) were finished using a 1-D VAM system installed on a conventional lathe [10]. A finish of 600 nm PV was achieved which exceeded the part specification.

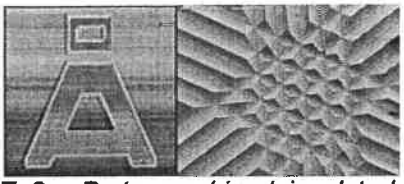

FIGURE 8. Parts machined in plated copper with the 2-D VAM system in Figure 4. (left) Angstrom symbol (right) 80 µm tall trihedrons.

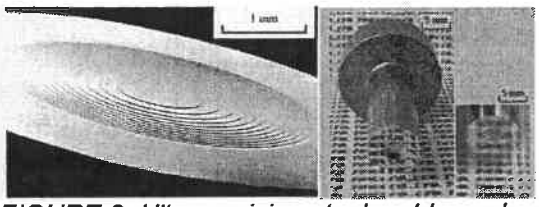

FIGURE 9. Ultraprecision steel molds made with the 2-D VAM system in Figure 3 (left) Fresnel lens mold (right) "Pick-up lens" lens mold [8]

CONCLUSIONS

The interrupted cutting characteristic of vibration-assisted machining leads to significant reduction in tool forces, extended tool life, and improved surface finish. The cutting dynamics differ between 1-D and 2-D VAM. Example applications are presented for both 1-D and 2-D VAM.

REFERENCES

[1] Moriwaki, T., Shamoto, E., "Ultraprecision Diamond Cutting of Hardened Steel by Applying Elliptical Vibration Cutting", 1999, *CIRP Annals* v48:1

[2] Negishi, N., "Elliptical Vibration-Assisted Machining with Single Crystal Diamond Tools", MS thesis, NCSU, 2003

[3] Shamoto, E., Moriwaki, T., "Study on Elliptical Vibration Cutting", 1994, *CIRP Annals* , v43:1

[4] Astashev, V., Babitsky, V., "Ultrasonic Cutting as a Nonlinear (Vibro-Impact) Process", 1998, *Ultrasonics*, v. 36

[5] Cerniway, M., "Elliptical Diamond Milling: Kinematics, Force, and Tool Wear", MS thesis, NCSU, 2001

[6] Weber, H., Herberger, J., Pilz, R., "Turning of Machinable Glass Ceramics with an Ultrasonically Vibrated Tool", 1984, *CIRP Annals* v33:1

{7] Jin, M., Murakawa, M., "Development of a Practical Ultrasonic Vibration Cutting Tool System", 2001, *J. of Materials Processing Technology*, v113

[8] Shamoto, E., *JSPE News*, Dec 2005

[9] Babitsky, V., Mitrofanov, A., Silberschmidt, V., "Ultrasonically-Assisted Turning of Aviation Materials: Simulations and Experimental Study", 2004, *Ultrasonics*, v42

[10] Gao, G., Zhao, B., Jiao, F., "Research on Influence of Cutting Conditions on Surface Microstructure of Ultra-thin Wall Parts in Ultrasonic Vibration Cutting", 2002, *J. of Materials Processing Technology*, v129:1-3

MICRO-STRUCTURE FABRICATION USING ELLIPTICAL VIBRATION-ASSISTED MACHINING (EVAM)[1]

D. E. Brehl, T. A. Dow, K. Garrard, and A. Sohn
Precision Engineering Center
North Carolina State University
Raleigh, North Carolina, USA

INTRODUCTION

"Elliptical vibration-assisted machining" (EVAM) is a diamond-tool machining process that can be used to create 3-dimensional micro-structures. In EVAM, the tool tip is driven very rapidly through a small (tens of micrometers) ellipse at multi-kHz frequencies; this elliptical motion is superimposed on the normal tool feed motion. EVAM shows potential for fabrication of micro-scale devices in true 3-D geometry, with greater material and shape flexibility than lithography methods derived from the semiconductor industry. When feature tolerances of ~200 nm suffice, it is more economical than methods such as micro-electro-discharge machining, focused ion beam, or laser ablation. EVAM also avoids problems of tool deflection, chatter, runout, and vibration associated with chip-making processes like micro-milling [1]. It can achieve cut edges which are virtually burr-free. Finally, because the tool is cutting in the workpiece for only part of each elliptical cycle, average cutting forces, and tool wear from mechanical and chemical effects, are reduced compared to conventional machining [2].

An EVAM tool, the Ultramill, has been used to make microstructures with binary and non-planar geometries, with minimum feature dimensions of 10 µm. In the future, the Ultramill will be used to machine functional devices that require complex 3-D geometry, minimum feature sizes smaller than 5 µm, aspect ratios greater than 1:1, and optical quality surfaces.

PROCESS DESCRIPTION

Figure 1 shows how EVAM can be achieved using two parallel piezoelectric actuators to drive a diamond tool. Applying cyclic voltages to the stacks causes them to change length in a cyclical manner. The toolholder acts as a linkage to convert the linear stack motion into an elliptical path. By changing the voltage amplitude and/or phase difference between the stacks, the ellipse geometry (aspect ratio, tilt, and dimensions) can be varied through a wide range.

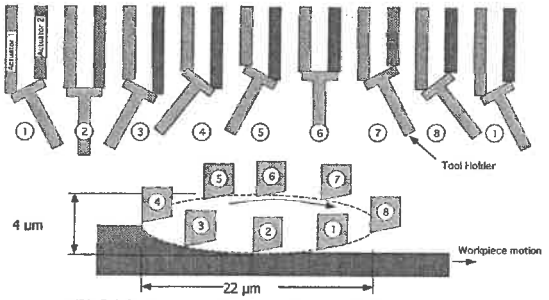

FIGURE 1. Ultramill EVAM concept

Figure 2 shows the tool motion in EVAM for two cutting cycles. During each cutting cycle, the work advances relative to the elliptical tool path. The overlapping toolpaths produce thin chips, resulting in greatly reduced tool forces compared to conventional cutting.

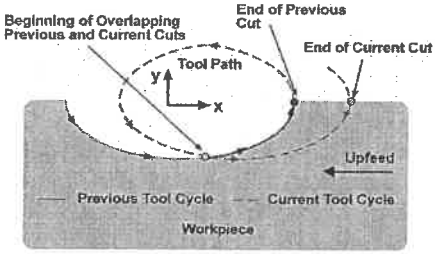

FIGURE 2. EVAM process cycle

Figures 3 and 4 show two different EVAM cutting conditions. In Figure 3, the depth of cut (DOC) is equal to or smaller than the length of the semi-minor axis of the toolpath ellipse. In this case the tool exits the workpiece each cutting cycle, creating small, discontinuous chips. This results in near-zero burr formation on the end and side edges of the cut. Figure 4 shows the case where the DOC exceeds the

[1] Work performed under NSF grant DMI-0423315, monitored by G. Hazelrigg. Additional support from Oak Ridge National Laboratory and Sandia National Laboratories.

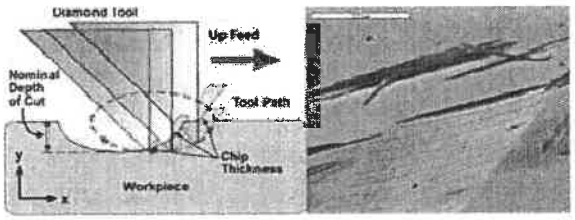

FIGURE 3. EVAM with DOC smaller than semi-minor axis of tool ellipse creates discontinuous chips and burr free edges.

semi-minor axis of the toolpath ellipse. In this case the tool still breaks contact with the uncut material during each cycle, but a long continuous chip remains attached to the workpiece. Thin segments are formed each cycle, attached to the continuous chip.

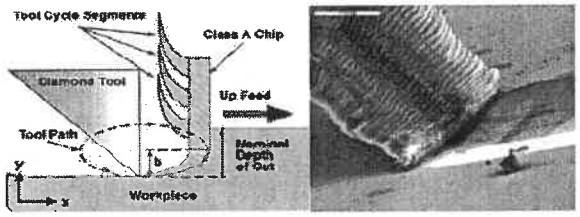

FIGURE 4. When DOC is greater than semi-minor axis of tool ellipse, EVAM produces a continuous chip with attached segments.

To create features that have a significant dimension in the depth direction, roughing passes can be made at a DOC larger than the semi-minor axis of the tool path ellipse. This economically achieves most of the required material removal. A finish pass is then made with DOC smaller than the ellipse semi-minor axis, to complete the part with burr free edges, excellent surface finish, and sub-micrometer feature tolerance.

EQUIPMENT

Figure 5 shows a cutaway view of the Ultramill. The two piezoelectric actuators are cooled by a dielectric fluid circulating continuously through the steel chamber. The hollow lightweight ceramic toolholder rests on alumina pins on the tops of the piezo stacks. A diamond tool is cemented to the toolholder. The titanium diaphragm exerts the required preload force on the piezo stacks and seals the coolant chamber. The Ultramill operates at frequencies up to 4 kHz.

Figure 6 shows the Ultramill installed on a diamond turning machine (DTM), which provides

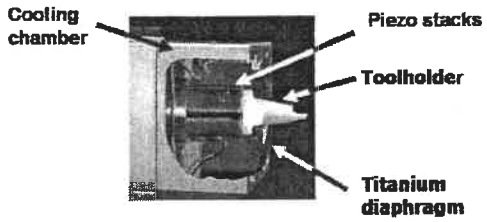

FIGURE 5. Ultramill EVAM tool

3-axis X-Y-Z motion for raster machining (the spindle is locked when using the Ultramill). The DTM's three axes are supported by hydrostatic oil bearings with nanometer-scale encoder resolution. The workpiece is held in place for machining by a vacuum chuck attached to the spindle. To facilitate touchoff, a video-microscope camera provides a view of the tool rake face and the work surface.

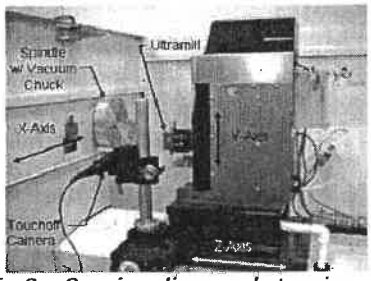

FIGURE 6. 3-axis diamond turning machine (DTM). Spindle is currently locked when using the Ultramill.

MACHINING RESULTS

Binary Microstructures

Figures 7 and 8 show white-light interferometer images of binary feature parts made with the Ultramill. These features are 500 nm tall. They were made using round-nosed diamond tools[2] with 0° rake angle and 10° clearance angle. The Angstrom symbols in Figure 9 are machined in hard-plated copper. The large Angstrom is 1 mm x 1 mm and was made with a 1 mm nose radius tool. The small Angstrom symbol (inset in Figure 7) is shown to the same scale as the large symbol, and is 200 µm x 200 µm. It was made using a tool with a 50 µm nose radius. Its smallest feature (vertical bar on the topknot symbol) is only 10 µm across. The Angstrom symbols have RMS surface roughness of 15-25 nm and are seen to be burr-free when imaged by SEM. The thunderbird logo in Figure 8 was machined in 17-4 stainless steel (34 RHC hardness, 0.1% carbon content) using a 1 mm

[2] Provided by Chardon Tool (Chardon, OH)

nose radius tool. It is approximately 1.08 mm x 1.08 mm, with surface roughness of 20 nm RMS with burr-free edges. Because of the shallow height of these structures, they were made with a DOC less than the semi-minor axis of the ellipse, as described in Figure 3.

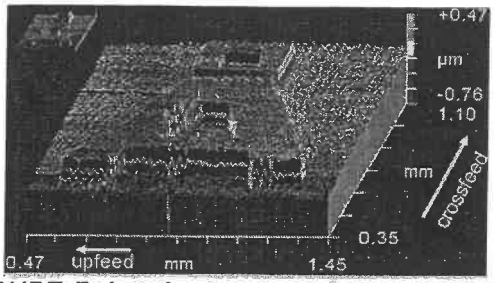

FIGURE 7. Interferegram of Angstom symbols in plated copper. Overall size 1 mm x 1 mm (main figure) and 200 µm x 200 µm (inset)

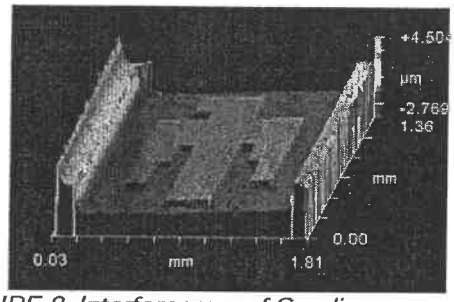

FIGURE 8. Interferogram of Sandia "thunderbird" logo in 17-4 PH stainless steel.

Non-planar Microstructures

Figure 9 shows an array of features with concave sculpted surfaces along the upfeed direction. The feature radius of curvature on the trailing side is 250 µm compared to 50 µm on the approach side. The features are 9 µm tall on a 9 µm deep background and were made in a single material removal pass. The depth dimension of the part is greater than the semi-minor axis of the ellipse (see Figure 4) so the tool entered and exited the workpiece at shallow angles to prevent burr formation.

To make non-planar surfaces, the motion of the center of the toolpath ellipse must be properly offset from the surface. For each point on the feature, the contact point on the toolpath ellipse is found which is mutually tangent to the surface. The ellipse center point location relative to the contact point is determined by the ellipse geometry, and is used in the DTM motion program. The offset from the surface contact point is different with different tangent slopes.

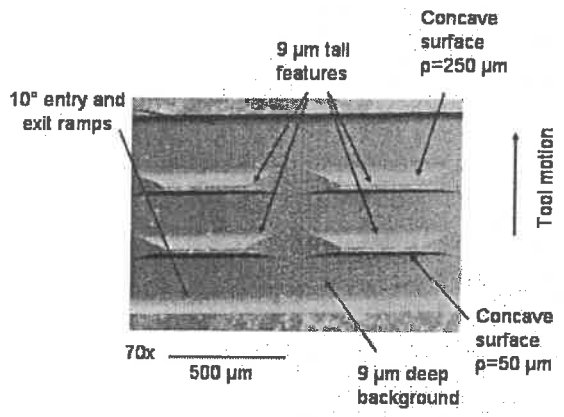

FIGURE 9. Non-planar microstructures with concave surfaces in direction of tool motion

Trihedrons

Figure 10 shows SEM images of trihedrons machined in hard-plated copper. The large trihedrons are 80 µm tall on a 112 µm side pitch. The small interstitial trihedrons are approximately 10 µm tall and show no burr at 4000x. These parts were created using a sharp diamond tool with an included angle of 70.6°, 0° rake angle, and 10° clearance angle. To make these parts, one set of parallel grooves was cut. The spindle was then rotated 60°, with the part also translating in X and Y as it was located off spindle center. The tool was moved to compensate for this translation and a second set of parallel grooves machined. Another 60° rotation was made and the process repeated for the last set of grooves. The interstitial features were obtained by offsetting the center of the machining coordinate system from the spindle center of rotation by 5 µm. Each groove was made by a series of roughing cuts 10 µm deep, followed by shallow finishing cuts to eliminate burrs.

ACTIVE and FUTURE PROJECTS

Microcontactor Pins

Figure 11 shows the contactor element for a microrelay. To increase device reliability, a groove pattern was machined into the contactor pins to provide clearance for particles that could otherwise interfere with operation. The contactor pins are 160 µm in diameter and made of a gold/glass matrix. The grooves are 5 µm deep with approximately a 1:1 aspect ratio. To make these small-scale features, a sharp-nose tool (included angle of 40°) was used. The pin tops have a sinusoidal profile of amplitude 2 µm in the upfeed direction.

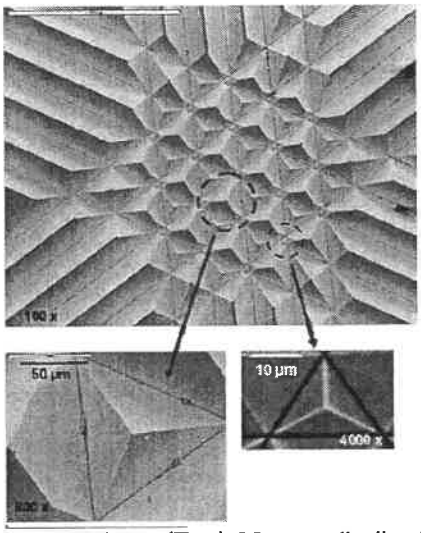

FIGURE 10. (Top) 80 µm tall trihedrons in plated copper. (Lower left) Detail of 80 µm trihedron (Lower right) Interstitial trihedron 10 µm tall.

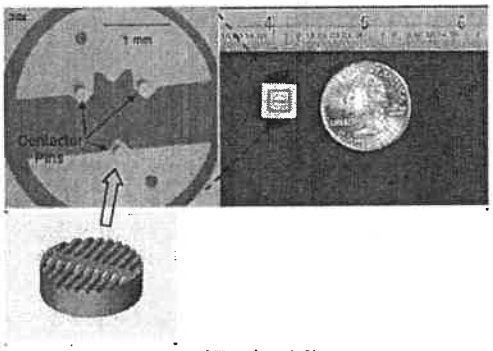

FIGURE 11. (Top) Microcontactor element (Lower left) Groove pattern to be machined onto each pin.

Machining the groove pattern into each pin required the Ultramill tool tip to be placed precisely on the part. Figure 12 shows a videomicroscope camera installed beside the Ultramill. This camera gives a plan view of the part. The X and Y axes are jogged to position the camera crosshairs on the part. The axes are then moved through a set offset distance (determined during setup) to place the tool tip at the desired location.

Microgripper

To demonstrate its ability to fabricate functional microdevices with integrated mechanical and optical elements, the Ultramill will make the microgripper shown in Figure 13. The transparent polycarbonate gripping elements act as light pipes. As the gap between the gripper tines changes, the amount of light coupled

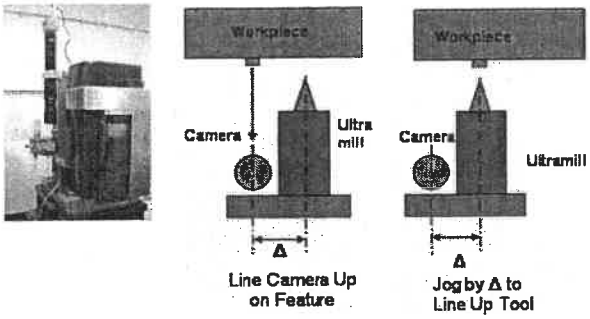

FIGURE 12. Tool tip positioning in X-Y coordinates, using Y-axis camera.

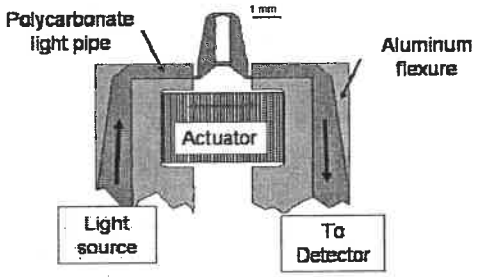

FIGURE 13. Microgripper

through the gap changes proportional to displacement. This provides feedback of gripper separation. When the gripper encounters an object, the light between the tines will be blocked. Successful operation of the gripper requires light pipe surfaces to be machined to an optical quality finish, to achieve total internal reflection. To facilitate fabricating the gripper's complex geometry, a rotational (C) axis will be added to the diamond turning machine, for precision angular positioning of the work relative to the tool tip.

CONCLUSIONS

The Ultramill has been used to create binary, nonplanar, and trihedron microstructures up to 80 µm tall. Diamond tools with round and sharp nose geometry have been used successfully. Roughing and finishing passes can be used to achieve large depth dimension features while avoiding burr formation. Fabrication is planned of functional devices with complex geometry and requiring optical quality finishes.

REFERENCES

1 Benivedes, G., "Meso-Machining Capabilities", M[4]: Workshop on Micro / Meso-Mechanical Manufacturing, Evanston, IL, May 2000.

2 Cerniway, M., "Elliptical Diamond Milling: Kinematics, Force, and Tool Wear", MS thesis, North Carolina State University, 2001.

FABRICATION OF MICRO-COMPONENTS USING VIBRATION-ASSISTED MICRO- EDM

Takashi Endo[1], Takayuki Tsujimoto[1], and Kimiyuki Mitsui[2]
[1]School of Integrated DESIGN Engineering
Keio University, Yokohama, Kanagawa, JAPAN
[2]Department of Mechanical Engineering
Keio University, Yokohama, Kanagawa, JAPAN

INTRODUCTION

Due to the advances in micro-machining technology, the development of a method for measuring both the profile and dimensions of micro-components has been in strong demand. One of the available methods is a small, three-dimensional profile-measuring apparatus with micro-probes. Related to this, we have investigated fabrication technologies using micro-electric discharge machining (micro-EDM) [1] for micro-probes that are used for a small, three-dimensional coordinate-measuring machine [2]. However, the machining of relatively complicated probes such as slanting probes is very difficult due to unstable machining conditions. Thus, a long time is required for probe fabrication, and it is sometimes impossible to perform normal machining due to the improper flow out of the cutting chip powder.

For this reason, we carried out some fundamental experiments on vibration-assisted micro-EDM, which is considered effective in improving machining stability [3]. The results clearly indicate that the oscillating tool electrodes have a major influence on the machining time. In this report, first the relation between the machining characteristics (machining time, electrode wear and surface roughness) and vibration-assisted micro-EDM are described. Then, we focus on the phenomenon called adhesion, which is considered to be a main cause of an unstable machining state, and investigate the relation of vibration and adhesion. These results reveal that vibration-assisted micro-EDM reduces adhesion and machining time. Finally, we describe our implementations of vibration-assisted micro-EDM to the micro-parts fabrication and machining of brass and especially titanium, which is difficult to machine with conventional machining methods such as cutting or grinding.

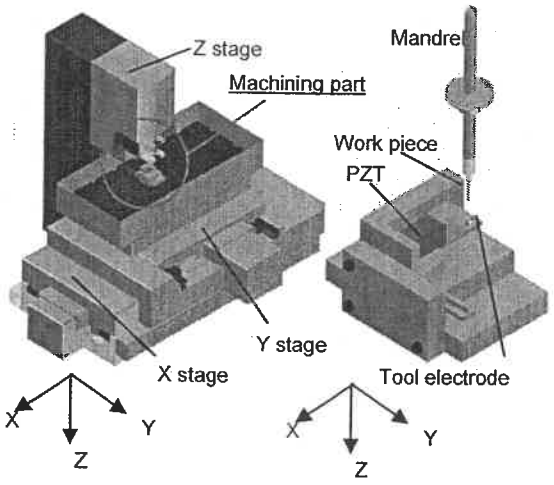

Figure 1: (Left) Overview of micro-electric discharge machine. (Right) Enlarged view of the machining part with the vibrating device.

EXPERIMENTAL SETUP

Figure 1 shows an outline of the micro-EDM machine (MG-ED72, Panasonic Electronic Devices Co., Ltd.) and an enlarged picture of the piezoelectric zirconate titanate (PZT) actuator holder. The tool electrode and the workpiece are set to negative and positive polarity, respectively. The pulse generator of the micro-EDM machine is an RC circuit and R=1.1 kΩ. Although Muro has reported on the relation of the feed rate and machining speed as well as the vibration frequency and machining speed for vibration-assisted micro-EDM [4], no systematic investigations have yet been conducted. In this research, a 20-mm-long laminating type PZT actuator (AE1010D16, Tokin Co., Ltd.) with a maximum displacement of 12 μm is used. A tool electrode is attached to a holder, which is joined to the PZT actuator. In our machining experiments, a workpiece of diameter 300 μm, which is held by a mandrel, is machined by the vibrating tool electrode (Ag-W, 10 mm × 10 mm × 1.2 mm), as shown in Fig. 2. The electrodes and workpieces are products of KAKOH Co., Ltd. The vibration amplitude used in the following description is measured in the air using a capacitive-type displacement sensor. However,

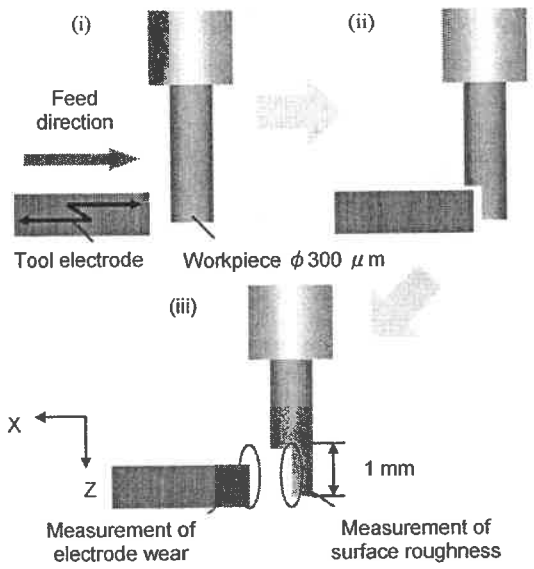

Figure 2: Machining process for the workpiece and the measurement locations.

the vibration amplitude of the PZT might be decreased because EDM is done in the EDM fluid. Therefore, the measurement results for the vibration amplitude in the air and in the EDM fluid are shown in Fig. 3. The vibration amplitude of the PZT was measured by using a strain sensor. In this experiment, it is shown that the vibration amplitude does not change much, even in the EDM fluid. Also, the feed direction on the tool electrode can be parallel to the PZT vibration direction, as shown in Fig. 4(a), and perpendicular to the PZT vibration, as shown in Fig. 4(b). In this paper, the vibration direction is assumed to be parallel to the feed direction, unless otherwise noted.

EXPERIMENTAL RESULTS

In this section, we describe the experimental results and two applications of vibration-assisted machining.

Characteristics of vibration-assisted machining

First, we describe the machining characteristics of the vibration-assisted micro-EDM in this study. The machining conditions are an open voltage of 100 V, a capacitance of the RC pulse generator of 3300 pF, a constant feed rate of 10 □m/s for a total feed of 150 μm in each experiment. Figure 5 shows the machining time until the 150 μm feed is achieved. From this figure, it is confirmed that vibration-assisted machining reduces the machining time. In addition, it seems that a higher frequency and larger amplitude of vibration is effective. Consequently, it is

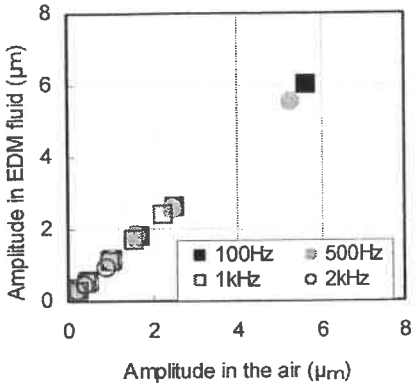

Figure 3. Effect of EDM oil on vibration amplitude in several frequencies.

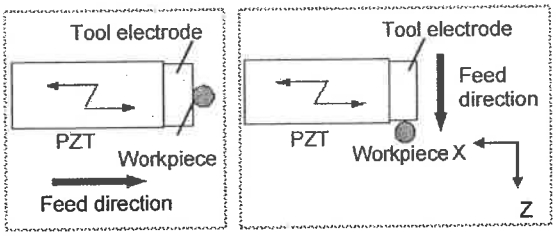

Figure 4: (Left) Vibration direction is parallel to feed direction. (Right) Vibration direction is perpendicular to feed direction.

confirmed that there are two factors involved in vibration-assisted machining. One is that discharge points are dispersed on the workpiece surface due to the oscillating of the electrode. And this leads to prevent an unusual discharge or concentration of discharge. The second factor is that a short circuit and adhesion (welding), which is described below, are avoided by flushing out of a cutting chip powder from the discharge gap. Higher frequency and larger amplitude of vibration is considered to be more effective in managing these factors, and, as a result, seems to reduce the machining time.

Figure 6 shows the electrode wear measured by using a surface roughness tester after machining. The machining was repeated in the same condition for three times in order to make the difference clear. According to this result, the amount of wear is almost the same in each condition. Figure 7 shows the surface roughness of the machined surface of the workpiece. The surface roughness was measured by a laser microscope. The measuring length was 0.5 mm for one measurement. Although the variations in each condition are large, it seems that vibration-assisted-machining has a minor effect on surface roughness.

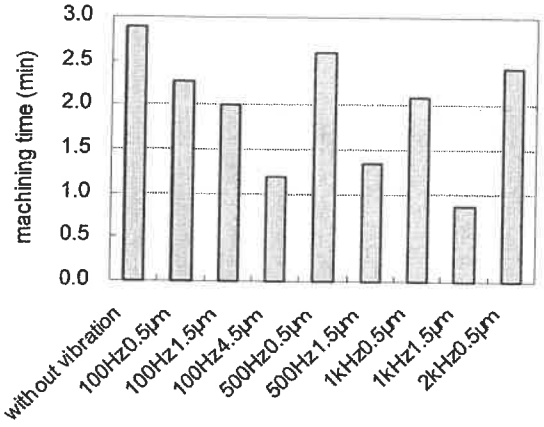

Figure 5. Machining time in vibration-assisted micro-EDM.

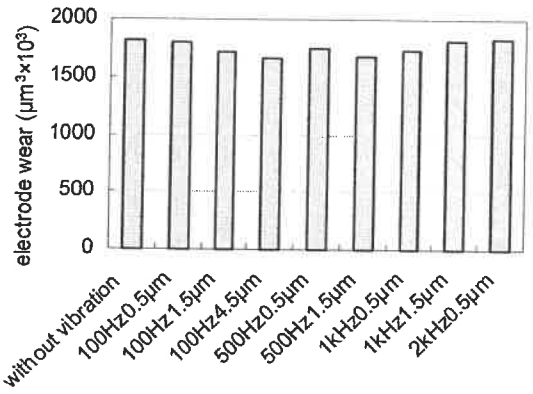

Figure 6. Electrode wear in vibration-assisted micro-EDM (result of machining three times).

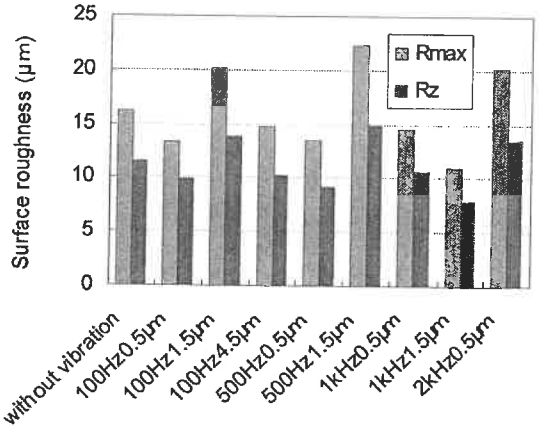

Figure 7. Surface roughness in vibration-assisted micro-EDM.

Effect of vibration on machining status

The micro-EDM machine employs a constant feed rate control for the feeding system, and feeding back action for a short circuit to maintain the gap distance between the workpiece and tool electrode. Therefore, under the unstable condition in which a short circuit occurs often, feeding back is needed often, and results in the increase of machining time. In order to investigate this machining stability, we measured the frequency of the discharge pulses with a current probe and simultaneously measured the table movement of the EDM machine in the X-direction (feed direction) with a laser displacement sensor. The data were recorded by an A/D converter (Maximum sampling frequency is 40 MHz), and then transferred the data to a personal computer.

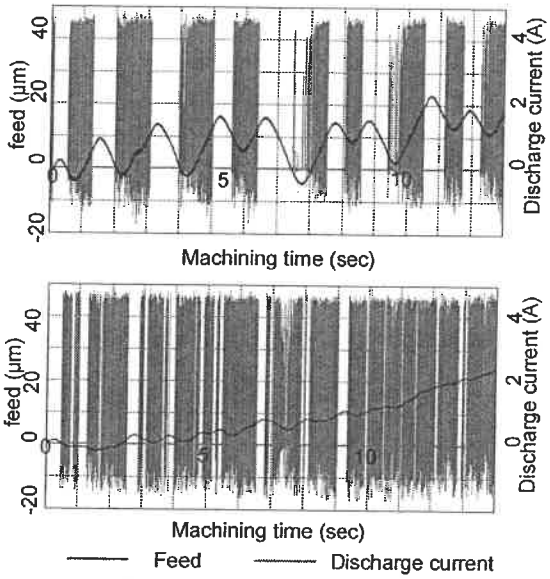

Figure 8: (Top) Discharge current and the movement of the worktable without vibration. (Bottom) Discharge current and the table movement with vibration (1 kHz, 1.5 μm).

Figure 8 shows the results of this measurement. In this experiment, the workpiece length is 7 mm in each condition and the sampling frequency is 1 MHz. The results indicate that the frequency of the discharge pulse increases when vibration is applied to the tool electrode. As for the table feeding back action due to a short circuit in vibration-assisted machining, the maximum table feeding back is rather small at around 3 μm. In other words, the EDM process is comparatively smooth. On the other hand, in machining without vibration, the table feeding back is large at about 20 μm, and frequent feeding back actions are also observed. From these experimental results, we confirmed the increase of the discharge pulse frequency and the decrease of the table feeding back action by applying vibration in the micro-EDM process. This leads to stabilization of the discharge current.

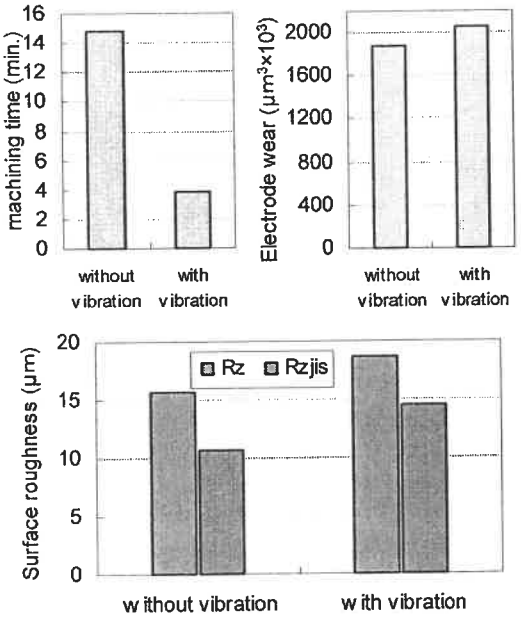

Figure 9: (Top Left) Machining time of titanium. (Top Right) Electrode wear of titanium. (Bottom) Surface roughness of titanium.

Applications of vibration-assisted micro-EDM

Here, we describe two examples of vibration-assisted micro-EDM. One is the machining of titanium. According to the $\lambda \cdot \theta$ theory, the machining of titanium with EDM is expected to be easy, but, in fact, it's just the opposite. This is attributed to the situation that the cutting chip powder of titanium tends to cause adhesion and a short circuit. As described above, vibration-assisted machining is considered to be effective in resolving the problem of adhesion and a short circuit, and so we attempted vibration-assisted machining of titanium. Figure 9 shows the characteristics of machining for titanium. In this example, the basic method of machining and measurement was the same as the machining for brass. From these figures, it is confirmed that vibration-assisted machining is highly effective in reducing the machining time.

As another example, we attempted the fabrication of a square shaft (50 μm × 50 μm) by vibration-assisted micro-EDM. The workpiece was brass and we machined the wokpiece three times in different conditions, as shown in Table 1. Figure 10 shows the results of the fabrication with vibration-assisted machining. The total machining time for fabrication without vibration was 16.15 min and that with vibration (1 kHz, 1.5 μm) was 8.60 min.

Table 1 Machining conditions for fabrication of a square shaft

	Open voltage (V)	Capacitance (pF)	cutting depth (μm)	feed rate (μm/s)
Roughing	-100	3300	90	7
1st finishing	-90	100	20	4
2nd finishing	-60	10	15	1

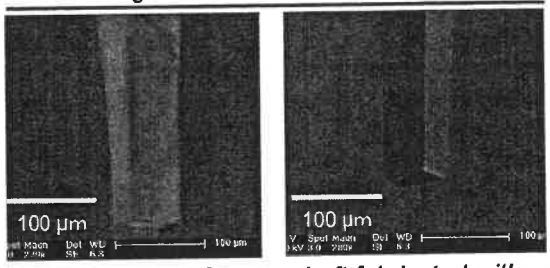

Figure 10: (Left) Square shaft fabricated without vibration. (Right) Square shaft fabricated with vibration.

CONCLUSIONS

The results obtained from the experiments are summarized as follows. A remarkable reduction of the machining time is observed by applying vibration to the tool electrode. We confirmed that higher frequency and larger amplitude vibration decreases the machining time. However, vibration-assisted machining has minor effects on electrode wear and surface roughness. Also, an increase of the discharge pulse frequency and a decrease of the table feeding back action is observed by applying vibration to the micro-EDM process. In addition, it is confirmed that vibration-assisted micro-EDM can be applied to the machining of titanium and the fabrication of a square shaft.

REFERENCES

1. Masuzawa T., Micro-EDM, In: Proceedings of International Symposium for Electromachining 13th. 2001, 3-19
2. Kawada M., Mitsui K., Fabrication of Probes for Profile Measurement of Micro-EDM Manufactured components, Nanotechnology and Precision Engineering, 2004, Vol.2, No.2, 124-131.
3. Hirai M., Kawada M., Endo T., Mitsui K., Fabrication of Probes for Profile Measurement of Microcomponents by Micro-EDM (Microprobe Fabrication and Effect of Vibration Assisted Micro-EDM on Machining time), Transactions of The Japan Society of Mechanical Engineers (c), 2005, Vol.72, No.709, 2819-2825. (in Japanese)
4. Muro M., Ikemoto Y., Gawa T., Masaki T., Furusawa Y., Micro-hole machining by vibration-assisted EDM, Proceedings of the Annual meeting of Japan Society of Electrical Machining Engineers, 1994, 19-20.

POLISHING OF SINGLE POINT DIAMOND TOOL BASED ON THERMO-CHEMICAL REACTION WITH COPPER

Masahiro Higuchi[1], Tomomi Yamaguchi[1], Shoichi Shimada[2], and Kazushi Obata[3]
[1]Kansai University, Dept. of Mechanical Systems Engineering
Suita, Osaka, Japan
[2]Osaka Electro-Comunication University, Dept. of Mechanical Engineering
Neyagawa, Osaka, Japan
[3]A.L.M.T. Diamond Corp.
Takino, Hyogo, Japan

Abstract:
This paper describes a new polishing method for diamond cutting tools. It is based on the principle of oxidization of copper and deoxidization of copper oxide by diamond. Practically speaking, a diamond tool is brought into contact with copper plates heated to a temperature range from 323 K to 523 K in air. The wear amount of the diamond increased almost exponentially with contact time and reached about 30 nm after 6 hours. In this erosion process, pre-existing microcracks on the diamond surface were eliminated. Accordingly, the thermo-chemically polished tool is highly resistant to chipping and yields a remarkable rise in tool life compared to the mechanically polished one.

1. Introduction

The cutting edges of a single point diamond tool are usually carefully formed by fine polishing with a scaife. However, mechanical polishing produces microcracks on the diamond surface because of the high polishing pressures and elevated temperatures. The microcracks lengthen as a result of the thermo-chemical erosion of oxygen at their tips, and thereby reduce the microstrength of the diamond [1]. This is thought to be the source of chipping that occurs on cutting edges during the tuning process. Hence, the elimination of microcracks is very important because the workpiece quality and/or tool life are reduced due to the occurrence of chipping.

To solve this problem, novel polishing methods have been proposed using various techniques, including the diffusion of carbon atoms into a certain sort of metals [2], the sputtering-off of carbon atoms by bombardment of energized ions [3], and tribochemical polishing combining mechanical abrasion and chemical dissolution of surface atoms [4]. These methods, however, possess drawbacks in terms of difficulty of use and high cost. Thus, a simpler polishing method, based on thermo-chemical reaction with copper, is proposed and discussed in this paper.

2. Principle of thermo-chemical polishing

Figure 1 shows the Ellingham diagram in which the change in Gibbs's free energy, ΔG^0_T, for oxide formation of copper and carbon for 1 mol oxygen is shown as a function of atmospheric temperature [5]. As seen from the diagram, the values of ΔG^0_T are negative. Hence, chemical reactions can occur between C and O_2, according to the equations: $C+O_2 \rightarrow CO_2$ and $2C+O_2 \rightarrow 2CO$. In addition, a reaction can occur between Cu and O_2, according to the equations: $2Cu+O_2 \rightarrow 2CuO$ and $4Cu+O_2 \rightarrow 2Cu_2O$. The diagram also shows that the values of ΔG^0_T for

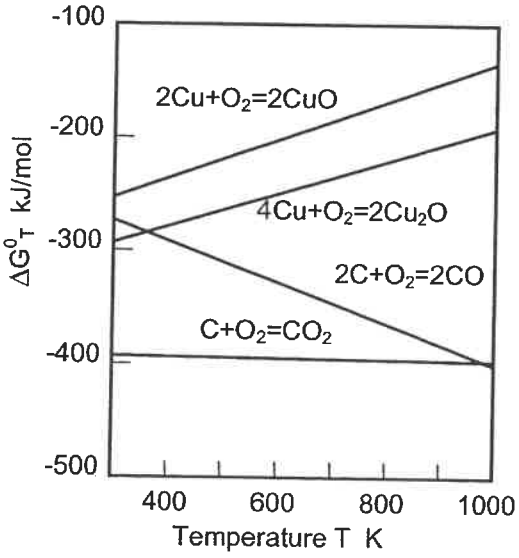

FIGURE 1. Change in Gibbs's free energy during oxide formation of copper and diamond for 1 mol oxygen.

the formation of CO_2 or CO are lower than those for the formation of CuO or Cu_2O. This suggests that when carbon atoms are close to copper oxide, they deoxidize it and are themselves oxidized. Therefore, by bringing diamond into contact with copper oxides at temperatures higher than room temperature in air, there is a very fair possibility of taking carbon atoms on its surface away.

3. Properties of thermo-chemical polishing

In order to ensure that the oxidization-deoxidization reaction mentioned above is applicable to the polishing of diamond tools in practice, erosion tests were carried out. A diamond specimen was brought into contact with copper plates heated to a range of temperatures from 323 K to 523 K in air. The specimen was natural monocrystalline diamond finished mechanically as smooth as the rake face of diamond tools. On its surface, a tiny ring crack was produced to measure its wear amount.

The erosion tests showed that the wear amount increased almost exponentially with contact time and reached about 30nm after 6 hours, as shown in Fig. 2. Figure 3 shows the Arrhenius plot of the wear rate versus the heating temperature. The decrease in wear rate is very nearly linear with decreasing temperature, and the apparent activation energy for the erosion of diamond in contact with copper is calculated to be 218 kJ/mol. According to Fig.1, a change in free energy ΔG^0_{523K} of more than 133 kJ/mol is required for the deoxidization of copper oxide by carbon at 523 K. Since the activation energy obtained exceeds ΔG^0_{523K}, it was confirmed that the carbon atoms on the diamond surface could be removed through oxidization accompanied by deoxidization of copper oxide.

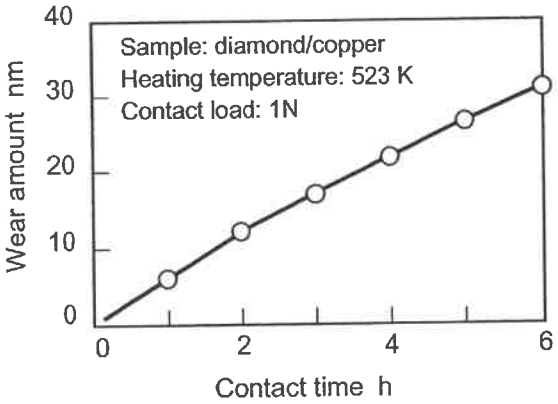

FIGURE 2. Variation in wear amount with contact time.

Next, Hertzian fracture tests were carried out in order to indirectly investigate whether surface microcracks can be eliminated by thermo-chemical polishing. The test involves pressing a spherical diamond indenter with a 50 μm tip radius on the flat specimen surface. If microcracks exist at the maximum tensile stress circle of the contact area, a ring crack fracture occurs. The average contact pressure at the moment yields the fracture strength of the specimen.

Figure 4 shows the change in fracture strength of the diamond specimens in contact with a copper plate or copper powder heated to 523 K. The strength of the diamond put in the copper power clearly decreases as the contact time

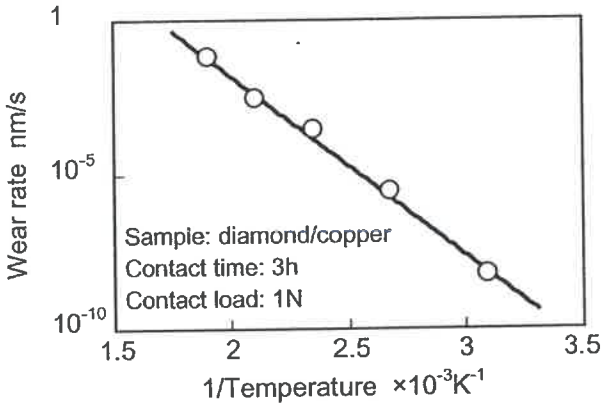

FIGURE 3. Arrhenius plot of wear rate versus temperature.

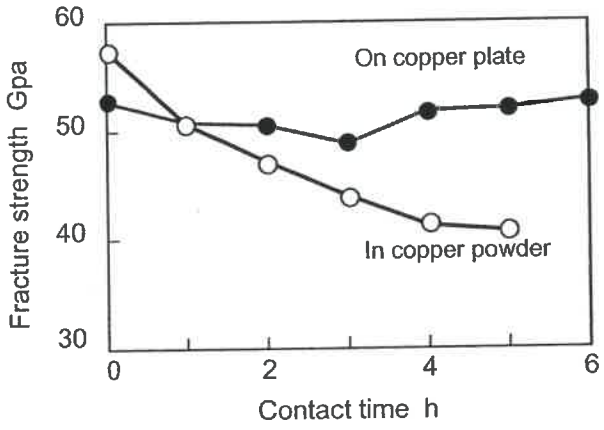

FIGURE 4. Change in fracture strength of diamond in contact with copper heated to 523 K.

increases. This phenomenon is explained as follows [1]. On the solid surface, thermally activated atoms frequently jump in and out of the surface. The carbon atoms which jump out of the crack tip are oxidized by thermally activated oxygen and eliminated as CO or CO_2. Simultaneously, vacancies diffuse into the bulk from the crack tip on the diamond surface, and the microcracks thereby lengthen and reduce the strength. In this case, the copper powder functions as a catalyst and accelerates the extension of the crack. On the other hand, the strength of the diamond placed on the heated copper plate decreases and then increases as the contact time increases. This increase in strength is probably due to the elimination of microcracks existing on the diamond surface. This is because when a diamond surface of few tens of nanometers is eroded by the oxidization-deoxidization reaction, the microcracks are also removed. This thermo-chemical polishing is thus very promising as a finishing technology of diamond tools.

4. Durability of thermo-chemically polished diamond cutting tool

In order to demonstrate the effects of thermo-chemical polishing on the wear resistance and life of a cutting tool, diamond turning of electrolytic deoxidized copper was carried out using the thermo-chemically polished diamond tool and a mechanically polished one. Table 1 shows the detailed tool geometries and cutting conditions that were used.

When turning copper, crater wear and notch wear occur on the rake face where the chip flows. Moreover, chipping occurs on the cutting edge, as shown in Fig. 5. These different types of tool failures can be measured by the following method [6].

TABLE 1. Tool geometries and cutting conditions.

Cutting tool	Material	Monocrystalline diamond
	Crystallographic orientation	(100) rake plane (110) front plane
	Included angle [deg]	130
	Rake angle [deg]	0
	Clearance angle [deg]	7
Workpiece	Material	OFHC (ASTM F6 Class 1)
Cutting conditions	Cutting speed [m/s]	15.7
	Feed rate [μm/rev]	3
	Depth of cut [μm]	6.7
	Blowed gas	Air

The level of wear can be distinguished by the qualitative difference in the dynamic component of the cutting force. When the tool wear is high, the cutting force fluctuates self-similarly, namely, $1/f^{\beta}$ noise with a spectral exponent of $\beta>1$ appears in the cutting force. On the other hand, when chipping occurs, acoustic emission (AE) due to fracture is released. This type of AE can be detected by the AE amplitude distribution spectrum follows the power law $N \sim a^{-m}$ with a scaling exponent of $m<2$, where N is the AE event rate and a is the AE amplitude. In addition, at the end of the life of diamond tools, the tool wears out and chipping of the cutting edge occurs simultaneously. Therefore, knowing that the spectral exponent is always greater than 1 for the cutting force and that the scaling exponent is always less than 2 for the AE, the end of the life of a tool can be effectively detected.

Judging from the criteria mentioned above, there is considerable difference in the wear resistance between the two tools. As seen from Fig. 6, comparing each cutting distance at which the $1/f^{\beta}$ noise appears in the cutting force, except for the period of the running-in cutting of the fresh tool, the distance for the thermo-chemically polished tool extends to about 1.4 times that of the mechanically polished one. Therefore, the thermo-chemically polished tool is clearly more resistant to wear. In addition, the thermo-chemical polishing manifests its beneficial effects in the form of suppression of chipping, as shown in Fig. 7. In turning with the thermo-

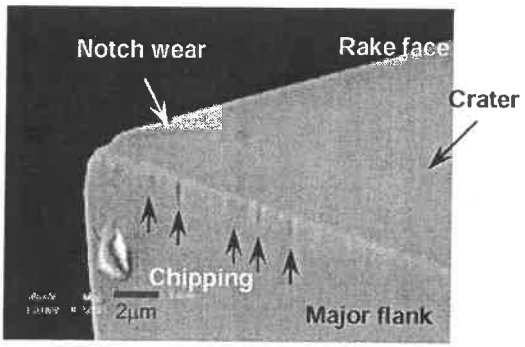

FIGURE 5. Wear pattern of a diamond tool at the end of its life when machining copper.

chemically polished tool, the scaling exponent is seldom less than 2, whereas this occurs often in turning with the mechanically polished tool. Accordingly, it is clear that the thermo-chemically polished tool is also resistant to chipping.

Thus, the improvement in wear resistance extends the durability of a tool. As seen from Figs. 6 and 7, when the cutting distance exceeded 345 km in the case of the mechanically polished tool, the spectral exponent became greater than 1 and the scaling exponent became less than 2. These changes in the signal indicate that the tool comes to the end of its life at a cutting distance of 345 km. On the other hand, the end of the life of the thermo-chemically polished tool was evaluated to occur at a cutting distance of 484 km. Thus, the thermo-chemically polished tool enjoys an unusually long life compared to the mechanically polished one. Our simple polishing method is thus very useful and effective to prolong the tool life.

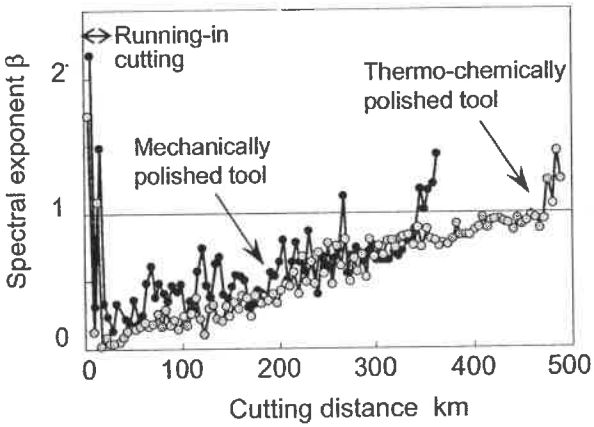

FIGURE 6. Variation in spectral exponent with cutting distance

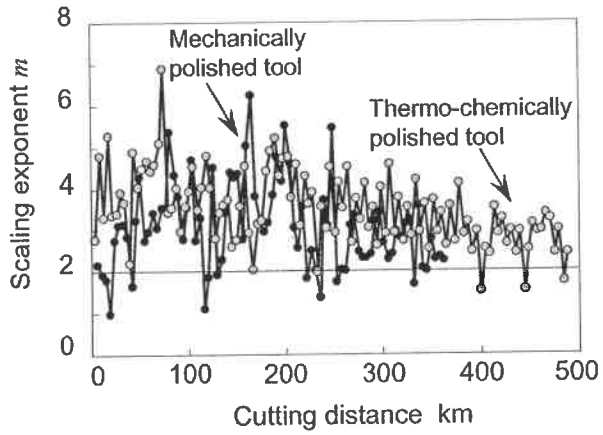

FIGURE 7. Variation in scaling exponent with cutting distance

5. Conclusions

In this paper, a new polishing method for diamond cutting tools has been discussed using thermo-chemical reaction with copper. It is a very simple and practical way of bringing a diamond tool into contact with a copper plate heated in air. Hertzian fracture tests showed that the microstrength of thermo-chemically polished diamond surface becomes higher because of the elimination of microcracks. In addition, the cutting experiments abundantly demonstrated that the thermo-chemically polished tool is superior in terms of the wear resistance and the tool life to the mechanically polished one. Accordingly, thermo-chemical polishing is recommended as a finishing technique for the diamond tool because of its efficiency.

6. Acknowledgments

This study was financially supported by a Grant-in-Aid for Scientific Research from The Japan Society for the Promotion of Science (JSPS No. 17560109-3655).

References

1. Tanaka, H., Shimada, S., Higuchi, M., Yamaguchi, T., Kaneeda, T. and Obata, K., 2005, Mechanism of cutting edge chipping and its suppression in diamond turning of copper, Ann of the CIRP, 54(1): 51-54.
2. Yang, C-F. and Yoshikawa, M., 1991, On Polishing of Diamond Film with Hot Metal, Polishing Mechanism, JSPE, 57(3): 504-509. (in Japanese).
3. Miyamoto, I., 1987, Ultra fine finishing of diamond tools by ion beams, Prec. Engg., 9(2): 71-78.
4. Haisma, J., van der Kruis F.J.H.M., Spierings, G.A.C.M., Oomen, J.M. and Fey, A.M.J.G., 1992, Damage-free tribochemical polishing of diamond at room temperature: a finishing technology, Prec. Engg., 14(4): 20-27.
5. The Japan Institute of Metals, 2003, Physical chemistry of metals, 198-210. (in Japanese).
6. Higuchi, M., Yamaguchi, T., Shimada, S. and Kaneeda, T., 2006, Monitoring of Tool Life in Diamond Turning of Electroless Ni-P, Proceedings of the 6th International conference euspen, Vol.2: 196-199.

TUNABLE HOLDER FOR BORING BARS

Lonnie Houck III[1], Tony L. Schmitz[1], and K. Scott Smith[2]
[1]Department of Mechanical and Aerospace Engineering
University of Florida, Gainesville, FL, USA
[2] Department of Mechanical Engineering and Engineering Science
University of North Carolina at Charlotte, Charlotte, NC, USA

INTRODUCTION

During metal cutting operations, vibratory motion between a cutting tool and work piece can lead to non-beneficial cutting performance. Such vibrations can cause the cutting tool, work piece, and/or machine to become damaged. Self-excited vibrations, or chatter, between the cutting tool and workpiece can cause poor surface finish, tool breakage, and other unwanted effects. When chatter does occur, the machining parameters must be changed and, as a result, productivity may be adversely affected.

One example of tools that may encounter excessive vibration is boring bars, which are typically used to fabricate deep holes. A primary difficulty in their use is that, because the holes tend to be deep and narrow, the boring bars must be long and have small diameters. Therefore, during machining, the variable cutting force causes the tool to deflect and leave a wavy surface behind. When the cutting edge encounters this wavy surface in the next revolution, additional forces and deflections may be caused which can lead to chatter.

Several methods for reducing boring bar vibration are currently used including, for example, internal vibration absorbers. Here, we describe a new method to reduce tool vibrations by providing a flexible holder with dynamics tuned to match the boring bar dynamics. The flexible holder supports the boring bar and acts as a dynamic absorber for the boring bar. The flexible holder natural frequency is matched to the clamped natural frequency of the tool, thereby reducing the amplitude of vibration at the free (cutting) end of the bar.

In this paper we present an analytical solution, which applies Euler-Bernoulli beam theory and receptance coupling techniques, and a finite element model for the assembly dynamics. A holder-boring bar is designed and frequency response measurements of the boring bar alone are compared to the measured response of a prototype holder-boring bar assembly.

RECEPTANCE COUPLING MODEL

Closed-form, Euler-Bernoulli beam receptances [1] were used to describe an ISO A10-SCLPR2 NE4 boring bar with a length to diameter (L:D) ratio of 6:1. This high L:D ratio was selected since the focus of this work is the improvement of the dynamic stiffness for these inherently low stiffness situations. A diameter of 15.9 mm was chosen because this is the smallest diameter for commercially available "tunable" boring bars (with dynamic absorbers located inside the bar). Figure 1 shows the analytical frequency response function (FRF) for the fixed-free (cantilever) beam model representing our steel, cylindrical boring bar.

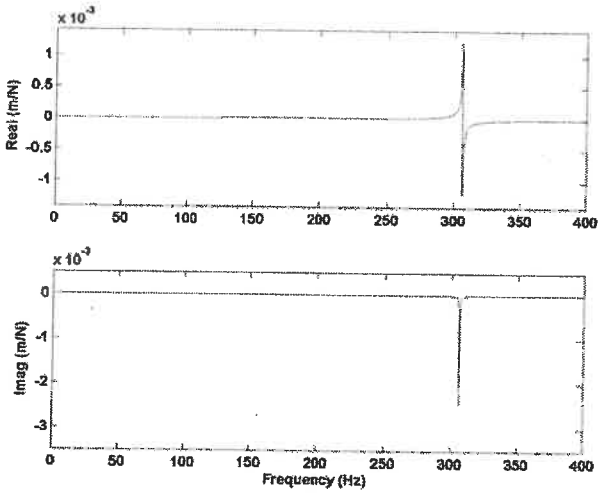

Figure 1: Cantilever response of 6:1 boring bar.

Using the peak picking method [2], a stiffness value of 6.35×10^5 N/m and a damping ratio of 6.5×10^{-4} were determined for the boring bar. A single degree of freedom (SDOF) representation of the cantilever holder was then defined with a stiffness value 20 times greater than the boring bar, but the same natural frequency and damping ratio. Next, the holder model was

coupled to a free-free model of the boring bar using the receptance coupling approach [3-8]. The FRF of the combined holder and boring bar is shown in Fig. 2.

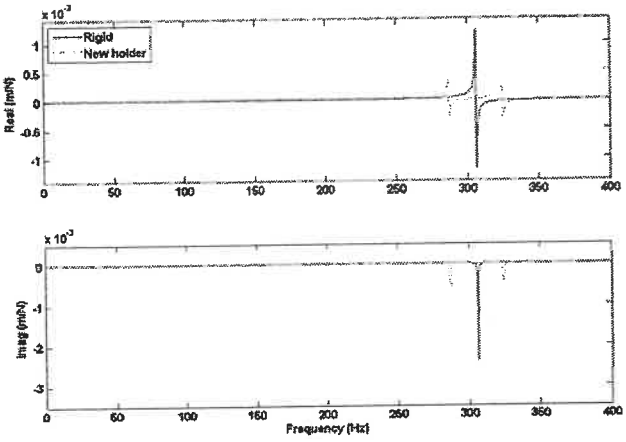

Figure 2: FRFs for the boring bar rigidly coupled to the holder (dotted line) and cantilever boring bar alone (solid line).

Figure 2 shows that the first bending mode of the boring bar is shifted down from 306 Hz to 287 Hz with a 74% reduction in amplitude. A second mode is also observed, but shifted up by the same amount to 324 Hz with the same amplitude. In the bandwidth shown, the system transforms from one bending mode (SDOF) to two bending modes (2DOF), split about the cantilever boring bar natural frequency, due to the addition of the holder. The increased dynamic stiffness of the coupled system is counter-intuitive (i.e., adding a flexible element increases the assembly stiffness), but is similar in nature to the well-known dynamic absorber effect.

FINITE ELEMENT MODEL

Finite element (FE) modeling was used to aid in the design and analysis of the holder. This enabled the convenient analysis of complicated geometries, which is more challenging when applying the analytical beam models that assume constant cross-sections [1]. All models were drawn using Autodesk Inventor 10 and imported into ANSYS Workbench 10 for analysis. Workbench subroutines were used to auto-generate part meshes; mesh refinement was introduced around critical areas. Solid three-dimensional (3D) elements were used and no cross section approximation or beam simplification was applied. Boundary conditions were implemented as appropriate. Each model was then checked for convergence and a final simulation was completed.

The ISO A10-SCLPR2 NE4 boring bar was modeled using cantilever boundary conditions and a harmonic analysis was carried out to identify its dynamic behavior. Figure 3 shows the results of the ANSYS model.

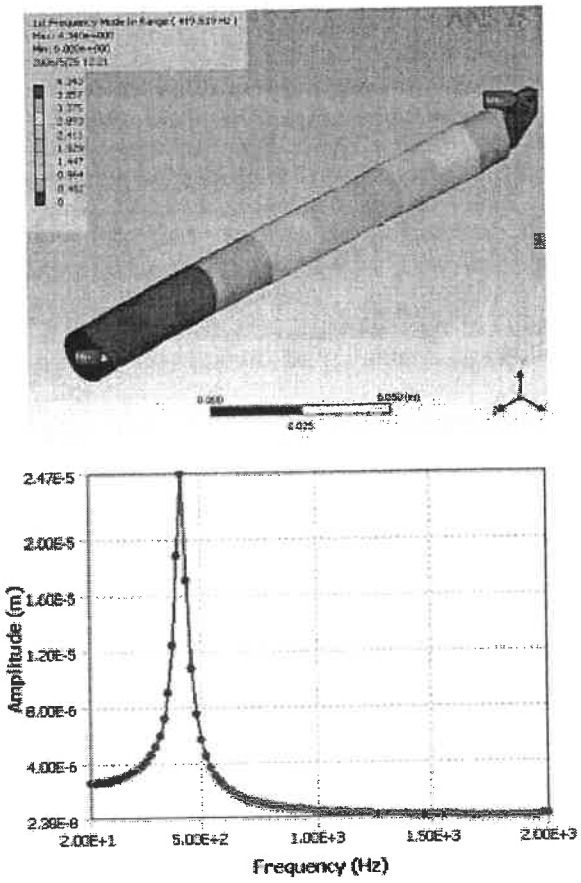

Figure 3: FE model of cantilever boring bar.

A notch-type flexure holder was selected to approximate a SDOF response. The notch and holder geometry were chosen to match the holder fundamental natural frequency to the FE boring bar results. Because high stiffness was required for the holder, the corresponding mass had to be large to realize the low natural frequency (419 Hz). A brass sleeve was clamped around the aluminum holder to obtain the desired response. Next, the boring bar was rigidly connected to the holder and the cantilever assembly FRF was computed; see Fig. 4. A 74% amplitude reduction relative to the boring bar alone (Fig. 3) is observed.

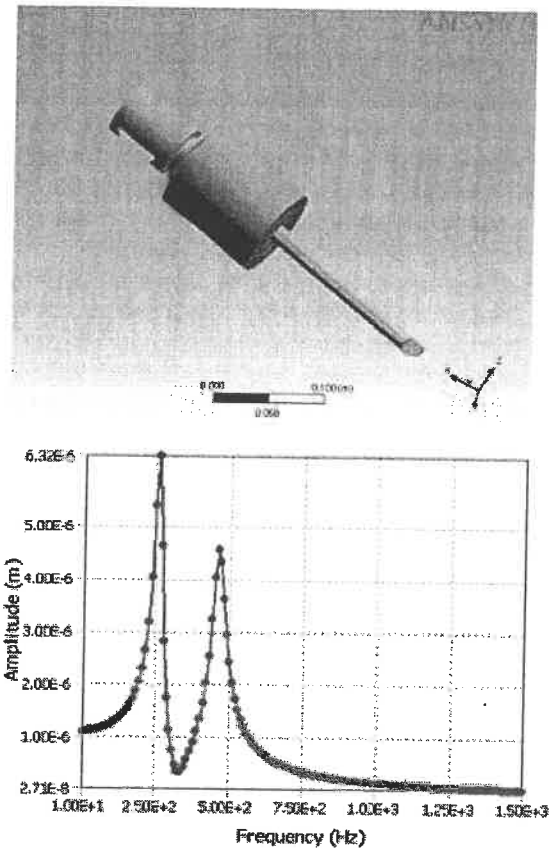

Figure 4: FE model of cantilever holder-boring bar assembly.

EXPERIMENTAL RESULTS

The 6061-T6 aluminum holder and brass sleeve were machined and two experimental setups were compared. In the first setup, a vise mounted to a machining center table was used to approximate a "grounded" boundary condition. In the second setup, the holder was clamped to a traditional dovetail tool post, again attached to the same machine table. The final holder and brass sleeve geometries are shown in Fig. 5. The outer diameter is the holder is 53 mm.

Vise setup

Before the boring bar was inserted into the holder, its cantilever FRF was recorded by clamping the boring bar directly in the vise at the 6:1 L:D ratio. The boring bar was then inserted in the holder using a thermal shrink fit connection. The assembly was also clamped in the vise and the FRF was measured at the free end of the boring bar. Figure 6 shows a comparison of the cantilever boring bar and assembly FRFs. A 53% reduction is amplitude is observed for the assembly.

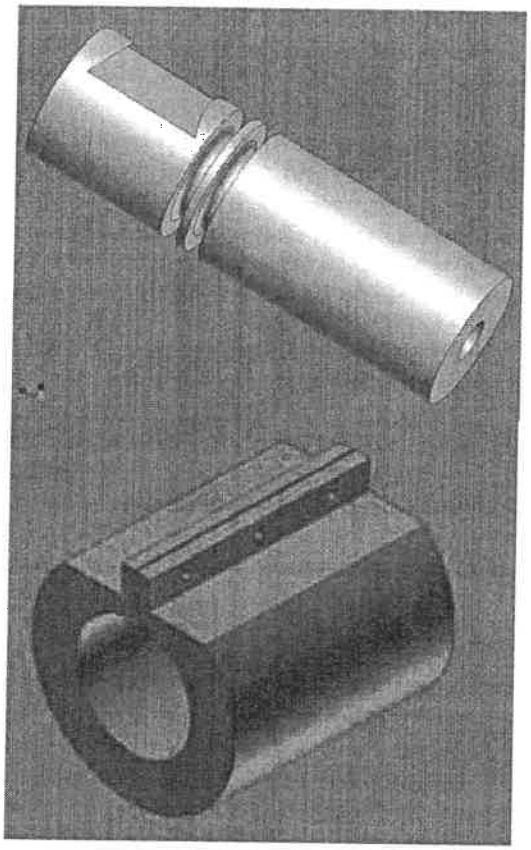

Figure 5: Geometry of holder and brass sleeve. The holder outer diameter is 53 mm.

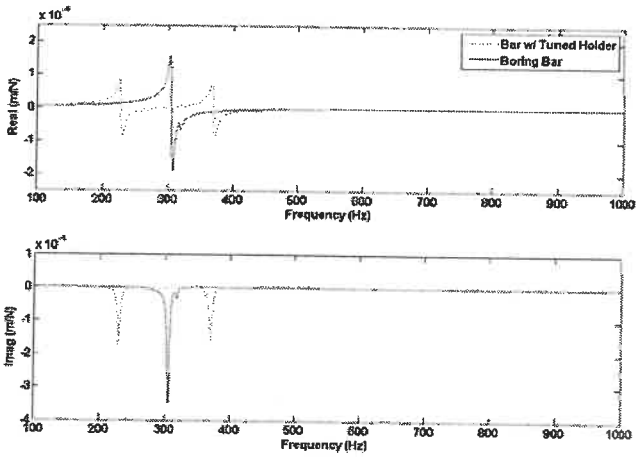

Figure 6: Comparison of cantilever boring bar (solid line) and holder-boring bar assembly (dotted line) FRFs. The assembly is 53% stiffer.

Dovetail setup

Finally, the assembly was attached to a standard dovetail tool post (see Fig. 7). The direct FRF at the free end of the boring bar was again measured. The results are shown in Fig. 8. Note that the scale for Fig. 8 is the same as for Fig. 6. It is seen that the response is slightly stiffer (68% amplitude reduction over the cantilever boring bar) and additional modes are present. This is presumed to be due to additional damping in the non-rigid dovetail connection.

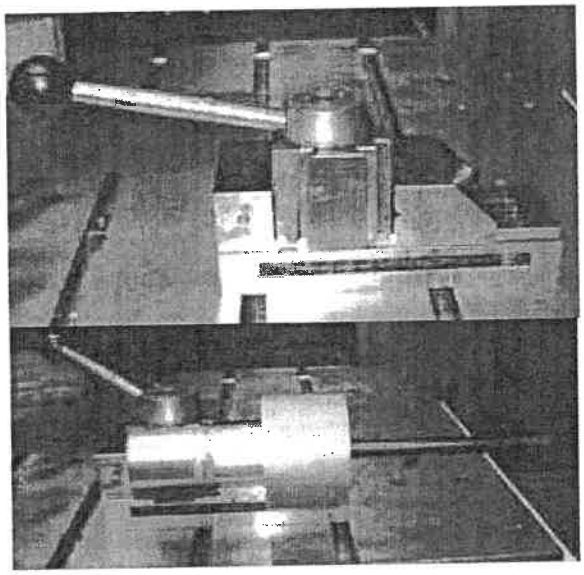

Figure 7: (Top) Photograph of dovetail tool post. (Bottom) Photograph of holder-boring bar assembly clamped to dovetail tool post.

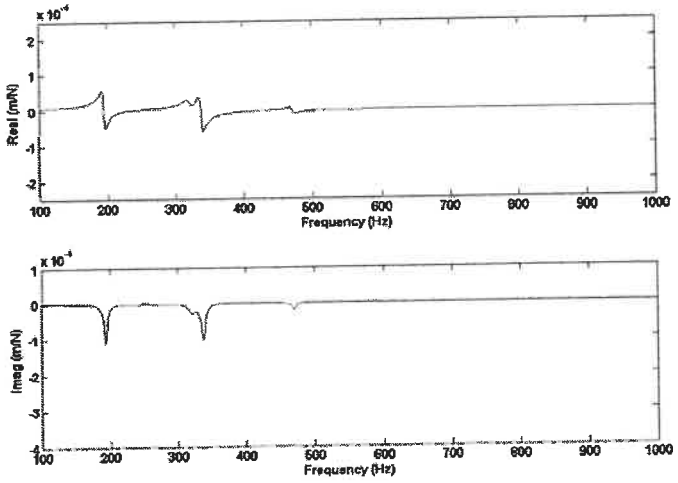

Figure 8: FRF of holder-boring bar assembly clamped to dovetail tool post.

CONCLUSIONS

This paper described a flexible tool holder which acts as a dynamic absorber for a boring bar. By introducing flexibility into the holder (using a notched flexure geometry) and matching its fundamental natural frequency to the first cantilever natural frequency of the boring bar, the holder effectively served as a dynamic absorber for the boring bar. An analytical approach was used to select the nominal holder response for an ISO A10-SCLPR2 NE4 boring bar with a 6:1 length to diameter ratio (15.9 mm diameter). Finite element models were used to refine the design. Components were machined and frequency response function measurements were completed. The dynamic stiffness of the holder-boring bar assembly was compared to the stiffness of the cantilever boring bar alone; Stiffness improvements up to 68% were observed for the holder-boring bar assembly.

ACKNOWLEGEMENTS

This work was supported by the National Science Foundation (DMI- 0555645).

REFERENCES

1. Bishop, R.E.D., Johnson, D.C., 1960, *The Mechanics of Vibration*, Cambridge University Press, Cambridge.
2. Ewins, D., 1995, *Modal Testing: Theory and Practice*, Research Studies Press, Ltd., Somerset, England.
3. Klosterman, A., McClelland, W., and Sherlock, I., 1977, Dynamic Simulation of Complex Systems Utilizing Experimental and Analytical Techniques, *ASME*, 75-WA/Aero-9.
4. Ren, Y., and Beards, C., 1993, A Generalized Receptance Coupling Technique, *Proceedings of the 11th International Modal Analysis Conference*, Kissimmee, FL, 868-871.
5. Ferreira, J., and Ewins, D., 1995, Nonlinear Receptance Coupling Approach Based on Describing Functions, *Proceedings of the 14th International Modal Analysis Conference*, Dearborn, MI, 1034-1040.
6. Schmitz, T., 2000, Predicting High-Speed Machining Dynamics by Substructure Analysis, *Annals of the CIRP*, 49/1: 303-308.
7. Schmitz, T., Davies, M., and Kennedy, M., 2001, Tool Point Frequency Response Prediction for High-Speed Machining by RCSA, *Journal of Manufacturing Science and Engineering*, 123: 700-707.
8. Schmitz, T., and Duncan, G.S., 2005, Three-Component Receptance Coupling Substructure Analysis for Tool Point Dynamics Prediction, *Journal of Manufacturing Science and Engineering*, 127/4: 781-790.

DEVELOPMENT OF CUTTING LOAD PREDICTION SYSTEM USING MONITORING DATA IN MICRO MACHINING

Naoto IKEDA[1], Motoo KONDO[2], Yoshikazu KOBAYASHI[2], and Kenji SHIRAI[2]
[1]Department of Computer Science, Nihon University
[2] College of Engineering, Nihon University
Nakagawara, Tokusada, Tamura-machi, Koriyama, Japan, 963-8642

1. INTRODUCTION

The development of machine tools in recent years has been remarkable [1]. In particular, accuracy and efficiency are rapidly improving in the machining of metal molds. Machining monitoring systems for grasping the machining conditions of machine tools and for preventing tool breakage and reduced machining accuracy are therefore required [2]. Devices with such functions are expensive but are indispensable in the specifications of machine tools. In addition, functions equivalent to the monitoring systems of machine tools such as conventional machining center are also required in micro machining systems for the micro fabrication of metallic cavities and cores, etc. However, the monitoring of the machining state in micro machining is difficult due to minimal load on the tool, resulting in lower machining accuracy and efficiency [3]. One of the solutions for this is to predict the machining load of the tool beforehand. In this study, first, machining state data was acquired, and then a cutting load prediction system was developed by regression analysis which is a data mining technique.

2. OUTLINE OF SYSTEM

Fig.1 shows the system configuration. This system is composed of a computer which controls the micro machining system main body and a machine tool. The machine tool is a surface texture generation device developed in this laboratory. This device has three axes, X, Y, and Z, enabling micro machining in the level of several ten μm [4]. The spindle speed is controlled by a spindle control device. *Fig.2* shows the flow of the internal processing of the control PC (Personal Computer), cutting load monitoring program, cutting load prediction program, and machining program in the PC. The load voltage of the main spindle is measured using an A/D (Analog/Digital) converter from the spindle control device by the cutting load

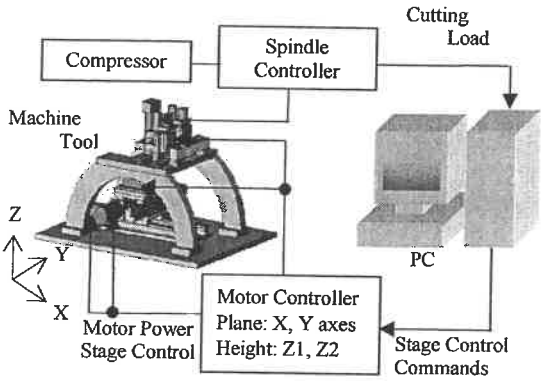

Fig.1 SYSTEM CONFIGURATION

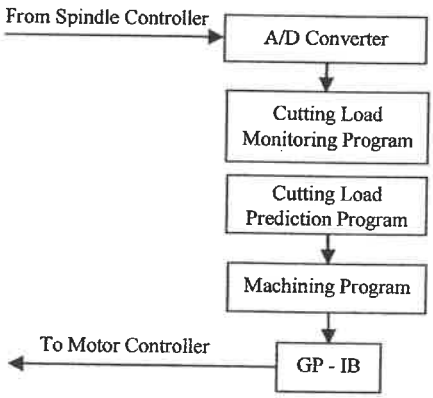

Fig.2 SYSYTEM PROCESSOR IN PC

monitoring program. Next, the cutting conditions are selected on the basis of prediction load calculated by the cutting load prediction program. Finally, control signals are transferred to the motor controller through a GP-IB (General Purpose Interface Bus).

3. CUTTING CONDITIONS FOR MACHINING STATE DATA ACQUISITION

Fig.3 shows the targeted work material shape in this study and *Table 1* shows the cutting conditions. In cutting experiments, straight line cutting of six lines was taken to be one cycle in the 5.0mm×5.0mm cutting range. The tool is a ball-end mill of 1.0mm in diameter. The spindle speeds were 30000, 40000 and 50000 rpm, and the feed rate was set at 30, 60, 90, 120, 150 and 180 mm/min for each spindle speed. The cutting depth was 0.05mm. The work material was pure aluminum, and the machining scraps were disposed by air blow.

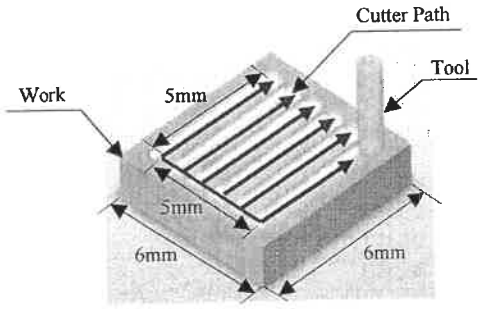

Fig.3 WORK PIECE

Table 1 CUTTING CONDITIONS

Work Piece	Al
Tool	Ball-end mill
Tool Diameter	R 1.0[mm]
Cutting Size	5.0×5.0[mm]
Feed Rate	30~180[mm/min]
Spindle Speed	30000,40000,50000[rpm]
Cutting Depth	0.05[mm]
Cutting Type	1 way

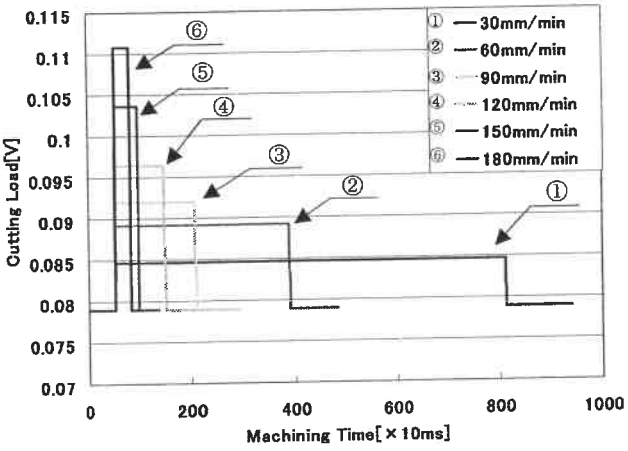

Fig.4 MONITIORING RESULT OF CUTING LOAD

4. ANALYSIS OF CUTTING CONDITIONS

Fig.4 shows the cutting load at the spindle speed of 30000 rpm. The cutting load is the mean value of the cutting load per cycle. The average voltage in free cut at this cutting condition was 0.079V, which is the cutting start point and cutting end point.

5. PREDICTION OF CUTTING LOAD

The data mining of the acquired monitoring data was carried out in order to predict the cutting load. Useful information was searched from an enormous volume of data including noise accumulated in the database [5]. There are various techniques for data mining, and regression analysis was used since the purpose of this study was prediction. Regression analysis is a technique which estimates the purpose variable X_p based on the explanatory variable Y by the regression formula. The basic regression formula is shown in the following.

The results of the analysis showed that the cutting load increases with the increase of the feed rate. Therefore, the cutting load can be predicted by fixing the feed rate.

$$Y = a_1X_1 + a_2X_2 + \cdots + a_pX_p + b \qquad (1)$$

Formula (1) a and b are respectively calculated by equation (2) and (3).

$$a = \frac{\sum_{i=1}^{n}\left(X_i - \bar{X}\right)\left(Y_i - \bar{Y}\right)}{\sum_{i=1}^{n}\left(X_i - \bar{X}\right)^2} \qquad (2)$$

$$b = \bar{Y} - a\bar{X} \qquad (3)$$

where

p : Number of explanatory variables

i : Data number

$\bar{X}$: Average of X

$\bar{Y}$: Average of Y

By substituting formula (1), the present prediction regression formula (4) can be obtained.

$$Y = aX + b \qquad (4)$$

where

Y : Prediction load [V]

X : Feed rate [mm/min]

a : Coefficient obtained by cutting load and regression analysis of feed rate

b : Coefficient obtained by calculated coefficient "a"

Table 2 RESULTS OF REGRESSION ANALYSIS

Spindle Speed	A	b
30000rpm	0.333	0.078
40000rpm	0.201	0.152
50000rpm	0.394	0.236

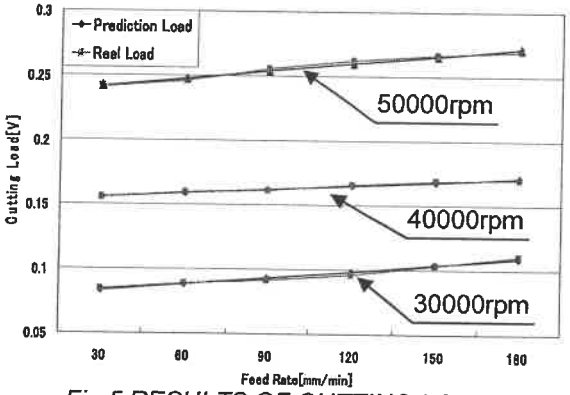

Fig.5 RESULTS OF CUTTING LOAD PEDICTIONN

Table 2 shows the results of the regression analysis and *Fig.5* shows the prediction load and actual loading at each spindle speed. It confirms that the prediction load and real load more or less agree at a difference of about 3% or less.

6. RELATION WITH PREDICTION LOAD AND CUTTING SURFACE

The reduction of cutting time and identification of the cutting surface are difficult by just prediction of the cutting load alone, and the optimum cutting conditions cannot be estimated. The effects of the estimated cutting load on the cutting surface were therefore verified. The roughness of the cutting surface using the sample cut in advance was measured using a scan-type white-light interferometer as the measuring device (*Fig.6*). *Fig.7* shows the results of measuring the roughness of the cutting surface, and the comparison of various cutting conditions. The spindle speed at which the roughness of the cutting surface could be

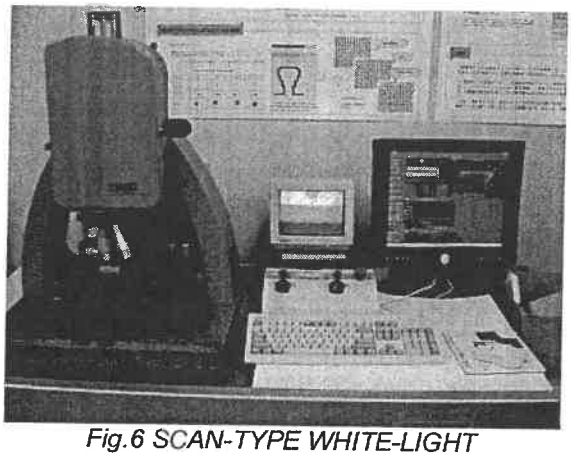

Fig.6 SCAN-TYPE WHITE-LIGHT INTEFEROMETER AS THE MEASURING DEVICE

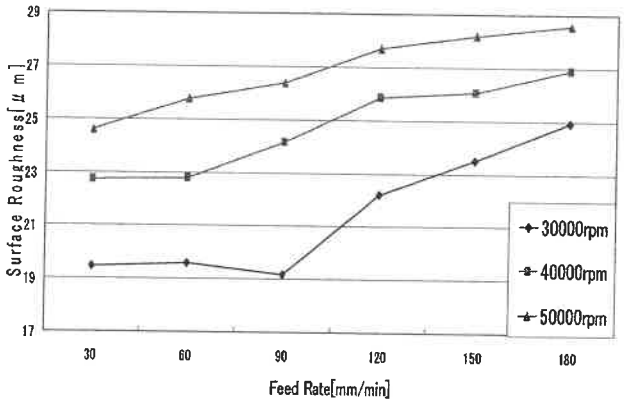

Fig.7 SURFACE ROUGHNESS OF CUTTING SURFACE

suppressed the most was 30000 rpm. In addition, the roughness of the cutting surface was found to rapid change from 90 mm/min to 120 mm/min, apparently due to the insufficient spindle speed for the feed rate. Moreover, it was proven that the roughness of cutting surface at the feed rate of 90 mm/min feed rate was 0.404 μm less than that at 60 mm/min. These results therefore suggest that high precision highly efficient cutting can be realized at the feed rate of 90mm/min for the spindle speed of 30000rpm.

7. CONCLUSION

To prevent reduced machining accuracy and efficiency in micro machining, a cutting load prediction system was developed by data mining of monitored data, and following conclusions were obtained.

(1) Using a cutting load monitoring program, machining state data could be obtained constantly.

(2) As a result of predicting the cutting load of the spindle by regression analysis, the error between the predicted load and real load was found to be about less than 3%.

(3) By comparing the relationship between the cutting load and roughness of the cutting surface, it was possible to control the roughness of cutting surface for each cutting condition.

REFERENCES

[1] Kouichi TOZAWA, Naohito TOIDA, Yoshikazu KOBAYASHI and Kenji SHIRAI: Evaluation of Machining Accuracy by Measurement of Surface Texture Pattern, ASPE CD-R, (2005)4.

[2] Masataka SAITO, Yoshikazu KOBAYASHI, and Kenji SHIRAI : Data Mining of Conditions for Machine Tools Based on Machining Information, ASPE Annual, 30(2003)375.

[3] Masataka SAITO, Yoshikazu KOBAYASHI, and Kenji SHIRAI : Cutting Load Analysis of Small Diameter Tool, JSDMT, Vol.19, No.13 (2004)42.

[4] Yoshikazu KOBAYASHI, Kenji SHIRAI, Masaaki SATO, Kouichi TOZAWA: Development of Surface Texturing System by Mechanical Machining, ASPE CD-R, (2004) 4.

[5] Teppei KAWAI, Toshiki HIROKAKI, Miho OHSAKI, Eiichi AOYAMA, Keiji OGAWA : Proposal of Manufacturing System Supported by Data Mining, JSPE CD-R, (2005) 1011-1012.

MANUFACTURING OF MICRO V-GROOVE WITH AN ELECTRICALLY CONDUCTIVE DIAMOND ELECTRODE IN EDM

Manabu Iwai[1], Sadao Sano[2], Weili Pan[3], Kenji Itagaki[3], Yoshihiko Murakami[4], Mei Wang[4], Tetsutaro Uematsu[1], and Kiyoshi Suzuki[3]

[1]Toyama Prefectural University, Imizu, Toyama, Japan
[2]Sodick Co. Ltd., Yokohama, Kanagawa, Japan
[3]Nippon Institute of Technology, Miyashiro, Saitama, Japan
[4]OSG Co., Ltd., Toyokawa, Aichi, Japan

INTRODUCTION

In order to realize successful fine and precise EDM, it is important to minimize the wear of the electrode under the condition of very small pulse duration. To cope with this issue, the authors focused attention on the electrically conductive CVD diamond (EC-CVD diamond here after) having very high thermal conductivity, and have already shown that an extremely low wear machining could be realized by using the EC-CVD diamond as an electrode [1, 2]. Subsequently, the authors proposed the use of PCD (polycrystalline diamond) material having adequately high thermal conductivity instead of expensive EC-CVD diamond, and have shown that the PCD also has superior wear resistance in EDM on die steel (SKD11 in JIS) similar to the EC-CVD diamond electrode [3].

In this study, fine EDM experiments were conducted using a PCD electrode having a knife edged shape with an included angle of 45°, for the purpose of realizing a practical use of PCD material as an electrode for fine and precise ED machining on tungsten carbide workpiece.

PCD MATERIAL USED

Table 1 shows the physical properties of typical PCD materials (Syndite, CTB-010 & CTH-025) as well as presently used electrode materials [4]. Each of the PCD materials has a thermal conductivity value falling between those of copper and EC-CVD diamond, and the thermal diffusivity calculated from the specific heat is also close to that of the EC-CVD diamond material. Therefore, PCD is expected to serve as a superior electrode material for precise micro-EDM on tungsten carbide materials. Such a superior thermal property is derived from the composition and structure of the PCD materials. Concretely, PCD is composed of micron-size diamond particles that are firmly bonded (intergrowth) with each other during the synthesis process under ultra-high pressure and high temperature with the help of metallic catalyst (cobalt in this case).

EDM PROPERTIES OF PCD ELECTRODES WITH FLAT SURFACE

EDM experiments on tungsten carbide (G5) were conducted using a flat surface of a PCD material with the setup shown in Fig.1 to investigate the properties of PCD as an electrode, and the results were compared with those of other electrode materials. The EDM conditions used were no-load voltage of u_i=90V, set peak current of i_P=3A, pulse duration of t_e=1 and 30μs for the PCD electrode. And for the Cu-W electrode the recommended condition, by an EDM machine maker, of u_i=120V, i_P=1.6A, t_e=0.5μs and the electrode polarity fluctuating between positive and negative were used because the electrode wear of the Cu-W is stated to be the lowest under these condition. The results of the experiments are shown in Fig.2.

Figure 2(a) shows a comparison of the electrode wear ratio (= electrode wear depth / workpiece removal ×100[%]) for the various electrode materials at a short pulse (t_e=1μs) as well as a long pulse (t_e=30μs) duration. A positive value shows electrode wear and a negative value shows an increase in the length of the electrode.

TABLE 1. Physical properties of various electrode materials.

	PCD (Syndite*2)		EC CVD diamond (CVDITE-CDE*2)	Exisitng electrode	
	CTB-010	CTH-025		Cu-W	Cu
Diamond size: μm	10	25	-	-	-
Density: g/cm^3	4.08	3.95	3.5	14	9.0
Binder	Cobalt	Cobalt	-	-	-
Binder: wt%/vol% *1	22.6/10.3	17.9/7.9	0	-	-
Diamond: wt%/vol% *1	77.4/89.7	82.1/92.1	100/100	-	-
Specific resistance: Ω·m *2	1.4×10^{-4}	-	$0.4\sim1\times10^{-3}$	6.8×10^{-9}	17×10^{-9}
Thermal conductivity: W/m·K *3	459	501	500~600	188~295	400
Thermal diffusivity: m^2/s *4	0.24×10^{-3}	0.27×10^{-3}	$0.27\sim0.33\times10^{-3}$	-	0.12×10^{-3}

*1 Calculated value, *2 Element Six Ltd. [4], *3 D.S. McLachlin [5],
*4 Calculated value from specific heat measured by Univ. of Limerick

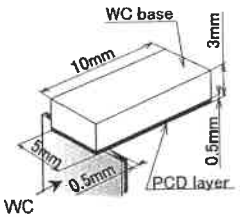

FIGURE 1. Schematic set up for EDM on tungsten carbide edge with PCD electrode.

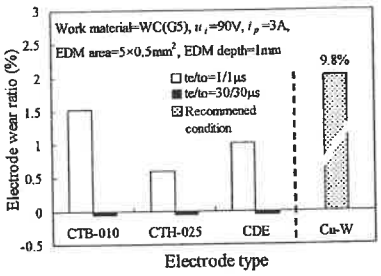

(a) Comparison of electrode wear ratio

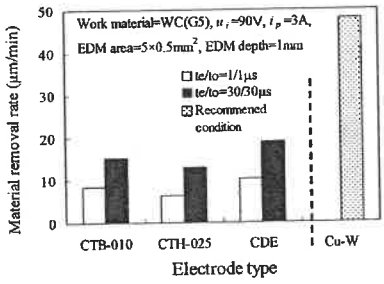

(b) Comparison of material removal rate

FIGURE 2. EDM properties of various electrode materials on tungsten carbide.

Here, the negative value means the adhesion of the graphitic carbon, which generated from the decomposition of the dielectric oil due to discharge, on the electrode surface. The wear on Cu-W electrode, generally used in conventional EDM on tungsten carbide workpiece, was very high about 10% even under the recommended condition. In addition to this, the electrode wear ratio was very low such as only 1.5% with CTB-010 (particle size 10μm) and 0.6% with CTH-025 (particle size 25μm) even at very short pulse duration of t_e=1μs. On the other hand, the electrode wear ratio showed negative value (adhesion of carbon) at t_e/t_o=30/30μs.

Figure 2(b) shows a comparison of the rate of material removal for the various electrodes. The rate of material removal of Cu-W electrodes is about 2.5~3 times higher than those of the PCD and EC-CVD diamond electrodes. But, it is believed to be meaningless to talk about material removal rate without considering electrode wear ratio.

EDM PROPERTIES OF PCD ELECTRODE WITH V SHAPE

(1) Shape of the PCD electrode: Two kinds of PCD materials with different grain sizes, namely, 10 and 25μm (Table 1), were formed to have a 45° V shape (knife edge shape) by wire EDM. Figure 3 shows an appearance of the knife-edge shape and the oblique plane. Nose radius of the edge is under 10μm for each case from the results of SEM observation.

(2) Fine groove machining condition: An attempt was made to create a fine groove on a tungsten carbide workpiece by performing an EDM operation up to a depth of 0.2mm in oil using the knife edge shaped electrode (Fig.4). In this experiment, the performance assessment of electrode in EDM was specially focused on the amount of wear of the electrode. Specifications

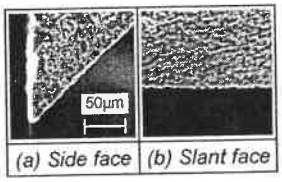

FIGURE 3. V-shaped PCD electrode formed by wire cut EDM machine.

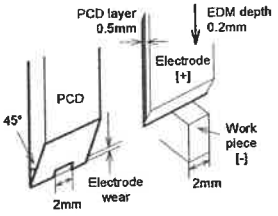

FIGURE 4. Experimental setup.

TABLE 2. Experimental conditions.

EDM machine	Die-sinking EDM machine (AQ35L, Sodick)
Working fluid	Kerosene (Vitol 2, Sodick)
V-shape electrodes	θ=45°, R=10μm 1) PCD (6×10×t2mm) (CTB-010, CTH-025, Element Six) 2) Copper tungsten (5×10×t3mm)
Workpiece	Tungsten carbide (G5)
EDM conditions	EDM width=2mm, EDM depth=0.2mm 1) For PCD: u_i=60~120V, i_P=0.5~4A, t_e=2~50μs, t_o=15μs 2) For Cu-W: Recommended from manufacturer

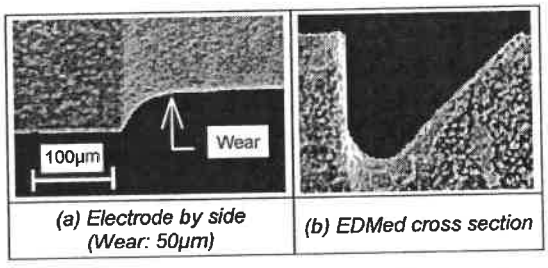

FIGURE 5. Cu-W electrode after EDM and groove profile on a workpiece (WC).

of the experimental apparatus and conditions are shown in Table 2. Effect of various parameters of EDM condition (ED voltage, ED current and ED duration) on the electrode wear was investigated.

EDM Characteristics With Cu-W Electrode

First, for comparison, a 2mm wide fine V-groove was machined on a WC workpiece using a Cu-

W electrode under the EDM conditions recommended by the machine manufacturer. Results are shown in Fig.5. Wear on the Cu-W electrode was relatively large, showing a depth of wear of 50μm on the edge after machining. The nose radius of the V-groove also became large.

EDM Characteristics Using PCD Electrode

The same EDM tests were carried out using other two kinds of PCD (CTB-010 and CTH025) electrodes. The relation between the EDM conditions and wear depths is shown in Fig.6. And, Figure 7 shows the results of the electrode wear and machined groove observed by SEM.

Effect of no-load voltage (Fig.6(a), Fig.7(a))

Varying the no-load voltage in the range of u_i=60~120V, an attempt was made to find out the condition where no wear machining was possible. For other conditions, set peak current of i_P=2A and rather long pulse duration of t_e=15μs (t_o=15μs) were used. Although the time required and machining efficiency are not discussed here, it is observed that the higher the voltage and current, the shorter the machining time was, e.g. the machining was completed in 5 minutes when i_P≥2A.

When no-load voltage was u_i=120V, the wear on both CTH025 and CTB010 was large as 15~20μm. But, by setting the voltage at 60V, electrode wear was largely reduced. Especially, almost no wear was observed with CTH025. By comparing the two different PCD electrodes, it has become clear that there is a tendency that a coarser grade PCD (CTH025) shows low wear than a finer grade PCD (CTB010).

Effect of set ED current (Fig.6(b), Fig.7(b))

In order to investigate the ED condition for low electrode wear, experimental test was carried out by varying the set ED current in the range of i_P=0.5-4A, and keeping the no-load ED voltage at u_i=60V. ED pulse was set at t_e/t_o=15/15μs. When the set current was as small as 0.5A, the electrode wear was large on the both PCD electrodes. However, it was revealed that low-wear machining was possible at the set current larger than 1A. In this experiment, the CTH025 electrode also proved to show lower wear than the CTB010 electrode.

Effect of ED duration (Fig.6(c), Fig.7(c))

Effect of ED duration (pulse-on time) was investigated by setting the conditions of ED voltage u_i=60V, ED current i_P=2A and off time t_o=15μm. At the short-pulse duration of t_e=2μs which is generally used to obtain a good surface, wear on the both PCD electrodes was between 20-30μm. On the other hand, it was revealed that, when te is larger than 15μs, CTH025 showed almost no wear. Moreover, in this case, wear on CTB010 electrode was also nearly zero.

From the above results, it has become clear that the problem of high electrode wear in fine EDM on tungsten carbide can be solved by using the proposed PCD electrode achieving almost zero wear. Cu-W electrode has never been able to achieve this. From now on, the authors plan to make a further study to investigate the machining efficiency and the dimensional accuracy of the groove.

CONCLUSION

Two types of PCD electrodes of different kind were applied to fine groove machining as well as flat surface machining on tungsten carbide and their machining characteristics were investigated. From the results, the following points have become clear.

1. PCD electrodes with flat surface show an almost zero wear at the long pulse duration and a significantly low wear of 0.6~1.5% at the short pulse duration compared to 10% wear of the Cu-W electrode at suggested

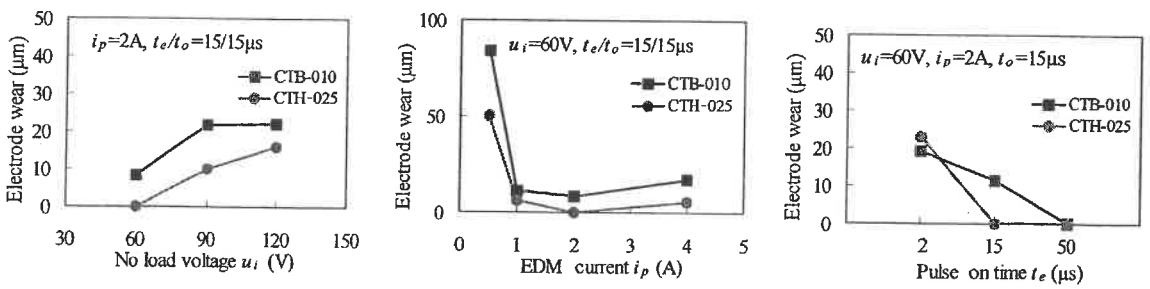

(a) Effect of no load voltage (b) Effect of EDM circuit (c) Effect of pulse on time

FIGURE 6. Comparison of electrode wears on various EDM conditions.

condition for EDM on tungsten carbide (G5).

2. The electrode wear is extremely less with PCD electrode compared to a Cu-W electrode and a zero wear machining is achieved by optimizing the ED conditions (u_i=60V, i_P=2A, t_e>15μs).
3. Thermal conductivity of PCD is different according to the diamond grain size of the PCD. In this study, it was expected that the electrode with higher thermal conductivity would show less wear. In fact, the result is just as expected, i.e. CTH025 exhibits less wear than CTB010.
4. As the diamond is an insulator, it was expected that the grain size of the diamond would affect ED performance. In order to investigate, how this would affect the electrode wear, various tests were carried out by varying the parameters under the ED condition. However, the result revealed that wear on CTH025 is less than CTB010 although CTH025 is thought to have more contributing factor to cause unstable ED performance.

ACKNOWLEDGMENTS

The authors would like to thank Element Six Ltd., for providing the PCD diamond material for this research. The authors would also express their heartfelt thanks to the Die and Mold Technology Promotion Foundation.

REFERENCES

1. Suzuki K., Iwai M., Sharma A., Uematsu T., Shoda K., and Kunieda M., 2003, Electrical Discharge Machining Using Electrically Conductive CVD Diamond as an Electrode, *7th Applied Diamond Conference / Third Frontier Carbon Technology Joint Conference, ADC/FCT2003*, 222.
2. Suzuki K., Iwai M., Sharma A., Ninomiya S., Uematsu T., and Sano S., 2005, Performance of an Electrically Conductive CVD Diamond Electrode for EDM and FEM Analysis for a Very Low Wear, *Abrasive Technology 8, Key Engineering Material*, 543.
3. Suzuki K., Iwai M., Ninomiya S., Sano S., Takeuchi K., and Uematsu T., 2005, Development of composite diamond electrode for EDM-1st report, *Proc. of Spring Conf., JSPE*, 1339. (in Japanese)
4. Element Six Ltd., *Catalogue.*
5. McLachlin D.S., 1984, Axial and surface resistivity of Syndite, Ultrahard Materials Applications Technology, De Beers Industrial Diamond Division, 3: 34.

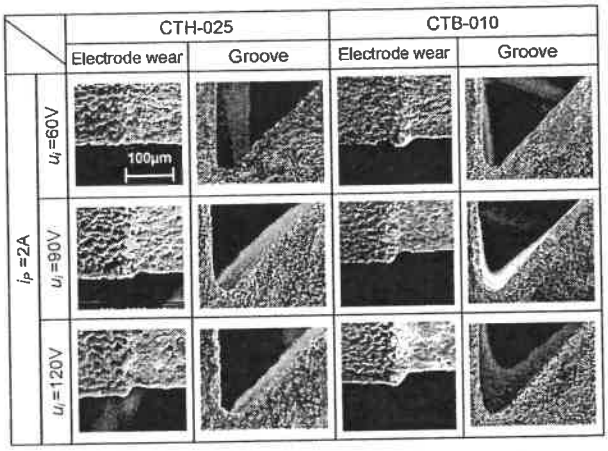

(a) Effect of no load voltage. (t_e/t_o=15/15μs)

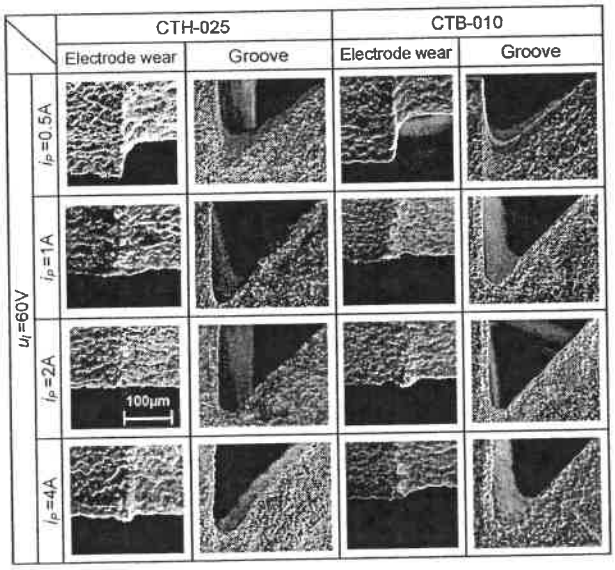

(b) Effect of applied set peak current. (t_e/t_o=15/15μs)

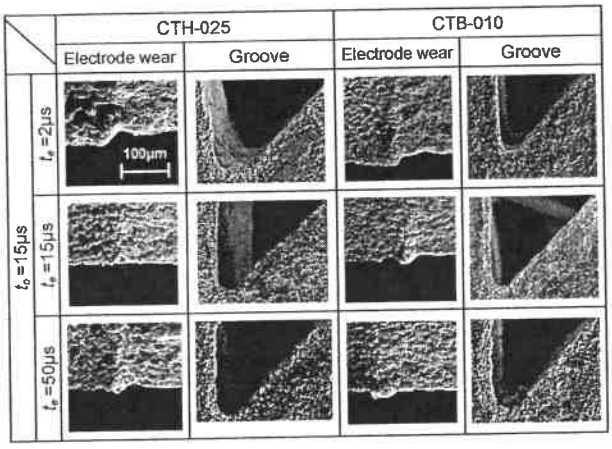

(c) Effect of pulse on time. (u_i=60V, i_P=2A)

FIGURE 7. Effect of EDM conditions on electrode wear and EDMed V groove.

CONDITION MONITORING OF MICRO-DRILLING PROCESSES ON GLASS BY USING MACHINE VISION

Hyun-Ho Kim[1], Siyon Chung [2], Seung-Chul Kim[1]
Won-Ho Jee[3] and Sung-Chong Chung[1]
[1]Hybrid Systems Design & Control LABoratory
Department of Mechanical Design and Production Engineering
Hanyang University, SungdongGu, Seoul 133-791, KOREA
[2]Faculty of Science, The University of Western Ontario, London, CANADA
[3]Shinhan Diamond Inc., Incheon 405-100, KOREA

ABSTRACT
Optical and medical devices require micro-drilling of holes on glass. Brittle fracture occurs during the drilling. Cone and radial cracks are generated due to impact load and walking when a drill hit a glass to make a hole. To produce good holes without cracks and fracture, a condition monitoring of glass drilling processes is required. In this paper, to develop a cost-effective direct monitoring system in micro-drilling processes on glass, a machine vision unit with the edge detection and 3D measurement functions is studied. It consists of a CCD camera with a zoom lens attached to the precision servo stage and a novel illumination unit. Performance of the developed machine vision system is verified in micro-drilling processes on glass using diamond and carbide drills.

KEYWORDS
Brittle fracture, Crack, Condition monitoring, Glass drilling, Micro-drilling, Machine Vision

INTRODUTION
Today, glass is widely used in various types of industries, such as semiconductors, optical components, flat panel displays, micro biochips, etc. The industries seek machining methods to fabricate smaller and smaller products, and therefore micro-hole drilling technology is required. As glass is manufactured isotropically, it is difficult to obtain precision micro-holes through machining processes. Some methods have introduced for micro-hole making. As EDM (Electric Discharge Machining) and laser machining have severe thermal damage and poor hole quality, micro-drilling through machining is preferred in the industries [1].

In a micro-hole drilling process on glass, blades of a micro-drill inflict impact loads on the glass. As the brittle material receive impact load, brittle fracture may occur as radial and/or conic cracks [2,3]. In order to find good drilling conditions and make good quality holes on glass parts, a direct type of condition monitoring system is required [4-6]. As general methods for measuring the hole quality in micro-drilling processes, SEMs (Scanning Electron Microscope) [7,8], Confocal microscopes [8], and laser-based sensing units have been used. However, they are very sensitive, expensive and difficult to be implemented in the working environments. Consequently, development of a cost-effective and rugged direct monitoring system is necessary.

In this paper, a precision 3D machine vision measurement system is proposed to measure hole quality and inspect drill wear in micro-drilling of glass material. Positional errors of fine holes, shape of cracks, and quality of hole surfaces are influenced by drilling conditions. In order to find good machining conditions, in which cracks do not occur and a clean machining surface is kept, qualities of fine holes and surfaces under different machining conditions should be constantly monitored. A machine vision system equipped with a zoom lens, a CCD camera and a novel illumination unit is developed. Using the edge detection method [9], hole quality, cracks due to brittle fracture, and drill wear are precisely quantized.

EXPERIMENTAL SET-UP
In the micro-drilling process, the machine accuracy affects the preciseness of micro holes. Therefore, a high-speed spindle with tight accuracy is required to increase the hole quality.

Cutting force on drill bits increases proportionally as the drilling depth increases. As the diameter of a micro-drill is less than 1 mm and has high slenderness ratio, it is easily broken as the drilling depth increases. The main reason for force increment and drill breakage is the chip created inside the hole and clogging due to the chip. In addition, heat caused by friction on flank and hole surfaces may cause thermal damage of drill bits.

In this paper, an air spindle is used to secure accuracy and drilling speed, and peck drilling is applied to evacuate the chip easily. Fig.1 shows the experimental set-up. The top shows an air spindle mounted on the CNC machine and the overall view of the machine vision system on the machine tool. The bottom shows the air spindle and the workpiece fixture.

To monitor cracks accurately on the glass surface, a precision servo stage is implemented for positioning and focusing of the image. A CCD camera is installed on the precision servo stage with 1 μm resolution and 3 μm repeatability. By controlling the stage, focused and defocused images are obtained. To measure drill abrasion around the periphery, a precision measurement spindle equipped with a rotary encoder is devised as shown in Fig. 2. In order to obtain clear images and reduce noise due to reflection, a diffusive illumination unit equipped with two halogen lights is devised. To find out the tendency of cracking, various cutting conditions are selected as shown in Table 1. For experiments, 0.3mm carbide micro-drills, 0.6mm diamond abrasive drills, and 1.0mm thickness soda-lime glass is used.

IMAGE PROCESSING PROCEDURE

Edge detection is applied to distinguish shapes of cracks at the entrance and exit of micro-holes. Sobel operator [9] is used for the edge detection and this method is also applied to measurement of drill wear.

Table1. Cutting conditions

Drill material	Cemented Carbide	Diamond
Drill diameter	0.3 mm	0.6 mm
Cutting speed	20,000 - 40,000 rpm	5,000 -15,000 rpm
Feedrate	1 - 20 mm/min	1 - 5 mm/min

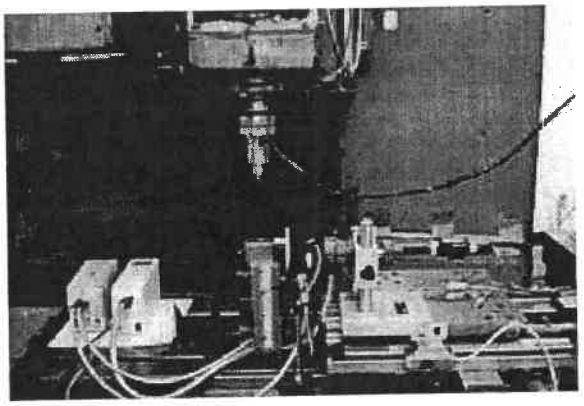

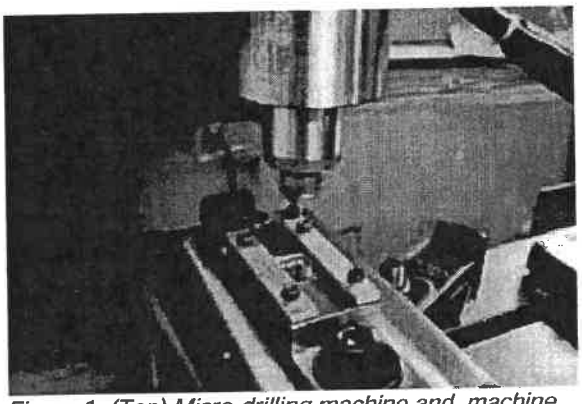

Figure 1: (Top) Micro-drilling machine and machine vision unit, (Bottom) Air spindle and workpiece fixture.

Figure 2: Illumination and measurement unit.

EXPERIMENTAL RESULTS

Cone, ring, radial, median, and lateral cracks have been reported in researches on brittle fracture [2-5]. Cone and ring cracks occur on the surface of specimens when light load is applied. As the load gets heavier, the cone crack spreads due to the principal tensile stress created in the material. If the load exceeds the critical load, radial and median cracks occur. Lateral crack occurs when the load is removed. Cone crack occurs just before the drill bit exits the hole. In the case of brittle materials, even when the applied load is light, deflection and

tensile stress increase as workpieces become thinner. As a result, minute crack developed in the drilling process spreads to the surface of the workpiece and creates cone crack. At this time, the radial and median cracks are separated from the workpiece as the size of the cone crack increases. Fig.3 shows various shapes of cracks in micro-drilling on glass.

Cracks created in the micro-drilling process occur due to deformation of glass caused by thrust force of drills. The thrust force may be lowered by changing cutting conditions. In this research, experiments are conducted to find the best cutting conditions that minimize the amount of crack. Cracks occur more on the exit of drills than entrance. In the case of 0.3mm cemented carbide micro-drills, the least amount of crack is found at the spindle speed of 35,000 rpm and feedrate of 3 mm/min. The crack has the maximum diameter of 379 μm and minimum diameter of 321 μm. Fig. 4 shows results of the cemented carbide micro-drilling. Cracks occur more at the exit than entrance.

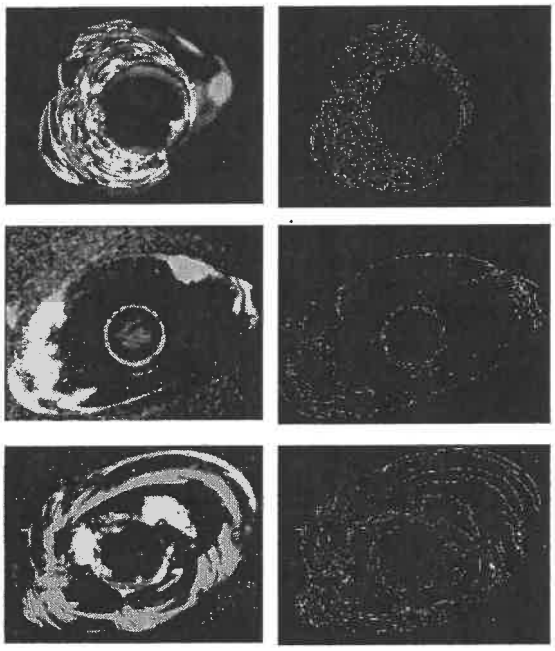

Figure 3: Shape of cracks in micro-drilling on glass.

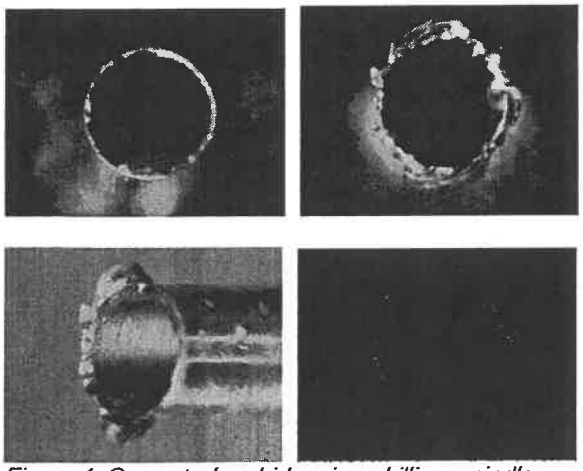

Figure 4: Cemented carbide micro-drilling; spindle speed of 35,000 rpm and feedrate of 3 mm/min.

In case of 0.6mm diamond abrasive drills, the drilling procedure, abrasive machining, is much different from micro-cutting of a 0.3mm cemented carbide drill. At the exit of the hole, cone crack of a large diameter occurs. Due to

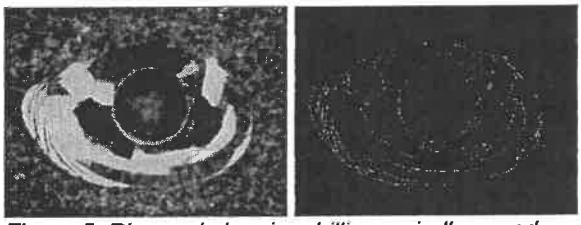

Figure 5: Diamond abrasive drilling; spindle speed 8,000 rpm and feedrate 5 mm/min.

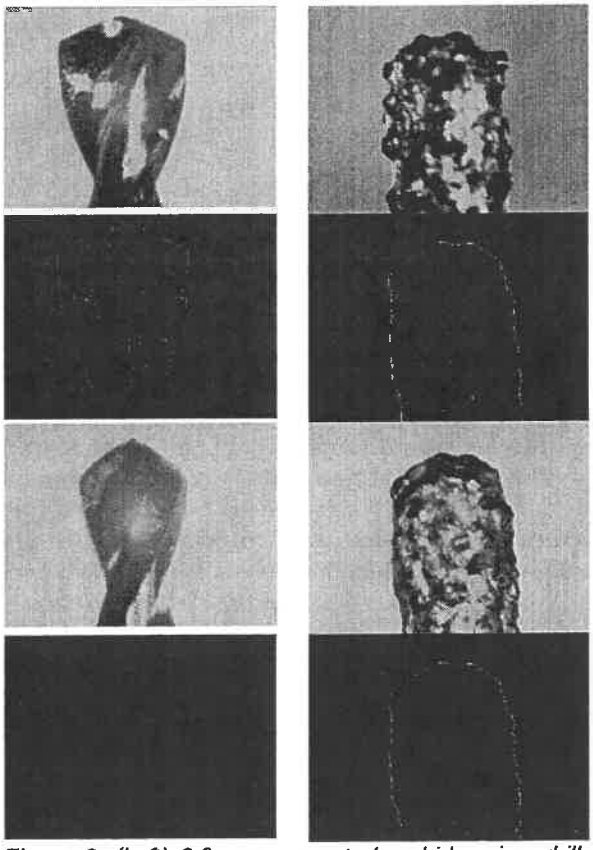

Figure 6: (Left) 0.3 mm cemented carbide micro-drill wear. (Right) 0.6 mm diamond micro-drill wear.

the large size of the cone crack, radial and median cracks rarely occur. Under the spindle speed of 8,000 rpm and feedrate of 5mm/min, both the maximum and minimum diameters of a crack are around 2,023 ㎛ and 1,238 ㎛, respectively. Fig.5 shows results of the diamond abrasive drilling.

Drill wear is measured on the precision measurement spindle unit shown in Fig. 2. After installation of the drill on the unit, edge detection is conducted at every rotational angle interval of the unit. Wear volume, length, and shapes are simultaneously measured and calculated through this process. The maximum diameter of the fresh cemented carbide micro-drill is 303 ㎛. After micro-drilling of 16 times, the maximum diameter of the drill decreases to 243 ㎛.

In the case of 0.6mm diamond drill, the maximum diameter of the fresh drill is 584 ㎛. After 12 times of drilling, it decreases to 563 ㎛. Fig. 6 shows features of the drill bit before and after drilling.

CONCLUSIONS

A machine vision system composed of a zoom lens, CCD camera, precision servo stage and two halogen lights is developed to measure different types of crack on glass and wear of drill bits. A control system is implemented to the precision servo stage to obtain accurate images of micro-holes and micro-drills with positioning resolution of 1 ㎛ and repeatability of 3 ㎛.

In case of the 0.3 mm cemented carbide micro-drill, the least amount of crack is obtained at the spindle of 35,000 rpm and feedrate of 3 mm/min. The crack has the maximum diameter of 379 ㎛ and minimum diameter of 321 ㎛.

In case of the 0.6 mm diamond drill, the crack created at the exit has the maximum diameter of 2,023 ㎛ and minimum diameter of 1,238 ㎛ under the spindle speed of 8,000 rpm and feedrate of 5mm/min,

In the case of the cemented carbide micro-drill, diameter of 60 ㎛ is worn out after 16 times of drilling. On the other hand, diameter of the diamond abrasive drill has wear of 21 ㎛ after 12 times of drilling.

REFERENCES

1. Yoon, H. S. and Chung, S. C., 2004, "Vision Inspection of Micro-drilling Processes on the Machine Tool," Transactions of the NAMRI/SME, Vol. 32, pp.391~398.
2. Gorham, D.A. and Salman, A.D., 1999, "Indentation Fracture of Glass and Mechanisms of Material Removal", Wear 233-235, pp. 151-156.
3. Smetana, W. and Reicher, R., 2000, "Preventing Failure of Soda Lime Cover Glass by Design Optimization", Engineering Failure Analysis 7, pp. 87-99.
4. Shih, A. J., M. Bakkal, S. B. McSpadden, and R. O. Scattergood, 2005, "Thrust Force, Torque and Tool Wear in Drilling the Bulk Metallic Glass," International Journal of Machine Tools and Manufacture, Vol. 45, pp. 863~872.
5. Jain, V.K., Choudhury, S.K. and Ramesh, K.M., 2002, "On the machining of alumina and glass," International Journal of Machine Tools and Manufacture, Vol. 42, pp. 1269~1276.
6. Matasumura T. and Ono, T., 2005, "Glass Machining with Ball End Mill," Transactions of the NAMRI/SME, Vol. 33, pp.319~326.
7. Nickel, J., A. N. Shuaib, B. S. Yilbas, and S. M. Nizam, 2000, "Evaluation of the Wear of Plasma-nitrided and TiN-coated HSS Drills using Conventional and Micro-PIXE Techniques," WEAR, Vol. 239, pp. 155~167.
8. Chen, Y. C. and Y. S. Liao, 2003, "Study on Wear Mechanisms in Drilling of Inconel 718 Superalloy," Journal of Materials Processing Technology, Vol. 140, pp. 269~273
9. Gonzalez, R. C. and R. E. Woods, 2002, Digital Image Processing, Prentice Hall, Inc., New Jersey.

MACHINING PARAMETER SELECTION BASED ON A COST-BASED OBJECTIVE FUNCTION AND PROCESS STABILITY

Mohammad H. Kurdi, Tony L. Schmitz, and Raphael T. Haftka
Department of Mechanical and Aerospace Engineering
University of Florida
Gainesville, FL, USA

INTRODUCTION

Machining optimization research has enjoyed a rich history. Initial theoretical work by Gilbert in 1950 used the Taylor tool life equation and two criteria, maximum production rate and minimum cost, to determine optimized cutting speed [1]. Subsequent research efforts have applied various optimization criteria, including sums of weighted objectives, and implemented multiple optimization techniques. The purpose of this paper is to demonstrate a single objective function optimization formulation for milling that simultaneously considers tool wear and process dynamics effects in an analytical framework. We compare the costs for optimized conditions and manufacturer-recommended values.

OBJECTIVE SELECTION

A natural candidate for the optimization objective is profit, P. Profit may be expressed as:

$$P = \int_{t_0}^{\infty} e^{-rt}(R - C)dt, \tag{1}$$

where t_0 is the current time, r is the discount rate that devalues future sales, R is revenue, and C is cost. Revenue is the product of price and the number of components. Cost, however, can have many inputs, which may be categorized into fixed and variable costs. Fixed costs include, for example, building and machinery depreciation, insurance, taxes, interest, indirect labor, engineering, rentals, general supplies, management expenses, and marketing/sales. Examples of variable costs are materials, tooling, labor, utilities/power, and maintenance. Cost considerations specific to machining include, e.g., setup time, part quality, CNC programming, inspection, cycle time, rework, finishing, part handling, fixturing, coolant use and disposal, and tool advance-retract-change times [2].

In job shop situations, the number of units to be sold, x, is typically known once a job is accepted. If we assume that the unit price is also known, then revenue is a fixed value and the objective becomes cost minimization. In the following sections, a method for including both process dynamics and tool wear in a cost minimization formulation is described.

APPROACH

The cost function, $C(x)$, is provided in Eq. 2, where C_f represents fixed costs and C_m is the machining-related cost per part.

$$C(x) = C_f + xC_m \tag{2}$$

We will minimize C_m (Eq. 3) subject to the two constraints shown.

$$\text{Minimize } C_m = t_m r_m + (t_{tch} r_m + C_t)\frac{t_c}{T} \tag{3}$$
$$\text{subject to } b \le b_{lim} \text{ and } \Omega_{min} \le \Omega \le \Omega_{max}$$

Here, t_m is the overall machining time, r_m is the machining cost per unit time, t_{tch} is the tool changing time, C_t is the cost per tool, t_c is the actual cutting time, and T is the tool life. Machining/cutting time and tool life are directly affected by: 1) the selected process parameters, including radial and axial depths of cut, a and b (limited by the process stability as indicated by the first constraint), spindle speed, Ω, and feed per tooth, f_t; and 2) the tool information, including the diameter, d, (which defines the cutting speed, $v = \pi d\Omega$, when combined with the spindle speed), cutting edge geometry, and the number of teeth, N.

The machining time depends on the part path. For simplicity, we define it here as:

$$t_m = L/f, \tag{4}$$

where L is the distance traveled by the tool and f is the feed rate, given by $f = \Omega N f_t$. The tool cutting time can be calculated as:

$$t_c = V/MRR, \quad (5)$$

where V is the volume to be removed and $MRR = abf_t\Omega N$ is the mean material removal rate. The tool changing time, t_{tch}, in Eq. 3 depends on the machining center and can range from less than one second (automated) to several minutes (manual). The machining cost per unit time depends on the manufacturing facility, machining center, and labor costs.

Tool Life Model

Coefficients for tool life models are typically determined from cutting test data. To demonstrate our approach, we have applied the data presented by Tsai *et. al.* [3] for a TiAlN-coated, tungsten carbide endmill (HFK UF440A-4ENSR-D10-R0.5) used to machine SKD61 tool steel. In [3], tool life is represented using an abductive polynomial network. The tool specifications are provided in Table 1 and the cutting conditions are listed in Table 2.

TABLE 1. Tool specifications from Tsai et al. *[3].*

d (mm)	N	Overall length (mm)	Helix angle (deg)	Corner radius (mm)
10	4	100	45	0.5

TABLE 2. Cutting conditions from Tsai et al. *[3].*

v (m/min)	Ω (rpm)	f_t (mm/tooth)	b (mm)	a (mm)
314-628	9994-19989	0.0075-0.15	0.5-1.5	0.5

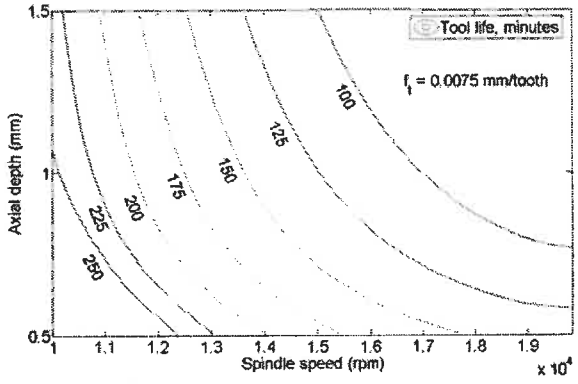

FIGURE 1. Tool life contours from Tsai et al. *[3].*

Tool life contours obtained using the abductive polynomial network for a 0.0075 mm/tooth feed per tooth value (within the Ω and b ranges given in Table 2) are shown in Fig. 1. As expected, the tool life decreases with increasing spindle speed, Ω, and axial depth of cut, b.

For optimization purposes, we wished to extend the allowable operating range beyond the cutting test conditions. Figure 2a shows extrapolated tool life contours for axial depths up to 3.5 mm and spindle speeds down to 2000 rpm. As seen, extrapolation of the abductive polynomial network yields unexpected results; the contours do not follow the general trend of decreased life with increased speed and axial depth. Therefore, we have used the data reported in [3] to generate a Taylor-type tool life model of the general form, $T = Cv^p f_t^q b^r$, where C, p, q, and r are constants. From the 42 tests completed using various v, f_t, and b values, the Taylor-type tool life equation coefficients were determined by least squares fitting:

$$T = 1.9549\text{x}10^6\, v^{-1.6265}\, f_t^{-0.1024}\, b^{-0.2837}, \quad (6)$$

where T is expressed in min, v in m/min, f_t in mm/tooth, and b in mm. In Fig. 2a, it is seen that the Taylor-type model exhibits the expected behavior. Figure 2b shows a comparison between the abductive polynomial network and Taylor-type model over the cutting test range. Reasonable agreement is observed.

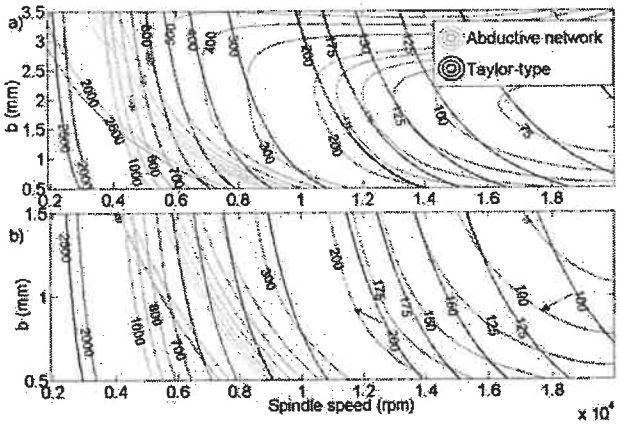

FIGURE 2. Comparison of tool life contours (in minutes) for abductive polynomial network and Taylor-type tool life models (f_t = 0.0075 mm/tooth). a) Extrapolation outside test range – abductive network shows unexpected results. b) Comparison of abductive and Taylor-type tool life models within the test range.

As noted, a key goal of this study was to compare manufacturer-recommended cutting conditions with those determined using the optimization approach. Because manufacturer

recommendations were not available for the tool-workpiece combination used in the Tsai *et al.* study, we selected an equivalent tool from Sandvik Coromant. This enabled us to use their recommended cutting conditions. Sandvik Coromant solid carbide tools with approximately the same coating as the tool in Table 1 have a grade designation GC1630. The SKD61 tool steel machined by Tsai *et al.* corresponds to an ISO CMC No. P03.11 high-alloy steel. The closest available Sandvik Coromant geometry was provided by an R216.34-10045-AC22N tool, p. A148 [4] (see Table 3). Additionally, cutting force coefficients for the ISO CMC No. P03.11 high-alloy steel were given as K_t = 2395x10^6 N/m^2 and K_n = 718x10^6 N/m^2 [4], which proportionally relate the tangential (*t*) and normal (*n*), or radial, direction cutting force components for the rotating cutter to the commanded chip area (i.e., the product of *b* and f_t).

TABLE 3. Sandvik Coromant tool specifications.

d (mm)	*N*	Overall length (mm)	Helix angle (deg)	Corner radius (mm)
10	4	72	45	Chamfer

Tool-Point Frequency Response Function

In order to determine the limiting axial depth of cut as a function of spindle speed (for the first constraint in Eq. 3), the tool point frequency response function (FRF) of the tool-holder-spindle combination must be known. To obtain the tool point FRF, we rigidly coupled models of the selected tool and a CoroGrip precision power chuck (392.410HMD-63 20 077, p. D113 [4]) with a cylindrical collet (393.CGS-20 10 52, p. D165 [4]) to a representative high-speed spindle (FRF determined experimentally) using Receptance Coupling Substructure Analysis [5-7]. Figure 3 shows the predicted assembly FRF as reflected at the tool point.

Process Stability Model

We applied the frequency domain approach given in [8] to predict the limiting axial depth of cut as a function of spindle speed. Inputs to the algorithm include the tool point FRF, cutting force coefficients, and radial depth of cut. Using the Fig. 3 FRF, K_t = 2395x10^6 N/m^2 and K_n = 718x10^6 N/m^2 cutting force coefficients [4], and *a* = *d*, the stability lobe diagram shown in Fig. 4 was obtained, where *b*-Ω combinations below the stability boundary indicate stable, or chatter-free, cutting.

RESULTS

We considered cost minimization for removing a cube of material with dimension *W* = 100 mm. For the full radial immersion conditions (*a* = *d*) shown in Fig. 5, the distance traveled by the tool is:

$$L = \frac{W}{b}\left(\frac{2W}{a}(W+d)+W\right). \qquad (7)$$

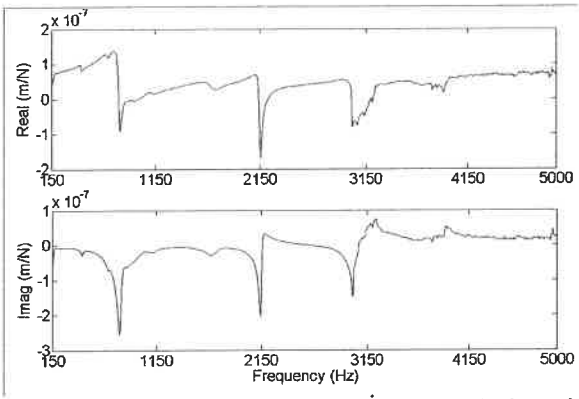

FIGURE 3. Tool point FRF for selected tool-holder-spindle combination.

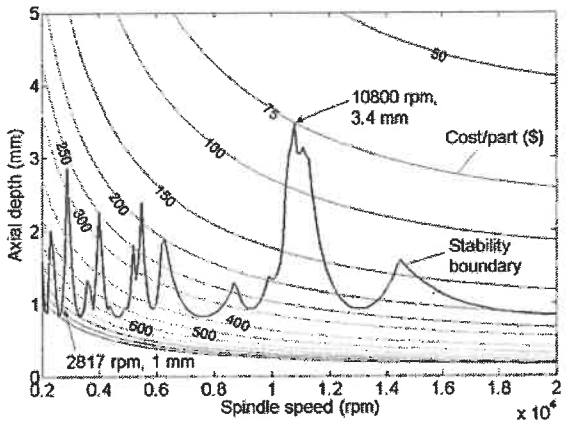

FIGURE 4. Stability lobe diagram for test case. Cost per part contours are also shown (f_t = 0.027 mm/tooth).

Based on the cost parameters listed in Table 4 and travel distance defined by Eq. 7, the cost per part was determined as a function of axial depth, *b*, and spindle speed, Ω (see contours in Fig. 4). It is seen that the minimum cost for chatter-free cutting corresponds to the highest possible combination of *b* and Ω defined by the stability boundary (3.4 mm and 10800 rpm). A gradient-based search algorithm with multiple guesses was implemented in Matlab (to handle

discontinuities in the stability boundary) and verified this operating point.

TABLE 4. Cost parameters for test case.

t_{tch} (sec)	C_t ($/tool)	r_m ($/min)
4	114	1

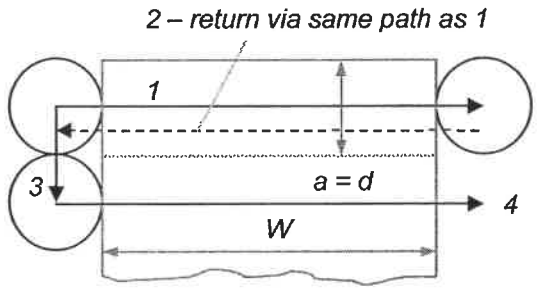

FIGURE 5. Part path for machining cube of dimension W = 100 mm. This path (1, 2, 3, 4, ...) is repeated in multiple axial levels as required by the limiting axial depth of cut.

The manufacturer-recommended cutting conditions for the selected tool-workpiece combination (p. A303, [4]) are listed in Table 5, where a correction factor of 1.18 was applied to obtain the recommended spindle speed corresponding to the SKD61 material hardness (p. A321, [4]). In a previous publication of the Sandvik Coromant handbook [9], the recommended axial depth for a slotting operation was listed as 50% of the tool diameter. This would correspond to b = 5 mm, which is in the unstable region for our test case.

TABLE 5. Manufacturer-recommended cutting conditions.

v (m/min)	f_t (mm/tooth)	Ω (rpm)	Depth (mm)
88.5	0.027	2817	$a \times b > d$

For the conditions listed in Table 5, if a stable depth of cut of 1 mm is selected (see Fig. 4 at 2817 rpm), the associated cost per part for machining the ISO CMC No. P03.11 high-alloy steel 100 mm cube is $775.44. If the optimized parameters are selected (10800 rpm, b = 3.4 mm), the cost is $76.78 – a 90% reduction. See Table 6. Even if a more conservative axial depth of 2.5 mm is used (to move away from the stability boundary), a cost reduction of 87% is still achieved. This simple example demonstrates the importance of considering the process dynamics, in addition to tool wear, for machining parameter selection.

TABLE 6. Cost comparison – the optimized conditions provide a 90% cost reduction.

Source	b (mm)	Ω (rpm)	C_m ($)
Sandvik	1.0	2817	775.44
Optimized	3.4	10800	76.78

CONCLUSIONS

In this paper we formulated a cost-based objective function which considered both tool life and process stability. Based on test data from the literature, it was shown that significant cost reduction relative to manufacturer recommendations could be achieved through the application of dynamic models within an optimization framework.

ACKNOWLEGEMENTS

This work was supported by the National Science Foundation (DMI-0238019), the Office of Naval Research (Young Investigator program), TechSolve, and the Naval Surface Warfare Center-Carderock Division. The authors also wish to thank G. Hazelrigg for many helpful discussions.

REFERENCES

1. Gilbert, W., 1950, Economics of Machining, *Machining – Theory and Practice*, American Society for Metals, Metals Park, OH, 465-485.
2. Stephenson, D. and Agapiou, J., 1997, Metal Cutting Theory and Practice, Marcel Dekker, Inc., New York, NY.
3. Tsai, M. K., Lee, B. Y., and Yu, S. F., 2005, A Predicted Modeling of Tool Life of High Speed Milling for SKD61 Tool Steel, *International Journal of Advanced Manufacturing Technology*, 26: 711.
4. Rotating Tools and Inserts Handbook, Sandvik Coromant, LIT-CAT 04-R.
5. Schmitz, T. and Donaldson, R., 2000, Predicting High-Speed Machining Dynamics by Substructure Analysis, *Annals of the CIRP*, 49/1: 303-308.
6. Schmitz, T., Davies, M., and Kennedy, M., 2001, Tool Point Frequency Response Prediction for High-Speed Machining by RCSA, *Journal of Manufacturing Science and Engineering*, 123: 700-707.
7. Schmitz, T. and Duncan, G.S., 2005, Three-Component Receptance Coupling Substructure Analysis for Tool Point Dynamics Prediction, *Journal of Manufacturing Science and Engineering*, 127/4: 781-790.
8. Altintas, Y. and Budak, E., 1995, Analytical Prediction of Stability Lobes in Milling, *Annals of the CIRP*, 44/1: 357.
9. Rotating Tools and Inserts Handbook, Sandvik Coromant, LIT-CAT 01-R.

CREATION OF V-SHAPED CURVED MICROGROOVES WITH TWO FLAT-ENDS BY NON-ROTATIONAL CUTTING TOOLS

Takamasa Moriya[1], Tohru Ishida[1], Koji Teramoto[1], Yoshimi Takeuchi[1]
[1]Department of Mechanical Engineering, Graduate School of Engineering, Osaka University, Suita, Osaka, Japan

INTRODUCTION

In recent years, attention is paid to diffractive optics for miniaturization and high performance of optical systems. Diffractive optics has surface shape like diffraction grating or Fresnel lens. It controls wavefront with diffraction effect. Then, a variety of machining methods are requested to effectively produce metal mold of diffractive optics, especially consisting of a variety of microgrooves with various shapes, where the expectation for so called flat-end microgrooves is growing.

Flat-end microgrooves mean microgrooves having no slope at the end, as illustrated in Fig.1. As the existence of the slope causes unnecessary diffraction lights and losses, the slope is requested to remove. However, flat-end microgrooves cannot be machined by conventional grooving methods.

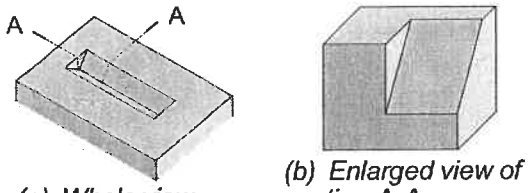

(a) Whole view. *(b) Enlarged view of section A-A.*

FIGURE 1. Flat-end V-shaped microgroove.

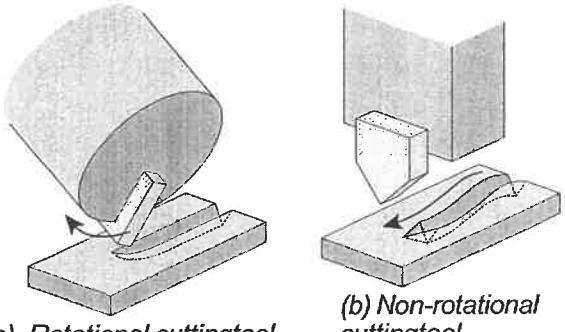

(a) Rotational cuttingtool. *(b) Non-rotational cuttingtool.*

FIGURE 2. Conventional microgrooving.

In microgrooving, two methods have mainly been used. One method is to fabricate microgrooves by use of a rotational cutting tool, as shown in Fig.2(a). The method is good in the shape accuracy and the surface quality, where the cutting speed can be kept high at any time. However, long slopes take place at microgroove ends by the geometrical properties.

The other method is to fabricate microgroove by employing a non-rotational cutting tool, as shown in Fig.2(b). By using the method, microgrooves with a variety of curvature can be fabricated. In addition, it is possible to shorten slopes at the microgroove ends since the entering angle can be controlled. However, the elimination of slopes was impossible, and the creation of the microgrooves with flat-ends has not been achieved before.

Thus, the creation of the flat-end shape was tried in the following manner[1]. At first, the cutting tool is stopped at the groove end so that the chips remain there, as shown in Fig.3(a). Then, the cutting tool removes the excessive parts of chips over the surface at the groove end, as shown in Fig.3(b). However, a microgroove with two flat-ends was not created because the attention was paid only to the creation of the flat end shape at one end. In addition, the shape of the microgroove was limited to the straight line. Accordingly, the study deals with the creation of the microgrooves with two flat-ends on the spherical surface by 6-axis control machining.

ULTRAPRECISION MACHINING CENTER

An ultraprecision machining center (FANUC Robonano) is used in the machining experiments.

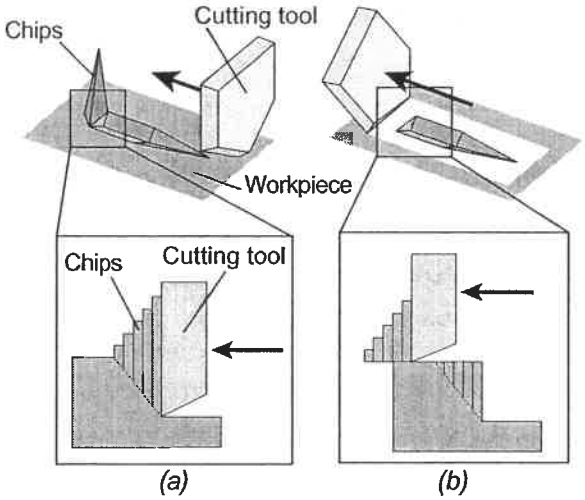

FIGURE 3. Machining method of a flat-end.

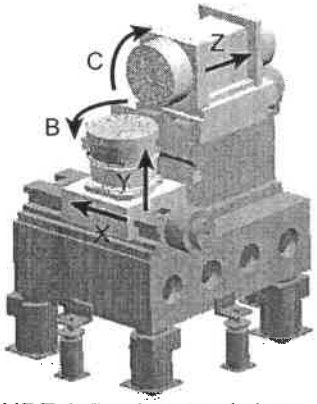

FIGURE 4. 5-axis control ultraprecision machining center.

The structure of the machining center is illustrated in Fig.4. The machining center is composed of three translational axes (X, Y, Z) and two rotational axes (B, C). By adding A axis spindle on B axis table, 6-axis control machining becomes possible. The minimum positioning accuracy of each translational and rotational axis is 1 nm and 0.00001 degree, respectively. A non-rotational cutting tool used in the machining is made of a single crystal diamond with the angle of 90 degrees. Flat-end microgrooves are created on an oxygen-free copper surface.

MACHINING METHOD OF V-SHAPED MICRO-GROOVES WITH TWO FLAT-ENDS

In microgrooving, chips are classified into the shear type shown in Fig.5(a) and the flow type shown in Fig.5(b). As flow type chips have smooth shape, a good machined surface can be expected. On the other hand, shear type chips are fragile and causes shearing slip easily. Moreover, even in case of materials with flow type, shear type chips may occur, depending on cutting conditions. It is confirmed that flow type chips are not suitable for creating a microgroove with flat-end shape since they are thin and wrinkle easily. The microgroove with a flat-end was created by using shear type chips in the previous research since shear type chips are thicker and steadier than flow type ones.

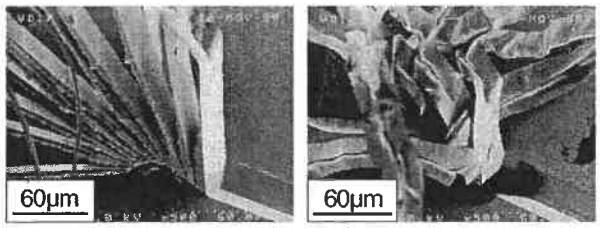

(a) Shear type chips. *(b) Flow type chips.*

FIGURE 5. Enlarged view of chips.

Cutting condition and machining method are shown in Table 1 and Fig.6, respectively. At first, a non-rotational cutting tool makes a V-shaped microgroove with slopes, as shown in Fig.6(a). Roughing is performed 19 times at 1μm depth of cut, and finishing twice at 0.5 μm depth of cut. As a result, the total depth of microgroove reaches to 20 μm. At the time, the generated chips are shear type in roughing and flow type in finishing. Then, the cutting tool is fed and stopped at the both groove ends so that the chips can be in layers and remain there, as shown in Fig.6(b) and 6(c). The generated chips are shear type since the depth of cut is constantly 1 μm. The feed rate up to this stage is 40 mm/min.

Finally, the cutting tool removes the excessive parts of chips over the surface at one end of microgroove, as shown in Fig.6(d), and the workpiece is then rotated to make the opposite groove end in the similar manner at 2 mm/min feed rate, as shown in Fig.6(e). If both ends are machined at a time, the machining time can be shortened, however the layered chips may flake off due to the tensile cutting force against the chips. Thus, each end is independently machined as explained.

TABLE 2. Cutting condition.

Microgroove	Total depth	20 μm
	Depth of cut	1 μm (roughing)
		0.5 μm (finishing)
	Feed rate	40 mm/min
Surface	Feed rate	2 mm/min

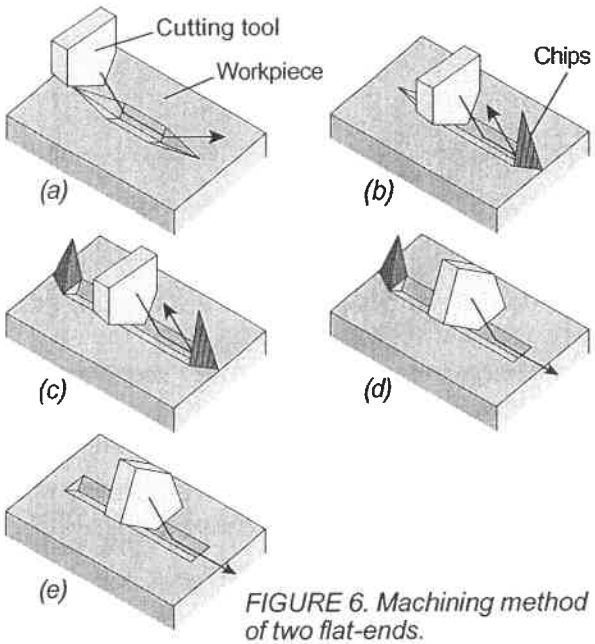

FIGURE 6. Machining method of two flat-ends.

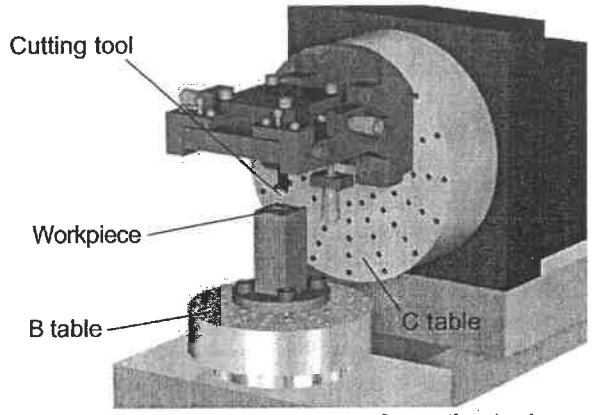

FIGURE 7. Arrangement of a cutting tool and a workpiece.

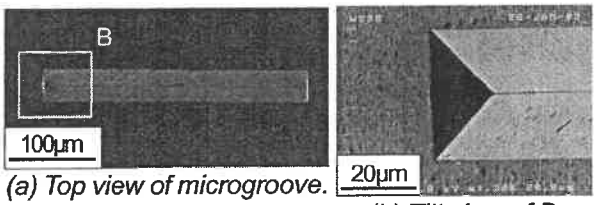

(a) Top view of microgroove. (b) Tilt view of B.

FIGURE 8. Enlarged views of liner microgroove.

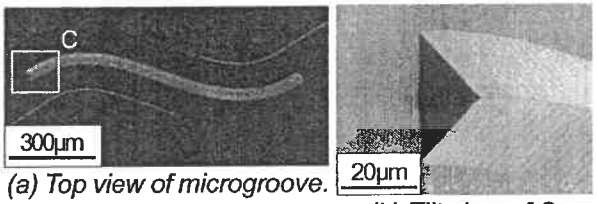

(a) Top view of microgroove. (b) Tilt view of C.

FIGURE 9. Enlarged views of curved microgroove.

CREATION OF V-SHAPED MICROGROOVES WITH TWO FLAT-ENDS ON PLANE SURFACE

In the experiment, the generality of the machining method is verified by creating two kinds of micro-groove on plane surface by use of 5-axis control machining. Figure 7 shows the arrangement of a non-rotational cutting tool and a workpiece.

The target shapes are a liner microgroove of 300 μm in length and a curved one of 900 μm in length. Figure 8 and Figure 9 show SEM images of the machined liner microgroove shape and the curved one, respectively. Figures 8(a) and 9(a) are the whole view of microgroove shapes taken from the above of workpiece. Figures 8(b) and 9(b) are flat-end shapes taken from the direction of 30 degrees upper against the surface of workpiece. It is found that the excellent microgrooves with two flat-ends are created without exfoliation of tips. From these figures, it is found that an excellent flat-end shape with sharp edge line is created. The machined roughness surface is from 30 to 50 nmRmax in the middle section of the microgroove and from 40 to 60 nmRmax at the vicinity of flat-ends. Both roughness values are smaller than 100 nm, and an excellent mirror surface is obtained.

CREATION OF V-SHAPED MICROGROOVE WITH TWO FLAT-ENDS ON SPHERICAL SURFACE

Then, a similar manner is applied to 6-axis control in order to create the microgroove on the spherical surface, assuming the lens shape. The arrangement of 6-axis control machining is shown in Fig.10(a). First of all, a cylindrical workpiece is installed in the air turbine spindle, and milled by using a tool blade, as shown in Fig.10(b), and fabricates a spherical surface of R1 at the tip of workpiece.

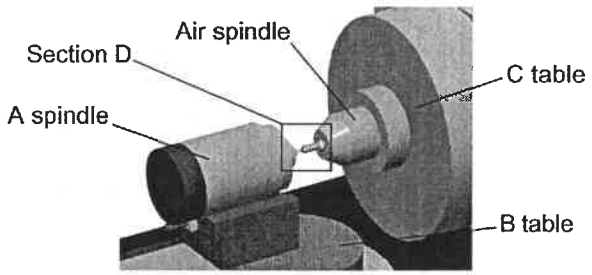

(a) Whole view of 6-axis setting.

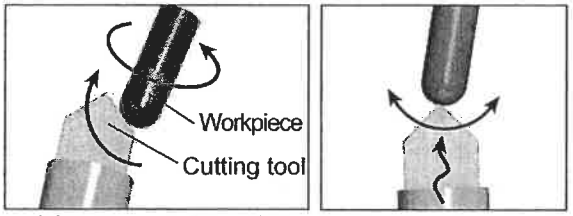

(b) Enlarged view of D at milling.

(c) Enlarged view of D at grooving.

FIGURE 10. Milling and grooving by 6-axis control machining.

Subsequently, the spindle is stopped, and the workpiece is fixed. Then, the microgroove is created by using tool top edge, as shown in Fig.10(c). Comparing 6-axis control machining with 5-axis control machining, the influence of positioning error appears due to the increase in the number of control axis. The errors due to the change in cutting tool and workpiece can be reduced by performing a series of machining with the same arrangement. Moreover, when the layered tips are removed, the workpiece is driven as well as sphere fabrication, as illustrated in Fig.10(b), to suppress the deviation between cutting surface and spherical surface.

Figure11 shows SEM images of the machined microgroove shape, where (a) is the whole view of microgroove shape taken from the above of spherical surface, (b), (c), and (d) are flat-end shapes taken from the direction of 45 degrees upper against the spherical surface. It is found that the curved microgroove is successfully created by 6-axis control grooving. An excellent flat-end shape with sharp edge line, as seen in Fig.11(c), is created as well as the case created on the flat surface. However, the top of flat-end at the cutting surface is not necessarily good, as seen in Fig.11(c), the cutting surface of the layered chips is located in a higher

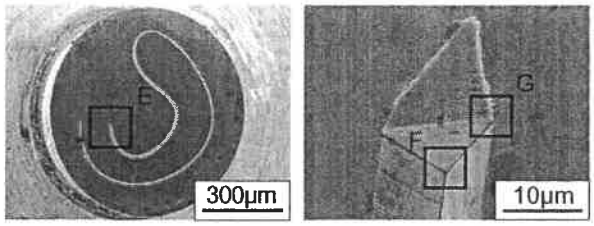

(a) Top view. (b) Enlarged view of E.

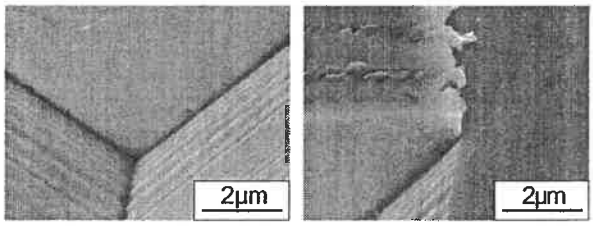

(c) Enlarged view of F. (d) Enlarged view of G.

FIGURE 11. Flat-end of curved microgroove on spherica surface.

position than the spherical surface. Although the sphere creation and microgrooving were performed with the same setting, ill flat-ends took place. This may be due to the air pressure change. To deal with the problem, the introduction of error correction method is requested, which measures errors and corrects NC code.

CONCLUSION

Although the flat-end shape was successfully created, it had only single end, and the microgroove shape was limited to the straight line. To widen the possibility of microgrooving technology, the study aims at developing a new machining method to create microgrooves with two flat-ends. As a result the straight and curved microgrooves with two flat-ends were successfully created on a flat surface and a spherical surface by a newly proposed machining method.

A part of the study is supported by Grant-in-Aid for Scientific Research B16360069.

REFERENCES

1. M. Murota, T. Suzumura, T. Ishida, Y. Takeuchi, T. Kawai, K. Sawada, "Creation of Ultraprecision V-shaped Micro Grooves with Flat-end," Journal of Japan Society for Precision Engineering, (in Japanese), 70, 5 (2004) pp. 677-682.

ULTRAPRECISION TURNING WITH BINDERLESS CBN

Dirk Oberschmidt[1], Martin Kurz[2], and Eckart Uhlmann[1]
[1]Micro Production Technology
Fraunhofer Institute for Production Systems and Design Technology
Berlin, Germany
[2]Manufacturing Technologies
Technical University Berlin, Institute for Machine Tools and Factory Management
Berlin, Germany

INTRODUCTION

Ultra precision machining of metals has an increasing importance for especially mould and die making. Depending on the machined materials, roughness values of Ra < 1 nm and form accuracies of less than one micron can be realised with ultra precision technologies by use of monocrystalline diamond as cutting material. With different replication technologies, it is possible to transfer these values to the final product. Injection molding, hot embossing and glass-pressing are of high potential for molding optical components. Until recently, manufacturing of metallic moulds and dies by cutting with geometrically defined cutting edges was limited to work piece materials that are traditionally machinable with monocrystalline diamond. These materials are non-ferrous metals and especially platings of electroless nickel-phosphorus (ElNiP). Ultraprecision machining of steel with geometrically defined diamond cutting edge is not yet a stable industrial process. Therefore the optical surface quality corresponding to the optical function on the final product is achieved by polishing, classically. Unfortunately, the form accuracy of the work piece is affected by polishing processes.

At the present time there are four different approaches to overcome the disadvantages of polishing by direct machining with ultraprecision technologies:

Approach I: Shortening the contact time between work piece and tool

Beside lattice faults, diamond wear is mainly caused by the transformation of diamond into graphite, which is the more stable phase of carbon at room temperature. This transformation results from high pressure and/or high temperature. The pressure and temperature values for the diamond-to-graphite conversion depend on the properties of the diamond used. Particularly with regard to natural diamond there is to observe a broad range of dispersion. Adequate accurate data are not available, especially for the necessary pressure. The temperature of graphitization can be specified as T > 550°C. With shortening the contact time between work piece and tool, the temperature of the cutting part can be reduced significantly. Thereby, in steel it is possible to achieve an arithmetical mean deviation of Ra = 5 nm [1].

Approach II: Tool cooling

With the same goal, the reduction of the cutting part temperature, tools are cooled in process. E.g. liquid nitrogen is used as coolant to reduce the temperature of the diamond cutting part. Up to now, no relevant advantage was obtained for steel machining by research activities [2].

Approach III: Work piece material modification

Initial point of this approach is a special characteristic of nickel. Nickel alloyed with phosphorus is diamond machinable while nickel itself is not. Free electrons that could react with carbon are bound by the alloying addition. Regarding this, efforts are made to use a similar effect for steel machining. With surface layer nitration of steel materials, first promising results were obtained [3].

Approach IV: Use of alternative cutting materials

Comprehensive investigations were made to substitute monocrystalline diamond as cutting material for ultra precision machining with geometrically defined cutting edge. Cutting materials used are e. g. aluminium oxide, cBN or diamond coated hard metal. Especially the application of cBN seems to be successful. 25CrMoS4 (60 to 65 HRC) was machined with PcBN BNX10 at a minimum roughness of Ra = 10 nm [4]. A roughness value of Ra = 65 nm has been achieved with monocrystalline cBN [5].

Objective

Starting from existing results mentioned above, objective of a research project at the Center for Production Technology (PTZ) in Berlin is to scrutinize the potential of Binderless cBN as cutting material for ultraprecision machining of steel with geometrically defined cutting edge. Goal is the complete machining by cutting of mould and die surfaces for the replication of optical components. At least, the process chain for the production of steel replication tools shall be shortened considerably by substituting process steps. Thus, a higher form accuracy of the final product will be achieved.

Experiments

Facing experiments with steel 40CrMnMoS8.6 were conducted. The material was used fully heat-treated by the manufacturer with a measured hardness of 54 HRC. The experiments were done at a 5-axis ultraprecision machining system Nanotech® 350 FG (Moore Nanotechnology Systems, Keene/USA). For measurements a confocal Laser-Scanning-Microscope LSM 5 Pascal (Carl Zeiss, Jena/Germany), a White-Light-Interferometer NewView 5010 (Zygo Corporation, Middlefield/USA), a Scanning-Electron-Microscope DSM 950 (Carl Zeiss SMT, Oberkochen/Germany), and a machine integrated optical tool setter were used.

Experimental Results with PcBN

First, experiments with PcBN were conducted. Within these tests, input parameters for the following experiments with Binderless cBN were identified.

TABLE 1. Parameters of PcBN-Tools

Cutting material	Tool corner radius r_ε /mm	Cutting edge roundness r_β /µm
HTC 2000	1.5	8
HTC 2000	3	8
BZN 9100	3	25

The cutting edge roundness is measured by ZEISS LSM 5 PASCAL (Objective Epiplan Neofluar 50/0.8), respectively. The particular roundness was determined as average value of 10 measurements on different tool corner positions. Thereby 3-point circle determination was used. The tool corner radii are measured by the optical tool setter.

During these experiments were varied cutting speed v, feed per revolution s, and depth of cut a. Regarding roughness as criteria for the surface quality, the best result was achieved with an arithmetical mean deviation of Ra = 27 nm. Best Peak-Valley value was P-V = 285 nm. The roughness was measured with a Zygo NewView 5010 (Objective 20/0.4) at a measuring length of 670 µm. The tool had a cutting part made of HTC 2000 and a corner radius of r_ε = 3 mm. Total tool path was $W_{(Ra)}$ = 40 m. As criterion of tool wear an increase of roughness value of 50% was defined. Used machining parameters were:

Cutting speed:	v = 145 m/min,
Depth of cut:	a = 5 µm,
Feed per revolution:	s = 10 µm/r.

These were the starting values of the facing experiment with Binderless cBN as cutting material.

Experimental Results with Binderless cBN

According to specifications provided by the manufacturer, Binderless cBN has the following properties:

Hardness:	45 GPa
Elasticity (Young's modulus):	710 GPa
Thermal stability on air:	1300°C
Grain size:	< 0.5 µm
cBN proportion:	99.7 %
Other constituents:	hbN.

It was not possible, due to the disposability of the cutting material, to use the same tool corner radii as for the PcBN experiments. The tests were made with the specifications mentioned in Table 2. The tool geometry measurements are done similarly to the PcBN tools.

TABLE 2. Characteristics of Binderless cBN-Tools

SEM image			
Tool No.	1	2	3
Tool corner radius	0.4 mm	0.8 mm	0.8 mm
Cutting edge roundness	3 µm	2.1 µm	1.4 µm
Rake face	raw	ground	finished

The scrutinized tools have a chip angle of $\gamma = 0°$ and a clearance angle of $\alpha = 8°$.

Starting with the previously mentioned and in the PcBN tests established cutting parameters, experiments were made under variation of v, s, and a. Regarding the roughness, it was found that best results were obtained at a cutting speed of $v = 135$ m/min and a feed per revolution of $s = 5$ µm. The results are listed in Table 3.

TABLE 3: Arithmetical mean deviation Ra as result of facing experiments with Binderless cBN (measured with a Zygo NewView 5010; objective 20/0.4; measuring length 900 µm)

Tool No.	Cutting distance m /m	Arithmetical mean deviation Ra /nm	
		Depth of cut a = 10 µm	Depth of cut ap = 5 µm
1	5	495	n. m.
	25	395	n. m.
	45	182	n. m.
2	5	77	***33***
	25	86	***30***
	45	73	***38***
3	5	***36***	84
	25	***36***	70
	45	***27***	42

The SEM image of a surface topography made with tool No. 3 is shown in Fig. 1. Fig. 2 is a white light interferometric image of the same surface.

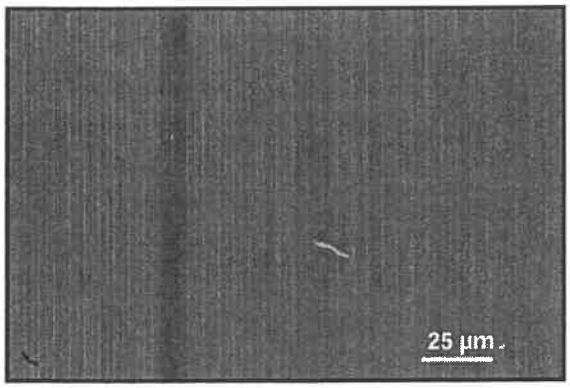

Figure 1. SEM image of a faced surface, machined with Binderless cBN; v = 135 m/min, s = 10 µm, a = 5 µm

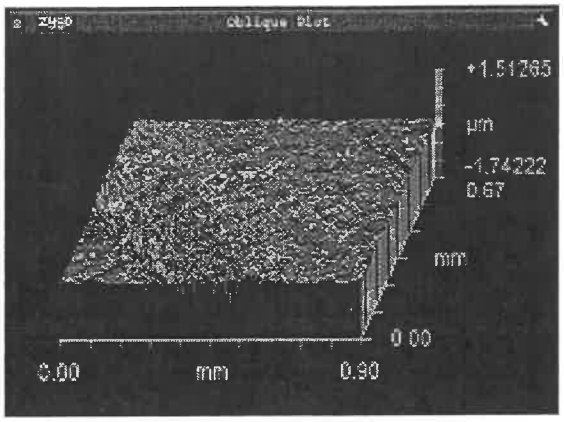

Figure 2. WLI image of a faced surface, machined with Binderless cBN; v = 135 m/min, s = 10 µm, a = 5 µm

Both images demonstrate a surface of high quality. Fig. 1 illustrates the formation of a homogeneous turned surface. Fig. 2 is to display the evenness of the surface. At the same time the image indicates the crossover between the different areas caused by different tool states.

During the experiments, there were different wear indications noticeable at the tool edges. E.g.: wear by cratering, flank wear, and cutting edge chipping. Fig. 3 shows the topology of the cutting edge of tool No. 2 during the machining. It also illustrates the potential of creation cutting edges with smaller cutting edge roundness.

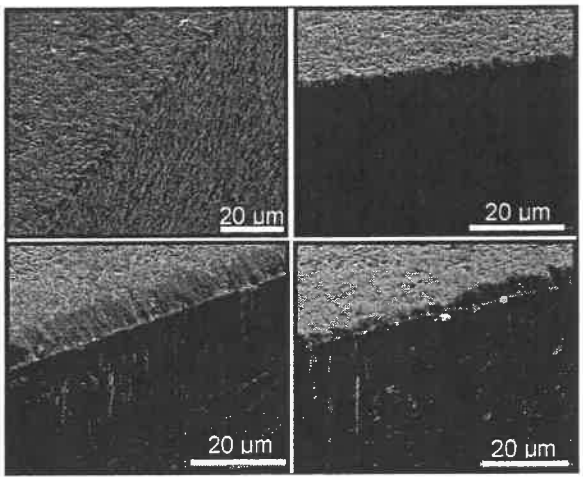

Figure 3. Topology of a Binderless cBN cutting edge during a facing experiment; unprocessed (top left), condition at the beginning of the machining (top right), condition during machining (bottom left), worn (bottom right); v = 135 m/min-1,sf = 10 µm, a = 5 µm

Four conditions can be distinguished:

Condition I: Unprocessed condition
The tool is unused. The cutting edge roundness is determined by the cutting edge preparation.

Condition II: Starting condition
There is to observe starting flank wear and thus leveling of the cutting edge roundness. This leads to machining condition.

Condition III: Machining condition
A quasi-stationary condition of the cutting edge is reached. At this condition, the best roughness values can be achieved.

Condition IV: Wear condition
Dominant wear indication is flank wear followed by adhesion of workpiece material onto the flank. It is assumed, that these adhesions lead to a stronger deflection of the tool. This causes tool vibration and chattering. The resulting impact load onto the cutting part leads to cracks and chipping of single grains out of the cutting edge. Thus it is reached the starting point for catastrophic tool wear.

Conclusion and Outlook
Successful ultraprecision facing experiments of fully heat-treated steel 40CrMnMoS8.6 has been made with Binderless cBN as cutting material. Results of roughness values Ra < 35 nm and peak to valley of P-V < 200 nm were achieved. Removal rate is Q > 0,1 mm³/s and the tool total path is about $W_{(Ra)}$ = 80 m. The generated surfaces show a homogeneous structure. Tools can be evaluated regarding geometrical characteristics and abrasion. Experiments show, that the cutting material Binderless cBN is of high potential regarding the machining of steel for moulds and dies. Despite the achieved roughness, the obtained surfaces are not ofoptical quality. This is documented by a Ra/P-V ratio of about 1/7. And despite the homogeneity, the surface is refractive and therefore appears rough.

In further research activities, particularly the preparation of the cutting edge has to be scrutinized. This is necessary to guarantee a stationary condition of the cutting edge from the beginning of the machining. With an adapted geometry of the cutting edge, this condition can be sustained considerably longer as currently possible. Further investigations must be carried out in the area of adapted cutting part geometry. This is essential for broadening the machinable material spectrum to stainless steel, too. Goal is the direct ultraprecision machining of different tool steels. That requires comprehensive analytic investigations in order to anticipate surely the in-process behaviour of the cutting edge and thus to increase process reliability.

REFERENCES

1. Moriwaki, T., Shamoto, E., 1999, Ultraprecision Diamond Cutting of Hardened Steel by Aplying Elliptical Vibration Cutting. Annals of the CIRP, 48/1999/1: 441-44.
2. Gläbe, R., 2004, Prozess- Und Schneidstoffentwicklungen zur ultrapräzisen Drehbearbeitung von Stahl. Forschungsberichte aus der Stiftung Institut für Werkstofftechnik Bremen, Band 24, Shaker Verlag, Aachen.
3. Brinksmeier, E., Dong, J., Gläbe, R., 2004, Diamond Turning of Steel Molds for Optical Applications. Proceedings of the 4th euspen International Conference, Glasgow, UK: 155-156.
4. Morantz, P., Maeda, C., Ueda, H., 2002, Ultra-precision machining hard metals: turning versus grinding. Proceedings of the 3rd euspen International Conference, Eindhoven, The Netherlands: 353-356.
5. Grimm, U. et al, 2004, Fabrication of surfaces in optical quality on pretentious tool steels by ultra precision machining. Proceedings of the 4th euspen International Conference, Glasgow, UK: 193-194.

CHATTER STABILITY BOUNDARY ANALYSIS USING NEURAL NETWORK

M.S. Oh [1], J.S. Jung[2], S.B. Sim[3] and M.C. Yoon[4] (corresponding author)
[1,3,4]School of Mechanical Engineering Pukyong National University
San100, Yongdang-Dong, Nam-Gu, Busan, Republic of Korea
[2]Workers Accident Medical Corporation Korea Orthopedics & Rehabilitation Engineering Center
47-3 Kusan-Dong, Pupyoung-Gu, Inchon, Republic of Korea

INSTRUCTION

A more important focus on chatter is the stability boundary analysis that is more practical and realistic in the sense that this analysis shows the chatter boundary region in all available cutting condition and the chatter state for the machinist in field to get the insight easily to avoid the chatter problem. Considering this points, a new method to get the chatter stability boundary is mainly discussed in this study. Present study about these kind of chatter stability boundary is the results of Kim and Yoon in the scope of basic knowledge[1-4]. Their study also have its roots on the study of Altintas[5]. There is some problem that cannot exactly discriminate the condition for specific cutting coefficient between that of half immersion and full immersion end-milling. Also in real calculation, the specific coefficient of different end-milling is considered as same. So it has some unreliable limitation in their results for concrete propose. However, the *RBNN* stability lobe analysis that is suggested in this study is more realistic than the conventional method in the means that this method uses the real experimental data as an input. So, it can represent the end-milling more realistic. In this study, the conventional *FFT* or time series spectrum is used for discriminating the chatter. After deciding the state of chatter in all condition, The state was coded and used as an input in all region with respect to an axial depth of cut and spindle revolution in the end-milling. In this paper, it was suggested to discriminate the chatter region by using the *RBNN* stability lobe algorithm. And it was verified that the output of the RBNN stability lobe also consists with the conventional stability lobe method. Further more it has some merit to represent the stability lobe considering experimental data using concrete data.

NEURAL NETWORK

A new *RBNN* stability lobe method is proposed and compared with the conventional stability lobe analysis[2,3] in this paper. This new method has the advantage of a fast convergence and a less error than other *BP* (back propagation) learning algorithm.

The proposed radial basis neural network has two hidden layer. One of them uses the radial basis function and the other does linear function as a transfer function. The output vector can be acquired by learning algorithm considering the weights and the bias. In *RBNN* algorithm, the dependent output parameter, ***a***, can be obtained by multiplying the weights ***w*** to input vector ***p*** and by adding the bias. The output, ***a***, become a new input in second hidden layer and a new output can be obtained with the same procedure. Fig.1 shows this architecture of *RBNN* algorithm. The left side of this figure shows the radial basis layer and the right side shows the linear layer. Fig. 2 shows the total architecture of the neural network. It has an input of two units, two hidden layer of seven units and an output of three units.

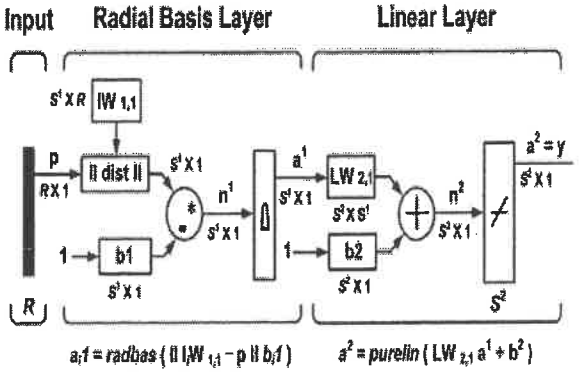

FIGURE 1. Architecture of the RBNN

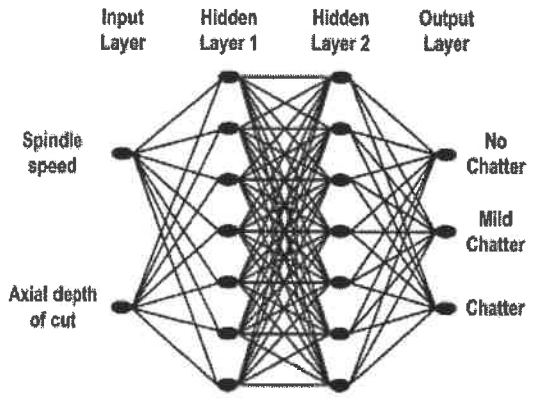

FIGURE 2. Architecture of the neural network

EXPERIMENTAL METHODS

An experiment was performed using a machining center (DOOMAC 40V) to acquire the signal of the cutting force during the end-milling operation, combined with a 15 *mm* _ 48.7 *mm* (diameter _ overhang), four fluted, high speed steel(HSS) helical end-mill, and a SM45C workpiece. The cutting force *Fx* and *Fz* was measured by a piezo-type tool dynamometer (Kistler:9272B) and recorded by a Pentium computer through a data acquisition system. The setup was further modified to obtain the cutting force signal including chatter properties. In the analysis, Microsoft Visual C++ was used for data arrangement for re-sampling. The tool dynamometer was used to acquire the cutting forces in three directions. The equipment specifications are summarized in Table 1. The sampling frequency for acquiring the cutting force is 10 *kHz* and the axial depth of cut ranging 1 ~ 8 *mm*, the spindle speed revolution ranging 100 ~ 1500 *rpm*, the radial depth of cut is set to 7.5 *mm*. And also the feed per minute is selected as 16, 24, 36, 40, 48, 56, 64, 72, 80, 88, 96, 104, 112, 120 *mm/min* and the feed per tooth is set constant as 0.02 *mm/tooth* in the end-milling.

TABLE 1 Experiment specification

Instrument	Specification
End-mill	_ 15, 4-flutes
Workpiece	SM45C
Machining center	Doosan machinery Co.
Dynamometer	Piezo type 9272B(Kistler Co.)
Charge amplifier	Type 5019A-4channels
A/D converter	DT3001

STABILITY LOBE ANALYSIS

Fig. 3 shows the stability lobe that was obtained by the conventional characteristic equation method. For this case the roots of the characteristic equation represent one of the stability boundary that match the integer *k=1, 2, ... , n*. In investigation the stability lobe[5,6], as the damping ratio increase the total boundary moves upward and the stability region becomes wide. But the boundary region moves downward for a large damping ratio and the size of stable region become smaller and narrower. If the natural frequency increases then the boundary curve moves right. And if it decreases on the contrary then the curve moves left[1].

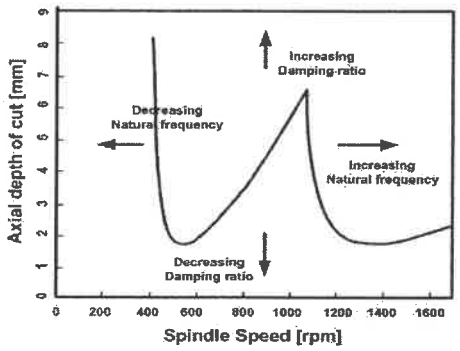

FIGURE 3. A rchitecture of the stability lobe behavior according to natural frequency and damping ratio

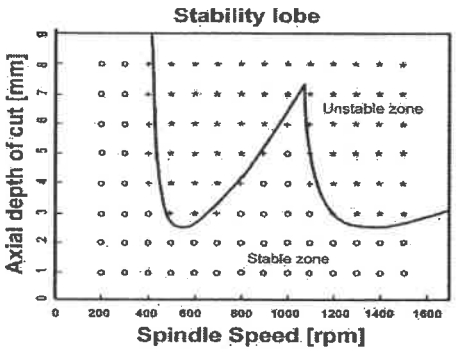

FIGURE 4. Distribution of chatter using experimental data and stability lobe for end-milling force Fx

Fig. 4 shows the superposition of the experimental pattern and the stability lobe of conventional characteristic equation method. In each spindle speed revolution, the classified pattern such as chatter(*), mild chatter(+) and no-chatter(o) is marked and the conventional stability lobe was superposed on the pattern.

The stability lobe approximated on this pattern is shown that the specific cutting coefficient K_t is 2100 N/mm^2, natural frequency $\_n$ = 234 Hz and damping ratio $\_$ = 0.33[2,3].

STABILITY LOBE ANALYSIS BY NEURAL NETWORK

The input vector that was used in this paper was defined after the cutting force in each condition is transformed in frequency domain using the time series spectrum. And if there is a peak mode in the power spectrum it is defined that the cutting force has chatter and if it does not have the mode more than 5 times larger than the minimum amplitude of power spectrum in all frequency range then it is considered no-chatter. With this criterion for chatter existence in each cutting condition, the experimental chatter pattern which is marked was classified in the Fig. 5. And the output vector is classified into three patterns such as chatter, mild chatter and no-chatter. With this input and output vector, after adjusting the weights and biases in the architecture of *RBNN*, the complete learning is accomplished by increasing the learning rate and reiterate. In learning algorithm, the radial basis function and linear function was used in each hidden layer. After reiterating, if the out vector converges to target vector and the total error is less than 0.01 % then the learning was stopped and the stability boundary was acquired. Fig. 5 shows three region classified by pattern mark, such as no-chatter(o), initial or mild chatter(+) and severe chatter(*). After passing through the neural network with input and output vector, a different boundary was calculated. The boundary **(A)** is the *RBNN* stability lobe for 10000 iterations and the boundary **(B)** is the *RBNN* stability lobe for 30,000 iterations. Fig. 5(a) shows the RBNN stability lobe that was calculated by passing the input vector through the radial basis neural network using cutting force *Fx*. After iterating about 10,000, the curve **(A)** is fitted and the final target curve **(B)** is obtained after iteration of 30,000. Also, the upper region is the unstable one where the chatter exists and the lower region is the stable region where the chatter does not exist after passing through the *RBNN*. Similarly, Fig. 5(b) shows the *RBNN* stability lobes using cutting force *Fz*. The curve **(A)** is the fitted *RBNN* stability lobe at an iteration number of 10,000 and the final target curve **(B)** is the fitted *RBNN* stability lobe at an iteration number of 30,000. As the iteration number increase, the RBNN stability lobe approximate the target curve exactly and the boundary consists with experimental pattern. As the pattern data is prepared widely with many points in all condition then the boundary curve becomes smoother. Also it matches well with the experimental result and more realistic stability lobe for chatter analysis. In general this *RBNN* algorithm has a faster convergence than the *BP* (back propagation) algorithm which is generally used. With this algorithm, it is shown that the *RBNN* stability lobe consist with experimental stability pattern.

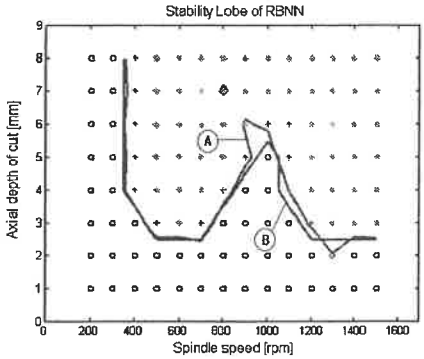

(a) Stability lobe surface for Fx

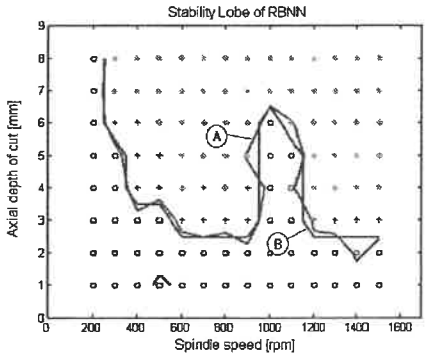

(b) Stability lobe surface for Fz

FIGURE 5. Stability lobe by radial basis neural network

Fig. 6(a) shows the three dimensional view of the chatter region that was calculated by passing the input vector through the radial basis neural network. And the input vector is discriminated by analyzing the cutting force *Fx* using power spectrum. In figure, the upper region is the unstable one where the chatter exists and the lower region is the stable region where the chatter does not exist. Fig. 6(b) shows the similar result of the chatter region that was calculated by passing the input vector using the cutting force *Fz* through the radial basis neural network. Similarly as the cutting force *Fx* in Fig.

6(a), the upper region is the unstable one where the chatter exists and the lower region is the stable region where the chatter does not exist. Similarly as the cutting force *Fx* in Fig. 6(a).

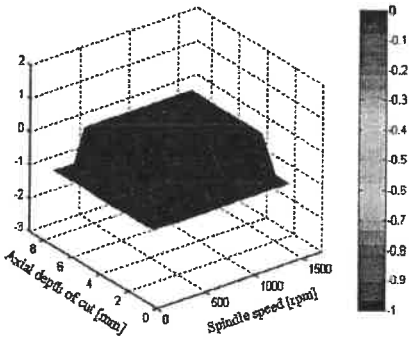

(a)Stability lobe surface for Fx

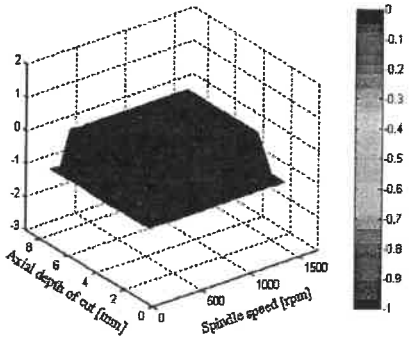

(b)Stability lobe surface for Fz

FIGURE 6. Stability lobe surface by RBNN algorithm

By investigating the two figures, the unstable chatter region appears wide in Fig. 6(b) than Fig. 6(a) which is the case using the cutting force *Fx*. This means that the chatter property is more dominant in cutting force *Fz* in the same cutting condition and the chatter appears more clearly in the cutting force *Fz*. So it is more appropriate to analyze the chatter using the cutting force *Fz*. This result is quite different to our common intuition that cutting force *Fx* may have more property of the chatter phenomenon than the cutting force *Fz*. Using this basic result, it is concluded that the selection of cutting force also have an effect on the appropriate chatter analysis. Also using this *RBNN* stability lobe, the operator can select the desirable cutting condition to avoid the chatter phenomenon. This result is more realistic than the conventional methods which use the characteristic equation for obtaining the chatter stability lobe because the conventional method have more deviation error according the stability boundary than the real chatter point with experiment. As a result, a more realistic axial depth of cut and spindle speed can be obtained to avoid the chatter using the suggested *RBNN* stability lobe in this study.

CONCLUSION

(1) Using the stability boundary analysis by *RBNN*, It is possible to discriminate the region between the stable and unstable region. With this method, a stability lobe that is a transition boundary between stable and unstable region with respect to the axial depth of cut and the revolution of spindle speed was suggested.

(2) Using the *RBNN*, A stability lobe that is consistent with that of the conventional method can be acquired with this algorithm. Even if the weighting factor and the bias is random value, the target value can be approximated by increasing the learning rate and repetitive number.

REFERENCES

1. M. C. Yoon, Y. G. Kim and K. H. Kim, 2006, The characteristics and stability boundary analysis of chatter using neural network, *J. of KSMPE,* 5/2: 16-21.
2. M. C. Yoon and Y. K. Kim, 2001, Chatter modeling and its diagnostics in end-milling, *Proceedings of ASPE*, 23: 481-484.
3. Y. G. Kim, M. C. Yoon, M. K. Ha and S. B. Sim, 2001, A study on the modeling and diagnostics on chatter in end-milling operation, *Proceeding of KSPE*, 971-974.
4. M. C. Yoon and D. H. Chin, 2006, Time series modeling and spectrum analysis for chatter mode in end-milling dynamics, *International Journal of AMT,* 29/11-12: 1125-1133.
5. Y. Altintas, 2000, Manufacturing Automation, *Cambridge Univ.* Press.
6. M. C. Yoon and Y. G. Kim, 2004, Cutting dynamic force modeling of end-milling operation, *Journal of MPT*, 156: 1383-1389.
7. M. C. Yoon, B. T. Kim and K. H. Kim, 2004, Natural mode estimation of cutting dynamics with time series modeling, *Journal of MPT*, 156: 1373-1382.
8. S. L. Oh, D. H. Chin, M. C. Yoon, I. I. Ryoo and M. K. Ha, 2005, Chatter mode and stability boundary analysis in turning, *Trans. of KSMTE*, 14/5, 7-12.
9. Matlab Manual, Mathwork Inc, 1997.

OPTIMIZING SAW TEETH DEFLECTION AND LUMBER THICKNESS VARIATION THROUGH PRECISION ENGINEERING APPROACH

Reynolds Okai
Department of Technology Education
University of Education, Winneba (Kumasi Campus)
P.O. Box 1277, Kumasi, Ghana

INTRODUCTION

Lumber size control is an essential element in maximizing recovery from both small and large diameter log because a small reduction in rough green target size could lead to substantial savings in wood fibre. It is an established fact that rough green target size is affected by shrinkage allowance, planer allowance, and sawing variation. It is therefore essential that studies be conducted into these components of rough green target size. The shrinkage allowance depends on the wood species, and in particular, species, which shrink more during drying, need to be sawn thicker initially than species, which shrink less. Sawing variation is an important component of target size, and useful information from sawing variation can be used for estimating target size in addition to troubleshooting machine centre problems. The sawing variation is an indicator of how accurately the wood is sawn into lumber, and consists of three components: within-board sawing variation, between-board sawing variation and total sawing variation.

Previous studies indicate that there is a difference between the accuracy and the precision of a saw machine. The accuracy relates to the capability of a saw to hit a target size. The precision relates to the degree of a saw's standard deviation. A third factor is reproducibility, which refers to the consistency of a saw machine to produce repeatedly similar patterns of variation. When repeated readings show erratic patterns of variation, the operation of a saw machine is not consistent and not reproducible. When accuracy and precision are under control, a system will demonstrate consistent reproducibility. We expect that a bigger side clearance could lead to excessive sawdust spillage between the cut surfaces and the saw blade if the bite per tooth is smaller than the clearance between the cut surface and the saw blade. The net effect is the inducement of friction. We also expect that a smaller side clearance would result in friction between the cut surface and the saw blade leading to overheating of the saw blade and consequently loss in saw tensioning. The loss in saw tensioning will create avenue for the saw blade to meander its way in the wood leading to excessive sawing variation. The work reported in this paper explains how the side clearance affects lumber thickness variation. A quadratic relationship between side clearance and lumber thickness variation has been established. As the side clearance of the saw increases, the sawing variation decreases until it reaches a minimum value and thereafter, further increase in side clearance of the saw teeth results in an increase in sawing variation. It was observed that an optimum side clearance of 0.69 mm under a saw blade thickness of 1.3 mm was required to produce on the average, a minimum value of 0.42 mm for within-board standard deviation, and 0.59 mm for the total standard deviation. An error margin of less than 1% was achieved when the experimental results for the optimum side clearance was compared with a theoretical assertion.

EXPERIMENTAL SETUP

A 1328 mm bandmill with auto feed carriage and rated motor power of 110 hp and spindle speed of 1440 revolutions per minute (rpm) was used for the study. Eight bandsaw blades comprising of four blades each of stellite-tipped and swage-set saws with similar dimensions and specifications were selected from ten bandsaw blades in random manner. The specifications of the saws are as follows: blade width; 152 mm, blade thickness; 1.3 mm, number of teeth; 209, tooth pitch; 45 mm, tooth height; 16 mm, and rake angle; 27 degrees. The stellite tipping was done by depositing a stellite material which is composed of 58% cobalt, 29% chromium and 9% tungsten on the teeth of the saws by the conventional method, that is, the rod of the stellite 3.2 mm in diameter was melted with an oxyacetylene flame and their melted pieces

were manually welded onto the rake faces of the swaged teeth. The four stellite-tipped saws were then sharpened and side-dressed with grinding wheels. The swage-set saws were prepared with manual swage-set machines. The kerf width of all the 209 teeth as well as the inner and outer side clearance of the eight bandsaw blades were measured with a vernier caliper and a side gauge respectively. The side gauge is a measuring device to indicate the amount of lateral (sidewise) projection of saw teeth beyond the surface of the saw.

In order to determine the sawing accuracy or sawing variation of stellite-tipped and swage-set saws, the eight bandsaw blades were used to rip-saw green *Triplochiton scleroxylon* of moisture content 63.6% into lumber of nominal thickness of 41 mm at a feed speed of 13 m/min and depth of cut of 420 mm. Ten boards were randomly sampled when each of the saws was used to rip-saw the beams. The thicknesses of the boards were measured with a vernier caliper at ten locations on each board along the top and bottom edges. The length of each board that was sampled for measurement was 3.66 m. The lumber thickness was measured at 330 mm from both ends of the board and subsequent measurements were taken at intervals of 750 mm. The influence of depth of cut on sawing accuracy was also examined. The depth of cut is the distance moved by successive teeth from a point where the teeth engage the workpiece to a point of exist from the workpiece in a direction perpendicular to the feed direction. The stellite-tipped saws were used to rip-saw *Triplochiton scleroxylon* into boards of nominal thickness of 41 mm and depth of cut of 320 mm, 420 mm, 500 mm, 610 mm, 750 mm, and 800 mm. Two displacement sensors were positioned 40 mm above the workpiece to measure the saw blade vibration.

In the next phase of the study, the inner and outer side clearances of the stellite-tipped saws were measured anytime the saws were sharpened. The saws were used to rip-saw *Triplochiton scleroxylon* beams into boards of nominal thickness of 41 mm and depth of cut of 420 mm. Ten boards were randomly selected from the first fifteen boards produced and the thickness of the boards measured at ten locations on the boards under identical side clearance and depth of cut. A complete randomised design (CRD) was used for data collection. Analysis of variance was used to test for significant differences between the kerf width of swage-set saws and stellite-tipped saws. The student's T-test was also used to test for significant differences between the inner and outer side clearance of the stellite-tipped saws.

EXPERIMENTAL RESULTS

The accuracy of kerf width of bandsaw teeth is influenced by the technique of setting and sharpening Murata, *et al* [1]. It is therefore essential that the saw teeth are prepared to maximum accuracy to ensure good sawing performance. Experimental results for the accuracy of kerf width of stellite-tipped and swage-set saws are presented in Table 1. It can be seen that the mean kerf width of the stellite-tipped saws are generally greater than the mean kerf width of the swage-set saws. On the average, the mean kerf width of the stellite-tipped saws was 4.2 mm whilst the mean kerf width of the swage-set saws was 3.06 mm. The results deviate from the assertion by Denig [2] that a simple rule for the required kerf of a blade is to multiply the blade thickness (1.3 mm) by two for which in this case the kerf width should have been 2.6 mm.

The results presented in Table 1 show that the accuracy of kerf width was best with stellite-tipped saws as indicated by the smaller standard deviation of the mean kerf width compared to a bigger standard deviation of the mean kerf width for swage-set saws.

TABLE 1. Kerf width of stellite-tipped and swage-set bandsaw blades

Saw No.	Types of saw setting			
	Stellite-tipped saws		Swage-set saws	
	Mean kerf width (mm)	SD (mm)	Mean kerf width (mm)	SD (mm)
1	4.02	0.2789	3.08	0.3511
2	4.48	0.2255	3.04	0.3940
3	4.25	0.2785	3.34	0.4341
4	4.04	0.1537	2.76	0.3739

SD: Standard deviation

Saw setting is intended to reduce friction by making the kerf wider than the thickness of the bandsaw blade. Spring setting, swage setting, and tipping are special types of saw setting. Each tooth on a saw must be given an equal amount of set if smooth and steady sawing is to

be obtained. Unevenly set teeth place a greater strain on some teeth than others. If the teeth are all set more on one side than the other the saw will lead to the side with the heaviest set and tooth marks and breakage will result.

Side clearance is provided on the saw teeth to reduce friction between the saw blade and the sawn lumber. Figure 1 shows the relationship between side clearance of stellite-tipped saw and sawing variation indicated by standard deviation of lumber thickness. A quadratic relationship between standard deviation of

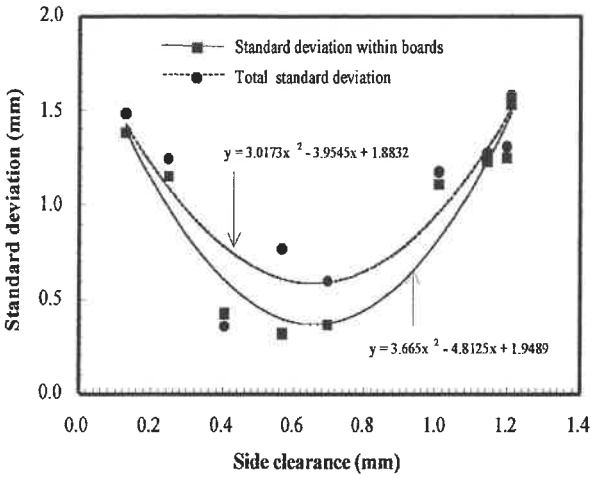

Figure 1. Relationship between side clearance and sawing variation of stellite-tipped saw indicated by standard deviation of lumber thickness.

Note: *Depth of workpiece: 420 mm*
Nominal thickness of board: 41 mm
Bite per tooth: 0.75 mm

lumber thickness and side clearance of the stellite-tipped saw can be observed. As the side clearance of the saw increases the standard deviation decreases until it reaches a minimum value of 0.37 mm for standard deviation within board, and a minimum value of 0.59 mm for the total standard deviation. Thereafter, further increase in side clearance of the saw teeth resulted in an increase in standard deviation. It can be deduced from Fig. 1 that the optimum side clearance of the saw teeth required to produce the minimum standard deviation of the lumber thickness is 0.66 mm, corresponding to a kerf-width of 2.62 mm for a blade thickness of 1.3 mm. This result is in agreement with the assertion by Denig [2] that the kerf-width should be twice the thickness of the blade for optimum efficiency. In this study, the thickness of the saw blade was 1.3 mm and the corresponding kerf-width based on the assertion by Denig [2] should be 2.6 mm. Clearly, there is less than 1% error margin and this demonstrates the reliability of our experimental results and further confirms the assertion by Denig [2].

The relationship between side clearance of the four stellite-tipped saws and standard deviation of lumber thickness is shown in Table 2. It can be deduced that on the average, an optimum side clearance of 0.69 mm of the saw teeth is required to produce an average minimum standard deviation of 0.42 mm within-boards, and an average total standard deviation of 0.59 mm when sawing *Triplochiton scleroxylon*. It also can be seen from Table 2 that minimum standard deviations within boards are obtained when the side clearance of the saw teeth ranges between 0.66 - 0.73 mm. For a side clearance greater than 0.75 mm, which was the average bite per tooth, there will be spillage of sawdust between the saw blade and the walls of the sawn lumber resulting in friction and consequently snaking of the saw. A side clearance of less than 0.66 mm could also lead to saw instability because the tissues of *Triplochiton scleroxylon* are fibrous and tend to increase the cutting resistance of the saw blade resulting in friction. The friction destabilises the saw allowing it to deviate from its true cutting position.

TABLE 2. Relationship between side clearance of stellite-tipped saws and standard deviation of lumber thickness

Saw No.	$X_{(max)}$	$S_{w(min)}$	$S_{t(min)}$
1	0.66	0.37	0.59
2	0.73	0.45	0.59
3	0.69	0.43	0.50
4	0.66	0.44	0.69

S_w = standard deviation within-boards;
S_t = total standard deviation;
x = side clearance
$X_{(max)}$ = optimum side clearance;
$S_{w(min)}$= minimum value of standard deviation within-boards
$S_{t(min)}$ = minimum value of total standard deviation

CONCLUSIONS

This study examined the influence of kerf-width and side clearance of bandsaw teeth on sawing variation when processing *Triplochiton*

scleroxylon with swage-set and stellite-tipped saws. A quadratic relationship was established between sawing variation and side clearance of stellite-tipped saws. The minimum lumber thickness standard deviations within-boards were obtained when the side clearance of the saw teeth ranges between 0.66 - 0.73 mm.

REFERENCES

1. Murata K, Nishimura K, Ikami Y, Ebihara M 1993, Sawing performance of band saws treated with new filling methods I. Journal of the Japan Wood Research Society, 39(11): 1231-1238.
2. Denig J, 1993 Small sawmill handbook. Miller Freeman Inc., San Francisco; 73-95.

CHARACTERISTICS OF MECHANICAL MICROMILLING USING TUNGSTEN CARBIDE TOOLS

O. Burak Ozdoganlar*, Sinan Filiz
Department of Mechanical Engineering
Carnegie Mellon University, Pittsburgh, Pennsylvania 15213-3890, USA

INTRODUCTION

Mechanical *micromachining* is one of the emerging techniques for creating three-dimensional micro-scale features on a wide range of materials [1]. Micromachining utilizes miniature cutting tools, such as micro-endmills, to perform machining processes at the micro scale. Due to scaling effects, the underlying phenomena that controls the tool-workpiece interaction are significantly different than those in conventional machining [2,3]. These differences influence micro-machinability characteristics considerably, and render our experience in machinability of materials from the macro scale not directly applicable [4].

This paper presents an experimental investigation of micromilling of OFHC copper 101 (ASTM B152 standard C10100) using tungsten carbide micro-endmills. The forces, surface roughness, and tool wear are analyzed under varying cutting speeds and feed rates. The variation of forces, surface roughness, and burr formation with wear is also studied. It was seen that the machinability characteristics are markedly different at the micro scale.

BACKGROUND

The commercially available micro-endmills are made of sintered micro-grain tungsten carbide (WC) and are fabricated by diamond grinding. A close-up image of a micro-endmill obtained using a Scanning electron microscope (SEM) is given in Fig. 1. The average grain size of micro-grain WC falls within the range of 0.4μm-0.7μm. These WC grains are held together by a cobalt (Co) binder. The grinding process used for fabricating these tools makes ductile fracture at the interface of the WC grains and Co binder energetically preferable to inter-granular fracture of the WC grains. As a result, the "flat" surfaces of the tool exhibit a smearing of Co over the WC grains, whereas the corners, including the cutting edges, show exposed WC grains with weak attachment to the binder. Therefore, the cutting edge radius (the sharpness of the cutting edges) is limited by the size of the WC grains.

The characteristics of micromachining are highlighted in the orthogonal cutting configuration depicted in Fig. 2, where h is the uncut chip thickness. The large edge radius imposes a large, negative *effective* rake angle (γ_e), which induces ploughing, elastic recovery, and subsurface damage.

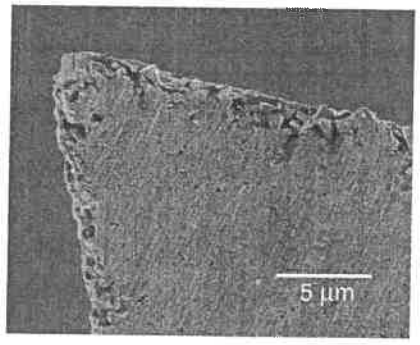

FIGURE 1: Cutting edge of a micro-endmill under SEM indicating large cutting edge and corner radius (Scale bar = 5μm). Individual grain of WC are also visible.

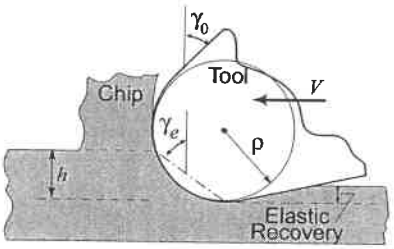

FIGURE 2: A schematic representation of (a) conventional machining and (b) micromachining

Another phenomenon, usually referred to as the *minimum chip thickness*, also arises from the rounded edge geometry. Below a critical chip thickness, the entire material is forced under the tool and elastically and plastically deformed, where the former recovers after the passing of the tool [5,6]. The minimum chip thickness is considered to be related to the resistivity of the material against plastic deformation, such as indentation hardness [5,7,8]. It is found to be strongly dependent on the ratio of chip thickness to cutting edge radius, and on the workpiece material/tool combination. Experimentally, the minimum chip thickness were observed to be within and 5% to 38% of the edge radius [5].

The *tool life* in micromachining is reached very

*Corresponding author: Ozdoganlar@cmu.edu

abruptly, and generally catastrophically [9]. The conditions that yield longer tool life at the macro scale generally do not correspond to those at the micro scale. Thermally induced wear phenomena, such as diffusion, are expected to become less important due to small size of the tool (large surface-to-volume ratio and reduced heat capacity), high-speed rotation, and the interrupted nature of the micromilling process [10]. On the other hand, the normal and frictional stresses at the flank face increase considerably due to the elastic recovery of the workpiece material with large cutting-edge radii [6, 11–14].

The *micromachining forces* exhibit different characteristics arising from the minimum chip thickness, elastic recovery, and ploughing phenomena [3, 15, 16], as well as the tool-tip runout [17]. A chip is not created before the instantaneous chip thickness exceeds the minimum chip thickness. Below the minimum chip thickness, the forces experienced are similar to indentation forces [4]. A majority of the material elastically recovers after the tool passes. When the instantaneous chip thickness exceeds the minimum chip thickness, a chip starts to form. The following cutting flute encounters the material left from the previous flute pass. For the region where a chip was not generated with the previous flute, the current flute experiences a larger chip thickness. When the feed is selected to be less than the minimum chip thickness a chip is generated only once in every several flute passes after a sufficiently large chip thickness is accumulated [2, 4].

The *specific energy* disproportionately increases at small uncut chip thicknesses experienced during micromachining. This phenomenon is usually referred to as the *size effect*, causes of which include ploughing of material under the tool due to large negative effective rake angles; the pressure applied to the flank face of the tool due to elastic recovery of the material; and strain-rate dependency and dislocation density/availability [8, 12–14, 18].

At small chip thicknesses, especially those below the cutting edge radius, the *surface roughness* increases due to elastic recovery and minimum chip thickness effects. For ultra-precision machining, elastic recovery has been empirically modeled as proportional to the edge radius and Young's modulus, and inversely proportional to the hardness of the material [6]. Therefore, a larger elastic recovery is expected from a larger edge radius, and material properties control the amount of elastic recovery for the same edge radius. At higher feed rates, the surface roughness increases with increased feed rate due to the process geometry [2].

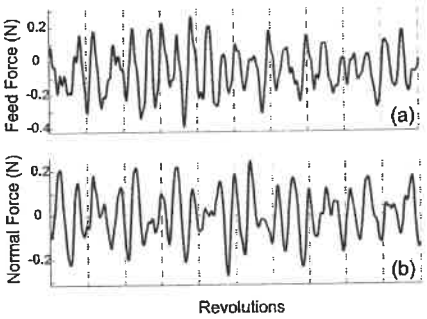

FIGURE 3: Feed and normal forces for $0.75\mu m$/flute feed rate.

EXPERIMENTAL SETUP

The experimental investigation presented here was conducted on a miniature machine tool (MMT) equipped with a 160,000 rpm air-turbine, air-bearing spindle. The spindle-axis offset is quoted by the manufacturer to be less than $2\mu m$. Feed motions are generated by three-axis Aerotech® ASL130-XYZ slide with 10 nm resolution, 250 mm/s maximum linear (feed) speed. A Kistler® three-axis mini-dynamometer (9256C1) with a 2 mN noise threshold is attached to the slides for measurement of forces.

The micro-endmills used during the experimentation were $254\mu m$ diameter, micro-grain, sintered tungsten carbide tools. These two-fluted micro-endmills had a 30 deg. helix angle. Prior to the experimentation, each micro-endmill was imaged using an SEM. The radii of the cutting edges were estimated from the SEM measurements to be $1.9\mu m$ in average, with a standard deviation of $0.35\mu m$.

This experimental study included full-immersion cuts at four feed rates (0.75-$6\mu m$/flute) and three cutting speeds (40, 80, and 120 m/min). The axial depth of cut was $30\mu m$ for all the tests.

CUTTING FORCES

Figures 3 and 4 give the feed and normal (to the feed) forces for feed rates of $0.75\mu m$/flute and $6\mu m$/flute, respectively. At small feed rates, micromilling forces exhibit erratic behavior, where the expected one-per-flute periodicity is absent. For higher feed rates, micromilling forces progressively resemble conventional milling forces (with runout effect).

The peak-to-valley (P-to-V) feed forces and associated standard deviations are compiled in Fig. 5. The effect of cutting speed is statistically significant only at the feed rate of $1.5\mu m$/flute, which is close to the average edge radius of $1.9\mu m$. At this feed rate, the intermediate cutting speed of 80 m/min produced the largest forces. The forces

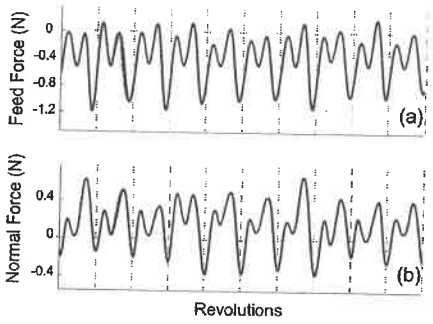

FIGURE 4: Feed and normal forces for 6μm/flute feed rate.

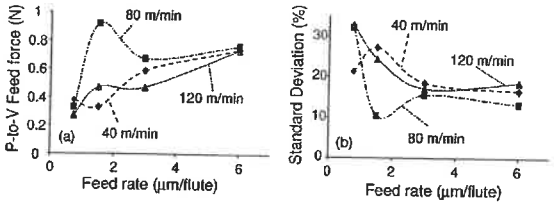

FIGURE 5: Average P-to-V feed forces and their standard deviation.

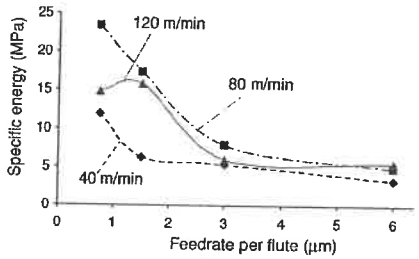

FIGURE 6: The change in average specific energy with feed rate and cutting speed.

showed a generally increasing trend with increasing feed rate, which is expected from the process geometry. The standard deviations were seen to reduce with increasing feed rate, possibly due to reduced effect of ploughing and minimum chip thickness.

Figure 6 shows the specific energies calculated from the average in-plane forces. The well-known size effect is observed. The cutting speed induced a strong effect at low feed rates, whereas it has almost no effect at higher feed rates.

SURFACE ROUGHNESS

To evaluate the effect of cutting conditions on the surface roughness, R_a values from the centerline of the bottom of the channels were measured using a white-light interferometer. These values are given in Fig. 7. As a reference, the *theoretical* R_a value calculated by considering the corner radius and the relief angle of the micro-endmills is also plotted. It can be seen that the effect of

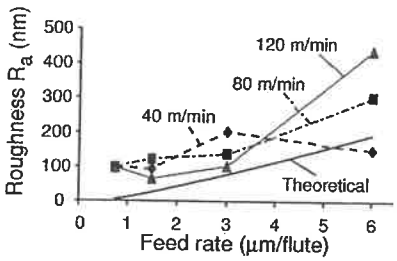

FIGURE 7: The surface roughness measured from the centerline of the channel floor.

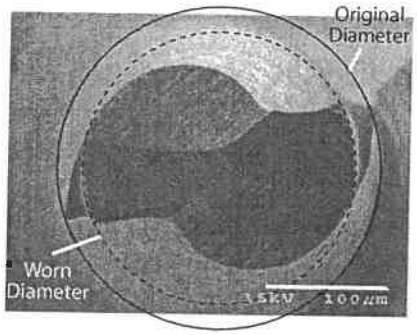

FIGURE 8: The change in tool diameter with progressed wear (Scale bar = 100μm).

both feed and cutting speed at low feed rates is small. However, the measured roughness values at these small feed rates are considerably higher than the theoretical roughness. This can be attributed to the effects of ploughing and minimum chip thickness.

As the feed rate is increased, the (theoretical) roughness due to the process geometry becomes more dominant. At feed rates of 3μm/flute and above, the theoretical and experimental roughness values become more similar. The roughness also markedly increases when the feed rate is increased from 3μm/flute to 6μm/flute. At the 6μm/flute feed rate, the speed is observed to have a strong effect.

TOOL WEAR

The wear behavior of the micro-endmills were investigated by cutting forty channels of 23mm length. The extent of wear was analyzed from the reduction in tool diameter from its original diameter at the completion of the operation.

Figure 8 shows an image of the worn tool and indicates the diameter reduction. The reduction in diameter after the completion of forty channels are given in Fig. 9 as a percentage of the initial tool diameter. The wear at low feed rates were seen to be severe with up to 20% reduction in tool diameter. The largest wear is observed at the lowest feed rate and the lowest speed. A rapid reduc-

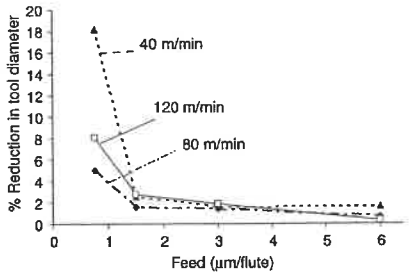

FIGURE 9: The reduction of tool diameter (as a measure of wear) with feed rate and cutting speed.

tion in wear is seen as the feed rate is increased to 1.5μm/flute, and a small amount of wear was seen for both 3μm/flute and 6μm/flute feed rates. The lowest diameter reduction of 0.3% was experienced at the highest feed rate and highest speed. An important conclusion here is that the cutting conditions that are generally considered as conservative in conventional milling—low feed rate and low cutting speed—induced the largest wear.

The mechanism of wear at small feed rates is the attrition wear in its most basic form. For the feed rates on the order of grain size, the cutting forces cause the weakly attached WC grains at the cutting edge to dislodge from the cobalt binder. When the feed rate is increased, the cutting forces are more evenly distributed, thereby reducing the attrition wear.

CONCLUSIONS

This paper presented an experimental study on micromilling of OFHC copper using tungsten carbide micro-endmills. The following conclusions are drawn from this work;

- The micromachining forces exhibit erratic behavior at feed rates less than the cutting edge radius. With increased feed rate, the forces resemble those from a conventional milling process.
- At small feed rates, the magnitude of the surface roughness is much higher than that calculated from the process geometry due to the effects of ploughing and minimum chip thickness. The geometrically induced surface roughness become more dominant as the feed rate is increased.
- Contrary to the experience from conventional milling, the largest wear in micromilling was observed for the lowest speed and the lowest feed rate, and the lowest wear was experienced at the highest speed and highest feed rate. The main mechanism of wear at low feed rates was seen to be the attrition wear.

REFERENCES

[1] Ehmann, K., Bourell, D., Culpepper, M., Hodgson, T., Kurfess, T., Madou, M., Rajurkar, K., and DeVor, R., 2005, *International assessment of research and development in micromanufacturing*. Baltimore, Maryland: World Technology Evaluation Center.

[2] Vogler, M. P., DeVor, R. E., and Kapoor, S. G., 2004, "On the modeling and analysis of machining performance in micro-endmilling, part i: Surface generation," Journal of Manufacturing Science and Engineering, Transactions of the ASME, **126**, no. 4, pp. 685 – 694.

[3] Vogler, M. P., Kapoor, S. G., and DeVor, R. E., 2004, "On the modeling and analysis of machining performance in micro-endmilling, part ii: Cutting force prediction," Journal of Manufacturing Science and Engineering, Transactions of the ASME, **126**, no. 4, pp. 695 – 705.

[4] Kim, C.-J., Bono, M., and Ni, J., 2002, "Experimental analysis of chip formation in micro-milling," Transactions of NAMRI/SME, **XXX**, pp. 247–254.

[5] Ikawa, N., Shimada, S., and Tanaka, H., 1992, "Minimum thickness of cut in micromachining," Nanotechnology, **3**, pp. 6–9.

[6] Arcona, C. and Dow, T. A., 1998, "An empirical tool force model for precision machining," ASME Journal of Manufacturing Science and Engineering, **120**, pp. 700–707.

[7] Lucca, D. A. and Seo, Y. W., 1993, "Effect of tool edge geometry on energy dissipation in ultraprecision machining," CIRP Annals - Manufacturing Technology, **42**, no. 1, pp. 83–86.

[8] Lucca, D. A., Seo, Y. W., Rhorer, R. L., and Donaldson, R. R., 1994, "Aspects of surface generation in orthogonal ultraprecision machining," CIRP Annals - Manufacturing Technology, **43**, no. 1, pp. 43–46.

[9] Tansel, I., Rodriguez, O., Trujillo, M., Paz, E., and Li, W., 1998, "Micro-end-milling-i. wear and breakage," International Journal of Machine Tools and Manufacture, **38**, pp. 1419–1436.

[10] Masuzawa, T., 2000, "State of the art of micromachining," CIRP Annals - Manufacturing Technology, **49**, no. 2, pp. 473–488.

[11] Friedrich, C. R. and Kulkarni, V. P., 2004, "Effect of workpiece springback on micromilling forces," Microsystem Technologies, **10**, pp. 472–477.

[12] Lucca, D., Rhorer, R., and Komanduri, R., 1991, "Energy dissipation in the ultraprecsion machining of copper," CIRP Annals - Manufacturing Technology, **40**, no. 1, pp. 69–72.

[13] Lucca, D. A. and Seo, Y. W., 1994, "A sliding indentation model of the tool-workpiece interface in ultra-precision machining," Tribology Symposium, 1994; presented at the Energy-Sources Technology Conference, New Orleans, LA, January 23-26, 1994, **61**, pp. 17–22.

[14] Lucca, D., Seo, Y., and Rhorer, R., 1994, "Energy dissipation and tool-workpiece contact in ultra-precision machining," Society of Tribologists and Lubrication Engineers (STLE) Tribology Transactions, **37**, no. 3, pp. 651–655.

[15] Bao, W. Y. and Tansel, I. N., 2000, "Modeling micro-end-milling operations. part i: analytical cutting force model," International Journal of Machine Tools and Manufacture, **40**, pp. 2155–2173.

[16] Xie, L., Brownridge, S., Ozdoganlar, O., and Weiss, L., 2006, "The viability of micromilling for manufacturing mechanical attachment components for medical applications," Transactions of the NAMRI/SME, **XXXIV**, pp. 445–452.

[17] Bao, W. Y. and Tansel, I. N., 2000, "Modeling micro-end-milling operations. part ii: tool run-out," International Journal of Machine Tools and Manufacture, **40**, pp. 2175–2192.

[18] Melkote, S. N. and Endres, W. J., February 1998, "The importance of including size effect when modeling slot milling," ASME Journal of Manufacturing Science and Engineering, **120**, pp. 68–75.

EFFECT OF LOW CUTTING SPEED ON ULTRA-PRECISION CUTTING OF TITANIUM ALLOY WITH COATED-CEMENTED-CARBIDE TOOL

Heiji YASUI[1], Akira SHINOZAKI[2], Akira TOYAMA[2], Shigehiko SAKAMOTO[1] and Yusuke KAJIWARA[2]

[1] Department of Mechanical System Engineering, Kumamoto University, Kumamoto city, JAPAN

[2] Graduate School of Science and Technology, Kumamoto University, Kumamoto city, JAPAN

INTRODUCTION

With the increase of the demand of high quality components, the technique of ultra-precision cutting for difficult-to-cut metals such as stainless steels, titanium metals and so on has been strongly required. In our previous researches, the coated-cemented-carbide tool is found so effective for ultra-precision cutting of those difficult-to-cut metals. The surface roughness formed by ultra-precision cutting of titanium alloys is below 200 nm(*Rz*) until the cutting length of L = 2,000 m [1, 2].

In order to improve furthermore the surface roughness and tool life, in the research, the effect of low cutting speed on ultra-precision cutting of a titanium alloy with coated-cemented-carbide tool is examined. The conditions of high depth of cut, in addition, is investigated for increasing removal rate at low cutting speed. Cutting speed and depth of cut range from below V = 1 m/min to 110 m/min and from d = 5 micro-meters to 1mm (=1,000 micro-meters), respectively.

EXPERIMENTAL PROCEDURE

The experiments are executed by face-turning beta titanium alloy (Ti-22V-4Al) at the cutting speed of below 1 m/min to 110 m/min with coated-cemented-carbide tool set on the ultra-precision turning machine as shown in FIGURE 1. Main experimental conditions are summarized in TABLE 1. Water-immiscible type of cutting fluid is directly supplied to cutting point with compressed air. The face-turned titanium alloy surface is evaluated by observing with a Nomarski differential interference microscope and measuring its surface roughness with surface interferometer (WYKO 3D). The wear of cutting tool is also observed with Scanning Electron Microscope (SEM).

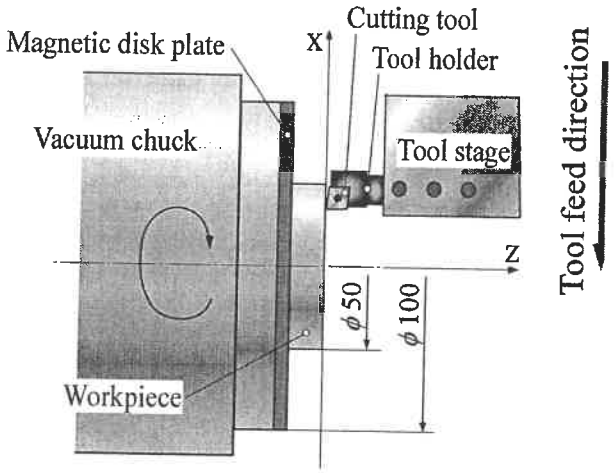

FIGURE 1. Ultra-precision face-turning set-up

TABLE 1. Experimental conditions

Machine tool: Ultra-precision lathe ULC-100A Toshiba Machine CO., LTD	
Cutting tool: Coated-cemented-carbide tool	
	Nose radius: R_θ = 0.4 mm
	Rake angle: θ_{ra} = 0 deg
	Relief angle: θ_{re} = 7 deg
Workpiece material: β titanium alloy (Ti-22V-4Al)	
Cutting fluid: Water-immiscible type	
Cutting conditions	Cutting speed: V = 0 - 110 m/min
	Depth of cut: d = 5 - 1,000 μm
	Feed rate: f = 2 μm/rev
	Cutting length: L = 212 m

RESULTS AND DISCUSSIONS

Effect of cutting speed on surface roughness

FIGURE 2 shows the workpiece surfaces after cutting at low cutting speed of $V < 1$ m/min and middle cutting speed of V = 42-60 m/min with coated-cemented-carbide tool. The total cutting length is L = 212 m. Crystal grain boundaries are not observed on the finished surface at $V < 1$ m/min. At V = 42-60 m/min, on the other hand, the crystal grain boundaries of about 100 micro-meters in size are clearly found. In addition to crystal grains, deep cutting grooves are observed on the finished surface. The 3D surface roughnesses formed at $V < 1$ m/min and 42-60 m/min are approximately 112 nm($Rz_{(3D)}$) and 164 nm($Rz_{(3D)}$), respectively. As shown in FIGURE 2 (c), the 2D surface roughnesses in feed direction at $V < 1$ m/min and V = 42-60 m/min are 84 nm(Rz) and 117 nm(Rz). As shown in FIGURE 2 (d), the surface roughnesses at $V < 1$ m/min and V = 42-60 m/min in cutting direction are about 30 nm($Rz_{(cut)}$) and 66 nm($Rz_{(cut)}$), respectively. The crystal grain boundary step on the finished surface at $V < 1$ m/min is about 30 nm($Rz_{(cut)}$). The step is much smaller than that of 66 nm($Rz_{(cut)}$) at the V = 42-60 m/min.

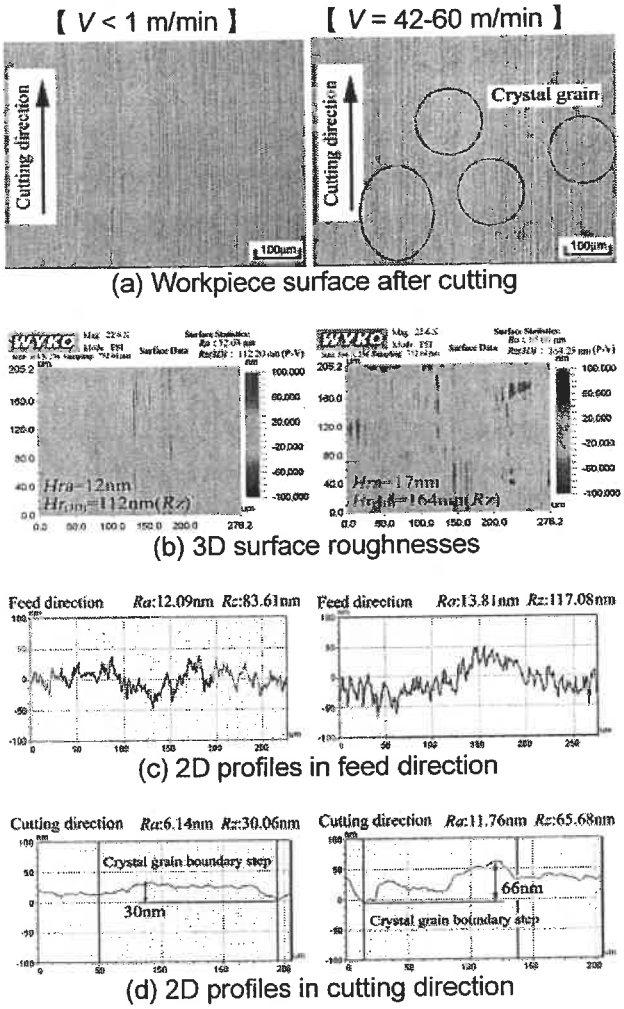

FIGURE 2. Comparison of beta titanium alloy surfaces face-turned at two kinds of cutting speed [f=2micro-meters/min, d=5micro-meters, Water-immiscible type cutting fluid]

FIGURE 3 shows the change of the surface roughness with cutting speed. At the cutting speed of V = 5-15 m/min, the surface roughness is almost the same as that at $V < 1$ m/min. At middle cutting speed of V = 42-60 m/min, the surface roughness becomes somewhat worse than that below V = 5-15 m/min. At high cutting speed of V = 80-110 m/min, the surface roughness becomes suddenly large and attains 600 nm(Rz). Omitting the photograph, irregular cutting groove and the large step of crystal grain boundaries are observed on the finished workpiece surface.

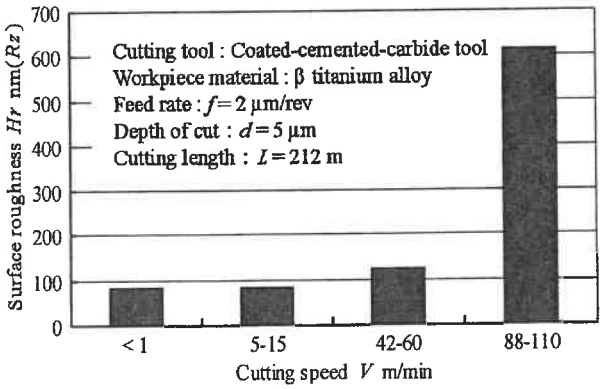

FIGURE 3. Influence of cutting speed on surface roughness

From the results mentioned above, the effect of low cutting speed on surface roughness in the ultra-precision cutting of titanium alloy is referred to be remarkably large. At the low cutting speed, as the result, the surface roughness can attain easily below 100nm (Rz) which attains so difficult at the high cutting speed.

Tool wear at low cutting speed

Tool wears of cutting edge after cutting of beta titanium alloy at cutting speed $V < 1$ m/min and V = 42-60 m/min are shown in FIGURE 4. At the cutting speed of $V < 1$ m/min, the width of the flank face wear land Vb_{max} is about 5.1

micro-meters. At the cutting speed of V = 88-110 m/min, on the other hand, the width of the flank face wear land Vb_{max} is about 14.8 micro-meters, and becomes clearly larger than that of V < 1 m/min.

FIGURE 5 shows the change of flank face wear of cutting tool with cutting speed. The flank face wear increases larger for higher cutting speed. At the cutting speed of V = 5-15 m/min, the width of the flank wear land Vb_{max} becomes 7.5 micro-meters. In middle cutting speed of V = 42-60 m/min, the wear width is about 8.9 micro-meters. At high cutting speed V = 88-110 m/min, the comparatively large tool flank wear occurs on the cutting point in short cutting length L = 212 m.

It is expected from the results mentioned above that the tool life at higher cutting speed becomes shorter because the tool wear at higher cutting speed which is related to the surface roughness is larger at the same cutting length. Accordingly the suitable cutting speed should be decided by considering the cutting efficiency.

Surface roughness at high depth of cut under low cutting speed

FIGURE 6 shows the finished surface and its surface roughness after cutting at low cutting speed of V < 1 m/min and high depth of cut of d = 100 micro-meters. On the surface, crystal grain boundaries are clearly observed. The 3D surface roughness is about 129 nm($Rz_{(3D)}$). The crystal grain boundary step in cutting direction is 38 nm($Rz_{(cut)}$). The 2D surface roughness in feed direction is about 90 nm(Rz), as shown in FIGURE 6 (c).

FIGURE 7 shows the change of the surface roughness with depth of cut. The cutting speed is V < 1 m/min of extremely low cutting speed. At depth of cut of 5 micro-meters, the surface roughness of the finished surface is about 70 nm(Rz). The surface roughness becomes larger as the depth of cut is larger. However it is below 100nm(Rz) at the depth of cut of 100 micro-meters. At the high depth of cut of 500 micro-meters, the surface roughness exceeds slightly 100 nm(Rz). At the high depth of cut of 1000 micro-meters (=1mm), the surface roughness attains suddenly about 200 nm(Rz).

In the low cutting speed, from the results, the extremely high depth of cut of ultra-precision cutting is referred possible. Compared with the high cutting speed, the depth of cut is possible over 10 times at least.

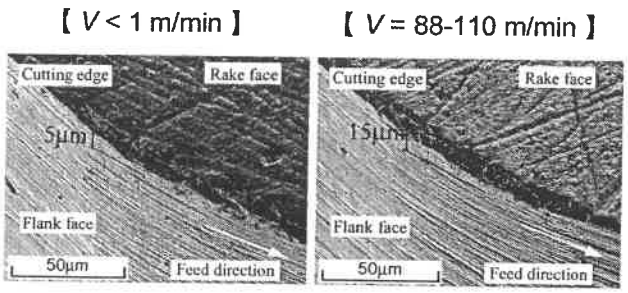

FIGURE 4. Comparison of flank wear face-turned at two kinds of cutting speed

[f=2micro-meters/min, d=5micro-meters, Water-immiscible type cutting fluid]

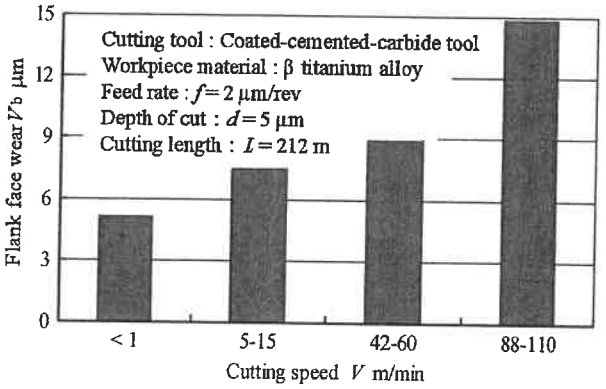

FIGURE 5. Influence of cutting speed on the flank face wear

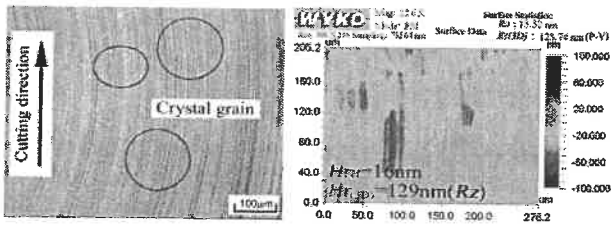

(a) Workpiece surface (b) 3D surface roughnesses

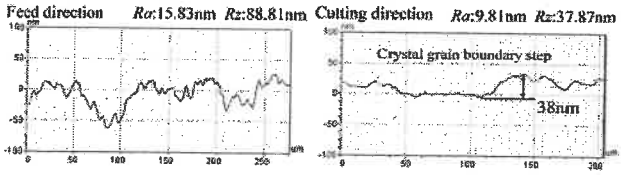

(c) WYKO 2D profiles in feed and cutting direction

FIGURE 6. Comparison of beta titanium alloy surface face-turned at depth of cut d = 100micro-meters under extremely low cutting speed

[V<1m/min, f=2micro-meters/min, L=212m, Water-immiscible type cutting fluid]

FIGURE 8 shows the tool edge before and after cutting of beta titanium alloy at cutting speed of V < 1 m/min and depth of cut of d = 100 micro-meters. From FIGURE 8 (b), the small flank face wear and the little adhesion of beta titanium alloy to cutting edge are observed.

FIGURE 9 shows the change of flank face wear with depth of cut under extremely low cutting speed of V < 1 m/min. The flank face wear increases steeply from Vb_{max} = 5.1 micro-meters at d = 5 micro-meters to Vb_{max} = 9.2 micro-meters at d = 100 micro-meters. Over d = 100 micro-meters, the flank face wear increases gradually larger for higher depth of cut. At the depth of cut of d = 500 micro-meters and 1,000 micrometers, the widths of the flank face wear land Vb_{max} are 9.8 micro-meters and 9.9 micro-meters, respectively. Compared with the flank face wear at depth of cut of 5 micro-meters under high cutting speed of V = 80-110 m/min, the wear is small. Therefore the wear at extremely low cutting speed is referred remarkably small.

CONCLUSIONS

The main conclusions obtained are as follows;

(1) Compared with the high cutting speed, the surface roughness formed by the ultra-precision cutting of titanium alloy at the low cutting speed with coated-cemented-carbide is remarkably small.

(2) In the high depth of cut over 100 micro-meters, the surface roughness formed at the extremely low cutting speed attains 100 nm(Rz).

(3) At low cutting speed, the tool wear becomes considerably a little. Under extremely low cutting speed of V < 1 m/min, the wear at the depth of cut of d = 1,000 micrometers is less than that at the depth of cut of d = 5 micrometers under high cutting speed V = 88-110 m/min.

ACKNOWLEGEMENTS

The authors would like to thank Yushiro Chemical Industry Co., Ltd., Daido Steel Co., UEX Co., Ltd. and Tungaloy Co., Ltd. for providing cutting fluids, workpiece materials and cutting tools. A part of the research is supported by GRANT-IN-AID for Scientific Research (2005) [Project No. 17656053], in Japan.

REFERENCES

1. Yasui H., Sakamoto S. and Kawada M., Ultra-precision Cutting of Titanium Alloys by Using Coated Carbide Bite, Journal of the JSPE, 2002; 68(7): pp. 928-932.
2. Sakamoto S., Yasui H. and Kawada M., Effect of Cutting Fluid on Surface Roughness Formed by Ultra-precision Cutting of Titanium Metal, Journal of the JSPE, 2003; 69(3): pp. 402-406.

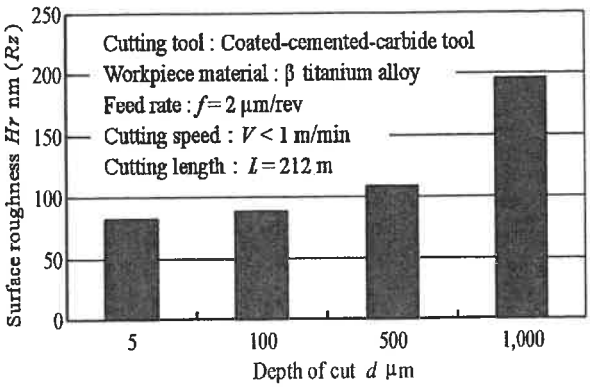

FIGURE 7. Influence of depth of cut on surface roughness under extremely low cutting speed

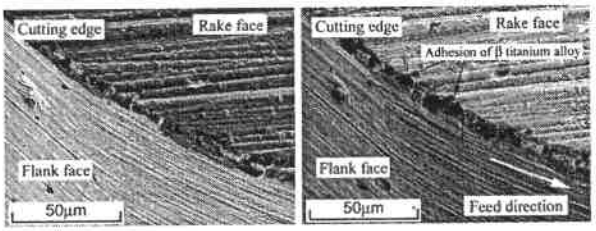

(a) Before cutting (b) After cutting

FIGURE 8. Flank wear due to cutting of beta titanium alloy at d = 100 micro-meters under V < 1 m/min [f=2micro-meters/min, Water-immiscible type cutting fluid]

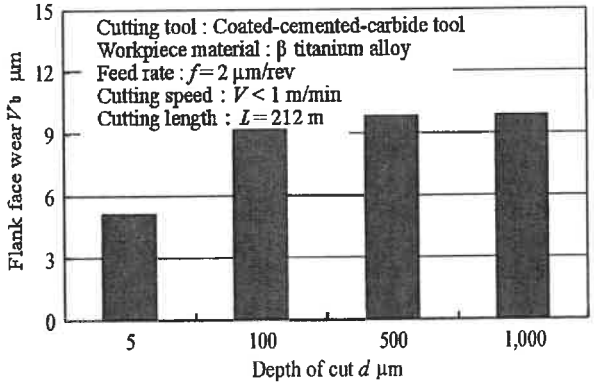

FIGURE 9. Influence of depth of cut on the flank face wear under extremely low cutting speed

SELF-ADJUSTMENT MODULE FOR PHONE CAMERA LENS ASSEMBLY

Chang-Woo Lee[1], Jun-Yeob Song[1]
[1]Intelligent Machine Systems Research Center,
Korea Institute of Machinery and Materials,
171, Jang-dong, Yuseong-gu, Daejeon, 305-343, S. Korea

INTRODUCTION

The 1.3-mega-pixel camera cellular phone was first released into the Korea market in October 2003. The major cellular phone companies released 2-mega-pixel camera cellular phone which supports zoom function and 2-mega-pixel camera cellular phone is settled down with the Korea cellular phone market. The table 1 shows that the market share of camera cellular phone was 14.6 % in 2003 and it is expecting that it holds a more than 75 % in 2007.

Table 1 : The world market trend of the cellular phone and the camera cellular phone [1]

(Unit : Million sets, %)

	2003	2004	2005	2006	2007
Cellular Phone	432	478	521	562	618
Rate of Increase	-	10.6%	9.0%	7.87%	9.96%
Camera Cellular Phone	63	135	266	365	464
Market Share	14.6%	28.3%	51%	65%	75%

As the market of a camera cellular phone of which lens module is manufactured by a manual work is getting larger in recent year, the need of automation is increased lately. In this industry, the customer's demand for the variety makes fast model change and the pixel resolution high form VGA to multi-mega pixel. The lens module of a camera cellular phone demands μm order accuracy to be assembled. The assembly system is designed to cope with phone camera model change and make the parts to be assembled arranged precisely. In general it makes the assembly system huge from size of view that the accuracy only depends on the mechanism stiffness. If there is utensil that compensates alignment error naturally, the assembly system can be small and manufactured as is cheap and corresponds easily to the cellular phone model change. In this paper the utensil is proposed and is called Self-Adjustment Module (SAM). The SAM that can compensate the alignment error reduces the tact time and also diminishes the inferior goods. The assembly system that has this SAM is not to have excessive stiffness so that it is designed to be smart and can correspond to the model change easily.

Function of Self-Adjustment Module (SAM)

The lens module consists of a holder, lenses, spacers and shield as shown in Fig. 1. The inside of a holder becomes the reference of assembly, and one after another are assembled lenses, spacers and shield. First a holder is situated at assembly position by a gripper with positioning error. Next a lens is moved to assembly position and then a holder and a lens are assembled with an alignment error. In general this alignment error can be compensated by using vision system.

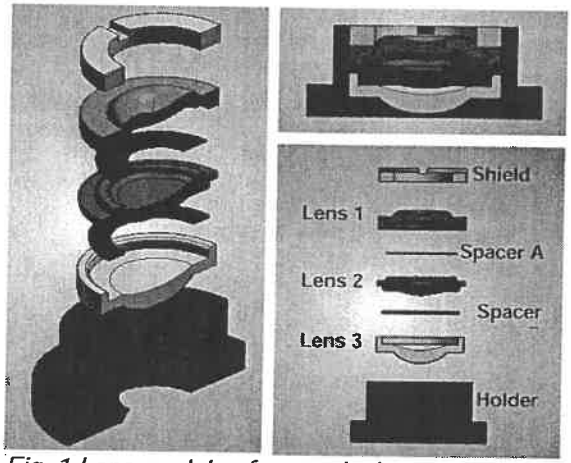

Fig. 1 Lens module of megapixel camera phone

If two parts are assembled and its direction is Z axis, the relative alignment errors has 5 ingredients as shown in Fig. 2. If SAM can make 5 directions free mechanically, two parts are assembled compensating alignment error

naturally. Fig. 3 shows the function of SAM schematically when a holder and a lens are assembled.

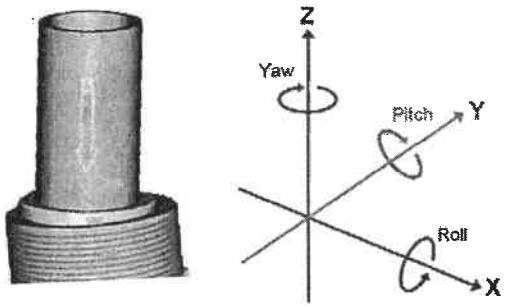

Fig. 2 Five alignment errors when assembly direction is Z axis

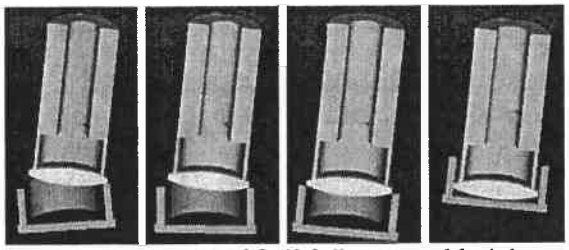

Fig. 3 Function of Self-Adjustment Module

Self-Adjustment Module (SAM) Design

The SAM only takes the stiffness in assemble direction and can be moved freely in the other direction so that it can make the parts assembled with the reference to the inside of a holder. Several types of SAM are proposed in the previous research [2][3]. This investigation suggests new two types of the SAM that can adjust one part to the inside of holder automatically and shows performance evaluation of SAM.

The first type is using hemisphere air bearing as shown in Fig. 4. This type consists of base that has five holes and hemisphere that has one hole. The pressure air that is supplied through center hole of base passes hole in hemisphere and make the holder housing floating freely. This function makes as holder housing has X, Y, Yaw 3 degree of freedoms. The other small holes in the base make the hemisphere floating on the base freely. This function makes as holder housing has Roll, Pitch 2 degree of freedoms. As a result, this device makes 5 degreed of freedoms free only with stiffness to Z axis direction.

The second type SAM consists of the porous air bearing that give three-degree of freedom free and the coil spring that give two-degree of freedom free as shown in Fig. 5. The air bearing can make a part moved without mechanical friction in X, Y direction and yaw motion and the coil spring also is able to get a part moved smoothly in roll and pitch motion.

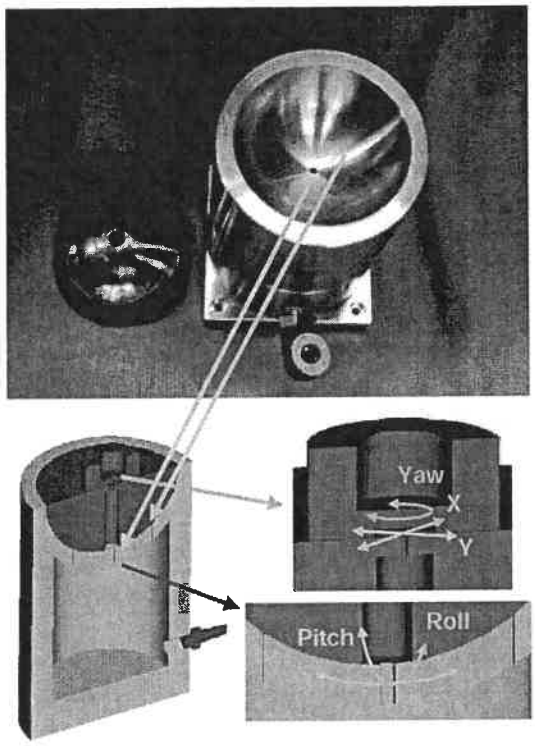

Fig. 4 Type 1 SAM using air bearing

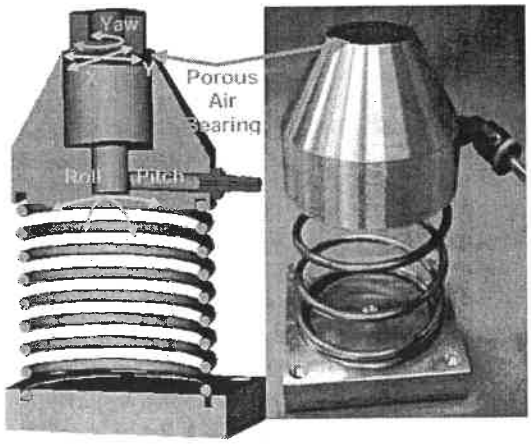

Fig. 5 Type 2 SAM using spring and air bearing

EXPERIMENTAL SETUP

Experiment has micro stage that can occur pitch, roll, X, Y direction alignment error independently as shown in Fig. 6. Also it has two gap sensors that can measurement X1, Y1 direction

displacement of holder housing and two-dimensional PSD (Position Sensitive Detector) sensor that can measurement pitch, roll of holder housing. The angle between gap sensor and micro stage is 45 ° mechanically, so the displacement of holder housing was expressed by X1, Y1. The gap sensors hold generating power 10 ㎷ per 1 ㎛ displacement. It tunes out that 1 ㎛ displacement of laser spot on the PSD results in output voltage of 1 ㎷. Pitch and roll is calculated in geometric relation from PSD displacement.

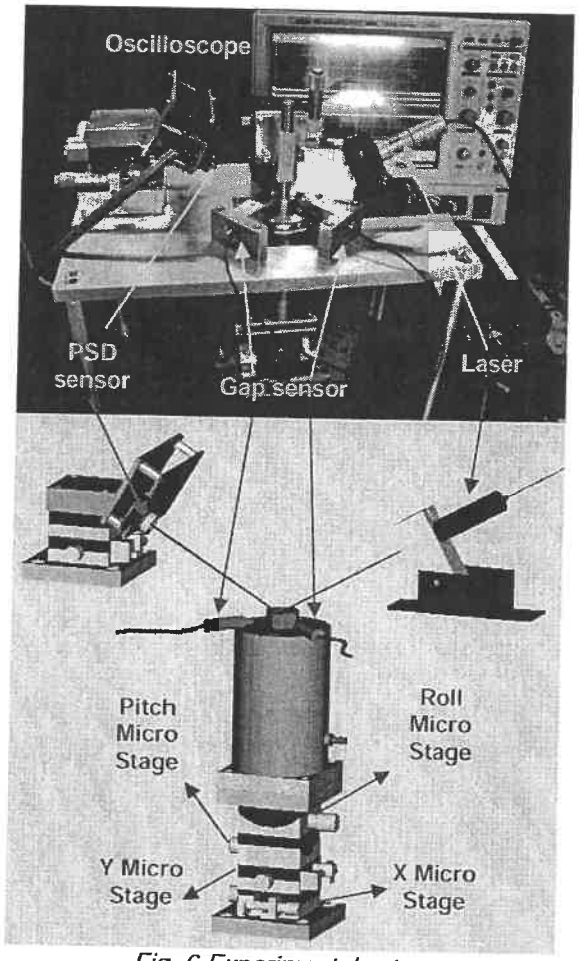

Fig. 6 Experimental setup

EXPERIMENTAL RESULTS

The experiment each type was carried out on 4 conditions.

First : X position error generated when pitch error was 0.3°, the other error is zero.

Second : Y position error generated when pitch error was 0.3°, the other error is zero.

Third : X position error generated when roll error was 0.3°, the other error is zero.

Fourth : Y position error generated when roll error was 0.3°, the other error is zero.

Because the center of micro stage that breed pitch, roll motion and that of holder housing differ, the micro stage can not move holder housing independently. If micro stage that breeds pitch, roll motion is moved, the position of the holder housing changes with X, Y, Z motion at the same time. In this research, the difference value in starting point was measured and calculated because the deviation is important. In general maximum alignment error is smaller than 0.1 ㎜ and 0.1°, so experimental condition is that displacement error is 0.5 ㎜ and angle error is 0.3°.

Type 1 SAM Result

X axis move, Y axis 0 ㎜, Pitch : 0.3° , Roll : 0.0°

X (㎜)	-0.5	-0.25	0	0.25	0.5
X1 (㎛)	4.9	-0.5	0	3.9	-1.3
Y1 (㎛)	10.6	7.5	0	0.5	-7.0
θ1 (arcsec)	18.1	19.7	0	-0.5	-11.0
θ2 (arcsec)	6.5	5.1	0	1.3	2.8

X axis 0 ㎜, Y axis move, Pitch : 0.3° , Roll : 0.0°

Y (㎜)	-0.5	-0.25	0	0.25	0.5
X1 (㎛)	-17.9	-6.0	0	-0.5	-1.5
Y1 (㎛)	8.2	6.0	0	10.6	13.3
θ1 (arcsec)	-5.9	-0.5	0	10.6	13.3
θ2 (arcsec)	19.7	17.3	0	-14.5	-14.5

X axis move, Y axis 0 ㎜, Pitch : 0.0° , Roll : 0.3°

X (㎜)	-0.5	-0.25	0	0.25	0.5
X1 (㎛)	13.3	2.8	0	-5.1	-18.4
Y1 (㎛)	13.4	18.1	0	-1.5	-4.9
θ1 (arcsec)	16.4	11.2	0	-9.6	-12.9
θ2 (arcsec)	6.0	1.3	0	7.3	-6.5

X axis 0 ㎜, Y axis move, Pitch : 0.0° , Roll : 0.3°

Y (㎜)	-0.5	-0.25	0	0.25	0.5
X1 (㎛)	-17.3	-10.6	0.0	5.3	18.4
Y1 (㎛)	5.1	15.8	0.0	-1.5	-4.9
θ1 (arcsec)	13.6	-5.9	0.0	4.9	7.7
θ2 (arcsec)	17.2	4.9	0.0	0.5	-11.0

Type 2 SAM Result

X axis move, Y axis 0 ㎜, Pitch : 0.3° , Roll : 0.0°

X (㎜)	-0.5	-0.25	0	0.25	0.5
X1 (㎛)	3.1	0.2	0	0.5	0.8
Y1 (㎛)	2.8	1.5	0	-1.2	-1.9
θ1 (arcsec)	7.9	6.1	0	1.2	-5.2
θ2 (arcsec)	2.1	2.7	0	-0.6	1.8

X axis 0 ㎜, Y axis move, Pitch : 0.3° , Roll : 0.0°

Y (㎜)	-0.5	-0.25	0	0.25	0.5
X1 (㎛)	-6.9	-3.5	0	0.2	-1.6
Y1 (㎛)	3.9	2.2	0	2.8	3.4
θ1 (arcsec)	-2.3	1.2	0	2.8	3.4
θ2 (arcsec)	6.1	5.1	0	-4.7	-4.7

X axis move, Y axis 0 ㎜, Pitch : 0.0° , Roll : 0.3°

X (㎜)	-0.5	-0.25	0	0.25	0.5
X1 (㎛)	3.4	1.8	0	-2.7	-5.3
Y1 (㎛)	4.0	9.3	0	-1.6	-3.1
θ1 (arcsec)	6.4	5.4	0	-4.1	-4.5
θ2 (arcsec)	3.5	-0.6	0	1.7	-2.1

X axis 0 ㎜, Y axis move, Pitch : 0.0° , Roll : 0.3°

Y (㎜)	-0.5	-0.25	0	0.25	0.5
X1 (㎛)	-5.1	-2.8	0	3.3	6.7
Y1 (㎛)	2.7	8.4	0	-1.6	-3.1
θ1 (arcsec)	3.6	-2.3	0	2.9	2.4
θ2 (arcsec)	7.3	2.9	0	-1.2	-5.2

CONCLUSIONS

In case of type 1 SAM, maximum displacement deviation is more than 35 ㎛ and maximum angle deviation is more than 34 arcsec. It is considered that the large deviation is caused by impertinent air bearing design, so air flow is unstable.

In case of type 2 SAM, maximum displacement deviation is smaller than 10 ㎛ and maximum angle deviation is smaller than 15 arcsec. The performance of type 2 SAM is improved little more, it is applicable in lens module assembly.

We confirmed that SMA compensated alignment error in some degree through this study.

ACKNOWLEGEMENTS

This work is one of The Next Generation New Technology Project. The author grateful for the support from the Ministry of Commerce, Industry and Energy and also Gyeongnam Regional Innovation Agency.

REFERENCES

1. Deutsch Bank, August, 2003
2. Song J.Y., Lee C.W. and Kim Y.G., "The design of an intelligent assembly robot system for lens module of phone camera." ICCAS(International Conference on Control, Automation, and System) 2005, pp. 649-652
3. Lee C.W., Song J.Y. and Ha T.H., "The design of a self adjustment module for μ-part assembly." In Proceeding of KSMTE, 2005, pp. 401-406

A STUDY ON THE ULTRA PRECISION PROGRESSIVE DIE MAKING FOR SHEET METAL FORMING BY COMPUTER SIMULATION

Sung-Bo Sim[1], Chung-Whan Kim[2], Gwi-Yun Park[1]
[1]School of Mechanical Engineering Pukyong National University
San100, Yongdang-Dong, Nam-Gu, Busan, Republic of Korea
[2]Graduate school of Mechanical Engineering Pukyong National University
San100, Yongdang-Dong, Nam-Gu, Busan, Republic of Korea

INTRODUCTION

A great deal of influence of development technology of progressive die for press tooling as a top rapidity operation with a minimizing costs is given to the production part by many kinds of factors, i.e. the complexity of die components of machining and its assembling, pressing machinery capacity, lot size of production part, materials of die components and its heat treatment, etc. The interactions of a whole of many factors to the die development with a optimized method are concerned by tool engineers. The important role of tool engineers is strip process layout design and computer aided FEM simulation with a existing data base and abundant field experiences. The prediction of result on the tryout is critical division on the die development. We used the part of precision production (Fig. 1) in electronic production line. Hence, this study needs a whole of press tool data, our field experiences, relative instructions, and ultra precision machine tools and its skilful operation and applications. The added process of this work was FEM simulation by DEFORM with 3D Unigraphics under the WINDOW environment. The result of this computer aided simulation was successful and very fine as the output coming in Fig. 4, Fig. 5. According to upper work, the optimum die design could be accomplished. Furthermore the goal of least defect could be obtained by the tryout and die revision.

ANALYSIS OF PART DRAWING

Fig. 1 shows the production part drawing in this study through the computer aided die design under the AutoCAD and Window environment. In this drawing the thickness of material is 0.8mm for bending part. The direction of burr is downward regularly, hence we designed strip process layout as the cut-off type progression through the modeling of 3D Unigraphics application. At this time, we could predict the completed actual strip process layout after tryout visually. Table 1 shows the mechanical properties of SPCC material.[1,2]

TABLE 1 Mechanical properties of SPCC

	Unit	Value
Young modules	GPa	200
Poison ratio	-	0.3
Tensile	MPa	760
Yield Strength	MPa	380

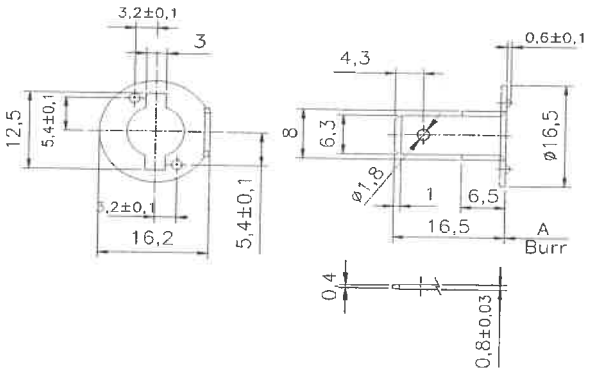

[Note]
1. Burr creating direction should be on the "A" surface to the downward.
Material : SPCC, Thickness : 0.8 mm

FIGURE 1 Production part drawing

DESIGN OF STRIP PROCESS LAYOUT

Fig. 2 shows the result of strip process layout in this study. For the increasing of material using ratio, we selected the couple row type method, at the same time the symmetrical disposition and guide line of pin method, pilot locating method were used to accurate process [3,4].

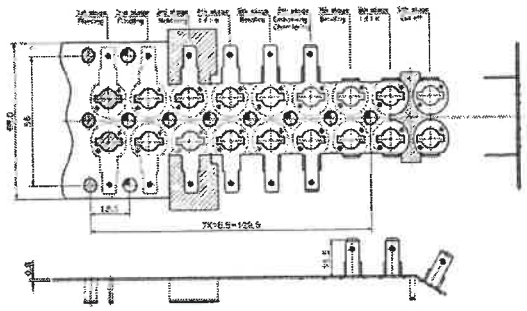

1st stage	Different shape piercing of central position and piercing to pilot
2rd stage	Indirected piloting process for accurate feeding
3nd tage	Symmetrical notching of bending portion
4th stage	Idle stage with consideration of die strength
5th stage	Left and right wing bending to upper direction
6th stage	Chamfering and embossing of edge portion
7th stage	90 degree bending of edge portion to the upper direction
8th stage	Idle stage as same effectiveness as 4th stage
9th stage	Cut-off stage with a consideration of burr direction for product obtaining

FIGURE 2 Strip process layout of couple rows

FEM SIMULATION OF STRIP LAYOUT

The FEM program used to simulate the strip process layout was DEFORM that is capable of material behaviour, deep and wide deformation and contrast between punch and die shapes. It was possible to determine the stress and strain of bending stage in the strip process.

SPRING BACK CREATING SIMULATION

In this Study, as a outer method of the common treatment of spring back of sheet metal bending, punch shoulder shape was considered coining type shape also it was simulated by DEFORM. Fig. 3 shows the bending punch shoulder shape with a coining method

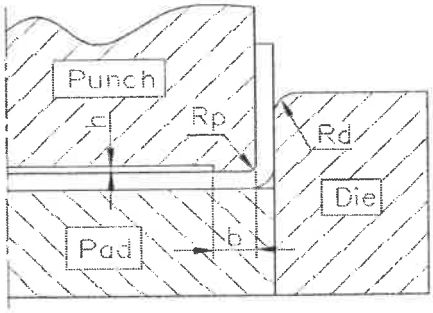

b	h					
	h1	h2	h3	h4	h5	h6
0.8mm (100%)	0.04 (5%)	0.08 (10%)	0.12 (15%)	0.16 (20%)	0.20 (25%)	0.24 (30%)

FIGURE 3 Bending punch shoulder shape and size of coining section

The conditions of DEFORM simulation were opened as same as following Table2

TABLE 2 Condition of DEFORM Simulation

Items	Contents
Press	Mechanical press SPM:60
Friction coefficient	0.09-0.12(0.12 fixed)

At this time, the conditions of bending formation were shown as the Table3.

TABLE 3 Condition of bending formation

Items	Contents
Punch radius	R 0.3mm fixed
Clearance	0.4-0.08mm
Die radius	0.8, 1.6, 2.4, 3.2mm
Height of Coining	0.04, 0.08, 0.12, 0.16, 0.20, 0.24mm

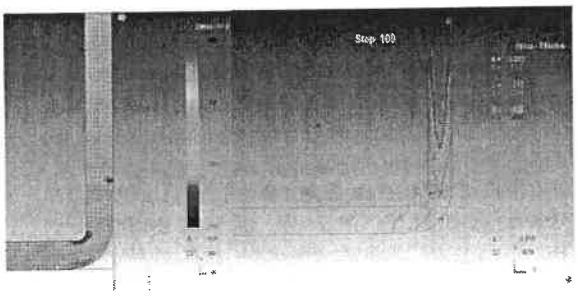

(a) Bending deformation rp=.3mm, rd=1.6mm

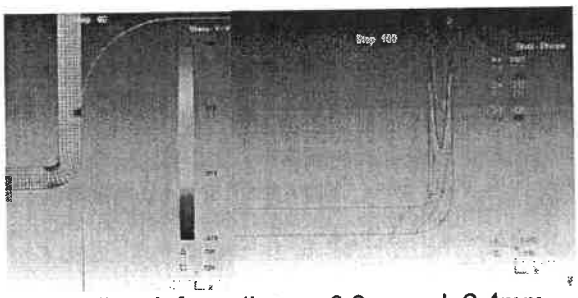

(b) Bending deformation rp=0.3mm, rd=2.4mm

FIGURE 4 FEM Simulation of bending Die radius

Fig. 4 shows the representatives of bending deformation among the conditions of bending formation as showing on the Table3. In this FEM simulation, it could be known that the bending die radius 1.6mm of couple times of material thickness of production part which was satisfied with a reduction of stress and strain under the relieving of transformation of material thickness. It was considered that the bending die radius 2.4mm was become to the lower effect of stress

and strain, hence, the actual production part by tryout was satisfied as a very important factor.

Fig. 5 shows the representatives of FEM simulation of stress and strain by DEFORM. At this time, bending die radius 2.4mm with a coining height 0.08mm pressing was satisfied with a lower stress and strain appearance but spring back phenomena occurred within 10% of material thickness. The production part could be predicted as a good quality.

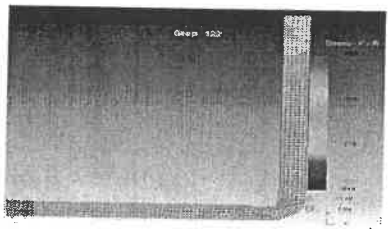

(a) FEM simulation of stress of 0.08 coining

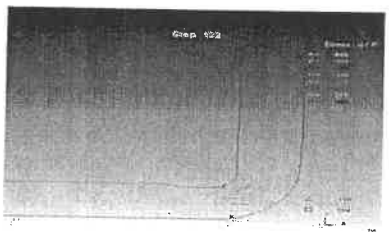

(b) FEM simulation of strain of 0.08 coining

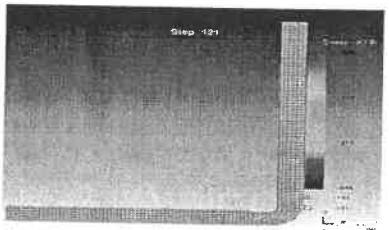

(c) FEM simulation of stress of 0.12 coining

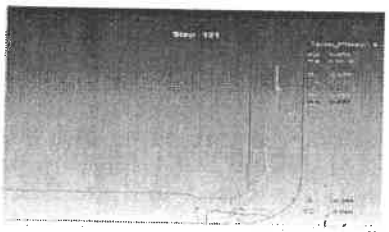

(d) FEM simulation of strain of 0.12 coining

FIGURE 5 Stress and Strain deformation of 0.08 and 0.12mm coining on the corner at the bending portion

DIE MAKING AND TRYOUT

Fig. 6 shows the assembling drawing of die design result. At this time, we considered the automatic roll feeding of strip for the mass production part above one hundred thousand pieces. Also, the die set was selected special type tool steel die with a outer and inner guide post. For aiding the roll feeding, the guide lifter pin was used[5-7].

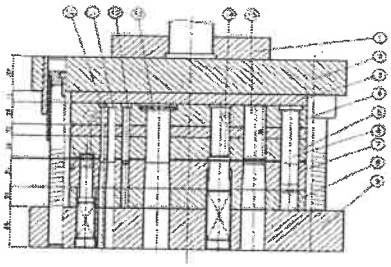

(a) Front view of assembly

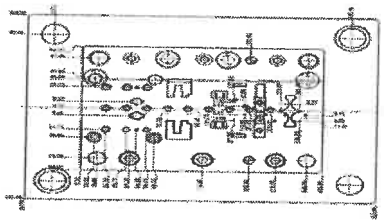

(b) Top view of Upper and Lower Die

FIGURE 6 Die assembling drawing

Fig. 7 shows the critical points of die making and assembling for increasing of accuracy

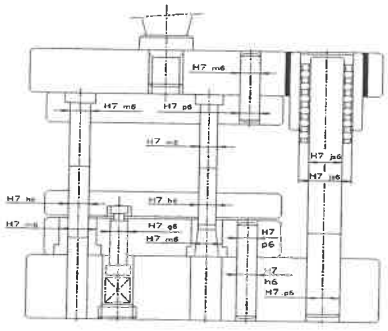

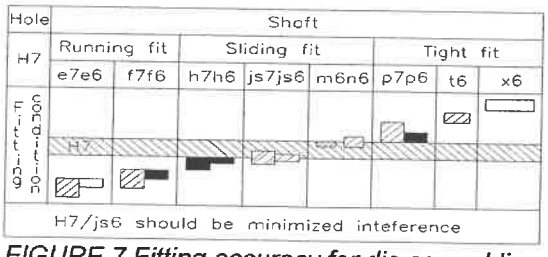

FIGURE 7 Fitting accuracy for die assembling

Fig. 8 shows the upper and lower die after die making at opening status. The SKD11 high alloy tool steel was selected for punch and die block as a cause of containing of minimized wear among whole of die materials. In this die making, we used many kinds of precision machine tools i.e. EDM, Wire-cut, jig grinding machine, tool, CNC machining center, mirror machine tool and vacuum type heat treatment furnace etc.

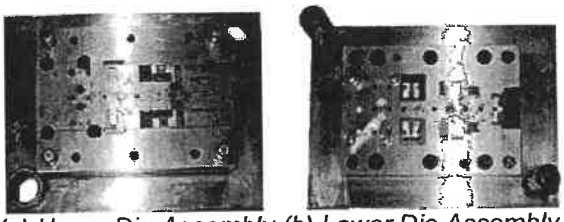

(a) Upper Die Assembly (b) Lower Die Assembly

FIGURE 8 Upper and lower die assembly

TRYOUT

Fig. 9 shows the actual production part after tryout completed. At this time it was confirmed that the result of tryout and its revision were preformed very exactly

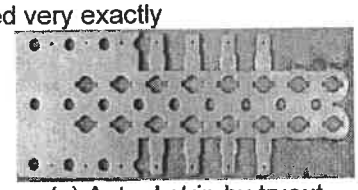

(a) Actual strip by tryout

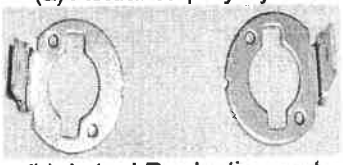

(b) Actual Production part

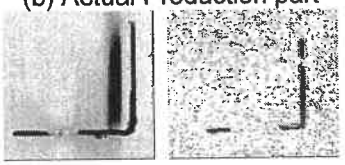

(c) Actual test part

FIGURE 9 Actual part and strip by tryout

CONCLUSION

The result of this study was obtained as follows.

1. Even in small details of production part, it could be considered sincerely. For the increasing of material using ratio, productivity, smoothing of strip feeding on the die block surface, and balancing of bending power, it could be fine method that is two lines blank disposition type strip process layout with 9 stages. Also it was applied to reduce the spring back phenomena by coining type punch shoulder. Then, it could be performed DEFORM simulation before the strip process layout design, die making, tryout and its revision through the analysis of actual production part. Upper methods produced outcome to coincide between simulation and tryout.
2. Under the condition of clearance of bending site 5~10% aided to material thickness of production part and die radius 2.0_3.0 times of material thickness of production part, the out view of actual production part was satisfied and the coining site of bending to 0.1_0.15 times of material thickness of production part was brought into existence in allowing tolerance.
3. It was possible that the prediction of result of tryout was successful through the FEM simulation. Also it could be done the optimizing design of strip process layout for the satisfied die making and tryout through the computer simulation

REFERENCES

1. Sim, Sung-Bo and Park, Sun-Kyu, 1999, May, Development of the Practical and Adaptive Die for Sheet Metals(1), *Proceedings of KCORE Conference*: 141-148
2. Sim, Sung-Bo, and Song, Young-Seok, 1999, Development for Practical and Adaptive Progressive Die for Design and Making of Marine Part Sheet Metals(1), *Inter. Jour. of Ocean Eng. and Tech, KCORE*, 2/2: 19-25.
3. Sim, Sung-Bo, Jang, Chan-Ho, and Sung Yul-Min, 2001, Development of the Pilotless Type Progressive Die for Thin Sheet Metal, *The Proceeding of KCORE Conference*: 289-294.
4. Sim, Sung-Bo, Jang, Chan-Ho and Lee, Sung-Taeg, 2002, A study on the Development of Two side carrier Type Progressive Die for Multi-Stage Drawing Process. *The Proceeding of the 2002 Autumn Conference of Korea Society Machine Tool Engineers*: 341-346.
5. Choi, Jung Il, Kim, Chang Bong, Kim, Byung Min and Choi, Jae Chan, 1999, August, Development of Integrated Computer-Aided Process Planning System for Press Working Products, *Journal of the Korean Society of Precision Engineering*,16/ 8: 59-70.
6. Karl and A.Keys, 1982, Innovation in Die Design, *SME*: 71-99.
7. B. Fogg and G. A. Jamieson, 1975, The Influencing Factors in Optimization Press Tool Die layouts and A Solution using Computer Aids, *Annual of the CIRP 24*: 429-434

A SINGLE DISCHARGE STUDY OF MICRO-EDM

Shawn P. Moylan[1] and S. Chandrasekar
School of Industrial Engineering
Purdue University
West Lafayette, IN, USA
[1]Presently at National Institute of Standards and Technology, Gaithersburg, MD, USA

INTRODUCTION

Increase in demand for micro/meso-scale parts and features (10 μm to 1 mm) brings an interest to machining processes capable of producing such features, and micro-electro-discharge machining (micro-EDM) is one process. However, understanding the micro-EDM process has proven significantly more difficult than traditional EDM because micro-EDM often employs discharges that last less than 10 ns and frequencies above 10 MHz. The approach taken here is that breaking micro-EDM down to its most basic component, the unit or single discharge, is the best path for gaining knowledge and improving understanding of the material removal process. Our idea is material removal by micro-EDM is the cumulative result of a sequence of discharges and therefore, studying the material removal characteristics of a single discharge and its relation to discharge parameters in a controlled way offers a path to better understanding of micro-EDM.

EXPERIMENTAL PARAMETERS

The main factors of the experiments were applied voltage, V, pulse width τ, and the combination of the two, or applied energy E, where:

$$E = \frac{V^2}{R} \cdot \tau \qquad (1)$$

(R is resistance).

Pulse forming transmission lines (PFL) (see Fig. 1) can be used to generate electrical discharges. The most common form of transmission line, a coaxial cable, allows creation of single electrical discharges typical of the micro-EDM process. The cable was semi-rigid copper, with a characteristic impedance of 50 Ω and capacitance of 90 pF/m. Each cable was two meters long, but several were connected together using standard subminiature version A (SMA) connectors for a maximum length of 20 m. Combining the resistance and capacitance of the coaxial cable with a direct current (DC) power supply and a charging resistor results in a resistance-capacitance (RC) circuit similar to those used in micro-EDM systems. The benefit of the PFL is that a switch can be added ahead of the coaxial cable allowing the circuit to discharge only once without recharging (see Fig. 1).

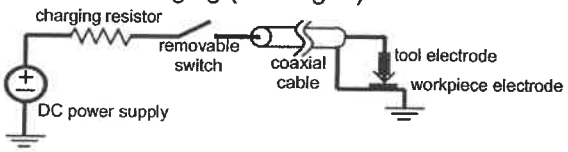

FIGURE 1. Schematic of the transmission line circuit used to create single micro-EDM discharges.

With the DC voltage source outputting a set voltage, the switch is closed to charge the line. After the switch is reopened, the line holds the charge until the tool comes close enough to the workpiece to breakdown the surrounding liquid dielectric, creating a spark and discharging the circuit. When the switch is open, the line does not recharge, preventing multiple discharges.

The duration of the pulses formed by this circuit are given by the transit time, τ, of the PFL

$$\tau = \sqrt{LC} = x\frac{\sqrt{\varepsilon_r}}{c} \qquad (2)$$

where the symbols represent L, inductance, C, capacitance, x, length of cable, ε_r, cable dielectric coefficient, and c, the speed of light in vacuum. It is important to note that τ, along with C, varies with the length of cable, which allows the pulse-width to be varied by simply changing the length of cable. In the present setup, τ is approximately 10 ns per meter of cable length.

A variety of applied voltages between 50 V and 200 V and pulse-width values between 45 ns and 250 ns were chosen to cover a broad area of applied energy values. The tool electrode employed was a 140 μm tungsten rod and the workpiece was a highly polished disc. Workpiece materials were aluminum, copper, iron, titanium, tungsten, zinc, and a steel

common to diesel engine fuel injector nozzles (AISI 8620 steel, a material commonly cut by EDM).

RESULTS

Plan views of micro-EDM craters created by a single electrical discharge (Figs. 2(a) and 2(b)) reveal that they are very similar to craters produced at larger energies [1]: circular in shape surrounded by a rim of re-solidified metal. However, unlike the rough, jagged craters often seen at larger energies, craters produced by micro-EDM appear smooth (see Fig. 2(a)). The profile, or cross-sectional views (Fig. 2(c)) are particularly revealing, showing that the rims of re-solidified metal are shorter in height than the depths of the craters, and that the craters are much wider (on the order of 20 μm in diameter) than they are deep (on the order of 2 μm). Thus the craters are not hemi-spheres, but spherical caps.

The volumes of craters produced on the workpiece varied linearly with applied energy, increasing in size with increasing energy. A scanning white-light interferometer was used to image the individual craters and determine the volume of material removed from the workpiece. The measurement uncertainty arising from random effects associated with this process is $u_c = 3\ \mu m^3$ (as obtained from device user's manual). As Fig. 3 illustrates, the volume data points fell along the same line regardless of whether the applied energy was varied by changing the pulse-width or the applied voltage. This implies that neither pulse-width nor voltage plays a large role in material removal. The combination of the two settings, i.e., discharge energy, determines the volume of material removed by a single micro-EDM discharge. In addition to crater volume, the crater diameter's variation with discharge energy was investigated (with measurement uncertainty $u_c = 2\ \mu m$, again from the device user's manual). Figure 4 shows the diameters of craters made in copper and a power law fit of that data. The power law fit is excellent ($R^2 = 0.97$) and the exponent is 0.325, or approximately 1/3. Sphere diameter is the cube-root of volume in geometry, as well as here experimentally, proving that the fits are valid.

Similar experiments were conducted on all workpiece materials, and the same metrics were examined, allowing for easy comparison of the results. Least squares fits were applied to the

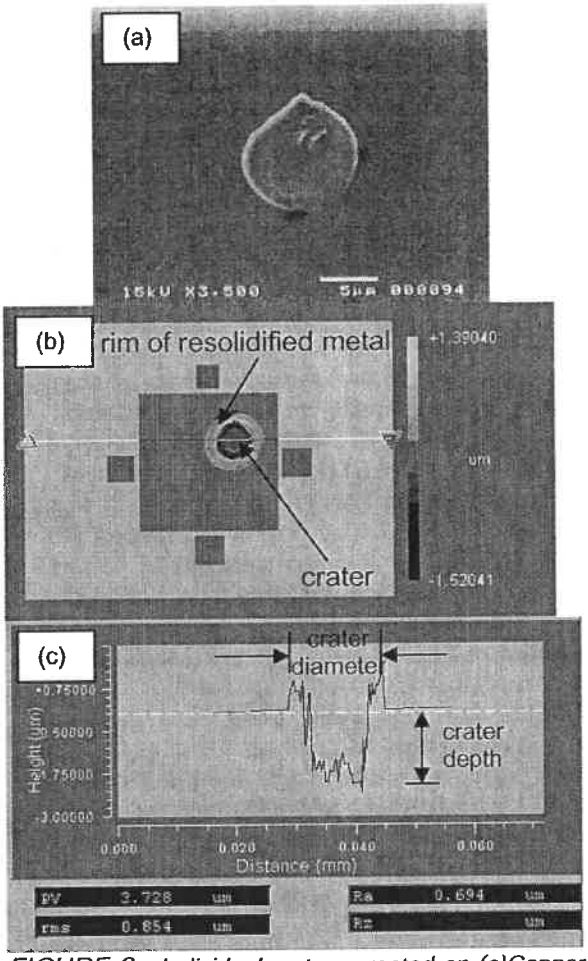

FIGURE 2. Individual craters created on (a)Copper (SEM micrograph), (b)Tungsten (scanning white light interferometry image), and (c)Zinc workpieces by various single discharges of micro-EDM (scanning white light interferometry profile).

volume data, and power law fits to the diameter data. Plots in Figs. 5 and 6 show all of the data. In each case, the exponent in the power law fit diameter data allow crater sizes to be estimated in any of these materials over a large range of discharge energies.

PREDICTING MATERIAL REMOVAL

One of the benefits of a single discharge study is that the results of the experiments lend themselves nicely to comparison with results from theoretical models. The fact that EDM is a thermal process means the EDM plasma discharge is often modeled as different types of heat sources.

An instantaneous point heat source (IPHS) is a logical model for the micro-EDM discharge and

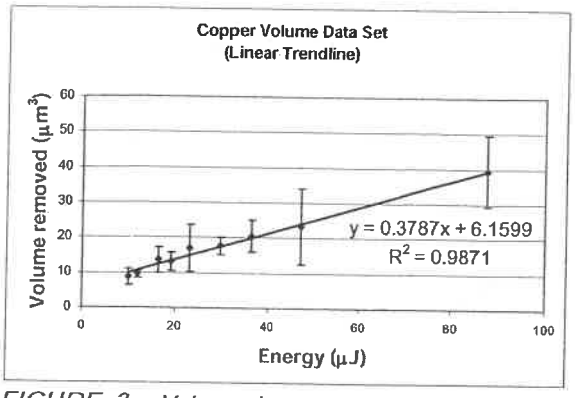

FIGURE 3. Volumetric removal of Copper due to single discharges of micro-EDM at various applied energies.

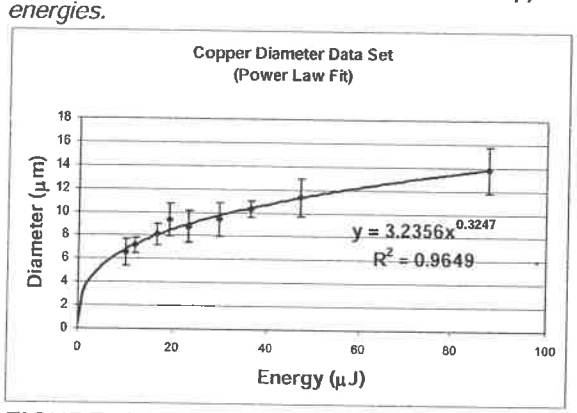

FIGURE 4. Diameters of craters created Copper due to single discharges of micro-EDM at various applied energies.

has indeed been used to accurately predict removal by die-sinking EDM at relatively high energies [2]. The differential equation of the conduction of heat in a solid is

$$\frac{\partial^2 T}{\partial x^2}+\frac{\partial^2 T}{\partial y^2}+\frac{\partial^2 T}{\partial z^2}=\frac{1}{\mathrm{K}}\frac{\partial T}{\partial t} \qquad (3)$$

and is satisfied by

$$T=\frac{Q}{8(\pi\kappa t)^{3/2}}e^{(x-x')^2+(y-y')^2+(z-z')^2} \qquad (4)$$

where T is temperature, Q is heat (equal to discharge energy divided by density, ρ, and specific heat, c_p) and κ is thermal diffusivity (equal to thermal conductivity, k, divided by density and specific heat). Following appropriate boundary and initial conditions, as discussed in Carslaw and Jaegar [3], one can obtain the temperature distribution due to an instantaneous point heat source

$$T=\frac{Q}{8(\pi\kappa t)^{3/2}}e^{\frac{r^2}{4\kappa t}}. \qquad (5)$$

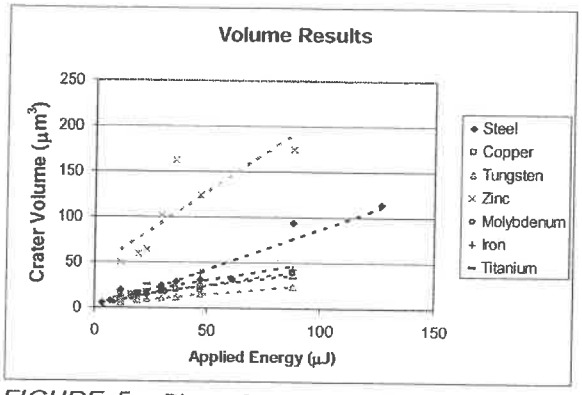

FIGURE 5. Plots of crater volume versus applied energy for all materials tested.

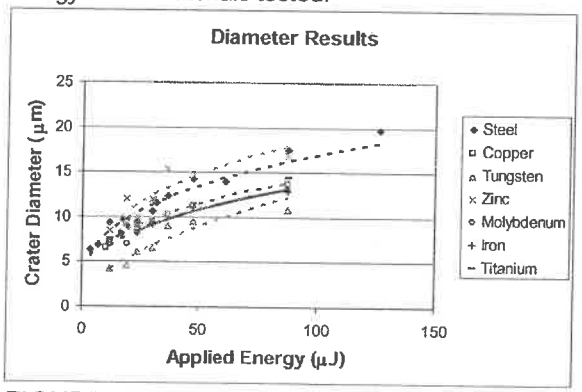

FIGURE 6. Plots of crater diameter versus applied energy for all materials tested.

Temperature reaches a maximum at time $t = r^2 / 6\kappa$. If this value is substituted into equation 5, the equation can be solved for radius.

$$r=\left(\frac{6}{\pi}\right)^{1/2}\left(\frac{Q}{8Te^{3/2}}\right)^{1/3}. \qquad (6)$$

Setting T equal to the melting point of the workpiece, equation 6 outputs the radius of a pool of molten material that has been raised above the melting point (*i.e.,* a melt pool).

The IPHS-predicted crater diameters are an order of magnitude smaller than the observed experimental values. This indicates that an IPHS is not an appropriate model for micro-EDM.

A possible reason that the IPHS predicts craters that are too small is that the point heat source may be too small to reasonably approximate the micro-EDM discharge. By taking the integral of the fundamental solution, (equation 5), using spherical coordinates, one may obtain an equation describing temperature change due to

an instantaneous spherical surface source. The temperature at any given distance r from the origin resulting from heat emitted by the spherical surface source with radius r' is given by

$$\Delta T = \frac{Q}{8\pi r'(\pi\kappa t)^{1/2}}\left(e^{\frac{-(r-r')^2}{4\kappa t}} - e^{\frac{-(r+r')^2}{4\kappa t}}\right). \quad (7)$$

Unfortunately it is difficult to solve this equation for radius r. Additionally, this equation has two unknowns, r and r'. However, equation 7 can be solved numerically, and the data collected during a single discharge study can be input into the equation. The question becomes, "what source radius, r', results in the temperature exceeding the material's melting point at the radius r observed in experiments?"

The validity of this model lies in the fact that the r' values obtained from numerical solutions at a given energy are very similar across all material melting points, as shown in Table 1. Knowledge of the approximate size of the spherical heat source radius allows prediction of the size of a crater created by a micro-EDM single discharge, and is true for any conductive material provided values for the thermal properties can be accurately obtained.

Fitting a curve to the average radii yields the equation:

$$r' = 2.67E^{1/3} \quad (8)$$

which allows one to calculate the size of the spherical source at any discharge energy.

While the crater diameters from the spherical heat source model more closely approach the observed crater diameters, this is, in part, due to the empirical nature of the solution. Additionally, the diameter of the heat source, r', does not imply any physical characteristic. This means the value should not be interpreted as representing the size of the discharge plasma channel nor the approximate gap between workpiece and tool.

CONCLUSION

Results of single discharge experiments are intriguing and allow a more accurate model of the micro-EDM discharge to be postulated. The crater resulting from a single discharge has a morphology similar to a spherical cap with a rim of re-solidified metal surrounding it. The volume of material removed by a single discharge varies linearly with applied energy while the diameters of the craters are proportional to the cube-root of applied energy. Use of a spherical surface heat source as a model of the micro-EDM discharge has allowed more accurate prediction of material removal.

TABLE 1. Radii of spherical heat source r', in micrometers, as computed by modeling the micro-EDM discharge as an instantaneous spherical heat source.

Energy	Cu	Fe	Ti	W	Zn	Steel	Average
9 μJ	5.8	5.2	5.8	3.8	7.4	5.3	5.62
11 μJ	6.2	5.5	6.2	4.1	8.4	5.7	6.02
16 μJ	6.9	6.2	7.0	4.8	9.6	6.4	6.83
19 μJ	7.4	6.6	7.4	5.2	10.2	6.8	7.27
23 μJ	7.8	7.0	7.9	5.7	10.8	7.2	7.74
29 μJ	8.5	7.6	8.5	6.3	11.6	7.8	8.39
36 μJ	9.1	8.2	9.1	6.8	12.6	8.4	9.03
47 μJ	9.6	8.9	9.9	7.6	13.8	9.2	9.83
87 μJ	12.1	11.0	12.0	9.6	16.9	12.1	12.14

REFERENCES

1. J.E. Greene and J.L. Guerrero-Alvarez, 1974, "Electro-Erosion of Metal Surfaces," *Metallurgical Transactions*, 5, pp. 695-706.
2. D.D DiBitonto, P.T. Eubank, M.R. Patel, and R.A. Barrufet, 1989, "Theoretical models of the electrical discharge machining process. I. A simple cathode erosion model," *Journal of Applied Physics*, 66(9), pp. 4095-4103.
3. H.S. Carslaw and J.C. Jaegar, 1959, *Conduction of Heat in Solids*, Clarendon Press, Oxford.

IMPROVEMENT OF MACHINING ACCURACY IN WIRE ELECTRICAL DISCHRAGE MACHINE

Yozo Sakai[1], Akihiro Goto[2], Toshio Nakashima[2], Atsushi Taneda[2], Takuji Magara[2], and Takashi Hashimoto [3]

[1]Indutrial Automation Machinery Marketing Division
Mitsubishi Electric Corporation, Tokyo, Japan
[2]Nagoya Works, Mitsubishi Electric Corporation, Nagoya, Aichi, Japan
[3]Advanced Technology R&D Center
Mitsubishi Electric Corporation, Hyogo, Japan

INTRODUCTION

Electrical Discharge Machine (EDM) is building up a major position in high accuracy die & mold manufacturing process. However, recently, there is a bigger demand for higher accuracy shapes and higher quality surfaces in die & mold industry as well as parts manufacturing industry. This is because of the facts that Japanese mold industry relies on high value added molds lately and also that Wire Electrical Discharge Machining (WEDMing) is replacing the grinding machining process in the area of super-high accuracy machining.

Although recent WEDMs have reached machining accuracy of 1-2 μm and surface roughness of 0.3-0.5 μmRz, better performance is still required.

The part straightness improvement in WEDM is reported [1], however, in this paper, the tip accuracy of narrow and long pin shape is also improved by proposing new method.

POWER SUPPLY FOR WEDM FINISHING

It is necessary to keep the energy of one discharge pulse small in order to have finer surface roughness in WEDMing. Recently, high frequency alternating current (HFAC) in the range of a few MHz to 10 MHz range is mainly used in WEDM (Figure 1) [2]. The performance of a HFAC power supply has achieved the surface roughness less than 1 μmRz .

PROBLEMS & ITS REASONS FOR MACHINING ACCURACY

The performance of HFAC power supply is good but still not enough for the recent demands of WEDM. One is to get adequate part straightness, and the other is the tip accuracy of narrow pin shape.

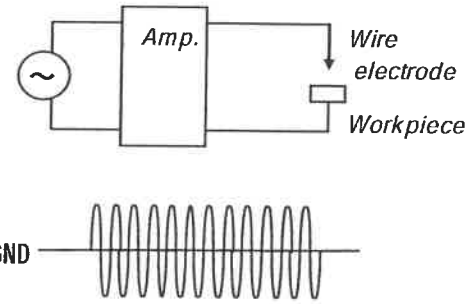

Figure 1: High-frequency AC power supply and its waveform

Reason of Part Straightness Deterioration

In general, good consistency can be obtained between surface roughness and part straightness when appropriate machining conditions are selected starting from rough to finish cuts. However, there is also the possibility that part straightness can be deteriorated by the repeated HFAC power supply usage.

The part shape becomes concave during finish cuts and conversely convex during rough and semi-finish cuts. The reason for this is considered to be the debate of the electrostatic gravitation and the discharge reaction forces acting between the workpiece and the wire electrode.[3]

Part shape becomes concave with relatively larger electrostatic gravitation force (typically shown in figure 2(a)), whereas the part shape becomes convex with relatively larger discharge reaction force (typically shown in figure 2(b)).

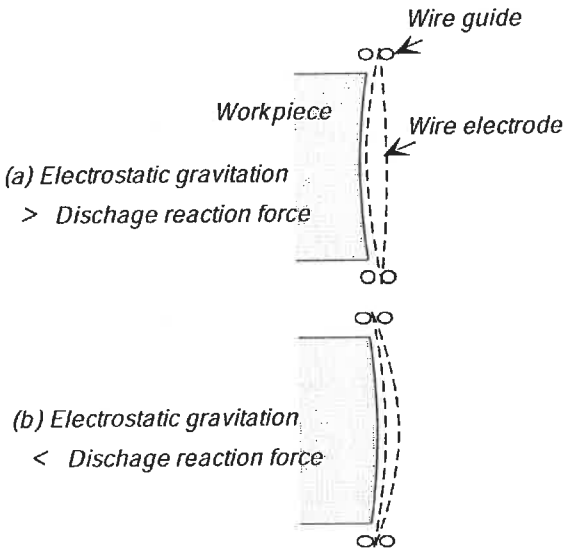

Figure 2 : Reason for the straightness change

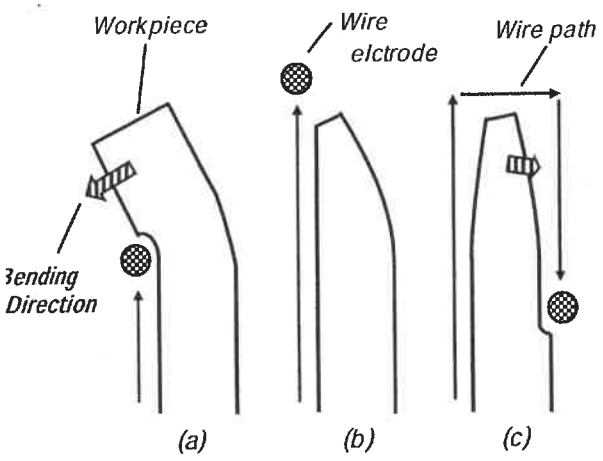

Figure 3: Tip accuracy of narrow pin shape

Reason of Tip Accuracy Deterioration

Miniaturization and lightweight-ization of IT related apparatus progresses, the core pin of the connector molding die is also miniaturized and requires narrower and longer shape

In case of the steel core pin of 0.2 mm thickness, 0.16 mm wide, and 0.5 mm pitch, It is very difficult to be machined by any other machine tools except WEDM. But, as for the length of a pin, 3.2 mm was considered to be the limit (length and width ratio (L/W) is 20), even at the small machining force which a workpiece receives from electrical discharging.

A standard HFAC power supply is easy to concentrate heat in machining area because of continuous discharging, and it is appeared that the machined part is deteriorated. A machining part has a tensile stress by the heat generated at the time of machining, and since bending occurs in the direction of the wire electrode path, especially the tip part is machined beyond necessity, and it is considered to become thin. Figure 3 show the process of the deterioration of the tip shape typically. Figure 3(a) shows the stage of machining one side. Figure 3(b) shows the stage of the finish of the side. Figure 3(c) shows the stage of the machining the opposite side of the pin.

NEW DEVELOPED HIGH PRECISION HFAC POWER SUPPLY

There are two requirements to solve the above problems, and one is to decrease electrostatic gravitation, another is to suppress concentration of heat.

In an AC high frequency power supply, if voltage is constantly applied between the wire electrode and the workpiece, the electrostatic gravitation force becomes large and so the workpiece shape gets concave. In order to decrease this electrostatic gravitation force, the experimental power supply with a switching circuit was built (Figure 4). According to Figure 4, T1 and T2 are called "ON Time" and "Rest Time", respectively. In addition, T1/ (T1 + T2) is called the "Duty" of this power circuit.

Moreover, this switching circuit can control discharge duration, it is expected to prevent concentration of heat.

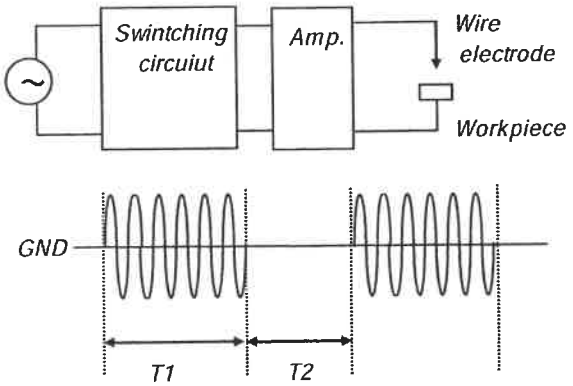

Figure 4: HFAC power supply with Switching circuit and its waveform

IMPROVEMENT OF STRAIGHTNESS

The relationship between the Duty of the HFAC power supply and part straightness was investigated with the workpiece of 18 mm thickness tool steel ,using brass wire electrode of φ 0.1 mm.

The experiments were conducted with four different Duties as presented in Table1. The voltage of the power supply was selected so that a surface roughness of approximately 1 μmRz could be obtained. Frequency was set to 13.5 MHz, and four finish cuts were applied under respective conditions with the HFAC power supply. Furthermore, the workpiece was first machined with WEDM before the HFAC power supply was applied (workpiece surface roughness of 4 μmRz and straightness of 0.5-0.6 μm).

Condition No.	ON Time (T1)	OFF TIME (T2)	Duty (%)
1	10μs	20μs	33
2	10μs	30μs	25
3	10μs	35μs	22
4	10μs	40μs	20

Table1 : Experiment Conditions

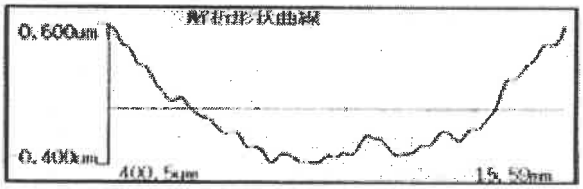

Figure 5: Waviness profile at 33% Duty (WT 0.9797 μm)

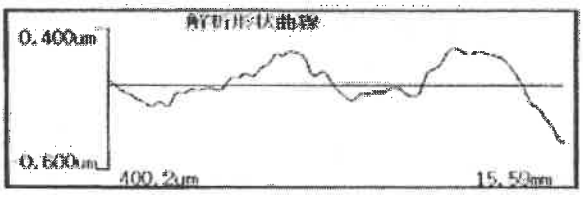

Figure 6: Waviness profile at 25% Duty (WT 0.6637 μm)

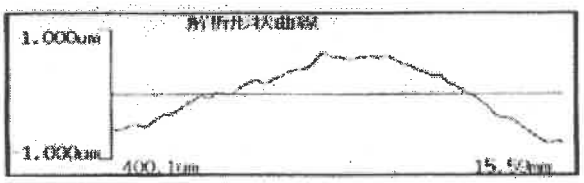

Figure 7: Waviness profile at 22% Duty (WT 1.3707 μm)

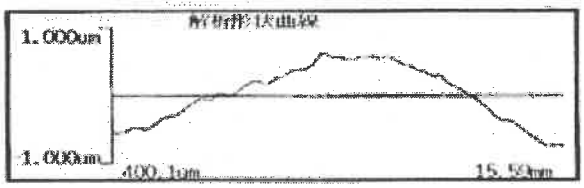

Figure 8: Waviness profile at 20% Duty (WT 1.6156 μm)

The part straightness profiles for four different Duties, after four finish cuts with HFAC power supply, are shown in Figure 5-8 respectively. The bigger the Duty, the more the shape becomes concave; whereas the smaller the Duty, the more it becomes convex. By the above data, it can be said that the Duty of 25% makes the best straightness.

Figure 9 shows the test piece of 80 mm thick cemented carbide assumed a tall punch for stamping die which was machined with the above proposed technology of 25% Duty, using brass wire electrode of φ 0.2 mm

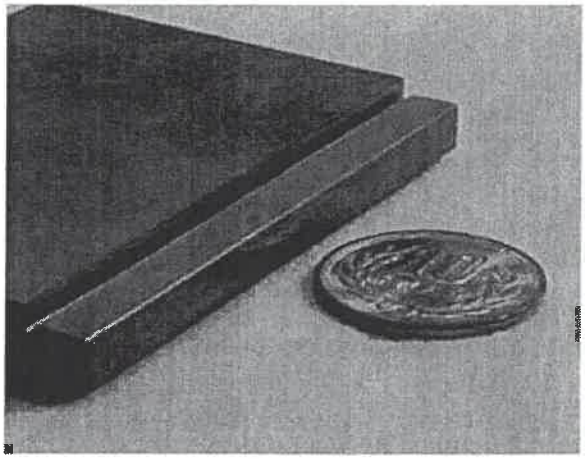

Figure 9: Test piece of Cemented carbide

The measurement result of the straightness is shown in figure 10 and it is 1.0 μm. And the

surface roughness is shown in Figure 11, and it is 0.475 μmRz. From these results, it can be said that the machining straightness in WEDMing can be achieved equivalent to that of surface grinding machining. It can be said that WEDMing is replacing some part of surface grinding process.

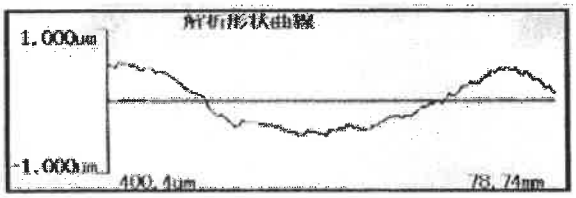

Figure 10: Waviness profile of Figure 9

Figure 11: Surface profile of Figure 9

IMPROVEMENT OF TIP ACCURACY

From the above-mentioned result, the same machining condition was applied to make a narrow pin shape. Figure 12 shows a core pin for connecter molding die which is 2 mm thick steel and 0.16 mm width.

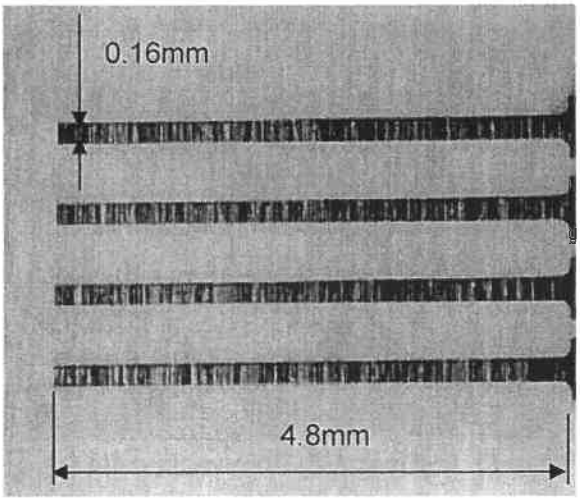

Figure 12: Core pin for connecter molding die

The length of pin is to 4.8 mm and length and width ratio (L/W) is achieved to 30, whereas it was limited to 20 without this new HFAC supply, as mentioned before. This is because that the switching circuit in the new HFAC power supply can control discharge duration, and prevent concentration of heat.

CONCLUSION

1) Part straightness with submicron surface roughness was investigated for an HFAC power supply. By controlling the duration of discharging, equivalent part straightness of a tall punch to in grinding machining process can be achieved. Because of the lack of high skilled operators and high manufacturing costs in grinding process, WEDMing is replacing some part of surface grinding process.

2) Tip accuracy of narrow pin shape in WEDMing was also investigated for an HFAC power supply. By using the same condition as part straightness improvement, the heat concentration is prevented and 150% of L/W can be achieved in 0.16 mm width

REFERENCES

1. A.Goto, T.Nakajima, A.Taneda, T.Magara, T.Hashimoto. Improvement of the accuracy in Wire Electrical Discharge Machining (in Japanese), Electrical Machining Technology, Vol.26, No84, pp.5-8, 2002
2. T.Magara, T.Yatomi, K.Kobayashi, Study on High-Precision Finishing by Wire-EDM - Micro-Finishing by High-Frequency AC Source - (in Japanese), Journal of the Japan Society of Electrical Machining Engineers, Vol.24, No.48, pp.45-64, 1991.
3. H.Obara, N.Ishizu, T.Kawai, T.Osumi, T.Hayashi, Simulation on Wire EDM (3rd Report) - Accuracy of Finish Cut – (In Japanese, Journal of the Japan Society of Electrical Machining Engineers, Vol.34, No.75, pp.30-37, 2000

A STUDY ON THE PERFORMANCE OF COPPER-GRAPHITE AS TOOL MATERIAL IN MICROMACHINING BY MICRO ELECTRO DISCHARGE MACHINING

Murali M. Sundaram [1], and Kamlakar P. Rajurkar[1]
[1] Center for Nontraditional Manufacturing Research,
University of Nebraska-Lincoln
Lincoln,NE, USA

INTRODUCTION

Micro products and components offer unique advantages. They occupy less space and consume less energy and material. They can be cheaper. Hence there is a strong demand for miniaturized components from diverse industries such as electronics, medical and aviation. Product miniaturization demands innovative manufacturing methods. Lithography based MEMS fabrication technologies are capable of producing micro and sub-micrometer size features. However the MEMS techniques do have limitations such as restricted choice of work materials, inability to produce complex geometries, huge capital investment and inevitable cleanroom environment. To complement MEMS techniques, various existing macro machining processes are being modified to perform micromachining. Electro discharge machining (EDM) is one such process used for the machining of electrically conductive materials especially hard metals. By reducing the tool dimensions and the discharge energy, EDM has been successfully downscaled to suit the requirements of micromachining such as reduced unit removal [1]. Unlike EDM, which typically uses a wide range of electrode materials such as graphite, copper, brass and their combinations, the micro EDM process predominantly uses tungsten as tool material due to its low wear [2]. However the major concern is that micro EDM is a slow process when compared to its mechanical counterparts like micro drilling, milling and turning. Search for alternate micro EDM tool material to increase the micro EDM productivity is a vibrant research area [3, 4].

This paper presents the outcome of experimental investigations carried out to assess the performance of copper-graphite as tool electrode material in micro EDM. Micro hole and micro slot machining were conducted on hardened tool steel. The results were compared with that of tungsten, the de-facto standard micro EDM tool electrode.

EXPERIMENTAL DETAILS

Micro EDM studies were conducted in Panasonic micro EDM (MG-ED72W) with standard setup. Experimental work involves spark erosion of three sets of micro holes and micro slot machining in tool steel using copper-graphite and tungsten electrodes. The experimental conditions are shown in *TABLE 1.*

TABLE 1. Experimental conditions.

Work material	Tool steel XW42
Tool material (Ø ~ 300 µm)	Copper-graphite Tungsten
Dielectric	Commonwealth 185
Open circuit voltage	110 (V)
Capacitance	3300 (pF)
Programmed feed	800,50 µm for micro hole, slot respectively
Programmed feed rate	3 µm/sec
Tool rotation	~ 3000 RPM
Polarity	Tool electrode negative and workpiece positive

The tungsten and copper-graphite tool electrodes were machined to Ø ~ 82 and 90 µm respectively, using the built-in wire electro discharge grinding process. The physical properties of the materials used are shown in *TABLE 2.*

The surface roughness was measured by WYKO laser interferometer. The micro holes were measured using optical microscope. Hitachi S-3000 N scanning electron microscope was used to examine the craters produced by micro EDM.

TABLE 2. Physical properties of the materials.

Property	XW42	Cu-graphite	Tung-sten
Density (g/cm^3)	7.86	3.05	19.3
Thermal conductivity (Wm^{-1}K^{-1})	26	-	174
Melting point (K)	1697	-	3695
Boiling point (K)	~ 3000	-	5828
Young's modulus (GPa)	200	-	345
Resistivity (μΩcm)	17.4	305	5.4

RESULTS AND DISCUSSION

Electrode wear

The programmed feed for the micro drilling is 800 μm. The hole depth and tool wear obtained for this feed for both the electrodes is shown in *FIGURE 1*. From the *FIGURE 1* it can be seen that the tool wear is more for copper-graphite electrode. The worn out graphite particle suspended in dielectric medium cause a reduction in the breakdown voltage of the dielectric and as a result both material removal rate and tool wear increases [5].

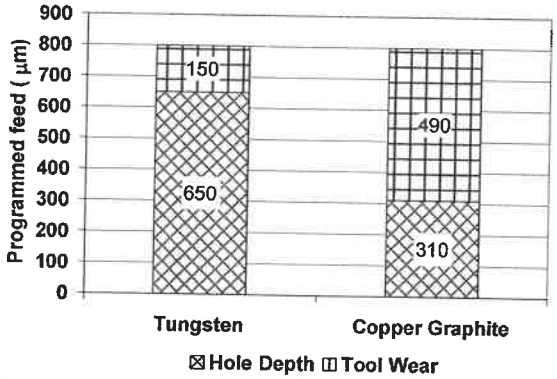

FIGURE 1. The hole depth achieved and the tool wear in tungsten and copper-graphite electrodes.

The time taken by the tool electrodes to attain the programmed feed is shown in *FIGURE 2*. The average feed rate achieved by copper-graphite is 2.83 μm/s, which is uniform through out the machining. For the tungsten electrode two phases can be seen. A feed rate of 1.63 μm/s is achieved up to about 600 μm. Above this, the feed rate has fallen to 0.69 μm/s. Since the density of copper-graphite, as can be seen from *TABLE 2*, is lower than the other two materials, the lighter debris produced by copper-graphite can be easily flushed out of the sparking zone.

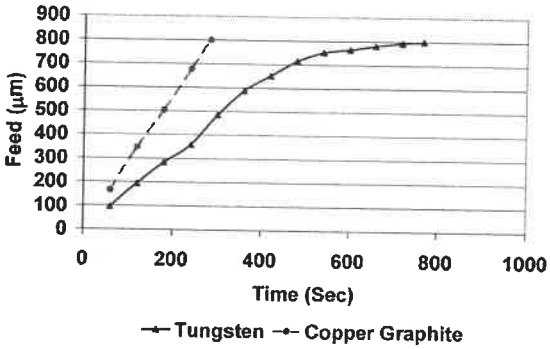

FIGURE 2. Feed vs. time for tungsten and copper graphite electrodes.

Moreover, from *FIGURE 1*, it is evident that most of the material removal in the case of copper-graphite is from the tool and hence the hole drilled is shallower and the debris removal is easier.Consequently, the feed rate achieved by copper-graphite is very close to the programmed feed rate of 3 μm/s. Similarly for tungsten too, higher feed rate is achieved for lower hole . depth. When the hole depth increases, debris removal becomes difficult and the machining process is hindered. Hence the feed rate falls down during latter stage. From *FIGURE 1* it is clear that the tool wear is much less for tungsten and hence it is preferable for applications requiring better profile accuracy.

Material removal rate

The material removal rate was calculated from the hole / slot depth and the machining time for both the electrodes and is given in *FIGURE 3*.

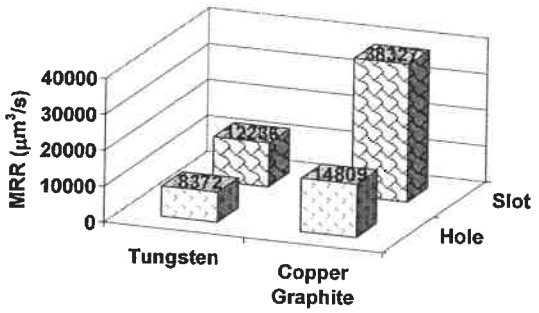

FIGURE 3. MRR for tungsten and copper-graphite electrodes during micro drilling and micro slot machining.

The MRR achieved by copper-graphite in micro drilling is about 77% higher than that of tungsten. This may be due to the material effect or it may be due to the easier debris removal in the case of copper-graphite, as discussed in the previous section. To clear this ambiguity, it was decided to machine shallow micro slots using

both the electrodes. The programmed depth of the micro slot was only 50 µm to keep it shallow. This facilitates easier debris removal and ensures smoother machining. The slots machined were measured using an optical microscope and found that the average volume of material removed in slot machining is 1541786 μm^3 and 766542 μm^3 respectively for the slots machined by tungsten and copper-graphite. The corresponding machining time were 126 seconds and 20 seconds. This clearly demonstrates the tool electrode material effect on MRR. Since the MRR is higher for the copper-graphite electrode, it can be used for bulk material removal, where profile accuracy is not relevant (e.g. through hole drilling).

Surface roughness

As the spark eroded surface is characterized by the overlapping of randomly spaced craters, the surface roughness is essentially based on the crater size and shape. The crater size is dependent on number of factors, such as discharge energy, material properties, flushing conditions etc. During the electrical discharge a plasma channel is formed between the tool and the workpiece as shown schematically in *FIGURE 4.*

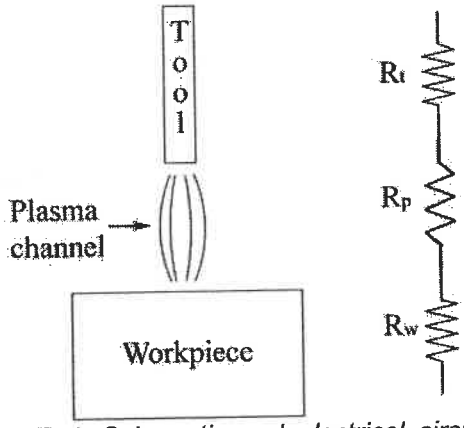

FIGURE 4. Schematic and electrical circuit of sparking zone.

The electrical resistance in the sparking zone is given by

$R=R_t+R_p+R_w$ (1)

where,

R_t = Resistance of the tool electrode

R_p = Resistance in the plasma channel

R_w = Resistance of the workpiece

When the workpiece is kept constant, the resistance (R) in equation 1 is dependent on the resistance of the tool electrode.

$$R \propto R_t \quad (2)$$

As per the Ohm's law, for the given discharge voltage (V), the relationship between the discharge current (I) and the resistance (R) is given by

$$I \propto \frac{1}{R} \quad (3)$$

Combaining equations 2 and 3, it is clear that the discharge current is dependent on tool electrode resistance as shown below.

$$I \propto \frac{1}{R_t} \quad (4)$$

Actually this discharge and current flow takes place between two asperities (points) in the tool and the workpiece. Considering a point current source on the surface of the workpiece, the current density (J_r) at any distance r from the point is given by

$$J_r = \frac{I}{2\pi r^2} \quad (5)$$

As per the electric field force hypothesis, if a critical current density J_c is required for the removal of a fragment of work material at radius r, the radius at which this current density exists is given by [6]

$$r = \sqrt{\frac{I}{2\pi J_c}} \quad (6)$$

From Equation 6 it is seen that the radius of the crater should be directly proportional to the discharge current. It is also clear from equations 4 and 6 that the crater radius is inversely proportional to the resistance of the tool electrode. Since the resistance of copper-graphite (see Table 2) is higher than that of tungsten, the crater produced by it is to be smaller than the crater produced by tungsten electrode according to the above discussion. The scanning electron microscope (SEM) image of the surfaces machined by the two tool electrodes are shown in *FIGURE 5.*

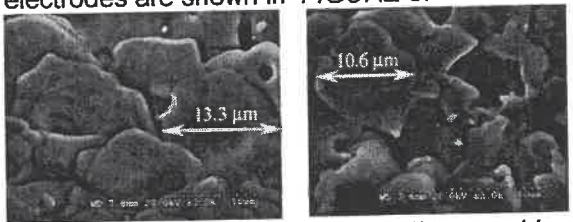

FIGURE 5. SEM images of the machined surfaces. (Left) Surface machined by tungsten electrode (Right) Surface machined by copper-graphite

It is noticed that the size (radius) of a typical crater produced by copper graphite electrode is smaller than the crater size produced by tungsten electrode. This experimental result confirms the theoretical prediction discussed above. Since the copper-tungsten electrode produces smaller craters, the surface roughness produced by this tool is expected to be smaller. The machined surfaces were inspected by laser interferometer to measure the surface roughness achieved by both the electrodes. The results are shown in *FIGURE 6*. As per the prediction, it is noticed that smoother surface is achieved when copper-graphite is used as tool electrode.

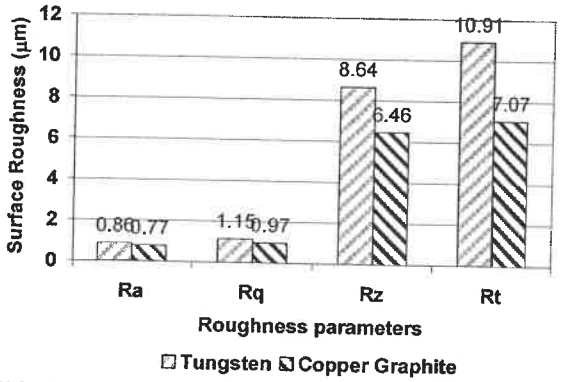

FIGURE 6. Surface roughness produced by tungsten and copper-graphite electrodes.

Spark gap

The spark gap resulted for tungsten and copper-graphite electrodes is shown in *FIGURE 7*.

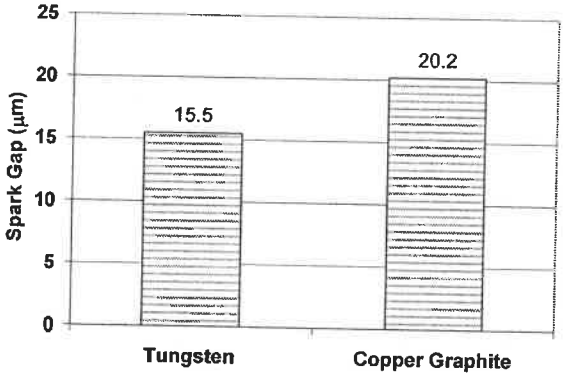

FIGURE 7. Spark gap produced by tungsten and copper-graphite electrodes.

It should be noted that the apparently high spark gaps are due to the rough machining conditions. Even under this rough machining conditions, the spark gap achieved by tungsten is lower that that of copper-graphite. As copper-graphite wears out more rapidly, the dielectric medium will be having more suspended powder materials. These suspended materials cause an increased gap distance. *FIGURE 7* indicates that the profile accuracy will be better when tungsten is used as tool electrode.

CONCLUSIONS

Experiments were carried out to asses the performance of copper-graphite as tool electrode in Micro EDM. Comparison of the results suggests that the productivity can be improved when copper-graphite is used as tool electrode. The machined surface is also smoother than that achieved with tungsten electrode. Hence copper-graphite can be used as tool electrode in applications such as through hole drilling. On the other hand, the tool wear and the spark gap are much lower when tungsten is used. Hence it is preferable to use tungsten as tool electrode for applications such as three-dimensional sculpture machining and micro mould machining where profile accuracy is important. Theoretical prediction and SEM image show that the typical crater size in the machined surface using copper-graphite electrode is smaller than that obtained with tungsten electrode.

ACKNOWLEDGEMENTS

The financial support from the NSF under grant number DMI-03553800 is acknowledged.

REFERENCES

1. Masuzawa, T., 2000, State of the Art of Micromachining, *Annals of the CIRP*, 49 (2): 473-488.
2. Tsai, Y.-Y. and Masuzawa, T., 2004, An index to evaluate the wear resistance of the electrode in micro-EDM, *Journal of Materials Processing Technology*, 149: 304-309.
3. Sundaram, M.M., Yeo, S. H., and Rajurkar K.P., 2005, A Study of Tool Electrode Materials and Flushing Techniques in Micro EDM *Proceedings of the ASPE Annual Meeting* 37: 492-495
4. Murali, M. and S. H. Yeo, 2004, A Novel Micro Erosion Technique for the Fabrication of High Aspect Ratio Micro-grooves, *Microsystem Technologies*, 10 (8-9): 628-632
5. Jeswani, M. L., 1981, Effect of the addition of graphite powder to kerosene used as the dielectric fluid in electrical discharge machining, *Wear*, 70: 133-139.
6. Williams, E. M., 1952, Theory of electric spark machining, *Electrical Engineering*, 71: 257-260.

A NEW PRECISION MAGNETIC FIELD ASSISTED FINISHING PROCESS FOR FERROMAGNETIC METALLIC MATERIALS USING PLURAL PERMANENT MAGNETS AS A TOOL

Yanhua Zou[1] and Takeo Shinmura[2]
[1] JSPS Postdoctoral Fellowship for Foreign Researcher
Graduate School of Engineering,
Utsunomiya University, Utsunomiya, Tochigi, Japan
[2] Graduate School of Engineering,
Utsunomiya University,
Utsunomiya, Tochigi, Japan

INSTRUCTION

Since the mirror finishing of a mold curvature is usually performed manually, a new mechanical process is now in demand for efficient and precise finishing. Magnetic field assisted machining process is a machining process using a magnetic particle brush with flexible machining behavior, this process can improve the surface accuracy while maintaining the form accuracy of the components [1].

It was known that the "Magnetic field assisted machining process" is very effective to the non-ferromagnetic workpiece. When the non-ferromagnetic workpiece was used, a strong magnetic field could be generated in the machining area, the magnetic particle brush can be formed between the magnetic pole and the workpiece, and consequently realizes the finishing of the workpiece surface [2].

The magnetic field assisted machining process of magnetic metallic material is an important subject to study because magnetic metallic material is popularly used for molds. However, It is very rather difficult to finish the surface of the ferromagnetic metallic materials by using the conventional "Magnetic field assisted machining process". If magnetic field assisted machining process is applied to a ferromagnetic metallic materials, the particle brush generates the phenomena of twist and agitation. These phenomena crush the magnetic particles into smaller particles, leave many residual particles on the surface of the workpiece, and reduce the number of particles actually working [3].

In this study, we propose a new process of machining magnetic workpieces using a magnetic tool. In the magnetic tool, a closed magnetic circuit can be created from more than one permanent magnet. Magnetic particles are attracted to the surface of the permanent magnet [4] [5] of the magnetic tool. This produces a magnetic particle brush along the magnetic field line of the magnetic circuit for machining. A closed magnetic circuit is created on the tool side to improve the coercive force that retains a group of magnetic particles. Moreover, in this process, the magnetic workpiece is machining while it is demagnetized by using the principle of loop attenuation demagnetization. This paper reports the feasibility and features of the machining process and the results of a machining experiment.

MACHINING PROCESS AND SYSTEM

Figure 1 shows a schematic of a conventional plane magnetic field assisted machining process. As the figure shows, a machining device is erected and mounted on a milling machine table. The magnetic field generated by the electromagnetic coil flows through a closed magnetic circuit that consists of the "iron core -

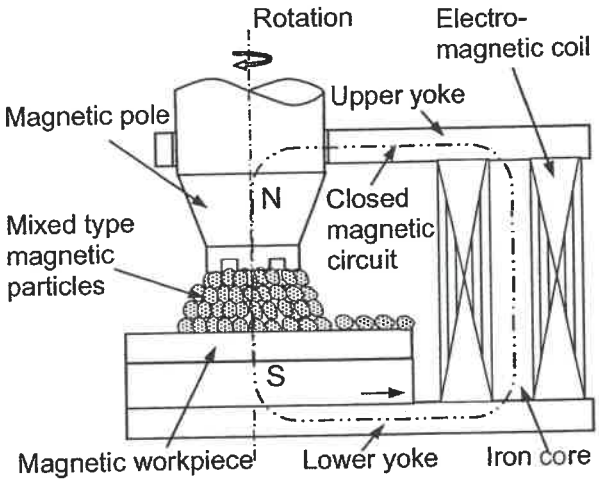

Figure 1: Schematic of the conventional plane magnetic field assisted machining process

upper yoke - rotary magnetic pole - workpiece - magnetic table - lower yoke - iron core." The uneven magnetic field distribution between the magnetic pole and the workpiece provides a strong magnetic field to the magnetic particles in the machining area to charge them intensively. When the magnetic tool is rotated at high speed, the magnetic particles also rotate accordingly to machine the surface of the workpiece.

If the workpiece is made of magnetic material, however, the workpiece surface is magnetized to the S pole, and magnetic particles contacting the surface of the workpiece receive a strong magnetic attraction force. This force makes it difficult for the front of the particle brush to follow the rotary magnetic pole. Therefore, the particle brush between the magnetic pole and the workpiece is twisted, and the magnetic particles are crushed into smaller particles. In addition, many residual magnetic particles are seen on the surface of the workpiece magnetized to the S pole.

Figure 2 shows a schematic of a new plane magnetic field assisted machining process proposed in this report. In the tool-side, a magnetic tool consisted of two permanent magnets, and in the workpiece- side, we do not

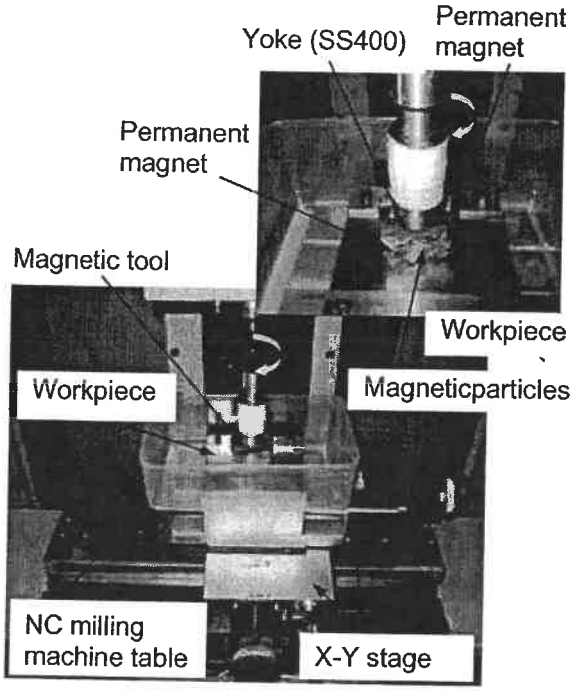

Figure 4: Machining system and an enlarged view of the machining section

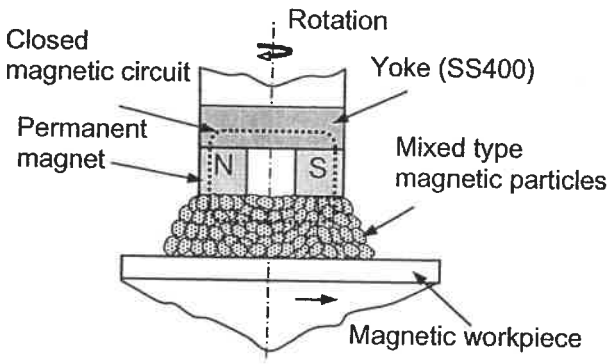

Figure: 2 Schematic of a new plane magnetic field assisted machining process

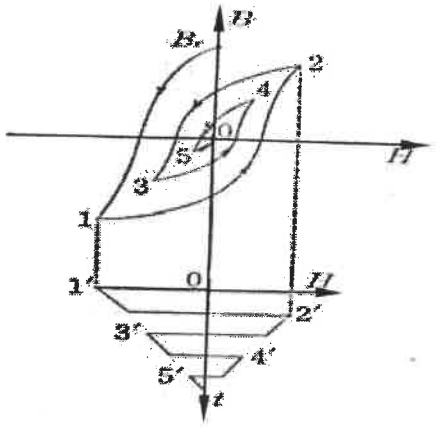

Figure: 3 Principle of the hysteresis loop attenuation demagnetization

use the magnetic poles as shown in Fig. 2. A closed magnetic circuit is formed with the magnetic tool, N magnet, yoke, S magnet and magnetic particles groups. It can reduce the influence of the magnetic field from the magnetic workpiece. In addition, the rotary magnetic tool of the N-S pair type produces an alternating magnetic field that affects one point on the surface of the magnetic workpiece. The size of this magnetic effect becomes small as the rotary tool moves. This action matches the principle of loop attenuation demagnetization [6] as indicated by the magnetizing-properties curve of the magnetic material.

Figure 3 shows a schematic of the principle of the loop attenuation demagnetization. To the magnetic substance which is a certain residual magnetism (*Br*) as shown in Fig. 3, when a positive and negative alternating magnetic field which attenuates for time act to that magnetic substance as shown under this figure, *Br* of the

magnetic substance is gradually decreased to approach attenuating to the starting point 0 along the hysterisis loop.

The machining of the magnetic workpiece becomes possible by using this process, that is, the magnetic workpiece was machining while the workpiece was demagnetized. This effect is expected at automatically demagnetize the surface of a magnetic workpiece and extremely reduce the residual magnetic particles.

EXPERIMENTAL SETUP AND CONDITIONS

Figure 4 is a photograph of the overall machining system and an enlarged photo of the machining section. As the photographs show, an X-Y stage is mounted on an NC milling machine table and a magnetic tool consisting of two permanent magnets is secured on the main shaft of the NC milling machine. With an SPCC magnetic steel plate as the workpiece, a machining experiment was conducted under the conditions listed in Table 1.

The magnetic tool was consisted of two Nd-Fe-B neodymium permanent magnets and a SS400 stainless steel yoke. The number of rotations of the magnetic tool was set to 650 min^{-1}. The feed speed of the workpiece was set to 18mm/min. The clearance between the surface of magnetic tool and the workpiece surface was set to 8mm. Electrolytic iron particles (330μm in mean diameter) and diamond grains (8 to 16μm in mean diameter) were used in this experiment.

TABLE 1.

Workpiece	SPCC steel plate, 80×60×1 mm
Magnetic tool	Magnet: Nd-Fe-B neodymium magnet, 20×10×10 mm, 2 pieces Yoke: SS400 (rolled steel). Number of rotations: 650 min^{-1}
Feed Speed	18 mm/min
Number of Machining Times	8 (stroke: 40 mm)
Clearance	8 mm
Magnetic Particle	Electrolytic iron powder (average particle size: 330 μm), 15 g
Abrasive	Diamond grains (average size: 8 to 16 μm), 2 g
Finishing Liquid	Water-soluble finishing liquid, 15 mL

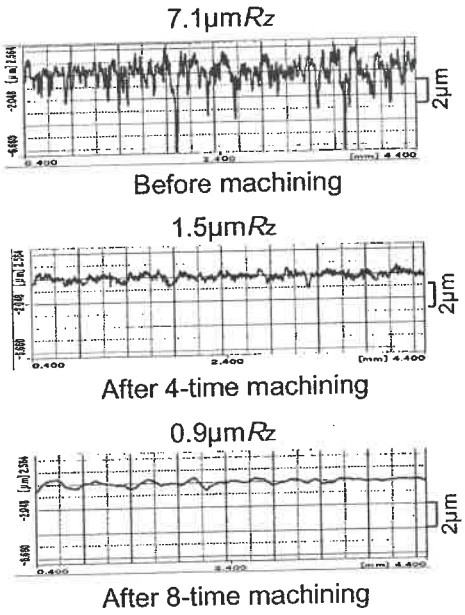

(a) Profiles of surface roughness before and after machining

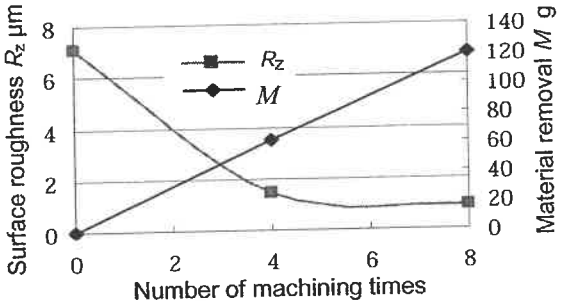

(b) Relationships between surface roughness Ra, material removal M and machining time

Figure :5 Change of surface roughness Rz, material removal M and profiles of the surface roughness

For premachining, the workpiece was manually processed with abrasive paper #120 to a surface roughness of 7.1μm*Rz*.

The experiment was stopped once after a four-time reciprocation. The workpiece was cleaned by ultrasonic cleaning, and then the material removal *M* and the surface roughness *Rz* were measured.

MACHINING RESULTS AND DISCUSSION

Figure 5 shows changes of the surface roughness, the material removal with the

Number of machining times, and also the profile of the surface roughness.

As the figure shows, four-time reciprocation machining made the workpiece surface almost smooth. The surface roughness improved from 7.1 μm *Rz* (0.76 μm *Ra*) to 0.90 μm *Rz* (0.16 μm *Ra*). The improvement slowed down after four-time reciprocation and became steady after eight-time reciprocation. The material removal increases linearly.

Figure 6 shows SEM photos of the workpiece surface before and after machining. The rough surface before machining was polished almost uniformly. Under the experimental conditions, the surface could not be mirror-finished. From the fine satin surface, however, we can imagine that particle brush machining is accompanied by the rolling of magnetic particles.

According to experimental observation, the new magnetic field assisted machining process of machining magnetic metallic material eliminated the phenomenon of the residual magnetic particle process [3] that was seen in the conventional magnetic brush system. This proves the process has the above mentioned effect of demagnetizing a workpiece. Thus, we clarified that this new process could realize the magnetic field assisted machining of the ferromagnetic metallic materials.

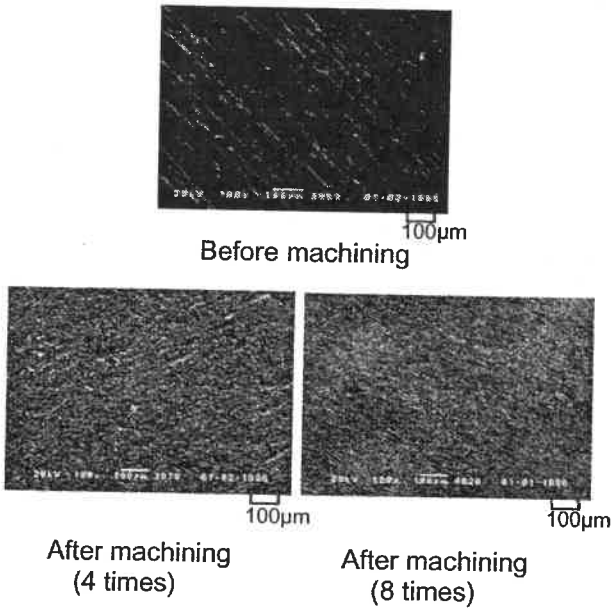

Figure 6: SEM photos of the workpiece before and after machining

CONCLUSIONS

For the magnetic field assisted machining of the ferromagnetic metallic materials, we propose a new process with a magnetic tool consisting of more than one permanent magnet. By an experiment using SPCC magnetic steel plates, we proved that this process could solve the phenomenon of residual magnetic particles and improve the workpiece surface roughness from 7.1μm *Rz* to 0.90μm *Rz*.

ACKNOWLEDGEMENT

This research is supported by the Japan Society for the Promotion of Science (Postdoctoral Fellowships for Foreign Researchers, Research Grants for JSPS Postdoctoral Fellows 1705076).

REFERENCES

[1]. Takeo Shinmura, 1987, Study on Free Form Surface Finishing Process (1st Report, Fundamental Experiments), Transactions of the Japan Society of Machanical Engineers.(C), 53 (485), 202-208. [in Japanese]

[2]. Takeo Shinmura, E. Hatano and K. Takazawa, 1986,Development of Plane Magnetic-abrasive Finishing Apparatus and Its Finishing Performance, Journal of the Japan Society of Precision Engineering, 52 (6), 1080-1086. [in Japanese]

[3]. Shaohui Yin and Takeo Shinmura, 2002, Study of magnetic field assisted machining process for ferromagnetic metallic materials –Development of new magnetic abrasive and its finishing performance-, Journal of the Japan Society for Abrasive Technology, 46 (3), 141-145. [in Japanese]

[4]. Yanhua Zou and Takeo Shinmura, 2004, A Study on the Magntic Field Assisted Machining Process for Internal Finishing Using a Magnetic Machining Jig, Key Engineering Material, 257-258, 505-510.

[5]. Yanhua Zou and Takeo Shinmura, 2004, Study on magnetic field assisted machining process using magnetic machining jig – Application to internal finishing of thick stainless steel tubing, Journal of the Japan Society for Abrasive Technology, 48 (8), 444 449. [in Japanese]

[6]. Hajime Yamada, Eijirou Miyazawa, Kazuo Bessho, 1975, Magnetics Fundamentals, Publishing house: Company Gakukensha, 54. [in Japanese]

DEVELOPMENT OF A STRUCTURE-CONTROLLED FIXED-ABRASIVE PAD FOR FINISHING OF AN OPTICAL GLASS

Toshiyuki Enomoto[1], Tsutomu Fujita[1], Shigeru Tominaga[2], and Makoto Suzuki[2]
[1]Department of Mechanical Engineering, Graduate School of Engineering
Osaka University, Suita, Osaka, JAPAN
[2]ROKI TECHNO CO., LTD., Shinagawa, Tokyo, JAPAN

INTRODUCTION

Loose-abrasive machining with ceria (cerium oxide) abrasive slurry is traditionally employed for finishing optical glass. However, the following major problems are associated with the process:
-low form accuracy, especially large edge roll off of workpiece due to the deformation of polishing pad
-high cost of slurry and polishing pad
-detrimental impact on environment (i.e. dirty working environment and a large amount of slurry disposal)

Therefore, it is strongly recommended that loose-abrasive machining be replaced with fixed-abrasive machining [1][2]. However, conventional fixed-abrasive tools such as fixed-abrasive pads have serious problem involving low finishing efficiency as compared with loose-abrasive machining. The reason for the low efficiency is considered to be that: 1) abrasives are coated with bonding resin in the state released from the fixed-abrasive tool, and results in the depression of the mechanical and chemical removal effect of the abrasives [3]; and 2) the effective cutting edge density is high due to the usage of fine or superfine abrasives and then the force on the cutting edge is too low [4].

One of the authors developed the lapping film utilizing agglomerative superfine abrasives to overcome the problem [4]. The finishing results for optical glass indicate that the high finishing efficiency and the high-quality surface finish can be achieved. The lapping film, however, has the limitation of applying only to specific film lapping machines and then it is required to develop a fixed-abrasive tool with pad type which can be used in general lapping or polishing machines.

In this study, a structure-controlled fixed-ceria abrasive pad is proposed for finishing optical glass in order to meet the above-mentioned requirement. The finishing performance is also evaluated.

STRUCTURE-CONTROLLED FIXED-ABRASIVE PAD

A structure-controlled, that is, spiral-structured fixed-ceria pad consists of fixed-ceria layer and fiber layer (Fig. 1). Table 1 shows the specifications of the developed pad.

The fixed-ceria layer consists of high-concentration (95 wt%) ceria abrasives (mean diameter 0.2 μm) and a small amount (5 wt%) of bonding resin (thermoplastic acrylic resin), resulting in the prevention of coating abrasive with resin. However, the pad wear is considered to be high, because the bonding strength is low due to a small amount of the resin. The fiber layer is, therefore, introduced in the pad for improving wear resistance. Moreover, the finishing efficiency is expected to be significantly improved, because the fiber brings high holding effect of abrasives and high friction with workpiece.

In the manufacturing process, ceria abrasives are first stirred into liquid acrylic resin and the resin is applied to fiber sheet. Next, the sheet is wound up applying adhesion polymer

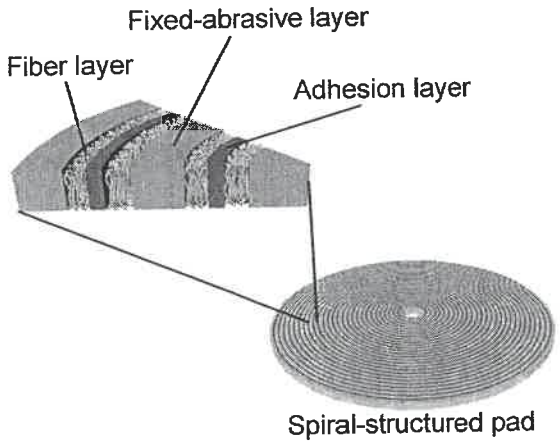

Figure 1: Schematic illustration of spiral-structured fixed-abrasive pad.

Table 1: Specifications of developed fixed-abrasive pad.

Size	Dia. 420 mm – t 3 mm
Abrasive	Cerium oxide Mean diameter 0.2 μm
Abrasive content in fixed-abrasive layer	95 wt%
Polymer of fixed-abrasive layer	Thermoplastic acrylic
Polymer of adhesion layer	Thermoplastic urethane
Thickness of fixed-abrasive layer	0.2 mm
Thickness of adhesion layer	0.07 mm

(thermoplastic urethane resin) and finally, the wound sheet is sliced in predetermined thickness.

The hardness of the manufactured pad was Hs 95 (durometer hardness type C), which was measured with rubber hardness tester (GS-703N, TECLOCK). From the result, it is expected that high flatness, that is, small edge roll off of workpiece can be achieved, considering that the hardness of commercial polishing pad, which is used in general polishing of glass, was low of Hs 50 to 60.

EXPERIMENTAL PROCEDURE

The finishing experiments for optical glass BK7 (75 mm - 75 mm - t 1 mm) were carried out in a single-sided polishing machine (LP-15F, Lapmaster Corp.), as shown in Fig. 2. Table 2 lists the finishing conditions. For comparison with finishing by the developed pad, conventional polishing with ceria slurry and a commercial polishing pad (urethane-foam pad containing ceria, Hs 55) was also performed. Polishing conditions were basically the same as those listed in Table 2. Ceria concentration of the slurry was set at 5 wt%, because the polishing efficiency reached the upper limit at the concentration.

As the finishing characteristics, a finishing efficiency, a finished surface roughness, an edge shape of workpiece and an abrasive consumption were evaluated. A finishing efficiency was calculated by the amount of weight reduction and the specific gravity of

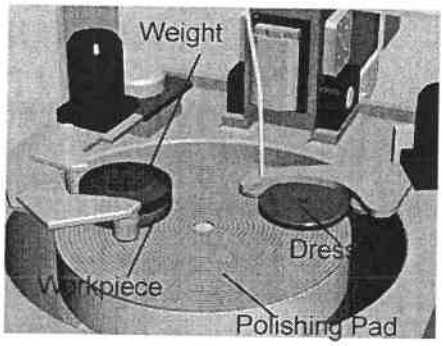

Figure 2: Experimental setup of single-sided finishing tests.

Table 2: Finishing conditions.

Workpiece	Optical glass BK7 75 mm – 75 mm – t 1 mm
Dresser	#60 diamond dresser
Finishing pressure	10 kPa
Dressing pressure	1.1 kPa
Rotation of workpiece	40 rpm
Rotation of pad	40 rpm
Rotation of dresser	50 rpm
Finishing time	10 min
Finishing fluid	Pure water
Supply rate	10 mL/min

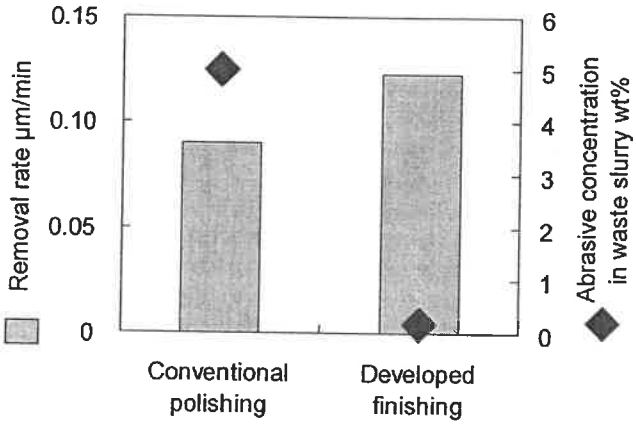

Figure 3: Finishing characteristics in comparison with conventional method.

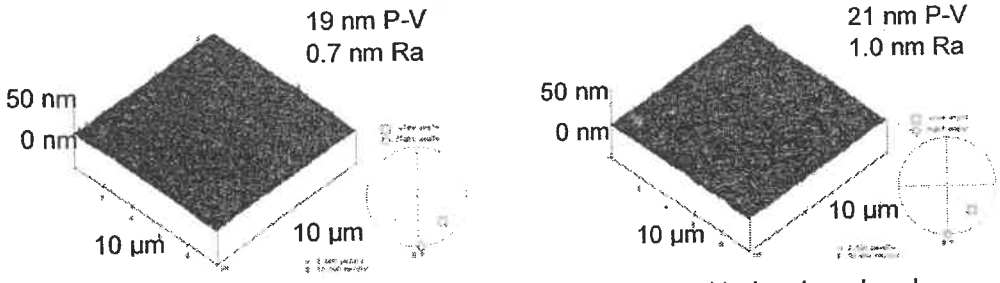

a) Conventional polishing

b) Finishing with developed pad

Figure 4: Finished workpiece surface.

workpiece. A surface roughness and an edge shape were measured with AFM (Dimension 3100, Veeco Instruments) and stylus profile instrument (SE3500K, Kosaka Laboratory Ltd.), respectively. The ceria concentration in waste slurry was evaluated as a substitute for the abrasive consumption.

EXPERIMENTAL RESULTS AND DISCUSSION

Figure 3 shows material removal rate and abrasive concentration in waste slurry. From the experimental result, it was found that the abrasive consumption was suppressed to about 1/30, while the finishing efficiency could be improved by 1.35 times, as compared with the conventional polishing. This indicates that the developed fixed-abrasive pad is extremely excellent in holding abrasives.

As for the surface roughness, the surface quality was as good as that obtained by the conventional polishing, as shown in Fig. 4.

The edge roll off could be significantly improved, as compared with the conventional polishing, as Fig.5 shows. The reason is thought to be that the hardness of the developed pad was 1.7 times higher than that of the commercial polishing pad.

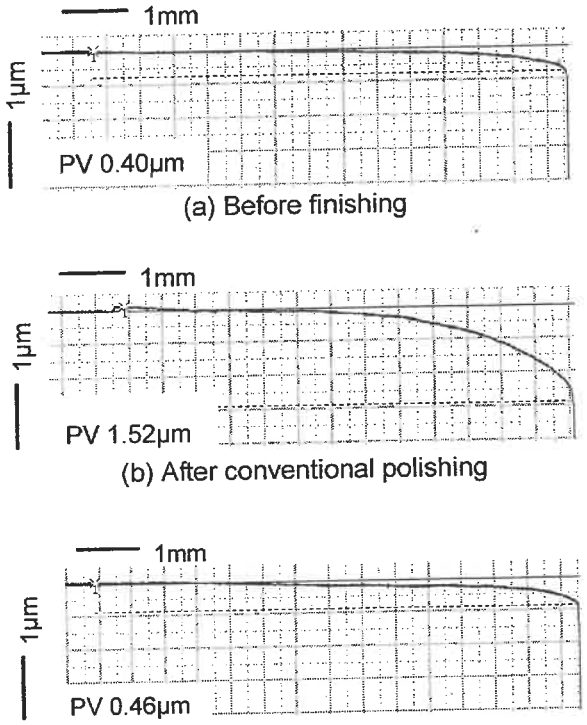

(a) Before finishing

(b) After conventional polishing

c) After finishing with developed pad

Figure 5: Edge shape of workpiece before and after finishing.

CONCLUSIONS

A structure-controlled, namely, spiral-structured fixed-abrasive pad was developed for finishing of an optical glass with slurry free. And, it was found that:

1. The surface quality obtained was as good as that obtained by conventional polishing and the finishing efficiency was much higher.

2. The edge roll off could be significantly improved, as compared with conventional polishing.

ACKNOWLEGEMENT

This research is supported in part by Osawa Scientific Studies Grants Foundation.

REFERENCES

1. Kim, H., Park, J., Jeong, H., Lee, H., Nam, C., Lee, S. and Kim, J., 2001, Development of Abrasive Capsulation Pad Using Water Swellable Polymer, Proceedings of 6th International Chemical-Mechanical Planarization for ULSI Multilevel Interconnection Conference, CA, USA, March, 197-203.
2. Sato, M., Kameyama, T. and Nonami, T., 2006, Polishing of ILD and STI by the LHA Pad, *Journal of the Japan Society for Precision Engineering*; 72 (1):79-83.
3. Hirokawa, K., Akatsuka, T. and Kodera, A., 2004, Polishing Tool, United States Patent Application, NO. 2004/0033771.
4. Enomoto, T., Zhang, J. and Endo, H., 2003, Development of a Lapping Film Utilizing Agglomerative Superfine Abrasives for Finishing of an Optical Glass, *Transactions of the Japan Society of Mechanical Engineers Series C*; 69 (684):234-239.

NOVEL CMP TECHNIQUE FOR COPPER SURFACE FINISHING WITH FULLERENE NANO-PARTICLE

Hiroki Tanada[1], Takashi Miyoshi[1], Yasuhiro Takaya[1], Terutake Hayashi[1], Keisuke Suzuki[2]
[1]Department of Mechanical Engineering, Osaka University
2-1 Yamadaoka Suita, 565-0871, Japan
[2]Advanced Product Development Sec. Product Technology Dept.
Nitta Haas Incorporated
3-17-1, Kannabidai, Kyotanabe, Kyoto 610-0333, Japan

1. INTRODUCTION

In recent years, CMP (Chemical Mechanical Polishing) technology has encountered turning for new direction such as planarization for new material of copper interconnects and Low-k dielectrics. The copper Dual-Damascene process based on CMP technology has been improved ULSI's performances in respect of planarization for multi-layer interconnections [1]. To meet the strong demand for faster semiconductor devices, copper layer should be finished with smoother surface in Cu-CMP process so that more interconnection layers are added to the semiconductor devices. However, conventional Cu-CMP technique could not achieve finishing accuracy for developing more than 9-layered interconnections.

As an essential solution for the problem, polishing procedure using finer abrasive grains is one of the basic ideas. In our research, fullerene C_{60} is proposed as primary abrasive grains due to its fineness. The purpose of this study is to develop slurry with fullerene nano particles, which can achieve local and global planarization on copper surface without any machining defects.

In our method, fullerene must be dispersed into water. However fullerene is normally low polar molecule, so it can be resolvent not to polar solvent such as water (solubility to water is 1.3×10^{-11}mg/ml) but to nonpolar solvent like toluene. To overcome this problem, poly-hydroxylated fullerene is applied as an abrasive for slurry. Poly-hydroxylated fullerene modified by many hydroxyl functions demonstrates high water solubility (up to 17.5mg/ml with about 10nm size in neutral condition).

This report describes fundamental experiments such as static etch rate experiments and polishing experiments to develop our proposed slurry.

2. PROPOSED MACHINING MECHANISM

Machining mechanism of proposed slurry is based on conventional Cu-CMP mechanism [2]. The polishing model of Cu-CMP is illustrated in Figure 1. The slurry contains abrasive grains and chemical agents.

Poly-hydroxylated fullerenes were applied as abrasive grains because of the following two advantageous features.

- The molecular size of less than 1nm as a primary particle is much smaller than any other kinds of abrasive grains such as aluminum oxide and colloidal silica. This feature makes it possible to improve the surface roughness with an accuracy of atomic order.
- The primary particle size is completely uniform so that global planalization is expected to achieve with high performance.

Secondly particles of poly-hydroxylated fullerenes aggregated by Van der Waals forces in water are expected to easily disgregate into primary particles due to mechanical forces by polishing pad in polishing process. Therefore these two features of primary particles are considered to be dominant in polishing process.

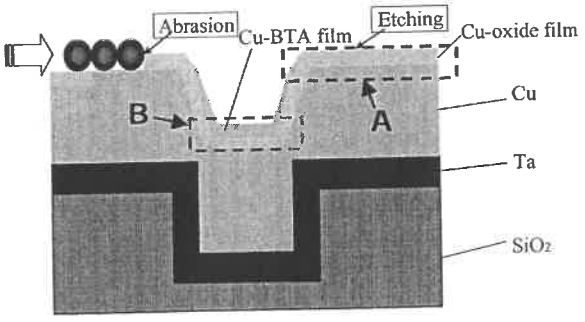

Figure 1 Polishing model of Cu-CMP.

Chemical agents, such as H_2O_2, benzotriazole (BTA), and chelating agents (ammonium phosphate and ammonium citrate) are also contained in slurry. First, copper reacts with the oxidation agent, H_2O_2, to form the porous copper oxide (CuO or Cu_2O) that is removed easily by abrasive grains. The oxidation film would react with chelating agents, ammonium phosphate and ammonium citrate, and then be dissolved as tetraamminecopper (II) ion. Besides such a reaction, the oxidation film simultaneously forms a highly inert Cu benzotriazolate (CuBTA) polymer on the surface reacting with benzotriazole. This polymeric film prevents etching and further oxidation of copper. A threshold pressure is required to obtain a significant mechanical removal of CuBTA film although the film is easier to be removed than the normal copper surface. As a result, the CuBTA film at convexity (area A in Figure 1) of the pattern is removed much faster than that at concavity (area B in Figure 1). The freshly exposed copper surface is oxidized again and "the oxidation-dissolution and passivation-abrasion cycle" repeats.

3. STATIC ETCH RATE EXPERIMENT

To develop novel slurry for Cu-CMP, characteristics of each chemical have to be investigated. Wet etch rate experiments are carried out for various concentrations of chemicals or temperatures. The copper wafer is immersed in reagent solutions. The etch rates are calculated with the time taken to completely dissolve a deposited copper layer whose thickness is about 16000 Å on SiO_2 substrate.

3.1 Effect of BTA concentration

Figure 2 shows wet etch rates of copper in reagent solutions at different BTA concentrations. The etch rate remains constant when BTA concentration is less than 0.06wt%. However with an increase in BTA concentration the etch rate decreases and is seemingly approaching 0 beyond 0.12wt% due to stronger passivation of CuBTA film on the surface.

3.2 Effect of H_2O_2 concentration

Figure 3 shows wet etch rates of copper in reagent solutions at different H_2O_2 concentrations and pH of these solutions. It seems that the value of pH remains constant in these low H_2O_2 concentratins. As to the etch rate, etching does not occur without H_2O_2. With an increase in H_2O_2 concentration the etch rate increases and reaches a maximum of about

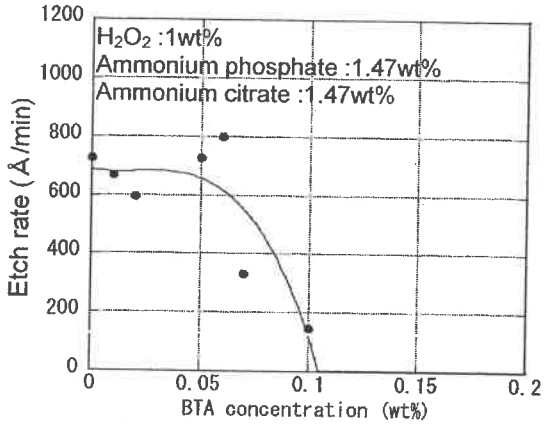

Figure 2 Effect of BTA concentration on wet etch rate.

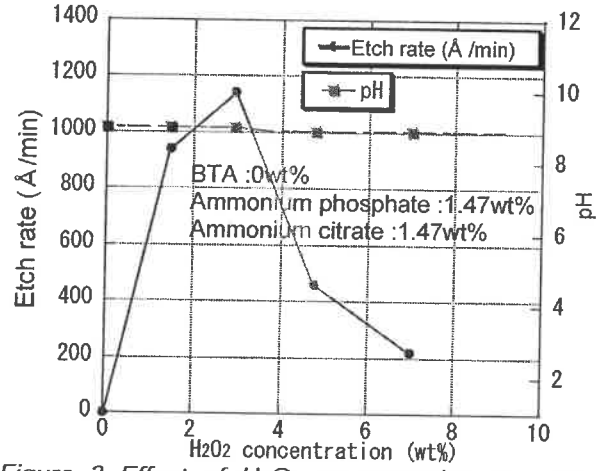

Figure 3 Effect of H_2O_2 concentration on wet etch rate and pH.

1100Å /min at 3wt% H_2O_2. With further increase in H_2O_2 concentration, the etch rate decreases drastically. This phenomenon is due to a strong passivation layer formed by the thickening of Cu oxide layer [3].

3.3 Effect of chelating agent concentration

Ammonium phosphate and ammonium citrate should be dissolved simultaneously into the solution because either of them can not etch effectively. Additionaly these chelating agents make abrasives aggregated by salting-out effect, which leads to micro scratchs, so they should be dissolved in concentrations as low as possible. Therefore in this experiment, mass ratio of two chelating agents is set at 1. Figure 4 shows wet etch rates of copper in reagent solutions at different chelating agent concentrations. The etch rate increases linearly with an increase in chelating agent concentration.

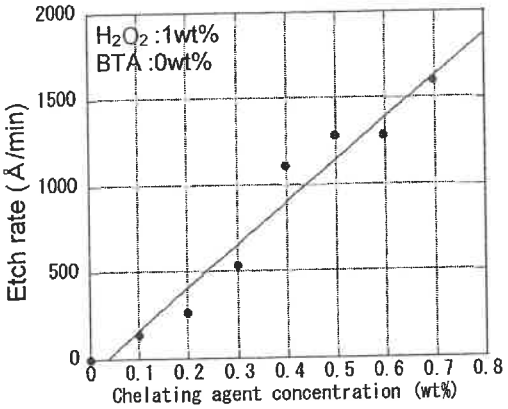

Figure 4 Effect of chelating agent concentration on wet etch rate.

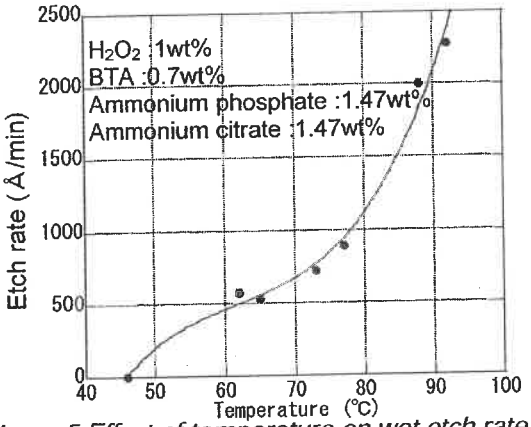

Figure 5 Effect of temperature on wet etch rate.

3.4 Effect of temperature

The temperature of solutions is controlled by a hotplate and is measured by a mercurial thermometer. Figure 5 shows wet etch rates of copper in reagent solutions at different temperatures. It is obvious that the escalation of temperature of the solution excites the wet etching reaction. This tendency contributes to the planarization because copper surface at convexity has higher frictional energy than that at concavity in CMP process.

4. POLISHING EXPERIMENT

The polishing experiment is carried out to examine the performance of proposed slurry. The schematic of CMP unit is illustrated in Fig 6. The polishing unit consists of polishing head for rotation of the test piece and XY stage for scaning the polising pad (Rodel Nitta SUBA400). The test piece with the size of □ 10 mm and the initial roughness of about 10 nm attached to the polishing head is rotated at 90 rpm under applied pressure of 25 kPa controlled by an air cylinder. The polishing pad with the size of ϕ 100

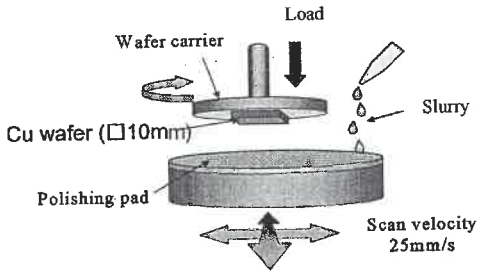

Figure 6 Schematic of CMP unit.

Table 1 Composition of slurry.

Component	Concentration (wt%)
Benzotriazole	0.12
H_2O_2	1
Ammonium phosphate	1.47
Ammonium citrate	1.47
Abrasive for slurry A $C_{60}(OH)_{36} \cdot 8H_2O$	0.1
Abrasive for slurry B $C_{60}H_4(OH)_{32} \cdot 6H_2O$	0.1

mm is fixed on the vacuum chuck. Before polishing experiments, 3ml of slurry are suppried on the polishing pad. And in polishing process, 0.5ml/min of slurry are added on polishing pad. Surface morphology studies of the copper are carried out by Atomic Force Microscopy (Dimension series 3100 AFM, Digital Instruments) using tapping mode Si probe. Three identical polishing experiments are conducted.

4.1 Polishing experiments using poly-hydroxylated fullerene

First, reagent solution was produced with the results obtained in section 3. Then two kinds of poly-hydroxylated fullerene were applied as abrasive particle in slurry, $C_{60}(OH)_{36} \cdot 8H_2O$ and $C_{60}H_4(OH)_{32} \cdot 6H_2O$ for slurry A and slurry B respectively. The composition of slurry is listed in Table 1.

Polishing experiments were performed for 5min. The cross sections and spatial frequency spectrum of the copper surface before and after polishing are shown in Figure 7. The initial surface roughness such as 10.4nm RMS (measured area of 25μm^2) with waviness was improved to approximately 2nm RMS using slurry A. As for Rmax, the surface polished using slurry A has smaller Rmax compared with

the surface polished using slurry B. From the spectrum analysis, it is also obviously described that the surface polished using slurry A has lower RMS roughness. These results indicate that the slight difference of structural formula between two kinds of poly-hydroxylated fullerenes causes a significant difference in the surface formed.

4.2 Relation between machining time and RMS

The relation between machining time and RMS using slurry A in Table 1 is investigated. The relation of RMS versus machining time and cross sections of the surface are shown in Figure 8. With an increase in machining time, RMS of cross section decreases from 9.38nm to 0.34nm. To conclude, highly planarized surface (i.e. 0.72nm RMS of 25μm^2 at 300sec.) is obtained and our proposed slurry performed well.

5. CONCLUSION

The main results obtained are as follows:

(1) The effect of chemicals contained in slurry such as BTA, H_2O_2 and chelating agent are investigated by the static etch rate experiments so that the effect of chemical reaction in machining mechanism is confirmed.

(2) The effect of temperature on chemical reaction is investigated also by the static etch rate. The escalation of temperature of the solution excites the wet etching reaction.

(3) Two kinds of poly-hydroxylated fullerene are applied as abrasive grains in slurry. Slurry with $C_{60}(OH)_{36} \cdot 8H_2O$ planarizes the copper surface well while another does not.

(4) The relation between machining time and RMS using slurry with $C_{60}(OH)_{36} \cdot 8H_2O$ was investigated. It is concluded that highly planarized surface is obtained with an increase in machining time (i.e. 0.72nm RMS of 25μm^2 at 300sec.).

These resluts indicate that our developed slurry polishes copper surface with low roughness taking advantageous of fullerene nano particles.

Acknowledgement

The authors would like to thank Dr. Ken Kokubo (Division of Applied Chemistry, Graduate School of Engineering, Osaka University) for providing poly-hidroxylated fullerene. This research was supported by the Ministry of Education, Science, Sports and Culture, Grant-in-Aid for Scientific Research, 16206017, 2006.

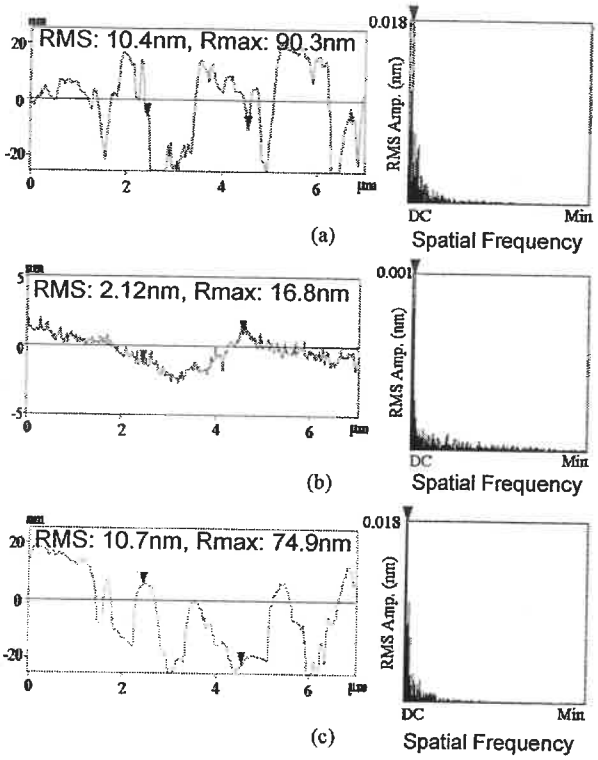

Figure 7 Cross sectional analysis and spectrum: (a) Before polishing, (b) After polishing with slurry A and (c) After polishing with slurry B.

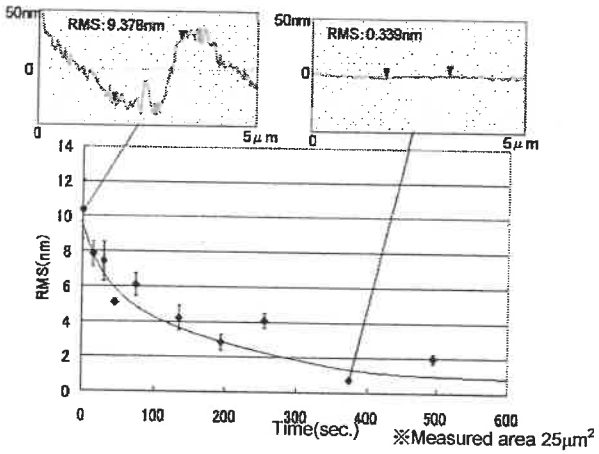

Figure 8 Effect of machining time on RMS of the copper surface polished with slully A.

REFERENCES

[1] T. Doi: Details of semiconductor CMP technology, Kougyotyosakai, Tokyo (2001)

[2] K.W. Chen, Y.L. Wang, C.P. Liu, L. Chang, F.Y. Li, Thin Solid Films 498 (2006) 50-55.

[3] Young-Jae Kang, Dae-Hong Eom, Jae-Hoon Song, Jin-Goo Park, Proceedings of Pac Rim-CMP (2004) 211-218

STUDIES ON OSCILLATION CONTROLLED LAPPING USING SMALL DIAMETER LAP TOOL

Michio UNEDA[1], Ken-ich ISHIKAWA[1], Hitoshi SUWABE[1] and Hiromasa TSUKADA[2]
[1]Kanazawa Institute of Technology
[2]Graduate School of Kanazawa Institute of Technology
7-1 Ohgigaoka, Nonoichi, Ishikawa, 921-8501 Japan

INTRODUCTIONS

With development of the recent semiconductor industry, the demands for the higher precision and productivity of silicon wafers used as the electronic element materials have grown up. Currently, silicon wafers with diameter as 300mm are generally used. Generally, the lapping of these wafers is performed using a "4 way lapping" system. In the 4 way system, the several wafers can be lapped simultaneously by rotating and revolving the several wafers and rotating the lapping plate. However, various problems are pointed out when the large diameter wafers are lapped in the 4 way system. Therefore, the single wafer lapping/polishing techniques which use the small diameter lap/polish tool have been discussed, recently.

This paper describes the basic characteristics of the Oscillation Controlled Lapping (OCL) method as the single wafer lapping technique. Figure 1 shows the schematic drawing of the OCL method. Especially, the OCL method discussed this paper has two parameters such as staying time and position. Furthermore, both Preston's equation expressed traction and genetic algorithm are used to the theoretical simulation for deciding the OCL parameters. In this paper, the provided results are described by the theoretical simulation and experiments.

BASIC LAPPING CHARACTERISTICS OF OCL METHOD

Experimental apparatus and method

Figure 2 shows a photograph of our experimental apparatus. In this apparatus, the workpiece on the lapping plate and the tool can rotate at an arbitrary rotating speed by exclusive servo motors. The lapping plate can be controlled own staying time and position because the electric cylinder is directly connected to the spindle bed of the lapping plate. Therefore, this apparatus controls the oscillatory movement of the workpiece. Moreover, this apparatus can give the lapping load by a dead weight method. The main experimental conditions are as shown in Table 1.

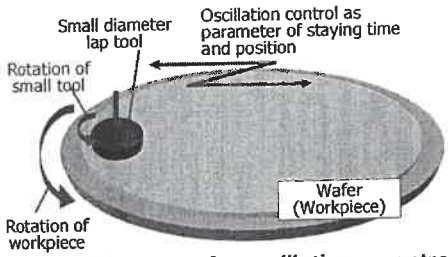
Small diameter lap tool
Oscillation control as parameter of staying time and position
Rotation of small tool
Wafer (Workpiece)
Rotation of workpiece

FIGURE1: Model of oscillation controlled lapping using small lap tool

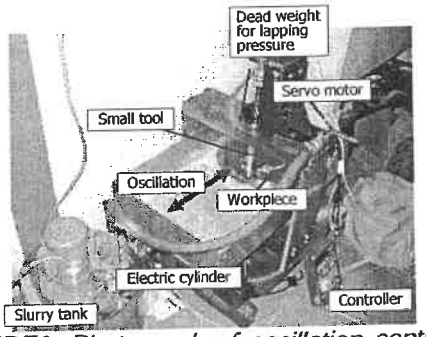

FIGURE2: Photograph of oscillation controlled lapping apparatus

TABLE1: Experimental conditions

Offset e	5,10,15,30,35,45,65,85,100,115mm
Lapping pressure	20kPa
Radius of workpiece $r_{w,max}$	150mm (ϕ300)
Radius of lap tool R_t	30mm (ϕ60)
Rotation velocity of tool and workpiece	30rpm ($\omega = \pi$ rad/s, CCW)
Slurry concentration	20wt% (GC#600)
Lapping time	From 0 to 120min in 30min step

On the other hand, it is necessary to clear the lapping characteristics in an arbitrary staying position of the workpiece for realizing the OCL method. Therefore, the several basic lapping experiments were done without the oscillatory control, and then, these results were evaluated as the basic lapping characteristics. In these experiments, the lapping staying position was defined through setting interval between the workpiece center and the tool center, and it was called as offset e.

Experimental results of basic lapping characteristics

Figure 3 shows six example results of the basic lapping characteristics for the offset e. Tests were actually conducted at ten offset as shown in Table 1. From our results, the lapping quantity and distribution change with changing the offset. Moreover, Fig.4 shows a tendency of the quantity of lapping volume for lapping speed $v(e)$. Note that the lapping speed $v(e)$ is given in ωe when the rotating direction and velocity ω of the tool are same as ones of the workpiece. From this result, the quantity of lapping volume is almost in direct proportion for lapping speed $v(e)$. However, the quantity of lapping volume becomes approximately constant when the lapping speed is beyond v_c. When judging these results from other references, this data is proper. Therefore, this paper supposes v_c to be 250mm/min.

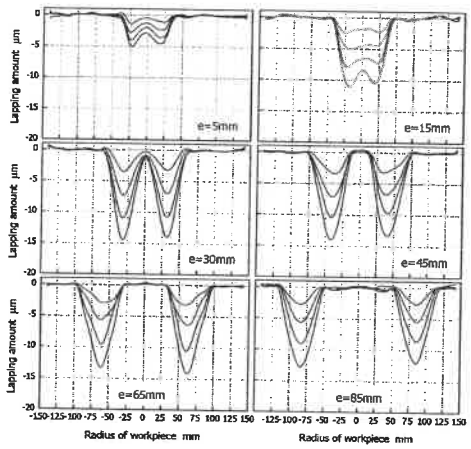

FIGURE3: Example results of lapping amount as a parameter of offset e in evaluating basic lapping characteristics (Four lines in each graph show the results in 30min, 60min, 90min, and 120min, respectively.)

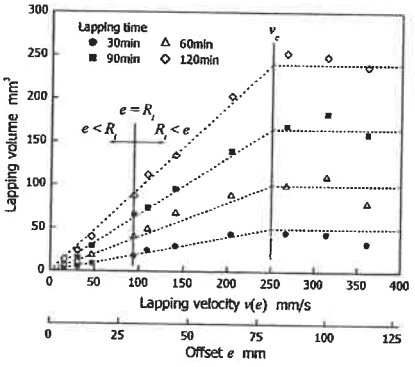

FIGURE4: Relation between lapping velocity and lapping volume (The dotted lines respectively show the tendency lines of each result.)

LAPPING THEORETICAL SIMULATION OF BASIC LAPPING CHARACTERISTICS BASED OUR EXPERIMENTAL RESULTS

It is necessary to express the lapping quantity and distribution in the theoretical simulation based on modeling of the lapping for realizing the OCL method. Therefore, this paper discusses the lapping theoretical simulation.

Theoretical simulation based on "Traction"

Preston reported the "Traction" phenomenon occurred between the tool and the workpiece in the polishing. Therefore, this paragraph shows the result on the traction consideration applying to the OCL method.

Figure 5 shows the geometric lapping model for considering the traction in the OCL method. This model presents a case of lapping the workpiece by the ring shaped tool at radius of R. The ring tool does not have width. Moreover, the workpiece is considered as aggregate of the ring shaped workpiece with width of dr_w.

Here, when considering the cases that the ring workpiece at radius from r_w to r_w+dr_w is lapped, the contact length between the ring tool and the ring workpiece is $ds(R)$. Therefore, with p being the lapping pressure and μ indicating the friction coefficient, the traction which occurs in $ds(R)$ can

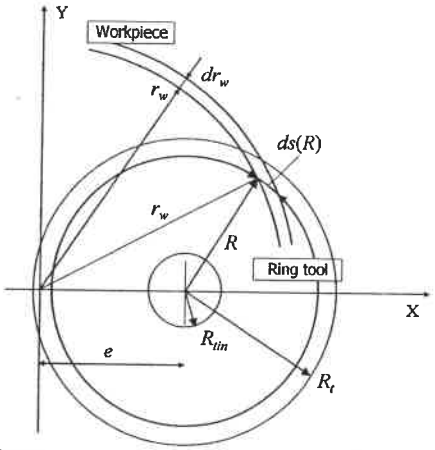

FIGURE5: Calculation model of traction between tool and workpiece

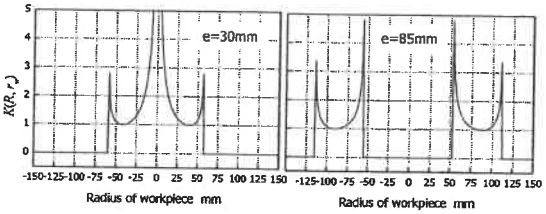

FIGURE6: Calculated results of $K(R, r_w)$ as a parameter of offset e when the radius of hollow ring tool R is R_t (=30mm)

be defined as follows:

$$\mu p \cdot ds(R) \quad (1)$$

Next, when assuming that the lapping efficiency is in direct proportion to the traction provided in Eq.(1), the lapping efficiency may thus be expressed as:

$$\mu p \cdot \omega e \cdot ds(R) \quad (2)$$

The surface area of considered ring workpiece is $2\omega r_w \cdot dr_w$. Therefore, the lapping rate per the unit workpiece area $L_{tra}(R, r_w)$ becomes:

$$L_{tra}(R, r_w) = \frac{\mu p \cdot \omega e \cdot ds(R)}{2\pi r_w \cdot dr_w} \quad (3)$$

We can represent Eq.(3) to Eq.(4) because ω and p are constant. Therefore, $L_{tra}(R, r_w)$ becomes:

$$L_{tra}(R, r_w) = \frac{\mu p}{2\pi} \frac{\omega e}{r_w} \frac{ds(R)}{dr_w} \quad (4)$$

Furthermore, with R_e being R/e, and r_{we} indicating r_w/e, we can get this follows:

$$\frac{ds(R)}{dr_w} = \frac{2r_w R_e}{e\sqrt{\left((1+R_e)^2 - r_{we}^2\right)\left(r_{we}^2 - (1-R_e)^2\right)}} \quad (5)$$

Finally, the theoretical lapping efficiency $L_{tra}(R, r_w)$ is represented as follows:

$$L_{tra}(R, r_w) = \frac{\mu p \omega}{2\pi} \frac{2R_e}{\sqrt{\left((1+R_e)^2 - r_{we}^2\right)\left(r_{we}^2 - (1-R_e)^2\right)}} = \frac{\mu p \omega}{2\pi} K(R, r_w) \quad (6)$$

where, $K(R, r_w)$ shows the non-dimension lapping efficiency.

Figure 6 shows the calculated result of $K(R, r_w)$ at the offset e of 30mm and 85mm in a case of ring tool radius R is R_t as examples. From these results, $K(R, r_w)$ shows very large value in both the most internal circumferences and the most circumferences parts in contact with the ring tool regardless of the offset. Therefore, the traction shows increase with increasing $K(R, r_w)$, and then, we conclude that it is easy to be lapped in these parts.

On the other hand, in the actual lapping process, it may be defined that $K(R, r_w)$ does not increase when $K(R, r_w)$ exceeds K_{th} which means upper limited value of $K(R, r_w)$, regardless $K(R, r_w)$ is obtained in Eq.(6). Therefore, with k being the lapping coefficient, the theoretical lapping efficiency $L_{tra}(r_w)$ obtained by the actual lap tool which is not the ring tool can be expressed below:

$$L_{tra}(r_w) = k \int_{R_{in}}^{R_t} L_{tra}(R, r_w) dR \quad (7)$$

Comparative examination of experimental results and theoretical results for basic lapping characteristics

First, we examine estimation K_{th} in this paragraph. Figure 7 shows the theoretical

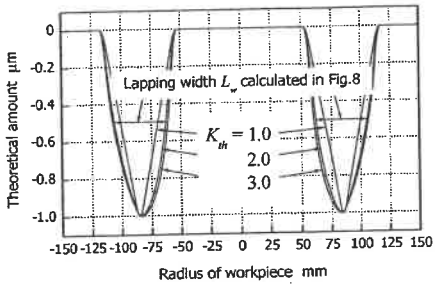

FIGURE7: Theoretical lapping amount as parameter of K_{th} at offset e of 85mm

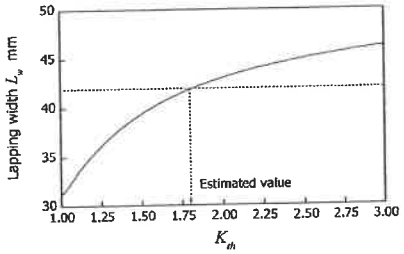

FIGURE8: Relationship between a parameter of K_{th} and lapping width at offset e of 85mm

lapping efficiency $L_{tra}(r_w)$ at offset e of 85mm with K_{th} to be changed from 1.0 to 3.0 with 1.0 step. Note that these results are converted the maximum value into as a standard. From this result, the shape of the theoretical lapping distribution changes by K_{th}, and then, the width of this shape decreases with decrease of K_{th}. Figure 8 shows the half width L_w of $L_{tra}(r_w)$ for changing of K_{th}. In Fig.8, a horizontal line shows the experimental value which equals 42mm in case that offset e is 85mm. From this result, the half width L_w increases with increase of K_{th}, moreover, we conclude that K_{th} can be estimated approximately 1.8.

Figure 9 shows six example results of the theoretical lapping efficiency $L_{tra}(r_w)$ for offset e. When comparing this result with Figs.3 and 9, $L_{tra}(r_w)$ in Fig.9 shows the results to accord the experimental results in Fig.3 regardless of offset. Moreover, Fig.10 shows relationship between the theoretical and experimental quantities of lapping volume. The theoretical quantity is obtained as follows:

$$V_{tra} = \int_0^{r_{w,max}} L_{tra}(r_w) dr_w \quad (8)$$

where $r_{w,max}$ is workpiece radius. Finally, there seems to be high correlation between theoretical and experimental results because the correlation coefficient shows 0.9878. Therefore, we conclude that above theoretical traction consideration can explain the actual lapping efficiency for the OCL method.

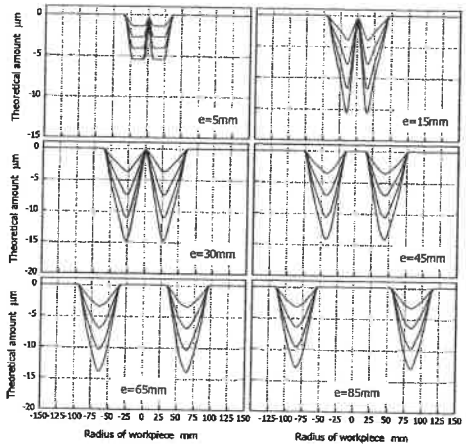

FIGURE9: Calculated results of theoretical lapping amount as a parameter of offset e in evaluating basic lapping characteristics

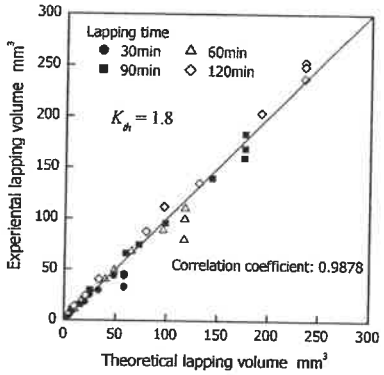

FIGURE10: Relation between theoretical lapping volume and experimental lapping volume

MICRO FORMING CHARACTERISTICS OF OCL METHOD

This chapter discusses the micro forming characteristics of the OCL method using above theoretical and experimental considerations on the basic lapping characteristics. The dotted line in Fig.11 shows the aimed profile by the micro forming using the OCL method. In this micro forming, the OCL parameters are given in the staying position as the offset and staying time. The other OCL conditions are as same as shown in Table 1.

The staying position and time as the OCL parameters were decided by the genetic algorithm. Moreover, in the limitation of used electric cylinder which oscillates the workpiece, 36 points were given as the staying positions.

Table 2 shows the OCL parameters obtained by the genetic operation, and then, the solid line in Fig.11 shows the experimental profile using Table 2 parameters. From this result, the

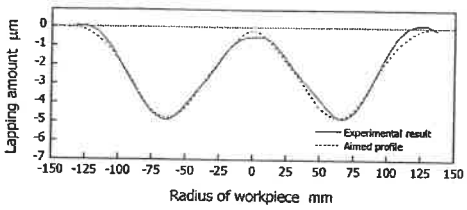

FIGURE11: Results of oscillation controlled lapping

TABLE2: Oscillation controlled conditions

Number	Absolute position mm	Relative position mm	Staying position mm	Staying time sec
1	33	0	33	260
2		-9	24	32
3		-8	16	246
4		-8	8	274
5		-6	2	298
6		-2	0	100
7	63	0	63	164
8		-9	54	278
9		-8	46	272
10		-8	38	62
11		-6	32	246
12		-2	30	6
13	88	0	88	278
14		-9	79	78
15		-8	71	254
16		-8	63	142
17		-6	57	230
18		-2	55	184
19	90	0	90	22
20		-9	81	50
21		-8	73	76
22		-8	65	8
23		-6	59	136
24		-2	57	158
25	98	0	98	264
26		-9	89	140
27		-8	81	96
28		-8	73	34
29		-6	67	98
30		-2	65	106
31	99	0	99	128
32		-9	90	186
33		-8	82	26
34		-8	74	260
35		-6	68	102
36		-2	66	274

experimental profile shows to accord with the aimed profiles within a range of ±0.5μm. Therefore, we conclude that this OCL method can make the workpiece high accuracy micro forming.

CONCLUSIONS

As the evaluation results of the OCL method, the following points have been noted.

(1) According to the theoretical and experimental results of the basic lapping characteristics, the lapping characteristics are remarkably changed as the offset.

(2) The lapping efficiency can be calculated using the traction consideration.

(3) The OCL method having parameters as staying position and time can make the workpiece high accuracy micro forming.

ACKNOWLEDGEMENT

The authors gratefully acknowledge a research grand from The Mazda Foundation for this work.

REFERENCES

1. Atsunobu UNE and Masaaki MOCHIDA, 2002, Oscillation-Speed-Control-Type Polishing with a Small Tool (1st Report), J. Jpn. Soc. Precision Eng., 68, 2: 201. (in Japanese).
2. F.W.Preston, 1927, The Theory and Design of Plate Glass Polishing Machines, J. Glass Tech, 11, 44: 214.

REAL TIME MEASUREMENT OF AXIAL FORCE AND TORQUE DURING POLISHING

Wesley B. Williams and Brigid A. Mullany
Department of Mechanical Engineering and Engineering Science
University of North Carolina at Charlotte
Charlotte, NC, USA

INTRODUCTION

Polishing is a crucial step in the fabrication of optics and other precision surfaces. Despite the criticality of the applications, mankind's long history of polishing and extensive research, there still remain significant gaps in our understanding of polishing mechanisms. Polishing processes are characterized by numerous chemical and mechanical properties related to the abrasives, setup kinematics, slurry, tool and workpiece. The large number of parameters within each of these categories makes it difficult to isolate the direct impact of any one on measurable attributes such as surface finish and material removal rate. The difficulty in separating out the relative influence is also increased as some of these parameters have secondary effects on other parameters [1], [2].

We have designed a novel polishing head that can potentially decouple some of these parameters by making certain real time measurements during polishing. The polishing head currently consists of a motor to drive the polishing tool as well as transducers to measure motor torque, and the contact force between the workpiece and tool. Additional instrumentation will be later incorporated to monitor process vibrations. The motor torque and contact force measurements will be used to calculate the coefficient of friction (CoF) between the tool and workpiece. Future monitoring of the process vibrations by accelerometers will potentially isolate the influence of tool properties (i.e. elasticity and plasticity) on process chatter. All of the quantitative information taken from the polishing tests will be correlated to material removal rates and surface finishes thus giving a better understanding of how a single process parameter change influences the overall polished surface quality. Such information has the potential to provide new insights into the fundamentals of polishing and bring about more economical polishing processes.

Real time measurements of friction have been used as a process control method in Chemical Mechanical Planarization (CMP) [2] as well as in studies of wear rates while polishing diamond with diamond abrasives [3]. Unlike previous studies, the methodology presented here does not pivot on motor current measurement and assumptions of motor efficiencies to calculate the CoF. Instead the CoF calculation is based on direct measurement of the reaction torque and axial loads experienced by the motor during polishing (described in detail in the next section). Care was also taken to ensure the polishing head could be used on different polishers and in different polishing configurations, thus offering greater flexibility. In the initial testing the polishing head will be used in a sub-aperture polishing configuration, i.e. the polishing tool is smaller than the workpiece. Both the polishing consumables (polishing tools and slurries) and workpieces will be those typically found in glass polishing. As previously stated, close attention will be given to material removal rates and resulting surface quality, whereby the processes used are expected to generate surfaces with low roughness values (<1nm) and minimal subsurface damage.

The initial testing assesses the ability of the newly designed polishing head to capture real time polishing events. The variations in torque and axial loading over several runs under identical conditions were assessed and the sources of large deviations isolated, i.e. are the variations induced by the process or by an un-optimized polishing head design. While early results are promising, testing shows that further work is necessary to eliminate non polishing related influences. Another set of polishing tests with varied loads and relative velocities were conducted and from these tests a Stribeck curve was generated. A Stribeck curve is an analysis tool adapted from the journal bearing industry that plots the CoF between two surfaces separated by a thin film of fluid against the Hersey number (a function of pressure, velocity

and the viscosity of the separating fluid film). Analysis of these curves can show the transition from a mixed elasto-hydrodynamic contact regime to a purely hydrodynamic contact regime. It was found for the tests conducted that the pressure is most influential in dictating the polishing contact mode.

POLISHING MEASUREMENT HEAD DESIGN

The polishing head design consists of a motor-gearbox assembly which is free to translate along and rotate about the motor's axis of rotation within an aluminum housing. The Maxon EC-max 30 motor (component 'a' in Figure 1) is a brushless DC motor with Hall effect sensors, which was chosen for its low noise characteristics as well as speed control. The motor is fitted with a planetary gearhead (component 'b') with an 18:1 reduction which provides a speed range of 0 to 328 rpm. Free rotation of this assembly within the aluminum housing is ensured by twelve ball nosed spring plungers placed at 60º apart (see 'k' for the placement of two of the plungers). The rotation and axial translation of the motor assembly is restricted by the placement of two miniature button load cells. The first load cell (component 'c') is imbedded in a threaded cap (component 'd') above the motor assembly and is aligned with the motor's axis of rotation. This load cell measures the load exerted by the polishing tool on the workpiece. The load is transmitted to the load cell through single point contact exerted by the Delrin sphere (component 'e'). This sphere is free to rotate within its holder and thus only transmits the axial load to the load cell. The second load cell (component 'f') is located in a mounting that extends from the bulk of the housing. This load cell contacts a fixture that extends in the radial direction from the motor surface (see component 'g'). This second load cell both restricts the rotation of the motor-gearbox assembly and measures the force component of the reaction torque generated opposite to the torque between the tool and workpiece. Again a Delrin sphere is used to transmit the load to this load cell. The two Delrin spheres along with the ball nosed spring plungers allow the motor assembly to freely translate and rotate with minimal frictional losses. This method of measuring the torque avoids pitfalls in extrapolating torque from the motor current due to variations in efficiency at different loads and speeds.

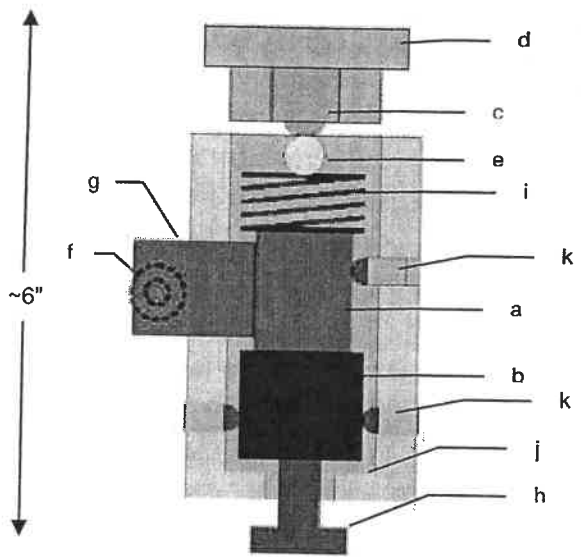

FIGURE 1. Representative Drawing of the Measurement Head. a) motor b) gearbox c) axial load cell d) threaded cap e) delrin sphere f) torque load cell g) torque fixture h) polishing tool i) spring j) internal ledge k) ball nosed spring plungers.

For polishing, the polishing tool (component h) is brought into contact with the workpiece such that the motor assembly translates up into the housing (to prevent the gearbox from dragging along the internal ledge indicated as 'j'). The axial loads are adjusted after the tool is brought into contact with the workpiece by screwing down the end cap which houses the axial load measuring load cell. This compresses a stack of wave springs (component i) between the load cell and motor which increases the axial load. The signals from the load cells are read into a data acquisition card and the measurements are collected through a Labview virtual instrument.

The CoF (μ) can be calculated from the measured load cell signals. The mathematical relationship is derived below. It assumes an even distribution of pressure across the polishing tool.

A=polishing tool area (in^2)
L[a]=measured axial load(pounds)
L[r]=load on a differential ring element (pounds)
L[t]=measured torque load (pounds)
M=moment arm at which the torque load is applied
μ=coefficient of friction (CoF)
R=pad radius (in)
r=radial distance (in)
P=pad pressure (psi)

T[r]=frictional torque on a differential ring element (lb.in)
T=total frictional torque summed over the pad (lb.in)

$$P = L[a]/A = L[a]/\pi R^2$$

$$L[r] = 2P\pi rdr$$

$$T[r] = 2P\mu\pi r^2 dr$$

$$T = \int_0^R 2P\mu\pi r^2 dr = \frac{2P\mu\pi R^3}{3} = \frac{2L[a]\mu R}{3} = L[t]M$$

$$\mu = \frac{3L[t]M}{2L[a]R}$$

EXPERIMENTAL SETUP

The polishing head is currently mounted to a 6-axis robot and is used in a sub-aperture polishing configuration. The polishing tool (component 'h') will polish a stationary glass workpiece. Throughout the process the workpiece surface will be wetted with a polishing slurry. For both sets of tests described below the polishing tool is covered with a foam backed Universal LPU polyurethane pad and the slurry used is a water based cerium oxide mixture (50g CeO_2/500ml water).
Two sets of experiments are conducted; the first is to assess the repeatability of the newly designed polishing head while the second is to measure CoF variations when polishing under varied loads and speeds.

Repeatability Test Setup

To assess the repeatability of the measurement head, a set of tests are conducted under a fixed load of 5 pounds with varying tool speeds. In the first test the speed is 28rpm, in the second it is 180 rpm and in the final test it is set at 328rpm. Three tests were carried out at each speed (run1, run2, run3). Each test was 2 minutes in duration. The average output and standard deviation of both the axial and torque load cell signals during each run was calculated. Tests were also conducted under no load conditions to determine the magnitude of the electrical and mechanical noise associated with the polishing head.

Varied Loads and Speed Test Setup

Individual sites on the glass workpiece were polished for 10 minutes each using combinations of three axial loads (5, 10 and 15lbs) and three rotational speeds (28, 180 and 328rpm). The average outputs from the load cells over the 10 minute runs were converted into coefficient of friction values by the method already outlined. The material removal rates for two extreme friction cases were also measured (low load low speed and high load-low speed).

EXPERIMENTAL RESULTS AND REMARKS

Repeatability Results

The average outputs from the axial and torque load cells during each run are shown in Figure 2. The error bars indicate the standard deviation of the signal during each run. On the right hand side of each graph the average of the three runs are shown. The error bars show the deviation over the three runs.

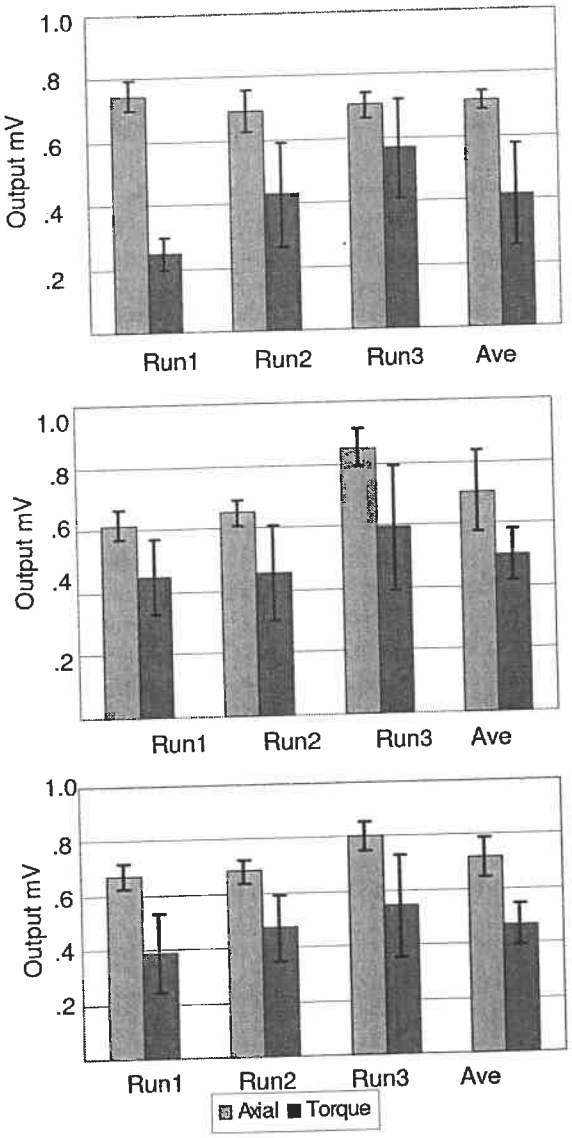

FIGURE 2. Repeatability Results. Top 27 rpm, Middle 180 rpm, Bottom 328 rpm.

Under all test conditions the measured torque load experienced larger deviations during the 2 minute run (in the order of 0.19mV). The axial load cell was more stable in its response with deviations in the order of 0.04mV. Under no load conditions the load cell deviations were 0.04mV and 0.02mV for the torque and axial signals respectively. This indicates that further work must be done to reduce noise sources associated with the polishing head. The data points on the right of each graph in Figure 2 depict the average recorded values over the three runs. It should be noted that 'run3' at both 180rpm and 328rpm are considered to be outliers attributed to a variation in the procedure for setting the axial load on those two trials. While the scatter is currently not insignificant it is expected that repetition of these tests after fine tuning of the process and reduction of inherent system noise will yield statistical proof of process repeatability.

Varied Load and Speed Results

As expected the calculated CoF changed with changing Hersey Number, see Figure 3. There is significant scatter in the CoF values at the lower Hersey numbers. More testing is required before definitive conclusions can be drawn. A preliminary examination of the material removal obtained at friction values of 0.533 and 1.011 was 1.5µm and 1.8µm respectively for the 10 minute test period. This is consistent with the expectation in polishing that higher levels of tool workpiece interaction (higher friction) will generate higher material removal rates.

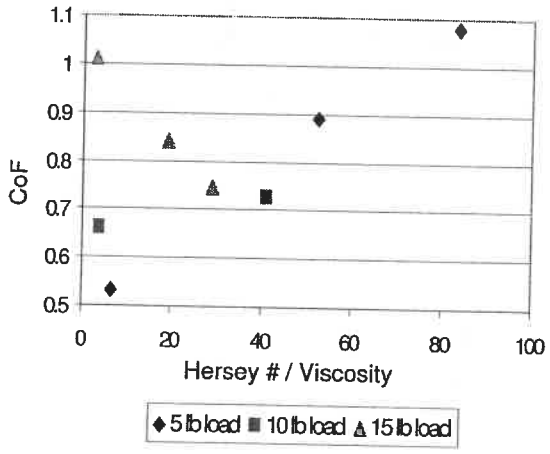

FIGURE 3. Stribeck Curve for Various Hersey Numbers.

CONCLUSIONS

From preliminary testing it appears that the presented polishing head design has the potential to be sufficiently sensitive and repeatable to provide useful quantitative process information. At present the system can clearly capture the changes in torque loading that accompany changes in the axial loading. Short term work is focusing on increased consistency in the mechanical setup and the reduction of system noise, more thorough signal analysis (i.e. FFT) and the addition of sensors to monitor process vibrations. We expect that reducing or accounting for these variations will result in a design that is sensitive to changes in numerous polishing parameters, that when coupled with material removal rates, surface finishes and subsurface damage will provide new information regarding polishing process fundamentals.

ACKNOWLEDGEMENTS

The authors would like to thank the Department of Mechanical Engineering at UNC Charlotte for supporting this work.

REFERENCES

1. C.J. Evans, et al., 2003, Material removal mechanisms in lapping and polishing, *CIRP Annals*, 52/1: 128-149.
2. R. Komanduri, et al., 1997, Technological Advances in Fine Abrasive Processes, *CIRP Annals*, 46/2: 545-596.
3. P.J. Backage, et al., 1999, Improved metal CMP endpoint control by monitoring carrier speed controller output or pad temperature, *Proc SPIE*, vol 3882: 118-125.
4. S.E. Grillo, et al., 2000, Diamond polishing: the dependency of friction and wear on load and crystal orientation. *J. Phys. D: Appl. Phys., 33:* 985–990.
5. B. Mullany, et al., 2003, The Effect of Slurry Viscosity on the Chemical Mechanical Polishing (CMP) of Silicon Wafers, *Journal of Materials Processing Technology, 132*: 28-34.

POLISHER LIFE IN ULTRA-SMOOTHNESS POLISHING OF MAGNETIC DISK SUBSTRATE USING NEW DOUBLE SIDE SURFACE POLISHING MACHINE

Heiji YASUI[1], Kanta YAMAGUCHI[2], Takuya NIKI[2],
Shingo OTSUKA[2], Tomohiko NAGATA[2]

[1] Department of Mechanical System Engineering, Kumamoto University, Kumamoto city, JAPAN
[2] Graduate School of Science and Technology, Kumamoto University, Kumamoto city, JAPAN

INTRODUCTION

To produce the low cost compact magnetic disk of high storage capacity, the high removal rate and ultra-smoothness polishing technique of the magnetic disk substrate has been strongly required. By using one side surface polishing machine, in the previous research, higher speed and/or higher pressure polishing than the present polishing condition is found effective for ultra-smoothness and high removal rate polishing of the substrate. The high speed and high pressure polishing, however, is considered difficult to be applied to double side surface polishing with the conventional polishing machine driven by gear mechanism because the carrier holding the substrate which is rotated by gear mechanism can not endure high polishing force generated from high polishing pressure and/or high speed drive. From the point of view, in the previous research [1], the gearless double side surface polishing machine in which the carrier is fixed during polishing is devised and manufactured on trial.
Using the new double side surface polishing machine, in the research, the polisher life which is one of the most important factors from the standpoint of the manufacturing cost is examined by polishing the electro-less nickel phosphorus plated aluminum substrate with colloidal silica abrasives.

GEARLESS DOUBLE SIDE SURFACE POLISHING MACHINE

In the conventional polishing machine, as shown in Fig.1, the carrier holding the substrate is rotated by sun gear and internal gear. Polishing is executed by the rotation of magnetic disk substrate accompanied with the carrier. The carrier can not endure high polishing force

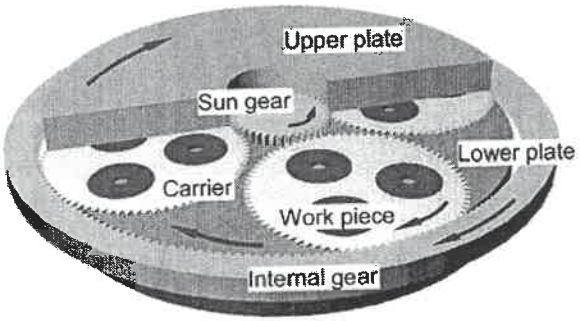

FIGURE 1. Schematic view of the mechanism in the conventional polishing machine

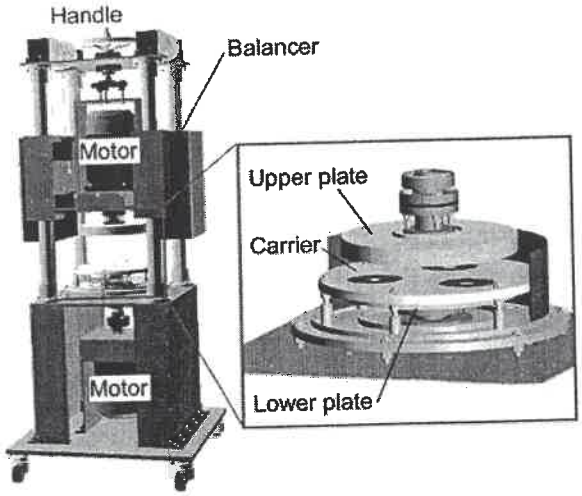

FIGURE 2. Appearance of new concept double side surface polishing machine

generated from high polishing pressure and/or high polishing speed drive because it is thin and weak.
To resolve the problem, the gearless double side surface polishing machine is devised. Appearance of double side surface polishing

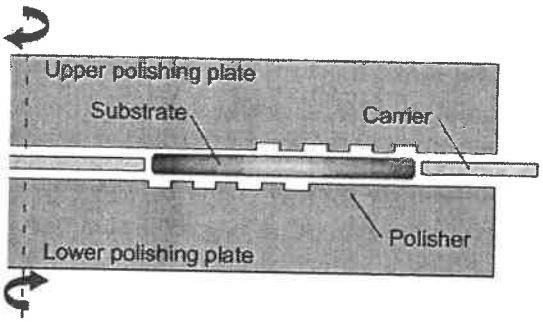

FIGURE 3. Schematic view of the rotating mechanism in the new concept machine

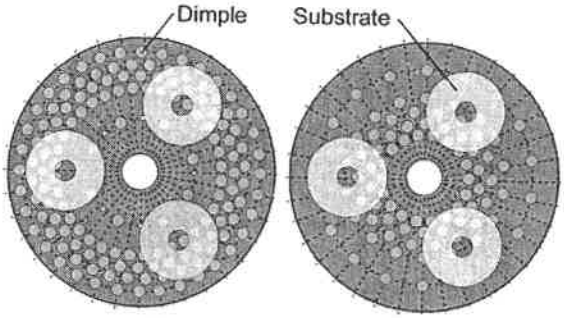

FIGURE 4. Schematic view of the polisher surface

machine is shown in Fig.2. In the gearless machine, the carrier is fixed and does not move the substrate set in the carrier. The rotating mechanism of the substrate depends on the couple of forces generated by the friction forces which are caused from the contact between the substrate and upper or lower polishing plate. Figure 3 shows the schematic view of the rotating mechanism of the new concept machine. The upper and the lower plate are rotated to reverse direction. In the upper plate side, the friction force between the substrate and polisher surface becomes larger at the outside of plate than the inside of plate because the contact area between the substrate and the polisher at the outside of plate is closer than the inside of plate. In the lower plate side, on the other hand, the friction force between the substrate and polisher surface becomes oppositely larger at the inside of plate than the outside of plate. As those results, the couple of forces which rotates the substrate operate to the substrate. Figure4 shows the schematic view of the polisher surface. A lot of circular dents are found on the polisher surface. The dents called "dimple"

TABLE 1. Experimental conditions

Work piece	NiP plated aluminum magnetic disk substrate (3.5inch type: ϕ 95× ϕ 25×1.27mm)
Polisher	Suede -Type (Single layer)
Polishing fluid	Abrasives : Colloidal silica Supply flux *Lg* : 50g/min
Polishing conditions	Polishing pressure *P* : 10kPa Polishing speed *Va* : 1.5m/s

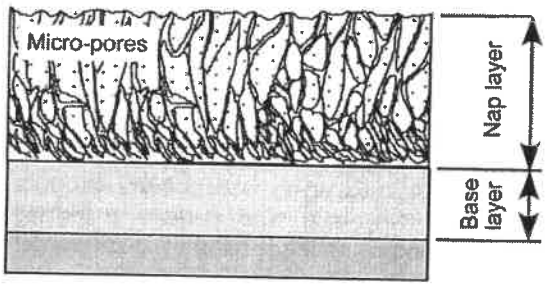

FIGURE 5. Schematic view of the polisher section

decrease the contact area between the polisher and substrate. The number of dimple in the upper plate side is more at the outside of plate than the inside of plate. The number in the lower plate side is more at the inside of plate than the outside of plate. The difference between the contact area due to the location of the substrate gives the large couple of forces to the substrate. As the result, high pressure and/or high speed double side surface polishing is possible.

EXPERIMENTS

To compare with the results obtained previously in the one side polishing experiments [2], in the research, the experiments are executed at polishing speed of 1.5m/s and polishing pressure of 10kPa which corresponds to the maximum ordinal polishing conditions. However the machine is available for the experiment up to polishing pressure of 60kPa and polishing speed of 18m/s in the specification of the design. The main experimental conditions are listed in Table 1. The aluminum substrate used is 3.5inch type. Supply flux is 50g/min. The polisher surface is observed with a differential interference microscope and SEM. Schematic view of the

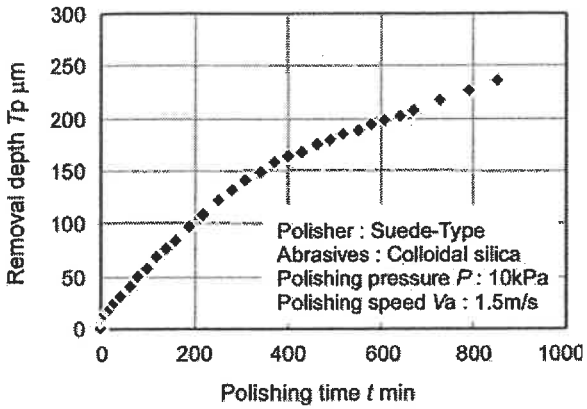

FIGURE 6. Change of removal rate with removal depth

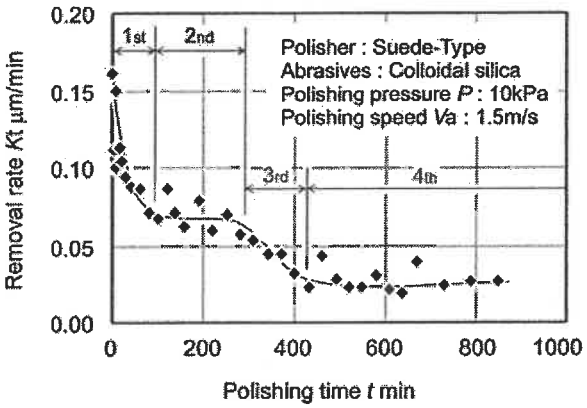

FIGURE 7. Change of removal rate with polishing time

polisher section is shown Fig.5. From the figure the polisher surface consists of large macroscopic holes and wall films having a lot of micro-pores. The substrate smoothness is evaluated from the standpoint of the average surface roughness Hra(Ra), which is obtained from the surface profiles of 256 micro-meter length measured with an interferometric surface profiler (WYKO). The data is obtained by averaging the values of two-dimensional profiles at five random positions on the three-dimensional WYKO images measured at four locations of substrate surface.

EXPERIMENTAL RESULTS AND DISSCUTIONS

FIGURE 6 shows the change of removal depth with polishing time. Polishing pressure and speed used are 10kPa and 1.5m/s, respectively. The removal depth increases steeply in the initial polishing process. Afterward the

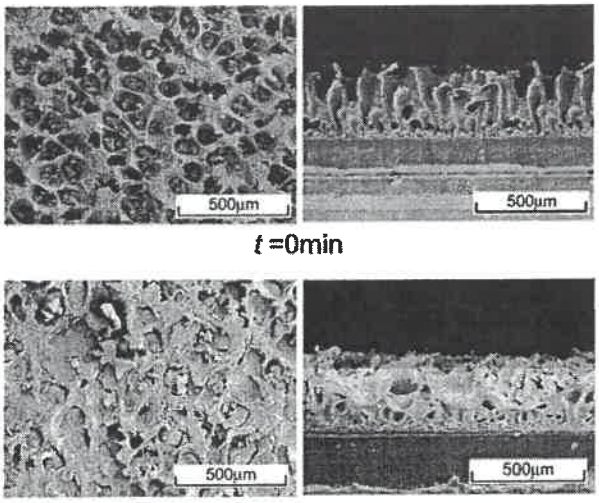

FIGURE 8. Comparison of the new polisher surface with that after polishing for 390min

〔 Colloidal Silica, Suede-type, Va=1.5m/s, P=10kPa, Lg=50g/min 〕

increasing rate decreases gradually. However the removal depth increases linearly from the polishing time of about 100 minutes to about 300minutes. From the polishing time of 300 minutes, the increasing rate of removal depth begins to become small again and finally converge to a extremely small value.

FIGURE 7 shows the change of removal rate with polishing time. The removal rate is high at the beginning of polishing. In the initial polishing process, however, the removal rate steeply decreases transiently with the increase of removal depth (1st stage). After the initial polishing process, the removal rate is kept steadily a constant value in the range of polishing time of about 200min (2nd stage). Over the range of steady state, the removal rate steeply decreases again (3rd stage). Finally the removal rate converges to extremely small values (Final 4th stage). The polisher life is defined when the removal rate comes to the final stage level. The change in the double side polishing machine is almost the same as that obtained previously in the one side polishing machine.

FIGURE 8 shows the comparison of polisher surface and surface section before and after polishing time of 300 minutes corresponding to life time. On the new polisher surface, large

empty pores of several 100 micro-meters are found. Thin film like wall around the pores is observed and has minute empty hole of below 1 micro-meter inside it. And the top of the film is consisted of the salience of nap. Compared with the new polisher surface, the polisher surface at the life time of t=390 min, is embedded mostly with colloidal silica abrasives. As the result, the real polishing pressure that is related to the removal rate decreases drastically because the polishing loading is applied to the embedded abrasives in addition to the surface of the thin film like wall. Thus the removal rate in polisher life is considered to become extremely small value.

FIGURE 9 shows the change of the terminal surface roughness with polishing time. However the terminal surface roughness means that the substrate smoothness converges finally to a value related to a given polishing condition after being improved by polishing. From the figure, the roughness, *Hra*, is the lowest in the 2nd stage and somewhat worse in the 1st stage. After the 3rd stage, the *Hra* tends to have extremely slight increase with the increase of polishing time. Accordingly the polisher surface condition is referred to influence little on polished substrate surface smoothness measured with WYKO.

FIGURE 10 shows the change of the three dimensional WYKO image with polishing time. The polishing time is found to have small influence on the surface smoothness.

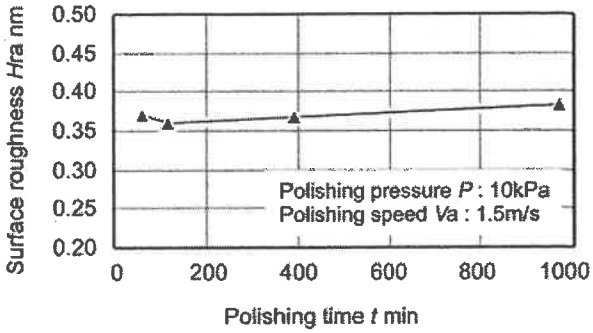

FIGURE 9. Change of the terminal surface roughness of substrate with polishing time

[Polisher :Suede-type , Abrasive :SiO2]

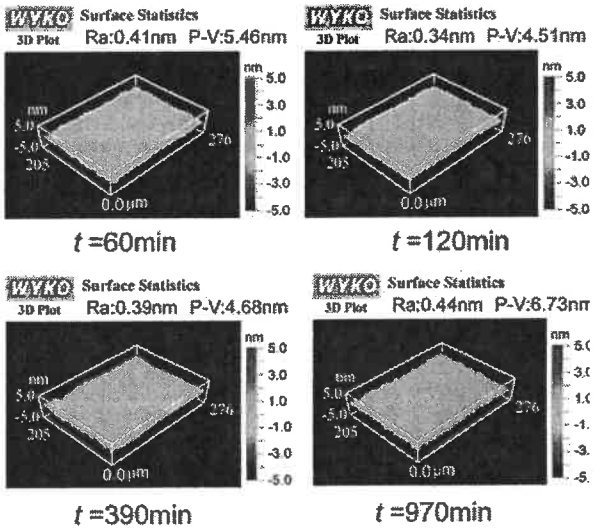

FIGURE 10. Change of WYKO image with polishing time

[Polisher :Suede-type , Abrasive :SiO2]

CONCLUSIONS

The main conclusions obtained are as follows:

(1) The removal rate with polishing process changes in the four stages, which are the initial removal rate reducing stage, the steady removal rate stage, the later removal rate reducing stage and the extremely small removal rate stage corresponding to the life time.

(2) The terminal surface roughness is at almost the same from the beginning of polishing to polisher life.

(3) The polisher life occurs when the small hole on the polisher surface is mostly embedded by colloidal silica abrasives.

ACKNOWLEGEMENTS

The authors would like to thank TOYO KOHAN Co. Ltd, FUJIBO EHIME Co. Ltd and KAO Co. Ltd for providing magnetic disk substrate, polisher and polishing fluid. A part of the research is supported by GRNT-IN-AID for Scientific Research (2005) [Project No. 17360065], in Japan

REFERENCES

1.H.Yasui, K.Yamaguchi, S.Kuribayashi:Development of Gearless Polishing Machine for High Removal Rate and Ultra-Smoothness Double Side Surface Polishing, Proc. 5th International Conference of the European society for precision engineering and nanotechnology, pp.465-468

2.H.Yasui, S.Kuribayashi, S.Matsukawa, Y.Yamasaki, K.Yamaguchi: Polisher Life in High Speed Ultra-Smoothness Polishing of NiP Plated Aluminum Magnetic Disk Substrate, Proc. ASPE 19th Annual Meeting, pp.737-740

LARGE AREA OPTICAL DEVICES WITH GLASS-PRESSED/METAL-EMBEDDED SUBWAVELENGTH GRATING

Kensuke Tsuchiya[1], Atsuto Komiya[2], Hideaki Suzuki[2], Takeshi Ooi[2]
Hiroshi Morii[2], Tetsuya Hamaguchi[2], and Masayuki Nakao[2]
[1]Institute of Industrial Science, The University of Tokyo,
Meguro-ku, Tokyo, JAPAN
[2]Department of Engineering Synthesis, The University of Tokyo,
Bunkyo-ku, Tokyo, JAPAN

INTRODUCTION

Optical devices with micro-features of about half the size of optical wavelengths have recently been gathering much attention [1]. Advancements in micro-fabrication have realized developing such optical devices with a variety of functionalities. For example, embedding metal in gratings (cyclic grooves) of sizes about half the optical wavelengths, produced on the surface of transparent material like glass or plastic, makes optical devices like color filters, polarizing filters, or photonic crystals [2]. The superior optical performance of glass gives it a lead as transparent substrate material.

Common forming methods of glass are pressing for mass production in case of smooth shapes like lenses. On the other hand, however, producing cyclic grooves on the surface in the sub-micron order requires lithography that repeats masking and etching or ion-beam etching. These processes consume large cost and time, thus are not suited for mass production. Press forming micro-structures can only reproduce forms to small areas and have not succeeded in forming larger areas in the millimeters to centimeters scale.

The study we report in this paper developed the entire sequence of processes starting with glass material with superior optical characteristics, pressing gratings with sizes of about half wavelengths of optical light on a large area, and embedding metal to the grooves. These processes produced guide light plates with cyclic micro-structures and ones with metal embedded in the grooves. We measured the optical performance of these plates to evaluate the effect of tolerances in our processes.

DESIGNING THE GLASS PRESSING PROCESS

We first pressed grating patterns to glass surfaces. The metal mold needed to satisfy three requirements of having durability against heat, the glass product coming off the mold easily, and micro-machinability. We thus picked CVD (Chemical Vapor Deposition)-SiC for the mold material, and Fast Atomic Beam (FAB) etching for the etching process because it etches bulk CVD-SiC over a larger area to form fine sub-micron form features.

For our study, we selected low transition point glass with a softening point of 408 and a glass transition point of 347 degrees Celsius (L-PHL1, OHARA Inc). Our preliminary tests found good pressing conditions of 3MPa at 380 degrees Celsius. Figure 1 shows SEM images of the pressing results at these conditions. Higher temperature caused defects in the glass, whereas, lower temperature made the pressing time too long. We reproduced micro-grooves with pitches of 400nm and 800nm onto the glass at these pressure and temperature to find the relation between the pressing time and the micro-groove filling. Figure 2 shows the results. Measuring the cross section of the product and mold with AFM, we found that the filling rate was approximately linear against the logarithm of time. The filling rate of 400nm pitched grooves were about half of that of 800nm pitched ones.

To evaluate the optical performance of our

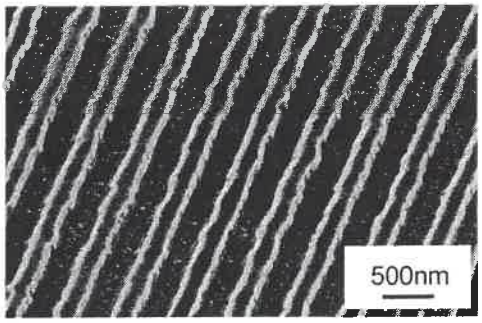

Figure 1: SEM images of the pressing results at the conditions of 3MPa at 380 degrees Celsius.

products, we produced guide-light plates with three different pitches of grooves using the above pressing process. In 12mm x 12mm areas on the mold surface, we cut three patterns of grooves; with width 170nm and pitch 340nm, width 200nm and pitch 400nm, and width 250nm and pitch 500nm. We then pressed them on glass substrates for one hour under the conditions of 3MPa and 380 degrees Celsius. From the back of these products, we injected white light at an angle of 60 degrees and measured the spectrum of the diffraction light that exits perpendicularly from the surface. Figure 3 and Figure 4 show the results. The graph has wavelengths in the horizontal axis and vertical axis is normalized a maximum value of 1.0 for the maximum light output from each grating. The figure shows that the spectrums peaked at 450, 526, and 651nm for pitches 340, 400, and 500nm. The output light wavelengths and grating pitches are related to each other in the following manner:

$$d=\lambda/n \sin\theta \qquad (1)$$

d: grating cycle λ: output light wavelength
n: diffraction index θ: input ray angle

Equation 1 gives the respective grating cycles of 344, 402, and 498nm from the measured output light wavelengths. The wavelengths, thus, only depends on the pitch and not on the grating cross-sectional shapes. Our results show that the pitches of the reproduced shapes were within a 1% tolerance of the designs.

DESIGNING THE PROCESS OF EMBEDDING METAL

The fine grooves made positioning difficult in locally embedding metal. We, therefore, first attached metal over the entire surface of the glass substrate with a film forming process and then later, removed the metal from the non-groove area. Figure 5 shows the concept of the process. For our study we used gold with high conductivity and resistance to oxidization, and adopted the sputtering process that produces a film with good adhesion. The removal process was dry etching FAB that is free of metal peeling and does not require cleaning. Sputtering followed by FAB does not flatten the glass surface, so we spin-coated resin with a FAB etching rate similar to that of gold after the sputtering process. Our preliminary tests showed an approximately 1:1 etching rate of gold and resin with FAB reaction gas SF6, and

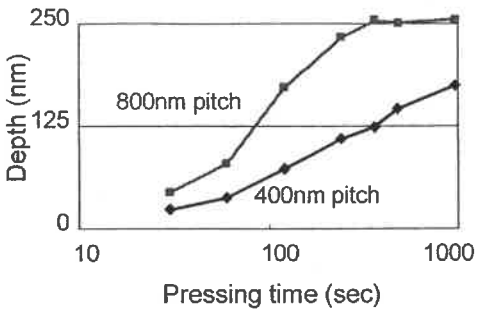

Figure 2: Measurement result of the relation between the pressing time and the micro-groove filling.

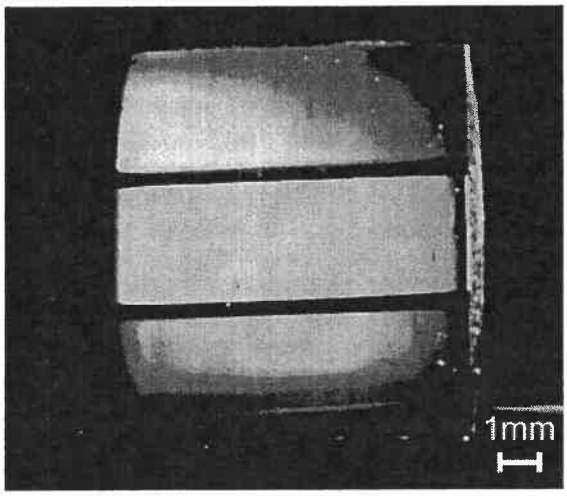

Figure 3: Glass substrate with reproduced micro grooves with pitch 340, 400 and 500nm.

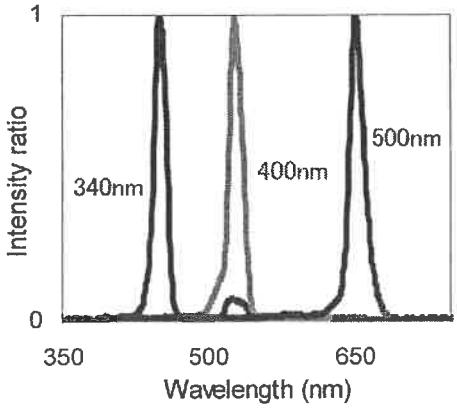

Figure 4: Spectrum of the diffraction light that exits perpendicularly from the surface of the pressed glass substrate.

we settled on using a positive type electron beam resist (ZEP-520, ZEON Corporation).
We applied the above processes to produce metal embedded gratings. With the target use of our gratings for polarization plates in mind, we ran numerical analyses of Finite Difference Time Domain Method (FDTD). Figure 6 shows the simulation results. Gratings without metal embedding passed most of both TE polarized (polarization with the electrical field vibration parallel to the gratings) and TM polarized (polarization with the electrical field vibration perpendicular to the gratings) lights. Metal embedded gratings, on the other hand, passed TE polarized light but reflected over half the TM polarized light. The degree of polarization is the rate of the polarized component to the entire light, thus by setting the polarization intensity of TE polarization to I_{te}, and that of TM polarization to I_{tm}, we obtain;

$$P=(I_{te}-I_{tm})/(I_{te}+I_{tm}) \quad (2)$$

. Here we sized the gratings to maximize the amount of polarization to a grating cycle of 400nm, and height 150nm.
Figure 7 shows the SEM images of the metal embedded gratings we produced. The figure demonstrates that our processes embed metal only in the grooves.
To further evaluate the optical performance, we injected white light to the gratings to find the degree of polarization from the transmitted light spectrums. Figure 8 shows the test results and the values from numerical analysis. The experiment results in blue lines show that the degree of polarization maximized when the injection light wavelength was about 640nm. The green lines in the graph are the calculated results for the rectangular groove model, and the red lines those for the trapezoid model. The latter better matched the measured results, thus, the actual crosses sections were probably closer to trapezoids due to fabrication error.
Probable causes of this error are the pressing process failing to fill glass to the end of the grooves, and void and crystal grain generation

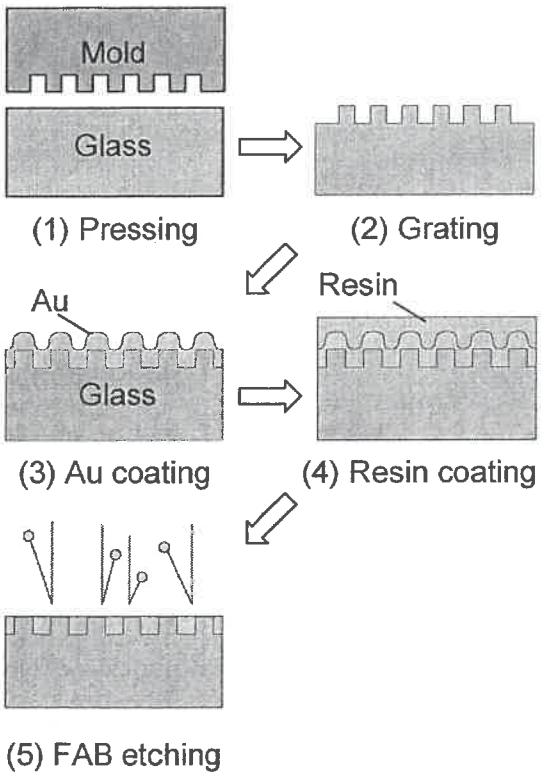

Figure 5: Concept of the process for embedding metal into the grooves.

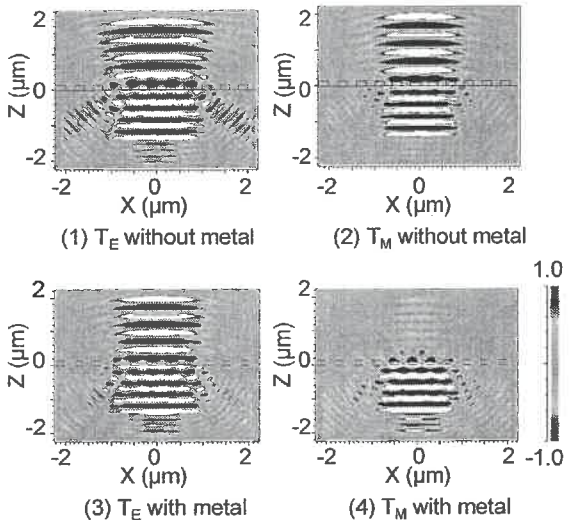

Figure 6: Simulation results of electromagnetic field around a metal-embedded polarizer.

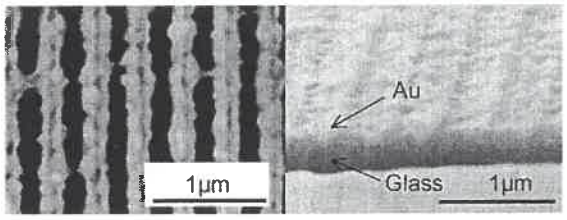

Figure 7: SEM images of the metal embedded gratings.

during the gold film forming with sputtering. Pressing the glass deeper into the mold would cause poor releasability of the product after its solidification, and we have to optimize the pressing conditions while keeping good releasability. The second problem will improve with better film forming conditions and different metal material. These results tell us that the cross section of gratings largely affect the degree of polarization. Optimizing the cross-sectional shape, therefore, can produce larger degrees of polarization.

CONCLUSIONS

Through our studies, we developed processes to reproduce micro-features to large areas and to embed metal to the grooves.

We designed and produced a mold for glass pressing. The mold was 12 x 12mm and had micro-grooves with a minimum width of 170nm and a minimum pitch of 340nm. The mold was made of bulk CVD-SiC and Fast Atom Beam (FAB) produced the micro-features. We determined the optimum press parameters for glass pressing with our mold, and we showed that the filling rate of pressing is approximately linear to the logarithm of time.

We also developed processes to produce metal embedded subwavelength gratings by sputtering a metal film on a glass substrate with micro-features, spin-coating resin to flatten the surface, and dry etching it with FAB.

We further evaluated the polarization device and found it had 0.9 degree of polarization to a light of wavelength 650nm. We confirmed the results by comparing the measured results with numerical analysis. For further enhancing the optical performance of the device, we need to optimize the grating cross-sectional shape and improve the precision of reproduction.

REFERENCES

1. M. L. M. Balistreri, J. P. Korterik, L. Kuipers, N. F. van Hulst, 2000, Photon scanning tunneling optical microscopy with a three-dimensional multiheight imaging mode, *Appl. Phys. Lett.*, 77(25): 4092-4094.
2. Bernd Schnabel, Ernst-Bernhard Kley, Frank Wyrowsky, 1999, Study on polarizing visible light by subwavelength-period metal-stripe gratings, *Opt. Eng.* 38(2): 220-226.

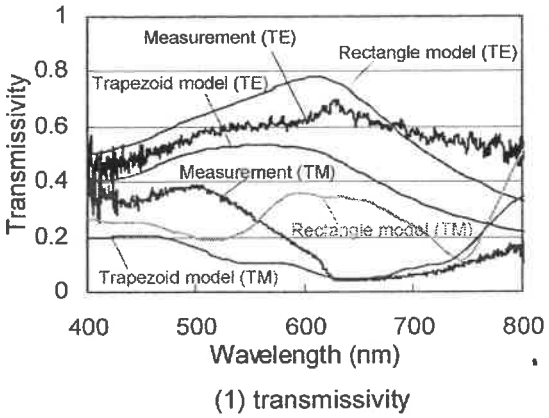

(1) transmissivity

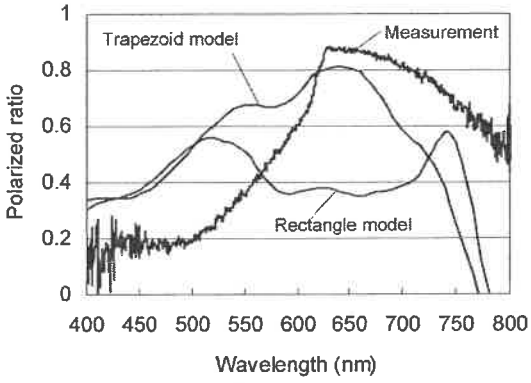

(2) Polarized ratio

Figure 8: Experimental result and the simulation results of intensity and polarized ratio of the polarized light from the metal embedded gratings.

CROSS CALIBRATION FOR PRIMARY ANGLE STANDARDS BY A PRECISION GONIOMETER WITH A SMALL ANGLE INTERFEROMETER

Huay-Chung Liou, Chih-Min Lin, Chao-Jung Chen, and Liang-Chih Chang
Center for Measurement Standards,
Industrial Technology Research Institute
Hsinchu, Taiwan, R.O.C.

INTRODUCTION

The traceability of angle standards like polygons, autocollimators and indexing tables can be accomplished by the circle closure principle or a primary artificial angular standard. The measuring system of primary standards with best positioning precision can be used to reduce the uncertainty for the calibration of polygons. Center for Measurement Standards (CMS) has built a primary standard by cross calibration method which combines a goniometer and a small angle interferometer, as shown in Fig. 1.

The goniometer was a high precision rotary air-bearing stage which was custom-made by Aerotech Company and provided a superior angular positioning performance. A Heidenhain RON905 incremental encoder was mounted on the shaft of the goniometer with positioning resolution of 0.035 arc second and positioning accuracy of 0.2 arc second. CMS designed and manufactured a sine bar mechanism upon the table of the goniometer. Two retro-reflectors were mounted on the each side of the rotation bar. A laser interferometer measured the relative displacement of those retro-reflectors. The length of the rotation bar was 400 mm, and the resolution of the laser interferometer was 10 nm. It could achieve an angular resolution of 0.035 arc second. The mechanism of the small angle interferometer was made of super Invar to reduce the deviation by temperature drift. All of the primary standard measuring system was supported by passive pneumatic isolators and covered in a black box to avoid the influences of temperature, airflow or light disturbance. It could get the best performance of the primary standard measuring system with minimum disturbance to reduce the measurement uncertainty.

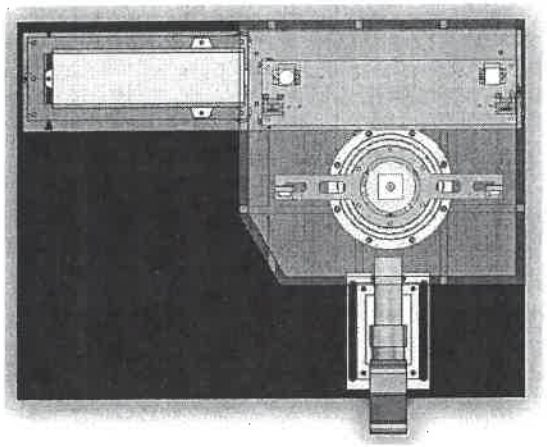

FIGURE 1. Assembly diagram of the goniometer and the small angle interferometer system

CROSS CALIBRATION METHOD

The schematic diagram of the cross calibration system is shown in Fig. 2. The n-sided polygon to be calibrated is fixed at the center of the goniometer which is also to be calibrated.

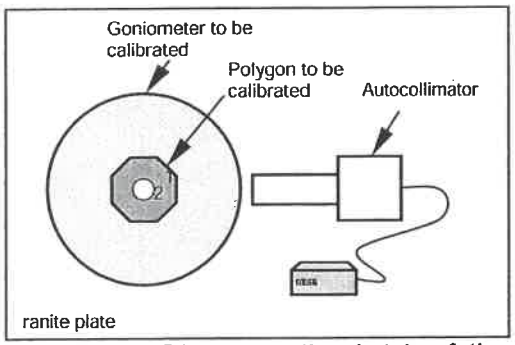

FIGURE 2. Diagrammatic sketch of the cross calibration system of the polygon and the goniometer.

Fig. 3 shows the measurement principle of the two adjacent faces from the polygon. In position 1, the face 1 of the polygon is located on the zero point of the goniometer and then aligned in order to bring it near the null of the autocollimator. At this moment, the readings of

the goniometer and the autocollimator are and , respectively. After rotating the goniometer with a nominal angle of the polygon and aligned the face 2 of the polygon near the null of the autocollimator, the readings of the goniometer and the autocollimator are and , respectively in position 2. The mathematical model could be represented by the following equation:

$$\begin{aligned} &\alpha_2 - \alpha_1 - \gamma - A_{1,2} = \beta_2 - \beta_1 - B_{1,2} \\ &B_{1,2} - A_{1,2} = -(\alpha_2 - \alpha_1 - \gamma + \beta_1 - \beta_2) = \alpha_{1,1} \end{aligned} \quad (1)$$

where is the angular error between the face 1 and 2 of the polygon, is the angular error between the position 1 and 2 of the goniometer, and is the first measurement result of the face 1 of the polygon located on the zero point of goniometer. Then, rotating the goniometer with gradually until it brings the face 1 back to a position near the autocollimator null and repeats the measurement sequence. The complete set of measurement equations as following:

$$\begin{aligned} &B_{1,2} - A_{1,2} = \alpha_{1,1} \\ &B_{2,3} - A_{2,3} = \alpha_{1,2} \\ &\quad\vdots \\ &B_{n-1,n} - A_{n-1,n} = \alpha_{1,n-1} \\ &B_{n,1} - A_{n,1} = \alpha_{1,n} \end{aligned} \quad (2)$$

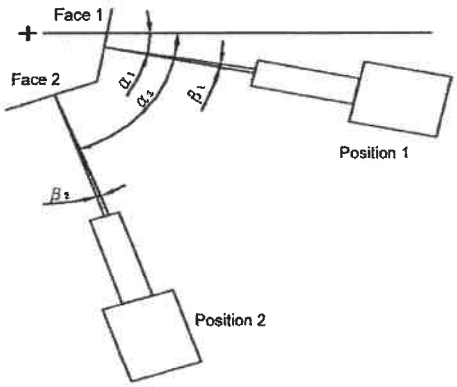

FIGURE 3. Measurement principle of two adjacent faces of the polygon.

Then, locating the face 2 of the polygon on the zero point of the goniometer and repeating the measurement mentioned above. We have linear equations:

$$\begin{aligned} &(B_{1,2} - A_{1,2}) = \alpha_{1,1} \\ &(B_{2,3} - A_{2,3}) = \alpha_{1,2} \\ &\quad\vdots \\ &(B_{n-1,1} - A_{n-3,n-2}) = \alpha_{n,n-1} \\ &(B_{n,1} - A_{n-2,n-1}) = \alpha_{n,n} \end{aligned} \quad (3)$$

There are two methods for analyzing the above equations. One is the direct summation method; another is the least square method [1].

On the basis of the direct summation method and the principle of circle closure:

$$\begin{aligned} &\sum_{i=1}^{n-1} A_{i,i+1} + A_{n,1} = 0 \\ &\sum_{i=1}^{n-1} B_{i,i+1} + B_{n,1} = 0 \end{aligned} \quad (4)$$

the deviations of the polygon and the goniometer can be separated directly, as shown in Tab. 1.

By dint of the least square method and the principle of circle closure, we combine the measurement relations, Eq. (3), with the two constraints, Eq. (4), and express the resultant set of linear equations in matrix form:

$$\begin{bmatrix} 1 & 0 & 0 & \cdots & 0 & 0 & -1 & 0 & 0 & \cdots & 0 & 0 \\ 0 & 1 & 0 & \cdots & 0 & 0 & 0 & -1 & 0 & \cdots & 0 & 0 \\ 0 & 0 & 1 & \cdots & 0 & 0 & 0 & 0 & -1 & \cdots & 0 & 0 \\ \vdots & \vdots & \vdots & \vdots & \vdots & \vdots & \vdots & \vdots & \vdots & \vdots & \vdots & \vdots \\ 0 & 0 & 0 & \cdots & 1 & 0 & 0 & 0 & 0 & \cdots & -1 & 0 \\ 0 & 0 & 0 & \cdots & 0 & 1 & 0 & 0 & 0 & \cdots & 0 & -1 \\ 1 & 0 & 0 & \cdots & 0 & 0 & 0 & -1 & 0 & \cdots & 0 & 0 \\ 0 & 1 & 0 & \cdots & 0 & 0 & 0 & 0 & -1 & \cdots & 0 & 0 \\ 0 & 0 & 1 & \cdots & 0 & 0 & 0 & 0 & 0 & \cdots & 0 & 0 \\ \vdots & \vdots & \vdots & \vdots & \vdots & \vdots & \vdots & \vdots & \vdots & \vdots & \vdots & \vdots \\ 0 & 0 & 0 & \cdots & 1 & 0 & 0 & 0 & 0 & \cdots & 0 & -1 \\ 0 & 0 & 0 & \cdots & 0 & 1 & -1 & 0 & 0 & \cdots & 0 & 0 \\ \vdots & \vdots & \vdots & \vdots & \vdots & \vdots & \vdots & \vdots & \vdots & \vdots & \vdots & \vdots \\ 1 & 0 & 0 & \cdots & 0 & 0 & 0 & 0 & 0 & \cdots & 0 & -1 \\ 0 & 1 & 0 & \cdots & 0 & 0 & -1 & 0 & 0 & \cdots & 0 & 0 \\ 0 & 0 & 1 & \cdots & 0 & 0 & 0 & -1 & 0 & \cdots & 0 & 0 \\ \vdots & \vdots & \vdots & \vdots & \vdots & \vdots & \vdots & \vdots & \vdots & \vdots & \vdots & \vdots \\ 0 & 0 & 0 & \cdots & 1 & 0 & 0 & 0 & 0 & \cdots & 0 & 0 \\ 0 & 0 & 0 & \cdots & 0 & 1 & 0 & 0 & 0 & \cdots & -1 & 0 \\ 1 & 1 & 1 & \cdots & 1 & 1 & 0 & 0 & 0 & \cdots & 0 & 0 \\ 0 & 0 & 0 & \cdots & 0 & 0 & 1 & 1 & 1 & \cdots & 1 & 1 \end{bmatrix} \begin{bmatrix} B_{1,2} \\ B_{2,3} \\ B_{3,4} \\ \vdots \\ B_{n-1,n} \\ B_{n,1} \\ A_{1,2} \\ A_{2,3} \\ A_{3,4} \\ \vdots \\ A_{n-1,n} \\ A_{n,1} \end{bmatrix} = \begin{bmatrix} \alpha_{1,1} \\ \alpha_{1,2} \\ \alpha_{1,3} \\ \vdots \\ \alpha_{1,n-1} \\ \alpha_{1,n} \\ \alpha_{2,1} \\ \alpha_{2,2} \\ \alpha_{2,3} \\ \vdots \\ \alpha_{2,n-1} \\ \alpha_{2,n} \\ \vdots \\ \alpha_{n,1} \\ \alpha_{n,2} \\ \alpha_{n,3} \\ \vdots \\ \alpha_{n,n-1} \\ \alpha_{n,n} \\ 0 \\ 0 \end{bmatrix} \quad (5)$$

or AX=Y, where A is an coefficient matrix, X is a column vector of the deviations of the goniometer and the polygon and Y is an vector. Hence, the least square solution is given by $X = (A^T A)^{-1} A^T Y$

TABLE 1. Data sheet of cross calibration of a polygon and a goniometer.

Angle spread of polygon / Angle spread of indexing table	0 ~ γ	γ ~ 2γ	⋯	(n - 2)γ ~ (n - 1)γ	(n - 1)γ ~ nγ	Accumulated value	Deviation of goniometer $B_{i,i+1}$
0 ~ γ	$B_{1,2} - A_{1,2}$	$B_{1,2} - A_{2,3}$	⋯	$B_{1,2} - A_{n-1,n}$	$B_{1,2} - A_{n,1}$	$nB_{1,2}$	$B_{1,2}$
γ ~ 2γ	$B_{2,3} - A_{1,2}$	$B_{2,3} - A_{2,3}$	⋯	$B_{2,3} - A_{n-1,n}$	$B_{2,3} - A_{n,1}$	$nB_{2,3}$	$B_{2,3}$
⋮	⋮	⋮	⋮	⋮	⋮	⋮	⋮
(n - 2)γ ~ (n - 1)γ	$B_{2,3} - A_{1,2}$	$B_{2,3} - A_{2,3}$	⋯	$B_{n-1,n} - A_{n-1,n}$	$B_{2,3} - A_{n,1}$	$nB_{n-1,n}$	$B_{2,3}$
(n - 1)γ ~ nγ	$B_{n,1} - A_{1,2}$	$B_{n,1} - A_{2,3}$	⋯	$B_{n,1} - A_{n-1,n}$	$B_{n,1} - A_{n,1}$	$nB_{n,1}$	$B_{n,1}$
Accumulated value	$-nA_{1,2}$	$-nA_{2,3}$	⋯	$-nA_{n-1,n}$	$-nA_{n,1}$	$\gamma = 360°/n$	
Deviation of polygon $A_{i,i+1}$	$A_{1,2}$	$A_{2,3}$	⋯	$A_{n-1,n}$	$A_{n,1}$	$\sum_{i=1}^{n-1} A_{i,i+1} + A_{n,1} = \sum_{i=1}^{n-1} B_{i,i+1} + B_{n,1} = 0$	

SMALL ANGLE INTERFEROMETER

The optical principle of the small angle interferometer system is shown in Fig. 4 as an illustration. The optical source starts from the laser head and the polarizing beam splitter divides the laser beam into two components. The split beams are reflected at two retro-reflectors mounted on the each side of the rotation bar and it recombined at the polarizing beam splitter. At the end, the interference signal is received at the detector. The rotating angle can be determined as the following relationship:

$$\sin(\theta) = \frac{d}{L} \Rightarrow \theta = \sin^{-1}(\frac{d}{L}) \qquad (6)$$

where d is the optical path difference between two retro-reflectors, and L is the length of rotation bar, this value can be obtained by a given standard angle and Eq. (6).

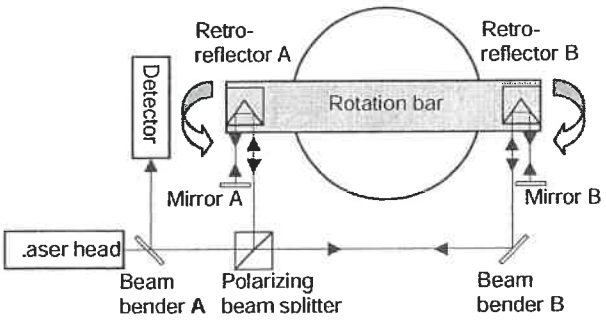

FIGURE 4. Design principle of the small angle interferometer system.

EXPERIMENTAL RESULTS

In order to calibrate an angle standard of the goniometer, it could be done by the cross calibration. A polygon and the goniometer were calibrated by an autocollimator simultaneously, and the deviations of the polygon and the goniometer could be obtained at the same time. We used the 18-sided and 24-sided polygons to perform the cross calibration operation. Fig. 5 shows the measurement deviations of the goniometer which was determined by the cross calibrations with the 18-sided and 24-sided polygons. The maximum deviations were 0.09 and 0.12 arc second with uncertainty of 0.04 and 0.06 arc second, respectively. Each value of Y-axis meant the deviation between the relative value of X-axis and its foregoing value. Fig. 5 shows both of the deviation curves were agreed with each other, and the maximum difference was 0.02 arc second.

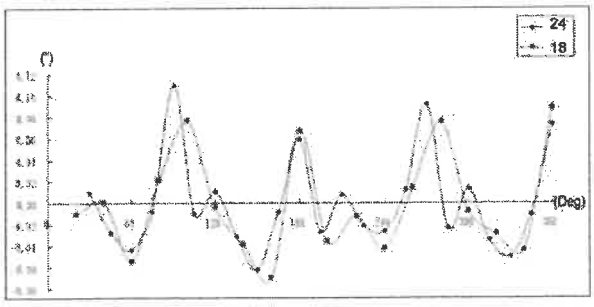

FIGURE 5. Deviation curves of the goniometer determined by the cross calibrations with the 18-sided and 24-sided polygons.

CONCLUSIONS

The measurement range of the small angle interferometer on the goniometer is less than 16 degree. From the cross-calibration results of the 24-sided polygon, we got the angle deviation of 15 degree angle position of the goniometer. A self-calibration is used to determine the bar length with this angle deviation. For the future work, we will evaluate the uncertainty for the small angle interferometer.

REFERENCES

1. Estler, W. T., 1998, Uncertainty Analysis for Angle Calibrations Using Circle Closure, Journal of the National Institute of Standards and Technology, 103(2): 141-151.

Authors Index

Adams, David Price 35, 403
Aketagawa, Masato 31, 427
Akilian, Mireille 439
Aoyama, Hisayuki 247
Arneson, David A. 195
Aso, Tasuku 301
Atkinson, Dennis P. 15
Bamberg, Eberhard 135, 239
Bardt, Jeffrey 283
Barraja, Mathieu 195
Bauza, Marcin B. 71
Bedillion, M. D. 127
Beltran, Michael J. 443
Brehl, David Edward 507, 511
Brouwer, Dannis M. 115, 275
Buice, Eric S. 175
Caballero-Ruiz, Alberto 199. 243
Callender, Matthew James 19
Canning, Jacqueline Suzanne 99
Castro, Carlos 207
Chan, C. K. 223
Chan, L. S. 223
Chandrasekar, S. 575
Chang, Andrew 27
Chang, L.-C. 615
Chau, W. C. 223
Chen, C.-J. 615
Chen, Shih-Chi 279, 283, 287
Chen, Yang 395
Cheng, Chi-Neng 191
Cheng, Chihung 131
Cheung, Chi-Fai 321
Chiba, Naoto 247
Chin, Do Hun 171
Choi, Heejin 279
Choi, Young-Man 183
Chon, Kwon Su 399
Chow, K. H. 223
Chow, W. Y. 223
Chu, David C. K. 67, 423
Chung, Sung-Chong 147, 255, 451, 455, 535
Chung, Carl 207
Chung, Siyon 147, 451, 535
Claudet, Andre A. 35, 333, 380, 403
Conklin, John William 341
Corbin, Brendan 135
Crawford, Thomas Mclendon 127
Culpepper, Martin L. 139, 279, 283, 287, 309, 313
Cuttino, James F. 87
de Boer, M. J. 275
de Jong, B. R. 115, 275
DeBra, Daniel B. 47, 59, 341
Demmer, Axel 395
Denkena, Berend 463
DeVries, Gary 435
Donaldson, Robert R. 207
Dow, Thomas A. 75, 507, 511
Duncan, G. Scott 131, 163
Dunn, Alison C 459
Efstathiou, Apostolos 19
Ellis, Jonathan David 345
Emig, Laura 135
Endo, Takashi 515
Endo, Toshiro 391
Enomoto, Toshiyuki 591
Eom, TaeBong 329
Evans, Christopher J. . . . . *
Fan, Xiaorui 487
Fang, Cheng-Yen 376
Filiz, Sinan 559
Fiske, Peter S. 27, 415
Fleig, Jon 435
Folkert, Karalyn F. 75
Forest, Craig Richard 443
Frank, Thomas 227
Fuchiwaki, Ohmi 247
Fujimaki, Kengo 349
Fujita, Toshinori 187
Fujita, Tsutomu 591
Fujiyama, Hirokazu 353
Fukuta, Masahiko 203
Furuhashi, Hideo 419
Furuya, Shogo 503
Fushiki, Atsuya 407
Gardopee, George 27, 415
Garrard, Kenneth P. 75, 91, 511
Gee, Anthony E. 19
Gill, David D. 35, 333, 403
Gleason Jr., Eugene A. 384
Gloess, Rainer 251
Golda, Dariusz 313
Goto, Akihiro 579
Gweon, Dae-Gab 183, 215
Hackel, Tobias 227
Haftka, Raphael T. 539
Haghighian, Behnoush 167
Hale, Layton C. 207
Hamaguchi, Tetsuya 107, 317, 611
Hamano, Toshiaki 259
Hardham, Corwin Thomas 59
Hashimoto, Takashi 579
Hatsuzawa, Takeshi 447

*Abstract unavailable at press time.

Hayashi, Terutake 291, 595
Heamawatanachai, Sumet 135
Heilmann, Ralf K. 51, 439
Heredia, Francisco 199
Higuchi, Masahiro 519
Higuchi, Sei 47
Hijikata, Yoshio 499
Hill, Martyn 372
Hiller, Bernhard 39
Hlavac, Marcus 467
Hocken, Robert J. 71, 175, 345
Hodges, V. Carter 35, 403
Hoffmeister, Hans-Werner. 467
Höhne, Günter. 227
Holt, Martin 123
Honda, Hiroshi. 31
Hoos, Axel 39
Hopkins, David J.. 207
Hopkins, Jonathan B. 139
Horiuchi, Osamu 211
Houck III, Lonnie 423, 523
Hughes, James D.. 15
Hung, C. Y.. 376
Hunter, Ian W. 443
Hwang, Jooho 365
Ikeda, Naoto 527
Ikeda, Shigeru 267
Inloes, Michael 43
Ishida, Tohru 543
Ishige, Masashi 31, 427
Ishikawa, Ken-ichi 491, 599
Itagaki, Kenji 531
Ito, Shuzo 267
Iwai, Manabu. 471, 531
Iwata, Futoshi 295
Jacobs, Stephen D.. 411
Jang, Min-Soo 255
Jansen, J. W.. 119
Jarausch, Konrad. . . . . *
Jee, Won-Ho 535
Jeong, Don Young 329
Jiang, Xiang-Qian 321
Johnson, Michael A.. 15
Joo, Byeong Gwon 337
Jordan, Scott. 287, 297
Jorgensen, J. Dean 239
Jung, Jin-seok 171, 551
Kagawa, Toshiharu 187
Kajihara, Yusuke 111
Kajiwara, Yusuke 563
Kamiya, Kazuhide 369
Kang, Dong-woo 215
Kang, Min Gu 337
Kang, Sung-hoon 215
Karodkar, Devendra D. 357
Kato, Shigeo 259, 263, 267
Kato, Takamichi 211
Kato, Tomonori 179
Kawashima, Kenji 179, 187
Kawashima, Takahiro 291
Kawasugi, Masaaki 427
Kibe, Yoshiyuki. 219
Kim, Chung Whan 571
Kim, Daekeun 279
Kim, Hyun-Ho 535
Kim, In 143
Kim, Jae Wan 329
Kim, Jeong Sik 337
Kim, Jong-Ahn 329
Kim, Jung-Jae 183
Kim, Ki-Hyun 183
Kim, Kyung-Don 147, 455
Kim, Seung-Chul 147, 255, 535
Kim, Seung-Woo 365
King, Christopher William 19
Klocke, Fritz. 395
Kobayashi, Masaaki 479
Kobayashi, Yoshikazu 527
Koelmans, W.. 127
Kolipaka, Janaki Prasad Santosh 431
Komiya, Atsuto 611
Kondo, Motoo 527
Kono, Akihiro 419
Kramer, Niklas J. 463
Kumanchik, Lee. 151
Kunieda, Hideyo 407
Kurdi, Mohammad H. 539
Kurihara, Ryo. 475
Kuriyama, Yutaka. 431
Kurz, Martin. 547
Kussul, Ernst 199
Kweon, Sung-Hwan. 143
Kwok, T. C.. 321
Lai, Barry. 123
Lambropoulos, John C. 411
Lamonds, Lucas 91
Lane, Ben 127
Langzettel, A. K. 127
Leach, Richard K. . . . . *
Lee, D. Chang-Woo 567
Lee, Hwa-Soo 479, 495
Lee, Jae-Ha. 155
Lee, K. S.. 223
Lee, Luke P.. 305
Lee, Wing-Bun. 321
Lewis, Andrew J. 19
Li, Huifen 321
Lin, C.-M.. 615
Liou, H.-C. 615
Lomonova, E. A. 119

*Abstract unavailable at press time.

Lotz, Markus 227
Lu, Xiaodong 63
Loychik, Neil 195
Lui, Kam-Wa 376
Ma, Hongshen 103
Ma, Li 387
Magara, Takuji 579
Makino, Eiji 291
Mansfield, Daniel I. 23
Mapoles, Evan R. 15
Marsh, Eric R. 167, 195, 361, 483
Maser, Jorg 123
Masuzawa, Toru 291
Matsuda, Kiyofumi 419
Matsuura, Fumio 427
Mauntler, Nathan A. 325, 459
McBride, John W. 372
Meyer, Piotr Jan 159
Miller, Michele H. 487
Min, Jin Young 215
Mineta, Takashi 291
Minowa, Yuzo 235
Misaki, Daigo 247
Mishima, Nozomu 231
Mitsui, Kimiyuki 219, 349, 515
Miyajima, Takashi 187
Miyamoto, Kensuke 503
Miyashita, Tsutomu 499
Miyoshi, Takashi 595
Mizoi, Tomohiro 235
Montesanti, Richard C. 15
Morgan, Christopher J. 305
Morii, Hiroshi 107, 317, 611
Morita, Hironori 495
Moriwaki, Toshimichi 499
Moriya, Takamasa 543
Moylan, Shawn P. 575
Mullany, Brigid A. 603
Munro, Logan 279
Muragishi, Takayuki 317
Murakami, Yoshihiko 531
Muralikrishnan, Bala 83
Murphy, Paul E. 435
Nagata, Tomohiko 607
Nakagawa, Kiyotaka 471
Nakamura, Masayoshi 353, 391, 475
Nakao, Masayuki 107, 317, 611
Nakao, Yohichi 235
Nakashima, Toshiro 579
Namba, Yoshiharu 399, 407
Neuschaefer-Rube, Ulrich 79
Niki, Takuya 607
Nishioka, Masahiko 203
Nomura, Takashi 369
Novotnak, Robert 127
O'Connor, Brian P. 127
O'Donohue, Stephen 435
Obata, Kazushi 519
Oberschmidt, Dirk 547
Ogasaka, Yasushi 407
Ogiso, Taro 187
Oh, Myungsuk 551
Okai, Reynolds 555
Okino, Tadashi 499
Okuno, Masaki 301
Oldfield, Simon 19
Oliver, Andrew D. 380
Ono, Manabu 259, 263, 267
Ooi, Takeshi 107, 317, 611
Orchard, Nick B. 55
Orino, Chris 239
Otsuka, Shingo 607
Otten, David 175
Overcash, Jerald Lee 87
Ozdoganlar, Burak O. 559
Pan, Weili 531
Park, Chun Hong 365
Park, Gwi Yun 571
Patamaporn, Chaikool 31
Pongs, Guido 395
Powell, K. B. 163
Preissner, Curt 123
Radler, Oliver 271
Rajurkar, Kamlakar P. 583
Rakwal, Dinesh R. 239
Reynolds, Jack L. 15
Rhorer, Richard L. 95
Roblee, Jeffrey W. 499
Ruiz-Huerta, Leopoldo 199, 243
Sakai, Yozo 579
Sakamoto, Ryushiro 503
Sakamoto, Shigehiko 563
Salsbury, James G. 43
Sano, Sadao 471, 531
Sasaki, Akira 295
Sawyer, W. Gregor 163, 459
Schattenburg, Mark L. 51, 439
Schmitz, Tony L. 99, 131, 151, 163, 325, 423, 459, 523, 539
Schwenke, Heinrich I. 79
Seugling, Richard M. 175
Shafrir, Shai N. 411
Shibata, Takayuki 211, 291
Shih, Ming Chang 191
Shilling, K. Meghan 380
Shimada, Shoichi 519
Shinmura, Takeo 587
Shinozaki, Akira 563
Shirai, Kenji 527
Shu, Deming 123

Sim, Sung Bo 551, 571
Slocum, Alexander H. 103
Smith, K. Scott 523
Smith, Stuart T. 71, 175, 345
Snyder, James J. 431
So, Peter 279
Soemers, Herman M. J. R. 115, 275
Sohn, Alex 91, 511
Song, Chang Kyu 337
Song, In-Ho 451, 455
Song, Jun-Feng John 387
Song, Jun-Yeob 567
Southwell, Larinn M. 333
Steel, Robert 19
Stephenson, Gregory B. 123
Stone Jr., Jack A. 83
Stoup, John R. 83
Ströhla, Tom 271
Subrahmanyan, Pradeep K. 27, 415
Suh, Ho Suhng 329
Sumomogi, Tsunetaka 353, 391, 475
Sun, Ke-Xun 59, 341
Sun, Wenjuan 372
Sundaram, Murali M. 583
Sung, Cheng-Kuo 376
Suwabe, Hitoshi 491, 599
Suzuki, Hideaki 611
Suzuki, Hirofumi 203, 499
Suzuki, Keisuke 595
Suzuki, Kiyoshi 471, 531
Suzuki, Makoto 591
Suzuki, Takachika 263
Swank, Aaron J. 59
Sweatt, William C. 35, 403
Takahashi, Satoru 111, 301
Takamasu, Kiyoshi 111, 301
Takaya, Yasuhiro 595
Takeuchi, Toru 111
Takeuchi, Yoshimi 543
Tanada, Hiroki 595
Tanaka, Katsutoshi 471
Tanaka, Miyuki 267
Taneda, Atsushi 579
Tashiro, Hatsuzo 369
Tawara, Yuzuru 407
Teramoto, Koji 543
Theska, René 227
To, Suet Sandy 321
Tominaga, Shigeru 591
Toyama, Akira 563
Tran, Hy D. 380
Trinkle, Christine Anne 305
Tröbs, Anita 227
Trujillo, Haydee 67
Trumper, David L. 51, 63, 175
Tsai, Ming-Hung 191
Tsuchiya, Kensuke 107, 317, 611
Tsuijimoto, Takayuki 515
Tsukada, Hiromasa 491, 599
Uchida, Yoshiyuki 419
Uematsu, Tetsutaro 471, 531
Uhlmann, Eckart 547
Uneda, Michio 491, 599
Ushiro, Yuki 295
Usuda, Takashi 247
Vallance, R. Ryan 167, 195, 361, 483
van de Veerdonk, R. J. M. 127
van Eijk, Jan 159
van Lierop, C. M. M. 119
Vandenput, Andre J. A. 119
Varadarajan, Kartik 309
Vasile, Michael J. 35, 403
Verma, Yogesh 415
Vogt, Stefan 123
Volkert, Ralf 271
Vorburger, Theodore V. 387
Walker, David 19
Wang, Mei 471, 531
Whiteside, Dean 55
Whitney, Evan 67
Williams, Wesley B. 603
Winarski, Robert 123
Wissmann, Mark Andre 79
Won, Dongki 163
Woody, Shane C. 71
Yamada, Takazo 479, 495
Yamaguchi, Kanta 607
Yamaguchi, Tomomi 519
Yamaguchi, Yoshiyuki 211
Yamamoto, Yuji 499
Yamamoto, Yuki 503
Yamashita, Koujun 407
Yanagida, Yasuko 447
Yang, Hua 175
Yang, Seung-Han 143, 155
Yasui, Heiji 503, 563, 607
Yazawa, Takanori 369
Yi, Allen Y. 395
Yoon, Gwon Ha 215
Yoon, Kwon Ha 399
Yoon, Moon-Chul 171, 551
Yoshida, Masashi 391, 475
Young, Jeff 67
Zapata, Raul Enrique 99
Zhao, Yong 51
Ziegert, John C. 99, 163, 283, 325
Zimmermann, Klaus 227
Zirn, Oliver 39
Zöppig, Veit 271
Zou, Yanhua 587

wavelength of the beam or less for polarized light measurement. We thus, applied FIB to open three 1.5μm x 0.2μm slits apart by a pitch of 0.4μm on the cantilever tip. Figure 5 shows the SEM photograph. The slit lengths were set so the open area approximately equals that of the circular aperture.

We used the above cantilever to verify that it could measure specific polarized lights when differently polarized lights coexisted. The specimens were made similarly to the previous section by sputtering metal on glass and removing part of the metal. The input beam was a laser from underneath. Figure 6-(1) shows the specimen with five 0.22μm x 2.5μm slits apart by a pitch of 0.53μm. We prepared 4 sets of such slit arrangement that were rotated by 90 degrees. Each slit on the specimen passes the input beam component with its direction of electrical field vibration perpendicular to the slit. Injecting a beam with its direction of electrical field vibration at a 45 degree angle with the slits would produce an outgoing beam with an electromagnetic field with polarized lights that are 90 degrees apart.

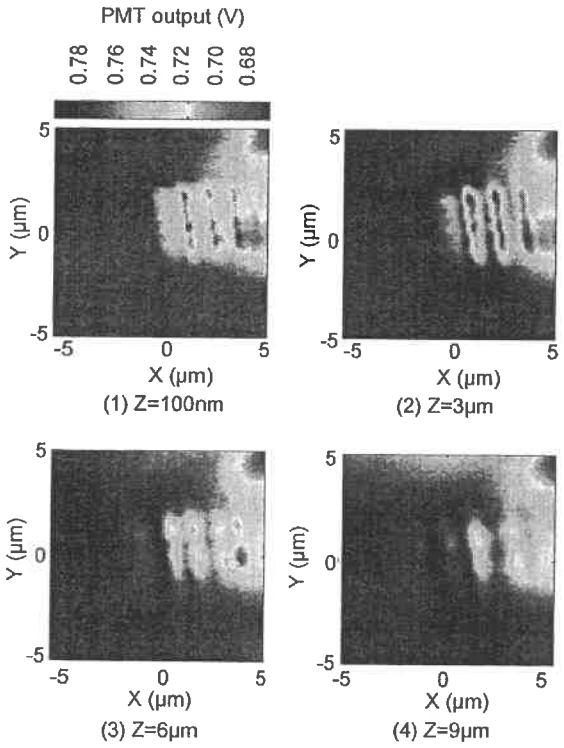

Figure 3: Measurement results of the electromagnetic field intensity distribution above a specimen.

We measured a 10μm x 10μm area above the specimen that covered the specimen slit area by reciprocate scanning of 100 lines at a speed of 1μm/sec. Using cantilevers with a circular aperture and slit apertures, we measured, with the method described in Section 2, the specimen surface configuration and the distribution of the electromagnetic field intensity in the area above the specimen.

Figure 6-(2)(3)(4) show the results. The cantilever with a circular aperture detected the beam output from all the slits. The cantilever with slit apertures, on the other hand, detected beam output only when the slits of the cantilever and those of the specimen were parallel. These results demonstrate that the cantilever with slit micro-apertures can measure the electromagnetic field intensities for specific

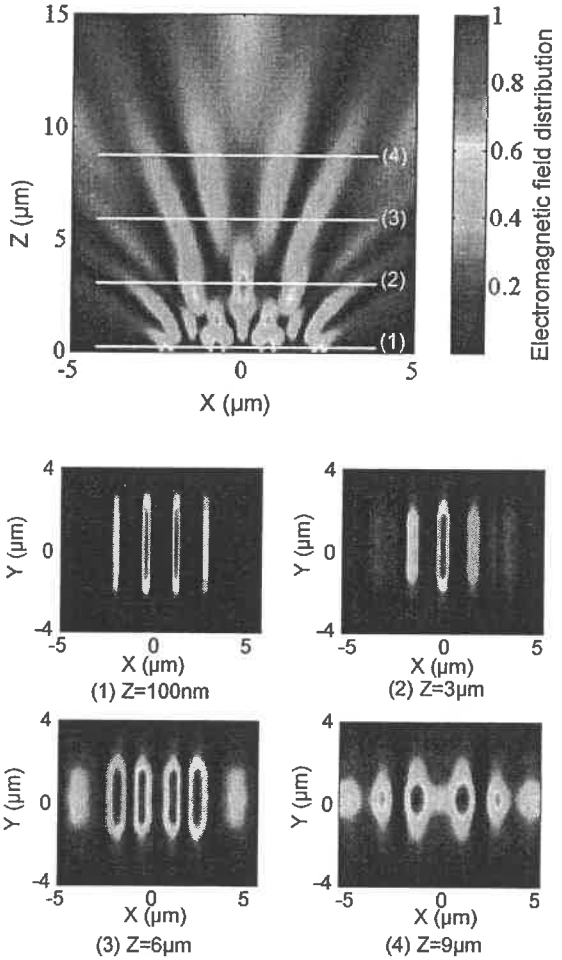

Figure 4: Simulation results of the electromagnetic field intensity distribution above a specimen with the similar conditions except with 3 slits.

polarized components. The slit apertures, however, failed to identify the optical interference like in the results of the previous section. This was due to the large apertures with sizes 1 to 2μm that caused lack of resolution.
To enhance the resolution, we need to reduce the aperture size, however, when they are made smaller than the beam wavelengths, the beams that pass the aperture turn into near-field beams and cannot reach the PMT. We need to develop mechanisms to convert a near-field beam into a diffusion beam by placing scatterer material like silver or carbon inside the apertures. The efficiency of conversion into a diffusion beam partially depends on the aperture shape. Since FIB allows freely aperture arbitrary shapes for the apertures, we can minimize the decay of light by sizing and forming adequate apertures depending on the wavelengths of the beams to detect.

CONCLUSIONS

This study developed a system to measure the surface configuration of optical devices and spatially measure the electromagnetic field intensity and polarized light in the near field. Micro-apertures at the tip of the cantilever beam on AFM allowed simultaneously measuring the device shape configuration and the electromagnetic field intensity. We also showed that slit shaped micro-apertures can measure the electromagnetic field intensity for specific polarized light components.

REFERENCES

1. M. L. M. Balistreri, J. P. Korterik, L. Kuipers, N. F. van Hulst, 2000, Photon scanning tunneling optical microscopy with a three-dimensional multiheight imaging mode, *Appl. Phys. Lett.*, 77(25): 4092-4094.
2. C. Peeters, E. Fluck, A. M. Otter, M. L. M. Balistreri, J. P. Korterik, L. Kuipers, 2000, Photon scanning tunneling microscopy of tailor-made photonic structures, *Appl. Phys. Lett.*, 77: 142-144.
3. E. Fluck, N. F. van Hulst, W. L. Vos, L.Kuipers, 2003, Near-field optical investigation of three-dimensional photonic crystals, *Physical Review E*, 68: 015601.
4. A. Nesci, R. Dandliker, M. Salt, H. P. Herzig, 2002, Measuring amplitude and phase distribution of fields generated by gratings with sub-wavelength resolution, *Optics Comunication*, 205: 229-238.
5. Th. Dziomba, Th. Sulzbach, O. Ohlsson, Cj. Lehrer, L.Frey, H. U. Danzebrink, 1999, Ion beam-treated silicon probes operated in transmission and cross-polarized reflection mode near-ingrated scanning near-field optical microscopy, *Surface And Interface Analysis*, 27: 486-490.
6. Quidant, J.-C. Weeber, A. Dereux, G. Leveque, J. Weiner, C. Girard, 2004, Addressing and imaging microring resonators with optical evanescent light, *Physical Review B*, 69: 081402.

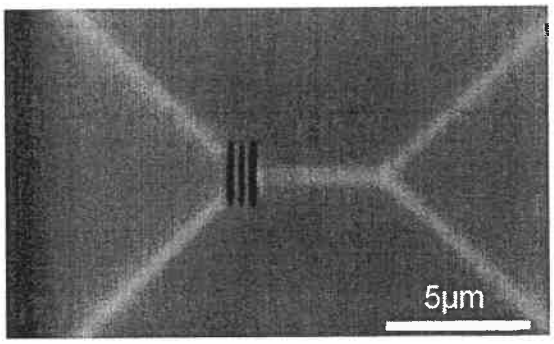

Figure 5: SEM images of the cantilever with slit shaped micro-apertures, which allows measuring the electromagnetic field intensity for specific polarized light components.

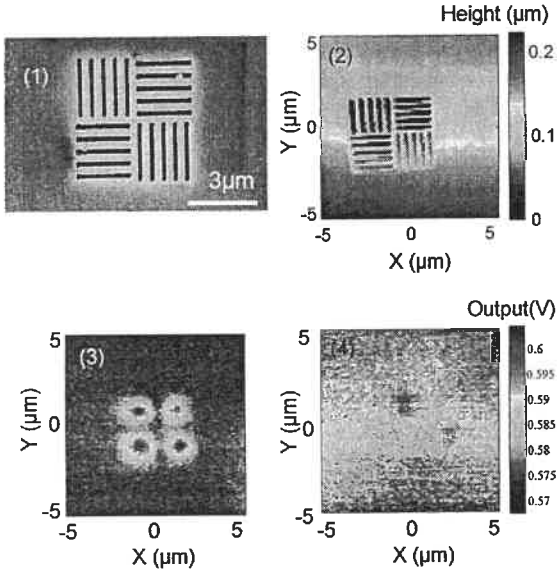

Figure 6: (1) SEM images of the specimen with five 0.22μm x 2.5μm slits apart by a pitch of 0.53μm, and measurement (2) AFM image, (3) optical image measured using cantilevers with a circular aperture, (4) optical image measured using cantilevers with slit apertures.